BIOSIGNALS 2008

International Conference on
Bio-inspired Systems and Signal Processing

Proceedings

Volume 2

Funchal, Madeira - Portugal · 28 - 31 January, 2008

TECHNICAL CO-SPONSORSHIP BY

IEEE EMB SIGART

CO-ORGANIZED BY

INSTICC UNIVERSIDADE da MADEIRA

IN COOPERATION WITH

aaai

INSTICC PRESS

BIOSIGNALS 2008

Proceedings of the
First International Conference on
Bio-inspired Systems and Signal Processing

Volume 2

Funchal, Madeira - Portugal

January 28 – 31, 2008

Co-organized by
INSTICC – Institute for Systems and Technologies of Information, Control and Communication
and
UMA – University of Madeira

Technical Co-sponsorship by
IEEE EMB – Engineering in Medicine and Biology Society
and
ACM SIGART- Special Interest Group on Artificial Intelligence

In Cooperation with
AAAI – Association for the Advancement of Artificial Intelligence

Edited by Pedro Encarnação and António Veloso

Printed in Portugal

ISBN: 978-989-8111-18-0

Depósito Legal: 268555/07

http://www.biosignals.org

secretariat@biosignals.org

BIOSIGNALS is part of BIOSTEC – International Joint Conference on Biomedical Engineering Systems and Technologies

BRIEF CONTENTS

INVITED SPEAKERS

Sérgio Cerutti

Polytechnic University of Milan

Italy

Kevin Warwick

University of Reading

U.K.

Fernando Henrique Lopes da Silva

University of Amsterdam

The Netherlands

Vipul Kashyap

Partners HealthCare System, Clinical Informatics R&D

U.S.A.

David Hall

Research Triangle Institute in North Carolina

U.S.A.

Albert Cook

University of Alberta, Faculty of Rehabilitation Medicine

Canada

ORGANIZING AND STEERING COMMITTEES

CONFERENCE CO-CHAIRS

Ana Fred, IST- Technical University of Lisbon, Portugal

Joaquim Filipe, INSTICC / Polytechnic Institute of Setúbal, Portugal

Hugo Gamboa, Telecommunications Institute, Portugal

Jorge Cardoso, University of Madeira - UMA / Madeira, Portugal

PROGRAM CO-CHAIRS

Pedro Encarnação, Catholic Portuguese University, Portugal

António Veloso, FMH, Universidade Técnica de Lisboa, Portugal

LOCAL CHAIR

Paulo Sampaio, University of Madeira - UMA, Portugal

PROCEEDINGS PRODUCTION

Paulo Brito, INSTICC, Portugal

Marina Carvalho, INSTICC, Portugal

Helder Coelhas, INSTICC, Portugal

Vera Coelho, INSTICC, Portugal

Andreia Costa, INSTICC, Portugal

Bruno Encarnação, INSTICC, Portugal

Bárbara Lima, INSTICC, Portugal

Vitor Pedrosa, INSTICC, Portugal

Vera Rosário, INSTICC, Portugal

Mónica Saramago, INSTICC, Portugal

CD-ROM PRODUCTION

Paulo Brito, INSTICC, Portugal

GRAPHICS PRODUCTION AND WEB DESIGNER

Marina Carvalho, INSTICC, Portugal

SECRETARIAT AND WEBMASTER

Marina Carvalho, INSTICC, Portugal

PROGRAM COMMITTEE

Andrew Adamatzky, University of the West of England, Bristol, U.K.

Cedric Archambeau, University College London, U.K.

Magdy Bayoumi, University of Louisiana, U.S.A.

Peter Bentley, University College London, U.K.

Paolo Bonato, Harvard Medical School, U.S.A.

Marleen de Bruijne, University of Copenhagen, Denmark

Zehra Cataltepe, Istanbul Technical University, Turkey

Gert Cauwenberghs, University of California San Diego, U.S.A.

Mujdat Cetin, Sabanci University, Turkey

Wael El-Deredy, University of Manchester, U.K.

Eran Edirisinghe, Loughborough University, U.K.

Eugene Fink, Carnegie Mellon University, U.S.A.

Luc Florack, Eindhoven University of Technology, the Netherlands

David Fogel, Natural Selection, Inc., U.S.A.

Alejandro Frangi, Universitat Pompeu Fabra, Spain

Sebastià Galmés, Universitat de les Illes Balears, Spain

Aaron Golden, National University of Ireland, Galway, Ireland

Rodrigo Guido, University of São Paulo, Brazil

Bin He, University of Minnesota, U.S.A.

Roman Hovorka, University of Cambridge, U.K.

Helmut Hutten, Graz University of Technology, Austria

Christopher James, University of Southampton, U.K.

Lars Kaderali, University of Heidelberg, Germany

Gunnar W. Klau, Free University Berlin, Germany

Alex Kochetov, Institute of Cytology and Genetics, Russian Federation

T. Laszlo Koczy, Budapest University of Technology and Economics, Hungary

Georgios Kontaxakis, Universidad Politécnica de Madrid, Spain

Igor Kotenko, St. Petersburg Institute for Informatics and Automation, Russian Federation

Narayanan Krishnamurthi, Arizona State University, U.S.A.

Arjan Kuijper, RICAM, Austria

Andrew Laine, Columbia University, U.S.A.

Anna T. Lawniczak, University of Guelph, Canada

Jason JS Lee, National Yang-Ming University, Taiwan, Province of China

Kenji Leibnitz, Osaka University, Japan

Marco Loog, University of Copenhagen, Denmark

David Lowe, Aston University, U.K.

Mahdi Mahfouf, The University of Sheffield, U.K.

Luigi Mancini, Universita di Roma La Sapienza, Italy

Elena Marchiori, VUA, the Netherlands

Fabio Martinelli, IIT-CNR, Italy

Martin Middendorf, University of Leipzig, Germany

Mariofanna Milanova, University of Arkansas at Little Rock, U.S.A.

Charles Mistretta, University of Wisconsin, U.S.A.

Gabor Mocz, University of Hawaii, U.S.A.

Kayvan Najarian, University of North Carolina at Charlotte, U.S.A.

Tadashi Nakano, University of California, Irvine, U.S.A.

Asoke K. Nandi, The University of Liverpool, U.K.

Antti Niemistö, Institute for Systems Biology, U.S.A.

Maciej J. Ogorzalek, Jagiellonian University, Poland

Kazuhiro Oiwa, National Institute of Information and Communications Technology, Japan

Jean-Chistophe Olivo-Marin, Institut Pasteur, France

Ernesto Pereda, University of La Laguna, Spain

Leif Peterson, The Methodist Hospital, U.S.A.

Gert Pfurtscheller, Graz University of Technology, Austria

Vitor Fernão Pires, ESTSetubal / IPS, Portugal

Chi-Sang Poon, MIT, U.S.A.

José Principe, University of Florida, U.S.A.

PROGRAM COMMITTEE (CONT.)

Chi-Sang Poon, MIT, U.S.A.

Jose Principe, University of Florida, U.S.A.

Nikolaus Rajewsky, Max Delbruck Center for Molecular Medicine, Germany

Dick de Ridder, Delft University of Technology, the Netherlands

Joel Rodrigues, Institue of Telecommunications / University of Beira Interior, Portugal

Marcos Rodrigues, Sheffield Hallam University, U.K.

Virginie Ruiz, University of Reading, U.K.

Heather Ruskin, Dublin City University, Ireland

William Zev Rymer, RIC/Northwestern University, U.S.A.

Gerald Schaefer, Aston University, U.K.

Dragutin Sevic, Institute of Physics, Belgrade, Serbia

Iryna Skrypnyk, University of Jyvaskyla, Finland

Alan A. Stocker, New York University, U.S.A.

Jun Suzuki, University of Massachusetts, Boston, U.S.A.

Andrzej Swierniak, Silesian University of Technology, Poland

Boleslaw Szymanski, RPI, U.S.A.

Asser Tantawi, IBM, U.S.A.

Lionel Tarassenko, University of Oxford, U.K.

Gianluca Tempesti, University of York, U.K.

Anna Tonazzini, Consiglio Nazionale delle Ricerche - CNR, Italy

Duygu Tosun, Laboratory of Neuro Imaging, U.S.A.

Bart Vanrumste, Katholieke Hogeschool Kempen, Belgium

Didier Wolf, CRAN CNRS UMR 7039, France

Andrew Wood, Swinburne University of Technology, Australia

Guang-Zhong Yang, Imperial College London, U.K.

Eckart Zitzler, ETH Zurich, Switzerland

AUXILIARY REVIEWERS

Qi Duan, Columbia University, U.S.A.

Soo-Yeon Ji, Virginia Commonwealth University, U.S.A.

Yuri Orlov, Genome Institute of Singapore, Singapore

Ting Song, Columbia University, U.S.A.

Bruno N. Di Stefano, Nuptek Systems Ltd., Canada

SELECTED PAPERS BOOK

A number of selected papers presented at BIOSIGNALS 2008 will be published by Springer, in a book entitled Biomedical Engineering Systems and Technologies. This selection will be done by the conference co-chairs and program co-chairs, among the papers actually presented at the conference, based on a rigorous review by the BIOSTEC 2008 program committee members.

OFFICIAL CARRIER

FOREWORD

This volume contains the proceedings of the *First International Conference on Bio-inspired Systems and Signal Processing* (BIOSIGNALS 2008), organized by the Institute for Systems and Technologies of Information Control and Communication (INSTICC) and the University of Madeira, technically co-sponsored by the IEEE Engineering in Medicine and Biology Society (EMB) and in cooperation with AAAI.

The purpose of the *International Conference on Bio-inspired Systems and Signal Processing* is to bring together researchers and practitioners from multiple areas of knowledge, including biology, medicine, engineering and other physical sciences, interested in studying and using models and techniques inspired from or applied to biological systems. A diversity of signal types can be found in this area, including image, audio and other biological sources of information. The analysis and use of these signals is a multidisciplinary area including signal processing, pattern recognition and computational intelligence techniques, amongst others.

BIOSIGNALS is one of three integrated conferences that are co-located and constitute the International Joint Conference on Biomedical Engineering Systems and Technologies (BIOSTEC). The other two component conferences are HEALTHINF (International Conference on Health Informatics) and BIODEVICES (International Conference on Biomedical Electronics and Devices).

The joint conference, BIOSTEC, has received 494 paper submissions from more than 40 countries in all continents. 65 papers were published and presented as full papers, i.e. completed work (8 pages/30' oral presentation), 189 papers reflecting work-in-progress or position papers were accepted for short presentation, and another 86 contributions were accepted for poster presentation. These numbers, leading to a "full-paper" acceptance ratio below 14% and a total oral paper presentations acceptance ratio below 52%, show the intention of preserving a high quality forum for the next editions of this conference.

The conference included a panel and six invited talks delivered by internationally distinguished speakers, namely: Sergio Cerutti, Kevin Warwick, F. H. Lopes da Silva, Vipul Kashyap, David Hall and Albert Cook. Their participation has positively contributed to reinforce the overall quality of the Conference and to provide a deeper understanding of the field of Biomedical Engineering Systems and Technologies.

The proceedings of the conference will be indexed by several major indices including DBLP, INSPEC and ISI-Proceedings and it will also be submitted for indexing to EI. A book with the revised versions of a short list of selected papers from the conference will be published by Springer-Verlag in the new CS book series: Communications in Computer and Information Science (CCIS). Additionally, a special issue of the IEEE Transactions on Biomedical Circuits and Systems will be edited based on the very best papers of the conference.

FOREWORD (CONT.)

The program for this conference required the dedicated effort of many people. Firstly, we must thank the authors, whose research and development efforts are recorded here. Secondly, we thank the members of the program committee and the additional reviewers for their diligence and expert reviewing. Thirdly, we thank the keynote speakers for their invaluable contribution and for taking the time to synthesise and prepare their talks. Fourthly, we thank the program chairs, Pedro Encarnação and António Veloso, whose collaboration was much appreciated. Finally, special thanks to all the members of the INSTICC team, especially Marina Carvalho at the conference secretariat, and the local organising committee from the University of Madeira, especially Jorge Cardoso and Paulo Sampaio, whose collaboration was fundamental for the success of this conference.

This year, the organization will distribute two paper awards at the conference closing session: the best paper award and the best student paper award. The decision was mainly based on the paper classifications provided by the Program Committee.

We wish you all an exciting conference and an unforgettable stay in the lovely island of Madeira. We hope to meet you again next year for the 2nd BIOSIGNALS, details of which are available at http://www.biosignals.org.

Joaquim Filipe

INSTICC/Polytechnic Institute of Setúbal

CONTENTS

INVITED SPEAKERS

KEYNOTE LECTURES

MULTIVARIATE, MULTIORGAN AND MULTISCALE INTEGRATION OF INFORMATION IN BIOMEDICAL SIGNAL PROCESSING

Sergio Cerutti
Department of Bioengineering, Polytechnic University, Milano, Italy
sergio.cerutti@polimi.it

Abstract: Biomedical signals carry important information about the behavior of the living systems under studying. A proper processing of these signals allows in many instances to obtain useful physiological and clinical information. Many advanced algorithms of signal and image processing have recently been introduced in such an advanced area of research and therefore important selective information is obtainable even in presence of strong sources of noise or low signal/noise ratio. Traditional stationary signal analysis together with innovative methods of investigation of dynamical properties of biological systems and signals in second-order or in higher-order approaches (i.e., in time-frequency, time-variant and time-scale analysis, as well as in non linear dynamics analysis) provide a wide variety of even complex processing tools for information enhancement procedures. Another important innovative aspect is also remarked: the integration between signal processing and modeling of the relevant biological systems is capable to directly attribute patho-physiological meaning to the parameters obtained from the processing and viceversa the modeling fitting could certainly be improved by taking into account the results from signal processing procedure. Such an integration process could comprehend parameters and observations detected at different scales, at different organs and with different modalities. This approach is reputed promising for obtaining an olistic view of the patient rather than an atomistic one which considers the whole as a simple sum of the single component parts.

BRIEF BIOGRAPHY

Sergio Cerutti is Professor in Biomedical Signal and Data Processing at the Department of Bioengineering of the Polytechnic University in Milano, Italy. In the period 2000-2006 he has been the Chairman of the same Department. His research interests are mainly in the following topics: biomedical signal processing (ECG, blood pressure signal and respiration, cardiovascular variability signals, EEG and evoked potentials), neurosciences and cardiovascular modelling. In his research activity he has put emphasis on the integration of information at different modalities, at different sources and at different scales in various physiological systems. Since 1983 he has taught a course at a graduate and a doc level on Biomedical Signal Processing and Modelling at Engineering Faculties (Milano and Roma) as well as at Specialisation Schools of Medical Faculties (Milano and Roma). He has been Elected Member of IEEE-EMBS AdCom (Region 8) in the period 1993-1996. He is actually Fellow Member of IEEE and of EAMBES and Associate Editor of IEEE Trans BME. He is a member of the Steering Committee of the IEEE-EMBS Summer School on Biomedical Signal Processing: he was the local organiser of four Summer Schools held in Siena. He has been Visiting Professor at Harvard-MIT Division Health Science and Technology, Boston, USA for an overall period of 1 year. He is the Author of more than 400 international scientific contributions (more than 180 on indexed scientific journals).

1 INTRODUCTION

Biomedical signals and imaging carry important information about the behavior of the living systems under studying. A proper processing of these signals and images allow in many instances to obtain useful physiological and clinical information. Actually, many advanced algorithms of digital signal and image processing are at disposal and therefore

important selective information is now obtainable even in presence of strong sources of noise or low signal/noise ratio. In most of the cases it is not sure whether such sources might derive even by complex and unknown interactions with other biological systems whose implications could be important from the physiological or clinical standpoints. Traditional stationary signal analysis together with innovative methods of investigation of dynamical properties of biological systems and signals in second-order or in higher-order approaches (i.e., in time-frequency, time-variant and time-scale analysis, as well as in non linear dynamics analysis) provide a wide variety of even complex processing tools for information enhancement procedures in the challenging studying of a better explanation of many physiological and clinical phenomena.

2 INTEGRATION BETWEEN SIGNAL PROCESSING AND PHYSIOLOGICAL MODELING

Another important innovative aspect to improve the information content from biomedical data is constituted by the integration between signal processing and modeling of the relevant biological systems, thus directly attributing patho-physiological meaning to the model parameters obtained from the processing; and, viceversa, the modeling fitting could certainly be improved by taking into account the results from signal/image processing procedures.

3 MONOVARIATE AND MULTIVARIATE SIGNAL PROCESSING

Other kinds of integration may be fulfilled, taking into account more signals from the same system in a multivariate way (i.e. from a single-lead vs multichannel EEG or ECG analysis) and combining also the action of different systems such as autonomic nervous system, cardiovascular and respiratory systems, etc. Sleep is a formidable example of multiorgan involvement in both physiological (sleep staging and correlation with cardiorespiratory system) and pathological conditions (sleep apnea, sleep deprivation, restless leg syndrome and so on).

4 MULTISCALE APPROACH

Further, modern rehabilition techniques (motor and /or cognitive) make use actually of objective indices obtained from the patient's biosignals and images to better "personalize" rehabilitation protocols (from EEG, EP's, ERP's, MRI, fMRI, NIRS, etc). In neurosciences such an integration process could comprehend parameters and observations detected also at different scales, from genome and proteome up to the single organ and to the entire body compartment. Examples will be described where an animal model (murine model) is developed by alterating a gene putative to a determined pathology (i.e.epilepsy) and changes in EEG signals are studied (spike/wave occurrences and modifications in signal power bands). In clinical applications, it is worth mentioning the important data fusion which could be fulfilled by the integration of simultaneous EEG recordings and fMRI in some epileptic patients during inter-critical or critical events.

Finally, another important integration can be obtained along different observation scales. Traditionally, biological signal analysis is carried out at the level of organ or system to be investigated (i.e., ECG or EEG signal, arterial blood pressure, respiration and so on). It is very clear the advantage of correlating this information with that one obtained about the same system, but at different scale level, i.e. at cellular level or even at subcellular level (for example, analyzing possible genetic correlates or typical patterns of proteins or even DNA/RNA sequences). Biomedical engineering as a dedicated discipline may strongly contribute to this multiscale information processing

Along this approach line, even the long-QT syndrome, can be efficiently studied at different scale level: a mutation in a portion of gene SCN5A which presents a phenotype compatible to long-QT3 type, is known to produce an altered function of Na+ channels. Through a proper model which describes the functioning of ventricular cells is possible to evidence that this alteration may induce a prolongation of QT duration, as detected on ECG tracing. This event is further correlated with an increased risk of ventricular tachyarrhythmias. Hence, the path is completed: from the genetic expression up to the disease manifestation (Clancy and Rudy, 1999), (Priori ey al., 2003). Many different signal processing and modeling are involved in this paradigmatic example: an integration along the various scales of observation may undoubtedly contribute to a better

understanding of the complex pathophysiological correlates.

A great effort is on course nowadays for creating very large databases and networking of models and technologies for integrating such information (Physiome project (Hunter et al., 2002), (Rudy, 2000) to be connected with Genome and Proteome projects and Virtual Physiological Human project – VPH – which is inserted into the activities of the 7th Framework Programme of EU).

Other examples are constituted by the studying of the profile of expressed proteins in 2D-gel supports, or after mass-spectrometry analysis, relative to a variety of pathologies (i.e. epilepsy, peripheral neuropathies or Amyotrophic Lateral Sclerosis (ALS), or in oncological studies) thus singling out the set of proteins which present a correlate with the pathology in respect to the control group.

This overall approach is reputed promising for obtaining an olistic view of the patient rather than an atomistic one which considers the whole as a simple sum of the single component parts.

REFERENCES

G. Baselli, S. Cerutti, S. Civardi, A. Malliani and M. Pagani, Cardiovascular variability signals: towards the identification of a closed-loop model of the neural control mechanisms, *IEEE Trans Biomed Eng*., vol.35(12):1033-46(1988).

E. N. Bruce, *Biomedical Signal Processing and Signal Modelling*, J. Wiley (2001).

C. E. Clancy and Y. Rudy, Linking a genetic defect to its cellular phenotype in a cardiac arrhythmia, *Nature*, vol. 400(6744):566-569 (1999).

A. Cohen, *Biomedical Signal Analysis*, Vol. I, II, CRC Press (1986).

P. Hunter, P. Robbins and D. Noble, The IUPS human physiome project, *Pflugers Arch-Eur. J. Physiol*., vol. 445:1-9 (2002).

R. I. Kitney, A nonlinear model for studing oscillations in the blood pressure control system*, J. Biomed. Eng*., vol I,n. 2: 88-89 (1979).

H. P. Koepchen, History of studies and concepts of blood pressure wave, in: *Mechanisms of blood pressure waves (*Miyakawa K., Koepchen, H.P., Polosa C. eds): 3-23, Springer-Verlag (1984).

M. C. Mackey and J.C. Milton, Dynamical diseases, *Ann N Y Acad.Sc.,* vol.504:16-32 (1987).

C.-K. Peng, S. Havlin, J.M. Hausdorff, J.E. Mietus, H.E. Stanley and A.L. Goldberger, Fractal mechanisms and heart rate dynamics long-range correlation and their breakdown with diseases, *Journal of Electrocardiology*, vol.28: 59-65 (1995).

S. G. Priori, P.J. Schwartz, C. Napolitano, R. Bloise, E. Ronchetti, M. Grillo, A. Vicentini, C. Spazzolini, J. Nastoli, G. Bottelli, R. Folli and D. Cappelletti, Risk stratification in the long-QT sindrome, *N Engl J Med*., May 8, vol.348(19):1866-74 (2003).

Y. Rudy, From Genome to Physiome: integrative models of cardiac excitation, *Ann. Biom. Engineer*, vol 28: 945-950 (2000).

Cerutti S, Esposti F, Ferrario M, Sassi R, Signorini MG, Long-term invariant parameters obtained from 24-h Holter recordings: a comparison between different analysis techniques, Chaos, vol.17(1):015108, (2007).

Foffani G, Ardolino G, Rampini P, Tamma F, Caputo E, Egidi M, Cerutti S, Barbieri S, Priori A., Physiological recordings from electrodes implanted in the basal ganglia for deep brain stimulation in Parkinson's disease: the relevance of fast subthalamic rhythms, Acta Neurochir Suppl, vol. 93:97-9, (2005).

OUTTHINKING AND ENHANCING BIOLOGICAL BRAINS

Kevin Warwick
University of Reading, UK

Keywords: Brain-Computer Interface, Biological systems, Implant technology, Feedback control.

Abstract: In this paper an attempt has been made to take a look at how the use of implant and electrode technology can now be employed to create biological brains for robots, to enable human enhancement and to diminish the effects of certain neural illnesses. In all cases the end result is to increase the range of abilities of the recipients. An indication is given of a number of areas in which such technology has already had a profound effect, a key element being the need for a clear interface linking the human brain directly with a computer. An overview of some of the latest developments in the field of Brain to Computer Interfacing is also given in order to assess advantages and disadvantages. The emphasis is clearly placed on practical studies that have been and are being undertaken and reported on, as opposed to those speculated, simulated or proposed as future projects. Related areas are discussed briefly only in the context of their contribution to the studies being undertaken. The area of focus is notably the use of invasive implant technology, where a connection is made directly with the cerebral cortex and/or nervous system.

Tests and experimentation which do not involve human subjects are invariably carried out *a priori* to indicate the eventual possibilities before human subjects are themselves involved. Some of the more pertinent animal studies from this area are discussed including our own involving neural growth. The paper goes on to describe human experimentation, in which neural implants have linked the human nervous system bi-directionally with technology and the internet. A view is taken as to the prospects for the future for this implantable computing in terms of both therapy and enhancement.

BRIEF BIOGRAPHY

Kevin Warwick is Professor of Cybernetics at the University of Reading, England, where he carries out research in artificial intelligence, control, robotics and cyborgs. He is also Director of the University KTP Centre, which links the University with Small to Medium Enterprises and raises £2.5 million each year in research income. As well as publishing 500 research papers, Kevin is perhaps best known for his experiments into implant technology. He has been awarded higher doctorates (DScs) both by Imperial College and the Czech Academy of Sciences, Prague. He was presented with The Future of Health Technology Award in MIT, was made an Honorary Member of the Academy of Sciences, St. Petersburg and in 2004 received The IEE Achievement Medal.

1 INTRODUCTION

Research is being carried out in which biological signals of some form are measured, are acted upon by some appropriate signal processing technique and are then employed either to control a device or as an input to some feedback mechanism (Penny et al., 2000), (Roitberg, 2005). In many cases neural signals are employed, for example Electroencephalogram (EEG) signals can be measured externally to the body, using externally adhered electrodes on the scalp (Wolpaw et al., 1990) and can then employed as a control input. Most likely this is because the procedure is relatively simple from a research point of view and is not particularly taxing on the researchers involved. However, reliable interpretation of EEG data is extremely complex – partly due to both the compound nature of the multi-neuronal signals being measured and the difficulties in recording such highly attenuated

In the last few years interest has also grown in the use of real-time functional Magnetic Resonance

Imaging (fMRI) for applications such as computer cursor control. This typically involves an individual activating their brain in different areas by reproducible thoughts (Warwick, 2007) or by recreating events (Pan et al., 2007). Alternatively fMRI and EEG technologies can be combined so that individuals can learn how to regulate Slow Cortical Potentials (SCPs) in order to activate external devices (Hinterberger et al., 2005). Once again the technology is external to the body. It is though relatively expensive and cumbersome.

It is worth noting that external monitoring of neural signals, by means of either EEG analysis or indeed fMRI, leaves much to be desired. Almost surely the measuring technique considerably restricts the user's mobility and, as is especially the case with fMRI, the situation far from presents a natural or comfortable setting. Such systems also tend to be relatively slow, partly because of the nature of recordings via the indirect connection, but also because it takes time for the individual themselves to actually initiate changes in the signal. As a result of this, distractions, both conscious and sub-conscious, can result in false indicators thus preventing the use of such techniques for safety critical, highly dynamic and, to be honest, most realistic practical applications. Despite this, the method can enable some individuals who otherwise have extremely limited communication abilities to operate some local technology in their environment, and, in any case, it can serve as a test bed for a more direct and useful connection.

The definition of what constitutes a Brain-Computer Interface (BCI) is extremely broad. A standard keyboard could be so regarded. It is clear however that various wearable computer techniques and virtual reality systems, e.g. glasses containing a miniature computer screen for a remote visual experience (Mann, 1997), are felt by some researchers to fit this category. Although it is acknowledged that certain body conditions, such as stress or alertness, can be monitored in this way, the focus of this paper is on bidirectional BCIs and is more concerned with a direct connection between a biological brain and technology, and ultimately a human and technology.

2 *IN VIVO* STUDIES

Non-human animal studies can be considered to be a pointer for what is potentially achievable with humans in the future. As an example, in one particular animal study the extracted brain of a lamprey, retained in a solution, was used to control the movement of a small wheeled robot to which it was attached (Reger et al., 2000). The lamprey innately exhibits a response to light reflections on the surface of water by trying to align its body with respect to the light source. When connected into the robot body, this response was utilised by surrounding the robot with a ring of lights. As different lights were switched on and off, so the robot moved around its corral, trying to position itself appropriately.

Meanwhile in studies involving rats, a group of rats were taught to pull a lever in order to receive a suitable reward. Electrodes were then chronically implanted into the rats' brains such that the reward was proffered when each rat thought (one supposes) about pulling the lever, but before any actual physical movement occurred. Over a period of days, four of the six rats involved in the experiment learned that they did not in fact need to initiate any action in order to obtain a reward; merely thinking about it was sufficient (Chapin, 2004).

In another series of experiments, implants consisting of microelectrode arrays have been positioned into the frontal and parietal lobes of the brains of two female rhesus macaque monkeys. Each monkey learned firstly how to control a remote robot arm through arm movements coupled with visual feedback, and it is reported that ultimately one of the monkeys was able to control the arm using only brain derived neural signals with no associated physical movement. Notably, control signals for the reaching and grasping movements of the robotic arm were derived from the same set of implanted electrodes (Carmena et al., 2003), (Nicolelis et al., 2000).

Such promising results from animal studies have given the drive towards human applications a new impetus.

3 ROBOT WITH A BIOLOGICAL BRAIN

Human concepts of a robot may involve a little wheeled device, perhaps a metallic head that looks roughly human-like or possibly a biped walking robot. Whatever the physical appearance our idea tends to be that the robot might be operated remotely by a human, or is being controlled by a simple programme, or even may be able to learn with a

microprocessor/computer as its brain. We regard a robot as a machine.
In a present project neurons are being cultured in a laboratory in Reading University to grow on and interact with a flat multi-electrode array. The neural culture, a biological brain, can be electronically stimulated via the electrodes and its trained response can be witnessed.

The project now involves networking the biological brain to be part of a robot device. In the first instance this will be a small wheeled robot. The input (sensory) signals in this case will be only the signals obtained from the wheeled robot's ultrasonic sensors. The output from the biological brain will be used to drive the robot around. The goal of the project initially will be to train the brain to drive the robot forwards without bumping into any object. Secondly, a separate biological brain will be grown to be the thinking process within a robot head (called Morgui) which houses 5 separate sensory inputs.

What this means is that the brain of these robots will shortly be a biological brain, not a computer. All the brain will know is what it perceives from the robot body and all it will do will be to drive the robot body around or control the robot head respectively. The biological brain will, to all intents and purposes, be the brain of the robot. It will have no life, no existence outside its robotic embodiment.

Clearly this research alters our concept of what a robot is, particularly in terms of ethical and responsibility issues. If a role of animal research is to open up possibilities for future human trials, then in this case the research could well be opening a window on the ultimate possibility of human neurons being employed in a robot body. All the 'human' brain would know would be its life as a robot.

4 HUMAN APPLICATION

At the present time the general class of Brain-Computer Interfaces (BCIs) for humans, of one form or another, have been specifically developed for a range of applications including military weapon and drive systems, personnel monitoring and for games consoles. However, by far the largest driving force for BCI research to date has been the requirement for new therapeutic devices such as neural prostheses.

The most ubiquitous sensory neural prosthesis in humans is by far the cochlea implant (Fin and LoPresti, 2003). Here the destruction of inner ear hair cells and the related degeneration of auditory nerve fibres results in sensorineural hearing loss. As such, the prosthesis is designed to elicit patterns of neural activity via an array of electrodes implanted into the patient's cochlea, the result being to mimic the workings of a normal ear over a range of frequencies. It is claimed that some current devices restore up to approximately 80% of normal hearing, although for most recipients it is sufficient that they can communicate to a respectable degree without the need for any form of lip reading. The typically modest success of cochlea implantation is related to the ratio of stimulation channels to active sensor channels in a fully functioning ear. Recent devices consist of up to 32 channels, whilst the human ear utilises upwards of 30,000 fibres on the auditory nerve. There are now reportedly well over 10,000 of these prostheses in regular operation.

Studies investigating the integration of technology with the human central nervous system have varied from merely diagnostic to the amelioration of symptoms (Warwick and Gasson, 2004). In the last few years some of the most widely reported research involving human subjects is that based on the development of an artificial retina (Rizzo, 2001). Here, small electrode arrays have been successfully implanted into a functioning optic nerve. With direct stimulation of the nerve it has been possible for the otherwise blind recipient to perceive simple shapes and letters. The difficulties with restoring sight are though several orders of magnitude greater than those of the cochlea implant simply because the retina contains millions of photodetectors that need to be artificially replicated. An alternative is to bypass the optic nerve altogether and use cortical surface or intracortical stimulation to generate phosphenes (Dobelle, 2000).

Most invasive BCIs monitor multi-neuronal intracortical action potentials, requiring an interface which includes sufficient processing in order to relate recorded neural signals with movement intent. Problems incurred are the need to position electrodes as close as possible to the source of signals, the need for long term reliability and stability of interface in both a mechanical and a chemical sense, and adaptivity in signal processing to deal with technological and neuronal time dependence. However, in recent years a number of different collective assemblies of microelectrodes have been successfully employed both for recording and stimulating neural activity. Although themselves of small scale, nevertheless high density

connectors/transmitters are required to shift the signals to/from significant signal processing and conditioning devices and also for onward/receptive signal transmission.

Some research has focussed on patients who have suffered a stroke resulting in paralysis. The most relevant to this paper is the use of a '3rd generation' brain implant which enables a physically incapable brainstem stroke victim to control the movement of a cursor on a computer screen (Kennedy, 2000), (Kennedy, 2004). Functional Magnetic Resonance Imaging (fMRI) of the subject's brain was initially carried out to localise where activity was most pronounced whilst the subject was thinking about various movements. A hollow glass electrode cone containing two gold wires and a neurotrophic compound (giving it the title 'Neurotrophic Electrode') was then implanted into the motor cortex, in the area of maximum activity. The neurotrophic compound encouraged nerve tissue to grow into the glass cone such that when the patient thought about moving his hand, the subsequent activity was detected by the electrode, then amplified and transmitted by a radio link to a computer where the signals were translated into control signals to bring about movement of the cursor. With two electrodes in place, the subject successfully learnt to move the cursor around by thinking about different movements. Eventually the patient reached a level of control where no abstraction was needed – to move the cursor he simply thought about moving the cursor. Notably, during the period that the implant was in place, no rejection of the implant was observed; indeed the neurons growing into the electrode allowed for stable long-term recordings.

Electronic neural stimulation has proved to be extremely successful in other areas, including applications such as the treatment of Parkinson's disease symptoms. With Parkinson's Disease diminished levels of the neurotransmitter dopamine cause over-activation in the ventral posterior nucleus and the subthalamic nucleus, resulting in slowness, stiffness, gait difficulties and hand tremors. By implanting electrodes into the subthalamic nucleus to provide a constant stimulation pulse, the over activity can be inhibited allowing the patient, to all external intents and purposes, to function normally (Pinter et al., 1999).

5 BRAIN WITHIN A BRAIN

Ongoing research, funded by the UK Medical Research Council, is investigating how the onset of tremors can be accurately predicted such that merely a stimulation current burst is required rather than a constant pulsing (Gasson et al., 2005: pp.16/1-16/4). This has implications for battery inter-recharge periods as well as limiting the extent of in-body intrusive signalling. The deep brain stimulator can be used to collect local field potential (LFP) signals generated by the neurons around the deep brain electrodes (Gasson et al., 2005: pp.16/1-16/4). Determining the onset of events can be investigated by using fourier transforms to transfer the time based signal to a frequency based spectrogram to determine the change in frequency at the critical time period. However, in addition to that, the frequency changes in the period of time immediately prior to the tremor occurrence can give important information.

Fig.1 shows the results of an initial attempt to train an artificial neural network to indicate not only that a Parkinsonian tremor is present but also that one is very likely to occur in the near future. The aim of this research is that, once a reliable predictor has been obtained, the stimulating pulsing will only be enacted when a tremor is predicted, in order to stop the actual physical tremor occurring before it even starts in the first place.

The bottom trace in Fig.1 shows emg (muscular) signals, measured externally, associated with movement due to the tremors. It can be seen that the tremors in this incident actually start at around the 45 to 50 second point. The trace just above this indicates the corresponding electrical data measured as deep brain Local Field Potentials in the Sub-Thalamic Nucleus of the patient involved. It can be witnessed how, in this case, the electrical data takes on a different form (in terms of variance at least) at around the 45 to 50 second point. The four top plots meanwhile indicate the outputs from 4 differently structured artificial neural networks, based on multi-layer perceptrons with different numbers of neurons in the hidden (middle) layer.

It can be seen how, for each network, the output of the network goes high (logic 1) at the 45 to 50 second point, to indicate the presence of a Parkinsonian tremor. This is all well and good, what is important however is that the output of the networks also briefly goes high around the 30

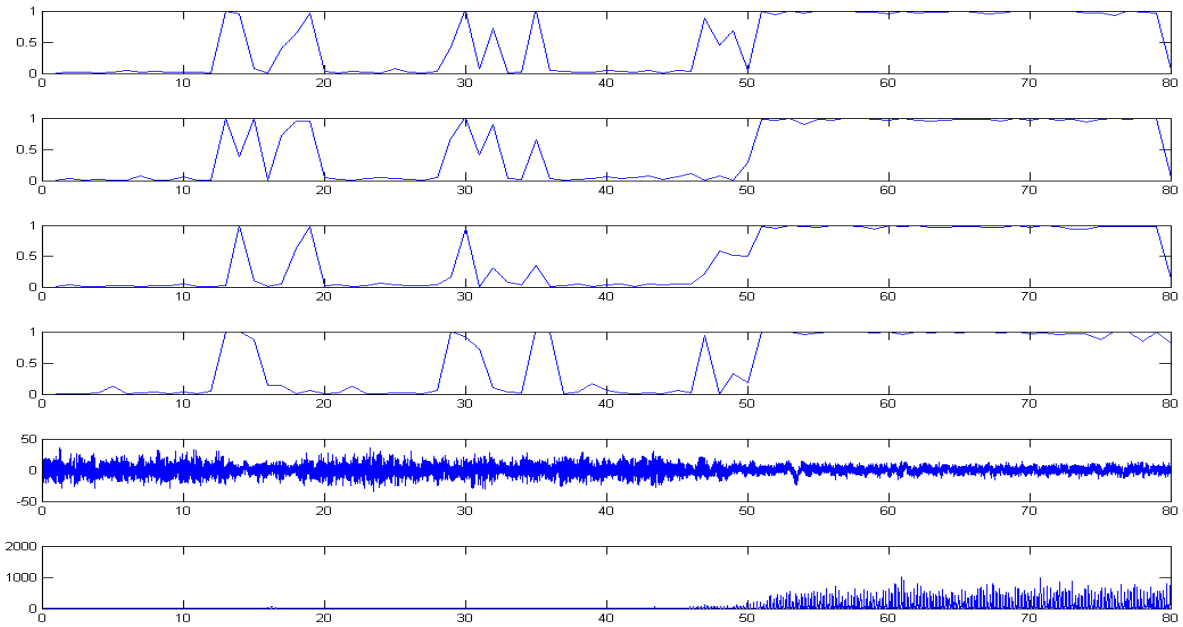

Figure 1: Time plot of the onset of a Parkisonian tremor incident with corresponding artificial neural network indicators.

second point and this can be seen as an indication of the fact that a tremor will shortly occur. Ongoing research is involved with selection of the type and number of inputs to the network, presently these being based on the energy spectrum in different frequency ranges. The networks are also being tested on considerable amounts of resting data, that is long periods of brain activity where no tremors at all actually occur in patients. Clearly the aim is that a network will not give false predictions of tremors.

In fact false positive predictions are not so much of a critical problem. The end result with a false positive is that a stimulation may occur when it is not strictly necessary. In any event no actual tremor would occur, which is indeed a good outcome, however unnecessary energy would have been used – in fact if numerous false predictions occurred the intelligent stimulator would tend toward the present 'blind' stimulator. Effectively the occasional false positive prediction is perhaps not a problem, unless it became a regular occurrence. The good news is that results show that the network can be readily tuned to avoid false positives anyway.

6 GENERAL IMPLANT STUDIES

Some of the most impressive human research to date has been carried out using the microelectrode array, shown in Figure 2. The individual electrodes are only 1.5mm long and taper to a tip diameter of less than 90 microns. Although a number of trials not using humans as a test subject have occurred (Branner and Normann, 2000), human tests are at present limited to two studies. In the second of these the array has been employed in a recording only role (Donoghue et al., 2002), (Donoghue et al., 2004), (Friehs et al., 2004), most notably recently as part of the 'Braingate' system. Essentially activity from a few neurons monitored by the array electrodes is decoded into a signal to direct cursor movement. This has enabled an individual to position a cursor on a computer screen, using neural signals for control combined with visual feedback. The first use of the microelectrode array (Figure 2) will be discussed in the following section as this has considerably broader implications which extend the capabilities of the human recipient.

A key selection point at the present time are what type of implant to employ, as several different possibilities exist, ranging from single electrode devices to multielectrode needles which contain electrode points at different depths to multielectrode arrays which either contain a number of electrodes which penetrate to the same depth (as in Figure 2) or are positioned in a banked/sloped arrangement. A further key area of consideration is the exact positioning of a BCI. In particular certain areas of the brain are, apparently, only really useful for monitoring purposes whilst others are more useful for stimulation.

Actually deriving a reliable command signal from a collection of captured neural signals is not necessarily a simple task, partly due to the complexity of signals recorded and partly due to time constraints in dealing with the data. In some cases however it can be relatively easy to look for and obtain a system response to certain anticipated neural signals – especially when an individual has trained extensively with the system. In fact neural signal shape, magnitude and waveform with respect to time are considerably different to the other signals that it is possible to measure in this situation.

If a greater understanding is required of neural signals recorded, before significant progress can be made, then this will almost surely present a major problem. This is especially true if a number of simultaneous channels are being employed, each requiring a rate of digitization of (most likely) greater than 20KHz in the presence of unwanted noise. For real time use this data will also need to be processed within a few milliseconds (100 milliseconds at most). Further, although many studies have looked into the extraction of command signals (indicating intent) from measured values, it is clear that the range of neural activity is considerable. Even in the motor area not only are motor signals present but so too are sensory, cognitive, perceptual along with other signals, the exact purpose of which is not clear – merely classifying them as noise is not really sufficient and indeed can be problematic when they are repeated and apparently linked in some way to activity.

It is worth stressing here that the human brain and spinal cord are linking structures, the functioning of which can be changed through electronic stimulation such as that provided via an electrode arrangement. This type of technology therefore offers a variety of therapeutic possibilities. In particular the use of implanted systems when applied to spinal cord injured patients, in whom nerve function is disordered, was described in (Warwick, 2004) as having the following potential benefits (among others):

1. Re-education of the brain and spinal cord through repeated stimulation patterns
2. Prevention of spinal deformity
3. Treatment of intractable neurogenic and other pain
4. Assisting bladder emptying
5. Improving bowel function
6. Treatment of spasticity
7. Improvement of respiratory function – assisting coughing and breathing
8. Reduction of cardiovascular maleffects
9. Prevention of pressure sores – possibly providing sensory feedback from denervated areas
10. Improvement and restoration of sexual function
11. Improved mobility
12. Improved capability in daily living, especially through improved hand, upper limb and truncal control

Sensate prosthetics is another growing application area of neural interface technology, whereby a measure of sensation is restored using signals from small tactile transducers distributed within an artificial limb (Fin and LoPresti, 2003). The transducer output can be employed to stimulate the sensory axons remaining in the residual limb which are naturally associated with a sensation. This more closely replicates stimuli in the original sensory modality, rather than forming a type of feedback using neural pathways not normally associated with the information being fed back. As a result it is supposed that the user can employ lower level reflexes that exist within the central nervous system, making control of the prosthesis more subconscious.

One final noteworthy therapeutic procedure is Functional Electrical Stimulation (FES), although it is debatable if it can be truly referred to as a BCI, however it aims to bring about muscular excitation, thereby enabling the controlled movement of limbs. FES has been shown to be successful for artificial hand grasping and release and for standing and walking in quadriplegic and paraplegic individuals as well as restoring some basic body functions such as bladder and bowel control (Grill and Kirsch, 2000). It must be noted though that controlling and coordinating concerted muscle movements for complex and generic tasks such as picking up an arbitrary object is proving to be a difficult, if not insurmountable, challenge.

In the cases described in which human subjects are involved, the aim on each occasion is to either restore functions since the individual has a physical problem of some kind or it is to give a new ability to an individual who has very limited motor abilities. In this latter case whilst the procedure can be regarded as having a therapeutic purpose, it is quite possible to provide an individual with an ability that they have in fact never experienced before. On the one hand it may be that whilst the individual in question has never previously experienced such an ability, some or most other humans have – in this

case it could be considered that the therapy is bringing the individual more in line with the "norm" of human abilities.

It is though also potentially possible to give extra capabilities to a human, to enable them to achieve a broader range of skills – to go beyond the "norm". Apart from the, potentially insurmountable, problem of universally deciding on what constitutes the "norm", extending the concept of therapy to include endowing an individual with abilities that allow them to do things that a perfectly able human cannot do raises enormous ethical issues. Indeed it could be considered that a cochlea implant with a wider frequency response range does just that for an individual or rather an individual who can control the curser on a computer screen directly from neural signals falls into this category. But the possibilities of enhancement are enormous. In the next section we consider how far things could be taken, by referring to relevant experimental results.

7 HUMAN ENHANCEMENT

The interface through which a user interacts with technology provides a distinct layer of separation between what the user wants the machine to do, and what it actually does. This separation imposes a considerable cognitive load upon the user that is directly proportional to the level of difficulty experienced. The main issue it appears is interfacing the human motor and sensory channels with the technology. One solution is to avoid this sensorimotor bottleneck altogether by interfacing directly with the human nervous system. It is certainly worthwhile considering what may potentially be gained from such an invasive undertaking.

Advantages of machine intelligence are for example rapid and highly accurate mathematical abilities in terms of 'number crunching', a high speed, almost infinite, internet knowledge base, and accurate long term memory. Additionally, it is widely acknowledged that humans have only five senses that we know of, whereas machines offer a view of the world which includes infra-red, ultraviolet and ultrasonic. Humans are also limited in that they can only visualise and understand the world around them in terms of a limited dimensional perception, whereas computers are quite capable of dealing with hundreds of dimensions. Also, the human means of communication, essentially transferring an electro-chemical signal from one brain to another via an intermediate, often mechanical medium, is extremely poor, particularly in terms of speed, power and precision. It is clear that connecting a human brain, by means of an implant, with a computer network could in the long term open up the distinct advantages of machine intelligence, communication and sensing abilities to the implanted individual.

As a step towards this more broader concept of human-machine symbiosis, in the first study of its kind, the microelectrode array (as shown in Figure 2) was implanted into the median nerve fibres of a healthy human individual (myself) in order to test *bidirectional* functionality in a series of experiments. A stimulation current direct onto the nervous system allowed information to be sent to the user, while control signals were decoded from neural activity in the region of the electrodes (Gasson et al., 2005:pp 365-375), (Warwick et al., 2003).

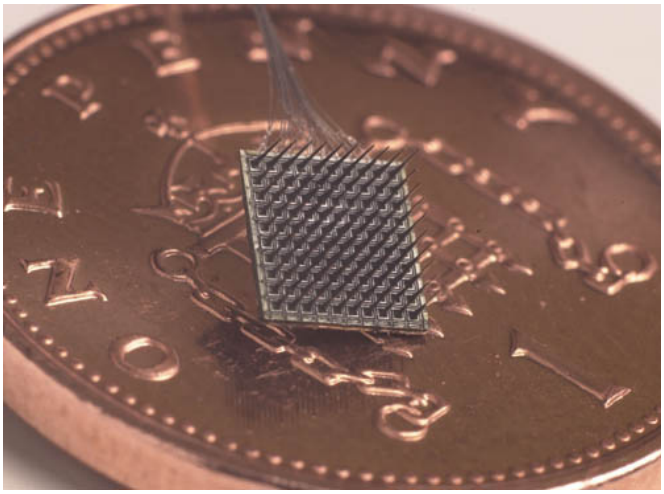

Figure 2: A 100 electrode, 4X4mm Microelectrode Array, shown on a UK 1 pence piece for scale.

In this way a number of experimental trials were successfully concluded (Warwick et al., 2004), (Warwick et al., 2005): In particular:

1. Extra sensory (ultrasonic) input was successfully implemented and made use of.
2. Extended control of a robotic hand across the internet was achieved, with feedback from the robotic fingertips being sent back as neural stimulation to give a sense of force being applied to an object (this was achieved between New York (USA) and Reading(UK))
3. A primitive form of telegraphic communication directly between the nervous systems of two humans was performed.
4. A wheelchair was successfully driven around by means of neural signals.
5. The colour of jewellery was changed as a result of neural signals – as indeed was the behaviour of a collection of small robots.

In each of the above cases it could be regarded that the trial proved useful for purely therapeutic reasons, e.g. the ultrasonic sense could be useful for an individual who is blind or the telegraphic communication could be very useful for those with certain forms of Motor Neurone Disease. However each trial can also be seen as a potential form of augmentation or enhancement for an individual. The question then arises as to how far should things be taken? Clearly enhancement by means of BCIs opens up all sorts of new technological and intellectual opportunities, however it also throws up a raft of different ethical considerations that need to be addressed directly.

8 ON STIMULATION

After extensive experimentation it was found that injecting currents below 80µA onto the median nerve fibers had little perceivable effect. Between 80µA and 100µA all the functional electrodes were able to produce a recognizable stimulation, with an applied voltage of 40 to 50 volts, dependant on the series electrode impedance. Increasing the current above 100µA had no apparent additional effect; the stimulation switching mechanisms in the median nerve fascicle exhibited a non-linear thresholding characteristic.

During this experimental phase, it was pseudo randomly decided whether a stimulation pulse was applied or not. The volunteer (myself), wearing a blindfold, was unaware of whether a pulse had been applied or not, other than by means of its effect in terms of neural stimulation. The user's accuracy in distinguishing between an actual pulse and no pulse at a range of amplitudes is shown in Figure 3.

In all subsequent successful trials, the current was applied as a bi-phasic signal with pulse duration of 200 µsec and an inter-phase delay of 100 µsec. A typical stimulation waveform of constant current being applied to one of the MEA's implanted electrodes is shown in Fig 4.

It was, in this way, possible to create alternative sensations via this new input route to the nervous system. Of the 5 enhancement features mentioned in the previous section, this one will be described, as an example, in further detail. Background information on the other enhancements can be found in a number of references, e.g. (Gasson et al., 2005:pp 365-375), (Warwick et al., 2003), (Warwick et al., 2004), (Warwick and Gasson, 2004).

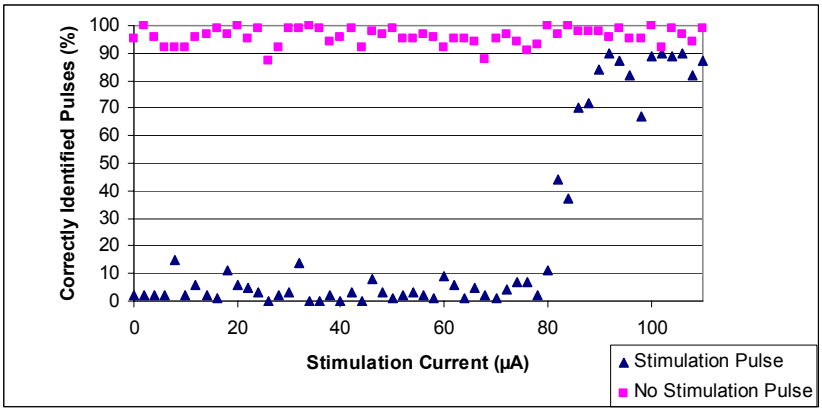

Figure 3: Effect of stimulation amplitude on the number of correctly identified pulses and absence of pulses (over 100 trials).

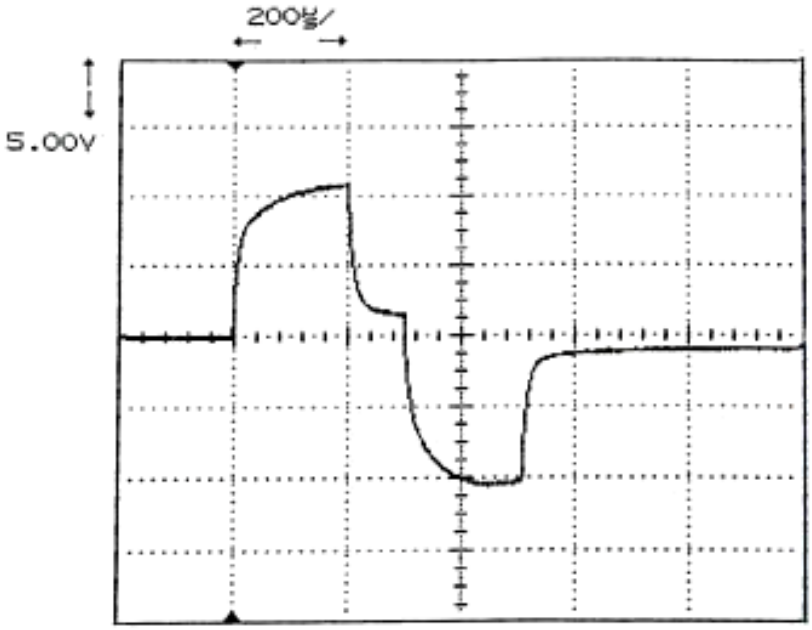

Figure 4: Voltage profile during one bi-phasic stimulation pulse cycle with a constant current of 80µA.

It must be reported that it took 6 weeks for my brain to repetitively recognize the stimulating signals accurately. This time period can be due to a number of contributing factors:

(a) The team had to learn which signals (what amplitude, frequency etc.) would be best in order to bring about a recognizable stimulation.

(b) The recipient's brain had to learn to recognize the new signals it was receiving.

(c) The bond between the recipient's nervous system and the implant was physically changing (becoming stronger).

9 EXTRA SENSORY EXPERIMENT

An experiment was set up to determine if the human brain is able to understand and successfully operate with sensory information to which it had not previously been exposed. Whilst it is quite possible to feed in such sensory information via a normal human sensory route, e.g. electromagnetic radar or infra-red signals are converted to visual, what we were interested in was feeding such signals directly onto the human nervous system, thereby bi-passing the normal human sensory input.

Ultrasonic sensors were fitted to the rim of a baseball cap (see Figure 5) and the output from these sensors, in the form of a proportional count, was employed to bring about a direct stimulation of the nervous system. Hence when no objects were in the vicinity of the sensors, no stimulation occurred, and as an object moved close by so the rate of stimulation pulses being applied increased in a linear fashion up to a pre-selected maximum rate. No increase in stimulation occurred when an object moved closer than 10cm to the sensors.

The ultrasonic sensors were open type piezoelectric ceramic transducers with conical metal resonators and operated at 40 KHz. These were used in a pair, one for transmit and one for receive, to give maximum sensitivity for small and distant objects. The most useful range for the experimentation was found to be 2 – 3m, this being also dependent on the size of object. A simple microcontroller was programmed to perform the echo ranging on the pair of transducers, and provide the range to the first detectable object only. This was translated into a stimulation pulse train, which operated on a single pin of the electrode array. Pins on the array had been tested for their suitability for stimulation by the earlier experimentation in which the recipient identified the presence or absence of stimulation pulse trains at various amplitudes and repetition frequencies.

Figure 5: Experimentation and testing of the ultrasonic baseball cap.

It was found that very little learning was required for the new ultrasonic sense to be used effectively and successfully – merely a matter of 5/6 minutes. This said it must be remembered that it had already taken several weeks for the recipient's brain to successfully, accurately recognize the current signals being injected.

As a result, in a witnessed experiment, the recipient, whilst wearing a blindfold, was able to move around successfully within a cluttered laboratory environment, albeit at a slower than normal walking pace. The sensory input was "felt" as a new form of sensory input (not as touch or movement) in the sense that the brain made a direct link between the signals being witnessed and the fact that these corresponded in a linear fashion to a nearby object.

10 CONCLUSIONS

External input-output interfaces with human and animal brains have been studied for many years. These are sometimes referred to as Brain-Computer Interfaces (BCIs) even though the interface may be external to the (human) body and its sensorimotor mechanism. In this paper an attempt has been made to put such systems in perspective. Emphasis has been placed on such interfaces that can be obtained by means of implanted devices through invasive surgery and actual direct neural connections. In particular a number of trials in this area have clearly shown the possibilities of monitoring, stimulating and enhancing brain functioning.

Although there is no distinct dividing line it is quite possible as far as humans are concerned to investigate BCIs in terms of those employed for direct therapeutic means and those which can have an enhanced role to play. It is clear that the interaction of electronic signals with the human brain can cause the brain to operate in a distinctly different manner. Such is the situation with the stimulator implants that are successfully used to counteract, purely electronically, the tremor effects associated with Parkinson's disease. Such technology can though potentially be employed to modify the normal functioning of the human brain and nervous system in a number of different ways.

The same stimulator, with slightly different positioning, has been shown to elicit feelings of sadness or happiness in the recipient. Given the nature of the intelligent stimulator described here it would appear to be possible to monitor, in real time, a human brain with a computer brain, and for the computer brain to predict when the human is going to feel sad – quite some time before they actually feel sad. In theory a signal could then be injected at

that time to make them feel happy, or at least to stop them actually ever feeling sad in the first place. Maybe this could be regarded as an electronic anti-depressant. There are of course questions about recreational use here – but this would need a deep brain implant which might well prove to be rather too onerous for most people.

Perhaps understandably, invasive BCIs are presently far less well investigated in University experiments than their external BCI counterparts. A number of animal trials have though been carried out and the more pertinent have been indicated here along with the relevant human trials and practice. In particular the focus of attention has been given to the embodiment of grown neural tissue within a technological body. Whilst only 1,000 or so neurons are involved this presents an interesting research area in a number of ways. But once the number of such neurons used increases 1,000 or 1,000,000-fold, it also raises enormous philosophical and ethical issues. For example is the robot 'thinking' and what rights should it have?

The potential for BCI applications for individuals who are paralysed is enormous, where cerebral functioning to generate command signals is functional despite the motor neural pathways being in some way impaired – such as in Lou Gehrig's disease. The major role is then either one of relaying a signal of intention to the appropriate actuator muscles or to reinterpret the neural signals to operate technology thereby acting as an enabler. In these situations no other medical 'cure' is available, something which presents a huge driver for an invasive implant solution for the millions of individuals who are so affected. Clearly though, bidirectional signalling is important, not only to monitor and enact an individual's intent but also to provide feedback on that individual's resultant interaction with the real world. For grasping, walking and even as a defensive safety stimulant, feedback is vital. This paper has therefore focussed on such studies.

Where invasive interfaces are employed in human trails, a purely therapeutic scenario often exists. In a small number of instances, such as use of the microelectrode array as an interface, an individual has been given different abilities, something which opens up the possibilities of human enhancement. These latter cases however raise more topical ethical questions with regard to the need and use of a BCI. What might be seen as a new means of communication for an individual with an extreme form of paralysis or a new sensory input for someone who is blind, opening up a new world for them, can also be seen as an unnecessary extra for another individual, even though it may provide novel commercial opportunities. What is therapy for one person may be regarded as an enhancement or upgrading for another.

Whilst there are still many technical problems to be overcome in the development of BCIs, significant recent experimental results have indicated that a sufficient technological infrastructure now exists for further major advances to be made. Although a more detailed understanding of the underlying neural processes will be needed in the years ahead, it is not felt that this will present a major hold up over the next few years, rather it will provide an avenue of research in which many new results will shortly appear through trials and experimentation, possibly initially through animal studies although it must be recognised that it is only through human studies that a full analysis can be made and all encompassing conclusions can be drawn. Nevertheless the topic opens up various ethical questions that need to be addressed and as such, research in this area should, I believe, only proceed in light of a pervasive ethical consensus.

ACKNOWLEDGEMENTS

The Author would like to acknowledge the considerable assistance and input of the Consultant Neurosurgeons Mr. Peter Teddy, Mr. Amjad Shad, Mr. Ali Jamous and Mr. Tipu Aziz and researchers Iain Goodhew, Mark Gasson, Ben Whalley and Ben Hutt. Ethical approval for the author's research was obtained from the Ethics and Research Committee at the University of Reading, UK and with regard to the neurosurgery aspect, the Oxfordshire National Health Trust Board overseeing the Radcliffe Infirmary, Oxford, UK.

REFERENCES

Branner, A. and Normann, R. (2000) A multielectrode array for intrafascicular recording and stimulation in the sciatic nerve of a cat, *Brain Research Bulletin*, Vol.51, pp.293-306.

Chapin, J.K. (2004) Using multi-neuron population recordings for neural prosthetics. *Nature Neuroscience*, 7, 452-454.

Carmena, J., Lebedev, M., Crist, R., O'Doherty, J., Santucci, D., Dimitrov, D. Patil, P., Henriquez, C. and Nicolelis, M. (2003) Learning to control a brain-

machine interface for reaching and grasping by primates, *Plos Biology*, Vol.1, Issue.2, article number e2.
Dobelle, W. (2000) Artificial vision for the blind by connecting a television camera to the visual cortex, ASAIO J, Vol.46, pp.3-9.
Donoghue, J. (2002) Connecting cortex to machines: recent advances in brain interfaces, *Nature Neuroscience Supplement*, Vol.5, pp.1085-1088.
Donoghue, J., Nurmikko, A., Friehs, G. And Black, M. (2004) Development of a neuromotor prosthesis for humans, Chapter 63 in *Advances in Clinical Neurophysiology, Supplements to Clinical Neurophysiology*, Vol.57, pp.588-602.
Finn, W. and LoPresti, P. (eds.) (2003) Handbook of Neuroprosthetic methods, CRC Press.
Friehs, G., Zerris, V., Ojakangas, C., Fellows, M. and Donoghue, J. (2004) Brain-machine and brain-computer interfaces, *Stroke*, Vol.35, Issue.11, pp.2702-2705.
Gasson, M., Hutt, B., Goodhew, I., Kyberd, P. and Warwick, K. (2005) Invasive neural prosthesis for neural signal detection and nerve stimulation, Proc. International Journal of Adaptive Control and Signal Processing, Vol.19, No.5, pp.365-375.
Gasson, M., Wang, S., Aziz, T., Stein, J. and Warwick, K. (2005) Towards a demand driven deep brain stimulator for the treatment of movement disorders, Proc. 3rd IEE International Seminar on Medical Applications of Signal Processing, pp.16/1-16/4.
Grill, W. and Kirsch, R. (2000) Neuroprosthetic applications of electrical stimulation, *Assistive Technology,* Vol.12, Issue.1, pp.6-16.
Hinterberger, T., Veit, R., Wilhelm, B., Weiscopf, N., Vatine, J. and Birbaumer, N. (2005) Neuronal mechanisms underlying control of a brain-computer interface, *European Journal of Neuroscience*, Vol.21, Issue.11, pp.3169-3181.
Kennedy, P., Bakay, R., Moore, M., Adams, K. and Goldwaith, J. (2000) Direct control of a computer from the human central nervous system, *IEEE Transactions on Rehabilitation Engineering*, Vol.8, pp.198-202.
Kennedy, P., Andreasen, D., Ehirim, P., King, B., Kirby, T., Mao, H. and Moore, M. (2004) Using human extra-cortical local field potentials to control a switch, *Journal of Neural Engineering*, Vol.1, Issue.2, pp.72-77.
Mann, S. (1997) Wearable Computing: A first step towards personal imaging, *Computer*, Vol. 30, Issue.2, pp. 25-32.
Nicolelis, M., Dimitrov, D., Carmena, J., Crist, R., Lehew, G., Kralik, J. and Wise, S. (2003) Chronic, multisite, multielectrode recordings in macaque monkeys, *Proc. National Academy of the USA*, Vol.100, Issue.19, pp.11041-11046.
Penny, W., Roberts, S., Curran, E., and Stokes, M. (2000) EEG-based communication: A pattern recognition approach, *IEEE Transactions on Rehabilitation Engineering*., Vol. 8, Issue.2, pp. 214-215.
Pinter, M., Murg, M., Alesch, F., Freundl, B., Helscher, R. And Binder, H. (1999) Does deep brain stimulation of the nucleus ventralis intermedius affect postural control and locomotion in Parkinson's disease?, *Movement Disorders*, Vol.14, Issue.6, pp.958-963.
Reger, B., Fleming, K., Sanguineti, V., Simon Alford, S., Mussa-Ivaldi, F. (2000) Connecting Brains to Robots: an artificial body for studying computational properties of neural tissues, *Artificial life*, Vol.6, Issue.4, pp.307-324.
Rizzo, J., Wyatt, J., Humayun, M., DeJuan, E., Liu, W., Chow, A., Eckmiller, R., Zrenner, E., Yagi, T. and Abrams, G. (2001) Retinal Prosthesis: An encouraging first decade with major challenges ahead, *Opthalmology,* Vol.108, No.1.
Roitberg, B. (2005) Noninvasive brain-computer interface, *Surgical Neurology*, Vol.63, Issue.3, p.195.
Warwick, K. (2004) I Cyborg, University of Illinois Press.
Warwick, K., Gasson, M., Hutt, B., Goodhew, I., Kyberd, P., Andrews, B., Teddy, P., Shad, A. (2003) The application of implant technology for cybernetic systems. *Archives of Neurology*, 60 (10), pp.1369-1373.
Warwick, K., Gasson, M., Hutt, B., Goodhew, I., Kyberd, P., Schulzrinne, H. and Wu, X. (2004) Thought Communication and Control: A First Step Using Radiotelegraphy, *IEE Proceedings on Communications,* Vol.151, No. 3, pp 185-189.
Warwick, K., Gasson, M., Hutt, B. and Goodhew, I. (2005) An Attempt to Extend Human Sensory Capabilities by means of Implant Technology. Proc. IEEE Int. Conference on Systems, Man and Cybernetics, Hawaii.
Wolpaw, J., McFarland, D., Neat, G. and Forheris, C. (1990) An EEG based brain-computer interface for cursor control, *Electroencephalogr. Clin. Neurophysiol*., Vol.78, pp.252-259.
Pan, S., Warwick, K., Gasson, M., Burgess, J., Wang, S., Aziz, T. and Stein, J. (2007) Prediction of parkinson's disease tremor onset with artificial neural networks", Proc. IASTED Conference BioMed 2007, Innsbruck, Austria, pp.341-345.
Warwick, K. (2007) The promise and threat of modern cybernetics, Southern Medical Journal, Vol.100, Issue.1, pp.112-115.
Warwick, K. and Gasson, M.N. (2004) Practical Interface Experiments with Implant Technology, in "Computer Vision in Human-Computer Interaction", Sebe, N., Lew, M.S and Huang, T.S. (eds.), Lecture Notes in Computer Science, Vol. 3058, pp.7-16.Xie, S., Yang, Z. and Yang, Y. (2004) Brain-computer interface based on event-related potentials during imitated natural reading, International Journal of Psychology, Vol.39, Issue.5-6, Supplement S., p.138.
Yoo, S., Fairneny, T., Chen, N., Choo, S., Panych, L., Park, H., Lee, S. and Jolesz, F. (2004) Brain-computer interface using fMRI: spatial navigation by thoughts, *Neuroreport*, Vol.15, Issue.10, pp.1591-1595.
Yu, N., Chen, J. and Ju, M. (2001) Closed-Loop Control of Quadriceps/Hamstring activation for FES-Induced Standing-Up Movement of Paraplegics, *Journal of Musculoskeletal Research*, Vol. 5, No.3, pp.173-184.

ANALYSIS AND MODELS OF BRAIN EPILEPTIC ACTIVITIES

Fernando Henrique Lopes da Silva
University of Amsterdam, The Netherlands

Abstract: The essence of epilepsy is the sudden occurrence of a qualitative change in the behaviour of neuronal networks of some specific areas of the brain. In general we may assume that neuronal networks possess multistable dynamics. We may simplify this concept considering the case that a neuronal network may display, at least, two dynamical states: an interictal state characterised by a normal on-going neural activity, as revealed in the Eletcroencephalogram of Magnetoencephalogram (EEG, MEG), that may be apparently random, and another one – the ictal state - that is characterised by the sudden occurrence of synchronous oscillations, most commonly with large amplitude. The latter becomes manifest as a paroxysmal change of behaviour and /of the state of consciousness of a patient, i.e. an epileptic seizure. In the terminology of the mathematics of non-linear systems, we may state that a neuronal network behaves as a bistable system with two attractors, to which the system converges depending on initial conditions and on the system's parameters.

We propose schematically that the transition between the normal on-going to the seizure activity can take place according to three basic models: Model I – a transition may occur due to random fluctuations of some system's parameters. These transitions are thus unpredictable. Models II and III – a transition may result from a gradual change of some unstable parameters, either due to endogenous (model II) or exogenous (model III). In these cases the change of parameter values causes a deformation of the attractor resulting in a transition from the basin of the attractor corresponding to the normal state, to the attractor corresponding to the seizure dynamical state. Some experimental findings obtained in different cases of epilepsy, both in human and in animals, are compatible with each of these 3 models. Some examples of these cases are illustrated.

BRIEF BIOGRAPHY

Fernando Henrique Lopes da Silva received his Medical Degree from the University of Lisbon in 1959, got his Ph.D. from the University of Utrecht in 1970, and in 1980 was appointed Full Professor of General Physiology at the Faculty of Science at the University of Amsterdam (since 2002 part of the Swammerdam Institute for Life Sciences). From 1993 to 2000 he was Director of the newly created Institute of Neurobiology of the University of Amsterdam, and member of the Scientific Directorate of the Graduate School Neurosciences Amsterdam. In 2000, when he reached the retirement age of 65, he became Emeritus Professor of the same University, and has at present a free-lance contract with the Swammerdam Institute for Life Sciences.

Since 1970, he supervised a large number of student trainees from different Universities and Faculties: Medical, Biology, Sciences, (Bio-medical) Engineering. Supervised 65 Ph.D. students (up to December 2006).

His research interests are centred on the biophysical aspects of electrical activity of the brain and the functional organization of neuronal networks, namely of the cerebral cortex and the limbic system, with a special interest in the generation and functional significance of brain rhythmic activities. He published more than 220 papers in peer-reviewed journals and contributed Chapters to 10 multi-authored books (of 6 he is co-editor), among which the Handbook "Electroencephalography: Basic principles, clinical applications and related fields", Niedermeyer, E. and Lopes da Silva, F.H. (Eds), published by Lippincott, Williams and Wilkins, Baltimore; 5 Editions: 1982, 1987, 1993, 1998, 2004. In addition he contributed chapters to to the Encyclopedia of Neuroscience (George Adelman, Barry H. Smith. Eds), Elsevier Science, 2003 (3rd edition), to the Encyclopedia of the Human Brain (Ed. V. S. Ramachandran), Academic Press, 2002, and to The Handbook of Brain Theory and Neural Networks (Ed. Michael A. Arbib), The MIT Press, 2003 (2nd edition).

Selection of Scientific Awards

- 1975 He received the Winkler Medal from the Netherlands Association for Neurology for scientific contributions in the field of neurosciences.
- 1985 Elected member of the Royal Netherlands Academy of Arts and Sciences.
- 1990 "Lord Adrian" Lecturer at the 12th World Congress of Electroencephalography and Clinical Neurophysiology in Rio de Janeiro, Brazil.
- 1992 Honorary President of the VIIth European Congress of Clinical Neurophysiology, Budapest, Hungary.
- 1995 Honorary Life Member of The British Society for Clinical Neurophysiology (Formerly The EEG Society), London, United Kingdom.
- 1997 Doctor Honoris Causa of the University of Lisbon (Portugal).
- 1997 Special "Berger" Lecturer at the 14th International Congress of EEG and Clinical Neurophysiology in Florence, Italy.
- 1999 Recipient of the Herbert H. Jasper Award, selected by the American Clinical Neurophysiology Society for his "lifetime of outstanding contributions to the field of clinical neurophysiology.''
- 2000 Recipient of the 'Storm van Leeuwen/ Magnus Prize' of the Dutch Society of Clinical Neurophysiology.
- 2000 Honorary member of the Portuguese Society of Electroencephalography and Clinical Neurophysiology.
- 2002 Recipient of the Ragnar Granit Prize for his work on the field of Bioelectromagnetism.
- 2002 Doctor Honoris Causa of the University of Porto (Portugal).
- 2004 Recipient of the first Prize "Universidade de Coimbra" for a (sic) "person of Portuguese nationality who has made a particular relevant and innovative contribution in the fields of culture or science."

General Honors

- 2000 High Officer of the Order of Santiago da Espada, for outstanding achievements in the field of Science/Art/Literature, awarded by the President of the Republic of Portugal.
- 2001 Knight of the Order of the 'Nederlandse Leeuw' awarded by the Queen of the Netherlands in appreciation for his achievements in science.

FROM THE BENCH TO THE BEDSIDE

The Role of Semantics in Enabling the Vision of Translational Medicine

Vipul Kashyap
Partners HealthCare System, Clinical Informatics R&D, USA

Abstract: Biomedical research and healthcare clinical transactions are generating huge volumes of data and information. At the same time, the results of biomedical research in the form of new molecular diagnostic tests and therapies are being increasingly used in the context of clinical practice. There is a critical need to speed "translation" of genomic research insights into clinical research and practice. In this talk, we will discuss challenges faced by a healthcare enterprise in realizing the vision of Translational Medicine, such as:

- The need to create structured and semantic representations of genotypic and phenotypic data such as clinical observations and molecular diagnostic tests.
- The need for cost-effective and incremental data integration for combining genotypic and phenotypic information at the point of care.
- The need for actionable decision support for suggesting molecular diagnostic tests and therapies in the context of clinical care.
- The need for knowledge update, propagation and consistency to keep abreast of the rapid pace of knowledge discovery being witnessed in the life sciences, a crucial pre-requisite to reduce the cost of knowledge acquisition and maintenance.

Semantics-based approaches to address the above-mentioned challenges, including the applicability of semantic web standard (RDF, OWL, Rules); and issues related to the value proposition of these technologies will be presented.

BRIEF BIOGRAPHY

Vipul Kashyap, PhD is a Senior Medical Informatician in the Clinical Informatics Research & Development group at Partners HealthCare System and is currently the chief architect of a Knowledge Management Platform that enables browsing, retrieval, aggregation, analysis and management of clinical knowledge across the Partners Healthcare System. Vipul received his PhD from the Department of Computer Science at Rutgers University in New Brunswick in the area of metadata and semantics-based knowledge and information management. He is also interested in characterization of the value proposition of semantic technologies in the enterprise context. Before coming to Partners, Vipul has held positions at MCC, Telcordia (Bellcore) and was a fellow at the National Library of Medicine. Vipul has published 2 books on the topic of Semantics, 40-50 articles in prestigious conferences and journals; and has participated in panels and presented tutorials on the topic of semantic technologies. Vipul sits on the technical advisory board of an early stage company developing semantics-based products, and represents Partners on the W3C advisory committee and the HealthCare Information Technology Standards Panel (HITSP).

THE CANCER INFORMATICS ECOSYSTEM

A Case Study in the Accretion of Federated Systems based on Service Oriented Architectures, Semantic Integration and Computing Grids

David Hall
Research Triangle Institute in North Carolina, USA

Abstract: Information technology is playing an increasingly critical role in health and life sciences research due to the profound expansion in the scope of research projects in the post-genomic age. Robust data management and analysis systems are becoming essential enablers of these studies. Driven by funding agency requirements, funding opportunities, and grass roots organizing, efforts are underway to develop standards and technologies to promote large-scale integration of publicly-funded systems and databases including infrastructure developed for individual studies. Predicted benefits include an enhanced ability to conduct meta-analyses, an increase in the usable lifespan of data, a funding agency-wide reduction in the total cost of IT infrastructure, and an increased opportunity for the development of third party software tools. This presentation will critically examine efforts towards developing publicly-accessible interoperable and distributed production systems in the health and life sciences via ontologies, formal metadata, service oriented architectures, and grid computing models with a focus on several projects under the direction of the author in the area of cancer informatics.

BRIEF BIOGRAPHY

David Hall is a Senior Software Project Leader at RTI International based in North Carolina, USA. He leads teams of up to 30 developers implementing computer systems that support large biomedical and biotechnological research enterprises in cancer research, drug discovery, genetic epidemiology, and plant biotechnology. His area of interest is the practical application of bioinformatics and medical informatics methods, technologies, and standards in the development of production software. Particular topics of interest include data visualization, semantic integration, systems integration, and high performance computing. Recent clients include the US National Institutes of Health, GlaxoSmithKline, Syngenta, and Duke University. Data systems developed by David's group manage clinical and research data for nearly one million patients. Applications include data warehouses, metadata registries, workflow systems, high resolution image databases, analytical applications, and web services. David is currently Principal Investigator of the Informatics Support Center for the National Cancer Institute's Breast and Colon Cancer Family Registries. He holds a Ph.D. in Genetics from the University of Georgia and a B.S. in Computer Science from Wake Forest University.

ICT AND PERSONS WITH DISABILITIES
The Solution or the Problem?

Albert M. Cook
Faculty of Rehabilitation Medicine, University of Alberta, Edmonton Alberta, Canada
al.cook@ualberta.ca

Keywords: Assistive technologies, information and computer technologies, persons with disabilities.

Abstract: In order to lead full and productive lives, persons with disabilities need to have the same access to information and communication systems as the rest of the population. Advances in information and communication technologies (ICT) are occurring quickly, and the capability of technologies to meet the needs of persons with disabilities is growing daily. Future developments in assistive technologies (AT) and the successful application of these technologies to meet the needs of people who have disabilities are dependent on exploitation of these ICT advances. AT also involves the development of specialized interfaces such as the brain computer interface (BCI), adaptive interfaces that accommodate for changes in the user's physical skills, cognitive interfaces that allow understanding of the human technology interface by individuals with intellectual disabilities and systems that accommodate for user needs based on environmental sensing (e.g., GPS interfaces) and downloading of profiles to meet specific user needs. Universal Design (or design for all) calls for the design of products and environments to be usable by all people, to the greatest extent possible, without the need for adaptation or specialized design. In the physical world this often means ramps, curb cuts and other adaptations to the built environment to accommodate individuals who have disabilities. In the ICT world the barriers to access are technological, and the goal for ICT universal design is to have an environment with enough embedded intelligence to be easily adaptable to the varying cognitive, physical and sensory skills of a wide range of individual's in order to meet their productivity, leisure and self care needs. If ICT advances are not adaptable enough to be accessible to persons with disabilities it will further increase the disparity between those individuals and the rest of the population leading to further isolation and economic disadvantage. On the other hand, availability of these technologies in a transparent way will contribute to full inclusion of individuals who have disabilities in the mainstream of society.

BRIEF BIOGRAPHY

Dr. Albert Cook is Professor of Speech Pathology and Audiology and currently Dean of the Faculty of Rehabilitation Medicine and Chair of the Health Sciences Council at the University of Alberta. Dr. Cook has worked with interdisciplinary teams to develop assistive devices and to assess the effectiveness of technology being used by persons with disabilities. Dr. Cook is also associated with the I CAN Centre the Glenrose Rehabilitation Hospital. He was formerly Professor of Biomedical Engineering at California State University, Sacramento where he established the graduate program in biomedical engineering and directed it for 12 years. He also served as Co-Director of the Assistive Device Center in Sacramento, California, helping over 500 persons with disabilities to identify and obtain assistive technologies.

He received his Bachelor of Science in Electrical Engineering at the University of Colorado, a Masters in Bioengineering and his doctorate from the University of Wyoming He is a member of Tau Beta Pi, Phi Kappa Phi and Gold Key honorary societies.

Dr. Cook co-authored with Janice Polgar, OTR, Cook and Hussey's Assistive Technologies: Principles and Practice 3nd edition, published in October 2007 by Elsevier. He has co-edited three other textbooks with John Webster and others and has written numerous chapters in rehabilitation and biomedical engineering texts and monographs.

Dr. Cook's research interests include augmentative and alternative communication, biomedical instrumentation and assistive technology design, development and evaluation. His most recent

research has focussed on the use of robotics with young children who have severe disabilities to develop and assess cognitive and linguistic skills. He has US and foreign patents and numerous publications and conference presentations in these areas. He has been principal investigator on research and training grants in augmentative communication, assistive technologies and biomedical engineering.
Dr. Cook is Past-President and Fellow of RESNA, a major professional society for assistive technology practitioners in North America. He has also served in national united States positions in the Institute of Electrical and Electronic Engineers Engineering in Medicine and Biology Society, the American Society for Engineering Education, the Biomedical Engineering Society, the International Society for Augmentative and Alternative Communication and the Association for the Advancement of Medical Instrumentation. Dr. Cook is a registered professional engineer (electrical) in California.

1 ICT AND PERSONS WITH DISABILITIES TECHNOLOGY AND PROGRESS

Societal Progress requires change much of which is accomplished through advances in technology. In his book, *A Short History of Progress*, Ronald Wright *(*2004) points out that this characteristic has been true for millions of years as societies have advanced through greater utilization of technology.

Wright goes on to describe the problems that technology typically creates such as over consumption, environmental ruin, and separation of classes. These problems are amplified for people who have disabilities, and they lead to a gap in the access to work, self care and community participation for persons with disabilities compared to the general population. Since people with disabilities often depend on technologies for societal participation, the lack of availability of accessible technology or the obsolescence of accessible technologies isolates them further. This is an extension of the concept of the "digital divide" that separates people along socioeconomic lines based on their access to ICT. I refer to it as the "disability gap".

2 ADVANCES IN INFORMATION AND COMMUNICATION TECHNOLOGIES (ICT)

The 21st Century is characterized by a continuous move from a machine-based to a knowledge based economy (Ungson & Trudel, 1999). In this shift, the basis of competence is changing to knowledge skills from machine skills. Information currently amounts to 75% of value added to products This will continually increase, and connectivity will be the key to business success. There is also a move from a regional or national scope of business influence to a global scope, in which virtual networks dictate organizational structures.

Key players in business development are becoming communication suppliers with the move from host-based to network based systems. Telephone, cable TV and internet service providers control commercial growth. Along with these changes networks will become more graphically-based moving increasingly from text-based systems. In order to lead full and productive lives, persons with disabilities need to have the same access to this new information and communication system as the rest of the population.

2.1 What Can we Expect from Technology in the Next 20 Years?

The cost of information technology is continually dropping for comparable or increased computing power and speed. There is also a greater understanding of the biological/physical interface for the control of computers. The human computer interface (HCI) is being developed to be more human-like, more user oriented and more intelligent-providing additional capabilities for searching, processing and evaluating information.

There are a number of changes that are likely to occur over the next few years (Applewhite, 2004). There will be an increase in automated transactions between individuals and organizations enabling people to complete all transactions without face-toface interactions. It is expected that we will achieve equalized access to the web and information between the developed and developing world. Embedded systems will dramatically increase with application such as "intelligence in the doorknob" that recognizes the owner and doesn't require key manipulation. We are likely to see much greater

understanding of the biological to physical interface for the control of computers.

2.2 Changes in Mainstream Tech with AT Implications

There are many examples of emerging mainstream technologies with potential for assisting people with disabilities to access ICT systems. A few of these are described in this section.

Display-based assistive technologies present an array of choices for a user to select from (Cook & Polgar, 2007). This often referred to as scanning since the choices are highlighted sequentially and then chosen using some sort of gross movement. One of the problems associated with this approach is that there must be a physical display for making selections. This often requires the overall system to be larger and more bulky or places a display between a user and a communication partner. A new development is a direct retinal display that creates image that overlays view of real object (Lewis, 2004). The retinal display is low powered because it is shined on retina directly. Scanning light into the eye allows the image to overlay an object such as a communication partner's face-enabling eye contact and small size. The scanning array could be the retinal image, since display scans across the retina power levels can be kept low kept low for safety.

Another development is 3-D displays that create a more intuitive view of objects, events and activities (Lewis, 2004). This type of display may be helpful to individuals who have cognitive disabilities. It might also create new challenges for individuals with visual limitations.

Embedded automatic speech recognition is being developed for PDAs because of the need for keyboards with more and more functions and the limitations of very small keyboards (Kumagai, 2004). This feature could be very useful to reduce individuals who have limited hand function or for those who cannot see the keyboard to make entries.

3 MEETING THE ICT NEEDS OF PERSONS WITH DISABILITIES

Over the centuries, our ability to make tools is what distinguishes us as human, but our tools ultimately control us by making us dependent on them (Wright, 2004). This dependence is less optional for people who have disabilities

3.1 Impact of Technology Advances on People who have Disabilities

Technology advances increase the gap between people who have disabilities and those who don't (Wright, 2004). All societies become hierarchical with an upward concentration of wealth (including aggregations of technology tools) that ensures that "there can never be enough to go around", and this disparity contributes to the "digital divide" and the "disability gap". As advances occur more quickly, the gap widens faster and the people who are poor and/or disabled loose out even more completely and faster. This is a characteristic of cultural and societal "progress" over centuries-technology drives change, and creates both positive and negative outcomes in the process

The prognosis is not good for people with disabilities unless there is considerable effort to keep them connected to ICT and thereby to commerce, employment and personal achievement. There two fundamental approaches to this problem (1) make mainstream technologies accessible to people who have disabilities, or (2) design special purpose technologies specifically for people with disabilities. The former approach is referred to as *universal design* or *design for all*. The second approach utilizes *assistive technologies*.

3.2 Implications for Assistive Technologies

Access to ICT for people with disabilities is a significant global problem, and it has major implications for assistive technologies. There is a constant challenge to keep ICT systems accessible to persons who have disabilities as mainstream advances occur and adaptations become potentially incompatible with the new systems. Communication technologies change rapidly, and each change may result in the need to re-design accessible interfaces. We are closer to goal of having assistive technology adaptations available when the mainstream consumer product ships, but there are still many problems with "workarounds" necessary to make mainstream operating system, productivity software and internet access accessible to people with disabilities.

Development and maintenance of access to ICT must be driven by the needs of people with disabilities. Developments which broaden the scope, applicability and usability of the human technology

interface will be driven, at least in part by the needs of people who have disabilities.

The Internet (e-mail and chat rooms) have the advantage of anonymity, and this can be a major benefit to individuals who have disabilities. Because the person's disability is not immediately visible, people who have disabilities report that they enjoy establishing relationships with people who experience them first as a person and then learn of their disability. For example, Blackstone, (1996) describes some of the advantages of e-mail for individuals who have disabilities. Since the receiver of the message reads it at a later time composition can be at a slower speed. The person with a disability can communicate with another person without someone else being present, establishing a greater sense of privacy than situations in which an attendant is required. It is also possible to work form any location-avoiding some transportation problems

3.3 Universal Design

Increasingly, commercial products are being designed to be usable by all people, to the greatest extent possible, without the need for adaptation or specialized design (NC State University, The Center for Universal Design, 1997).

3.3.1 General Principles of Universal Design

Features are built into products to make them more useful to persons who have disabilities (e.g., larger knobs; a variety of display options--visual, tactile, auditory; alternatives to reading text--icons, pictures) are built into the product. This is much less expensive than modifying a product after production to meet the needs of a person with a disability. The North Carolina State University Center for Universal Design, in conjunction with advocates of universal design, have compiled a set of principles of universal design, shown in Box 1. This center also maintains a Web site on universal design (www.design.ncsu.edu/cud).

3.3.2 Universal Design for ICT

In universal design for ICT the barriers are technological rather than political and economic barriers that characterize architectural and commercial product design (Emiliani, 2006). The goal of universal design for ICT is to have an environment with enough embedded intelligence to be easily adaptable. The features of future information services are that there will be no clearly predefined service and little distinction between interpersonal communication and access to information. Services will need to be highly interactive, inherently multimedia, sensory multimodal (i.e., access via auditory or visual means is equally possible). To achieve this cooperation between users or representatives of users is critical in a variety of contexts of use. The overall goal is to have access to information involving communities of users with a wide range of motor, sensory and cognitive skills.

ONE: EQUITABLE USE
The design is useful and marketable to people with diverse abilities.
TWO: FLEXIBILITY IN USE
The design accommodates a wide range of individual preferences and abilities.
THREE: SIMPLE AND INTUITIVE USE
Use of the design is easy to understand, regardless of the user's experience, knowledge, language skills, or current concentration level.
FOUR: PERCEPTIBLE INFORMATION
The design communicates necessary information effectively to the user, regardless of ambient conditions or the user's sensory abilities.
FIVE: TOLERANCE FOR ERROR
The design minimizes hazards and the adverse consequences of accidental or unintended actions.
SIX: LOW PHYSICAL EFFORT
The design can be used efficiently and comfortably and with a minimum of fatigue.
SEVEN: SIZE AND SPACE FOR APPROACH AND USE
Appropriate size and space is provided for approach, reach, manipulation, and use regardless of user's body size, posture, or mobility.

Box 1: Principles of Universal Design From North Carolina State University, The Center for. Universal Design, 1997.

In addition to Universal Design for ICT, access to capabilities of mainstream technologies includes individualized assistive technologies that are easily – customized. This in return requires an increased understanding of the biological/physical interface for the control of assistive technologies and expanded availability of embedded systems networks.

3.4 A Working Definition of Assistive Technologies

The *International Classification of Functioning, Disability and* Health (ICF) is a system developed by the World Health Organization (WHO) that is designed to describe and classify health and health related states. These two domains are described by

body factors (body structures and functions) and individual and societal elements (activities and participation) (WHO, 2001). The ICF recognizes two contextual factors that modify health and health related states: the environment and personal factors (WHO, 2001). Environmental elements include assistive technologies in relation to activities of daily living, mobility, communication, religion and spirituality as well as in specific contexts such as education, employment and culture, recreation and sport (WHO, 2001). Other environmental elements such as access to public and private buildings, and the natural and built outdoor environments, also have implications for assistive technologies.

A commonly used definition of assistive technology is from the Technical Assistance to the States Act in the United States (Public Law (PL) 100-407): ***Any item, piece of equipment or product system whether acquired commercially off the shelf, modified, or customized that is used to increase, maintain or improve functional capabilities of individuals with disabilities.***

3.4.1 Hard and Soft Technologies

Odor (1984) has distinguished between hard technologies and soft technologies. Hard technologies are readily available components that can be purchased and assembled into assistive technology systems. The main distinguishing feature of hard technologies is that they are tangible. On the other hand, soft technologies are the human areas of decision making, strategies, training, concept formation, and service delivery as described earlier in this chapter. Soft technologies are generally captured in one of three forms: (1) people, (2) written, and (3) computer (Bailey, 1997). These aspects of technology, without which the hard technology cannot be successful, are much harder to obtain. Soft technologies are difficult to acquire because they are highly dependent on human knowledge rather than tangible objects. This knowledge is obtained slowly through formal training, experience, and textbooks such as this one. The development of effective strategies of use also has a major effect on assistive technology system success. Initially the formulation of these strategies may rely heavily on the knowledge, experience, and ingenuity of the assistive technology practitioner. With growing experience, the assistive technology user originates strategies that facilitate successful device use. There is a false belief that progress is solely driven by "hard" technological change The gap between the general public and persons with disabilities can only be closed by gains in both soft and hard technologies

3.4.2 Mainstream Technologies to Specially Designed Technologies: A Range of Options

As illustrated in Figure 1, the needs of people with disabilities can be met in a number of ways. Off the shelf "standard" (i.e., mainstream technologies) commercially available devices (especially those designed using the principles of universal design) can often be used by people with a variety of disabilities. For example, standard personal computers designed for the general population are often used by persons with disabilities. Sometimes these need to be modified however, to make them useable. Another type of commercially available device is one that is mass-produced but specifically designed for individuals with disabilities *(special commercially available devices)*. These devices often need to be modified to meet the needs of a specific individual. Our goal is to reduce the amount of modification necessary and to make mainstream technologies as accessible as possible. However, there will always be a portion of the disabled population that will require specifically designed assistive technologies.

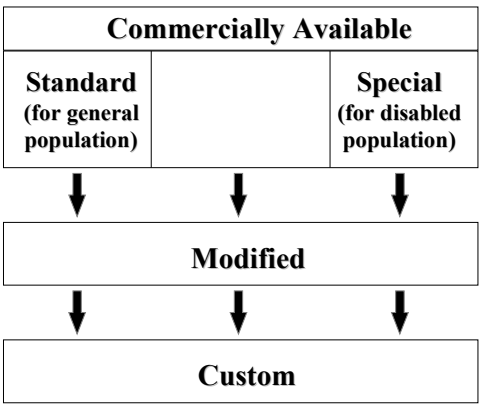

Figure 1: This diagram shows the progression from commercially available devices for the general population and commercially available devices for special populations to modified devices and custom devices. From Cook and Polgar, (2007).

3.5 The Human Technology Interface for ICT

3.5.1 General Concepts

It is estimated that as many as 40 million persons in the United States alone have physical, cognitive, or sensory disabilities (Lazzaro, 1999). The world-wide impact is significantly larger. If these people are to compete on an equal basis with non-disabled individuals, then it is extremely important that the internet be accessible to all. As the internet becomes more and more dependent on multimedia representations involving complex graphics, animation, and audible sources of information, the challenges for people who have disabilities increase. In order for access to the Internet to be useful to people with disabilities, the accessibility approach must be independent of individual devices. This means that users must be able to interact with a *user agent* (and the document it renders) using the input and output devices of their choice based on their specific needs. A **user agent** is defined as software to access Web content (www.w3.org/wai). This includes desktop graphical browsers, text and voice browsers, mobile phones, multimedia players, and software assistive technologies (e.g., screen readers, magnifiers) that are used with browsers. The person with a disability interacts with technology through the Human Technology Interface (HTI) (Cook and Polgar, 2007).

The graphical user interface (GUI) has both positive and negative implications for persons with disabilities. The positive features are those that apply to non-disabled users (e.g., use of icons, recognition rather than recall memory, screen icons for the same task look the same, operations such as opening and closing files are always the same). The GUI is the standard user interface because of its ease of operation for novices and its consistency of operation for experts. The latter ensures that every application behaves in basically the same way. People with motor disabilities may not have the necessary physical (eye-hand coordination) and visual skills to navigate the GUI. Modification of the GUI to allow specialized access (see Figure 1) can also be more challenging for GUI-based operating systems.

As networks are expanded and more devices (e.g., cell phones, PDAs) have open architectures, it will be possible to download profiles, adaptations and special instructions that enable adaptable systems to be developed to meet the needs of people who have disabilities. Some examples are (1) trainable hearing aids that adjust automatically to the environments in which they are used; (2) a "Smart House" that assesses occupants current state and the state of various home utilities to aid with common activities of daily living, provides feedback should residents become disoriented or confused and report medical emergencies automatically; an orientation and direction finding device that senses the current location (via GPS) and gives directions to a desired location for individuals who cannot read maps because of visual or cognitive disabilities.

3.5.2 Access for Motor Impairment

There are a significant number of people who cannot effectively use standard keyboards, mouse controls or switches. It is likely that we will see a much greater understanding of the biological/physical interface for the control of computers in the future (Applewhite, 2004).

One approach that may offer promise is the brain computer interface (BCI). BCI systems may be grouped into a set of functional components including the input device, amplification, feature extraction, feature translation and user feedback (Mason and Birch, 2003). Signals are mathematically analyzed to extract features useful for control (Fabiani, Mcfarland, Walla, and Pfurtscheller 2004). Features or signals that have been used include slow cortical potentials, P300 evoked potential, sensorimotor rhythms recorded from the cortex and neuronal action potentials recorded within the cortex). A typical task for a user is to visualize different movements or sensations or images.

Another approach to cursor control is the use of a digital camera and image recognition software to track a particular body feature to control an on-screen mouse cursor (Betke, Gips and Fleming, 2002). The most easily tracked feature is the tip of the nose, but the eye (gross eye position not point of gaze), lip, chin and thumb have also been used. Non-disabled subjects used this approach and fund that the camera mouse was accurate but slower than a typical hand-controlled mouse. Using an on-screen keyboard the camera mouse was half as fast as a regular mouse in a typing task, but the accuracy obtained was equivalent on each system. More and more computers have built-in cameras, so the camera mouse requires only software to capture the body feature image and interpret its movement as mouse commands. This may lead to wider application of this technique.

There are many other approaches that are used to provide access to and control over technologies for people with severe motor disabilities (Cook and Polgar, 2007) \. These range form keyboards of various type, to automatic speech recognition to mouse and mouse emulators systems to single and multiple switches.

3.5.3 Access for Cognitive Impairment

Cognitive disabilities include a wide range of skills and deficiencies. Learning disabilities typically involve significant difficulties in understanding or in using either spoken or written language, and these difficulties may be evident in problems with reading, writing, mathematical manipulation, listening, spelling or speaking (Edyburn, 2005). These limitations make it increasingly difficult to access complicated Web sites that may include flashing pictures, complicated charts, and large amounts of audio and video data. While there are assistive technologies that are specifically designed to address these areas (discussed later in this chapter), many of the technological tools are useful for all students, and are part of instructional technology (Ashton, 2005). Even the so-called assistive technologies have features (e.g., multimedia, synthetic speech output, voice recognition input) that are useful to all learners.

For individuals with acquired cognitive disabilities due to injury (e.g., traumatic brain injury) or disease (e.g., stroke (CVA) or dementia) changing features such as font size, background/ foreground color combinations, contrast, spacing between words, letters and paragraphs and using graphics can all improve access to screen-based information. Another technological concept for these individuals is a cognitive prosthesis, which is a custom-designed computer-based compensatory strategy that directly assists in performing daily activities[1]. It may also include additional technologies such as a cell phone, pager, digital camera or low tech approaches

Persons with intellectual disabilities have difficulties with memory, language use and communication, abstract conceptualization, generalization and problem identification/problem solving. Characteristics of the HTI that are important for these individuals include simplicity of operation, capacity of the technology to support repetition, consistency in presentation, and inclusion of multiple modalities (e.g., speech, sounds and graphical representations) (Wehmeyer, Smith and Davies, 2005).

An example of technology designed for cognitive needs is the Planning and Execution Assistant and Trainer (PEAT). It is a PDA-based personal planning assistant designed to assist individuals with cognitive disorders due to brain injury, stroke, Alzheimer's disease, and similar conditions (Levinson, 1997). PEAT employs artificial intelligence to automatically generate plans and also to revise those plans when unexpected events occur. PEAT uses a combination of manually entered schedules and a library of stored scripts describing activities of daily living (e.g., morning routine or shopping). Scripts can be used for both planning and for execution. Planning involves a simulation of the activity with key decision points presented and prompts (auditory and visual) supplied necessary to aid the individual through the planning process. The plan to be executed can be either the stored script or a modified script based on the simulation. The PEAT artificial intelligence software generates the best strategy to execute the required steps in the plan (LoPresti, Mihailidis, and Kirsch, 2004). PEAT also automatically monitors performance, and corrects schedule problems when necessary.

3.5.4 Access for Auditory Impairment

Since web pages are a mixture of text, graphics, and sound, people who are deaf may be prevented from accessing some information unless alternative methods are available. The primary approach for thee individual is the use of the Microsoft Synchronized Accessible Media Interchange (SAMI), which allows authors of Web pages and multimedia software to add closed captioning for users who are deaf or hard of hearing. This approach is similar to the use of closed captioning for television viewers. The W3C WAI SMIL (www.w3.org/WAI) is designed to facilitate multimedia presentations in which an author can describe the behavior of a multimedia presentation, associate hyperlinks with media objects, and describe the layout of the presentation on a screen

Trainable hearing aids adjust automatically to the environments in which they are used through access to embedded information networks. This allows automatic adaptation to changing noise levels and environments.

[1] Institute for Cognitive Prosthetics, http://www.brain-rehab.com/definecp.htm

3.5.5 Access for Visual Impairment

The W3C WAI user agent guidelines are based on several principles that are intended to improve the design of both types of user agents. The first is to ensure that the user interface is accessible. This means that the consumer using an adapted input system must have access to the functionality offered by the user agent through its user interface. Second, the user must have access to document content through the provision of control of the style (e.g., colors, fonts, speech rate, and speech volume) and format of a document. A third principle is that the user agent help orient the user to where he is in the document or series of documents. In addition to providing alternative representations of location in a document (e.g., how many links the document contains or the number of the current link), a well-designed navigation system that uses numerical position information allows the user to jump to a specific link. Finally, the guidelines call for the user agent to be designed following system standards and conventions. These are changing rapidly as development tools are improved.

Communication through standard interfaces is particularly important for graphical desktop user agents, which must make information available to assistive technologies. Technologies such as those produced by the W3C include built-in accessibility features that facilitate interoperability. The standards being developed by the W3C WAI provide guidance for the design of user agents that are consistent with these principles. The guidelines are available on the W3C WAI Web page (www.w3.org/wai).

3.5.6 Other ICT Access

Cellular telephones are becoming more powerful with capabilities approaching that of personal computers. This expanded capability will provide significant advantages for people with disabilities, especially those with low vision or blindness. describes Three changes will be particularly valuable to people who have disabilities:: (1) standard cell phones will have sufficient processing power for almost all the requirement of persons with visual impairments, (2) software will be able to be downloaded into these phones easily, (3) wireless connection to a worldwide network will provide a wide range of information and services in a highly mobile way (Fruchterman, 2003). Because many of these features will be built into standard cell phones the cost will be low and reachable by persons with disabilities. A major advance will occur if the cell phone industry moves away from proprietary software to an open source format providing the basis for a greater diversity of software for tasks such as text-to-speech output, voice recognition and optical character recognition in a variety of languages. Many applications for people with disabilities will be able to be downloaded from the internet. With expanded availability of embedded systems, it will be possible for a user to store their customized programs on the network and download them as needed form any remote location.

Downloading a talking book program into a cell phone can provide access to digital libraries for persons who are blind. Outputs in speech or enlarged visual displays can be added as needed by the user. With a built-in camera and network access a blind person could obtain a verbal description of a scene by linking to on-line volunteers who provide descriptions of images. These applications will depend on the increasing application of universal design in information technology products (Tobias, 2003). These applications include ATMs, cell phones, vending machines and other systems that are encountered on a daily basis (Tobias, 2003).

4 INFRASTRUCTURE FOR FUTURE ACCESSIBILITY

The infrastructure for future accessibility consists of: (1) an expanded, smarter and more available "real" and "virtual" internet, (2) Home automation systems that are smarter and have greater interconnectivity, (3) universal design principles that are applied more widely, (4) alternative approaches for accessing information technologies, and (5) special-purpose assistive technologies.

The Infrastructure for future accessibility will depend on several factors. These include: Web-based virtual systems, home automation, universal design for ICT, alternatives for accessing information technologies and special-purpose assistive technologies. In addition there is n on going need for the development of soft technology tools.

If ICT advances are not adaptable enough to be accessible to persons with disabilities it will further increase the disparity between those individuals and the rest of the population leading to further isolation and economic disadvantage. On the other hand, availability of these technologies in a transparent way will contribute to full inclusion of individuals who have disabilities in the mainstream of society.

5 CONCLUSIONS

The move to the information age offers great promise for persons with disabilities. It also holds great threats for persons with disabilities. Constant vigilance is required to insure that information technologies remain accessible and responsive to the needs of persons with disabilities. The future for persons with disabilities will not be driven by advances in technology, but rather by how well we can take advantage of those advances for the accomplishment of the many tasks of living that require technological assistance

6 SUMMARY

Anticipated changes in technologies coupled with the focus on the social aspects of disability, provide a significant opportunity for major advances in the degree to which individuals with disabilities can participate in all aspects of life, including work, school, leisure and self care.

Technological advances will be particularly important as the percentage of the population that is elderly rises. Concepts from universal design will be important in ensuring that this segment of the population remains active and is able to participate in society. This new group of elderly individuals will also be more experienced with computers and other technologies than their predecessors and they may well demand greater performance and adaptability from both assistive technologies and mainstream ICT (e.g., telephones, internet communication).

The percentage of individuals with long-term disabilities who join the over 65 age group will also increase. These individuals will have been long-term users of assistive technologies, and their experience will have major implications for developments to meet future needs.

While much of what I have described is conjecture, it is based on modest extrapolation from the current state of the art. There are some things that we know with a high degree of certainty. We know that computer systems will be faster, have more memory be smaller and be less expensive for the same or greater functionality. We also know that the communication channel bandwidth will continue to increase allowing much more information and much more sophisticated information processing. Finally, it is clear that people with disabilities will continue to assert their right to fully participate in society.

Technological advances also raise questions for people who have disabilities. The most important of these is whether accessibility will keep pace with technological developments. For example, will assistive technologies for input and output be compatible with the user agents and operating systems of tomorrow. A second major question is whether the needs of persons with disabilities will be a driving force in future technological developments. Will people who have disabilities have to adapt to the existing technologies based on characteristics for non-disabled people or will universal design become a greater reality? In the latter case, adaptations will become less important and accessibility will become the rule rather than the exception.

For people who have disabilities, there are significant implications of emerging information processing technologies. If not closely monitored, these could result in less rather than more access to the new information economy for persons with disabilities. Despite the wider use of universal design principles, there will still be a need for effective assistive technology design and application if individuals with disabilities are to realize the full potential of the new information age.

REFERENCES

Applewhite A: (2004). 40 years: the luminaries. *IEEE Spectrum,* 41(11), 37-58.

Ashton T.M. (2005). Students with learning disabilities using assistive technology in the inclusive classroom, pp. 229-238, in Edyburn D., Higgins K.. & Boone R. (eds.): *Handbook of Special Education Technology Research and Practice,* Whitefish Bay, Wisconsin: Knowledge by Design, Inc.

Bailey, R.W: (1996). *Human performance engineerin.,* ed 2, Upper Saddle River, NJ, , Prentice Hall.

Betke M., Gips J. & Fleming P: (2002). The camera mouse: Visual tracking of body features to provide computer access for people with severe disabilities. *IEEE Trans. Neural Systems and Rehabilitation Engineering,* 10(1): 1-10.

Blackstone S. (1996). The Internet: what's the big deal *Augment Commun News* 9(4):1-5.

Cook A.M. & Polgar J.M. (2007). *Cook and Husey's Assistive Technologies: Principles and Practice*, 3rd ed St. Louis: Elsevier.

Edyburn D.L. (2005). Assistive technology and students with mild disabilities: from consideration to outcome measurement, pp 239-270, in Edyburn D, Higgins K. & Boone R. (eds.): *Handbook of Special Education Technology Research and Practice,* Whitefish Bay, Wisconsin: Knowledge by Design, Inc.,

Emiliani, P.L. (2006). Assistive technology (AT) versus Mainstream Technology (MST): The research perspective. *Tech Disab*, 18, 19-29,

Fabiani G.E., Mcfarland D.J., Wolpaw J.R., & Pfurtscheller G (2004). Conversion of EEG activity into cursor movement by a brain-computer interface (BCI). *IEEE Trans. Neural Systems and Rehab Engr*, 12: 331-338.

Fruchterman J.R: (2003) In the palm of your hand: A vision of the future of technology for people with visual impairments. *J Vis Impair Blindness, 97*(10), 585-591.

Kumagai, J. (2004).Talk to the machine. *IEEE Spectrum,* 39(9): 60- 64.

Lazzaro J.L. (1999). Helping the web help the disabled, *IEEE Spectrum* 36(3): 54-59

Levinson R.L. (1997): The planning and execution assistant and trainer. *J. head trauma rehabilitation*, 12(2): 769-775.

Lewis, J.R. (2004). .In the eye of the beholder*, IEEE Spectrum,* 41(5)24- 28.

LoPresti E.F., Mihailidis A. & Kirsch N. (2004): Assistive technology for cognitive rehabilitation: State of the art. *Neuropsychological Rehabilitation,* 14(1): 5-39.

Mason S.G. & Birch G.E: (2003).A general framework for brain-computer interface design. *IEEE Trans. Neural Systems and Rehab Engr*, 11, 70-85.

Odor P. (1984): Hard and soft technology for education and communication for disabled people, *Proc Int Comp Conf*, Perth, Western Australia,

Tobias J: (2003). Information technology and universal design: An agenda for accessible technology. *J Vis Impair Blindness, 97*(10), 592-601.

Ungson G.R. and Trudel J.D. (1999). The emerging knowledge-based economy. *IEEE Spectrum*, 36(5):60-65.

Wehmeyer M.L., Smith S.J., Palmer SB, Davies D.K. & Stock S.E: (2004). Technology use and people with mental retardation. *International Review of Research in Mental Retardation,* 29: 291-337.

World Health Organization (2001): *International classification of functioning disability and health*-ICF, Geneva, World Health Organization

Wright, RA. (2004). *A Short History of Progress*, Toronto: Anansi Publications.

SHORT PAPERS

MODEL ORDER ESTIMATION FOR INDEPENDENT COMPONENT ANALYSIS OF EPOCHED EEG SIGNALS

Peter Mondrup Rasmussen, Morten Mørup, Lars Kai Hansen
Informatics and Mathematical Modelling, Technical University of Denmark
Richard Pedersens Plads, bld. 321, DK-2800 Kgs. Lyngby, Denmark
peter.mondrup@gmail.com, mm@imm.dtu.dk, lkh@imm.dtu.dk

Sidse M. Arnfred
Cognitive Research Unit, Department of Psychiatry, University Hospital of Copenhagen, Hvidovre
Brøndbyøstervej 160, DK-2605 Brøndby, Denmark
Sidse.Arnfred@hvh.regionh.dk

Keywords: EEG, Event related potentials, Independent component analysis (ICA), Molgedey Schuster, TDSEP, Model selection, Cross validation.

Abstract: In analysis of multi-channel event related EEG signals indepedent component analysis (ICA) has become a widely used tool to attempt to separate the data into neural activity, physiological and non-physiological artifacts. High density elctrode systems offer an opportunity to estimate a corresponding large number of independent components (ICs). However, too large a number of ICs leads to overfitting of the ICA model, which can have a major impact on the model validity. Consequently, finding the optimal number of components in the ICA model is an important problem. In this paper we present a method for model order selection, based on a probabilistic framework. The proposed method is a modification of the Molgedey Schuster (MS) algorithm to epoched, i.e. event related data. Thus, the contribution of the present paper can be summarized as follows: 1) We advocate MS as a low complexity ICA alternative for EEG. 2) We define an epoch based likelihood function for estimation of a principled unbiased 'test error'. 3) Based on the unbiased test error measure we perform model order selection for ICA of EEG. Applied to a 64 channel EEG data set we were able to determine an optimum order of the ICA model and to extract 22 ICs related to the neurophysiological stimulus responses as well as ICs related to physiological- and non-physiological noise. Furthermore, highly relevant high frequency response information was captured by the ICA model.

1 INTRODUCTION

The electroencephalogram (EEG) is a recording of electrophysiological brain activity and the major benefit of EEG relative to other brain imaging modalities is a high temporal resolution. The basic electrophysiology of the EEG signal implies that it may be modelled as a linear mixture of multiple sources of neural activity, non-brain physiological artifacts such as eye blinks, eye movements, and muscle activity, and non-physiological artifacts such as line noise, and electrode movement (Onton et al., 2006; Hesse and James, 2004). By electrical conductance these source signals instantaneously project to the scalp electrodes used for acquisition (Onton et al., 2006). Assuming linear addition of these relatively independent source signals at the scalp electrodes motivates the use of instantaneous independent component analysis (ICA) as a technique for extracting a set of underlying sources from the recorded EEG signals (James and Hesse, 2005; Makeig et al., 2002; Hyvarinen and Oja, 2000). The EEGLAB software is widely used for decomposing EEG using ICA (Delorme and Makeig, 2004). More accurate modeling of the signal component(s) including residual delayed correlations can be achieved using so-called convolutive ICA in a subspace of components extracted by the initial instantaneous ICA (Dyrholm et al., 2007).

Epochs extracted from an EEG experiment are described by the data matrix $X \in \mathbb{R}^{M \times N}$, where M is the number of electrode channels and N is the number of sampling time points. In the following N is the total time consisting of a certain number of epochs, i.e., individual experiment. The epochs may be separated by variable time intervals according to the specific experimental design. It is a specific point in the following, where we are going to invoke temporal correlation based models, that we do not compute temporal

correlations across epoch boundaries.

In general the ICA model can be written as

$$X = AS \qquad X_{n,t} = \sum_{k=1}^{K} A_{n,k} S_{k,t}, \qquad (1)$$

where $X_{n,t}$ is the signal at the $n'th$ sensor at $t'th$ time point and *K* is the number of sources or independent components (ICs). $A \in \mathbb{R}^{M \times K}$ is denoted the mixing matrix and $S \in \mathbb{R}^{K \times N}$ the source matrix. In this model the sources as well as the mixing coefficients are unknown. The random signal X is observed, and from this A and S are estimated. It is impossible to determine the variance (energy) of the sources, since any scalar multiplier in one of the sources could be cancelled by dividing the corresponding column in A with the same multiplier. Therefore, the sources are often assumed to have unit variance, which can be achieved by normalizing the source signals and multiply the corresponding column of the mixing matrix. Specifically, there is a sign ambiguity, if we change the sign of a source signal and change the sign of the corresponding column in the mixing matrix, the same reconstructed signal is obtained by multiplication. Finally, the ordering of components is arbitrary. We may order independent component according to variance of their contribution to the reconstructed signal.

The recovery of the mixing matrix and the sources is not possible from the covariance matrix alone, hence, by principal component analysis (PCA). Additional information is needed. ICA is often based on a non-Gaussianity assumption of the sources (Bell and Sejnowski, 1995) or by assumed differences in source auto-correlation (Molgedey and Schuster, 1994).

The number of EEG channels M may be different from the number of sources K, thus it is relevant to estimate K. Estimation of the correct number of sources can have a major impact on the validity of the ICA solution and prevents overfitting (James and Hesse, 2005). One approach to prevent overfitting is based on pre-processing by PCA, where the number of sources is determined by the number of dominant eigenvalues which account for a high proportion of the total variance in the data set. However this procedure has been criticized for sensitivity to noise (James and Hesse, 2005). Another approach is based on stepwise extraction of sources until a specified accuracy is achieved (James and Hesse, 2005). However this method is highly dependent on the choice of the accuracy level. In this paper we present a method for model order selection, based on a probabilistic framework. This approach was earlier proposed in a multimedia contexts (Kolenda et al., 2001). However, the approach requires large amount of memory for long signals and is inapplicable to EEG signals that are epoched due to temporal discontinuities where epochs are merged. Here we present a method that is customized to epoched data with the additional benefit of reducing the memory requirement. In our method PCA leads to a number of model hypotheses, of which an ICA model is estimated using a modified version of the Molgedey Schuster (MS) algorithm (Molgedey and Schuster, 1994). The MS algorithm is chosen because it is based on source autocorrelation, which is very relevant to EEG, and because of its relative low computational complexity. We take further advantage of the epoched nature of the signals, and split the data set into a training- and a test set. Model selection, i.e., estimating K, is then based on evaluating the likelihood of each model hypothesis using the test set in order to ensure generalization.

The paper is organized as follows. First we give a description of our method and we compare by simulation study the modified MS algorithm with the currently used ICA methods for EEG TDSEP (Ziehe et al., 2000) and infomax ICA (Bell and Sejnowski, 1995). We then test our model selection scheme within the simulated data and apply our method on real event related EEG data from an experiment involving visual stimulus.

2 METHODS

In the following, a description of PCA and the MS algorithm will be given. This is followed by a description of the probabilistic modelling. Finally the procedures for model order selection is presented.

2.1 PCA

Using PCA it is possible to reduce the dimensionality of the ICA model. In EEG $M \ll N$ which leads to the singular value decomposition (SVD) $X = UDV^T$, where $U \in \mathbb{R}^{M \times M}$, $D \in \mathbb{R}^{M \times N}$, and $V \in \mathbb{R}^{N \times N}$. By selecting the first K eigenvectors in U as a new basis, the signal space $\mathcal{S}$ is reduced to K dimensions. ICA is performed in $\mathcal{S}$, where A is the ICA basis projected onto the PCA subspace. The mixing matrix in the original vector space and the source signals are then given by

$$\tilde{A} = UA \qquad (2)$$

$$S = A^{-1} D V^T. \qquad (3)$$

The noise space $\mathcal{E}$ is spanned by the remaining $M-K$ eigenvectors.

2.2 Molgedey Schuster Separation

The Molgedey Schuster approach is based on the assumption that the autocorrelation functions of the independent sources are non-vanishing, and can be used if the source signals have different autocorrelation functions (Molgedey and Schuster, 1994; Hansen et al., 2000; Hansen et al., 2001). Time shifted data matrices X_τ and S_τ are defined followed by the definition of the cross-correlation function matrix for the mixture signals

$$C(\tau) \equiv \frac{1}{N_e} X_\tau X^T, \tag{4}$$

where $C \in \mathbb{R}^{M\times M}$ and N_e is the epoch length. For $\tau = 0$ the usual cross-correlation matrix is obtained. Due to the epoched nature of the signals $C(\tau)$ is estimated within each epoch and averaged, since the cross-correlation is not valid over epoch boundaries. Now we define the quotient matrix $Q(\tau) \equiv C(\tau)C(0)^{-1}$ which is rewritten, using the relation $X = AS$, as

$$\begin{aligned} Q(\tau) &= C(\tau)C(0)^{-1} \\ &= \frac{1}{N_e} X_\tau X^T (\frac{1}{N_e} X X^T)^{-1} \\ &= (AS_\tau)(AS)^T((AS)(AS)^T)^{-1} \\ &= AS_\tau S^T A^T A^{-T}(SS^T)^{-1}A^{-1} \\ &= AD(\tau)D(0)^{-1}A^{-1}, \end{aligned} \tag{5}$$

where $D(\tau) \equiv \frac{1}{N_e} S_\tau S^T$ in the limit $N_e \to \infty$ is the diagonal source cross-correlation matrix at lag τ. It is now seen, that the eigenvalue decomposition of the quotient matrix

$$Q\Phi = \Phi\Lambda \tag{6}$$

leads to $A = \Phi$ and $\Lambda = C(\tau)C(0)^{-1}$. τ is estimated as described in (Kolenda et al., 2001).

2.3 Probabilistic Modeling

The ICA model is defined in terms of the model parameters i.e. the mixing matrix A. Using Bayes theorem the probability of specific model parameters given the observed data $P(A|X)$ can be written as

$$P(A|X) = \frac{P(X|A)P(A)}{P(X)}, \tag{7}$$

where $P(X|A)$ is the likelihood function, and $P(A)$ is the prior probability of a specific model. This likelihood function is rewritten as

$$\begin{aligned} P(X|A) &= \int P(X,S|A)dS \\ &= \int P(X|S,A)P(S)dS \\ &= \int \delta(X - AS)P(S)dS \end{aligned} \tag{8}$$

Evaluating the integral in (8) gives

$$P(X|A) = P(A^{-1}X)\frac{1}{||A||}, \tag{9}$$

where $||A||$ is the absolute determinant of A.

In order to write the likelihood function we need the likelihood for the reduced signal space $\mathcal{S}$ as well as for the noise space $\mathcal{E}$. Since the sources are statistically independent we have $P(S) = \prod_{i=1}^{K} P(s_i)$, where s_i denotes the i'th source. If the sources are assumed stationary, independent, have zero mean, possess time-autocorrelation and are Gaussian distributed, then the source distribution is given by (Hansen et al., 2001; Hansen et al., 2000)

$$P(S) = \prod_{i=1}^{K} \frac{1}{\sqrt{|2\pi\Sigma_{s_i}|}} \exp\left(-\frac{1}{2} s_i^T \Sigma_{s_i}^{-1} s_i\right), \tag{10}$$

where $\Sigma_{s_i} = E[s_i s_i^T] = Toeplitz([\gamma_{s_i}(0), ..., \gamma_{s_i}(N_e - 1)])$ and γ_{s_i} are the source autocorrelation function values. The autocorrelation function values are estimated in each epoch and averaged. This estimate of the source distribution leads to a formulation of the likelihood for the signal space as

$$\begin{aligned} P(\mathcal{S}|A) = \prod_{i=1}^{K} \frac{1}{\sqrt{|2\pi\Sigma_{s_i}|}} \left(\frac{1}{||A||}\right)^{N_e} \\ \times \exp\left(-\frac{1}{2} s_i^{-1} \Sigma_{s_i}^T s_i)\right). \end{aligned} \tag{11}$$

The noise space $\mathcal{E}$ is assumed to be isotropic with noise variance $\sigma_\mathcal{E}^2 = (M-K)^{-1}\sum_{i=K+1}^{M} D_{ii}^2$. It can be shown (Kolenda et al., 2001; Minka, 2001) that

$$\begin{aligned} P(\mathcal{E}|\sigma_\mathcal{E}^2) = \left(2\pi\sigma_\mathcal{E}^2\right)^{-\frac{N_e(M-K)}{2}} \\ \times \exp\left(-\frac{N_e(M-K)}{2}\right). \end{aligned} \tag{12}$$

The signal and noise space are assumed independent which leads to the likelihood function

$$P(X|A) = P(\mathcal{S}|A)P(\mathcal{E}|\sigma_\mathcal{E}^2). \tag{13}$$

2.4 Model Order Selection

PCA reduction of dimensionality leads to a set of *M* model hypotheses. Since the data set consists of a

large number of epoch e.g. 105, we have the opportunity to split the data set into a training set $\mathcal{D}_{train}$ and a test set $\mathcal{D}_{test}$. Using $\mathcal{D}_{train}$ the model parameters A and Σ_{s_i} in (11) are estimated. The negative logarithm of the likelihood function (13) is then evaluated using $\mathcal{D}_{test}$, where (11) is rewritten as

$$-\log\left(P(\mathcal{S}|A)\right) = N_e \log(||A||) + \frac{1}{2}N_e + K\log(2\pi) + \frac{1}{2}\sum_{i=1}^{K}\log(\left|\Sigma_{s_{i,train}}\right|) + \frac{1}{2}\sum_{i=1}^{K} Tr(\Sigma_{s_{i,test}}\Sigma_{s_{i,train}}^{-1}), \quad (14)$$

where N_e is the number of samples in each epoch , $||A||$ is the absolute determinant of A estimated from $\mathcal{D}_{train}$, K is the dimension of $\mathcal{D}$ and $\Sigma_{s_{i,train}}$ and $\Sigma_{s_{i,test}}$ are estimated from $\mathcal{D}_{train}$ and $\mathcal{D}_{test}$ respectively. By observing (13) model order selection is performed by identifying the model order having minimal generalization error.

3 EXPERIMENTAL EVALUATION

Simulation experiments was conducted to investigate the performance of the MS algorithm and the test set procedure for model order selection. The data sets are constructed from three sources s_1, s_2, and s_3 which show bursts at frequencies of 14, 19, and 11 Hz respectively. The simulated source signal matrix S consist of 80 epochs of bursts with random intra epoch interval. A 50 Hz noise source s_4 is included after generation of the 80 epochs. Electrode signals are created by mixing the simulated source signals with a specified mixing matrix A, and Gaussian noise E is added to the electrode signals leading to a specic signal-to-noise ratio (SNR) (a description of noise generation is found in Appendix). Epochs are extracted from the mixed signals using EEGLAB (Delorme and Makeig, 2004).

3.1 Algorithm Performance Results

By PCA the dimensionality of the simulation was reduced to 4 dimensions, and the ICA model estimated by TDSEP, the infomax ICA implementation of EEGLAB, and our modified MS algorithm. To evaluate the separation performance of our algorithm, we use the correlation between original- and estimates sources as well as the source-to-interference ratio (SIR) (Fevotte et al., 2005; Vincent et al., 2006) measure

$$SIR = 10\log_{10}\frac{||s_{target}||^2}{||e_{interf}||^2}, \quad (15)$$

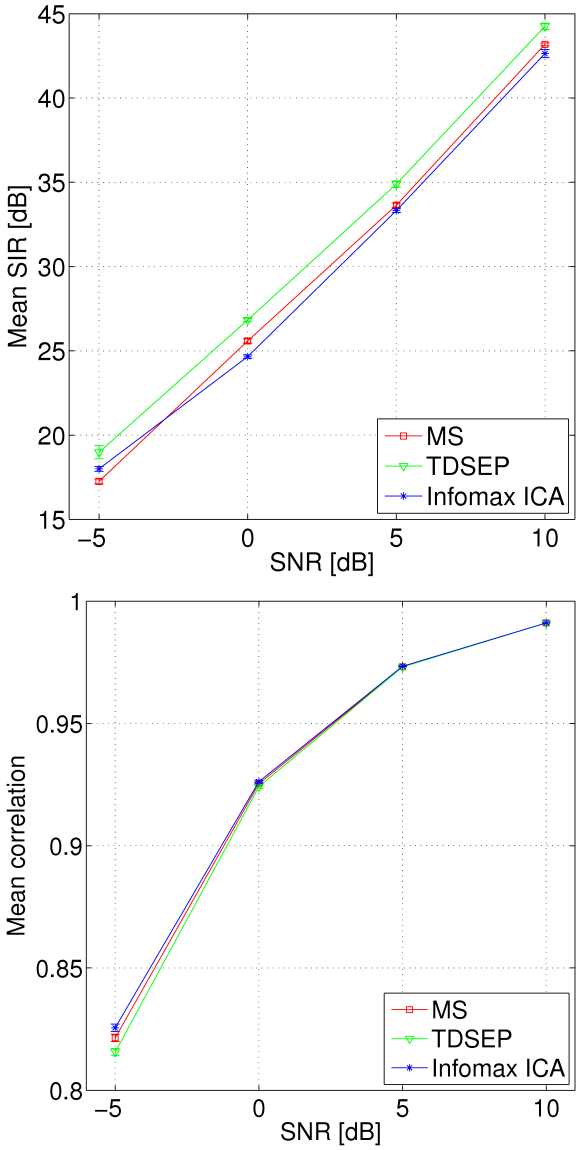

Figure 1: Simulation experiment. Results for source separation for TDSEP (Applied with default timelags 0,1), EEGLAB's implementation of infomax ICA, and our epoch modified MS algorithm. The simulation data is constructed from four signal sources mixed out in 32 channels, Gaussian noise is added. Dimensional reduction to four dimensions by PCA. Experiment repeated 10 times, error bars indicate three standard deviations of the mean. Top: Performance of source estimation measured in terms of mean SIR. Bottom: Performance measured in terms of mean correlation between true sources and estimates.

where s_{target} represents the target source or true source and e_{interf} represents interferences of unwanted sources. The SIR was calculated using the BSS_EVAL toolbox (Fevotte et al., 2005), where the performance measure is computed for each estimated source $\hat{s}_i$ by comparing it to the true source s_i and

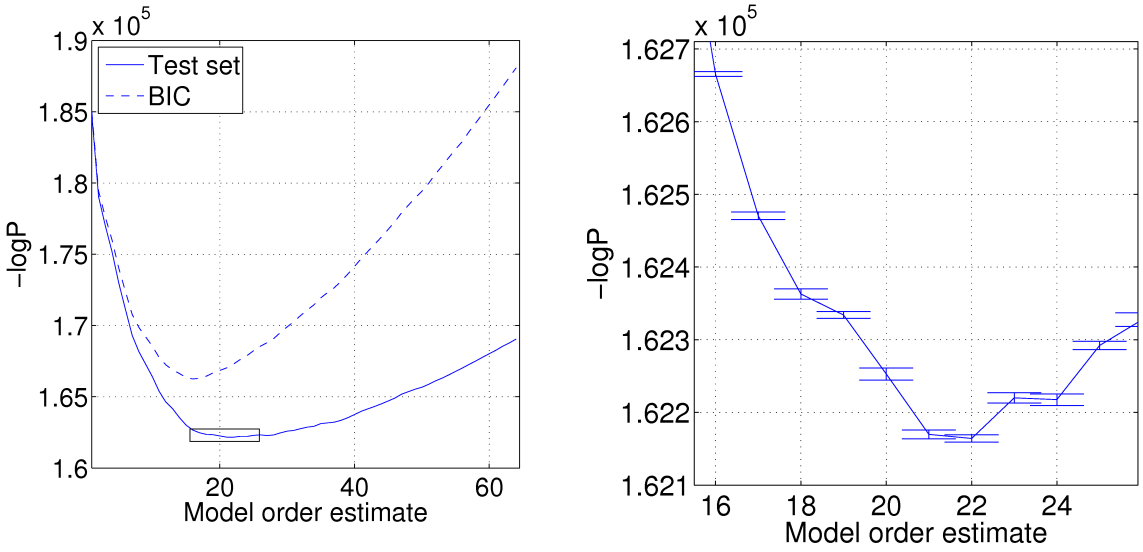

Figure 3: Left: Negative log likelihood for each of the 64 model hypotheses. Test set curve is averaged over 10 experiments, and minimum is found at 22 dimensions, suggesting an ICA model with 22 ICs. BIC is more conservative and estimates 16 ICs. Right: Zoom of the minimum region in the test set curve indicated by the box on left plot. Errorbars indicate three standard deviations of the mean.

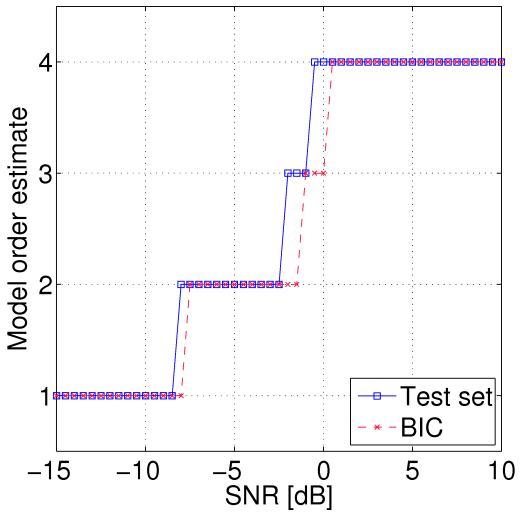

Figure 2: Simulation experiment. Results for model order selection for the test set procedure and for BIC estimation. The simulation is constructed from four signal sources mixed out in 32 channels, and Gaussian noise is added. BIC underestimates the number of sources at 0 dB whereas the test set procedure remains stable until -1 dB.

other unwanted sources $(s_j)_{j\neq i}$. In general SIR levels below 8-10 dB indicate failure in separation (Boscolo et al., 2004). Figure 1 shows that source estimates achieved with the modified MS algorithm are comparable with results from the alternative ICA algorithms. The MS algorithms has the advantages that it is fast compared to infomax ICA and TDSEP. Furthermore, there exists a heuristic for estimation of the time lag parameter τ.

3.2 Model Estimation

Model order selection is performed using the test set likelihood function (13) as evaluated using 10-fold cross-validation. Figure 2 shows model order estimates for a wide range of SNR. Here the proposed cross-validation procedure is compared to the Bayesian Information Criterion (BIC) (MacKay, 1992). The experiment indicates, that the cross-validation procedure is more robust than BIC estimation but it also has a tendency to underestimate the number of sources at low SNR.

4 APPLICATION ON EEG DATA SET

Our model selection procedure was applied on a data set from a visual stimulation experiment with experimental details described in (Mørup et al., 2006) and paradigm described in (Herrmann et al., 2004). EEG was recorded with 64 scalp electrodes arranged according the the International 10-10 system, sampling frequency 2048 Hz, band pass filter 0.1-760 Hz. Data

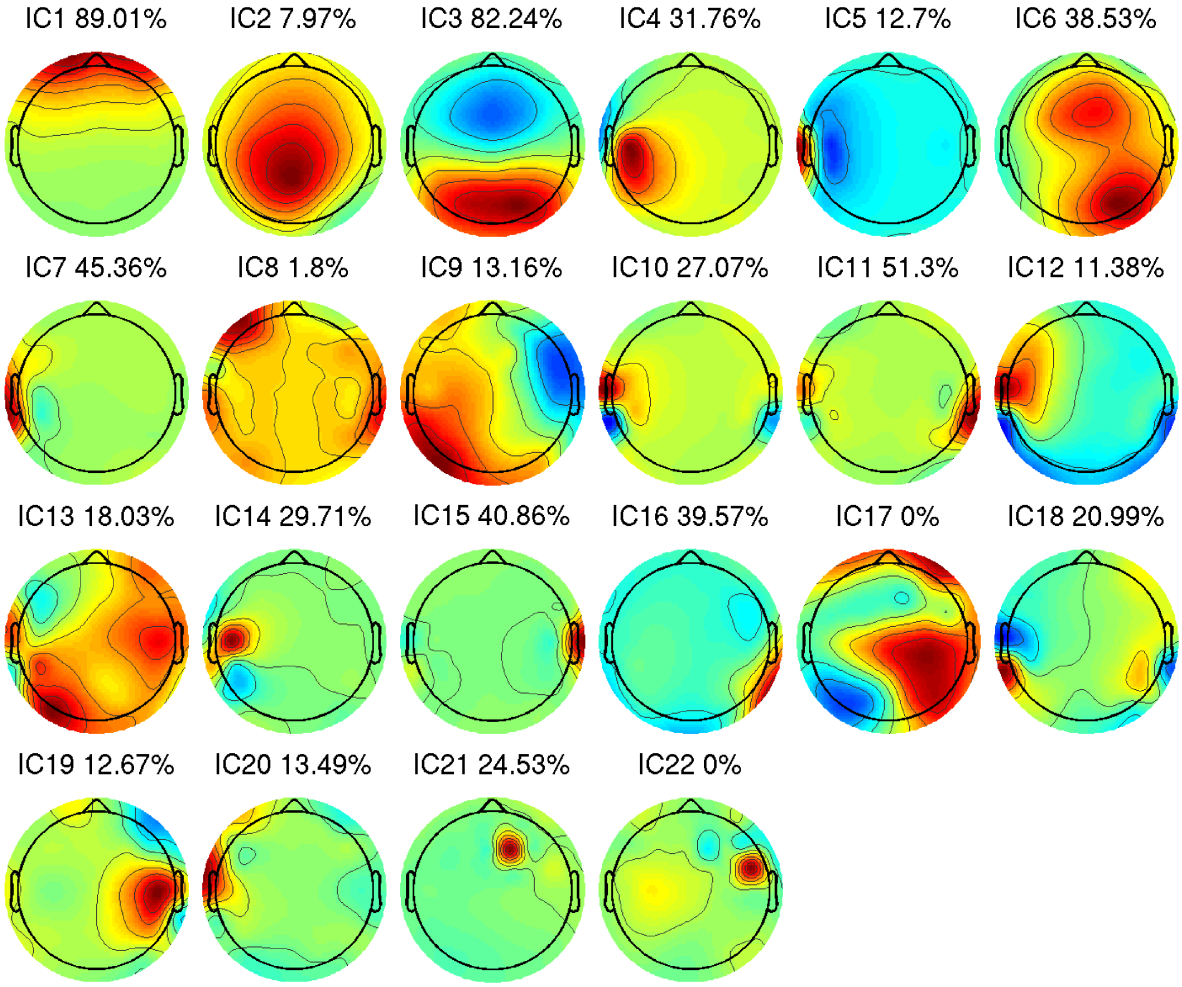

Figure 4: Interpolated scalp maps individually scaled to maximum absolute values. Dimensionality of the data from 64 scalp electrodes reduced to 22 by PCA. ICs estimated by MS algorithm, and components are sorted according to variance. The percentage at each IC indicates how much variation is explained by the respective IC of the average ERP at the electrode, where the respective IC project the strongest, calculated as $(||X_k||_F^2 - ||X_k - P_k||_F^2)/||X_k||_F^2$, where X_k is the ERP at electrode k and P_k is the projection ERP of the respective IC onto electrode k. Estimated ICs represents different types of sources, for example, IC1 reflects eye artifacts, IC2, IC3, IC4, IC6 reflect brain sources and IC21, IC22 reflect electrode noise.

was high pass filtered at 3 Hz in EEGLAB, and line noise removed using a maximum likelihood 50 Hz filter. The data were referenced to digitally linked earlobes, down sampled to 256 Hz and cut into 105 epochs (-500 to 1500 ms).

PCA leads to a set of 64 model hypotheses. For each hypothesis the negative logarithm of the likelihood function (13) was evaluated using 10-fold cross-validation. The experiment was repeated 10 times with different splits of training- and test sets. Figure 3 shows model order estimation by the test set procedure and BIC estimation.

According to model order estimation the dimensionality of the data set was reduced to 22 by PCA. ICs were estimated by the MS algorithm and sorted according to variance. Figure 4 shows all IC scalp maps. To categorize components each scalp map and averaged event related potentials (ERPs) were examined, where for example IC2, IC3, IC4 and IC6 reflect brain sources, IC1 reflects physiological eye artifacts, and IC21 and IC22 reflect electrode noise.

Further analysis of IC3 is performed by creating ERP images (Delorme and Makeig, 2004) as shown in Figure 5 top, from the PO4 electrode signal and IC3 projected onto electrode PO4. Generally the electrode signal has a larger amplitude than the projection of IC3, however, the major dynamics of the ERP seems to be captured by IC3. Another common analy-

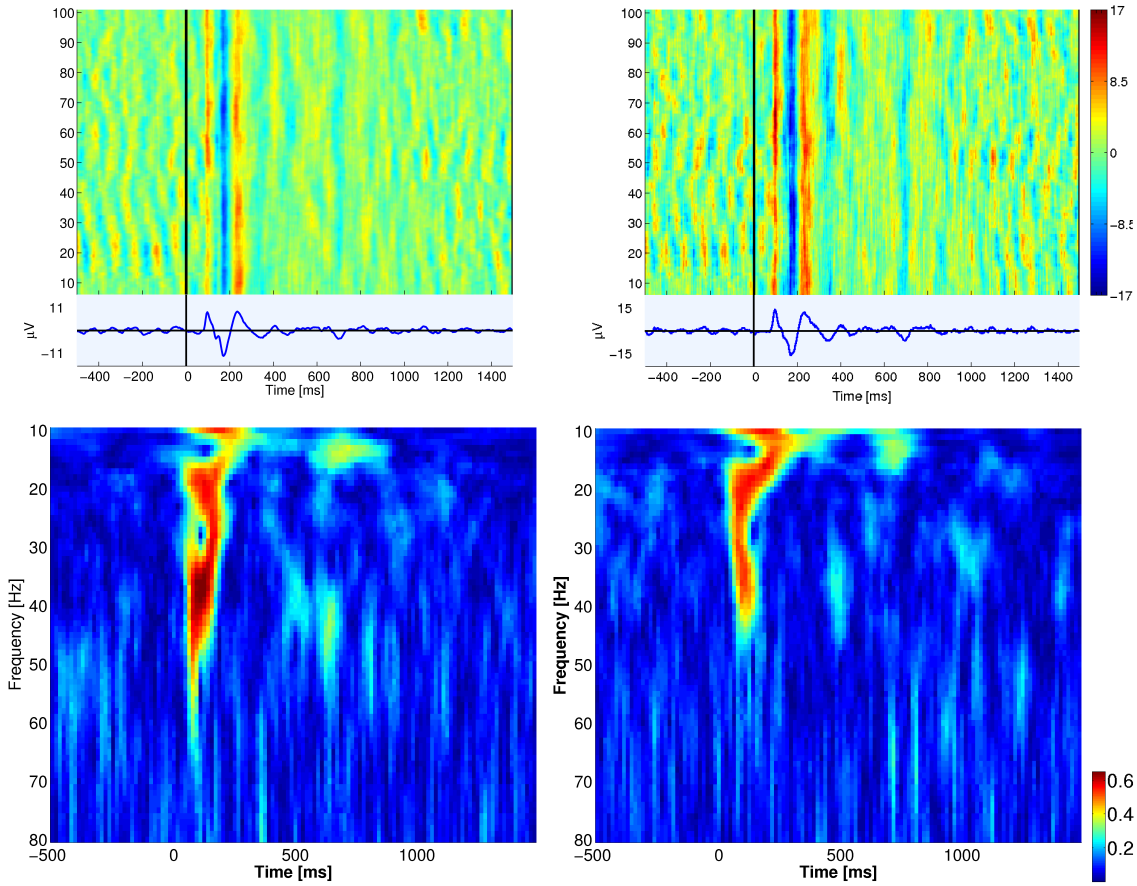

Figure 5: Top panel; ERP images, scaled to same color scale, epochs sorted by epoch number. Left; Image of IC3 projected onto electrode PO4. Right; Electrode signal at PO4. The electrode signal has a larger amplitude than the projection of IC3, however, the major dynamics of the ERP seems to be captured in IC3. Bottom panel; Time-frequency plots of the ITPC scaled to same color scale. Left; IC3 projected onto electrode PO4. Right; Electrode signal at PO4. IC3 reveals prominent evoked activity in the gamma band around 40 Hz compared to the raw electrode signal.

sis tool is time-frequency analysis of ERPs (Delorme and Makeig, 2004; Mørup et al., 2007), where different time-frequency measures exist. By ERPWAVELAB (Mørup et al., 2007) we wavelet transformed the data using the complex Morlet wavelet and calculated the inter-trial phase coherence (ITPC)

$$ITPC(c,f,t) = \frac{1}{N}\sum_{n=1}^{N}\frac{X(c,f,t,n)}{|X(c,f,t,n)|}, \qquad (16)$$

where $X(c,f,t,n)$ denotes the time-frequency coefficient at channel c, frequency f, time t and epoch n. ITPC measures phase consistency over epochs. Figure 5 bottom shows time-frequency plots of ITPC for the PO4 electrode signal and IC3 projected onto electrode PO4. It is evident that IC3 reveals prominent evoked activity in the gamma band around 40 Hz compared to the raw electrode signal. Gamma band activity is consistent with earlier findings (Mørup et al., 2006; Herrmann et al., 2004). Accordingly, relevant high frequency response information is captured in IC3, whereas noise contributions are isolated in other ICs.

5 CONCLUSIONS

Based on a probabilistic framework, we have formulated a cross-correlation procedure for ICA and a model order selection scheme applicable to epoched EEG signals. Our procedure is an extension of the Molgedey Schuster approach to ICA and utilizes the epoched nature of the signals. The approach is based on assuming source autocorrelation, which is very relevant to EEG. In our model selection procedure we split data into a training- and a test set to obtain an

unbiased measure of generalization. Based on the unbiased test error measure we perform model order selection for ICA of EEG. Applied to a 64 channel EEG data set we were able to determine the order of the ICA model and to extract 22 ICs related to the neurophysiological stimulus responses as well as ICs related to physiological- and non-physiological noise. Furthermore, relevant high frequency response information was captured by the ICA model. In this study we have applied our model selection procedure to EEG signals. However, our approach may also be applicable to other types of signals.

REFERENCES

Bell, A. and Sejnowski, T. (1995). Blind separation and blind deconvolution: an information-theoretic approach. *Acoustics, Speech, and Signal Processing, 1995. ICASSP-95., 1995 International Conference on*, 5:3415–3418.

Boscolo, R., Pan, H., and Roychowdhury, V. (2004). Independent component analysis based on nonparametric density estimation. *IEEE Transactions on Neural Networks*, 15(1):55–65.

Delorme, A. and Makeig, S. (2004). Eeglab: an open source toolbox for analysis of single-trial eeg dynamics including independent component analysis. *Journal of Neuroscience Methods*, 134(1):9–21.

Dyrholm, M., Makeig, S., and Hansen, L. K. (2007). Model selection for convolutive ica with an application to spatiotemporal analysis of eeg. *Neural Computation*, 19(4):934–955.

Fevotte, C., Gribonval, R., and Vincent, E. (2005). Bss eval toolbox user guide. Technical Report 1706, IRISA, Rennes, France. http://www.irisa.fr/metiss/bss eval/.

Hansen, L., Larsen, J., and Kolenda, T. (2001). Blind detection of independent dynamic components. *Acoustics, Speech, and Signal Processing, 2001. Proceedings. (ICASSP '01). 2001 IEEE International Conference on*, 5:3197–3200.

Hansen, L. K., Larsen, J., and Kolenda, T. (2000). *On Independent Component Analysis for Multimedia Signals*. CRC Press.

Herrmann, C. S., Lenz, D., Junge, S., Busch, N. A., and Maess, B. (2004). Memory-matches evoke human gamma-responses. *BMC Neuroscience*, 5:13.

Hesse, C. and James, C. (2004). Stepwise model order estimation in blind source separation applied to ictal eeg. *Engineering in Medicine and Biology Society, 2004. EMBC 2004. Conference Proceedings. 26th Annual International Conference of the*, 1:986–989.

Hyvarinen, A. and Oja, E. (2000). Independent component analysis: algorithms and applications. *Neural Networks*, 13(4-5):411–430.

James, C. J. and Hesse, C. W. (2005). Independent component analysis for biomedical signals. *Physiological Measurement*, 26(1):R15.

Kolenda, T., Hansen, L. K., and Larsen, J. (2001). Signal detection using ICA: Application to chat room topic spotting. *Third International Conference on Independent Component Analysis and Blind Source Separation*, pages 540–545.

MacKay, D. (1992). Bayesian model comparison and back prop nets. *Proceedings of Neural Information Processing Systems 4*, pages 839–846.

Makeig, S., Westerfield, M., Jung, T.-P., Enghoff, S., Townsend, J., Courchesne, E., and Sejnowski, T. (2002). Dynamic brain sources of visual evoked responses. *Science*, 295(5555):690–694.

Minka, T. P. (2001). Automatic choice of dimensionality for PCA. *Proceedings of NIPS2000*, 13.

Molgedey, L. and Schuster, H. (1994). Separation of a mixture of independent signals using time delayed correlations. *Physical Review Letters*, 72(23):3634–3637.

Mørup, M., Hansen, L., and Arnfred, S. (2007). Erpwavelab. *Journal of Neuroscience Methods*, 161(2):361–368.

Mørup, M., Hansen, L. K., Herrmann, C. S., Parnas, J., and Arnfred, S. (2006). Parallel factor analysis as an exploratory tool for wavelet transformed event-related eeg. *NeuroImage*, 29(3):938–947.

Onton, J., Westerfield, M., Townsend, J., and Makeig, S. (2006). Imaging human eeg dynamics using independent component analysis. *Neuroscience and Biobehavioral Reviews*, 30(6):808–822.

Vincent, E., Gribonval, R., and Fevotte, C. (2006). Performance measurement in blind audio source separation. *IEEE Transactions on Audio, Speech and Language Processing*, 14(4):1462–1469.

Ziehe, A., Muller, K.-R., Nolte, G., Mackert, B.-M., and Curio, G. (2000). Artifact reduction in magnetoneurography based on time-delayed second-order correlations. *IEEE Transactions on Biomedical Engineering*, 47(1):75–87.

APPENDIX

Definition of SNR

Let N be the number of samples and M the number of electrodes. The signal to noise ratio is defined by $SNR = \frac{\|AS\|_F^2}{\|E\|_F^2}$, where $\|E\|_F^2 = NM\sigma^2$. Then the variance of the additive noise is $\sigma^2 = \frac{\|AS\|_F^2}{NM \cdot SNR}$. In decibels the signal to noise ratio is $SNR_{dB} = 10\log_{10}(SNR)$.

BALLISTOCARDIOGRAPHIC ARTIFACT REMOVAL FROM SIMULTANEOUS EEG/FMRI RECORDING BY MEANS OF CANONICAL CORRELATION ANALYSIS

S. Assecondi, P. Van Hese, H. Hallez, Y. D'Asseler, I. Lemahieu
Department of Electronics and Information Systems, MEDISIP, Ghent University-IBBT-IBiTech
De Pintelaan 185, B-9000 Ghent, Belgium
sara.assecondi@ugent.be

A. M. Bianchi
Department of Biomedical Engineering, Polytechnic University, Milan, Italy

P. Boon
Laboratory of Clinical and Experimental Neurophysiology (LCEN),Department of Neurology
Ghent University Hospital, Ghent, Belgium

Keywords: Electroencephalogram (EEG), Blind source separation (BSS), Canonical correlation analysis (CCA), Ballistocardiographic artifact (BCG).

Abstract: The electroencephalogram (EEG) is a standard technique to record and study the brain activity with a high temporal resolution. Blood oxygenation level dependent functional magnetic resonance imaging (BOLD fMRI) is a non-invasive imaging method that allows the localization of activated brain regions with a high spatial resolution. The co-recording of these two complementary modalities can give new insights into how the brain functions. However, the interaction between the strong electromagnetic field (3T) of the MR scanner and the currents recorded by the electrodes placed on the scalp generates artifacts that obscure the EEG and diminish its readability.
In this work we used canonical correlation analysis (CCA) in order to remove the ballistocardiographic artifact (BCGa). CCA is applied to two consecutive windows in order to take into account both spatial and temporal information. We showed that users can easily remove the artifact through a graphical user interface by adjusting the number of components to be removed according to visual inspection of the signal, its power spectrum, the cumulative explained variance and the correlation coefficients.

1 INTRODUCTION

The simultaneous registration of EEG and fMRI has become a valuable tool for the understanding of the functionalities of the brain during cognitive and behavioral studies. The good temporal resolution of the EEG and the high spatial resolution of the fMRI offer an insight into the brain dynamics not achievable with any other non-invasive technique. However, the presence of the strong magnetic field of the MR scanner generates artifacts on the EEG, such as the ballistocardiographic artifact (BCGa), which obscure the brain activity. The origin of the BCGa is still unclear but it is believed to be related to blood flow in scalp arteries leading to electrode movements.

Different methods have been suggested in literature in order to remove this artifact, all of them based either on blind source separation (Niazy et al., 2005; Benár et al., 2003; Srivastava et al., 2005) or averaging techniques (Allen et al., 1998). These methods can be applied either to a time window containing all the EEG channels, considering only spatial correlation or independence, or to a window containing a delayed version of the same channel, taking into account only temporal correlation. It should be noted, however, that BCGa is periodic and affects all the electrode sites. Both periodicity and topographical similarity of the BCGa can be exploited to identify the source or sources responsible for the artifact.

In this work we propose a framework based on canonical correlation analysis (CCA) to remove the BCGa. The advantage of using CCA applied to two consecutive windows is that the algorithm takes into account both spatial and temporal information.

2 MATERIALS AND METHOD

2.1 Data

The data consist of 12 fragments of EEG recorded from an epileptic patient during fMRI. Information about dataset are shown in table 1. In these data BCGa were identified by visual inspection. The electroencephalographic data were recorded using an EEG/fMRI compatible equipment (BE-MRI EBNeuro, Medtronic). The fMRI data were recorded using a 3T MR scanner (Siemens TRIO). The electrodes were positioned according to the 10-20 international system and an average reference was used. The sampling rate was 4096 Hz in order to allow removal of the gradient artifact using the BE-MRI toolbox . After gradient artifact removal the signal was then subsampled to 512 Hz and band-pass filtered between 0.5 Hz and 40 Hz. No epileptic activity was identified in the recording. The final EEG segment considered consisted of 20 channels.

Table 1: Data description: NRC is the number of components removed to clean the dataset, EV is the variance explained by the removed components, CORR is the lowest correlation of the removed components. Mean value (mean) and standard deviation (STD) are also shown.

dataset	n. of BCG	NRC	EV	CORR
setA1	18	6	0.89	0.97
setA2	19	5	0.84	0.98
setA3	18	5	0.85	0.98
setA4	18	5	0.84	0.98
setB1	17	6	0.88	0.97
setB2	14	5	0.84	0.98
setB3	17	6	0.87	0.96
setB4	18	6	0.87	0.97
setC1	16	5	0.84	0.98
setC2	16	6	0.87	0.96
setC3	15	6	0.87	0.97
setC4	18	6	0.88	0.97
mean		5.6	0.86	0.97
std		0.55	0.02	0.09

2.2 Blind Source Separation

Blind source separation (BSS) techniques aim at decomposing the original signal into a set of components or sources. Let $\mathbf{X} = [\mathbf{x_1}(t) \dots \mathbf{x}_M(t)]^T, t = 1 \dots N$ with N the number of samples, be a matrix containing the time series recorded through M sensors. The signals can be expressed as follows:

$$\mathbf{X} = \mathbf{A}\,\mathbf{S} \tag{1}$$

where $\mathbf{A}$ is the $(M \times M)$ unknown mixing matrix and $\mathbf{S} = [\mathbf{s}_1(t) \dots \mathbf{s}_M(t)]^T, t = 1 \dots N$ is the matrix containing the time course of the sources.
BSS estimates the unmixing matrix $\mathbf{W}$, in such a way that the sources are maximally independent (Independent component analysis) or uncorrelated (Principal component analysis). The estimated sources $\widehat{\mathbf{S}}$ can then be recovered using the following formula:

$$\widehat{\mathbf{S}} = \mathbf{W}\,\mathbf{X} \tag{2}$$

2.3 Canonical Correlation Analysis

CCA (Hotelling, 1936) is a multivariate technique that finds two sets of basis vectors, one in each signal space, such that the correlation between the signals in the new subspaces is maximized and the covariance matrix is diagonal.

Consider two sets of zero-mean random variables $\mathbf{X} = [\mathbf{x}_1(t) \dots \mathbf{x}_M(t)]^T, t = 1 \dots N$ and $\mathbf{Y} = [\mathbf{y}_1(t) \dots \mathbf{y}_M(t)]^T, t = 1 \dots N$. We can then define two linear combinations of $\mathbf{x}$ and $\mathbf{y}$ as follows:

$$\begin{aligned} \mathbf{U} &= \Omega_{\mathbf{X}}^T \mathbf{X} \\ \mathbf{V} &= \Omega_{\mathbf{Y}}^T \mathbf{Y} \end{aligned} \tag{3}$$

$\mathbf{U}$ and $\mathbf{V}$ are called *canonical variates* and $\Omega_{\mathbf{X}} = [\omega_{x_1}, \dots \omega_{x_M}]^T$ and $\Omega_{\mathbf{Y}} = [\omega_{y_1}, \dots \omega_{y_M}]^T$ are the *regression weights*. In order to find the regression weights, we maximize the correlation between the two new variables with respect to $\Omega_{\mathbf{X}}, \Omega_{\mathbf{Y}}$. The correlation can be expressed as follows:

$$\rho(\Omega_{\mathbf{X}}, \Omega_{\mathbf{Y}}) = \frac{\Omega_{\mathbf{X}}^T \mathbf{C}_{\mathbf{XY}} \Omega_{\mathbf{Y}}}{\sqrt{(\Omega_{\mathbf{X}}^T \mathbf{C}_{\mathbf{XX}} \Omega_{\mathbf{X}})(\Omega_{\mathbf{Y}}^T \mathbf{C}_{\mathbf{YY}} \Omega_{\mathbf{Y}})}} \tag{4}$$

where ρ is a matrix containing the correlations between $\mathbf{X}$ and $\mathbf{Y}$ and the covariance matrices $C_{\mathbf{XX}}$, $C_{\mathbf{YY}}$ and $C_{\mathbf{XY}}$ are estimated from the data.

2.3.1 Implementation of CCA

One possible implementation of CCA relies on the computation of the principal angles between two orthogonal subspaces (Golub and Van Loan, 1996). Let us consider $\widetilde{\mathbf{X}} = \mathbf{X}^T$ and $\widetilde{\mathbf{Y}} = \mathbf{Y}^T$. First we compute two orthogonal subspaces $\mathbf{Q}_{\widetilde{\mathbf{X}}}$ and $\mathbf{Q}_{\widetilde{\mathbf{Y}}}$ of the original signal spaces:

$$\begin{aligned} \widetilde{\mathbf{X}} &= \mathbf{Q}_{\widetilde{\mathbf{X}}} \mathbf{R}_{\widetilde{\mathbf{X}}} \\ \widetilde{\mathbf{Y}} &= \mathbf{Q}_{\widetilde{\mathbf{Y}}} \mathbf{R}_{\widetilde{\mathbf{Y}}} \end{aligned} \tag{5}$$

Next, we compute the singular value decomposition of $\mathbf{Q}_{\widetilde{\mathbf{X}}}^T \mathbf{Q}_{\widetilde{\mathbf{Y}}}$:

$$\mathbf{Q}_{\widetilde{\mathbf{X}}}^T \mathbf{Q}_{\widetilde{\mathbf{Y}}} = \mathbf{E}\mathbf{C}\mathbf{F}^T \tag{6}$$

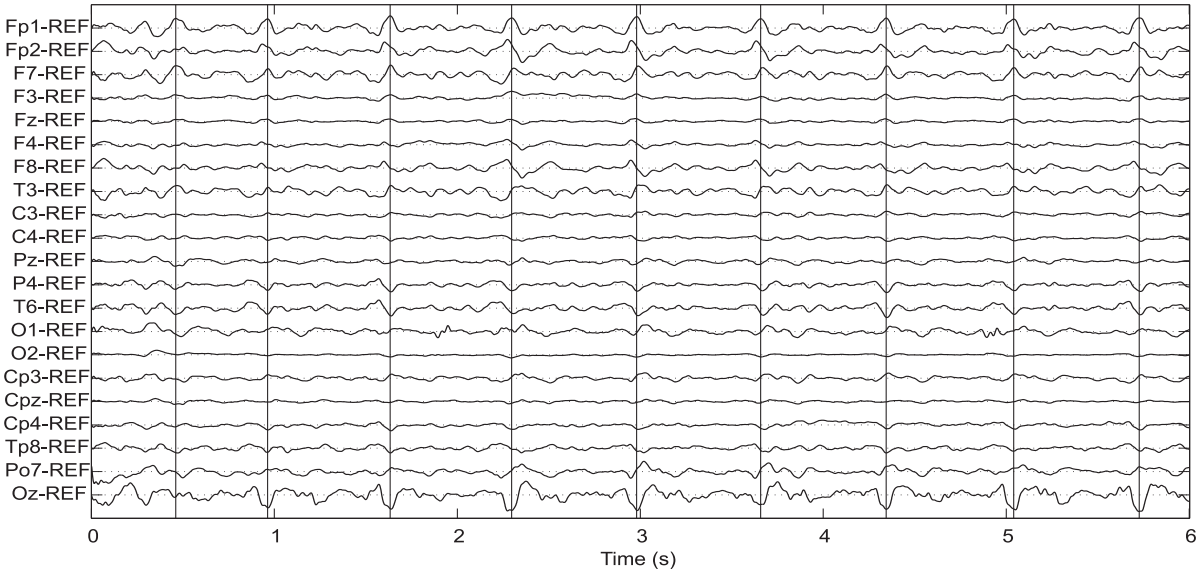

Figure 1: Simultaneous EEG/fMRI recording before BCG artifact removal.

where $\mathbf{C}$ is a diagonal matrix containing the correlation coefficients associated to each variate in decreasing order. We can then compute the canonical variates:

$$\begin{aligned} \mathbf{U}^T &= \mathbf{Q}_{\widetilde{\mathbf{X}}}\mathbf{E} = \widetilde{\mathbf{X}}\mathbf{R}_{\widetilde{\mathbf{X}}}^{-1}\mathbf{E} = \widetilde{\mathbf{X}}\Omega_{\mathbf{X}} \\ \mathbf{V}^T &= \mathbf{Q}_{\widetilde{\mathbf{Y}}}\mathbf{F} = \widetilde{\mathbf{Y}}\mathbf{R}_{\widetilde{\mathbf{Y}}}^{-1}\mathbf{F} = \widetilde{\mathbf{Y}}\Omega_{\mathbf{Y}} \end{aligned} \tag{7}$$

2.3.2 Signal Reconstruction

Once the canonical variates are calculated, a subset of them can be used to reconstruct the original signal. The specific variates are selected by setting to zero the regression coefficients corresponding to the unwanted variates. The new signal approximation can be computed using the new regression weights $\widetilde{\Omega}_{\mathbf{X}}$ and $\widetilde{\Omega}_{\mathbf{Y}}$,as follows:

$$\begin{aligned} \widehat{\mathbf{X}} &= (\widetilde{\Omega}_{\mathbf{X}}^{-1})^T\mathbf{U} = \widetilde{\Omega}_{\mathbf{U}}^T\mathbf{U} \\ \widehat{\mathbf{Y}} &= (\widetilde{\Omega}_{\mathbf{Y}}^{-1})^T\mathbf{V} = \widetilde{\Omega}_{\mathbf{V}}^T\mathbf{V} \end{aligned} \tag{8}$$

2.4 Method

The artifact removal procedure involves the following six steps:

1. identification of the BCG artifacts on the EEG,
2. segmentation of the EEG around the artifact,
3. application of CCA to two consecutive windows,
4. detection of artifactuated canonical variates,
5. removal of the artifactuated sources,
6. reconstruction of the original signal.

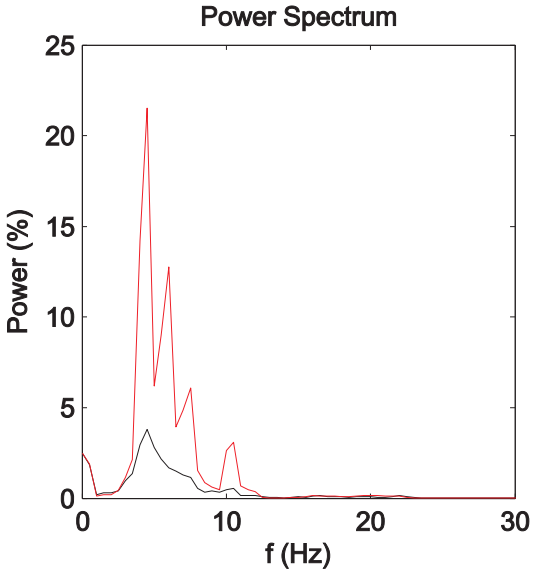

Figure 2: Normalized power spectrum of the Fp1 channel before (red line) and after (black line) artifact removal, when six components are removed.

Figure 1 shows the original EEG. The artifacts are easily distinguishable on the EEG channels and are marked by vertical lines. At first inspection the artifact appears synchronized over the channels but with different amplitude. Moreover the shape changes over time whereas the relative contribution of the artifact to different electrode sites is time-independent. For these reasons, CCA was applied to two consecutive windows: this allows the extraction of components that share the same topography over time.

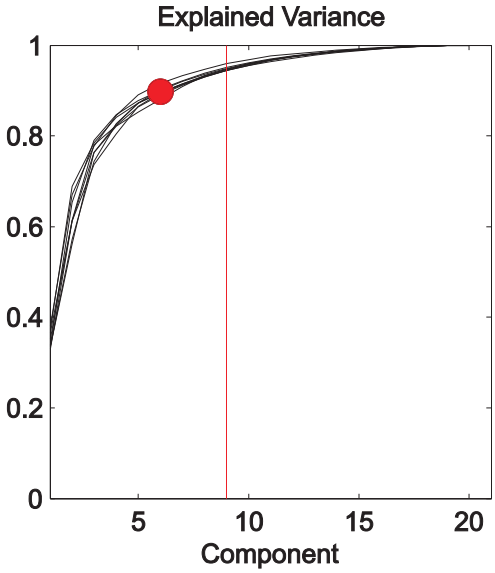

Figure 3: Cumulative explained variance for each BCG occurrence plotted as a function of the number of components: the vertical line marks the component where the 95% of the total variance is explained for all the BCG artifact. The red dot represents the variance explained by the first six components.

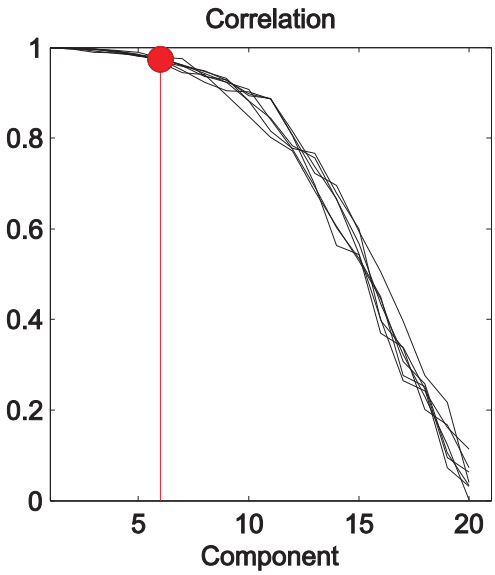

Figure 4: Correlation coefficients calculated by CCA plotted for each BCG as a function of the components: the vertical line marks the component where the correlation coefficient is lower than 95% in all BCG's.. The red dot represents he correlation of the sixth component.

The artifacts are manually identified on the EEG. The data are then segmented by considering a window of 300 ms (the approximate duration of the artifact) around each artifact occurrence. CCA is applied to two consecutive windows ($m \times n$, where n is the number of points and m is the number of channels) and the canonical variates are calculated. The sources outputted by the CCA algorithm are ordered according to their correlation (see equation 6). The basic assumption is that the artifact is determined by the same sources active during two consecutive time-windows, superimposed to EEG activity uncorrelated to the artifact.

In order to guide the choice of the number of components to remove, the following three features are considered: the normalized power spectrum of the Fp1 channel, where the artifact has high amplitude, the cumulative explained variance and the correlation coefficients given by CCA. Figure 2 represents the normalized power spectrum of the Fp1 channel, where the artifact has high amplitude, before and after artifact removal. In figure 3 the cumulative explained variance for each BCG occurrence is plotted as a function of the number of components considered: the vertical line marks the component where the 95% of the total variance is explained for all the BCG artifacts. In figure 4 the correlation coefficients calculated by CCA are plotted for each BCG as a function of the components: again the vertical line marks the component where the correlation coefficient is lower than 95% in all BCG's.

A graphical user interface (GUI), shown in figure 5, was developed in order to facilitate the artifact removal procedure. A sliding bar allows the user to increase the number of removed components from 0 to k: at each step of the sliding bar, the first k components, i.e. the k canonical variates associated to the highest correlation, are removed. Simultaneously the EEG before and after artifact removal is plotted, as well as the normalized power spectrum of the Fp1 channel, the explained variance and the correlation coefficients. A black dot represents the position of the current component with respect to the explained variance and the correlation. The value of the explained variance and the correlation at each step are also given as the average over the BCG's shown in the GUI. At every step of the sliding bar, the plots and the values of explained variance and correlation are updated. In this way the user can determine the number of components to remove based on visual inspection of both EEG and its power spectrum (the smaller the harmonics, the cleaner the signal), until the EEG appears readable and the power spectrum does not change significantly. Moreover the user can avoid excessive removal of EEG activity by monitoring the explained variance and the correlation of the component at the current step.

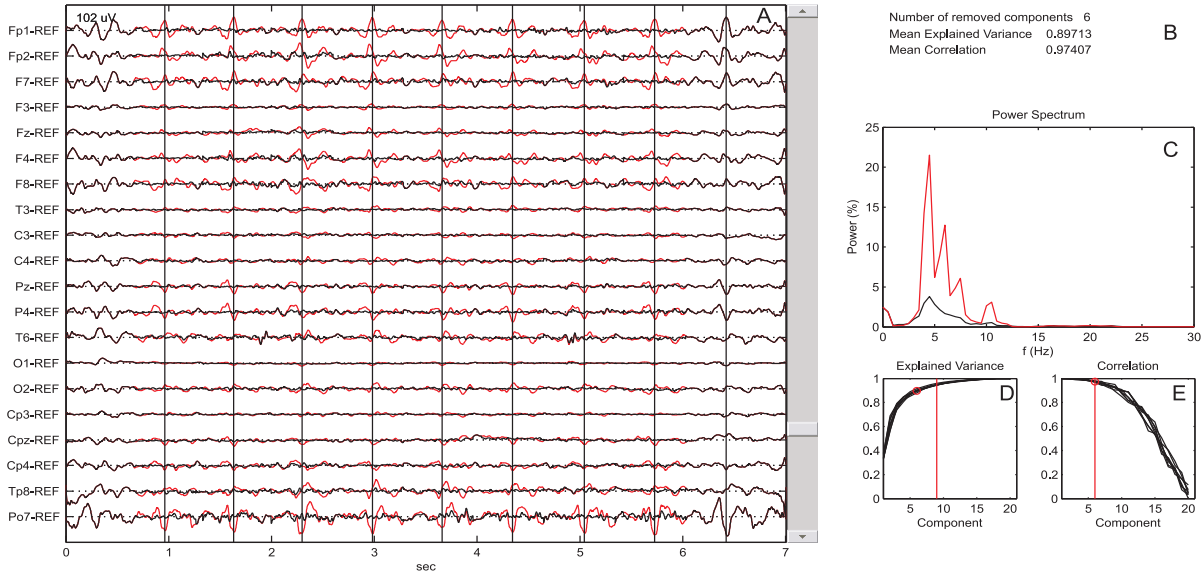

Figure 5: Screenshot of the graphical user interface (GUI) developed to remove the BCGa from EEG data. Panel A is updated at every step of the sliding bar by a superposition of the original and the clean data. In panel B the number of component removed at the current step are reported, as well as the explained variance and correlation, as the mean over the BCG occurrences shown in panel A, for the particular number of components. Panel C represents the normalized power spectrum of FP1 before (dashed line) and after (solid line) artifact removal. In panel D the cumulative explained variance for each BCG occurrence shown in A is plotted as a function of the components. In E the correlation coefficients resulting from the application of CCA to each BCG occurrence are also plotted as a function of the components.

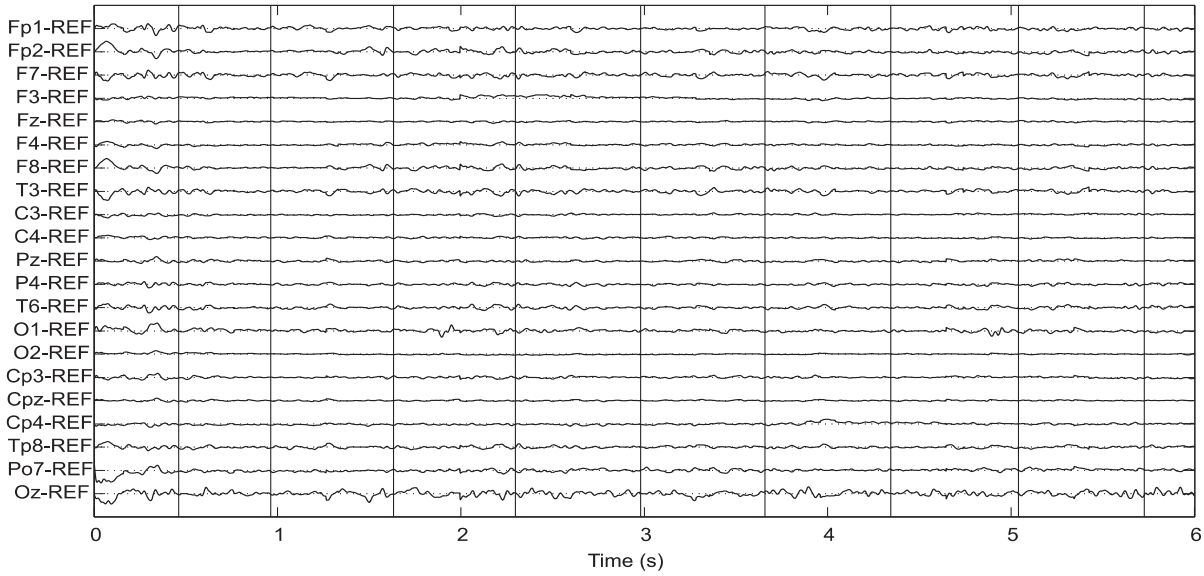

Figure 6: Simultaneous EEG/fMRI recording after BCG artifact removal.

3 RESULTS AND DISCUSSION

Figure 6 shows the EEG after artifact removal, the vertical lines define the time occurrence of the artifact. In this case the first six components were removed (explained variance = 0.90; correlation = 0.97). The high amplitude artifact-related activity is not visible anymore. Moreover, by monitoring the explained variance and the correlation coefficients, we are able to preserve information in background EEG. Table 1 shows how the number of removed components is adaptively chosen, so that the algorithm can

cope with the intrinsic subject variability.

Figure 2 shows the normalized power spectrum of the channel Fp1 before and after artifact removal when the first six components were removed. The harmonic components disappeared. Moreover, removing more than the first five components does not significantly change the power spectrum of the data. We can infer that the first six components were artifact related, whereas the remaining sources were EEG-related.

Therefore, the results confirm the presence of artifactual sources that share the same topographies over time.

4 CONCLUSIONS

We demonstrated that CCA can be a valuable tool in removing the BCG artifact from simultaneous EEG/fMRI recording.

We believe that CCA is able to take into account the physiology of the artifact. The identification of sources whose topographies do not change over time allows the use of both spatial and temporal information during the identification of the artifact. The use of a moving window also allows the topographies to adapt to the physiological variation of the blood flow. This makes CCA an extension with respect to those methods, like ICA or PCA, in which only the spatial information is considered. Moreover CCA is less sensitive than ICA to the window length (Hyvarinen et al., 2001), allowing the use of a time window that matches the artifact characteristics.

Further research has to be done in order to automatically detect the BCGa on the EEG data and automatically identify the number of components to remove, in such a way that an optimal reconstruction is achieved in each window. In order to assess the reliability of the procedure, the application of the method to a larger database of human recording is also necessary. Moreover a simulation study is needed in order to test the performances of the algorithm with respect to noise and artifact characteristics.

REFERENCES

Allen, P. J., Polizzi, G., Krakow, K., Fish, D. R., and Lemieux, L. (1998). Identification of EEG events in the MR scanner: the problem of pulse artifact and a method for its subtraction. *Neuroimage*, 8:229–239.

Benár, C., Aghakhani, Y., Wang, Y., Izenber, A., Al-Asmi, A., Dubeau, F., and Gotman, J. (2003). Quality of EEG in simoultaneous EEG-fMRI for epilepsy. *Clin Neurophysiol*, 114:569–580.

Golub, G. and Van Loan, C. (1996). *Matrix Computations*. The Johns Hopkins University Press, Baltimore, 3rd edition.

Hotelling, H. (1936). Relations between two sets of variates. *Biometrika*, 28(3/4):321–377.

Hyvarinen, A., Karhunen, J., and Erkki Oja, E. (2001). *Independent Component Analysis*. Wiley, John & Sons, Incorporated.

Niazy, R., Beckmann, C., Iannetti, G., Brady, J., and Smith, S. (2005). Removal of fMRI environment artifacts from EEG data using optimal basis sets. *NeuroImage*, 28:720–737.

Srivastava, G., Crottaz-Herbette, S., Lau, K., Glover, G., and Menon, V. (2005). ICA-based procedures for removing ballistocardiogram artifacts from EEG data acquired in the MRI scanner. *NeuroImage*, 24:50–60.

INVESTIGATION OF ENTROPY AND COMPLEXITY MEASURES FOR DETECTION OF SEIZURES IN THE NEONATE

Ehsan Chah
UCD School of Electrical, Electronic and Mechanical Engineering, University College Dublin, Dublin 4, Ireland
ehsan.chah@ee.ucd.ie

Barry R. Greene
Neonatal Brain Research Group, Dept. of Electrical Engineering, University College Cork, Ireland
barryg@rennes.ucc.ie

Geraldine B. Boylan
Neonatal Brain Research Group and the Department of Paediatrics and Child Health, University College Cork, Ireland
g.boylan@ucc.ie

Richard B. Reilly
UCD School of Electrical, Electronic and Mechanical Engineering, University College Dublin, Dublin 4, Ireland
and The Cognitive Neurophysiology Laboratory, St Vincent's Hospital, Fairview, Dublin, Ireland
richard.reilly@ucd.ie

Keywords: Entropy, complexity, neonatal, seizures, EEG.

Abstract: The performance of three Entropy/complexity measures in detecting EEG seizures in the neonate were investigated in this study. A dataset containing EEG recordings from 11 neonates, with documented electrographic seizures, was employed in this study. Based on patient independent tests Shannon Entropy was found to provide the best in discrimination between seizure and non-seizure EEG in the neonate. Lempel-Ziv complexity and Multi-scale Entropy were second and third respectively, while Sample Entropy did not prove a useful feature for discriminating seizure patterns from non-seizure patterns.

1 INTRODUCTION

Seizures are one of the few neurological conditions in the neonate that require immediate medical attention and represent the most distinctive sign of central nervous system dysfunction (Volpe, 2001). Neonatal seizures occur in 6% of low birth-weight infants and in approximately 2% of all newborns admitted to a neonatal ICU. An automatic neonatal seizure detector would be a significant aid in newborn monitoring given that expert EEG interpretation is not available on a 24-hour basis. The current state of the art in neonatal seizure detection does not offer the reliability or robustness necessary for use in a neonatal ICU. A multi-signal approach has been proposed (Greene et al., 2007), based on the extraction of pertinent features from EEG and ECG signals. Choice of which features to extract is an area of active research in neonatal seizure detection.

The aim of this study was to compare the applicability of four measures of signal entropy and complexity, which measure the degree of regularity or complexity in a single channel EEG, as possible features for use in a neonatal seizure detection system.

2 AUTOMATIC NEONATAL SEIZURE DETECTION

The block diagram in Fig.1 describes the detection method employed in this study to compare

complexity and entropy measures. Initially, the EEG channel was processed, extracting features or parameters to facilitate subsequent discrimination in a pattern classifier between seizure and non-seizure EEG.

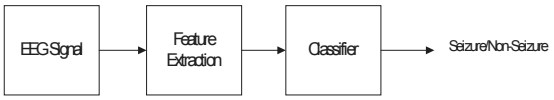

Figure 1: Detection method block diagram.

The focus of this study was on the feature extraction phase, with entropy and complexity being the feature extracted.

3 DATA SET

The dataset for this study comprised multi-channel EEG recordings from 11 babies from two different test centers. Recordings from Kings College Hospital, London (8 babies) were made on Telefactor Beehive Video EEG machine and sampled at 200Hz. Recordings from the Unified Maternity Hospitals, Cork (3 babies) were on a Viasys NicOne Video EEG machine and sampled at 256Hz.

Table 1: Data set.

Patient	Num of seizure segments	Num of non-seizure segments	Total recording time in minutes
1	30	43	73
2	44	21	65
3	51	24	75
4	55	44	99
5	7	15	22
6	10	22	32
7	31	33	64
8	26	39	65
9	22	26	48
10	16	13	29
11	21	15	36

Electrographic seizures in each multi-channel recording were labeled such by an expert in neonatal EEG (author GBB).

Recordings for each patient were then split into 1-min single channel segments either containing seizure or non-seizure EEG. Only EEG channels that were determined (by the electroencephalographer) to contain definite seizure activity were included in the analysis.

The data set employed was 608 min i.e. 10.13 hours, containing 5.22 hours of seizure EEG and 4.92 hours of non-seizure EEG. Table 1 summarizes the dataset for this study.

4 ENTROPY MEASURES

Four entropy/complexity measures were compared, namely Multiscale Entropy, Sample Entropy, Shannon Entropy and Lempel-Ziv complexity. Entropy and complexity are dependent on signal properties and each method quantifies randomness or complexity of a signal from a different perspective.

4.1 Sample Entropy

Sample Entropy (SampEn) is the negative natural logarithm of an estimate of the conditional probability that sub-series (epochs) of length m that match point-wise within a tolerance r also match at the next point (Richman and Moorman, 2000).

$$SampEn = \ln \frac{B}{A} \tag{1}$$

where B is the total number matched m patterns, and A is the total number of matched $m+1$ patterns.

4.2 Multiscale Entropy

Multiscale Entropy (MSE) (Goldberger et al., 2000) is a modified version of Sample Entropy and quantifies the degree of regularity or conversely randomness.

MSE calculation involves two main procedures: firstly the data (x) of length N is divided into smaller segments of length τ, and then the series of average of each data segment is computed and used to obtain the "coarse-graining" series $y_j^{(\tau)}$.

$$y_j^{(\tau)} = \frac{1}{\tau} \sum_{i=(j-1)\tau+1}^{j\tau} x_i \tag{2}$$

Where j can take values between:

$$1 \le j \le \frac{N}{\tau} \tag{3}$$

SampEn is calculated from this coarse graining series.

4.3 Lempel-Ziv Complexity

Lempel-Ziv (LZ) (Lempel and Ziv, 1976) quantifies complexity of a time series, by observing a number of unique sequences in a given dataset. One dimensional time series *X(t)* is converted into series *P(n)* of ones and zeros by comparing it to threshold T_d. Then the transformed series is scanned from left to right and number of unique sequences *c(n)* is computed.

$$\text{Let } b(n) = \frac{n}{\log_\alpha(n)} \tag{4}$$

Where *n* is the length of *P* and *α* is the size of alphabet, in zero-one conversion α = 2, .then the normalized LZ complexity =

$$\frac{c(n)}{b(n)} \tag{5}$$

4.4 Shannon Entropy

Shannon Entropy (ShEnt) (Shannon, 1948) has been defined as a measure of uncertainty of a signal or degree of orderliness of the data.

$$\text{ShEnt} = -\sum_{i=1}^{n} p_i \log p_i \tag{6}$$

Where p_i is an estimate of the probability density function. A histogram of the signal with k bins is constructed and from this the probability distribution can be estimated.

Entropy measures MSE, SampEnt, and LZ complexity all use sequences of data to determine complexity or regularity of the signal. Shannon entropy considers only signal amplitude in order to measure degree of regularity.

5 METHODS

To assess the applicability of each of these measures, a detection system was implemented, as shown in Fig. 1.

Data acquired from the recording equipment was processed to extract each measure. Calculation of each entropy/complexity measure assumes that the number of data points is large, i.e. $N \longrightarrow \infty$. The International Federation of Clinical Neurophysiology (IFCN) recommends that 10 sec is the minimum electrographic seizure duration if the EEG background is abnormal (De Weered, 1999). This suggests a maximum deployable window length. A longer duration window may result in the detector missing short duration seizures. The length of the window was chosen to be 10 sec, similar to a study by Gotman (Gotman et al., 1997), the window employed in this study was non-overlapping.

To assess the utility of each entropy feature, a Linear Discriminant (LD) classifier model was employed in this study. An LD classifier model finds the best linear combination that separates between two or more classes using Fishers discriminant ratio.

Cross fold validation is used to provide an estimate of the potential utility of these complexity and entropy based features when employed in a patient independent seizure detection system. The classifier model is trained on (*n-1*) patients and tested on the n^{th} patient. Each fold contains all features from a single patient i.e. given 11 patients, thus fold 1 corresponds to Patient 1 and fold 2 to Patient 2 etc. Four features are extracted from each 10s EEG epoch.

Experiments were carried out to determine the optimum values of parameters used in SampEnt and MSE calculations:

5.1 Sample Entropy Parameter r

For SampEnt a tolerance value for accepting matches, *r*, must be chosen. In literature (Costa et al, 2005) it is common to have parameters *m = 2* and *r* between 0.1 and 0.2. in this study *m* = 2 and *r* = 0.2 were chosen.

5.2 Multi-Scale Entropy Parameters

In Multi-scale Entropy (MSE) two parameters, scale *τ* and tolerance *r* must be chosen.

5.2.1 Scale τ

Scaling is averaging data points in non-overlapping windows of size *τ*. In other words when using scaling we reduce the number points on which Sample Entropy is calculated, i.e. when using *τ* = 10 with a window size of 10 sec (2000 data points) SampEnt is calculated for 200 points only. In this study parameters *m* and *r* were fixed (*m=2, r =0.2*) and the scale *τ* = 10 was chosen.

5.2.2 Tolerance For Accepting Matches r

In this study $r = 0.2$ was chosen.

5.3 Lempel-Ziv Complexity Parameters

In biomedical signal processing it is common to convert a time series into a series of ones and zeros by comparing it to a threshold T_d. T_d is commonly chosen as the median of the signal (Aboy et al., 2006), thus in this study EEG signals were transformed into 1's and 0's by comparing it to the median of the signal. Converting to a binary sequence has the advantage of being simple to implement in hardware and software and computationally less expensive.

5.4 Shannon Entropy Parameters

The histogram method was used in order to calculate Shannon Entropy. The histogram count was constructed with $k = \sqrt{n}$ bins, where n is the total number data points in each window.

6 PERFORMANCE MEASURES

The performance of each of the complexity and entropy based features employed in this study were determined using the following measures: Accuracy, Sensitivity, Specificity and ROC curve area.

Accuracy (Acc) is the percentage of each 10 s EEG epoch correctly classified by an epoch based seizure detector.

Sensitivity (Sens) is defined as the percentage of labeled 10s seizure EEG epochs correctly classified as a seizure epoch by the classifier.

Similarly, specificity (Spec) is the percentage of labeled 10s non-seizure EEG epochs correctly identified as non-seizure epochs by the detection method.

A receiver operating characteristic curve (ROC) (Zweig and Campbell, 1993) is a plot of sensitivity versus specificity for different thresholds. Trapezoidal numerical integration is used to calculate the area under the curve, this area gives an indication of how well a given feature discriminates between seizure and non-seizure epochs. An area of 1 corresponds to a perfect discrimination, while a ROC area of 0.5 is a result of a random discrimination. The closer the ROC area value is to unity the better the discrimination between classes.

7 RESULTS

To obtain an estimate of the patient independent performance of the measures the classifier was trained on the data available and then tested on a data recorded from a patient that was not included in the training.

The results in Table 2 shows that Shannon Entropy (ShEnt) gives the best performance out of the four entropy/complexity measures, however combining different entropy measures improves the detection scheme.

Table 2: Patient independent results.

Entropy /complexity	Acc (%)	Sens (%)	Spec (%)	ROC Area
ShEnt	69	71	66	0.73
LZ	64	68	58	0.67
MSE	57	58	56	0.59
SampEnt	55	66	43	0.53
Combination of all four measures	73	75	71	0.80

Table 3: Performance of individual patients.

Patient	Acc (%)	Sens (%)	Spec(%)
1	79	79	78
2	71	75	63
3	63	59	75
4	69	69	67
5	44	45	43
6	51	53	50
7	97	99	94
8	80	91	74
9	87	98	78
10	52	57	47
11	82	83	81

Table 3 shows the individual performances of each patient in the dataset when all four entropy/complexity measures are combined and fed to the classifier.

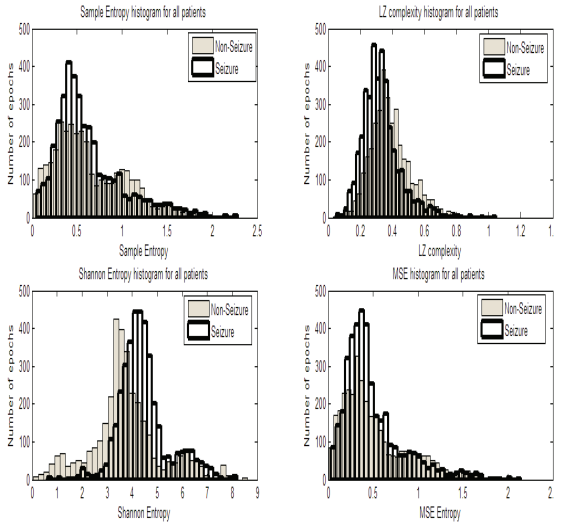

Figure 2: Histogram of entropy features (all patients combined).

Figure 2 shows histograms for each entropy/complexity measures for all patients combined, providing a graphical comparison on how these measures discriminate between seizure and non-seizure EEG segments.

The histograms show that the best separation between seizure and non-seizure EEG epochs through the application of Shannon Entropy to EEG data, the next best feature can be seen to be the Lempel-Ziv complexity, and thus these measures contribute the most in overall detection scheme.

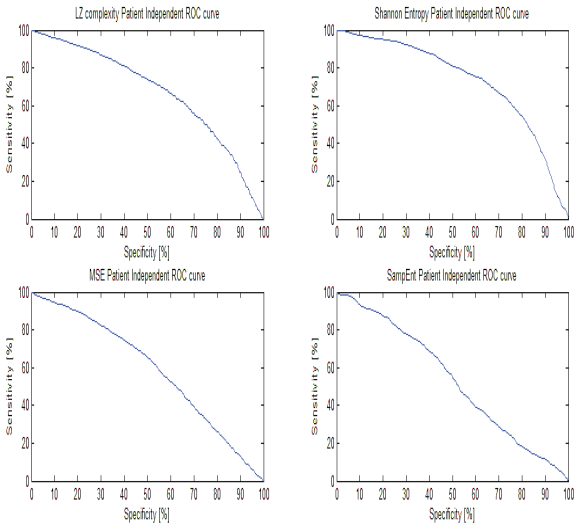

Figure 3: Patient independent ROC curves for individual features. ShEnt Roc area 0.73, LZ ROC area 0.67, MSE ROC area 0.59, SampEnt ROC area 0.53.

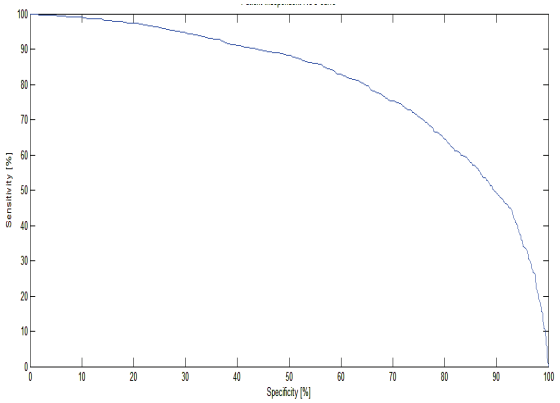

Figure 4: Patient independent ROC curve (all features combined) ROC area 0.8.

From the ROC curves in Fig. 3 it can be observed that SampEnt does not provide a good discrimination. We can omit Sample Entropy from the feature extractor in the patient independent test and obtain equal results based on the remaining three entropy measures.

8 DISCUSSION

In this study four Entropy/complexity measures were applied to neonatal seizure EEG. Results indicate that Shannon Entropy gives better performance than other entropy/complexity measures in discriminating seizure EEG from non-seizure EEG.

The main reason Shannon Entropy outperforms other entropy measures in neonatal seizure is probably due to the fact that Shannon Entropy considers amplitude of the signal when calculating entropy and so is suitable for detecting high amplitude seizures.

The poorest performing entropy measure applied in this study was Sample Entropy. The patient independent results showed that if Sample Entropy is omitted from the feature extractor, equal results are obtained from the three remaining entropy measures.

The results also showed that combining different entropy and complexity measures (with the exception of SampEn) improved the overall detection system Acc by 4% compared to the system when ShEnt is extracted alone. The results also show that Sample Entropy gives the lowest Acc results of 55% and a ROC area of 0.53 which is not much better than a random detection. Thus we

conclude that SampEn does not provide a good discrimination.

From Fig. 2 is can be observed that while Sample Entropy and Lempel-Ziv complexity values decrease as a seizure is occurring, Shannon Entropy and Multi-Scale Entropy increase as a seizure is taking place. Similar behavior of entropy measures were reported in (Costa et al., 2005) for ECG analysis and (Ferenets et al., 2006) for EEG analysis. Ferenets et al explain that ShEnt "is indifferent to the time order of the signal", while SampEnt and LZ are dependent on the order of signal thus this might explain the behavior mentioned above.

In a recently reported EEG based detection method (Greene, 2006) six features were extracted, one being Spectral Entropy. The patient specific results reported in (Greene, 2006) showed that the best performing feature was line length, while Spectral Entropy and Non-linear Energy were second best performing features. Therefore, it would be beneficial to investigate if adding Spectral Entropy to the list of features extracted in this study will improve the overall performance of the detection method.

In this study, the total amount of data employed was 10.13 hours. In order to attain a clinically relevant performance estimate for the method proposed, a much larger data set would be required. Using the features, with the parameter values chosen from this study, on a new larger dataset containing multi-channel continuously recorded EEG, would further validate the effectiveness of these measures in neonatal seizure detection.

9 CONCLUSIONS

The conclusion drawn from this study is that out of the four entropy/complexity measures investigated. Shannon entropy provides the best discrimination between seizure and non-seizure EEG in the neonate.

ACKNOWLEDGEMENTS

B. R. Greene was supported by Science Foundation Ireland (SFI/05/PICA/1836).

REFERENCES

Aboy, M., Hornero, R., Abasolo, D., Alvarez, D., 2006. Interpretation of the Lempel-Ziv Complexity measure in the context of biomedical signal analysis. *IEEE Transactions on Biomedical Engineering,* 53(11), p. 2282-2288.

Costa, M., Goldberger, A. L., Peng, C. K., *2005.* Multiscale Entropy Analysis of Biological Signals. *Physical Review,* E*;71:021906*.

De Weered, A. W., Despland, P. A., Plouin, P., 1999. Neonatal EEG. The International Federation of Clinical Neurophysiology. *Electroencephalography Clinical Neurophysiology,* 52, p. 149-157.

Ferenets, R., Lipping, T., Anier, A., Jantii, V., Melto, S., Hovilehto, S., 2006. Comparison of entropy and complexity measures for the assessment of depth of sedation, *IEEE Transactions on Biomedical Engineering*, 53(6). p. 1067-1077, JUNE.

Goldberger, A. L., Amaral, L.A N., Glass, L., Hausdorff, J. M., Ivanov, Mark, P. C. R. G., Mietus, J. E., Moody, G. B., Peng, C., Stanley, H. E., 2000. PhysioBank, PhysioToolkit, and PhysioNet, Components of a New Research Resource for Complex Physiologic Signals. *Circulation* 101(23),e215-e220.

Gotman, J., Flanagan, D., Zhang, J., Rosenblatt, B., 1997. Automatic seizure detection in newborns: methods and initial evaluation. *Electroencephalography and clinical Neurophysiology,* 103, p. 356-362.

Greene, B., Boylan, G., Reilly, R., de Chazal, P., Connolly, S., 2007. Combination of EEG and ECG for improved automatic neonatal seizure detection, *Clinical Neurophysiology.* 118, 1348-1359.

Greene, B. R., 2006, Quantification and classification of Electrophysiological Markers of Seizure in the Neonate. *PhD thesis*, University College Dublin, National University of Ireland.

Lempel, A., Ziv, J., 1976. On the complexity of finite sequences. *IEEE Transactions on Information Theory,* IT-28(1), p. 75-81.

Richman, J. S., Moorman, J. R., 2000. Physiological time-series analysis using approximate entropy and sample entropy. *American Journal of Physiology - Heart Circulatory Physiology,* 278(6). H2039-H2049.

Shannon, C. E., A mathematical theory of communication. 1948. *Bell System Technical Journal,* 27. p. 379-423.

Volpe, J. J., 2001. Neurology of the newborn. 4th ed. Philadelphia PA.: Saunders.

Zweig, M., Campbell, G., 1993. Receiver-Operating Characteristic (ROC) plots: a fundamental evaluation tool in clinical medicine. *Clinical Chemistry,* 39(4), p. 561-577.

EEG HEADSET FOR NEUROFEEDBACK THERAPY
Enabling Easy Use in the Home Environment

Joran van Aart, Eelco R. G. Klaver, Christoph Bartneck, Loe M. G. Feijs and Peter J. F. Peters
Department of Industrial Design, Eindhoven University of Technology, Den Dolech 2, Eindhoven, The Netherlands
design@joran.eu, e.r.g.klaver@student.tue.nl, {c.bartneck; l.m.g.feijs; p.j.f.peters}@tue.nl

Keywords: Headset, neurofeedback therapy, electroencephalography, EEG, brain waves, home environment, wellbeing, impedance measurement.

Abstract: In this article we present the design of an EEG headset together with the context and vision that motivated us to undertake the described design work. There is a variety of potential advantages and potential difficulties associated with neurofeedback therapy. Both are analyzed informally and we argue in favour of a change in perspective, moving away from treatment of illness towards prevention and giving the user an active and responsible role. To structure the discussion we will deploy the closed loop diagram. We identify elements from the world of gaming that will have added value over a pure training approach, notably elements that improve enjoyment and motivation. We describe several of the design steps of the headset that has been designed to achieve enjoyable neurofeedback therapy in the home environment and conclude with an evaluation of this headset.

1 INTRODUCTION

With neurofeedback therapy we can make brainwave patterns explicit by for example a computer screen, patterns we normally cannot influence since we are unable to see or feel them. This feedback provides us the ability to influence and change them. With neurofeedback therapy we are literally reconditioning and retraining the brain (Hammond, 2007).

In order to provide a structure and discuss the wide variety of potential advantages and potential difficulties associated with neurofeedback therapy, we start by introducing the closed loop diagram of Figure 1. In this diagram, G(s) is the user, patient, sportsman, etcetera and H(s) is the external training equipment together with services of the therapist. To give an easy biofeedback example, let u be a desirable value for the BMI (Body Mass Index) and let y be the patient's or user's weight. Then H includes the calculation y/(length^2), but also a display function. By informing the user of the difference between desired and actual BMI, the user is supposed to eat and move wisely and adjust his weight. This example actually has been realized as the Smart Mirror by Philips Electronics (Van Splunter, 2002).

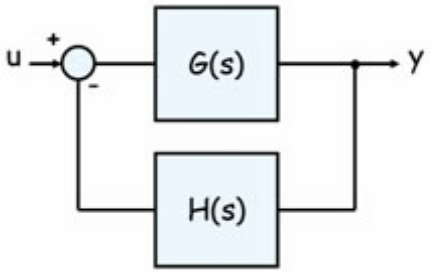

Figure 1: Closed loop diagram with user G(s) and training equipment and services H(s).

Feedback theory has been the backbone of mechanical and electrical engineering since almost a century - and it still is. It is outside the scope of this article to try and develop precise models of the controlled system and the feedback function, we just use it to structure the debate. One remark is in order: it is of the utmost importance to be aware of the complexity of the human mind-body system G(s). Its subsystems include the skeletal, digestive, muscular, lymphatic, endocrine, nervous, and cardiovascular, urinary and reproductive systems. The nervous system includes the brain and its higher functions such as perception, cognition, and control. The subsystems are not only coupled, they also have internal feedback loops. This being said, we can begin.

2 OPEN QUESTIONS

In this section we begin with some preliminary observations and open questions regarding neurofeedback (NF). Some of the questions are speculative and possibly controversial. We take them as a source of inspiration; several of the issues embedded in these questions will be addressed more seriously in the subsequent sections.

Neurofeedback therapy (Evans, 1999) is about training the mind in a non-intrusive way using EEG signals, stimulating or discouraging certain brain functions. Experiences with neurofeedback therapy might seem promising, however for some reason it hasn't been adopted by the general public yet. One of the causes might be that in present day society, there seems to be a tendency to focus on the physical aspect of health and on curing the symptoms rather than fighting the cause. For example, people with ADHD are drugged with Ritalin, which reduces symptoms of hyperactivity, but doesn't cure it. In contrast, the main focus of neurofeedback is on mental issues.

Another problem might be that neurofeedback therapy is based on a 'mind over matter' perspective, implying that physical and mental wellbeing are interconnected (Fox, 1999; Kendell, 2001). However, for some reason it seems difficult to accept this perspective. Prejudices have been formed, perhaps as a result of the natural fear of the unknown. Still, although neurofeedback therapy has shown to have a positive influence on numerous disorders (Lubar, 1995), proof of absence of possible side-effects has not been supplied yet. Whether this is a potential issue for the therapy not to be accepted, remains open for debate. However, it has been said that if some or another medication could be as broadly and effectively applicable as neurofeedback therapy, it would already be available at every pharmacy in the world. (Roskamp, 2007). Maybe we should focus on a vision in which neurofeedback therapy could eventually become as easy as taking an aspirin.

Professional athletes use neurofeedback to improve their already exceptional performances by entering a state of 'relaxed focus', a moment of optimal performance reached by this so-called peak-performance training. This raises the question whether neurofeedback could actually be applied to elevate our general wellbeing in the way athletes do. Heinrich et al (2007) formulate the following promising statement: 'In addition, 'normal' subjects may improve cognitive functions (e.g., attention and working memory) and performance in real-life situations by means of NF'.

3 ANALYSIS

EEG products are mainly distinct in the number of electrodes that are used for measurements. Products range from the ElectroCap with 19 sensors (Figure 2) (ElectroCap International Inc., 2004), to two-channel products only using 2 sensors and clips on each earlobe. However, in either case scalp contact is optimized by removing dead skin cells and parting hair out of the way. Conducting gel is applied in most cases, although products with dry sensors are being developed as well. Recent products include the g.EEGcap (Guger Technologies OEG, 2007) and other techniques for measuring, like Project Epoc (Emotiv Systems Inc., 2007) and SMART BrainGames PlayStation System (SMART BrainGames, 2007).

Figure 2: ElectroCap (image courtesy of ElectroCap International Inc., 2004)

Referring to Figure 1 we decompose both G(s) and H(s) to identify various difficulties and opportunities. This also allows us to position our own contribution, which includes the design of the headset reported in section 5.

First we consider H(s), consisting of (1) the services provided by the therapist and (2) the training equipment. There are several good reasons why the therapist is involved. These include the professional judgment on the needs and on the progress of the patient, checking for counter-indications together with the personal attention and motivation given to the patient by the therapist. But at present the therapist is also needed to (a) position the EEG cap or headset onto the patient's head, (b)

add conducting gel and (c) set-up the equipment. The latter reasons a-c, although indispensible at present, form at the same time a bottleneck. They are a bottleneck in the following sense:

- the therapist gets involved only after the user has been diagnosed to be ill or has been classified according to a certain disorder. The user has become a patient. In other words, feedback training is not used as a preventive tool, which could help a user to maintain a healthy equilibrium;
- the therapist is needed to take care of positioning the cap, applying conducting gel and setting-up equipment, in other words: without the therapist the neurofeedback training cannot happen. The user cannot train at home. This limitation in turn, limits the number of training sessions, both in frequency and duration;

There is one conclusion which we draw immediately, namely that if the practical difficulties related to the cap, the gel and the equipment can be solved or relieved, home usage and preventive usage are much more likely to happen.

But the contribution of the therapist is larger. There is no substitute for his or her professional judgment and personal attention. So the therapist keeps a role, although perhaps not during each session. This leaves a question about the unsupervised sessions. The question is how the user will keep him or herself motivated to train regularly. Our answer is simple: training should be fun. Phrased differently, there have to be motivational elements built-in to the training equipment (gaming, flow). We shall address this in the next section.

Now let's have a closer look at the user. G(s) is an intertwined mind-body complex. The output of the training equipment enters the user through suitable interface elements first at his or her bodily level: ears, eyes, perhaps touch. This is not very problematic because excellent interface elements such as loudspeakers, earphones, video screens etc. are readily available. There is also no lack of pleasant and aesthetic audio-video content. The user's output, the EEG signal, is also wiretapped at a physical level. This is a source of difficulties, as already mentioned. That is why we consider the design of an easy-to-use headset to be an essential step.

At a higher level inside the user there are processes of perception, cognition, volition and consciousness going on. It is at this level that issues of attention and attention deficit become noticeable, as in ADHD. But it is also at this level where fun, beauty and motivation occur.

4 PRACTICAL AND MOTIVATIONAL ELEMENTS

To enable neurofeedback training in the home context, the product should be designed according specific requirements, aiming at improving the training methods and enabling users to operate independently. These requirements should include the ability to (a) easily locate sensor positions, (b) apply sensors and gel without help, (c) measure electrode impedance and to act accordingly and (d) easily clean and reuse the system.

Bringing neurofeedback training to the home environment would also benefit the financial aspect, reducing the cost of training as a result of decreasing expert involvement. Furthermore, only an EEG measurement device and software would have to be acquired, since we can assume that most households already have a computer.

In addition to the requirements, the training software should be intrinsically motivating (playful) (Rauterberg, 2004) as mentioned before. For designing training software, we formulated the following assumptions based on observations and experiences:

- A_1: that it is helpful to give the user rewards based on performance;
- A_2: that it is helpful to simulate elements from an assumed context of use;
- A_3: that it is helpful to provide the user with quantitative performance data.

Taking a closer look at these assumptions, we find several opportunities to apply concepts of gaming to the proposed neurofeedback training software, for example:

- reward schemes with levels, credits, bonuses, etc. (A_1);
- sound generation and rendering of high-resolution real-time environments (A_2);
- statistics and graphs etc. (A_3);

Acknowledging this overlap and the fact that intrinsic motivation is found in gaming (Malone, 1980), implies stimulating concentration and motivation. We suggest to incorporate gaming aspects in neurofeedback training software (e.g. ‘Brainball’ of Hjelm (Hjelm, 2003) is considered to be an interesting example).

We aim for neurofeedback training applied in such a practical and motivational way that it can be considered a game. In the next section we describe the creation of a product in which we applied the aforementioned shift from treatment to play, in an attempt to show it is not only desirable but also achievable. However, we have to consider the fact that the rich media and gaming experience people are used to, has its influence on the expectancy for neurofeedback software; we could say that neurofeedback training has to keep pace with gaming.

5 DEVELOPMENT OF EEG HEADSET

In order to reach the aims as discussed earlier, we developed a headset which gives the user the opportunity to retrieve EEG signals from his scalp in a convenient way. Combined with neurofeedback in the form of a 3D environment, this headset is the first step to the vision that combines gaming, EEG signals and therapy within the home environment. In contrast to the traditional ElectroCap, the headset (Figure 3) can be put on the head with ease and without professional help. Operations as locating contact points, attaching sensors and applying conducting gel are all integrated in the headset, enabling neurofeedback applications for non-expert users in the home environment. The product includes a headset, electronics, sensors, hard- and software.

Figure 3: EEG headset.

The headset has a flexible construction to adapt to a variety of head dimensions. The material flexibility enables a one-size fits all design, reckoning with a head breadth variety of 1.3 inch. This figure is based on difference in dimensions of children age 6 (5^{th} percentile girls, 5.1 inch) to adults (95^{th} percentile male, 6.4 inch) (Woodson, Tillman, & Tillman, 1992). The mechanical properties of the material make sure that the headset is stable on the head, which is necessary for the sensors to work properly. Soft cushion pads on the sides provide the headset with more stability and comfort.

Embedded electronics take care of the 2-channel EEG signal amplification, enhancing signal strength. Two sensors (positioned on points C3 and C4 of the international 10-20 system) measure EEG signals while the sensor positioned on the Cz location acts as a ground (a common reference electrode placement). The fourth sensor is placed near the Fz position and acts as an active electrode, according to the 'driven right leg' (DRL) principle (Webster, 1998) to minimise distortion. This position has been chosen for its symmetric location relative to points C3 and C4, preventing topographic distortion. Moreover, it increases the stability of the headset by restricting the headset to tilt when nodding or moving the head otherwise.

The sensors (Figure 4) can be clicked in and out of slots in the headset. Those slots enable two degrees of freedom (translation and rotation), enabling the sensors to adapt to different head shapes and dimensions autonomously. A flexible material between the sensor and the headset allows for vertical sensor translation and applies a force, pushing the sensor on the scalp. Additionally, the shape of the sensor slots enables a 20˚ rotation to both sides. The combination of translation and rotation assures that the sensors can adapt to different head shapes and helps to maintain a stable signal.

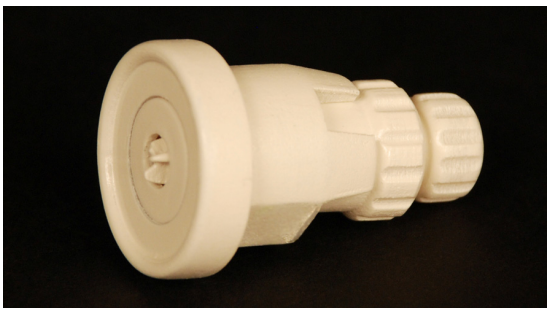

Figure 4: EEG headset sensor.

The detachable sensors measure EEG signals on the scalp. Therefore the scalp has to be scratched in

order to gently remove dead skin cells that disturb the signals, this is achieved by simply twisting a part of the sensor called 'scratcher'. Furthermore, a container for conducting gel is implemented in the scratcher. The gel can simply be applied by pushing a plunger. By doing so, the gel connects the tin (Sn) electrode with the scalp, bridging the gap caused by the hair. Currently, the sensors need to be filled with gel using a syringe, but in the future gel capsules or disposable sensors will be developed to nullify this inconvenience.

The 2 channel EEG signal retrieved from the sensors is magnified by the analogue pre-amplifier in the headset. This signal is converted using an A/D converter, which is located in an external box. The box also contains a power source and an opto-coupler for safety reasons. The signal is send to a computer, which feeds the retrieved bio-signals back through a 3D environment. This 3D environment includes different sessions for neurofeedback training, where the user learns to train specific brain capacities using goals and instant brain feedback (e.g. the intensity of a fire is related to the level of concentration, see Figure 5).

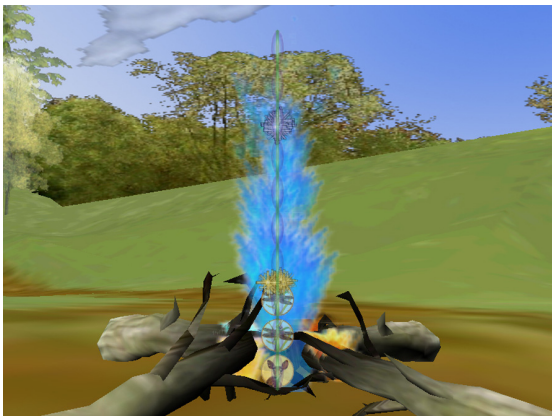

Figure 5: Screenshot of 3D environment 'AdventurePark'.

6 EVALUATION

To test the quality of the headset, we developed an initial functional prototype since the actual headset has not been manufactured yet. This prototype was used in an evaluation of the headset principle.

6.1 Research Question

An impedance limit of 5 kΩ is often mentioned for clinical use of the EEG, in order to prevent signal distortions (Heinrich, 2007). In this project however, we allow ourselves a 10 kΩ impedance limit because of two reasons. Firstly, we assume that the distortion level depends on the length of the wires, which is reduced by embedding the preamplifier in the headset. Secondly, the embedded DRL system filters a lot of distortion, ensuring a relatively high quality EEG signal. This leads to the following formulation of the research question:

All sensors of the headset have impedance lower than 10 kΩ when placed on the head of the participants.

6.2 Method

We conducted an experiment in which we compared the impedance values of the sensors against the requirements of 10 kΩ.

6.2.1 Apparatus and Measurements

To prevent for extreme cases influencing the reliability of the experiment, head dimensions of the participants have been measured by the experimenters (Figure 6). A tape measurer has been used to measure the ear to ear distance along the skull (from the points of attachment of the ears along the centreline of the international 10-20 electrode placement system). For the head breadth, measured straight above the ears, a self-made sliding calliper has been used (Figure 7).

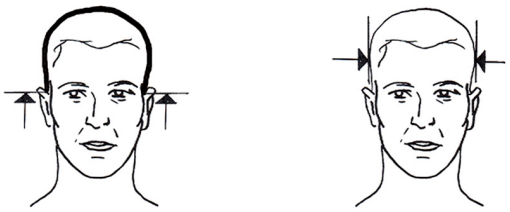

Figure 6: Head dimension measurement method.

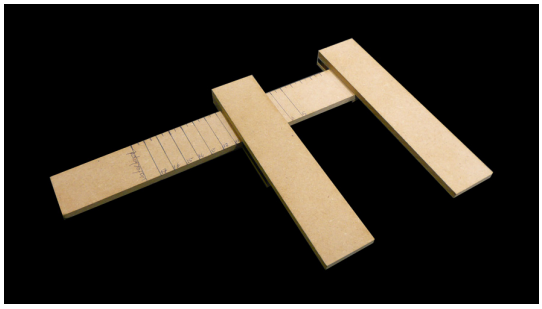

Figure 7: Self-made sliding calliper.

The impedance of the sensors C3, C4 and Fz were measured relatively to sensor Cz. For this, the 2-

Channel EEG MindSurfer Standard hardware has been used. The value was determined by reading an analogue gauge implemented in the Jukebox mental training software installed on a notebook (NEC Versa P520). The gauge was calibrated on forehand with resistors with fixed values.

The functional prototype (Figure 8) was made of 4mm thick Plexiglass and shaped according the headset design.

6.2.2 Participants and Procedure

Twenty students (17 male, 3 female, age 20-24) participated in this test. The tests took place in an cutoff room. After welcoming the participants, they were asked to sit in a comfortable chair.

Figure 8: Picture user test participant.

After a short introduction the participant was asked to put on the headset. The experimenters assisted in positioning the headset and parting the hair out of the way. Participants gently scratched their own head with the sensor scratchers and applied the gel. The participants were able to see the impedance value on the notebook screen and were instructed to optimise the conductance by trying to bring this value down to less than 10 kΩ. They were told to achieve this by using the sensor scratchers and by shaking the headset slightly, allowing the gel to settle. After optimising the conductance for about one minute, the researcher recorded the impedance value of each sensor. This value indicates the impedance between sensor Cz and sensors C3, C4 and Fz. 2-Channel EEG hardware was used, whereas three values had to be recorded. Therefore the C3 sensor wire was connected to the Fz sensor after recording its value, the C4 wire was disconnected at that time.

After each test, all gel was removed from the sensors and new gel was inserted, to ensure the same conditions for all participants.

6.3 Results

We calculated the mean and standard deviations of all measurements and report on them in Table 1 and illustrate them in
Figure 9.

A t-test showed that the mean impedances for C3 ($t(19)=-4.616$, $p<.001$), C4 ($t(19)=-4.082$, $p=.001$) and Fz ($t(19)=-7{,}452$, $p<.001$) were significantly lower than 10 kΩ.

The head dimensions of the participants are within the 5th and 95th percentile as defined in the Human Factors Design Handbook (Woodson et al., 1992).

Table 1: Head dimensions and sensor impedances.

	mean	std dev
Head breadth (cm)	15.01	0.52
Ear to ear distance (cm)	31.75	1.40
Sensor C3 (kΩ)	6.70	3.20
Sensor C4 (kΩ)	7.10	3.18
Sensor Fz (kΩ)	5.40	2.76

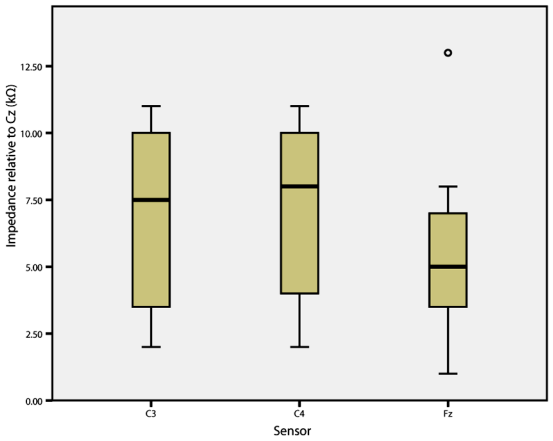

Figure 9: Median, quartile ranges and outliers of result set.

6.4 Conclusions

Based on the results of this evaluation we can state that the functional prototype reaches impedances significantly lower than the desired 10 kΩ limit. In addition, based on our experience there seem to be some aspects that would probably decrease the impedance even more, although it should be mentioned that no extensive testing of these aspects has been done. Firstly, based on our own experience, it seems that having some experience with the headset plays an important role in creating good conductivity. Given a certain amount of training, most users are likely to achieve impedance levels

below 5k. Secondly, the impedance measurements were recorded after approximately one minute of having the gel applied on the head, yet our experience gives the impression that the impedance tends to decrease a bit over time.

The results are considered promising and in manufacturing the headset, there should be aimed for the same characteristics as the functional prototype. However, this doesn't imply that the manufactured headset will actually behave in the exact same way and therefore we propose an evaluation of the final product as well.

7 DISCUSSION

We identified several possible issues holding back the development and implementation of neurofeedback therapy. New aims of neurofeedback are suggested, including: 1) a focus shift in healthcare from cure to prevention, 2) increasing the focus on mental wellbeing in healthcare, 3) elevating the standard of living by enabling users to consciously train brain signals 4) implementing gaming approaches in neurofeedback to increase intrinsic motivation.

In an attempt to make neurofeedback training more accessible by combining the therapy with gaming in the home environment, we designed a headset that can be used all by oneself in combination with a 3D gaming environment for desktop pc. We evaluated a prototype of the headset and proved that the impedances of the sensors were significantly below 10 kΩ. Of course, future work will have to imply the actual realization and testing of this headset, more iteration steps will have to be made before starting large volume production.

To our knowledge, this headset is one of the first attempts to apply enjoyable neurofeedback in the home environment. It can be used without supervision of a medical expert and can be operated by a single user, lowering the practical barriers of neurofeedback therapy, combined with motivational elements in the form of an entertaining 3D game. Hopefully, this will increase the societal acceptance of neurofeedback

We argue to continue developing headsets implementing EEG sensors, in order to stimulate the ease of use. Future work could include gel capsules to prevent hassle with syringes and cleaning, or even dry EEG sensors. Furthermore, a focus should remain on using gaming as motivational tool in neurofeedback therapy and to support society adopting neurofeedback training to increase overall mental wellbeing. Neurofeedback therapy already exists for over a decade; still the general public is unaware of the broad spectrum of opportunities neurofeedback could provide. Curing mental illnesses is of course a big opportunity, but neurofeedback has the potential to go much further. Instead of curing, it could prevent mental illness to happen or even exceed current human capabilities. For this to be realized, the neurofeedback research community should focus on practical and motivational issues that hold back the implementation of neurofeedback therapy, and create a shift towards a society that greatly benefits from its possibilities.

ACKNOWLEDGEMENTS

We would like to thank Joep Frens, Chet Bangaru, Jacques Terken and Geert van den Boomen from the Department of Industrial Design, Eindhoven University of Technology, who helped shaping our thoughts and enabled the design of the headset. Furthermore we would like to thank Geert-Jan Driessen, Pierre Cluitmans and Frans Tomeij for sharing their knowledge and insights on the matter. The Mind Connection in Maastricht has been a contributor of the project.

REFERENCES

ElectroCap International Inc. (2004). ElectroCap International Inc. Retrieved April 3, 2007, from http://www.electro-cap.com

Emotiv Systems Inc. (2007). Project Epoc. Retrieved July 13, 2007, from http://www.emotiv.com

Evans. (1999). *Introduction to quantitative EEG and neurofeedback*.

Fox, K. R. (1999). The influence of physical activity on mental well-being. *Public Health Nutr, 2*(3A), 411.

Guger Technologies OEG (2007). g.EEGcap. Retrieved July 13, 2007, from http://www.gtec.at/products/Accessories/gEEGcap.htm

Hammond, D.C. (2007). What is neurofeedback. *Journal of Neurotherapy, 10*(4), 25.

Heinrich, H., Gevensleben, H., Strehl, U. (2007). Annotation: neurofeedback - train your brain to train behaviour. *J Child Psychol Psychiatry, 48*(1), 3-16.

Hjelm, S. I. (2003). Research + design: the making of Brainball. *interactions, 10*(1), 26-34.

Kendell, R. E. (2001). The distinction between mental and physical illness. *Br J Psychiatry, 178*, 490.

Lubar, J. F. (1995). Evaluation of the effectiveness of EEG neurofeedback training for ADHD in a clinical setting as measured by changes in T.O.V.A. scores,

behavioral ratings, and WISC-R performance. *Biofeedback Self Regul, 20*(1), 83.

Malone. (1980). *What Makes Things Fun to Learn?: A Study of Intrinsically Motivating Computer Games.* Ph.D. dissertation, Department of Psychology, Stanford University.

Rauterberg, M. (2004). Positive effects of entertainment technology on human behaviour. In Rene Jacquart (Ed.), *Building the Information Society* (pp. pp. 51-58): IFIP, Kluwer Academic Press.

Roskamp, H. (2007, feb/mar 2007). Wordt baas in eigen brein. *Bright, 14,* 57-61.

SMART BrainGames (2007). SMART BrainGames PlayStation System. Retrieved July 13, 2007, from http://www.smartbraingames.com/product.asp?id=1289

Splunter, J. van (2002). Building Technology for People. Retrieved October 29, 2007, from http://ww5.newscenter.philips.com/assets/Downloadablefile/CEBIT-Asia-Keynote-speech-Van-Splunter(1)-3734-1440.pdf

Webster, J. G. (1998). *Medical Instrumentation* (3rd ed.). New York: John Wiley & Sons.

Woodson, W. E., Tillman, B., & Tillman, P. (1992). *Human Factors Design Handbook* (2nd ed.): McGraw Hill.

RULE OPTIMIZING TECHNIQUE MOTIVATED BY HUMAN CONCEPT FORMATION

Fedja Hadzic and Tharam S. Dillon
Digital Eciossytems and Business Intelligence Institute (DEBII), Curtin Universityof Technology, USA
fedja.hadzic@postgrad.curtin.edu.au, t.dillon@curtin.edu.au

Keywords: Data Mining, Rule Optimization, Feature Selection.

Abstract: In this paper we present a rule optimizing technique motivated by the psychological studies of human concept learning. The technique allows for reasoning to happen at both higher levels of abstraction and lower level of detail in order to optimize the rule set. Information stored at the higher level allows for optimizing processes such as rule splitting, merging and deleting, while the information stored at the lower level allows for determining the attribute relevance for a particular rule.

1 INTRODUCTION

During the rule optimization process a trade-off usually needs to be made between the misclassification rate (MR), and coverage rate (CR) and generalization power (GP). MR corresponds to the number of incorrectly classified instances and it should be minimized. CR is the number of instances that are captured by the rule set and this should be maximized. Good GP is achieved by simplifying the rules. The trade-off occurs especially when the data set is characterized by continuous attributes where a valid constraint on the attribute range needs to be determined for a particular rule. Increasing the attribute range usually leads to the increase in CR but at the cost of an increase in MR. Similarly if the rules are too general they may lack the specificity to distinguish some domain characteristics and hence the MR would increase.

In this paper we extend the rule optimizing method presented in (Hadzic & Dillon, 2005; Hadzic & Dillon, 2007). The method was used to optimize the rules learned by a neural network and in this work it is extended to be applicable to rules obtained using any knowledge learning methods. The extension allows reasoning to happen at both higher level of abstraction and lower level of detail. The information about the relationships between the class attribute and the input attributes will be available for determining the relevance of rule attributes at any stage of the rule optimizing (*RO*) process. The attributes irrelevant for a particular rule can then be deleted. Furthermore, attributes previously found as irrelevant can be re-introduced if found relevant at a later stage in the process. The proposed method is evaluated on the rules learned from publicly available real world datasets and the results indicate the effectiveness of the method.

2 MOTIVATION

Concept or category formation has been studied extensively in the psychology area. Generally it refers to the process by which a person learns to sort specific observations into general rules or classes. It allows one to respond to events in terms of their class membership rather than uniqueness (Bruner et al., 1956). This process is the elementary form by which humans adjust to their environment. Relevant attributes need to be identified and a rule has to be learned, developed or applied for formulating a concept (Sestito & Dillon, 1994). Human subjects consistently seek confirming information by actively searching they environment for appropriate examples which can confirm or modify the newly discovered concepts (Kristal 1981; Pollio 1974, sestito & Dillon 1994). Hence, there exists one level at which the concepts or categories have been formed and there is another level where the observations are used for confirming or adjusting the learned concepts and their relationships (Rosch 1977). When a formed belief appears to be contradictory for some observations one may go into thinking at the lower level of detail to investigate the constituents of that belief and what example

observations formed it. An update of the belief can then occur whereby some pre-conditions are added or removed from the constituents of that particular belief. Re-introducing new features previously found as irrelevant or removing the irrelevant one, can occur quite frequently while learning occurs and until some reliable belief is formed.

Being able to perform this type of task is desirable for the rule optimizing process. The higher level of abstraction would correspond to the rules with the attribute constraints and the predicting class values, while at the lower level the relationships between attribute values and the occurring class values are stored. This information can be used to determine the relevance of attributes in predicting of the class value that a particular rule implies. Integrating the feature selection criterion with the rule optimizing stage is advantageous since initial bad choices made about the attribute relevance could be corrected as learning proceeds.

3 METHOD DESCRIPTION

The method takes as input a file describing the rules detected by a particular classifier and the domain dataset from which the rules were learned. The rules are represented in a graph structure (*GS*) where each rule has a set of attribute constraints and points to one or more target values. The *GS* contains the high level information about the domain at hand in form of rules and is used for reasoning at the higher level of abstraction.

3.1 Graph Structure Formation

In order for the *GS* to be formed two files are read, one describing the rules detected by a classifier and the other containing the total set of instances from which the rules were learned. The rules are in form of attribute constraints while the implying class of each rule is ignored. The reason is that during the whole process of *RO*, the implying class values can change as some clusters will be merged or split. Rather the domain dataset is read according to which the weighted links between the rules and class values are set. The implying class value of a rule becomes the highest weighted link to a particular class value node. This class value has most frequently occurred in the instances which were captured by the rule. An example of the GS after a dataset is read in is shown in Figure 1. The implying class of Rule1 and Rule 3 would be class value 1 while for Rule2 it is class value 2. Even though it is not shown in the figure, each rule has a set of attribute constraints associated with it, which we refer to as the weight vector (*WV*) of that rule. The set of attribute values occurring in the instance being processed are referred to as the input vector (*IV*). Hence, to classify an instance we match the *IV* against the *WV*s of the available rules. A constraint for a continuous attribute is given in terms of a lower range (lr) and an upper range (ur) indicating the set of allowed attribute values.

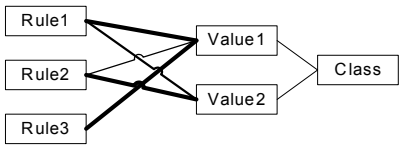

Figure 1: Example graph structure from high level.

3.2 Storing Lower Level Information

Previous sub-section has explained the *GS* formation at the top level which is used mainly for determining the implying class values of the rules. In this section we discuss how lower level instance information is stored for each rule. This low level information is necessary for the reasoning at the lower level.

As previously mentioned each rule has a set of attribute constraints associated with it, which are stored in its *WV*. For each of the attributes in the *WV* we collect the occurring attribute values in the instances that were captured by that particular rule. Hence each attribute has a value list (*VL*) associated with it which stores all the occurring attribute values. Furthermore, each of the value objects in the list has a set of weighted links to the occurring class values in the instance where that particular value occurred. This is necessary for the feature selection process which will be explained later. For a continuous attributes there could be many occurring values and values close to one another are merged into one value object when the difference between the values is less than a chosen merge value threshold. Hence the numerical values stored in a list of a continuous attribute will be ordered so that a new value is always stored in an appropriate place and the merging can occur if necessary. Figure 2 illustrates how this low level information is stored for a rule that consists of two continuous attributes A and B. The attribute A has the lower range (lr) and the upper range (ur) in between which the values v1, v2 and v3 occur. The ‘lr’ of A is equal to the value of v1 or the ‘lr; of v1 if v1 is a merged value object,

while the 'ur' of A is equal to the value of v3 or the 'ur' of v3 if v3 is a merged value object.

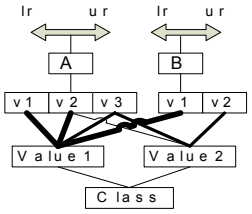

Figure 2: Storing low level instance information.

3.3 Reasoning at the Higher Level

Once the implying classes are set for each of the rules the dataset is read in again in order to check for any misclassifications and update the rule set accordingly. When a rule captures an instance that has a different class value than the implication of the rule, a child rule will be created in order to isolate the characteristic of the rule causing the misclassification. The attribute constraints of the parent and child rule are updated so that they are exclusive from one another. The child attribute constraint ranges from the attribute value of the instance to the range limit of the parent rule to which the input attribute value was closest to. The parent rule adopts the remaining range as the constraint for the attribute at hand.

After the whole dataset is read in there could be many child rules created from a parent rule. Some child rules may be merged together first but explanation of this is to come later once we discuss the process of rule similarity comparison and merging. If a child rule points to other target values with high confidence it become a new rule and this corresponds to the process of rule splitting, since the parent rule has been modified to exclude the child rule which is now a rule on its own. On the other hand if the child rule still mainly points to the implying class value of the parent rule it is merged back into the parent rule (if they are still similar enough). An example of a rule which has been modified to contain a few children due to the misclassifications is displayed in Figure 3. The reasoning explained would merge 'Child3' back into the parent rule since it points to the implying class of the parent rule with high weight. This is assuming that they are still similar enough. On the other hand Child1 and Child2 would become new rules since they more frequently capture the instances where the class value is different to the implying class of the parent rule. Furthermore if they are similar enough they would be merged into one rule.

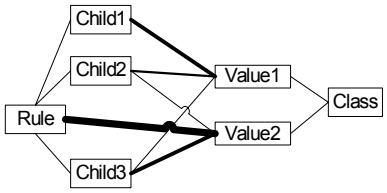

Figure 3: Example of rule splitting.

In order to measure the similarity among the rules we make use of a modified Euclidean distance (*ED*) measure. This measure is also used to determine which rule captures a presented instance. An instance is always assigned to the rule with the smallest *ED* to the *IV*. Even though one would expect the *ED* to be equal to 0 when classifying instances this may not always be the case throughout the *RO* process. The *ED* calculation is calculated according to the difference in the allowed range values of a particular attribute. The way that *ED* is calculated is what determines the similarity among rules, and therefore we first overview the *ED* calculation and then proceed onto explaining the merging of rules that may occur in the whole *RO* process.

3.3.1 ED Calculation

For a continuous attribute a_i occurring at the position i of WV of rule R, let '$a_i$lr' denote the lower range, '$a_i$ur' the upper range, and 'a_iv' the initial value if the ranges of a_i are not set. The value from the i-th attribute of IV will be denotes as iva_i. The i-th term of the ED calculation between IV and WV of R for continuous attributes is:

- case 1: a_i ranges are not set
  - 0 iff $iva_i = a_i v$
  - $iva_i - a_i v$ if $iva_i > a_i v$
  - $a_i v - iva_i$ if $iva_i < a_i v$
- case 2: a_i ranges are set
  - 0 iff $iva_i \geq a_i lr$ and $iva_i \leq a_i ur$
  - $a_i lr - iva_i$ if $iva_i < a_i lr$
  - $iva_i - a_i ur$ if $iva_i > a_i ur$

The input merge threshold used for continuous attribute (*MT*) also needs to be set with respect to the number of continuous attributes in the set. It corresponds to the maximum allowed sum of the range differences among the WV and IV so that the rule would capture the instance at hand.

When calculating the *ED* for the purpose of merging similar rules there are four possibilities that need to be accounted with respect to the ranges being set in the rule attributes, and the *ED* calculation is adjusted. For rule R_1 let r_1a_i denote the attribute occurring at the position i of WV of rule R_1, let '$r_1a_i$lr' denote the lower range, '$r_1a_i$ur' the upper range, and 'r_1a_iv' the initial value if the ranges of r_1a_i are not set. Similarly for rule R_2 let r_2a_i denote the attribute occurring at the position i of WV of rule R_2, let '$r_2a_i$lr' denote the lower range, '$r_2a_i$ur' the upper range, and 'r_2a_iv' the initial value if the ranges of r_2a_i are not set. The i-th term of the *ED* calculation between the WV of R_1 and WV of R_2 for continuous attributes is:

- case 1: both r_1a_i and r_2a_i ranges are not set
  - 0 iff r_1a_iv = r_2a_iv
  - r_1a_iv - r_2a_iv if r_1a_iv > r_2a_iv
  - r_2a_iv - r_1a_iv if r_1a_iv < r_2a_iv
- case 2: r_1a_i ranges are set and r_2a_i ranges are not set
  - 0 iff r_2a_iv ≥ $r_1a_i$lr and r_2a_iv ≤ $r_1a_i$ur
  - $r_1a_i$lr - r_2a_iv if r_2a_iv < $r_1a_i$lr
  - r_2a_iv – $r_1a_i$ur if r_2a_iv > $r_1a_i$ur
- case 3: r_1a_i ranges are not set and r_2a_i ranges are set
  - 0 iff r_1a_iv ≥ $r_2a_i$lr and r_1a_iv ≤ $r_2a_i$ur
  - $r_2a_i$lr – r_1a_iv if r_1a_iv < $r_1a_i$lr
  - r_1a_iv – $r_2a_i$ur if r_1a_iv > $r_2a_i$ur
- case 4: both r_1a_i and r_2a_i ranges are set
  - 0 iff $r_1a_i$lr ≥ $r_2a_i$lr and $r_1a_i$ur ≤ $r_2a_i$ur
  - 0 iff $r_2a_i$lr ≥ $r_1a_i$lr and $r_2a_i$ur ≤ $r_1a_i$ur
  - min($r_1a_i$lr - $r_2a_i$lr, $r_1a_i$ur - $r_2a_i$ur) iff $r_1a_i$lr > $r_2a_i$lr and $r_1a_i$ur > $r_2a_i$ur
  - min($r_2a_i$lr - $r_1a_i$lr, $r_2a_i$ur -$r_1a_i$ur iff $r_2a_i$lr > $r_1a_i$lr and $r_2a_i$ur > $r_1a_i$ur
  - ($r_1a_i$lr – $r_2a_i$ur) iff $r_1a_i$lr > $r_2a_i$ur
  - ($r_2a_i$lr – $r_1a_i$ur) iff $r_2a_i$lr > $r_1a_i$ur

For a rule to capture an instance or for it to be considered sufficiently similar to another rule the *ED* would need to be smaller than the *MT* threshold.

3.3.2 Rule Merging

As mentioned at the start of Section 3.3 the child rules may be created when a particular rule captures an instance that has a different class value than the implying class value of that rule (i.e. misclassification occurs). After the whole file is read in the child rules that have the same implying class values are merged together if the *ED* between them is below the *MT*. Thereafter the child rules either become a new rule or are merged back into the parent rule, as discussed earlier. Once all the child rules have been validated the merging can occur among the new rule set. Hence if any of the rules have the same implying class value and the *ED* between them is below the *MT* the rules will be merged together and the attribute constraints updated. After this process the file is read in again and any of the rules that do not capture any instances are deleted form the rule set.

3.4 Reasoning at the Lower Level

Once the rules have undergone the process of splitting and merging, the relevance of rule attributes should be calculated as some attributes may have lost their relevance through merging of two or more rules. Other attributes may have become relevant as a more specific distinguishing factor of a new rule which resulted from splitting of an original rule. For this purpose we make use of the symmetrical tau (Zhou & Dillon, 1991) feature selection criterion whose calculation is made possible by the information stored at the lower level of the graph structure. We start this section by discussing the properties of the symmetrical tau and then proceed onto explaining how the relevance cut-off is determined and the issue of choosing the merge value threshold for the value objects in a value list.

3.4.1 Feature Selection Criterion

Symmetrical Tau (τ) (Zhou & Dillon, 1991) is a statistical measure for the capability of an attribute in predicting the class of another attribute. The τ measure is calculated using a contingency table which is used in statistical area to record and analyze the relationship between two or more variables. If there are I rows and J columns in the table, the probability that an individual belongs to row category i and column category j is represented as P(ij), and P(i+) and P(+j) are the marginal probabilities in row category i and column category j respectively, the Symmetrical Tau measure is defined as (Zhou & Dillon, 1991):

$$\tau = \frac{\sum_{j=1}^{J}\sum_{i=1}^{I} P_{ij}^2/P_{+j} + \sum_{i=1}^{I}\sum_{j=1}^{J} P_{ij}^2/P_{i+} - \sum_{i=1}^{I} P_{i+}^2 - \sum_{j=1}^{J} P_{+j}^2}{2 - \sum_{i=1}^{I} P_{i+}^2 - \sum_{j=1}^{J} P_{+j}^2}.$$

For the purpose of feature selection problem one criteria in the contingency table could be viewed as an attribute and the other as the target class that needs to be predicted. In our case the information contained in a contingency table between the rule attributes and the class attributes is stored at the

lower level of the graph structure as explained in Section 3.2. The τ measure was used as a filter approach for the feature subset selection problem in (Hadzic & Dillon, 2006). In the current work its capability of measuring the sequential variation of an attribute's predictive capability is exploited.

3.4.2 Determining Relevance Cut-off

For each of the rules that are triggered for multiple class values we calculate the τ criterion and rank the rule attributes according to the decreasing τ value. The relevance cut-off point is determined as the point in the ranking where the τ value of an attribute is less than half of the previous attribute's τ value. All the attributes below the cut-off point are considered irrelevant for that particular rule and are removed from the rule's WV. On the other hand, if some of the attributes above the relevance cut-off point were previously excluded from the WV of the rule, they are now re-introduced since their τ value indicates their relevance for the rule at hand.

As mentioned in Section 3.2 when the occurring values stored in the value list of an attribute are close together they are merged and the new value object represents a range of values. The merge value threshold chosen determines when the difference among the value objects is sufficiently small for merging to occur. This is important for appropriate τ calculation. Ideally a good merge value threshold will be picked with respect to the value distribution of that particular attribute. However, this information is not always available and in our approach we pick a general merge threshold of around 0.02. This has some implications for the calculated τ value since when the categories of an attribute A are increased more is known about attribute A and the error in predicting attribute B may decrease. Hence, if the merge value threshold is too large many attributes will be considered as irrelevant since all the occurring values could be merged into one value object which points to many target objects and this aspect would indicate no distinguishing property of the attribute. On the other hand, if it is too small many value objects may exist which may wrongly indicate that the attribute has high relevance in predicting the class attribute.

4 METHOD EVALUATION

The proposed method was evaluated on two rule sets learned from publicly available real world datasets (Blake et al., 1998). The rule optimizing process was run for 10 iterations for each of the tested domains.

The first set of rules we consider has been learned from the 'Iris' dataset using the continuous self-organizing map (Hadzic & Dillon, 2005) so that we can compare the improvement of the extension to the rule optimizing method. The merge cluster threshold *MT* was set to 0.1 and the merge value threshold *MVT* for attribute values was set to 0.02. The rules obtained using the CSOM technique (Hadzic & Dillon, 2005) are displayed in Figure 4. When the rules obtained after retraining were taken as input by our proposed rule optimization method the resulting rule set was different in only one rule. The rule 4 was further simplified to exclude the attribute constraint from sepal-width and the new attribute constraint was only that petal-width has to be between the values of 0.667 and 1.0 for the class value of Iris-virginica. Hence the process was able to detect another attribute that has become irrelevant during the *RO* process. The predictive accuracy remained the same.

C#	Constraints	TargetVector	MR
1	0.24 < SL < 0.694 0.08 < SW < 0.58 0.42 < PL < 0.695 0.36 < PW < 0.62	Ivs – 26 Ivg – 1	1
2	0.41 < SL < 0.556 0.2 < SW < 0.49 0.64 < PL < 0.78 0.54 < PW < 0.75	Ivg – 9	
3	0 < PW < 0.167	Is – 33	
4	0.25 < SW < 0.75 0.75 < PW < 1	Ivg – 21	
5	0.194 < SL < 0.22 0.37 < PW < 0.41	Ivs – 2	
6	0.375 < SW < 0.5 0.625 < PW < 0.7	Ivg – 5 Ivs – 1	1

C#	Constraints	TargetVector	MR
1	0.24 < SL < 0.75 0.08 < SW < 0.58 0.42 < PL < 0.695 0.36 < PW < 0.62	Ivs – 17 Ivg – 1	1
2	0.41 < SL < 0.556 0.2 < SW < 0.49 0.64 < PL < 0.78 0.54 < PW < 0.75	Ivg – 1	
3	0 < PW < 0.208	Is – 15	
4	0.2 < SW < 0.75 0.667 < PW < 1	Ivg – 12	
5	0.19 < SL < 0.22 0.37 < PW < 0.41	Ivs – 1	
6	0.375 < SW < 0.5 0.625 < PW < 0.7	Ivs – 1	

Figure 4: Iris rule set as obtained by using the traditional rule optimizing technique.

With respect to using CSOM to extract rules from the 'Iris' domain we have performed another experiment. The initial rules extracted by CSOM without the network pruning and retraining of the network were optimized. When network pruning occurs the network should be re-trained for new abstractions to be properly formed. In this experiment we wanted to see how the *RO* technique performs by itself without any network pruning or retraining.

Rules	Implying class
0.33 < PL < 0.678 0.375 < PW < 0.792	Iris-versicolor
0.208 < SW < 0.542 0.627 < PL < 0.847 0.54 < PW < 1.0	Iris-virginica
0.778 < SL < 1.0 0.25 < SW < 0.75 0.814 < PL < 1.0 0.625 < PW < 0.917	Iris-virginica
0.0 < SL < 0.417 0.41 < SW < 0.917 0.0 < PL < 0.153 0.0 < PW < 0.208	Iris-setosa

Figure 5: Optimized initial rules extracted by CSOM Notation: SL – sepal_length, SW – sepal_width, PL – petal _length, PW – petal_width.

By applying the *RO* technique the rule set was reduced to four rules as displayed in Figure 5. However, not as many attributes were removed from each of the rules and two instances were misclassified. Hence, performing network pruning and retraining prior to *RO* may achieve a more optimal rule set. However, in the cases where retraining the network may be too expensive the *RO* technique can be applied by itself. In fact compared to the initial set of rules detected by CSOM, which consisted of nine rules with three misclassified instances this is still a significant improvement.

The second set of experiments was performed on the complex 'Sonar' dataset which consists of sixty continuous attributes. The examples are classified into two groups one identified as rocks (R) and the second identified as metal cylinders (M). The learned decision tree by the C4 algorithm (Quinlan, 1990) consisted of 18 rules with the predictive accuracy equal to 65.1%. These rules were taken as input in our *RO* technique and the *MT* was set to 0.2 while the *MVT* was set to 0.0005. The optimized rule set consisted of only two rules i.e 0.0 < a11 <= 0.197 → R and 0.197 < a11 <= 1.0 → M. When tested on an unseen dataset the predictive accuracy was 82.2 % i.e. 11 instances were misclassified from the available 62. Hence the *RO* process has again proved useful in simplifying the rules set without the cost of increasing the number of misclassified instances.

5 CONCLUSIONS

This paper has presented a rule optimizing technique motivated by the psychological studies of human concept information. The capability to swap from the higher level reasoning to the reasoning at the lower instance level has indeed proven useful for determining the relevance of attributes throughout the rule optimizing process. The method is applicable to the optimization of rules obtained from any data mining techniques. The evaluation of the method on the rules learned from real world data by different classifier methods has shown its effectiveness in optimizing the rule set. As a future work method needs to be extended so that categorical attributes can be handled as well. Furthermore, it would be interesting to explore the possibilities of the rule optimizing method in becoming a stand-alone machine learning method itself.

REFERENCES

Blake, C., Keogh, E. and Merz, C.J., 1998. UCI Repository of Machine Learning Databases, Irvine, CA: University of California, Department of Information and Computer Science., 1998. [http://www.ics.uci.edu/~mlearn/MLRepository.html].

Bruner, J.S., Goodnow, J.J., and Austin, G.A., 2001. *A study of thinking*, John Wiley & Sons, Inc., New York, 1956.

Hadzic, F. & Dillon, T.S., 2005. "CSOM: Self Organizing Map for Continuous Data", *3rd Int'l IEEE Conf. on Industrial Informatics*, 10-12 August, Perth.

Hadzic, F. and Dillon, T.S., 2006 "Using the Symmetrical Tau (τ) Criterion for Feature Selection in Decision Tree and Neural Network Learning", *2nd Workshop on Feature Selection for Data Mining: Interfacing Machine Learning and Statistics*, in conj. with SIAM Int'l Conf. on Data Mining, Bethesda, 2006.

Hadzic, F. & Dillon, T.S., 2007. "CSOM for Mixed Data Types", *4th Int'l Symposium on Neural Networks*, June 3-7, Nanjing, China.

Kristal, L., ed. 1981, *ABC of Psychology*, Michael Joseph, London, pp. 56-57.

Pollio, H.R., 1974, The *psychology of Symbolic Activity*, Addison-Wesley, Reading, Massachusetts.

Quinlan, J.R., 1990. "Probabilistic Decision Trees", Machine Learning: An Artificial Intelligence Approach Volume 4, Kadratoff, Y & Michalski, R., Morgan Kaufmann Publishers, Inc., San Mateo, California.

Roch, E. 1977, "Classification of real-world objects: Origins and representations in cognition", in *Thinking: Readings in Cognitive Science*, eds P.N. Johnson-Laird & P.C. Wason, Cambridge University Press, Cambridge, pp. 212-222.

Sestito, S. and Dillon, S.T., 1994. *Automated Knowledge Acquisition*. Prentice Hall of Australia Pty Ltd, Sydney.

Zhou, X., and Dillon, T.S., 1991. "A statistical-heuristic feature selection criterion for decision tree induction", *IEEE Transactions on Pattern Analysis and Machine Intelligence*, vol. 13, no.8, August, pp 834-841.

BIOMIMETICS AND PROPORTIONAL NOISE IN MOTOR CONTROL

Christopher M. Harris
Centre for Theoretical and Computational Neuroscience, Universityv of Plymouth, Plymouth, Devon PL4 8AA, U.K.
cmharris@plymouth.ac.uk

Keywords: Human movement, optimal control, minimum variance, minimum jerk, channel capacity, neuromorphic engineering, biomimicry, size principle, saccade, arm reaching.

Abstract: Proportional noise, in which the standard deviation of signal noise is proportional to signal mean, is a fundamental constraint on human motor performance but why it occurs is unknown. We show that for neural networks with binary thresholded units, channel capacity is maximised with a recruitment strategy that produces PN. The size principle also emerges, in agreement with observation. We therefore argue that Fitt's law, speed-accuracy trade-off, and the minimum variance trajectories (including minimum jerk trajectories for limiting brief movements), which are observed in most human point-to-point movements, have evolved as optimal strategies resulting from maximising channel capacity. We conclude that biomimicry of minimum variance and minimum jerk trajectories in robotics is probably only of aesthetic value when using standard technology. In contrast, biomimicry using neuromorphic technology in which networks are built from stochastic silicon 'neurons' with thresholds, is functional biomimetics and optimization of channel capacity will produce behaviours that are human-like.

1 INTRODUCTION

A fundamental tenet of biomimetics is that naturally occurring systems have intrinsically 'good' qualities. By mimicking natural systems, it is believed that these qualities will transfer to synthetic systems. While there are some positive examples (eg. 'gecko tape' Geim et al, 2003), it is not always obvious what true benefits accrue from biomimicry, and building copies of nature may become an aesthetic end in itself. Natural systems evolve and adapt to solve problems of survival and reproduction, often by optimizing performance and structure within a particular environment or constraint. Mimicking the behaviour or structure without understanding the natural constraints may not be beneficial and may be quite suboptimal if the context/constraints are not relevant to the synthetic system. To translate nature's solutions to synthetic systems requires a scientific understanding of the problem nature is attempting to solve.

Mimicking human movements in robots is a particularly pertinent example. It is well-known that human movements that redirect an effector (limb, eye, etc.) from one point to another in space, such as reaching or saccadic eye movements, are highly stereotyped with characteristisc 'smooth' trajectories. For brief (rapid) movements, velocity profiles tend to be symmetrical, 'bell-shaped' and rather straight. Historically, this behaviour was first captured by the 'minimum jerk' trajectory (MJ) (Hogan, 1984; Flash & Hogan 1985) which purported to show that observed trajectories minimised the square of jerk (derivative of acceleration) integrated over the movement duration. It was argued that the MJ trajectory was a maximally 'smooth' trajectory. Subsequently, the MJ has been mimicked as a control objective in numerous robotic systems, presumably because of the smoothness performance (it is also easy to compute). However, from a biological viewpoint, the MJ hypothesis has been criticised because of the lack of plausibility of smoothness as a biological relevant performance criterion. Much smoother trajectories are feasible (Harris, 2004) and the MJ model cannot explain why longer movements have asymmetrical velocity profiles. So why build robots with MJ trajectories? – is it aesthetic biomimicry or does it build 'good' robots?

A more recent optimal control model of human movement is the minimum variance model (MV) (Harris & Wolpert, 1998) in which it is proposed that trajectories minimise the inaccuracies caused by

proportional noise (PN), which is a specific kind of signal-dependent noise where the standard deviation of noise on a signal is proportional to the mean of the signal.

$$\sigma_x = Kx \tag{1}$$

where K is a constant. The MV model captures many features of observed trajectories including increasing asymmetry with duration and the ubiquitous Fitt's law (see below). In this model, 'smoothness' is a by-product - not an objective - of the optimization because rapid changes in effector position cause more output variance. We are now beginning to see the incorporation of MV objectives in robotic systems (Simmons & Demiris, 2005). Again though, why build robots with MV trajectories? – is it biomimicry for its own sake, or does it build 'better' robots?

There is no doubt (mathematically) that the 'smoothness' cost function is a by-product of the PN constraint, but why does PN occur in natural systems? Indeed is PN optimal itself for some deeper constraint, and for roboticists is this deeper constraint even relevant to robotics? This is the question we wish to address.

Human movement appears to be tightly constrained by the effects of PN. Most point-to-point movements (such as arm reaching) can be described by the empirical Fitt's law in which the duration of a movement depends only on the ratio of target distance to target width. This invariance implies that that the standard deviation of end-point error is proportional to target distance (ie. PN). Physiological measurements have confirmed the existence of PN in isometric force production (Schmidt et al., 1979; Jones et al, 2002). For low-pass systems (such as muscles), PN on the input command leads directly to a speed-accuracy trade-off. Faster transitions at the ouput require more intense commands which are noisier because of PN, which in turn lead to greater end-point error. For a given muscle plant, there is a unique trajectory that minimises end-point variance (for a given duration) which has been shown to be in close agreement with the observed bell-shape velocity profiles (Harris & Wolpert, 1998, 2006).

It is important to distinguish PN from the noise encountered in renewal point processes (eg. Poisson process), which we call Renewal Noise (RN). The firing rate of neurons has often been modelled as a renewal point process, but in RN it is the *variance* that is proportional to the mean rate, where the constant of proportionality (Fano factor F) depends on the inter-spike interval distribution:

$$\sigma_x = (Fx)^{1/2} \tag{2}$$

PN does not emerge as a 'natural' property of a renewal process (Harris, 2002). Simple mixing of renewal processes does not produce PN, but tends to produce an ever more Poisson-like renewal process (Cox & Miller, 1977). PN must emerge in some other way.

In this paper, we consider an idealised motor recruitment network, or 'channel', and show analytically that there is an optimal recruitment strategy to maximise the number of signals that can be transmitted for a given error probability. PN emerges as the optimal noise for binary sub-channels. We then consider the implications for dynamic motor control.

2 THE IDEALISED CHANNEL

The idealised recruitment channel consists of a parallel network of a large number of noisy sub-channels (eg. motor neurons) each driven by the same input, $x(t)$. The channel output, $y(t)$, is a linear weighted sum of the sub-channel outputs (fig.1).

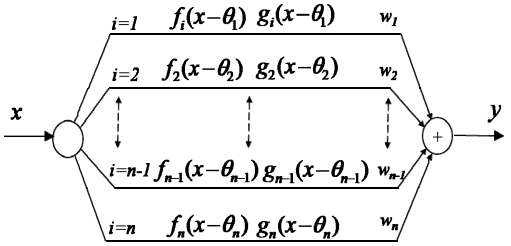

Figure 1: An idealised recruitment channel.

Each sub-channel has a thresholded response function, so that when the instantaneous value of the input exceeds the threshold of the sub-channel, the sub-channel is switched on and generates a noisy signal. When the input is below threshold, the sub-channel is switched off and generates no output and no noise. We denote the output of the ith sub-channel ($i = 1, N$) by

$$z_i(t) = \begin{cases} f_i(x(t) - \theta_i) & x(t) > \theta_i \\ 0 & x(t) < \theta_i \end{cases} \tag{3}$$

where $f_i(.)$ denotes the response characteristic of the ith sub-channel, and θ_i is a constant threshold for that sub-channel.

Each sub-channel generates noise when switched on, which we assume to be mutually independent

from the noise of any other channel. We denote the instantaneous noise variance at the output of each sub-channel by:

$$\sigma_i^2(t) = \begin{cases} g_i(x(t)-\theta_i) & x(t) > \theta_i \\ 0 & x(t) < \theta_i \end{cases} \quad (4)$$

where $g_i(.)$ denotes how noise variance depends on the sub-channel input. The output of the whole channel is then given by

$$y(t) = \sum_{i=1}^{N} w_i z_i(t) \quad (5)$$

where w_i is a fixed positive weight. The total output variance is given by

$$v(t) = \sum_{i=1}^{N} w_i^2 \sigma_i^2(t) \quad (6)$$

We assume that $f_i(.)$ and $g_i(.)$ are pre-specified functions determined by the characteristics of the sub-channels. For convenience, we drop the time dependence and consider only steady-state responses (we will return to the dynamic case later).

Because of the redundancy in the system, it is obvious that there are many ways we can generate a specified output value, *y*, for a given input value *x*, by suitable choice of weights and thresholds. However, in general, each way will produce a different $v(t)$. Therefore, our goal is to find the distribution of weights and thresholds that optimises $v(t)$ according to some cost function. To do this we develop the problem using continuous functions to allow us to use variational calculus to find the optimal weights and thresholds.

2.1 Continuous Recruitment Equations

We approach this problem analytically by assuming that there are a large number of sub-channels so that we can approximate summations in equations 5 and 6 with integrals. In anticipation of a possible singularity occurring at $x = 0$, we also assume that the input can range only over $\varepsilon \le x \le x_{\max}$ where ε is a small positive constant $0 \le \varepsilon << x_{\max}$. We next assume that there is a 'density' of units with thresholds $\theta = x$ denoted by $\rho(x)$, which is constrained by:

$$N = \int_{\varepsilon}^{x_{\max}} \rho(x)dx \quad (7)$$

The weights of sub-channels are approximated by the continuous function $w(x)$. The output can then be written as a convolution integral:

$$y(x) = \int_{\varepsilon}^{x} w(x')\rho(x') f_{x'}(x-x')dx \quad (8)$$

Where $f_x(.)$ is the response characteristic of subchannels with threshold at *x*. The output variance is similarly:

$$v(x) = \sigma_y^2(x) = \int_{\varepsilon}^{x} w^2(x')\rho(x') g_{x'}(x-x')dx \quad (9)$$

2.2 Channel Capacity

We now consider how to optimise the channel's performance when the expected value of channel output is required to follow the input (ie. a unity gain linear channel).

$$y(x) = x \quad \varepsilon \le y \le x_{\max} \quad \varepsilon \le x \le x_{\max} \quad (10)$$

The channel is required to transmit signals of different values at different times. We assume that these signal values are uniformly distributed over the range $\varepsilon \le x \le x_{\max}$, and that the channel is memoryless with no expectation of which signal is to be transmitted.

We consider the input to be deterministic, so that the noise perturbing the output is due to the internal noise of the recruited sub-channels, which we assume to be Gaussian. Let us now assume that we wish to transmit *M* signals spread across the range. Consider three adjacent input signals, x_{j-1}, x_j x_{j+1} (fig.2). We can see that the output y given x_j could deviate sufficiently from the expected value $y(x_j)$ such that a maximum likelihood detector could make an error by attributing the output to be more likely to arise from x_{j-1} or x_{j+1} (shaded tails in fig.2). Assuming noise variance changes slowly with *x*, then the probability of the detector being correct is

$$p_c \approx erf\left(\frac{\Delta_i \sqrt{2}}{\sigma_{y_i}}\right) \quad (11)$$

where Δ_i is the width of the region of correct response. We argue that, of all the possible channel configurations, the one that maximises the number of signals that can be transmitted for a specified probability of correct detection per signal is the best configuration.

Assuming Δ_i to be small so that we can make a continuous approximation, the number of signals that can be transmitted is:

$$M \approx \int_{\varepsilon}^{x_{max}} \frac{1}{\Delta(x)} dx \tag{12}$$

It follows from eq.11 that for a fixed probability of correct response, we need to maximise the benefit function

$$M \approx \int_{\varepsilon}^{x_{max}} \frac{b}{\sigma(x)} dx = \int_{\varepsilon}^{x_{max}} \frac{b}{v^{1/2}(x)} dx \tag{13}$$

where $b = \sqrt{2}/erf^{-1}(p_c)$. This optimization is, however, constrained by the channel's possible output variance functions, eq(9), which are determined by the weighting function $w(x)$ and the threshold density function $\rho(x)$ which must also yield the desired output $y(x)$ according to eq.10. Finally the density function must also be constrained by the total number of sub-channels according to eq.7. We solve this is variational problem analytically for simple binary sub-channels.

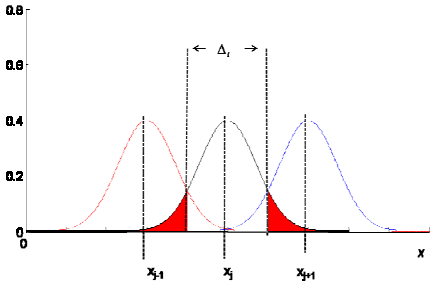

Figure 2: Output of subchannels for deterministic input.

3 BINARY CHANNELS

We now consider a 'neuromorphic' example in which each sub-channel is a 'neuron' with an output signal given by a spike train with a mean firing rate of unity. We assume that the spike-train is a renewal point process so that its variance is proportional to the mean according to eq.2. We further assume that when the neuron is switched on, the mean firing rate does not change with increasing input, ie, the neuron response function is a step function (see figure 3).

$$u(t-\theta) = \begin{vmatrix} 1 & t > \theta \\ 0 & t < \theta \end{vmatrix} \tag{14}$$

The recruitment equation (8) then simplifies to:

$$y = x = \int_{\varepsilon}^{x} w(x')\rho(x')u(x-x')dx' = \int_{\varepsilon}^{x} w(x')\rho(x')dx' \tag{15}$$

which has the solution

$$w(x)\rho(x) = 1 \tag{16}$$

The variance will be given by:

$$v(x) = F\int_{\varepsilon}^{x} w^2(x')\rho(x')dx' \tag{17}$$

or

$$v(x) = F\int_{\varepsilon}^{x} \frac{1}{\rho(x')} dx' \tag{18}$$

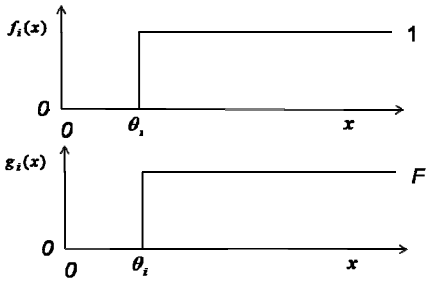

Figure 3: Binary sub-channel. Signal and variance are step-functions.

Differentiating we have

$$\rho(x) = \frac{F}{v'(x)} \tag{19}$$

where the dash means the derivative with respect to x. Substituting into eq.7, we have the constraint:

$$N = \int_{\varepsilon}^{x_{max}} \frac{F}{v'(x)} dx \tag{20}$$

3.1 Isoperimetric Problem

We recognise that maximising the benefit function (eq.13) subject to the integral constraint (eq.20) forms an isoperimetric problem in variational calculus. The Lagrangian is:

$$L(x, v, v') = \frac{b}{v^{1/2}} + \frac{\lambda F}{v'} \tag{21}$$

where λ is a constant Lagrange multiplier. The Euler-Lagrange equation is

$$\frac{b}{v^{3/2}} - \frac{4\lambda F v''}{(v')^3} = 0 \tag{22}$$

which has the solution of the form

$$v(x) = (Kx)^2 \tag{23}$$

where K is a positive constant. This is a maximum and for positive v' it satisfies the Weierstraussian condition for a strong extremum (not shown here). Since we have $y = x$, we can write the output variance as

$$v = (Ky)^2 \tag{24}$$

which is proportional noise.

3.2 Singularity

The threshold density function can now be found by substituting eq.23 into eq20:

$$\rho(x) = \frac{F}{2K^2 x} \tag{25}$$

which will require an infinite threshold density at the origin. This is not physically realizable, so we consider $0 < \varepsilon << x_{\max}$. In this case we see from eq.20 that

$$N = \frac{F}{2K^2} \ln\left(\frac{x_{\max}}{\varepsilon}\right) \tag{26}$$

Thus it appears that we can come arbitrarily close to the origin if we are willing to devote a large enough number of channels. It also appears from eq.25 that reducing K, is very expensive in sub-channels since

$$K = \sqrt{\frac{F}{2N} \ln\left(\frac{x_{\max}}{\varepsilon}\right)} \tag{27}$$

As a numerical example, consider ε to be 0.1% of $x_{\max}$, then if we used a N=1000 sub-channels, then K~0.06 for a Poisson sub-channel renewal process (F=1).

An important property of this optimization is that a size principle emerges. From eq.25 we see that the number of sub-channels deceases with increasing output, but from eq.16 we have

$$w(x) = \frac{1}{\rho(x)} = \frac{2K^2 x}{F}. \tag{28}$$

The weights (or strengths) increase with increasing signal. In human movement physiology, the size principle is a well-known phenomenon, but we see that it an inevitable emergent property of optimizing the channel.

Thus far we have only considered positive signals. To handle signals of either sign, we employ two channels of different polarities with a common origin, so that:

$$\sigma = K|x| \tag{29}$$

We note that there are other configurations in which the two channels could be active simultaneously by having shifted origins (co-activation). This could overcome problems with the singularity, but we do not explore this here.

4 DYNAMICS

We now consider the dynamics of the optimal channel. We will only give an outline to emphasise some remarkable emergent properties, as some aspects have already been dealt with in depth elsewhere and others have yet to be explored experimentally.

4.1 Fano Factor and Bandwidth

It can be seen from above, that the resources needed for the optimal channel also depend on the Fano factor F of the sub-channels. Thus fewer sub-channels are needed if we can reduce F (eq.26). However, for spike trains, reducing F comes at a price, since it reduces bandwidth.

So far we have dropped the dependence on time. Indeed, the above derivation is independent of time provided there are no bandwidth restrictions on the sub-channel response characteristics. However, for the neuromorphic embodiment of sub-channels, the output $z_i(t)$ depends on the firing rate of a motor neuron (sub-channel). Modelling the motor neuron spike train as a renewal point process, the response of $z_i(t)$ will therefore depend on the inter-spike interval probability distribution. For exponential interval distributions, the rate process is Poisson (F=1) with an autocovariance given by a delta function. Thus a Poisson process yields a fast temporal response, but requires a high F. In fact motor neuron firing rates are not Poisson, but have considerable lower Fano factors. This will result in a broader autocovariance function and hence more sluggish impulse response function (Cox & Miller, 1977). The relationship between the impulse response function and the spike-interval distribution is complex and non-stationary, so we will approximate it by a first-order impulse response function with a time-constant τ:

$$R_z(t) = e^{-t/\tau} / \tau \tag{30}$$

4.2 Linear Plant Considerations

Assume that we use our optimal channel to drive a physical effector plant, such as a real muscle, a robotic arm, a prosthetic limb, etc.. We approximate the plant as linear 2nd-order with mass/inertia, viscosity, and elasticity. The drive to this plant is the output of our channel, $y(t)$ which is not only perturbed by PN, but also has its own dynamics because of the non-Poisson statistics of the firing rates. We must therefore consider an augmented plant with a higher order, which will be *at least* 3rd order (given eq.31) (fig.4).

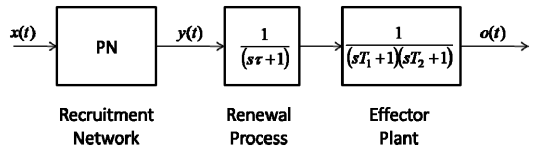

Figure 4: Simplified lumped linear model of a motor system driven by the optimized recruitment channel. The channel generates a drive with PN which then is passed to a 3rd order system including the response function of the motor neuron renewal process and the actual 2nd order effector plant.

Denote the augmented plant impulse response by, $p(t)$ with Laplace transform given by:

$$P(s) = \frac{1}{(s\tau + 1)(sT_1 + 1)(sT_2 + 1)} \tag{31}$$

Then the variance at the output of the plant is given by the convolution (Harris 1998):

$$\sigma_o^2(t) = K^2 \int_0^t x^2(t')p^2(t-t')dt' \tag{32}$$

Note that the kernel is the square of plant impulse response, and causes the variance response to be more sluggish (and less intuitive) than the signal response.

4.3 Optimal Trajectories

PN and its transfer through a linear system (eq.33) has far reaching implications when we are required to move an effector from one point to another, as in reaching or saccadic eye movements. If we want to move more quickly then we clearly need a larger input signal, $x(t)$ but this will lead to a larger output variance and hence larger pointing errors (end-point errors). Conversely, if accuracy is important then the input needs to be small and the movement will take a longer time. The speed-accuracy trade-off implies that for a given movement duration, there is a unique trajectory (velocity profile) that minimises end-point error. This has been found numerically and analytically (Harris & Wolpert 1998, 2006). In two dimensions trajectories tend to be straight.

For very brief movements, a 3rd order system becomes dominated by the 3rd derivative (jerk) and the kernel in eq. 33 tends towards the square of jerk. Thus the variance at the end of the movement is given by:

$$\sigma_o^2(T) \xrightarrow[T\to 0]{} K^2 \int_0^T \left(\frac{d^3 o(t')}{dt'^3} \right)^2 dt' \tag{33}$$

Minimising jerk is therefore minimising variance in the limit for a 3rd order system. However, this is only approximate for brief movements. Careful analysis of data using Fourier analysis reveals that arm reaching and saccades are not MJ but closer to MV (Harris & Harwood, 2005; Harwood et al., 1999). For longer movements velocity profiles become quite asymmetric and cannot be fit by the MJ model.

In summary, a vast amount of human goal-directed dynamic motor behaviour is explicable as an optimal trade-off between speed and accuracy, which a direct result of PN. Perhaps most remarkable, is that this can all be attributed to maximising channel capacity!

5 DISCUSSION

If we start with a collection of noisy binary sub-channels (units) with thresholds, then the optimal pattern of threshold levels and weights is to recruit sub-channels according to equations 25 and 28. This arrangement maximises the number of different signals we can transmit for a given error probability per signal. It emerges that the output signal of such a configuration exhibits proportional noise (PN) (eq.1). This result is consistent with known neurophysiology which has shown that PN emerges from the orderly recruitment of motor units in human arm movements (Jones et al, 2001). The configuration of thresholds and weights is also consistent with the well-known empirical size principle in which stronger motor units are recruited at higher thresholds. We have only considered binary sub-channels, but it appears that a similar result could occur for other types of rapidly saturating sub-channels away from the origin (not shown here). We propose, therefore, that PN is itself is an optimal strategy that has evolved to maximise channel capacity.

Once PN has emerged, it places a trade-off between speed and accuracy for point-to-point movements, which leads to an optimal trajectory (the minimum variance trajectory), which fits observations remarkably well (Harris & Wolpert 1998). For brief movements, the MV trajectory becomes bell-shaped and similar to (but not exactly the same as) the minimum jerk (MJ) profile. This is why the MJ trajectory seems to fit observation quite well (but only for brief movements).

Our overall conjecture is that through evolution/adaptation multiple noisy sub-channels with thresholds will ultimately and inevitably lead to smooth straight movements.

5.1 The Biomimetic Question

Clearly we could build synthetic systems (robots etc.) that mimic the smooth straight trajectories made by humans simply because they look like human movements. This is aesthetic biomimicry. Incorporating minimum jerk (MJ) trajectories in robots is probably as example of this kind of mimicry. It could be argued that smoothness is useful in reducing wear-and-tear, but there are much smoother trajectories than MJ (Harris, 2004). One would need to trade-off the cost of wear-and-tear against poor dynamic performance. In any case, human movements are not MJ, and are much better described by minimum variance (MV) trajectories in which PN inaccuracies are optimally traded against duration. MJ trajectories are just a limiting case of MV trajectories for brief durations. But copying human trajectories, albeit more precisely with MV profiles, is still aesthetic mimicry unless PN exists in the synthetic system.

In contrast to aesthetic mimicry, functional biomimetics copies the control objective of human movement and incorporates it into the constraints in the synthetic system. For example if the control signal in a synthetic system were perturbed by stationary additive Gaussian noise, making an accurate and rapid movement would probably be achieved by a bang-bang control solution. It only makes sense to incorporate an MV controller if the synthetic control signal is perturbed by PN, which in our experience, is not common in conventional engineered systems. One could, of course, introduce PN deliberately, but this would just be aesthetic mimicry.

5.2 The Neuromorphic Approach

Building synthetic systems with artificial neurons is a fundamentally different proposition. Neuromorphic technology can now produce silicon neurons with thresholds and stochastic spike trains. When configured optimally for movement control, they should produce PN because, as we have shown here, PN emerges at the output of the optimal channel (at least for binary channels). For robots built on this technology, MV trajectories would be an optimal solution for speed and accuracy. This is *functional* rather than *aesthetic* biomimetics.

But, why should synthetic systems employ artificial neurons? Is this not just another level of aesthetic mimicry? We suggest that the neuromorphic argument runs deeper. Over eons, biological functions and structures have improved survival through natural selection. Optimal solutions to problems emerge (without mathematical premise) that are not obvious to us, and not even achievable with current technology. In the case of neural systems, it is only by building them neuromorphically, that we can discover these solutions.

REFERENCES

Fitts P.M. (1954) The information capacity of the human motor system in controlling the amplitude of movement. *Journal of Experimental Psychology* 47: 381– 391.

Cox, D.R. Miller, H.D. (1977) *The theory of stochastic processes.* Chapman & Hall, London.

Flash, T., Hogan N. (1985) The coordination of arm movements: an experimentally confirmed mathematical model. *Journal of Neuroscience* 5: 1688–1703, 1985.

Geim A.K., Dubonos S.V., Grigorieva I.V. et al. (2003) Microfabricated adhesive mimicking gecko foot-hair *Nature Materials* 2: 461-463

Hogan N. (1984), An organizing principle for a class of voluntary movements, *Journal of Neuroscience* 4, 2745-2754.

Harris C.M. (1998) On the optimal control of behaviour: a stochastic perspective. *Journal of Neuroscience Methods* 83: 73-88.

Harris C.M. (2004) Exploring smoothness and discontinuities in human motor behaviour with Fourier analysis. *Mathematical Biosciences* 188: 99-116.

Harris, C.M., 2002. Temporal uncertainty in reading the neural code (proportional noise). *Biosystems* 67, 85-94.

Harris C.M., Harwood M.R. (2005) Boundary conditions in human movement III: Fourier analysis of reaching. In *Proceedings of the IASTED International Conference Biomedical Engineering,* ACTA Press Anaheim USA, 629-640.

Harris C.M. & Wolpert D.M. (1998) Signal-dependent noise determines motor planning *Nature* 394, 780-784.

Harris C.M. & Wolpert D.M. (2006) The main sequence of saccades optimizes speed-accuracy trade-off *Biological Cybernetics* 95, 21-29.

Harwood M, Mezey, L, Harris CM. (1999) The spectral main sequence of human saccades. *Journal of Neuroscience* 19: 9098-9106.

Jones, K.E., Hamilton. A.F., Wolpert D.M. (2001) Sources of signal-dependent noise during isometric force production. *Journal of Neurophysiology* 88, 1533-1544.

Schmidt R.A., Zelaznik H., Hawkins B., Franks J.S., Quinn J.T.J. (1979) Motor output variability: a theory for the accuracy of rapid motor acts. *Psychological Review* 86, 415–451.

Simmons G. & Demiris Y. (2005) Optimal robot arm control using the minimum variance model. *Journal of Robotic Systems* 22: 677-690

A HYBRID METHOD BASED ON FUZZY INFERENCE AND NON-LINEAR OSCILLATORS FOR REAL-TIME CONTROL OF GAIT

J. C. Moreno[1,2], J. L. Pons, E. Rocon
[1]*Bioengineering Group, Industrial Automation Institute, the Spanish National Research Council (CSIC), 28500 Madrid, Spain*
[2]*Technaid S.L., 28500 Madrid, Spain*
moreno@iai.csic.es, jlpons@iai.csic.es, juan.moreno@technaid.com

Y. Demiris
Intelligent Systems and Networks Group, Imperial College London, SW7 2BT London, UK
y.demiris@imperial.ac.uk

Keywords: Fuzzy inference systems, non-linear oscillators, inertial sensing, gait compensation.

Abstract: Robust generation of motor commands for real-time control of locomotion with artificial means is crucial for human safety. This paper addresses the combination of fuzzy inference for determination of rules with a non linear oscillator system, as generators of motor commands for the control of human leg joints during walking, by means of external gait compensators, e.g. exoskeletons, functional electrical stimulation or hybrid systems. The response of the proposed method is evaluated for variations in stride frequency and step length. The testing during gait conditions is performed considering inertial sensing as feedback in a simulation study. The reference data considered is obtained in multiple experiments with healthy subjects walking with a controllable exoskeleton designed to compensate quadriceps weakness. A model of the operation of the knee joint compensation provided by the exoskeleton is obtained as reference to evaluate the method based on real data. The results demonstrate the benefits of both incorporating a) the fuzzy inference system in cyclical decision making for generation of motor commands and b) the dynamic adaptation of the timing parameters of the external compensator provided by the van der Pol oscillator.

1 INTRODUCTION

Robust generation of motor commands for real-time control of locomotion with artificial means is crucial for human safety. Broadly, current active external compensators of pathological gait under research can be configured as functional electrical stimulators (FES), (Popovic et al., 1999), (Skelly and Chizeck, 2001) controllable leg exoskeletons or orthoses, (Blaya and Herr, 2004), (Irby et al., 1999), (Moreno et al., 2005) or as a combination of both, known as hybrid systems, (Gharooni et al., 2000), (Goldfarb and Durfee, 1996). From the control point of view, the design of robust controller of locomotion with such devices, towards real life application, must be easy to customise, adapt dynamically to typical variations in gait pase and preferably should incorporate a coordinated development with the user.

1.1 Gait Compensation

A wide range of external gait compensators, e.g. exoskeletons, functional electrical stimulation or hybrid systems, have been considered to restore human gait. In particular leg exoskeletons or orthoses, can be prescribed for cerebrovascular accident, polyo myelitis or cerebral palsy patients with leg muscle weakness, in order to provide knee stability, reducing falling risk and enabling a certain degree of mobility.

In order to control an exoskeleton, it is not clear the hypothesis that instantaneous control of trajectory of the joint angle is essential for the lower limb system, since the reduced mechanical output —joint torque— limits its transitory response, in relation with the inertial properties of the musculoskeletal system (Franken, 1995). Velocity or position control loops are more appropriate and safe in training and rehabilitation applications where controlled generation of joint trajectories is required, with application of oscillatory signals and modulation techniques during gait

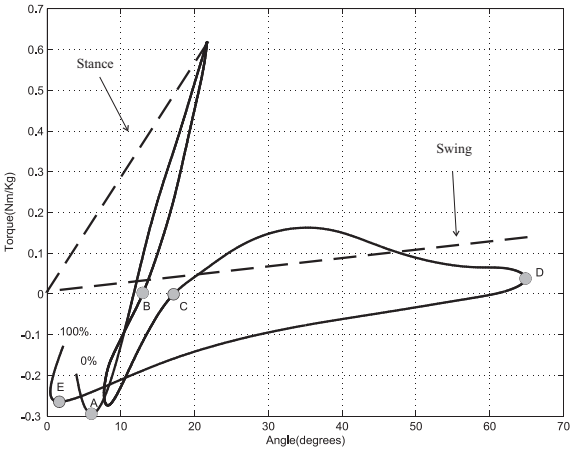

Figure 1: Mechanical adaptation for gait compensation during one gait cycle at the knee joint.

cycles for training subjects following neural/motor injuries.

Our previous work has consisted in the implementation of intermittent control of resistance of the knee joint with an unilateral exoskeleton applying selectively different constant stiffnesses depending on gait phase, to approach more natural profiles and avoid collapsing of the knee and risk of falling, see fig. 2.

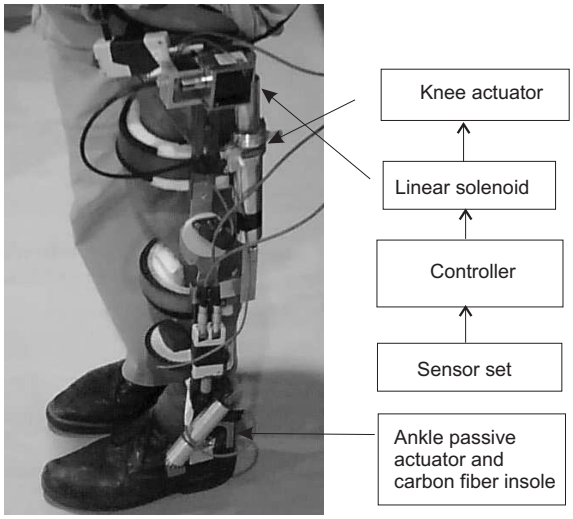

Figure 2: Controllable ambulatory exoskeleton.

Under this approach, a knee actuator is controlled to apply a given impedance K_1 in the stance phase, during a period of time ensuring the joint stability and shift during swing phase releasing the joint for a free swing while applying K_2 ($K_1 >> K_2$), for smooth transition and storage/recover of energy to assist the leg extension, see figure 1.

1.2 Rule based Control

Reliability of control in such a wearable solution for pathological cases is a critical issue that has an impact in human safety.

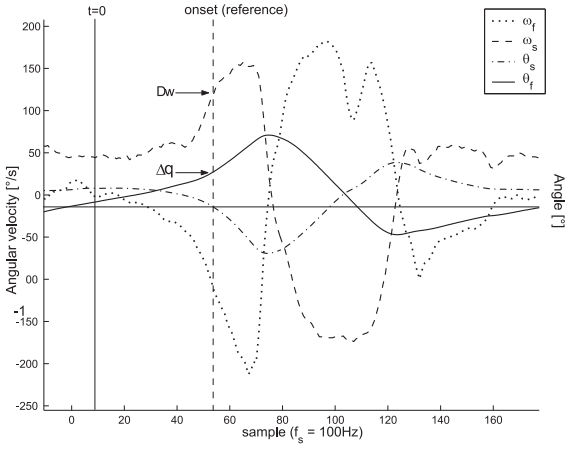

Figure 3: Typical normal gait pattern of foot and shank segments rotations and rotational velocities (sagittal plane) during a walking task at 34 m/min speed, with the cable-driven exoskeleton, after training of the subject. A system with a cable triggers the knee mechanism (onset) depending on a fixed degree of dorsiflexion.

The output of the controller is the motor command for the actuator, characterized by two parameters: activation *onset* and *period*. The activation onsets during each stride are calculated by rule-based conditions, evaluated according to segments orientation or rate velocity (See pattern during stance phase, figure 3). The system is a reactive controller performing according to the motion of the leg. The criteria to cyclically adapt the activation period (pulse width) of the actuator is defined considering temporal parameters relative to stance phase of current S(k) and past S(k-1) strides, and initial conditions S(0), given by average expected values.

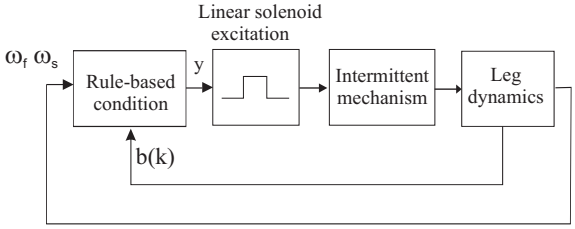

Figure 4: Control scheme for walking.

Experimental trials have demonstrated short-term adaptation of human motor system when applying functional compensations with customized tunning of the discrete rule-based controllers ,(Moreno,

2006). The adaptation of cyclical activation, has demonstrated proper results at self-preferred constant speeds. The next proposed method is an improvement intended to provide the required dynamical adaptation to changes of step frequency/length by the user.

1.3 Bipedal walking with Central Pattern Generators (CPGs): Simulation

It has been demonstrated previously how the use of the dynamical systems paradigm can realize a walking behavior in robotic walking platforms (Veskos and Demiris, 2006). The neural architecture has demonstrated successful operation in swinging and planar walking in a bipedal platform, incorporating van der Pol oscilators as generators of motor commands.

Medium and short term application of a walking real-time controller for the mentioned application scenarios, ought include mechanisms that provide adaptability and stable response to variations of frequency in the feedback signals, can led to an approach of cooperative development with the user/environment. In the following, the analysis of the response of the proposed hybrid controller to variations in gait frequency is evaluated with real data measured with the orthotic walking platform.

2 METHODS

2.1 Gait Patterns with Knee Joint Compensator

Subjects wearing an exoskeleton, need to adapt their walking strategy to drive the system to successfully switch between two knee spring damper configurations. During the entrainment of the subject with the controllable exoskeleton it is necessary to reach a certain ankle dorsiflexion angle which is variable during normal gait. Although this angle is adjustable, subjects change their gait pattern until they learn to use the exoskeleton. The learning process (which can be seen as an adaptation) in the use of the controllable exoskeleton has been previously studied in (Forner-Cordero et al., 2006). In order to obtain sampled data of different gait speeds, experimental trials with a healthy subject have been conducted after the adaptation process, consisting in walking back and forth along a 10 meter path, with definition of the step length with marks on the floor and the gait speed by means of a metronome, and systematic adjustments of the cable mechanism to provide a comfortable gait pattern (see table 1). The gait velocity and step length variations were defined according to average values taken from Perry, (Perry, 1999), consisting in feasible combinations of 100%, 70%, 60% and 50%. Rate gyroscopes fixed at the shank and leg segments of the external device were used to measure rotational velocities along the sagittal plane. Motions of interest occur at normal (2.6 km/h) and low (2 km/h) gait speeds, and therefore, signals outside the band frequency related to gait kinematics (0.3–20 Hz), are rejected from the sensor outputs with -3 dB low pass filters, refer (Moreno et al., 2006) to for details. A precision angular position sensor was fixed at the knee joint to track the knee joint angle in the sagittal plane. A resistive pressure sensor (5 mm in diameter active area, 0.30 mm thickness) is used to monitor the activation status of the knee actuator.

Collection of input/ouput data is utilized to generate training and checking data sets, of both multiple speed trials, and constant speed separated trials.

2.2 Validation Model

A robust Model describing the dynamics of the knee-orthotic hinge system during cyclic walking conditions can be used as a reference to analyze the performance of the advanced control system. We propose the identification of the model the activation patterns provided by the cable driven exoskeleton, with time-series of kinematic data. A broadly used signal processing paradigm is the state-space model. Defined by two equations, the state-space model has been broadly applied in signal processing (Smith and Brown, 2003). A first equation describes how the hidden state or latent process is observed and a second (state) equation that defines the evolution of the process through time. Based on the formulation given by (Haverkamp et al., 1996), we propose identification of a multiple-input single-output continuous-time model from the experimentally collected input and output data.

Considering the state-space model in the innovations form

$$\frac{dx(t)}{dt} = Ax(t) + Bu(t) \quad (1)$$

$$y(t) = Cx(t) + Du(t) \quad (2)$$

where $u(t)$ denotes the sampled inputs, being the foot and shank rotations in the sagittal plane during walking, for continuous measurements at 100 Hz sampling frequency, with transitions from low to high speed, and progressive variations in step length and given the measured output reference; $y(t)$, as the entrained knee joint status (actuator activation period)

Table 1: Systematic variations of healthy subject walking with the cable driven prototype (* Not feasible combinations).

Percentage	Step length[m]	Stride length[m]	Speed[m/s]			
100	0.73	1.46	1.35	0.94	0.81	0.67*
70	0.51	1.02	0.94*	0.66	0.56	0.47
60	0.44	0.88	0.81*	0.56	0.48	0.40
50	0.37	0.73	0.67*	0.47	0.40	0.33
		Cadence (step/min)	111	78	67	56
		Metronome (bpm)	1.85	1.30	1.11	0.93

for normal walking, $x(t)$ is the internal state of the system and $[A,B,C,D]$ are the deterministic system matrices.

The reference sampled input and output data $u(t)$ and $y(t)$ is obtained from experiments with healthy subjects wearing a orthotic walking platform, manually adjusted at each velocity to trigger the knee actuator based on the ankle dorsiflexion.

The goal of the state-space model identification process implemented in MATLAB is to find the system matrices $[A,B,C,D]$ according to the model structure. This resulted in a second order model as the best to the input-output behavior of the system, selected upon the analysis of the singular values (1st order, 53.23; 2nd order, 3.77; 3rd order, 0.34; 4th, 0.30).

The continuous-time model describes the relation between the foot and shank segments angular velocities and the output activation at the knee joint actuator for the range of tested speeds, by the state differential equation 1 and the output equation 2, where

$$A = \begin{bmatrix} 0.994 & -0.063 \\ -0.003 & 0.933 \end{bmatrix}; \quad (3)$$

$$B = \begin{bmatrix} -3.05e^{-6} & -8.28e^{-6} \\ -2e^{-5} & -3.39e^{-5} \end{bmatrix}; \quad (4)$$

$$C = \begin{bmatrix} 14.55 & -0.009 \end{bmatrix}; \quad (5)$$

Assuming the initial state as zero, from the evaluation of the transient (impulse) response of the second order system, it can be concluded a stable system with t_p = 0.5 s, as the time to reach the peak value, and a settling time t_d of approximately 10 s, after persistent excitation.

Evaluation of the response of the model compared against the external compensator operation is then performed, with the checking data set corresponding to multiple speeds. The crossing zeros (time interpolation) of the oscillatory output signal during the steady state are detected as equivalent onset and offset timings of the measured events. The correlation coefficient r^2, calculated for the modeled and measured outputs is 0.999.

2.3 Architecture

The control scheme consists of different modules (see figure 6). A fuzzy inference system with two inputs and a single output node is identified and trained to map the inputs and trigger the actuator. The crisp output of the fuzzy inference system during each cycle is critical in providing transition between restrained knee flexion in stance to a free swinging leg. The activation period of the knee actuator (pulse width) during the swing phase is cyclically adapted by a second module composed by an nonlinear oscillator. This nonlinear system incorporates real-time estimated gait temporal parameters as feedback in the generation of an oscillatory signal which adapts the duty cycle of an external compensator.

2.3.1 Fuzzy Inference System

Conventional PID controllers have been applied in the control of cyclical movements in legs of paraplegic subjects (Franken, 1995). Introduction of dynamical adaptation of the rules commanding FES systems has been investigated, in order to cover a wider range of unsafe and uncertain situations in application of stimulation . A Sugeno system is suited for modeling nonlinear systems. A training scheme with a fuzzy modeling network structure has been combined to develop a gait synthesis learning scheme, (Horikawa et al., 1990).

Obtaining a fuzzy system corresponds with approximated reasoning, which refers to methodologies to describe physical systems which include complexity due to nonlinearities and uncertainties. Let us suppose that our unknown system is a black box only capable of measuring a set of inputs x_1,...,x_n and outputs y_1,... ,y_m. A fuzzy system with a crisp output and the following type of rules is to be obtained

$$R_i : \text{IF } x_1 \text{ es } S_{i1} \text{ and...and } x_m \text{ es } S_{im}, \text{ THEN } \textit{and} \text{ es } c_i \quad (6)$$

The fuzzy inference system is generated by means of the grid partition method. For the identification a

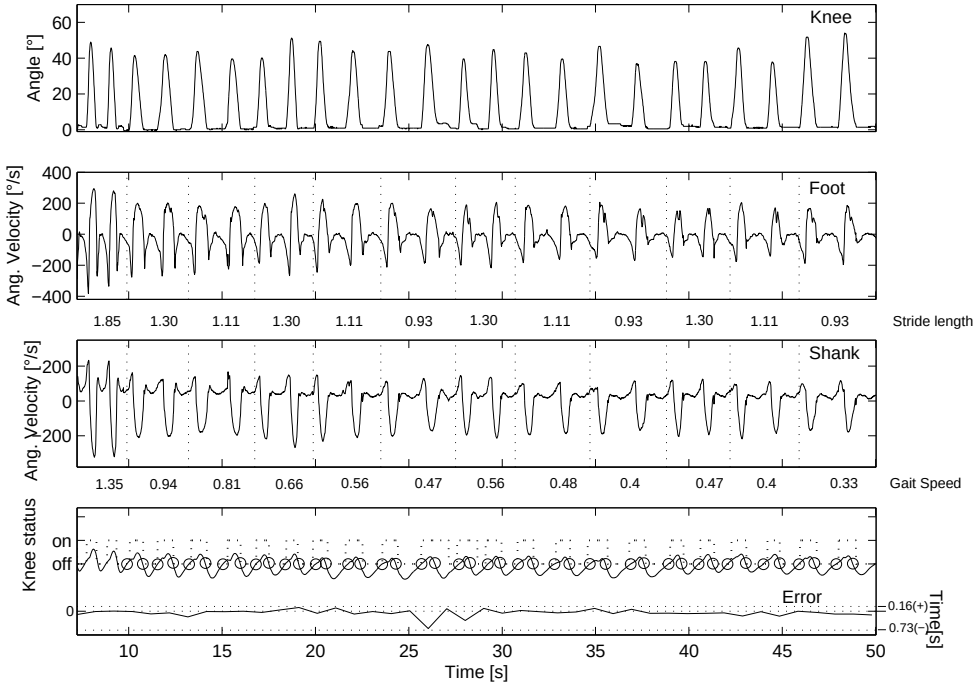

Figure 5: Data of measured input/ouputs of healthy subject with the compensator, after adaptation, at multiple gait speeds and space-state model performance. (a) Knee joint measured angle with external compensation, checking data set of (b) Foot angular velocity and (c) Shank angular velocity; (d) the measured activation status of the actuator (dotted line), model ouput (dashed line) onset and offset timings given by the model (circles), and time difference per cycle.

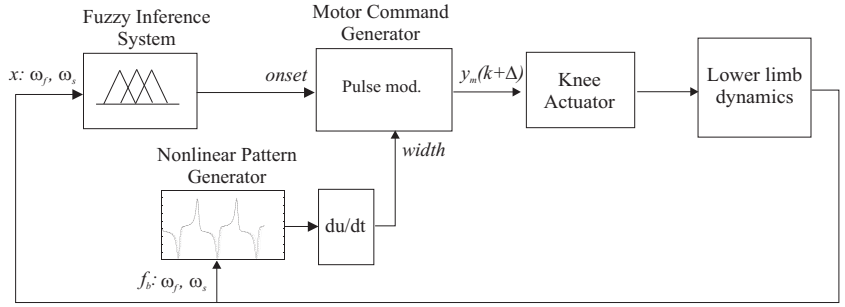

Figure 6: Hybrid architecture for control of gait external compensation at knee level, based on inertial sensing data. First module contains the fuzzy inference system with a crisp output The second module contains a nonlinear system predicting the activation period of the knee actuator as function of gait frequency (forced oscillator), with proprioceptive feedback.

training data set is generated from the experimentation. The identification method consists in the application of the adaptive network fuzzy inference system (ANFIS) proposed by Jang, (Jang, 1993), in order to build the fuzzy rules with membership functions to generate input/output data pairs. Iteratively, input parameters of the membership functions are learnt by means of back-propagation in an adaptive network and while the parameters of output functions are optimized by the least squares fitting method. The *adaptive network* is a feedforward multilayered network, with a supervised learning scheme. The functions of given nodes in a layer are similar. For means of simplicity, we consider a first order Sugeno type model, as the inference system. Having the kinematic inputs, the output $E(t)$ and n fuzzy rules:

$$\begin{aligned} R_n \quad : \quad & \text{IF } \dot{\theta}_s \text{ is } A_n, \text{ AND } \dot{\theta}_f \text{ is } B_n \\ & \text{THEN } E = p_1\dot{\theta}_s + \dot{\theta}_f + t \end{aligned} \tag{7}$$

Gaussian membership functions have been selected for smooth transition. A total of 4 Sugeno

type fuzzy rules were defined, with a network with 21 nodes. These rules were of AND (minimum) type antecedent. The defuzzification method, calculating the output, is performed by the centroid method. The clustering radius r = 0.2 was adjusted for tunning. The optimization process spanned 13 epochs, with the training data set. The figure depicts the output surface of the final identified system given the two inputs.

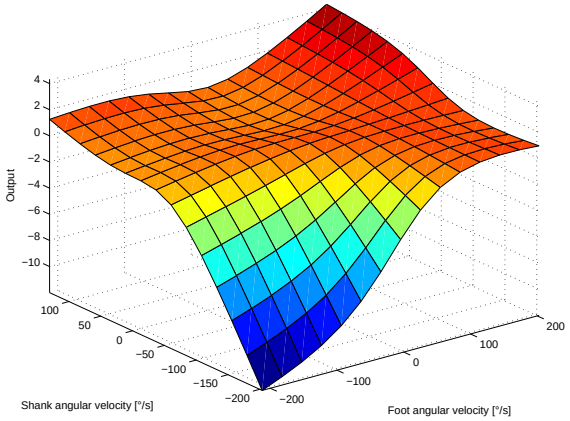

Figure 7: Inputs (foot and shank angular velocities) output (knee actuator activation) surface of the fuzzy system.

2.3.2 Forced Nonlinear Oscillator

The dynamic robustness of a pattern generator to noise and other external disturbances can be improved by incorporating nonlinearities to the system. A van der Pol oscillator, requires a reduced number of parameters, and has the advantages of robustness and ease of computational implementation. Such nonlinear system can be applied as an adaptive oscillator during the swing phase to determine the time of activation of the external compensator. To unlock the frequency of the oscillator and provide it with adaptability to the leg motion, the nonlinear system is forced to oscillate at a frequency, which depends on the spatio-temporal behavior of gait. Let us consider the forced nonlinear oscillator

$$[!top]\dot{x} = y \quad (8)$$

$$\dot{y} = -\mu(x^2-1)y - \omega x + A\cos\theta t \quad (9)$$

with ω as the natural frequency μ as the damping parameter, θ as the forcing frequency and A as the amplitude of the forcing function. An approximate solution of the non-linear system, satisfying the initial conditions x = 0, y = 0 is calculated during each cycle i with

$$\theta_i = \frac{T_{ST}}{R} \quad (10)$$

where T_{ST} is the stance phase period in cycle i, and R, a frequency scaling factor. T_{ST} is estimated from consecutive local minima (peak) values from the foot rotational velocity, as described in (Moreno et al., 2006).

2.4 Hybrid Controller

Local minima values are detected from the output of the fuzzy system, upon numerically integration. The sensitivity of the local minima detector is given by δ, which corresponds to the minimum difference in amplitude with the neighbor samples. With the calibrated gyroscopes raw data, a δ = 40 was satisfactory for all conditions. Thus, cyclically the fuzzy system provides the activation *onset*, the controller incorporates the output of the nonlinear oscillator to predict the *width* τ or duration period for the knee external compensator, with

$$\tau = \frac{D}{2\omega} \quad (11)$$

where D determines the duty cycle percentage. Incorporating the prediction given by the forced oscillator, D = 0.8 was defined and remained constant in all further experiments.

An example of the hybrid controller for cyclic gait at 0.94 m/s (stride length, 1.46 m) is depicted in fig. 8

3 RESULTS

The performance of the hybrid controller is compared with the validation model and the testing data set. The mean errors and standard deviations are calculated, considering 4 continuous gait cycles per each condition, for the output of the fuzzy inference system module and the nonlinear oscillator module (see Table 2). A negative error (in seconds) means anticipation with respect to the reference. For the tested conditions, the maximum average error for the fuzzy rule-based detection was 0.19 *s* demonstrating the robustness of a single fuzzy model to drastic variations in stride frequency. The discrete rule-based method, previous tests showed significantly better performance for the application of thresholds, during slow gait velocities in comparison with the results with higher velocities. The response with the fuzzy rule-based method can be regarded as uniform for the tested conditions. The maximum average error for the oscillator was 0.32 *s* and therefore, the robustness to the variations in the timing of the generated motor commands was observed. The evaluation with the continuous data set provide a good indication of the accuracy and robustness of the hybrid method.

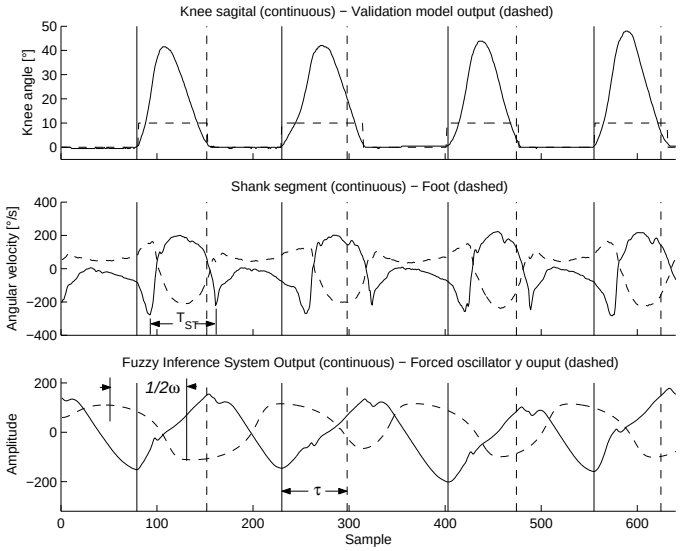

Figure 8: Example of the simulation results of the hybrid system at a relative fast speed. Measured knee angle and reference output given by validation model (top); Inputs (middle); Fuzzy inference system and forced linear oscillator outputs. The hybrid system generates the triggers (continuous vertical lines) and activation periods (dashed vertical lines).

Table 2: Results of the hybrid controller for the 12 testing conditions. Mean errors and standard deviations with respect to the evaluation model output are calculated taking 4 continuous gait cycles per each condition.

		Fuzzy System		**Forced oscillator**	
Step length[m]	Speed [m/s]	Mean error [s]	SD	Mean error [s]	SD
1.46	1.3505	0.0995	0.0123	0.005	0.0451
1.46	0.94535	0.041	0.0744	-0.025	0.0719
1.46	0.8103	0.154	0.1847	-0.245	0.0806
1.022	0.6617	0.0685	0.0296	-0.06	0.051
1.022	0.5672	-0.042	0.0238	-0.17	0.0497
1.022	0.4726	-0.13	0.1238	-0.1775	0.1072
0.876	0.56721	0.0335	0.023	-0.1275	0.0629
0.876	0.48618	-0.0125	0.0728	-0.1725	0.083
0.876	0.4051	-0.1075	0.12	-0.32	0.0668
0.73	0.47267	0.0025	0.031	-0.16	0.0462
0.73	0.4051	-0.1205	0.0689	-0.0625	0.0998
0.73	0.3376	-0.1915	0.1003	0.15	0.2149

4 CONCLUSIONS

The evaluation with the continuous data set provide a good indication of the accuracy and robustness of the hybrid method. For the tested conditions, the results demonstrate a proper means to combine a learning method which incorporates fuzziness with the adaptive nature of a non lineal oscillator, to generate motor commands to control gait. A validation model has been used in order to simulate the real mechanical system (human leg and exoskeleton) in this study. Further work includes a simulation study of the response of the methos to external perturbations (foot contact with the ground during the swing and obstacles) and testing with subjects of the embedded application.

ACKNOWLEDGEMENTS

The authors would like to thank Paschalis Veskos. The work presented in this paper has been partially founded by I3P programme of the Spanish Scientific Research Council.

REFERENCES

Blaya, J. and Herr, H. (2004). Adaptive control of a variable-impedance ankle-foot orthosis to assist drop foot gait. *IEEE Trans Neural Syst Rehabil Eng*, 12(1):24–31.

Forner-Cordero, A., Moreno, J., Cullell, A., Navarro, E., and Pons, J. (2006). Evaluation of mental load to wear an actuated knee ankle foot orthosis. In *International Congress on Gait and Mental Functio*, Madrid, Spain.

Franken, H. (1995). Cycle to cycle control of swing phase of paraplegic gait induced by surface electrical stimulation. *Medical and Biological Engineering and Computing*, 33:440–451.

Gharooni, S., Heller, B., and Tokhi, M. (2000). A new hybrid spring brake orthosis for controlling hip and knee flexion in the swing phase. *IEEE Transactions on Rehabilitation Engineering*, 9(1):106–107.

Goldfarb, M. and Durfee, W. K. (1996). Design of a controlled-brake orthosis for fes-aided gait. *IEEE Transactions on Rehabilitation Engineering*, 4(1):13–24.

Haverkamp, B., Chou, C., Verhaegen, M., and Johansson, R. (1996). Identification of continuous-time mimo state space models fromsampled data, in the presence of process and measurement noise. In *IEEE 35th Decision and Control*.

Horikawa, S., Furuhashi, T., Okuma, S., and Uchikawa, Y. (1990). a fuzzy controller using a neural network and its capability to learn experts control rules. In *Proc. Int. Conf. Fuzzy Logic and Neural Networks*, page 103106.

Irby, S., Kaufmaun, K., Wirta, R., and Sutherland, R. (1999). Optimization and application of a wrap-spring clutch to a dynamic knee-ankle-foot orthosis. *IEEE Transactions on Rehabilitation Engineering*, 7(2):130–4.

Jang, J. (1993). Anfis: Adaptive-network-based fuzzy inference system. *IEEE Systems, Man and Cybernetics*, 23:665–684.

Moreno, J. (2006). *Exosqueletos Robticos para Valoracin y Compensacin funcional de Marcha Patolgica*. PhD thesis, Universidad Politcnica de Madrid.

Moreno, J., Brunetti, F., Pons, J., Baydal, J., and Barbera, R. (2005). Rationale for multiple compensation of muscle weakness walking with a wearable robotic orthosis. In *International Conference on Robotics and Automation*, pages 1914–1919.

Moreno, J., Rocon, E., Ruiz, A., Brunetti, F., and Pons, J. (2006). Design and implementation of an inertial measurement unit for control of artificial limbs: application on leg orthoses. *Sensors and Actuators B*, 118(1-2):333–337.

Perry, J. (1999). *Gait Analysis: Normal and Pathological Function*. McGraw-Hill Inc.

Popovic, D., Stein, R., Namik Oguztoreli, M., Lebiedowska, M., and Jonic, S. (1999). Optimal control of walking with functional electrical stimulation: a computer simulation study. *Rehabilitation Engineering, IEEE Transactions on [see also IEEE Trans. on Neural Systems and Rehabilitation]*, 7(1):69–79.

Skelly, M. and Chizeck, H. (2001). Real-time gait event detection for paraplegic fes waking. *IEEE Transactions on Neural Systems and Rehabilitation Ingenieering*, 9(1):59–68.

Smith, A. and Brown, E. (2003). Estimating a state-space model from point process observations. *Neural Computation*, 15(5):965–91.

Veskos, P. and Demiris, Y. (2006). Neuro-mechanical entrainment in a bipedal robotic walking platform. In *Biro-net Symposium*, Bristol, UK.

BIOPHYSICAL MODEL OF A MUSCLE FATIGUE PROCESS INVOLVING Ca^{2+} RELEASE DYNAMICS UPON THE HIGH FREQUENCY ELECTRICAL STIMULATION

Piotr Kaczmarek
Poznań Univeristy of Technology, Insitute of Control and Information Engeenering, Piotrowo 3a, 60-395 Poznań, Poland
Piotr.Kaczmarek@cie.put.poznan.pl

Keywords: Electrical stimulation, Muscle model, Calcium release, Muscle fatigue.

Abstract: The aim of this study is to create a model which enables to explain the muscle fibre contraction due to various stimulation programs. The model accounts for Ca^{2+} release dynamics both as a result of an action potential and of a stimulus shape, duration and frequency. It has been assumed that the stimulus can directly activate the voltage-dependent receptors (dihydropiridine receptors) responsible for a Ca^{2+} release. The stimulation programs consisted of standard stimulation trains made of low and middle frequency square pulses. High frequency modulating harmonic signals have been tested to investigate the fibre fatigue effect. It has been observed that fatigue effect factors depend on the selected stimulation program. The results reveal that the fatigue effect could be minimized by changing the shape and frequency of the stimulation waveform. Such the model could be useful for a preliminary selection and optimization of the stimulus shape and the stimulation trains, thus reducing the number of in vivo experiments.

1 INTRODUCTION

Electrical stimulation is a rehabilitation technique applied to increase muscles force, reduce spasticity, muscular atrophy and to decrease pain effects. It is also used to restitute a motion in handycaped subjects via Functional Electrostimulation (FES). In order to get an efficient FES system, the optimal stimulation programs have to be worked out. The former investigations revealed that muscle fatigue effect is greater as a result of electrical stimulation than as a result of a voluntary contraction (Kostyukov et al., 2000; Gissel, 2000). It has been reported that stimuli train frequency and a single pulse shape have the significant impact on the fatigue effect (Bennie et al., 2002). Therefore, the optimization of the stimulation programs is one of the most important aspects of the FES method. As far, the optimization has been limited to the identification of the optimal frequency of a stimulation pattern (Ding et al., 2003; Chou et al., 2005) or to a search for variable frequency pulse trains. (Mourselas and Granat, 1998).

The studies on the high frequency stimulation programs (>200Hz) as well as on the single pulse shapes as related to the muscle fatigue effect are missing.

The dynamics of Ca^{2+}ions transportation plays an important role in the muscle contraction process (Bottinelli and Reggiani, 2000; Benders et al., 1997; Delbono and Meissner, 1996). The change of the Ca^{2+}release rate is an important factor of the fatigue effect (Westerblad et al., 2000; Gissel, 2000). Therefore a majority of models reflecting potentiation and fatigue effects have been based on the Ca^{2+}dynamics. (Otazu et al., 2001; Ding et al., 2003; Riener and Quintern, 1997). In these models the impact of the stimulus shape as well as of the pulse width on the fatigue effect were not addressed. It is only assumed there that a single stimulus evokes an action potential (AP) in the muscle fibre, which activates a voltage-dependent dihydropiridine receptor (DHPR) resulting in Ca^{2+}release from the sarcoplasmic reticulum (SR). The amount and the release profile of the liberated Ca^{2+}ions are assumed to be constant, even though the physiological variability of the AP amplitude and shape (in the t-tubular system) is observed.

The in vivo experiments demonstrated that the stimulus amplitude and duration affect the calcium concentration ($[Ca^{2+}]$)(Delbono and Meissner, 1996;

Bakker et al., 1996; Benders et al., 1997). However, the direct influence of a neuro-muscular electrical stimulation (NMES) on the DHPR receptor behaviour was ignored in the models. Therefore the applicability of these models for testing stimulation trains composed of wider pulses is dubious and the trains frequency should be restricted to the maximal physiological frequency of the AP generation ($f_{stim} < 100$Hz).

The aim of this work is to analyse the influence of the stimulation parameters on the muscle contraction and fatigue effect. We present a novel model of a muscle fibre. The model is an extension of already known models, by introducing the direct interaction between the stimulus and the DHPR receptor activity as well as by incorporating the calcium release dynamics. These adds-on enable to study the muscle fatigue effect during various stimulation programs. In particular we analyse the influence of a train frequency and a single pulse-duration on the dynamics of calcium concentration and on the fatigue effect.

2 PHYSIOLOGICAL BACKGROUND

2.1 Excitation-Contraction Coupling

Depolarization of sarcolemma due to the physiological action potential (AP) or to stimulation, activates a sarcoplasmic reticulum (SR) Ca^{2+}release. The voltage signal is transformed into the Ca^{2+} release via a voltage-sensitive dihydropiridine receptor (DHPR), which activates some of the Ca^{2+}channels (ryanoidine receptor - RyR) in SR. This process is called Dihydripiridine-Induced Calcium Release (DICR). The amount of the activated RyRs is dependent on the stimulus intensity and the muscle fibre type. The number of RyR coupled with DHPR depends strongly on a fibre type, and is the largest for the slow fibres (Delbono and Meissner, 1996; Benders et al., 1997).

The uncoupled RyRs are activated as a result of the sarcoplasmic $[Ca^{2+}]$ increase. This effect, called Calcium-Induced Calcium Release (CICR), generates a positive feedback in the Ca^{2+}liberation process. Ca^{2+}ions are transported by a Ca^{2+}-ATPase pump from cytosol into SR. The pump efficiency is dependent on the $[Ca^{2+}]$ in the sarcoplasm. At the resting state the Ca-ATPase pump maintains the Ca^{2+}ions concentration about 10^4 higher in SR than in cytosol (Bottinelli and Reggiani, 2000).

Ca^{2+}diffuses in cytosol from the proximity of SR surface to the interior of the myofibrils, where a troponin (TN) is localized. TN is a part of a thin filament proteins. Whenever TN binds to Ca^{2+}, actin (the part of thin filaments) and myosin (the part of thick filaments) are able to interfere resulting in the myofibril contraction. In the sarcoplasmic space the Ca^{2+}can be buffered also by parvalbumin (PARV). The CaTN and CaPARV buffers decrease the concentration of free Ca^{2+}ions in cytosol.

2.2 Fatigue Effect

There is an experimental evidence that the muscles are subject to the faster fatigue under the electrical stimulation than during the voluntary contraction. Moreover, the stimulation of muscles having majority of the fast-type fibres induces stronger fatigue effect than with the slow-type muscles (Delbono and Meissner, 1996; Gissel, 2000).

The following reasons of the muscle fatigue are reported:

1. RyR receptor has an inactivating binding site for Ca^{2+}(Glukhovski et al., 1998) resulting in the inhibition of CICR during long-lasting stimulation as well as in response to APs.
2. The AP amplitude and shape changes in the t-tubular system under long-lasting AP (Wallinga et al., 1999; Bakker et al., 1996).
3. The Ca^{2+}liberation is inhibited due to the increase of Mg^{2+} concentration and decrease of [ATP] (Westerblad et al., 2000).
4. Calcium-phosphate precipitation in the SR (Westerblad et al., 2000)
5. Structural degeneration of the muscle fibres as a result of the eccentric, low frequency contraction (Westerblad et al., 2000).

In this paper only the two first factors will be discussed.

3 PROCESS MODEL

The proposed muscle fibre model is based on the model of Otazu et al. (Otazu et al., 2001), originally applied to study a potentiation and a catch-like effects in muscle fibres. It consisted of two blocks: the activation dynamics block (AD) and the contraction dynamics block (CD). The input to the AD subsystem is a potential of the sarcolemma activating the voltage-dependent DHPR receptors. In the original model it has been assumed that the muscle contraction is evoked only by APs. Each AP generates the

same membrane potential profile and thus the amplitude and dynamics of DCICR is kept constant during simulation.

The model proposed here accounts for the depolarization of the sarcolemma under direct influence of the stimulation pulses. Thereby it takes into account the fact that DICR profile and amplitude depend on the stimulus shape, amplitude and train frequency. Such a model let to study the muscle fibre behaviour under a high-frequency or a wide-pulse stimulation, when APs are not generated. Such the model could enable the preliminary optimization and selection of the stimuli and the stimulation trains reducing the number of *in vivo* experiments.

The model of a voltage activated channel reflects some properties of the DHPR receptor recorded *in vivo* during the stimulation with a high amplitude and the long lasting depolarization pulses (Delbono and Meissner, 1996; Bakker et al., 1996). The AD block produces the concentration of the TN bounded to the Ca^{2+}ions ([CaTN]).

3.1 Activation Dynamics

In this section the description of the myofibril model has been limited only to the aspects necessary for the analysis of stimulation effects. The full model with parameters values have been presented by Otazu *et al.* (Otazu et al., 2001).

The intracellular Ca^{2+}concentration is described by the stoichiometric equation:

$$\frac{d[Ca^{2+}]_{PROX}}{dt} = \gamma_{DICR} + \gamma_{CICR} + \gamma_{LEAK} - \gamma_{PUMP} - \frac{[Ca^{2+}]_{PROX} - [Ca^{2+}]_{DIST}}{\tau_{PROX}}, \quad (1)$$

where: γ_{DICR} is the rate of Ca^{2+}liberation process elicited by the voltage-dependent DHPR receptor (see section 3.2), γ_{CICR} is a rate of the Ca^{2+}release from SR through uncoupled-RyR, γ_{LEAK} denotes a constant Ca^{2+}efflux leakage, while γ_{PUMP} is a Ca-ATPase pump rate. $[Ca^{2+}]_{PROX}$ denotes a Ca^{2+}concentration nearby SR surface, while $[Ca^{2+}]_{DIST}$ is a Ca^{2+}concentration in the interior of the myofibrillar space, τ_{PROX} denotes a time constant of a diffusion process.

Previous results (Glukhovski et al., 1998) revealed that the RyR channel has two calcium binding sites: the first one for couple Ca^{2+} ions (activating site) and the second one for a single Ca^{2+} ion (inactivating site). The Ca^{2+} release rate is described by the probability of binding of two Ca^{2+}ions to the activation site (a) and the probability that the inactivation site is bound to a single Ca^{2+}molecule (i).

$$\gamma_{Ca} = f_{Ca}(1-i)a \quad (2)$$

$$\frac{da}{dt} = \alpha_a(1-a)[Ca^{2+}]^2 - \beta_a a \quad (3)$$

$$\frac{di}{dt} = \alpha_i(1-i)[Ca^{2+}] - \beta_i i \quad (4)$$

where f_{Ca} denotes the maximum rate of Ca^{2+} release through the uncoupled-RyR. The probability of binding of Ca^{2+} ion to the activation or inactivation site is represented by a coefficient α and depends on $[Ca^{2+}]$. A durability of the bond is characterized by β.

3.2 Voltage Activated Channel

It is difficult to evaluate unambiguously a relationship between the sarcolemma potential and the Ca^{2+} liberation rate (via the coupled RyRs) based on the recent experimental evidence, because the CICR effect is strictly dependent on the DICR effect. The interaction between the DICR and the CICR results in a complex dynamical system, therefore the decomposition of these two effects is difficult (Bakker et al., 1996; Delbono and Meissner, 1996). For the sake of simplicity, it is assumed that DICR release rate is proportional to the depolarization potential. Model of the RyR coupled with DHPR receptor reflects a voltage-dependent factor generating a slow decline in the Ca^{2+}release rate as an effect of the long-lasting depolarization (Delbono and Meissner, 1996). Moreover, the threshold depolarization potential (V_{th}), which reflects DHPR excitability, is taken into consideration (Delbono and Meissner, 1996; Bakker et al., 1996).

$$\gamma_{DICR} = g_{DHPR}(1-i_V)(V_m - E_{rest}) \quad (5)$$

$$\frac{di_V}{dt} = \alpha_V(1-i_V)(V_m - E_{rest}) - \beta_V i_V \quad (6)$$

where V_m is the sarcolemma potential, E_{rest} denotes a resting potential of the sarcolemma, g_{DHPR} denotes a proportional coefficient, i is related to the voltage-dependent DICR decline.

The parameters in eq. (5) and (6) were estimated based on *in vivo* results available for a soleus muscle (Delbono and Meissner, 1996), under the assumption that the refractory period of the DHPR is similar to a refractory period of sarcolemma (8ms). The value of g_{DHPR} was calculated assuming that AP (which amplitude reaches 20mV (Wallinga et al., 1999; Bakker et al., 1996)) generates the Ca^{2+}release according to Otazu et al. (Otazu et al., 2001). The V_{th} is calculated from the Voltage dependent of SR Ca^{2+}release results and the coefficients α_V and β_V were estimated by using least square method and digitalized results of the time dependence Ca^{2+}release. The obtained estimates are presented in tab. 1

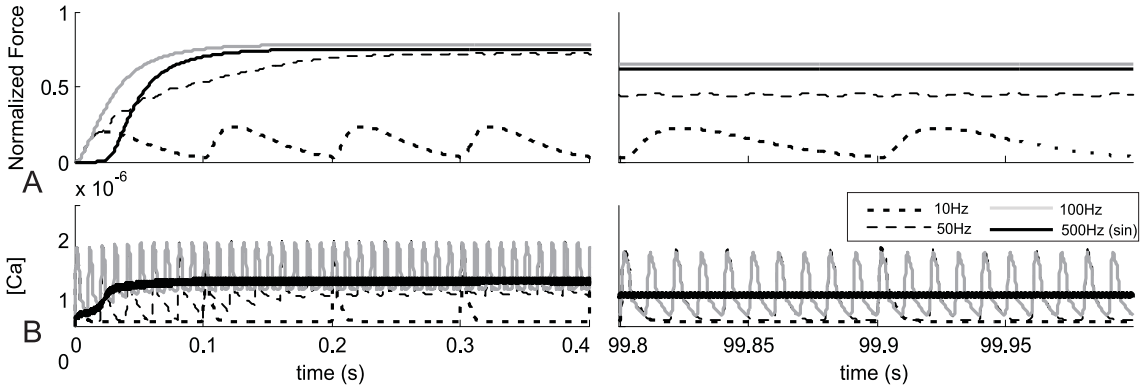

Figure 1: The contraction profiles (A) and $[Ca^{2+}]$ concentration (B) recorded at the beginning and at the end of 100s stimulation period for 10,50,100Hz trains of square-wave and modulated harmonically pulses (500Hz).

Table 1: Parameters of the voltage activated channel.

g_{DHPR} $M(mV\cdot s)^{-1}$	α_V $(mV\cdot s)^{-1}$	β_V s^{-1}	E_{rest} mV	V_{th} mV
$1.0e-3$	1.29	125	-80	-50

3.3 Contraction Dynamics

The input to the block modelling the contraction dynamics is a concentration of TN bound to Ca^{2+}([CaTN]) (Otazu et al., 2001). The contraction dynamics is described by a linear second-order element connected with two nonlinear elements: a threshold-type (connected to the input) and a Hill-type saturation (connected to the output). Such the behavioural model, accounts for the following physiological observations: the threshold level of the [CaTN] above which the contraction occurs, and the saturation of the [CaTN]-Force curve (Bottinelli and Reggiani, 2000).

4 SIMULATIONS

4.1 Comparison of Two Modes of Stimulation

In our experiment the fatigue effect was studied during stimulation of the myofibril model lasting 100s. The standard stimulation with short stimuli (0.1ms) and frequency in the range of (2÷100)Hz was used. Each pulse was assumed to trigger an AP. Moreover, the persistent stimulation by (250÷1500)Hz sinusoidal trains was investigated. It was assumed that during transcutaneous NMES, the muscle fibre was depolarized by both positive and negative half-periods. The pulse polarity has a little influence on muscle activation as compared to the pulse amplitude. The intensity magnitude must be above the DHPR threshold (V_{th}) (Green and Laycock, 1990). The stimulation amplitude was selected in order to obtain myofibril contraction at the level observed with a traditional stimulation at the range (50Hz÷100)Hz. It has been assumed that the persistent stimulation inhibits the generation of APs (as in a TENS effect)(Bakker et al., 1996).

4.2 Evaluation of Fatigue Effect as Related to the Pulse-width

The influence of the depolarization on the fatigue effect was investigated in the following experiment. First the square stimulation pulses at the frequency 10, 30 and 50Hz with varying width in the range of 4÷20ms have been applied. Then, the modulation of the corresponding stimulation pulses with the harmonic 500Hz signal were applied with respect to 30Hz stimulation sequence. In both cases the generation of AP at the beginning of each stimulation period (30Hz) was enabled. The aim of this study was to determine whether the pulse-width or the pulse modulation can reduce the fatigue effect.

In our paper, the fatigue effect is characterized by two parameters: the relative force decrease (RFD) and the relative Ca^{2+}concentration decrease (RCD). These parameters are defined as:

$$RFD = \frac{F_{max}-F_{min}}{F_{max}}\cdot 100\% \quad (7)$$

$$RCD = \frac{[Ca^{2+}]_{max}-[Ca^{2+}]_{min}}{[Ca^{2+}]_{max}}\cdot 100\% \quad (8)$$

where F_{max} denote maximal force and $[Ca^{2+}]_{max}$ is a maxiumum calcium concentration, while F_{min} and

$[Ca^{2+}]_{min}$ are maximal a force and a calcium concentration, respectively at the end of stimulation experiment lasting 100s.

5 RESULTS AND CONCLUSIONS

5.1 Frequencial Effects

The fatigue effect under the traditional square-wave stimulation (1÷100)Hz is similar to the results of *in vivo* experiments (Westerblad et al., 2000; Chou et al., 2005). The relative force decrease (RFD) is greater for sub-tetanic (50Hz) contractions than for the fused tetani (100Hz) stimulation (fig. 1A and, 2A). However, this result does not reflect the change in Ca^{2+}concentration. The relative $[Ca^{2+}]$ decrease (RCD) is greater for the 100Hz than for the 50Hz stimulation (fig. 2B). The muscle stimulated with 100Hz pulses is more fatigue-resistant due to the nonlinear relationship between the [CaTN] and the contraction force. The saturation of this function ensures that during fused contractions, the force changes are small even if the calcium concentration changes are significant (Westerblad et al., 2000). In the case of unfused contractions (1-30Hz) the rise of the stimulation frequency increases the fatigue effect (RFD) and RCD as well (fig. 2). However the RFD and the RCD values are lower in that case than during sub-tetani contractions (50Hz). In each case, the calcium concentration decrease is due to the inhibition of uncoupled-RyR (see eq. 4). The inhibition level depends on mean as well as on maximal calcium concentration. This can be observed in the frequency-RCD relation (fig. 2). Moreover such a significant force decrease in the case of sub-tetani contraction (50Hz) is due to the decay of the potentiation effect (Otazu et al., 2001). The results obtained with the harmonic high-frequency stimulation (HFS) reveal that the observed RFD is similar as for the 100Hz traditional stimulation (fig. 1A) and slightly depends on the pulse base-frequency (fig. 2A). However the RCD value is two times larger here than in the case of the traditional stimulation (fig. 2B). The calcium concentration decrease cannot be explained here as a result of uncoupled-RyR inhibition, because the maximal $[Ca^{2+}]$ level is significantly lower than during the traditional stimulation (fig. 1B), so the inhibition level must be lower as well. Therefore the main factor resulting in RCD increase must be the coupled RyRs habituation (eq. 6).

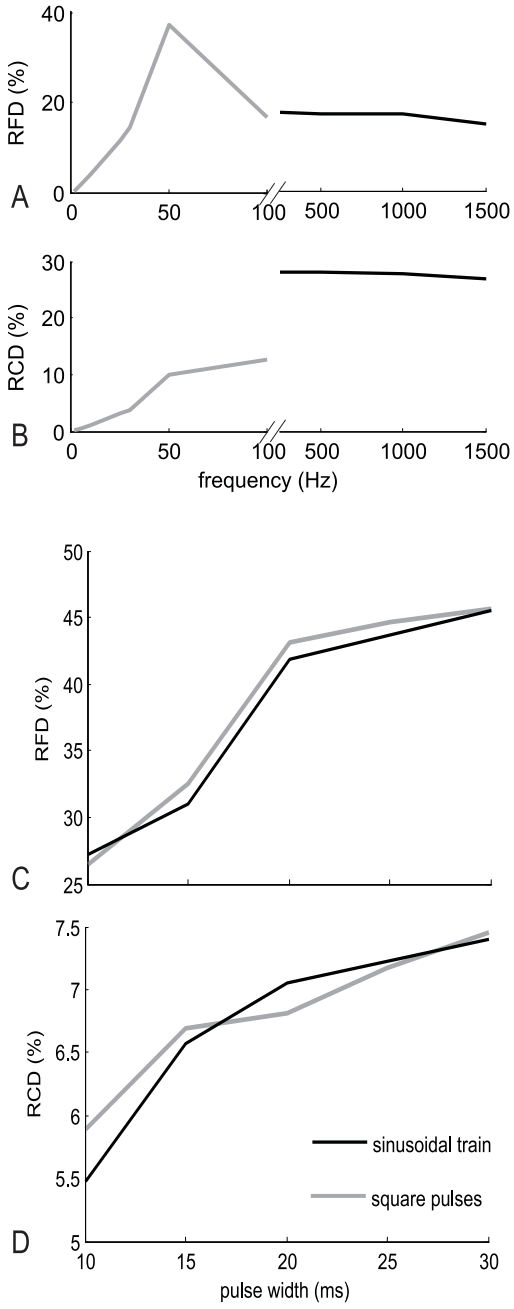

Figure 2: A relative force decrease (RFD) (A,C) and Ca^{2+}concentration decrease (RCD) (B,D) as a function of the stimulation frequency (A,B) and the pulse-width (C,D).

5.2 Pulse width Effect

The analysis of the pulse width influence on the muscle fatigue does not reveal any significant differences between the square pulses and the modulated sinusoidal stimulation (fig. 2B,C). However the sinus-modulated trains seem to be slightly better. Fatigue effect increases here as the pulse width grows, how-

ever for short pulses (10-15ms) it is significantly lower then for the traditional stimulation at 50Hz (fig. 2). In case of the modulated HFS, the RCD is over five times lower in comparison to the results of the harmonic persistent stimulation. This observation can be explained on the basis of the DICR model, because the modulated sinusoidal stimulation ensures the refractory period for the DHPR receptor.

5.3 Discussion

Presented myofibril model reflects effects of Ca^{2+} release from SR as a result of sarcolemma depolarization. It does not take into consideration the properties of the sarcolemma and other tissues which are stimulated during NMES. Thereby, the effect of direct influence of a transcutaneous stimulus on DHPR receptor can not be clearly established. It could be explained only on the basis of *in vivo* experiment results and on a muscle model reflecting myofibril properties, muscle fibres recruitation during stimulation and electrical properties of the skin and other tissues combined.

Modulated HFS trains seem to do better than the traditional stimulation programs, however the influence of such a stimulation on the fibre degeneration process should be investigated. Although the amplitude of repolarization pulses during HFS stimulation are 50% lower as compared to the short-pulses stimulation, the mean stimulation current is significantly higher (Bennie et al., 2002). In comparison with the wide-pulse stimulation the modulated HFS seems to be less painful due to the lower tissue impedance at a higher frequency. It should be mentioned that the presented model and results can be useful to evaluate stimulation programs under the hypothesis that the transcutaneus stimulation can trigger the DICR effect.

ACKNOWLEDGEMENTS

The work was partially supported by the Polish Ministry of Education and Science, project no. 1445/T11/2004/27

REFERENCES

Bakker, A. J., Head, S. I., and Stephenson, D. G. (1996). Measurement of membrane potential and myoplasmic [ca2+] in developing rat myotubes at rest and in response to stimulation. *Cell Calcium*, 19(5):409 – 418.

Benders, A. A., Oosterhof, A., Wevers, R. A., and Veerkamp, J. H. (1997). Excitation-contraction coupling of cultured human skeletal muscle cells and the relation between basal cytosolic ca2+ and excitability. *Cell Calcium*, 21(1):81 – 91.

Bennie, S. D., Petrofsky, J. S., Nisperos, J., Tsurudome, M., and Laymon, M. (2002). Toward the optimal waveform for electrical stimulation of human muscle. *Eur J Appl Physiol*, 88(1-2):13 – 19.

Bottinelli, R. and Reggiani, C. (2000). Human skeletal muscle fibres: molecular and functional diversity. *Progress in Biophysics & Molecular Biology*, 73:195 – 262.

Chou, L.-W., Ding, J., Wexler, A. S., and Binder-Macleod, S. A. (2005). Predicting optimal electrical stimulation for repetitive human muscle activation. *J Electromyography Kinesiology*, 15:300–309.

Delbono, O. and Meissner, G. (1996). Sarcoplasmic reticulum ca2+ release in rat slow- and fast-twitch muscles. *J. Membr. Biol.*, 151(2):123 – 130.

Ding, J., Wexler, A. S., and Binder-Macleod, S. A. (2003). A mathematical model for fatigue minimization during functional electrical stimulation. *Journal of Electromyography and Kinesiology*, 13:575–588.

Gissel, H. (2000). Ca2+ accumulation and cell damage in skeletal muscle during low frequency stimulation. *Eur J Appl Physiol*, 83(2-3):175 – 180.

Glukhovski, A., Adam, D., Amitzur, G., and Sideman, S. (1998). Mechanism of ca2+ release from the sarcoplasmic reticulum: a computer model. *Ann Biomed Eng*, 26:213–229.

Green, R. and Laycock, J. (1990). Objective methods for evaluation interferential therapy in the treatment of incontinence. *IEEE Trans Biomed Eng*, 37(6):615–623.

Kostyukov, A. I., Hellstrom, F., Korchak, O. E., Radovanovic, S., Ljubisavljevic, M., Windhorst, U., and Johansson, H. (2000). Fatigue effects in the cat gastrocnemius during frequency-modulated efferent stimulation. *Neuroscience*, 97(4):789 – 799.

Mourselas, N. and Granat, M. H. (1998). Evaluation of patterned stimulation for use in surface electrical stimulation systems. *Medical Engineering and Physics*, 20:319–324.

Otazu, G. H., Futami, R., and Hoshimiya, N. (2001). A muscle activation model of variable stimulation frequency response and stimulation history, based on positive feedback in calcium dynamics. *Biol Cybern*, 84(3):193 – 206.

Riener, R. and Quintern, J. (1997). A physiologically based model of muscle activation verified by electrical stimulation. *Biochemistry and Bioenergetics*, 43:257–264.

Wallinga, W., Meijer, S. L., Alberink, M. J., Vliek, M., Wienk, E. D., and Ypey, D. L. (1999). Modelling action potentials and membrane currents of mammalian skeletal muscle fibres in coherence with potassium concentration changes in the t-tubular system. *Eur Biophys J*, 28(4):317 – 329.

Westerblad, H., Bruton, J. D., Allen, D. G., and Lannergren, J. (2000). Functional significance of ca2+ in long-lasting fatigue of skeletal muscle. *Eur J Appl Physiol*, 83(2-3):166 – 174.

IMPLEMENTING AN ARTIFICIAL CENTIPEDE CPG
Integrating Appendicular and Axial Movements of the Scolopendromorph Centipede

Rodrigo R. Braga
Departament of Electronic and Computer Engineering, Federal University of Rio de Janeiro, Rio de Janeiro, Brazil
rodovalho@ufrj.br

Zhijun Yang
School of Engineering and Electronics, Edinburgh University, Edinburgh EH9 3JL, UK
zhijun.yang@ed.ac.uk

Felipe M. G. França
Systems Engineering and Computer Science Program, Federal University of Rio de Janeiro, Rio de Janeiro, Brazil
felipe@cos.ufrj.br

Keywords: Centipede locomotion, central pattern generator, distributed algorithms, post-inhibitory rebound, scheduling by multiple edge reversal.

Abstract: In nature, a high number of species seems to have purely inhibitory neuronal networks called *Central Pattern Generators* (CPGs), allowing them to produce biological rhythmic patterns in the absence of any external input. It is believed that one of the mechanisms behind CPGs functioning is the *Post-Inhibitory Rebound* (PIR) effect. Based in the similarity between the PIR functioning and the *Scheduled by Multiple Edge Reversal* (SMER) distributed synchronizer algorithm, a generalized architecture for the construction of artificial CPGs was proposed. In this work, this architecture was generalized by integrating, in a single model, the axial and appendicular movements of a centipede in the fastest gait pattern of locomotion.

1 INTRODUCTION

Central Pattern Generators (CPGs) are neural circuits that can, without any sensory input, produce rhythmic patterned outputs (Marder et alli, 1995). These networks underlie the production, in a large spectrum of species, of a wide variety of rhythmic motor patterns such as walking, swimming or flying. For that reason, the scientific community devotes enormous efforts to full comprehend it and, as fast as new biological explanations are proposed to explain the mechanism underlying the functioning of CPGs, several mathematically strict models are developed with the purpose of encompass their effects to fields like robotics, computing and artificial intelligence.

The most common approach to the development of models for CPGs is based on dynamical system theory (Golubitsky et alli, 1997). Usually, the behaviour of the neurons in CPGs is modelled through the help of non-linear coupled oscillators. As one may know, the strategies to solve those types of systems cover a vast and sophisticated mathematical ground governed by differential equations. The difficulty to analyse those systems increases even more when the biochemical processes involved in the modelling of CPG activity are considered. On the other hand, a discrete and generalized model approach could produce the same results with the advantage of modularity and quick development without any lost of accuracy. In this work, we intend to use one of these models to reproduce the locomotion of a centipede, hoping to demonstrate the power of such models.

A special class of topology-independent graph dynamics called *Scheduling by Multiple Edge Reversal* (SMER), developed initially with the purpose of solve some problems in distributed computing, present itself as an interesting way of predict and reproduce the behavior of many biological oscillatory neuronal networks.

In the following sections we will try to briefly explain the SMER algorithm and show how, starting from it, we can develop a model for the inner biological behavior of CPGs. After that, we will hold some discussions on centipedes, its axial and appendicular movements, and lastly, an experimental model will be draw as much as the conclusions.

2 SMER AND ARTIFICIAL CPGS

SMER is an algorithm used in Distributed and Parallel Computation as a tool to allow a given number of processes sharing a finite number of resources among them, without the occurrence of *deadlock* or *starvation*. SMER is a generalization of the *Scheduling Edge Reversal* (SER) graph dynamics. In order to understand SER, consider a given number of processes and resources as part of a neighbourhood-constrained system represented by an acyclic graph. Processes are represented by nodes and resources by oriented edges. Each node will be in one of two possible states: *operating* or *idle*; also, each edge will be always point to the process that has the resource turn available to. So, when a node has all the shared edges pointing towards it, i.e., has all the resources turns available, it changes from the idle state to the operating state (in this case, this node is also called *sink* node). Once this operating process has finished operation, it reverses all its oriented edges to its neighbours. Although that is not the purpose of this work, it's possible to prove that if the initial graph is acyclic, then no process will be idle forever and, more importantly, the system will oscillate (see Figure 1). More than that, at any cycle of oscillation, every process will operate the exactly same number of times (Barbosa, 1996).

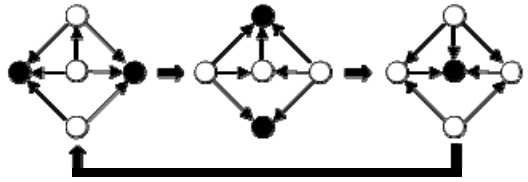

Figure 1: An example of the SER graph dynamics. Black nodes represent operating processes; white nodes represent idle processes.

Note that, even though the above described SER mechanism is enough to solve much of the problems of resource sharing, there is no differentiation among the node's time of task execution. It's fair to imagine that under certain circumstances some processes will need of its shared resources for a longer period of time than the others. To encompass this scenario, the SMER algorithm was created as a generalization of SER. In this new algorithm, all the characteristics of the SER persist with the difference that each node will have associated with it an natural number *r*, called *reversibility*, and between any two nodes is allowed to exist any number of oriented edges. Once a node has pointing towards it, from all of its neighbours, a number at least equal to its reversibility, this node is allowed to operate. When operation has finished, a node will reverse a number of edges equal to his reversibility to all of its neighbours (see Figure 2). Among the characteristics of SMER, one very important is that for any system with arbitrary reversibilities of its nodes, there is always at least one possible periodic SMER solution.

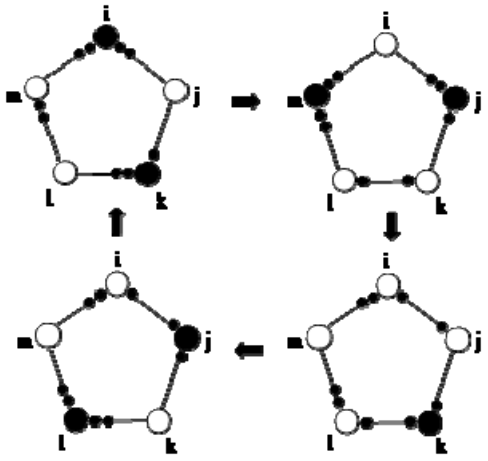

Figure 2: An example of a SMER graph. Note that to avoid the existence of several arrows connecting two nodes, a different representation of resource dependency is adopted. In this example the reversibilities are $i=l=m=2$, $j=k=1$.

Once we have defined what SMER is and how it works, it's important to clarify exactly how it connects with CPGs. As said before, CPGs are the underlying mechanism of a series of rhythmic patterns of locomotion. Although it is not completely clear how it exactly works, some biological mechanisms have been found and are credited as small units in the construction of CGPs. One of those real neuronal mechanisms is called *post-inhibitory rebound* (PIR) and is capable of

produce an alternate cycle of activity in a group of inhibitory neurons in the absence of external stimulus (Pirtle and Satterlie, 2007). Although the PIR phenomenon is a complex subject, it is interesting to note that it matches perfectly to the mutual exclusion activity between neighbouring nodes coupled under SMER. It will be the theory behind the construction of modules that, in our model, will act just like a set of interconnected inhibitory neurons exhibiting PIR. These modules will be called *Oscillatory Building Blocks* (OBBs). So, instead of modeling electrophysiological activities of interconnected neurons based on membrane potential functions, we build an artificial CPG network with SMER-based OBBs for the exploration of the collective behaviour networks of purely inhibitory neurons.

3 THE ARTIFICIAL CENTIPEDE

Centipedes form a very special species of arthropods. They are capable of, combining axial and appendicular movements, attaining great speed with energetic efficiency. These unique characteristics of the centipedes stimulate a great number of biologists to study his static anatomy and the kinematics of his locomotion leading to a great amount of interesting information about this animal. For instance, biologists thru the use of high-speed cameras discovered that the number of legs touching the ground at a high-speed movement decreases when compared to the low-speed one , leading to a bigger distance between the supporting legs. In the extreme, a centipede can be supported for only four legs. Also, there is a direct correlation between the axial pattern of undulation and the speed. Nevertheless, whatever the speed is, in each segment contralateral legs will always step alternately (Anderson, Shultz and Jayne, 1995). All this aspects have to be taken into account while modeling the centipede's movement.

As a simple observation of a moving centipede may suggest, the challenge is the integration between two different components: the appendicular and the axial. It's reasonable to infer that a good way of tackle this problem could be made through the analysis of each movement separately, defining its period and trying to construct a SMER-based OBB for a later synchronization between the two. Although it seems a good strategy, it lacks an important aspect of the problem: the two types of movements are connected in a much deeper level. For example, it's impossible to see a real centipede to put two contralateral legs in any position different that the one caused by alternately stepping. Therefore, this approach would not reproduce that subtle aspect of the locomotion of the centipede.

To correctly model the locomotion of a centipede, with the maximum similarity to its complex behavior, one has to construct the OBB with eight nodes, i.e., motor neurons, enclosing one whole segment. In this case, the network responsible for the connection of these OBBs has to be one that follows the full length of the animal, from the anterior to the posterior segment. But before we see in detail the whole model, let's see more of each centipede's movement as a way to understand how this OBB will be made and how the connections among them will be put. Consider in the following a scolopendromorph centipede in the fastest pattern gait of locomotion, i.e., the amplitude of lateral bending has the largest value and the fastest speed of dislocation is attained. Also, it is important to note that this kind of centipede has 21 leg bearing segments linked by flexible membranes serving as the only intersegmental articulation.

3.1 Appendicular Movement

As said before, in any given speed of the centipede, two legs from the same segment are always in opposite positions, i.e., when the left leg of a segment is flexing the other in that segment is extending. Also, it is important to note that the legs that are in the concave side of an undulating wave are always extending. The last statement is the most important one since ties the axial and the appendicular movements.

For the sake of simplicity and without any loss of generality, let's assume the appendicular movement being defined as the action of two antagonic muscles: flexor and extensor. The first one is responsible for lifting a leg from the ground and the later one for doing the opposite. In this simplification, let's also assume that when a leg is touching the ground it is also pushing it backwards, allowing the effective movement of the animal.

3.2 Axial Movement

In the fastest speed a centipede can attaining approximately 1.5 times his length per second ($1.5Ls^{-1}$) with a correspondents $f = 3.45Hz$ and $\lambda = 11$ (Anderson, Shultz and Jayne, 1995). As a result, we infer that each concave section of the undulating wave it is composed for approximately 5 body segments. Also, for the sake of simplicity and

without any lose of generality, let's suppose the lateral bending of a centipede as the result of a pair of antagonic muscles: one causing the left and the other causing the right bending.

4 EXPERIMENTAL EXPLORATIONS

Our artificial centipede was designed to reproduce the macroscopic features of its real counterpart. Following the before mentioned characteristics and simplifications, each segment will have six artificial muscles: two pairs of extensors and flexors (one pair per leg), one muscle responsible for the lateral bending to the right and another for the left. As a didactic resource, Figure 3 shows the schematic representation of our artificial centipede's segment taking into the account the artificial muscles mentioned before. The intersegmental articulation is represented by a single pivot. Once more, note that we consider that the extensor muscle is in action, the respective leg is producing traction.

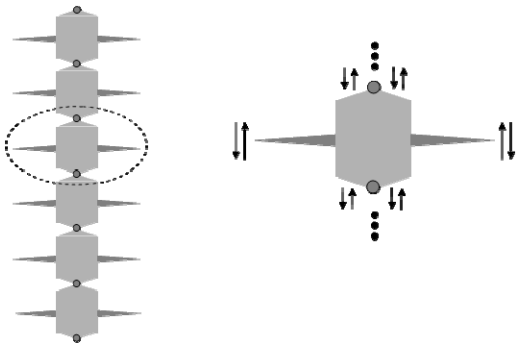

Figure 3: The Artificial Centipede design. In the left it is displayed 6 of the 21 segments of the model. In the right, the degrees of freedom in one segments is showed.

4.1 The Centipede OBB

As we saw before, to integrate the two types of movements, the OBB has to enclose the whole animal's segment. So, in this model we have to generate a SMER-based network capable of reproducing all the intermediate positions that each muscle assumed during the periodic movement. At this point, all the information retrieved during the analyses of real centipedes comes together.

In this OBB there are also two additional nodes, represented in the middle of Figure 4, that are responsible for the connection among the OBBs, represented by the dotted line, and for the activation of the others nodes, the artificial muscles. Note also that the reversibility of those two connection-nodes is 5, meaning that both of them are only activated when each connected edge is fully directed to them. Under another point of view, this also means that the others nodes, the artificial muscles, will be activated for a period of time five times longer them those two, since its reversibility is one.

The above mentioned reversibility, i.e., $r = 5$, was obtained from the analysis of the undulating wave that covers the centipede from the anterior to the posterior segment (see Figure 5.b). It is half of the wavelength.

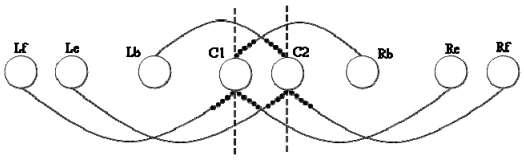

Figure 4: The resulting Oscillatory Building Block (OBB). C1 and C2 are the inter-segment connection nodes; dotted lines display the connection to other OBBs. Lb and Rb are nodes representing the artificial motor neurons/muscles responsible for the left and right bending, respectively. Le and Re are nodes representing the artificial motor neurons/muscles responsible for the extension of the left and right legs, respectively. Finally, Lf and Rf are the nodes representing the artificial muscles responsible for the flexion of left and right legs, respectively.

4.2 The SMER Network

Now that the OBB is built, it is necessary to connect them in a network that will reproduce the body behaviour of the animal. Since the locomotion pattern of the centipede is an undulating wave covering the whole body, the design of the network started with this perception and tried to reproduce this characteristic. Fortunately, this proposition proved correct and the SMER-based network, responsible for the connection of the OBBs is one that produces the activation of each OBB in the same direction as the travelling wave (see Figure 5).

.

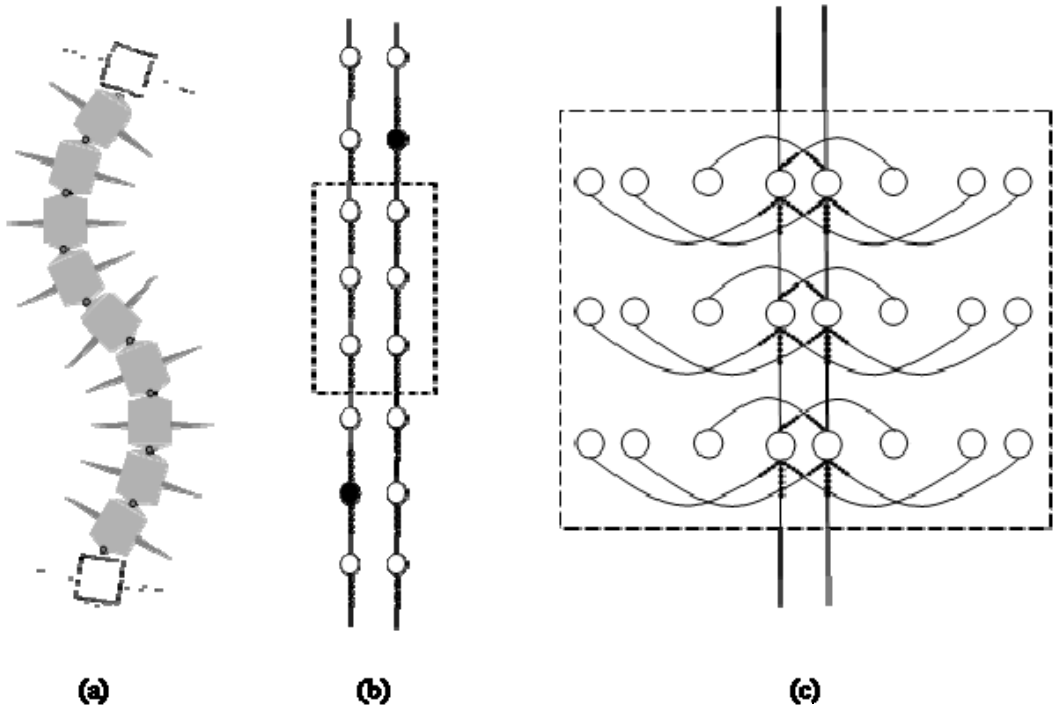

Figure 5: (a) The artificial centipede scheme (only 11 segments shown); (b) The functioning axial SMER-based network (without the OBB details); (c) SMER-based OBBs (3 OBBs shown).

5 CONCLUSIONS

Since the beginning of the study of Central Pattern Generators, one of the most critical problems was to understand and to model the biological macroscopic cyclic behaviour observed in terms of small nonlinear units. As an alternative to the usual continuous numerical methods applied in this field, the use of a discrete and generalized model to mimic the cyclic behaviour of CPGs was proposed in this work. In this aspect, the use of distributed algorithms avoids the usual complexity of the usual approach without losing expressivity or generality.

The present work shows the application of one of these algorithms (SMER) to model the complex locomotion of a centipede at its fastest gait pattern speed. Although others ways of reaching that objective may exist, we believe that our approach showed significant advantages in aspects like time consumed, facility and acceptable correlation with the reality. We believe that the strategy adopted in this work could help biologists and neurophysiologists to not only test the current theories in Central Pattern Generator's functioning, but also develop new points of view in the construction of complete explanations to the phenomenon of the generation of rhythmic patterns in animals.

REFERENCES

Barbosa, V.C., 1996. *An Introduction to Distribuited Algorithms*, The MIT press, 1nd edition.

Marder, E., Nandim, F., Calabrese, R.L., 1995. Principles of rhythmic Motor Pattern Production, Physiological Reviews.

Anderson, B.D., Shultz, J.W., Jayne, B.C., 1995. Axial Kinematics and muscle activity during terrestrial locomotion of the centipede Scolopendra Heros. The Company of Biologists Limited.

Golubitsky, M., Stewart, I., Buono, P., Collins, J.J., 1997. A modular network for legged locomotion. N.H. Elsevier.

Pirtle, T. J., Satterlie, R.A., 2007. The role of post-inhibitory rebound in the locomotor central-pattern generator of Clione limacine, Integr. Comp. Biol.

Yang, Z., França, F.M.G., 2003. A generalized locomotion CPG architecture based on oscillatory building blocks, Biol. Cybern., Springer-Verlag.

BIO-INSPIRED IMAGE PROCESSING FOR VISION AIDS

C. Morillas, F. Pelayo, J. P. Cobos, A. Prieto
Department of Computer Architecture and Technology, University of Granada, Spain
cmorillas@atc.ugr.es, fpelayo@ugr.es, juanp@atc.ugr.es, aprieto@ugr.es

S. Romero
Department of Computer Science, University of Jaén, Spain
sromero@ujaen.es

Keywords: Bioinspired real-time image processing, vision aids, neuromorphic encoding, visual neuroprostheses.

Abstract: We present in this paper a system conceived to perform a bioinspired image processing and different output encoding schemes, oriented to the development of visual aids for the blind or for visually-impaired patients. We remark some of its main features, as the possibility of combining different image processing modalities (colour, motion, depth, etc.) and different output devices (Head Mounted Displays, headphones, and microelectrode arrays), as well as its implementation on a reconfigurable chip (FPGA) or a specific VLSI chip, which allows working in real time on a portable equipment. A software design environment has been developed for the simulation and the automatic synthesis of the processing models into a hardware platform.

1 INTRODUCTION

Visual impairment is considered as one of the 4 main causes for the loss of self-sufficiency among elderly people. With different affection degrees, visual impairment affects about a 25% of persons over 65 years old, and a 15% of adults between 45 and 65 years old. In addition, the progressive ageing of the population in developed countries makes these numbers grow forth, propitiating a remarkable loss in visual acuity and a reduction of the visual field. In this context, retinal degenerations (especially the age-related macular degeneration, ARMD), cataracts, glaucoma, diabetic retinopathy, optic nerve damage, and ocular traumas, yield a relevant amount of blindness cases, often non-curable.

Visually impaired patients require optical aids (microscopes, magnifiers, telescopes, optic filters) to enhance their quality of life, exploiting their remaining functional vision. However, there is no a unique aid able to provide this enhancement under any circumstance. Electronic aids, as (LVES, 1994) V-MAX, or the recent (JORDY, 2007) provide a more efficient use of the visual functional remains of the patient by magnifying images, enhancing light/darkness and colour contrasts, but none of these systems are able to implement an efficient control of local gain to produce clear and sharp images in a variety of lighting situations. These devices also use to be relatively heavy (0.5 to 1 Kg.), quite expensive and difficult to manipulate during motion. These reasons led us to propose the system described in this paper, which is inspired by the way the biological retina works, and is fully adaptable and configurable to each patient.

The retina-like design, not only at a functional level, but also at an architectural level, is a key aspect in the development of a robust and efficient system able to apply in real time local spatio-temporal contrast processing of the visual information. The final system has been developed on a reconfigurable hardware platform in order to provide real-time and portable solutions for visual processing that fit to the particularities of the visual impairment of every person, and which can be tuned according to its evolution with time. According to diversity of affections, different output encoding modalities have been considered, including acoustic encoding, high resolution image for Head Mounted Displays and neuromorphic encoding for neuroprostheses.

The next section is devoted to explain the bioinspired image processing in the system we present, and its main architecture. In section 3, a spike event encoding method is detailed, that is able to produce trains of electrical signals intended to

stimulate neurons of the human visual system. Section 4 describes an acoustic signal generation module, that allows to the blind to localize those objects in the visual environment that produce higher activity levels. Finally real-time hardware implementation is presented and conclusions are summarized.

2 BIOINSPIRED IMAGE PROCESSING

The development of a bioinspired system for visual processing is being pursued by several research groups, as the tuneable retinal encoder, by (Eckmiller, 1999), or the computational models of retinal functions described by (Koch, 1986). The CORTIVIS (Cortical Visual Neuroprosthesis for the Blind) consortium has also implemented a bioinspired retinal processing model as part of a system designed to transform the visual world in front of a blind individual into multiple electrical signals that could be used to stimulate, in real time, the neurons at his/her visual cortex (Cortivis, 2002; Romero, 2005).

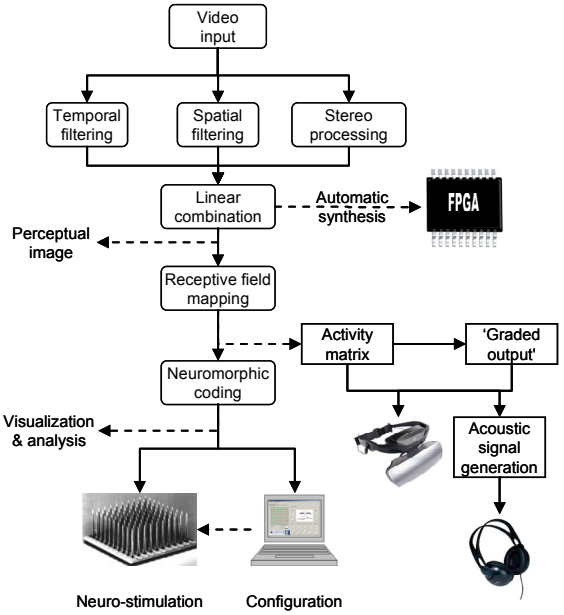

Figure 1: Reference architecture of the bioinspired image processing system for the development of visual aids. After obtaining a linear combination of spatial, temporal and depth-related features, different outputs for a variety of applications are possible. The choices include automatic synthesis for programmable devices; sending the information to the patient by means of HMD, headphones for acoustic signalling, or delivering neurostimulation to the neural tissue to evoke visual perceptions.

Even though the main objective of the CORTIVIS project, in which our research group has been involved, was the design of a complete system for neurostimulation, a part of the system is useful as a processing scheme which can be adapted to match the requirements aforementioned, and, this way, develop non-invasive aids for visualization, or sensorial transduction to translate visual information into sound patterns.

Figure 1 shows the reference architecture illustrating all the capabilities developed up to this moment. The input video signal is processed in parallel by three modules for the extraction or enhancing of image features, according to different processing modes. The first module performs a temporal filtering, as natural retinae also respond and remark temporal changes in the visual input; see for example (Victor, 1999). In our platform this temporal enhancement is implemented by remarking the differences between two or more consecutive frames, and with different strength in the periphery of the visual field (foveated model) as in natural retinae (Morillas, 2007).

For the spatial processing, an intensity and colour-contrast filtering is applied to different combinations of the three colour planes (red, green and blue) composing a frame. This spatial filtering emulates the function of bipolar cells in the retina, in the form of difference of Gaussians filters.

Our platform offers a variety of bioinspired predefined and parameterized filters, including Gaussians (1), difference of Gaussians (2) and laplacian of Gaussians (3). Even more, we can include new filters in the form of any Matlab (Mathworks, 2007) expression over the colour or intensity channels.

$$G_{\sigma 1}(x,y)=\frac{1}{\sqrt{2\pi\sigma_1^2}}\exp\left[-\frac{x^2+y^2}{2\sigma_1^2}\right] \quad (1)$$

$$DoG=G_{\sigma 1}-G_{\sigma 2}=\frac{1}{\sqrt{2\pi}}\left[\frac{1}{\sigma_1}e^{-(x^2+y^2)/2\sigma_1^2}-\frac{1}{\sigma_2}e^{-(x^2+y^2)/2\sigma_2^2}\right] \quad (2)$$

$$LoG=\Delta G_{\sigma}(x,y)=\frac{x^2+y^2-2\sigma^2}{\sigma^4}e^{-(x^2+y^2)/2\sigma^2} \quad (3)$$

The stereo processing module obtains disparity maps at different resolutions, starting from image pairs captured by two head mounted cameras. Figure 2 shows examples of application where disparity maps are used as a weighting term for the output of a spatio-temporal filtering combination, emphasizing closer objects which produce a higher activity levels.

The next stage in figure 1 gathers the results obtained by each of the processing modalities. Its objective is to integrate as much information as possible into a single compact representation, so it requires a maximum degree of compression to allow

the integration of the most relevant features. Given a real scene, we intend to remove all the background content, so only the closest objects are remarked, which are considered to be the most relevant information for an application like the one described in this paper, conceived for basic visual exploration tasks and obstacle-avoidance navigation. After some initial experiments with a portable prototype, we considered the need for incorporating an ultrasonic range finder, which provides a measurement of the distance to the closest object that can be used to ponderate the output of later stages, based on proximity.

According to the kind of application, the resolution for the output will be different; however, we can consider a general reduction of the resolution. For a neuroprosthesis, this resolution will match the number of available electrodes in the physical interface, which is currently in the order of hundreds of channels (Fernández, 2005). If we apply this scheme for a sensorial transduction system for the translation of visual information into audible patterns, we will be restricted by the amount of different sounds that the patient is able to distinguish without interfere his/her normal perception capabilities.

The reduction of spatial resolution is based on the concept of receptive field, which can be defined as a zone of the image (set of pixels) that contribute to the calculation of the value resulting in the reduced representation, which we call "activity matrix".

The default configuration performs a partition of the image into rectangular non-overlapping areas of equal size, however we have also developed a tool for the definition of more complex structures, allowing even different sizes and shapes, which also can be variable, depending on its localization, from the centre of the visual field to its periphery.

Once the system has computed the activity matrix, depending on the specific application we will use it in a different way. In the case of a neuroprosthesis, the next stage is the recoding of this information into a neuromorphic representation, as a sequence of stimulation events (spikes), which will be later used to drive a clinical stimulator. Another possible use is the display of this information by means of specialized portable screens as HMD (Head Mounted Displays), to assist low-vision patients suffering a visual deficiency but still holding a functional remain of his/her vision.

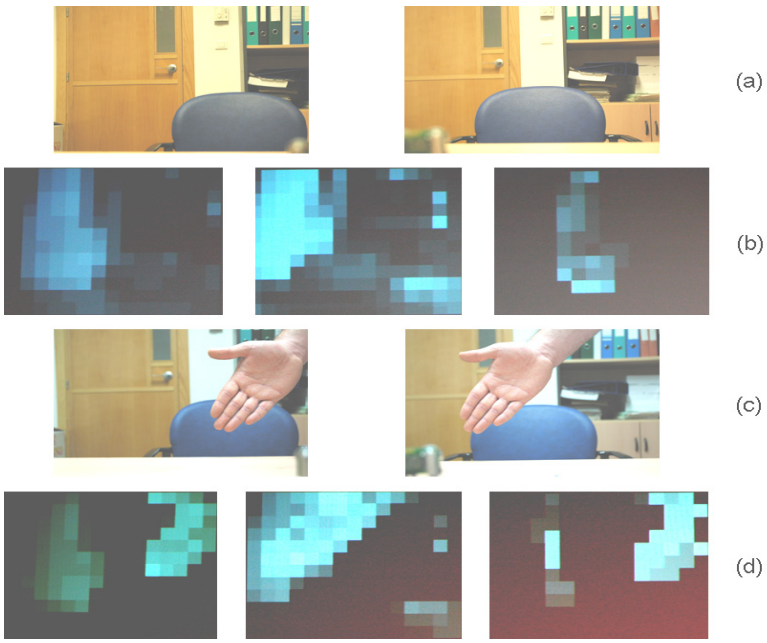

Figure 2: Stereo processing results obtained with the hardware implementation described in section 5. (a) Left and right images from the stereo cameras. (b) Activity matrices for a combination of spatial filters on the left input (left), right input (centre) and disparity weighting (right), the door is detected as relevant for spatial filters, but the chair, that is closer, is enhanced by the disparity computation. (c) A new closer object (the hand) appears in the visual field. (d) The disparity filter (on the right) detects this new object as the most relevant, due to its higher activity at the output matrix. The disparity output image is referred to the filtered left image in all cases.

The information provided by the activity matrix has been also employed in our system to locate the most relevant zones of the scene and translate them into sound patterns that include 3D spatial information. This way, the system can point out the location of the highest activity levels in the scene for the patient.

3 NEUROMORPHIC ENCODING

Features extracted by the image processing stage can be used in a complete neural stimulation system, being transformed by a spiking neuron model that is able to translate numerical activity levels into spike trains that the stimulation device can handle.

Different neuron models can be found in the literature (Gerstner, 2002), and we decided to implement an integrate-and-fire spiking neuron model, including a leakage factor, because of the simplicity to be implemented in a discrete system.

The selected spiking neuron model, depicted in figure 3, needs a set of accumulators which gather activity levels resulting of the current frame processing. When a value is integrated, the result is compared to a previously defined threshold, and if reached, the accumulator is initialized and a spike event is raised. The leakage factor avoids unexpected events due to ambient noise or residual activity from previously processed frames.

Each spike event generated is delivered to the stimulation device which has to form the corresponding electric waveform to be applied to the neural tissue.

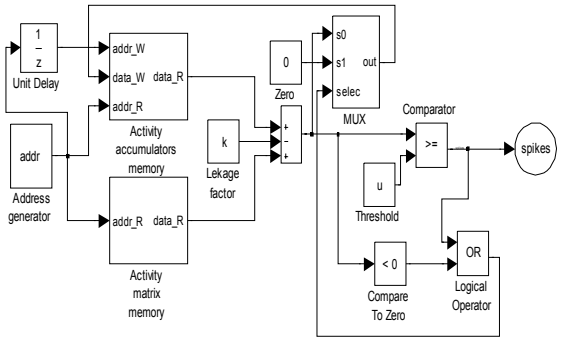

Figure 3: Block diagram of the neuromorphic coding subsystem for a sequential implementation.

All the events generated during a stimulation session can be stored for analysis. Figure 4 shows a graphic representation of all the events produced by a white horizontal bar moving from bottom to top on a black background, considering a 10 by 10 channels stimulation device. In this example the retina function is approximated by a simple model described by the expression (4):

$$retina = \frac{1}{5} \cdot I + F_{temp} \quad (4)$$

where I is the input pixel intensity and the temporal filter F_{temp} compares, for each pixel, the current intensity value with the average of the five previous frames.

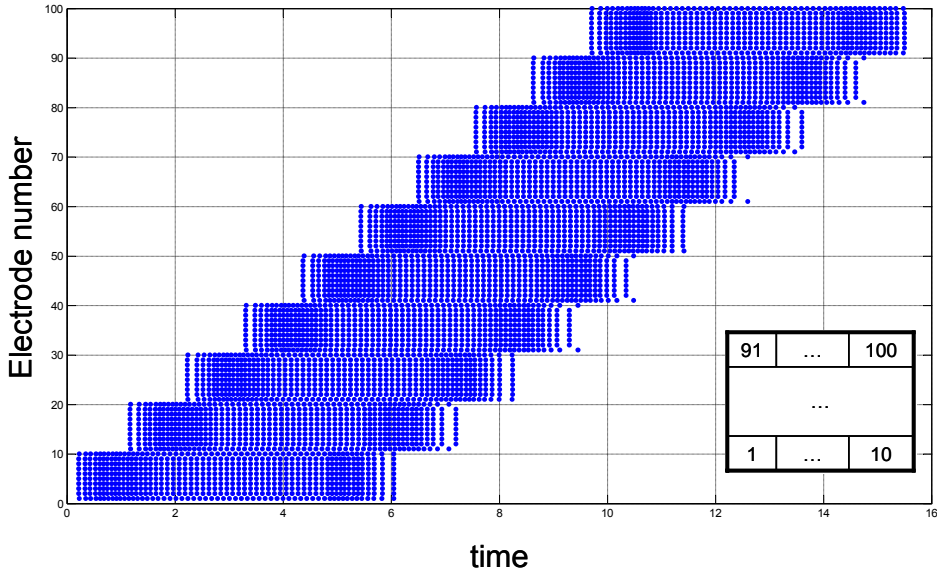

Figure 4: Spike event trains produced by a horizontal bar pattern moving from bottom to top of the image, and illustration of stimulation channels numbering (see text for details).

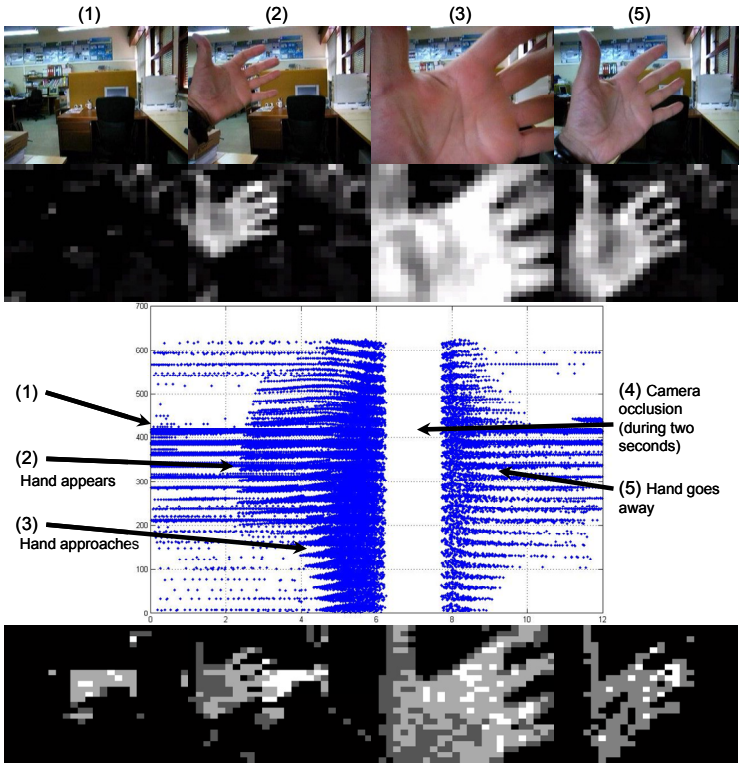

Figure 5: Image processing and coding example, including the inverse activity restoration stage. First row shows four instants of a video sequence. In the second row we can see the corresponding activity matrix obtained with a certain spatial filtering combination. Graphics shows the representation of the spike events produced by the image sequence, and finally, the bottom row represents the reconstruction of each activity matrix.

In order to test the effectiveness of this information coding method, we have developed a procedure for restoring activity matrix values from the temporal sequence of spike events (i.e. an inverse spike to activity conversion). Each spike produces an increment of the accumulated value of the corresponding activity matrix component, while a leakage factor is applied every simulation time step. A visual comparison between original and restored activity matrices was done, reporting successful results. However, a better evaluation method was implemented. Restored activity matrix was applied again to the neuromorphic pulse coding stage, producing very precise results with almost imperceptible differences. Results obtained from the restoring stage are illustrated in figure 5

4 GENERATION OF ACOUSTIC SIGNALS

As we have mentioned above, an object detected by the image processing stage can be encoded by a sound that will represent the position in which it has been detected (see figure 1).

We will represent the position of an element in the visual space by means of a sound pattern coming (apparently) from the actual spatial location of that element. This location is determined by three parameters (see figure 6): straight-line distance between the observer and the object, *d*, elevation of the object over the horizontal plane containing the head, *e*, and azimuth or horizontal angle between the front and the sides of the head, *a*.

The mechanism of spatial sound location carried out by the binaural biological system is highly dependent on the individual, making difficult the set up of an artificial system for universal filtering (Algazi, 2001). As a first approach, we have made use of the results obtained by (Gardner, 1994) in order to create sounds including spatial localization

information. In their study, they placed a KEMAR (Knowles Electronics Manikin for Acoustic Research) model inside a soundproof cabin. Then, the authors played pseudo-random sound stimuli, and measured the response at the input of each of the pinnae.

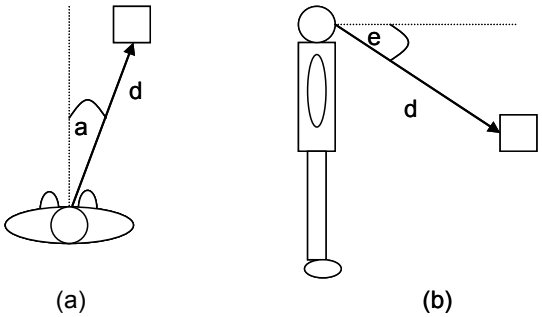

Figure 6: Basic parameters for the 3D location of sounds. See text for more details.

This way, they obtained an ample set of measurements of the HRTF (Head-Related Transfer Functions) which model the physical and mechanical features of the head acoustic system. These functions are described as a set of multiple pairs of coefficient sets of a FIR filter, one for each spatial location and auditory channel.

This technique is expressed in (5):

$$y(t) = \sum_{i=1}^{N} h(i)x(t-i) \qquad (5)$$

where h is the set of coefficients of the FIR filter, x represents the samples of base sound to which we want to add spatial information, and y is the resulting sound.

5 REAL-TIME HARDWARE IMPLEMENTATION

This section describes the implementation of our system into a programmable circuit. This choice is based on the customization needs of the application. The kind of processing to be carried out depends strongly on the specific features of the disability of the patient, which also can vary with the evolution of the illness, so the system requires being able to adapt its configuration to those changes.

Furthermore, the systems that are based on reconfigurable logic chips (FPGA) present some other features that make them suitable for this field of development, as the short time required to obtain a working prototype, its small size, allowing for portability and the integration of some other interfacing circuitry.

The description of the different modules has been written in Handel-C language, from (Celoxica, 2007), within its DK synthesis environment.

The prototyping platform selected for our tests is the Celoxica's RC300 board, which incorporates a 6 million gates FPGA and all the peripherals required for our application, as a dual video capture system to grab input images for each visual channel, VGA video outputs, and specific circuitry to obtain stereo audio. Figure 7 shows the experimental setup based on the RC300.

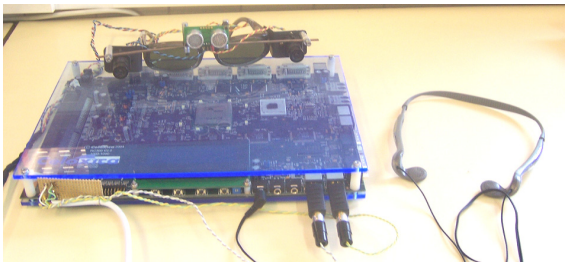

Figure 7: Experimental hardware prototype composed by two cameras, an ultrasonic range finder, headphones and a RC300 board.

This kind of devices let us implement a high degree of parallelism, so that most of the modules can process in parallel. The design has been made to exploit this capability, and a pipelined architecture has been implemented, with a high number of stages that operate concurrently.

Figure 8 shows the schematic organization of the building blocks for the image processing subsystem.

The combination of an image grabbing process to store the frame, and another process to read this information feeds constantly the computational pipeline, and achieves an uncoupling between the image capture rate and the processing carried out by the rest of the system. The information read from the memory banks is delivered to the spatial filtering module, which performs the convolution over the input images with different masks. The outputs from this stage are put together by a weighting module. The results obtained with this module will be used to perform the receptive field based mapping, in which the mean value of all the pixels in the contributing zone is stored for every point of the activity matrix.

Once the activity levels are computed for every zone of the image, the maximum values are identified, as they indicate the presence of the most relevant objects in the scene, which need to be reported to the patient. The user can select the amount of information that he/she is receiving

through this system by varying the number of different zones (K) of the image that he/she prefers to be reported about. This means that we will generate K audible patterns, modulating each of them to include information regarding the location of the image from which it has been extracted, so the patient can perceive their origin.

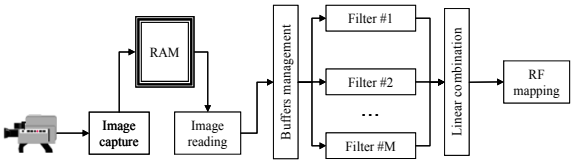

Figure 8: Architecture for the implementation of the image processing system in a Celoxica RC300 Board. The output of this common sub-system can be used for sensorial transduction, low-vision enhancing, or neurostimulation, as depicted in figure 1.

Although the working frequency for the global system is not very high, about 40 MHz, the performance-oriented design architecture allows reaching a 60 fps rate of processing, more than enough to consider the system is working in real time.

6 CONCLUSIONS

Image processing is a key stage for any device conceived to provide an aid to visually-impaired persons. We present a system that incorporates a bioinspired vision preprocessing stage which selects the most relevant objects in a visual scene to perform later processing that can be applied to different impairments. When this later translation is encoded into a stream of events for electrode addresses, the system can be applied for a visual neuroprosthesis. If we perform a sensorial transduction, the results can be translated into sound patterns, providing 3D binaural information related to the location of obstacles in the visual field. In any case, the system is highly flexible and parametric, and can be synthesized to fit into a portable, restricted power consumption board, which is suitable for a wearable aid. Our system is able, as described, of integrating different aspects of the image, as depth, colour and luminance contrast, and temporal changes detection.

We show some results on how the image analysis is performed for a variety of tuneable aspects, and specific data related to the synthesis of the processing scheme on a FPGA.

ACKNOWLEDGEMENTS

This work has been supported by the National Spanish Grants DPI-2004-07032 and IMSERSO-150/06, and by the Junta de Andalucía Project: P06-TIC-02007.

REFERENCES

Algazi, V.R., Duda, R.O., Thompson, D.M., Avedano, C., 2001. 'The CIPIC HRTF Database', *2001 IEEE Workshop on the Applications of Signal Processing to Audio and Acoustics*, pp. 99-102.

Celoxica. http://www.celoxica.com [2007].

Cortivis website. http://cortivis.umh.es [2002].

Eckmiller, R., Hünermann, R., Becker, M., 1999. Exploration of a dialog-based tunable retina encoder for retina implants. *Neurocomputing* 26-27: 1005-1011.

Fernández, E., Pelayo, F., Romero, S., Bongard, M., Marin, C., Alfaro, A., Merabet, L., 2005. Development of a cortical visual neuroprosthesis for the blind: the relevance of neuroplasticity. *J. Neural Eng.* 2: R1–R12.

Gardner, B., Martin, K., 1994. HRTF Measurements of a KEMAR Dummy-Head Microphone, *Media Lab Perceptual Computing Technical Report* #280.

Gerstner, W. and Kistler, W., 2002. *Spiking Neuron Models*, Cambridge: Cambridge University Press.

JORDY, Enhanced Vision. [2007]. http://www.enhancedvision.com

Koch, C., Torre, V. and Poggio, T., 1986. Computations in the vertebrate retina: motion discrimination, gain enhancement and differentiation. *Trends in Neuroscience* 9: 204-211.

LVES, University John Hopkins, Baltimore in collaboration with NASA. [1994] http://www.hopkinsmedicine.org/press/1994/JUNE/199421.HTM

Mathworks website, The. [2007] http://www.mathworks.com.

Morillas, C., Romero, S., Martínez, A., Pelayo, F., Reyneri, L., Bongard M., Fernández, E., 2007. A Neuroengineering suite of Computational Tools for Visual Prostheses. *Neurocomputing* 70(16-18): 2817-2827.

Romero, S., Morillas, C., Martínez, A., Pelayo, F., Fernández, E., 2005. A Research Platform for Visual Neuroprostheses. In *SICO 2005, Simposio de Inteligencia Computacional*, pp. 357-362.

Victor, J., 1999. Temporal aspects of neural coding in the retina and lateral geniculate. *Network* 10(4): 1-66.

BI-LEVEL IMAGE THRESHOLDING
A Fast Method

António dos Anjos and Hamid Reza Shahbazkia
Faculty of Sciences and Technology, University of Algarve, DEEI - ILab 2.57, 8005-139 Faro, Portugal
aanjos@ualg.pt, hshah@ualg.pt

Keywords: Bioinformatics, Medical image processing, Image thresholding.

Abstract: Images with two dominant intensity levels are easily manually thresholded. For automatic image thresholding, most of the effective techniques are either too complex or too eager of computer resources. In this paper we present an iterative method for image thresholding that is simple, fast, effective and that requires minimal computer processing power. Images of micro and macroarray of genes have characteristics that allow the use of the presented method for thresholding.

1 INTRODUCTION

It is known that, in the context of image processing, thresholding (Sezgin and Sankur, 2004) is a simple, but powerful tool to separate objects from the background. There is a vast number of applications for thresholding such as document image analysis (Kamel and Zhao, 1993), map processing (cad,), scene processing and quality inspection of materials (Sezgin and Tasaltin, 2000). Gene images (Diachenko, 1996)(Zhang, 1999) of micro and macro-arrays, where dots of cDNA need to be extracted from the background and electrophoresis and two-dimensional electrophoresis (Dowsey and Yang, 2003) gels, where blots need to be extracted from the background, to determine protein expression, are more recent applications for image thresholding. The quality of the subsequent steps (e.g. spot detection, quantification) will often depend on the quality of the image thresholding.

In this paper it is presented a method of image thresholding that aims to be simple – allowing a rapid implementation in any computer programming language, fast – requiring low computing power – and effective – giving results that can be compared with other reference methods of image thresholding. First it will be presented an overview of what lead us to the proposed method, then, the method itself will be described. Finally, there will be presented some results and comparative data with reference methods of thresholding.

2 STATISTICAL APPROACH

After statistically (Kilian, 2001) analysing several histograms of genomic images with two dominant intensity classes, the background intensity class and the foreground intensity class, with one of them being dominant over the other, for example, the background class being dominant over the foreground class (see fig. 1), it was noticed that when the histogram grows substantially near the dominant peak, the variance, from the lowest intensity level to the intensity level where the big growth happens, decreases relatively to the variance from the lowest intensity level to that intensity level minus one.

In the case of figure 1, the decrease on variance, obviously, happens because the background is highly dominant. From the intensity level where that change occurred to a very fair threshold level there is a distance of about minus one standard deviation of the whole image histogram. With images with a great contrast between background and foreground, the standard deviation is bigger, and the contrary also happens. Thus, the goal was to find where the decrease of variation occurred and then subtract one standard deviation of distance. Very good results were achieved with images where the background was the dominant class but, as long there is one dominant class, it doesn't matter which is the dominant one.

If the variance is measured starting on the first intensity level to any level before the least dominant peak, a decrease on the variance may happen before reaching the most dominant one. Ideally, the

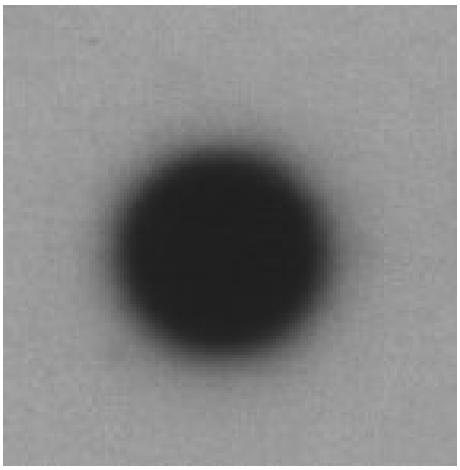

(a) Macroarray dot.

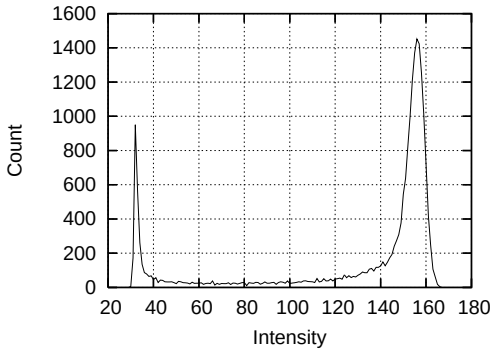

(b) Histogram of 1(a).

Figure 1: Two-dominant intensities image.

decrease should be measured having, as first ending level, the level where we find the depression between the two peaks, but, if that could easily be found, there wouldn't be needed to proceed, because that is what we are trying to find. For that reason, the mean intensity level of the image was used as the first ending level.

Clearly, if the mean is above the point where the variance starts to decrease, which happens if the least dominant class (peak) has very little representation in contrast with the dominant class, the method will not work, even if there is an important contrast between classes. Nevertheless, for images where the mean was below the point of decrease on variation, this solution finds a fairly good threshold level. So, the variance was measured, starting from the first intensity level until the mean intensity, towards the dominant peak, comparing the result of each step with the previous one.

Knowing that an image is a 2D grayscale intensity function with N pixels with graylevels from 1 to L and the number of pixels of graylevel i is denoted by f_i, we can define the mean until level l as:

$$\mu_l = \sum_{i=0}^{l} \frac{i \times f_i}{\sum_{i=0}^{l} f_i}; \tag{1}$$

and the variance until level l as:

$$\sigma_l^2 = \frac{1}{\sum_{i=0}^{l} f_i} \sum_{i=0}^{l} f_i \times (i - \mu_l)^2. \tag{2}$$

Assuming that the dominant peak is on the right side of the histogram (as in image 1(b)), the level l where σ_l^2 will decrease relatively to σ_{l-1}^2, can be defined as the first occurrence of:

$$l^* = \{l \mid \sigma_l^2 < \sigma_{(l-1)}^2 \wedge \mu_L \leq l < L\}; \tag{3}$$

then, the threshold level T, would be:

$$T = l^* - \sqrt{\sigma_L^2}. \tag{4}$$

where $\sqrt{\sigma_L^2}$ is the standard deviation of the whole image.

As an example, take the case of the image I in figure 1(a). The mean intensity of I is $\mu_L = 130$ and the standard deviation is $\sigma_L = 43$, with $L = 256$. Calculating the variances σ_l^2 with l being the ending levels for calculation of the variance and $\mu_L \leq l < L$, all the variances will rise until the gray level is 153 (see fig. 2), where $\sigma_{154}^2 < \sigma_{153}^2$. Consequently, $l^* = 154$, and the estimated threshold level is calculated by subtracting the standard deviation of the image from l^*. In this way, we get a threshold value of $T = 111$ (see fig. 3). Applying the well known Otsu (Otsu, 1979) thresholding method, the achieved threshold level was of 100. Taking in consideration that in many circumstances an acceptable threshold level for this image could be between the intensities 40 and 140, 111 is a good threshold level. For the specific case, any threshold level between 60 and 120, would be a very good threshold level. When manually thresholding the same image, the optimum threshold was found as 76. With $T = 76$, the diffuse area that separates background and foreground was almost completely eliminated.

As can be seen on figure 2, the variance decreases when the selected part of the histogram starts to grow more in height than in spread, meaning that all the intensity values until l^* or higher will be closer to the mean. On a histogram with both intensity classes equally expressed, the growth of any of the existing intensities will decrease the variance. Observing figure 2, it can be stated that the variance decreases after the histogram is more or less balanced between

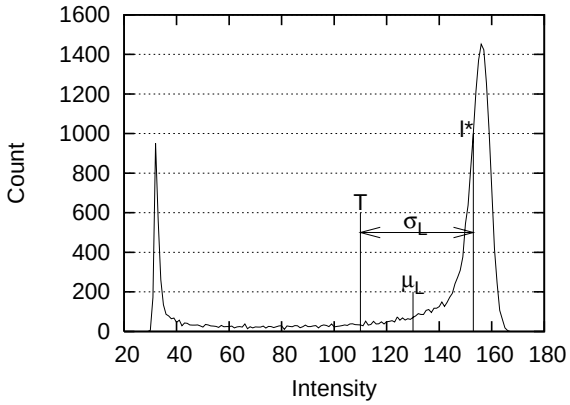

Figure 2: Calculation of T.

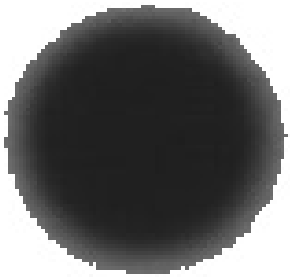

Figure 3: Image 1(a) thresholded with T=110.

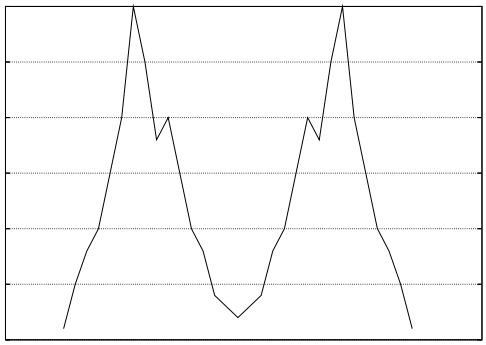

(a) Balanced Histogram.

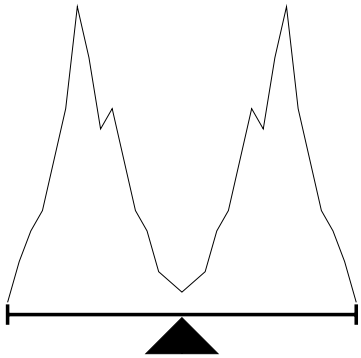

(b) Histogram over a lever.

Figure 4: Perfectly balanced histogram.

the first intensity level and level l^*. Also, considering a histogram with only two intensities, the maximum variance will be reached when both intensities are equally expressed. Any increase or decrease to any of the intensities of the histogram, will result in the decrement of the variance, because one of the intensities will be dominant.

As stated before, the previous approach would need images with very specific characteristics and, that is not allways possible. Although this was not a good technique for image thresholding it gave us some ideas on how to find a good thresholding level, as explained on the next section.

3 WEIGHTING A HISTOGRAM

If a perfect balanced histogram, i.e. a histogram that has the same distribution of background and foreground, could be placed over a lever, it wouldn't fall for any side (see fig. 4). Also, notice that the optimum threshold level would be right in the centre of the lever.

Looking at figure 5, which represents an unbalanced histogram, it can be observed that the lever falls to the side where the histogram is heavier. The idea is to try to balance the unbalanced histogram. Once again, there is the assumption that the image has two dominant classes (peaks), one representing the foreground and the other representing the background. In this case, there is no need of one being highly dominant over the other. So, how can an unbalanced histogram be balanced? The proposed way of doing it is to figuratively put the unbalanced histogram over a lever, as in figure 5, and then start to remove the excess weight from the heavier side. The next step is to adjust the base triangle to the new middle position.

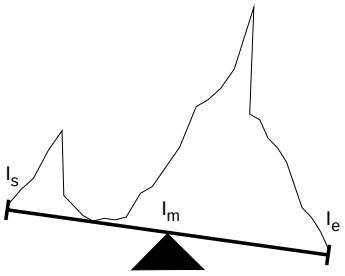

Figure 5: Unbalanced Histogram.

Let I_s (Intensity Start) be the first graylevel intensity occurrence and I_e (Intensity End) the last. Now the position of the base triangle can be defined as:

$$I_m = \frac{I_s + I_e}{2}. \tag{5}$$

Remembering that an image is a 2D grayscale intensity function with N pixels with graylevels from 1 to L and the number of pixels of graylevel i denoted by f_i, we can define the weights of the left and right sides as:

$$W_l = \sum_{i=I_s}^{I_m} f_i \tag{6}$$

and

$$W_r = \sum_{i=I_{m+1}}^{I_e} f_i \tag{7}$$

so that initially $W_l + W_r = N$, we can define the following algorithm:

Algorithm
3.1: GET-THRESHOLD(f, I_s, I_e)

$I_m \leftarrow \frac{I_s+I_e}{2}$
$W_l \leftarrow \sum_{i=I_s}^{I_m} f_i$
$W_r \leftarrow \sum_{i=I_{m+1}}^{I_e} f_i$
while $W_r > W_l$
do { $W_r \leftarrow W_r - f_{I_e}$; $I_e \leftarrow I_{e-1}$; **if** $\frac{I_s+I_e}{2} < I_m$ **then** { $W_l \leftarrow W_l - f_{I_m}$; $W_r \leftarrow W_r + f_{I_m}$; $I_m \leftarrow I_m - 1$ }
return (I_m)

The same algorithm will apply when the dominant peak is on the left side, only mirrored. Another solution is to invert the histogram and apply the algorithm the same way. But for now, it will be assumed that the most dominant peak (heaviest) is at the right side of the least dominant one. What happens in this algorithm is that after determining I_s and I_e, I_m, the position of the base triangle is calculated (see eq. 5). After that, two classes are created, W_l with all the intensities at the left of I_m (see eq. 6) and W_r with all the intensities at the right of I_m (see eq. 7). Now, while the heaviest class (W_r in this case) weights more than the lightest, columns are subtracted from the heaviest peak, starting at the outer side of it. Then, if there is a need to adjust the position of the base triangle, moving it to the left, both classes are adjusted accordingly, W_l loosing one bar to W_r. The result of applying the algorithm on the histogram represented by figure 5 can be seen on figure 6(a).

At the end, I_m is the position which is in between the two peaks that may work as a threshold level. Another estimate for the threshold can be the lowest value between the highest peak at the left of I_m and the highest peak at the right of I_m or, by other words, the lowest value between the two peaks. That in not very hard to find now that we have I_m. There is another approach that generally seams to produce better results. That approach consists of drawing a horizontal line over the top of the lowest of the two dominant peaks and determine its intersection with the highest peak. Then the middle distance between the top of the lowest dominant peak and that intersection, can be used as a threshold, as demonstrated by figure 6(b).

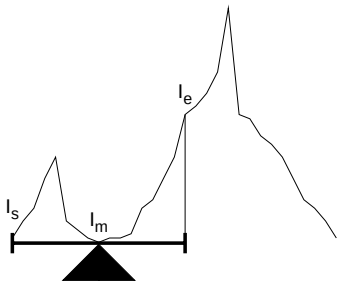

(a) Threshold is I_m.

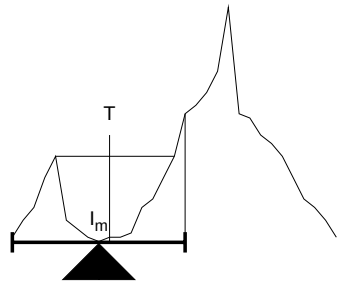

(b) Threshold is T.

Figure 6: Processed Histogram.

If the image is noisy, the histogram may have some intensities represented with very low frequency and usually they will be noticed in the histogram as tails before the first peak and after the last one. In this case, using the approach presented by algorithm 3.1 to find a threshold level may fail. For example, if the least dominant peak has a big tail (see fig. 7), I_s will be placed very far away from the representative

area of the least dominant peak, moving I_m closer to the least dominant peak. The approach represented on figure 6(b) can correct this problem only if the resulting I_m is still between the two peaks. In the case that it's the most dominant peak that has the big tail, that may cause the side that should be the lighter one, to be the heavier, not allowing to find the right thresholding level. In order to solve this problem, there have been found two main approaches. One consists of passing a parameter to the algorithm that will work as the least quantity that will be representative and, thus, accounted for the calculation of I_s and I_e. The other approach consists of performing a mean smoothing of the image. This may eliminate all the intensities that have almost no representativity.

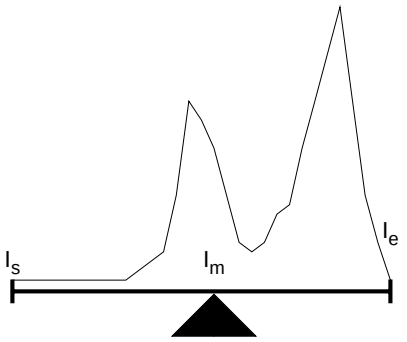

Figure 7: Big tail at the left of least dominant peak.

4 PROPOSED METHOD

The method presented in the previous section (see alg. 3.1) has a caveat that makes it unreliable in some cases. This algorithm will tend to approach I_m to the lowest peak, proportionally to the degree of growing and height of the highest peak. That happens, of course, because each bar of the highest peak will correspond to more than one of the lowest peak bars. This may be a minor problem if the contrast is very high, but will be noticed in low contrast images with one of the peaks much higher than the other and with high accentuation of growth. To solve this problem it was applied the same reasoning presented in section 3. For example, if the right side of the histogram is the heavier, we will remove bars from the right side of the histogram. The stop condition for algorithm 3.1 is when the right side gets lighter then the left side. At this point, the histogram will have its left side heavier than the right side and, thus, it's unbalanced. Applying the same algorithm (mirrored) to the histogram, the right side will become the heaviest side again, and so on. The result is that I_s and I_e will get closer until they are equal to I_m. This approach is represented by algorithm 4.1.

Algorithm
4.1: GET-THRESHOLD-FINAL(f, I_s, I_e)

$I_m \leftarrow \frac{I_s+I_e}{2}$
$W_l \leftarrow \sum_{i=I_s}^{I_m} f_i$
$W_r \leftarrow \sum_{i=I_{m+1}}^{I_e} f_i$
while $I_s \neq I_e$
do
- **if** $W_r > W_l$
  - **then**
    - $W_r \leftarrow W_r - f_{I_e}$
    - $I_e \leftarrow I_{e-1}$
    - **if** $\frac{I_s+I_e}{2} < I_m$
      - **then**
        - $W_l \leftarrow W_l - f_{I_m}$
        - $W_r \leftarrow W_r + f_{I_m}$
        - $I_m \leftarrow I_{m-1}$
- **else if** $W_l \geq W_r$
  - **then**
    - $W_l \leftarrow W_l + f_{I_s}$
    - $I_s \leftarrow I_{s+1}$
    - **if** $\frac{I_s+I_e}{2} > I_m$
      - **then**
        - $W_l \leftarrow W_l + f_{I_m+1}$
        - $W_r \leftarrow W_r - f_{I_m+1}$
        - $I_m \leftarrow I_{m+1}$

return (I_m)

In this way I_m will tend to move to the lowest area of the depression in the histogram. With this approach it won't matter how fast the highest peak grows because I_m will be centred, once again, if I_m's initial position is located in between the two peaks. There is still the concern of the big tails in the histogram, if I_m's initial position is outside of the depression in the histogram.

As a final matter, there is the situation when there is very low contrast between background and foreground. In this case we only have a peak. This will result on a all or nothing threshold, because the histogram will allways be heavier from the same side. I_s will still get to be equal to I_e, but the threshold level may not be correct. When the histogram has two peaks, bars will be removed from both sides of the histogram, so, the solution that was found to this problem was to place a flag in each of the places where bars removal occurs. This way we know if it's a one or two peaks histogram or if it's a one peak histogram only. In the case of a one peak histogram, a good approximation for the threshold level may be the mean of the original histogram minus some constant or some percentage.

5 RESULTS

For test and comparison of the presented method, there were used scanned radioactive images of gene macro arrays. Due to the existence of gradient in the global image, obviously there could not be used an optimum global threshold level, so the image was split in to tiles of spot images (see fig. 8).

Table1, presents the result of applying this algorithm to those images and compares it to the result of applying various reference methods. Results are presented in the following order: Manual threshold, Otsu's, IsoData, Maximum Entropy, Mixture Modelling and the proposed method's threshold levels. For the IsoData, Maximum Entropy and Mixture Modelling threshold methods, it was used ImageJ's (Rasband, 2006) implementation.

Table 1: Results of the various thresholding methods.

Spot	*Man*	*Otsu*	*Iso*	*Max*	*Mix*	*Pro*
1	66	80	78	101	113	69
2	60	68	66	89	12	50
3	59	66	64	85	13	55
4	58	83	81	101	118	67
5	80	90	88	107	118	77
6	55	68	66	89	12	54
7	92	92	90	105	116	84
8	57	69	67	94	104	50
9	60	73	71	96	111	59
10	65	78	77	96	112	72

As can be seen in table 1, the proposed method is the one that, generally, finds lower values for thresholding. As the spot starts to blend with the foreground (the diffuse area) there will be the depression in the histogram. That diffuse area increases in intensity level and in quantity of pixels as it goes from the spot to the foreground. It is normal, then, that the proposed method will find the lower threshold levels because, as stated before, I_m will tend to move to the lowest area of the depression of the histogram. Figure 8 is shown just to present an idea of the criteria that was used in the manual threshold calculation (the ground truths).

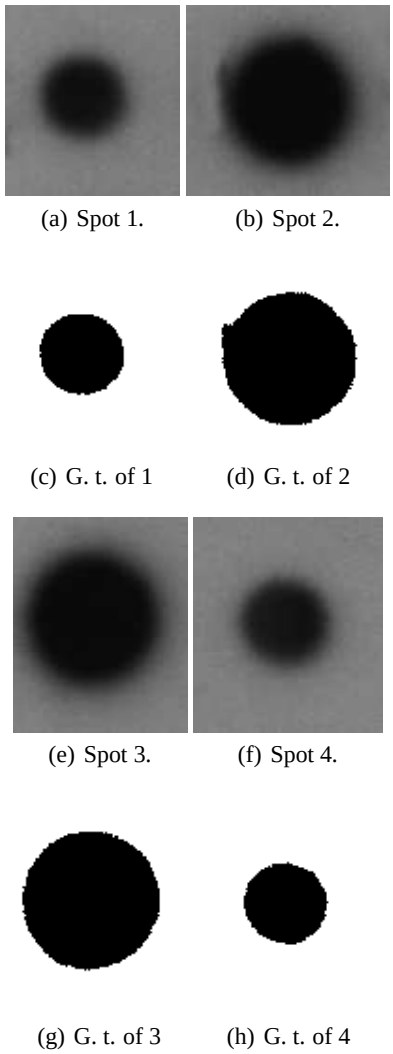

(a) Spot 1. (b) Spot 2.

(c) G. t. of 1 (d) G. t. of 2

(e) Spot 3. (f) Spot 4.

(g) G. t. of 3 (h) G. t. of 4

Figure 8: First four of the tested sample images and their ground truths.

6 CONCLUSIONS

This is a very fast method that works very well on images that have a fair amount of background and foreground representation, and with a reasonable contrast between both, as is the case of scanned radioactive images of macroarrays. It is a good approach when the objective is to find the spot without the diffuse area. If the diffuse area is to be included, Otsu or Isodata may be better. The presented method is already being used on a bioinformatics software (Anjos and Ascenso, 2007) for analysis of gene expression data of macroarray images.

REFERENCES

Anjos, A., S. H. and Ascenso, R. (2007). Maq - a bioinformatics tool for macroarray analysis. *(Internal Report - ILAB - UAlg)*.

Diachenko, L., e. a. (1996). Suppression subtractive hybridization: A method for generating differentially

regulated or tissue-specific cdna probes and libraries. *Proc. Natl. Acad. Sci. USA*, 93(12):6025–6030.

Dowsey, Andrew, D. M. and Yang, G.-Z. (2003). The role of bioinformatics in two-dimensional gel electrophoresis. *Proteomics*, 3(8):1567–1596.

Kamel, M. and Zhao, A. (1993). Extraction of binary character/graphics images from grayscale document images. *Graphical Model and Image Processing*, 55(3):203–217.

Kilian, J. (2001). Simple image analysis by moments. *OpenCV library documentation*.

Otsu, N. (1979). A threshold selection method from gray-level histograms. *IEEE Trans. Systems Man Cybernet*, 9:62–69.

Rasband, W. (1997-2006). Imagej. *U. S. National Institutes of Health, Bethesda, Maryland, USA*, page http://rsb.info.nih.gov/ij/.

Sezgin, M. and Sankur, B. (2004). Survey over image thresholding techniques and quantitative performance evaluation. *Journal of Electronic Imaging*, 13:146–165.

Sezgin, M. and Tasaltin, R. (2000). A new dichotomisation technique to multilevel thresholding devoted to inspection applications. *Pattern Recognition Letters*, 21:151–161.

Zhang, M. (1999). Large-scale gene expression data analysis: a new challenge to computational biologists. *Genome Research*, 9:681–688.

ACOUSTIC INDICES OF CARDIAC FUNCTIONALITY

Guy Amit[1], Jonathan Lessick[2,3]
[1]*School of Computer Science, Tel-AvivUniversity, Tel-Aviv, Israel*
[2]*Department of Cardiology, Rambam Medical Center, Haifa, Israel*
gamit@tau.ac.il, j_lessick@rambam.health.gov.il

Noam Gavriely[3], Nathan Intrator[1]
[3]*Rappaport Faculty of Medicine, Technion-Israel Institute of Technology, Haifa, Israel*
gavriely@tx.technion.ac.il, nin@tau.ac.il

Keywords: Heart sounds, time-frequency analysis, feature extraction, cardiac functionality.

Abstract: The mechanical processes of the cardiac cycle generate vibratory and acoustic signals that are received on the chest wall. We describe signal processing and feature extraction methods utilizing these signals for continuous non-invasive monitoring of cardiac systolic function. Vibro-acoustic heart signals were acquired from eleven subjects during a routine pharmacological stress echocardiography test. Principal component analysis, applied to the joint time-frequency distribution of the first heart sound (S1), revealed a pattern of an increase in the spectral energy and the frequency bandwidth of the signal associated with the increase of cardiac contractility during the stress test. Novel acoustic indices of S1 that compactly describe this pattern showed good linear correlation with reference indices of systolic functionality estimated by strain-echocardiography. The acoustic indices may therefore be used to improve monitoring and diagnosis of cardiac systolic dysfunctions.

1 INTRODUCTION

The human heart is a mechanical system whose primary function is to pump blood throughout the body in order to provide adequate perfusion of organs. This function is achieved by a complex interplay between the cardiac muscle, the vascular system and the blood, highly regulated by mechanical and neural control mechanisms. Cardiovascular diseases, such as coronary artery disease, hypertension and cardiomyopathy, may impair the mechanical functionality of the heart, leading to the clinical syndrome of heart failure (HF). As these diseases are major public health problems worldwide, technologies for improving early diagnosis and patient monitoring are essential.

The low-frequency vibratory and acoustic signals, produced by the mechanical processes of the cardiac cycle and received on the chest wall, provide a direct and simple way for assessing the mechanical functionality of the cardiovascular system (Tavel, 1978). However, the utilization of these signals in the clinical setting has been mostly limited to qualitative assessment by manual methods, as research and development efforts in recent years focused on modern imaging technologies such as echocardiography and cardiac computerized tomography. These valuable techniques require complex equipment, as well as expert operators and interpreters. In particular, these imaging tools can not be used continuously or outside of the hospital environment. Consequently, long-term non-invasive monitoring of mechanical functionality remains unavailable in the common medical practice.

In this work, we revisit the problem of quantitative analysis of mechanical vibro-acoustic heart signals using modern signal processing tools. In an earlier study, we have shown the feasibility of using vibro-acoustic signals to extract temporal information about the phases of the cardiac cycle (Amit, 2005). In the current study, we address the potential of continuously assessing the global systolic functionality of the left ventricle using indices extracted from the first heart sound, S1. According to Rushmer's theory of the origin of heart sounds, S1 is generated by the vibrations of the entire cardiohemic system, as a result of blood acceleration and deceleration following the onset of ventricular contraction and the closure of the

atrioventricular valves (Rushmer, 1978). The amplitude of S1 has been previously shown to be related to the pressure gradient (dP/dt) developing in the left ventricle during isovolumetric contraction (Sakamoto, 1965). A good correlation was also reported between dP/dt and the instantaneous frequency of S1 (Chen, 1997). While these previous studies were performed on anesthetized dogs, the relation between the characteristics of S1 and global left-ventricular systolic functionality has not been studied in humans in routine clinical settings.

We study the relationship between acoustic indices, extracted from the time-frequency energy distribution of S1, and reference echocardiographic indices that are related to left-ventricular systolic functionality. To achieve dynamic, yet controllable, hemodynamic conditions, we used clinical settings of a routine echocardiography pharmacological stress test. In the following sections, we describe the signal processing and feature extraction methods applied to the vibro-acoustic heart signal, introduce novel acoustic indices of systolic functionality and present quantitative results on the correlation between these indices and echocardiography-derived measures. We conclude by discussing the potential applicability of our methods for continuous non-invasive monitoring of cardiac systolic function.

2 METHODS

2.1 Patients and Protocol

The study was approved by the local ethics committee for medical research. Data was acquired from eleven male subjects of ages 36-79 (mean 60±14), referred to a routine Dobutamine stress echo test (DSE) for assessment of ischemic heart disease. The referral indications included positive ergometry stress test, atypical chest pain and chest pain during physical activity. Two of the subjects had a history of coronary artery disease. These two subjects were diagnosed as positive for myocardial ischemia in the DSE test. The remaining nine patients were diagnosed as negative for ischemic heart disease. Prior to data recording, the patients signed an informed consent form. The standard DSE protocol consisted of four 3-minute stages of increasing Dobutamine dosage, from 10 to 40μg/kg/min. If the target heart rate, defined as 0.85 * (220 – Age), was not achieved at the end of the final stage, 0·25 mg boluses of atropine were given at 1-min intervals, up to a maximum of 1 mg.

2.2 Data Acquisition

Vibro-acoustic heart signals were recorded using a digital data acquisition system constructed in our lab. The system consisted of 4 piezoelectric contact transducers (PPG Sensor Model 3, OHK Medical Devices, Haifa, Israel), an ECG sensor (EKG-BTA, Vernier Software & Technology, Beaverton, OR), a preamplifier with high input impedance and a linear frequency range of 1Hz – 4KHz (A.S. ZLIL, Bnei-Brak, Israel), a 16-bit analog-to-digital converter (PMD-1608FS, Measurement Computing Corp., Norton, MA), and a designated signal recording software running on a portable personal computer.

The transducers were placed at the apex area, the aortic and pulmonary areas (second intercostal space, right and left sternal border, respectively) and at the right carotid artery, and were firmly attached using either elastic straps or adhesive bands. The patients were lying on their left side. Vibro-acoustic and ECG signals were continuously recorded during the stress test (30-45 minutes long) at a sample rate of 4KHz. Echocardiography images were acquired using a GE Vivid 7 ultrasound machine (General Electric Healthcare, Wauwatosa, WI). Two-dimensional echo cine loops of a single heart beat were captured before the beginning of the stress test (baseline), during each stage of the test and following the test (recovery), from three apical views (4-chamber, 2-chamber and apical long axis) at a high frame rate of 70-100 FPS.

2.3 Echo Data Processing

The captured echo cine loops were post-processed using EchoPAC Dimension ’06 software (GE Healthcare Wauwatosa, WI) in order to extract quantitative echocardiographic indices of systolic functionality. The indices used were peak systolic velocity (PSV) and peak systolic strain rate (PSSR), shown to be strongly correlated with left-ventricular systolic functionality (Greenberg, 2002). These indices were first calculated separately for each cardiac wall (septal, lateral, inferior, anterior, posterior, and anteroseptal) and for three segments per wall (basal, middle and apical), and then averaged to obtain a global functionality index. Index calculation was done using 2D strain analysis, based on speckle tracking technique. This modality allows objective analysis of the entire myocardial motion throughout the heart cycle by tracking natural acoustic markers in the image. It was shown to provide accurate strain measurements, compared with tagged MRI (Amundsen, 2006). Strain indices

were successfully calculated for 10 patients. One patient was excluded due to inadequate quality of the captured echo images.

2.4 Acoustic Signal Processing

Each of the four recorded signal channels was first pre-processed by a applying a digital band-pass filter in the frequency range of 20-250Hz (Figure 1a). The signal was then partitioned into cardiac cycles using the peaks of the ECG-QRS complexes as reference points (Figure 1b). Signal segments with noisy ECG were excluded from the analysis. The signal cycles were aligned by their starting points and their amplitudes were color-coded to create a two-dimensional signal map, showing the time-domain dynamics of the first and second heart sounds throughout the stress test (Figure 1c). Fast Fourier transform (FFT) was applied to each cycle of the first heart sound (S1), defined as the cycle segment from 50ms before the QRS peak to 200ms after the QRS peak. The logarithm of the power spectrums was color-coded to generate a spectral map of S1 throughout the recording (Figure 1d).

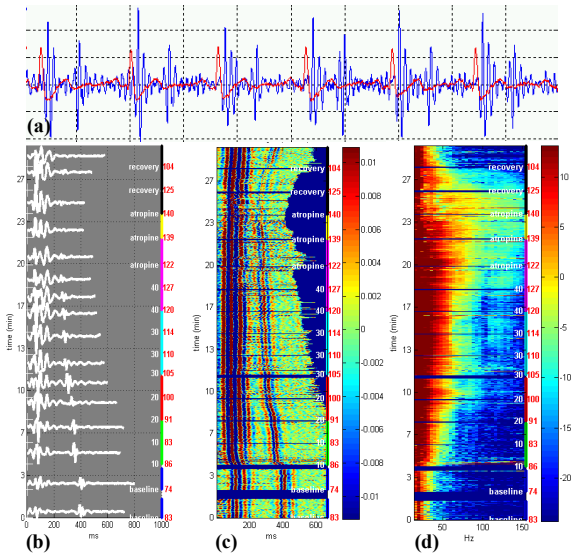

Figure 1: Generation of time-domain and frequency-domain signal maps in a healthy subject: (a) the heart sound signal (blue), segmented using the ECG (red). (b) aligned multiple sound signal cycles throughout the test (left y-axis), with heart rate (red labels) and test staged (white labels and colored segments), (c) continuous color-coded map of segmented sound signals (d) continuous color-coded power spectrum of the first heart sound (S1).

In order to characterize the joint time-frequency energy distribution of S1, S-transform was applied to each cycle of S1. S-transform (Stockwell, 1996) is a linear transform that provides frequency-dependent resolution, while maintaining a direct relationship with the Fourier spectrum. It is defined by:

$$S(\tau, f) = \int_{\Re} s(t) \frac{|f|}{\sqrt{2\pi}} e^{-\frac{(\tau - t)^2 f^2}{2}} e^{-i2\pi f t} dt$$

Where *s(t)* is the original signal, τ is the time delay and *f* is the frequency. The progressive resolution of the transform provides a time-frequency resolution superior to Fourier-based techniques, while its linearity ensures accurate decomposition without artifactual cross-terms that are typical to quadratic transforms. S-transform is therefore suitable for analysis of non-stationary multi-component signals such as heart sounds.

After applying S-transform to each cycle of S1, the resulting time-frequency representations were grouped by the stages of the stress test and averaged to produce a small number of representative time-frequency maps (Figure 2).

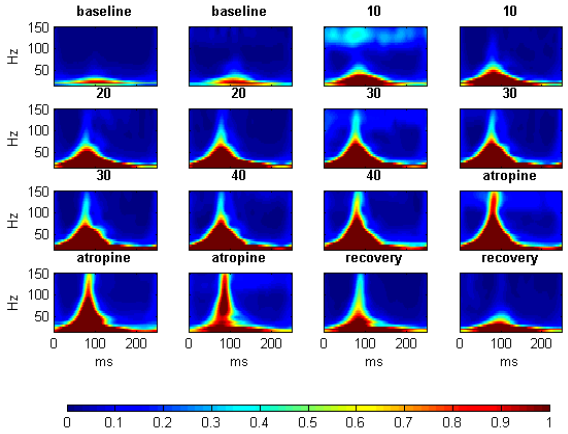

Figure 2: S-transform time-frequency representation of S1 acoustic signal obtained in a representative healthy subject during the stages of the stress test. Each plot represents an average of the S-transform of all S1 cycles over a specified period of the test.

2.5 Acoustic Feature Extraction

The purpose of feature extraction is to find a compact representation of high dimensional data, without significant loss of information content. Principal component analysis (PCA) is a well-known statistical technique for dimensionality reduction (Duda, 1973). The principle of PCA is to project the data on a new orthogonal basis, such that the variances of the linearly transformed data are sorted in descending order along the coordinates, with the maximal variance on the first coordinate

(first principle component), the second largest variance on the second coordinate, and so on. The projection of the original data on the first few principal components provides a low-dimensional representation of the data, which emphasizes the significant features (in terms of statistical variability) in the data. The choice of the significant principal components is done by examining their associated eigenvalues.

PCA was applied on the aggregation of segmented S1 signals. The analysis was performed on both the frequency domain spectral maps (Figure 1d) and on the time-frequency representations produced by the S-transform (Figure 2), vectorized by concatenating adjacent columns. The most significant principal components, having eigenvalues greater than 10% of the first eigenvalue, were selected and weighted by their relative eigenvalues. The projection of the data on this weighted combination of the significant principal components was chosen as a one-dimensional feature representing the dynamic characteristics of the acoustic signal during the stress test. To obtain an interpretable trend line, this feature was normalized by the median value of the baseline stage and smoothed by a moving average filter. The resulting index, denoted acoustic variability index (AVI) is interpreted as the trend of relative change in the spectral energy distribution of S1.

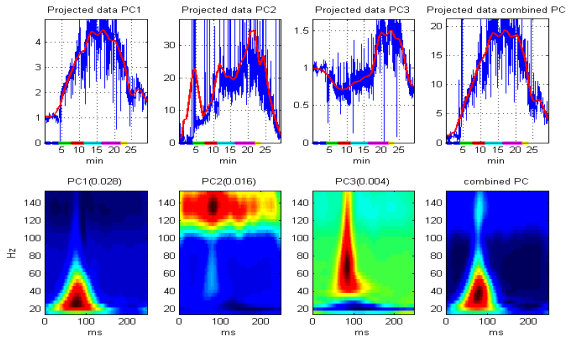

Figure 3: Principal component analysis applied to the vectroized time-frequency representation of S1 cycles during a stress test. The bottom plots show the coefficients of the first 3 principal components (PC), and their linear combination, weighted by the eigenvalues (shown in parenthesis). The upper plots show the AVI index during the entire stress test, obtained by projecting the data on the respective PC. The red lines are the result of smoothing the projected data with a moving-average filter.

Figure 3 illustrates an example of applying PCA to the time-frequency data shown in Figure 2, and calculating the time-frequency AVI.

A second feature extracted from the spectrum of each cycle of S1 was the frequency bandwidth of the signal, defined by the highest frequency with significant energy content. Prior to calculating this feature, signal cycles with a high wide-band energy content, compared to their local environment, were classified as noise and excluded from further processing. The bandwidth feature was calculated for each cycle by searching the spectrum for the first frequency whose energy is at least 10dB below the maximal energy. The feature trend line obtained from all cycles was normalized by the median value of the baseline stage, and denoted Acosutic Spectral Index (ASI).

3 RESULTS

The color-coded signal map in figure 1c illustrates the time-domain characteristics of the heart sound signal during the stress test. As expected, there are noticeable changes in the duration of ventricular systole and diastole, as the heart rate increases in exercise and decreases in recovery. However, there are no apparent morphological changes in the signal that can be associated with the stress response. Fourier analysis uncovers a pattern of an ascent in the spectral energy of the first heart sound as the Dobutamine dose is increased, and a descent back to baseline levels during recovery figure 1d. In addition to the overall energy rise, there is also an increase in the frequency bandwidth of S1, as higher frequency components in the range of 50-150Hz emerge and strengthen. The time-frequency representation, obtained by S-transform, enables localization of these spectral changes in time (Figure 2): the high-frequency components are centered about 80ms after the beginning of the signal (30ms after the peak of ECG-QRS complex), growing up to 150Hz in the highest Dobutamine dose, then falling back to the baseline upper-limit frequency of 50Hz in the recovery phase. There is no apparent time shift of the signal's energy distribution throughout the test.

Principal component analysis, applied to the spectral maps of S1, was able to identify the major frequency bands that contribute to the data variability. When applied to the vectorized time-frequency distributions, PCA also pointed out the temporal location of these frequency bands. Figure 3 shows a representative example of the coefficients of the first three principal components (PC), and the projection of the time-frequency data on these principal components. The first PC, representing the axis with the largest data variability, captures the

pattern already observed qualitatively in the time-frequency distributions in Figure 2: it varies from 30ms to 120ms relative to the beginning of the cycle, and from frequency of 20Hz to 70Hz, thus showing the strengthening of the signal's low-frequency components. The second PC captures the variability of the high frequency components between 110 to 150Hz for the entire duration of the S1 signal. The third PC shows a wide-band variability of frequency ranging from 40Hz to 150Hz, localized in time around 80ms from the beginning of the cycle. This component strengthens during the peak stress response. A combination of the most significant principal components, weighted by their eigenvalues, and the projection of the data on this combined PC provide a one-dimensional feature, denoted time-frequency acoustic variability index (TF-AVI), which summarizes the dynamics of the joint time-frequency energy distribution of S1 throughout the stress test.

The TF-AVI trend lines, extracted separately from each of the four transducers in two representative subjects are plotted in Figure 4, along with the stages of the stress test, the heart rate and blood pressure trends and the relative change in the echocardiographic indices of peak systolic velocity (PSV) and peak systolic strain rate (PSSR). While the TF-AVI provides a continuous line with one point per cardiac cycle, the reference echocardiographic indices are available only at discrete time points of each stage in the stress test. Nevertheless, there is a noticeable correlation between the two indices: for the plot in Figure 4a (subject #5), the correlation coefficients between the echo indices PSV and PSSR and the corresponding TF-AVI, averaged over all transducers were 0.91 and 0.89 respectively. For the plot in Figure 4b (subject #6) the correlation coefficients were 0.97 and 0.83 ($p < 0.05$ in all cases).

Both paired and unpaired t-test showed that the absolute values of the acoustic spectral index (ASI) at the end of low-dose Dobutamine induction were significantly higher than the baseline values ($p<0.04$ for the 10ug stage, $p<0.003$ for the 20ug stage, Figure 5). The correspondence between the ASI and the echocardiographic indices in all of the subjects was tested by comparing the values of the relative index change at the end of the low-dose Dobutamine stages. These points were selected since the inotropic effect is more prominent at the early stages of the test. In addition, the higher heart rates at later stages of the test reduce the reliability of the tissue tracking procedure used to extract the reference echocardiographic indices. As shown in Figure 6, a good linear correlation ($r=0.78$, $p<0.01$) was observed between ASI calculated from the apex signal and the relative PSSR at the end of the 20ug stage. At the end of the 10ug stage the correlation coefficient between the two indices was 0.68 ($p< 0.03$).

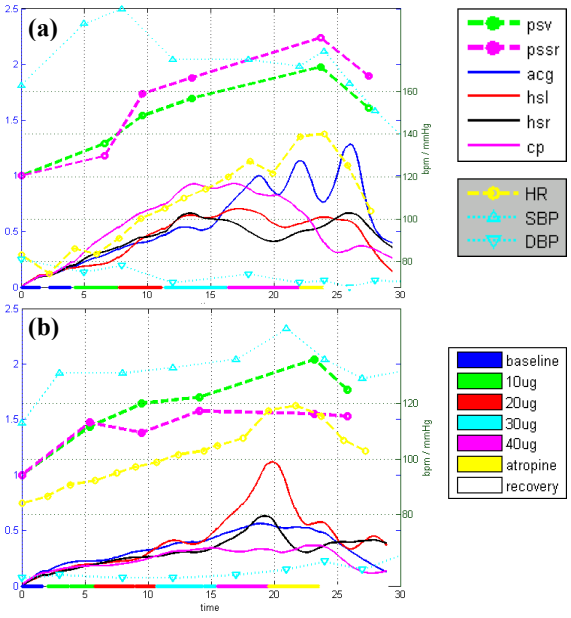

Figure 4: TF-AVI indices of subjects #5 (a) and #6 (b). Each plot displays the trend lines of TF-AVI from the transducers at the apex (acg), aortic area (hsr) pulmonary area (hsl) and carotid artery (cp), along with the relative echo indices PSV and PSSR, trend lines of heart rate and blood pressure, and color-coded stages of the stress test. See text for details.

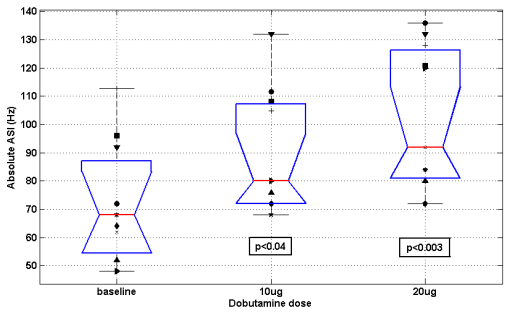

Figure 5: Absolute ASI values of all subjects at baseline and after low-dose Dobutamine induction (10 and 20 ug/kg/min). The box plot displays the median, lower quartile, upper quartile and data extent. Each marker symbol represents a different subject. The p-values represent a t-test comparison to the baseline values.

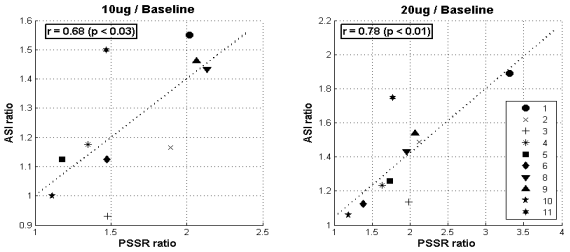

Figure 6: The correlation and regression line between relative PSSR index and relative ASI at the end of first (10ug) and second (20ug) low-dose Dobutamine induction. Each marker symbol represents a different subject.

4 DISCUSSION

More than 40 years ago, Sakamoto et al. reported a nearly linear relationship between the amplitude of the first heart sound, S1, and the maximum of the time derivative of the left ventricular systolic pressure (dP/dt) in dogs (Sakamoto, 1965). Later it was shown that myocardial infarction in humans caused a shift of the maximum energy of S1 to a lower frequency range (Adolph, 1970), and that a reduction in the spectral energy of S1 correlated well with the presence of significant coronary artery disease (Clarke, 1978). More recently, Chen et al. showed a good cross-correlation between the instantaneous frequency of S1 and dP/dt of dogs in various contractile states (Chen, 1997). They suggested that the resonant frequency of S1 is proportional to the fractional power of the tension of the left-ventricular myocardium during contraction, which relates to the left ventricular pressure gradient by Laplaces's law. The results of the current study are in agreement with these previous studies regarding the relation between the amplitude and frequency spectrum of the first heart sound and the dynamics of left ventricular contraction. The acoustic indices developed in the current study exhibited a marked correlation with the pattern of inotropic and chronotropic changes throughout the Dobutamine stress test. The increase in the spectral energy, along with the emergence of higher frequency components was consistently observed in multiple recording locations in all of the subjects. Although the study was conducted on a small group of subjects, statistically significant differences were observed across-subjects between baseline and low-dose Dobutamine stages, confirming the reliability of the results. The good correlation obtained with the reference strain echocardiography indices suggests that the acoustic indices truly characterize the variations in the myocardial systolic functionality. The relationship between the cardiovascular physiological processes and their acoustic manifestation on the chest wall is complex and most probably non-linear. This relationship is affected by neurohormonal modulation of the heart's inotropic and chronotropic states, as well as by changes in the properties of the thoracic cavity conducting the acoustic vibrations. Nevertheless, this work provides a framework and a set of computational tools for robust quantitative analysis of vibro-acoustic heart signals that can be utilized for non-invasive, continuous monitoring of cardiac functionality.

The capability of this framework to diagnose a pathologic functionality reduction could not be addressed quantitatively in this work, due to the small number of subjects and the fact that the great majority of the subjects had normal cardiac functionality. Interestingly, the single subject that was diagnosed in the echocardiography examination with a reduced segmental wall motion during stress, due to myocardial ischemia (subject #10) had the lowest values of absolute and relative ASI, as well as the lowest values of PSSR, indicating that the compromised wall motion might result in a frequency reduction of the first heart sound.

The usage of strain-echocardiography indices for evaluation of left-ventricular function is still not a part of the common clinical practice. Nevertheless, there are strong research evidences for the relation between peak strain rate and the invasive contractility measure of peak elastance (Greenberg, 2002), and for the ability of global strain indices to detect left-ventricular systolic dysfunction. (Reisner, 2004). Strain echocardiography was therefore used in this research as a quantitative 'gold-standard' reference, which can be obtained non-invasively during the routine protocol of the stress test.

One of the major challenges of extracting meaningful physiological information from signals acquired in routine clinical settings is noise robustness. The data used in this work was contaminated with various types of noise, including body movements, interferences of the ultrasonic transducer and audible sounds. The signal analysis methods used in this work were specifically designed to cope with these types of noise. In particular, the statistical approach of transforming the data to a new orthogonal basis of the principal components was able to accentuate physiologically meaningful patterns, while diminishing noisy-related components.

5 CONCLUSIONS

We have described a signal analysis framework for robust extraction of systolic functionality indices from acoustic heart signals. The developed tools were constructed and tested on data from a pharmacological stress test, with strain echocardiography as the gold standard reference. Using principal component analysis on the time-frequency representation of the first heart sound we have characterized the pattern of spectral changes occurring during the stress test, and associated this pattern to the alternations in systolic functionality by showing it is linearly correlated to echocardiography derived indices of cardiac contractility. Our analysis framework and proposed indices can be applied to real-time continuous monitoring of cardiac functionality, thus enabling improved diagnosis and management of cardiac dysfunction.

ACKNOWLEDGEMENTS

We would like to express our gratitude to the team of the Echocardiography lab at the Rambam medical center, for their kind assistance in data collection.

We would like to thank Dr. Zvi Friedman and Dr. Peter Lysyansky from GE Healthcare for providing the strain echocardiography analysis tools.

REFERENCES

Adolph, RJ., Stephens, JF., Tanaka, K., 1970. The clinical value of of frequency analysis of the first heart sound in myocardial infarction, Circulation 41:1003-1014.

Amit, G., Gavriely, N., Lessick, J., Intrator, N., 2005. Automatic Extraction of Physiological Features from Vibro-Acoustic Heart Signals: Correlation with Echo-Doppler, Computers in Cardiology 2005:299-302.

Amundsen, BH., Helle-Valle, T., Edvardsen,, T., Torp, H., Crosby, J., Lyseggen, E., Støylen, A., Ihlen, H., Lima, JAC., Smiseth, OA., Slørdahl, SA., 2006. Noninvasive Myocardial Strain Measurement by Speckle Tracking Echocardiography, J Am Coll Cardiol, 47:789-793.

Chen, D., Durand, LG., Lee, HC., Wieting, DW., 1997. Time-frequency analysis of the first heart sound: Part 3, Med. Biol. Eng. Comput. 35;455-461.

Clarke, WB., Austin, SM., Pravib, MS, Griffen, PM., Dove, JT., McCullough, J., Schreiner, BF., 1978. Spectral Energy of the Fist Heart Sound in Acute Myocardial Ischemia, Circulation 57;593-598.

Duda, RO., Hart, PE., 1973. Pattern Classification and Scene Analysis. Wiley New-York.

Greenberg, NL., Firstenberg, MS., Castro, PL., Main, M., Travaglini, A., Odabshian, JA., Drinko, JK., Rodriguez, LL., Thomas, JD., Garcia, MJ., 2002. Doppler-Derived Myocardial Systolic Strain Rate Is a Strong Index of Left Ventricular Contractility, Circulation 105:99-105.

Reisner, SA., Lysyansky, P., Agmon, Y., Mutlak, D., Lessick, J., Friedman, Z., 2004. Global Longitudinal Strain: A Novel Index of Left Ventricular Systolic Function, J Am Soc Ehocardiogr 17:630-633.

Rushmer, RF., 1978. Cardiovascular Dynamics, WB Saunders Co. Philadelphia, 4th edition.

Sakamoto, T., Kusukawa, R., MacCanon, DM., Luisada AA., 1965. Hemodynamic Determinants of the Amplitude of the First Heart Sound, Circ. Res. 16;45-57.

Stockwell, R., Mansinha, L., Lowe, R., 1996. Localization of the complex spectrum: the S transform, IEEE Transactions on Signal Processing,, 44:998-1001

Tavel, ME., 1978. Clinical Phonocardiography & External Pulse Recording. Year Book Medical Publishers Inc. Chicago, 3rd edition.

INFLUENCES OF DIGITAL BAND-PASS FILTERING ON THE BCG WAVEFORM

Mikko Koivuluoma[1], Laurentiu Barna[1], Teemu Koivistoinen[2]
1) Institute of Signal Processing, Tampere University of Technology, Korkeakoulunkatu 1, Tampere, Finland
mikko.koivuluoma@tut.fi

Tiit Kööbi[2], Alpo Värri[1]
2) Department of Clinical Physiology, Tampere University Hospital, Tampere, Finland

Keywords: Ballistocardiogram, ProHeMon, EMFi.

Abstract: The band pass filter is used to attenuating breathing originated signal from the heart originated BCG signal. The bandwidth of the both signals slightly overlap, hereby the complete attenuation of the breathing is not possible without also altering the heart originated BCG waveforms and the parameters which are obtained from the BCG. In our study we investigated the optimal lower cut-off frequency, and 1.3 Hz was found as the reasonable compromise between the attenuation of the breathing and the altering of the heart originated BCG.

1 INTRODUCTION

The developments in sensors, recording devices, and signal processing techniques, experienced over the past two decades, significantly increase the analysis possibilities of the ballistocardiogram (BCG). The potential of BCG to provide valuable information about the condition of the heart was clearly demonstrated even from early stages, when it was used to predict the evolution of ischemic myocardial diseases. Other clinical studies in which BCG proved useful include prognosis, monitoring, physical conditioning, stress tests, evaluation of therapy, and cardiovascular surgery (Marinelli 1991). The use of BCG has also been reported in epidemiological and cardiovascular screening studies (Star and Wood, 1961; Kiessling, 1970; Lynn and Wolf, 1974). Because during the signal measurement stage, no electrodes need to be attached to the body of the subject, BCG presents great potential for modern healthcare, especially in the case of home care monitoring.

The majority of modern BCG analysis methods rely on two separate stages, the signal measurement and the offline signal analysis with the help of a digital computer. When this is the case, one can closely look into the measured signal and decide about the filtering methods appropriate for each particular measurement. Such offline or visual analysis of BCG signals is time consuming and the costs associated with it are considerable. A better solution was offered by the advances of computers and electronic technology that provide a good basis for automatic cardiac performance monitoring and heart disease diagnosis, by assisting clinical practice and thus saving diagnosis time.

Because the raw BCG signal is usually corrupted with breathing and movement artifacts, a pre-processing of the raw data is necessary before the interpretation stage can take place. For a real-time automatic BCG analysis system, one should know in advance how this preprocessing will affect the BCG waveform. In the mid sixties the subjects were asked to hold their breath for some part of the recording, in order to eliminate the respiration effect on the BCG signal. Although this technique increases the quality of the raw BCG signal, it cannot be performed over long periods of time and it is rather uncomfortable for the subject. For these reasons digital filtering was proposed as an alternative, but was not pursued until recently due to the limitations of computing power at that time.

This study was made to investigate how bandpass filtering the raw BCG signal at different cut-off frequencies affects the BCG waveform, with respect to the BCG waveform parameters usually taken into consideration as meaningful diagnostic information.

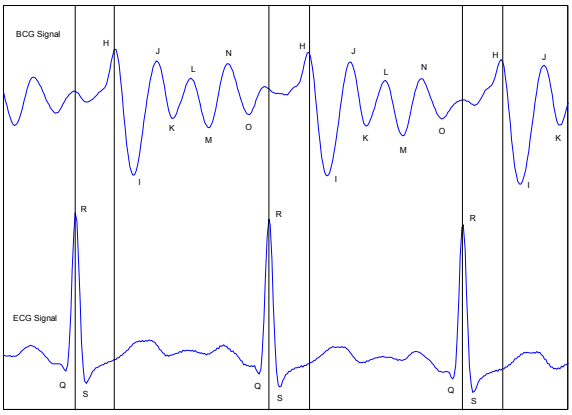

Figure 1: One dimensional BCG (top) and ECG (bottom) signals from a normal healthy subject during breath suppression.

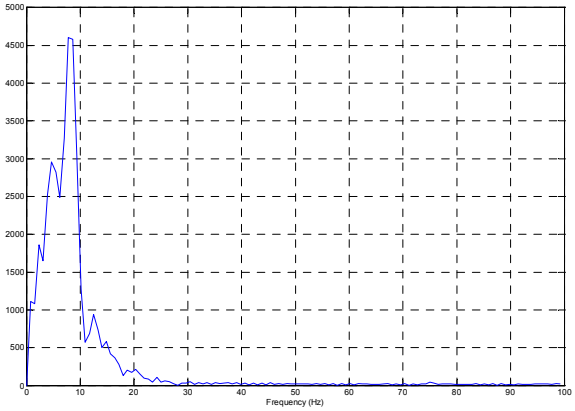

Figure 2: Power spectrum of the BCG wave shown in Fig. 1. As it can be seen, the spectra power are mostly within 20Hz.

2 THE BALLISTOCARDIOGRAM

BCG is a measure of the heart's mechanical activity associated with the flow of blood out of the heart's chambers. It was studied very actively from the 1940s until the mid-1970s when research activity in this area ended almost completely due to the technical limitations of sensors, signal conditioning electronics, recording devices and the high diagnostic value of the already available electrocardiogram (ECG). With the advance of technology, BCG signals can now be easily recorded, unobtrusively, both on supine and sitting positions using noninvasive modern techniques.

The idealized BCG waveform consists of seven components, labeled the H through N wave (Starr and Noordergraaf, 1967) with the IJK-complex being the predominantly identifiable segment (see Fig. 1). In time, typically the BCG will trail the ECG by about 0.1-0.3s (Braunstein and Thomas, 1953).

A simple spectral analysis of the BCG signal shows that the spectra power of the BCG waveform is mostly within 20Hz (see Fig. 2) but in literature is was reported that the BCG waveform lies between 0.1 Hz and 40 Hz.

BCG waves change with respiration and from one patient to another making BCG analysis a rather difficult task. Moreover, usually the raw BCG signal is also corrupted with movement artifacts, which makes the recognition of characteristic BCG waveforms almost impossible (see Fig. 3). In order to eliminate the respiration effect, seen as a drift from the baseline of the signal, various bandpass digital filters have been used and reported in literature with the most common frequency range

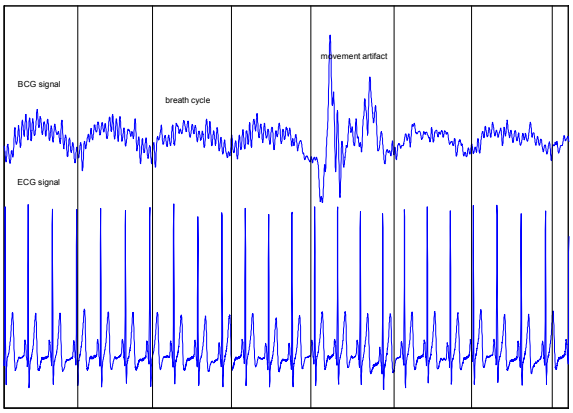

Figure 3: One dimensional BCG (top) and ECG (bottom) signals from a normal healthy subject. Notice the breathing effect on the BCG signal as a drift from the baseline and the movement artifact that causes abnormalities in the signal and makes the detection of the BCG peaks difficult.

being between 1 Hz and 20 Hz. Filtering above 1 Hz should eliminate the respiration effect but as different people have different respiration frequencies the filter could be selected at a lower or higher cut-off frequency, depending on the parameters studied. Because the BCG signal has components below 1 Hz as well and any kind of digital filtering will affect those components, it is important to know how the BCG waveform will be affected by filtering at different cut-off frequencies in order to know the tradeoff between the selected cut-off frequency and the changes suffered by the BCG waveform due to filtering.

Traditionally the physicians interpret different parameters of the measured BCG waveforms and calculate relevant indicators to determine whether or not the heart shows signs of cardiac diseases.

The various reported off-line analysis methods use different relations between the BCG peaks to classify the waveforms. The average cardiac stroke volume can be estimated as follows (Starr et al 1940):

$$ACSV = 7\sqrt{(3I + 2J)AC^{3/2}} \quad (1)$$

where I and J are the BCG waves (in mm), A the subject's aortic internal diameter (in cm^2) and C the duration of the cycle (in seconds). From the ACSV, the cardiac output can be further calculated (Brown, Hoffman and De Lalla 1950, Starr et al 1940).

The amplitudes of the H-I, I-J, and J-K segments and their expiratory and inspiratory ratios HI_E/HI_I, IJ_E/IJ_I, JK_E/JK_I were used to express respiratory variation in BCG waves and the HI_M/IJ_M and JK_M/IJ_M ratios of the averaged mean amplitudes were used as amplitude ratios (Onodera 1964, Scarborough 1953, March 1955). The time amplitudes (TA) obtained by dividing the amplitude of a segment by its interval measured in expiratory and inspiratory phases investigated on H-I, I-J, and J-K intervals have also been reported. Other intervals measured in the literature are: the P-H interval measured from the beginning of the P wave of the electrocardiogram to the tip of the H of the Ballistocardiogram the Q-H, Q-I, Q-J and Q-K measured from the beginning of the Q wave of the electrocardiogram to the H, I, J, and K tips of the Ballistocardiogram (Onodera 1964).

3 PATIENTS AND METHODS

In this study we used a subset of 15 subjects from the signal database recorded during the ProHeMon project (Koivistoinen et al. 2004). All the measurements were conducted by an experienced research nurse at the Department of Clinical Physiology of the University Hospital from Tampere, Finland. The study protocol was approved by the Ethical Committee of Tampere University of Tampere and a written consent was obtained from each subject measured. Part of the measurement protocol included the parallel measurement of ECG, impedance cardiogram (ICG) and two BCG channels. The subjects were divided into three groups (5 subjects in each group):

1. 20-30-year old healthy students
2. healthy 50-70-year old men
3. 50-70 year old men with myocardial infarct in their medical history

Figure 4: Recording setup. In this case, no ICG leads were connected.

All measurements were done with CircMon™, a commercially available circulation monitor (Jr Medical Ltd). The ECG and ICG leads were connected to their own dedicated channels of CircMon and two BCG signals were connected to auxiliary input channels. A measurement chair with electromechanical film (EMFi™) (Kirjavainen 1987) foils and a dedicated BCG amplifier specially designed and built for this study were used to record and amplify the BCG signals from the back and the seat of the chair (Junnila et al 2004, Barna et al 2005, Junnila et al 2005). The quality of the signals was visually inspected and assessed by specialist medical doctors. In this setup CircMon functioned as an A/D converter and a sampling frequency of 200 Hz was used for each recording. The recordings lasted for about 13 minute per subject. At the beginning of the recording, the subject was placed in supine position and no BCG signal was recorded. This study does not include the study of the ICG signals obtained. The gain of the BCG amplifier was increased after the first group was recorded, so the absolute signal values between groups are not comparable.

The BCG signal, was filtered offline with a Parks-McClellan optimal equiripple band-pass Finite Impulse Response (FIR) filter designed in Matlab® 7.2 (The MathWorks Inc.). The advantage of using an FIR filter is that the phase of the input signal is not distorted and the delay introduced by the filter can be easily calculated, the information about the time location of the BCG waveform being preserved. The lower cut-off frequency of the pass-band was varied between 0.7 Hz and 4.6 Hz with a step of 0.1 Hz and the upper cut-off frequency was fixed at 20.5 Hz. A ripple of 0.1 dB was set for the pass-band and attenuation of 60 dB for both stop-

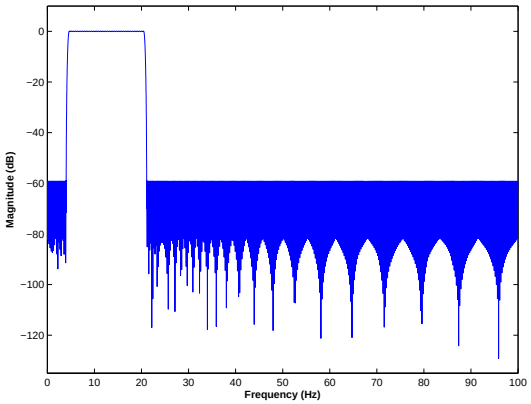

Figure 5: One FIR filter used in study. This filter have passband from 4.6 to 20.5 Hz.

bands. The transition band width was set to 0.6 Hz (see Fig. 5 for example). The order of the filters used was rather high (N = 848), which resulted in a high computation time at filtering.

After filtering, the locations of the BCG waveforms were determined using the R spikes of the parallel ECG tracing. The BCG signal was divided into sections of 151 samples. A mean BCG waveform ($BCGM_{NB}$) was calculated as the mean of 50 % of the most similar BCG waveforms found from the artifact free epochs of the recording. Cross correlation was used as the measurement of the similarity, and no visual inspection was involved. For each mean BCG waveforms the following parameters were calculated:

- the amplitudes of the mean H-I and I-J waves
- HI_M/IJ_M ratios of the mean H-I and I-J waves

4 RESULTS

In this section, a sample recording is first analyzed, followed to an overall assessment for all the recordings involved in this study.

In the Figure 6, the original signal (A01) with six heartbeats is shown. The respiratory signal can be clearly seen as a low frequency drift from the baseline of the signal. In this example, the measurement of characteristic BCG waveforms is not difficult, because the heart originated component has relatively high amplitudes compared to the respiratory signal. Figure 7 shows the same section of the BCG signal, band-pass filtered at different cutt-off frequencies. When the lower cut-off frequency is between 1.3 Hz (row one, column two) and 2.5 Hz (row four, column four), the shape of the signal is almost constant. Therefore, an optimal lower cut-off frequency of about 1.3 Hz is recommended. By studying the changes in amplitudes of the different waveforms and HI_M/IJ_M ratio, we can find a more accurate cut-off frequency.

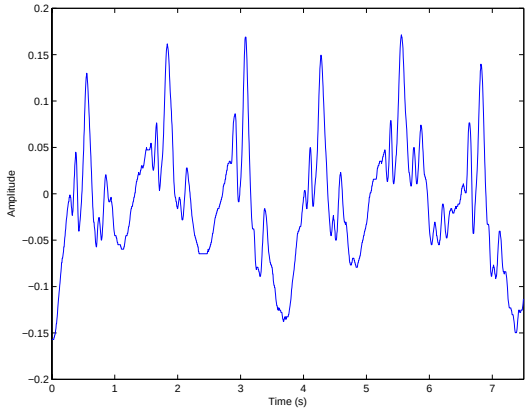

Figure 6: Raw BCG signal (subject A01).

The changes of different parameters resulted from filtering, and expressed as function of the lower cut-off frequency are shown in figure 8. As seen from the previous graphics, the parameters remain relatively constant between 1.3 Hz and 2.5 Hz, with significant changes occurring between 1 Hz and 1.2 Hz, and after 2.6 Hz. A lower cut-off frequency can be therefore selected between 1.3 Hz and 2.5 Hz without greatly compromising the BCG parameters.

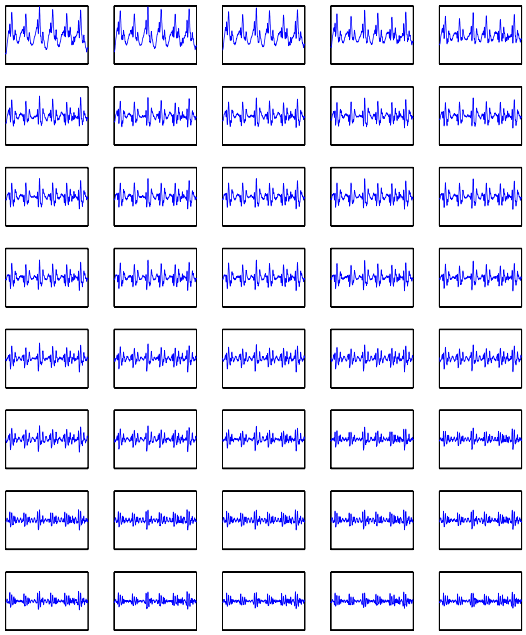

Figure 7: The section of the BCG-signal filtered with 40 different band pass filter. In the upper left corner is the output of the filter with pass band from 0.7 Hz to 20.5 Hz, and in the lower right corner is the output of the filter with pass band from 4.6 Hz to 20.5 Hz.

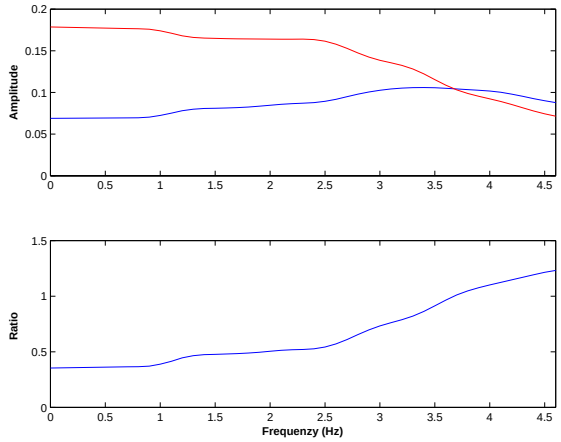

Figure 8: The different parameters as the function of the lower cut-off frequency. Up: mean I-J amplitude (red) and mean H-I amplitude (blue). Down: HI_M/IJ_M ratio.

Figure 9, shows the HI_M/IJ_M ratios of the all recordings used in this study. In the most cases, HI_M/IJ_M ratios present a flat section between 1.3 Hz to 2.2 Hz, the mean HI_M/IJ_M ratio and approximate derivative of the mean HI_M/IJ_M, shown in Figure 10 supporting this observation.

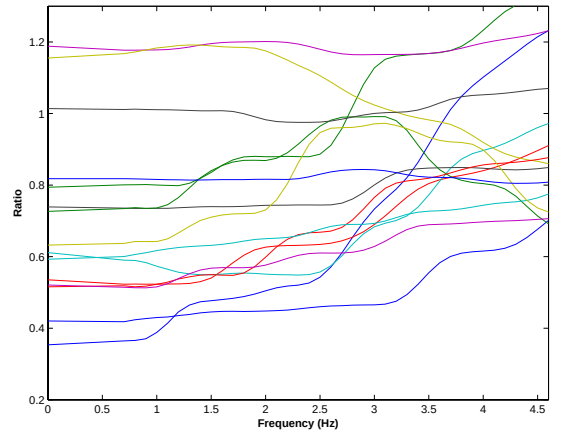

Figure 9: HI_M/IJ_M ratios of the recordings used in this study. Although up to 1Hz the ratios remain rather flat and between 1Hz and 1.3Hz they get significantly changed, when filtering at 1Hz the effect of respiration is still visible in the signal, but at 1.3Hz this effect gets eliminated (this being better for a visual inspection of Starr classes).

Based on the observations made upon the entire set of BCG recordings employed, the optimal lower cut-off frequency recommended is of 1.3 Hz. For this value, most of the signal remains unaltered, and the major effects of the respiration are removed.

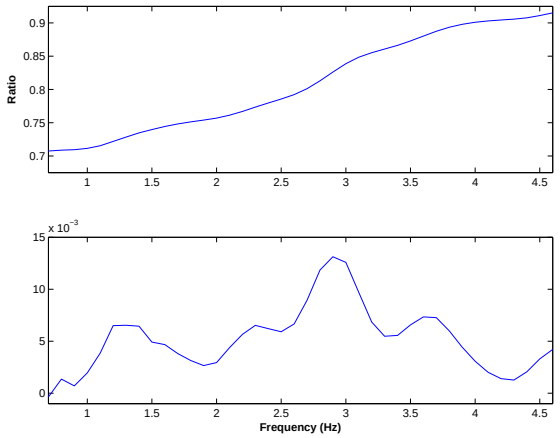

Figure 10: Up: the mean HI_M/IJ_M ratio. Down: Approximate derivative of the mean HI_M/IJ_M ratio.

5 DISCUSSION

Setting the cut-off frequency of the BCG band-pass filter is a trade-off between attenuating breathing and altering the heart-originated components of the raw BCG signal. Individual cut-off frequencies might be optimal, but that would make the comparison between patients more difficult. By using a cut-off frequency 1.3 Hz, a reasonable compromise was found.

Our results also show that changes of BCG components as a result of filtering can be estimated and accounted for in reporting BCG derived measures and ratios. By analyzing BCG data from recordings involving breath suppressed epoch, we expect to refine our results in a future study.

In this study no attempts have been made to link the amplitudes and ratio calculated from the BCG signal to any of the cardiovascular variables such as stroke volume

The equation presented in section "The Ballistocardiogram" for the average cardiac stroke volume was not feasible because no calibration has been performed for the BCG system used and the subjects were recorded in sitting position, unlike Starr et al, in which the recordings were performed in supine position. As future improvements, we plan to combine the information available in the ECG and ICG recordings with the one obtained from BCG..

REFERENCES

Barna, L.C., Koivuluoma, M., Värri, A., "Heart-rate detection using EMFi sensors on a normal looking

chair", *Proceedings of the 3rd European Medical & Biomedical Engineering Conference, IFMBE European Conference on Biomedical Engineering, EMBEC 2005*, Prague, Czech Republic, 20-25 November, pp. 5 p, 2005

Braunstein, J., Thomas, C., "The ballistocardiogram, a dynamic record of the heart," Springfield, IL: Springfield, 1953

Brown, H.R., Hoffman, M.J., De Lalla, V., "Ballistocardiographic findings in patients with symptoms of angina pectoris," *Circulation*, vol. 1, pp. 132-140, January 1950

Jr Medical Ltd, "U.S. Patent No. 6,228,033 B1: Apparatus and methods for a noninvasive measurement of physiological parametres," May 8 2001.

Junnila, S., Koivistoinen, T., Kööbi, T., Niittylahti, J., Värri, A., "A Simple Method for Measuring and Recording Ballistocardiogram," in Proc. 17th Int. EURASIP Conference BIOSIGNAL 2004, Brno, Czech Republic, June, pp. 232–234, 2004

Junnila, S., Barna, L., Koivistoinen, T., Koivuluoma, M., Alametsä, J., Kööbi, T., Turjanmaa, V., Niittylahti, J., Värri, A., "Development of a wireless proactive ballistocardiograph chair," *In: Linden, G. (ed.). Proceedings of the Proactive Computing Workshop PROW 2004*, Helsinki, Finland, 25-26 November, pp. pp. 25 - 28, 2004

Junnila, S., Akhbardeh, A., Koivistoinen, T., Värri, A., "An EMFi-film Sensor based Ballistocardiographic Chair: Performance and Cycle Extraction Method," *Proc. IEEE Workshop on Signal Processing Systems*, Athens, Greece, 2-4 Nov 2005

Kiessling, C.E., "A preliminary appraisal of the prognostic value of ballistocardiography," *Bibl. Cardiol.*, vol. 26, pp. 292-295, 1969

Kirjavainen, K., "U.S. patent #4654546: Electromechanical film and procedure for manufacturing same," 1987.

Koivistoinen, T., Barna, L., Alametsä, J., Junnila, S., Koivuluoma, M., Kööbi, T., Turjanmaa, V., Värri, A. "*Ballistocardiograms from young adults in sitting position using EMFi sensors*," Proceedings of the 31st Annual Meeting of Computers in Cardiology 2004, Chicago, Illinois, USA, 19-22 September, pp. 5 p, 2004

Koivistoinen, T., Junnila, S., Värri, A., Kööbi, T., "A new method for measuring the ballistocardiogram using EMFi sensors in a normal chair," *Proc. 26th Annual International Conference of the IEEE Engineering in Medicine and Biology Society*, San Francisco, California, USA, 1-5 September, pp. 4 p, 2004

Lynn, T.N., Wolf, S., "The prognostic significance of the ballistocardiogram in ischemic heart disease," *Am. Heart J.*, vol. 88, pp. 277-280, 1974

March, H.W., "Three-Plane Ballistocardiography: The Effect of Age on the Longitudinal, Lateral, and Dorsoventral Ballistocardiograms," *irculation*, vol. 12, pp. 869, 1955

Marinelli, R.A., Penney, D.G., Marinelli, W.A., Baciewicz, F.A., Jr., "Rotary motion in the heart and blood vessels: A Review," *J. Appl. Cardiol.*, vol. 6, pp. 421-431, 1991

Onodera, K., "A study on ballistocardiogram recorded during valsalva maneuver in healthy persons and patients with abnormal blood pressure," *Jpn Circ J.*, vol. 28, pp. 493-504, July 1964

Scarborough, W.R., Davis, F.W., Baker, B.M., Mason, R.E., Singewald, M.L., Lore, S.A., Fox, L.M., "A ballistocardiographic study of 369 apparently normal persons; an analysis of normal and borderline ballistocardiograms," *Am Heart J.*, vol. 45, pp. 161-89, February 1953

Starr, I., Schroeder, H.A., "Ballistocardiogram. II. Normal standards, abnormalities commonly found in diseases of the heart and circulation, and their significance", *J Clin Invest.*, vol. 19, pp. 437–450, May 1940

Starr, I., and Wood, E.C., "Twenty years studies with the Ballistocardiograph, the Relation between the amplitude of the first record of 'health' adults and eventual mortality and morbidity form heart disease," Circulation, vol. 23, pp. 714–732, 1961

Starr, I., Noordergraaf, A., "Ballistocardiography in cardiovascular research," Philadelphia (PA): JB Lippincott, pp. 166-189, 1967

ANT COLONY INSPIRED METAHEURISTICS IN BIOLOGICAL SIGNAL PROCESSING

Hybrid Ant Colony and Evolutionary Approach

Miroslav Bursa, Michal Huptych and Lenka Lhotska
Dept. of Cybernetics, Czech Technical University in Prague, Technicka 2, Prague 6, Czech Republic
bursam@fel.cvut.cz, huptycm@fel.cvut.cz, lhotska@fel.cvut.cz

Keywords: Electrocardiogram Signal Processing, Evolutionary Algorithm, Ant Colony Optimization, Electroencephalogram Processing, Biological Signal Processing.

Abstract: Nature inspired metaheuristics have interesting stochastic properties which make them suitable for use in data mining, data clustering and other application areas, because they often produce more robust solutions. This paper presents an application of clustering method inspired by the behavior of real ants in the nature to biomedical signal processing. The main aim of our study was to design and develop a combination of feature extraction and classification methods for automatic recognition of significant structure in biological signal recordings. The method targets the speed-up and the increase in objectivity of identification of important classes and may be used for online classification, so it can be used as a hint in the expert classification process. We have obtained significant results in electrocardiogram and electroencephalogram recordings, which justify the use of such kind of methods.

1 INTRODUCTION

This study aims at design and development of feature extraction and classification methods for automatic recognition of important patterns in biological signal recordings. The doctors often work under pressure (time and fatigue) and the error ratio of the expert increases when working under high load (both psychical and physical fatigue). Automated methods are designed to speed up and objectify the identification of relevant classes and may be used for online classification. However, they should be provided as a hint to the doctor only, as they do not consider many other aspects (medication, diagnosis, treatment, patient history, etc.).

With the oncoming boost in personal medical electronics and portable monitoring technology, there is still growing amount of data which must be processed and evaluated by the physicians.

Nowadays, many data-mining algorithms with still growing number of modifications exist, see for example (Abraham et al., 2006) or (Panos M. Pardalos, 2007). Such modifications aim at speeding up the data mining process, increase its robustness and stability. But even with rapidly increasing computational power of modern computers, the analysis of huge databases is very expensive (in terms of computer time and/or memory and therefore also financially). This is why scientists instantly search and develop novel and robust techniques to analyze and process large amount of data.

Biological signal processing workflow consists of the following main processes: signal pre-processing, signal transfer and/or storage, digital signal processing and feature extraction, clustering of the similar data (mainly in long-term recordings), signal interpretation (classification) and expert validation. In the majority of the processes mentioned, the ant-colony inspired methods can be used with more or less success (Bursa et al., 2006). Usually some kind of suitable feature processing and filtering is also performed.

1.1 Clustering

In many industrial, business and scientific areas we can see still growing use of computers and computational appliances, and a huge amount of vari-

ous data must be stored, processed and evaluated. Such data are often mixed from different sources, containing many different data types, unusual coding schemes, and seldom come without any errors (or noise). Datamining is not only an important scientific area, but also an important tool in industry and business and still gaining its importance in healthcare and biomedical applications.

This is where data clustering can significantly help. By clustering we mean constructing partitioning scheme on the data set while minimizing the distance inside each cluster (intra-cluster distance) and maximizing distance between clusters (inter-cluster distance). Note that a similarity (or distance) measure must be specified in order to the clustering being applicable.

Data clustering, referred as *cluster analysis* (Rousseeuw and Kaufman, 1990), numerical taxonomy, typological analysis, etc., is a common unsupervised learning technique aimed at accumulation of similar patterns into groups (clusters): partitioning of a data set into subsets (clusters), so that the data in each subset (ideally) share some common aspect. Review of main clustering methods (partitioning methods, hierarchical methods, density-based methods and grid-based methods) can be found in (Jain et al., 1999).

If the final (correct) classification is not known, different techniques for measuring cluster validity exists: Dunn index (Dunn, 1974), Davis-Bouldin index (Davies and Bouldin, 1979), Silouhette index (Rousseeuw, 1987), etc.

1.2 Electrocardiogram

The electrocardiogram (ECG) analysis is still one of the most important non-invasive diagnostic techniques used in patient diagnostics process.

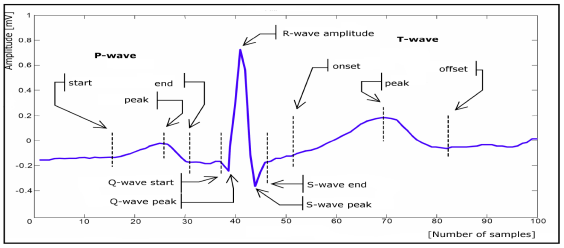

Figure 1: Electrical recording of a heart action (an electrocardiogram, ECG). The most important features are marked. The graph shows amplitude dependency on time (record samples).

With Holter ECG recordings (long-term ECG recordings, lasting usually 24 and more hours), wearable medical electronics and patient auto-diagnostic (and monitoring) appliances, also a huge amount of data has to be transferred and furthermore processed.

In clinical praxis it is hardly acceptable for the physician to accept longer than five minutes for the patient long-term recording (Holter) to be processed (Chudacek and Lhotska, 2006). Thus efficient and robust algorithms must be used, opening wide area of application for nature inspired methods and artificial intelligence methods which can be used in exploratory analysis.

1.3 Electroencephalogram

Electroencephalogram (EEG) is one of the most important methods for studying maturation degree of human brain. A newborn infant typically sleeps approximately 70 % of an 24 hour interval. In adult sleep, the characterization of recorded bioelectrical signals is mainly performed using spectral frequency analysis. In the case of newborns, different methods have been often used (Scher, 2004), e.g. fractal analysis, dimensional analysis and nonlinear analysis.

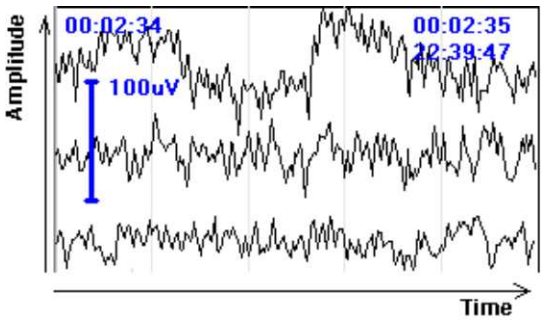

Figure 2: Electrical recording of human brain (an electroencephalogram, EEG). Three channels are shown. The graph shows amplitude dependency on time (record samples).

Active newborn sleep is characterized by irregular breathing, saccadic eye movements, small body movements and twitches. In contrast to adult REM sleep, peripheral motor pathways are not depressed during active sleep in neonates, making movements possible. During quiet sleep, breathing is regular, and eye and bodily movements are absent. These states have EEG correlates: EEG in quiet sleep shows either continuous high-voltage low-frequency (HVLF) activity or trace alternant, where HVLF activity alternates with quiet periods in cycles of few seconds duration. In active sleep, the EEG is relatively quiet (Teofilo and Lee-Chiong, 2006).

2 METHODS

2.1 Methods Inspired by Ant Colonies

The inspiration of the ant inspired algorithms comes from the *foraging* behavior of real ant colonies (Deneubourg et al., 1990) which has been observed in nature and which has been studied by biology scientists. The idea of ant colony technique for optimization was introduced in the early 1990s by M. Dorigo and the ant colony metaheuristics has been thoroughly studied (Dorigo et al., 1999).

The Ant Colony Optimization metaheuristic technique (Dorigo et al., 1999) is a model of the ant behavior used for combinatorial problems. This method is inspired by the process the real ants use to construct a path using chemical substance (*pheromone*). A modification of Ant Colony Optimization can also be used for dynamic optimization such as network routing (R. O. Schoonderwoerd, 1996). Review of ant colony inspired methods can be found for example in (Dorigo and Blum, 2005).

The method for optimization in continuous space has been also developed. It uses probabilistic density function with Gaussian kernel which represents the spatial distribution of pheromone has been proposed (Bilchev and Parmee, 1993), (Socha, 2004). The method presented by K. Socha (Socha, 2004) is the most related with ant-inspired techniques.

2.1.1 Ant Based Clustering

Also a method for data clustering inspired by ant cemetery organization of some ant colonies has been studied (Dorigo et al., 1999) and implemented. It models the way the ants search the space and collect similar objects together. For example, the *Messor sancta* ants organize dead corpses into clusters; brood sorting has been studied in ant colony of *Leptothorax unifasciatus*. This approach has been modeled (Lumer and Faieta, 1994), (Deneubourg et al., 1990) to perform a clustering of data. It is very sensitive to the similarity measure used (e. g. Euclidean distance, etc.) and the range of agent perception. Note, that no pheromone is used in this method. Also some methods using pheromone exist, namely A^2CA (Vizine et al., 2005).

Another approach can be seen the work of J. Handl in (Handl et al., 2006) (an ATTA algorithm), which introduce modified neighborhood function (penalizing high dissimilarities), short-term memory with lookahead (jumping ants), increasing radius of perception, time-dependent modulation of the neighborhood function. The work also introduces modified threshold function for picking and dropping the data. The work is followed by the work of Tan et al. (Tan et al., 2006) which removes the ant metaphor from the method and presents a deterministic version of ant-clustering algorithm.

2.2 ACO_DTree method

As described in (Abraham et al., 2006), nature inspired methods can be successfully used in data mining process. The method ACO_DTree (Bursa et al., 2007) uses an evolutionary approach combined with ant colony optimization approach. The ACO_DTree method works with a population of classifier trees (a decision-tree like structure): a hierarchical binary structure of nodes where each node divides data set into two parts using a single if-rule (e.g. `if (feature(i) < value)` then `pass_data_left` else `pass_data_right`). The population is continuously evaluated, new individuals are continuously added and worst solutions removed. Only the best individuals can contribute in pheromone laying process (in compliance with (Dorigo et al., 1999)). New individuals are inductively created using the pheromone matrix, preferring important features (features selected by the best individuals).

2.2.1 Decision Tree Construction

By a classification tree we mean hereby a tree-like structure composed of similar nodes. Each node can have left and right sub node. Each node is represented by a decision rule with two parameters (feature index $feature_j$ and decision value *decVal*) which can be described in the following way for an item s_i:

```
1  if (s(i).getFeature(j) < decVal)
2    classifyToLeftBranch
3  else
4    classifyToRightBranch
```

The same applies to the root node. The tree is constructed as follows: first, a random feature index is selected (for the root node). The decision value is also chosen randomly. Then, for each subnode, its subnode is created with certain probability (inversely proportional to the level in the tree). The feature index is selected using the pheromone matrix: successful edges are strongly preferred. The decision value is determined randomly. The random selection of decision value does not present a problem, because even the randomly selected values perform acceptable solution. However, the population is then trained (the decision values are optimized). See section 2.2.5.

By level in the tree we mean the distance from the given node to the root node. Tree height is a maximum level in the tree. Depending on the classification

tree, the data are divided into subgroups which should have similar properties (minimization of intra-cluster distance) and the classes should be different as much as possible (maximization of inter-cluster distance). This process is known as data clustering.

2.2.2 Decision Tree Evaluation

Each tree can be assigned a real number which can be called fitness function. This number represents the classification efficiency of the tree. In the presented method this number is determined by the ratio of incorrectly classified data over the total data in the class (in this paper it is called error ratio). The goal of our method is to obtain tree with the lowest error ratio on the given dataset.

For method evaluation, the training data set is used. The testing data set is used to evaluate the tree on the unknown data (data which have never been presented to the tree). If the classification of the testing data is not known, cluster validation techniques can be used. See section 1.1 for more details.

2.2.3 Parameter Estimation

The following parameters are the most important parameters of the proposed method: population size, number of new solutions added in each step, maximal number of iterations, max. tree height, pheromone lay/evaporate rate and the percent of ants which can deposit pheromone (elitist ratio). The overall results are better when the first four parameters increase, but the computational time rises. For other parameters, an optimum must be determined.

Based on the results of preliminary experiments, population size and number of new solutions added has been fixed to reflect the number of features and $1/2$ of the solutions respectively. These parameters actually increase/decrease the number of solutions generated over time. Similar effect can be obtained by adjusting the maximum iteration limit. Elitist ratio (number of best solutions which can deposit pheromone has been also fixed to the value of $1/2$ of the population (with minimum of 5).

2.2.4 Parameter Adaptation

In order to avoid premature convergence and maintain diversity in the population of solutions, adaptive techniques have been used. First, the pheromone amount on the edge is limited and can be in the range $\langle 0.05; 1.05 \rangle$, the evaporation rate and lay rate is adaptively changed to maintain an average pheromone value over the whole pheromone matrix (if the average pheromone drops by 10 % the pheromone lay rate is increased, similar policy is applied to the pheromone evaporate rate; both the values are bounded by the minimum and maximum value). This could lead to saturation of pheromone values, thus a countermeasure to maintain number of saturated edges on the minimum is also used. The balanced process diversifies the population and avoids getting stuck in local minima.

As a measure to speed up the process and to increase the preference of trees with lower height, the maximum height parameter is continuously increased with the iterations (at about $1/4$ of total iterations the parameter is increased up to its maximal value).

2.2.5 Tree Optimization

In the ACO_DTree method we have presented an optimization strategy (local search) which optimalizes the decision value of each node in the tree. Newly added solutions are first optimized. This improves the overall fitness of the population.

Also after certain period (experimentally determined $1/10$ of total iterations), the population is re-optimized (not the structure, but decision values in the nodes). The method used is Particle Swarm Optimization (Kennedy and Eberhart, 1995), but any other kind of local search can be used. The use and degree of the optimization has to be considered, because it can lead to over-training of the tree: the tree adapts to the training data set and performs badly on the validation (and testing) set, thus reducing robustness of the solution.

3 DATA

This section describes data (biological signals), which have been used in this study: Electrocardiogram (EEG) and Electroencephalogram (EEG).

3.1 Electrocardiogram

Extracted features are the basic ECG parameters. Input signals are taken from a MIT-BIH database (Goldberger et al., 2000), which contains annotated records. In (Goldberger et al., 2000), certain description of the data can also be found (together with some basic anonymous description of the patients, their medication and treatment). The classification into more classes is nearly impossible due to lack of the data (mainly abnormal heart action signal) in some signals. By using only PVC (Premature Ventricular Contraction) beat as abnormal heart actions, more records

Table 1: The table shows results for the the ACO_Dtree algorithm for generating classification trees.

Task	ACO_Dtree
ECG Classification	97.11 %
EEG Classification	71.30 %
EEG Active/quiet sleep	96.38 %
EEG Noise removal	91.02 %

Table 2: The table shows results for the WEKA Random Tree algorithm for generating classification trees.

Task	WEKA Rand. Tree
ECG Classification	96.53 %
EEG Classification	66.21 %
EEG Active/quiet sleep	95.37 %
EEG Noise removal	90.80 %

from the MIT-BIH database can be correctly processed. Another approach can be to divide all heart actions in two classes: normal and abnormal.

From the ECG signal, the following eight features have been automatically extracted, see (Chudacek and Lhotska, 2006): amplitudes of Q, R, S, positive T and negative T wave, amplitude ratio of Q/R, R/S and R/T waves. For processing, the features have been normalized into the interval of $\langle 0.0; 1.0 \rangle$.

3.2 Electroencephalogram

All recordings used in this work contain eight EEG channels (these are FP1, FP2, T3, T4, C3, C4, O1, O2), Electrooculogram (EOG), Electromyogram (EMG), Respiratory channel (PNG) and Electrocardiogram (ECG). All the data have been annotated by an expert into four classes (wake, quiet sleep, active sleep, movement artifact).

For accurate classification it is necessary to determine and/or calculate the most informative features. In our previous study a method based on power spectral density (PSD) has been applied to each EEG channel. Features derived from EOG, EMG, ECG and PNG signals have been also used. The most informative one is the measure of regularity of respiration in PNG signal. The following methods, which have been used for feature extraction, are in detail described in (Gerla et al., 2006).

4 RESULTS

Using the presented method with Particle Swarm Optimization, we have obtained 97.11 % accuracy over the training set (training set has been randomly selected from the whole data set in the ratio of 66 % and 33 % of training respective testing data vectors).

Using the EEG recordings of patients we obtained an accuracy of 82 % in the artifact removal process. The overall classification accuracy is 71.3 %.

The results are summarized in Table 1 and Table 2. The ACO_Dtree method outperformed the Random Tree method in all cases.

5 CONCLUSIONS

In this paper we have presented a hybrid method which can be used for data partitioning, data classification and also feature selection. The method is based on the hybrid combination of evolutionary algorithm with ant colony optimization. This combination allows better convergence and leads to increased robustness. The method has been compared with a simple evolutionary algorithm, which does not use pheromone and with Random tree generation method (from the WEKA (Witten and Frank, 2005) toolkit). The hybrid method outperformed the other method in all cases. The method has been (after preliminary tests on smaller datasets) applied to the MIT-BIH database with more than 80.000 records. The EEG data contains about 450.000 instances.

Certain parameters of the method have been experimentally determined. The population size should equal the number of features in the signal (the square root of the size of pheromone matrix). PSO re-optimization of the individuals is very important, however with vigorous optimization, the advantage of robustness is lost (the results on training data set are excellent, but very poor on the testing data set).

Lower accuracy on the EEG set is manly due to high amount of expert misclassification in the data (the neurologists obtain classification consensus in about 70 % of the cases).

The results show that the approach is suitable for biological data clustering. The advantage is that it produces clear structure with clinical use.

ACKNOWLEDGEMENTS

This research has been supported by the research program No. MSM 6840770012 "Transdisciplinary Research in the Area of Biomedical Engineering II" of the CTU in Prague, sponsored by the Ministry of Education, Youth and Sports of the Czech Republic. This work has been developed in the BioDat research group `http://bio.felk.cvut.cz`.

REFERENCES

Abraham, A., Grosan, C., and Ramos, V. (2006). *Swarm Intelligence in Data Mining (Studies in Computational Intelligence)*. Springer.

Bilchev, G. and Parmee, I. C. (1993). The ant colony metaphor for searchin continuous design spaces. *Proc. of AISB Workshop on Evolutionary Computing Lecture Notes inComputer Science*, pages 25–39.

Bursa, M., Huptych, M., and Lhotska, L. (2006). The use of nature inspired methods in electrocardiogram analysis. *International Special Topics Conference on Information Technology in Biomedicine [CD-ROM]. Piscataway: IEEE*.

Bursa, M., Lhotska, L., and Macas, M. (2007). Hybridized swarm metaheuristics for evolutionary random forest generation. *Proceedings of the 7th International Conference on Hybrid Intelligent Systems 2007 (IEEE CSP)*, pages 150–155.

Chudacek, V. and Lhotska, L. (2006). Unsupervised creation of heart beats classes from long-term ecg monitoring. *Conference: Analysis of Biomedical Signals and Images. 18th International EURASIP Conference Biosignals 2006. Proceedings.*, 18:199–201.

Davies, D. L. and Bouldin, D. W. (1979). A cluster separation measure. *IEEE Transactions on Pattern Recognition and Machine Intelligence*, 1 No. 2:224–227.

Deneubourg, J. L., Goss, S., Franks, N., Sendova-Franks, A., Detrain, C., and Chretien, L. (1990). The dynamics of collective sorting robot-like ants and ant-like robots. In *Proceedings of the first international conference on simulation of adaptive behavior on From animals to animats*, pages 356–363, Cambridge, MA, USA. MIT Press.

Dorigo, M. and Blum, C. (2005). Ant colony optimization theory: A survey. *Theoretical Computer Science Issues 2–3*, 344:243–278.

Dorigo, M., Caro, G. D., and Gambardella, L. M. (1999). Ant algorithms for discrete optimization. *Artif. Life*, 5(2):137–172.

Dunn, J. C. (1974). Well separated clusters and optimal fuzzy partitions. *Journal of Cybernetics*, 4:95–104.

Gerla, V., Lhotska, L., Krajca, V., and Paul, K. (2006). Multichannel analysis of the newborn eeg data. *IEEE ITAB International Special Topics Conference on Information Technology in Biomedicine. Piscataway: IEEE*.

Goldberger, A. L., Amaral, L. A. N., Glass, L., Hausdorff, J. M., Ivanov, P. C., Mark, R. G., Mietus, J. E., Moody, G. B., Peng, C.-K., and Stanley, H. E. (2000). PhysioBank, PhysioToolkit, and PhysioNet: Components of a new research resource for complex physiologic signals. *Circulation*, 101(23):e215–e220.

Handl, J., Knowles, J., and Dorigo, M. (2006). Ant-based clustering and topographic mapping. *Artificial Life 12(1)*, 12:35–61.

Jain, A., Murty, M. N., and Flynn, P. J. (1999). Data clustering: A review. *ACM Computing Surveys*, 31:264–323.

Kennedy, J. and Eberhart, R. C. (1995). Particle swarm optimization. *Proceedings IEEE International Conference on Neural Networks*, IV:1942–1948.

Lumer, E. D. and Faieta, B. (1994). Diversity and adaptation in populations of clustering ants. *From Animals to Animats: Proc. of the 3th Int. Conf. on the Simulation of Adaptive Behaviour*, 3:501–508.

Panos M. Pardalos, Vladimir L.Boginski, A. V., editor (2007). *Data Mining in Biomedicine*. Springer.

R. O. Schoonderwoerd, e. a. (1996). Ant-based load balancing in telecommunications networks. *Adaptive Behavior 5*, pages 169–207.

Rousseeuw, P. and Kaufman, L. (1990). *Finding Groups in Data: An Introduction to Cluster Analysis*. John Wiley & Sons.

Rousseeuw, P. J. (1987). Silhouettes: a graphical aid to the interpretation and validation of cluster analysis. *J. Comp App. Math*, 20:53–65.

Scher, M. S. (2004). *Automated EEG-sleep analyses and neonatal neurointensive care*.

Socha, K. (2004). Aco for continuous and mixed-variable optimization. *Proceedings of ANTS 2004 Lecture Notes in Comput Science, Springer*, 3172:25–36.

Tan, S. C., Ting, K. M., and , S. W. T. (2006). Reproducing the results of ant-based clustering without using ants. *CEC 2006. IEEE Congress on Evolutionary Computation*, pages 1760–1767.

Teofilo, L. and Lee-Chiong (2006). *SLEEP: a comprehensive handbook*. Johm Wiley & Sons, Inc., Hoboken, New Jersey.

Vizine, A. L., de Castro, N. L., Hruschka, E. R., and Gudwin, R. R. (2005). Towards improving clustering ants: An adaptive ant clustering algorithm. *Informatica 29*, pages 143–154.

Witten, I. H. and Frank, E. (2005). *Data Mining: Practical machine learning tools and techniques, 2nd Edition*. Morgan Kaufmann, San Francisco.

ADAPTATIVE SIGNAL SAMPLING AND SAMPLE QUANTIZATION FOR RESOURCE-CONSTRAINED STREAM PROCESSING

Deepak S. Turaga, Olivier Verscheure, Daby M. Sow and Lisa Amini
IBM T.J. Watson Research Center, 19 Skyline Drive, Hawthorne, NY, USA
turaga@us.ibm.com, ov1@us.ibm.com, sowdaby@us.ibm.com, aminil@us.ibm.com

Keywords: Remote Health Monitoring, ECG Compression, Low-complexity, Non-Uniform Sampling, Quantization.

Abstract: We propose a low-complexity encoding strategy for efficient compression of biomedical signals. At the heart of our approach is the combination of non-uniform signal sampling together with sample quantization to improve the source coding efficiency. We propose to jointly extract and quantize information (data samples) most relevant to the application processing the incoming data in the backend unit. The proposed joint sampling and quantization method maximizes a user-defined utility metric under system resource constraints such as maximum transmission rate or encoding computational complexity. We illustrate this optimization problem on electrocardiogram (ECG) signals, using the Percentage Root-mean-square Difference (PRD) metric as the utility function measuring the distortion between the original signal and its reconstructed (inverse quantization and linear interpolation) version. Experiments conducted on the MIT-BIH ECG corpus using the well-accepted *FAN* algorithm as the non-uniform sampling method show the effectiveness of our joint strategy: Same PRD as '*FAN* alone' at half the data rate for less than three times the (low) computational complexity of *FAN* alone.

1 INTRODUCTION

Remote Health Monitoring is an emerging technology allowing medical practitioners to extend their services to patients outside of traditional hospital settings. Common remote health monitoring systems are leveraging pervasive devices such as cellular phones to collect biomedical readings on patients and relay the data to servers while being non-intrusive and not restricting the mobility of patients (Mohomed et al., 2006). This usage of pervasive devices differ significantly from traditional client server usage models where the pervasive device acts as a client *receiving* data from a more powerful server. In the current model, the roles are reversed. Pervasive devices are used to *stream* data to back-end servers. Their resource scarceness creates interesting research challenges dictating the need for efficient, low complexity signal encoding schemes. This work proposes a generic method for streaming continuous signals under very strict resource constraints while minimizing the loss in valuable information the original signals carry.

While our method is applicable to a wide variety of signals, we describe it in the context of efficient, low complexity compression of electrocardiogram (ECG) signals. An ECG signal provides essential information to the cardiologist and is used for both monitoring and diagnostic purposes. An ECG monitoring device essentially measures the electrical impulses that stimulate the heart to contract. Between 125 and 500 sample points are collected every second, each coded on 8 or 12 bits (Nygaard et al., 2001). Thus, a single-lead uncompressed ECG signal requires between 1 kbps and 6 kbps of sustained wireless bandwidth. Any application based on wireless transmission of even moderate amounts of data must deal with the reality that usage of wireless spectrum will always incur some monetary cost. Efficient, low complexity compression is thus crucial to make remote health monitoring via low-end pervasive devices a reality.

The main goal of any compression technique is to achieve maximum data volume reduction while preserving the significant signal morphology features upon reconstruction (Jalaleddine et al., 1990). In ECG signal compression algorithms the goal is to achieve a minimum information rate, while retaining the relevant diagnostic information in the reconstructed signal. Compression techniques for ECG waveforms can be broadly classified into two main groups: direct time-domain techniques (Barr, 1988; Cox et al., 1968), and transform-domain techniques (Bradie, 1996; Hilton, 1997; Addison, 2005). Transform-based methods (e.g., wavelet-based) usually outperform time-domain techniques but require

a computational power beyond what a mainstream pervasive device can handle. Instead, well-accepted time-domain techniques, such as FAN (Barr, 1988) and AZTEC (Cox et al., 1968), rely on simple heuristics so as to non-uniformly sample the original waveform and retain only those data samples that contribute the most to the quality of the reconstructed (interpolated) signal.

Another well-known compression strategy is *quantization*. There are two types of quantization. Vector quantization, where the input symbols are gathered together in groups called vectors and processed to give the output, and scalar quantization, where each input symbol is treated separately in producing the output. Scalar quantization has a low computational complexity, is easy to implement and can achieve reasonably good compression performance if applied properly. There has been recent interests in the scientific community to design schemes performing jointly both quantization and uniform sampling in order to match the underlying system resource constraints (Derpich et al., 2006). Uniform sampling involves discarding samples of the data regularly to reduce the data rate. While uniform sampling can reduce the stream rate appropriately it does not guarantee the retention of all samples of interest (features), especially when the frequency characteristics of the signal are not well-behaved, which is clearly the case for ECG waveforms.

This work investigates the benefit of jointly performing non-uniform sampling (e.g., FAN or AZTEC) and quantization operations in the context of remote health monitoring. The paper is organized as follows: Section 2 introduces some notations and describes, in generic terms, the concept of joint non-uniform sampling and quantization. This concept applied to signal compression is the subject of Section 3, while Section 4 formulates the problem specifically for ECG compression under resource constraints using FAN (Barr, 1988) as the non-uniform sampling technique. The problem is posed as an optimization problem. The optimization problem is solved in Section 5. Finally, our strategy is validated in Section 6. And, Section 7 gives concluding remarks.

2 SIGNAL COMPRESSION: NON UNIFORM SAMPLING AND QUANTIZATION

Let $x[k], 0 \leq k < N$ denote a discrete time signal represented with b_u bits per sample.

2.1 Non Uniform Sampling

Non uniform sampling of $x[k]$ extracts $N_{SOI} \leq N$ samples of interests (SOI) from $x[k]$. We denote such sampling by the operator $\mathcal{S} : x[k] \rightarrow x[k_i]$ where k_i corresponds to the location of the retained samples of interest. The operator $\mathcal{S}$ is often lossy, and only an approximation to the original signal $x_r[k]$ may be recovered by interpolating $x[k_i]$ appropriately. If, after sampling, we retain N_{SOI} out of N samples, the achieved compression ratio is $\frac{N_{SOI} b_u}{N b_u}$, corresponding to a rate $\frac{N_{SOI} b_u}{N}$ bits per sample. Additionally, in the compressed rate we also need to include the bits required to encode the locations of the retained samples, i.e. an additional b_{loc} bits per sample. The selectivity of the sampling operator $\mathcal{S}$ is controlled by a sampling sensitivity parameter ε, with low values of ε corresponding to low selectivity, i.e. most samples from $x[k]$ are retained. To explicitly indicate the dependence of $\mathcal{S}$ on ε, we present it as $\mathcal{S}_\varepsilon$.

2.2 Quantization

Quantization is another well known lossy technique used to reduce the signal rate, when applications can tolerate the resultant distortion. We denote the quantization operator as $\mathcal{Q} : x[k] \rightarrow \hat{x}[k]$ where $\hat{x}[k]$ uses $b_q < b_u$ bits per sample, thereby reducing the average data rate of the stream by a factor $\frac{b_u}{b_q}$.

Given a periodic signal such as ECG, with relatively stationary probability density function (under known context, i.e. physical activity, health state etc.) the quantizer sensitivity is controlled only by the number of desired reconstruction levels[1] $L = 2^{b_q}$. As before, to explicitly indicate the dependence of $\mathcal{Q}$ on L, we represent it as $\mathcal{Q}_L$.

2.3 Joint Non-uniform Sampling and Quantization

Quantization, when used in conjunction with non-uniform sampling can further reduces the rate of the stream. When quantization is applied prior to sampling we have the resultant signal $\mathcal{S}_\varepsilon(\mathcal{Q}_L(x[k]))$ and when the signal is sub-sampled before quantization, the resultant signal is $\mathcal{Q}_L(\mathcal{S}_\varepsilon(x[k]))$. Note that these operators are not commutative, and the two cases are likely to achieve different compression factors. The compression gain is multiplicative, i.e. the corresponding rate of signal $\mathcal{Q}_L(\mathcal{S}_\varepsilon(x[k]))$ is $\frac{N_{SOI} b_q}{N} + b_{loc}$ bits per sample.

[1] The optimal values of these reconstruction levels are known for a standard MSE quantizer

3 DESIGN OF JOINT NON-UNIFORM SAMPLING AND QUANTIZATION BASED COMPRESSION

We can exploit the multiplicative gain in compression achieved by joint sampling and quantization to design better signal compression schemes. However, different types of signals and applications can tolerate different levels of quantization noise and require different numbers of samples of interest. Hence the joint design of quantization and non-uniform sampling needs to be performed carefully. Consider the two different operator options $\mathcal{S}_\varepsilon(Q_L)$ and $Q_L(\mathcal{S}_\varepsilon)$, and let the corresponding rates be $\frac{N_{SOI}^{\mathcal{S}_\varepsilon(Q_L)} b_q^{\mathcal{S}_\varepsilon(Q_L)}}{N} + b_{loc}^{\mathcal{S}_\varepsilon(Q_L)}$ and $\frac{N_{SOI}^{Q_L(\mathcal{S}_\varepsilon)} b_q^{Q_L(\mathcal{S}_\varepsilon)}}{N} + b_{loc}^{Q_L(\mathcal{S}_\varepsilon)}$. In order to design a good compression scheme, we also need to formally define a distortion metric. Let $x_r[k]$ represent the reconstructed signal, after decompression, i.e. $x_r[k] = \mathcal{S}_\varepsilon^{-1}(Q_L^{-1}(Q_L(\mathcal{S}_\varepsilon(x[k]))))$ or $x_r[k] = Q_L^{-1}(\mathcal{S}_\varepsilon^{-1}(\mathcal{S}_\varepsilon(Q_L(x[k]))))$. Then the utility associated with the compression may be defined in terms of $x[k]$ and $x_r[k]$ as $\mathcal{U}(x[k], x_r[k])$. The goal of designing the right compression scheme is to maximize this utility under a rate constraint. If the desired rate constraint is b_{con} (in bits per sample), the optimal compression scheme may be designed by solving the following constrained optimizations:

$$\{Q_{opt}, \mathcal{S}_{opt}\} = argmax_{\{Q_L, \mathcal{S}_\varepsilon\}} [\mathcal{U}(x[k], x_r[k])] \quad \text{subject to } \frac{N_{SOI}^{Q_L(\mathcal{S}_\varepsilon)}(b_q^{Q_L(\mathcal{S}_\varepsilon)})}{N} + b_{loc}^{Q_L(\mathcal{S}_\varepsilon)} \leq b_{con} \tag{1}$$

and

$$\{\mathcal{S}_{opt}, Q_{opt}\} = argmax_{\{\mathcal{S}_\varepsilon, Q_L\}} [\mathcal{U}(x[k], x_r[k])] \quad \text{subject to } \frac{N_{SOI}^{\mathcal{S}_\varepsilon(Q_L)}(b_q^{\mathcal{S}_\varepsilon(Q_L)})}{N} + b_{loc}^{\mathcal{S}_\varepsilon(Q_L)} \leq b_{con} \tag{2}$$

As mentioned earlier, designing the quantizer Q_L requires determining the number of quantization levels L and designing the non-uniform sampling $\mathcal{S}_{epsilon}$ strategy requires determining the optimal value for ε for a given non uniform sampling scheme. We thus reduce the problem of finding Q_{opt} and $\mathcal{S}_{opt}$ to the identification of the values of L and ε that maximizes the utility. Consequently, since $b_q^{Q_L(\mathcal{S}_{epsilon})} = \lceil \log_2 L \rceil$,1 and 2 can be rewritten as:

$$\{\varepsilon_{opt}, L_{opt}\} = argmax_{\{L,\varepsilon\}} [\mathcal{U}(x[k], x_r[k])] \quad \text{subject to } \frac{N_{SOI}^{Q_L(\mathcal{S}_\varepsilon)}(\lceil \log_2 L \rceil)}{N} + b_{loc}^{Q_L(\mathcal{S}_\varepsilon)} \leq b_{con} \tag{3}$$

and

$$\{\varepsilon_{opt}, L_{opt}\} = argmax_{\{\varepsilon,L\}} [\mathcal{U}(x[k], x_r[k])] \quad \text{subject to } \frac{N_{SOI}^{\mathcal{S}_\varepsilon(Q_L)}(\lceil \log_2 L \rceil)}{N} + b_{loc}^{\mathcal{S}_\varepsilon(Q_L)} \leq r_{con} \tag{4}$$

If the order of the quantization and non-uniform sampling also needs to be determined, we may compare the optimal utilities in the two cases to determine the best order. Solving the joint optimization presented in equations 4 and 3 is non-trivial. This optimization is heavily dependent on the relationships between $\mathcal{U}$ and N_{SOI} and the pair (ε, L). For a generic sampling algorithm, for a signal with arbitrary characteristics, it is likely to be very difficult to determine the optimal solution without some form of computationally complex exhaustive search. In some cases, however, for sampling algorithms such as FAN, and for well-behaved signals such as ECG, we show that these relationships can be estimated experimentally, and modeled using simple parametric functions. This enables tractable, and low complexity algorithms to solve the optimization in real time. In the following sections, we present several parametric model based approaches to trade-off computational complexity for accuracy, while solving this optimization for the FAN algorithm with MSE quantization for the ECG signal.

4 ENCODING ECG SIGNALS FOR REMOTE HEALTH MONITORING

We illustrate our approach to jointly quantize and sample non uniformly waveforms by focusing on the representation of electrocardiogram (ECG) signals. This proposed technique implements adaptive sampling before quantization (i.e. $\mathcal{S}$ before Q).

4.1 Brief Background on ECG Signals

A typical electrocardiogram monitoring device generates large volumes of digital data. Depending on the intended application, the sampling rate may range from 125 to 1000 Hz, with each data sample digitized to a 8-16 bit value. This translates to a minimum data rate of 15 KB per minute. Transmitting this signal over a low-bandwidth channel, especially when aggregating data from multiple sensors, requires compression. The data needs to also be recorded over long periods, often as much as 24 hours, and doctors may wish to build a database of ECG recordings for their patients. Minimizing the storage resources also requires data compression.

4.2 Adaptive Sampling

FAN (Barr, 1988) is a standard sampling technique for ECG signal compression and was reported in 1964 by (Gardenhire, 1964). It extracts samples of interest by approximating the signal using a piecewise linear representation, and discards all but the terminal points along these line segments. More precisely, the FAN algorithm replaces the signal with straight line segments such that none of the original points lies further from the line segment than some predetermined maximum deviation threshold τ. Figure 1 visually describes the algorithm. The first point $x[k_0]$ is accepted as non-redundant (permanent sample). Two slopes $\{L_1, U_1\}$ are drawn between $x[k_0]$ and $\{x[k_1]-\tau, x[k_1]+\tau\}$. The third sample point $x[k_2)]$ falls within the area bounded by the two slopes. Thus new slopes $\{L_2, U_2\}$ are calculated between $x[k_0]$ and $x[k_2]\pm\tau$ respectively. Then the two pairs of slopes are compared and the most restrictive are retained: $U_2 = \min(U_2, U_1)$ and $L_2 = \max(L_1, L_2)$. Since sample $x[k_1]$ lies inside the range it is thus discarded; while $x[k_2]$ is accepted as a permanent sample and the procedure above is repeated, comparing future sample values to the most restrictive lines. During signal reconstruction, the discarded samples are linearly interpolated from their neighboring retained samples.

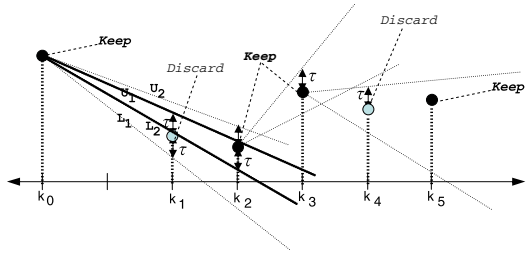

Figure 1: FAN algorithm for non-uniform sampling.

The deviation threshold τ determines the quality of the approximation with large τ leading to more samples being discarded, and coarser signal approximation. In our setting, this threshold τ maps directly to the sampling sensitivity ε, and we use the two interchangeably. The FAN algorithm has been used widely for ECG signal compression as it is extremely computationally lightweight ($O(N)$ for N samples), and performs reasonably well in practice, in terms of retaining samples and features of interest. However, for small target bit-rates (under 2 bits per sample), the FAN algorithm often underperforms computationally more complex ($O(N^2)$) algorithms such as Cardinality Constrained Shortest Path (CCSP). In this bit-rate range, we wish to improve the performance of FAN by combining it with quantization. Combination with a simple quantization can retain the low-complexity nature of FAN, while improving its compression quality.

4.3 Joint FAN Sampling and Quantization

The reconstruction quality of compressed ECG signals is often captured using the percentage root-mean-square difference (PRD) between the original signal and its reconstructed (inverse quantization and linear interpolation) version. The reconstructed signal $x_r[k]$ is determined from the sampled and quantized signal by inverse quantization and linear interpolation.

Hence, the utility function is defined as:

$$\mathcal{U}(x[k], x_r[k]) = -100 * \sqrt{\frac{\sum_{j=1}^{N}(x[j]-x_r[j])^2}{\sum_{j=1}^{N}x[j]^2}} \quad (5)$$

Finally the joint sampling and quantization problem, given a rate constraint b_{con} (in bits per sample), may be written as the following optimization:

$$\begin{aligned} \{\varepsilon_{opt}, L_{opt}\} &= argmax_{\{\varepsilon,L\}}\left[\mathcal{U}(x[k], x_r[k])\right] \\ \text{subject to } &\frac{N_{SOI}^{S_\varepsilon(Q_L)} b_q^{S_\varepsilon(Q_L)}}{N} + b_{loc}^{S_\varepsilon(Q_L)} \leq b_{con} \end{aligned} \quad (6)$$

The search complexity for a naive implementation of the solution to this problem is $O(|\Omega_\tau| \times |\Omega_L|)$ where Ω_ε is the set of possible values for ε, Ω_L is the set of possible values for L and $|\bullet|$ is the cardinality operator. This is a constant factor that multiplies the complexity of the FAN algorithm (thereby linearly increasing the complexity). However, this is a worst case metric as it assumes no apriori knowledge of the underlying ECG signal. Due to the periodic nature of the ECG signal, the designed answer is likely to change slowly with time (across consecutive windows of N samples each), and hence we can distribute this complexity over several windows. This may be done by either solving the optimization once every Z windows, thereby reducing the overhead complexity to $O(\frac{|\Omega_\varepsilon| \times |\Omega_L|}{Z})$ or by reducing the space of possible search values, i.e. the number of elements in each set (allowing only for small variations in the previously designed values).

Additional improvement in performance may be obtained by actually designing the complete quantizer (including the design of the optimal resonstruction levels) dynamically. This however comes at a cost of increased complexity. In the worst case, a standard k-means based implementation of quantizer design has complexity $O(N^L)$. Of course, this cost may also be distributed across several windows (due to the nature

of the ECG signal) to reduce the computational complexity. The design of optimal low-cost quantizers in conjunction with the sampling is an interesting direction of future research.

5 MODEL BASED SEARCH STRATEGY

A model based search strategy is enabled by the reasonably stationary characteristics of the ECG signal, and the somewhat predictable behavior of the FAN algorithm. Specifically, we observe, that in a particular operating region (defined by the rate constraint, e.g. number of bits per sample, and the corresponding quality metric, i.e. PRD) we may develop simple parametric models that capture the effect of L and ε on the utility (PRD) and the rate (bits per sample). As an example, we run the FAN algorithm several times on a real ECG signal with different values of ε and plot the resulting number N_{SOI} of samples retained, and the corresponding distortion *PRD* in Figure 2.

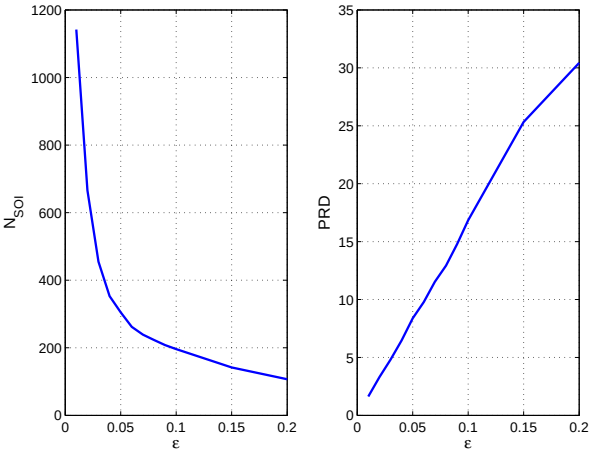

Figure 2: N_{SOI} and *PRD* as functions of ε.

As is clear, N_{SOI} has an almost exponentially decaying relationship with ε, while the *PRD* has a near-linear relationship with ε, and we can capture these relationships very simply as follows

$$N_{SOI}(\varepsilon) = \mu e^{-\nu\varepsilon} \tag{7}$$

and

$$PRD(\varepsilon) = \alpha + \beta\varepsilon \tag{8}$$

where μ, ν, α, and β are the model parameters. If we now combine this sampling with quantization using L levels, we can derive the resulting bit-rate for the compressed signal (in bits per sample) as

$$b_q^{Q_L(s_\varepsilon)} = \frac{N_{SOI} log_2(L)}{N} \tag{9}$$

Using Equation 7, we may rewrite this as

$$b_q^{Q_L(s_\varepsilon)} = \frac{\mu e^{-\nu\varepsilon} log_2(L)}{N}. \tag{10}$$

In order to build a similar model for the *PRD* as a joint function of ε and L, we plot the resulting PRD (after FAN followed by quantization) in Figure 3. Clearly,

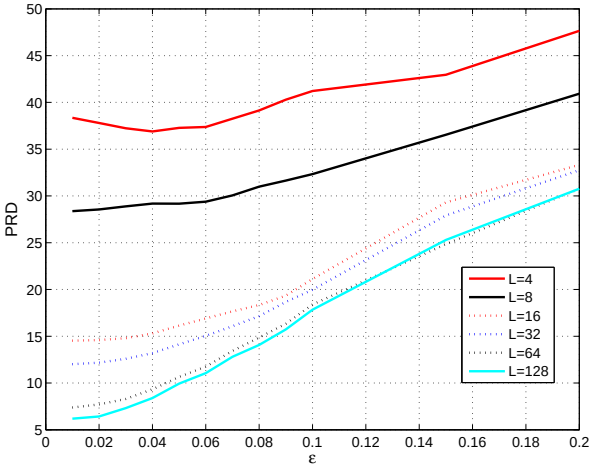

Figure 3: *PRD* as function of ε and L.

the slope and intercept of the line relating *PRD* to ε change with L. After further investigation, we find that this relationship may be captured as

$$\alpha(L) = \gamma e^{-\rho L} \tag{11}$$

and

$$\beta(L) = \eta \times log(\xi L_Q). \tag{12}$$

Combining these equations, we may rewrite the model for *PRD* after joint sampling followed by quantization as

$$PRD = \gamma e^{-\rho L_Q} + \eta\varepsilon log(\xi L_Q) \tag{13}$$

These models for *PRD* and $b_q^{Q_L(s_\varepsilon)}$ are validated for a real ECG signal in Figure 4 and Figure 5. While the models tend to underestimate the real values (especially for small ε), the shapes of the curves remain similar allowing for a search strategy using this model.

5.1 Three Times FAN Strategy

In order to compress the ECG signal under a rate constraint, we first partition it into fixed size windows (each with W samples[2]). Then per window, we run

[2]Note that since we process the window independently, we have $N = W$

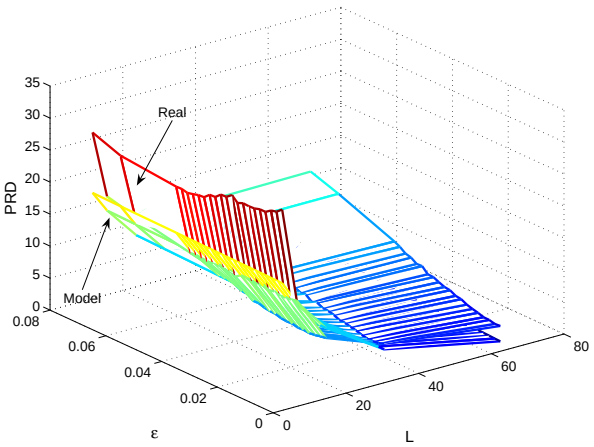

Figure 4: *PRD*: Real value versus model prediction.

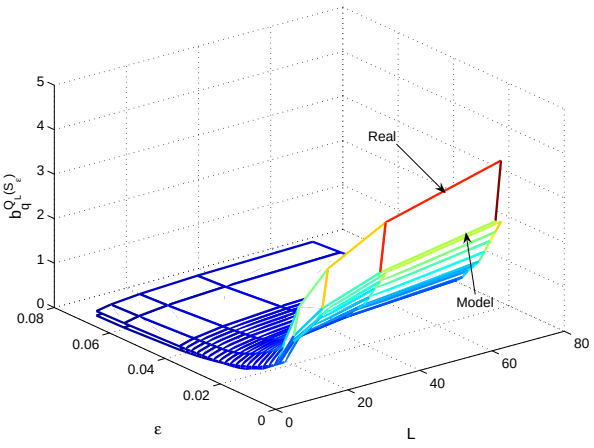

Figure 5: b_q: Real value versus model prediction.

the FAN algorithm for two different values of ε (a high value and a low value), to determine two values for N_{SOI} followed by quantization with two different numbers of levels L (a high value and a low value) to determine four values of *PRD*. The four values of *PRD* provide us with four equations to solve for parameters γ, ρ, η and ξ. Similarly, the two values of N_{SOI} provide us with two equations to solve for parameters μ and ν. Once we determine the model for a given window, it is straightforward to determine the optimal parameter settings for ε and L under any specified rate constraint. Once we determine the optimal parameter settings, we then need to run FAN once with the selected ε_{opt} followed by quantization with L_{opt} levels. Hence, per window we run the FAN algorithm three times.

5.2 Two Times FAN Strategy

We exploit the near stationarity of the ECG signal characteristics to reduce the complexity of the Three Times FAN strategy. Specifically, while for the first window we employ the same approach (with two times FAN followed by two times quantization) for every subsequent window we run the FAN algorithm for only one additional value of ε followed by quantization with two different values of L. This provides us with two values of *PRD* and one value of N_{SOI}. In order to compute the model parameters, we then combine this with two values of *PRD* and one value of N_{SOI} computed from the previous window. We alternate between recomputing the *PRD* and N_{SOI} for the high ε, and the *PRD* and N_{SOI} for the low ε (correspondingly reusing these for the low ε and high ε, respectively, from the previous window), for every successive window. Note that it is possible to easily extend this approach to recompute the model parameters only once every Z windows, to further reduce complexity. We examine some of the tradeoffs between complexity and accuracy by comparing the performance of these algorithms, and using that to identify trends for other extensions.

6 EXPERIMENTAL RESULTS

We evaluate the performance of these algorithms on ECG signals from the MIT-BIH database. Specifically, we use a subset of this database, consisting of 10 different ECG signals, of duration 8000 samples each. For these signals we evaluate the different strategies described in Table 1. We compare FANEX, FANQEX, FANQMS-3 and FANQMS-2 in terms of their distortion (PRD)-rate (bits per sample) curves, and also in terms of their computational complexity. We present results for different processing window sizes (W) to identify the general performance trend variations. Each window consists of W samples of the signal, and is analyzed and processed independently by the different algorithms, specifically in terms of computing the optimal parameters ε and L, and using the FAN algorithm with these parameters. We limit the search space for the exhaustive search strategies by considering a finite small set of possible values that ε and L can take. For our experiments we have $\varepsilon \in \{0.002, 0.004, \cdots, 0.04, 0.05, 0.06\}$ and $L \in \{4, 8, 16, 32, 64\}$. We first consider a processing window of size $W = 1000$ samples, and present the distortion-rate (D-R) curve averaged across these signals (across the 8 windows per signal) for the four different algorithms in Figure 6.

In Figure 6 we observe that the schemes with joint

Table 1: Algorithms Considered.

Name	Uses Quantization	ε only or (ε, L) search strategy
FANEX	No	Exhaustive
FANQEX	Yes	Exhaustive
FANQMS-3	Yes	Model Based - Three Times FAN
FANQMS-2	Yes	Model Based - Two Times FAN

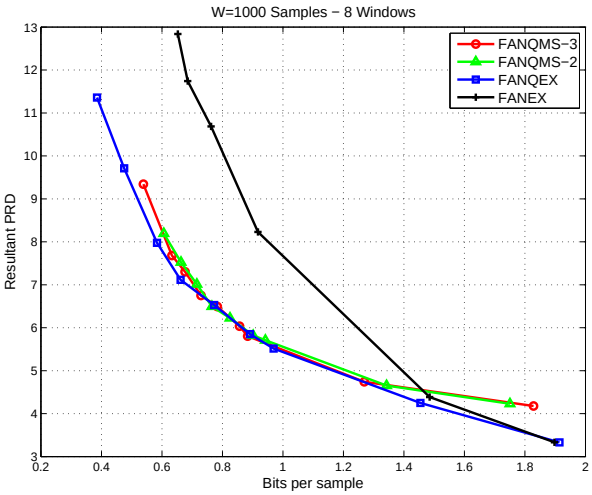

Figure 6: D-R Curves: $W = 1000$.

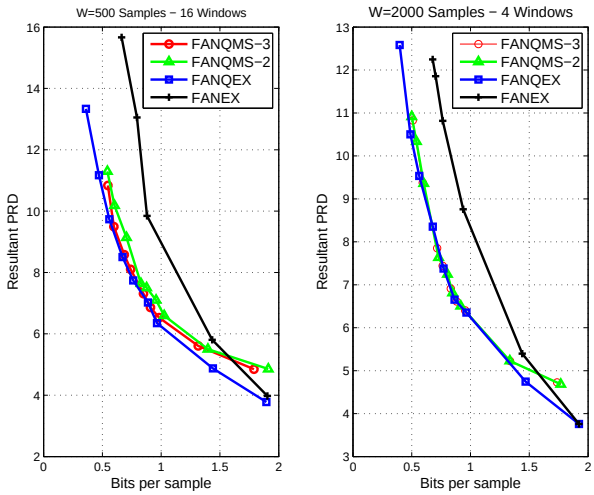

Figure 7: D-R Curves: $W = 500$(left), $W = 2000$(right) .

quantization and FAN significantly outperform the FAN only scheme, a compression factor of 2 for the same PRD. This makes the performance of the FAN algorithm comparable to the state-of-the art compression algorithms (with significantly higher complexity). Furthermore, we find that the model based searches FANQMS-3 and FANQMS-2 have performance very close to that achieved by the exhaustive search for target bit-rates less than 2 bits per sample. As the target bit-rate starts to approach 2 bits per sample, the model based search strategies underperform the FANEX strategy, as the models are inaccurate[3] for this range. However, note that for this higher bit-rate range, the performance of the FAN algorithm by itself is comparable to the best ECG compression algorithms presented, thereby limiting any gains obtained by additionally quantizing the signal. We also repeat these experiments for a smaller window ($W = 500$) and a larger window ($W = 2000$, and the results are presented in Figure 7.

From Figure 7, the same performance trend is observed as in Figure 6 for the four algorithms, however it is clear that the performance of FANQEX, FANQMS-2, and FANQMS-3 are closer to each other for larger W. This may be explained by the fact that a larger window size allows the model based algorithms to fit better parameterized curves, improving the performance of the model based search schemes. This is also evident from the fact that on average, the PRD for the same target bit rate decreases with increasing W. We also compare the computational complexity of these algorithms in terms of the amount of CPU time consumed per window. These CPU times are labeled t_{FANEX}, t_{FANQEX}, $t_{FANQMS-2}$ and $t_{FANQMS-3}$ respectively. We also label the time taken to run the FAN algorithm on one window as t. Instead of presenting absolute numbers, we present relative ratios of the complexity of these algorithms to hide the dependency on the underlying computer architecture, operating system etc. These complexity ratios for the different algorithms are presented in Table 2.

It is evident from Table 2 that FANQMS-3 has 29 (FANQMS-2 has 45 times) lower complexity than FANQEX and 4 times (FANQMS-2 has 7 times) lower complexity than FANEX. Further, as expected, FANQMS-2 has lower complexity than FANQMS-3. This observation holds across the two different window sizes considered. Furthermore, FANQMS-3 has 4 times the complexity of FAN, while FANQMS-2 has 3 times the complexity of running FAN one time. This implies that the search for the optimal ε and L has the complexity 1.5 times that of the FAN algorithm. Note that by reusing the model parameters

[3] Assumptions on linear, exponential and log-linear relationships are violated in this range.

Table 2: Complexity Comparison.

W	$\frac{t_{FANQEX}}{t_{FANQMS-3}}$	$\frac{t_{FANEX}}{t_{FANQMS-3}}$	$\frac{t_{FANQMS-3}}{t}$	$\frac{t_{FANQEX}}{t_{FANQMS-2}}$	$\frac{t_{FANEX}}{t_{FANQMS-2}}$	$\frac{t_{FANQMS-2}}{t}$
500	29.18	4.50	4.18	47.75	7.35	2.80
1000	29.06	4.49	4.21	46.07	7.12	2.64

across more windows (updating model infrequently), this overhead can also be significantly reduced. This is also indicated by the comparing the rows of Table 2, as the complexity gains for FANQMS-2 increase as W increases from 500 to 1000 (the ratio $\frac{t_{FANQMS-2}}{t}$ decreases from 2.80 to 2.64).

7 CONCLUSIONS

We present a low-complexity joint non-uniform sampling and quantization based strategy for signal compression. Specifically, we combine the FAN algorithm with a minimum mean-squared error quantization strategy to compress ECG signals. We first formulate the joint design of non-uniform sampling and quantization for compression, as a constrained optimization problem in terms of maximizing the relevant distortion metric given the desired compression rate. The solution of this optimization yields the optimal sampling sensitivity, and the number of levels to be used by the quantizer. In general, and for arbitrary signals, it may not be possible to solve this optimization efficiently. However, for ECG signals, we show that we can develop simple parametric models to capture the impact of the FAN algorithm and quantization on the resulting distortion (PRD) and rate, especially in very low bit-rate operating regions. Using these models we can efficiently determine the optimal FAN selectivity parameter ε and quantization levels L to minimize the PRD for a given rate constraint. We design two model based algorithms, one that re-estimates model parameters for every window (W samples), and another that updates model parameters every alternate window. We show that with these strategies, we can achieve up to 2 times the compression rate of FAN (for the same PRD) with a complexity less than 3 times that of FAN alone. We also show that the performance of these algorithms approaches (within 10% in rate when $\varepsilon < 1.8$) an exhaustive search based strategy for different signals, and window sizes. Given the low complexity of FAN our algorithms still remain significantly lower complexity than state-of-the-art transform based compression schemes, while achieving comparable performance. Directions for future research include design of the optimal search strategy to re-estimate model parameters (how often, optimal window size etc.), theoretical analysis of the signal frequency and statistical properties as well as algorithm complexity for rate-distortion-complexity optimal joint sampling and quantization, and application of these ideas for other multi-dimensional medical signals.

REFERENCES

Addison, P. S. (2005). Wavelet transforms and the ecg: a review. In *Physiological Measurement*, volume 26.

Barr, R. C. (1988). Adaptive sampling of cardiac waveforms. In *Journal of Electrocardiology*, volume 21, pages 57–60.

Bradie, B. (1996). Wavelet packet-based compression of single lead ecg. In *IEEE Transactions on Biomedical Engineering*, volume 43, pages 493–501.

Cox, J., Fozzard, H., Nolle, F. M., and Oliver, G. (1968). Aztec: A preprocessing system for real-time ecg rhythm analysis. In *IEEE Transactions on Biomedical Engineering*, volume 15, pages 128–129.

Derpich, M., Quevedo, D., Goodwi, G., and Feue, A. (2006). Quantization and sampling of not necessarily band-limited signals. In *IEEE International Conference on Acoustics, Speech and Signal Processing*, volume 3.

Gardenhire, L. W. (1964). Redundancy reduction the key to adaptive telemetry. In *National Telemetering Conference*, pages 1–16.

Hilton, M. L. (1997). Wavelet and wavelet packet compression of electrocardiograms. In *IEEE Transactions on Biomedical Engineering*, volume 44, pages 394–402.

Jalaleddine, S., Hutchens, C., Strattan, R., and Coberly, W. (1990). Ecg data compression techniques-a unified approach. In *IEEE Transactions on Biomedical Engineering*, volume 37, pages 329–343.

Mohomed, I., Ebling, M. R., Jerome, W., and Misra, A. (2006). Harmoni: Motivation for a health-oriented adaptive remote monitoring middleware. In *UbiHealth'06, Fourth International Workshop on Ubiquitous Computing for Pervasive Healthcare Applications*, Irvine, CA, USA.

Nygaard, R., Melnikov, G., and Katsaggelos, A. (2001). A rate distortion optimal ecg coding algorithm. In *IEEE Transactions on Biomedical Engineering*, volume 48, pages 28–40.

UNVEILING INTRINSIC SIMILARITY
Application to Temporal Analysis of ECG

André Lourenço
Instituto de Telecomunicacoes, Instituto Superior de Engenharia de Lisboa, Portugal
alourenco@deetc.isel.ipl.pt

Ana Fred
Instituto de Telecomunicacoes, Instituto Superior Tecnico, Lisboa, Portugal
afred@lx.it.pt

Keywords: Visualization, Unsupervised Learning, Clustering, Evidence Accumulation Clustering, Co-association Matrix, ECG Analysis, Behavior Identification.

Abstract: The representation of data in some visual form is one of the first steps in a data-mining process in order to gain some insight about its structure. We propose to explore well known visualization and unsupervised learning techniques, namely clustering, to improve the understanding about the data and to enhance possible relations or intrinsic similarity between patterns. Specifically, Clustering Ensemble Methods are exploited separately and combined to provide a clearer visualization of data organization. The presented methodology is used to improve the understanding of ECG signal acquired during Human Computer Interaction (HCI).

1 INTRODUCTION

Critical to the understanding of data is the ability to provide its pictorial or visual representation. This process is particularly relevant for analyzing large volumes of complex data (e.g. multidimensional) that are available from a variety of sources. The human visual system has an enormous capacity for receiving and interpreting data efficiently (Treinish and Goettsche, 1989).

There are many numerical and statistical techniques that can be used to analyze structural information from multidimensional data. Discovery and understanding of the structure in the data has many applications in science and business. Examples of structure include clusters, regular patterns, outliers, distance relations, proximity/similarity of data points, etc... (Post et al., 2003).

The underlying tool for most of the pattern recognition methods is a distance function, or more generally a similarity or dissimilarity measure. In the literature there are many proposed similarity/dissimilarity measures (see (Fred, 2002) and the references therein). Moreover each clustering algorithm induces a similarity measure between data points, according to the underlying clustering criteria (Fred and Jain, 2006). The representation of such similarities is the focus of this paper.

Multidimensional scaling (MDS) techniques enable the representation of multidimensional data (embedded in an n-dimensional space) in lower dimensional spaces such that the structural properties of the data are preserved. Given a dissimilarity (or similarity) pairwise matrix (containing pairwise information), MDS techniques represent the objects in a low-dimensional space, preserving all pairwise, symmetric dissimilarities between data objects (Pekalska and Duin, 2003).

Data clustering and Unsupervised learning is used in many disciplines and contexts, as an exploratory data analysis (EDA) tool. Ensemble methods, namely the evidence accumulation clustering (EAC) technique (Fred and Jain, 2005), represent state of the art in data clustering methods, and a way of learning the pairwise similarity between the data in order to proper partitioning the data points (Fred and Jain, 2006).

In this paper we present a methodology based on data Clustering techniques, aiming at improving the understanding about the data, enhancing its intrinsic structure. We apply this methodology to electrophysiological data, namely ECG, provided under the scope of a HCI study.

The paper is organized as follows: in section 2 we briefly present the MDS techniques; in section 3

we formalize the clustering problem and present several methods to enhance the intrinsic data structure: in subsection 3.1 using the dissimilarity matrix; and in subsection 3.2 mapping the associations in a new similarity measure using the evidence accumulation clustering method. Finally, in section 4, this methodology is presented in the analysis of ECG data. Throughout the paper we present illustrative examples.

2 MULTIDIMENSIONAL SCALING

Multidimensional scaling (MDS) in wide sense refers to any technique that produces a geometric representation of data, on a low dimensional space, usually Euclidean, where quantitative or qualitative relationships in data are made to correspond with geometric relationships in the geometric representation (Cox and Cox, 1994) (de Leeuw, 2000). Data objects judged to be similar to one another result in points being close to each other in this geometric representation (Pekalska and Duin, 2003). For more technical details about MDS techniques consult Cox and Cox (Cox and Cox, 1994) or Pekalska and Duin (Pekalska and Duin, 2003).

As input for these techniques it is required a measure of similarity (or dissimilarity - inversely related to similarity) between objects in the high-dimensional space. Consider δ_{ij} a measure of dissimilarity (usually called *disparity*) between the data objects i and j, and d_{ij} the estimated geometric distance in the low dimensional space used to represent data objects i and j. The *raw stress*, is the most elementary MDS loss function, which quantitatively characterizes a given geometric configuration for the data representation:

$$S^{raw}(X) = \sum_{i=1}^{n-1} \sum_{j=i+1}^{n} (\delta_{ij} - d_{ij})^2 \qquad (1)$$

An iterative optimization process can be used to find a geometric configuration that minimizes the loss function presented above (or other given in the literature).

Consider as an illustrative example of the MDS technique a 2-dimensional representation of a set of 4-dimensional gaussian data (R^4), with identical covariance matrices ($\Sigma = 0.5I_4$), and centered, respectively in $\mu_1 = [3,0,0,0]$, $\mu_2 = [0,3,0,0]$, $\mu_3 = [0,0,3,0]$ and $\mu_4 = [0,0,0,3]$. Figure 1(a) represents the matrix plot of the multidimensional data (that is: the i-th row and j-th column of this matrix is a plot of X_i variable versus X_j variable; the main diagonal represents the histograms of each variable). Figure 1(b) presents the

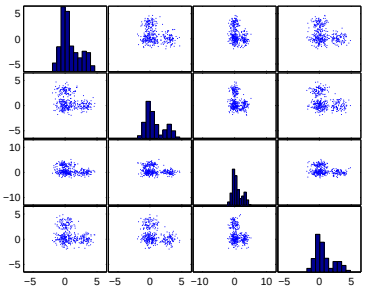

(a) Matrix Plot

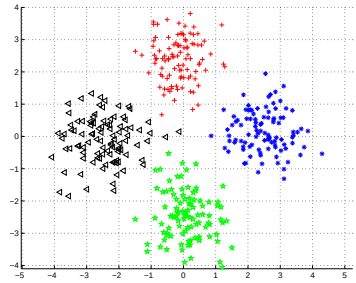

(b) MDS

Figure 1: Multidimensional data representation. Projections in 2-D dimensional spaces. MDS configuration.

obtained configuration in the 2-D euclidean space, using as optimization criteria the Kruskal's normalized stress1 criterion (equation above). For better understanding of the obtained representation, different colors and shapes where used to represent each of the different gaussians. In the next section we will briefly review the methods that unsupervisely group data objects.

3 CLUSTERING

The goal of clustering is to enhance the interpretability of the data by organizing data in meaningful groups (or clusters) such that the patterns in a cluster are more similar to each other than patterns in different clusters (Jain and Dubes, 1988), (Pekalska and Duin, 2003). Each clustering algorithm visualizes data in a different way, inducing different similarity measures between data points according to the underlying clustering criteria (Fred and Jain, 2006).

There are a number of problems with clustering methods. The most important one is that there are

Clustering is a difficult problem, hundreds different techniques have been proposed in the literature, yet no single algorithm is able to identify all sorts of

cluster shapes and structures that are encountered in practice.

A recent trend in clustering, that constitutes the state-of-the art in the area, are the clustering combination techniques (also called ensemble methods). They attempt to find a robust data partitioning by combining different partitions produced by a single or multiple clustering algorithms. Several combination methods have been proposed (Fred, 2001; Strehl and Ghosh, 2002; Fred and Jain, 2002; Topchy et al., 2004) to obtain the combined solution.

3.1 Dissimilarity Matrix

There is some work in visual approaches for assessing cluster tendency (Bezdek and Hathaway, 2002) based directly on visualizing the dissimilarity matrix obtained from the data. In (Bezdek and Hathaway, 2002) Bezdek and *al.* presented an algorithm - the visual assessment of cluster tendency (VAT) - which reorders the dissimilarity data so that possible clusters can be enhanced.

The images in Figure 2 are intensity image, where the intensity or gray level of the pixel (i,j) depend on the value of δ_{ij}, the dissimilarity between sample i and j. The value 0 corresponds to pure black; and the pure white represent the maximum dissimilarity. They were obtained with Euclidean distance for the gaussian data set presented previously. The figure 2(a) represents the obtained dissimilarity images when the samples are randomly positioned, and the figure 2(b) when the samples are re-organized so that the samples that are close together are as near as possible (as described in VAT (Bezdek and Hathaway, 2002)). By analyzing this dissimilarity image we identify dark rectangular areas, characteristic of items that are close together and that could constitute a cluster.

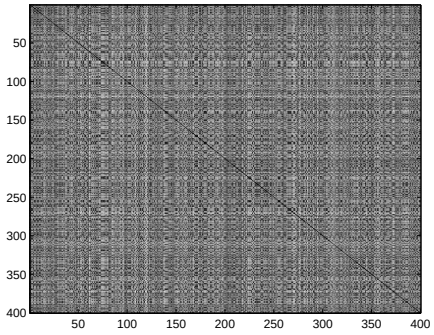

(a) Dissimilarity Matrix

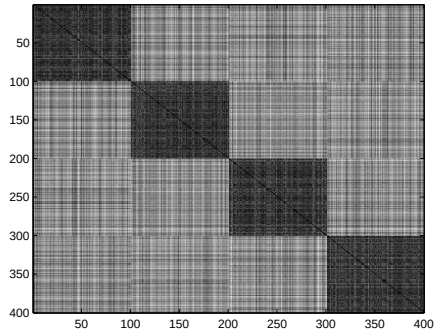

(b) VAT

Figure 2: Dissimilarity Images.

3.2 Evidence Accumulation Clustering

The Evidence Accumulation Clustering (EAC), proposed by Fred and Jain in (Fred, 2001) (Fred and Jain, 2005), is one of the clustering combinations techniques proposed in the literature. This method combines different visions over the data set, obtained by different algorithms or a single algorithm with different initializations, aiming to find the intrinsic similarity of the data. The different partitions obtained by the clustering algorithms, are called the *clustering ensemble*.

The EAC is based on the mapping of the relationships between pairs of patterns into a $n \times n$ co-association matrix, $\mathcal{C}$. This matrix accumulates the co-occurrence of pairs of samples in the same cluster over the N clusterings of the clustering ensemble $\mathbb{P}$ according to the equation:

$$\mathcal{C}(i,j) = \frac{n_{ij}}{N}, i,j \in 1,..,N \qquad (2)$$

where n_{ij} represents the number of times a given sample pair (i,j) has co-occurred in a cluster over the N clusterings. Assuming that patterns belonging to a "natural" cluster are very likely to be co-located in the same cluster in different clusters of the partitions of the clustering ensemble, the co-occurrences of pairs of patterns summarizes the inter-pattern structure perceived from these clusterings. Each co-occurrence of a pair of samples in the same cluster are taken as a vote for the association of those samples. For that reason this method is also known as majority voting combination scheme. In order to recover the natural clusters, and to emphasize the neighborhood relationships, in (Fred, 2001), the Single-link hierarchical algorithm (Jain and Dubes, 1988) is applied on the new feature space represented by the co-association matrix, yielding the combined data partition P^*. Other algorithms may be applied in this final step (Fred and Jain, 2005).

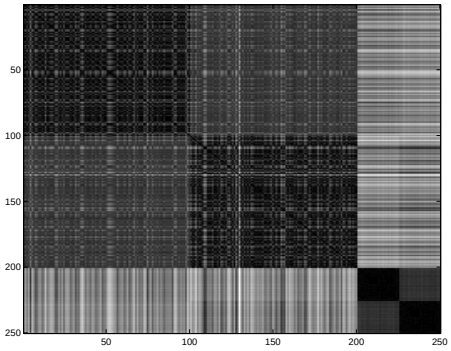

(a) Dissimilarity Matrix.

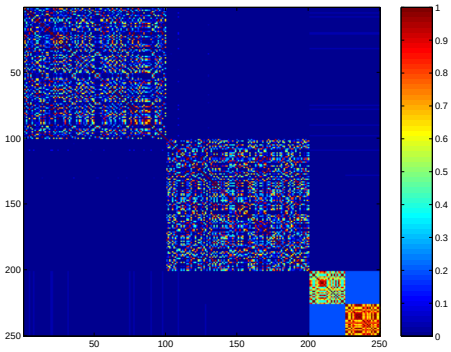

(b) Co-association matrix based on the ensemble.

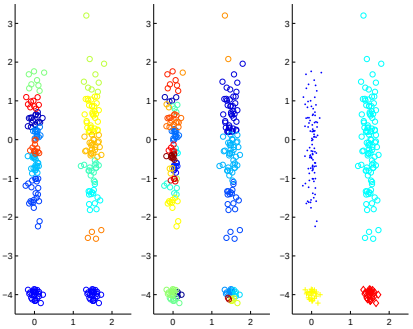

(c) One of the partitions of the ensemble, k=14

(d) One of the partitions of the ensemble, k=28

(e) EAC combined partition.

Figure 3: Individual clusterings and combination results on the cigar data-set using a k-means ensemble.

Figure 3 presents a typical application of the EAC method on an artificial data set (cigar data-set). An ensemble of 25 partitions was produced using the k-means algorithm with random initialization and with k randomly chosen in the interval [10,30]. Examples of obtained partitions are illustrated in (c) and (d). The combination result is presented in (e). The *co-association* matrix (illustrated in (b)), corresponds to a new similarity between samples based on the information accumulated from the partitions in the clustering ensemble. In figure the axis represent the samples of the data set, organized such that samples belonging to the same cluster are displayed contiguous (as described in section 3.1). The color scheme in the figure ranges from red to blue, corresponding to a gradient in similarity. Pure Red corresponds to the highest similarity. It can be seen that, although individual data partitions are quite different, neighboring patterns occur in the same cluster in most of the partitions. As a result, the true structure of the clusters becomes more evident in the co-association matrix: notice the more clear separation between clusters (large blue zones) and more evident block diagonal structure in figure 3(b) as compared to the original dissimilarity matrix in figure 3(a).

In the described method each partition is given an equal weight in the combination process and all clusters in each partition contribute to the combined solution. Other approaches were taken, for example, weighting/selecting the partitions based on the quality of the overall partitions. More recently, instead of evaluating the overall performance of a clustering algorithm based on the final partition produced by it, in (Fred and Jain, 2006) it is assumed that each algorithm can have different levels of performance in different regions of the multidimensional space. It is proposed to learn pairwise similarity based on meaningful clusters, which can be identified based on cluster stability criteria. Thus only those clusters passing the stability test will contribute to the co-association matrix an to the learned similarity matrix yielding a more robust solution. Figure 4 presents this matrix for the same data set as above. We observe that the rectangular areas are perfectly defined clearly distinguishing the underlying clustering structure. When represented via MDS this matrix yields 4 separate points in the 2-dimensional space.

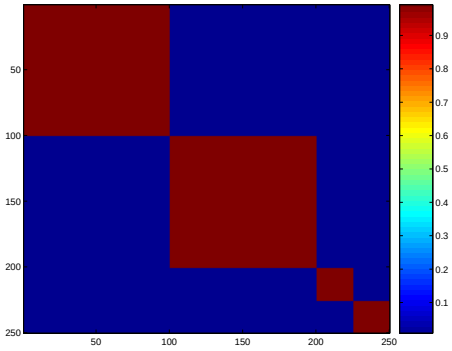

Figure 4: Learned co-association matrix.

4 ECG ANALYSIS

We applied the previous methodology to the analysis of ECG recordings, performed during the execution of a cognitive task using the computer, based on the work on (Silva et al., 2007). The ECG acquisition was part of a wider multi-modal physiological signal acquisition experiment aiming personal identification. The task consisted on a concentration task where two grids with 800 digits were presented, with the goal of identifying every pair of digits that added 10 and was designed for an average completion time of 10 minutes. A collection of 53 features were extracted from mean ECG waves for groups of 10 heart-beat waveforms (without overlapping): 45 amplitude values measured at sub-sampled points and 8 latency and amplitude features were also extracted (for more details see (Silva et al., 2007)).

Instead of using the ECG features for personal identification, herein we study the data in a data-exploratory perspective, trying to find its underlying time evolution. The task was designed to induce stress in the subject (for more details see (Silva et al., 2007)) thus the ECG characteristics should vary over time. The aim of this preliminary analysis is access typical patterns of temporal evolution over the subjects based on the ECG extracted features.

For each subject, the temporal evolution of the ECG characteristics was performed as follows: each time window, represented by the 53 features, constitutes a sample; the application of clustering over these samples reveals groups of samples representing 'stable' phases of temporal behavior over the ECG. According to the previous ensemble methodology, we constructed a clustering ensembles of $N = 75$ K-means partitions with varying number of clusters, $k \in [2, 30]$, applying the EAC approach and analyzed the induced similarity matrix.

We applied this technique over the 26 subjects that performed the task. Figure 5 presents one example of the typical structures obtained in the analysis. Figure 5(a) represents the obtained co-association matrix. In this co-association matrix adjacent patterns (in rows and columns) represent time aligned samples (0 represents the beginning of the test) of the ECG recording. It is interesting to note its block diagonal structure revealing time relationships between the patterns. This structure is not so evident as in the previous toy example, but a similar diagonal pattern can be inferred.

Using the Ward's link and the life time criteria for choosing the number of clusters, 6 clusters are obtained. In figure 5(b) we present the temporal evolution of such clusters: x-axis correspond to the samples order by time; and the y-axis the discovered clusters $\{1, 2, \ldots, 6\}$. Analyzing this figure, we can perceive that over the time the changes in cluster are only between adjacent clusters: cluster 1 evolutes only to cluster 2; cluster 2, evolutes only between clusters 1 or 3, ..., cluster i evolutes only between $i-1$ and $i+1$. Note that this adjacent clusters are more similar that not adjacent ones. If we consider that each cluster represent a temporal behavior, this reveals a continual evolution of these behaviors, not observing drastic changes over time. These changes in the temporal behavior of the features could have been caused by the increasing stress levels induced by the test that was being resolved by the subjects.

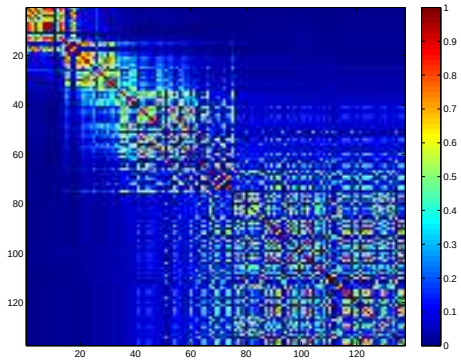

(a) Co-association Matrix based on the ensemble.

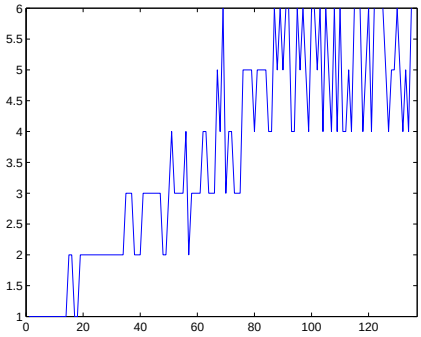

(b) Cluster Temporal-Evolution.

Figure 5: ECG Analysis based on induced similarity using the EAC algorithm over an ensemble of 75 k-means partions (with varying number of clusters).

Figure 6 presents the MDS representation of the data, based on the EAC induced similarity. The represented clusters (in different colors and shapes) are the same presented in figure 5(b). It is possible to note that samples of adjacent clusters are represented adjacently as previously discussed in the temporal evolution of clusters.

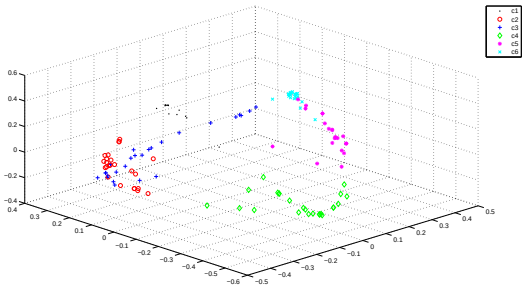

Figure 6: MDS representation of the data based on the EAC induced similarity. The clusters were obtained using the Ward's link and the life time criteria for choosing the number of clusters.

5 CONCLUSIONS

We presented a short overview of state of the art in data visualization and unsupervised learning techniques, to improve the understanding about the data.

Examples shown that the visualization either by dissimilarity matrix observation (using VAT), or co-association observation (obtained via EAC) or using Multidimensional Scalling (MDS), provide pictorial or alternative visual representations of multidimensional data important to gain insight about the data.

The preliminary analysis of the ECG signal demonstrates the potential of these visualization techniques in biosignal analysis. The results have shown typical patterns of time evolution of clusters which can be related with increasing stress levels.

REFERENCES

Bezdek, J. and Hathaway, R. (2002). Vat: A tool for visual assessment of (cluster) tendency. In Press, I., editor, *IJCNN 2002*, pages 2225–2230.

Cox, T. F. and Cox, M. A. A. (1994). *Multidimensional Scaling*. Chapman and Hall.

de Leeuw, J. (2000). Multidimensional scaling. Dep. of Statistics, UCLA. Paper 2000010108.

Fred, A. (2001). Finding consistent clusters in data partitions. In Kittler, J. and Roli, F., editors, *Multiple Classifier Systems*, volume 2096, pages 309–318. Springer.

Fred, A. (2002). *Pattern Recognition and String Matching*, chapter Similarity measures and clustering of string patterns. Kluwer Academic.

Fred, A. and Jain, A. (2002). Data clustering using evidence accumulation. In *Proc. of the 16th Int'l Conference on Pattern Recognition*, pages 276–280.

Fred, A. and Jain, A. (2005). Combining multiple clustering using evidence accumulation. *IEEE Trans Pattern Analysis and Machine Intelligence*, 27(6):835–850.

Fred, A. and Jain, A. (2006). Learning pairwise similarity for data clustering. In *Proc. of the 18th Int'l Conference on Pattern Recognition (ICPR)*, volume 1, pages 925–928, Hong Kong.

Jain, A. and Dubes, R. (1988). *Algorithms for Clustering Data*. Prentice Hall.

Pekalska, E. and Duin, R. P. W. (2003). *The Dissimilarity Representation for Pattern Recognition: Foundations And Applications*. World Sci. Pub. Company.

Post, F. H., Nielson, G. M., and Bonneau, G.-P., editors (2003). *Data Visualization: The State of the Art*. Kluwer.

Silva, H., Gamboa, H., and Fred, A. L. N. (2007). One lead ecg based human identification with feature subspace ensembles. In *Proc Machine Learning and Data Mining in Pattern Recognition*, pages 770 – 783, Leipzig, Germany.

Strehl, A. and Ghosh, J. (2002). Cluster ensembles - a knowledge reuse framework for combining multiple partitions. *J. of Machine Learning Research 3*.

Topchy, A., Jain, A., and Punch, W. (2004). A mixture model of clustering ensembles. In *Proceedings SIAM Conf. on Data Mining*.

Treinish, L. A. and Goettsche, C. (1989). Correlative visualization techniques for multidimensional data. Technical report, National Space Science Data Center NSSDC-NASA.

SHORT-TERM CEPSTRAL ANALYSIS APPLIED TO VOCAL FOLD EDEMA DETECTION

Silvana Cunha Costa
Federal Center of Techological Education of Paraíba-CEFET-PB, Federal University of Campina Grande-UFCG
Av.1º de Maio, 720, João Pessoa, Paraíba, Brazil
silvana@cefetpb.edu.br

Benedito G. Aguiar Neto
Federal University of Campina Grande-UFCG, Intitute of Technology of Washington
University of Washington
Tacoma, USA
bganeto@u.washington.edu

Joseana Macêdo Fechine
Federal University of Campina Grande-UFCG, Campina Grande,Paraíba, Brazil
joseana@dsc.ufcg.edu.br

Menaka Muppa
Intitute of Technology of Washington -University of Washington Tacoma, USA
mmupa@u.washington.edu

Keywords: Acoustic voice analysis, speech processing, acoustic features, *cepstral* parameters, disordered voices, speech pathology.

Abstract: Digital signal processing techniques have been used to perform an acoustic analysis for vocal quality assessment due to the simplicity and the non-invasive nature of the measurement procedures. Their employment is of special interest, as they can provide an objective diagnosis of pathological voices, and may be used as complementary tool in laryngoscope exams. The acoustic modeling of pathological voices is very important to discriminate normal and pathological voices. The degree of reliability and effectiveness of the discriminating process depends on the appropriate acoustic feature extraction. This paper aims at specifying and evaluating the acoustic features for vocal fold edema through a parametric modeling approach based on the resonant structure of the human speech production mechanism, and a nonparametric approach related to human auditory perception system. For this purpose, LPC and LPC-based cepstral coefficients, and mel-frequency cepstral coefficients are used. A vector-quantizing-trained distance classifier is used in the discrimination process.

1 INTRODUCTION

A great range of diseases causes modifications in the voice. These are related to the vocal tract pathologies, as well as many others which are provoked by neuro-degenerative diseases (Davis, 1979; Quek et al, 2002).

Voice quality of patients have been evaluated by several techniques, most of which are based on listening to the patient's voice and on the inspection of the vocal folds through laryngoscopy. The first method is subjective, which could provide different results, depending of the professional experience. The second one has the advantage of being more accurate, but it requires high cost tools such as special light sources and specialized video-camera equipments. In addition, it is considered an invasive technique, which may cause discomfort to the patients

Non-invasive techniques based on acoustic analysis of the speech signal can be used to

diagnosis and evaluation of medical treatments of diseases which provoke vocal disorders. Moreover, acoustic analysis can be employed to the precocious detection of pathologies in the vocal folds or the evaluation of the vocal quality of patients subject to surgical processes in the vocal folds.

Some researchers have dedicated their efforts for obtaining efficient methods to discriminate normal and pathological voices using acoustic analysis (Godino-Llorente et al, 2006; Shama et al, 2007; Murphy and Akande, 2007; Dibazar et al, 2006; Umapathy et al, 2005). Those methods have employed techniques based on the estimation of glottal noise, feature extraction from decomposed time-frequency parameters, linear prediction modeling-based measures and measures based on auditory modeling. However, there is limited agreement on which parameters are more suitable for acoustic modeling of particular pathology. An efficient and reliable acoustic modeling of the pathology is necessary, when pattern classification of vocal disorders is being used. Thus, the vector of acoustic characteristics of the pathological voice should be carefully chosen to be quite representative.

In this research, techniques of digital signal processing are used to carry out an acoustic analysis of pathological voice. The study is focused on the case of voice disorders provoked by edemas in the vocal folds, using the evaluation of following features: LPC coefficients, LPC-based cepstral coefficients and mel-frequency cepstral coefficients. The irregularities in the features of the normal voice in comparison with the pathological voice are observed and analyzed. A vector quantization technique (VQ) was used associated with a distortion measurement to classify the speech signal. The VQ was trained with voices affected by the considered pathology.

The results can be used in order to build an effective method basis for detecting pathological voices. The outline of the paper is as follows: basis for an acoustic modeling of disordered voices, database and methods, results and conclusions.

2 ACOUSTIC MODELING BASIS

Feature extraction of speech signals is frequently employed to acoustic evaluation of pathological voices. Specific statistical parameters based on the linear model of speech production can be used as significant acoustic features. It is known that the voice signal is produced as a result of glottal pulses or a signal varying randomly, like noise excitation filtered by the vocal tract (Rabiner and Schafer, 1978).

Vocal fold pathology such as vocal fold edema affects the vocal fold or other components of the vibratory system, producing an irregular vibration. In fact, it is widely known that pathological vocal folds can present variation in the cycle of the vibratory movement because of changes in the vocal folds elasticity. This occurs due to incomplete closure of the vocal folds in all glottal cycles. The changes in the vocal folds morphology can provoke significant modifications to the acoustic signal. Although the pathology is located in the vibratory system it can affect the regular articulatory movement during the speech production. Furthermore, components of the resonating system can be affected, resulting in changes of the vocal shape, producing irregularities on the spectral properties. A modification in the fundamental frequency and on the spectral shape can be observed as a result of the vocal disorders (Godino-Llorente et al, 2006).

The understanding of changes in the acoustic features involving excitation and resonance effects is the key to an efficient disordered voices modeling. The speech signal contains information about both vocal tract and excitation source.

The handle of the variability present in the speech signal is one of the main challenges of acoustic modeling. The variability arises from the dynamic nature of the vocal tract. Thus, speech is dynamic or time-varying and the modeling needs to consider two aspects: 1) the explicit temporal dependencies of the pathological voice, and 2) the estimation of the features have to be based on statistical short-time analysis. The model has to represent the irregularities behaviour introduced by the pathology itself.

Two parametric methods based on the linear model for the human speech production mechanism approaches have been considered on the literature so far: 1) linear predictive coding (LPC) analysis; 2) LPC-based cepstral analysis (Godino-Llorente et al, 2006, Marinaki et al, 2004, Parsa and Jamieson, 2001; Gavidia-Ceballos, 1996).

The LPC estimates each speech sample based on a linear combination of the p previous samples; a larger p enables a more accurate model. It provides a set of speech parameters that represent the vocal tract (Rabiner and Schafer, 1978). It is expected that any change in the anatomical structure of the vocal

tract, because of pathology, affects the LPC coefficients. A linear predictor with p prediction coefficients, α_k is defined as a system whose output is

$$\tilde{s}(n) = \sum_{k=1}^{p} \alpha(k) s(n-k) \quad (1)$$

In the LPC-based cepstral analysis is considered that speech signal is the result of convolving excitation with vocal tract sample response by cepstral analysis, and it is possible to separate the two components. One step in cepstral deconvolution transforms a product of two spectra into a sum of two signals. In practice, the complex cepstrum is not needed. The real cepstrum suffices, obtained with digital algorithm as follows (Rabiner and Schafer, 1978; O'Shaugnessy, 2000):

$$c(n) = \frac{1}{N} \sum_{k=0}^{N-1} \log[X(k)] e^{j2\pi kn/N} \quad n = 0, 1, ..., N\text{-}1 \quad (2)$$

Cepstral coefficients can be computed recursively from the linear predictor coefficients, α_i, by means of (Furui, 1981):

$$\begin{cases} c(1) = -\alpha(1) \\ c(i) = -\alpha(i) - \sum_{k=1}^{i-1} (1 - \frac{k}{i}) \alpha(k) c(i-k) \quad 1 < i \le p \end{cases} \quad (3)$$

Other authors have investigated the use of mel-frequency cepstral (MFC) analysis which is a measure based on the human auditory perception system (O'Shaughnessy, 2000). A nonparametric MFC-based approach can be derived from fast Fourier transform (FFT-MFC) (Godino-Llorente et al, 2006, Dibazar et al, 2006, Murphy and Akande, 2007, Bou-ghazale and Hansen, 2000).

Cepstrum analysis is based on the human auditory perception system, which incorporates some aspects of audition. This method provides a logarithm relationship between the real and the perceived frequency scales (mels). Mel-frequency cepstral coefficients $c(n)$ are calculated by means of (O'Shaughnessy, 2000):

$$c(n) = \sum_{k=1}^{M} \log(S_k) . \cos[n(k - \frac{1}{2})] . \frac{\pi}{\mathrm{M}} \quad n = 0, 1, ..., \mathrm{M}, \quad (4)$$

where M is the number of mel bands in the mel scale and $S(k)$ is given by

$$S(k) = \sum_{j=1}^{NFFT} W_k(j) . X(j) \quad k = 1, ..., M, \quad (5)$$

where $W_k(j)$ is the triangular weighting windows associated with the mel-scales, and $X(j)$ is the NFFT-point magnitude spectrum (Godino-Llorente et al, 2006, O'Shaughnessy, 2000).

A common model for the relationship between frequencies in mel and linear scales is as follows (O'Shaughnessy, 2000):

$$F_{mel} = 2595 \cdot \log_{10}(1 + \frac{F_{linear}(Hz)}{700}), \quad (6)$$

where F_{linear} is the linear frequency (in Hertz), and F_{mel} is the perceived frequency (in Mel).

3 DATABASE AND METHODS

The database used in this work was recorded by the Massachusetts Eye and Ear Infirmary (MEEI) Voice and Speech Lab (Kay Elemetrics, 1994). It includes more than 1,400 voice samples (i.e., sustained /a/) from approximately 700 subjects. The database including samples from patients with a wide variety of voice disorders, was collected in a controlled environment with the following features: low-noise-level, constant microphone distance, direct digital 16-bit sampling and robust signal conditioning. Sampling rates of 25 kHz (pathological voices) or 50 kHz (normal voices) were employed. The normal voice signals were downsampled to 25 kHz, to maintain the same sample frequency to all signals.

The selected cases of people presenting edemas in the vocal folds are: 33 women (17 to 85 years old) and 11 men (23 to 63 years old), most of them (32) with bilateral edema. The database of normal voices is composed of 53 patients - 21 male (26 to 59 years old), and 32 female (22 to 52 years old). We also used 23 signals, under other pathologies, such as cysts, nodules and paralysis (07 male and 16 female voices).

First, a 20 ms Hamming window with an overlap of 50% is employed to obtain frames from the dataset for the short-term voice analysis.

A Vector Quantization technique is employed in the classification process, associated with a distortion measurement to discriminate among voices affected by vocal fold edema, normal voices and voices presenting other vocal fold pathologies. The Vector Quantization is carried out individually for each feature using just voices under vocal fold edema. Thus, different VQ-trained distance classifiers are obtained by the discrimination process. The VQ-classifiers are applied to static

feature vectors, which are computed for every 10 ms frame of the speech samples over a dynamic input sustained vowel /a/.

A codebook is generated, after the feature extraction, consisting of N discrete level generation that each input vector could assume. An N-level vector quantizer can be defined as a mapping Q of a K-dimensional Euclidean space R^K into a finite subset W of R^K, such as $Q:R^K \rightarrow W$.

The codebook $W=\{\boldsymbol{w}_i ; i=1, 2, ...N\}$ is the set of codevectors, K is the dimension of the quantizer and N is the number of codevectors in W.

The mapping Q assigns to a K-dimensional real-valued input vector $\boldsymbol{x}$ a K-dimensional codevector $\boldsymbol{w}_i=Q(\boldsymbol{x})$. VQ defines a partitioning of the K-dimensional Euclidean space into non-intercepting cells $S_i = \{\boldsymbol{x} : Q(\boldsymbol{x}) = \boldsymbol{w}_i\}$, $i = 1, 2, \ldots, N$.

As the Voronoi cell, S_i, collects together all input vector mapping to the i-th codevector, the codevector w_i may be viewed as a pattern-class label of the input patterns belonging to S_i.

The mapping of the input vector $\boldsymbol{x}$ to a codevector w_i occurs if the distortion function is such as $d(\boldsymbol{x},\boldsymbol{w}_I) < d(\boldsymbol{x},w_i), \forall_i \neq I$.

It follows the nearest neighbour rule is applied to find the codevector that presents the greatest similarity to $\boldsymbol{x}$. In this work, LBG algorithm and the least mean square distance were used (Linde et al, 1980).

4 RESULTS AND DISCUSSION

To reduce the dimensionality of feature vectors, a Vector Quantizer (VQ) to each parameter was employed, using dimension K=12 and *N=64 levels.* The VQ was trained with 20 voice signals under vocal fold edema. In the test phase 53 normal voices, 24 signals under vocal fold edema and 23 speech signals of speakers, affected by other vocal fold pathologies as nodules, cysts and paralysis, were used. The Euclidean distance measure to classify the signals was used to analyze the effect of pathologies in vocal tract response. For this purpose, LPC, cepstral and mel-cepstral coefficients were extracted from the database signal.

A predictor order *p=12* was applied the LPC analysis. The LPC coefficients were obtained using the autocorrelation method by Levinson-Durbin algorithm (Rabiner and Schafer, 1978). Figure 1 shows the distribution of vocal fold edema, normal voices and other pathologies. It is clear the excellent separation of the two classes analyzed: normal voices and voices affected by vocal fold edema. This results in a high correct rejection rate. In comparison, the edema behaviour and the other pathologies have a certain similarity that suggests difficulties in recognizing each pathology.

A threshold value to provide the best separation between the classes in the classification process was chosen. For cepstral analysis it was used an algorithm based on Eq. (3). A number of 12 coefficients were obtained and the same process of quantization used to LPC method was employed.

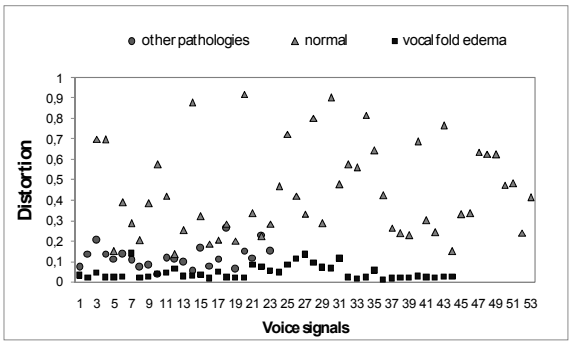

Figure 1: Distortion behaviour for normal, vocal fold edema and other pathologies, obtained by Euclidian distortion on LPC method.

The behaviour of classes, on cepstral analysis, is shown in Figure 2. The graphic provides a great way to observe the relevance of each parameter in classifying a pathological voice. The good separation of normal and pathological voices is well defined as in LPC method.

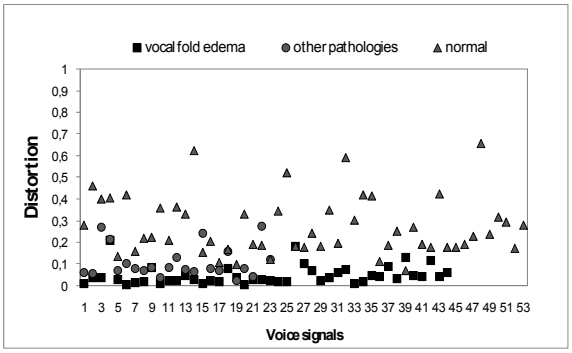

Figure 2: Distortion behaviour for normal, vocal fold edema and other pathologies obtained by Euclidian distortion on cepstral method.

The number of filter bank bands employed to MFCC method was 30 (3ln(*Fs*), where *Fs* is the sampling frequency (*Fs* = 25kHz) and a number of 12 MFC coefficients were obtained as described in section 2. An algorithm of Voicebox - Speech Processing Toolbox for MATLAB (http://www.ee.ic.ac.uk/hp/staff/dmb/voicebox) was used.

The behaviour of classes in mel-cepstral method is presented in Fig. 3. In this method, as in the others, it has a good separation of normal and pathological voices. However, the differences among the pathologies are not evident. LPC and cepstral methods seem to be better in representing the pathologies specificities.

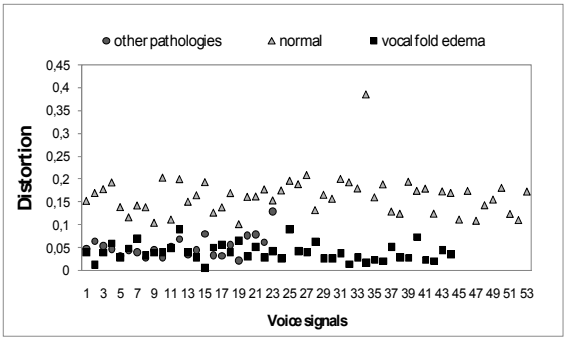

Figure 3: Distortion behaviour for normal, vocal fold edema and other pathologies obtained by Euclidian distortion on mel-cepstral method.

The evaluation of performance was made by the use of the following measurements: 1) Correct acceptance rate (CA), in which the presence of the pathology is detected when that is really present; 2) Correct rejection (CR), that gives the rate of the detection of the correct absence of the pathology; 3) False acceptance rate (FA) that detects the presence of the pathology when it is not present; 4) False rejection rate (FR), that quantifies the rejection of the presence of the pathology when, in fact, it is present.

Related to the rates mentioned it was computed:

- Specificity - SP: represents the likelihood that the pathology is detected when it is present, given by $SP=CR/(CR+FA)$x100.
- Sensitivity – SE: represents the likelihood that the pathology is detected when it is present, obtained by SE(%)=(CA/(CA+FR)x100.
- Efficiency-E: gives the correct classification of a given class when that is present given as E(%)=(CR+CA)/(CR+CA+FA+FR)x100.

Figure 4 presents results to the measurements above obtained for the three applied methods considering other pathologies as a separate class of edema. It is seen that LPC gives the best method. However, the false rejection rate obtained for this method was 27%. It is important to emphasize that the classifier was trained to accept vocal fold edema signals and reject any other signal as being pathological.

It is also observed that mel-cepstral method was not efficient in discriminating each pathology class. Mel-cepstral analysis represents the perceptual auditory aspect that is similar in some vocal fold pathologies as nodule, cyst and edema.

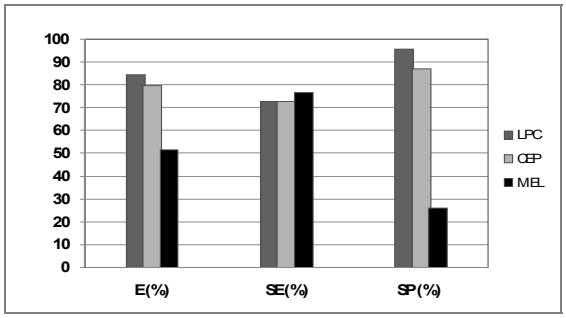

Figure 4: Performance evaluation considering vocal fold edema and the other pathologies as different classes.

The hoarseness and severely noisy-speech are some of common aspects that occur to speakers affected by the mentioned pathologies. The ability of MFCC method in representing the irregular vibration of vocal folds is common in the pathologies in this study and it is reflected on the results. The behaviour of the pathological signals is similar in mel-cepstral domain. Therefore, to discriminate pathologies occurring on vocal folds is not an easy task.

Figure 5 shows a comparison of the LPC, cepstral and mel-cepstral methods, when using the classifier to all pathologies in the same classes. It is clear that mel-cepstral method is better than the other methods in representing the behaviour differences of the pathological signals relating to normal cases.

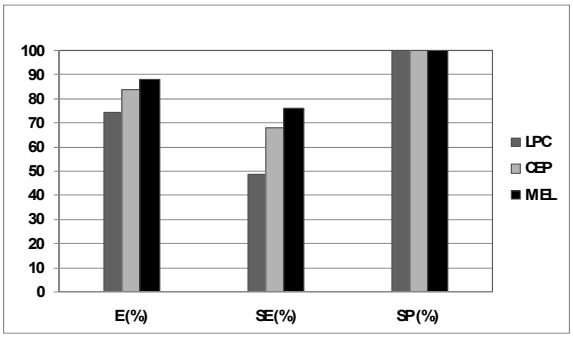

Figure 5: Performance evaluation considering vocal fold edema and the other pathologies in the same class.

The ability of methods employed in rejecting correctly the classes out of classifier training class is excellent (SP).

Figure 6 shows results obtained for Specificity, Efficiency and Sensitivity comparing pathological voices under vocal fold edema and normal voices.

The other pathologies are not considered here. The ability of FFT-MFCC in modeling the irregular vibration of the vocal folds provoked by the pathology is shown in the results. Good results are also obtained to LPC and cepstral analysis.

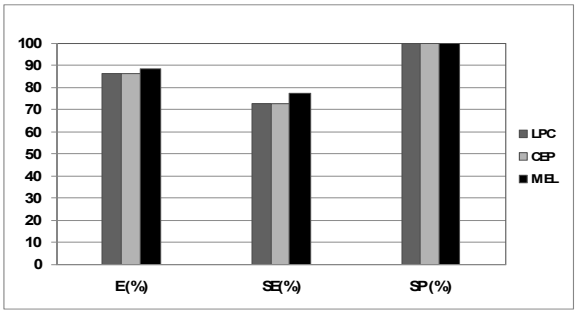

Figure 6: A comparison of the performance evaluation of LPC, cepstral and mel-cepstral analysis to the cases of vocal fold edema and normal voices.

5 CONCLUSIONS

The changes on LPC, cepstral and mel-cepstral coefficients describe the abnormal behaviour of the vocal folds movements caused by the pathologies. The efficiency in characterizing pathological voices using short-time cepstral analysis is well described by results.

It is noted that mel-cepstral coefficients are very good to detect the presence of pathology. They provide a good separation of normal and pathological voices. However, this method is not efficient in discriminating distinct pathologies. The differences among pathologies which belong to similar class of diseases are not evident. LPC and cepstral methods seem to be better in representing the pathologies specificities.

In order to improve the performance of the classification process, two aspects are suggested: 2) the use of non-linear analysis to improve the acoustic modeling of non-linear characteristics inherent to speech signal, and 2) the employment of other classifiers based on Artifitial Neural Networks or Hideen Markov Models, for example.

REFERENCES

Bou-Ghazale, S.E., Hansen, J.H.L., 2000. A Comparative Study of Traditional and Newly Proposed Features for Recognition of Speech Under Stress. *IEEE Transactions on Speech & Audio Processing*. Vol. 8, no. 4, pp. 429-442, July.

Davis, S. B, 1979. Acoustic Characteristics of Normal and Pathological Voices. *Speech and Language: Advances in Basic Research and Practice*. Vol. 1, pp. 271–335.

Dibazar, A. A., Berger, T.W., and Narayanan, S. S., 2006. Pathological Voice Assessment. *Proceedings of the 28th IEEE EMBS Annual International Conference*. New York, USA, Aug. 30-Sept. 3.

Furui, S., 1981. Cepstral Analysis Technique for Automatic Speaker Verification. *IEEE Transactions on Acoustics, Speech and Signal Processing*. Vol. 29, No. 2, pp 254-272, April.

Gavidia-Ceballos, Liliana and Hansen, John H. L., 1996. Direct Speech Feature Estimation Using an Interactive EM Algorithm for Vocal Fold Pathology Detection. *IEEE Trans. on Biomedical Engineering*. Vol. 43, No. 4, April.

Godino-Llorente, J. I., Gomes-Vilda, P. and Blanco-Velasco M., 2006. Dimensionality Reduction of a Pathological Voice Quality Assessment System Based on Gaussian Mixture Models and Short-Term Cepstral Parameters. *IEEE Transactions on Biomedical Engineering*. Vol. 53, No. 10, pp. 1943-1953, October,

Kay Elemetrics Corp. Disordered Voice Database, 1994. Model 4337, 03 Ed.

Linde, Y., Buzo, A., and Gray, R. M., 1980. An Algorithm for Vector Quantizer Design, *IEEE Transaction on Communications*. Vol. COM-28, N0.I, pages 84-95, January.

Marinaki, M., Contropoulos, C., Pitas, I., and Maglaveras, N., 2004. Automatic Detection of Vocal Fold Paralysis and Edema, *Proc. of 8th Conf. Spoken Language Processing (Interspeech 2004)*. Jeju, Korea, October.

Murphy, Peter J. and Akande, Olatunji O., 2007. Noise Estimation in Voice Signals Using Short-term Cepstral, *Journal of the Acoustical Society of America*. pp. 1679-1690, Vol. 121, No. 3, March.

O'Shaughnessy, Douglas, 2000. *Speech Communications: Human and Machine*. 2nd Edition, NY, IEEE Press.

Parsa, Vijay and Jamieson, Donald G., 2001. Acoustic Discrimination of Pathological Voice: Sustained Vowels versus Continuous Speech. *Journal of Speech, Language, and Hearing Research*. Vol. 44, pp 327–339, April.

Quek, F., M. Harper, Haciahmetoglou, Y., Chen, L. and Raming, L. O., 2002. Speech pauses and gestural holds in Parkinson´s disease. *Proceedings of International Conference on Spoken Language Processing*. pp. 2485-2488.

Rabiner L. R. and Schafer R. W., 1978. *Digital Processing of Speech Signals*. New Jersey: Prentice-Hall.

Shama, K., Krishna, A. and Cholayya, N. U., 2007. Study of Harmonics-to-Noise Ratio and Critical-Band Energy Spectrum of Speech as Acoustic Indicators of Laryngeal and Voice Pathology. *EURASIP Journal on Advances in Signal Processing*. Vol. 2007.

Umapathy, K., Krishnan, S., Parsa, V., and Jamieson D., 2005. G. Discrimination of Pathological Voices Using a Time-Frequency Approach. *IEEE Transactions on Biomedical Engineering*. Vol. 52, No. 3, March.

APPLICATION OF WALSH TRANSFORM BASED METHOD ON TRACHEAL BREATH SOUND SIGNAL SEGEMENTATION

Jin Feng, Farook Sattar
School of Electrical& Electronic Engineering, Nanyang Technological University, Singapore
jinf0001@ntu.edu.sg, efsattar@ntu.edu.sg

Moe Pwint
Dept. of Information Science, The University of Computer Studies, Yangon, Myanmar
moepwint@pmail.ntu.edu.sg

Keywords: Segmentation, Walsh Transform, Refinement Scheme, Inspiratory/Expiratory Phase, Various Types of Tracheal Breath Sounds, End-Inspiratory/Expiratory Pause.

Abstract: This paper proposes a robust segmentation method for differentiating consecutive inspiratory/expiratory episodes of different types of tracheal breath sounds. This has been done by applying minimal Walsh basis functions to transform the original input respiratory sound signals. Decision module is then applied to differentiate transformed signal into respiration segments and gap segments. The segmentation results are improved through a refinement scheme by new evaluation algorithm which is based on the duration of the segment. The results of the experiments, which have been carried out on various types of tracheal breath sounds, show the robustness and effectiveness of the proposed segmentation method.

1 INTRODUCTION

For early detection of diverse illnesses, accurate estimation of respiratory rate is very important (Sierra et al., 2005). Many adventitious lung sounds, which are indications of infectious and respiratory diseases, can be clinically characterized by their duration in respiratory cycle and relationship to the phase of respiration (Meslier et al., 1995). Therefore, segmentation of respiratory sound into individual respiratory cycles and further subdividing into its inspiratory and expiratory phases is necessary in quantifying adventitious sounds.

Generally, phonopneumography or spirometer together with sound recording devices are always used in respiratory sound analysis, in which amplitude of the sound signal is displayed simultaneously with the airflow as a function of time. Signals can be segmented into consecutive inspiratory phase, end-inspiratory pause, expiratory phase, and end-expiratory phase according to the provided Forced Expiratory Volume (FEV) readings (Taplidou and Hadjileontiadis, 2007)(Cortés et al., 2005). However, it could be difficult to carry out a spirometric test for patients with high obstruction in tracheal (Cortés et al., 2005).

Acoustical flow estimation is one of the first attempts to relate respiratory sounds and flow. In (Hossain and Moussavi, 2002) and (Golabbakhsh, 2004), airflow has been estimated using the respiratory sounds by applying different models, while exponential model between flow and averaged sound power has been found with the highest estimation accuracy. The model coefficients calculation in the above mentioned methods require samples of breath sound with known flow. However, the calibration process is not always possible. Therefore, a modified entropy-based linear model describing relationship between flow and tracheal sound has been derived in (Yadollahi and Moussavi, 2006) without prior acoustical flow knowledge. Also, other segmentation methods using spectral and temporal analysis of transformed respiratory sounds have been developed in (Hult et al., 2000)(Sierra et al., 2004). As these researches are still in preliminary stage, the segmentation is restricted to normal tracheal breath and the accuracy depends mainly on signal-to-noise ratio (SNR) for various types of tracheal breath sounds.

In this paper, an automatic and robust respiratory sound signal segmentation method is developed. The proposed method is based on the modification of input sound signal using a modified analysis and synthesis

scheme based on Walsh basis functions. Without the aid of any other features, a decision module is then applied on the modified signal by adaptive thresholding for segmentation. The preliminary segmentation result is optimized lastly by the refinement scheme based on the segment duration. This scheme ensures the segmentation process to perform equally accurate irrespective of flow and types of tracheal breath sounds. The proposed method is tested to be effective for both normal tracheal breath sounds as well as adventitious respiratory sounds such as, wheeze and stridor.

2 BACKGROUND

The Walsh transform is a matrix consisting of a complete orthogonal function set having only two values +1 and -1 over their definition intervals (Beauchamp, 1984). The motivation for using Walsh transform rather than other transforms is its computational simplicity giving a realistic processing time. The Walsh function of order N can be represented as

$$g(x,u) = \frac{1}{N}\prod_{i=0}^{q-1}(-1)^{b_i(x)b_{q-1-i}(u)} \qquad (1)$$

where $u = 0,1,...,N-1$, $N = 2^q$ and $b_i(x)$ is the i--th bit value of x. In this context, the Walsh functions are arranged into sequential order, the number of zero crossings of Walsh function per definition interval, to obtain a set of basis functions. The number of zero crossings increases with the order of basis functions $W = [\phi_0,\ \phi_1,\ \cdots\ ,\phi_{N-1}]$.

3 PROPOSED SEGMENTATION METHOD FOR RESPIRATORY SOUND SIGNAL

The proposed respiratory sound signal segmentation approach is based on segmentation of the respiratory sounds using Walsh functions. The segmentation method is based on the reconstruction/modification of the analyzed signals by efficient linearly combined Walsh functions. A simple decision scheme is then followed for segmentation of our recorded respiratory sound signals based on the statistics of the modified/reconstructed signal. The details of our minimal Walsh functions based segmentation method is presented here.

3.1 Modification of Signal

The modification of the input signal consists of two stages - sinusoidal signal analysis (Arfib et al., 2002) followed by our signal reconstruction scheme using minimal Walsh functions.

3.1.1 Signal Analysis

The input signal $x(n)$ is multiplied by a Hann window to yield successive windowed segments of $x_s(n)$. These window segments are mapped into the spectral domain by using FFTs. In this way, a time varying spectrum $X_s(n,k) = |X_s(n,k)|e^{j\varphi(n,k)}$ with $n = 0,1,...,N-1$ and $k = 0,1,...,N-1$ for each windowed segment is obtained. Here, $X_s(n,k)$ denotes the spectral component of the input signal at frequency index k and time index n, while $|X_s(n,k)|$ and $\varphi(n,k)$ denote the time-varying magnitude and phase responses, respectively.

3.1.2 Modified Signal Synthesis

The recorded input respiratory signal is reconstructed as a modified sequence based on our modified analysis/synthesis approach. Prior to synthesis, each s--th windowed segment is modified as the weighted sum of the magnitude $|X_s(n,k)|$ using binary Walsh basis functions. Using basis functions, the number of parameters required to track along the variations of the inspiration and expiration phases of the noisy signal can be reduced. For this reason, SVD (Singular-Value Decomposition) is used to determine the minimal number of Walsh basis functions to be applied. The detailed procedure for the identification of the minimal number of Walsh basis functions and the new modified basis function used based on the selected basis functions, are described in the following section. Applying the i-th basis function ϕ_i, a modified sequence, $y_s(n)$, for each windowed segment is then obtained as

$$y_s(n) = \sum_{k=0}^{N-1}|X_s(n,k)|.\phi_i(k) \qquad (2)$$

All the modified segments are finally concatenated to generate an output signal $y(n)$ having the time-varying magnitude responses.

$$y(n) = \sum_{s=0}^{S-1} y_s(n-sN) \qquad (3)$$

3.1.3 Selection of Minimal Walsh Functions for Modified Synthesis

It is very important to select appropriate basis functions so that variations between the dynamics of

the two phases can be captured more precisely. A method used to select the global natural scale in discrete wavelet domain (Quddus and Gabbouj, 2002) is adopted to determine the minimal number of basis functions. This method adaptively selects the optimal scale using SVD, while decomposition is being carried out. Consider an input noisy respiratory signal x of length $\mathcal{V}$, and $y_d(\nu)$ be its modified sequence obtained by applying the basis functions of order d into Eq(2) and Eq(3). Modified sequences $\{y_d(\nu)\}_{d=0}^{D-1}$ can be represented as a matrix of size $D \times \mathcal{V}$. To determine the order of basis functions with dominant eigenvalues, the SVD of the $D \times \mathcal{V}$ matrix is calculated adaptively begin with the first two orders (i.e. ϕ_0 and ϕ_1) while adding the Walsh functions of higher orders.

Here, the proposed algorithm defines the minimal order of basis functions N_{min} as 3 throughout the simulations and found very robust against various situations. In the original algorithm (Quddus and Gabbouj, 2002), optimal scale is defined as the average of the details from the first level to the natural scale, the level associated with the dominant eigenvalue. However, this averaging may introduce clipping effect for the signals at low signal level. To avoid this effect, a shifting operator which swaps the right and left halves of the basis function coefficients is applied first. Then a good estimate of a modified binary Walsh basis function within dominant eigenvalues is defined as

$$\phi_m = \frac{\phi_0 - \sum_{i=1}^{N_{min}} CS(\phi_i)}{\max\{|\phi_0 - \sum_{i=1}^{N_{min}} CS(\phi_i)|\}} \tag{4}$$

where $N_{min} = 3$ is the largest order referring to the most prominent eigenvalues and $CS(\cdot)$ is the shifting operator. This new basis function ϕ_m provides sharper representation and higher discriminating features.

3.2 Decision Strategy

3.2.1 Preliminary Decision Module

First, 0-order basis function, ϕ_0 is used to produce a modified sequence, $y_0(\nu)$, to get the global information of the original sample signals. This modified sequence is used as a reference or pilot sequence as used in the areas of telecommunication. Containing the local characteristics, another modified signal, $y_m(\nu)$, is formed using the new basis function ϕ_m. From this new sequence, locations and durations of inspiration and expiration phases can be located more precisely even for adventitious respiratory sounds such as wheeze and stridor. In this way, approximate locations of inspiration and expiration segments are first determined from the modified signal, $y_0(\nu)$. Then, the results to determine respiratory phases can be improved by using the second modified signal, $y_m(\nu)$, which contains the detailed information. Applying the reconstructed signals y_0 and y_m, the procedure of detection scheme can be described as below:

- Extract two sequences of local minima, $\{\alpha_{0i}\}_{i=1}^{L}$ and $\{\alpha_{mi}\}_{i=1}^{L}$, where L is the number of frames, from every 4 ms frame of $y_0(\nu)$ and $y_m(\nu)$.
- Set thresholds, τ_0 and τ_m, for each minima sequence which are obtained using a simple statistics: $\tau_0 = \mu_0 - \kappa\delta_0$ and $\tau_m = \mu_m - \kappa\delta_m$, where μ_0 and δ_0 are the mean and the standard deviation of the first set of local minima, and μ_m and δ_m are those of the second set of local minima while κ is a positive value which depends on the dynamic range of modified sequence $y_0(v)$.
- Set threshold coefficient, κ, which is the same for τ_0 and τ_m. As shown by Eq(5), κ is proportional to global average of $y_0(v)$, and a is a constant value. After experimenting with 10 reconstructed waveforms of different respiration types (stridor and wheeze, normal tracheal breath for adult and infant), a is found to be 3.4, and universal for all types of tracheal breath sounds.

$$\kappa = a \times \frac{1}{N} \sum_{v=0}^{N-1} y_0(v) \tag{5}$$

- Declare a frame as an respiration frame if either $\alpha_{0i} < \tau_0$ or $\alpha_{mi} < \tau_m$. As it is mentioned earlier, respiratory cycle is divided into four consecutive phases: inspiratory phase, end-inspiratory pause, expiratory phase, and end-expiratory pause. Respiration frames is defined in this context as the frames belong to either inspiratory or expiratory phases. In this way, the respiration frame indices are obtained from $y_0(\nu)$ and $y_m(\nu)$ as $\mathcal{R}$ and $\mathcal{T}$:

$$\mathcal{R} = \{r_1, r_2, ..., r_P\} \tag{6}$$
$$\mathcal{T} = \{t_1, t_2, ..., t_Q\} \tag{7}$$

- Combine the two initial boundary decisions as follows:

$$\mathcal{C} = \mathcal{R} \cap \mathcal{T} \tag{8}$$

where $\mathcal{C}=\{c_1, c_2, ..., c_J\}$ is the set of elements common to $\mathcal{R}$ and $\mathcal{T}$. Considering that the members of $\mathcal{C}$ are the indices of either inspiration or expiration frames, the final decision for detecting respiration frames are obtained.

In the above, we decide that there exist respiration frames whenever some or all of the prominent local

minima obtained from the first modified signal $y_0(\nu)$ would coincide with the local minima found from the second modified signal $y_m(\nu)$. For those detected frames when their corresponding local minima are not obtained from both modified sequences of $y_0(\nu)$ and $y_m(\nu)$, are discarded as outliers.

3.2.2 Refinement Scheme

Due to the quasi-stationary nature of the adventitious respiratory sounds and their relatively small dynamic range due to shallow breath, there are chances where frames are wrongly identified because of the inflexibility of the global threshold value used: small spikes happen during end-inspiratory/expiratory pauses being wrongly identified as respiration segments which are denoted by peaks; and small fluctuations during inspiration/expiration might be wrongly identified as pause segments which are denoted by troughs as indicated in Fig.1(c). In order to ensure the accuracy of the segmentation, the results obtained from the preliminary decision module will be fine-tuned by the refinement scheme to avoid wrong identification of the respiratory frames. The scheme consists of two stages:

- Identify error segments with durations shorter than threshold σ_t, where σ_t varies for patients with different respiratory rate. Since the duration of end-inspiratory/expiratory pauses range from 0% to 30% and inspiration time range from 10% to 80% of a complete breath cycle (Li, 2004), we defined error segment to be with duration less than 5% of individual's averaged breath cycle. Therefore σ_t is defined as:

$$\sigma_t = 5\% \times \frac{60}{RR} \times F_s \tag{9}$$

  where RR as Respiration Rate, is the number of breath cycle per minute and F_s is the sampling rate of the signal. Since the averaged RR is the highest for infant which is 44 breaths/min (Keszler and Abubakar, 2004), the scheme adopts this value to minimize the wrong identification. The selected parameter values are listed in Table 1. The error segments are then divided into error respiration segments and error pause segments, where the number of segments for each error segment type is counted.

Table 1: Values of parameters for refinement scheme.

Parameter	Value
F_s	8000 Hz
RR	44 breaths/min
σ_t	545 samples

- Evaluate the error segments based on segment duration. This process is applied for evaluating error respiration segments first. The procedure can be described using our following pseudo code, where respiration segment is denoted by R(s) and pause segment by P(s) and s is the positional index of the segment along time line.

```
Begin
    T = threshold;
    Pd(s) = duration of P(s);
    Rd(s) = duration of R(s);
    I = number of error R(s);
    for i=1:I,
        locate first error R(s);
        if duration of Pd(s-1) & Pd(s) < T
            if Pd(s) > Pd(s-1)
                R(s) combine with R(s-1);
            else
                R(s) combine with R(s+1);
        else if Pd(s-1) < T or Pd(s) < T
           R(s) combine with R(s-1) or R(s+1);
        else
           R(s) is considered as pause segment;
        end
    end
End.
```

This procedure is then applied for the second time to evaluate error pause segments by interchanging R(s) with P(s) in the pseudo code.

4 EXPERIMENTAL RESULTS

4.1 Data and Parameter Selection

Five different types of tracheal sound signals are chosen from (Lehrer, 1993) and (Wilkins et al., 2004). Tracheal breath sound is chosen due to its relatively larger amplitude compared with the sounds recorded over chest. Also, it has distinct inspiratory/expiratory phases and is related closely to respiratory flow.

The segmentation algorithm has been tested on total 10 sound signals, each consists of 8 breathing cycles. Four phases are distinct in every breathing cycle for all signals chosen. Since the segmentation method is working based on the overall trend instead of the detail fluctuations of the signals, the order m for reconstructed signal $y_m(v)$ should be kept low. Therefore, $m = 3$ is used in the experiments.

4.2 Illustrative Results and Analysis

Fig.1 illustrates the outputs of individual segmentation steps on a signal of inspiratory stridor and expiratory moderate wheeze. Fig.1(a) shows the original

signal containing wheeze and stridor whereas Fig.1(b) shows its transformed version, the reference modified sequence $y_0(v)$, together with the reference threshold τ_0. In Fig.1(c), output of preliminary decision module is depicted. As indicated by arrows A, B, C, D, there are 4 locations of preliminary results containing error segments. Being optimized by the refinement scheme, the final segmentation result is displayed in Fig.1(d).

Also, the results for infant normal tracheal breath are shown by Fig.2. By comparing these two figures, no error segments are detected in Fig.2(c). This is due to the different nature of the signals: The quasi-stationary nature of wheeze and stridor signals gives them more prominent components at low frequency, while the fast transient nature of the normal tracheal breath makes it emphasize more on the high frequency components. Since $y_0(v)$ focusses on the signal trend which is represented by the low frequency components, it captures more spikes (low frequency details) for wheeze and stridor, but provides smoother waveforms for normal breath sound signal. Therefore, after thresholding by τ_0, segments with short duration are detected for abnormal breath sound signals. However, due to the optimization by refinement scheme, the final segmentation results are equally accurate for both normal tracheal breath sounds and adventitious breath sounds.

Moreover, illustrative results of the segmentation algorithm for different types of respiratory sound signals are shown by Fig.3(a)-(e). These results demonstrate the robustness of our proposed method on different types of tracheal breath.

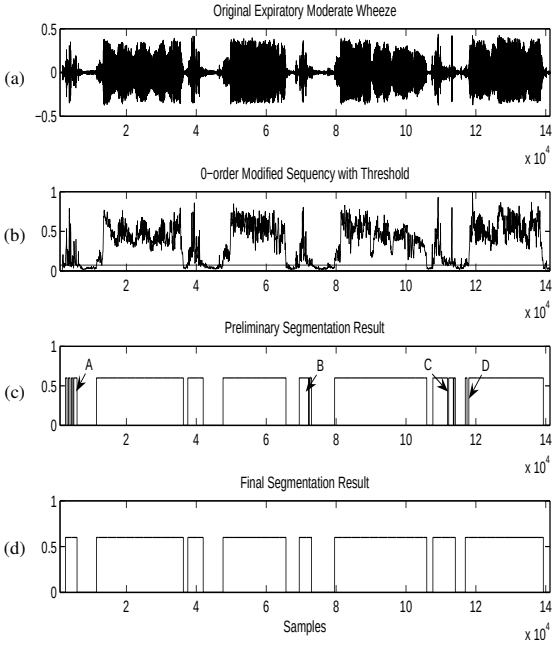

Figure 1: (a) Original signal waveform; (b)0-order modified sequence $y_0(v)$ with threshold τ_0; (c) preliminary segmentation result; (d) final segmentation result for inspiratory stridor and expiratory moderate wheeze.

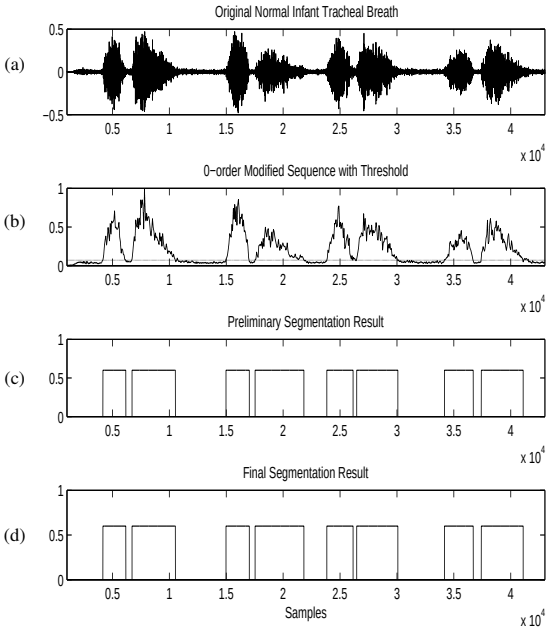

Figure 2: (a) Original signal waveform; (b)0-order modified sequence $y_0(v)$ with threshold τ_0; (c) preliminary segmentation result; (d) final segmentation result for infant normal tracheal breath.

5 DISCUSSION

In this paper, we have presented an algorithm to locate and differentiate inspiratory/expiratory phases with end-inspiratory/expiratory pauses for different types of tracheal breath sounds. The use of binary Walsh transform simplifies the proposed algorithm to a large extend and left only few parameters for adjustment. This makes the algorithm fast and automatic even in the absence of any *a priori* information of the input signal types. It performs equally accurate for both normal as well as adventitious sounds due to the incorporation of refined decision module. Thus it is more robust compared to existing methods as by using these conventional methods, accurate segmentation is still restricted within normal breath sounds.

As the only limitation, the proposed method does not perform well on raw recorded tracheal breath sound signals. This is due to the presence of the prominent heartbeat. Since the frequency range of heartbeat is below 300Hz, it interferes with the normal breath sounds and contaminates the signal with

large amount of low frequency components. This can be solved by taking recording at positions with low heart sound to respiratory sound amplitude ratio, or preprocessing using a notch filter to suppress the effect of heartbeat. However, the algorithm is immune to other ambient noises due to the wide spectrum occupied by the noises.

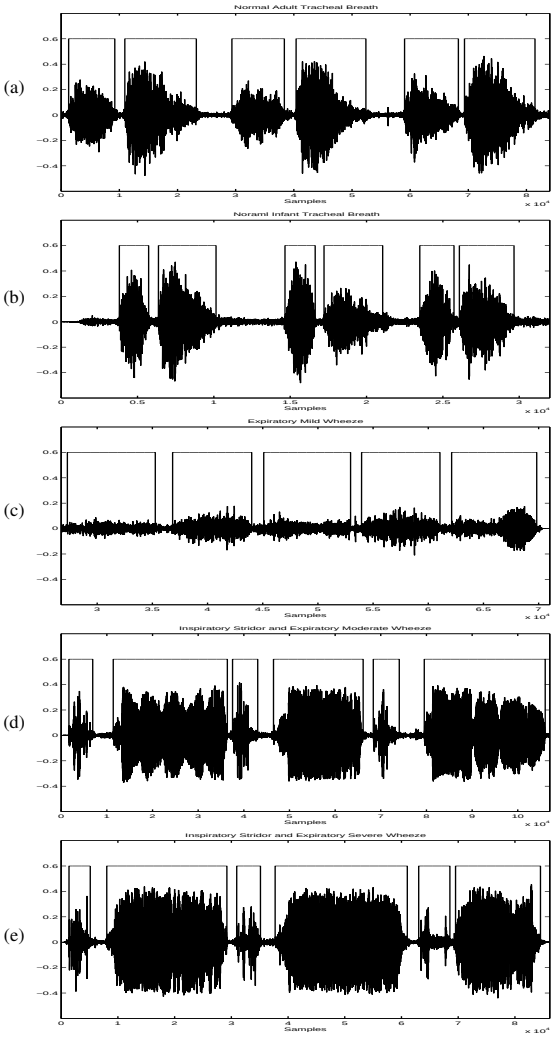

Figure 3: The segmentation results displayed with original signal waveform for (a)-(b) normal tracheal breath of adult/ infant; (c) expiratory mild wheeze; (d)-(e) inspiratory stridor and expiratory moderate/ severe wheeze.

REFERENCES

Arfib, D., Keiler, F., and Zöler, U. (2002). *DAFX - Digital Audio Effects*. John Wiley Publisher.

Beauchamp, K. G. (1984). *Applications of Walsh and Related Functions*. Academic Press.

Cort*é*s, S., Jan*é*, R., Fiz, J. A., and Morera, J. (Sept, 2005). Monitoring of wheeze duration during spontaneous respiration in asthmatic patients. *IEEE Proceedings of Engineering in Medicine and Biology*, pages 6141–6144.

Golabbakhsh, M. (2004). Tracheal breath sound relationship with respiratory flow: Modeling, the effect of age and airflow estimation. *M. Sc. theses, Electrical and Computer Engineering Department, University of Manitoba*.

Hossain, I. and Moussavi, Z. (2002). Respiratory airflow estimation by acoustical means. *[Engineering in Medicine and Biology, 2002. 24th Annual Conference and the Annual Fall Meeting of the Biomedical Engineering Society] EMBS/BMES Conference, 2002. Proceedings of the Second Joint*, 2.

Hult, P., Wranne, B., and Ask, P. (2000). A bioacoustic method for timing of the different phases of the breathing cycle and monitoring of breathing frequency. *Medical Engineering and Physics*, 22:425–433.

Keszler, M. and Abubakar, K. (2004). Volume guarantee: Stability of tidal volume and incidence of hypocarbia. *Pediatric Pulmonology*, 38(3):240–245.

Lehrer, S. (1993). *Understanding lung sounds, Audio CD*. Saunders.

Li, T. (2004). Invasive mechanical ventilation. *Respiratory problems: Invasive mechanical trainee manual*.

Meslier, N., Charbonneau, G., and Racineux, J. L. (1995). Wheezes. *European Respiratory Journal*, 8(11):1942–1948.

Quddus, A. and Gabbouj, M. (2002). Wavelet-based corner detection technique using optimal scale. *Pattern Recognition Letters*, 23:215–220.

Sierra, G., Telfort, V., Popov, B., Durand, L. G., Agarwal, R., and Lanzo, V. (2004). Monitoring respiratory rate based on tracheal sounds. first experiences. *Annual International Conference of the IEEE Engineering in Medicine and Biology*.

Sierra, G., Telfort, V., Popov, B., Pelletier, M., Despault, P., Agarwal, R., and Lanzo, V. (2005). Comparison of respiratory rate estimation based on tracheal sounds versus a capnograph. *Annual International Conference of the IEEE Engineering in Medicine and Biology*.

Taplidou, S. A. and Hadjileontiadis, L. J. (2007). Nonlinear analysis of wheezes using wavelet bicoherence. *Computers in Biology and Medicine*, 37:563–570.

Wilkins, R. L., Hodgkin, J. E., and Lopez, B. (2004). *Fundamentals of lung and heart sounds, Audio CD*. Mosby.

Yadollahi, A. and Moussavi, Z. (2006). A robust method for estimating respiratory flow using tracheal sounds entropy. *IEEE Transactions on Biomedical Engineering*, 53(4):662–668.

PHASE SEGMENTATION OF NOISY RESPIRATORY SOUND SIGNALS USING GENETIC APPROACH

Feng Jin, Farook Sattar
School of Electrical & Electronic Engineering, Nanyang Technological University
Nanyang Avenue, Singapore 639798
jinf0001@ntu.edu.sg, efsattar@ntu.edu.sg

Moe Pwint
Dept. of Information Science, The University of Computer Studies, Yangon, Myanmar
moepwint@pmail.ntu.edu.sg

Keywords: Noisy Respiratory Sound Signals, Phase Segmentation, Sample Entropy(SampEn), Genetic Algorithm (GA).

Abstract: In this paper, a new approach to automatically segment noisy respiratory sound signals is proposed. Segmentation is formulated as an optimization problem and the boundaries of the signal segments are detected using a genetic algorithm (GA). As the estimated number of segments present in a segmenting signal is initially obtained, a multi-population GA is employed to determine the locations of segment boundaries. The segmentation results are found through the generations of GA by introducing a new evaluation function, which is based on the sample entropy and a heterogeneity measure. Illustrative results for respiratory sound signals contaminated by loud heartbeats and other high level noises show that the proposed genetic segmentation method is quite accurate and threshold independent to find the noisy respiratory segments as well as the pause segments under different noisy conditions.

1 INTRODUCTION

Respiratory rate (RR) monitoring plays an important role in many clinical situation. Correct timing of individual respiratory phases can be useful in studying flow in the heart (Hult et al., 2000), quantifying adventitious respiratory sounds and many other situations. Different airflow measurements, such as mouthpiece pneumotachograph or chest movement measurement, are the most widely applied methods in monitoring RR and respiratory phases. However, it would be difficult to apply such methods under certain circumstances, especially when studying children with neurological impairments (Yadollahi and Moussavi, 2006). Hereby, acoustical analysis of respiratory sounds has recently provided an alternative way to detect respiratory phases and therefore RR.

Tracheal breath sound refers to respiratory sound recorded over suprasternal notch. It can be segmented into four successive phases: inspiratory phase, expiratory phase, end-inspiratory pause, expiratory phase, and end-expiratory pause. It is chosen due to its distinct phases and relatively larger amplitude compared with sounds recorded over chest, as well as its close relationship to respiratory flow. A few attempts have been done to estimate flow for segmentation through tracheal sounds in the past. Among all, one of the effective method is the signal analysis approach uses the temporal and frequency variables of tracheal sounds as well as disturbance characteristics (Hult et al., 2000). It is able to identify different respiratory phases but it requires more than one microphone to capture the ambient noise and it is sensitive to disturbance. To avoid such problems, in (Yadollahi and Moussavi, 2006), flow estimation using Shannon entropy of the bandpass filtered tracheal sounds is proposed.

Both the above mentioned methods are generally effective on preprocessed tracheal sounds which are free of heartbeats and ambient noise. However heartbeat as one of the most influential noise for respiratory sounds are usually unavoidable during signal recording. It has the frequency range of [0 300]Hz which interferes with that for respiratory sounds; and it masks the respiratory sounds because of its high intensity. When the recorded signals which are corrupted by heartbeats or other unknown types of high level noises, the segmentation becomes tough and thus it is difficult to locate the boundaries of respiratory phases accurately. To deal with this problem, a

genetic algorithm (GA) is employed for the first time to segment accurately the noisy respiratory signal.

The aim of this paper is to propose an genetic algorithm for automatic phase segmentation of respiratory sounds corrupted by heartbeats and other unknown types and levels of noises. The segmentation method described here is based on a stochastic global search method. To guide the search space of generic algorithm, an evaluation function combined sample entropy and heterogeneity measure is introduced.

2 GENETIC ALGORITHM BASED RESPIRATORY PHASE SEGMENTATION

As for our phase segmentation, the locations of the segment boundaries are detected using our genetic algorithm. Depending on the total number of segments as prior information or estimated using any existing technique(e.g. using an onset detection algorithm), an initial population is randomly generated.

To guide the search space of GA, a new evaluation function is introduced. First the irregularity in the time series (i.e. input sequence) is investigated using *sample entropy* (*SampEn*). Measuring the *homogeneity* and *heterogeneity* of the candidate segments, the fitness of the evaluation function is designed. Through the generations of GA, the locations of segment boundaries are then optimized.

2.1 Sample Entropy

In this GA based segmentation method, a similarity measure of times series (sample entropy) is employed to determine the boundaries of respiratory segments. Sample entropy (*SampEn*) is applied here to measure the complexity and regularity of time series signals' similarities. $SampEn(m,r,N)$ is chosen as it does not count self-matches of the time series. This ensures the consistency of the measurement and reduces the dependency on the signal length. It is defined in (Richman and Moorman, 2000) as the negative natural logarithm of the conditional probability that a data set of length N, having repeated itself within a tolerance r for m points, will also repeat itself for $m+1$ points, without allowing self-matches.

For an input signal u of length N, $\{u(j) : 1 \leq j \leq N\}$ forms the $N-m+1$ vectors $x_m(i)$ for $\{i|1 \leq i \leq N-m+1\}$, where $x_m(i) = \{u(i+k) : 0 \leq k \leq m-1\}$ is the vector of m data points from $u(i)$ to $u(i+m-1)$. In this context, only the first $N-m$ vectors of length m are considered to ensure that, $x_m(i)$ and $x_{m+1}(i)$ are defined for $1 \leq i \leq N-m$. Let $B^m(r)$ is the probability that two sequences will match for m points and $A^m(r)$ is the probability that two sequences will match for $m+1$ points. $B_i^m(r)$ is defined as $(N-m-1)^{-1}$ times the numbers of vectors $x_m(j)$ within r of $x_m(i)$, where $1 \leq j \leq N-m$, and $j \neq i$ to exclude self-matches. Then $B^m(r)$ is defined as

$$B^m(r) = (N-m)^{-1} \sum_{i=1}^{N-1} B_i^m(r) \tag{1}$$

Similarly, $A_i^m(r)$ is defined as $(N-m-1)^{-1}$ times the numbers of vectors $x_{m+1}(j)$ within r of $x_{m+1}(i)$, where $1 \leq j \leq N-m$ and $j \neq i$. Then set $A^m(r)$ as

$$A^m(r) = (N-m)^{-1} \sum_{i=1}^{N-1} A_i^m(r) \tag{2}$$

Finally, sample entropy (*SampEn*) is calculated by

$$SampEn(m,r,N) = -\ln \frac{A^m(r)}{B^m(r)} \tag{3}$$

SampEn measures the regularity of data sequence. A low value of *SampEn* reflects a high degree of self-similarity in time series. With increasing irregularity, a larger value of *SampEn* is obtained. The *SampEn* increases for respiratory segments and decreases during the appearance of pause segments. Hence, the dynamics of segmenting respiratory signal can be investigated through the sample entropy sequence. And sample entropy can be applied as a useful tool to determine the locations of the respiratory segments as well as pause segments for a noisy respiratory sound signal.

2.2 Genetic Algorithm

GAs are numerical optimization algorithms inspired by both natural selection and natural genetics (Coley, 2001). GAs operate on a population of strings, that is, a group of potential solutions of a problem. To measure how good or bad the solutions within the population, fitness of each string is calculated in decoded form (solution vector) applying an evaluation function. At each generation, a new set of solutions are produced by selecting the fittest strings in the problem domain and through the application of the genetic operators such as crossover and mutation. A review for the fundamental operations of a simple GA can be found in (Tang et al., 1996). The procedure of a simple GA can be described as follows, where the population of candidate solutions at time t is represented by P(t):

```
begin
        t = 0;
        initialize P(t);
        while not termination criteria do
        begin
                t = t + 1;
                select P(t) from P(t-1);
                reproduce pairs in P(t);
                evaluate P(t);
        end
end
```

2.2.1 Initial Population

In order to detect both start and end locations of each segment, a population of GA is generated with strings whose length is two times the total number of segments as obtained earlier. A string is a real-valued string representing the locations of the candidate segment boundaries in increasing order. Although the binary-coded GAs are the most commonly used representation, a more natural real-valued representation is used in this system to increase the efficiency of GA. Using the real-valued strings, there is no need to convert strings to solution vectors to evaluate their fitness. Thus it would be faster in computation.

2.2.2 Evaluation Function

In GAs, an evaluation function or fitness function is usually used to evaluate the performance of the strings in the problem domain. In order to obtain accurate boundaries of each segment, an evaluation function is designed using the heterogeneity measure and sample entropy. This function simultaneously maximize the homogeneity within the segments and heterogeneity among different segments using sample entropy.

In this context, *SampEn* of the original segmenting signal is calculated first to investigate the dynamics. To prevent the requirement of large computational time (to obtain the feasible computation time and to make the proposed algorithm to be tractable), *SampEn* is calculated on each data set of length 100 (i.e. N=100) within a tolerance r of $0.15 \times SD$ for 1 point (i.e. m=1). Here, SD is the standard deviation of the data set. Let H_w be the total within-segment homogeneity and H_b denotes the total between-segment heterogeneity, a segmentation evaluation function is defined as

$$H = \frac{H_b + 1}{H_b + H_w + 1} \tag{4}$$

where total within-heterogeneity H_w is defined as

$$H_w = \frac{\sum_{i=1}^{S} L_i \sigma_i^2}{L} \tag{5}$$

where L is the total length of the segmented signal, L_i is the length of i-th segment, σ_i^2 is the variance of the sample entropy of the i-th segment and S is the number of segments in the segmented signal. The between-segment heterogeneity, H_b, is defined as the average Euclidean distance between the mean value of the sample entropy of any two adjacent segments.

$$H_b = \frac{\sum_{(i,j) \in adjacent, i \neq j} \|\mu_i - \mu_j\|^2}{ns} \tag{6}$$

where ns is the total number of the adjacent segments in the segmented signal, μ_i and μ_j are the mean value of the sample entropy of the i-th and j-th segments. H becomes one when the internals of all segmented respiratory signals are completely homogeneous.

2.2.3 Evolution Procedure

In order to effectively search the solution space, and to take advantage of the parallelism of GAs, the proposed algorithm applies the multiple subpopulations approach provided by (Chipperfield et al., 1995) for the evolutionary process. Using multiple populations the quality of the results obtained can be improved compared to GAs with single population. This approach divides the population into a subpopulations where each of them can evolve independently using parallel processing technique. It can search in parallel different subspaces of the search space, thus making it less likely to become trapped by low-quality subspaces. Multiple populations GA is a widely used parallel GA model where multiple subpopulations evolve independently toward different optima. More diverse subpopulations can be maintained by exchanging genetic materials between subpopulations. The premature convergence effect of simple GA can then be mitigated by this approach. To reduce the required computational time, it is implemented through the use of high-level genetic operator functions and exchanging individuals between subpopulations.

Over generations, each subpopulation is evolved as in traditional simple genetic algorithm (SGA) using the basic operators: *crossover* and *mutation*. Depending on the migration interval (i.e. the number of generations between successive migration) and the migration rate (i.e. the number of individuals to be migrated from one subpopulation to another), individuals from one subpopulation migrate to another from time to time. The initial population is created using 8 subpopulations containing 20 individuals each. At each generation, 90% of the individuals with higher fitness values within each subpopulation are selected for breeding using a *stochastic universal sampling*

function which has minimum spread and zero bias.

In GAs, the recombination operator is usually used to produce the new offsprings. By applying *discrete recombination crossover*, a uniform crossover for real-valued representation, the new offsprings within each subpopulation are produced. Normally, offsprings are mutated after recombination to prevent the population from converging to local minima. And the new possible solutions can be introduced to the population by mutating the offsprings. In this system, a mutation rate of $1/nvar$ is used, where *nvar* is the length of an individual.

When the offsprings produced are less than the size of the original population, the new offsprings have to be reinserted into the population to maintain the size of the original population. Similarly, when not all the offsprings are to be used at each generation, or if the offsprings produced are more than necessary, a reinsertion scheme must be used. This scheme determines which individuals should be replaced by the offsprings produced and which individuals should be inserted into the new population.

In this segmentation method, offsprings are inserted into the appropriate subpopulations depending on *fitness-based reinsertion* with a rate of 0.9. In this multi-population GAs, migration of individuals between subpopulations is performed at every 20 generations with a migration rate of 0.2. After GA iterates for *maxgen* times (here *maxgen*=80), the evolution of this GA stops. The best individual with the maximum fitness value presents the optimized solution for the boundaries of the segments of the segmented signal.

3 SIMULATION RESULTS

In this section, performance of the method is presented for the noisy respiratory sound signals. Both the standard preprocessed normal tracheal breath sound from (Lehrer, 2002; Tilkian and Conover, 2001; R. L. Wilkins and Lopez, 2004) and normal recorded data as corrupted with heartbeats(Phonocardiogram, PCG) and ambient noise, are used to test the segmentation method.

3.1 Acquisition of Respiratory Sounds

The recording environment and equipments are chosen based on the standard given by (Rossi et al., 2000). Short-term recordings have been done in sitting position in audio laboratory which provides a quiet environment. One electret condenser microphone (ECM-77, Sony, Inc., Tokyo, Japan) has inserted into a hemispherical rubber chamber 2cm in diameter, and placed at suprasternal notch of the test subjects to record the tracheal breath sounds. Recording software WAVEPAD (V3.05, NCH Swift Sound Software) has been used and the signal clips have been recorded and saved as mono-channel *.wav file at sampling frequency of 8 kHz. Test subjects have been asked to breath normally, and 20s recording are saved each time.

3.2 Test Respiratory Data

Tracheal breath sounds signals from 10 healthy students of Nanyang Technological University have been used as the dataset of the performance test. The sample size of 10 consists of 6 females and 4 males, each producing two clips of 20s recording. All clips have been testified to be normal tracheal breath by Dr. Daniel Goh from National University Hospital of Singapore.

3.3 Results

This section presents the simulation results using noisy respiratory sound signals. Four different examples regarding segmentation of normal noisy breath sounds are given below. The sampling frequency used is 8 kHz.

Example 1: In this example, the segmentation results for a normal infant tracheal sound from the standard data set, are demonstrated. In contrary to the existing phase segmentation methods, the proposed method is able to function with the presence of heartbeats and provides accurate segmentation results at different levels of PCG (varying with a scaling factor of α)(See Fig. 1). Fig. 1(a) shows the segmentation result for 3 cycles of infant tracheal breath, whereas Figs. 1(b)-(c) show the results with the superimposed PCG. Comparing the results in Fig. 1, it is found that the present method performs well irrespective of PCG level without using any threshold parameter.

Example 2: In this example, segmentation results for the recorded adult normal tracheal breath sound are shown. Both the original signal and the noisy recorded signal interfered with heartbeats, are considered here for illustration. Unlike the infant breath (Fig. 2(a)), the adult breath in Fig. 2(a) has different time evolution (i.e. slower respiration rate) and shallow. The segmentation results in the presence of heartbeats are still found effective like the previous case.

Example 3: In this example, segmentation results are shown for a signal of noisy recorded respiratory sound due to background White Noise (WN) of varying noise variance as ambient noise (see Fig. 3(a)-

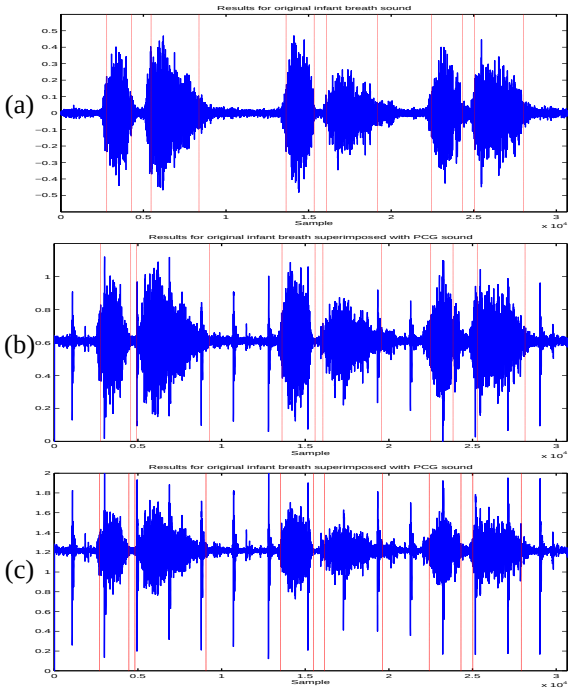

Figure 1: Segmentation results of the standard infant tracheal breath sound: (a) without PCG sound; (b)-(c) with PCG sound added with scaling factor α=1 and 2, respectively.

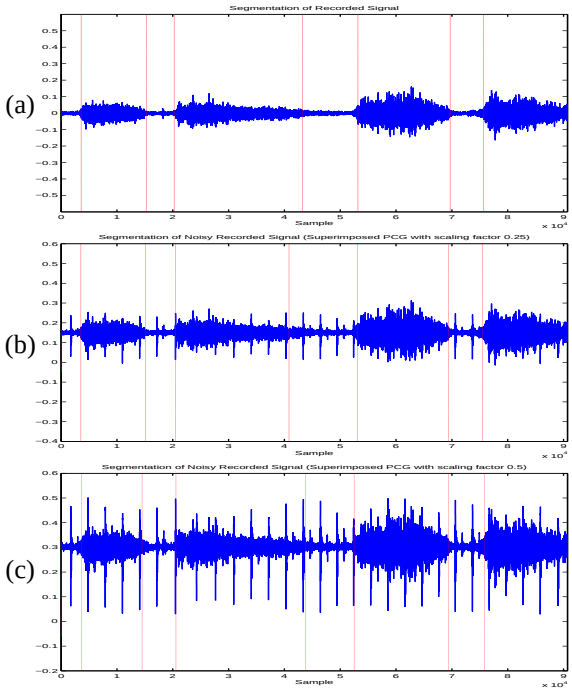

Figure 2: Segmentation results of: (a) preprocessed recorded tracheal breath sound; (b) original recorded tracheal breath sound with heartbeats; (c) recorded tracheal breath sound with superimposed PCG for scaling factor α=0.5.

(b)). Also, simulation result in the presence of both white noise and PCG (heartbeats) is illustrated in Fig. 3(c). As it is seen in Fig. 3 that the segmenation method provides good results for white background noise and heartbeats.

Example 4: In this example, segmentation results are presented, Fig. 4(a)-(b), for the noisy recorded signal corrupted by background Colored Noise (CN) with varying noise level. Also, a simulation example for both ambient colored noise and PCG interference is shown in Fig. 4(c). The colored noise is realized as EEG noise, $v(n)$, which is simulated by an ARMA process described as $v(n) = \frac{C(z^{-1})}{A(z^{-1})}e(n)$ where $e(n)$ is the zero-mean white Gaussian noise and $C(z^{-1})$ and $A(z^{-1})$ are third-order polynomials in the backward shifting operator z^{-1}. The coefficents of $C(z^{-1})$ and $A(z^{-1})$ are chosen in a way that makes the spectrum of the ARMA precess approximates the EEG process.

The estimation error is defined as

$$\varepsilon = \frac{1}{N}\sum_{n=1}^{N} \mid \frac{P_{est}^{n} - P_{ref}^{n}}{P_{ref}^{n}} \mid \qquad (7)$$

where P_{est}^{n} is the starting/ end position of the nth segment for a noisy signal and P_{ref}^{n} is that for a preprocessed signal without white noise, colored noise, and PCG. For performance of segmentation method on real Recorded Tracheal Sound (RTS) with different types of noises imposed onto it as indicated in Figs. 2-4, the error is calculated for each subject using Eq. 7 and then averaged between the subjects.

Table 1: The estimation errors of the segmentation method for different types of noisy signals.

Type of Signal	Segmentation Error
RTS (Fig. 2(b))	0.014 ± 0.011
RTS with PCG (Fig. 2(c))	0.016 ± 0.010
RTS with WN (Fig. 3(a))	0.016 ± 0.013
RTS with WN & PCG (Fig. 3(c))	0.015 ± 0.009
RTS with CN (Fig. 4(a))	0.013 ± 0.009
RTS with WN & PCG (Fig. 4(c))	0.018 ± 0.018

4 CONCLUSIONS

In this paper, effective segmentation of noisy respiratory sound signals is introduced based on genetic (GA) approach. Using sample entropy, a regularity measure of the time sequence and heterogeneity measure, the evaluation function of GA is designed.

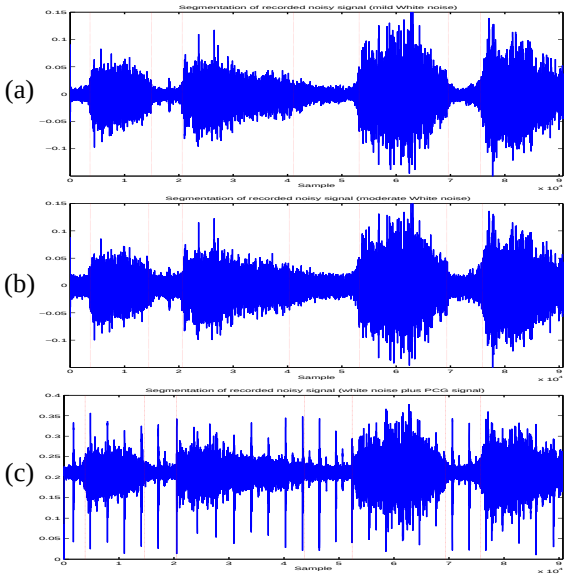

Figure 3: Segmentation results of the noisy recorded breath signal together with (a)-(b) varying white noise;(c) white noise and PCG.

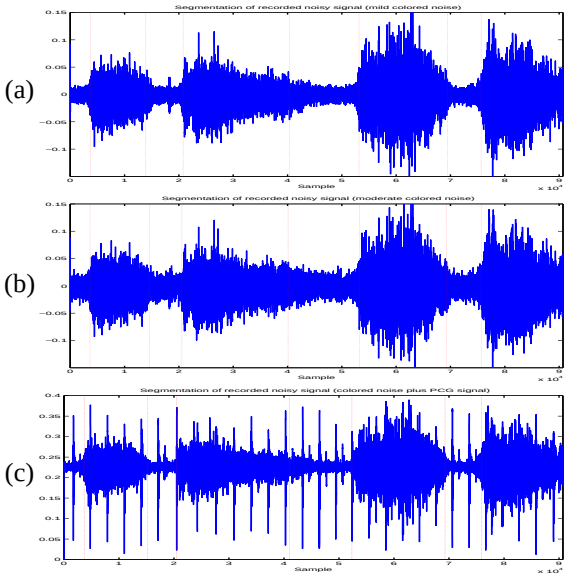

Figure 4: Segmentation results of the noisy recorded breath signal together with (a)-(b) varying colored noise;(c) colored noise and PCG.

The segmentation results for normal tracheal breath sounds corrupted with heartbeats and ambient noise are found quite accurate, especially when the existing methods only perform well on the processed signals without these noise. The method is found effective in the presence of various types and levels of noise.

Furthermore, many approaches for initial segment number estimation (e.g. onset or other detection techniques) are suitable for the proposed segmentation method. As the performance of the proposed method does not depend heavily on the accuracy of the total segment number estimated, only a rough estimation by using any detection technique is required. Moreover, the independency on threshold values makes the method very robust and suitable for segmentation of recorded respiratory sound signals.

REFERENCES

Chipperfield, A., Fleming, P., Pohlheim, H., and Fonseca, C. (1995). Genetic algorithm toolbox. *Department of Automatic Control and Systems Engineering, University of Sheffield.*

Coley, D. A. (2001). *An Introduction to Genetic Algorithms for Scientists and Engineers*. World Scientific.

Hult, P., Wranne, B., and Ask, P. (2000). A bioacoustic method for timing of the different phases of the breathing cycle and monitoring of breathing frequency. *Medical Eng. and Physics*, 22:425–433.

Lehrer, S. (2002). *Understanding Lung Sounds*. Philadelphia, PA: Saunders, Audio CD.

R. L. Wilkins, J. E. H. and Lopez, B. (2004). *Fundamentals of Lung and Heart Sounds*. Mosby, Audio CD.

Richman, J. S. and Moorman, J. R. (2000). Physiological time-series analysis using approximate entropy and sample entropy. *Am J Physiol Heart Circ Physiol*, 278(6):H2039–2049.

Rossi, M., Sovijarvi, A. R. A., P. Pirila, L. V., Dalmasso, F., and Vanderschoot, J. (2000). Environmental and subject conditions and breathing manoeuvres for respiratory sound recordings. *European Respiratory Review*, 10(77):611–615.

Tang, K. S., Man, K. F., Kwong, S., and He, Q. (1996). Genetic algorithms and their applications. *Signal Processing Magazine, IEEE*, 13(6):22–37.

Tilkian, A. G. and Conover, M. B. (2001). *Understanding Heart Sounds and Murmurs: with an Introduction to Lung Sounds*. Philadelphia, PA:Saunders 2001; Audio CD.

Yadollahi, A. and Moussavi, Z. (2006). A robust method for estimating respiratory flow using tracheal sounds entropy. *Biomedical Engineering, IEEE Transactions on*, 53(4):662–668.

BIOLOGICALLY INSPIRED BEAMFORMING WITH SMALL ACOUSTIC ARRAYS

Douglas L. Jones, Michael E. Lockwood, Albert S. Feng and Bruce C. Wheeler
Beckman Institute, University of Illinois at Urbana-Champaign, 405 N. Mathews, Urbana, IL, USA
dl-jones@uiuc.edu, melockwo@uiuc.edu, afeng1@uiuc.edu, bwheeler@uiuc.edu

Keywords: Beamforming, hearing aids, biologically inspired beamformers, cocktail party.

Abstract: Many biological hearing systems perform much better than existing signal processing systems in natural settings. Two biologically inspired adaptive beamformers, one mimicking the mammalian dual-delay-line localization system, show SNR gains in challenging cocktail-party scenes substantially exceeding those of conventional adaptive beamformers. A "zero-aperture" acoustic vector sensor array inspired by the parasitoid fly *Ormia ochracea* and accompanying algorithms show even better performance in source recovery than the binaural beamformers, as well as the ability to localize multiple nonstationary sources to within two degrees. New experimental studies of the performance of the biologically inspired beamformers in reverberation show substantial reduction in performance in reverberant conditions that hardly affect human performance, thus indicating that the biologically inspired algorithms are still incomplete.

1 INTRODUCTION

Many biological hearing systems exhibit remarkable performance that greatly exceeds that of current engineered systems. An example is the parasitoid fly, *Ormia ochracea*, which orients toward its cricket prey to within two degrees by use of an ear about a millimeter in maximum extent (Robert et al., 1996). The dominant frequency of the cricket's call is about 5 kHz, so *Ormia* achieves this remarkable accuracy with an aperture that is well less than 1/50th of a wavelength, and at a range exceeding that of cricket females. *Ormia* thus exceeds the traditional Rayleigh resolution by well more than an order of magnitude.

The human hearing system also demonstrates remarkable performance in many respects. With only two ears, it achieves lateral directional accuracy similar to *Ormia* and considerable ability to localize complex natural sounds in elevation as well. Its ability to recover a desired speech source in the presence of multiple simultaneous speech interferers (the "cocktail party" environment) with only two ears is unequaled by conventional signal processing methods; current beamforming or source-separation algorithms fail when the number of sources exceeds the number of sensors. The human hearing system is also remarkably tolerant to reverberation and time-varying environments.

For comparison, consider that conventional engineered beamforming systems require a many-element array of about half-wavelength spacing between elements to achieve the high directional accuracy demonstrated by *Ormia*. An array of at least as many sensors as sources, again with an appropriate aperture, would be required to perform acceptable signal recovery at a cocktail party in an anechoic chamber; tens of elements would be required to accomplish this in the presence of the modest reverberation in a typical room.

Clearly, the performance of these biological systems far exceeds that of current electronic systems, at least for their specific biological application. By drawing ideas and inspiration from these systems, we have developed new algorithms that greatly advance the state-of-the-art in acoustic signal recovery of speech and similar natural systems in complex real-world environments. These new methods show promise for many applications, including hearing aids, hands-free telephony in noisy or reverberant environments, and surveillance.

2 CONVENTIONAL BINAURAL BEAMFORMERS

Acoustic beamforming for hearing aids presents a special challenge because the total aperture on a single behind-the-ear (BTE) array is well less than two centimeters. This is well below half a wavelength for

the audio frequencies with most speech energy; arrays of only two, or at most three, microphones can be used, and resolution well beyond the Rayleigh limit is required for significant directionality.

The minimum-variance distortionless response (MVDR) (also known as linearly constrained minimum variance (LCMV)) methodology introduced by Capon (Capon, 1969) is the most common approach for super-resolution adaptive beamforming. MVDR beamformers minimize the output energy of the best linear combination of the microphone inputs, subject to the constraint that any signal from the desired target (or "look" direction) is exactly preserved. The minimum-energy objective causes maximal rejection of unwanted sources from other directions or noise, while the distortionless response constraint prevents the beamformer from attenuating or otherwise distorting the desired signal. The distortionless-response constraint is captured in a "steering" vector, $\mathbf{e}$, which represents the relative magnitudes and phases of a signal from the target look direction, and the linear constraint equation on the beamformer weights, $\mathbf{w_{opt}}$, is $\mathbf{e}^H\mathbf{w_{opt}} = 1$. Capon derived the constrained optimal linear weights for scalar (instantaneous mixing or narrowband signals) beamforming:

$$\mathbf{w_{opt}} = \frac{\mathbf{R}^{-1}\mathbf{e}}{\mathbf{e}^H\mathbf{R}^{-1}\mathbf{e}} \tag{1}$$

Capon's method has several major limitations. The beamformer will work successfully only if the number of interfering sources is less than the number of sensors. It requires accurate knowledge of the steering vector; errors in $\mathbf{e}$ cause the beamformer to cancel the desired signal as well as the interference. The super-resolution capability of Capon's beamformer also amplifies this problem, because even small errors can be sufficient to allow self-cancellation. In particular, any reverberation manifests itself in this framework as a single source with an altered, composite steering vector; self-cancellation is usually so severe as to render Capon's adaptive beamformer unusable in hearing aids. Finally, Capon's original approach applies only to narrowband sources or instantaneous mixtures.

Frost (Frost III, 1972) and later Griffiths and Jim (Griffiths and Jim, 1982) overcame this last limitation by applying the Capon MVDR criterion to beamformers with filters, rather than just scalar, weights on each array channel. These algorithms avoid the computational complexity and numerical instability of inverting large matrices by applying the LMS algorithm to iteratively converge toward the optimal constrained filter weights. Griffiths' and Jim's GSC algorithm is generally used for wideband adaptive beamforming, and several attempts have been made to apply it to directional or binaural hearing-aid arrays. In carefully controlled laboratory settings with a single interferer, it has shown considerable gain, but with additional interferers or even modest reverberation, the performance collapses, often producing a negative signal-to-noise (SNR) gain.

Figure 3 summarizes the performance of a carefully optimized GSC beamformer in anechoic conditions for speech recovery in the presence of one, two, three, and four speech interferers from different directions in the front half-plane. (Use of Greenberg's adaptive step-size was essential to avoid misconvergence during intervals of silence in the target speech and to obtain positive SNR gain (Greenberg, 1998).) As can be seen in the figure, the beamformer performs well for a single interference, but the performance drops dramatically when the total number of sources exceeds the number of sensors. For applications such as hearing aids that are limited to two or three microphones and must perform well in the cocktail-party context, the conventional beamforming approach is inadequate.

3 BIOLOGICALLY INSPIRED BINAURAL BEAMFORMERS

The GSC beamformer performance is perfectly consistent with beamforming theory, but psychophysical studies, as well as the personal experience of every human being with normal hearing, show that humans perform much better in the cocktail-party environment. Using only two ears, humans can localize as many as six simultaneous sources (Bronkhorst and Plomp, 1992) and gain a very significant binaural advantage in terms of ability to understand a desired speech source among multiple spatially separated interferers. Clearly, biology holds some secrets unknown to engineering for improved performance with small arrays in crowded acoustic environments for speech sources.

3.1 A Biologically Inspired Beamformer

The remarkable performance of the human binaural hearing system in the cocktail-party environment has prompted us to develop new biologically inspired beamforming algorithms. The mammalian hearing system has been extensively studied by physiologists; while a great deal remains to be deciphered, much is now known. Mammals' brains use several cues to determine direction, including the interaural time difference (ITD), which is equivalent to phase delay for narrowband signals, interaural intensity (or level)

difference (IID), and spectral shaping for elevation (Yost and Gourevitch, 1987). The cochlea act as filter-banks that separate the signals at each ear into different frequency bands, which are processed in parallel. Based on physiological studies that have located and identified the specific neural circuitry, Jeffress (Jeffress, 1948) modeled the mammalian interaural time-difference mechanism as a dual delay-line circuit as illustrated in Figure 1.

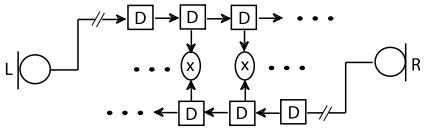

Figure 1: The mammalian interaural time-delay dual delay-line circuit.

The neural response to the sound passes, in opposite directions and in parallel for each frequency band, through counter-flowing delay lines. The signals at corresponding positions in the delay lines are in effect cross-correlated over short time intervals, and the delay yielding the peak coincidence produces a strong response, indicating a dominant source in the corresponding direction at that frequency and time. It is less well understood how higher stages of the neural processing use this information.

Based on this model, we developed a biologically inspired binaural beamforming algorithm with much better performance in the cocktail-party scenario than the conventional GSC. Following the mammalian ITD system, the method in Liu *et al.* (Liu et al., 2000) transforms the signal to the short-time frequency domain via an overlapped FFT filter-bank (this differs somewhat from mammalian ears, in which the filter bandwidths vary across frequency). Independently at each frequency and delay-line pair, a running short-time sum-of-absolute-differences (SAD) is computed to create a frequency-delay map of the strength of coincidence. The neural system sharpens the directional responses via inhibition of weaker neighboring responses; the algorithm mimicks this by locating local peaks and thresholding to create a binarized, sparse map of the dominant signal directions as a function of both frequency and direction. For broadband sources such as speech, integrating this map across frequency provides a composite graph that clearly indicates the directions of several simultaneous sources active at that time. The peaks in this composite directional map are thresholded to determine the number and direction of all significant active sources. This completes the "localization" step of the method.

The desired source is recovered, or "extracted" from the interference, via guided frequency-domain null-steering beamforming (Liu et al., 2001). The source (as identified from the localization step) closest in direction to that of the target is recovered by applying a different constrained beamformer in each frequency band that passes the desired source and nulls the dominant interferer in that band. Figure 2 illustrates the method.

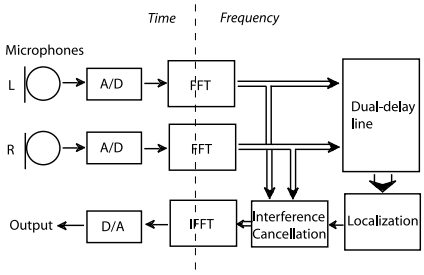

Figure 2: A block diagram of the biologically inspired localization/extraction beamformer.

Liu *et al.* report excellent performance; for four simultaneous speech sources in an anechoic environment, intelligibility weighted SNR gains ranged from 8 to 9.1 dB (Liu et al., 2001). The SNR gain ranged from 4.6 to 6.7 dB in a test room with a reverberation time of 0.4 sec. These performances far exceed that of the conventional GSC beamformer for such conditions.

3.2 A DSP-friendly Biologically Inspired Beamformer

While closely resembling the biological system, the localization/extraction method described above is computationally expensive when implemented on a conventional electronic computer. The characteristics of neural systems (massively parallel and relatively slow) and current electronic hardware (much less parallel and extraordinarily fast) differ enough that direct mapping of the neuronal algorithm to electronics may not be the most effective engineering solution. Accordingly, we developed an alternate biologically inspired algorithm that captures some of the essential features of the mammalian hearing system while being much more amenable to real-time DSP implementation.

The mammalian auditory system exhibits key characteristics, exploited by the biologically inspired algorithm, that allows its excellent performance. The mammalian hearing system processes auditory signals within frequency bands and dynamically over short-time intervals; that is, it performs some type of rapidly adapting time-frequency processing. It is essential to note that the mammalian auditory system is not designed for the narrowband signals or white Gaussian noise for which most signal process-

ing algorithms are optimized; such signals are rare in natural environments. The signals, and the interference, of most relevance to humans are transients and speech, which are rapidly time-varying, have considerable harmonic structure, and are relatively sparse in time-frequency. For example, even continuous speech has many short intervals of silence, and speech has formants, at many times strong harmonic structure (voiced speech), and other distinct and relatively sparse structure in frequency as well. In the short-time-frequency domain, the average number of interferers in any time-frequency bin is much less than the number of sources. Thus, while beamforming theory shows that only fewer interferers than sensors can be cancelled for narrowband frequency or broadband noise sources, with frequency decomposition and rapid adaptivity, the inherent time-frequency sparseness can be exploited to cancel most of several "simultaneous" interferers.

With this biologically inspired insight, new approaches better matched to implementation with current DSP hardware can be derived that still demonstrate performance approaching that of the more biologically faithful algorithm of Liu *et al.* Time-frequency decomposition to expose the sparsity of the sources and interferers, and rapid adaptation to take advantage of it, are the key elements that allow a binaural system to overcome multiple interferers in a cocktail-party environment. We have developed a particular frequency-domain MVDR beamformer implementation (FMV) that provides similar interference rejection and is easily implementable in a low-power, fixed-point, real-time DSP system such as a digital hearing aid (Lockwood et al., 2003). Like the L/E algorithm described earlier, the algorithm begins with overlapped short-time FFTs of the individual input channels, and subsequently processes each channel independently. This exposes the time-frequency sparsity of the interference. This transformation produces the added advantage that the beamformers in each frequency bin are scalar. Running short-time cross-correlation matrices are computed at each frequency via an efficient recursive update. In most frequency-domain MVDR implementations, the GSC algorithm is used to slowly adapt the beamformer due to the $O(N^3)$ complexity and stability challenges of the matrix inverse. However, for a *binaural* beamformer, implemented in the frequency domain, $N = 2$ in each independent channel, and direct solution for the optimal Capon weights according to (1) requires only a few operations after algebraic simplification. We also apply a multiplicative (energy-normalized) regularization to provide some robustness to the short-time correlation estimates (Cox et al., 1987). Just as in the first algorithm, the optimal beamforming weights are applied at each frequency and the extracted signal of interest is recovered via an inverse FFT.

Figure 3 shows the performance in terms of SNR gain of a 15 cm two-element free-field array in an anechoic environment with one through four interferers. The initial SNR for the desired source was about -3 dB, representing a challenging cocktail-party situation at about the lower threshhold at which people with normal hearing can follow conversational speech. Each of these conditions summarizes many runs with at least four different configurations of positions of the interferers (the target was always positioned at broadside, or perpendicular to the line of the array), and at least eight combinations of different male and/or female talkers for each configuration. For comparison, the performance of our best implementation of the conventional GSC beamformer is also shown. As is clear from the figure, the performance of the biologically inspired FMV beamformer substantially exceeds that of the GSC, particularly (as expected) for cases with more than one simultaneous interferer. The FMV algorithm's performance may be somewhat inferior to the L/E method (which is too expensive to perform the complete battery of tests for direct comparison), but FMV clearly captures some of the strengths of the biological system. The slow convergence of the LMS-based iterative GSC adaptation prevents it from reacting fast enough to exploit the time-frequency sparseness of the interference. (Each test is only 2.4 seconds long and both beamformers are initialized to a conventional summing beamformer, so GSC's somewhat inferior performance even for one source also reflects slower convergence. For one source and after convergence, the performance of both beamformers is comparable.) The results strongly suggest that the FMV beamformer, like the L/E method, has captured at least one of the special "tricks" that the human hearing system uses to perform well with only two ears in the cocktail-party context.

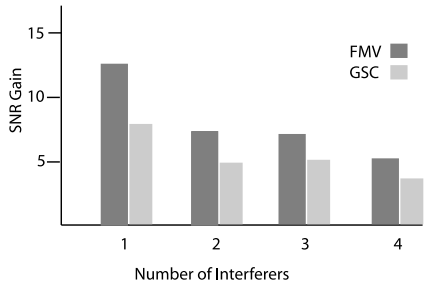

Figure 3: SNR gains for one, two, three, and four simultaneous speech interferers of the FMV (dark) and GSC (light) adaptive beamformers.

4 BIOLOGICALLY INSPIRED BEAMFORMING WITH A ZERO-APERTURE ArrAy

Miles *et al.* have found that *Ormia ochracea* obtains its amazing directional accuracy of less than two degrees with an ear about a millimeter across by a precise mechanical coupling of the common (omni-directional) and differential modes of oscillation between the left and right sections of the ear (Miles et al., 1995). A unique connecting structure with precise mechanical tuning causes even slightly off-center sound direction to induce much larger vibrations in the nearer ear-plate. Inspired by this system, Miles and collaborators are developing single-chip silicon MEMS arrays of two orthogonal differential and one omni-directional microphones (Miles et al., 2001), each only slightly larger than *Ormia*'s ear. The total aperture of this array is only a few millimeters on a side. An array with a similar acoustic response but in all three dimensions can be constructed out of three gradient (figure-8 pattern) hearing-aid microphones arranged orthogonally in three dimensions (X,Y, and Z axes) and one omni-directional microphone to form an acoustic vector sensor with a total extent of well less than a centimeter in any dimension (see (Lockwood and Jones, 2006) for a photograph of such an array used for the experiments reported below.)

The relative gains of a signal from direction θ and elevation ϕ on the three directional (X,Y, and Z) and one omni-directional (O) microphones are

$$g_O = 1 \tag{2}$$

$$g_X = \cos(\theta)\cos(\phi) \tag{3}$$

$$g_Y = \sin(\theta)\cos(\phi) \tag{4}$$

$$g_Z = \sin(\phi) \tag{5}$$

and are unique for any arrival direction. Since this array requires no spatial separation to distinguish the direction of arrival, is small, and the microphones are located right next to each other, we colloquially refer to this as a "zero-aperture" array.

4.1 Super-Resolution Direction-Finding With a Zero-Aperture Array

A unique mechanical structure combines the common (omni) and differential (directional gradient) modes of *Ormia*'s ear to form a highly directional response. Inspired by this remarkable biological system, we can combine these modes electronically to form a super-resolution beamformer. While Capon's MVDR beamformer is usually applied to spatially separated arrays with equal gains and for which relative phase differences between elements distinguishes the source direction, Capon's formulation applies as well to amplitude and phase or amplitude-only differences in directional response, a fact which has been exploited in underwater acoustic vector sensor arrays (Nehorai and Paldi, 1994) (D'Spain et al., 1992), and which has been shown to improve the performance of the FMV binaural beamformer on the head (Lockwood and Jones, 2006).

For narrowband or broadband noise sources, the MVDR beamformer can only localize fewer sources than sensors. Many engineering applications may require more, so we have combined the biological inspirations of *Ormia*'s directional microphone array and the mammalian hearing system to develop a method for doing so. With the acoustic vector sensor array, we imitate the interaural level difference system in the mammalian brain. As described above, the mammalian system exploits the time-frequency sparsity of natural sources to localize more sources than sensors by identifying the locations of sources in time-frequency bins in which only one source dominates.

Mohan *et al.* have developed a signal-processing-friendly approach for achieving the same goal (Mohan et al., 2003a) (Mohan et al., 2003b). As in the FMV algorithm described earlier, the inputs from all microphones are short-time Fourier transformed and cross-correlated within each frequency band. A sinple rank test is performed on each short-time-frequency correlation matrix to estimate the number of significant sources in that bin. Any bin of full rank (equal or more sources than sensors) is ignored; any bin of lower rank (more sensors than sources) can be used to estimate the direction of its dominant sources. To each low-rank bin we apply either an MVDR or MuSIC (Schmidt, 1986) beamformer using the directional array responses in (2), (3), (4), (5) to form the steering vectors, and form a composite localization map by summing (usually with normalization) these individual high-resolution directional maps. The number of sources and their locations are then determined in the usual manner by finding and threshholding the peaks of this composite response.

In both simulation and with real data, this algorithm achieves directional accuracy comparable to *Ormia* (less than two degrees of error variance) and locates more sources than sensors (Mohan et al., 2003a). It can be applied to, and performs similarly with, binaural arrays (Mohan et al., 2003b).

4.2 Speech Source Recovery With a Zero-Aperture Array

The *Ormia*-inspired acoustic vector sensor array can also be combined with the FMV algorithm for higher performance speech source recovery in the cocktail-party scenario with a much smaller aperture than even the binaural array. Since Capon's formulation supports steering vectors with direction-dependent amplitude, as well as phase, differences, FMV can be applied almost without modification other than forming steering vectors according to the relative responses of the directional microphones in the target direction.

Figure 4 shows the performance in terms of SNR gain of a 15 cm two-element free-field array in an anechoic environment with one through four interferers. The physical experiments from which these data are created are identical to those used to create Figure 3. Since all sources were in the horizontal plane, we used only three microphones, the X and Y directional microphones and the omni.

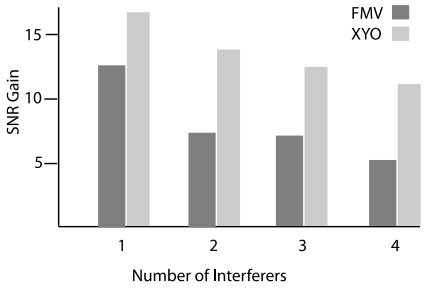

Figure 4: SNR gains for one, two, three, and four simultaneous speech interferers of binaural and XYO arrays with the FMV adaptive beamformer.

The performance of the FMV beamformer with the XYO microphone array is considerably better than with the binaural array. We believe that this is mainly because the relative difference in the response of the directional microphones is relatively independent of frequency and is greater at the lower frequencies comprising most of the speech signal energy; at these frequencies, the separation of the binaural array is much less than half a wavelength, and separation of the sources becomes progressively more difficult. The extra microphone may also play a lesser role.

5 ADAPTIVE BEAMFORMER PERFORMANCE WITH REVERBERATION

The human hearing system performs well in complex natural environments, which usually include at least modest, and sometimes quite substantial, reverberation. As described earlier, adaptive beamforming algorithms are particularly sensitive to reverberation, which alters the effective steering vectors of the source. This makes the desired source appear to come from a different direction, and the super-resolution interference suppression of the adaptive beamformer then allows it to cancel the target even if these errors are small. It is essential to evaluate our biologically inspired algorithms, which only capture some of the features of the complex biological system, for their robustness to the reverberation found in typical listening situations.

Figure 5 shows the performance of the binaural beamformer in the presence of reverberation for the same set of tests shown above. The "anechoic" steering vectors were obtained by measuring impulse responses from microphones near the center of a sound-treated room and truncating these after the initial response was complete and before arrival of the first reflections. The steering vectors thus capture the response of the microphones and recording electronics but not the room. The impulse responses in multiple rooms, such as typical and large conference rooms and offices, were measured at various distances at fifteen-degree increments, to allow the synthesis of many realistic scenes with various positions and numbers of interferers.

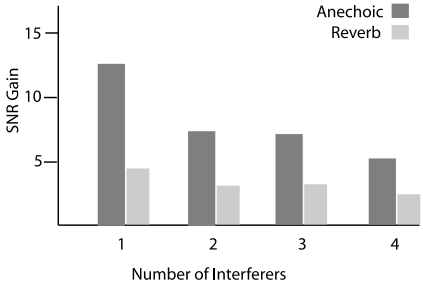

Figure 5: SNR gains for one, two, three, and four simultaneous speech interferers of the FMV beamformer in anechoic and reverberant conditions.

Figure 5 shows the performance in terms of SNR gain for the FMV algorithm in a typical medium-sized conference room, with a reverberation time (T_{60}) of less than 0.4 seconds, for target and interfering speech sources at a 1 meter distance, at which the direct sound substantially exceeds the reverberation. Even in these relatively benign conditions, the performance of the beamformer, while still positive, drops dramatically in the presence of reverberation. The reduced performance even with a single interferer indicates that it is mostly due to mismatch of the steering vector for the target source, rather than changes in the response to the interferers; other tests too numerous

to describe here support this diagnosis. Humans perform as well or even slightly better under conditions of modest reverberation compared to anechoic conditions, so this performance loss is due to limitations of the algorithm rather than the intrinsic difficulty of the problem.

Robust beamforming methods attempt to overcome this problem. Cox, *et al.* show that several criteria for robustness are optimized by regularization of the correlation matrix in Capon's formulation (Cox et al., 1987). This has the effect of controlling self-cancellation for small deviations in the steering vector, but at the price of reducing the interference suppression. Many other methods have been introduced that minimize the worst-case performance or introduce additional constraints to prevent self-cancellation over an uncertainty region, but again these methods sacrifice interference cancellation to obtain robustness. As mentioned earlier, the human hearing system's performance has been shown to *improve* somewhat with modest reverberation, which indicates that it works on very different principles. We speculate that it learns, adapts to, and exploits the actual room response, thus avoiding the trade-off between performance and robustness of current signal-processing approaches. We are currently working on practical techniques to do the same.

6 CONCLUSIONS

The excellent performance of the biologically inspired binaural adaptive beamformers with more speech sources than microphones strongly suggests that the biologically inspired algorithms capture some of the essential features of the mammalian hearing system that allow humans to perform so well in these conditions. These key elements are exploitation of the time-frequency sparseness of natural source signals via short-time frequency decomposition and rapid, separate adaptation in each band to take maximal advantage of it. Similarly, the comparable performance in directional localization accuracy of the binaural algorithm based on the Jeffress auditory model to that of humans, as well as that of the acoustic vector sensor array of collocated directional microphones with that of the parasitoid fly *Ormia ochracea*, suggests that these localization algorithms have identified some of the key principles of the biological systems.

The substantial degradation in performance of the FMV beamformer with levels of reverberation easily tolerated by humans suggests, on the other hand, that key features of human auditory processing of great importance to real-world application are missing from the model. Preliminary evidence that the localization-extraction method (which is based more directly on the physiological model) degrades less under reverberant conditions may eventually yield some hints as to what is missing. Current robust beamforming algorithms tolerate reverberation by limiting the damage to performance due to errors in the steering vector (often at substantial sacrifice to performance under good conditions); biological systems, on the other hand, seem to adapt to and even exploit the real-world conditions. We are currently exploring new strategies for robust beamforming that attempt to learn and exploit the variations in response introduced in real-world conditions, with the ultimate goal of building algorithms approaching the remarkable robustness shown by biological signal processing systems.

The characteristics of biological and electronic devices are very different, particularly in terms of complexity of function, parallelism, and speed, so the best biologically inspired signal processing systems may involve different implementations at the "hardware" level. We thus believe that biological *inspiration*, based on discernment of the underlying physical or signal processing principles exploited by the biological system, usually yields better results than biological *imitation*. However, physiology only indirectly indicates the signal processing principles exploited by the auditory sensors and the brain, so the development of effective and efficient biologically inspired signal processing algorithms is rarely straightforward. Close collaboration between physiologists, psychophysicists, and signal processors can yield insights and ultimately signal processing systems that would be difficult to conceive individually.

ACKNOWLEDGEMENTS

We gratefully acknowledge the research support of the Mary Jane Neer Foundation, Phonak USA, Inc., the National Institutes of Health NIH-NIDCD 1R01DC005782-01A1, DARPA DAAD17-00-0149, and the National Science Foundation ITR CCR-0312432.

REFERENCES

Bronkhorst, A. and Plomp, R. (1992). Effect of multiple speechlike maskers on binaural speech recognition in normal and impaired hearing. *Journal of the Acoustical Society of America*, 92:3132–3139.

Capon, J. (1969). High-resolution frequency-wavenumber spectrum analysis. *Proceedings of the IEEE*, 57(8):1408–1418.

Cox, H., Zeskind, R., and Owen, M. (1987). Robust adpative beamforming. *IEEE Trans. Acoust., Speech, Signal Processing*, 35(10):1365–1376.

D'Spain, G., Hodgkiss, W., Edmonds, G., Nickles, J., Fisher, F., and Harriss, R. (1992). Initial analysis of the data from the vertical DIFAR array. *Proc. Mast. Oceans Tech.(Oceans. 92)*, pages 346–351.

Frost III, O. (1972). An algorithm for linearly constrained adaptive array processing. *Proceedings of the IEEE*, 60(8):926–935.

Greenberg, J. (1998). Modified LMS algorithms for speech processing with an adaptive noise canceller. *IEEE Transactions on Speech and Audio Processing*, 6(4):338–351.

Griffiths, L. and Jim, C. (1982). An alternative approach to linearly constrained adaptive beamforming. *IEEE Transactions on Antennas and Propagation]*, 30(1):27–34.

Jeffress, L. (1948). A place theory of sound localization. *J. Comp. Physiol. Psychol*, 41(1):35–39.

Liu, C., Wheeler, B., O.Brien Jr, W., Bilger, R., Lansing, C., and Feng, A. (2000). Localization of multiple sound sources with two microphones. *Journal of the Acoustical Society of America*, 108:1888.

Liu, C., Wheeler, B., O.Brien Jr, W., Lansing, C., Bilger, R., Jones, D., and Feng, A. (2001). A two-microphone dual delay-line approach for extraction of a speech sound in the presence of multiple interferers. *Journal of the Acoustical Society of America*, 110:3218.

Lockwood, M. and Jones, D. (2006). Beamformer performance with acoustic vector sensors in air. *Journal of the Acoustical Society of America*, 119:608.

Lockwood, M., Jones, D., Bilger, R., Lansing, C., O.Brien Jr, W., Wheeler, B., and Feng, A. (2003). Performance of time-and frequency-domain binaural beamformers based on recorded signals from real rooms. *Journal of the Acoustical Society of America*, 115:379.

Miles, R., Gibbons, C., Gao, J., Yoo, K., Su, Q., and Cui, W. (2001). A silicon nitride microphone diaphragm inspired by the ears of the parasitoid fly Ormia ochracea. *Journal of the Acoustical Society of America*, 110:2645.

Miles, R., Robert, D., and Hoy, R. (1995). Mechanically coupled ears for directional hearing in the parasitoid fly Ormia ochracea. *Journal of the Acoustical Society of America*, 98:3059.

Mohan, S., Lockwood, M.E., Jones, D.L., Su, Q., and Miles, R.N. (2003). Sound source localization with a gradient array using a coherence test. *Journal of the Acoustical Society of America*, 114(4 pt. 2):2451.

Mohan, S., Kramer, M., Wheeler, B., and Jones, D. (2003). Localization of nonstationary sources using a coherence test. *IEEE Workshop on Statistical Signal Processing*, pages 470–473.

Nehorai, A. and Paldi, E. (1994). Acoustic vector-sensor array processing. *IEEE Transactions on Signal Processing*, 42(9):2481–2491.

Robert, D., Read, M., and Hoy, R. (1996). The tympanal hearing organ of the parasitoid fly Ormia ochracea (Diptera, Tachinidae, Ormiini). *Cell and Tissue Research*, 275(1):63–78.

Schmidt, R. (1986). Multiple emitter location and signal parameter estimation. *IEEE Trans. Antennas Propag*, pages 276–280.

Yost, W. and Gourevitch, G. (1987). *Directional hearing*. Springer-Verlag New York.

CARDIAC BEAT DETECTOR
A Novel Analogue Circuitry for the First Heart Sound Discrimination

Shinichi Sato
Department of Physiology, Akita University School of Medicine, 1-1-1 Hondo, Akita, Japan
bigwave@med.akita-u.ac.jp

Keywords: Non-invasive, piezoelectric transducer (PZT), analogue circuit, heart rate, respiration sounds, mice.

Abstract: Cardiac beat detector, which is an analogue circuitry installed in a novel non-invasive system for measuring heart rate in mice by using a piezoelectric transducer (PZT) sensor, performs an critical role in detecting the first heart sound (S1) in heart sounds. The PZT sensor detects heartbeat vibration and converts it to an electrical signal, namely the heart sounds. The measurement in intervals of S1s in the heart sounds is required to calculate heart rate, however, it is not simple because a S1 is a vibrating signal and has multiple peaks, which fluctuate in interval and in magnitude. In addition, respiration sound noise, which has frequency components similar with that of S1, makes S1 detection difficult and complex. The cardiac beat detector made it possible to overcome these problems by transforming multi-peaked S1 signal into a quasi-digital pulse. This technique is also available for the use in humans. Thus, the cardiac beat detector would contribute to the progress in the non-invasive heart rate measurement when it is installed in various, novel phonocardiogram-based equipments for the use in the fields of clinical and basic science in medicine.

1 INTRODUCTION

In experiments using small animals such as mice, a clip ECG electrode is often used for ECG recording (Yamada et al., 2001). However, investigators often encounter the problem with ECG signal deterioration or instability during long recording due to the hairy limbs and drying up of electrolytic paste between the limbs and the clip electrodes particularly in small animals. Moreover, there is an undeniable possibility that the pain induced by the electrode attachment might activate the sensory neurons and influence on the physiological state even in an anesthetized animal (Sato, 2007).

To overcome these problems, we recently developed a non-invasive cardiorespiratory monitor system for small animals using a piezoelectric transducer (PZT) sensor, which converts cardiac beats into an electrical signal when a small animal was simply placed on it (Sato et al., 2006; US patent 7174854). The PZT cardiorespiratory monitor enables stable and long measurement of heart rate of sleeping or anesthetized animals. Only placing an animal on the PZT sensor is required to monitor heart rate, and therefore, it gives no pain to animals. To calculate the heart rate, it is required to detect the first heart sound (S1) in a heartbeat signal detected by the PZT sensor. However, it is not simple to detect S1 constantly by distinguishing from noises of a frequency range similar to that of S1 because a S1 is composed of multi-peaked vibrating signal (Rangayyan and Lehner, 1988) and its magnitude decreases in anesthetized animals and humans (Manecke et al., 1999). A cardiac beat detector, which is made of a custom-designed analogue circuitry for S1 detection, was strikingly effective for detecting S1 and the second heart sound (S2) and for computing heart rate with a simple microprocessor algorithm.

2 METHOD

2.1 PZT Cardiorespiratory Monitor

The PZT cardiorespiratory monitor system consists of a PZT sensor device and a main unit, which contains two band-pass filters, a cardiac beat detector, a breathing movement detector, microprocessors and a temperature controller for the PZT sensor device. The sensor device consists of a disk-shaped thin PZT placed in a hole cut in a copper plate and covered by 0.5 mm-thick insulating sheets, which all were mounted on an electronic controlled heater (Sato et al., 2006) (Fig. 1).

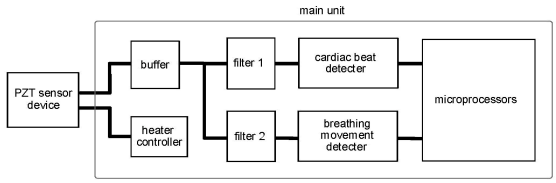

Figure 1: Block diagram of PZT cardiorespiratory monitor.

2.2 Signal Separation by Filters

Heart sound and breathing movement signals were separated from the PZT output signal by filters with pass band of 280-1000 Hz and 0.4-2.6 Hz for heart sounds and breathing movements, respectively, as shown in Fig. 2.

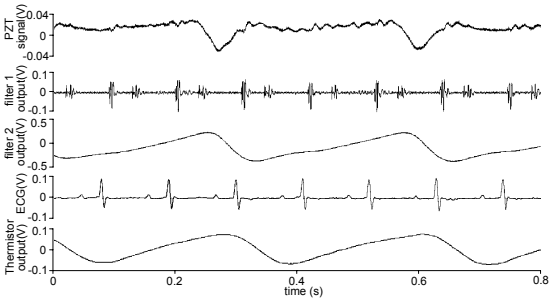

Figure 2: PZT output signal, Heart sounds, breathing movement signal, ECG and thermistor airflow sensor.

However, it was found that the presence of respiration sound noise, which was produced by airflow in airway, disturbs the detection of S1 (S2) when the magnitude of S1 (S2) declined in anesthetized mice (Fig. 3; upper trace). In addition, airway secretion produced marked, large-amplitude respiratory noise (Fig. 3; lower trace). These respiration-related noises were hardly possible to be removed by a filter because the frequency component of them were similar to that of S1; the period of vibrating signal of S1 (Ts) and respiration sound noise (Tr) was ranged between 1.4 and 4.0 ms (average = 2.4 ms, n = 50) and between 3.5 and 7.7 ms (average = 5.4 ms, n = 50), respectively. The frequency components of both S1 and respiration sound noise fluctuated, and therefore, they ranged widely and overlapped each other.

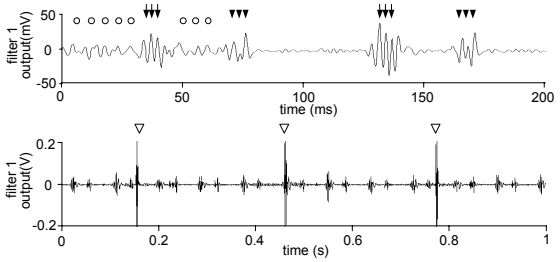

Figure 3: Representative traces of respiration sound noise (open circles; upper trace) and large-amplitude respiratory noise (open triangles; lower trace). Arrows and arrowheads indicate S1 and S2, respectively.

2.3 Cardiac Beat Detector

Since it was difficult to accomplish effective removal of the respiration sound noise from heart sounds by a filter because they have similar frequency components and fluctuate, we have developed a novel cardiac beat detector circuit, which consists of two diode detectors connected to a differential amplifier, an AC amplifier, and a hysteresis comparator (Fig. 4a). This circuit has three functions; (1) S1 emphasizing, (2) transforming S1 into a quasi-digital pulse and (3) automatic threshold controlling (Sato et al., 2006).

2.3.1 S1 Emphasizing Function

As described above, frequency components of S1 are at slightly higher range than those of respiration sound noise, although the both components fluctuate and overlap in part. To overcome the fluctuation, the cardiac beat detector was designed to emphasize always a higher frequency sounds over relatively lower frequency sounds. The S1 emphasizing function is produced by the combination of two diode detectors, which work as envelop detectors, and a differential amplifier (Fig.

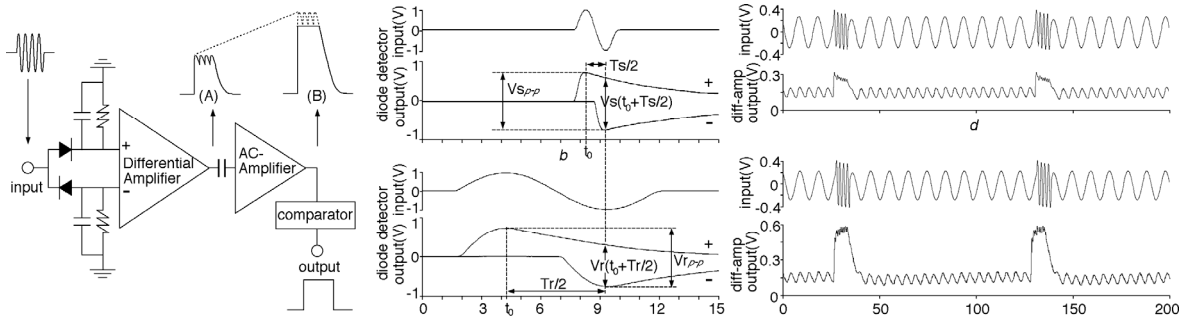

Figure 4: Function of the cardiac beat detector.

4a).

The two-diode detectors produce positive and negative envelopes with ripples when a sine wave is input. The voltage of the positive envelope during the declining phase (V(t)) is determined by a time constant RC as

$$V(t) = V_p\, e^{-t/RC} \quad (1)$$

where R and C are the resistance and the capacitance of the diode detectors and t is the time after a time of positive peak in the input and V_p is the voltage of the peak.

Output voltage difference between the two diode detectors at t = T/2 (V(T/2)) is calculated as

$$V(T/2) = V_p\,(1 + e^{-T/2RC}) \quad (2)$$

where T is the period of the input signal. Therefore, the higher input signal frequency, the larger voltage difference the diode detectors output. In fact, output voltage difference for an input sine wave of higher frequency ($Vs(t_0+Ts/2)$; Fig. 4b) is larger than that of lower frequency ($Vr(t_0+Tr/2)$; Fig. 4c).

This voltage difference appears equally in the differential amplifier output. Responses of the diode detectors to an input of a synthesized waveform, which consisted of alternating 4 cycles of a 500Hz sine wave (artificial S1) and 10 cycles of a 100Hz sine wave (artificial respiration sound), are shown in Fig. 4d and e. The artificial S1 is enhanced as compared to the artificial respiration sound when amplitudes of both inputs are almost the same (Fig. 4d), while the artificial S1 is largely enhanced when it is slightly larger than the artificial respiration sound in input signal (Fig. 4e). Fig. 4d demonstrates that the diode detectors have the S1 emphasizing function, while Fig. 4e shows an additional contribution of a rectifying property of diode, which abruptly reduces its resistance to the signal that exceeds about 0.3V, to the S1 emphasizing function.

Fig. 5 shows an example of quasi-digital pulses output from the differential amplifier when a real filtered heart sound signal was input ((A); Fig. 4a). The amplitude ratio of the S1 signal (filled circle) to the respiration sound noise (open circles) was enhanced from 3-fold in the input (broken lines; upper trace) to 10-fold in the output (lower trace) (Fig. 5). In addition, the cardiac beat detector combines the multi peaks of S1 into a quasi-digital pulse, which is helpful for the comparator to detect S1 easily. The unique combination of these effects enabled the emphasizing of S1 of higher frequency over the respiration sound noise of lower frequency, thus enabling a great improvement in the S/N ratio of the quasi-digital pulse.

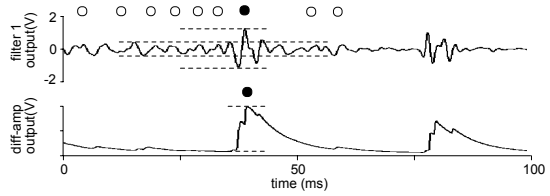

Figure 5: S1 emphasizing function of cardiac beat detector.

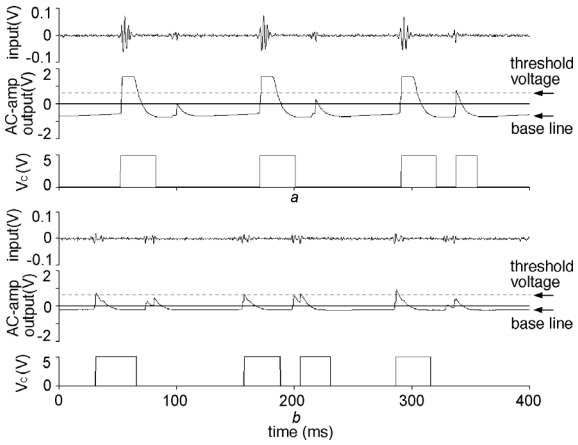

Figure 6: Automatic threshold adjustment controlled by the cardiac beat detector.

2.3.2 Automatic Threshold Controlling Function

The quasi-digital pulse (Fig. 5; lower trace) output from the differential amplifier was fed into the AC amplifier. The AC amplifier lowers the baseline of the differential amplifier output (quasi-digital pulse) to the negative direction when the magnitude of the quasi-digital pulse becomes larger (Fig. 6a), while the baseline approaches 0V when the pulse height declines (Fig. 6b). These responses of the AC amplifier to the change in magnitude of the quasi-digital pulse act as an automatic threshold control, which help comparator to detect the S1 signal with a higher sensitivity (Fig. 6).

2.4 Heart Rate Calculation by Microprocessor Program

The cardiac beat detector improved the incidence of S1 detection by removing the influence of respiration sound noises, however, large-amplitude respiratory noises, which were elicited by an airflow

in airway with airway secretion, still remained and induced errors in S1-S1 interval detection for heart rate calculation. Discrimination between S1 and S2 is also required for the heart rate calculation. I made a microprocessor program to overcome these problems. The major algorithms adopted in the program are; (1) to calculate the correct HR by selecting four S1-S1 intervals of less error from eight consecutive intervals and (2) to set a non-detection period of 75 ms after a S1 (or S2) for the discrimination of S1 from S2 (Sato et al., 2006).

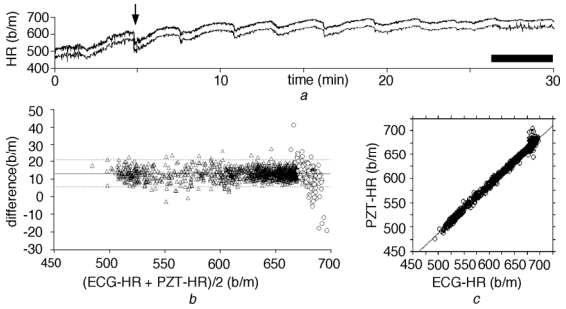

Figure 7: Comparison between the heart rate calculated by the PZT system and ECG for 30 min. Output of the PZT system (lower trace) and the heart rate calculated from the R-R intervals in ECG (upper trace) (a), their difference plot (b) and cross-correlogram (c). Black bar in (a) indicates the duration where large-amplitude respiratory noise appeared. Lower trace in (a) is lowered to show almost complete agreement between the two traces.

3 RESULT

Heart rate output from D/A converter in the PZT system (PZT-HR) and that calculated from ECG reading (ECG-HR) averaged over every 1 s were compared using 6 anesthetized adult C57BL/6 mice.

The PZT-HR and the ECG-HR were highly correlated (Fig. 7a). Difference plot between them also showed good correlation (Fig. 7b) even during the period when large-amplitude respiratory noise appeared (open circles; Fig. 7b). The difference plot demonstrated the highly reliable detection of HR by the PZT system; 96.2% (1,729/1,798) of total points fell within ±2 SD of the mean value. The PZT-HR also closely followed a rapid decrease in HR at a rate of 33 b/m/s (arrow in Fig. 7a). Cross-correlation coefficient between PZT-HR and ECG-HR was 0.995±0.003 (mean±SD, n = 6; Table 1, Fig. 7c).

Table 1: Correlation between PZT-HR and ECG-HR.

mouse	*r*	difference (%)
1	0.995	1.9±0.5
2	0.990	1.8±1.7
3	0.992	2.9±1.6
4	0.997	1.3±0.6
5	0.999	2.4±1.3
6	0.997	2.1±0.6

4 DISCUSSIONS

Since the high-frequency component of S1 is comprised of multi peaks of vibrating signal, the program code for heart rate calculation would be a complex one in the case without the use of the cardiac beat detector although recent developments in digital signal processing of the phonocardiogram have been reported (Durand and Pibarot, 1995; Wang et al, 2001). All intervals between peaks of S1 and S2 in addition to respiration sound noises, which are all composed of multi-peaked signal and fluctuate in interval and/or in magnitude, should be measured quickly and the initial point of the S1 should be properly identified almost instantaneously during each heart cycle of less than 100 ms. In contrast to such considerably complex digital signal processing, making the quasi-digital pulse from vibrating S1 signal with enhancing S/N ratio using the cardiac beat detector ensures the easier digital conversion of the S1 signal for the heart rate calculation.

In conclusion, the present study demonstrated that the cardiac beat detector has a performance suitable for the non-invasive detection of S1 in the heart sounds of small animals. It should be noted that the cardiac beat detector is available not only for anesthetized small animals but also unanesthetized animals and humans at sleep or rest. Indeed, the PZT system can be applied to unanesthetized newborn mice (Sato et al., 2007), human infants (Sato et al., 2006) or bedridden patients after some alteration to the sensor construction. As the cardiac beat detector greatly reduces the program code for S1 detection, it would help us to create novel phonocardiogram-based equipments for a wide range of fields in clinical and basic sciences in medicine.

ACKNOWLEDGEMENTS

I wish to thank Prof. Kyoichi Ono, Prof. Nobuya Inagaki and Prof. Katsuya Yamada for helpful advice and suggestions.

REFERENCES

Durand, LG., Pibarot, P., 1995. "Digital signal processing of the phonocardiogram: review of the most recent advancements", *CRC Crit Rev Biomed Eng* 23: 163–219

Manecke, GR. Jr., Nemirov, MA., Bicker, AA., Adsumelli, RN., Poppers, PJ., 1999. "The effect of halothane on the amplitude and frequency characteristics of heart sounds in children", *Anesth Analg* 88: 263–267.

Rangayyan, RM., Lehner, RJ., 1988. "Phonocardiogram signal analysis: a review", *CRC Crit Rev Biomed Eng* 15: 211–236.

Sato, S., K, Yamada., N, Inagaki., 2006. "System for simultaneously monitoring heart and breathing rate in mice using a piezoelectric transducer", *Med Biol Eng Comput* 44(5): 353-362.

Sato, S., Ishida, A., Kawamura, N., Nakajima, W., Takada, G., Inagaki, N., 2006. "A new PZT (piezoelectric transducer)-based heartbeat and breathing monitor system for newborn", *Pediatric Academic Society's Annual Meeting* San Francisco, California.

Sato, S., 2007. "Heart rate drop in newborn mice caused by attaching ECG electrodes", *J Physiol Sci* 57(suppl): S136.

Wang, W., Guo, Z., Yang, J., Zhang, Y., Durand, LG., Loew, M., 2001. "Analysis of the first heart sound using the matching pursuit method", *Med Biol Eng Comput* 39(6): 644-8.

Yamada, K., Ji, JJ., Yuan, H., Miki, T., Sato, S., Horimoto, N., Shimizu, T., Seino, S., Inagaki, N., 2001. "Protective role of ATP-sensitive potassium channels in hypoxia-induced generalized seizure", *Science* 292(5521): 1543-6.

DYNAMICAL PROPERTY OF PERIODIC OSCILLATIONS OBSERVED IN A COUPLED NEURAL OSCILLATOR NETWORK FOR IMAGE SEGMENTATION

Tetsuya Yoshinaga and Ken'ichi Fujimoto
Faculty of Medicine, The University of Tokushima
3-18-15 Kuramoto, Tokushima, 770-8509 Japan
(yosinaga—fujimoto)@medsci.tokushima-u.ac.jp

Keywords: Coupled oscillator, image segmentation, dynamical system, bifurcation.

Abstract: We consider image segmentation using the LEGION (Locally-Excitatory Globally-Inhibitory Oscillator Network), and investigate dynamical properties of a modified LEGION, described by noise-free or deterministic continuous ordinary differential equations. We clarify a phenomenon of image segmentation corresponds to the appearance of a synchronized periodic solution, and the ability of segmentation depends on its symmetric properties. We study bifurcations of periodic solutions by using a computational method based on the qualitative dynamical system theory.

1 INTRODUCTION

Image segmentation technique underlies perceptual processes such as identification, recognition, and separation of different objects in a natural image. Various methods of image segmentation based on statistic, filtering, and machine learning techniques were presented (Russ, 2002). A practical image segmentation technique using the LEGION (Locally-Excitatory Globally-Inhibitory Oscillator Network) has also been proposed (Wang and Terman, 1995; Terman and Wang, 1995). It can segment different areas in an image, and then the segmented areas are rapidly exhibited in time-series. Because of the high ability of LEGION, there has been a lot of research on application to medical images (Shareef et al., 1999), implementation of analog electronic circuit (Cosp et al., 2004), and so on.

The LEGION is a coupled oscillator network consisting of oscillators, each of which has an excitatory unit and an inhibitory unit, and a global inhibitor. The dynamics of LEGION is described by nonlinear ordinary differential equations with a noise term. It is know that LEGION segments different image areas temporally and spatially, based on its own dynamics. Although its fundamental dynamics has been studied (Terman and Wang, 1995), there are no investigations for detailed dynamical structure and property of oscillations observed in the coupled oscillator network. Properties of the oscillations observed in LEGION are related to its fundamental ability for image segmentation, therefore analysis of the dynamical properties enable us to design the parameters of LEGION so that it achieves optimal image segmentation.

In this paper we study dynamical properties of oscillations observed in LEGION. Because the dynamics of the original LEGION (Wang and Terman, 1995) is a stochastic dynamical system with noise terms, in order to simplify our discussion, we study a noise-free LEGION, which is a deterministic dynamical system. Bifurcation analysis is useful for designing system parameter. Through the bifurcation analysis, we clarify that a phenomenon of image segmentation corresponds to the appearance of a synchronized periodic solution, and the ability of segmentation depends on its symmetric properties.

2 MODEL DESCRIPTION

The LEGION consists of a global inhibitor and oscillators which are arranged in grid; and the number of oscillators corresponds to the number of pixels in target image. We illustrate single oscillator which consists of an excitatory unit EU_i and an inhibitory unit IU_i in Fig.1 (a). The excitatory unit couples with the other excitatory units in its four-neighborhood

each other, and all excitatory units also connect to the global inhibitor. The architecture of LEGION is shown in Fig.1 (b). Figure 1 (c) illustrates the behavior of LEGION and schematic diagram of an image segmentation procedure. The dynamics of an oscillator indexed by i ($i = 1, 2, \ldots, n$) is described by

$$\frac{dx_i}{dt} = 3x_i - x_i^3 + 2 - y_i + I_i + C_i \quad (1)$$

$$\frac{dy_i}{dt} = \eta\left[\gamma(1 + \tanh(x_i/\beta)) - y_i\right]. \quad (2)$$

We eliminated noise terms from the original LEGION (Wang and Terman, 1995) so that the system becomes a deterministic dynamical system. The variables x_i and y_i represent the states of the excitatory and inhibitory units, respectively. The symbol I_i denotes external stimulation to the oscillator. Its value is determined by the i-th pixel value. The symbol C_i represents the summation of the coupling strength among oscillators, which is defined by

$$C_i = \sum_{k \in N(i)} W_{ik} S(x_k, \theta_x) - W_z S(z, \theta_{xz}) \quad (3)$$

where

$$S(x, \theta) = \frac{1}{1 + \exp(-K(x - \theta))}. \quad (4)$$

Here $N(i)$ indicates the four-neighborhood of the i-th oscillator, W_{ik} denotes the coupling strength between the i-th oscillator and the other k-th oscillator in $N(i)$, and W_z denotes the coupling strength between the i-th oscillator and the global inhibitor. Using the sigmoidal function, described by Eq.(4), instead of the Heaviside function in the original LEGION, the dynamics of the global inhibitor is defined by

$$\frac{dz}{dt} = \phi\left(S\left(\sum_{k=1}^{n} S(x_k, \theta_{zx}), \theta_{zx}\right) - z\right) \quad (5)$$

where γ, β, θ_x, θ_{xz}, θ_{zx}, K, and ϕ indicate parameters, which are fixed as the same values of the original

$$\gamma = 6.0, \quad \beta = 0.1, \quad \theta_x = -0.5$$
$$\theta_{xz} = \theta_{zx} = 0.1, \quad K = 50, \quad \phi = 3.0 \quad (6)$$

and η is a bifurcation parameter.

We treat binary images shown in Figs. 2–3; the indexes of the pixels are also shown in the same figures. For the binary images, the value of I_i is determined by

$$\begin{cases} I_i > 0, & \text{if the } i\text{-th pixel is white} \\ I_i < 0, & \text{if the } i\text{-th pixel is black.} \end{cases} \quad (7)$$

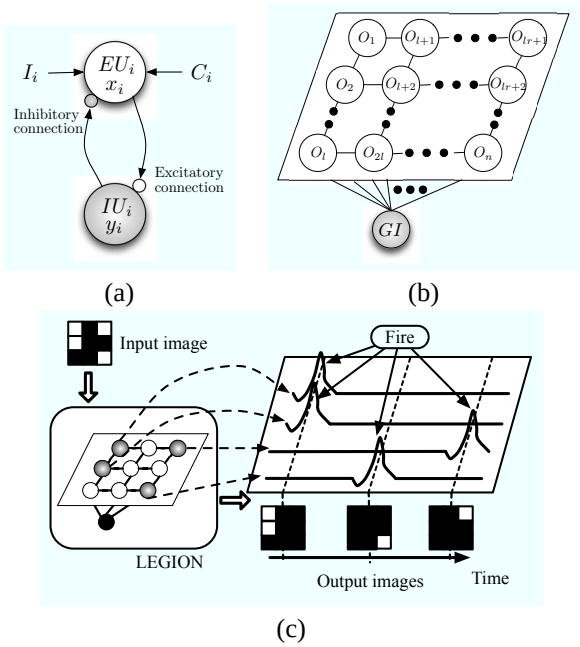

Figure 1: (a), (b) Architecture of LEGION, and (c) behavior of LEGION and schematic diagram of image segmentation.

1	4	7
2	5	8
3	6	9

(a) Input image (b) Index number of each pixel

Figure 2: (3×3)-pixel image and its index number of each pixel.

3 METHOD OF ANALYSIS

We summarize methods for calculating bifurcations in the deterministic LEGION defined in the preceding section. Let us consider an N-dimensional general autonomous differential equation consisting of Eqs.(1)–(5) such that

$$\frac{d\mathrm{x}}{dt} = f(\mathrm{x}). \quad (8)$$

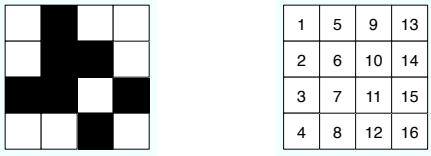

1	5	9	13
2	6	10	14
3	7	11	15
4	8	12	16

(a) Input image (b) Index number of each pixel

Figure 3: (4×4)-pixel image and its index number of each pixel.

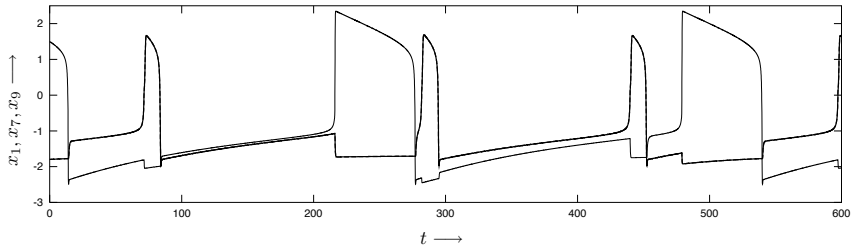

(a)

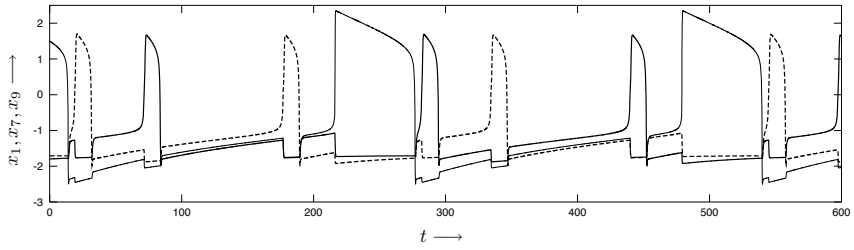

(b)

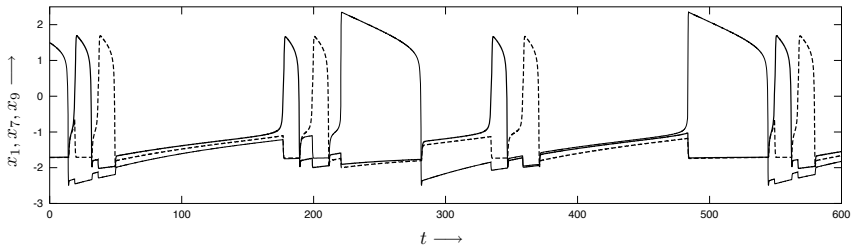

(c)

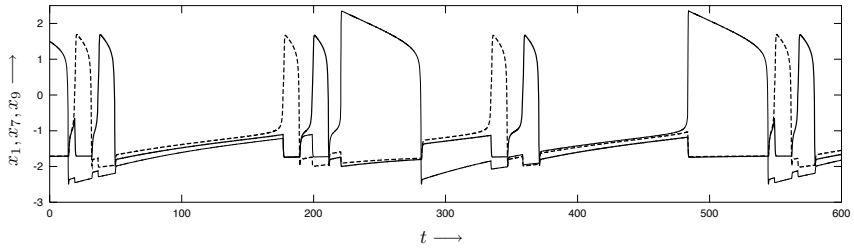

(d)

Figure 4: Waveforms of stable periodic solutions under $\eta = 0.02$. The thin solid curve indicates the states of the oscillators x_1 and x_2; and the heavy solid curve and the dashed curve denote the states of the oscillators x_7 and x_9, respectively.

The state vector $\mathrm{x} \in R^N$ corresponds to the set $\{x_1, y_1, x_2, y_2, \ldots, x_n, y_n, z\} \in R^{2n+1}$, where n denotes the number of oscillators. Note that $f(\mathrm{x})$ is C^∞-class function for all state variables and all parameters. We assume that there exists a solution with initial condition, $\mathrm{x} = \mathrm{x}_0$ at $t = t_0$, described by $\mathrm{x}(t) = \varphi(t; \mathrm{x}_0)$ for all t.

We consider a local manifold Σ in the N-dimension state space with the scalar condition $g(\mathrm{x}) = 0$, which is described by

$$\Sigma = \left\{ \mathrm{x} \in R^N \mid g(\mathrm{x}) = 0,\ g : R^N \to R \right\}. \qquad (9)$$

We arrange a local section $\Pi \subset R^{N-1}$ in Σ called the Poincaré section. Using the coordinate transformation h described by

$$h\ :\ \Sigma \to \Pi \subset R^{N-1}; \quad \mathrm{x} \mapsto \mathrm{u}, \qquad (10)$$

we define the Poincaré map T as

$$T\ :\ \Pi \to \Pi; \quad \mathrm{u} \mapsto h \circ \varphi\left(\tau(h^{-1}(\mathrm{u})); h^{-1}(\mathrm{u})\right) \quad (11)$$

where $\tau(h^{-1}(\mathrm{u}))$ is the time in which the trajectory emanating from a point $\mathrm{u} \in \Pi$ at $t = t_0$ will go across the Π again. Then an m-periodic solution in Eq.(8) corresponds to a fixed point of T^m, i.e., m-periodic point of T. Hence, one of analyses of m-periodic solutions observed in Eq.(8) can be reduced to an analysis of a fixed point of T^m.

Let $u^* \in R^{N-1}$ be a fixed point of T^m such that

$$u^* - T^m(u^*) = 0. \qquad (12)$$

Then the characteristic equation of the fixed point is defined by

$$\chi(\mu) = \det\left(\mu I_{N-1} - \frac{\partial T^m(u^*)}{\partial u}\right) = 0 \qquad (13)$$

where I_{N-1} is the $(N-1) \times (N-1)$ identity matrix. By using the Poincaré map T^m we totally have $2(N-1)$-different-type hyperbolic fixed points. The topological property of a hyperbolic fixed point is determined by the value of characteristic multipliers μ_i, $(i = 1, 2, \ldots, N-1)$: if all characteristic multipliers are in the unit circle on the Gaussian plane, then the fixed point is stable; the fixed point is unstable if one or more characteristic multipliers are outside the unit circle. Hence, we can discuss topological property of the fixed point based on the value of the characteristic multipliers. Let us classify fixed points into two types ${}_kD$ and ${}_kI$, where k is the number of characteristic multipliers outside the unit circle; it also represents the dimension of unstable subspace. The types D and I correspond to the even and odd numbers of characteristic multipliers in the range of $(-\infty, -1)$ on the real axis, respectively. Bifurcation of a fixed point occurs when its topological property is changed by the variation of a system parameter. The types of bifurcations are tangent bifurcation, period-doubling bifurcation, the Neimark-Sacker bifurcation, and D-type of branching. Bifurcation sets of a fixed point are computed (Kawakami, 1984) by solving the simultaneous equation which consists of Eqs.(12)–(13).

Now, let us discuss a symmetrical property of the system in Eq.(8). Assume that there exists a transformation Q satisfying $Q(f(\mathrm{x})) = f(Q(\mathrm{x}))$. Then such a system may have a periodic solution satisfying $Q(\varphi(t; \mathrm{x}_0)) = \varphi(t + L; \mathrm{x}_0)$ for all t, where $L \geq 0$ is a phase difference. We call it a (Q, L)-symmetric periodic solution.

4 RESULTS AND DISCUSSION

This section is devoted to show and discuss numerical results obtained from bifurcation analysis of a couple of examples.

4.1 Example 1

We investigate periodic solutions observed in the deterministic LEGION for 3×3 pixel image shown in Fig.2. Each external stimulus I_i, $i = 1, 2, \ldots, 9$, is defined as

$$\begin{cases} I_i = 0.2, & \text{if the } i\text{-th pixel is white} \\ I_i = -0.02, & \text{if the } i\text{-th pixel is black.} \end{cases} \qquad (14)$$

Because the pixels indexed by 1, 2, 7, and 9 are white, we observe oscillatory responses from the oscillators with the same indices, and non-oscillatory responses from the other oscillators. Note that, because the set satisfying $x_7 \equiv x_9$ and $y_7 \equiv y_9$ is an invariant subspace in the state space, the system is symmetric with respect to the transformation, say Q_1, swapping (x_7, y_7) and (x_9, y_9).

For oscillatory solutions we use symbolic sequence of strings representing the continuation of in-phase firing assigned by the oscillator indices and non-firing assigned by dot (“.”). For example, the set of $(12.79.7.9)$ indicates a sequence in the order of firing: oscillators 1 and 2 (instantaneously in-phase), oscillators 7 and 9 (instantaneously in-phase), oscillator 7, and oscillator 9, periodically.

Figure 4 shows waveforms of stable periodic solutions observed in the system at $\eta = 0.02$. The symbolic sequences corresponding to Figs.4 (a)–(d) are, respectively, as follows: (a) $(12.79.79.12.79)$; (b) $(12.7.9.7.12.9.7.9)$; (c) $(12.7.9.7.9.12.7.9)$; and (d) $(12.9.7.9.7.12.9.7)$. The solutions shown in Figs.4 (a) and (b) are $(Q_1, 0)$- and $(Q_1, \tau/2)$-symmetric two-periodic solutions, respectively, where τ denotes the

period of solution. While, each of the solutions shown in Figs.4 (c) and (d) has no symmetric property itself, however, it is reflectional with respect to the transformation Q_1 each other. We show the time-series of output images from LEGION in Fig.5, which corresponds to the solution of Fig.4 (b). The connected white pixels, the first pixel and the second pixel, always appear instantaneously in-phase. Then three different image areas are segmented temporally and spatially.

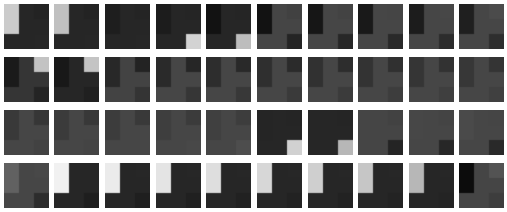

Figure 5: Snapshots of time-series output in LEGION which corresponds to the periodic solution shown in Fig. 4 (b). These output images sequentially appear from on the top-left to the bottom-right; then its appearance in each line starts from the left.

We investigate bifurcations of periodic points based on the Poincaré section defined by

$$\Pi = \left\{ \mathrm{x} \in R^N \mid x_1 - 1.5 = 0,\ \frac{dx_1}{dt} < 0 \right\}. \qquad (15)$$

Figure 6 shows a one-parameter bifurcation diagram of a $(Q_1, 0)$-symmetric two-periodic solution as shown in Fig.4 (a). In the bifurcation diagram, the heavy curve denotes stable $(Q_1, 0)$-symmetric two-periodic solution, and the dashed curve indicates its destabilized solution. The circled point labeled by I^2 denotes the parameter value $\eta = 0.08098952872$, at which we observe a period-doubling bifurcation. By decreasing the value of η across the point, the following bifurcation formula occurs:

$$ {}_1I^2 \to {}_0D^2 + {}_1D^4 \qquad (16)$$

where the left- and right-hand sides of the arrow indicate the periodic points before and after the bifurcation, respectively. Hence, a stable two-periodic solution ${}_0D^2$ and a saddle-type four-periodic solution ${}_1D^4$ simultaneously occur, i.e., they coexist in a certain parameter region. Let us discuss the basin of the stable solution. Figure 7 (a) shows periodic points of the Poincaré map at $\eta = 0.0808$, projected to the (x_7, x_9)-plane. The points a and b indicates two-periodic point ${}_0D^2$, and the points c and d correspond to a $(Q_1, \tau/2)$-symmetric two-periodic solution, which is irrelative to the bifurcation in Eq.(16). The periodic points of the coexisting ${}_1D^4$ are near the point a. It can be confirmed by the phase portrait shown in Fig.7 (b), an enlarged figure of Fig.7 (a); the points e and f denote a

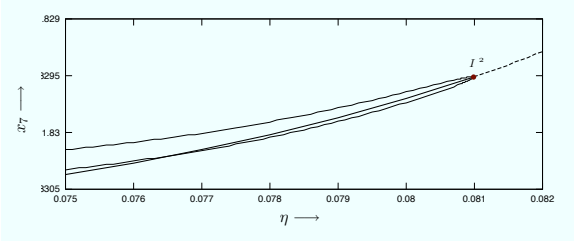

Figure 6: One-parameter bifurcation diagram of x_7 for the parameter η. The thin solid curve, the heavy solid curve, and the dashed curve denote the unstable four-periodic point, the stable two-periodic point, and its destabilized two-periodic point, respectively.

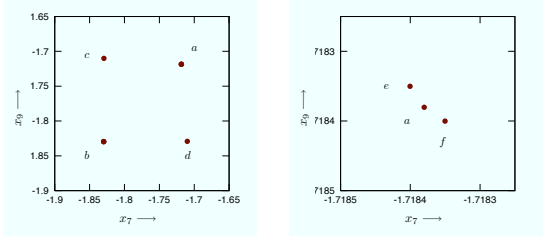

(a) (b)

Figure 7: Phase portrait of periodic points on the (x_7, x_9)-plane under $\eta = 0.0808$. The right figure is the enlarged figure around the point a in the left figure.

part of four-periodic points ${}_1D^4$. The period-doubling bifurcation of ${}_1I^2$ occurs so that its symmetry is broken, then the placement of the periodic points are reflected in the topological property which can be explained by its eigenvector. Besides, the basin boundary of ${}_0D^2$ is separated by the stable manifold of ${}_1D^4$. That is, we can observe ${}_0D^2$ when the initial value is placed only near its periodic point.

4.2 Example 2

As the second example we treat 4×4 pixel image shown in Fig.3. The value of each external stimulus I_i, $i = 1, 2, \ldots, 16$, is defined by Eq.(14); its index number i is shown in Fig.3 (b). Due to the pixels indexed by 1, 2, 4, 8, 9, 11, 13, 14, and 15 are white, the dynamical system has two symmetries for two swapping operators. One is described by $Q_2(f(\mathrm{x})) = f(Q_2(\mathrm{x}))$ where Q_2 is the transformation that swaps (x_1, y_1, x_2, y_2) with (x_4, y_4, x_8, y_8), respectively. The other symmetry is described by $Q_3(f(\mathrm{x})) = f(Q_3(\mathrm{x}))$ where Q_3 is the transformation that swaps (x_{11}, y_{11}) with (x_{16}, y_{16}). In this example, we investigate periodic solutions with the following relations: $(x_1, y_1) = (x_2, y_2)$, $(x_4, y_4) = (x_8, y_8)$, and $(x_9, y_9) = (x_{13}, y_{13}) = (x_{14}, y_{14})$. Periodic solu-

tions in Table 1 are observed under $\eta = 0.02$. Note that we employed the symbols $a, b, c, \ldots, g$ instead of the double-digit index numbers $10, 11, 12, \ldots, 16$, respectively. Besides, the symbols *A*, *B*, *C*, *D*, and *E* represent kinds of periodic solutions. All solutions in the category *A* are $(Q_2, 0)$-symmetric two-periodic solutions; the solutions A_1 and A_2 are reflectional symmetry for Q_2, then A_3 and A_4 are also reflectional symmetry for Q_3. The category *B* indicates $(Q_3, 0)$-symmetric two-periodic solution, then B_1 and B_2 are reflectional symmetry for Q_2. The category *C* denotes $(Q_3, \tau/2)$-symmetric two-periodic solution, then C_1 and C_2 are also reflectional symmetry for Q_2. Each periodic solution in *D* has two symmetries. The category D_1 is a two-periodic solution with $(Q_2, 0)$- and $(Q_3, 0)$-symmetric properties; the others D_2, D_3, and D_4 are two-periodic solutions with $(Q_2, 0)$-symmetric and $(Q_3, \tau/2)$-symmetric. All solutions in *E* are asymmetric two-periodic solutions, however, respective pairs of solutions (E_1, E_2) and (E_3, E_4) are reflectional symmetry for Q_3. The solutions (E_2, E_3) and (E_1, E_4) are also reflectional symmetry for Q_2, respectively. Besides, in the solutions A_3, A_4, B_3, B_4, C_3, C_4, D_1, D_4, and E_5, the image area connected white pixels, indexed by 9, 13, and 14, synchronously fire with the other white area, e.g., the pixels indexed by 1, 2, 4, or 8. This synchronization is interesting from a viewpoint of nonlinear science. However, it is inappropriate for image segmentation.

Table 1: Periodic solutions by symbolic sequences.

Category	Periodic solutions
A_1	(1248.b.g.9de.b.g.1248.b.g.9de)
A_2	(1248.g.9de.b.1248.g.b.9de.g.b)
A_3	(12489de.g.b.g.b.12489de.g.b)
A_4	(12489de.b.g.b.g.12489de.b.g)
B_1	(12.48.bg.9de.12.bg.48.9de.bg)
B_2	(12.9de.bg.48.12.bg.9de.48.bg)
B_3	(129de.bg.48.129de.bg.48.bg)
B_4	(12.bg.489de.12.bg.489de.bg)
C_1	(12.g.9de.b.48.g.12.b.9de.g.48.b)
C_2	(12.g.48.b.9de.g.12.b.48.g.9de.b)
C_3	(129de.g.b.48.g.129de.b.g.48.b)
C_4	(12.g.b.489de.g.12.b.g.489de.b)
D_1	(12489de.bg.12489de.bg.bg)
D_2	(1248.g.9de.b.g.1248.b.9de.g.b)
D_3	(1248.b.g.9de.b.1248.g.b.9de.g)
D_4	(12489de.g.b.g.12489de.b.g.b)
E_1	(12.g.b.48.9de.g.b.12.48.g.b.9de)
E_2	(12.b.g.48.9de.b.g.12.48.b.g.9de)
E_3	(12.b.g.9de.48.b.g.12.9de.b.g.48)
E_4	(12.g.b.9de.48.g.b.12.9de.g.b.48)
E_5	(12.b.g.489de.12.b.g.489de.b.g)

5 CONCLUDING REMARKS

We have investigated dynamical properties of periodic solutions observed in the deterministic LEGION, which is a modification from the original one by eliminating noise terms and replacing the Heaviside function with a sigmoidal function, in order to investigate dynamical properties and ability of LEGION. The main results obtained from the analysis using our method for computing bifurcation sets, are summarized as follows: (1) The dynamical system has various kinds of symmetric properties corresponding to the input image. Indeed we see that symmetric and asymmetric periodic solutions can be observed. Its patterns are based on the symmetric dynamical structure of LEGION; (2) A stable symmetric periodic solution bifurcates under a certain parameter. Moreover, then its basin boundary is determined by the stable manifolds of the coexisting saddle-type periodic solution; and (3) We also observed periodic solutions such that different image areas fire synchronously. The intrinsic objective of image segmentation in LEGION is that different image areas are not exhibited at the same time. Therefore, the appearance of the periodic solutions is inappropriate for this objective.

Their analyzed dynamical properties are directly related to fundamental abilities of LEGION. For higher quality of the segmentation, a mechanism for desynchronizing in-phase periodic solutions is required in the coupling system.

REFERENCES

Cosp, J., Madrenas, J., Alarcon, E., Vidal, E., and Villar, G. (2004). Synchronization of nonlinear electronic oscillators for neural computation. *IEEE Trans. Neural Networks*, 15(5):1315–1327.

Kawakami, H. (1984). Bifurcation of periodic responses in forced dynamic nonlinear circuits: computation of bifurcation values of the system parameters. *IEEE Trans. Circuits Syst.*, CAS-31(3):246–260.

Russ, J. (2002). *The image processing handbook, fourth Ed.* CRC Press.

Shareef, N., Wang, D., and Yagel, R. (1999). Segmentation of medical images using legion. *IEEE Trans. Medical Imaging*, 18:74–91.

Terman, D. and Wang, D. (1995). Global competition and local cooperation in a network of neural oscillators. *Physica*, D81:148–176.

Wang, D. and Terman, D. (1995). Locally excitatory globally inhibitatory oscillator networks. *IEEE Trans. Neural Networks*, 6(1):283–286.

COGNITIVE STATE ESTIMATION FOR ADAPTIVE LEARNING SYSTEMS USING WEARABLE PHYSIOLOGICAL SENSORS

Aniket A. Vartak[1], Cali M. Fidopiastis[2], Denise M. Nicholson[2], Wasfy B. Mikhael[1]
[1]*Department of Electrical Engineering and Computer Science,* [2]*Institute of Simulation & Training*
Univerisity of Central Florida,Orlando, FL, U.S.A.
aniket@ucf.edu, cfidopia@ist.ucf.edu, dnicholson@ist.ucf.edu, mikhael@mail.ucf.edu

Dylan D. Schmorrow
Office of Naval Research, U.S.A.
Dylan.Schmorrow@navy.mil

Keywords: Intelligent tutoring, psychophysiological metrics, augmented cognition, signal processing, wearable sensors.

Abstract: This paper presents a historical overview of intelligent tutoring systems and describes an adaptive instructional architecture based upon current instructional and adaptive design theories. The goal of such an endeavor is to create a training system that can dynamically change training content and presentation based upon an individual's real-time measure of cognitive state changes. An array of physiological sensors is used to estimate the cognitive state of the learner. This estimate then drives the adaptive mitigation strategy, which is used as a feed-back and changes how the learning information is presented. The underlying assumptions are that real-time monitoring of the learners cognitive state and the subsequent adaptation of the system will maintain the learner in an overall state of optimal learning. The main issues concerning this approach are constructing cognitive state estimators from a multimodal array of physiological sensors and assessing initial baseline values, as well as changes in baseline. We discuss these issues in a data processing block wise structure, where the blocks include synchronization of different data streams, feature extraction, and forming a cognitive state metric by classification/clustering of the features. Initial results show our current capabilities of combining several data streams and determining baseline values. Given that this work is in its initial staged the work points to our ongoing research and future directions.

1 INTRODUCTION

The design of metrics to determine cognitive state changes in real-time of persons performing tasks in their work environment is an emerging field of research. For example, Human Factors and Augmented Cognition research endeavors suggest the use of psychophysiological measures to determine best practices when developing trainers for military (Nicholson et al., 2006) and medical (Scerbo, 2005) occupations in an effort to optimize the learning state of the user. Further, a valid and reliable metric of cognitive state has far reaching utility in the field of intelligent tutoring, which has further implications for cognitive rehabilitation and assistive brain-computer interfaces.

This type of research is not possible without portable, unobtrusive psychophysiological sensing devices. However, utilizing physiological metrics such as electroencephalography (EEG) is difficult due to the many factors that influence cognitive processes intra and interpersonally. Some such factors include external demands (e.g., loud noises), trait characteristics (e.g., personality), and physical states (e.g., levels of fatigue). More importantly, the neurobiology underlying constructs defining cognitive states (e.g. working memory) are not fully elucidated (Cabeza & Nyberg, 2003), thus operationally defining "cognitive state" is difficult as is identifying a theoretical approach for studying it. Thus, the most straight forward approach to developing these metrics is by establishing a convergent methodology that is multimodal in nature (Karamouzis, 2006).

In this paper, we discuss the historical aspects of developing adaptive intelligent tutoring using psychophysiological metrics. Additionally, we describe our Adaptive Instructional Architecture,

which features multimodal sensors. We discuss challenges in developing a convergent methodology for using multimodal sensors. Finally, we present initial work on data fusion techniques necessary for driving the adaptive tutoring system.

2 ADAPTIVE TUTORING SYSTEMS

In 1958, Skinner challenged educators to become more efficient and effective in their teaching strategies by using "teaching machines". These machines would not only deliver learning content, but also allow the learner to interact with the system in a manner appropriate for learning to occur. The strength of this approach was the potential for customized instruction in an anytime anywhere format. However, teaching machines from this era neglected the knowledge base of the learner and focused more on "contingencies of reinforcement" or the presentation of learning material (Wenger, 1987).

"Intelligent Tutoring Systems" (ITS) was first coined by Sleeman & Brown (1982); however, it was Wenger (1987) who advocated for cross-talk among education, cognitive, and artificial intelligence researchers to shape the future of ITS design. This collaborative approach shifted emphasis from purely computational solutions to those that integrated Cognitive Psychology constructs (e.g., working memory) and new research in Education Psychology (e.g., experiential learning). The improved flexibility of these designs supported the successful transition of some adaptive systems into classrooms and workplaces (Anderson, et. al., 1995; Parasuraman et. al., 1992).

While previous ITS theories emphasized the knowledge state of the learner, current instructional design methods consider the learner's cognitive state, (i.e., cognitive load state) as more predictive of learning outcomes (Paas et. al., 2004). Cognitive load theorists contend that learning complex tasks (e.g., performing surgery) is optimal when the learning environment matches the cognitive architecture of the learner (Sweller, 1999). Thus, the learning environment should account for individual differences in the unique ways that individuals cognitively process data.

Physiological metrics of cognitive load such as pupil dilation and heart rate may map a learner's cognitive state to the learning task (Paas et al, 2003, p. 66). Another suggested use of psychometric data is to drive the adaptive response in the ITS (Karamouzis, 2006; Scerbo, 2006). In previous work, we have proposed an Adaptive Instructional Architecture (AIA) that merges the constructs of experiential learning, cognitive load, and adaptive trainers into a testbed simulation capable of measuring multimodal psychophysical responses (Nicholson et al., 2007). In the next sections we provide an overview of the AIA and give a description of the sensors used within the training environment. In addition, we provide pilot data from current studies which use multiple sensors to determine the learner's cognitive states. These studies are discussed in the context of data fusion strategies and point to future work in the field

3 OVERVIEW AIA, SENSORS, FEATURE EXTRACTION & DATA FUSION

3.1 Adaptive Instructional Architecture Overview

Figure 1 provides an overview of the Adaptive Instructional Architecture (AIA) within a simulator testbed. As shown the learner interacts with context based stimuli that follow the continuum from real world to simulated real world multi-sensory content. The psychophysiological sensors (e.g., heart rate) attached to the learner collect information about the learner's cognitive state. The sensor data streams are sent through a signal processing block (Figure 3) where data fusion techniques determine such constructs as learner engagement, arousal, and workload.

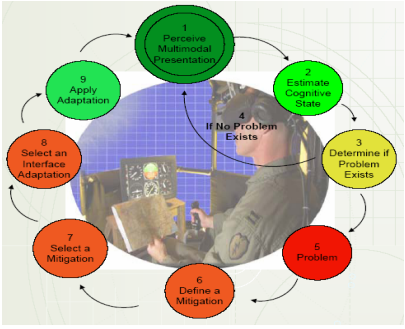

Figure 1: Adaptive Instructional Architecture Overview.

If the learner is experiencing higher than baseline values of these state references, the system chooses an appropriate mitigation strategy from a database of options. The system interface is then

adapted to adjust to the learner and the training scenario continues. This decision tree cycle is continued until the training session ends.

The novel features of the AIA are the potential to assess the cognitive state changes of the learner in real-time, change the learning scenario as the learner transitions in knowledge states, and assess performance outcomes concomitantly with the cognitive state assessment. Two main design issues faced are: 1) defining metrics derived from the mutimodal data streams that reliably predict the learner's cognitive state and 2) determining the relationship of the metric and that of mitigation selection. Our current focus is on deriving meaningful metrics from the multimodal data stream. In the next sections, we introduce the psychophysical sensors and measures that we are currently exploring.

3.2 Physiological Sensors and Cognitive State Estimation

Various proposed cognitive states such as arousal, and workload are quantified in terms of physiological parameters. For example, heart rate variability (HRV) can provide a measure of arousal (Hoover & Muth, 2005). Eye position tracking may indicate visual attention and stress. The EEG can provide brain based measures of psychological constructs such as cognitive workload. Thus, a multi-modal data acquisition strategy may be necessary for accurate cognitive state estimation (Erdogmus et al., 2005; Cerutti et al., 2006). However, synchronizing and determining relevant meaning of the multiple data streams is an ongoing issue.

Figure 2 represents examples of state-of-the-art psychophysiological sensing devices within our lab. The ASL 6000 eye tracker (www.a-s-l.com) shown in Figure 2 utilizes a head tracker with pan tilt capabilities to track the corneal reflection of the user. The B-Alert EEG (www.b-alert.com) provides classifications for engagement, mental workload, distraction and drowsiness (Berka et al., 2005). The Wearable Arousal Meter (WAM, www.ufiservingscience.com) also measures arousal however does so by utilizing inter-heartbeat interval (IBI) changes associated with task performance. Changes in IBI reflect the Respiratory Sinus Arrhythmia (RSA), which correlates with autonomic nervous system states (Hoover & Muth, 2004). Also shown are the respiratory, temperature, and GSR sensors of Thought Technologies InfinitiPro wireless system (www.thoughttechnologies.com). Overall, the sensors provide a portable solution for capturing real-time neural and behavioral responses training in a naturalistic environment.

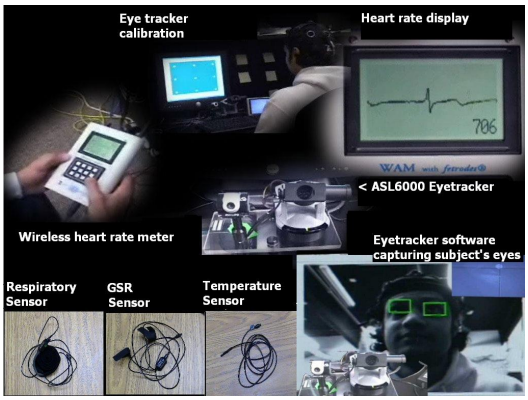

Figure 2: Sensor suite examples.

3.3 Block-wise Multimodal Signal Processing/ feature Extraction

The data generated from various sensors over time is enormous. To draw meaningful conclusions and to classify cognitive state in real-time, while also providing the feedback to the learner, the data may be effectively handled in a block processing procedure. Figure 3 provides a general overview of block processing as it applies to multimodal signal processing.

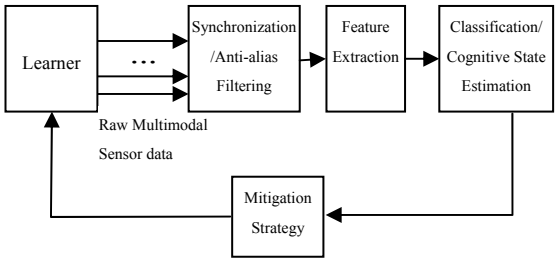

Figure 3: Multi-modal signal processing block.

The first block of the system synchronizes the data from various sensors. Multi-rate Digital Signal Processing (DSP) techniques such as decimation/interpolation are used to match the sampling frequency of various sensors. The data also needs to be time-synchronized to a unique clock-time, so that there is no error interpreting the data in further blocks.

The next block of feature extraction is a very important step in processing the data emanating from the sensor suite. The physiological measure will dictate what type of feature is to be extracted and the level to which this feature will provide

meaningfulness to the derived metric. In the following sub-section we will give an overview of typical features used from various sensors in the literature.

3.3.1 Heart Rate Features

The most popular feature used from the ECG data is the power spectral density (PSD) of the IBI. The PSD analysis provides a means to evaluate various autonomic nervous system influences on the heart efficiently. Most of the recent research focuses on quantifying the change in RSA as a measure of vagal tone activity influencing the heart (Hoover & Muth, 2005; Keenan & Grossman, 2006; Aysin & Aysin, 2006).

3.3.2 Blood Pressure Features

Blood pressure also affects heart rate modulation through the baroreceptor reflexes (Sleight & Casadei, 1995). The main challenge is to obtain a continuous measure of arterial blood pressure (ABP). The photoplethysmogram (PPG) signal is much more accessible and easily acquired in continuous manner as compared to direct measurement of the ABP signal. Recent work by Shaltis et al, (2005) discusses the calibration of the PPG signal to ABP signal.

3.3.3 Eye Tracking Features

The ASL 6000 eye tracker uses an IR camera to capture images of the eye. An image processing algorithm detects the dark pupil area in the eye and the glint of light coming off of the eye. Using these two measures, the learner's point of gaze (POG) is calculated. After proper calibration, the learner's POG can be transformed into a point on the screen correspond to where he or she is looking.

Various features could be extracted from the horizontal and vertical co-ordinate data, such as fixation intervals, speed of eye movement, and direction of eye movement. Marshall (2007) used these features as inputs to a neural network to classify cognitive states such as *relaxed/engaged, focused/distracted,* and *alert/fatigued.* The authors also state that as the data captured at the rate of 60-250 Hz, the states could be predicted in real time.

3.4 Data Fusion, Cognitive State Estimation

Once appropriate features psychometric data are extracted, a strategy is needed for defining the mathematical relationship between the feature the state change. For example, Marshall (2007) used features extracted from the eyetracker (e.g., eye blinks, eye movement, pupil size, and divergence) to classify cognitive activity into 'low' and 'high' activity measures. The authors used discriminant function analysis to create a linear classification model. A feed-forward neural network architecture was trained with backpropagation learning scheme to create a non-linear classification using the eyetracker features.

We are in the process of creating multidimensional classifiers based upon feature analysis across multiple psychophysiological metrics. These classifiers will eventually index levels of cognitive state, which in turn will drive the mitigation selection process of the AIA. The pilot work presented in the next section highlights current results.

4 PRELIMINARY RESULTS

4.1 Sensor Sensitivity in Cognitive State Estimation

We are currently investigating the sensitivity of the multimodal sensors to define cognitive state changes dynamically. For example, Figure 4 shows eyetracker data merged with the instantaneous arousal level of the observer, as the observer passively views a series of varying visual stimuli. The arousal metric is calculated from the heart rate data and was obtained using the WAM (Hoover & Muth, 2005).

In Figure 4(d), the ellipse represents the current viewing location of the observer. When the observer moves his or her eyes in a vertical direction, the major axis of the ellipse appears as vertical. A diagonal movement of the eyes will produce a circle as shown in Figure 4(a) and 4(c). Fixations are illustrated in 4(c). As the observer fixates onto a point of interest, the ellipse becomes a dot. The fixation time can be presented along with the fixation point in real-time or in an after action review format.

The arousal levels are mapped to the ellipse via colors ranging from red for high, yellow for medium, and green for low. The scale used to change the color will be verified experimentally using a variation of the International Affective Picture Sort (Lang et al., 2005). These transformed features may further be used to develop

multidimensional metrics with which to predict visual attention and arousal states of the learner.

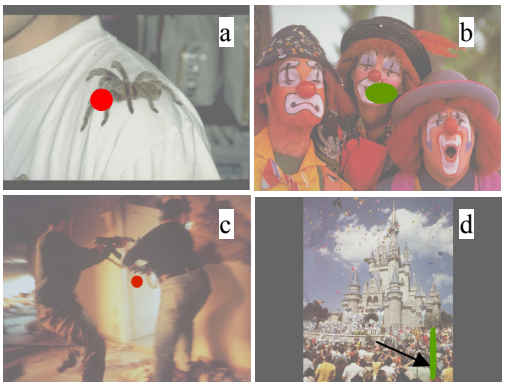

Figure 4: Four screen captures from our system, showing the observer's current gazing location along with the arousal (Images: Lang et al., 2005).

4.2 Identifying Baseline Values

Understanding how multimodal psychometric data combine to predict cognitive states is only one part of the problem in AIA design. Another issue is identifying initial baseline values that will set the system indices and determine the appropriate classification of the learner's cognitive state. Not only will these baseline values vary based upon individual difference, they may also vary during the training session.

In a recent study, we monitored the arousal state of persons placed in a mixed reality scenario representing an every day social experience. The social interaction was classified as friendly (e.g., mutual regard) or rude (e.g., confrontational). Figure 5 shows the percent high engagement as measured by the EEG and the mean skin conductance for a single participant. We used a multiple baseline approach to identify points in the scenario that may indicate a new baseline score.

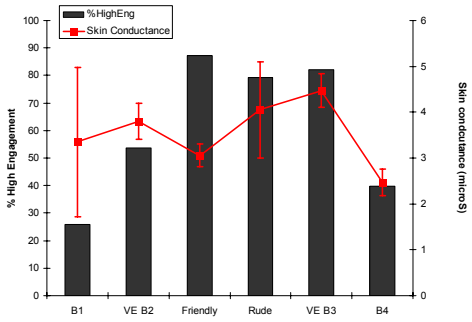

Figure 5: Skin conductance mean amplitude with 95% Confidence Interval and % High Engagement as measured by the EEG.

As shown, high engagement alone would not capture the change in state of the participant accurately. Regardless of variability, the sustained arousal carried over from experiencing the rude interaction may indicate a change in baseline that must be account for in order to appropriately select the next mitigation. Multimodal data is necessary to construct an appropriate metric to capture this type of sustained effect.

5 CONCLUSIONS

In this paper we reviewed the historical aspects of ITS design and discussed a new direction in combining current learning theory with adaptive system theory. The resulting AIA represents a step forward in providing on-demand training in a complex and contextually relevant training environment. The addition of physiological measures to estimate the cognitive state of the learner is not a novel; however, the data fusion techniques and the use of the multimodal data drive mitigation selection may present a worthwhile contribution to the field.

ACKNOWLEDGEMENTS

This work was supported by the Office of Naval Research and an In-House Grant provided by UCF's Institute for Simulation and Training.

REFERENCES

Nicholson, D., Stanney, K., Fiore, S., Davis, L., Fidopiastis, C., Finkelstein, N., & Arnold, R. 2006, 'An adaptive system for improving and augmenting human performance', *In D.D. Schmorrow, L.M. Reeves, and K.M. Stanney (eds.): Foundations of Augmented Cognition* 2nd Edition, Arlington, VA: Strategic Analysis, Inc., pp. 215-222.

Scerbo, M. 2005 'Biocybemetic systems: Information processing challenges that lie ahead', *Proceedings of the 11th International Conference on Human-Computer Interaction.*

Cabeza, R., Nyberg, L. 2000, 'Imaging cognition II: An empirical review of 275 PET and fMRI studies', *Journal of Cognitive Neuroscience,* vol. 12, pp. 1–47.

Karamouzis, S. 2006, 'Artificial Intelligence Applications and Innovations', *IFIP Intemational Federation for Information Processing,* Vol. 204, Springer, Boston, pp. 417-424.

Sleeman, Brown, J. 1982, *Intelligent tutoring systems,* New York: Academic Press.

Nicholson, D., Fidopiastis, C., Davis, L., Schmorrow, D. & Stanney, K. 2007, 'An adaptive instructional architecture for training and education', *Proceedings of HCI International (in press).*

Skinner, B. 1958, *Teaching Machines,* Science 128, pp. 969-77.

Wenger, E. 1987, *Artificial Intelligence and Tutoring Systems: Computational and Cognitive Approaches to the Communication of Knowledge,* Morgan Kaufmann Publishers, Inc., Los Altos, CA.

Anderson, J., Corbett, A., Koedinger, Pelletier, K. 1995, 'Cognitive Tutors: Lessons Learned', *Journal of the Learning Sciences*, vol. 4, no. 2, pp. 167-207.

Parasuraman, R., Bahri, T., Deaton, J. E., Morrison, J. G., & Barnes, M. 1992, *Theory and design of adaptive automation in adaptive systems (Progress Report No. NAWCADWAR–92033–60).* Warminster, PA: Naval Air Warfare Center, Aircraft Division.

Paas, F., Renkl, A., & Sweller, J. 2004, 'Cognitive load theory: Instructional implications of the interaction between information structures and cognitive architecture', *Instructional Science,* vol. 32, pp. 1–8.

Sweller, J. 1999, *Instructional Design in Technical Areas*. Australian Council for Educational Research Press, Camberwell, Australia.

Paas, F., Tuovinen, J., Tabbers, H., & Van Gerven, P.W. M. 2003 'Cognitive load measurement as a means to advance cognitive load theory', *Educational Psychologist*, vol. 38, pp. 63–71.

Hoover, A., Muth, E. 2005, 'A real-time index of vagal activity', *International Journal of Human-Computer Interaction*, vol. 17 no. 2, pp. 197-209.

Erdogmus, D., Adami, A., Pavel, M., Lan, T., Mathan, S., Whitlow, S., Dorneich, M. 2005, 'Cognitive state estimation based in EEG for augmented cognition', *Proceedings of the 2nd International IEEE EMBS Conference in Neural E engineering,* Arlington, Virginia, March 16-19.

Downs, J., Downs, T., Robinson, W., Nishimura, E., Stautzenberger, J. 2005, 'A new approach to fNIR: The optical tomographic imaging spectrometer', *Proceedings of the 1st International Conference on Augmented Cognition,* Las Vegas, NV, 22-27 July 2005.

Berka, C., Levendowski, D., Cvetinovic, M., Davis, G., Lumicao, M., Zickovic, V., Popovic, M., Olmstead, R. 2005, 'Real-time analysis of EEG indexes of alertness, cognition, and memory acquired with a wireless EEG headset', *International Journal of Human-Computer Interaction*, vol. 17 no. 2, pp. 151-170.

Takahashi, M., Kubo, O., Kitamura, M., Yoshikawa H. 1994, 'Neural network for human cognitive state estimation', *Proceedings of the IEEE/RSJ/Gi International Conference on Intelligent Robots and Systems '94*.

Cerutti, S., Bianchi, A., Reiter, H. 2006, 'Analysis of sleep and stress profiles from biomedical signal processing in wearable devices', *Proceedings of the 28th IEEE EMBS Annual International Conference*, New York City, USA, Aug 30-Sept 3.

Crosby, M., Ikehara C. 2005, 'Using physiological measures to identify individual differences in response to task attributes', *In D.D. Schmorrow, L.M. Reeves, and K.M. Stanney (eds.): Foundations of Augmented Cognition* 2nd Edition, Arlington, VA: Strategic Analysis, Inc., pp. 162-168.

Keenan, D., Gorssman, P. 2005, 'Adaptive filtering of heart rate signals for an improved measure of cardiac autonomic control', *International Journal of Signal Processing,* vol. 2, no. 1, pp. 52-8.

Aysin, B., Aysin, E. 2006, 'Effect of respiration in heart rate variability (HRV) analysis', *Proceedings of the 28th IEEE EMBS Annual International Conference*, New York City, USA, Aug 30-Sept 3.

Sleight, P., Casadei, B. 1995, 'Relationships between Heart rate, respiration and blood pressure variabilities', *Heart Rate Variability,* Futura Publishing Company, Armonk, NY.

Shaltis, P., Reisner, A., Asada, H. 2005, 'Calibration of the photoplethysmogram to arterial blood pressure: capabilities and limitations for continuous pressure monitoring', *Proceedings of the 27th IEEE EMBS Annual International Conference*, Shanghai, China, Sept 1-4.

Salvucci, D., Anderson, J. 1998, 'Tracing eye movement protocols with cognitive process models', *Proceedings of the Twentieth Annual Conference of the Cognitive Science Society,* pp. 923-8.

Marshall, S., 2007, 'Identifying cognitive state from eye metrics', *Aviation, Space and Environmental Medicine,* Vol. 78, no. 5, pp. 165-75.

Lang, P., Bradley, M., Cuthbert B. 2005, 'International affective picture system (IAPS): Affective ratings of pictures and instructional manual", *technical report A-6,* University of Florida, Gainesville, FL.

A VOCAL TRACT VISUALISATION TOOL FOR A COMPUTER-BASED SPEECH TRAINING AID FOR HEARING-IMPAIRED INDIVIDUALS

Abdulhussain E. Mahdi
Department of Electronic & Computer Engineering, University of Limerick, Limerick, Ireland
hussain.mahdi@ul.ie

Keywords: Speech Production, Vocal Tract Models, Articulatory Training, Linear Prediction Coding.

Abstract: This paper describes a computer-based software prototype tool for visualisation of the vocal-tract, during speech articulation, by means of a mid-sagittal view of the human head. The vocal tract graphics are generated by estimating both the area functions and the formant frequencies from the acoustic speech signal. First, it is assumed that the speech production process is an autoregressive model. Using a linear prediction analysis, the vocal tract area functions and the first three formants are estimated. The estimated area functions are then mapped to corresponding mid-sagittal distances and displayed as 2D vocal tract lateral graphics. The mapping process is based on a simple numerical algorithm and an accurate reference grid derived from x-rays for the pronunciation of a number English vowels uttered by different speakers. To compensate for possible errors in the estimated area functions due to variation in vocal tract length between speakers, the first two sectional distances are determined by the three formants. Experimental results show high correlation with x-ray data and the PARAFAC analysis. The tool also displays other speech parameters that are closely related to the production of intelligible speech and hence would be useful as a visual feedback aid for speech training of hearing–impaired individuals.

1 INTRODUCTION

The process of learning to speak in the case of people with normal hearing is primarily aided by auditory feedback. However, for those who suffer from deafness, learning to speak naturally is a very difficult process. With limited auditory capability, a hearing-impaired person often lacks models of speech targets necessary to produce normal speech. In an effort to overcome this difficulty, many attempts have been made to provide a substitute for the feedback mechanism with visual speech display devices (Choi, 1982; Bunnell et. Al., 2000; Mashie. 1995). However, without any articulatory correlate, the benefits of such devices were limited. In order to produce a natural and intelligible speech, a speaker needs to know how to use the vocal organs in regards to correct position of the articulators, breathing, loudness, rhythm and nasalization (Eriksson, et. al., 2005) . Hence the availability of visual information regarding these aspects would greatly help the hearing-impaired improving their speaking abilities.

This paper describes a system which visualises a speaker's vocal tract by means of mid-sagittal graphical plots of the human head. The vocal tract shapes, and other related speech parameters, are graphically displayed on a PC-monitor using information extracted directly from the acoustic speech signal as picked up by a microphone or loaded from an audio file. To estimate the necessary parameters, it is assumed that the speech production process is an autoregressive (AR) model. The vocal tract area functions, log spectra and the first three formants are then estimated, by employing a linear prediction (LP) analysis, and used to construct the corresponding vocal tract graphics and other parameters display.

2 SPEECH ANALYSIS MODEL

Speech is the acoustic wave that is radiated from the vocal system when air is expelled from the lungs and the resulting flow of air is perturbed by a constriction somewhere in the vocal tract. This speech production process can be practically modelled using the well-known all-pole source-filter approach, which represents the speech signal in terms of an AR model (Quatieri, 2002). According

to this model, speech is split into a rapidly varying excitation signal, generated by an impulse train input or a random noise generator, and a slowly varying filter representing the vocal tract. Voiced speech is produced by taking the impulse train as excitation. In unvoiced segments, the random white noise is used as the excitation. The output speech is produced by passing the excitation through the vocal tract filter. Hence, changes in the vocal tract configuration, reflected by the filter, produces corresponding changes in the spectral envelope of the speech signal. Therefore to estimate the vocal tract shape form the speech signal, an inverse filter model has to be used (Miller & Mathews, 1963).

The speech analysis model used in this work is shown schematically in Figure 1. In this model, it is assumed that the speech to be analysed is limited to periodic non-nasalised voiced sounds so that the filter in Figure 1 is driven by an impulse train. This means that the filter includes all the contributions from the glottal wave, the vocal tract and the radiation impedance at the lips. The inverse filter is assumed to be a linear filter with only zeros in its transfer function, and the power spectral envelope of the speech is assumed to be approximated by poles only. Accordingly, the transfer function of the inverse filter can be expressed in terms of z-transform notation as:

$$A(z) = \sum_{i=0}^{M} a_i \, z^{-i} \,, \quad a_0 = 1 \tag{1}$$

where a_i are the coefficients of the inverse filter, M is the order of the filter, $z = e^{j\omega T}$ and T is the sampling period. Here, a_0 affects only the gain of the system, hence no generality is lost by setting $a_0 = 1$. The objective of this analysis is to obtain a close representation of the vocal tract. To obtain this representation, one needs to estimate the coefficients of the optimal inverse filter described by equation (1). Wakita (Wakita, 1973) has shown that $A(z)$ is also an inverse transfer function of a non-uniform acoustic tube model of the all-pole vocal tract model. Thus the optimal inverse filter process in the above speech analysis model can be equivalently replaced by a filtering process of an acoustic tube of length l, which is the assumed length of the vocal tract, divided into arbitrary number, M, of sections with equal length Δl, provided that:

(a) The continuity conditions for the volume velocity and sound pressure are satisfied at each junction between two adjacent sections;

(b) The length of the individual tube sections, Δl, are kept short compared to the wavelength at the highest frequency of interest;

(c) No losses are accounted for, and

(d) It should also be noted that the identity of the filtering process of the above described acoustic tube to that of the optimum inverse filter is obtained under the condition $z = e^{j\omega 2\Delta l / c} = e^{j\omega T}$, where c is the velocity of sound. Consequently, the sampling frequency $F_s = 1/T$ and the number of sections $M = l/\Delta l$ is constrained by (Wakita, 1973):

$$F_s = \frac{M\,c}{2l} \tag{2}$$

Therefore, as long as F_s is constant, the vocal tract length, l, is assumed to be fixed here and M, i.e. number of the sections or the filter's order, has to be chosen to satisfy equation (2).

3 MODELLING THE VOCAL TRACT

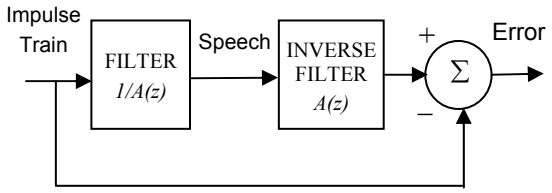

Figure 1: The speech analysis model.

The vocal tract can be modelled as an acoustic tube of varying diameter. If we abstract from the vocal tract curvature, the acoustic tube can be divided into cylindrical sections of equal lengths. Depending on the shape of the acoustic tube, a sound wave travelling through it will be reflected in a certain way so that interferences will generate resonances at certain frequencies. These resonances are called formants. Their location largely determines the speech sound that is heard.

It is well known that the linear prediction (LP) analysis of speech signals is based on an AR speech production model (Markel & Gray, 1976). It has also been shown by several researchers that the LP process is equivalent to the filtering process of a non-uniform acoustic tube model where the tube is divided into an arbitrary number of sections of equal length (Wakita, 1973; Markovic, 1999). Thus, if the conditions stated at the end of Section 2 are satisfied, and if the speech signal is pre-emphasis to compensate for the spectral characteristics of the glottal excitation source and for the lips radiation impedance, then estimates of the vocal tract area functions can be obtained by computing the

reflection coefficients at the junctions between adjacent sections of the equivalent acoustic tube. This can be done by using an LP model of the appropriate order and the following relation:

$$\mu_i = \frac{A_{i+1} - A_i}{A_{i+1} + A_i} \quad \Leftrightarrow \quad A_i = A_{i+1}\frac{1-\mu_i}{1+\mu_i} \qquad (3)$$

where A_i and A_{i+1} are the cross-sectional areas of two adjacent sections of the non-uniform acoustic tube indexed in ascending order from the lips to the glottis, and μ_i is the reflection at the junction between these two sections.

4 SYSTEM DESIGN AND DESCRIPTION

Using the vocal tract model described in Section 3, a PC-based prototype system for visualisation of the human vocal tract shapes and other associated speech parameters has been designed and developed. The system uses the PC's sound card operating with 8 kHz sampling frequency and 16-bit resolution, to extract the necessary speech parameters directly from the acoustic speech waveform. shows The block diagram given in Figure 2 depicts the functionality and main processing blocks of the developed system.

For simplicity, our system uses an initial assumption that the vocal tract is 17 cm long. As the PC's sound card samples the speech at the rate of 8 kHz, thus satisfying equation (2) requires M to be equal to 8, i.e. the initial use of an acoustic tube with 8 sections. Consequently, an 8th order LP analysis model is employed by the system.

4.1 Estimation of the Area Functions

The speech signal is segmented into 30 ms frames using a hamming window of an appropriate length. A pre-emphasis of an approximately 6 dB/octave is applied to the current frame using an FIR high-pass filter of the form:

$$y_n = x_n - 0.9375\,x_{n-1} \qquad (4)$$

The reflection coefficients are computed by applying an 8th order LP analysis model using an autocorrelation method that uses LPC uses the Levinson-Durbin recursive algorithm due to its simplicity and ease of its implementation within the chosen computing environment. Equation (3) is then used to estimate the corresponding vocal tract area functions as discussed in Section 3. As an example, Figure 3 (the upper half) shows the normalised area functions for the English vowel /UH/, as computed by the system using an 8-section acoustic tube model. The LP model is also used to obtain the log spectra, whose peaks are then marked to identify and estimate the first three formants, as also illustrated in lower half of Figure 3.

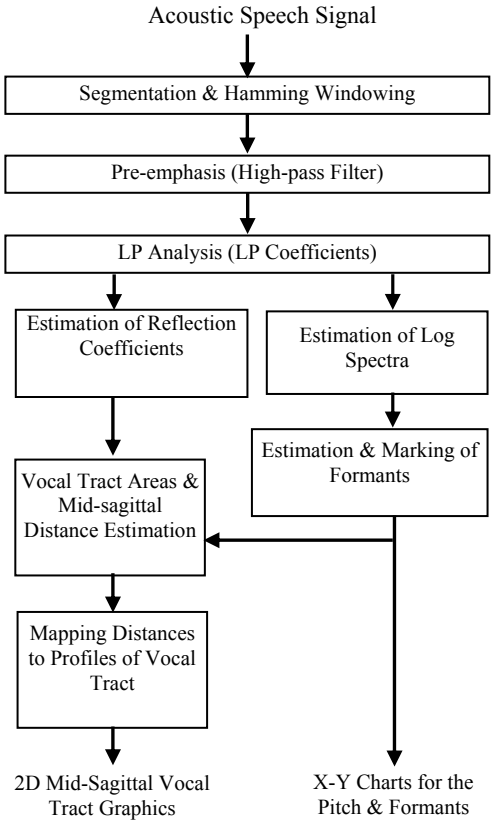

Figure 2: Functional block diagram of the system.

4.2 Mapping to Mid-sagittal Distances

Since the human vocal tract does not resemble an exact circular tube, there is therefore a need to modify the above computed area functions such that they map correctly into mid-sagittal distances of the vocal tract profiles. Several areas to profile transformation techniques have been developed (Heinz & Stevens, 1965). Most such techniques rely on derivation of suitable application-specific transformation parameters using complex analysis of x-ray and cine-fluorograms of various speakers. A common technique is the $\alpha\beta$ model (Heinz & Stevens, 1965), which is described by:

$$A_i = \alpha_i\, d_i^{\beta_i} \quad \Leftrightarrow \quad d_i = \left(\frac{A_i}{\alpha_i}\right)^{1/\beta_i} \qquad (5)$$

where A_i is the cross-sectional area of a given section, d_i is the mid-sagittal distance and α_i and β_i are section dependent parameters. In our system, we

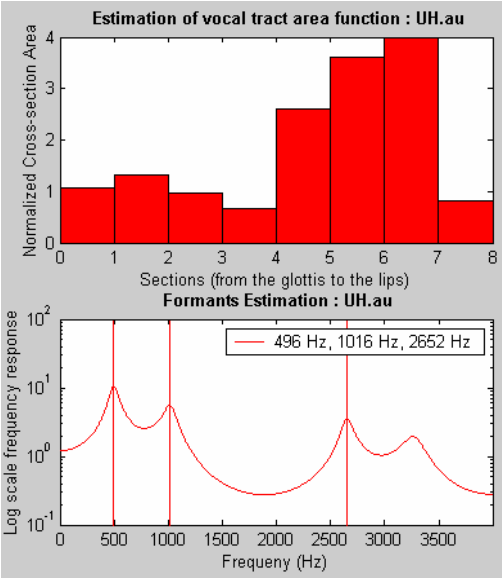

Figure 3: Vocal tract area functions and the first three corresponding formants for the vowel /UH/.

employ a new method based on the above model to measure the mid-sagittal distances along the lines of a semipolar grid (*See Figure 4)* according to the following procedure:

(a) The vocal tract was assumed to be divided into 18 equal sections.

(b) In the vocal organs, the shortest path from the upper to the lower part of each section was selected.

(c) The upper jaw was assumed to be fixed and the lower jaw was movable.

(d) A reference grid for the upper jaw based on x-ray data of the lateral shape of the vocal tract and on results of the PARAFAC analysis (Harshman, et. al., 1977) was designed, as shown in Figure 4. In this grid, straight perpendicular lines were drawn through the centre of each section, in accordance with (b) above.

(e) The 8 area functions estimated by the 7th order LP model were re-sampled and redistributed to fit the 18-section vocal tract configuration used in the system.

(f) Based on equation (5), a simple numerical procedure is used to estimate the values of the coefficients α and β that minimize the root mean squared error between the area functions estimated in (e) above and those derived from measurement data obtained from (Harshman, et. al., 1977) for pseudo-sagittal dimensions of the tongue position for five speakers each saying ten English vowels. The estimated area functions are then interrupted as functions of α and β, as given in equation (5), to compute the mid-sagittal distances.

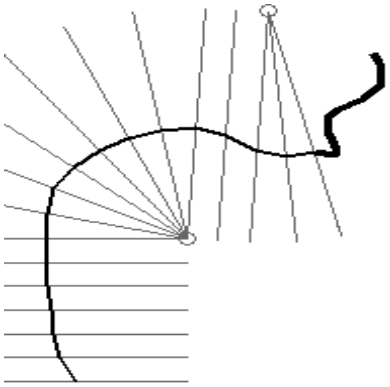

Figure 4: The reference upper jaw grid used in the system.

As indicated previously, initially the vocal tract is modelled in our system with an assumption that it is 17 cm long. It is known, however, that the vocal tract length for the utterance of various sounds varies even for a single speaker. In addition, the male vocal tract is generally slightly longer than 17 cm, while children and females have shorter vocal tracts (Kirlin, 1978). Hence, the above assumption may cause an error in the distribution of the area functions along the assumed vocal tract configuration. To compensate for this possible source of error, the first two mid-sagittal distances have been determined from the three estimated formants F_1, F_2 and F_3 as follows (Ladefoged, et. al., 1978):

$$X_1 = C_1 F_2 + C_2 F_2 F_3 + C3 F_1 / F_2 + C_4 \qquad (6)$$

where X_1 is the mid-sagittal distance between the lips in cm, $C_1 = 0.3\times10^{-3}$, $C_2 = -0.343\times10^{-6}$, $C_3 = 4.143$, $C_4 = -2.865$. The mid-sagittal distance between the upper and lower teeth, X_2, is estimated by:

$$X_2 = \frac{X_1 + X_3}{2} \qquad (7)$$

where X_3 is the mid-sagittal distance extracted from the vocal tract area function that corresponds to section 3. In addition, the estimated formants have been used to adjust the rounding degree of the lips and the height of the jawbone on the designed vocal tract lateral graphics.

5 RESULTS AND DISCUSSION

The vocal tract visualisation tool has been designed to operate with MS Windows-based PC environment. The multi-display window and other user's features of the complete system are shown in Figure 5. As can be seen, the system's screen is divided into four windows for displaying the vocal tract graphics, the sound intensity, the pitch and the first three formants of the speech signal. The system can operate in two main modes: (a) near real-time mode, whereby the speech signal is picked up by a microphone connected to the PC sound card (as with the case shown in Figure 5), and (b) non real-time mode, whereby the speech signal is either recorded by the system or read from a stored audio file, and its features are then displayed. It also allows the saving of speech/sound signals. For the vowel articulation, the user can compare the shape of his/hers vocal tract to a reference trace (shown with a dashed line in Figure 5) for the correct tongue position derived from the measurements data reported in (Miller & Mathews, 1963). The deviation from the reference trace is given for this case in the form of a computed mean squared error (MSE) of all the estimated mid-sagittal distances.

Figure 6 shows the vocal tract profiles for 10 American English vowels, as estimated by the system (dashed lines represent reference trace for tongue position). For comparison and evaluation purposes, the deviations, in terms of MSE values, from the reference tongue position data adopted from (Harshman, et. al., 1977) are also indicated. In general, the obtained results seem to correlate well with the reference data. They were also found to correlate well with x-ray data and the PARAFAC analysis. Referring to the MSE values shown in Figure 6, the system seems to perform particularly well in the cases of all the 'front vowels', such as /IY/, /EY/, /IH/, /EH/ and /AE/, with the MSE increasing as the vowel height decreases. With the exception of /AA/ and /UH/, the results show relatively less accurate correlation with the reference data for the cases of the 'back vowels'. As vowel classification into front and back vowels is related to the position of the tongue elevation towards the front or the back of the mouth, we believe that the higher accuracy in the cases of the front vowels is attributed to the formant-based added adjustments of the lips, jawbone and front sections of the vocal tract we used in our approach.

On the other hand, the relative length of the vowel's vocalisation seems to affect the accuracy of the estimated area functions and hence the displayed vocal tract shape. In specific, the system seems to give relatively lower accuracy for relatively longer vowels, such as /AO/, and complex vowels which involve changes in the configuration of the mouth during production of the sound, such as /OW/. We believe this is due to the fact that the system, in its current design, bases its estimation of the speech parameters on information extracted from the 2-3 middle frames of the analysed speech waveform.

6 CONCLUSIONS

We have described the process of designing and development of a computer-based system for the near real-time and non real-time visualisation of the vocal tract shape during vowel articulation. Compared to other similar systems, our system uses a new approach for estimating the vocal tract mid-sagittal distances based on both the area functions and the first three formants as extracted from the acoustic speech signal. It also utilises a novel and simple technique for mapping the extracted information to corresponding mid-sagittal distances on the displayed graphics. The system is also capable of displaying the sound intensity, the pitch and the first three formants of the uttered speech. It extracts the required parameters directly from the acoustic speech signal using an AR speech production model and LP analysis. Reported preliminary experimental results have shown that in general the system is able to reproduce well the shapes of the vocal tract, with real-time sensation, for vowel articulation. Work is well underway to optimise the algorithm used for extraction of the required acoustics information and the mapping technique, such that dynamic descriptions of the vocal tract configuration for long and complex vowels, as well as vowel-consonant and consonant-vowel are obtained. Enhancement of the system's real-time capability and features, and facilitation of an integrated speech training aid for the hearing-impaired are also being investigated.

REFERENCES

Choi, C.D., 1982. A Review on Development of Visual speech Display Devices for Hearing Impaired Children. *Commun. Disorders*, 5, 38-44.

Bunnell, H.T., Yarrington, D. M. & Polokoff, 2000. STAR: articulation training for young children. In *Intl. Conf. on Spoken Language Processing (INTERSPEECH 2000),* 4, 85-88.

Mashie, J.J., 1995. Use of sensory aids for teaching speech to children who are deaf. In *Spens , K-E. and Plant, G.*

(Eds.), Profound Deafness and Speech Communication, 461-491, Whurr Publishers Ltd.

Eriksson, E., Balter,, O., Engwall, O., Oster, A-M. & Sidenbladh-Kjellstrom, H., 2005. Design recommendations for a computer-based speech training system based on end-user interviews. In. *SPECOM 2005*, *10th Intl. Conf. on Speech and Computer*, 483-486.

Quatieri, T.E., 2002. *Discrete-time Speech signal Processing, Principles and Practice*, Prentice Hall. NJ, USA.

Miller, J.E. & Mathews, M.V., 1963. Investigation of the glottal waveshape by automatic inverse filtering. *J. Acoust. Soc. Am.*, 35, 1876-1884.

Wakita, H., 1973. Direct Estimation of the Vocal Tract Shape by Inverse Filtering of Acoustic Speech Waveforms. *IEEE Trans. on Audio and Electroacoustics*, AU-21, 417-427.

Markel, J. & Gray, A., 1976. *Linear Prediction of Speech*, Springer-Verlag. New York, USA.

Markovic, M., 1999. On determining heuristically decision threshold in robust AR speech model identification procedure based on quadratic classifier. In *ISSPA'99, 5th Intl. Symp. Sognal Process. And its Applications*. 131-134.

Heinz, J.M. & Stevens, K.N., 1965. On the relations between lateral cineradiographs area functions and acoustic spectra of the speech. In *5th Int. Congress of Acoustics*. Paper A44.

Harshman, R., Ladefoged, P. & Goldstein, L., 1977. Factor analysis of tongue shapes. *J. Acoustics Soc. Am*., 62, 693-706.

Kirlin, R.L., 1978. A posteriori estimation of vocal tract length. *IEEE Trans. Acoust., Speech, Signal Process.*, ASSP—26, 571-574.

Ladefoged, P., Harshman, R., Goldstein, L., & L. Rice, 1978. Generating vocal tract shapes from formants frequencies. *J. Acoustics Soc. Am*., 64, 1027-1035.

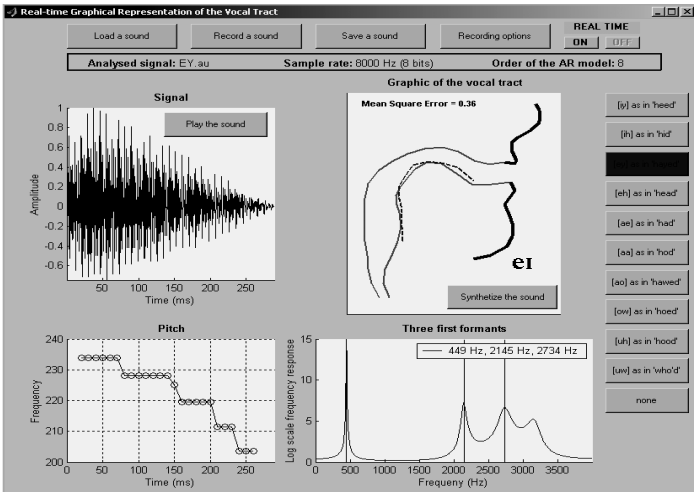

Figure 5: System's multi-pane screen display and user's extracted features.

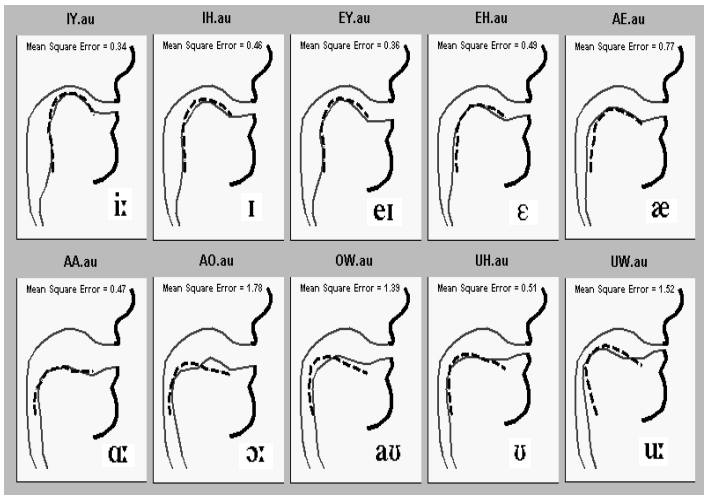

Figure 6: Vocal tract profiles for 10 American English vowels as estimated by the system (dashed lines represent reference traces for tongue positions).

PHONETOGRAPHY DATABASE FOR ELDERLY WOMEN

Lídia Cristina da Silva Teles, Maria Inês Pegoraro-Krook
Departament of Speech pathology of Faculdade de Odontologia de Bauru, University of São Paulo
Al. Octávio Pinheiro Brisola 9-75, Bauru, Brazil
lidiactm@usp.br,_mikrook@usp.br

Marcos Kenned Magalhães
Departament of Eletric Engineering of Escola de Engenharia de São Carlos, University of São Paulo
Avenida Trabalhador São-carlense 400, São Carlos, Brazil
marcoskm@usp.br

Keywords: Speech pathology, voice evaluation, phonetography, signal processing, database.

Abstract: The aim of this work was to create a software that, from the phonetography measures of elderly women, generates the phonetogram, evaluates its area, vocal extension (VE), and the dynamic extension (DE) and elaborates a database. The phonetography exams were carried out based on the European Phoniatrics Rules. The software tools used for development were Delphi® and Paradox®. The results related to the voice evaluation of elderly women compares favorably with the normal aging process. The software stores and recovers the exams data as well as evaluates voice characteristics and presents graphical outputs in an appropriate way.

1 INTRODUCTION

The speech has its origin at the vocal folds level, through the air flux coming from the lungs, passing throughout the larynx constriction, the equalized by the vocal tract and radiated by the lips (Boone and McFarlane, 1994).

The voice exam only is complete when the sound properties are stored and analised in some way (Damsté, 1970).

The phonetography is a exam that allows to evaluate both the frequency extension and dinamic range for each frequency value. The result of this method produce a graphic called phonetogram. This exam allows to identify changes in the voice associated with common pathological conditions to verify the progression resulting from the vocal therapy or simply to follow the voice development of the individual (Damsté, 1970; Gramming, 1988; Higgins and Saxman, 1991; and Teles-Magalhães, Pegoraro-Krook and Pegoraro, 2000).

The rapid growth of elder population has brough some concern in the last few decades. The concern is more related to the added life in years than the added years in the life (Leden, 1977). These considerations bring some questions like : what is the vocal extension of elderly people? What is the boundary between aging and pathological conditions in the vocal changes ?

Several papers about voice in the aging have maked clear that there is a great interest in better knowing the voice characteristics of this population. So the effects of the age on the voice have to be clearly defined in order to stablish the healthy range of the voice characteristics.

The effects of the age on the vocal behavior seems to be different in type and level for men and women (Higgins et al., 1991). In this work just the women voices are considered.

The informatic has auxilied the speech therapists in their diagnosis efforts. Unfortunately, for the phonetography case, the few softwares commercially available do not present database facilities or have prohibitive cost, making the storage or recovery of data cumbersome.

Taking in account all this shortcomings, the objective of this work was to elaborate a software that from the measures of phonetography of elderly women elaborates the phonetogram, evaluation of its area, of the vocal extension (VE) and the dinamic extension (DE) storing all this information in a database.

2 MATERIAL AND METHODS

2.1 Phonetography

Forty volunteers women from Bauru city, São Paulo state participated of this work, aging from 60 to 84 years old ($\overline{X}$=68,2 ± 5,74 years old). All of these women were interviewed besides the submission of perceptive and audiologic exams.

The exam procedures follow the standards proposed by Shultte e Seidner (1993) and recommended by the European Phoniatrics Union. Basically the exams were issued in a acoustic room of the Experimental Phonetic Laboratory of the Hospital de Reabilitação de Anomalias Craniofaciais, of the São Paulo University. A Casio Model CA-110, miniorgan was used to generate the musical notes, and an Entelbra 142 analogical sound level meter (sound pressure level gauge) to obtain the intensity measurements.

2.2 Database Program

Equipment (hardware): one IBM-PC® presenting the following characteristics: Pentium IV® processor (3.0 GHz), RAM memory 512 Kb, hard disk of 80 Gb and CD_ROM Creative® was used. The video resolution was 800 x 600 pixels per inch. Also has been used a HP Deskjet 692C.

Programs (software): the software was developed in Windows XP® using Delphi® from Borland Inprise Corporation (version 5.0) and Paradox® from Paradox Corporation for the database.

2.3 Parameters Evaluated from Phonetography

Vocal Extension evaluation: by using the fundamental frequencies values (F_0), in semitones (st), it is applied the following formula:

$$EV = F_0 \text{ max} - F_0 \text{ min} \quad (1)$$

Where:

- EV = Vocal extension (st);
- F_0 max = Maximum frequency (st) produced by the individual;
- F_0 min = Minimum frequency (st) produced by the individual;

All evaluations related to the frequency are made using semitones (st).

Dynamic Extension and Maximum Dynamic Extension: after all obtained values for maximum and minimum magnitude for each frequency to be introduced, the following formula for dynamic extension is applied:

$$DE = \text{Int max} - \text{Int min} \quad (2)$$

where:

- DE = Dynamic extension (dB);
- Int max = Higher magnitude (dB) produced by the individual;
- Int min = Lower magnitude (dB) produced by the individual.

The maximum dynamic extension (MDE) is the higher dynamic extension found among all tested frequencies.

Phonetogram Area Evaluation: the area evaluation follows the standard proposed by Shultte e Seidner (1993). In order to evaluate the area the following formula is used:

$$A = \sum_{i=1}^{n-1} \frac{\left(I_{\max_i} - I_{\min_i}\right) + \left(I_{\max_{i+1}} - I_{\min_{i+1}}\right)}{2} \cdot \left(st_{i+1} - st_i\right) \quad (3)$$

where:

- A = Area of the phonetogram (cm^2);
- Int max = Higher magnitude (dB) produced by the individual;
- Int min = Lower magnitude (dB) produced by the individual;
- St = Semitone where the maximum and minimum magnitude were evaluated;
- n = Number of elements (semitones) of the phonetogram.

3 RESULTS

3.1 Exam Data Evaluation

Related to the minimum frequencies, their values varied from 110 Hz or 33 st to 220 Hz or 45 st. The average value for minimum frequencies was 154 ± 24,98 Hz or 38,68 ± 2,80 st.

For the maximum frequencies of vocal extension, the higher value was 659 Hz or 64 st, and the lower value was 330 Hz or 52 st. The average value for the maximum frequencies was 478,88 ± 56,11 Hz or 58,35 st ± 2,04 st for all sample.

For the vocal extension, the maximum value was 609 Hz and the lower was 172 Hz or 10 st, with average of 324,05 ± 56,97 Hz or 19,70 ± 3,09 st.
The maximum dynamic estension (MDE) varied from 16 to 43 dB. The average value found in the sample was 29,08 ± 7,09 dB.
As far as the area of the phonetogram is concerned, the lower area found was 162,0 dB.st or 7,3 cm2 and the higher area was 654,5 dB.st or 29,5 cm2. The average value for this parameter considering all the sample was 404,8 ± 135,1 dB.st corresponding to 18,2 ± 6,1 cm2.

3.2 The Software

The computer program developed, that managing the database of phonetography generating the phontogram, is compose by eight modules for diferents tasks:

Menu – this module shows all available options of the program.

Patient schedule – This module contains all information about the patient and, allows to include or make alterations in the schedule.

Phonetography Schedule – The user can manipulate the data related to phonetography (frequency values (st) and magnitudes (dB)). Through these values, the program can evaluates the Vocal Extension (VE), the Maximum Dynamic Extension (MDE) and the graphic area. Also, protocols of palate evaluation, speech, voice and larynx have been included in this module.

Phonetogram Comparisons – in this module, comparisons between 2 or more (maximum 6) phonetograms can be done. Any phonetogram can be choose by the user from database.

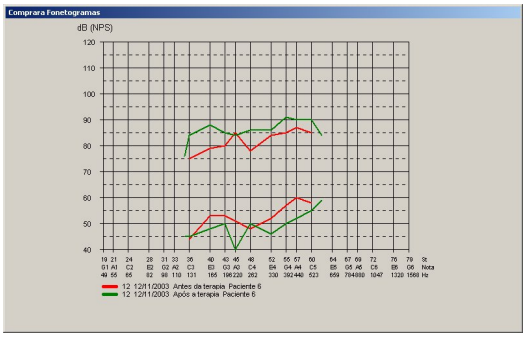

Figure 1: Comparison between phonetograms.

Data Filter – this module allows the user to select any specific class of patients. For example, it is possible to select all patients from 50 to 55 years old or all patients with a specific larynx dysfunction.

Printer Configuration – this module runs a Windows® routine to configure the system printers.

Software Information – this module shows all information related to the program.

End of Program – this module asks for the end procedure and, through the confirmation, closes the database and concludes the process.

4 DISCUSSION AND CONCLUSION

4.1 Characteristics of Elderly Women Voice

Certainly the advance of the age causes lower performance of the biologic systems. Particularly, the vocal behavior of women studied in this work confirms the procedure of normal aging.

Considering the results, it can be observed that:

- Vocal extension was expanded for low frequencies;
- Reduction of higher boundary of the vocal extension;
- Decreasing of the number of tones of vocal extension;
- Restriction of the boundaries of the minimum magnitudes;
- Restriction of the boundaries of the maximum magnitudes;
- Reduction of the maximum dynamic extension;
- Reduction of the phonetogram area;
- Better control of the vocal magnitude at 262 Hz or 48 st, showing high vocal comfort at this frequency.

4.2 Database Utilization

The easy use of the exam information of the database has become a useful tool for the voice specialist. The better flux information saves time with schedule or data files in different places of the hard disk.

The fast parameters evaluation, after the frequency and magnitude data insertion, helps the diagnosis. In many cases, the phonetogram area evaluation can not be at the clinical practice because demands a more complex mathematical formula.

The over plot facility makes the comparison instantaneous. In this way, the comparison among patients or even between pre and pos-therapy makes

the software an attractive tool. Also the visual feedback can helps the patient to correct his vocal gesture.

In conclusion, this software is a potential auxiliary tool for voice specialists by presenting quantitative values of the voice and allowing recording and comparing the voice at distinct times of the rehabilitation procedure.

REFERENCES

Boone, D. R., McFarlane, S. C., 1994. *A Voz e a Terapia Vocal*. Porto Alegre: Artes Médicas, Tradução: Sandra Costa, 300p, 5ª. Edição.

Damsté, P. H., 1970. *The Phonetogram*, Pract. Oto-rhinolaryng, v. 32, p. 185-187.

Gramming, P., 1988. *Non-organic dysphonia. II. Phonetograms for normal and pathological voices*, Acta Otolaryngol, Oslo, v. 106, n. 5-6, p. 468-476.

Higgins M. B., Saxman J. H., 1991. *Comparison of selected phonatory behaviors of healthy aged and young adults*, Journal of Speech Res. v. 34, p. 1000-1010.

Leden, H. V., 1977. *Speech and hearing problems in the geriatric patient*, Journal of America Geriatric Society 25:422-426.

Schutte, H. K., Seidner, W., 1983. *Recommendation by the Union of European Phoniatricians (UEP): standardizing voice area measurement/phonetography*, Folia Phoniatric (Basel) v. 35, n. 6, p. 286-288.

Teles-Magalhães, L. C., Pegoraro-Krook, M. I., Pegoraro, R., 2000. *Study of the Elderly Females Voice by Phonetography*, Journal of Voice, New York, v. 14, n. 3, p. 310-321.

VOICE SIGNALS CHARACTERIZATION THROUGH ENTROPY MEASURES

Paulo Rogério Scalassara, María Eugenia Dajer, Carlos Dias Maciel and José Carlos Pereira
School of Engineering of São Carlos, University of São Paulo, Avenida Trabalhador São-carlense, 400, São Carlos, Brazil
prscala@sel.eesc.usp.br, eugedajer@yahoo.com.ar, maciel@sel.eesc.usp.br, pereira@sel.eesc.usp.br

Keywords: Voice, entropy, phase space reconstruction, nodule, predictability.

Abstract: Human voice has been a matter of interest for different areas as technological development and medical sciences. In order to understand the dynamic complexity of healthy and pathologic voice, researchers have developed tools and methods for analysis. Recently nonlinear dynamics has shown the possibility to explore the dynamic nature of voice signals from a different point of view. The purpose of this paper is to apply entropy measures and phase space reconstruction technique to characterize healthy and nodule affected voices. Two groups of samples were used, one from healthy individuals and the other from people with nodule in the vocal fold. They are recordings of sustained vowel /a/ from Brazilian Portuguese. The paper shows that nonlinear dynamical methods seem to be a suitable technique for voice signal analysis, due to the chaotic component of the human voice. Since the nodule pathology is characterized by an increase in the signal's complexity and unpredictability, measures of entropy are well suited due to its sensibility to uncertainty. The results showed that the nodule group had a higher entropy values. This suggests that these techniques may improve and complement the recent voice analysis methods available for clinicians.

1 INTRODUCTION

The human voice is one of the principal means of communication, and the acoustic signal carries significant information about some individual characteristics. The complex normal or pathologic voice production mechanism involves different variables. Vocal fold biomechanics in association with aerodynamic variables play an important role in voice production and they are linked to the voice quality changes.

In order to study normal voice and the different voice disorders, scientists from diverse areas developed several methods and tools for measurement, diagnosis and voice treatment. Therefore traditional acoustic analysis is an essential and familiar tool for physicians and speech therapists.

Traditionally, voice has been modeled as a linear process and acoustic analysis tools are based in linear system theory. Acoustic parameters evaluate perturbation or noise contents in the voice signal. The classical perturbation parameters evaluate jitter (fundamental frequency variation), and shimmer (amplitude variation). Two parameters used to determine the voice signal noise quantity are the deterministic Harmonic to Noise Ratio (HNR) and the Coefficient of Excess (EX) that evaluate the noise from a statistical point of view (Davis, 1979).

Another interesting parameter is the pitch amplitude (PA), which is a normalized measure of the amplitude of the pitch period peak of the residue signal autocorrelation function. It has a high value for healthy vowel signals that have clearly defined pitch period. However, for breathy pathological voices, the PA is low because the signals have weak periodicity (Davis, 1979).

Although, these linear tools have been used over the years, they are based in the assumption that voice is a linear phenomenon. But, voice production is a complex mechanism that involves different variables and exhibits nonlinearities (Kumar and Mullick, 1996). Considering human voice production (healthy and pathologic) as a nonlinear system, it can be described by a number of observable output states. Therefore it can be used in the construction of a state

space description of the system behavior. Voice signal, as a time series data, makes available the study of an underlying dynamic and provide the necessary information to obtain a reconstruction of the state space behavior of the system. Thus, phase space reconstruction technique can be used for voice characterization.

Nowadays, the use of entropy measures is widespread in many fields of science, whether applied to stochastic processes or dynamical systems. As presented by (Amigó et al., 2007), the application of entropy to discrete phase space is very natural, since its concept has been extended from deterministic continuous dynamics to stationary random processes and discrete dynamical systems. (Amigó et al., 2007) present a quantity called discrete entropy to deal with finite-state systems. This quantity asymptotically converges to conventional entropy, as evidenced by several examples.

As an example of the applicability of entropy, (Kirk and Jenkins, 2004) show that the Kolmogorov entropy is used to investigate software metrics, allowing early assessment of the design quality of software project. Also, in (Lake et al., 2002), an entropy measure called sample entropy was proposed. The objective was to improve the diagnosis of neonatal sepsis by monitoring the heart rate characteristics. The rate variability is interpreted as changes in the complexity of the underlying physiological processes. Despite the fact the method showed sensitivity to other signal's parameters, the results were interesting and could be used for monitoring at-risk infants.

Measures of entropy are intimately related to the predictability of signals. These measures can be used to evaluate forecast skill of a system. According to (Kleeman, 2002), some progress has occurred in using processes ensemble spread as an indicator of predictability. This is formalized in a parameter called predictive power (Schneider and Griffies, 1999).

Natural processes seem to be unpredictable due to several reasons, as described in (Crutchfield and Feldman, 2003). The most important reasons are: unknown rules that govern the system, existence of intrinsic mechanisms that amplify fluctuations, observer-induced sources of randomness, insufficient volume of data, and, perhaps, the dynamics is too complicated to have predictions evaluated.

Since the presence of pathologies on the vocal folds results in behavior change of the voice production system, the produced signals are going to be less predictable than the healthy ones. This work aims to try to detect these changes using simple entropy measures to differentiate two kinds of signals: healthy and pathological. For this paper, the pathology studied is the presence of nodule in the vocal folds.

In Theory a brief description of the entropy estimation is presented and also an explanation about the vocal fold nodule pathology. In Materials and Methods the voice samples used in the study are described in some details. After that, the phase space reconstruction and entropy estimation methods are presented. Also, a small discussion is made about the voice samples' processing. In Results examples of signals' phase space analysis are shown with the general results of entropy measures. In Conclusion the final comments about the work is presented.

2 THEORY

In this section a brief explanation of the entropy theory is presented. Also, a description of vocal fold nodules is shown.

2.1 Entropy

According to (Cover and Thomas, 1991), entropy is a quantity defined for any probability distribution with properties that agree with the intuitive notion of information measures.

One of the entropy's first concepts was presented in (Shannon, 1948) as the definition of a measure of uncertainty of a random variable. Considering a random variable X that assumes values $x \in \chi$ where χ is a finite set, the entropy $H(X)$ can be defined by Equation (1), with units in bits.

$$H(X) = -\sum_{x \in \chi} p(x)\, log_2\, p(x) \qquad (1)$$

The probability of x, $Pr\{X = x\}$, is denoted by $p(x)$. If $p(x) = 0$, $p(x)\, log_2\, p(x) = 0$ by convention. This quantity is dependent on the distribution of X instead of the actual values of the random variable. As discussed in (Crutchfield and Feldman, 2003), the entropy measures the average amount of bits necessary to store outcomes of the random variable.

2.2 Vocal Fold Nodules

Individuals with vocal nodules constitute a large part of the client population at voice clinics (Colton and Casper, 1996). They are commonly seen in women, children, salesmen, and teachers who have to use their voice too frequently. The main symptoms are hoarseness, breathiness, easy vocal fatigue, and throat discomfort. The voice is better in the morning and worsens in the afternoon after voice use (Fisher, 1996).

The vocal nodule is as a benign lesion occurring on both sides of the vocal folds, strictly symmetric on

the border of the anterior and middle third of the vocal fold and usually immobile during phonation. The lesion is confined to the superficial layer of the *lamina propria* (Rosen and Murry, 2000; Hirano, 1991).

The vocal folds are subject to several forms of mechanical stress during phonation. Vocal fold vibration during phonation leads to impact stress during collision between the left and right vocal fold surfaces. According to different studies, nodules mostly occur at the midpoint of the membranous vocal folds, where impact forces are the largest and they are mostly bilateral (Titze, 1994; Jiang and Titze, 1994).

During the closing phase of the folds' vibration, the presence of nodules on the outer layer of vocal folds' tissue inhibits them from being completely folded on each other. Consequently the glottis closure is uncompleted, adding turbulent air to the voice signal. In order to reduce this effect, the subject increases the muscle tension and the subglottal pressure, consequently rising the vocal fold collision forces (Hillman et al., 1990).

Nodule voice shows perceptually strained/pressed voice quality and breathiness with various degrees of turbulent noise. Frequently, the voice also presents vibrations irregularities, such as roughness and instability, as well as vocal fry/creak (Hammarberg, 1998).

The nodules are responsible for pitch frequency and air flow volume changes, also amplitude and mucosal wave reduction and the noise-like turbulence of airflow in the vocal folds. This is mainly due to the incomplete closure of the vocal folds, glottal air leakage, and their asymmetrical vibration because of their biomechanical parameter alterations (Hugh-Munier et al., 1997).

3 MATERIALS AND METHODS

In this section the voice samples are addressed showing the groups and acquisition method. After that, the phase space reconstruction technique and the entropy estimation method are presented. Finally, the voice signals' analysis method is shown.

3.1 Voice Samples

For this study, 28 voice signals divided in two equal groups were used. The first group was composed of healthy people with no voice complaints or laryngeal pathology. The second group was composed of people with vocal fold nodules in different stages of disease evolution according to (Scalassara et al., 2007). These voice signals are part of a voice database of the Group of Bioengineering of the School of Engineering of São Carlos at the University of São Paulo, Brazil. These signals were collected along the past ten years and used in several studies (Rosa et al., 2000; Dajer et al., 2005).

All volunteers were diagnosed by physicians of the Otolaryngology sector and the Head and Neck Surgery sector of the Clinical Hospital in the Faculty of Medicine at Ribeirão Preto, Brazil (`http://www.hcrp.fmrp.usp.br`) by means of videolaryngoscope and stroboscope light.

The data recording was performed using a protocol similar to the one presented in (Uloza et al., 2005). The subjects were asked to produce a sustained vowel /a/ at a comfortable pitch and loudness level for about 3 seconds. The used microphone was in accordance to the standards established in Brazil. It was placed at a distance of 5 cm from the person's mouth. Consecutive trials were performed, selecting the signal with less voice variability.

As presented in (Davis, 1979), vowel sounds are generally used in studies of pathological speech because the vocal folds are vibrating during vowel phonation. Also, acoustics assessment of laryngeal function relates to adequacy of sustained vocal fold vibration. Therefore, in order to collect the data, the sustained /a/ phoneme was used to evaluate the acoustical parameters of the samples. In English, this phoneme is equivalent to "a" in "dogma".

At voice acquisition, it was necessary to check if the individual could cope with the phonation interval and, in negative case, he was asked to stop uttering. This procedure was important because the maintenance of the utterance causes an increase of the voice fundamental frequency and an artificial stability on its production (Rosa et al., 2000). In order to avoid the influence of transitory phenomena, the start and ending of the acquired voice signal were discarded. Then, it was possible to ensure that the beginning and ending of voicing did not influence the final result.

After that, the amplitude of the signal was normalized according to its absolute maximum value. It was necessary to eliminate the influence of different sound levels from the signals collected. All voices samples were quantized in amplitude with 16 bits and recorded in mono-channel WAV format to preserve the fidelity of the signal. The sampling frequency was 22050 Hz.

3.2 Phase Space Reconstruction Technique

In order to describe the nonlinear dynamic characteristics of voice signals, sustained vowel data set was analyzed with ANL (*Análise Não-Linear*) software

(Dajer et al., 2005). This piece of software was developed using Matlab 7.0 and the Tisean Package (Hegger et al., 1999; Kantz and Schreiber, 2004). The ANL is based in the phase space reconstruction technique and represent the vocal folds vibration as an orbit trajectory in phase space with time evolution.

The voice signal can be represented by the time series $x(t_i)$, $t_i = t_0 + iT$, with $i = 1,2,\ldots,N$, where N is the length of the signal and T is the sampling period (Rabiner and Schafer, 1978). The phase space reconstruction of this signal is performed by plotting the time series $x(t_i)$ against itself at some time delay (Ott et al., 1994; Packard et al., 1980).

In order to create the reconstructed space for the time series $x(t_i)$, the method of delays is used (Fraser and Swinney, 1986; Hegger et al., 1999). A set of m vectors, called the embedding space, are formed from time delayed values of $x(t_i)$, Equation (2). In this set, m is the embedding dimension and τ is the time delay.

$$X(t_i) = \{x(t_i), x(t_i - \tau), \ldots, x(t_i - (m-1)\tau)\} \quad (2)$$

When $m > 2D + 1$, where D is the Hausdorff dimension, the reconstructed phase space is topologically equivalent to the original phase space (Fraser and Swinney, 1986). The delay τ is obtained by the first local minimum of the mutual information function of the signal (Fraser and Swinney, 1986).

3.3 Entropy Estimation

In order to estimate the signal entropy, an algorithm was developed based on the one presented in (Moddemeijer, 1989) with the optimizations shown in (Moddemeijer, 1999). The method is based on a simple histogram algorithm with bias correction and minimum mean square error estimation. In the cited paper, the author presents several examples that evaluate the algorithm showing its reliability.

The principle of the method is to try to estimate the probability distribution function (PDF) of the signal under study. This is performed by dividing the function in a rectangular grid with I equally Δx-sized cells. The occurrences of the signal's points in each cell, k_i, are summed. Then, the probabilities of each cell, p_i, is replaced by the estimative k_i/N, where N is the total number of samples of the signal. Therefore, the entropy estimator of Equation (3) is obtained, since the logarithms have base 2, the units are in bits. The bias correction for this estimator for discrete systems is given in Equation (4).

$$\hat{H}_x = -\sum_i \left(\frac{k_i}{N} log_2 \frac{k_i}{N} \right) + log_2 \Delta x \quad (3)$$

$$E\{\hat{H}_x\} \approx H_x - \frac{I-1}{2N} \quad (4)$$

An example of the use of this algorithm is now shown. It is taken from R. Moddemeijer website: `http://www.cs.rug.nl/~rudy/matlab/doc/entropy.html`. A normal distributed random noise is generated with zero mean and unity standard deviation. The signal and its histogram, obtained using 30 bins, are presented in Figures 1 and 2 respectively. The expected entropy of this signal is 1.4189 nat. Using the estimator the result is 1.3643, what gives an error of 3.85%.

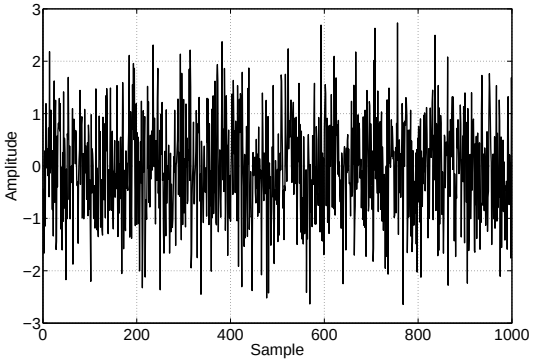

Figure 1: Signal of a normal distributed random noise generated with zero mean and unity standard deviation used to illustrate the entropy algorithm.

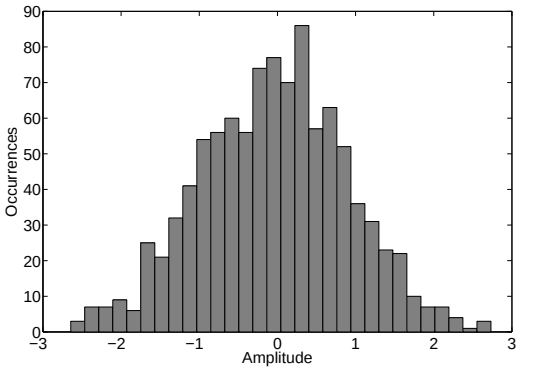

Figure 2: Histogram of the random noise signal used to illustrate the entropy algorithm. This histogram was obtained using 30 bins.

3.4 Analysis Method

Each voice sample was analyzed by a speech therapist and had its most stationary part selected. This stationarity was further analyzed by checking the result's power spectrum density (PSD), verifying if only

minor changes occur. This is a simple form of obtaining wide sense stationary (WSS) signals (Hayes, 1996).

For all the samples, this procedure resulted in at least one second of voice sample. The result was divided in parts with length of 1000 points (approximately 50 milliseconds). Each of these signals were normalized by the absolute of its maximum value.

The PDF of these normalized signals were estimated according to the proposed method in order to evaluate their entropy. Since each signal has the same length and amplitude range, the entropy estimator does not favor any of them. The analysis is perfomed with the mean and standard deviations values of the signal's entropies.

4 RESULTS

Healthy and nodule voice samples analyzed by means of phase space reconstruction technique with ANL showed different visual patterns for each group.

In order to determinate the visual pattern characteristics, three kind of orbits' dynamic behavior were observed: a) number of loops, b) attractor course regularity, and c) attractor trajectories distribution (divergence and convergence of attractor orbits' trajectories).

For healthy voice signals, phase space reconstruction for sustained vowel /a/ presents a typical visual pattern. First, it is characterized by many concentric loops of different dimensions. The orbits' loops are correlated to the interaction between the fundamental frequency (F_0) and the harmonic frequencies (F_1, F_2, F_3, ...) of the signal. This configuration links the voice signal complexity and the number of harmonic frequencies amplified and contained in sustained /a/ vowel. Second, the attractor course is flat and regular and, third, the attractor trajectories are very close to each other showing convergence tendency.

Figure 3 shows a typical healthy voice signal of a sustained vowel /a/. Figure 4 shows its phase space reconstruction with time delay τ according to (Fraser and Swinney, 1986).

For nodule voice signals, phase space reconstruction of sustained vowel /a/ presents different patterns. In general, the nodule's pattern is characterized firstly by a single and irregular orbit loop differing from the healthy ones. Although the harmonic components are present in the glottal pulse, the higher muscle tension and subglottal pressure unbalance the (F_0)/harmonic frequencies ratio and the compensatory vocal tract gesture contributes to atenuate the harmonic frequencies, consequently producing a single trajectory loop.

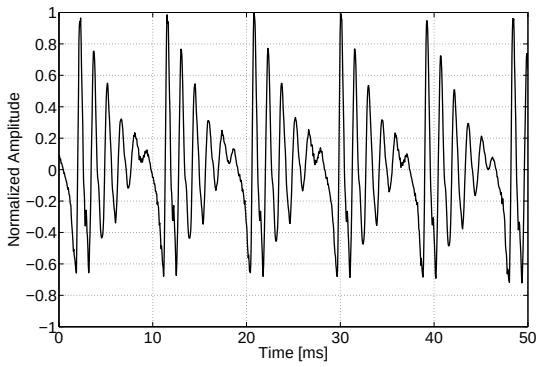

Figure 3: Example of a typical healthy voice signal of a sustained vowel /a/.

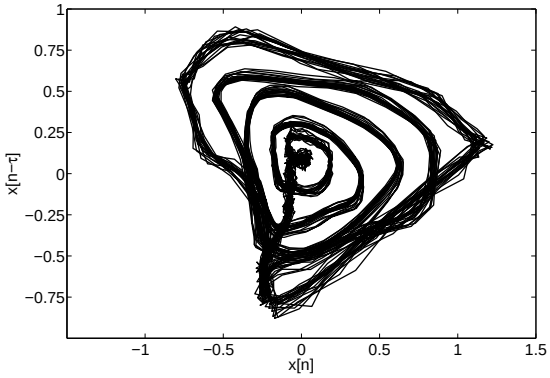

Figure 4: Phase space reconstruction of the typical healthy voice signal of a sustained vowel /a/.

Secondly, the attractor course is irregular and curly because of the incomplete closure of the vocal folds, turbulence of airflow and the asymmetrical vibration. Thirdly, the attractor trajectories present a disperse tendency caused by air flow volume changes and the mucosal wave variation. This irregularity can happen in some specific regions or even in different regions of the orbits.

Figure 5 shows a typical nodule voice signal of a sustained vowel /a/. Figure 6 shows its phase space reconstruction with time delay τ according to (Fraser and Swinney, 1986).

After the proper stationary regions of the signals were selected using the perceptual acoustic analysis and study of the phase space, the entropy estimations were performed. Since these selected samples had at least one second of voice, they were decomposed in 20 signals of 1000 points each. Figure 7 presents the mean and standard deviation entropy values of the results of these 20 signals for each of the 14 healthy and 14 nodule voice samples. These samples are ordered by their evaluation, therefore they are not paired.

As can be seen in the figure, the mean values of

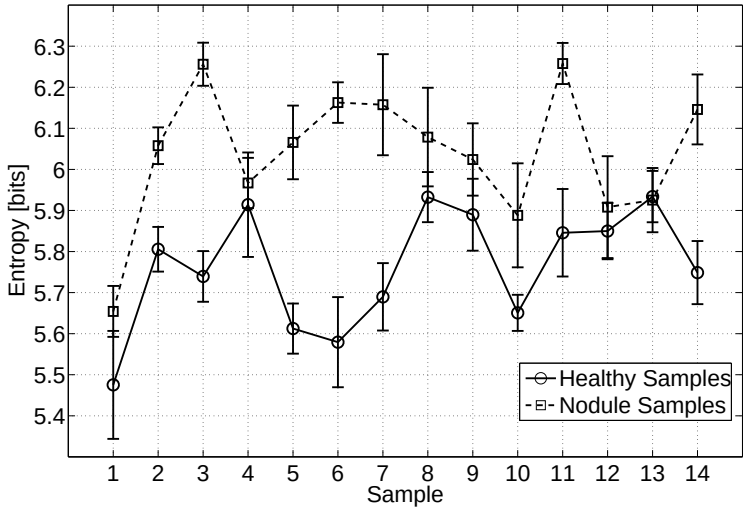

Figure 7: Entropy estimation results for the two groups of voice signals, healthy and nodule affected, each with 14 samples. Every point is a mean (with standard deviation) of entropy values of 20 signals (50 milliseconds each). The nodule group presented higher values than the healthy group, 99.75% probability in a Student-t test (significance level of 5%).

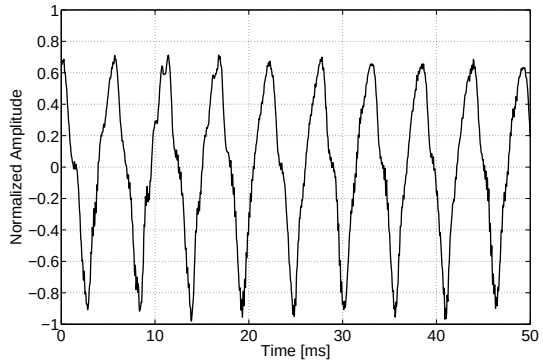

Figure 5: Example of a typical nodule voice signal of a sustained vowel /a/.

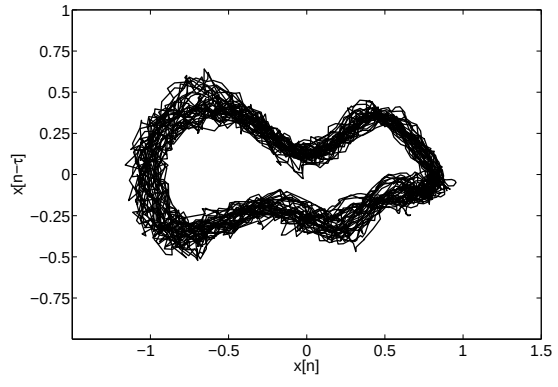

Figure 6: Phase space reconstruction of the typical nodule voice signal of a sustained vowel /a/.

the nodule samples seem to be higher than that of the healthy samples. According to the standard deviation values, the two classes seem to be separated. The mean entropy value of the healthy group is 5.76 bits with standard error of 0.14 bits, while the mean and standard error values of the nodule group is 6.04 and 0.16 respectively. The individual values obtained for these samples are shown in Table 1. An unpaired Student-t test with a significance level of 5% was performed on the data. It shows that the mean of the nodule group is indeed higher than that of the healthy group with a probability of 99.75%.

Table 1: Mean and standard deviation (Std) of the entropy values, in bits, of the results of the 20 signals of each of the 14 healthy and 14 nodule voice samples.

Healthy Samples		**Nodule Samples**	
Mean	Std	Mean	Std
5.48	0.13	5.65	0.06
5.81	0.05	6.06	0.04
5.74	0.06	6.26	0.05
5.91	0.13	5.97	0.06
5.61	0.06	6.07	0.09
5.58	0.11	6.16	0.05
5.69	0.08	6.16	0.12
5.93	0.06	6.08	0.12
5.89	0.09	6.02	0.09
5.66	0.04	5.89	0.13
5.85	0.11	6.26	0.05
5.85	0.07	5.91	0.12
5.93	0.06	5.93	0.08
5.75	0.08	6.15	0.09

Table 2: Mean values and standard deviations of jitter, shimmer and pitch amplitude (PA) for the signals under analysis (percentual values).

Samples	Jitter	Shimmer	PA
Healthy	0.47 ± 0.39	3.34 ± 0.88	54 ± 12
Nodule	3.37 ± 3.22	10.04 ± 4.74	36 ± 15

In order to compare the performance of the proposed method, the voice signals were analyzed aiming to extract vocal acoustic parameters. This was performed by a commercial software called *Análise de Voz* (Voice Analysis) version 6.0. The mean values (and standard deviations) of jitter, shimmer and pitch amplitude (PA) over the 14 samples of each group of signals are presented in Table 2.

The jitter and shimmer mean values are smaller for the healthy group, as expected, and present narrow probability distribution. For the nodule group the distribution is much wider. This variation can be interpreted as an increase of the uncertainty of these signals. The mean PA is higher for the healthy group because the signals have a more defined period, the cause of the smaller jitter values.

The higher variability of the parameters for the nodule group is probably due to physiological differences among the occurences of the pathology. Nodules can be manifested in several ways along the vocal folds, some layers of tissue may be modified or not. Therefore, the system dynamic alterations can lead to much different voice signals. It is interesting to observe that the presented parameters compare favorably to the results obtained by the entropy method.

5 CONCLUSIONS

In this work, there was an attempt to look into voice as a dynamical signal and, consequently, explore new processing techniques for healthy and vocal nodule's voice signals. A practical application and advantages of dynamical analysis were also presented. Thus, we believe that nonlinear dynamics tools, as entropy measures and phase space reconstruction, may help in a review of many of the voice dynamic characteristics.

We presented a study of the use of entropy measures to two groups of voice signals. They were composed by samples of healthy and nodule in the vocal folds affected individuals. The samples were analyzed by a speech therapist with aid of phase space plots. The most stationary parts of these signals (in the WSS sense) were selected. The entropy method developed by (Moddemeijer, 1989) was used to estimate the entropy of samples of 50 milliseconds of each of the signals. The results obtained for the mean and standard deviation values were tested with a Student-t test being clearly separable. This is an indication of the behavior of the entropy of nodule signals, at least in the voice samples studied.

The nodule group showed a higher entropy value than the healthy group. This was expected because this vocal fold pathology is characterized by increase of the signal's complexity (Hammarberg, 1998; Hillman et al., 1990). This effect is reflected in an increase of the uncertainty of the signal, that is, the signal becomes less predictable (Crutchfield and Feldman, 2003; Schneider and Griffies, 1999).

The results were compared to jitter, shimmer and pitch amplitude values of the samples, which were obtained with a commercial software. The variability of the parameters for the nodule affected group was significantly higher than that of the healthy group, therefore presenting a behavior that compares favorably to that obtained with the entropy method.

This work is still an initial study, but phase space analysis helps to depict the vowel pattern in a dynamical way. This technique allows to visualize the differential dynamics between healthy voices and voices with vocal folds nodules. Future works intend to use predictability measures to improve the understanding of the relation of pathologies with the complexity of the voice signal. Also, measures applied directly to the phase space of the signals are planned as well.

ACKNOWLEDGEMENTS

The authors acknowledge the Research Foundation of the State of São Paulo (FAPESP) and the Program of Students - Post-graduation Agreement (PEC-PG) for the support and scholarship. We also thank the School of Engineering of São Carlos (EESC/USP) for the research facilities and the use of its voice database.

REFERENCES

Amigó, J. M., Kocarev, L., and Tomovski, I. (2007). Discrete entropy. *Physica D: Nonlinear Phenomena*, 228(1):77–85.

Colton, R. H. and Casper, J. K. (1996). *Understanding voice problems: a physiological perspective for diagnosis and treatment*. Williams & Wilkins, Baltimore.

Cover, T. M. and Thomas, J. A. (1991). *Elements of Information Theory*. John Wiley and Sons, Inc., New York.

Crutchfield, J. P. and Feldman, D. P. (2003). Regularities unseen, randomness observed: levels of entropy convergence. *Chaos*, 13(1):25–54.

Dajer, M. E., Pereira, J. C., and Maciel, C. D. (2005). Nonlinear dynamical analysis of normal voices. In *Seventh IEEE International Symposium on Multimedia (ISM 2005)*, pages 765–771, Irvine, CA, USA.

Davis, S. B. (1979). *Speech and language: advances in basic research and practice*, chapter Acoustic characteristics of normal and pathological voices, pages 271–314. Academic Publishers, New York.

Fisher, K. V. (1996). Vocal fold nodules. *Curr. Op. Otol. Head Neck Surg.*, 4:166–171.

Fraser, A. M. and Swinney, H. L. (1986). Independent coordinates for strange attractors from mutual information. *Phys. Rev. Lett.*, 33(2):1134–1140.

Hammarberg, B. (1998). Perception and acoustics of voice disorders: a combined approach. In *Proceedings of VOICEDATA98, Symposium on databases in voice quality research and education*, pages 1–6, Utrecht, The Netherlands. Utrecht Institute of Linguistics.

Hayes, M. H. (1996). *Statistical Digital Signal Processing and Modeling*. John Wiley & Sons, Inc., New York.

Hegger, R., Kantz, H., and Schreiber, T. (1999). Practical implementation of nonlinear time series methods: The tisean package. *Chaos*, 9(2):413–435.

Hillman, R. E., Holmberg, E. B., Perkell, J. S., Walsh, M., and Vaughan, C. (1990). Phonatory function associated with hyperfunctionally related vocal fold lesions. *Journal of Voice*, 4(1):52–63.

Hirano, M. (1991). *Phonosurgery assessment and surgical management of voice disorders*, chapter Phonosurgical anatomy of the larynx, pages 34–36. Raven Press, New York.

Hugh-Munier, C. M., Scherer, K. R., Lehmann, W., and Scherer, U. (1997). Coping strategies, personality, and voice quality in patients with vocal fold nodules and polyps. *Journal of Voice*, 11(4):452–461.

Jiang, J. J. and Titze, I. R. (1994). Measurements of vocal fold pressure and impact stress. *Journal of Voice*, 8(2):132–145.

Kantz, H. and Schreiber, T. (2004). *Nonlinear Time Series Analysis*. Cambridge University Press, Cambridge, 2nd edition.

Kirk, S. R. and Jenkins, S. (2004). Information theory-based software metrics and obfuscation. *The Journal of Systems and Software*, 72(2):179–186.

Kleeman, R. (2002). Measuring dynamical prediction utility using relative entropy. *Journal of the Atmospheric Sciences*, 59(13):2057–2072.

Kumar, A. and Mullick, S. K. (1996). Nonlinear dynamical analysis of speech. *Journal of the Acoustic Society of America*, 100(1):615–629.

Lake, D. E., Richman, J. S., Griffin, M. P., and Moorman, J. R. (2002). Sample entropy analysis of neonatal heart rate variability. *Am. J. Physiol. Regul. Integr. Comp. Physiol.*, 283(3):R789–R797.

Moddemeijer, R. (1989). On estimation of entropy and mutual information of continuous distributions. *Signal Processing*, 16(3):233–248.

Moddemeijer, R. (1999). An efficient algorithm for selecting optimal configurations of ar-coefficients. In *20th Symp. on Information Theory in the Benelux*, pages 189–196, Haasrode (B).

Ott, E., Sauer, T., and Yorke, J. A. (1994). *Coping with Chaos*. John Wiley & Sons, Inc., New York.

Packard, N. H., Crutchfield, J. P., Farmer, J. D., and Shaw, R. S. (1980). Geometry from a time series. *Phys. Rev. Lett.*, 45(9):712–716.

Rabiner, L. R. and Schafer, R. W. (1978). *Digital Processing of Speech Signals*. Prentice Hall, Englewood Cliffs, NJ.

Rosa, M. O., Pereira, J. C., and Grellet, M. (2000). Adaptive estimation of residue signal for voice pathology diagnosis. *IEEE Trans. Bio. Eng.*, 47(1):96–104.

Rosen, C. A. and Murry, T. (2000). Nomenclature of voice disorders and vocal pathology. *Otolaryngol. Clin. North. Am.*, 33(5):1035–1046.

Scalassara, P. R., Maciel, C. D., Guido, R. C., Pereira, J. C., Fonseca, E. S., Montagnoli, A. N., Barbon, S., Vieira, L. S., and Sanchez, F. L. (2007). Autoregressive decomposition and pole tracking applied to vocal fold nodule signals. *Pattern Recognition Letters*, 28(11):1360–1367.

Schneider, T. and Griffies, S. M. (1999). A conceptual framework for predictability studies. *Journal of Climate*, 12(10):3133–3155.

Shannon, C. E. (1948). A mathematical theory of communication. *The Bell System Technical Jounal*, 27:379–423, 623–656.

Titze, I. R. (1994). Mechanical stress in phonation. *Journal of Voice*, 8(2):99–105.

Uloza, V., Saferis, V., and Uloziene, I. (2005). Perceptual and acoustic assessment of voice pathology and the efficacy of endolaryngeal phonomicrosurgery. *Journal of Voice*, 19(1):138–145.

ON-CHIP FLUORESCENCE LIFETIME EXTRACTION USING SYNCHRONOUS GATING SCHEME

Theoretical Error Analysis and Practical Implementation

Day-Uei Li, Bruce Rae, David Renshaw, Robert Henderson
Institute for Integrated Micro and Nano Systems, The University of Edinburgh, The King's Buildings
Mayfield Rd., Edinburgh EH9 3JL, UK
David.Li@ed.ac.uk

Eleanor Bonnist
School of Chemistry and the Collaborative Optical SpectroscopyMicromanipulation and Imaging Centre (COSMIC)
University of Edinburgh, West Mains Rd., Edinburgh EH9 3JJ, UK
e.y.m.bonnist@sms.ed.ac.uk

Keywords: Fluorescence lifetime imaging microscopy (FLIM). Error analysis. On-chip implementation. Rapid lifetime determination (RLD). Single photon avalanche diode (SPAD). Time-correlated single-photon counting (TCSPC). Data fitting. Pipe-lined RLD. Instrumental response function (IRF).

Abstract: A synchronous gating technique was proposed for fluorescent photon collecting. The two- and multi-gate rapid lifetime determination (RLD) technique was applied to implement on-chip fluorescence lifetime extraction. Compared with all available iterative least square method (LSM) or maximum likelihood estimation (MLE) based general purpose FLIM analysis software, we offer a method for the direct calculation of lifetime based on the photon counts stored in on-chip memory and deliver faster analysis to enable real-time applications. Theoretical error analysis of the two-gate RLD technique was derived for comparison. The performance of the algorithms were tested on a single-exponential histogram obtained from a CMOS SPAD detector chip using a 468nm laser diode light source with optimized gate width. Moreover, a multi-exponential pipelined RLD FLIM technique was also proposed and tested on a four-exponential decay DNA sample containing a single adenine analogue 2-aminopurine.

1 INTRODUCTION

Fluorescence lifetime measurements have been used widely to study various scientific and practical applications on optics, chemistry, biology, medicine, medical diagnosis. A large number of different techniques including time-domain and frequency-domain methods have been well developed for measuring fluorescence lifetime (Apanasovich and Novikov, 1992). In time-domain methods, the fluorescence intensity decay is measured through a time-correlated single photon-counting (TCSPC) card after excitation with a short pulse of laser light (Cubeddu et al, 2002), whereas in frequency-domain methods, the fluorescent sample is illuminated with a periodic light source to obtain a measured phase difference between the light source and the fluorescent emission. Irrespective of the method used (Jo et al, 2004), the lifetime extraction is done using computer software. For general purpose time-domain analysis tools for scientific research demanding high accuracy down to the picosecond timescale or for practical medical/clinical diagnostic applications demanding fast results, a wide range of faint multi-exponential fluorophores must be computed with a lifetime resolution better than 50ps (Becker, 2005). Due to the incapability of the LSM or MLE to resolve a small lifetime with a coarse channel width, the number of bits of resolution of TDCs on photon counting cards is therefore expected to be larger than 11-bit (Becker, 2005). To use LSM or MLE properly, the measurement window is usually set as large as possible otherwise the software would treat the measured data as having a DC offset part and therefore the laser pulse repetition rate is kept low, which further lowers the photon collection speed. Data therefore can be gathered in several days. Moreover, because

fluorescence lifetimes in imaging are determined on a pixel-by-pixel basis, iterative methods can be quite time consuming and make real-time image processing almost impossible. Although one can drop the requirement for short laser pulses by using frequency-domain methods, lifetime extraction still relies on software analysis, which also makes real-time image processing difficult to achieve. As process technology advances, integration of high speed laser drivers and laser diodes on chip is becoming feasible.

2 THEORETICAL ERROR ANALYSIS

The recorded fluorescence intensity $f(t)$ is related to the true decay function I(t) through the integral

$$f(t) = \int_0^t I(t-\tau) IRF(\tau)\, d\tau \qquad (1)$$

where $IRF(t)$ is the instrumental response function, or the convolution of transition spread of the detector and the pulse function of the laser source. The true response $I(t)$ could be obtained through an on-chip digital de-convolution calculation. However, we need to evaluate whether the enhanced precision can justify the cost of the extra chip area for digital de-convolution. Here we assume $I(t) = A\exp(-t/\tau)$, and the ratio of the full width half maximum (FWHM) of $IRF(t)$ over the lifetime is denoted as r. The recorded response $f(t)$ is obtained from (1). As r is larger than 1, it is difficult to obtain a clear response because of the effects of noise and it is inefficient to accumulate enough photon counts for a certain SNR criteria. The smaller the ratio r, the more efficiently and accurately the lifetime can be extracted. Considering the 10ps jitter in the light source, the 80ps transition spread of our SPAD structure, and the 30ps jitter of gate transitions, the overall FWHM is about 100ps. Thus, without on-chip de-convolution function, the smallest lifetime that can be obtained is of the order of 200ps. For first time implementation, we simplify by using longer-lifetime samples as test cases. The assumption of $f(t)$ as a single exponential is quite reasonable. In this paper, we applied the RLD method for simplicity.

2.1 Theory

The simplest way of calculating fluorescence lifetime is to use the RLD technique with two consecutive gates (Ballew and Demas, 1989) called

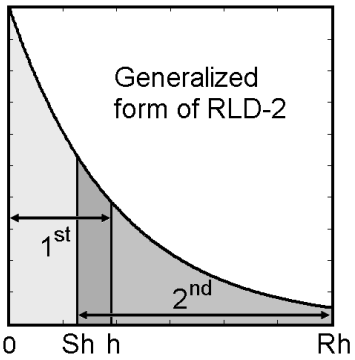

Figure 1: Generalized form of two-gate RLD.

standard RLD. Unlike the LSM or MLE based methods, it is a direct calculation method. The disadvantage of standard RLD is its high sensitivity to the gate width selection. This can be explained by reasoning that when dealing with a short lifetime, the photons are mostly located in the first gate, and the relatively low counts in the second gate becomes the major source of error. To overcome this problem, a gate overlap approach was introduced to the standard RLD (Sharman and Periasamy, 1999) trying to offer greater insensitivity to the Possion noise in the second gate. This method did offer better resolvability for a range of short lifetimes, but it sacrificed precision for the longer lifetimes. Another approach called SWRLD is proposed (Chan et al, 200) using a square wave driven LED as a light source. SWRLD offers uniform high precision in a much wider range of gate width. However, this method does not easily extract lifetimes shorter than 1ns because the 1ns edge speed of the fastest available LED dictates the minimum lifetime extraction limit, Thus an example of a long lifetime of 2ms has been chosen as an illustration. The second challenge is that SWRLD needs many filters to separate fluorophore emission from scattered laser emission (the IRF). Beyond these limits, SWRLD is indeed a precise method for long lifetime extraction (>> 10ns). A better approach to achieve better precision for long lifetimes is make the second gate wider than the first and therefore tolerate much higher counts (Moore et al, 2004). This method, however, needs an iteration method to do lifetime extraction. Plus for on-chip implementation, asymmetric gates require the generation of two synchronized clocks with different pulse widths and thus increase the circuit complexity. The best theoretical solution is not necessarily the right one in terms of cost and feasibility. All the amended algorithms mentioned require Monte Carlo to do error analysis. We derive a generalized formula here

for calculating the standard deviation of lifetimes much more conveniently and therefore facilitate location of the optimized lifetime region or measurement window. Figure 1 shows the generalized form of two-gate RLD. The counts N_1 and N_2 in the two gates are related as

$$g(x) = N_2(1-x) - N_1(x^S - x^R) = 0, \quad (2)$$

where $x = \exp(-h/\tau)$ and

$$N_1 = N_c(1-x)/(1-x^R), \sigma N_1 = \sqrt{N_1},$$
$$N_2 = N_c(x^S - x^R)/(1-x^R), \sigma N_2 = \sqrt{N_2}. \quad (3)$$

with σN_1 and σN_2 being the standard deviations in N_1 and N_2, respectively for Poisson noise and N_c the total count number. Together with (2), we have

$$\sigma g(x) = \sigma x \cdot |g'(x)|, \quad (4)$$

$$\sigma g = \sqrt{\sigma N_2^2 (1-x)^2 + \sigma N_1^2 (x^S - x^R)^2}, \quad (5)$$

$$|g'(x)| = N_2 + N_1(Sx^{S-1} - Rx^{R-1}), \quad (6)$$

$$\text{and} \quad \sigma x/x = h\sigma\tau/\tau^2. \quad (7)$$

From (2) to (7), we could obtain

$$\frac{\sigma\tau}{\tau} = \frac{\tau h^{-1}\sqrt{(1-x^R)k(x)}/\sqrt{N_c}}{\left[(S-1)x^{S+1} - (R-1)x^{R+1} - Sx^S + Rx^R\right]} \quad (8)$$
$$k(x) = (1-x)(x^S - x^R)^2 + (1-x)^2(x^S - x^R).$$

2.2 Comparison of RLD-*2*s and RLD-*N*

To demonstrate the ability of different RLD schemes, we fix the measurement window (MW). First we compute the standard deviation over the lifetime SNR = $\sigma\tau/\tau$ in dB. Figure 2 shows the SNR in the range of τ/MW within 0.05 and 1, and gate number N within 2 and 128 under total counts of 2^{17}. It shows the SNR plot converges as $N > 8$ and RLD-*2* shows the best resolvability for small lifetime region, but both RLD-*2* and RLD-*N* could not resolve those less than 0.1. It means that with a laser source of repetition rate of 100MHz, they could not resolve those less than 1ns. Moreover, the complexity of implementing *N*-gate RLD on chip is too large. In terms of implementation, the RLD-2 is much easier than RLD-*N*. Figure 3 shows a comparison plot of lifetime SNR versus lifetime normalized by measurement window (MW) for theoretical equation (8), equation for the multi-gate scheme not shown here, Monte-Carlo RLD methods and the maximum likelihood estimator (MLE) (Kollner and Wolfrum, 1992).

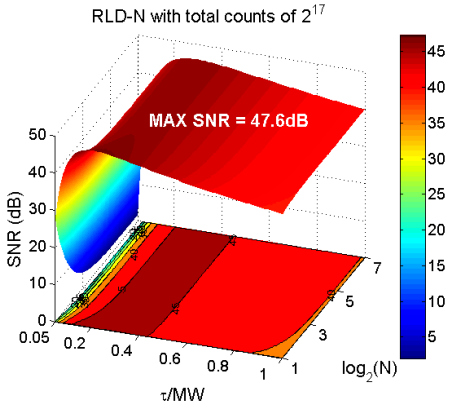

Figure 2: SNR plot for RLD-*N* under total counts of 2^{17}.

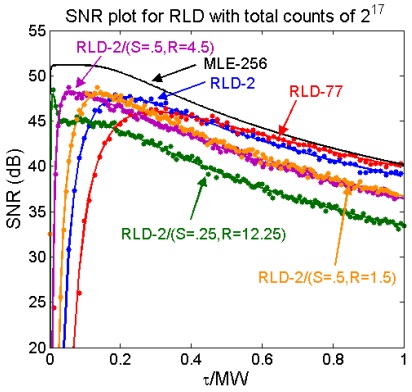

Figure 3: SNR plot for RLD-*N* with total counts of 2^{17}.

This plot shows the range of lifetime resolvable by each extraction method for a certain laser repetition rate. The results obtained by theoretical equations are marked as solid lines whereas those by Monte-Carlo methods are indicated by dots. They match well. We also compare the MLE results and find that the peak value of the RLD-2 occurs at τ/MW = $\tau/(2h)$ ~ 0.2 which is coincident with previously reported literature. The plot shows the RLD-77 has best precision and closest to that of MLE only in high lifetime region, while it has the worst resolvability for low lifetime region. Un-equal gate scheme (S = 0.5, R = 4.5) offers better resolvability than the equal gate-width one (S = 0.5, R = 1.5). The one with S = 0.25 and R = 12.25 suggested by (Moore et al, 2004) offers the best resolvability for small lifetime region but sacrifices some precision in the high lifetime region. In terms of implementation complexity, feasibility, and limitations on chip, the equal gate width scheme is the simplest. Of course, if we insist on implementing an un-equal one given

that we have conquered the problem of transition spread of the IRF, we could build an on-chip look-up table to simplify lifetime extraction. For first time on-chip implementation, we simplify by using the equal gate and non-overlap scheme. The overlap scheme will be implemented in the future. Table 1 lists the summary of RLD schemes. Except the RLD-*N*, the others are all possible candidates.

Table 1: Comparison and summary of RLD schemes.

	Closed Form	τ/MW < 0.1 Resolvability	On-chip Feasibility
Standard RLD-2	Yes	No	Yes/Look-up Table
Standard RLD-*N* (N > 2)	Yes	No	No
Overlap RLD-2 (R = 1+S)	Yes	Yes	Yes/Look-up Table
Overlap RLD-2 (R ≠ 1+S)	No	Yes	Yes/Look-up Table

2.3 Synchronous Gating Scheme

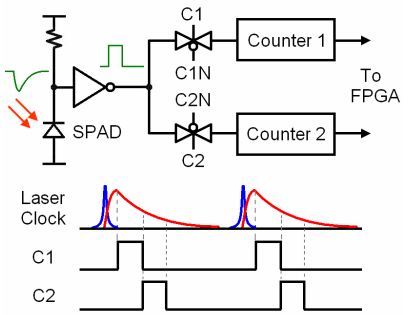

Figure 4: Timing diagram for synchronous gating technique.

Figure 4 shows the block diagram for the photon counting process. The fluorescence emission is detected by a SPAD detector, and the detected signal is converted into a digital one by a comparator and then sent into two synchronous counters controlled by clocks C1 and C2, respectively. And the photon counts on counters 1 and 2 are sent to a FPGA for post processing.

2.4 Pipelined RLD-2 for Multi-Decays

The above analysis is based on the assumption that the fluorescence emission follows a single-lifetime function. When trying to resolve multi-lifetime fluorescence decay, we need a simple algorithm. Figure 5 shows an algorithm for lifetime extraction in a two-lifetime fluorescence histogram similar to the concept of pipelined analog-to-digital converters, called pipelined RLD-2 (PL-RLD-2). The lifetime extraction procedure uses RLD-2 to extract the larger lifetime and intensity with the first memory, and subtraction of the extracted extrapolation function from the photon counts stored in the second memory to obtain the second lifetime and intensity. Pipelined algorithms for higher (> 2) decays can follow this procedure until the last lifetime is finally calculated.

3 EXPERIMENTAL RESULTS

3.1 Single-decay

The chip including a 4×16 SPAD array and digital readout circuits was implemented on 0.35µm high voltage CMOS process. The die had the polymide passivation removed providing around 3-5x increase in photon detection probability in the 500nm range. Each pixel contains a single 15µm-diameter CMOS SPAD (Niclass, 2006).

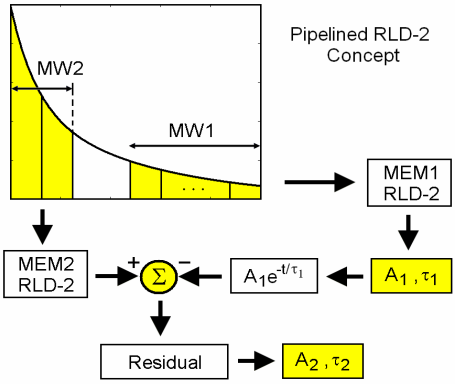

Figure 5: Block diagram of pipelined RLD-2.

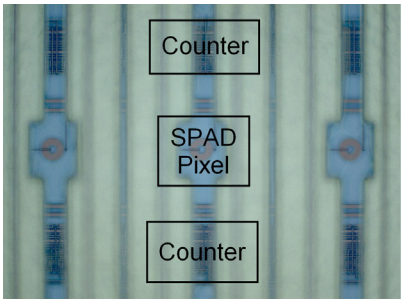

Figure 6: SPAD pixel and two ripple counters.

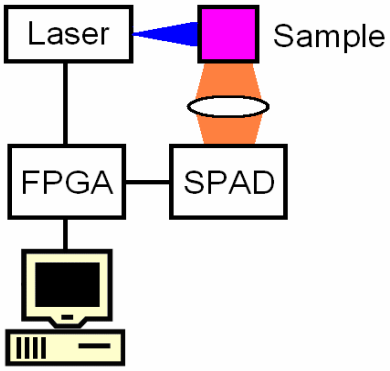

Figure 7: SPAD pixel and two ripple counters.

Figure 6 shows a SPAD pixel with two ripple counters up and down. The gating width could be adjusted over a 48ns range with a 408ps resolution. The imager is controlled by a FPGA and photon count histograms are captured and displayed on a PC. The measurement setup is shown in Figure 7. It consists of a laser diode emitting 88ps pulses at 468nm, 5mW average power, synchronized to the system clock. Without using any photon counting card, the photon emitted is converted into a digital signal and processed by on-chip ripple counters in Figure 4. The fluorophore sample is 1 micro-molar Rhodamine B. Table 2 shows the extracted lifetime using the RLD-2 and the LSM based software. The difference between them is about 7%. Jitter performance of the synchronous gate might contribute some error, because a phase-locked loop PLL has not been integrated to minimize the jitter.

Table 2: Comparison of lifetimes extracted by RLD-2 and software.

Sample	RLD-2	Software
Rhodamine B	2.33ns	2.175ns

3.2 Multiple-decays

The second example is used to test the proposed pipelined RLD-2 algorithm. This data set comes from the fluorophore 2-aminopurine (2AP) inside a singly-labelled 14 base-pair DNA duplex and was measured in an Edinburgh Instruments spectrometer equipped with TCC900 photon counting electronics (Neely et. al, 2005). The excitation source was a Ti-Sapphire femtosecond laser system producing pulses of ~200fs at 76MHz repetition rate. The output of the laser was passed through a pulse picker to reduce the repetition rate to 4.75MHz and then frequency tripled to give an output at 320nm. The emission from the sample was collected orthogonal to the excitation direction through a polarizer. The fluorescence was passed through a monochromator, and detected by a Hamamatsu PMT (R3809U-50). The instrument response was 50ps FWHM. Florescence decay curves were recorded at emission wavelength of 390nm on a timescale of 50ns, resolved into 4096 channels, to a total 10,000 counts in the peak channel. Decay curves were analyzed using the proposed PL-RLD-2 and using the F900 software with standard iterative reconvolution method, assuming a multi-exponential decay function in the following equation.

$$I(t) = \sum_{i=1}^{4} A_i \exp\left(-\frac{t}{\tau_i}\right), \quad (9)$$

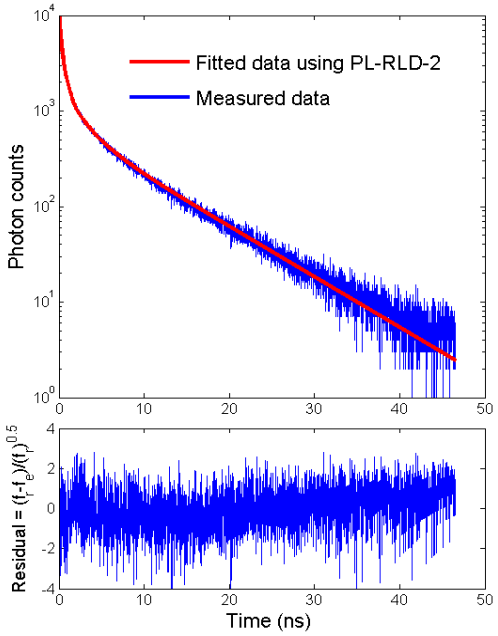

Figure 8: Fitted data and residual using PL-RLD-2.

Table 3: Comparison of lifetimes (ns) and fractional amplitudes (%) extracted by PL-RLD-2 and F900 software.

τ_i(ns)/A_i(%)	PL-RLD-2	F900 Software
τ_1/A_1	0.136/27	0.14/47
τ_2/A_2	0.481/55	0.47/39
τ_3/A_3	2.179/11	2.19/9
τ_4/A_4	8.225/7	8.15/5

where A_i is the fractional amplitude and τ_i is the fluorescence lifetime of the i-th decay component. Figure 8 shows the logarithmic plot for the measured photon counts starting from the channel with peak counts 10,000 and the fitted data using the proposed PL-RLD-2. The residual plot reveals that the proposed method fits well with the experimental data. The extracted lifetimes and fractional

amplitudes using the PL-RLD-2 and the F900 software are listed in Table 3. The Table shows the extracted lifetimes differ within 4% whereas the amplitudes differ in a significant range. That is why recent literature (Philip, 2003) suggests that fluorescence lifetime measurements offer better precision. These results highlight the potential of RL-RLD-2 for on-chip multiple exponential lifetime extraction, if adaptive gating width technique could also be introduced on-chip.

4 CONCLUSIONS

On-chip fluorescence lifetime extraction including a SPAD array and digital readout circuitry is for the first time implemented on 0.35μm CMOS process using the two-gate RLD. Theoretical error equations for several RLD-2/RLD-*N* schemes were derived and compared to determine a possible implementation strategy. To implement RLD-2, a non-overlap synchronous gating is applied for photon counting. The first on-chip attempt is mainly focused on dealing with single-exponential fluorescence emission, and the extracted result matches with the true value well within 10% including possible contribution from gating jitter. For possible future on-chip implementation for multi-exponential fluorescence lifetime extraction, we proposed a pipelined RLD-2 (PL-RLD-2) and we test this method on a four-exponential experimental data, and the extracted lifetimes match well with those obtained by iteration based software within 4%.

ACKNOWLEDGEMENTS

This work has been supported by the European Community within the Sixth Framework Programme IST FET Open MEGAFRAME project (contract No. 029217-2, www.megaframe.eu). The measurements have been performed using the COSMIC laboratory facilities at the University of Edinburgh.

DISCLAIMER

This publication reflects only the authors' views. The European Community is not liable for any use that may be made of the information contained herein.

REFERENCES

Apanasovich, V. V. and Novikov, E. G. (1992) 'Methods of analysis of fluorescence decay curves in pulsed fluorometry (Review)', *Journal of Applied Spectroscopy*, Vol. 56, No. 4, pp. 317-327.

Cubeddu, R., Comelli, D., D'Andrea, C., Taroni, P. and Valentini, G. (2002) 'Time-resolved fluorescence imaging in biology and medicine', *J. Phys. D*: *Applied Physics*, Vol. 35, pp. R61-R76.

Jo, J. A., Fang, Q., Papaioannou, T. and Marcu, L. (2004) 'Novel ultra-fast deconvolution method for fluorescence lifetime imaging microscopy based on the Laguerre expansion technique', *Conference Proceedings*, 26th Annual International Conference of the IEEE EMBS, pp. 1271-1274.

Becker, W. (2005), *Advanced Time-Correlated Single Photon Counting Techniques*, Wolfgang, Springer.

Ballew, R. M. and Demas, J. N. (1989), 'An error analysis of the rapid lifetime determination method for the evaluation of single exponential decays', *Ana. Chem.*, Vol. 61, pp. 30-33.

Sharman, K. K. and Periasamy, A. (1999), 'Error analysis of the rapid lifetime determination method for double-exponential decays and new windowing schemes', *Ana. Chem.*, Vol. 71, pp. 947-952.

Chan, S. P., Fuller, Z. J., Demas, J. N., Ding, F. and DeGraff, B. A. (2001), 'New method of rapid luminescence lifetime determination using square-wave excitation', *Applied Spectroscopy*, Vol. 55, No. 9, pp. 1245-1250.

Moore, C., Chan S. P., Demas, J. N. and DeGraff, B. A. (2004), 'Comparison of methods for rapid evaluation of lifetime of exponential decays', *Applied Spectroscopy*, Vol. 58, No. 5, pp. 603-607.

Kollner, M. and Wolfrum, J. (1992), 'How many photons are necessary for fluorescence-lifetime measurements?', Chemical Physics Letters, Vol. 200, No. 1,2, pp. 199-204.

Niclass, C. L. et al, (2006), 'A single photon avalanche diode array fabricated in deep submicron technology', *Conference Proceedings*, Design, Automation, and Test Europe Conference, pp. 81-86.

Neely, R. K., Daujotyte, D., Grazulis, S., Magennis, S. W., Dryden, D. T. F., Klimasauskas, S. and Jones, A. C., (2005), 'Time-resolved fluorescence of 2-aminopurine as a probe of base flipping in M.Hhal-DNA complexes', *Nucleic Acids Research*, Vol. 33, No. 22, pp. 6953-6960.

MULTIPLE SCALE NEURAL ARCHITECTURE FOR RECOGNISING COLOURED AND TEXTURED SCENES

Francisco Javier Díaz-Pernas[1], Míriam Antón-Rodríguez[2], Víctor Iván Serna-González[3]
José Fernando Díez-Higuera[4] and Mario Martínez-Zarzuela[5]
Department of Signal Theory, Communications and Telematics Engineering, Telecommunications Engineering School
University of Valladolid, Valladolid, Spain
[1]pacper@tel.uva.es, [2]mirant@tel.uva.es, [3]vsergon@ribera.tel.uva.es, [4]josdie@tel.uva.es, [5]marmar@tel.uva.es

Keywords: Computer Vision, neural classifier, texture recognition, colour image segmentation, Boundary Contour System, Feature Contour System, ART, colour-opponent processes.

Abstract: A dynamic multiple scale neural model for recognising colour images of textured scenes is proposed. This model combines colour and textural information to recognise coloured textures through the operation of two main components: segmentation component formed by the Colour Opponent System (COS) and the Chromatic Segmentation System (CSS); and recognition component formed by pattern generation stages and Fuzzy ARTMAP neural network. Firstly, the COS module transforms the RGB chromatic input signals into a bio-inspired codification system (L, M, S and luminance signals), and then it generates the opponent channels (black-white, L-M and S-(L+M)). The CSS module incorporates contour extraction, double opponency mechanisms and diffusion processes in order to generate coherent enhancing regions in colour image segmentation. These colour region enhancements along with the local textural features of the scene constitute the recognition pattern to be sent into the Fuzzy ARTMAP network. The structure of the CSS architecture is based on BCS/FCS systems, thus, maintaining their essential qualities such as illusory contours extraction, perceptual grouping and discounting the illuminant. But base models have been extended to allow colour stimuli processing in order to obtain general purpose architecture for image segmentation with later applications on computer vision and object recognition. Some comparative testing with other models is included here in order to prove the recognition capabilities of this neural architecture.

1 INTRODUCTION

In biological vision, we can distinguish two main operating modes: pre-attentive and attentive vision. The first one performs a parallel and instantaneous processing which is independent of the number of patterns being processed, thus covering a large region of the visual field. Attentive vision, nevertheless, acts over limited regions of the visual field (small aperture) establishing a serialised search by means of focal attention (Julesz & Bergen, 1987).

The proposed model works on the pre-attentive and attentive mode: pre-attentive segmentation and attentive recognition. In the pre-attentive process, the network processes, in a consistent way, colour and textural information for enhancing regions and extracting perceptual boundaries to form up the segmented image. In the attentive mode, the model merges textural information and the intensity of the region enhancement in order to punctually recognise scenes that include complex textures, both natural and artificial.

The skill of identifying, grouping and distinguishing among textures and colours is inherent to the human visual system. For the last few years many techniques and models have been proposed in the area of textures and colour analysis (Gonzalez & Woods, 2002), resulting in a detailed characterisation of both parameters as well as certain rules that model their nature. Many of these initiatives, however, have used geometric models, omitting the human vision physiologic base and so, wasting the context dependence. A clear example of such a feature is the illusory contour formation, in which context data is used to complete (Grossberg, 1984) the received information, which is partial or incomplete in many cases.

The architecture described in this work extracts both colour and textural features from a scene, segments it into textural regions and brings this information to an ART classifier, which categorizes

the textures using a biologically-motivated learning algorithm. Humans learn to discriminate textures by looking at them and becoming sensitive to their statistical properties in small regions (Grossberg and Williamson, 1999).

The proposed neural model architecture is based on the later version of BCS/FCS neural model (Grossberg et al., 1995; Mingolla et al., 1999), and on the Fuzzy ARTMAP recognition architecture (Carpenter et al., 1992). The BCS/FCS model suggests a neural dynamics for perceptual segmentation of monochromatic visual stimuli and offers a multiple scale unified analysis process for different data referring to monocular perception, grouping, textural segmentation and illusory figures perception. The BCS system obtains a map of image contours based on contrast detection processes, whereas the FCS performs diffusion processes with luminance filling-in within those regions limited by high contour activities. Consequently, regions that show certain homogeneity and are globally independent are intensified.

In pre-processing, the main improvement introduced to the BCS/FCS original model hereby in this paper, resides in offering a complete colour image processing neural architecture for extracting contours and enhancing the homogeneous areas in a colour image. In order to do this, the neural architecture develops processing stages, coming from the original RGB image up to the segmentation level, following analogous behaviours to those of the early mammalian visual system. This adaptation has been performed by trying to preserve the original BCS/FCS model structure and its qualities, establishing a parallelism among different visual information channels and modelling physiological behaviours of the visual system processes. Therefore, the envisaged region enhancement is based on the feature extraction and perceptual grouping of region points with similar and distinctive values of luminance, colour, texture and shading information.

The adaptive categorization and predictive theory is called Adaptive Resonance Theory, ART. ART models are capable of stably self-organizing their recognition codes using either unsupervised or supervised incremental learning (Carpenter et al., 1991). ARTMAP theory extends the ART designs to include supervised learning. Fuzzy ARTMAP architecture falls into this supervised theory. In Fuzzy ARTMAP, the ART chosen categories learn to make predictions which take the form of mappings to the names of output classes. And thus many categories can map the same output name.

In section 2, each of the stages composing the architecture will be explained. Afterwards, section 3 studies its performance over input images presenting complex textures in order to, in section 4, establish the conclusions of the analysis and finally assess the validity of the model depicted here.

2 PROPOSED NEURAL MODEL

The architecture of the proposed model (Figure 1) is composed of two main components, colour segmentation module and recognition module. The first component consists of two systems called Colour Opponent System (COS) and Chromatic Segmentation System (CSS). The recognition module is made up by a feature smooth stage, an orientational invariances stage, and a Fuzzy ARTMAP neural network.

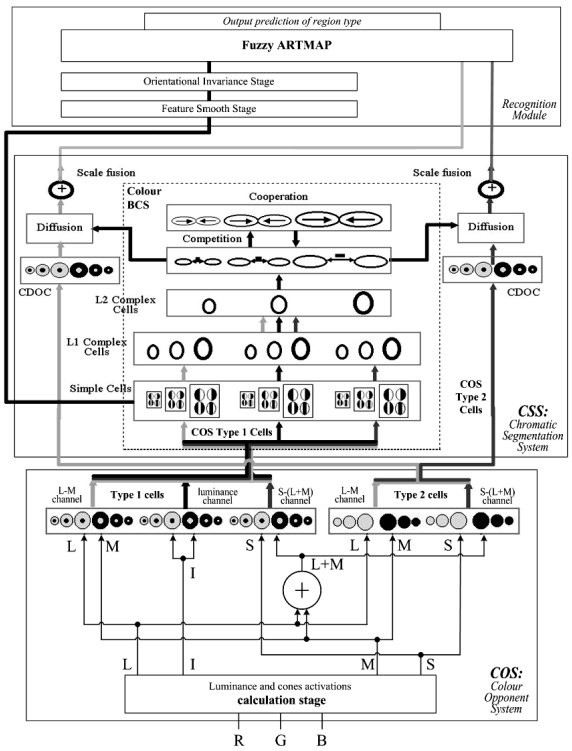

Figure 1: Proposed model architecture. At the bottom, the detailed COS module structure: on the left, it shows type 1 cells whereas on the right, elements correspond to type 2 opponent cells. In the middle, the detailed structure of the Chromatic Segmentation System (CSS) based on the BCS/FCS model. At the top, the recognition module, based on a Fuzzy ARTMAP network.

The COS module transforms the chromatic components of the input signals (RGB) into a bio-

inspired codification system, made up of two opponent chromatic channels, L-M and S-(L+M), and an achromatic channel.

Resulting signals from COS are used as inputs for the CSS module where the contour map extraction and two intensified region images corresponding to the enhancement of L-M and S-(L+M) opponent chromatic channels are generated in multiple scale processing, according to various perceptual mechanisms (perceptual grouping, illusory contours, discounting the illuminant and emergent features). The two enhanced images along with the textural response from the simple cells form up the punctual pattern of features that will be sent to the recognition module where the Fuzzy ARTMAP architecture generates a context-sensitive classification of local patterns. The final output of the proposed neural architecture is a prediction class image where each point is associated to the texture class label which it belongs to.

2.1 Colour Opponent System (COS)

The COS module performs colour opponent processes based on opponent mechanisms that are present on the retina and on the LGN of the mammalian visual system (Hubel, 1995). Firstly, luminance (I signal) and activations of the long (L signal), middle (M signal), short (S signal) wavelength cones and (L+M) channel activation (Y signal) are generated from R, G and B input signals. The luminance signal (I) is computed as a weighted sum (Gonzalez & Woods, 2002); the L, M and S signals are obtained as the transformation matrix (Hubel & Livingstone, 1990).

In the COS stage, two kinds of cells are suggested, called type 1 and type 2 cells (see Figure 1). These follow opponent profiles intended for detecting contours (type 1, simple opponency) and colour diffusion (type 2 cells initiate double opponent processes).

2.1.1 Type 1 Opponent Cells

Type 1 opponent cells perform two opponent L-M, S-(L+M), and luminance (Wh-Bl) channels (see Figure 1). These cells are modelled through two centre-surround multiple scale competitive networks, and form the ON and OFF channels composed of ON-centre OFF-surround and OFF-centre ON-surround competitive fields, respectively. These competitive processes establish a gain control network over the inputs from chromatic and luminance channels, maintaining the sensibility of cells to contrasts, compensating variable illumination, and normalizing image intensity (Grossberg & Mingolla, 1988). The equations governing the activation of type 1 cells ((1) and (2)) have been taken from the Contrast Enhancement Stage in the original models (Grossberg et al., 1995; Mingolla et al., 1999), but adapted to compute colour images. The equations for the ON and OFF channel are:

$$y_{ij}^{g+} = \left[\frac{AD^{+} + BS_{ij}^{c} - CS_{ij}^{sg}}{A + S_{ij}^{c} + S_{ij}^{sg}} \right]^{+} \quad (1)$$

$$y_{ij}^{g-} = \left[\frac{AD^{-} + CS_{ij}^{sg} - BS_{ij}^{c}}{A + S_{ij}^{sg} + S_{ij}^{c}} \right]^{+} \quad (2)$$

where A, B, C and D are model parameters, $[w]^{+}=max(w,0)$ and:

$$S_{ij}^{c} = \sum_{pq} e_{i+p,j+q}^{c} G_{pq}^{c} \text{ and } S_{ij}^{sg} = \sum_{pq} e_{i+p,j+q}^{sg} G_{pq}^{sg} \quad (3)$$

with e^{c} as central signal, e^{s} as peripheral signal (see Table 1), the superscript g=0,1,2 with suitable values for the small, medium and large scales. The weight functions have been defined as normalised Gaussian functions for central (G^{c}) and peripheral (G^{sg}) connectivity.

Table 1: Inputs of different channels on type 1 opponent cells.

	L-M Opponency		S-(L+M) Opp.		Luminance	
	L^{+}-M^{-}	L^{-}-M^{+}	S^{+}-Y^{-}	S^{-}-Y^{+}	W^{+}-Bl^{-}	W^{-}-Bl^{+}
e^{c}	Lij		Sij		Iij	
e^{sg}	Mij		Yij		Iij	

2.1.2 Type 2 Opponent Cells

The type 2 opponent cells initiate the double opponent process that take place in superior level, chromatic diffusive stages (see Figure 1). The double opponent mechanisms are fundamental in human visual colour processing (Hubel, 1995).

The receptive fields of type 2 cells are composed of a unique Gaussian profile. Two opponent colour processes occur, corresponding L-M and S-(L+M) channels. Each opponent process is modelled by a multiplicative competitive central field, presenting simultaneously an excitation and an inhibition caused by different types of cone signals (L, M, S and Y as sum of L and M). These processes are applied over three different spatial scales in the multiple scale model shown. Equations (4) and (5) model the behaviour of these cells, ON and OFF channels, respectively.

$$x_{ij}^{g+} = \left[\frac{AD^{+} + BS_{ij}^{+g}}{A + S_{ij}^{\mathrm{Eg}}} \right]^{+} \quad (4)$$

$$x_{ij}^{g-} = \left[\frac{AD^{-} + BS_{ij}^{-g}}{A + S_{ij}^{\mathrm{Eg}}} \right]^{+} \quad (5)$$

where A, B, C and D are model parameters, $[w]^{+}=max(w,0)$ and:

$$S_{ij}^{+g} = \sum_{pq} G_{pq}^{g} \left(e_{i+p,j+q}^{(1)} - e_{i+p,j+q}^{(2)} \right) \quad (6)$$

$$S_{ij}^{-g} = \sum_{pq} G_{pq}^{g} \left(e_{i+p,j+q}^{(2)} - e_{i+p,j+q}^{(1)} \right) \quad (7)$$

$$S_{ij}^{\mathrm{Eg}} = \sum_{pq} G_{pq}^{g} \left(e_{i+p,j+q}^{(1)} + e_{i+p,j+q}^{(2)} \right) \quad (8)$$

with $e^{(1)}$ and $e^{(2)}$ being the input signals of the opponent process (see Table 2). The weight functions have been defined as normalised Gaussians with different central connectivity (G^{g}) for the different spatial scales g=0, 1, 2:

Table 2: Inputs for different type 2 cells channels.

	L-M Opponency		S-(L+M) Opponency	
	L^{+}-M^{-}	L^{-}-M^{+}	S^{+}-Y^{-}	S^{-}-Y^{+}
$e^{(1)}$	Lij		Sij	
$e^{(2)}$	Mij		Yij	

2.2 Chromatic Segmentation System (CSS)

As previously mentioned, the Chromatic Segmentation System bases its structure on the modified BCS/FCS model (Grossberg et al., 1995; Mingolla et al., 1999), adapting its functionality to chromatic opponent signals, for colour image processing. The detailed structure of CSS can be seen in Figure 1.

The CSS module consists of the Colour BCS stage and two chromatic diffusive stages, processing one chromatic channel each.

2.2.1 Colour BCS Stage

The Colour BCS stage constitutes our colour extension of the original BCS model. It processes visual information from three parallel channels, two chromatic and a luminance channels to obtain a unified contour map. Analogous to the original model, the Colour BCS module has two differentiated phases: the first one (simple and complex cells) extracts real contours from the output signals of the COS and the second is represented by a competition and cooperation loop, in which real contours are completed and refined, thus generating contour interpolation and illusory contours (see Figure 1). Colour BCS preserves all of the original model perceptual characteristics such as perceptual grouping, emergent features and illusory perception.

The achieved output coming from the competition stage is a contour map and it will act as a control signal serving as a barrier in chromatic diffusions.

The simple cells are in charge of extracting real contours from each of the chromatic and luminance channels. In this stage, the filters from the original model have been replaced by two pairs of Gabor filters with opposite polarity, due to their high sensibility to orientation, spatial frequency and position (Daugman, 1980). Their presence has been proved on the simple cells situated at V1 area of visual cortex (Pollen & Ronner, 1983). Figure 2 shows a visual representation of Gabor filter pair profiles.

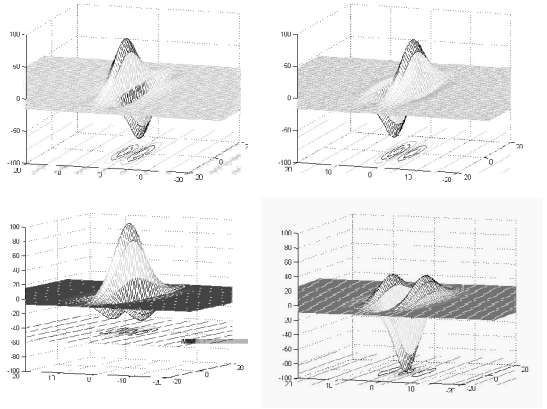

Figure 2: Receptive fields of the filters used to model simple cells. Top-left: Anti-symmetric light-dark receptive field. Top-right: Anti-symmetric dark-light receptive field. Bottom-left: Symmetric receptive field with central excitation. Bottom-right: Symmetric receptive field with central inhibition.

The complex cell stage, using two cellular layers, fuses information from simple cells giving rise to a final map which contains real contours for each of the three scales used (see Figure 1).

Detected real contours are passed into a cooperative-competitive loop, as it is shown in Figure 1. This nonlinear feedback network detects, regulates, and completes boundaries into globally consistent contrast positions and orientations, while it suppresses activations from redundant and less important contours, thus eliminating image noise. The loop completes the real contours in a consistent way generating, as a result, the illusory contours. In order to achieve this feature it makes use of a short-

range competition, and a long-range cooperation stage (Grossberg et al., 1995; Mingolla et al., 1999).

Cooperation is carried out by dipole cells. Dipole cells act like long-range statistical AND gates, providing active responses if they perceive enough activity over both dipole receptive fields lobes (left and right). Thus, this module performs a long-range orientation-dependent cooperation in such a way that dipole cells are excited by collinear (or close to collinearity) competition outputs and inhibited by perpendicularly oriented cells. This property is known as spatial impermeability and prevents boundary completions towards regions containing substantial amounts of perpendicular or oblique contours (Grossberg et al., 1995). The equations used in competitive and cooperative stages are taken from the original model (Grossberg et al., 1995).

2.2.2 Chromatic Diffusive Stages

As mentioned above, the chromatic diffusion stage has undergone changes that entailed the introduction of Chromatic Double Opponency Cells (CDOC), resulting in a new stage in the segmentation process. CDOC stage models chromatic double opponent cells. The model for these cells has the same receptive field as COS type 1 opponent cells (centre-surround competition), but their behaviour is quite a lot more complex since they are highly sensitive to chromatic contrasts. Double opponent cell receptive fields are excited on their central region by COS type 2 opponent cells, and are inhibited by the same cell type. We apply double opponency to the L-M and S-Y channels. This is to say, we apply a greater sensibility to contrast as well as a more correct attenuation toward illumination effects, therefore bringing a positive solution to the noise-saturation dilemma.

The mathematical model that governs the behaviour of chromatic double opponent cells is the one defined by (1) and successive equations, by varying only their inputs. These inputs are now constituted by the outputs of the COS type 2 opponent cells for each chromatic channel (see Table 3).

Table 3: Inputs of the included Chromatic Double Opponent Cells.

	L-M Opponency		S-(L+M) Opponency	
	L^+-M^-	L^--M^+	S^+-Y^-	S^--Y^+
e^c	$(L^+\text{-}M^-)_{ij}$	$(L^-\text{-}M^+)_{ij}$	$(S^+\text{-}Y^-)_{ij}$	$(S^-\text{-}Y^+)_{ij}$
e^{sg}	$(L^+\text{-}M^-)_{ij}$	$(L^-\text{-}M^+)_{ij}$	$(S^+\text{-}Y^-)_{ij}$	$(S^-\text{-}Y^+)_{ij}$

Chromatic diffusion stages perform four nonlinear and independent diffusions for L-M (ON and OFF) and S-Y (ON and OFF) chromatic channels. These diffusions are controlled by means of a final contour map obtained from the competition stage while the outputs of CDOC are the signals being diffused.

At this stage, each spatial position diffuses its chromatic features in all directions except those in which a boundary is detected. By means of this process, image regions that are surrounded by closed boundaries tend to obtain uniform chromatic features, even in noise presence, and therefore producing the enhancement of the regions detected in the image. The equations that model the diffusive filling-in can be found in (Grossberg et al., 1995).

As in previous stages, diffusion is independently performed over three spatial scales in an iterative manner, obtaining new results from previous excitations, simulating a liquid expansion over a surface.

Scale fusion constitutes the last stage of this pre-processing architecture. A simple linear combination of the three scales, see equation (9), obtains suitable visual results at this point.

$$V_{ij} = A_0(F_{ij}^{01} - F_{ij}^{02}) + A_1(F_{ij}^{11} - F_{ij}^{12}) + A_2(F_{ij}^{21} - F_{ij}^{22}) \quad (9)$$

where A_0, A_1 and A_2 are linear combination parameters, F_{ij}^{gt} represents diffusion outputs, with g indicating the spatial scale ($g=0,1,2$) and t denoting the diffused double opponent cell, *1* for ON and *2* for OFF.

2.3 Recognition Module

The attentive recognition process generates a pattern by merging the textural response information coming from the simple cells and the diffusion intensities of the chromatic channels from the scale fusion stage. The assorted pattern will be made up with the responses from the three scales of the receptive fields, small, medium, and large, the k orientations, and its two last components being the chromatic diffusion intensities from the scale fusion stage of L-M and S-(L+M) channels. Thus a n-dimensional pattern from each point of the scene will be created and sent to the Fuzzy ARTMAP architecture to be learned in the supervised training process or be categorized in the prediction process. The ART architecture must learn a mapping from the input space populated by these feature vectors to a discrete output space of associated region class labels. The architecture's output corresponds with an image of the class prediction labels in each point.

The recognition stage is composed of three components: texture feature smooth stage,

orientational invariances stage, and the Fuzzy ARTMAP neural network stage.

2.3.1 Texture Feature Smooth Stage

Due to the high spatial variability shown in Gabor's filters response a smooth stage is proposed through a Gaussian Kernel convolution with σ_{smooth} deviation, in all orientations.

2.3.2 Orientational Invariance Stage

In the pattern categorization process some orientational invariances are generated by means of the group displacement of components following the pattern's existing orientations.

The two last components from diffusion do not participate in this displacement. Thanks to these invariances it's achieved that the same texture pattern may be viewed from different angles.

3 TESTS AND RESULTS

This section introduces our tests' simulations over the proposed architecture.

The recognition process takes place by generating patterns in every position of the scene, obtaining them from the outputs of the simple cells. Those patterns contain textural and colour information. The textural information for pattern generation is obtained of the luminance channel. The colour information is included in the diffusion components inserted into the pattern.

In order to shape the patterns, the responses coming from two simple cells filters are used, the Anti-symmetric light-dark receptive field and the Symmetric receptive field with central excitation (see Figure 2). With them, we used three spatial scales y four orientations. Thus, obtaining a 24-dimensional textural vector, which, with the two intensities coming from the scale fusion stage, generate a 26-dimensional pattern to use as input to the recognition stage.

In order to show processing nature of the depicted model, its responses will be analysed and compared versus other methods, using images which include complex textures. We begin with a first test "two textures problem". The textures image (see Figure 3a) is composed of two near-regular textures (weave and brick) which are widely used in texture benchmarks (Grossberg and Williamson, 1999).

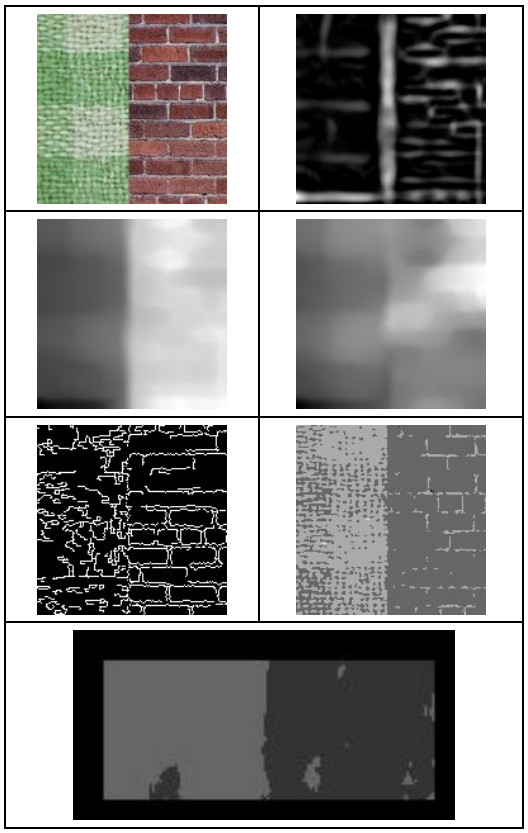

Figure 3: Images of the "two textures test". a) Original image, 128x128 pixels. b) Image of the contours map for large scale, c) Output of the scale fusion stage for the L-M channel, d) Output of the scale fusion stage for the S-(L+M) channel, e) Image of extracted contours using Canny's extractor, f) Image segmentation with a pyramidal method, g) Classification result of 'two textures' test. The darker grey level corresponds to the brick texture prediction while the lighter grey level corresponds to the weave texture prediction.

Figures 3b, 3c and 3d, display the different stage outputs of the proposed model. Figure 3b includes the contour map for large scales, Figures 3c and 3d include the two outputs coming from the diffusion stages. Those outputs will constitute the last two components of the recognition patterns. Figure 3e include the results from the Canny extractor, using the cvCanny() with 1, 100, and 70 as parameters; and 3f shows the output of the pyramidal segmentation using function cvPyrSegmentation() with 30000, 30000, and 7 as parameters. cvCanny() and cvPyrSegmentation() are functions from Intel Computer Vision Library, OpenCv (Intel, 2006).

Comparing the results, it can be clearly observed that the proposed architecture behaves in a compatible manner with the human visual system. The presented system detects a texture boundary contour map with perceptual behaviour by extracting

the illusory contour which marks off both textures. The shown model perceptually differentiates two textures through filling-in processes controlled by the illusory vertical contour. Those two comparative methods do not exhibit a concordance with the Visual System, and so both extraction and segmentation obtain worse quality visual results.

Another recognition test was run with a two textures image. A smooth value of σ_{smooth}=4.85 was chosen for the textural patterns, which corresponds to a 8x8 resolution, that is, each patch of 8x8 pixels in the input image yields a single pixel in an output image for each orientation (Grossberg and Williamson, 1999). The image was divided into lower and upper parts. The patterns from the lower half were taken for Fuzzy ARTMAP network training using a vigilance parameter of 0.95. The network was then tested using the patterns coming from the upper half part. In the supervisory process, the categories created for the patterns on the left texture (weave) were associated to a class prediction pictured light grey, while the patterns coming from the right texture (brick) where associated to another class prediction depicted in a darker grey.

In the training process as well as in the testing one a frame of 10 pixels were left without any processing. In Figure 3g we can see its resulting class prediction. The errors committed in the upper half prediction were of 115 points in the left side (weave texture) and 112 points in the right side (brick texture) which brings the error toll to a 3.17% (96.83% of success). Those statistics are of a similar magnitude to those obtained in (Grossberg and Williamson, 1999), where a score of 95.7% was obtained for a texture mosaic test with 5 textures instead of two like in our case.

Figure 4: 8-colour texture database (t1 a t8) and multitex test image.

In order to accomplish this comparison of texture recognition methods, a test was run, similar to the "10-texture library problem" proposed in (Grossberg and Williamson, 1999). We took 8 different classes of textures with 3 colour images per class (see Figure 3, only one of each class is presented). Each texture image consists of 128x128 pixels.

Those 8 classes are included or are of similar complexity to the black & white image texture database used in (Grossberg and Williamson, 1999). Our architecture was trained with points from two of the images from each class. The training phases were executed using three different resolutions like in (Grossberg and Williamson, 1999), 8x8, 16x16, and 32x32. The third image from each class was used to evaluate the prediction level of our architecture. Both training and testing was performed with two different levels of vigilance, ρ=0.95 and ρ=0.98 for training and ρ=0.9 and ρ=0.97, respectively for testing. The results are shown in Table 4, where the statistics for each class of texture are depicted. It can be observed that the success rate of the predictions increase with low resolutions. The global results are shown in the last row of Table 4. Our recognition system achieved 96,4%, 98.0% and 97.4% corrects with ρ=0.95; and 98.0%, 99.6% and 97.4% corrects with ρ=0.98 in 8x8, 16x16 and 32x32 resolution, respectively. The ARTEX system proposed in (Grossberg and Williamson, 1999) achieved worse results in the two first resolutions. ARTEX system achieved 95.8%, 97.2% and 100.0% corrects with all its features and one training epoch (no information about the vigilance parameter is given). In Table 4, it can be seen that the first texture sharply decreases the success rate because it is a highly irregular (no regular brick size and colour). The others statistical values are over those obtained by ARTEX system.

Table 4: 8-textures recognition statistics for each texture class and global.

	ρ=0.95			**ρ=0.98**		
	8x8	**16x16**	**32x32**	**8x8**	**16x16**	**32x32**
T1	90.0	86.9	80.3	90.9	87.2	79.3
T2	97.3	100	100	97.1	100	100
T3	98.1	98.5	99.0	98.8	99.8	100
T4	98.7	99.8	99.8	99.9	100	100
T5	97.8	100	100	99.2	100	100
T6	99.9	99.9	100	100	100	100
T7	97.6	100	100	99.9	100	100
T8	92.1	98.5	100	98.4	100	100
total	96.4	98.0	97.4	98.0	99.6	97.4

Our architecture was also trained and tested over a "multitex problem", analog but more complex than

the "texture mosaic problem" proposed in (Grossberg and Williamson, 1999). Our mosaic includes 9 textural areas versus the 5 textural areas from (Grossberg and Williamson, 1999). As explained before, with the third image from each texture class, we built a 210x210 pixels multitex test image (see Figure 4 row 3-right) in order to evaluate the frontier precision between textures in the prediction of our architecture. Both the training and the testing was performed with two different levels of vigilance, ρ=0.95 and ρ=0.98 for training and ρ=0.9 and ρ=0.97, respectively for testing. The results are shown in Table 5. Those results show a better class rate in all resolutions and vigilance levels than those obtained in (Grossberg and Williamson, 1999) as our worst result (95.89%) beats the best result (95.7%) shown in this work.

Table 5: Multitex prediction statistics.

Resolution	Train vigilance parameter	Samples /class	Class rate (%)
8x8	0.95	300	**95.89**
16x16	0.95	125	**96.67**
32x32	0.95	40	**97.30**
8x8	0.98	300	**99.75**
16x16	0.98	125	**99.48**
32x32	0.98	40	**99.18**

The images of the predictions can be seen in Figure 5 where only those corresponding to a vigilance parameter value of ρ=0.95 are shown. Each prediction class is depicted with a level of grey, from black to white. Those images reveal two remarkable points. First, the best prediction for the interior points shows up for a 32x32 resolution. However, it is the 8x8 resolution the one which accurately resolve texture transitions.

The main differences between our architecture and the one shown in (Grossberg and Williamson, 1999) are basically the inclusion of colour information (the two output signals coming from the chromatic channels in the diffusion stage) and the use of one additional receptive field in the pattern's textural components. Our architecture also includes in the patterns the processing of the symetric receptive field with central excitation simple cells.

REFERENCES

Carpenter, G.A., Grossberg, S., Markuzon, N. and Reynolds, J.H. (1992). Fuzzy ARTMAP : A Neural Network Architecture for Incremental Supervised Learning of Analog Multidimensional Maps. Neural Networks, 3, 5, 698 -713.

Daugman, J.G. (1980) Two-dimensional spectral analisis of cortical receptive field profiles. Vision Research, 20, 847-856.

Gonzalez, R.C. and Woods R.E. (2002), Digital Image Provessing, 2/E, Prentice Hall.

Grossberg, S. (1984). Outline of a theory of brightness, colour, and form perception. In E. Degreef and J. van Buggenhault (Eds.) Trends in mathematical psychology. Amsterdam: North Holland.

Grossberg, S. and Hong, S. (2006). A Neural Model of Surface Perception: Lightness, Anchoring, and Filling-In. Spatial Vision, 19, 2, 263-321.

Grossberg, S. and Williamson, J.R. (1999). A self-organizing neural system for leaning to recognize textured scenes, Vision Research, 39, pp. 1385-1406.

Grossberg, S., and Mingolla, E. (1988). Neural dynamics of perceptual grouping: textures, boundaries, and emergent segmentations. In Grossberg, S. (Ed.): The adaptive brain II. Chap. 3. Amsterdam, North Holland, 1988.

Grossberg, S., Mingolla, E. and Williamson, J. (1995). Synthethic aperture radar processing by a multiple scale neural system for boundary and surface representation. Neural Networks, 8, 1005-1028.

Hubel D.H. (1995) Eye, Brain and Vision. Scientific American Library, No. 22., WH Freeman, NY. p. 70.

Hubel, D.H., and Livingstone, M.S. (1990). Color and contrast sensitivity in lateral geniculate body and Primary Visual Cortex of the Macaque Monkey. The Journal of Neuroscience, 10, 7, 2223-2237.

Intel Corporation (2006). Open Source Computer Vision Library. http://www.intel.com/technology/computing/opencv/

Julesz, B., and Bergen, R. (1987), Textons, The Fundamental Elements in Preattentive Vision and Perception of Textures. In Fischer and Firschen (eds.). Readings in Computer Vision, 243-256, 1987.

Mingolla, E., Ross, W. and Grossberg, S. (1999) A neural network for enhancing boundaries and surfaces in synthetic aperture radar images. Neural Networks, 12, 499-511, 1999.

Pollen, D.A. and Ronner, S.F. (1983) Visual cortical neurons as localized spatial frequency filters. IEEE Transactions on Systems, Man, and Cybernetics, SMC-13, No 15, 907-916.

A NEW ALGORITHM FOR NAVIGATION BY SKYLIGHT BASED ON INSECT VISION

F. J. Smith
School of Electronics, Electrical Engineering and Computer Science
Queens University, Belfast, N. Ireland
Fj.smith@qub.ac.uk

Keywords: Polarization, skylight, navigation, insect vision, POL, insect celestial map, robot, drone.

Abstract: Many insects can navigate accurately using the polarised light from the sky when the sun is obscured. They navigate using two different types of optical features: one is a set of three ocelli on the top of the head and the second is a celestial compass based on several photoreceptors on the dorsal rims of the compound eyes. Either feature can be used alone, but the dorsal rim receptors appear to be more accurate. Robots have been built that navigate using three photoreceptors, or three pairs of orthogonally oriented photoreceptors, but none has been designed which uses a full set of photoreceptors similar to those in the dorsal rim. A new model of the function of the dorsal rim compass is proposed which relies on the four azimuths at which the polarization angle $\chi = \pm\pi/4$. A simulation shows that this could provide an accurate navigational tool for a robot (or insect) in lightly clouded skies.

1 INTRODUCTION

Due to the scattering of light within the earth's atmosphere, skylight is partially linearly polarized, discovered by the Irish Scientist Tyndall (1869). Two years later a full mathematical description of the phenomenon was given by Lord Rayleigh (1871) for the scattering by small particles in the atmosphere (the particles we now know are air molecules). That an insect can use this polarization to navigate was first discovered in experiments with bees by Karl von Frisch (1949).

It took another 25 years before the nature of the insect's celestial compass began to be clarified (Kirshfeld et al., 1975; Bernard and Wehner, 1977). There are two different types of optical features involved: the first is a set of ocelli, generally 3 in number, on the top of the head (Goodman, 1970) and the second depends primarily on a specialized part of the insect compound eye, a comparatively small group of ommatidia situated in the dorsal rim area. Normally the ocelli and dorsal rim are probably used together to navigate, in some way still unknown, but experiments with desert ants (Fent and Wehner, 1985) have shown that either feature can be used successfully alone with the other blacked out. It was also found in these experiments that the ocelli are more erratic and less accurate for navigation than the dorsal rim photoreceptors.

Further insight on the dorsal rim came from Rudiger Wehner and co-workers working with desert ants and bees (Labhart, 1980; Rossel and Wehner, 1982; Wehner, 1997). It was found that each ommatidium in the dorsal rim has two photoreceptors with axes of polarization at right angles to one another and each strongly sensitive to the E-vector orientation of plane polarized light. One of the axes of polarization of these ommatidia has a fan shaped orientation that has been shown in experiments to provide a map for the polarised sky, a map which the insect can use as a compass (Rossel, 1993). Recently this insect map of celestial E-vector orientation has been found represented within the central complex of the brain of an insect, the cricket (Heinz and Homberg, 2007). We return to this later.

Therefore much is known about this celestial compass and how it is represented within the brain. However, relatively few contributions deal with the physical mechanism underlying the compass, the principal subject of this paper. Only one attempt has been made (to our knowledge) to design a navigational aid for a drone or robot based on this compass; this uses only 3 pairs of photoreceptors (Wehner,1997; Lambrinos et al, 1998), different from the typical fan of 50 -100 pairs of receptors

used by an insect or used in the design proposed here. NASA has also built robots navigating by skylight, but these use three photoreceptors with different axes of polarization, probably the underlying principle behind navigation by the ocelli (NASA, 2005). Few details have been released on the above systems, so comparison with our new algorithm has not been possible.

In the following we first derive mathematical expressions for the light intensities measured by the photoreceptors, before showing how these can give the direction of the sun.

2 THEORY

2.1 Measured Intensity

We begin with the assumption that the sky is blue, with no cloud. Then it is well known (Rayleigh, 1871) that the light observed from any patch of sky is partially polarised, with an elliptical profile for the electric vector (although not elliptically polarised) in which the major axis of the ellipse, is at right angles to both the direction of the sun, represented by the unit vector **S,** and to the direction of the observed patch of sky, **k'**. We let **k'** be one of three mutually orthogonal vectors **i', j'** and **k'**, with **i'** in the direction of the major axis of the ellipse, and **j'** in the direction of the minor axis. The electric vector in the direction of the major axis is often called the E-vector. The angle which this makes clockwise in the ellipse from the plane of the zenith, is called the polarization angle, χ. In the ideal situation where all of the light observed is scattered once only, the ratio of the size of the minor axis to the size of the major axis is known to be cos *(θ)* where θ is the angle between **S** and **k'**.

Let $\mathbf{E_S}$ be the scattered electrical vector being observed. Then

$$\mathbf{E_S} = E[\cos(\phi)\,\mathbf{i'} + \cos(\theta)\sin(\phi)\,\mathbf{j'}] \qquad (1)$$

where E is the magnitude of the unpolarized electric field. The angle ϕ determines the direction of the vector within the ellipse; so it equals 0 when the electric vector is parallel to the major axis.

When the partially polarised light enters an ommatidium in the dorsal rim its intensity is measured by two photoreceptors, each of which can measure polarised light with parallel structures called microvilli. The two directions of the microvilli are at right angles to one another, and define two orthogonal axes of polarization, represented here by the orthogonal unit vectors **i** and **j**, known as the X and Y photoreceptors. The third mutually orthogonal vector, **k**, is in the same direction as the observed patch of sky, so **k** = **k'**. The angle which the vector **i** makes with the vertical plane by rotation about **k** is called ξ.

We can now write the previous unit vectors in Equation (1) in terms of **i** and **j** using the transformation:

$$\begin{aligned} \mathbf{i'} &= +\cos(\chi - \xi)\mathbf{i} + \sin(\chi - \xi)\mathbf{j} \\ \mathbf{j'} &= -\sin(\chi - \xi)\mathbf{i} + \cos(\chi - \xi)\mathbf{j} \end{aligned} \qquad (2)$$

We look at the orientations of the microvilli in the dorsal rim of the honey bee by Sommer (1979), as copied in Figure 1. The fan shape of the microvilli is apparent.

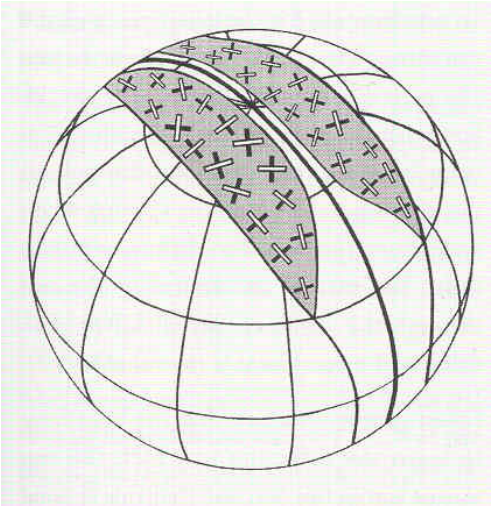

Figure 1: The paired orthogonal photoreceptors in the dorsal rims of a bee. The Y photoreceptors are dark, the X photoreceptors light (Sommer, 1979).

The observation of sky by the photoreceptors is known to be contralateral, i.e. they observe the sky on the opposite side of the head. An examination of the figure shows that the axes of the X photoreceptors are approximately parallel to the meridians passing through the patches of sky being observed contralaterally. The same approximate parallel pattern was found in Desert Ants by Wehner and Raber (1979). So we assume that the angle ξ that the X polarization axis makes with this meridian is always zero. This greatly simplifies our later algorithm for a small insect brain.

We can now substitute for **i**' and **j**' from Eq.(2) in Eq.(1) to obtain an expression for the partially polarised vector $\mathbf{E_S}$ in terms of the unit vectors **i** and

j. For example, part of this is the magnitude, E_X, of the vector in the direction **i** to be measured by the microvilli of the X photoreceptor:

$$E_X = E\left(\cos(\chi)\cos(\phi) - \sin(\chi)\cos(\theta)\sin(\phi)\right) \qquad (3)$$

However, each receptor can only measure a light intensity, which is proportional to the summation of the square of the amplitudes of the electrical vectors for all angles ϕ. So, for receptor X, the measured intensity, S_X, is found by first integrating the square of the amplitude in (3) over all angles and then multiplying by a factor, $2R$, which depends on terms derived by Lord Rayleigh (1871) and on the measuring capability of the photoreceptor.

Before writing down the result of the integration we note that in the real world the sky is often not always blue, but has a degree of haze or cloud differing with direction. The light then entering the ommatidia can be viewed as make up of two components, one partly polarised as in the above equations, and the second totally unpolarized due to multiple scattering. We let U be the intensity of unpolarized light measured by both photoreceptors. Then we find

$$S_X = RE^2\left[1-\sin^2(\theta)\sin^2(\chi)\right]+U \qquad (4)$$

$$S_Y = RE^2\left[1-\sin^2(\theta)\cos^2(\chi)\right]+U \qquad (5)$$

It has been shown by Labhart(1988) that the POL neuron at the bottom of each ommatidium of a cricket records the difference between the two signals, or rather the difference between the log of the two signals, not the signals themselves; so the signal recorded is

$$S_{XY} = Ln(S_X) - Ln(S_Y) \qquad (6)$$

We set RE^2 = 1 in Figure (2) to illustrate the variation in these signals as the azimuth angles of the ommatidia vary.

Some of the above is known, but to proceed further we need the polarization angle, χ. This depends on the azimuth and elevation of the sun.

2.2 Solar Azimuth and Elevation

The angles θ and χ are related to the azimuth, a_s, and elevation, h_s, of the sun. It is convenient to introduce a third set of orthogonal axes, **i'', j''** and **k''** fixed on the earth, with **i''** and **j''** in the plane of the ground and **k''** vertically upwards. For a photoreceptor to find θ and χ we need also the azimuth, a_o, and elevation, h_o, of the sky being observed by the photoreceptor, i.e. towards the centre of the patch of sky being observed. So we let the unit vector **i''** point along the ground in this direction.

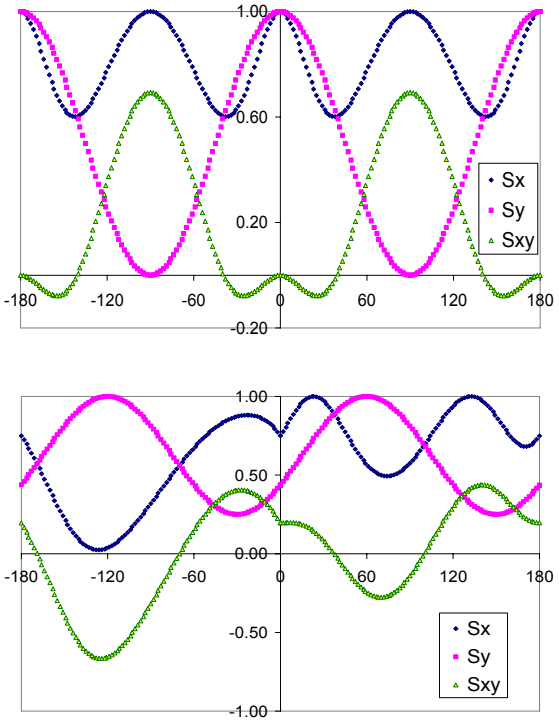

Figure 2: Illustration of the signals S_X and S_Y with U=0, and S_{XY} with U=1, as they vary with the azimuth of the fan of observations, a_o, measured from the central axis of the insect. Top graph: h_s=0, a_s=0. Bottom: h_s=30, a_s=60. Note that a_s=a_o at a maximum of S_Y and that there are 4 azimuths where S_{XY}=0, called zeros.

In terms of these new unit vectors we write the vector pointing in the direction of the sun as **S** = S_1**i''** + S_2**j''** + S_3**k''** where

$$S_1 = \cos(h_s)\cos(a_s - a_o);$$
$$S_2 = \cos(h_s)\sin(a_s - a_o); \qquad (7)$$
$$S_3 = \sin(h_s)$$

We can write down two equations for the direction of the sun. First we know that the vector **k',** which points at the observed patch of sky, makes an angle θ relative to the direction of the sun, **S**. We also know that the E-vector, in the direction represented by the unit vector, **i'**, is at right angles to the plane containing the solar unit vector, **S**, and the vector, **k'**. So

(a) **k'.S** = *cos(θ)*, and (b) **i'.S** = *0*. (8)

We now express the unit vectors **i',** describing the E-vector, and **k'** in terms of the new axes **i'', j''**

and **k''** fixed in the earth. Since **k'** and **k''** are in the same vertical plane it follows that

$$\mathbf{k}' = \cos(h_o)\mathbf{i}'' + \sin(h_o)\mathbf{k}'' \quad (9)$$

Noting that **i'** is at right angles to **k'** and that the angle χ represents the orientation of the major axis of the polarised light about the vector **k'**, it follows that

$$\mathbf{i}' = [-\sin(h_O)\mathbf{i}'' + \cos(h_O)\mathbf{k}'']\cos(\chi) - \sin(\chi)\mathbf{j}'' \quad (10)$$

Substitute and Equations (8a and b) become

$$\cos(\theta) = \cos(h_O)\cos(a)\cos(h_S) + \sin(h_O)\sin(h_S) \quad (11)$$

$$0 = \cos(\chi)\cos(h_O)\sin(h_S) - \cos(\chi)\sin(h_O)\cos(a)\cos(h_S) - \sin(\chi)\sin(a)\cos(h_S) \quad (12)$$

where $a = a_s - a_o$ is the azimuth of the sun relative to the azimuth of the observed sky.

A new unexpected equation was derived from (11) and (12) after some analysis:

$$\sin(\theta)\cos(\chi) = \sin(a_s - a_o)\cos(h_s) \quad (13)$$

This can also be derived geometrically, or from the relation **k'** x **S** = *sin(θ)***i'.** It simplifies the calculation of the angle χ, although not its sign. But more significantly, by substitution in (5), it changes the expression for the measured intensity S_Y:

$$S_Y = RE^2\left[1 - \sin^2(a_s - a_o)\cos^2(h_s)\right] \quad (14)$$

This surprising result shows first that it is the same for all elevations of the sky being observed and second that, as the azimuth a_o round the fan of receptors varies, the position of the maximum value of S_Y gives a new measure for the azimuth of the sun, for all elevations of the sun (see Figure 2). Unfortunately, finding this maximum is not possible if an insect is only measuring the difference in the two log signals as in Equation (5). But this does not stop a robot from using this strategy to find the solar azimuth. But it can only be approximate as finding the exact position of a maximum is always difficult.

2.3 A Precise Compass

We begin with a question - why have two orthogonal photoreceptors, instead of one? A possibility is that the contrast between the two signals is improved near the maximum of one of them. Unfortunately this is often obscured by the $sin^2(\theta)$ term in Equations (4) and (5), as evident in Figure (2). Also we are left with the problem of the lack of precision in the determination of the position of any maximum, even enhanced.

The photoreceptors can only measure intensities, but absolute intensities of light from the sky are so variable that only comparisons between intensities from the same region of the sky are meaningful computationally. An example is the ratio of the two intensities from the pair of orthogonal receptors in one ommatidium. Although this ratio can be measured accurately, the inclusion of an unknown amount of unpolarized light, U, makes it meaningful only when the two are equal (the easiest factor to measure). Equating S_X and S_Y puts $S_{XY} = 0$ in Equation (6), eliminates U, RE^2 and θ and we get simply: $\sin^2(\chi) = \cos^2(\chi)$.

This makes $\chi = \pm\pi/4$. So finding where $S_{XY}=0$, the quantity measured for each ommatidium, tells us the precise azimuths a_o where $\chi = \pm\pi/4$. We call this a zero. An examination of Figure (2) shows that in these two cases there are 4 zeros. Curves similar to this were drawn for a range of solar azimuths and solar elevations and the zeros found. The zeros for different solar azimuths are shown in Figure (3) for one solar elevation. This and other examples show that in almost all cases there are 4 zeros, usually 2 on either side of the head, but sometimes 4 on one side and none on the other. When the elevation of the sun is above the elevation of the observed patch of sky there may be no zeros.

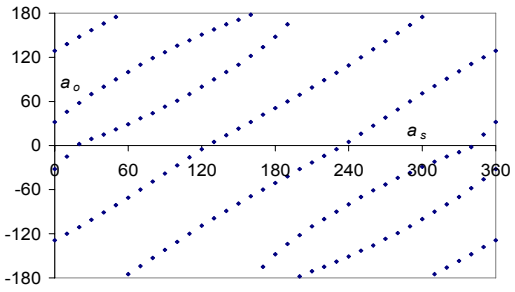

Figure 3: Graph of azimuths, a_o, of the observation at which $S_{xy} = 0$ (called zeros) for different values of the solar azimuth, a_s, at solar elevation, $h_s = 30^o$. Zeros occur when the two orthogonally polarized intensities are equal, making $\chi = \pm\pi/4$. There are usually 4 zeros, just enough to uniquely define the azimuth and elevation of the sun.

We now show how we can use these 4 zero to make a precise measurement of the sun's position. Noting that $\cos(\chi) = 1$ and $\sin(\chi) = \pm 1$ at the zeros, Equation (12) becomes:

$$\cos(a_s - a_o)\sin(h_o) \pm \sin(a_s - a_o) = \cos(h_o)\tan(h_s) \quad (15)$$

Solving this for a_s, the azimuth of the sun, gives

$$a_s = a_o \pm \gamma \pm \delta \qquad (16)$$

in which for each azimuth, a_o there is a different γ and δ given by $\gamma = arccos(1/K)$ and $\delta = arcsin(tan(h_s)cos(h_o)/K)$ where $K^2 = 1 + sin^2(h_o)$. The angle γ is fixed for each ommatidium; so it might be stored as $a_o \pm \gamma$ within the corresponding neurons. It needs to be corrected with the angle δ (unless the sun is on the horizon, when $\delta=0$); but this correction needs the observation of 4 zeros, as discussed in the next section. If 4 zeros cannot be observed because the region of observed sky is restricted the insect can only use $a_o \pm \gamma$, leaving an error of δ. Such errors have been found in experiments. So Equation (16) may be the mathematical basis of at least part of the celestial map in an insect brain.

The 4 alternatives in Equation (16) can also regenerate exactly the results in Figure (3), but in an inverted form. An example is shown in Figure (4). In Figures (3) and (4) the elevations of the sky being observed have been chosen to vary between 45° (at azimuths 0° and 180°) and 80° (at azimuths ±90°). However, these elevations are not critical: if all ommatidia examine the sky at a constant high elevation the algorithm described below is still valid and the curves in Figures (3) and (4) all become straight lines. There are still 4 zeroes, but none at high solar elevations where $sin(\delta) > 1$.

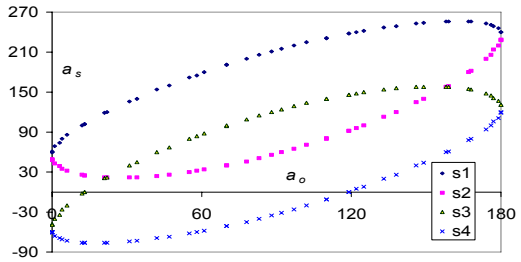

Figure 4: Inverted graph of a_s for positive a_o calculated using Equation (16) for h_s =60°, showing the contribution of the different ± combinations: s1: a_o +γ +δ; s2: a_o +γ -δ; s3: a_o –γ +δ; s4: a_o –γ -δ.

We have built a simulator that can calculate the position of the sun using the above equations. We illustrate first with an example in which the elevation of the sun is 30° and the solar azimuth is 20 °; in this example the four zeros are at the azimuths: a_o = 53°, 145 °, -5 °, and -110 °. For each of these there are 4 alternatives given by Equation (16), but an insect or a robot which is only measuring intensities would not know which is correct. Four alternatives for 4 zero angles makes a total of 16 possibilities as in the array in Table 1.

Table 1: Example of array of 4 possible solar azimuths for each of 4 zeros (where $S_X - S_Y = 0$) when the elevation of the sun is 30°. Note that the correct azimuth (marked in bold) is found once in each of the four rows corresponding to the four zeros. This occurs only for the correct solar elevation.

Zeros	γ+δ	+γ-δ	–γ+δ	–γ-δ
52	180	**20**	85	-75
145	-89	125	165	**20**
-5	131	**20**	-31	-142
-110	**20**	-148	-72	120

So the algorithm is simple:

1. find the 4 zeros where $S_X = S_Y$;
2. obtain for each the two angles $a_o \pm \gamma$;
3. choose a possible solar elevation;
4. find the 4 possible azimuths for each zero from Equation (16) and put in an array of 16 angles (as in the example);
5. scan the array for one angle in all 4 rows, within a small tolerance (e.g. 1 degree). If found, it is the solar azimuth;
6. if not found, increase the elevation (e.g. by 1 degree) and return to step 3.

Figure (5) shows how this algorithm converges to the correct result for the example in Table 1.

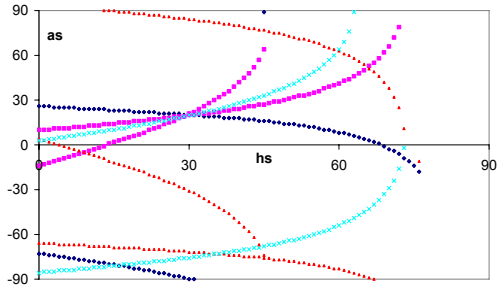

Figure 5: Graph showing, as the solar elevation h_s varies, how four of the elements in the 16 array elements in Table 1 converge on the correct result at the solar azimuth a_s=20° when h_s=30°. (Only half of the graph is shown.).

Simulations with about 1000 examples have shown that this algorithm succeeds is almost every case with no ambiguity within a tolerance of 1 degrees. Occasional errors or failure occur only at low or high solar elevations (< 3° or > h_o). Four zeros are needed: three zeros give a typical 40% error rate. The algorithm takes only a page of code, and once it is given the positions of the 4 zeros it calculates the

solar azimuth in less than a second on a PC. It can easily be built into the processor of any robot.

Besides the accuracy of the method it has the advantage that it gives the solar azimuth anywhere within 360^o, with no ambiguity of π as in some other algorithms. It is partially independent of environmental conditions since some ommatidia may be looking at blue sky while others are looking at lightly clouded sky. The position of the zeros is unchanged as long as a polarization pattern is detectable below the cloud, which is more likely for ultraviolet light detectors (Pomozi et al., 2001).

So the greatest difficulty in building a skylight compass for a robot based on this algorithm is the detection of the four zeros. One design uses an array of about 100 pairs of orthogonal photoreceptors in a circle round the robot. The problem is that each pair would have to observe a patch of sky with an accurate azimuth; the elevation, due to Equation (14), would be less critical. In another design the robot has one accurate pair of photoreceptors which is rotated continually through 360^o (like radar) measuring the azimuth as it moves at a constant high elevation (e.g. 70^o).

3 CONCLUSIONS

We have shown that an accurate celestial compass for a robot can be built round the principle of finding 4 zeros in the differences between the two signals obtained from pairs of orthogonally polarised photoreceptors. The algorithm was derived from published studies on the anatomy of insect eyes and on published experiments with insect navigation. In particular Equation (16) explains why errors occur when the view of an insect is restricted. The algorithm is also simple enough for the small brain of an insect; so we believe that the algorithm, or something like it, is part of the celestial compass within the brain of an insect.

At the heart of the algorithm are searches in arrays of exactly 16 elements as in Table 1. So we might expect evidence for this within the brain of an insect. It is interesting to note that a topographic representation of E-vector orientation has been found to underlie the columnar organisation of the central complex of the brain of a locust, and this consists of stacks of arrays, each composed of a linear arrangement of 16 columns (Heinze and Homberg, 2007).

REFERENCES

Bernard, G D, Wehner, R, 1977. Functional similarities between polarization vision and color vision, Vision Res., 17, 1019-28.

Fent, K, Wehner, R, 1985. Ocelli: A celestial compass in the desert ant Cataglyphis, Science, 228, 192-4.

Goodman, L. J., 1970. The structure and function of the insect dorsal ocellus. Adv. Insect Phys., 7, 97-195.

Heinze, S, Homberg, U, 2007. Maplike Representation of Celestial E-Vector Orientations in the Brain of an Insect, Science, 315, 995-7.

Kirschfeld, K, Lindauer, M, Martin,H, 1975. Problems in menotactic orientation according to the polarized light of the sky, Z. Naturforsch, 30C, 88-90.

Labhart, T, 1980. Specialized Photoreceptors at the dorsal rim of the honeybee's compound eye: Polarizational and Angular Sensitivity, J Comp. Phys., 141, 19-30.

Labhart, T, 1988. Polarised-opponent interneurons in the insect visual system, Nature, 331, 435-7.

Lambrinos, D, Maris, M, Kobayashi, H, Labhart, T, Pfeifer, P, Wehner, R, 1998. Navigation with a polarized light compass, Self-Learning Robots II: Bio-Robotics (Digest 1998/248) IEE, London, 7/1-4.

NASA, 2005. www.nasatech.com/Briefs/Oct05/ NPO_41269.html

Pomozi, I, Horvath, G, Wehner, R., 2001. How the clear-sky angle of polarization pattern continues underneath clouds, J. Expt. Biol, 204, 2933-42.

Rayleigh, Lord, 1871. On the light from the sky, its polarisation and colour, Phil Mag,, 41, 107-20, 274-9.

Rossel, S, 1993. Mini Review: Navigation by bees using polarised skylight, Comp. Biochem. Physiol, 104A, 695-705.

Rossel, S, and Wehner, R, 1982. The bee's map of the e-vector pattern in the sky, Proc. Natl. Acad. Sci. USA, 79, 4451-5.

Sommer, E W, 1979. Untersuchungen zur topo-graphischen Anatomie der Retina und zur Sehfeldoptologie im Auge der Honigbiene, Apis mellifera (Hymenoptera). PhD Thesis,Un.Zurich.

Tyndall, J, 1869. On the blue colour of the sky, the polarisation of skylight, and on the polarisation of cloudy matter, Proc. Roy. Soc., 17, 223.

Von Frisch, K, 1949. Die Polarisation des Himmelslichts als Orientierender Faktor bei den Tanzen der Bienen, Experientia, 5, 142-8.

Wehner, R, 1989. The hymenopteran skylight compass: matched filtering and parallel coding, J Exp. Biol., 146, 63-85.

Wehner, R, 1997. The Ant's celestial compass system: spectral and polarization channels, In Orientation and Communication in Arthropods, Ed. M. Lehler, Birkhauser, Berlag, Basel, Switzerland, 145-85.

Wehner, R, and Raber, F, 1979. Visual spatial memory in desert ants, Cataglyphis bicolor (Hymenoptera: Formicidae), Experientia, 35, 1569-71.

TWO-STAGE CLUSTERING OF A HUMAN BRAIN TUMOUR DATASET USING MANIFOLD LEARNING MODELS*

Raúl Cruz-Barbosa and Alfredo Vellido
Dept. de Llenguatges i Sistemes Informàtics, Universitat Politècnica de Catalunya
Edifici Omega, Campus Nord, C. Jordi Girona, 1-3, Barcelona, 08034, Spain
{*rcruz, avellido@lsi.upc.edu*}

Keywords: Brain tumours, MRS, Generative Topographic Mapping, two-stage clustering, outliers.

Abstract: This paper analyzes, through clustering and visualization, Magnetic Resonance spectra of a complex multi-center human brain tumour dataset. Clustering is performed as a two-stage process, in which the models used in the first stage are variants of Generative Topographic Mapping (GTM). Class information-enriched variants of GTM are used to obtain a primary cluster description of the data. The number of clusters used by GTM is usually large and does not necessarily correspond to the overall class structure. Consequently, in a second stage, clusters are agglomerated using K-means with different initialization strategies, some of them defined *ad hoc* for the GTM models. We evaluate if the use of class information influence the brain tumour cluster-wise class separability resulting from the process. We also resort to a robust variant of GTM that detects outliers while effectively minimizing their negative impact in the clustering process.

1 INTRODUCTION

Medical decision making is usually riddled with uncertainty, especially in sensitive settings such as non-invasive brain tumour diagnosis. The brain tumour data analysed in this study are obtained by Magnetic Resonance Spectroscopy (MRS). Information derived from the MR spectra can contribute to the evidence base available for a particular patient, providing support to clinicians.

The fields of Machine Learning and Statistics coexist with data analysis as a common target. An example can be found in Finite Mixture Models (Figueiredo and Jain, 2002). In practical scenarios, such as medical decision making, these models could benefit from data visualization. Finite Mixture Models can be endowed with visualization capabilities provided certain constrains are enforced, such as forcing the mixture components to be centred in a low-dimensional manifold embedded in the observed data space, as in Generative Topographic Mapping (GTM) (Bishop et al., 1998), which can be seen as a probabilistic alternative to Self-Organizing Maps (SOM) (Kohonen, 1995) for data clustering and visualization. When available class information can also be integrated as part of the GTM training to enrich the cluster structure definition (Cruz and Vellido, 2006). The resulting models will be used in our experiments to analyze a complex MRS dataset.

GTM-based models do not place any strong restriction on the number of mixture components (or clusters), in order to achieve an appropriate visualization of the data. This richly detailed cluster structure does not necessarily match the more global cluster and class structures of the data. In this scenario, a two-stage clustering procedure may be useful to uncover such global structure (Vesanto and Alhoniemi, 2000). GTM and its variants can be used in the first stage to generate a detailed cluster partition in the form of a mixture of components. The centres of these components can be further clustered in the second stage. For that role, the well-known K-means algorithm is used in this study.

The first goal of the paper is assessing to what extent the introduction of class information improves the final cluster-wise class separation. The issue remains of how we should initialize K-means in the sec-

*Alfredo Vellido is a Ramón y Cajal researcher and acknowledges funding from the MEC project TIN2006-08114. Raúl Cruz-Barbosa acknowledges SEP-SESIC (PROMEP program) of México for his PhD grant. Authors gratefully acknowledge the former INTERPRET project centres (http://azizu.uab.es/INTERPRET) for making available and managing the data for this study.

ond clustering stage. Random initialization (Vesanto and Alhoniemi, 2000) does not make use of the prior knowledge generated in the first stage of the procedure and requires a somehow exhaustive search of the initialization space. Here, we propose two different ways of introducing such prior knowledge as fixed initialization. These procedures, resulting from GTM properties, allow significant computational savings.

In section 2, we summarily introduce the GTM and its *t*-GTM and class-enriched variants, as well as the two-stage clustering procedure with its alternative initialization strategies. Several experimental results are provided and discussed in section 3, while a final section outlines some conclusions.

2 TWO-STAGE CLUSTERING

2.1 The GTM Models

The standard GTM is a non-linear latent variable model defined as a mapping from a low dimensional latent space onto the multivariate data space. The mapping is carried through by a set of basis functions generating a constrained mixture density distribution. It is defined as a generalized linear regression model:

$$\mathbf{y} = \phi(\mathbf{u})\mathbf{W}, \tag{1}$$

where ϕ are M basis functions $\phi(\mathbf{u}) = (\phi_1(\mathbf{u}),...,\phi_M(\mathbf{u}))$. For continuous data of dimension D, spherically symmetric Gaussians are an obvious choice of basis function; $\mathbf{W}$ is a matrix of adaptive weights w_{md} that defines the mapping, and $\mathbf{u}$ is a point in latent space. To avoid computational intractability a regular grid of K points $\mathbf{u}_k$ can be sampled from the latent space. Each of them, which can be considered as the representative of a data cluster, has a fixed prior probability $p(\mathbf{u}_k) = 1/K$ and is mapped, using (1), into a low dimensional manifold non-linearly embedded in the data space. This latent space grid is similar in design and purpose to that of the visualization space of the SOM. A probability distribution for the multivariate data $\mathbf{X} = \{\mathbf{x}_n\}_{n=1}^N$ can then be defined, leading to the following expression for the log-likelihood:

$$L = \sum_{n=1}^{N} \ln\left\{ \frac{1}{K} \sum_{k=1}^{K} \left(\frac{\beta}{2\pi}\right)^{D/2} \exp\left\{ \frac{-\beta\|\mathbf{y}_k - \mathbf{x}_n\|^2}{2} \right\} \right\} \tag{2}$$

where $\mathbf{y}_k$, usually known as *reference* or *prototype* vectors, are obtained for each $\mathbf{u}_k$ using (1); and β is the inverse of the noise model variance. The EM algorithm is an straightforward alternative to obtain the Maximum Likelihood (ML) estimates of the adaptive parameters of the model, namely $\mathbf{W}$ and β.

The class-GTM model is an extension of GTM that makes use of the available class information. The main goal of this extension is to improve class separability in the clustering results of GTM. For the Gaussian version of the GTM model (Sun et al., 2002; Cruz and Vellido, 2006), this entails the calculation of the posterior probability of a cluster representative $\mathbf{u}_k$ given the data point $\mathbf{x}_n$ and its class label c_n, or class-conditional *responsibility* $\hat{z}^c_{kn} = p(\mathbf{u}_k|\mathbf{x}_n, c_n)$, as part of the E step of the EM algorithm. It can be calculated as:

$$\begin{aligned} \hat{z}^c_{kn} &= \frac{p(\mathbf{x}_n, c_n|\mathbf{u}_k)}{\sum_{k'=1}^{K} p(\mathbf{x}_n, c_n|\mathbf{u}_{k'})} \\ &= \frac{p(\mathbf{x}_n|\mathbf{u}_k)p(c_n|\mathbf{u}_k)}{\sum_{k'=1}^{K} p(\mathbf{x}_n|\mathbf{u}_{k'})p(c_n|\mathbf{u}_{k'})} \\ &= \frac{p(\mathbf{x}_n|\mathbf{u}_k)p(\mathbf{u}_k|c_n)}{\sum_{k'=1}^{K} p(\mathbf{x}_n|\mathbf{u}_{k'})p(\mathbf{u}_{k'}|c_n)}, \end{aligned} \tag{3}$$

and, being T_i each class,

$$p(\mathbf{u}_k|T_i) = \frac{\frac{\sum_{n;c_n=T_i} p(\mathbf{x}_n|\mathbf{u}_k)}{\sum_n p(\mathbf{x}_n|\mathbf{u}_k)}}{\frac{\sum_{k'} \sum_{n;c_n=T_i} p(\mathbf{x}_n|\mathbf{u}_{k'})}{\sum_n p(\mathbf{x}_n|\mathbf{u}_{k'})}} \tag{4}$$

The rest of the model's parameters are estimated following the standard EM procedure.

For the Gaussian GTM, the presence of outliers is likely to negatively bias the estimation of the adaptive parameters, distorting the clustering results. In order to overcome this limitation, the GTM was recently redefined (Vellido, 2006; Vellido and Lisboa, 2006) as a constrained mixture of Student's *t* distributions: the *t*-GTM, aiming to increase the robustness of the model towards outliers. The mapping described by Equation (1) remains, with the basis functions now being Student's *t* distributions and leading to the definition of the following mixture density:

$$\begin{aligned} &p(\mathbf{x}|\mathbf{W},\beta,\nu_k) = \\ &\frac{1}{K}\sum_{k=1}^{K} \frac{\Gamma(\frac{\nu_k+D}{2})\beta^{D/2}}{\Gamma(\frac{\nu_k}{2})(\nu_k\pi)^{D/2}} \left(1+\frac{\beta}{\nu_k}\|\mathbf{y}_k-\mathbf{x}_n\|^2\right)^{\frac{\nu_k+D}{2}} \end{aligned} \tag{5}$$

where $\Gamma(\cdot)$ is the gamma function and the parameter $\nu = (\nu_1,\ldots,\nu_K)$ represents the degrees of freedom for each component k of the mixture, so that it can be viewed as a tuner that adapts the level of robustness (divergence from normality) for each component. This density leads to the redefinition of the model log-likelihood and, again, the estimation of the corresponding adaptive parameters using EM. The extension to class-*t*-GTM is straightforward and is omitted here for the sake of brevity.

2.2 Two-Stage Clustering based on GTM

In the first stage of the proposed two-stage clustering procedure, the GTM models are trained to obtain the representative prototypes (detailed clustering)

of the observed dataset. In this study, the resulting prototypes $\mathbf{y}_k$ of the GTM models are further clustered using the K-means algorithm. In a similar two-stage procedure to the one described in (Vesanto and Alhoniemi, 2000), based on SOM, the second stage K-means initialization in this study is first randomly replicated 100 times, subsequently choosing the best available result, which is the one that minimizes the error function $E = \sum_{c=1}^{C} \sum_{\mathbf{x} \in G_c} \|\mathbf{x} - \mu_c\|^2$, where C is the final number of clusters in the second stage and μ_c is the centre of the K-means cluster G_c. This approach seems somehow wasteful, though, as the use of GTM instead of SOM can provide us with richer a priori information to be used for fixing the K-means initialization in the second stage.

Two novel fixed initialization strategies that use the prior knowledge obtained by GTM in the first stage are proposed. They are based on the Magnification Factors (MF) and the Cumulative Responsibility (CR). The MF measure the level of stretching that the mapping undergoes from the latent to the data spaces. Areas of low data density correspond to high distorsions of the mapping (high MF), whereas areas of high data density correspond to low MF. The MF is described in terms of the derivatives of the basis functions $\phi_j(\mathbf{u})$ in the form:

$$\frac{dA'}{dA} = \det{}^{1/2}\left(\psi^{\mathbf{T}}\mathbf{W}^{\mathbf{T}}\mathbf{W}\psi\right), \tag{6}$$

where ψ has elements $\psi_{ji} = \partial\phi_j/\partial u^i$ (Bishop et al., 1997) and dA' and dA are, in turn, infinitesimal rectangles in the manifold and latent spaces. If we choose C to be the final number of clusters for K-means in the second stage, the first proposed fixed initialization strategy will consist on the selection of the class-GTM prototypes corresponding to the C non-contiguous latent points with lowest MF for K-means initialization. That way, the second stage algorithm is meant to start from the areas of highest data density.

The CR is the sum of responsibilities over all data points in $\mathbf{X}$ for each cluster k:

$$CR_k = \sum_{n=1}^{N} \hat{z}_{kn}^c \tag{7}$$

The second proposed fixed initialization strategy, based on CR, is similar in spirit to that based on MF. Again, if we choose C to be the final number of clusters for K-means in the second stage, the fixed initialization strategy will now consist on the selection of the GTM prototypes corresponding to the C non-contiguous latent points with highest CR. That is, the second stage is meant to start from those prototypes that are found in the first stage to be most responsible for the generation of the observed data.

3 EXPERIMENTS

3.1 Human Brain Tumour Data

The multi-center data used in this study consists of 217 single voxel PROBE (PROton Brain Exam system) MR spectra acquired in vivo for six brain tumour types: meningiomas (58 cases), glioblastomas (86), metastases (38), astrocytomas (22), oligoastrocytomas (6), and oligodendrogliomas (7). For the analyses, the spectra were grouped into three types (typology that will be used in this study as class information), as in (Tate et al., 2006): high grade malignant (metastases and glioblastomas), low grade gliomas (astrocytomas, oligodendrogliomas and oligoastrocytomas) and meningiomas. The clinically relevant regions of the spectra were sampled to obtain 200 frequency intensity values. The high dimensionality of the problem was compounded by the small number of spectra available, which is commonplace in MRS data analysis.

3.2 Experimental Design and Settings

The GTM, *t*-GTM and their class-enriched counterparts were implemented in MATLAB®. For the experiments reported next, the adaptive matrix $\mathbf{W}$ was initialized, following a PCA-based procedure described in (Bishop et al., 1998). This ensures the replicability of the results. The grid of latent points $\mathbf{u}_k$ was fixed to a square 20x20 layout for the MRS dataset. The corresponding grid of basis functions ϕ was equally fixed to a 5x5 square layout.

The goals of these experiments are fourfold. First, we aim to assess whether the inclusion of class information in the first stage of the procedure results in any improvement in terms of cluster-wise class separability (and under what circumstances) compared to the procedure using standard GTM. Second, we aim to assess whether the two-stage procedure improves, in the same terms, on the use of direct clustering of the data using K-means. Third, we aim to test whether the second stage initialization procedures based on MF and the CR of the class-GTM, described in section 2.2, retain the cluster-wise class separability capabilities of the two-stage clustering procedure in which K-means is randomly initialized. In fourth place, we aim to explore the properties of the structure of the dataset concerning atypical data. For that, we use the *t*-GTM (Vellido, 2006), as described in section 2.1.

The clustering results of all models will be first compared visually, which should help to illustrate the visualization capabilities of the models. Beyond the visual exploration, the second stage clustering results

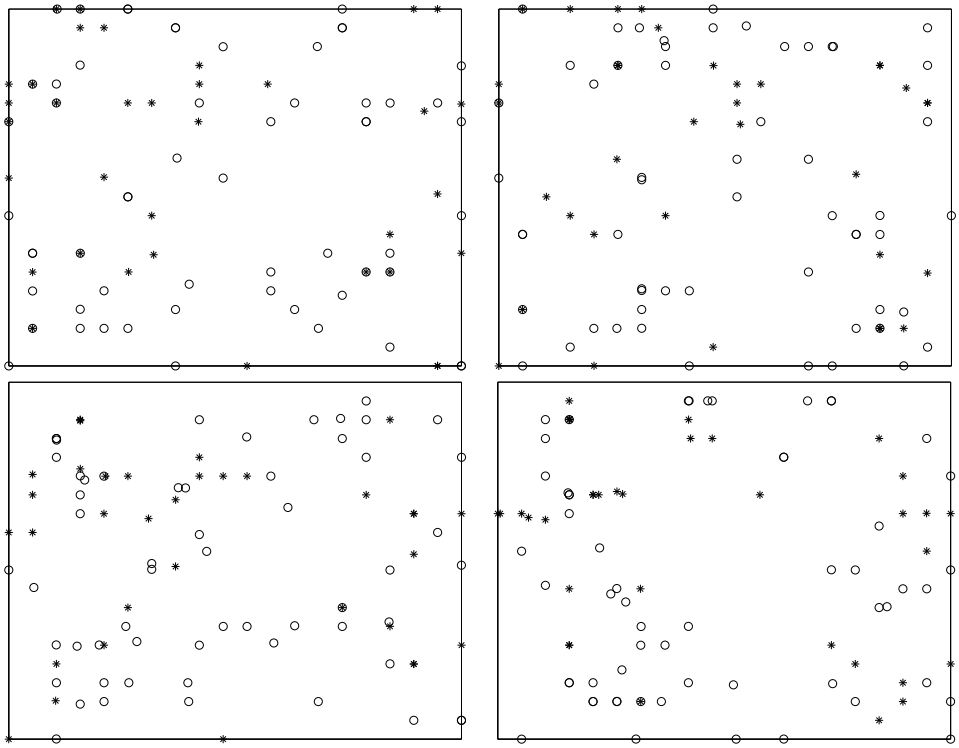

Figure 1: Representation, on the 2-dimensional latent space of GTM and its variants, of a part of the tumour dataset. It is based on the mean posterior distributions for the data points belonging to low grade gliomas ('*') and meningiomas ('o'). The axes of the plot convey no meaning by themselves and are kept unlabeled. (Top left): GTM without class information. (Top right): class-GTM. (Bottom left): *t*-GTM without class information. (Bottom right): class-*t*-GTM.

should be explicitly quantified in terms of cluster-wise class separability. For that purpose, the following entropy-like measure is proposed:

$$E_{G_c}(\{T_i\}) = -\sum_{\{G_c\}} P(G_c) \sum_{\{T_i\}} P(T_i|G_c) \ln P(T_i|G_c) = -\sum_{c=1}^{C} \frac{K_{G_c}}{K} \sum_{i=1}^{|\{T_i\}|} p_{ci} \ln p_{ci} \quad (8)$$

Sums are performed over the set of classes (tumour types) $\{T_i\}$ and the K-means clusters $\{G_c\}$; K is the total number of prototypes; K_{G_c} is the number of prototypes assigned to the c^{th} cluster; $p_{ci} = \frac{K_{G_c i}}{K_{G_c}}$, where $K_{G_c i}$ is the number of prototypes from class i assigned to cluster c; and, finally, $|\{T_i\}|$ is the cardinality of the set of classes. An entropy of 0 corresponds to the case of no clusters being assigned prototypes corresponding to more than one class.

Given that the use of a second stage in the clustering procedure is intended to provide final clusters that best reflect the overall structure of the data, the problem remains of what is the most adequate number of clusters. In this paper we do not use any cluster validity index and we just evaluate the entropy measure for solutions from 2 up to 10 clusters.

3.3 Results and Discussion

In the first stage of the two-stage clustering procedure, GTM, *t*-GTM and their class-enriched variants class-GTM and class-*t*-GTM were trained to model the human brain tumour dataset. The resulting prototypes $\mathbf{y}_k$ were then clustered in the second stage using the K-means algorithm. This last stage was performed with three different initializations, as described in section 2.2. In all cases, K-means was forced to yield a given number of final clusters, from 2 up to 10. The entropy was calculated for all settings.

Before considering the entropy results, visualization maps (obtained using the mean of the posterior distribution: $\sum_{k=1}^{K} \mathbf{u}_k \hat{z}_{kn}$ or $\sum_{k=1}^{K} \mathbf{u}_k \hat{z}^c_{kn}$) of all the trained models in the first stage were generated. Three hypotheses were made for the clustering results visualized here. First, the use of class information in the clustering models should yield visualization maps where classes are separated better than in those models which do not use it. Second, the use of *t*-

GTM should help to diminish the influence of outliers and the visualization maps generated with these models should show the data more homogeneously distributed throughout the visualization maps than in Gaussian GTM, which do no use it. Thirdly, since the tumour dataset is stronly class-unbalanced, we hypothesized that the small classes would consist mainly of atypical data. The second and third hypotheses will be tested using the *t*-GTM variants.

For the sake of brevity, we only provide one of these illustrative visualizations in Fig. 1.

Here, two tumour groups (low grade gliomas and meningiomas) are shown. The right column of Fig. 1, where the models that include class information are located, provides some preliminary support for the first hypothesis since the class separation between both classes is better than that of the models that do not use class information, located in the left column. This can be observed in the form of a more pronounced overlapping of both classes in the left hand-side models of Fig. 1. This is reinforced by the entropy results provided later on in the paper.

The use of *t* distributions in the models represented in the bottom row yields a similar data spread to that of the standard Gaussian GTM models of the top row. This is an indication that there might be not too many clear outliers in the two classes visually represented. Therefore, the second hypothesis cannot be supported at this stage.

We now turn our attention to the third hypothesis. In (Vellido and Lisboa, 2006) it was shown that a given data instance could be characterized as an outlier if the value of

$$O_n^* = \sum_k \hat{z}_{kn} \beta \|\mathbf{y}_k - \mathbf{x}_n\|^2 \qquad (9)$$

was sufficiently large. The histogram in Fig. 2 displays the values of O_n^* from (9) for the brain tumour dataset. We did the same for the class-*t*-GTM model and the corresponding values of O_n^* are displayed in Fig. 3.

First of all, and supporting our previous impression, not too many data could be clearly characterized as outliers according to these histograms. Somehow surprisingly, given the complex tumour typology of the dataset under study, these results do not support the third hypothesis, as most of the spectra that might be considered as outliers actually belong to the largest and best represented tumour types, such as meningiomas and glioblastomas. Interestingly, few metastases and astrocytomas are amongst the most extreme outliers.

The entropy measurements quantifying the cluster-wise class separation for the brain tumour dataset are shown in Fig. 4. Two immediate conclusions can be drawn: First, all the two-stage clustering procedures based on GTM perform much better than the direct clustering of the data through K-means in terms of cluster-wise class separation. The two-stage procedure based on class-GTM also performs much better than its counterpart without class information based on the standard GTM (right hand side of Fig. 4). On the contrary, it can also be observed that the two-stage clustering based on class-*t*-GTM does not perform better than the *t*-GTM model. This is explained by the fact that the adjustment of the model provided by *t*-GTM, which is blind to class information by itself, alters the accordance between class and cluster distributions, especially in a strongly class-unbalanced dataset such as the one under analysis. This result draws the limits out of which the addition of class information is not necessarily useful in terms of cluster-wise separation. The second main conclusion to be drawn is that the random initialization in the second stage of the clustering procedure, with or without class information, does not entail any significant advantage over the proposed fixed initialization strategies across the whole range of possible final number of clusters, while being far more costly in computational terms.

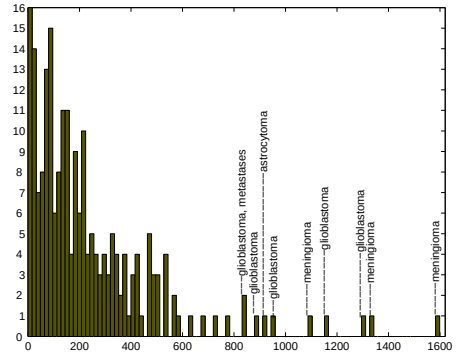

Figure 2: Histogram of the statistic (9) for the *t*-GTM model; outliers are characterized by its large values. As an example, the ten largest values are labeled.

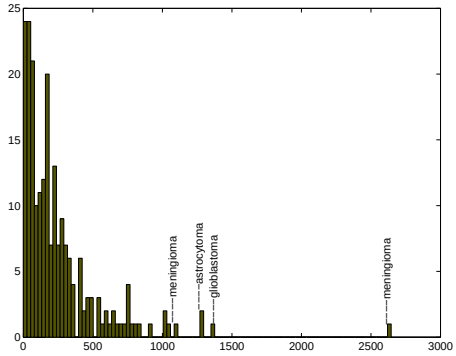

Figure 3: Histogram of (9) for class-*t*-GTM. As an example, the four largest values are labeled.

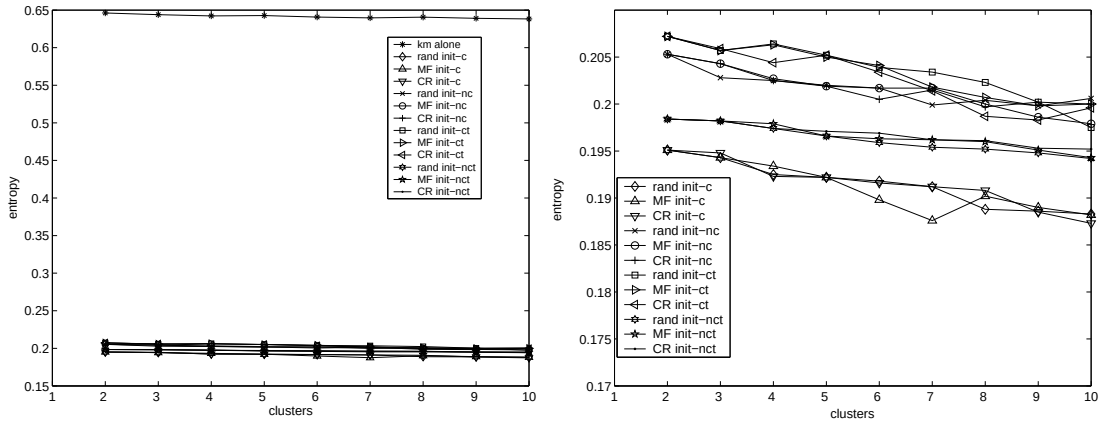

Figure 4: Entropy for the two-stage clustering of the tumour dataset, with different initializations (MF init, CR init and rand init) and K-means alone. The 'c' and 'nc' symbols refer to models that, in turn, use and not use class information. The 't' in the legend means that *t*-GTM was used in the first stage. (Left): all models are shown. (Right): only the GTM, *t*-GTM and their class-enriched variants are shown.

The entropy measure in (8) quantifies the level of agreement between the clustering solutions and the class distributions. In terms of the overall cluster-wise class separation provided by the Gaussian distributions-based GTM clustering models, it has been shown that the addition of class information consistently helps. As a result, these class-enriched models would be useful in a semi-supervised setting in which new undiagnosed tumour cases were added to the database.

4 CONCLUSIONS

In this paper we have analyzed the influence exerted by the inclusion of class information in the two-stage clustering of a complex human brain tumour MRS dataset. We have also introduced two economical and principled fixed initialization procedures for the second stage of the procedure. The existence of atypical data or outliers in the human brain tumours MRS dataset under study and its influence on the clustering have also been explored.

REFERENCES

Bishop, C. M., , Svensén, M., and Williams, C. K. I. (1997). Magnification Factors for the GTM algorithm. In *Proceedings of the IEE fifth International Conference on Artificial Neural Networks*, pages 64–69.

Bishop, C. M., Svensén, M., and Williams, C. K. I. (1998). The Generative Topographic Mapping. *Neural Computation*, 10(1):215–234.

Cruz, R. and Vellido, A. (2006). On the improvement of brain tumour data clustering using class information. In *Proceedings of the 3rd European Starting AI Researcher Symposium (STAIRS'06), Riva del Garda, Italy.*

Figueiredo, M. A. T. and Jain, A. K. (2002). Unsupervised learning of finite mixture models. *IEEE Transactions on Pattern Analysis and Machine Intelligence*, 24(3):381–396.

Kohonen, T. (1995). *Self-Organizing Maps*. Springer-Verlag, Berlin.

Sun, Y., Tiňo, P., and Nabney, I. T. (2002). Visualization of incomplete data using class information constraints. In Winkler, J. and Niranjan, M., editors, *Uncertainty in Geometric Computations*, pages 165–174. Kluwer Academic Publishers, The Netherlands.

Tate, A. R., Underwood, J., Acosta, D. M., Julià-Sapé, M., Majós, C., Moreno-Torres, A., Howe, F. A., van der Graaf, M., Lefournier, V., Murphy, M. M., Loosemore, A., Ladroue, C., Wesseling, P., Bosson, J. L., Cabañas, M. E., Simonetti, A. W., Gajewicz, W., Calvar, J., Capdevila, A., Wilkins, P. R., Bell, B. A., Rémy, C., Heerschap, A., Watson, D., Griffiths, J. R., and Arús, C. (2006). Development of a decision support system for diagnosis and grading of brain tumours using in vivo magnetic resonance single voxel spectra. *NMR in Biomedicine*, 19:411–434.

Vellido, A. (2006). Missing data imputation through GTM as a mixture of *t*-distributions. *Neural Networks*, 19(10):1624–1635.

Vellido, A. and Lisboa, P. J. G. (2006). Handling outliers in brain tumour MRS data analysis through robust topographic mapping. *Computers in Biology and Medicine*, 36(10):1049–1063.

Vesanto, J. and Alhoniemi, E. (2000). Clustering of the Self-Organizing Map. *IEEE Transactions on Neural Networks*, 11(3):586–600.

ROBUST CENTROID-BASED CLUSTERING USING DERIVATIVES OF PEARSON CORRELATION

Marc Strickert, Nese Sreenivasulu
Leibniz Institute of Plant Genetics and Crop Plant Research Gatersleben, Germany
stricker@ipk-gatersleben.de, srinivas@ipk-gatersleben.de

Thomas Villmann
Clinic for Psychotherapy, University of Leipzig, Germany
thomas.villmann@medizin.uni-leipzig.de

Barbara Hammer
Institute of Computer Science, University of Clausthal, Germany
hammer@in.tu-clausthal.de

Keywords: Centroid-based clustering, correlation, quantization cost optimization.

Abstract: Modern high-throughput facilities provide the basis of -omics research by delivering extensive biomedical data sets. Mass spectra, multi-channel chromatograms, or cDNA arrays are such data sources of interest for which accurate analysis is desired. Centroid-based clustering provides helpful data abstraction by representing sets of similar data vectors by characteristic prototypes, placed in high-density regions of the data space. This way, specific modes can be detected, for example, in gene expression profiles or in lists containing protein and metabolite abundances. Despite their widespread use, k-means and self-organizing maps (SOM) often only produce suboptimum results in centroid computation: the final clusters are strongly dependent on the initialization and they do not quantize data as accurately as possible, particularly, if other than the Euclidean distance is chosen for data comparison. Neural gas (NG) is a mathematically rigorous clustering method that optimizes the centroid positions by minimizing their quantization errors. Originally formulated for Euclidean distance, in this work NG is mathematically generalized to give accurate and robust results for the Pearson correlation similarity measure. The benefits of the new NG for correlation (NG-C) are demonstrated for sets of gene expression data and mass spectra.

1 INTRODUCTION

Massive data sets with a high number of samples and/or attributes create challenges in *de novo* data analysis. Particularly, high-throughput biomedical devices like mass spectrometers or gene expression arrays generate thousands of data points in parallel for which accurate data models are required in order to faithfully reduce the data complexity and to facilitate the analysis.

Centroid-based data representations provide most intuitive interpretations, because a centroid can be regarded as noise-free prototype of its surrounding cloud of data. Especially for many data vectors, centroids can be much more easily assessed than results from hierarchical clustering, for example. Some well-known clustering algorithms are freely available (de Hoon et al., 2004), implementing widely used methods of Eisen et al. (Eisen et al., 1998).

As a matter of fact, self-organizing maps (SOM) and k-means clustering are frequently used methods for extracting a pre-defined number of centroids from the data (Kohonen, 2001; MacQueen, 1967). While centroids in k-means get specialized by an iterative averaging procedure applied to data that they do currently represent, SOM is a cooperative model with updates of the best-matching centroid and also of its neighbors. Since SOM neighbors are related to lateral centroids arranged on a grid structure, the SOM update triggers a mapping of similar high-dimensional data vectors onto similar positions of that usually low-dimensional grid, often, a 2D-plane for visualization. Due to topological constraints induced by the grid, quantization accuracy, i.e. data representation, of the SOM centroids is often not optimum (Villmann and Claussen, 2006). Thus, if the dimension reduction

feature of SOM is not needed, better representations are obtained without grid structure. This can be realized by a SOM-like algorithm called neural gas (NG) that will be of interest here.

Data condensation requires similarity criteria in order to gather related items. Besides Euclidean distance, Pearson correlation is one of the most often used comparison criteria in biological studies. In principle, a wide range of similarity measures, expressed as Minkowski metric or correlation, is available in self-organizing maps (SOM) and k-means.

There is a commonly overlooked problem connected to similarity rating and model update, though. SOM centroids, for example, are defined by their closeness to data points, and it is thus straight-forward to describe closeness by task-specific similarity measures. Yet, the SOM update rule 'make close centroids more similar to the data' is traditionally implemented as a claim for identity: centroids are moved on straight lines in *Euclidean* space, in portions depending on their closeness, towards presented data points. There is thus a difference between the update rule for a strict one-to-one correspondence of all centroid components with those of the represented data vectors, and the more relaxed desire of merely representing high similarity. Although, for vector pairs, identity is equivalent to maximum similarity, the situation is different for a single centroid representing many data points; then, similarity constraints do usually allow more degrees of freedom for the centroid placement than strict identity constraints. Analogous considerations apply to the k-means clustering method, in which custom measures define data assignments to centroids, but in which average data centroids are strictly computed (by averaging) in Euclidean space.

The discrepancy between similarity computation and subsequent update of data models can be circumvented by coupling the update procedure with analytic properties of the selected similarity measure. In cost function frameworks the model parameters can be adapted by optimization of similarity relationships. Here, gradient-based optimization of centroid locations is discussed for Pearson correlation similarity. Correlation is often used in biomedical analysis tasks. It has got favorable pattern matching characteristics, and it allows to calculate formal derivatives and can be directly used in gradient methods such as the Heskes variant of SOM (Heskes, 1999), neural gas (Martinetz and Schulten, 1991), and generalized learning vector quantization (Sato and Yamada, 1995). The subsequent derivative is integrated into the highly accurate neural gas clustering method, for which superior performance is demonstrated for gene expression data and mass spectrum data.

2 METHODS

Faithful data representation requires robust centroid locations within the data. Self-organizing maps (SOM) realize a cooperative centroid placement strategy by iterative presentation of data points that trigger further improvements of previously placed centroids. A general formulation of this simple procedure is given in Algorithm 1.

Algorithm 1 SOM / NG centroid update

repeat
  chose randomly a data vector $\mathbf{x}$
  $k \leftarrow \arg\min_i \{ \mathrm{d}(\mathbf{w}^i, \mathbf{x}) \}$
    $\{$ $\mathbf{w}^k$ is closest centroid to data vector $\mathbf{x}$ $\}$
  for all m centroids j **do**
    $\mathbf{w}^j \leftarrow \mathbf{w}^j + \gamma \cdot \mathrm{h}_\sigma \left(D(\mathbf{w}^k, \mathbf{w}^j) \right) \cdot U(\mathbf{x}, \mathbf{w}^j)$
      $\{$ $\gamma, \mathrm{h}, \sigma, D, U$: see text $\}$
  end for
until no more major changes

SOM Mode of Algorithm 1. Since SOM centroids cooperate laterally on a grid structure, updates imply spatial specialization with similar grid neighbors. Grid dependencies between centroids k and j are expressed by the neighborhood index $D(\mathbf{w}^k, \mathbf{w}^j)$. For example, rectangular 2D grids possess four direct neighbors $\mathcal{N}_k$ of non-boundary centroids with $D(\mathbf{w}^k, \mathcal{N}_k) = 1$. The σ-range of neighborhood cooperation is expressed by the decreasing function h_σ, with maximum value at $\mathrm{h}_\sigma(0) = 1$. Often a Gaussian bell $\mathrm{h}_\sigma(D) = e^{-D^2/\sigma^2}$ is put upon the grid, contracted during update by shrinking $\sigma \to 0$. In addition to neighborhood characterization, the update strategy of centroid $\mathbf{w}^j$ facing data vector $\mathbf{x}$ is described by $U(\mathbf{x}, \mathbf{w}^j)$. As said above, centroids are most often moved on straight Euclidean lines towards the data vector, i.e. by the term $U(\mathbf{x}, \mathbf{w}^j) = (\mathbf{x} - \mathbf{w}^j)$, in small steps depending on the update rate $\gamma < 1$.

NG Mode of Algorithm 1. The neural gas algorithm works exactly the same as described in the previous SOM mode, except for one crucial exception: the centroid neighborhood is no longer defined on a pre-defined grid structure. Instead, the neighborhood changes dynamically in course of data presentation. The centroid closest to the currently presented data vector $\mathbf{x}$ is assigned a rank of zero, the runner-up gets a rank of one, and so forth. In general, the neighborhood is defined by the ranks relative to only the data vector: $D(\mathbf{w}^k, \mathbf{w}^j) = D(\mathbf{w}^j) = \mathrm{rnk}(\mathbf{x}, \mathbf{w}^j)$ with

$$\mathrm{rnk}(\mathbf{x}, \mathbf{w}^j) = \left| \{ \mathrm{d}(\mathbf{x}, \mathbf{w}^i) < \mathrm{d}(\mathbf{x}, \mathbf{w}^j), i = 1 \ldots m \} \right| .$$

In contrast to SOM, the best-matching centroid $\mathbf{w}^k$ does not induce a specialized structure on the grid neighbors, and the rank-based neighborhood is always data optimum. Centroid update profits from ranks, because they are useful for breaking ties, i.e. for differentiation of very similar data. Ranks are exponentially wrapped by $\mathrm{h}_\sigma(D) = e^{-D/\sigma}$, again $\sigma \to 0$ during update iterations. As for SOM, $U(\mathbf{x}, \mathbf{w}^j) = (\mathbf{x} - \mathbf{w}^j)$ and $\gamma < 1$.

Its is known that the NG algorithm asymptotically realizes a stochastic gradient descent on the cost function (Martinetz et al., 1993):

$$\mathrm{E}(\mathbf{W}, \sigma) = \frac{1}{C(\sigma)} \cdot \sum_{j=1}^{m} \sum_{i=1}^{n} \mathrm{h}_\sigma(\mathrm{rnk}\left(\mathbf{x}^i, \mathbf{w}^j\right)) \cdot \mathrm{d}(\mathbf{x}^i, \mathbf{w}^j)\,. \tag{1}$$

The scaling factor $C(\sigma) = \sum_{i=0}^{m-1} \mathrm{h}_\sigma(i)$ is used for normalization. In the limit $\sigma \to 0$, the NG mode of Algorithm 1 leads to a centroid placement that minimizes the total quantization error, defined by $\mathrm{d}(\mathbf{x}^j, \mathbf{w}^i)$, between m centroids and n data vectors. This property does not hold for the SOM version. Even worse, in general the mathematical optimization target of SOM is undefined (Cottrell et al., 1994), unless the costly modification proposed by Heskes is implemented (Heskes, 1999).

The benefits of neural gas are: mathematical understanding of centroid specialization, high reproducibility of results, neighborhood cooperation for robustness against initialization, and easy implementation. Very importantly, the generic formulation of the neural gas algorithm allows to create modifications with respect to the choice of the data similarity measure. A minor drawback of NG is the sorting operation, i.e. a computing complexity of $O(n \log n)$, required for rank calculation. Therefore, a fast batch version of neural gas with quadratic convergence based on Newton's method has been proposed recently (Cottrell et al., 2006), complementing the iterative online approach discussed here. The authors do also present a method for clustering data only defined by a similarity matrix. For its simplicity, we stick to Algorithm 1 in the following, and we introduce a derivation making full use of the analytic properties of Pearson correlation for an improved centroid update rule.

Neural Gas Clustering with Pearson Correlation. Pearson correlation is our focus of choice, because it provides a certain degree of invariance to additive or multiplicative effects induced by measuring devices or biochemical probe concentrations. Thus, pattern-based analysis is enhanced by choosing Pearson similarity for data vectors and centroids, mathematically described with abbreviation $\mathsf{r}(\mathbf{x}, \mathbf{w}) = \frac{\mathscr{B}}{\sqrt{\mathscr{C} \cdot \mathscr{D}}}$ by

$$\mathsf{r}(\mathbf{x}, \mathbf{w}) = \frac{\sum_{i=1}^{d} (x_i - \mu_\mathbf{x}) \cdot (w_i - \mu_\mathbf{w})}{\sqrt{\left(\sum_{i=1}^{d} (x_i - \mu_\mathbf{x})^2\right) \cdot \left(\sum_{i=1}^{d} (w_i - \mu_\mathbf{w})^2\right)}}\,. \tag{2}$$

In principle, the covariance of $\mathbf{x}$ and $\mathbf{w}$ gets standardized by the product of the individual variances of $\mathbf{x}$ and $\mathbf{w}$. However, due to dynamic centroid update, there is no much use in making the implicit standardization explicit by data preprocessing, such as z-score transformation. Furthermore, in cases when correlation is just a building block, like in the dissimilarity measure $(1 - \mathsf{r})^p$ (Zhou et al., 2002), it is much more natural to think in terms of a self-contained equation (Eqn. 2) than in terms of statically preprocessed data.

Correlation described by Eqn. 2 can be plugged into the cost function Eqn.1 being optimized by gradients along partial derivatives of E with respect to coordinates of all centroids $\mathbf{w}$. In general, these derivatives indicate contributions of the k-th centroid component of $\mathbf{w}$ to the distance or similarity measure.

For the squared Euclidean distance $\mathrm{d}^2(\mathbf{x}, \mathbf{w}) = \sum_{i=1}^{d} (x_i - w_i)^2$ this corresponds to the previously mentioned term $U(\mathbf{x}, \mathbf{w}) = (\mathbf{x} - \mathbf{w})$:

$$\frac{\partial \mathrm{d}^2(\mathbf{x}, \mathbf{w})}{\partial w_k} = -2 \cdot (x_k - w_k) \propto U(x_k, w_k)\,.$$

For Pearson correlation the derivative is

$$\frac{\partial \mathsf{r}(\mathbf{x}, \mathbf{w})}{\partial w_k} = \frac{(x_k - \mu_\mathbf{x}) - \frac{\mathscr{B}}{\mathscr{D}} \cdot (w_k - \mu_\mathbf{w})}{\sqrt{\mathscr{C} \cdot \mathscr{D}}}\,. \tag{3}$$

Since the cost function should be minimized, correlation r is turned by negative sign into a dissimilarity measure. Therefore, the term $U(x_k, w_k) = -\partial \mathsf{r}(\mathbf{x}, \mathbf{w}) / \partial w_k$ is inserted into Algorithm 1 which constitutes the new version of neural gas for correlation-based centroid placement, NG-C for short. It can be shown that this correlation-based update rule yields a valid gradient descent also at the boundaries of the receptive fields. A proof, originally for the Euclidean case, is provided by (Martinetz et al., 1993), where a vanishing contribution of the ranks was presented. Since the proof does not rely on specific properties of the Euclidean metric, a direct transfer to Pearson correlation is possible. Therefore, Eqn. 1 is still a cost function that gets optimized by the neural gas algorithm.

Usually, good convergence is reached after 50–1000 repeated data cycles, depending of the size n of the data set and the number m of centroids. Thereby, the neighborhood range σ is exponentially decreased from a starting size of $\sigma = m$ to a small value of $\sigma = 0.001$. This involves all prototypes strongly in the beginning, contracting centroids towards the data

'center', and it leads to a fine-tuning of data-specific centroids in the final phase.

3 RESULTS

The following three applications show the superiority of NG-C clustering over traditional methods with Pearson correlation. As demonstrated, cost function optimization by NG-C provides better data representations and higher reproducibility of results.

3.1 Single Cluster Representation of Gene Expression Data

A first proof of concept is given for the simple, but illustrative task of finding only a single centroid position. This points out structural differences between Euclidean- and correlation-based centroid update. We use an exemplary 14-dimensional gene expression data set, where macroarrays were used to cover 14 temporal developmental stages in the endosperm tissue of developing barley grains, sampled from day 0 after flowering in steps of two days to day 26. After quality-based filtering, 4824 highly reliable genes were obtained. Conforming to standards, expression values were quantile normalized and $\log_2$-transformed. However, for maintaining overall expression levels, z-score was not applied to the 14-dimensional expression series. For illustration, the set was further reduced to 344 genes of prominent temporal up-regulation with more than 10 transitions $x_t^j < x_{t+1}^j$.

Neural gas has been run with Euclidean update $U(\mathbf{x},\mathbf{w}) = (\mathbf{x}-\mathbf{w})$ and with updates based on the derivative of correlation according to Eqn. 3. Both approaches have been re-run 50 times with random centroid initialization. Each run has been carried out with 100 update iterations using $\gamma = 0.001$ for the approach Euclidean and $\gamma = 0.01$ for the correlation-based one. Neighborhood size σ does not have any influence and even d is not important for data assignments, because there is only one centroid to be assigned to. Thus, only the effect of the derivative of d on the centroid specialization is studied here.

The results are displayed in the plot panel of Fig. 1. The plots show the 14-dimensional expression series together with their centroids, projected by PCA and embedded by multi-dimensional scaling (MDS) in two dimensions. PCA represents the Euclidean view on the data, MDS the correlation-based view. To summarize the displayed results, Euclidean update is very stringent in both data views, the top left panel indicating that all 50 centroids are almost perfectly located in the center of gravity at point (0,0), which is the k-means solution for $k = 1$. Complementary to that, correlation-based update exhibits many degrees of freedom in Euclidean view, but shows very high specificity in the correlation view – which is exactly what is has been designed for.

In addition to visual validation, which might suffer from shortcomings of the built-in dimension reduction, quantization errors have been calculated. For the average data vector, analog to the deterministic k-means result with $k = 1$, an average correlation of $r = 0.96226$ to the data vectors is found. The Euclidean NG-update yields a result with an average correlation of the generated centroids of $r = 0.96222 \pm 5.583 \cdot 10^{-5}$, which is virtually the result of the avarage vector, affected by minor update-specific fluctuations. Correlation-based centroid update yields the best results with an average correlation of $r = 0.96403 \pm 8.173 \cdot 10^{-5}$. In combination with the bottom left panel in Fig. 1 it can be concluded that there are non-unique solutions that can be reached only, if Euclidean constraints are relaxed to updates operating in correlation space. Despite of the small differences for the presented data set, the results are quite fundamental, because they show that better solutions exist beyond averages. On a good mathematical basis, similarity-specific updates induce less constraints on the cost function and yield better data representations.

3.2 Clustering of Gene Expression Data

Mining for principal shapes in large lists of gene expression patterns is a central tool for the identification of co-expressed genes. Neural gas with correlation is used to meet this purpose for the data set described in the last paragraph containing 4824 gene expression levels at 14 time points. For comparison, Eisen's implementation of k-means and Gasch's and Eisen's fuzzy k-means are taken as reference models (de Hoon et al., 2004). Both make use of Pearson correlation for creating sets of similar patterns for centroid calculation, but they compute centroid positions in Euclidean space. Calculations were done with 100 cycles for neural gas, i.e. 482,400 centroid updates, and 100 cycles for the k-means models.

A number of 23 centroids was used in all models, because fuzzy k-means is, due to its built-in PCA, limited to $3\times$#experiments+2=$3\times14+2 = 44$ prototypes of which only 23 were identified as unique by fuzzy k-means (Gasch and Eisen, 2002). Contrary to the k-means methods, unused prototypes do not occur in NG-C, because of its neighborhood cooperation. The exponential NG-C neighborhood influence is realized as exponential decay from $\sigma = 23$ to $\sigma = 0.001$,

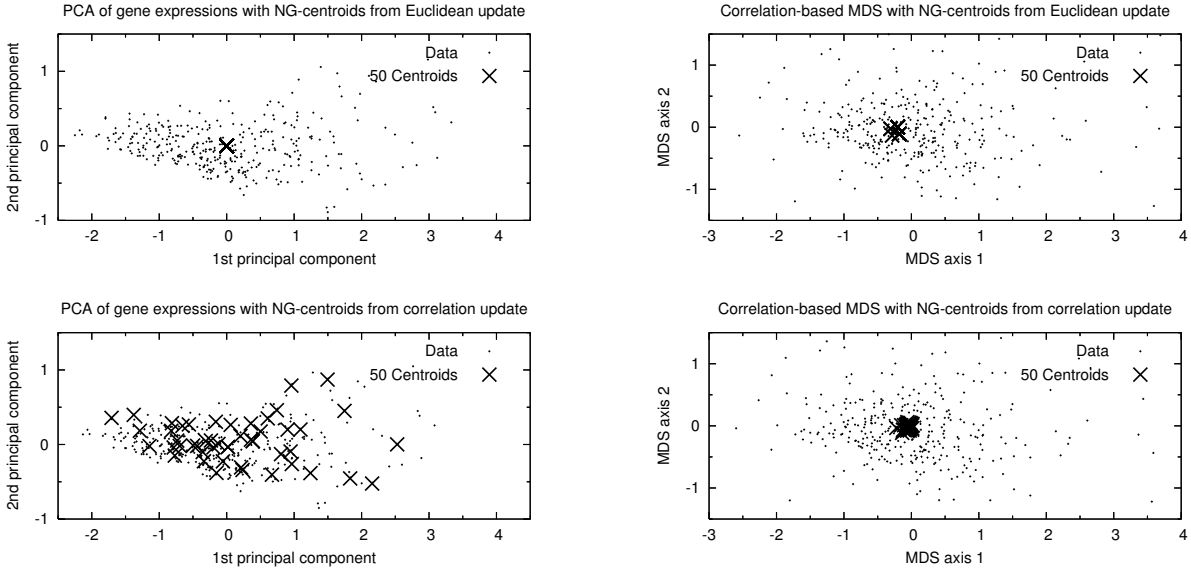

Figure 1: Centroid specialization for single cluster representation. Top row: Euclidean update rule, bottom row: update based on derivative of Pearson correlation. Left column: principal component plots, right column: multidimensional scaling of $(1-r)$ data relationships. In 50 individual NG runs, Euclidean updates (top row) show high specificity for both the Euclidean data view (shown as PCA) and the correlation-based view (shown as MDS). Correlation-based updates (bottom row) exhibit large diversity in Euclidean view (PCA) and high specificity in correlation view (MDS).

the update rate is set to $\gamma = 0.001$. Two quality criteria are considered for model comparison: reproducibility of the obtained centroids for different runs of the algorithms and quantization accuracy.

Reproducibility of Clusters. One major aspect of clustering is the consistency of the results. This has been tested by running NG-C and k-means 10 times from random starting configurations of the 23 centroids. For fuzzy k-means the standard initialization is fixed, which makes repeats unnecessary. Visual comparison is thus restricted to NG-C and k-means. An informative comparison between both methods is displayed in Figure 2, created using the free TreeView software. Both horizontal intensity bars contain the 23 centroids of 10 runs, i.e. 230 columns. Shades of gray denote specific gene expression intensities. Patterns of temporal up- and down-regulations present in the underlying data set are nicely captured by centroids of both models. The tic marks attached to the bottom of the NG-C bar point out 23 prominent bands that reflect a high reproducibility of the centroids contained therein, independent of their random initialization. For k-means, displayed in the row above, the result is very different: an unspecific continuous range of final states is obtained, which supports the experience of many users of k-means who complain about the poor reproducibility of results.

Quantization Accuracy. Table 1 provides a summary of the quantization accuracy of the found clusters. For each run, the average correlation of expression patterns with their corresponding centroids are measured, and the respective standard deviations are also calculated. These two values are averaged over all centroids. Finally, mean values for the 10 experiments are determined and listed in Table 1. As a major outcome, NG-C shows a superior data representation over k-means and fuzzy k-means. The fuzzy k-means is a little better than simple k-means, but its major disadvantage is the limitation to 44 centroids of which 21 are even unused. The good results of NG-C, however, are not too much surprising, because neural gas has been mathematically designed to optimize the goal of

Table 1: Average correlations between data samples and their centroids for 10 independent runs of NG-C and k-means. The deterministic result of the fuzzy k-means is 0.9335 ± 0.07216. In terms of quantization accuracy and data assignment variability NG-C performs best. Both k-means and its fuzzy k-means yield slightly worse quantizations, but fuzzy k-means covers data more homogeneously.

NG-C	
mean	std.-dev.
0.9516±0.0001	0.0573±0.0004
k-means	
mean	std.-dev.
0.9329±0.0017	0.0881±0.0038

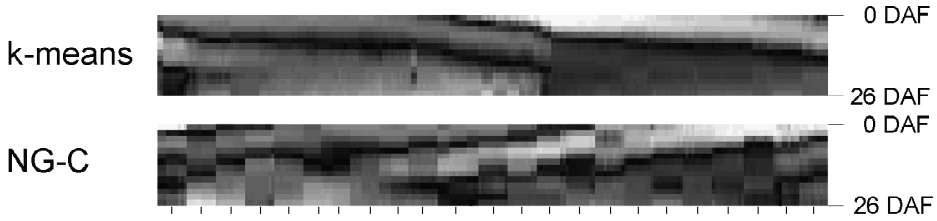

Figure 2: Cluster reproducibility for correlation-based neural gas (NG-C) and k-means. Both models, corresponding to the upper and lower bar, were run 10 times with random initialization. For the considered number of 23 centroids this yields a total of 230 centroids (gray columns) for comparison. While the final states of k-means cover a continuum of centroid locations, exhibiting only one major break, the final states of NG-C are highly conserved and displayed as 23 characteristic bands containing approx. 10 specific centroids.

maximum quantization accuracy (minimum quantization error), while the k-means methods are acting on assumptions about Euclidean data centers iteratively assessed by averaging.

3.3 Clustering of Mass Spectra

The last application concerns clustering of mass spectrum data from a clinical cancer study with 1050 mass spectra taken from sliced frozen tissue probes, using a linear MALDI-TOF MS, Autoflex, in a range of 2000-10000Da (by courtesy of Bruker Daltonik GmbH, Bremen). The data preparation protocol of the measured spectra followed the default workflow for baseline correction, alignment and peak picking. Robust peaks with signal to noise ratio S/N > 5 were used for further analysis, and only maxima of the extracted peaks were considered. This led to a high quality data set of 1050 samples, each described by 32 peaks. Clustering assists in tasks of data inspection and hypothesis generation.

Neural gas is applied in two manners to address the task of deriving tissue-specific spectrum centroids from the 32-dimensional data: one with Pearson correlation for centroids assignment, but with Euclidean update, the other fully correlation-driven for both pattern matching and update.

A small number of 11 clusters has been chosen in order to force sparse representations and to make the constraints of stringent Euclidean updates apparent. Both approaches have been trained in 10 independent runs using 1000 data cycles, i.e. 1000 x 1050 iterations, starting with randomly initialized centroids. Euclidean update was performed with an update rate of $\gamma = 0.01$. A value of $\gamma = 10^4$ was used for the correlation-based update. This large value compensates for the very small variability of the derivatives of correlations, which are caused by very similar mass peak profiles.

Both methods yield accurate data abstractions, as shown in Fig. 3. The MDS visualization faithfully displays the correlation relationships of the 32-dimensional centroids and the data. Since similar scatter points correspond to highly correlated data vectors, excellent reproducibility of the final configurations and a good data coverage can be observed. With respect to quantization, centroids from Euclidean update correlate on average at a level of $r = 92.8106 \pm 0.0043$ with the represented data. Update by Pearson correlation yields an improvement to $r = 93.4854 \pm 0.0790$ for the same number of prototypes. The small standard deviation for Euclidean update again points out (indirectly) the very strong attraction to the final centroid configuration, which is, however, not optimum in terms of quantization accuracy (data representation), for which the correlation update is clearly a better choice.

4 CONCLUSIONS

Based on the mathematical derivative of the Pearson correlation coefficient, we developed a new approach to maximize correlation in prototype-based data models. Particularly, the derivative can be directly plugged into the update step of a generalized version of the neural gas clustering method. Well-reproducible high-quality clusters were obtained by the new NG-C method. For the data clustered here, k-means and fuzzy k-means, although offering correlation similarity, are clearly outperformed by NG-C. In general, correlation-based centroid matching combined with Euclidean update, as usually realized in k-means and SOM implementations, leads to suboptimal data representations.

Although Pearson correlation is one of the gold standards in biomedical data analysis, the above concept can be easily generalized by replacing the derivative of Pearson correlation by that of other suitable similarity measures. This opens directions to process

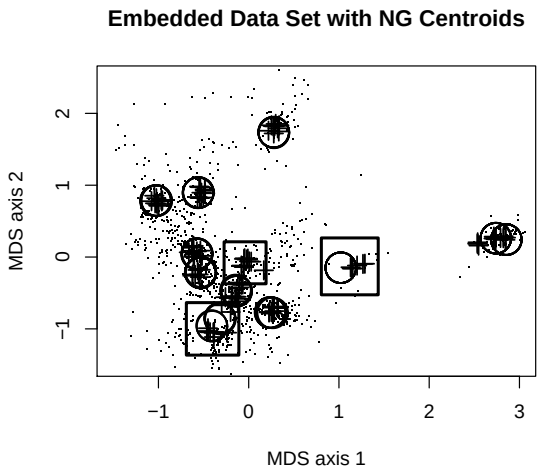

Figure 3: Visualization of data (small dots) and neural gas (NG) centroids (circles and crosses). Centroids correspond to 10 independent runs of NG, each run comprising 11 centroids, for two different update rules. Circles correspond to NG centroids obtained by Euclidean update; they do exhibit an extremely high reproducibility. Crosses correspond to centroids with correlation-based update; their final states are less stringently fixed, but their quantization quality is better (see text). In many cases, both update rules yield similar final configurations, but the boxes highlight regions with sytematic differences.

data from wide scientific fields where domain knowledge needs to be carefully considered.

ACKNOWLEDGEMENTS

Thanks to Frank-Michael Schleif (University of Leipzig) for the mass spectrum data and for fruitful discussions. This work is supported by the Ministry of Culture of Saxony-Anhalt, grant XP3624HP/0606T.

REFERENCES

Cottrell, M., Fort, J., and Pagès, G. (1994). Two or three things that we know about the Kohonen algorithm. In Verleysen, M., editor, *European Symposium on Artificial Neural Networks (ESANN)*, pages 235–244. D-facto Publications.

Cottrell, M., Hammer, B., Hasenfuss, A., and Villmann, T. (2006). Batch and median neural gas. *Neural Networks*, 19(6–7):762–771.

de Hoon, M., Imoto, S., Nolan, J., and Miyano, S. (2004). Open source clustering software. *Bioinformatics*, 20(9):1453–1454.

Eisen, M., Spellman, P., Brown, P., and Botstein, D. (1998). Cluster analysis and display of genome-wide expression patterns. *PNAS*, 95(25):14863–14868.

Gasch, A. and Eisen, M. (2002). Exploring the conditional coregulation of yeast gene expression through fuzzy k-means clustering. *Genome Biology*, 3(11):1–22.

Heskes, T. (1999). Energy functions for self-organizing maps. In Oja, E. and Kaski, S., editors, *Kohonen Maps*, pages 303–316. Elsevier, Amsterdam.

Kohonen, T. (2001). *Self-Organizing Maps*. Springer-Verlag, Berlin, 3rd edition.

MacQueen, J. (1967). Some methods for classification and analysis of multivariate observations. In *Proceedings of 5-th Berkeley Symposium on Mathematical Statistics and Probability*, pages 281–297. University of California Press.

Martinetz, T., Berkovich, S., and Schulten, K. (1993). "Neural-gas" network for vector quantization and its application to time-series prediction. *IEEE Transactions on Neural Networks*, 4(4):558–569.

Martinetz, T. and Schulten, K. (1991). A "neural-gas" network learns topologies. *Artificial Neural Networks*, pages 397–402.

Sato, A. and Yamada, K. (1995). Generalized Learning Vector Quantization. In Tesauro, G., Touretzky, D., and Leen, T., editors, *Advances in Neural Information Processing Systems 7 (NIPS)*, volume 7, pages 423–429. MIT Press.

Villmann, T. and Claussen, J. (2006). Magnification control in self-organizing maps and neural gas. *Neural Computation*, 18(2):446–469.

Zhou, X., Kao, M.-C., and Wong, W. (2002). Transitive functional annotation by shortest-path analysis of gene expression data. *PNAS*, 99(20):12783–12788.

ENDOCARDIAL SEGMENTATION IN CONTRAST ECHOCARDIOGRAPHY VIDEO WITH DENSITY BASED SPATIO-TEMPORAL CLUSTERING

Prashant Bansod, U. B. Desai
SPANN Lab., Electrical Engg. Department, Indian Institute of Technology, Bombay, India
ppbansod@iitb.ac.in, ubdesai@ee.iitb.ac.in

Nitin Burkule
Cardiologist, Asian Heart Hospital and Research Center, Mumbai, India
nitinburkule@prontomail.com

Keywords: Contrast echocardiography, Left ventricle, Segmentation, Spatio-temporal clustering.

Abstract: We present a spatio-temporal clustering algorithm for detection of endocardial contours in short axis (SAX) contrast echocardiographic image sequences. A semiautomatic method for segmentation of left ventricle in SAX videos is proposed which uses this algorithm and at the same time requires minimal expert intervention. Expert is required to specify a few candidate points belonging to the contour, only in the first frame of the sequence. The initial contour is approximated by fitting an ellipse in the region defined by the points specified. This region is identified as the principal cluster corresponding to the left ventriclular cavity. Later the density based clustering was applied for regularization on the inital contour. We have extended the DBSCAN algorithm for identification of the principal cluster corresponding to the left ventricle from the image. The algorithm also incorporates the temporal information from the adjacent frames during the segmentation process. The algorithm developed was applied to 10 data sets over full cardiac cycle and the results were validated by comparing computer generated boundaries to those manually outlined by one expert. The maximum error in the contours detected was $\pm 2.9mm$. The spatio-temporal clustering algorithm proposed in this paper offers an efficient semiautomatic segmentation of heart chambers in 2D contrast echocardiography sequences.

1 INTRODUCTION

Amongst the various medical imaging modalities, two dimensional (2D) echocardiography is valuable for patients with heart diseases. It is noninvasive, real time, easy to use in clinical environment and offers relatively low cost solution as compared to other modalities (Bridal et. al, 2003). However, for evaluation of cardiac functional parameters, segmentation is to be carried out. Manual segmentation as routinely carried by experts is time consuming and tedious due to large image data in different standard echo views over a full cardiac cycle. Again the manual method also suffers from inter-observer and intra-observer variability in measurements (Maes et. al, 1993). Many researchers have shown image processing applications to enhance clinical utility of echocardiography by automated and semiautomated endocardial border delineation and for evaluation of functional cardiac parameters (Noble and Boukerroui, 2006). In fact there is a continuous growing demand for the automated segmentation and quantification to support professionals in diagnosis. In recent years automated segmentation of heart chambers and in particular the left ventricle has received significant attention in 2D and 3D echocardiograms. However automatic edge definition and subsequent segmentation in echocardiograhic images is difficult due to presence of speckle noise, poor contrast, inherent dropouts, inter-cavity structures and variability of data along with orientation and positioning of transducer (Setaredhan and Soragham, 1996).

In recent years numerous clinical studies have shown the clinical utility of myocardial contrast echocardiography (MCE) in quantification of myocardial perfusion, left ventricle (LV) volumes, LV contours and cardiac functional parameters (Cohen et.al., 1998). There have been few reports of research attempts towards the semiautomatic and fully automatic segmentation of left ventricle from 2D contrast enhanced echo images (Wolfer et. al, 1999). A very rigorous work for the segmentation problem

in low mechanical-index contrast echocardiography is reported (Zwirn et. al, 2006). It has been shown that the use of temporal continuity results in better segmentation as it follows the approach of human expert in delineation (Mullet-Parada and Noble, 1998). Typically the dropouts present in the image can be recovered by the use of boundary information from the neighboring frames (Choy et. al, 1998). Researchers have reported active contour approach (Morales et. al, 2002), trained deformable models (Garcia et. al, 2003) and active shape model (Pickard et. al, 2004). Many of the proposed methods have shown results comparable to expert delineation for good quality images (Mishra et. al, 2003). However none of the methods has a generalized applicability for fully automatic or semiautomatic segmentation for the images acquired in routine clinical environment.

Few researchers have extended the application of well established data clustering approaches in the field of medical image segmentation (Celebi et. al, 2005). In this work we have extended the Density-based Clustering (DBSCAN) approach by including temporal data and applied for the segmentation of contrast echo sequences. Our spatio-temporal clustering algorithm has shown good results in the segmentation of endocardial borders in frames of a sequence by accommodating temporal information. The user intervention is minimal and is of the form of specifying five or more candidate points for contour on the first frame of the sequence.

The paper is organized as follows: In section II we discuss the density based clustering and its extension in spatio-temporal clustering technique. In section III, we present the application of the algorithm for segmentation of endocardial border after fitting the ellipse in the first frame through the points specified by the user and then to subsequent frames in the sequence. The contours thus obtained are post processed and smoothened to obtain final endocardial borders. In section IV we present the results of the proposed algorithm and, finally conclusions drawn and future work is discussed in Section VI.

2 CLUSTERING

Clustering is an important technique in data mining for finding data distributions and patterns in the underlying one or more dimensional data (Jain and Dubes, 1988). It has been a active field of research since last two decades and many novel approaches have been reported in the literature (Jain et. al, 1999). Clustering has number of upcoming application fields, such as statistical data analysis, pattern recognition, image processing, segmentation and many others. It is the task of grouping similar objects together with respect to a distance , connectivity, continuity, relative density in the space or other similarity measure.

In formal mathematical definition cluster is defined as (Fung, 2001): Let $X \in \mathbb{R}^{m \times n}$ be a set of data items representing a set of m points in x_i in $\mathbb{R}^n$. The goal is to partition X into K groups C_k such that every data that belongs to the same group are more alike than data in different groups. Each of the K groups is called a cluster. The result of the algorithm is an injective mapping $X \longmapsto C$ of data items X_i to clusters C_k. The number K might be preassigned by the user or it can be unknown determined by the algorithm . There are many approaches to data clustering that vary in their complexity and effectiveness. For our application we have focussed our attention on a single cluster $(K = 1)$, pertaining to the heart chamber specifically, the left ventricle in the contrast echcocardiographic view. In our work we call it as principal cluster. The assumption of defining only one principal cluster is valid because the spatial coordinates of the boundary objects of this principal cluster reflect the endocardial contour.

2.1 Dbscan for Principal Cluster

Density-based algorithms typically regard clusters as dense regions of objects in the data space separated by regions of low density. Thus the main objective lies in finding regions of high and low densities (Bradley and Fayyad, 1998). This approach is also capable of finding arbitrarily shaped clusters in the data space. Another advantage of these algorithms is that they are independent of the prior knowledge of the number of clusters. Hence these are very useful in situations very clustering can be confined to only in the region of interest (Han and Kamber, 1998). In contrast enhanced short axis echo sequence, the chamber cavities are filled with micro-bubbles which contribute in achieving their opacity. This results in a bright regions corresponding to the blood filled areas in an echo image (Fedele et. al, 1998). In the SAX images of the left ventricle (LV), a single bright region in the center of the acoustic window corresponds to the LV cavity. We treat this central bright region as a single cluster of interest. As stated earlier it is termed as the principal cluster for this application. The two global parameters of density based clustering algorithms are:

- Eps: Maximum radius of the neighborhood.
- $MinPts$: Minimum number of points in the Eps neighborhood of a point.

The ellipse fitted through the expert specified points in the first frames is taken as the starting point for the density based cluster algorithm. The maximum radius of the neighborhood Eps is chosen as half of the major axis of the ellipse. The parameter $MinPts$ was chosen to be 100 after a study of end systole images in 44 patients. The core point of the principal cluster is chosen as the center point of the ellipse fitted through the points specified by the expert in the first frame. We have chosen four local parameters for grouping the objects (pixels) in a cluster. These parameters include the features of the objects like pixel intensity, gradient threshold, gradient angle and the angular gradient with respect to the center point of the region. For cavity boundary, only negative intensity changes are identified along radial lines from center point. Again the threshold for gradient (G_T) was obtained automatically from the histogram statistics and the coordinates and intensities of the pixels specified by the expert. The algorithm for our application is framed as:

- *The center of the ellipse is taken as core point.*
- *The maximum radius is assigned the value of semi major axis in the first frame.*
- *Gradient threshold is obtained by histogram of the frame.*
- *Density reachable points around the core point are identified.*
- *Above steps are repeated for all the frames in the sequence.*
- *Border objects of the cluster are determined.*

2.2 Spatio-temporal Dbscan

An image is a 2-dimensional(2D) array of pixels defined on a $W \times H$ rectangular lattice $S = [\ (x,\ y) : 1 \leq x \leq W, 1 \leq y \leq H\ ]$, and is indexed by the coordinate $(x,\ y)$. Each pixel in a given frame can be represented by a feature vector. In a video stream, image frames are continuous along the time axis. Thus a video sequence can be expressed in spatio-temporal domain. Temporal dimension can be incorporated in many ways. One of the way is separating the frames of the sequence with respect to discrete time and to stack consecutively. We follow this approach in our application. In a video sequence, the frame to frame variation in shape and dimension of a given object depends upon its deformity and forces acting on it. Hence it is possible to recover a missing segment or to correct any outlier in the contour from the adjacent frames if the frame to frame variation is not significant. The outliers are detected with the radius of curvature of the extracted contour and the corresponding points in adjacent frames. We propose temporal continuity in the neighborhood of three frames:

1. For i^{th} frame the j^{th} border pixel will lie in the bounds setup by $(i-1)^{th}$ and $(i+1)^{th}$ frame.
2. Presence of drop out pixels in a frame was taken by temporal continuity from adjacent frames over an interval of three fames.

We have used parameter λ as the correction factor which governs the closeness of the corrected segment with the temporal frames. Correction is incorporated at 360 equidistant points on the contour i.e $j = [1,2,.....360]$. The clustering is recursively carried out to regroup the cluster on the basis of modified distance and density parameters. These parameters in turn are function of λ during recursive calls of DBSCAN.

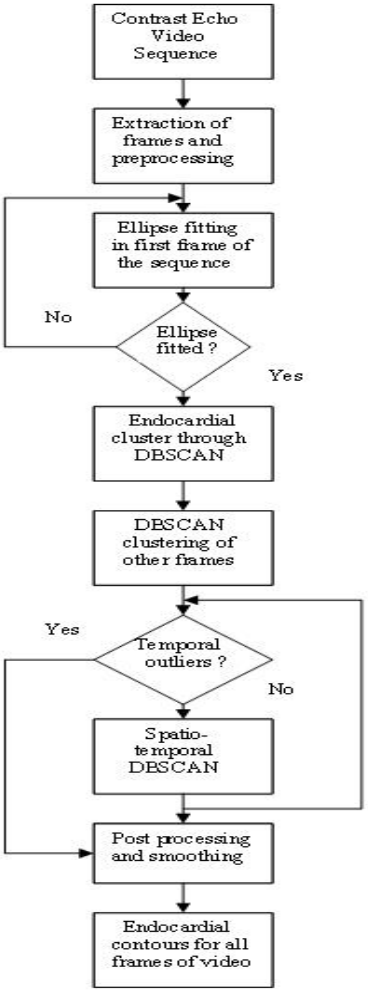

Figure 1: Flow chart for segmentation procedure.

3 SEGMENTATION WITH T-DBSCAN

In this work, we have applied the spatio-temporal clustering algorithm to segment the endocardial border in the contrast enhanced echocardiography videos of 10 patients. Figure 1. shows the flowchart of the segmentation procedure. After preprocessing of the image frames, user specifies candidate boundary pixels of the left ventricle in the first frame of the first frame of the sequence by mouse. The ellipse is fitted through these points and its parameters are stored for subsequent processing.

3.1 Image Processing

The echocardiographic videos used in this study were contrast enhanced short axis apical images at various levels of LV. These were obtained from different subjects for two to four cardiac cycles. The videos were acquired on GE Vingmed Ultrasound, VIVID7 in hospital environment under expert guidance. The frames in each video were 434 x 636 true color with 8 bit bitdepth in DICOM format. Gray scale conversion with 256 levels was done. The video sequences for one complete cardiac cycle were used for estimation of LV border. Echo images contain speckle noise which lead to incorrect gradient estimation. Hence speckle reducing anisotropic diffusion (SRAD) filtering was used (Yongjian and Scott, 2002). They have suggested edge sensitive diffusion for reducing speckles. In the numerical implementation we used $\delta t = 0.008$ and threshold of 5. This reduced the speckles and at the same time preserved the edge information for further feature extraction.

3.2 Elliptical Boundary Approximation

The Initial boundary approximation is carried out in the first frame of the sequence by fitting a ellipse through the points specified by the expert. The best fit ellipse through the points specified is done using Least Squares Criterion (Fitzgibbon et. al, 1999) A minimum of five points are to be specified by the expert, which strongly belong to the endocardial border for that particular frame. This is the only user intervention which is required in our scheme. The standard *impixel* function of MATLAB is used which gives the spatial coordinates of the selected points along with their intensities. The intensities returned by the function were used in the subsequent procedure for the search.

The generalized CONIC equation of the Ellipse is given by:

$$ax^2 + by^2 + cx + dy + exy + f = 0 \qquad (1)$$

with a, b and c not all zero and $b^2 < 4ac$, where all of the coefficients are real. Again, more than one solution, defining a pair of points (x, y) on the ellipse, exists. It can be expressed in matrix notation as;

$$\mathbf{X^T A X} = 0 \qquad (2)$$

where $\mathbf{X}$ and $\mathbf{A}$ are given by

$$\mathbf{X} = [1\ x\ y]' \qquad (3)$$

$$\mathbf{A} = \begin{bmatrix} f & 0.5c & 0.5d \\ 0.5c & a & 0.5e \\ 0.5d & 0.5e & b \end{bmatrix} \qquad (4)$$

The coordinates of the N chosen points $(N >= 5)$ as marked by the expert and the equations (2-4) are used for the determination of the parameter matrix of the conic representation. The orientation and tilt of the ellipse is sought by coefficients in the equation (1) and incorporated in the evaluation of final ellipse parameters using square completion method. Figure 2 shows the first frame of SAX apical sequence with the detected ellipse and its center point.

Figure 2: Ellipse Fitted in the first frame of the sequence.

3.3 Spatio-temporal Clustering

The DBSCAN clustering algorithms is recursively called for incorporating corrections in the outliers with the parameter λ. In our implementation we have used $\lambda = 0.5$ distance units, which gave optimum results.

3.4 Post Processing and Smoothing

The contour thus obtained was smoothed out by locally weighted scatter plot smoothing using least squares linear polynomial fitting. A span of 10 *percent* was used to implement this standard

MATLAB function. Further smoothing was carried out by fitting spline through the data points with minimizing the maximum square distance between the data points.

Figure 3: Detected contour in frame No.1.

Figure 4: Detected contour in frame No.8.

Figure 5: Detected contour in frame No.15.

4 EXPERIMENTAL RESULTS

The proposed methods for ellipse fitting, DBSCAN and Spatio-temporal DBSCAN were implemented in MATLAB 2006a on P-IV 2.1 GHz PC. Figures 3 to 7 show the result of application of the proposed algorithm. The endocardial border estimation was done on more than 10 video sequences of various standard contrast echo views. The contour estimated by computer in each frame of every sequence was compared with that drawn by expert.

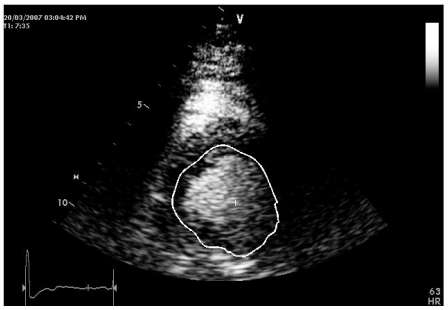

Figure 6: Detected contour in frame No.25.

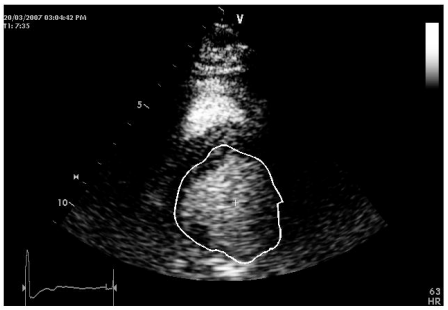

Figure 7: Detected contour in frame No.32.

5 CONCLUSIONS

The proposed method for semi automatic estimation of endocardial border of heart chambers in short axis contrast echocardiographic sequences is based on ellipse fitting and subsequent spatio-temporal recursive density-based clustering. The results show the effectiveness of the method and its utility in the recovery of the dropouts during image acquisition. The method requires user intervention only in the first frame of the sequence. The contour for each frame so obtained may be utilized for the determination of the cardiac parameters like, wall motion, area and for 3D visualization. Further work is required before the method can be employed in clinical environment for evaluation of cardiac functional parameters. The issues involved are the testing robustness, computational complexity of the method along with its sensitivity to the expert points. The algorithm requires fine tuning of parameter λ for determination of optimum number of iterations. In future work, we also intend to test the proposed method on large number of data sets for its further validation for images acquired in routine clinical environment.

ACKNOWLEDGEMENTS

The authors would like to thank Echocardiology department of Asian Heart Hospital, Mumbai for extending its support for contrast echo data and suggestions during analysis and interpretation.

REFERENCES

S.L.Bridal, S.L. Correas, Saied, A. and Laugier, P.(2003) Milestones on the road to higher resolution, quantitative, and functional ultrasonic imaging. In *Proc. IEEE*,vol.91, no.10, pp.1543-1561.

Maes, L. Bijnens, B. Suetens, P. and Verf, F.V. Automatic Contour Detection of the Left Ventricle in short Axis views in 2D Echocardiograms. In *Machine vision and Applications, Springer-Verlag.*, 6:1-9.

Noble, J.A. and Boukerroui, D.(2006). Ultrasound Image Segmentation: A Survey. In *IEEE Trans. Med. Imag.*, vol. 25, pp. 987-1010.

Setaredhan, S. K. and Soragham, J. J.,(1996) Automatic Cardiac LV Boundary Detection and Tracking Using Hybrid Fuzzy Temporal and Fuzzy Multiscale Edge Detection. In *IEEE Trans. Med. Imag.*, vol. 46, pp. 1364-1378.

JL Cohen et.al.(1998) Improved left ventricular endocardial border delineation and opacification with optison, a new echocardiographic contrast agent. In *J Am Coll Cardiol*, 32, pp: 746:752.

Wolfer, J. Lee, SH. Sandelski, J. Summerscales, R. Soble, J. and Roberge, J.(1999) Endocardial Border Detection in Contrast Enhanced Echocardiographic Cineloops using a Pulse Coupled Neural Networks. In *IEEE Conference on Computers in Cardiology*, pp. 185-188.

Zwirn, G. Beeri, R. Gilon, D. and Akselrod, S.(2006). Automatic Endocardial-Boundary Detection in Low Mechanical-Index Contrast Echocardiography. In *IEEE Trans.on Biomedical Engg.*, Vol.53, No. 11, pp:2310- 2322.

Mulet-Parada, M and Noble, J.A.(1998). 2D+T Acoustic Boundary Detection in Echocardiography. In *MICCAI'98.* LNCS 1496, pp. 806-813.

Choy, M.M. and Jin, J.S.(1998) Extracting endocardial Borders from sequential Echocardiographic Images. In *IEEE Engineering in Medicine and Biology*, pp. 116-121.

MA Morales, MA. Positano, V. Rodriguez, O. Passera, M. Lombardi, M. and Rovai, D., (2002) Tracking of the Left Ventricle in Contrast Enhanced Echocardiography by Anisotropic Filtering and Active Contours Algorithm. In *IEEE Conference on Computers in Cardiology*, pp. 65-68.

Garcia,J. Rotger, D. Carreras, F. Leta, R. and Radeva, P. (2003) Contrast Echography Segmentation and Tracking by Trained Deformable Models In *IEEE Conference on Computers in Cardiology*, pp. 173-176.

J.E. Pickard, J.E. R.L. Janiiczek, R.L. S.T. Acton, S.T. J. Sklenar, J. J.A. Hossack, J.A. and S. Kaul, S.,(2004) Segmentation of the Myocardium from Myocardial Contrast Echocardiography. In IEEE Conference on Signals, Systems and Computers, Volume 2, pp: 1616-1619.

Mishra, A. Dutta, P. Ghosh, M.K.(2003) A GA Based Approach for boundary Detection of Left Ventricle with Echocardiographic Image Sequences, In *Image and vision Computing* vol.21, pp. 967-976.

Celebi, M.E. Aslandogan, Y.A. and Bergstresser, P.R.(2005) Mining biomedical Images with Density-based Clustering. In *Proceedings of IEEE Conference on Information Technology: Coding and Computing(ITCC05)*.

Jain, A.K. Dubes, R.C. (1998). *Algorithms for Clustering Data*. Prentice Hall, Upper Saddle River, New Jersy.

Fung, G. (2001) A Comprehensive Overview of Basic Clustering Algorithms In *Technical Report*

Jain, A.K. Murty, M.N. Flynn, P.J.(1999). *Data Clustering: a Review*. In ACM Surveys, 31(3):264-323.

Bradley, PS. Fayyad, U. and Reinna, C.(1998) Scaling Clustering algorithms to large data bases.

Han,J. and Kamber, M. (1998) Data Mining: Concepts and Techniques. *Morgan Kaufmann, San Francisco*, 2000.

Fedele F, Trambaiolo P, Magni G, De Castro S and Cacciotti L, New modalities of regional and global left ventricular function analysis;State of the art. In *American Journal of Cardiology*, 81:49G-57G.

Yu, Y. and Acton, S.T., (2002) Speckle Reducing Anisotropic Diffusion In *IEEE Trans.Image Processing.*,vol 11,No.11, pp. 126-1270.

Fitzgibbon, A. Pilu, M. and Fisher, R.B. (1999) Direct Least Square fitting of Ellipses, In *Pattern Analysis and Machine Intelligence*, vol.21, no.5.

LEVEL SET BRIAN SEGMENTATION WITH AGENT CLUSTERING FOR INITIALISATION

Fast Level Set Based MRI Tissue Segmentation with Termite-Like Agent Clustering for Parameter Initialization

David Feltell and Li Bai
School of Computer Science & IT, Nottingham University, Triumph Rd, Nottingham, UK
dzf@cs.ac.uk, bai@cs.ac.uk

Keywords: Level Set, Multi Agent Clustering, Image Segmentation.

Abstract: This paper presents a novel 3D brain segmentation method based on level sets and bio-inspired methodologies. Level set segmentation methods, although highly promising, require manual selection of seed positions and thereshold parameters, along with manual reinitialisation to a new level set surface for each candidate region. Here, the use of swarm intelligent mechanisms is used to provide all the statistical data and sample points required, allowing automatic initialisation of multiple level set solvers. This is shown by segmentation of white matter, grey matter and cerebro-spinal fluid in a simulated T1 MRI scan, followed by direct comparison between a commercial level application - FMRIB's FAST - and the ground truth anatomical model.

1 INTRODUCTION

The solution to initial value problems by level set methods has transformed the study of evolving interfaces and, along with the surge in available processing power, provides a unique and promising methodology for three-dimensional image segmentation. However, the initialization of surfaces and tuning of parameters almost universally requires human intervention. By using agent based clustering and segmentation algorithms, we can hope to automate this process to a large extent, thus no longer relying on expert knowledge or requiring multiple tedious trials for an acceptable result.

The paper begins by reviewing the history of level set methods, leading to the method currently used in this work. Following this is a brief review of the mechanisms of swarm intelligence, leading to previous attempts at data clustering and image segmentation using agent based principles. Next, the implementation details are given of the level set solver, followed by the agent-based initialization algorithm. Finally, preliminary results of the system are shown along with a discussion of its merits and the project's future direction.

1.1 Level Set Method

Level set methods for image segmentation rely on an evolving closed surface defined by a moving interface, the front, which expands from a point out into the image, fitting itself to the region it is released within, and smoothing any noise. Among the advantages of level set methods is the natural ability for a single surface to seemingly split apart and merge without losing its identity. To accomplish this we add a further spatial dimension, ϕ, to our problem space, then we can in effect have a single surface in $(n+1)$-dimensional space, even though from observation of n dimensions we see two or more spatially distinct closed surfaces. This is the essence of the level set method and allows for topological changes to be handled naturally. This is easily visualised in the 2D case: for example Figure 1, where two 2D surfaces are projected to a 3D volume, where it is shown they are mathematically part of the same object. Numerically, each point in space U includes a scalar ϕ that can vary dynamically as time progresses, via a speed function F. Functionally, by taking a slice at time t of all points in U where $\phi = 0$, we are taking the 0^{th} *level set* of the function ϕ.

If we initialise ϕ to the signed distance from an initial closed surface, then we can visualise ϕ as the height at a certain point, and all the points in space with a height of 0 make up our surface. Thus, as well as handling topological changes naturally, the level set approach also has the advantage that the gradient across the surface at any given point on the interface can be found using $\nabla\phi$, meaning the local curvature can be determined. A curvature term gives the signed

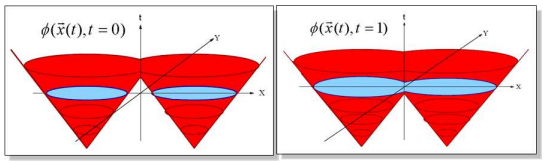

Figure 1: Illustration of level set function surface S (red) and evolution of moving interface/zero level set (blue). Topological change of two separate fronts (left) into a single front (right) handled naturally via higher dimensional function. After (Sethian, 1996).

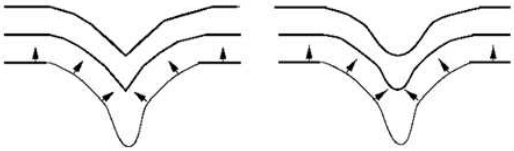

Figure 2: Illustration of surface evolution without curvature (left) and using a curvature term (right). After (Sethian, 1996).

'sharpness' of the interface at a point, allowing for a smoothing effect, overcoming noise and preventing leaks. This is illustrated in Figure 2. The typical formulation for the ϕ update function then becomes:

$$\phi_t = |\nabla\phi|(\alpha F + (1-\alpha)\nabla \bullet \frac{\nabla\phi}{|\nabla\phi|}) \qquad (1)$$

Where: ϕ_t is the time derivative of ϕ; α controls the the level of smoothness in the surface; F is the data-dependent speed function; $\nabla \bullet \frac{\nabla\phi}{|\nabla\phi|}$ gives local curvature at a given point.

Updating the values of ϕ at each point in space requires a numerical technique to evolve the zero level set from an initial specification. Naively then, we could initialise a surface in space, create a suitable speed function F, and numerically integrate until some condition is met and the surface extracted as all points where $\phi = 0$ (for example (Phillips, 1999)). An advantage here is sub-cell accuracy - the ϕ values can be interpolated to find points on a scale that is more accurate than the discrete embedding it is operating within. The first problem here is that the whole state-space must be evaluated each iteration, rather than just the surface. Secondly a small timestep is required to prevent numerical instabilities. These two caveats make the naive method undesirable for use outside of specialist fields.

Algorithms have been developed to overcome these issues by only performing updates on regions near the surface, rather than integrating over the entire state space. The most well-known is the Narrow Band approach (D. Adalsteinsson, 1995; Sethian, 1999), where numerical integration is performed within a band of points initialised around the surface, though when the zero level set reaches the edge of this band, the band must be reset. This dramatically increases efficiency over the naive method, with little or no effect on accuracy. However, further optimization in this vein has come in the form of the Sparse Field approach (Whitaker, 1998). With this method the narrow band is reduced to the smallest workable size and the reinitialisation requirement is based on a purely local update, rather than a global update of the entire band. The reduction in accuracy is tolerable for most applications and its implementation has allowed the level set family of methods to achieve real-time performance levels in complex 3D applications (for example see (Lefohn et al., 2003; Lefohn et al., 2004)).

The Sparse Field approach has been taken even further in the work of (Karl, 2005), and is the method presented here. In this work the narrow band is lowered to simply two linked lists operating in a discrete space, L_{in} and L_{out}, representing the inside and outside boundaries of the zero level set, respectively. No attempt at sub-cell accuracy is made and most operations use integer math. The values of ϕ are also kept constant depending on their status and are updated discretely. There are four such values representing inside, inside edge, outside edge, and outside the volume, set so that a rough gradient can be found at any point (for example: $3, 1, -1, -3$, respectively). The level set algorithm approximation itself is implemented in a two-pass process:

In the first pass elements in L_{in} and L_{out} are checked using the speed function F. If an expansion/contraction is provoked, the relevant list element is switched to the opposing list. If an element finds itself surrounded by cells with ϕ values of opposite sign, it is removed from its list. This fact allows for splits and merges in the topology.

The second phase involves an approximate Gaussian smoothing term G, that is, taking the (weighted) average of ϕ values from the area surrounding an element of L_{in} or L_{out}. Depending on the outcome of G, expansion/contraction adjustments to the lists and ϕ values are performed, similar to expansion via F. This has the effect of smoothing away noise as well as sharp protuberances in the surface.

Unlike previous algorithms, the process of expansion via the speed function and contraction via curvature are not intrinsically linked into the same update. In this algorithm, F is run on L_{in} and L_{out} a number of times. After this initial expansion phase a number of G runs are similarly done on L_{in} and L_{out}. The ratio of F to G runs determines the smoothness of the solution (in an analogue to the α parameter in (1)).

Further optimization can be made when the ratio of F runs is much higher than G runs. Elements visited on the list that have reached a locally optimal position will remain in that position on the next run of the speed function. Therefore they can be removed from successive F runs on that pass.

As mentioned in their paper title, this method departs almost entirely from the PDE based methods, but maintains many of the advantages. Sub cell accuracy is not possible in this generic form, but it would a simple addition to use this method as a prototype generator for slower, but more accurate methods. The inclusion of the ϕ embedding, albeit much simplified, allows local topology to be determined at any point to discrete-level accuracy. Thus, the Gaussian function has the information required to approximate the 'sharpness' at a point, and to expand or contract as a result (in a reasonable approximation to the effect of curvature). The lack of the requirement to solve PDEs holds several advantages. No timestep is required in the update process - the algorithm is entirely discrete. The method maintains the implicit ability of splits and merges along the front, without relying on any gradient calculation, eliminating the need for expensive entropy-satisfying spatial derivative schemes.

Parameter selection for level set segmentation generally requires at least some level of human interaction. Specifically in the case of image segmentation, initialization of a level set solver requires at minimum seed locations, an ideal data value, and an acceptable noise threshold to be preset. Also, differing data classes in the same problem space, for example tissue types in medical scans, each require their own level set surface with their own set of initialization parameters. Ideally the task of assigning seed locations and calculating level set parameters would be automated. These issues lend themselves well to an agent based approach, which will be discussed in the following section.

1.2 Multi-Agent Swarm Based Algorithms

Agents are independent entities existing in some environment - sensing, processing and modifying the environment based on internal reasoning. For multi-agent systems, the swarm intelligence and self-organisation paradigms have become popularized in many disciplines as an explanation for the apparent mismatch in complexity of agent versus complexity of task (Camazine et al., 2001), and as a unique engineering metaphor (Bonabeau et al., 1999). Such systems of agents can focus on simple stimulus-response functions using purely local stimuli with little or no cognition or direct communication. Tasks are accomplished by exploiting the non-linearity inherent in such a massively parallel system, rather than relying on individual agent complexity. An agent modifying the environment at a particular location allows another agent in that same location at a later time to sense this new state and respond accordingly. In this way the environment is used for indirect communication, termed *stigmergy*. Stigmergy in biological systems is further enhanced by the complexity of the environment, for example diffusion is utilized in many biological processes to spread information in the form of chemical gradients. Activation/attraction and inhibition/repulsion functions can thus be designed to control agent interactions based solely on local environmental state and any internal state, relying on quantitative information reinforcement and decay as well as qualitative signaling via the environment to control the weighting between possible responses. A global-level task or structure may then be many times more complex than an individual can perceive or accomplish, yet through parallel application of simple rules with indirect non-linear couplings, we see the spontaneous emergence of a solution. Given this non-linearity, a tiny change in a parameter can result in a drastically different solution, but (if the system is well formed) one that still conforms to a valid set of stable solutions - that is, the system exhibits *multistability*. We have demonstrated this engineering paradigm previously in modeling the building behaviour of *Macrotermes* termites (Feltell and Bai, 2004; Feltell et al., 2005). The use of an attractive cement pheromone to coordinate soil clustering behaviour has provided the inspiration for the swarm-intelligent clustering mechanism used here.

Swarm based clustering algorithms have been developed to cluster sets of n-dimensional data, generally projected onto a 2D grid, by taking inspiration from brood sorting and corpse clustering in ants (Monmarche et al., 1999; Monmarche, 1999; Kanade and Hall, 2003; Schockaert et al., 2004) as well as building behaviour in termites (Vizine et al., 2005). The approach does not need any prior knowledge of the problem space or number of clusters, and as a bonus gives a visual representation of the clusters on the 2D grid.

Agent based approaches have also been developed to directly segment an image, again using inspiration from natural systems such as ant pheromone trail networks (Ramos and Almeida, 2000), artificial life (Liu et al., 1997; Liu and Tang, 1999; Bocchi et al., 2005), social spiders (Bourjot et al., 2003), and even termites, bloodhounds and children (Fledelius and Mayoh, 2006). Here the agents interact directly

within the n-dimensions of the problem space, rather than outside it. This distinction from swarm based data clustering allows spatially localized regions to be processed independently - possibly requiring only a subset of the image space to be explored.

If the two perspectives can be combined, along with other swarm-inspired mechanisms, we could ideally form a localized data clustering algorithm, whereby ideal seed locations and other parameters would be found by agents within the image environment as they cluster similar voxels together.

Swarm intelligent systems emphasize robustness and diversity over accuracy, and so find solutions to complex problems that are 'good enough', but which require minimal agent capability in terms of both cognition and interaction. One of the major lures of level set algorithms is the tolerance for error, both in the problem space and, within limits, the initialization parameters. As long as 'good enough' seed location, ideal value and acceptable range parameters can be determined, the solution to the level set equations should be near-optimal in all but the hardest cases. With this assumption in mind, well located seeds can then be acceptable sample points used to approximate the voxel mean and range within a class.

2 IMPLEMENTATION

2.1 Level Set Solver

The level set solver is derived from the model of Shi & Karl (Karl, 2005). We define two sets of discretized points, representing the inside and outside layers between which lies the level set surface. As well as updating these sets as the surface expands or contracts we must maintain the values of ϕ, such that $\phi = 3$ inside the volume enclosed by the level set surface, $\phi = 1$ along the inside layer, $\phi = -1$ along the outside layer, and $\phi = -3$ outside the volume (note: the sign is reversed here compared to the original algorithm to be more in line with other level set methodologies). Finally, we must ensure that no orphaned points exist. That is, inside points must always have at least one outside point adjacent to them, and similarly outside points must always have at least one inside point adjacent. The update routine for both inside and outside layers is similar, though varies in parameter value. Following is a summary of the general update routine:

Let:

- Current time step be t.
- Two sets of points defining our two discretized layers be S_i and S_j.
- ϕ constants in space be: b_i along S_i; b_j along S_j; a_i in the volume beyond S_i; a_j in the volume beyond S_j.
- Three-dimensional cartesian point vector, $\mathbf{p} = (pi + pj + pk)$.
- Neighbourhood of $\mathbf{p}$, $N(\mathbf{p}) = \{(pi + i + pj + pk), (pi - i + pj + pk), (pi + pj + j + pk), (pi + pj - j + pk), (pi + pj + pk + k), (pi + pj + pk - k)\}$.
- Context dependent speed function, $F(\mathbf{p}) : \Re \longrightarrow \Re$, with condition f_i required for update to occur. Here and throughout this work it is assumed voxel intensity value is in $[0,1] \in \Re$.

Then, for each $\mathbf{p} \in S_i$, iff $F(\mathbf{p}) \Longrightarrow f_i$:

1. Increment time step, t.
$$t \longleftarrow t + 1 \tag{2}$$
2. $\mathbf{p}$ is added to S_j
$$S_j \longleftarrow \{S_j \cup \{\mathbf{p}\}\} \tag{3}$$
3. ϕ at point $\mathbf{p}$ is set to constant, b_j.
$$\phi(\mathbf{p},t) \longleftarrow b_j \tag{4}$$
4. $\mathbf{p}$ is removed from S_i, whilst all relevant neighbours of $\mathbf{p}$ are added to S_i.
$$S_i \longleftarrow \{S_i - \{\mathbf{p}\}\} \cup \{\forall \mathbf{r} \in N(\mathbf{p}) \mid \phi(\mathbf{r},t) = a_i\} \tag{5}$$
5. ϕ at all relevant neighbours of point $\mathbf{p}$ is set to constant, b_i.
$$\phi(\{\mathbf{r} \mid \phi(\mathbf{r},t) = a_i\},t) \longleftarrow b_i, \forall \mathbf{r} \in N(\mathbf{p}) \tag{6}$$
6. All points in S_i that are in not neighboured by a point in S_j are orphaned points and must be removed.
$$S_i \longleftarrow S_i - \{\forall \mathbf{r} \in S_i \mid N(\mathbf{r}) \cap S_j = \emptyset\} \tag{7}$$
7. ϕ at all orphaned points in S_i is set to constant, a_j.
$$\phi(\{\mathbf{r} \mid N(\mathbf{r}) \cap S_j = \emptyset\},t) \longleftarrow a_j, \forall \mathbf{r} \in S_i \tag{8}$$

In practice, all these steps can be combined into a single update loop. The update loop is performed on both the inside and outside layers. Let our inside surface be S_{in} and the outside surface be S_{out}, then: $a_{in} = 3$, $a_{out} = -3$, $b_{in} = 1$, $b_{out} = -1$, $f_{in} \Leftrightarrow (F(\mathbf{p}) > 0)$, $f_{out} \Leftrightarrow (F(\mathbf{p}) < 0)$. The steps (3)..(6) deal with the surface evolution. The steps (7) and (8) handle shock propagation, that is, they remove points as the curve crosses over itself to maintain an unambiguous closed surface.

The algorithm is then:

Let:

- $D(\mathbf{p})$ be the problem specific data term, specifically the voxel gray level value at point $\mathbf{p}$.
- $J(\mathbf{p})$ be the problem specific speed function, specifically: $J(\mathbf{p}) = 1$ for $|(D(\mathbf{p}) - T)| < \varepsilon$ and $J(\mathbf{p}) = -1$ for $|(D(\mathbf{p}) - T)| > \varepsilon$, where: T is the ideal data value; ε is the acceptable error.
- $G(\mathbf{p})$ be a Gaussian smoothing approximation, specifically $G(\mathbf{p}) = \big(\phi(\mathbf{p},t) + \sum_{\mathbf{r}\in N(\mathbf{p})} \phi(\mathbf{r},t)\big)/7$. With the condition $G(\mathbf{p}) = 0$ iff $|G(\mathbf{p})| < 1$, tighter areas can be explored, as smoother curves will neither contract nor expand. This produces more accurate solutions in most cases, but tends to give less smooth surfaces.
- t_J be the number of speed runs to perform; t_G be the number of Gaussian smoothing runs to perform.

Then:

A Initialize S_{in} and S_{out} to small surface(s) about given seed locations.

B Perform (2)..(8) with: $i = out$; $j = in$; $F(\mathbf{p}) = J(\mathbf{p})$.

C Perform (2)..(8) with $i = in$; $j = out$; $F(\mathbf{p}) = J(\mathbf{p})$.

D Repeat from (B) while $t < t_J$.

E Perform (2)..(8) with: $i = out$; $j = in$; $F(\mathbf{p}) = G(\mathbf{p})$.

F Perform (2)..(8) with $i = in$; $j = out$; $F(\mathbf{p}) = G(\mathbf{p})$.

G Repeat from (E) while $t < t_J + t_G$.

H Set $t = 0$. Repeat from (B) for t_S iterations.

2.2 Swarm based Parameter Initialization

The parameter specification for the level set solver as well as the number of tissue types requiring individual segmentation is beyond the capability of a level set algorithm alone. Instead, in this work we show how we can use a collection of agents following similar rules to previous agent clustering algorithms, but with the agents embodied within the image space itself, finding good seed locations as well as performing minor preprocessing functions.

Agents have real-valued position and direction, using simple nearest neighbour approximation when sensing the underlying discrete image voxels. They wander the image in an initially random direction, however as they move they lay a quantity of attractive 'pheromone' in visited voxels. The quantity of pheromone is proportional to the divergence of voxel intensity $|\nabla^2 \cdot D|$ at their current location. A high divergence value often indicates a heterogeneity in the image - specifically an interface between two regions. Here, pheromone deposition further has the restriction $D > 0.1$ to avoid segmenting irrelevant black regions. Pheromone diffuses through the image lattice, with the edge of the lattice and near-black ($D < 0.1$) voxels acting as sinks. The addition of a positive reinforcement pheromone mechanism allows the agents to use gradient following behaviour in coordinating toward promising seed locations. As pheromone diffuses away it causes that area to receive less attention, ultimately meaning less suitable seed locations are abandoned. This reflects in many ways the clustering behaviour of termites in nest construction (Bruinsma, 1979), where heterogeneities stimulate deposits of soil laden with a cement pheromone, which in turn attracts other termite builders to the site.

This clustering behaviour, in the termite case, creates regular spaced piles or pillars of soil. Piles close to one-another thus compete for the termites attentions, eventually resulting in regularly spaced pillars. In this work, as with the termite paradigm, this mechanism means seed locations tend not to become too localised. The combined effect ultimately increases the agents' sampling efficiency within large images.

The generalised update routine for an individual agent is given as follows:

Let:

- t be the current time step of an agent.
- Real-valued point vector, $\mathbf{p}$ be the current position of an agent
- Scalar pheromone field, $\rho(\mathbf{p})$ be the pheromone concentration at location $\mathbf{p}$.
- Speed, s be a scalar speed value for the agent.
- Vector $\mathbf{v}$ be the continuous direction vector of the agent.

Then:

1. Increment time step, t.
$$t \longleftarrow t + 1 \tag{9}$$
2. Lay pheromone proportional to the logarithm of the absolute divergence. Logarithmic scale is used here to avoid floating point accuracy overflow.
$$\log(\rho(\mathbf{p})) \longleftarrow \log\big(\rho(\mathbf{p}) + |\nabla^2 D(\mathbf{p})|\big) \tag{10}$$
3. Calculate new direction vector from weighted gradient of $\log\rho$.
$$\mathbf{v} \longleftarrow \mathbf{v} + \alpha(\mathbf{v} - \nabla \log\rho) \tag{11}$$

4. Calculate speed scalar based on local density of ρ.

$$s \longleftarrow 1 + \frac{\beta}{1 + \log(\rho(\mathbf{p}))} \tag{12}$$

5. Calculate updated position based on normalized direction vector and speed value.

$$\mathbf{p} \longleftarrow \mathbf{p} + \frac{\mathbf{v}}{||\mathbf{v}||} \cdot s \tag{13}$$

Where: α is the weighting of pheromone gradients in movement; β controls the maximum speed of an agent.

The full agent algorithm is then:

A Initialize set of n agents, M, each with random position within the image and random direction.

B Perform (9)..(13) for each $m \in M$.

C Diffuse pheromone: $\partial_t \rho = d \cdot \nabla^2 \rho$

D Repeat from (B) while $t < t_A$ time steps.

E Select the top C voxel locations with highest pheromone level ρ, to get full seed list, Q.

F Run k-means clustering on Q, classifying into prespecified number of sets, Q_i, where $i = \{1,2,..,q\}$.

G Within each Q_i calculate mean $\mu(Q_i)$ and standard deviation $\sigma(Q_i)$, giving ideal data value $T = \mu(Q_i)$ and error threshold $\varepsilon = \sigma(Q_i) + k$, where k is a constant, within a class.

Once T and ε have been calculated for a seed set Q_i, the level set routine can be run, initialising L_{in} and L_{out} surfaces as pseudo-spheres about each seed location in Q_i. The agent algorithm need only be run once, then the level set algorithm run once for each seed set.

Additionally, in practice the diffusion step can be moved into a separate thread to take advantage of modern day multiple core processors. With the simplest distributed setup, with little control on synchronization or load balancing, the algorithm can still function correctly - an implicit advantage of the robust swarm metaphor.

The image is finally extracted as all voxel positions where $\phi > 0$, thus all points lying on and within L_{in}.

3 RESULTS

The dataset used comes from BrainWeb's online MRI simulator (McConnell BIC, 2007) with default parameters: modality T1, slice thickness 1mm, noise 3% and non-uniform intensity 20%. For comparison with ground truth and FAST (Zhang et al., 2001) the number of classes is set $q = 3$. The various parameters, unless otherwise stated, are set as follows:

$\alpha = 2; \beta = 2.5; d = 0.015; k = 0.02; t_S = 10; t_A = 3000; t_J = 30; t_G = 3$

The parameter values above for α, β, d and k, were found in part using a real-valued genetic algorithm, using the similarity to the ground truth images, minus the similarity between one another, as a fitness function. This process has proven useful so far, yet is only partially utilised here and remains a direction for future work. Other values are chosen intuitively to balance execution time and accuracy.

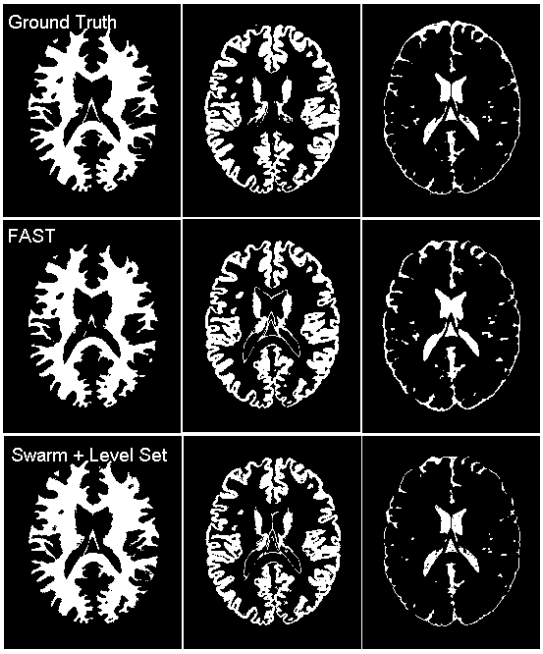

Figure 3: Comparison of ground truth to FAST and the swarm initialised level set solution presented here. Images used in both FAST and the present work have been preprocessed by BET. From left to right: white matter; gray matter; cerebro-spinal fluid.

From Figure 3 it can be seen how the approach, even in this early stage, can compete with popular solutions such as FMRIB's FAST, which uses a method based on Markov random fields. In both solutions, preprocessing has been performed using FMRIB's popular BET (Smith, 2002) to skull strip and normalise the image voxels.

Quantitative measurement on accuracy is approximately possible given the hand segmented ground truth images available. In the above case, FAST achieves approximately 92%, 85% and 57% accuracy, whereas the swarm initialised level set algorithm

achieves 86%, 83% and 55%, for white matter, grey matter and cerebro spinal fluid, respectively. FAST remains superior, but the small score difference certainly indicates the presented approach is well worth further investigation.

In terms of execution time, from the point of file loading to final file output, FAST outdoes the performance of the presented work by just over double. The above solution was found by the swarm initialised level set algorithm in approximately 17 mins, whereas FAST finished in approximately 8 mins. It is worth noting that the swarm approach presented is still in early development, and as discussed in the next section, has the advantage of naturally supporting a distributed implementation.

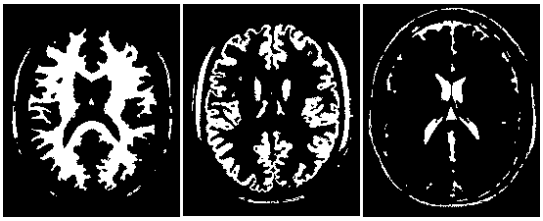

Figure 4: Solution found using current algorithm without BET preprocessing. All parameters are set similar - the number of classes remaining at 3. From left to right: white matter, gray matter, cerebro-spinal fluid.

4 DISCUSSION AND FUTURE WORK

The level set solver is an approximate discrete solution to a continuous problem. Although the algorithm used in this work is particularly fast, it simply does not have the power of a narrow band or even sparse field approach. These methods not only reflect the naive approach more directly, but also have sub-cell accuracy, where actual surface points can be interpolated within image voxels using the real-valued gradient of ϕ. They can also vary in speed along different areas of the surface, allowing for a more global curvature force effect. The discretisation of ϕ values to simply the set $\{-3,-1,1,3\}$ means the curvature term is much more rigid, and does not distinguish on a local level between corners of differing sharpness. Ideally the current level set solver approximation would work as a rapid prototype for a more accurate narrow band based method. This remains a direction for future work.

One benefit of using a swarm based system is in the robustness to a noisy environment. In this regard it should be possible to include an atlas mechanism, using only the most minimal registration with the candidate image, and restrict agent interaction within or near the atlas template for a given region. This would give the agents' environment a significant amount of extra information, which can be used to focus agent efforts - increasing efficiency and allowing for segmentation of more difficult (too smooth/too noisy) regions.

The preprocessing by BET could be removed for future versions. BET simplifies segmentation significantly, and prevents areas such as the skull being segmented as part of brain matter. However, preliminary results of segmentation without BET preprocessing are promising in their own right, though show several mismatched regions (see Figure 4), and it is likely that with more classes and ground truth samples, along with evolutionary algorithm parameter tuning, the method can be applied to multiple modalities and varying image spaces without the need for any preprocessing.

Another benefit of the multi-agent paradigm is its naturally distributed nature. As has been eluded to, the diffusion of pheromone can already be ported to another processing unit to greatly increase efficiency. A further extension could see the image space and/or agents split to run parallel. Certainly each region's level set solver could in future run on separate processes to dramatically decrease execution time.

REFERENCES

Bocchi, L., Ballerini, L., and Hssler, S. (2005). A new evolutionary algorithm for image segmentation. *Applications on Evolutionary Computing*, pages 264–273.

Bonabeau, E., Dorigo, M., and Theraulaz, G. (1999). *Swarm Intelligence: From Natural to Artificial Systems*. Oxford University Press.

Bourjot, C., Chevrier, V., and Thomas, V. (2003). A new swarm mechanism based on social spiders colonies: From web weaving to region detection. *Web Intelligence and Agent System*, 1(1):13–32.

Bruinsma, O. (1979). *An Analysis of Building Behaviour of the Termite Macrotermes Subhyalinus (Rambur)*. PhD thesis, Landbouwhogeschool, Wageningen.

Camazine, S., Deneubourg, J.-L., Franks, N., Sneyd, J., Theraulaz, G., and Bonabeau, E. (2001). *Self-Organization in Biological Systems*. Princeton University Press.

D. Adalsteinsson, J. S. (1995). A fast level set method for propagating interfaces. *J. Comp. Phys.*, 118:269–277.

Feltell, D. and Bai, L. (2004). Swarm robotics for construction. In *24th SGAI International Conference on Innovative Techniques and Applications of Artificial Intelligence*, Cambridge, UK.

Feltell, D., Bai, L., and Soar, R. (2005). Bio-inspired emergent construction. In *IEEE 2nd Intl. Swarm Intelligence Symposium*, Pasadena, CA, USA.

Fledelius, W. and Mayoh, B. (2006). A swarm based approach to medical image analysis. In *24th IASTED International Conference on Artificial Intelligence and Applications (AIA 2006)*, pages 150–155, Anaheim, CA, USA. ACTA Press.

Kanade, P. and Hall, L. (2003). Fuzzy ants as a clustering concept. In *22nd International Conference of the North American Fuzzy Information Processing Society (NAFIPS)*, pages 227–232.

Karl, Y. S. W. (2005). A fast level set method without solving pdes. In *IEEE International Conference on Acoustics, Speech, and Signal Processing (ICASSP 2005)*, volume 2, pages 97–100.

Lefohn, A. E., Cates, J. E., and Whitaker, R. T. (2003). Interactive, gpu-based level sets for 3d segmentation. In *Medical Image Computing and Computer-Assisted Intervention (MICCAI 2003)*, pages 564–572.

Lefohn, A. E., Kniss, J. M., Hansen, C. D., and Whitaker, R. T. (2004). A streaming narrow-band algorithm: Interactive computation and visualization of level sets. *IEEE Transactions on Visualization and Computer Graphics*, 10:422–433.

Liu, J. and Tang, Y. (1999). Adaptive image segmentation with distributed behavior-based agents. *IEEE Transactions on Pattern Analysis and Machine Intelligence*, 21:544–551.

Liu, J., Tang, Y., and Cao, Y. (1997). An evolutionary autonomous agents approach to image feature extraction. *IEEE Transactions on Evolutionary Computation*, 1:141–158.

McConnell BIC (2007). Brainweb: Simulated brain database, Montreal Neurological Institute. http://www.bic.mni.mcgill.ca/brainweb/.

Monmarche, N. (1999). On data clustering with artificial ants. In Freitas, A. A., editor, *Data Mining with Evolutionary Algorithms: Research Directions*, pages 23–26, Orlando, Florida. AAAI Press.

Monmarche, N., Slimane, M., and Venturini, G. (1999). On improving clustering in numerical databases with artificial ants. In *ECAL '99: Proceedings of the 5th European Conference on Advances in Artificial Life*, pages 626–635, London, UK. Springer-Verlag.

Phillips, C. L. (1999). The level set method. *The MIT Undergraduate Journal of Mathematics*, 1:155–164.

Ramos, V. and Almeida, F. (2000). Artificial ant colonies in digital image habitats - a mass behaviour effect study on pattern recognition. In *2nd Int. Workshop on Ant Algorithms (ANTS 2000)*, pages 113–116, Brussels, Belgium.

Schockaert, S., Cock, M. D., Cornelis, C., and Kerre, E. E. (2004). Fuzzy ant based clustering. In *International Workshop on Ant Colony Optimization and Swarm Intelligence (ANTS 2004)*, pages 342–349, Brussels, Belguim.

Sethian, J. (1996). Level set methods: An act of violence - evolving interfaces in geometry, fluid mechanics, computer vision and materials sciences. *American Scientist*.

Sethian, J. (1999). *Level Set Methods and Fast Marching Methods*. Cambridge University Press.

Smith, S. (2002). Fast robust automated brain extraction. *Human Brain Mapping*, 17(3):143–155.

Vizine, A., de Castro, L., Hruschka, E., and Gudwin, R. (2005). Towards improving clustering ants: An adaptive ant clustering algorithm. *Informatica*, 29(2):143–154.

Whitaker, R. (1998). A level-set approach to 3d reconstruction from range data. *International Journal of Computer Vision*, 29(3):203–231.

Zhang, Y., Brady, M., and Smith, S. (2001). Segmentation of brain mr images through a hidden markov random field model and the expectation maximization algorithm. *IEEE Trans. on Medical Imaging*, 20(1):45–57.

A REGION BASED METHODOLOGY FOR FACIAL EXPRESSION RECOGNITION

Anastasios C. Koutlas
Dept. of Medical Physics, Medical School, University of Ioannina, Ioannina, Greece
me01697@cc.uoi.gr

Dimitrios I. Fotiadis
Unit of Medical Technology and Intelligent Information Systems, Dept. of Computer Science
University of Ioannina, Ioannina, Greece
fotiadis@cs.uoi.gr

Keywords: Facial expression recognition, Gabor filters, filter bank, artificial neural networks, Japanese Female Facial Expression Database (JAFFE).

Abstract: Facial expression recognition is an active research field which accommodates the need of interaction between humans and machines in a broad field of subjects. This work investigates the performance of a multi-scale and multi-orientation Gabor Filter Bank constructed in such a way to avoid redundant information. A region based approach is employed using different neighbourhood size at the locations of 34 fiducial points. Furthermore, a reduced set of 19 fiducial points is used to model the face geometry. The use of Principal Component Analysis (PCA) is evaluated. The proposed methodology is evaluated for the classification of the 6 basic emotions proposed by Ekman considering neutral expression as the seventh emotion.

1 INTRODUCTION

Facial expression recognition is an active research field that spawns across different subjects such as Human Computer Interaction (HCI), Smart Environments and medical applications. Recognizing facial expressions is a difficult task and therefore several limitations exist such as limitation due to lighting conditions, facial occlusions or facial hair.

In 1971 Ekman et.al determined 6 basic emotions; anger, fear, surprise, happiness, disgust and sadness (Ekman and Friesen, 1971). The neutral face expression is usually considered as the seventh basic emotion. Basic emotions are universal and exist in different human ethnicities and cultures. Even though the term emotion is used for categorization, emotions do not rely solely on visual information (Fasel and Luettin, 2003).

The task of Facial Expression Recognition can be divided into three main steps which are face recognition so that the face in an image is known for further processing, facial feature extraction which is the method used to represent the facial expressions and finally classification which is the step that classifies the features extracted in the appropriate expressions.

In general there are two approaches to represent the face and consequently the facial features. The first, often referred to as holistic approach, treats the face as a whole. Essa (Essa and Petland, 1997) treated the face holistically using optical flow and measured deformations based on the face anatomy. Donato (Donato et. al. 1999) has used several methods for facial expression recognition. Fisher linear discriminates (FLD) were used to project the images in a space that provided the maximal separability between classes and Independent Component Analysis (ICA) to preserve higher order information.

Instead of using the whole face, one can isolate and use the prominent features of a face, such as eyes, eyebrows, mouth, etc. Using fiducial points to model the position of the prominent features one can symbolize the face geometry in a local manner. The number of fiducial points used varies and mainly depends on the desired representation, as it is reported that different positions hold different

information regarding the expressions (Lyons et. al., 1999). The way that these fiducial points are identified in an image can either be automatic (Gu et. al., 2005) or manual (Lyons et. al. 1999), (Guo and Dyer, 2005), (Zhang et. al. 1998).

It has been shown that simple cells in the primary visual cortex can be modeled by Gabor functions (Dougman, 1980), (Dougman, 1985). This solid physiological connection between Gabor functions and human vision has yielded several approaches to facial expression recognition (Lyons et. al. 1999), (Gu et. al., 2005), (Guo and Dyer, 2005), (Zhang et. al. 1998), (Liu and Wang, 2006), (Lyons and Akamatsu, 1998). Zhang (Zhang et. al., 1998) compared the Gabor function coefficients with the coordinate positions of the fiducial points and concluded that the first represent the face better than the latter. Donato (Donato et. al., 1999) reported that Gabor functions performed better than any other method used in both analytic and holistic approaches.

In this work we present a methodology for the classification of human emotions which is based on Gabor coefficients of the fiducial points. The methodology is based on Gabor coefficients which are extracted from a region around the fiducial points. It is noted in the literature that the feature vector is formed using single pixel values at the locations of the fiducial points. The proposed approach forms the feature vector from a region around each fiducial points gathering more information and avoiding in such a way artifacts which might exist close to the fiducial point. Furthermore, an alternate set of fiducial points is presented using just 19 landmark positions. We also attempted to reduce the number of fiducial points and to make the approach more efficient using PCA. The methodology is evaluated using the Japanese Female Facial Expression (JAFFE) database (Lyons and Akamatsu, 1998) in two cases: (a) using its full annotation and (b) excluding fear.

2 MATERIALS AND METHODS

The proposed methodology includes three stages (a) construction of the Gabor Filter Bank, (b) extraction of the Feature vector and (c) classification (Fig. 1).

2.1 Gabor Function

A two dimensional Gabor function $g(x,y)$ is the product of a 2-D Gaussian-shaped function referred as the envelop function and a complex exponential

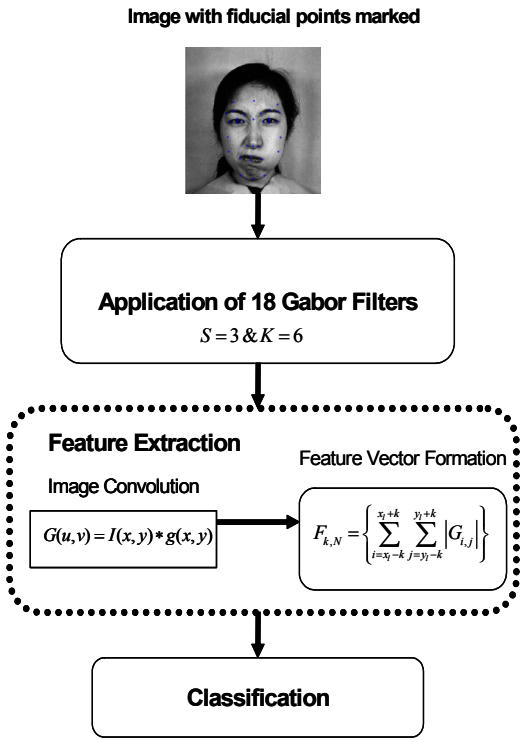

Figure 1: Flow chart of the proposed method.

(sinusoidal) known as the carrier and can be written as (Dougman, 1980), (Dougman, 1985), (Manjunath and Ma, 1996):

$$g(x,y)=\left(\frac{1}{2\pi\sigma_x\sigma_y}\right)\exp\left[-\frac{1}{2}\left(\frac{x^2}{\sigma_x^2}+\frac{y^2}{\sigma_y^2}\right)+2\pi jW\right], \quad (1)$$

where x,y are the image coordinates, σ_x,σ_y are the variances in the x,y coordinates respectively and W is the frequency of the sine wave.

Its Fourier Transform $G(u,v)$ can be written as:

$$G(u,v)=\exp\left\{-\frac{1}{2}\left[\frac{(u-W)^2}{\sigma_u^2}+\frac{v^2}{\sigma_v^2}\right]\right\}, \quad (2)$$

where $\sigma_u=1/2\pi\sigma_x$ and $\sigma_v=1/2\pi\sigma_y$.

2.2 Gabor Filter Bank

A Gabor filter bank can be defined as a series of Gabor filters at various scales and orientations. The application of each filter on an image produces for each pixel a response. The above representation (Eq. (1)) combines the even and odd Gabor functions as are defined in (Dougman, 1980).

If $g(x,y)$ is the mother function, we can derive the Filter bank functions using a series of rotations and dilations on the mother function:

$$g'(x,y) = g(x',y'), \quad \begin{pmatrix} x' \\ y' \end{pmatrix} = \begin{pmatrix} \cos\theta & -\sin\theta \\ \sin\theta & \cos\theta \end{pmatrix} \begin{pmatrix} x \\ y \end{pmatrix}, \tag{3}$$

where $\theta = n\pi / K$, K is the total number of orientations and $n = 0, 1, \ldots, K-1$.

Manjunathan showed that Gabor filters form a nonorthogonal basis and that redundant information is included in the images produced by the filter (Manjunath and Ma, 1996), (Guo and Dyer, 2005). This leads to the following equations for the filter parameters a, σ_u and σ_v:

$$a = \left(\frac{U_h}{U_l}\right)^{\frac{1}{S-1}}, \quad W = a^m U_l, \tag{4}$$

$$\sigma_u = \frac{(a-1)W}{(a+1)\sqrt{2\ln 2}}, \tag{5}$$

$$\sigma_v = \tan\left(\pi/2K\right)\sqrt{\frac{W^2}{2\ln 2} - \sigma_u}, \tag{6}$$

where a is the scaling factor, S is the number of scales, $m = 0, 1, \ldots, S-1$, and U_h and U_l are the high and low frequencies of interest.

In this work we have chosen $U_h = \sqrt{2}/4$, $U_l = \sqrt{2}/16$ with three scales ($S = 3$) and six orientations ($K = 6$) differing each by $\pi/6$. Thus 18 complex Gabor filters were defined in total which will be used to extract the feature vector for each image. In Figure 2 the real part of the resulting filters is displayed.

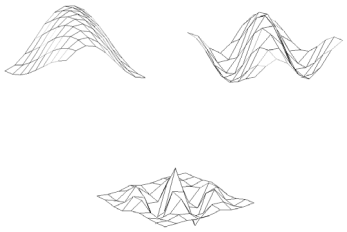

Figure 2: The real part of the Gabor filter when $\theta = 2\pi/6$ at all scales used.

2.3 Gabor Features

For any given image $I(x,y)$ its Gabor decomposition at any given scale and orientation can be obtained by convolving the image with the particular Gabor filter.

$$G(u,v) = I(x,y) * g(x,y) \tag{7}$$

The magnitude of the resulting complex image is given:

$$|G| = \sqrt{Re(G)^2 + Im(G)^2} \tag{8}$$

All features derive from $|G|$ and the feature vector $F_{k,N}$ is formed according to the following formula:

$$F_{k,N} = \left\{ \sum_{i=x_l-k}^{x_l+k} \sum_{j=y_l-k}^{y_l+k} |G_{i,j}| \right\}, \quad l = 0,1,..,N, \quad k = 0,1,..,5, \tag{9}$$

where N is the number of the fiducial points, equalled to 19 and 34 respectively here. k is the number of neighbouring pixels used to form the regions. The feature vector can be portrayed as a square 1-norm of the matrix when $k \neq 0$, which corresponds to the intensity values of the mask around each fiducial point.

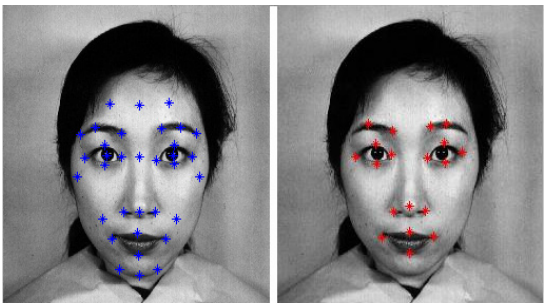

(a) (b)

Figure 3: Typical Positions of fiducial points (a) 34 points (b) 19 points.

2.4 Artificial Neural Networks

Artificial Neural Networks (ANNs) are well known classifiers and can be used in multi-class problems. In the presented work we employed feed forward back propagation ANNs. The architecture of the ANNs consists of three layers. The first layer (input layer) consist of T input nodes where T is the dimension of the feature vector ($F_{k,N} \in R^T$). The second layer (hidden layer) consists of $T+C/2$ neurons, where C is the number of the classes. The sigmoid function is used as activation function for these hidden neurons. Finally the third layer (output

layer) consists of C neurons. The activation function of the output neurons is the linear function. In order to train the ANNs the mean square error function is used and the number of epochs are 500.

2.5 Principal Component Analysis

In several cases T is quite large (for example when N in Eq. (9) is set to 34, the resulting feature vector has a dimension of 612). PCA is applied to reduce the input number features so that the retained features account for 95% of the total variance (sum of variances).

2.6 Dataset

The JAFFE (Lyons and Akamatsu, 1998) database was used for the evaluation of the proposed method. It features ten different Japanese women posing 3 or 4 examples for each basic emotion containing a total of 213 images. Including in the annotation of the dataset, neutral position is considered as a seventh basic emotion.

An alternate dataset derives from JAFFE database containing 181 images when fear is excluded. This can be justified in (Zhang et. al., 1998). Hereafter the two different datasets would be addressed as JAFFE-7 and JAFFE-6 with the latter excluding fear.

3 RESULTS

Several different sets of experiments were contacted with respect to:

i. The annotation used for classifications (i.e. either JAFFE-6 or JAFFE-7 datasets)
ii. The number of fiducial points used (N in Eq. (9) is equal to 19 or 34)
iii. The neighborhood size used to construct the feature vector (Single Pixel, 3x3, 5x5, 7x7, 9x9, 11x11)
iv. The employment or not of PCA for dimensionality reduction

The combination of the aforementioned sets leads to 48 different feature sets. For the evaluation the ten fold stratified cross validation method was used.

In the tables that will be presented below the abbreviations used correspond to the emotions, (SU for surprise, DI for disgust, FE for fear, HA for happy, NE for neutral, SA for sadness and finally AN for anger).

3.1 JAFFE-7

In this series of experiments the full annotation of the JAFFE dataset was used along with both facial representations (34 and 19 fiducial points). Table 1 displays the accuracy of each approach; the best performance was obtained when a neighborhood 11x11 of pixels was used with 34 fiducial points representing the face. When 19 fiducial points were used the accuracy declined only by 0.9% at max.

Table 1: Performance using the JAFFE-7 Dataset.

Region	34 Points	34 PCA	19 Points	19 PCA
Single Pixel	72.8%	53.5%	63.4%	47.4%
3x3	81.7%	74.6%	73.2%	60.1%
5x5	84.0%	79.3%	78.4%	71.4%
7x7	85.0%	78.9%	82.2%	73.7%
9x9	87.3%	82.6%	84.0%	80.8%
11x11	87.8%	83.6%	86.9%	82.6%

Table 2 displays the confusion matrix for the best performing approach. It can be seen that the poorest performance was obtained for the emotions of disgust and fear where the first was classified often as anger and the latter as sadness. Following the reasoning of Zhang (Zhang et. al., 1998) a second series of experiments were conducted.

Table 2: Confusion matrix for 34 fiducial points and 11x11 region.

	SU	DI	FE	HA	NE	SA	AN
SU	30	0	0	0	0	0	0
DI	0	24	0	0	0	1	4
FE	1	1	23	2	1	3	1
HA	0	0	0	27	3	1	0
NE	0	0	0	0	29	1	0
SA	1	0	1	1	1	27	0
AN	0	2	1	0	0	0	27

3.2 JAFFE-6

In this series of experiments fear was excluded from the classification process. The accuracy for each approach is shown in Table 3. The best performance was still obtained when using 34 fiducial points with accuracy 92.3%. Still the alternate dataset with 19 fiducial points provided similar results with accuracy 90.1%.

Table3: Performance using the JAFFE-6 Dataset.

Region	34 Points	34 PCA	19 Points	19 PCA
Single Pixel	75.7%	60.2%	65.2%	53.0%
3x3	85.6%	79.0%	76.8%	68.5%
5x5	87.3%	81.2%	81.8%	72.9%
7x7	89.5%	82.9%	84.0%	79.0%
9x9	91.7%	85.1%	85.6%	85.1%
11x11	92.3%	87.3%	90.1%	86.2%

In Table 4 and Table 5 the confusion matrices of these best performing experiments are presented. Disgust still is confused with anger in both cases. This yields that both these sets of fiducial points are not adequate enough to separate correctly these two emotions.

Table 4: Confusion matrix for 34 fiducial points and 11x11 region excluding fear.

	SU	DI	HA	NE	SA	AN
SU	29	0	0	1	0	0
DI	0	24	0	0	2	3
HA	0	0	31	0	0	0
NE	0	0	0	30	0	0
SA	3	0	1	1	26	0
AN	0	3	0	0	0	27

Table 5: Confusion matrix for 19 fiducial points and 11x11 region excluding fear.

	SU	DI	HA	NE	SA	AN
SU	29	0	0	1	0	0
DI	0	24	0	0	2	3
HA	0	0	31	0	0	0
NE	0	0	0	30	0	0
SA	3	0	1	1	26	0
AN	0	3	0	0	0	27

4 DISCUSSION

A facial expression recognition method, using a Gabor Filter Bank was presented. All redundant information in the construction of the filter bank was avoided by specially designing the filters. Two different facial representations were used using 19 and 34 fiducial points, respectively. Furthermore, the employment of a region based approach was investigated to avoid misclassification due to artefacts.

The manual feature reduction performed with the alternate dataset has reduced the feature vector by a factor of 0.4. The use of PCA, produced competitive results and has decreased the dimension of the feature vector by a factor of 0.9. In this work the fiducial points in the image were marked manually. This approach is possible to introduce errors, for example choosing a different point of interest instead of the one indented. By using regions the possibility of such errors taking place was minimized. The classifier performed weakly when tried to classify disgust and anger. Larkin (Larkin et. al., 2002) reported that males also made errors when decoding facial expressions of disgust, confusing it with anger. Facial expression recognition is a multi-class problem. Zhang (Zhang et. al. 1998), using a slightly different ANN, have reported accuracy ~90% when dealing with JAFFE-7 and 92.2% when using JAFFE-6. Guo (Guo and Dyer, 2005) had used JAFFE-7 and compared the performance of different classifiers. When the same feature vector was used (dimension equaled to 612) they reported accuracy 63.3% for the Simplified Bayes, 91.4% when using linear Support Vector Machines and 92.3% when using non linear (Gaussian Radial Basis Function Kernel) Support Vector Machines. Both of these approaches use a pixel-based feature extraction approach; in our case we employed a region-based feature extraction process, which permits some flexibility in the selection of the fiducial points and the affect of artifacts is minimized.

Further improvement of the presented method consists primarily of making the method automated. This is mainly related to the identification of the fiducial points that currently are manually marked. Furthermore, the use of a three-dimensional filter bank will be investigated by using time as a third constant and applied in a new, preferably video based, dataset.

ACKNOWLEDGEMENTS

This work was partly funded by the European Union and the General Secretariat for Research and Technology of the Hellenic Ministry of Development (PENED 2003 03OD139).

REFERENCES

Ekman, P, Friesen, WV, 1971, “Constants Across Cultures in the Face and Emotion”, *J. Pers. Psycho.,* vol. 17, no. 2, pp. 124-129.

Fasel, B, Luettin, J, 2003, "Automatic Facial Expression Analysis: a survey", *Pattern Recognition,* vol. 36, no. 1, pp. 259-275.

Essa, I, Pentland, 1997, "Coding, Analysis, Interpretation, Recognition of Facial Expressions", *IEEE Trans. Pattern Analysis and Machine Intelligence,* vol. 19, no. 7, pp. 757-763.

Donato, G, Bartlett, MS, Hager, JC, Ekman, P, Sejnowski, TJ, 1999, "Classifying Facial Actions", *IEEE Trans. Pattern Analysis and Machine Intelligence,* vol. 21, no. 10, pp. 974-989.

Lyons, MJ, Budynek, J, Akamatsu, S, 1999, "Automatic Classification of Single Facial Images", *IEEE Trans. Pattern Analysis and Machine Intelligence,* vol. 21, no. 12, pp. 1357-1362.

Gu, H, Zhang, Y, Ji, Q, 2005, "Task Oriented Facial Behaviour Recognition with Selective Sensing", *Computer Vision and Image Understanding,* vol. 100, no. 1-2, pp. 385-415.

Guo, G, Dyer, CR, 2005, "Learning From Examples in the Small Sample Case: Face Expression Recognition", *IEEE Trans. System, Man and Cybernetics-Part B: Cybernetics,* vol. 35, no. 3, pp. 477-488.

Zhang, Z, Lyons, M, Schuster, M, Akamatsu, S, 1998, "Comparison Between Geometry Based and Gabor Wavelet Based Facial Expression Recognition Using Multi Layer Perceptron", In *Proc. 3rd Int. Conf. Automatic Face and Gesture Recognition,* pp. 454-459.

Dougman, J, 1980, "Two-Dimensional Spectral Analysis of Cortical Receptive Field Profiles", *Vision Research,* vol. 20, pp. 846-856.

Dougman, J, 1985, "Uncertainty Relation for Resolution in Space, Spatial Frequency and Orientation Optimized by Two-Dimensional Visual Cortical Fields", *J. Opt. Soc. Am. A.,* vol. 2, no. 7, pp. 1160-1169.

Liu, W, Wang, Z, 2006, " Facial Expression Recognition Based on Fusion of Multiple Gabor Features", In Proc. 18th Int. Conf. on Pattern Recogntion,vol. 3, pp. 536-539.

Lyon, M, Akamatsu, S, 1998, "Coding Facial Expressions with Gabor Wavelets", In *Proc. 3rd Int. Conf. Automatic Face and Gesture Recognition,* pp. 200-205.

Manjunath, BS, MA, WY, 1996, "Texture Features for Browsing and Retrieval of Image Data", *IEEE Trans. Pattern Analysis and Machine Intelligence,* vol. 18, no. 8, pp. 837-842.

Larkin, KT, Martin, RR, McClain, SE, 2002, "Cynical Hostility and the Accuracy of Decoding Facial Expressions of Emotions", *J. Behavioural Medicine,* vol. 25, no. 3, pp. 285-292.

ANALYSIS OF FOCUSES OF ATTENTION DISTRIBUTION FOR A NOVEL FACE RECOGNITION SYSTEM

C. Spampinato
Department of Informatics and Telecommunication Engineering, University of Catania
Viale Andrea Doria,6, 95125, Catania, Italy
cspampin@diit.unict.it

M. Nicotra, A. Travaglianti
Catania Territorio d'Eccellenza – ICT E1, Municipality of Catania, Viale Vigo, 95100, Catania, Italy
nicotra.massimiliano@gmail.com, a.travaglianti@gmail.com

Keywords: Face Recognition, Bottom-up Attentive Analysis, FOAs distribution.

Abstract: In this paper we propose an automated approach to recognize human faces based on the analysis of the distribution of the focuses of attention (FOAs) that reproduces the ability of the humans in the interpretation of visual scenes. The analysis of the FOAs (distribution and position), carried out by an efficient and source light independent visual attention module, allows us to integrate the face features (e.g., eyes, nose, mouth shape) and the holistic features (the relations between the various parts of the face). Moreover, a remarkable approach has been developed for skin recognition based on the shifting of the Hue plane in the HSL color space.

1 INTRODUCTION

Face recognition is a research area of biometrics that for its complexity and importance is becoming one of the most interesting topics of study in the image analysis and understanding field. A general statement of the face recognition problem is as follows: given a video image of a scene, identify one or more persons in the scene using a stored database of faces. The problem of face recognition is open, because an effective model has not been proposed yet, and the shortcomings of these systems are evident when compared to the human capability to recognize the faces.

Several approaches for automating the process of face recognition have been proposed in the last twenty years. Generally, a face recognition involves automating three related tasks: 1) Face Detection, 2) Features Extraction and 3) Face Matching.

The automatic systems have to execute all the three tasks above.

For *face detection* the majority of the approaches are based on the skin pixels segmentation using the color spaces processing (Brand et al., 2001), (Ikeda, 2003).

An interesting algorithm is proposed in (Phung et al., 2002) where a human skin color model in the YCbCr color space is presented, and the k-means algorithm is proposed for clustering the skin pixels in three Gaussian clusters. The pixels are considered belonging to one of three clusters on the basis of the Mahalanobis distance.

For the *face features extraction* various methods have been developed. Methods based on deformable templates seem to be the most effective. Yuille et al. (Yuille et al., 1991) describe the use of deformable templates called "snakes" (Kass et al., 1998), based on simple geometrical shapes to locate eyes and mouths. Several methods use the active shape model (ASMs), (Jiao et al., 1998) and (Wang et al., 2000), with different approaches (e.g. wavelet, Gabor filter, etc.) for the detection of the features. Cootes et al. (Cootes et al., 1995) have proposed an effective model for interpretation and coding of face images with results in the range [70%-97%], but in their approach the landmarks to detect the main facial features are manually located.

One of the most relevant algorithms for *face matching* is the eigenfaces proposed in (Pentland et al., 1994). The eigenfaces, based on the eigenpictures, removes the data redundancy within

the face images. Other approaches have pointed out the structural coupling of the face features. One of the most effective is the Elastic Bunch Graphic Matching (Wiskott et al., 1997) which uses the wavelet functions.

All the mentioned methods are not effective in all the possible scenarios, and require a high processing time and great amounts of memory for features storaging.

A techniques commonly used for features dimensionality reduction are Principal Components Analysis (PCA) (Yang et al., 2004) and Linear Discriminant Analysis (LDA) (Etemad et al, 1997). The main goal of PCA is to reduce the dimensionality of the data, while retaining as much as possible of the variation present in the original dataset. The reduction is obtained by selecting a set of orthogonal vectors maximizing the variance overall the samples.

Instead LDA seeks to find the direction in the dataset that maximizes between-class scatter and minimizes the within-class scatter.

Although these two methods reduce the space dimensionality, they face the computational difficulty when the dimension of the data is too huge. Moreover a critical issue of the LDA method is the singularity and instability of the within-class scatter matrix. Indeed, especially in face recognition problems, there are a large number of features available, while the total number of training patterns is limited, commonly less than the dimension of the features space. This implies that the within-class scatter matrix might be singular and instable (Jain et al, 1982).

In order to overcome the singularity problem, an alternative method, called Fisherfaces (Belhumeur et al, 1997), was proposed. Such method is a two stage dimensionally reduction technique carried out by: 1) performing PCA to project the n-dimensional image space onto a lower dimensional subspace and 2) applying LDA to the best linear discriminant features on such subspace.

Although Fisherfaces method solves the singularity problem, often the instability remains a huge drawback. Several methods, based on Fisherfaces, were proposed to bypass such limitation (Liu et al, 1993), (Thomaz et al, 2003).

The aim of our paper is to propose an algorithm that avoids the computational costs inherent to an high features space dimensionality by using a restricted number of features face. Moreover our method shows a reasonable accuracy comparable with the best existing methods as shown in the section results. Sect. 2 outlines the overall face recognition system, Sect. 3, Sect .4 and Sect. 5 illustrate, respectively, the subsystems Face Detection, Face Features extraction, and Face Matching of the algorithm. Results and future work are focused, respectively, in the last two sections.

2 PROPOSED SYSTEM

Many researchers in computer science, neuroscience and psychology have pointed out the importance of either the *face features* (e.g., mouth shape, nose shape, etc.) or the *holistic features* (such as the distance between the nose and the mouth or the distance between the eyes, etc.) for the face recognition. For example, Bruce in (Bruce et al., 1998) has attentioned the holistic features. Other studies support the hypothesis that the face recognition in human relies only on the *face features* (e.g., big ears, crooked nose, etc.). For example, in (Faro et al., 2006) an attentive system, based on the Itti and Koch model of visual attention (Itti et al., 2000), recognizes faces by analyzing and classifying only the face features, located by using the Active Contour Model and Active Shape Model.

The use of only face features has been criticized, based on the evidence provided in the Barlett and Searcy study (Barlett et al., 1993) using the *Thatcher Illusion*. In fact, inverting the main features of a face (i.e. putting the mouth in place of the eyes) the result is an strange object that is not recognized as a face.

This supports the importance of the holistic features in the face recognition process.

The proposed recognition system integrates both theories and is based on the hypothesis that in the recognition process humans memorize the distribution of some particular points, called "focuses of attention" (FOAs) that bind both face and holistic features. It consists of four main parts (shown in fig.1):

- **Face Detection:** by a suitable clustering algorithm based on color processing;
- **Visual Attention for Features Extraction:** where the points of interest are focused by a pure bottom-up attention module;
- **Features Extraction:** by a suitable analysis of the identified FOAs;
- **Face Matching:** where the features (face and holistic ones), extracted by the previous module, are compared with the others stored in the database for face matching.

The FOA extraction module is based on the emulation of the human capability to interpret

complex visual scenes. In fact, humans have a remarkable ability to interpret scenes in real time, in spite of the limited speed of the neuronal hardware available for such tasks. Visual processes appear to select a subset of the available sensory information before further processing (Tsotsos et al., 1995), most likely to reduce the complexity of scene analysis. This selection seems to be implemented in the form of a spatially circumscribed region of the visual field, called "focus of attention" (FOA), which scans the scene (by using sequence of eye movements, called *saccades*) both in a rapid, bottom-up, saliency-driven, and task-independent manner as well as in a slower, top-down, volition-controlled, and task-dependent manner. Bottom-up attention directs the gaze to salient regions (image-based saliency cues), while topdown attention enables goal directed visual search (task-dependent cues).
In particular, our algorithm implements the architecture proposed by Koch and Ullman (Koch et al., 1985) where human visual search strategies are explained by the "feature integration theory," based on the *saliency map* that defines the relationships between the components of a scene depending on the importance that the components have for the generic observer.

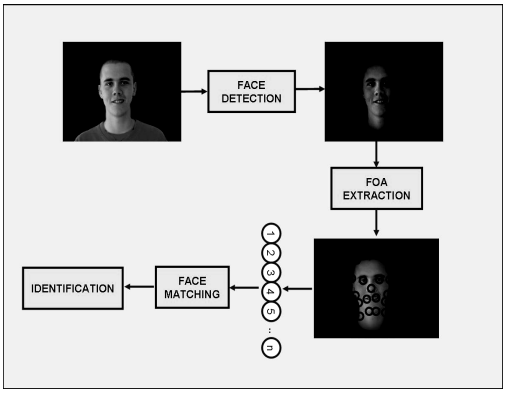

Figure 1: The Overall System.

3 FACE DETECTION

Usually, the face detection process depends strongly from the illumination of the scene. For this reason in our algorithm the HSL (Hue, Saturation, Luma) space color has been chosen. In this space H=0 represents red while H = 255 is violet (fig. 2(a)). For the Caucasian, Mongolian and American races, the pixels of the skin are close to the red color, hence for a better analysis we have defined a new space called HrSL (Hue centered on Red-Saturation-Luma) obtained by shifting the HSL space (see Fig. 2). In the new space the red color is represented by the value H=127 and not by 0 as in the HSL space. This shifting allows us to realize an effective thresholding of the skin pixels as is shown in fig.3.

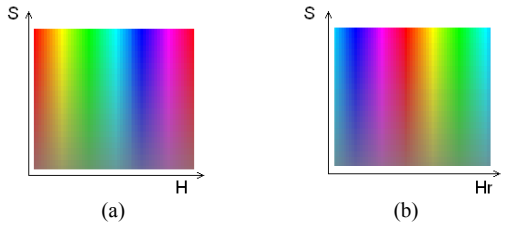

(a) (b)

Figure 2: (a) HSL space, (b) HrSL space.

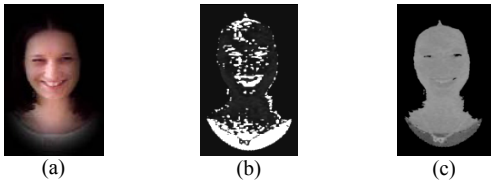

(a) (b) (c)

Figure 3: (a) Original Image. Images obtained by a suitable thresholding in the HSL space (b) and in the HrSL space (c).

The face detection process (shown in fig. 4) uses a clustering algorithm, which consists of three steps:

- Identification of three clusters ;
- Selection of the winner cluster ;
- Filtering the input image with a mask obtained by a smoothing of the winner cluster

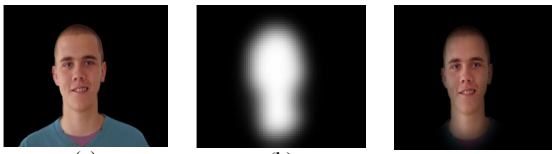

(a) (b) (c)

Figure 4: (a) Imput Image, (b) Mask obtained by a smoothing of the winner cluster, (c) Final Image with face detection.

More in details the clustering algorithm used is based on a modified version of the k-means algorithm. The first step aims to divide the Hr plane of the input image in a lot of the clusters using the minimization of the Euclidean Distance between each one points value of the Hr plane and the centroid value, which represents the mean of the values of each one region of the image. A very great number of cluster produces an increasing of the CPU time and the merging problem, whereas few clusters could be non sufficient to separate the main parts of

the Hr plane. In according to experimental test, we choose three clusters.

After the clustering algorithm we divide the image in cluster to identify the **winner cluster,** which is the cluster whose the RGB value is nearest at (195,145,155). Applying a suitable filtering we obtain the face mask that allows us to detect the face.

4 VISUAL ATTENTION FOR FEATURES EXTRACTION

The output image of the face detection step is the input image for the algorithm that extracts features based on a visual attention system. The visual attention module proposed in this paper detects salient regions from a color image simulating saccades of human vision using a saliency map similar to the one proposed by Itti & Koch (Itti et al., 2000). The differences in computing the saliency map are: 1) we don't apply Gaussian pyramid, thus reducing the computational complexity and increasing the spatial resolution of the processed images and 2) we don't use the double color opponent mechanism, and therefore the dependence of attention module on the illumination source is reduced, 3) the HSL space is the best representative of how the humans perceive the colors.

The first step to compute the saliency map is to convert the image, obtained by the face detection module, in the HrSL space. Experimentally, we have noticed that the Saturation plane is unnecessary for the computation of the saliency map, while Hr and L planes allow us, respectively, to detect the contours and the shapes of the face (e.g. eyes, nose, mouth, etc…). After having extracted the Hr and L planes, the following filters have been applied to the both planes, obtaining the images partially shown in fig. 5:

- Directional Prewitt filters (oriented at 0°, 45°, 90°, 135°) obtaining $Hr\_Prewitt^{0°}$, $Hr\_Prewitt^{45°}$, $Hr\_Prewitt^{90°}$, $Hr\_Prewitt^{135°}$ and $L\_Prewitt^{0°}$, $L\_Prewitt^{45°}$, $L\_Prewitt^{90°}$, $L\_Prewitt^{135°}$,features;
- Canny Filter to both planes, obtaining the Hr_Canny_map and L_Canny_map;

The images, processed with the above non-linear filters, are combined with the aim to obtain the *features maps* as follows:

1. All the Hr images processed with Prewitt filters are summed obtaining the *Hr-Prewitt Features Map;*
2. All the L images processed with Prewitt filters are summed giving more weight to the 90° Map, obtaining the so called *L-Prewitt Features Map;*
3. The Hr_Canny map and L_Canny map are processed using a normalization function N(·) that implements the mechanism of *iterative spatial inhibition* by using the DoG (Difference of Gaussian) filter proposed in (Itti et al., 2000). The obtained maps are called respectively *Hr-Edge Map* and *L-Egde Map.*

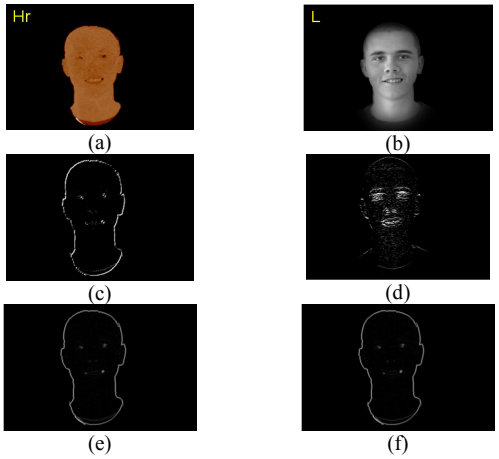

Figure 5: (a) Hr plane of the detected face, (b) L plane of the detected face, (c) Hr-Prewitt$^{90°}$ Map, (d) L-Prewitt$^{90°}$ Map, (e) Hr-Canny Map, (f) L-Canny Map.

Applying the normalization factor N(·) to both the *Hr-Prewitt Features Map* and *Hr- Egde-Map* and summing these two maps we obtain the *Hr-Saliency Map* (fig.6(a)).

The same procedure is applied for *L-Saliency Map* (fig.6(b)) which is obtained by summing the L-Prewitt Features Map and L-Egde Map. Finally, the *Saliency Map* (fig.6(c)) is computed by summing the L-Saliency (with a greater weight) with the Hr-Saliency Map.

After having extracted the saliency map, the first Focus of Attention (FOA) is directed to the most salient region (the one with the highest grey level in fig.6(c)).

Afterwards, this region is inhibited according to a mechanism called *inhibition of return (IOR)*, allowing the computation of the next FOA.After the FOAs distribution extraction, a FOAs analysis has been carried out in order to identify the eyes, the

ellipse surrounding the face and the mouth. For the eyes position detection, we consider the most two salient regions of the obtained FOAs distribution.

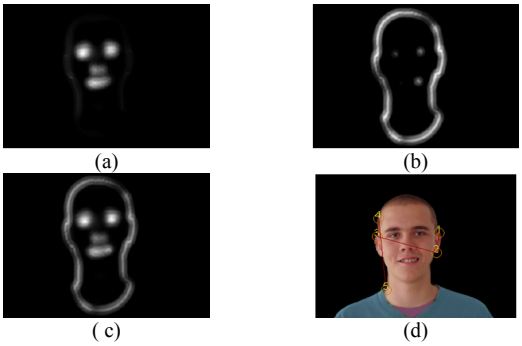

Figure 6: (a) L_Saliency Map, (b) Hr_Saliency Map, (c) Saliency Map, (d) Some identified FOAs.

For the ellipse identification the algorithm computes a set of distances from each extracted FOA. All the FOAs, which distance by the centre is greater than a suitable threshold, are considered as belonging to the face boundaries. By an interpolation of these FOAs we obtain the searched ellipse. By analyzing the remaining FOAs, we are able to extract the mouth. After the feature extraction the holistic face features have been extracted.

5 FEATURES EXTRACTION

The aim of this module is to extract the *face features* and the *holistic features* starting from the most important FOAs previously identified. The identified *holistic features* are:

- The normalized area ($\mathbf{A_N}$) and the eccentricity (**E**) of the ellipse that best fits the contour FOAs, as described below:

$$E = 100 \cdot sign(A_y - A_x) \cdot \sqrt{1 - \frac{\min(A_x, A_y)^2}{\max(A_x, A_y)^2}}$$

$$A_N = \frac{A_x \cdot A_y}{\sqrt{A_x^{\,2} + A_y^{\,2}}}$$

Where A_x and A_y are, respectively, the horizontal and the vertical axes of the ellipse;

- the distance between the central point of the FOAs eyes ($\mathbf{C_0}$) and the center of the such ellipse ($\mathbf{C_{Em}}$);
- the focal distance between the eyes ($\mathbf{C_f}$);
- the vertical distance (**Yb**) between the central point of the mouth ($\mathbf{C_m}$) and the center of the ellipse ($\mathbf{C_{Em}}$);
- the distance between the eyes and the mouth: computed as the distance between the central point of the eyes FOAs $\mathbf{C_0}$ and $\mathbf{C_m}$;
- the distribution of the 20 most salient FOAs;

Overall the computed holistic features are shown in fig.7. For the *face features* we consider the position of the most relevant FOAs and starting from these locations we apply the snakes, as in (Faro et al., 2006), that allow us to extract the searched features.

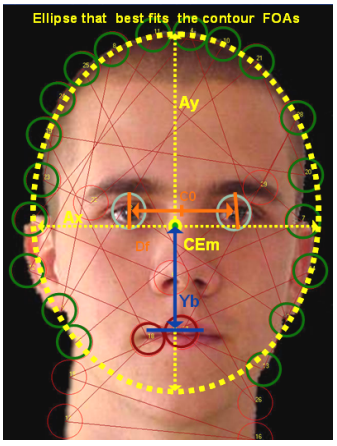

Figure 7: Extracted Holistic Features.

The final step is to match the extracted features with the ones stored in the database. The considered features for the matching are:1) FOAs Distribution, 2) Face Features and 3) Holistic Features.

The face matching must be independent from the rotation, the scaling and the translation. For this reason the first step is to apply a Procrustes analysis (Bin et al., 1999) to the FOAs distribution. After this transformation we extract the holistic (based on the FOAs distribution) and the face features and finally we compute the fitting value that is given by the following formula:

$$Fit = \alpha_1 \cdot T_1 + \alpha_2 \cdot T_2 + \alpha_3 \cdot T_3$$

where T_1 is the fitting value of the distribution, T_2 the fitting value for the features extracted by using the FOAs dist., and T_3 the fitting value for the facial features extracted by deformable models. The recognized person is the one whose *Fit* value is the

greatest, and if it is greater than a threshold, otherwise nobody is recognized.

6 EXPERIMENTAL RESULTS

The proposed method has been tested on a database of 114 subjects. Each subject is represented by 5 images in different positions (side view with an angle of 45°, frontal view with serious expression, side view with angle 135°; frontal view showing no teeth and frontal view showing the teeth). Each image is characterized by a spatial resolution of 640*480, with a uniform background and natural light. Subject's age is between 18 and 50 years.

For face matching, the features of the side view with an angle of 45°, frontal view with serious expression, and side view with angle 135° of each person have been used to create the face model; the remaining two images of each person (frontal view showing no teeth and frontal view showing the teeth) have been used for the testing phase.

Concerning face detection, the success rate is 100%. For the features extraction on all the detected images, the percentage of success is about 93%. The 66% of the images whose features have been extracted correctly, has been used for the model face creation. The test for face identification has been carried out on the remaining images (181 images, corresponding to the 34%).

The experimental results are shown in Table 1.

Table 1: Experimental results.

Algorithm	N° Test images	Correct Evaluation	Success rate
Face Detection	570	570	100 %
Features Extraction	570	531	93.1%
Face Matching	181	170	93.9%

The overall recognition rate of our method is 87.42%. The classification performances are more than satisfying, especially if compared with other well-know methods in literature. Indeed Eigenfaces (Pentland et al., 1994) shows an average recognition rate of 88.0%, Fisherfaces(Belhumeur et al, 1997) 86%, Liu Method(Liu et al, 1993) 86.5%.

7 CONCLUSIONS AND FUTURE WORKS

An automated face recognition system based on the emulation of the human capability to interpret complex visual scenes has been proposed. The system proves effective due to the integration of the face and holistic features.

This integration is attained by applying both the FOAs distribution analysis and the algorithm proposed in (Etemad et al, 1997).

An important peculiarity of the system is the independence from both the illumination source and the dimension of the face to be recognized. The independence from the illumination source has been obtained by using the proposed HrSL color space.

Moreover, the HrSL allows us to best detect the skin pixels. The independence from the face dimension has been carried out adopting the Procrustes analysis.

An improvement that generalizes the system regards the face detection module; in fact, the high accuracy of the method is due to the background uniformity of the used images. In other cases for a better clustering it will be necessary to associate at the color processing module a spatial processing system.

In addition, the system is set to work only with Caucasian, Mongolian and American races; for a correct functioning with the other races it is sufficient to shift the Hue color plane. Although the features extraction and the face matching systems have shown good results, they should be tested especially with different face images with different orientation and non-uniform background.

For this reason it will be very interesting to develop a parallel system able to analyze at the same time different locations of the scene, especially for complex scenes with many faces and other objects.

Finally, we plan to apply the proposed approach not only for face recognition but also for gesture recognition.

ACKNOWLEDGEMENTS

This paper has been partially supported by the project "Catania Territorio d'eccellenza – ICT E1" of the Catania municipality. Moreover we would to thank the CVL and ŠCV, PTERŠ, Velenje for the face database.

REFERENCES

Brand, J.D., Mason, J.S.D., Pawlewski, M.: Face detection in colour images, *Proceedings of the IEEE ICIP 2001*, Thessaloniki, Greece, October 7-10, 2001.

Ikeda, O.: Segmentation of faces in video footage using HSV color for face detection and image retrieval, *Proceedings of the IEEE ICIP 2003*, Barcelona, Catalonia, Spain, September 14-18, 2003.

Phung, S.L., Bouzerdoum, A., Chai, D.: A novel skin color model in YCbCr color space and its application to human face detection, *Proceedings of the IEEE ICIP 2002*, Rochester, New York, USA, September 22-25, 2002.

Yuille, A. L.: Deformable templates for face detection *Journal of Cognitive Neuroscience*, Vol. 3, No. 1, pp. 59-70, 1991.

Kass, M., Witkin, A., Terzopoulos, D.: Snakes: Active countorn models, *International Journal of Computer Vision*, pages 321–331, 1998.

Jiao, F., Li, S., Shum, H. and Schuurmans, D.: Face allignment using statistical models and wavelet features. *Proc. of CVPR'03 IEEE*, pages 1063–1069, 2003.

Wang, W., Shan, S., Gao, W., Cao, B. and Baocai, Y.: An improved active shape model for face alignment. *Vision Research*, 40:1489–1506, 2000.

Cootes, T. F., Taylor, C. J., Cooper, D. H. and Graham, J.: Active shape model their training and application. *Computer vision graphics and image understanding*, 61:38–59, 1995.

Pentlad, A., Moghaddam, B., Starner, T. , Oliyide, O. and Turk, M.: View based and modular eigeispaces for face recogntion. *M.I.T. Media Laboratory,* Percentual Computing section-Technical report, 245, 1994.

Wiskott. L., Fellous, J.-M., and von der Malsburg, C.:Face Recognition by Elastic Bunch Graph Matching, *IEEE Trans. on PAMI*, Vol.19, pp.775-779, 1997.

Yang, J., Zhang, D., Frangi, A.F., Yang, J.Y., Two dimensional PCA: a new approach to appearance-based face representation and recognition", *IEEE Trans. On PAMI*, Vol.26, No.1, pp 131-137, 2004.

Etemad, K., Chellapa, R.: Discrimant analysis for recognition of human face images, *Journal of the Optical Society of America A*, Vol.14, No.8, pp.1724-1733, 1997.

Jain, A.K., Chandrasekaran, B.: Dimensionality and sample size consideration in pattern recognition practice, *Handbook of Statistics*, P.R. Krishnaiah and L.N. Kanal Eds., North Holland, vol.2, pp.835-855, 1982.

Belhumeur, P.N., Hespandha, J.P., Kriegman, D.J., "Eigenfaces vs Fisherfaces recognition using class specific linear projection", *IEEE Trans. On PAMI*, Vol.19, No.7, pp.711-729, 1997.

Liu, K., Cheng, Y.Q., Yang, J.Y., Algebraic feature extraction for image recognition based on an optimal discriminant criterion", *Pattern Recognition*, Vol.26, No. 6, pp 903-911, 1993.

Thomaz, C.E., Gillies, D. F., A new Fisher-Based method applied to Face Recognition, *Lecture Notes on Computer Science* 2756, pp.596-605, 2003.

Bruce, V., Hancock, P., and Burton, A.: Human face perception and identification, In Wechsler, Philips, Bruce, Fogelman-Soulie, and Huang, editors, *Face Recognition: From Theory to Applications,* pages 5 1-72. Springer-Verlag, 1998.

Faro, A., Giordano, D. and Spampinato, C.: An Automated Tool For Face Recognition using Visual Attention and Active Shape Model Analysis, *Proc. of IEEE EMBC 2006*, New York, USA, August 29-30, 2006.

Itti, L. and Koch, C.: A saliency-based search mechanism for overt and covert shifts of visual attention. *Vision Research*, 40:1489–1506, 2000.

Barlett, J. C., Searcy, J.: Inversion and Configuration of Faces, *Cognitive Psychology* 25, 281-316, 1993.

Tsotsos, J.K., Culhane, S.M. , Wai, W.Y.K., Lai, Y.H. , Davis, N. and Nuflo, F.: Modelling Visual Attention via Selective Tuning," *Artificial Intelligence*, vol. 78, no. 1-2, pp. 507–545, Oct. 1995.

Koch, C. and Ullman, S. : Shifts in Selective Visual Attention: Towards the Underlying Neural Circuitry," *Human Neurobiology*, vol. 4, pp. 219–227, 1985.

Bin L., Hancock, E.R.: Matching Point-sets using Procrustes Alignment and the EM Algorithm, *Proc. of BMV99*, Manchester, United Kingdom, July 1999.

A NOVEL TEMPLATE HUMAN FACE MODEL WITH TEXTURING

Ken Yano and Koichi Harada
Graduate School of Engineering, Hiroshima University
1-4-1 Kagamiyama, Higashi-Hiroshima, Japan
d064016@hiroshima-u.ac.jp, harada@mis.hiroshima-u.ac.jp

Keywords: Geometric modeling, 3D face scan, surface fitting, human face, triangular mesh.

Abstract: We present a method to fit a template face model to 3D scan face. We first normalize the size and align the orientation then fit the model roughly by scattered interpolation method. Secondly we run the optimization method based on Allen's work. We are able to generate face models which have "poin-to-point" correspondence among them. We also suggest a way to transfer any facial texture image over this fitted model.

1 INTRODUCTION

Creating realistic 3D human face is a difficult task. Since human face has very complex geometry, and its difference between races and ages is large. Although 3D human face model has been created for many application, it can be said that there is no standard way of making human face model from scratch. Making a realistic human face is still a challenging task. Related study have been reported to create morphable or animatable human face from 3D face scan, however there are still many known or unknown issues relating human face model (Ekman and V.Friesen, 1975) (Parke, 1972).

In this paper, we propose a method for creating face model which has full correspondence among different faces. By having such a model with full correspondence, it becomes an easy task to animate face with known parameters among different face models. With this model, it becomes a trivial task to group face by comparing the corresponding geometry or morphing between different faces. It would also be possible to use this face model to recognize human face if the quality of created face model improves more.

The main contribution of this paper is a template-based face registration technique for establishing a point-to-point correspondence among a set of face model. Our method of creating such a face model is based on the Allen's work (Allen et al., 2003). Starting from the 3D scan face data, we try to fit our template face to those scan data with as less as human interactions intervened. The fitting process runs semi-automatic except that facial markers have to be marked by human at first. We describe our fitting method from a template face to any 3D-face scan taken from real human in this paper. We also suggest one method of transferring facial image over this face model.

2 RELATED WORK

Blantz and Vetter (Blanz and Vetter, 2003) create a morphable face model by taking images of several faces using a 3D scanner and putting them into "one-to-one" correspondence by expressing each shape using the same mesh structure. Using the morphable model, it is possible to group changes in vertex position together for representing common changes in shape among several surfaces. Using principal component analysis, they succeeded to find a basis for expressing shape changes between faces.

Concept of morphable model face model has been extended by many researchers. For instance Vlasic (Vlasic et al., 2005) published a method for expressing changes in face shape using a multi linear model, accounting for shape changes not only based on a person's identity but also based on various expression.

Model with full correspondence is also studied by Praun and co-workers work (Praun et al., 2001). In order to establish full correspondences between models, they create a base domain which is shared between models, then apply a consistent parameterization. They search for topologically equivalent patch boundaries to create base domain mesh. Since our

domain is limited to only Human face model, a base domain would be prepared in advance.

3 OVERVIEW

The task of the template face model fitting is to adapt a model face to fit an individual's 3-D scan face. As input to this process, we took several 3D face scan with Vivid700 (MINOLTA, 1999). We created the template face model with a commercial modeling software. Our template face contains 435 vertices and 822 triangles. Boundary of the shape is the contour of face. We first crop the 3D scan data outside of the face contour. We preprocess the surfaces so that the shape of boundary of template face model and 3D scan face is almost the same. However this is not a strict demand, but doing so makes the fitting result better empirically. Our fitting method are comprised of two part. We first fit the template face model roughly by using scattered interpolation method, then refine the fitting by minimizing the error energy function which describes the quality of the match. For visual richness of 3D surface especially for facial expression, texturing is very important topic. We suggest a method of transferring any facial textual image over the fitted model with full correspondence among them.

4 3D SURFACE FITTING

If the two face model's shapes differ substantially, optimization framework could stuck in local minima and will not result in desirable face model. So our method first fit the template face model roughly by using scattered data interpolation, then use the optimization framework suggested by Allen (Allen et al., 2003). This way makes our fitting process more robust than (Allen et al., 2003). Before starting fitting, we normalize the size of each model by resizing the bounding box of its model and align the center of the model. Scattered data interpolation is described in 4.1, and optimization framework is described in 4.2.

4.1 Scattered Data Interpolation

We first locate the same number of facial feature points on both on template face model and 3D scan face data manually. The number of marker points is 13 in our case. Once we have set markers which have one-to-one correspondence between template face and 3D scan face, we construct a smooth interpolation function that gives the 3D displacements between the 3D scan face and the new adapted position for every vertex in the template face model.

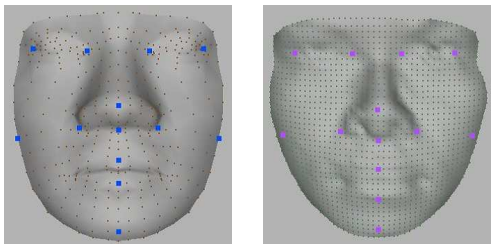

(a) (b)

Figure 1: Facial markers. (a) Facial markers v_i on template face. (b) Facial markers m_i on 3D scan face.

Given a set of known displacements $u_i = v_i - m_i$ away from the 3D scan face positions at every marker position i, construct a function that gives the displacement u_j for every non-constrained vertex j in the template face model. We use a method based on radial basis functions, that is the function of the form

$$f(v) = \sum_i c_i \phi(\| v - v_i \|) + Mv + t \qquad (1)$$

where $\phi(r)$ are radially symmetric basis functions. M and t are affine components. To determine the coefficient c_i and the affine components M and t, we solve a set of linear equations that include the interpolation constraints $u_i = f(v_i)$, as well as the constraints $\sum c_i = 0$ and $\sum c_i v_i^T = 0$, which remove affine contribution from the radial basis functions. Many different functions for $\phi(r)$ have been proposed. We have chosen $\phi(r) = |r|^2 \log(|r|)$ for our function. We have applied this interpolation for each coordinate, X, Y, and Z.

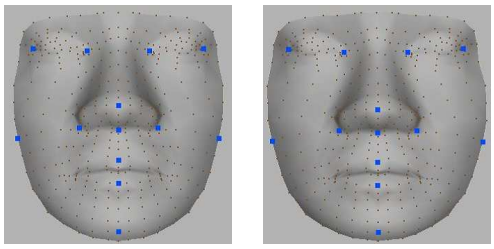

(a) (b)

Figure 2: Scattered data interpolation. (a) Original template face. (b) Template face after RBF interpolation.

4.2 Model Data Fitting Optimization

After fitting roughly by scattered interpolation method described above. We improve the quality of fitting by minimizing the fitting error metric by adapting Allen's method (Allen et al., 2003). We describe

this method for fitting template face model to 3D scan face. Each vertex v_i in the template surface is influenced by a 3x4 affine transformation matrix T_i. We try to find a set of transformations that move all of the points in the template face to 3D scan face surface.

The quality of the match is evaluated using a set of error functions: data error, smoothness error, and marker error. These error terms are described in the following sections.

Marker error. Equal number of Facial feature points are placed on both the template face and the 3D scan face at the locations which are characteristic for faces. About 13-20 features markers are suffice to locate facial feature locations. We call the 3D location of the markers on the 3D scan face $m_{1...m}$, and the corresponding vertex index of markers on the template face $t_{1...m}$. The marker error term E_m minimizes the distance between each marker's location on the template face and the 3D scan face:

$$E_m = \sum_{i=1}^{m} \parallel T_{t_i} v_{t_i} - m_i \parallel^2 \quad (2)$$

Data error. We fit the marker first, then fit all the remaining points in the template face. We define a data error term E_d as the sum of the squared distances between each vertex in the template face and the 3D scan face surface.

$$E_d = \sum_{i=1}^{n} \delta_i dist^2(T_i v_i, D) \quad (3)$$

where n is the number of vertices in template face, δ_i is a weighting term to control the validity of the match, and the $dist()$ function computes the distance to the closest point on the 3D face scan. If the surface normals at the corresponding points are more than 90°, set δ_i to 0 otherwise set to 1.

Smoothness error. Allen (Allen et al., 2003) suggested that simply moving each vertex in the template face to its closest point in the 3D scan separately will not result in a well arranged mesh, because neighboring parts of the template face could be mapped to disparate parts of the 3D scan face. To constraint the problem, we adopted the smoothness error, E_s (Allen et al., 2003). we formulate the constraint between every two points that are adjacent in the template face:

$$E_s = \sum_{\{i,j|\{v_i,v_j\} \in edges(T)\}} \parallel T_i - T_j \parallel_F^2 \quad (4)$$

where $\parallel \cdot \parallel$ is the Frobenius norm. By minimizing E_s we prevent adjacent parts of the template face from begin mapped to disparate parts of the 3D scan face.

Combining each error. Our complete objective function E is the weighed sum of the three error functions above:

$$E = \alpha E_m + \beta E_d + \gamma E_s \quad (5)$$

where the weights α, β, and γ are adjusted to guide the optimization. We use a quasi-Newtonian solver, L-BFGS-B (Zhu et al., 1994).

We first run the optimization using the relatively low resolution mesh of the template face compared with the 3D scan face. After that we subdivide the resulting template face by inserting a new vertex between every edges of the mesh. Newly inserted vertex position and its affine transformation is interpolated between the two vertices of the edge.

We vary the weights, α, β, and γ, so that marker point fits first then the remaining vertice move to the appropriate position so that overall surface of the template face fit to the 3D scan face. We run our optimization as following

At the first stage (Low resolution of the template face)
1. Fit the markers first: α=10, β=1, γ=1
2. Make the data error term to dominate: α = 1, β=10, γ=1

At the second stage (High resolution of the template face)
1. Continue the optimization: α=5, β=1, γ=0
2. Make the data error term to dominate: α = 0, β=10, γ=1

Template face after fitting sometimes have ripple over high curvature area. We have applied laplacian smoothing (Taubin, 1995) to this surface and get more smooth surface as seen in Fig 4.

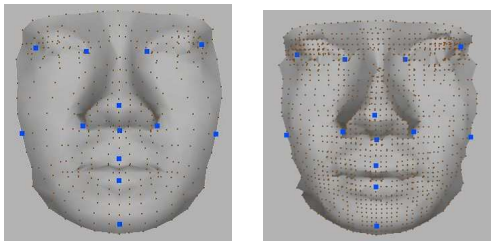

(a) (b)

Figure 3: Fitting template face. (a) Template face after fitting to 3D face scan. (b) Subdivided template face after fitting.

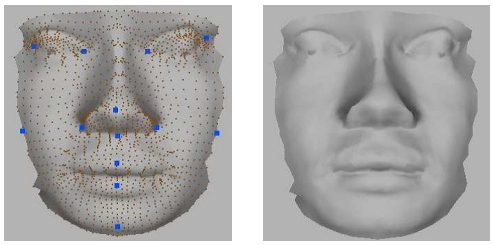

(a) (b)

Figure 4: (a)Smoothing face model after fitting. (b) display in shading mode.

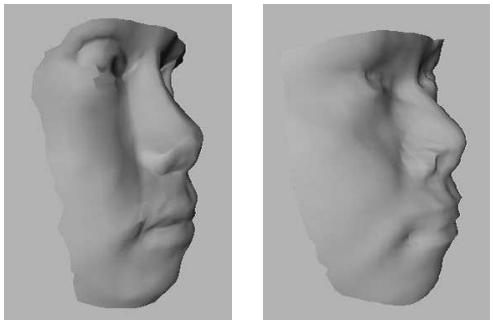

(a) (b)

Figure 5: (a)Fitted template face from another angle. (b) Target 3D face scan from the same angle.

5 CONSTRAINED FACIAL TEXTURE MAPPING

We propose a method based on radial basis function (RBF) technique to apply a facial texture image to our template based 3D face model. Fist we calculate the mapping from 3D template face surface to 2D parameter space. With this mapping we obtain the template face image. Then user specifically assigns the corresponding 2D points in the sample facial image to those points in the template face image. We employ RBF to morph the sample face image with the constraint of these feature points. Our method is characteristic in that we do not re-calculate the 2D mapping parameter for each face model, but use the common parameterization prepared in-advance with the morphed face image.

5.1 Template Face Image

Texture mapping or parameterization of 3D mesh is to compute a mapping between a discrete surface patch and an isomorphic planner mesh through a piecewise linear mapping. This piecewise linear mapping is simply defined by assigning each mesh node a pair of coordinate (u,v) referring to its position on the planer region. A number of work on parameterization has been published, and almost all techniques explicitly aim at producing least-distorted parameterization. We employ the intrinsic parameterizations (Desbrun et al., 2002) for our parameterization method. Summary of the intrinsic parameterization is described in Appendix. Fig 6 shows the result when we apply this parameterization to our template face model. We call the resulting 2D image the template face image.

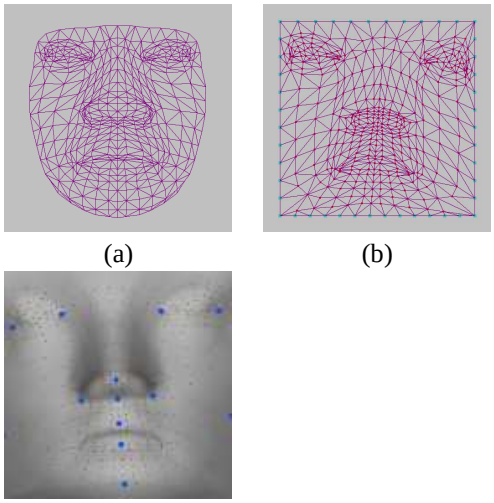

(a) (b)

(c)

Figure 6: (a)3D template face. (b) 2D parameterization. (c) template face image.

5.2 Face Image Morphing

2D image Morphing method we employ is basically same as 4.1. The energy-minimization characteristic of RBF ensures that the mapping function smoothly interpolates constraints with non-deformation properties. User manually assign corresponding 2D points in the sample texture image. User can set an arbitrary set of constrained points, although for simplicity this could be the same set of facial feature points as we use in 4.1. The morphing result is in Fig 7. We transform this morphed face image over the face model after fitting in Fig 8. Fig 9 shows various texture image applied to our template face model.

6 CONCLUSIONS

We have succeeded to make face models which have full point correspondence among them by fitting the generic template face model to each 3D face scan. Although initially it requires human interaction to locate facial feature markers on each model, fitting process

(a) (b)

Figure 7: Locate facial feature points int the original texture image which correspond to the facial feature points of the template face image in Fig 6 (c). We then apply RBF based image morphing with the constrained feature points. (a)original texture image. (b) morphed texture image.

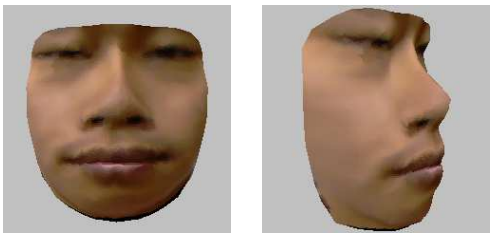

(a) (b)

Figure 8: Texture mapping after fitting. (a)textured face model. (b) view from another angle.

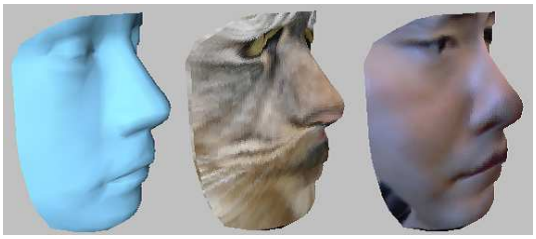

Figure 9: Various texture mapping to template face model.

proceeds automatically. The resulting face model is nicely fitted to the target 3D scan face. Although the fitted face surface sometime is not as smooth as we desire, we can smooth the surface by using laplacian smoothing method without blurring the facial feature points. Since our template face is created by ad-hoc method, it calls for the way to create a ideal template face. Praun et al (Praun et al., 2001) create a base domain model by tracing patch boundaries to represent overall shape of the model. Although created base domain is too abstract for our template model, it could be generated from its base domain. In stead of using a triangular mesh, several studies have been made to fit a spline surface over dense polygon mesh or points. Besides of the patch boundary issue relating to spline surfaces, it is a more suitable model for animation and provide a fine but more expensive model for rendering.

Since we have a face model with consistent parameterization, it is a simple application to morph between any two faces. Although our face model after fitting looks very similar to the original scan face, we haven't evaluated how accurate the fitting is. One possible method is to construct a graph which consists of geodesic paths between every pair of the facial marker points. The accuracy of the fitting could be done by comparing these graphs.

We suggested one method to map texture image over our template based face model. With this method user doesn't have to adjust texture coordinate for each different face model, but rather morph the image with the constraint of matched feature points between the template face image and itself. For the restricted domain as human face model this method was found to produce pleasing result.

REFERENCES

Allen, B., Curless, B., and Popovic, Z. (2003). The space of human body shapes. In *International Conference on Computer Graphics and Interactive Techniques*. ACM SIGGRAPH.

Blanz, V. and Vetter, T. (2003). Face recognition based on fitting a 3d morphable model. In *IEEE Transactions on Pattern Analysis and Machine Intelligence*.

Desbrun, M., Meyer, M., and Alliez, P. (2002). Intrinsic parameterization of surface meshes. In *Eurographics 2002, Computer Graphics Proceedings*. Eurographics.

Ekman, P. and V.Friesen, W. (1975). *Unmasking the Face. A guide to recognizing emotions from facial clues*. Prentice-Hall.

MINOLTA, K. (1999). Non-contact 3d laser scanner. http://se.konicaminolta.us/products/3dscanners/index.html.

Parke, F. I. (1972). Computer generated animation of faces. In *Proceedings ACM annual conference*.

Praun, E., Sweldens, W., and Schröder, P. (2001). Consistent mesh parameterizations. In *SIGGRAPH 2001, Computer Graphics Proceedings*. ACM Press / ACM SIGGRAPH.

Taubin, G. (1995). A signal processing approach to fair surface design. In *Computer Graphics*.

Vlasic, D., Brand, M., Pfister, H., and Popovic, J. (2005). Face transfer with multilinear models. In *ACM Transactions on Graphics*.

Zhu, C., Byrd, R., Lu, P., and Nocedal, J. (1994). Lbfgs-b: Fortran subroutines for large-scale bound constrained optimization. In *LBFGS-B: Fortran subroutines for large-scale bound constrained optimization, Report NAM-11, EECS Department*.

APPENDIX

Parameterization of 3D mesh is to compute a mapping between a discrete surface patch and an isomorphic planar mesh with least distortion. Desbrun at el (Desbrun et al., 2002) describe a general distortion measure E, which is given by Dirichlet Energy E_A and Chi Energy E_χ

$$E = \lambda E_A + \mu E_\chi$$

where λ and μ are two arbitrary real constants.

$$E_A = \sum_{edges \in (i,j)} cot\alpha_{ij} |u_i - u_j|^2$$

where $|u_i - u_j|$ is the length of the edge(i, j) in the parameter domain, and α_{ij} is the opposite left angle in 3D as shown in Fig 10.

$$E_\chi = \sum_{j \in N(i)} \frac{(cot\gamma_{ij} + cot\delta_{ij})}{|x_i - x_j|^2} (u_i - u_j)^2$$

where the angles γ_{ij} and δ_{ij} are define in Fig 10.

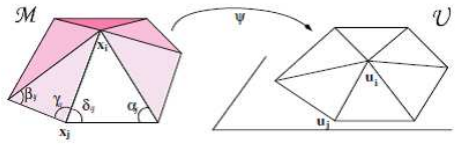

Figure 10: 3D 1-ring and its associated flattened version.

Since the gradient of E is linear, computing a parameterization reduces to solving the following sparse linear system:

$$MU = \begin{bmatrix} \lambda M^A & + & \mu M^\chi \\ 0 & & I \end{bmatrix} \begin{bmatrix} U^{internal} \\ U^{boundary} \end{bmatrix} = \begin{bmatrix} 0 \\ C^{boundary} \end{bmatrix} = C$$

where U is the vector of 2D-coordinates to solve for. C is a vector of boundary conditions that contains the positions where the boundary vertices are placed. M^A and M^χ are sparse matrices where coefficients are given respectively by:

$$M^A_{ij} = \begin{cases} \cot(\alpha_{ij}) + \cot(\beta_{ij}) & \text{if } j \in N(i) \\ -\sum_{k \in N(i)} M^A_{ik} & \text{if } i = j \\ 0 & \text{otherwise,} \end{cases}$$

$$M^\chi_{ij} = \begin{cases} (\cot(\gamma_{ij}) + \cot(\delta_{ij}))/|x_i - xj|^2 & \text{if } j \in N(i) \\ -\sum_{k \in N(i)} M^\chi_{ik} & \text{if } i = j \\ 0 & \text{otherwise,} \end{cases}$$

ILLUMINATION NORMALIZATION FOR FACE RECOGNITION
A Comparative Study of Conventional vs. Perception-inspired Algorithms

Peter Dunker and Melanie Keller*
Fraunhofer Institute for Digital Mediatechnology (IDMT), Ehrenbergstrasse 29, 98693 Ilmenau, Germany
**Robert Bosch GmbH, Daimlerstrasse 6, 71229 Leonberg, Germany*
peter.dunker@idmt.fraunhofer.de, melanie.keller@de.bosch.com

Keywords: Illumination normalization, face recognition, perception-inspired, retinex, diffusion filter, local operations.

Abstract: Face recognition has been actively investigated by the scientific community and has already taken its place in modern consumer software. However, there are still major challenges remaining e.g. preventing negative influence from varying illumination, even with well known face recognition systems. To reduce the performance drop off caused by illumination, normalization methods can be applied as pre-processing step. Well known approaches are linear regression or local operations. In this publication we present the results of a two-step evaluation for real-world applications of a wide range of state-of-the-art illumination normalization algorithms. Further we present a new taxonomy of these methods and depict advanced algorithms motivated by the pre-eminent human abilities of illumination normalization. Additionally we introduce a recent bio-inspired algorithm based on diffusion filters that outperforms most of the known algorithms. Finally we deduce the theoretical potentials and practical applicability of the normalization methods from the evaluation results.

1 INTRODUCTION

Artificial face recognition is in the focus of challenging research and besides a widely used technology in a multitude of applications. The targeted application of this paper is the field of person recognition in real-world photo archive scenarios, e.g. unsupervised consumer photo archive management.

In the task of face recognition under real-world conditions, different factors hinder the recognition process e.g. pose, facial expression and illumination. In this publication we concentrate on the impact of varying illumination that can change the appearance of one person more than the difference of appearance between two persons (Adini et al., 1997).

The purpose of this work is an experimental evaluation of state-of-the-art illumination normalization methods for real-world applications. We draw the hypothesis that well performing algorithms under controlled conditions can worsen results under uncontrolled real-world conditions versus other algorithms.

We focus on algorithms that can be summarized as pre-processing techniques. Commonality of that methods is the ability to process single images without the need of further information.

The contemplated pre-processing algorithms differ manifestly in their method concerning the impact of illumination and the manner to normalize it. They range from well-know histogram manipulations that directly produce normalized images to sophisticated methods e.g. adopting human visual concepts that return illumination estimations for normalizing process. These algorithms follow the idea that illumination $L(x,y)$ and reflecting facial information $R(x,y)$ are distributed in different frequencies of image information $I(x,y)$ depicted in Figure 1.

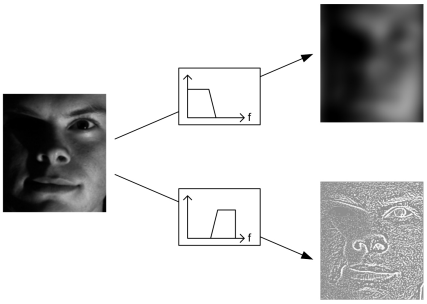

Figure 1: Most illumination estimation algorithms for face recognition assume high spatial frequency of facial information and low frequency of interfering illumination.

To allow systematic analysis of the different algorithms a novel taxonomy of the state-of-the-art normalizations is introduced. Furthermore we present an advanced regression algorithm and a novel

perception-inspired approach for illumination normalization based on diffusion filters.

2 TAXONOMY OF NORMALIZATION METHODS

2.1 Homogenous Point Operations

Homogenous point operations conduct transformations on gray scale values of an intensity image $I(x,y)$ independent from their position using a general transformation function F:

$$I'(x,y) = F(I(x,y)) \quad (1)$$

Several studies e.g. (Shan et al., 2003) evaluated homogeneous point operations for illumination normalization. In our experiments we use the *Histogram Equalization (HE)*, *Histogram Matching (HM)*, *Histogram Stretching (HS)*, *Normal Distribution (ND)* and *Logarithmic Transformation (LOG)*. The LOG refers to dynamics compression for better resolutions of dark regions in human perception (Savvides and Kumar, 2003).

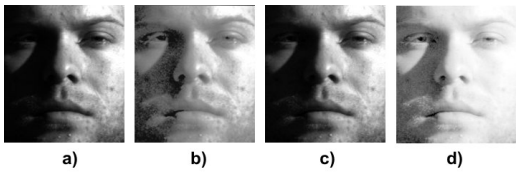

Figure 2: Illumination normalization results of homogenous point operations a) original, b) HE, c) HS, d) LOG.

Figure 2 shows the results of selected algorithms. In general these algorithms yield an improved visual impression of the distracting illumination impact. However they are not able to eliminate local illumination effects like shadows since disregarding any spatial information.

2.2 Local Point Operations

The homogenous point operations can also be applied in a local window. That type of normalization for face recognition was first introduced by (Villegas-Santamaria and Paredes-Palacios, 2005) and (Xie and Lam, 2006). In our experiments we use the *Local Histogram Equation (LHE)*, *Local Histogram Matching (LHM)* and *Locale Normal Distribution (LND)*.

A common advanced local algorithm is the *Limited Adaptive Histogram Equalization (LAHE)*. The LAHE limits the contrast in homogenous regions and interpolates values of the neighbourhood to avoid

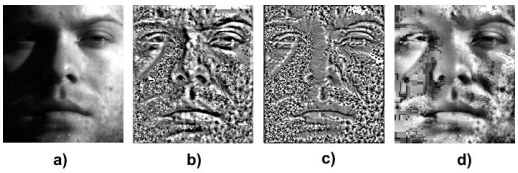

Figure 3: Normalization results of different local point operations with distinct intensity of artefacts: a) original, b) LHM, c) LHE, d) LAHE.

artefacts. In our experiments we use the LAHE developed by (Zuiderveld, 1994).

The results of local point operations show improved consideration on local effects of illumination by concomitant degrease of image quality for human impression, depicted in Figure 3.

2.3 Statistical Illumination Estimation

(Ko et al., 2002) introduced the *Linear Regression (LREG)* model to estimate the influence of illumination in face recognition as a regression plane. Applied on image data the regression plane Y' can be calculated with an approximated regression factor B. B can be calculated with the vectorized image X and its coordinates Y by a least square fit:

$$Y' = B \cdot X \quad with \quad = (X^T \cdot X)^{-1} \cdot X^T Y \quad (2)$$

The illumination normalization is achieved by inverting the resulting regression layer and substraction of the original image. For a more adaptive illumination estimation we introduce the *Nonlinear Regression (NLREG)* for illumination normalization in face recognition. The NLREG uses an n-th order polynomial as regression function. To prevent over fitting of the regression to facial contours we use only a 2D quadratic polynomial (QDREG):

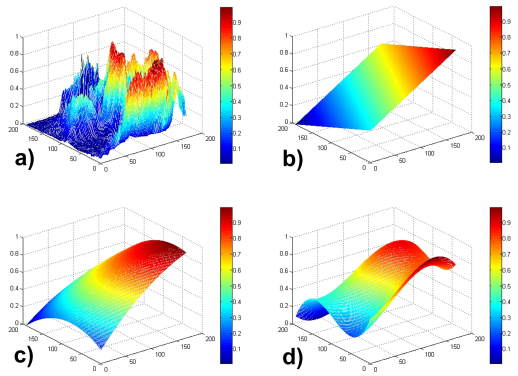

Figure 4: Approximations of different regression methods of an face image with strong shadows: a) original face, b) LREG , c) QDREG, d) CBREG.

$$L(x,y) = a_0 + a_1 \cdot x + a_2 \cdot y + a_3 \cdot x^2 + a_4 \cdot y^2 + a_5 \cdot xy \quad (3)$$

and a 2D cubic polynomial (CBREG) for our experiments. The regression coefficients a_i can be determined by least squares estimation. Figure 4 shows the different regression results.

All of these regression methods result in a quite similar visual impression depicted in Figure 5. This behavior depends on the same overall slope of the regression layers and the smooth influence of the polynomial characteristics.

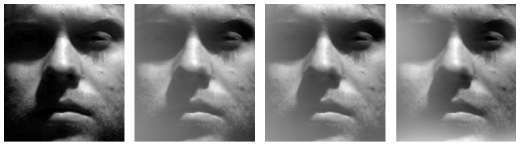

Figure 5: Illumination normalization results of statistical algorithms: a) original, b) result LINREG, c) result QDREG , d) result CBREG.

2.4 Retinex Methods

The retinex model, named after retina and cortex, was introduced by (Land, 1977) to entitle its model of the human visual perception. It describes the human visual cognition of color and illumination by considering retina and cerebral cortex. The most interesting point for illumination normalization is the assumption, that perception depends on the relative or surrounding illumination. It means that reflector $R(x,y)$ equals the quotient of intensity $I(x,y)$ and the illumination $L(x,y)$ calculated by the neighborhood of $I(x,y)$. The following algorithms estimates the illumination based on the pixel neighborhood.

Single-Scale Retinex (SSCRET) introduced by (Jobson and Woodell, 1995) defines a Gaussian kernel to estimate the neighborhood illumination. Within the SSCRET a logarithmic transformation of the image data is used as human perceptional oriented dynamic compression. These step is an additional requirement of the retinex theory (Levine et al., 2004). For SSCRET Equation 4 with a single Gaussian can be used.

$$R(x,y) = \sum_{s=1}^{S} (\log[I(x,y)] - \log[I(x,y) * G_s(x,y)]) \quad (4)$$

Multi-Scale Retinex (MSCRET) describes an extension to the SSCRET and uses multiple Gaussian kernels (Rahman et al., 1996). The aim of using different Gaussian filters with varying σ_s is a better approximation. The multiple results are combined by accumulating the single normalizations. Figure 6 shows the results of SSCRET and MSCRET.

The *Self Quotient Image (SLFQUO)* was developed by (Wang et al., 2004) and estimates an illumination free image Q as quotient of the intensity image

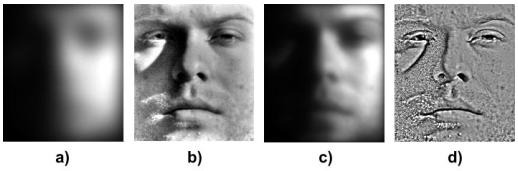

Figure 6: Illumination estimations and normalization results of Single/Multi-Scale Retinex algorithms: a) illumination est. SSCRET, b) result SSCRET, c) illumination est. MSCRET, d) result MSCRET.

I and I convolved with a filter F.

$$Q = \frac{I}{I * F} \quad (5)$$

The image Q equals to the reflection R and the filtered image I equals to the approximated illumination L. Similar to the MSCRET, multiple Gaussian filters were used. In contrast, a special weighted Gaussian kernel is designed and used in equation 4 instead of normal Gaussian kernel G.

In addition to the retinex theory the illumination estimation according to (Gross and Brajovic, 2003) *(GROBRA)* uses further information from the human perceptional research. Psychological experiments show that the ability of human visual perception to dissolve intensity change ΔI depends proportionally to the absolute intensity I. That behavior is described in Weber's law (Wandel, 1995) as:

$$\frac{\Delta I}{I} = \rho \quad (6)$$

Instead of Gaussian filters the GROBRA uses an minimization approach to estimate the illumination L.

$$\begin{aligned} E(L) = &\int\int_{\Omega} \rho(x,y) \cdot [L(x,y) - I(x,y)]^2 dxdy \\ &+ \lambda \int\int_{\Omega} (L_x^2 + L_y^2) dxdy \end{aligned} \quad (7)$$

The weighting function $\rho(x,y)$ is applied to handle the local contrast ratio based on equation 6. The second term of equation 7 describes a smoothing constraint with λ as weighting factor. To solve the minimization problem a linear partial differential equation system based on Euler-Lagrange equation is used.

The GROBRA seems to be the most sophisticated retinex algorithm but Figure 7 shows that at least the visual result yields the best by visual impression. The following section describes a novel diffusion filter approach that relates to the group of retinex algorithms.

3 DIFFUSION FILTER APPROACH

The theory of (Cohen and Grossberg, 1984) about neural dynamics of brightness perception indicates

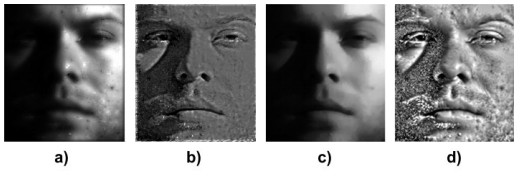

Figure 7: Illumination estimation and normalization result of SLFQUO and GROBRA algorithms: a) illumination est. SLFQUO, b) result SLFQUO, c) illumination est. GROBRA, d) result GROBRA.

that diffusion processes are proceeded in human perception. Qualities of features like brightness spread diffusively up to boundary contours in visual cortex.

In image processing the diffusion approach was introduced as *Scale-Space-Theory (SST)* by (Witkin, 1983). The concept of the SST is to describe structured elements by a multi-resolution pyramid that is generated by convolutions of the original image $I_0(x,y)$ with multiple Gaussian filters.

$$I(x,y,t) = I_0(x,y) * G(x,y,t) \tag{8}$$

The varying parameter t results in different sized images. Another form to describe that context is the diffusion equation as used by (Koenderink, 1984):

$$\partial_t I = \nabla^2 I = (I_{xx} + I_{yy}) \tag{9}$$

The motivation behind that approach is the assumption that structured elements can be better described by increasing the number of resolution planes. With rising the number of planes a floating approximation of the image structure can be processed.

Disadvantage of the SST is the linear isotropic behavior which means diffusion spread out to all directions without responding to edges. Further nonlinear algorithms e.g. (Perona and Malik, 1990) consider edges and reduce the diffusion by a diffusion coefficient c that depends on image gradients intensity.

$$\partial_t I = \nabla \cdot (c \cdot \nabla I) \tag{10}$$

Considering additionally the direction of edges in the diffusion process, leads to nonlinear anisotropic diffussion (Weickert, 1998). The different impacts on noisy images are depicted in Figure 8.

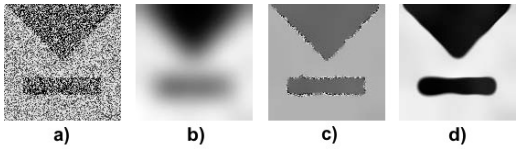

Figure 8: Different behaviors of diffusion filter for noise reduction with attention to structured elements: a) original, b) linear isotropic, c) nonlinear isotropic, d) nonlinear anisotropic (Weickert, 1998).

For illumination normalization the diffusion filtered image can be interpreted as the illumination estimation $L(x,y)$. With use of $L(x,y)$ a normalization in multiplicative Retinex context can be processed. Following a systematization of diffusion filters by (Weickert, 1998) we use the algorithm of (Perona and Malik, 1990) in our experiments as *Nonlinear Isotropic Diffusion Filter (NLISODIF)* that weakens the diffusion at edges by the intensity of the gradient.

Additionally we introduce the novel use of a diffusion tensor based *Nonlinear Anisotropic Diffusion Filter (NLANISODIF)* algorithm for illumination normalization. That approach uses a gradient direction related tensor D instead of diffusion coefficient c to weaken the diffusion process.

The diffusion tensor D according to (van den Boomgaard, 2004) is based on a rotation matrix and can be measured as:

$$D = \frac{1}{(I_x)^2 + (I_y)^2} \cdot \begin{pmatrix} d_1(I_x)^2 + d_2(I_y)^2 & (d_2 - d_1)I_x I_y \\ (d_2 - d_1)I_x I_y & d_1(I_y)^2 + d_2(I_x)^2 \end{pmatrix} \tag{11}$$

Figure 9 shows the normalization results of NLISODIF and NLANISODIF.

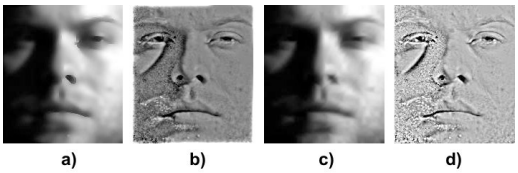

Figure 9: Illumination estimation and normalization results for different diffusion filter: a) illumination est. NLISODIF, b) result NLISODIF, c) illumination est. NLANISODIF, d) result NLANISODIF.

The visual impression of the diffusion results is similar to the related retinex methods. Based on the algorithmic the NLISODIF resembles the GROBRA while NLISODIF uses the gradient as weighting function and GROBRA the Weber contrast.

4 EVALUATION

4.1 Concept

The evaluation concept is based on the hypothesis that pre-processing methods with ability to solve the single problem of varying illumination possibly reduce recognition rate in real-world environment by removing necessary facial information.

For that reason we decided to conduct a two-step evaluation. First we tested under controlled conditions with small changes in pose and facial expression. This *pretest* should measure the ability of each

algorithm to normalize illumination changes and assure a comparability to other publications.

The second step measures the recognition rates under real-world uncontrolled conditions. This *real-world test* should evaluate changes within and between normalization groups compared by controlled and uncontrolled conditions. Further it allows to draw more practical oriented and reliable conclusions for the given use cases.

4.2 Face Recognition Algorithms

The choice of recognition algorithms plays an important role in the evaluation of the normalization methods. We decided to choose well known and common algorithms for eased comparability with other publication results.

We use the *eigenface* (Turk and Pentland, 1991) and *fisherface* (Belhumeur et al., 1997) approaches which are appearance based subspace methods for face recognition. These algorithms interpret pixels of images as coordinates in a high-dimensional space and transform them into low dimensional subspace called facespace. Therefore a training process with observations of reference persons is needed.

4.3 Databases

We used the following setup for our experiments: For pretest we choose the Yale Face Database B. It is well suited for evaluation of lightning influence as shown in (Georghiades et al., 2001).

We use four already defined database subsets with similar illumination conditions as shown in Figure 10.

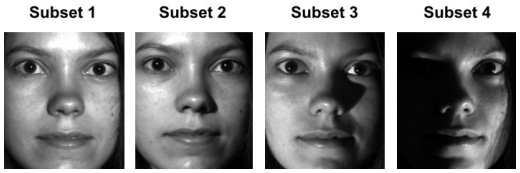

Figure 10: Examples of the Yale Face Database B subsets used for the pretest.

In our experiments we used all possible combination of these subsets. This procedure is oriented at realistic conditions, where different lighting environments can be used as reference and test data. Based on that procedure we get 4 by 4 recognitions rates. The final result is estimated as mean of this 16 rates.

Publicly available face recognition databases are usually based on controlled environmental conditions and focus on varying specific properties. Regarding the given use case with real-world conditions we created a new special database. It is set-up from private consumer photos that were taken by individual photographers, with different camera types, at very different situations, day-times and mimics. The only restriction is a frontally pose. Figure 11 shows examples of this database. It contains 25 persons with four observations of each person. Because of the small number of images per person we iterative changed the train and test observation to get four results for each person by using three training images per person.

Figure 11: Examples of the new real-world database that contains frontal face images varying in all possible aspects.

4.4 Results and Discussion

Figure 12 shows the results of our two-step evaluation. All algorithms went through pretest and real-world test with eigenface and fisherface recognition approaches. In addition each algorithm was separately evaluated with a preliminary and subsequent histogram equalization (HE). The subsequent HE improves the results clearly so that we present in each case only the best combination. The first data set in the diagram (ORG) represents the initial recognition rate without any normalization as reference.

As expected, the homogenous point operations leads to the lowest recognition rates of the test field. All algorithms supply similar results at least in the real-world test. Most of the algorithms could reach there results only by using a preliminary or subsequent HE. Based on that fact we ascribe most of the improvements to the HE.

Local point operations obtain the best results beneath the retinex methods. Within the local methods, especially by evaluating the LND, we could prove our hypothesis that transferring algorithms from controlled to uncontrolled environments can decrease performance. Reason for the decline of LND towards the LAHE could be the worse artefacts of LND that arise by filtering without paying attention to different contrast in local window. In real-world test LAHE is leading in its group and outperforms most of all other algorithms.

Statistical regression methods lead to good overall but not best results. On real-world test the nonlinear extensions come up with better results then LINREG

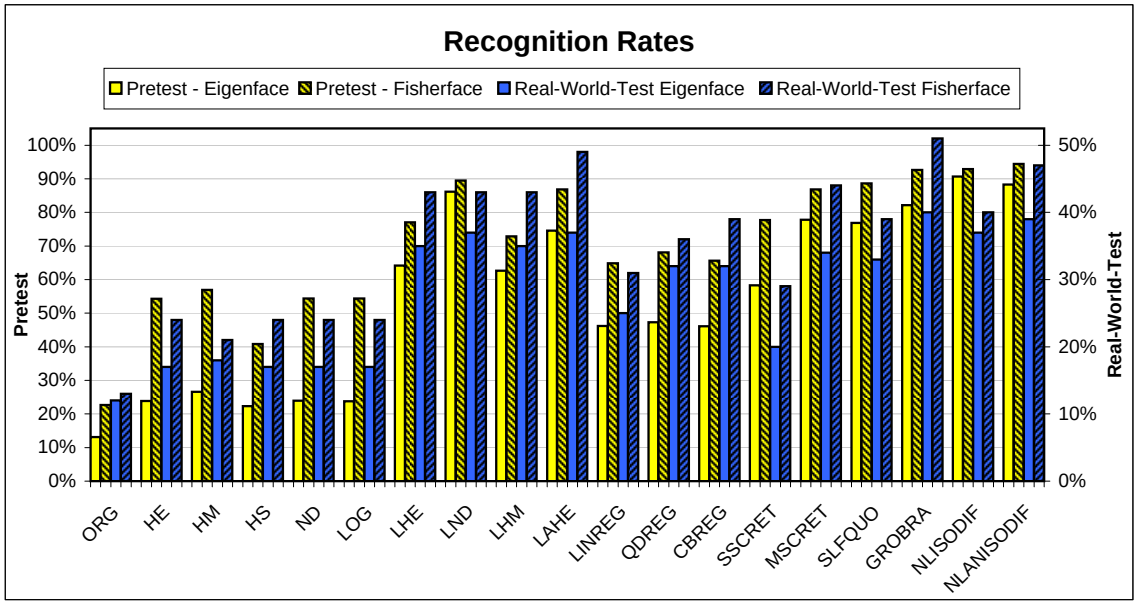

Figure 12: Results of two-step evaluation for pretest and real-world test as well as eigenface and fisherface approach.

but within pretest the results are equal. That behavior can be explained by the heavy cast shadows within pretest images which results in strong shadow lines that could not be approximated by the 2th and 3rd order polynomials. In most real-world images these strong shadow-light contours appear rarely, so that CBREG can improve recognition by 8 %.

The group of human perceptional algorithms based on retinex theory contains with NLANISODIF and especially GROBRA the outperforming algorithms of our experiments. A reason for that could be the consequent transfer of human visual processing techniques based on the perceptional concepts e.g. use of gradient information to approximate the illumination estimation. Following this conclusion SLFQUO with its weighted Gaussian filter that attempts to use gradient information could not convince within real-world test.

However, within the pretest the new diffusion filter based algorithms lead the overall results with 94 % recognition rate. Within the real-world test the Weber contrast proportion used by GROBRA seems to be more applicable. The GROBRA becomes the overall leading algorithm in real-world test with 51 % recognition rate which also supports our hypothesis.

Besides LAHE the GROBRA and NLANISODIF algorithms are of high practical relevance.

5 CONCLUSIONS

In this paper we presented a new taxonomy of illumination normalization methods. We introduced an algorithm motivated by human perception and based on known diffusion filter concepts. Further we presented the results of a two-step evaluation of 18 different algorithms to verify best approaches under controlled and uncontrolled real-world conditions. Our experiments suggest a number of conclusions:

- Our experiments showed that variation only in illumination can be normalized up to nearly consummate recognition rates of 94 %.
- We demonstrated that recognition rates for real-world data can be improved with eigenface from 12 % to 40 % and fisherface from 13 % to 51 %.
- Furthermore we verified our hypothesis that well-performing algorithms under controlled conditions can be worse under real-world conditions depicted on the overall leading algorithm of pretest and real-world test.
- Human perception related algorithms outperformed nearly all other algorithms.
- The group of local operations brought up multiple well-performing algorithms.

However, the real-world test results clearly show that illumination normalization is just one step to an entire face recognition system. There are a number of issues to be addressed in future work. First, analyze

in detail which factors influence the recognition rates to what extent. Second, evaluating of normalizing algorithms for different aspects e.g. pose or facial expression under real-world conditions. Finally, evaluation of further face recognition techniques is needed e.g. Hidden Markov Model (M. Bicego and Murino, 2003) or 2D Gabor Wavelet (Wiskott et al., 1997).

ACKNOWLEDGEMENTS

Parts of the presented research were realized within an ongoing partnership with the MAGIX AG. The publication was supported by grant No. 01MQ07017 of the German THESEUS program.

REFERENCES

Adini, Y., Moses, Y., and Ullman, S. (1997). Face recognition: The problem of compensating for changes in illumination direction. *IEEE Transactions on Pattern Analysis and Machine Intelligence*, 19(7):721–732.

Belhumeur, P. N., Hespanha, J. P., and J.Kriegman, D. (1997). Eigenfaces vs. fisherfaces: Recognition using class specific linear projection. *IEEE Transactions on Pattern Analysis and Machine Intelligence*, 19(7):711–720.

Cohen, M. A. and Grossberg, S. (1984). Neural dynamics of brightness perception: Features, boundaries, diffusion, and resonance. *Perception and Psychophysics*, 36(5):428–456.

Georghiades, A. S., Belhumeur, P. N., and Kriegman, D. J. (2001). From few to many: Illumination cone models for face recognition under variable lighting and pose. *IEEE Transactions on Pattern Analysis and Machine Intelligence*, 23(6):643–660.

Gross, R. and Brajovic, V. (2003). An image preprocessing algorithm for illumination invariant face recognition. *4th International Conference on Audio- and Video-Based Biometric Person Authentication*, pages 10–18.

Jobson, D. J. and Woodell, G. A. (1995). Properties of a center/surround retinex: Part 2 - surround design. Technical report, NASA Technical Memorandum 110188.

Ko, J., Kim, E., and Byun, H. (2002). A simple illumination normalization algorithm for face recognition. In *PRICAI '02: Proceedings of the 7th Pacific Rim International Conference on Artificial Intelligence*, pages 532–541. Springer-Verlag.

Koenderink, J. (1984). The structure of images. *Biological cybernetics*, pages 363–370.

Land, E. H. (1977). The retinex theory of color vision. *Scientific American*, 237(6):108–120, 122–123, 126, 128.

Levine, M. D., Gandhi, M. R., and Bhattacharyya, J. (2004). Image normalization for illumination compensation in facial images.

M. Bicego, U. C. and Murino, V. (2003). Using hidden markov models and wavelets for face recognition. In *12th International Conference on Image Analysis and Processing*, pages 52–56.

Perona, P. and Malik, J. (1990). Scale-space and edge detection using anisotropic diffusion. *IEEE Transactions on Pattern Analysis and Machine Intelligence*, 12(7):629–639.

Rahman, Z., Jobson, D. J., and Woodell, G. A. (1996). Multi-scale retinex for color image enhancement. *International Conference on Image Processing*.

Savvides, M. and Kumar, B. V. K. V. (2003). Illumination normalization using logarithm transforms for face authentication. *Audio- and Video-Based Biometric Person Authentication: 4th International Conference*, pages 549–556.

Shan, S., Gao, W., Cao, B., and Zhao, D. (2003). Illumination normalization for robust face recognition against varying lighting conditions. *IEEE International Workshop on Analysis and Modeling of Faces and Gestures*, pages 157–164.

Turk, M. A. and Pentland, A. P. (1991). Face recognition using eigenfaces. *IEEE Proceedings of Computer Vision and Pattern Recognition*, pages 586–591.

van den Boomgaard, R. (2004). Geometry driven diffusion. Lecture Notes at University of Amsterdam.

Villegas-Santamaria, M. and Paredes-Palacios, R. (2005). Comparison of illumination normalization for face recognition. *Third COST 275 Workshop Biometrics on the Internet*, pages 27–30.

Wandel, B. (1995). Foundations of vision. *Sunderland MA: Sinauer*.

Wang, H., Li, S. Z., and Wang, Y. (2004). Face recognition under varying lighting conditions using self quotient image. *Sixth IEEE International Conference on Automatic Face and Gesture Recognition*, pages 819–824.

Weickert, J. (1998). *Anisotropic Diffusion in Image Processing*. Teubner-Verlag, Stuttgart.

Wiskott, L., Fellous, J.-M., Krger, N., and von der Malsburg, C. (1997). Face recognition by elastic bunch graph matching. *IEEE Transactions on Pattern Analysis and Machine Intelligence*, 19(7):775–779.

Witkin, A. P. (1983). Scale space filtering. *Proceedings International Joint Conference on Artificial Intelligence*, pages 1019–1023.

Xie, X. and Lam, K.-M. (2006). An efficient illumination normalization method for face recognition. *Pattern Recognition Letters*, 27(6):609–617.

Zuiderveld, K. (1994). Contrast limited adaptive histogram equalization. *Graphics gems IV*, pages 474–485.

A NEW METHOD FOR ICG CHARACTERISTIC POINT DETECTION

Maria Rizzi, Matteo D'Aloia and Beniamino Castagnolo
Dipartimento di Elettrotecnica ed Elettronica – Politecnico di Bari, via E. Orabona, 4 70125 Bari, Italy
rizzi@deemail.poliba.it, matteo.daloia@libero.it, castagno@poliba.it

Keywords: ICG, C point detection, wavelet transform, parallel filter banks, time frequency analysis, signal processing, parallel computing

Abstract: Impedance Cardiography is a cost-effective, non-invasive technique particularly useful in measuring cardiac functions. It evaluates systolic time intervals and stroke volume measuring thorax bioimpedance. In this paper, adopting the time-frequency analysis method, a new design has been developed to study the first derivative of impedance cardiography signal. The application of parallel wavelet filter banks has been investigated and a new method for ICG signal characteristic point detection has been developed. Test results show the improvement of the method in sensitivity and the feasibility of an easy implementation by design tools. Moreover, the algorithm noise immunity has been investigated.

1 INTRODUCTION

Impedance Cardiography (ICG) is a technique to study cardiac functions through measurements of the thorax electrical impedance. It has been widely adopted because it is noninvasive, easy to use and suitable for long-term and continuous monitoring of hemodynamic function (Jensen, 1995). Moreover, the ICG signal can be correlated with other significant signals (i.e. ECG) to generate alarm in critical situations.

In the past difficulties associated in ICG signal processing have been motion artefacts, muscle noise, pacemakers, etc. The most recent ICG devices have shown improved accuracy. Therefore the ICG has established a role in the management of outpatients with hypertension, heart failure and other chronic diseases (Treister, 2005). The use of ICG in therapeutic decision making regarding patients with critical diseases is primarily based on its ability to identify presence or absence of hemodynamic abnormalities. For these reasons many researches have been developed both to study physiological mechanisms for understanding origin and meaning of ICG signals and to improve effectiveness and applicability of ICG diagnostic test adopting advanced signal processing techniques (Wang, 1995).

Many efforts have been done to implement automatic detection of reference points in biological signal. However, existing peak detection algorithms are difficult to automate for generic use because either they rely on a number of parameters that need to be customized for a particular application of the algorithm or they use reference informations that is highly specialized for a particular application.

Most of the proposed methods make use of filtering technique (band pass filtering and temporal filtering) (Leski, 1992), (Pan, 1984), or adaptive thresholding technique (Sun, 1992), (Suppappola, 1994). All the previous techniques exhibit limitations when real signal are adopted (Sun, 2005). In fact, the first drawback of filtering-based approach is that frequency variations in the signal under test (due to different causes such as, for instance, cardiac frequency changes) may adversely affect the method performance. For instance, the frequency band of some biological signal, such as ECG, differs for different subjects and can change for the same subject due to particular events. The second problem in the filter based algorithms is the frequency band overlapping of noise and some biological signals. Therefore, the choice of a suitable bandwidth is a trade off between noise and high frequency details while the duration of the sliding window is a trade off between false and missed detections.

Whereas, the main problem of the thresholding techniques is their sensitivity to baseline variations and signal intensity. This high noise sensitivity can

be a problem for some types of signals having low signal to noise (S/N) ratio.

An extensive overview of various algorithms for peak detection in ECG signals can be found in (Kohler, 2002) which includes approaches based on neural networks, adaptative filters, Hidden Markov models and Hilbert transform, too.

The purpose of this paper is to introduce an improved signal processing technique able to provide an easy implementation in design tools. It adopts the wavelet transform for ICG waveform characteristic point detection. Moreover, for parallel computing and for implementation by design tool, parallel filter banks have used in the adopted technique. Experimental results show the method validity and its high sensitivity parameter. In fact, sensitivity reliable results with minimum interferences from noise and artifact have been obtained.

2 ICG TECHNIQUE

Impedance cardiography is the study of cardiac function by means of thorax electrical impedance measurements. High frequency (20-100KHz), low intensity current (1-5mA rms) is injected through the thorax by some electrodes and the impedance change is sensed by measuring a voltage across other electrodes. No risk of physiological effects have been found because various tissues of human body are not excitable at this frequency and at this low current level (Patterson, 1989). The impedance variation can be used for diagnostic information and for the stroke volume (SV) estimation by using blood flow appropriate model. The term SV indicates the amount of blood pumped by the heart left ventricle in one contraction.

Figure 1 shows a typical impedance waveform obtained from electrodes in which the characteristic points are indicated.

Pulsating blood flow through the thoracic aorta causes shifts in the thoracic impedance as a function of changes in blood volume. This oscillating component of the total thoracic impedance can be expressed as its derivative (dZ/dt). Measurements of the changes in the thoracic impedance (dZ/dt waveform) during the cardiac cycle are used to calculate SV. This can be done in several ways (Kubicek, 1974), (Sramek, 1982), (Bernstein, 1986). Generally all the equations take into account position and value of C-point related to B-point and X-point.

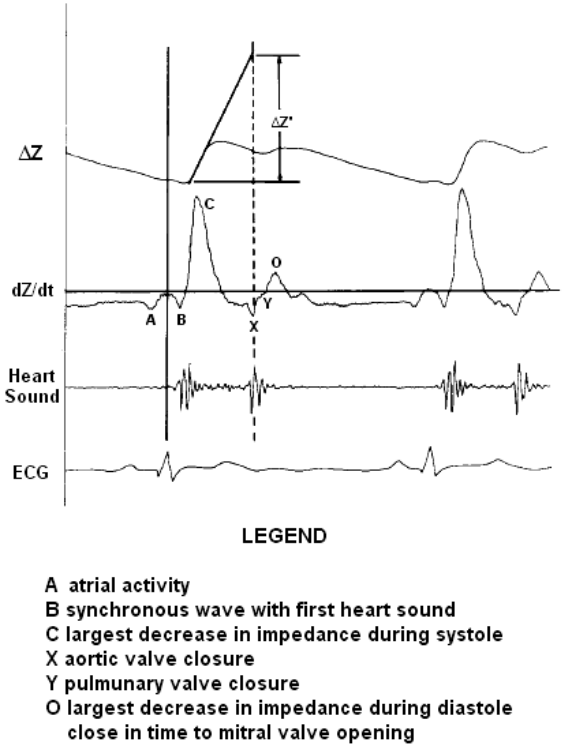

Figure 1: Typical impedance waveforms from the thorax of a human subject.

3 WAVELET TRANSFORM

Wavelet transform provides temporal and spectral information simultaneously, so it is suited for determining characteristic points of non stationary and fast transient signals, such as ICG signals. This feature is suitable to distinguish the ICG signal from noise and interferences.

The wavelet method decomposes a time variant signal into several components having various scales or resolutions. A suitable time and frequency limited wavelet is chosen as the "*mother*". Scaling and shifting the mother wavelet, a family of functions called "*daughter*" wavelet is generated. For small value of the scale factor, the wavelet is constructed in the time domain and gives information about fine details of signals. Therefore a global view of the signal is obtained by the scale factor large value. The wavelet transform of a time signal at any scale is the convolution of the signal and a time-scaled daughter wavelet.

There are essentially two types of wavelet decompositions: the redundant ones (continuous wavelet transform (CWT)), and the nonredundant ones (orthogonal, semi-orthogonal, or biorthogonal

wavelet bases) (Unser, 1996). The first type is preferable for feature extraction because it provides for a description that is truly shift-invariant. The second type is preferable for data reduction, or when the orthogonality of the representation is an important factor. However, the choice between these types of decompositions has to take into account computational considerations, too. A decomposition in terms of wavelet bases using Mallat fast algorithm is typically orders of magnitude faster than a redundant analysis, even if the fastest available algorithms are used (Rioul, 1992), (Unser, 1994).

As the aim of this paper is the implementation of a fast parallelized algorithm, a nonredundant wavelet decompositions has been chosen. To determine the best wavelet function to be used, the ICG signal properties have been studied, such as the shape and the time localization of events. Temporal signal shape is an important parameter, so orthogonal wavelets are unsuitable to be used. In fact they are unable to provide symmetry in the time domain and they introduce non-linear phase shift. The signal shape is maintained if the phase shift is linear. Thus the wavelet to be adopted should be a symmetrical function (Dinh, 2001). Spline wavelets have properties satisfying the previous requirements. The higher order of the Spline wavelet results in the sharper frequency response of the equivalent FIR filter, that is always desirable. But the FIR equivalent filter of the higher order Spline wavelet has longer coefficient series leading to more computational time consumption. Therefore, the cubic spline wavelet is assumed to have an order high enough for this application.

Traditional wavelet theory (Cohen, 1996) considers a decomposition algorithm with an iterative structure (in particular an asymmetrical tree structure) that does not efficiently merge with the novel computational techniques, such as parallel processing, concurrent programming and design tools. In this study the a' trous and the Mallat algorithms for parallelized filter bank design have been used (Yang Li, 2005). The algorithm generates a set of parallelized perfect-reconstruction filter banks for an arbitrary number of end-nodes of a traditional tree structure (Koh, 2003).

4 PEAK DETECTOR METHOD

The method presented in this section processes the first derivate of the impedance signal and allows to determine the time domain absolute position of C Peak (figure 1).

ICG signal (figure 2) is sampled at a frequency of 250 Hz. The input hardware stores sequentially all the sample in a high speed frame which is then processed in real time by the system.

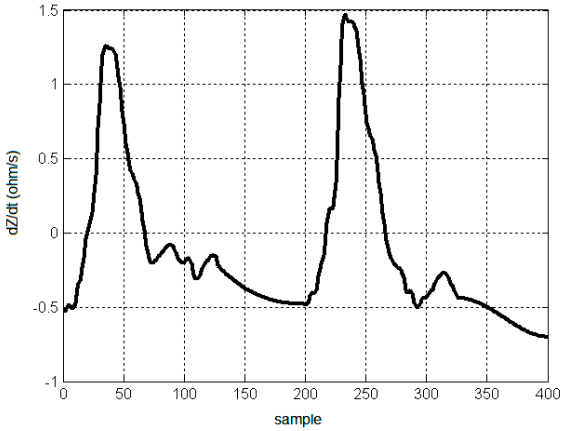

Figure 2: ICG signal.

In figure 3 the algorithm model is represented. The starting signal is indicated with 'ICG Signal', while the results with:

- 'C_point_Number' that evaluates the number of peaks presents in the processed frame;
- C_Indices' whose aim is the determination of the position of samples which corresponds to peaks

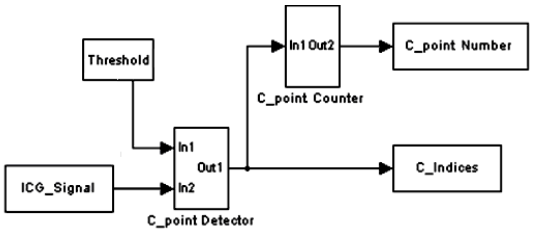

Figure 3: Algorithm model realized with the software tool MATLAB Simulink®.

The 'C_point Detector' subsytem (figure 4) determines the ICG signal peaks.

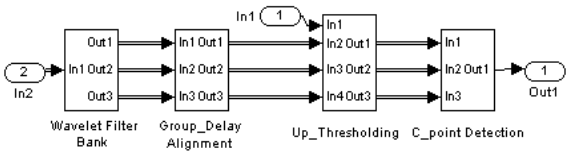

Figure 4: 'C point detector' subsystem model.

It uses an evolution of the classical Mallat decomposition, called a' trous algorithm. The a'

trous algorithm for non-ortogonal wavelet uses a filter bank structure as the Mallat algorithm (Mallat, 1989), but differs only for the filters design. It has been demonstrated that after the application of wavelet filters for j-times, the precision of a' trous algorithm is 2j time higher then the Mallat algorithm (Table 1) (Shensa, 1992).

Table 1: Precision of Mallat algorithm and a' trous algorithm varying decomposition level

Algorithm	Precision level 1	Precision level 2	…	Precision level j
Mallat	1/512	1/256	…	2^j/1024
a' trous	1/1024	1/1024	…	1/1024

For the tree structure of the algorithm, the previous structure is not suitable for parallel computing and for implementation in design tools. To overcome this limit equivalent parallel filter banks have been used. As it is known, the output signal realignment is necessary only to put just the delay introduced by each filter (figure 5).

A cubic spline wavelet (wavelet 'bior3.3') has been chosen because it makes possible the perfect signal reconstruction (figure 6).

For ICG signal processing, six dyadic scales have been used to decompose the signal (figure 7).

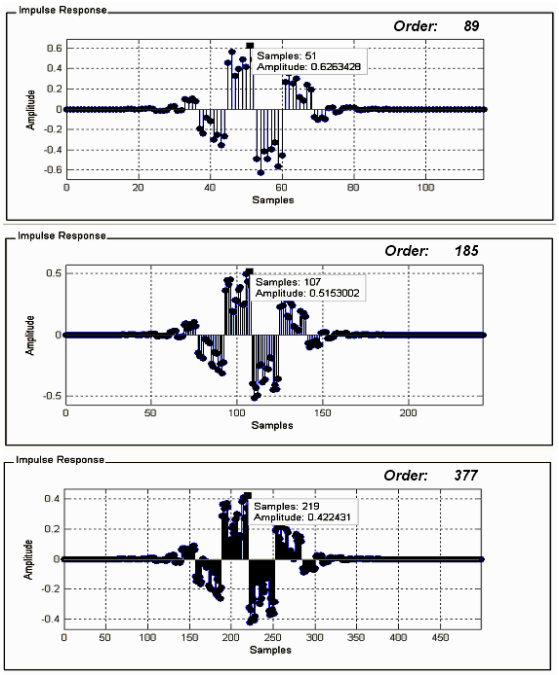

Figure 5: Pulse response of FIR filters equivalent to levels 4, 5, 6.

With a soft treesholding technique applied to level 1, 2, 3, the noise has been reduced and then the signal reconstructed in the time domain.

To localize characteristic points inside signal, detail levels 4, 5, 6 have been considered because they contain the highest number of C signal frequencies.

In respect to each singularity in ICG signal, a point of maximum value in detail coefficient signal is present. The proposed method searches local maximum points in the positive region of scale 4, scale 5 and scale 6 using a thresholding technique. Various tests have indicated the local maximum in the lower scale as the best points for the real signal peak localization

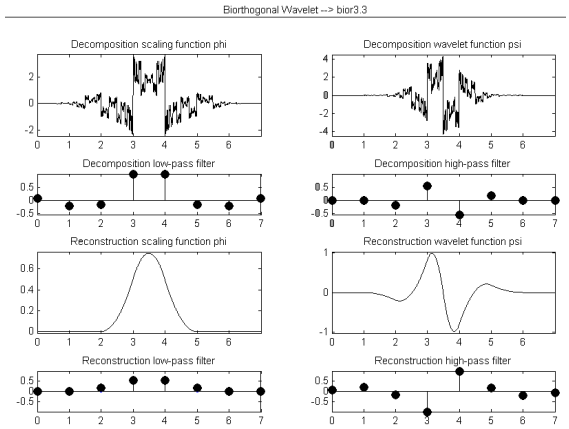

Figure 6: Wavelet 'bior3.3'.

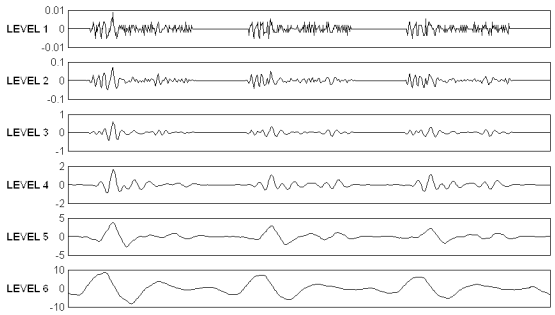

Figure 7: Decomposition of ICG signal over six scales.

5 RESULTS AND DISCUSSION

Real ICG signal (fig.8) has been tested with good results. Moreover the test has been repeated adding Gaussian noise with zero average and variable variance. In this situation the algorithm noise immunity has been evaluated.

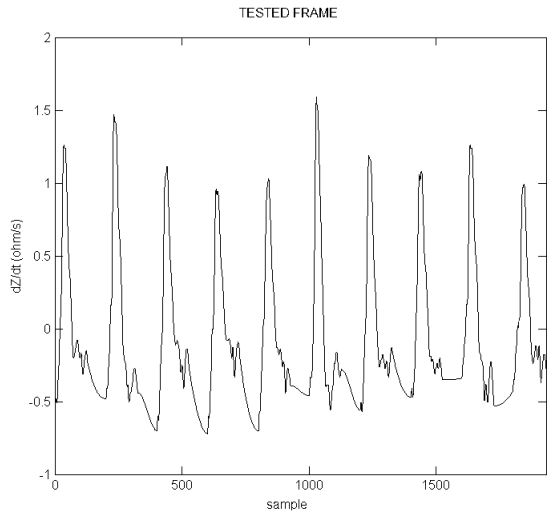

Figure 8: Frame tested.

The software detection algorithms for medical applications requires the evaluation of the detection performance according to ANSI/AAMI standard. Two parameters are used to evaluate algorithms:

Sensitivity:

$$Se = \frac{TP}{TP + FN} \quad (1)$$

Positive Prediction:

$$P = \frac{TP}{TP + Fp} \quad (2)$$

where:

- TP is the number of true positive detections;
- FN (the number of false negatives) is the number of C points present in the signal that the algorithm is not able to detect;
- FP (the number of false positives) is the number of C points detected by the algorithm but really not present in the signal.

Tested Frame presents C-peak value fluctuations in the range [1÷1.5Ω/s]. Other local maximum points are all in the negative region. Algorithm has individuated the 50% of the maximum value of the wavelet in each windowed segment of data as the optimal threshold value.

The obtained sensitivity parameter is very satisfactory and appears quite independent from noise (figure 9). Predictivity is fairly good but decreases as noise increases (figure 10).

Anyway it is to be noted that very heavy noise conditions have been chosen to test the algorithm noise immunity. An additional Gaussian noise signal with $v=0.1(\Omega/s)^2$ corrupts heavily the ICG signal; in particular the noise, besides changing the ICG signal shape, introduces many false peaks while cancels a minor number of true peaks.

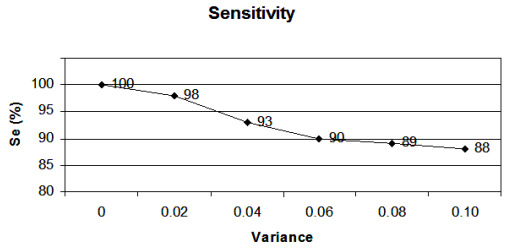

Figure 9: Sensitivity.

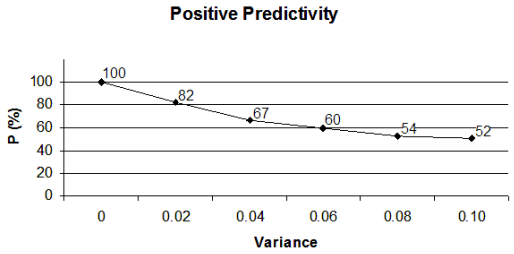

Figure 10: Positive Predictivity.

6 CONCLUSIONS

The real-time C-point detection algorithm presented in this paper has demonstrated to have high sensitivity.

The method computational time has been optimized adopting a parallel procedure to analyze the ICG signal. Therefore the realized procedure is suited to be implemented in real applications. Practical performance is to be improved for positive predictivity that appears to be sensible to noise level. Moreover, the absence of standard and validated ICG data bases, such as those used for ECG signals, makes the algorithm efficiency evaluation difficult and provides results poorly reproducible and comparable.

REFERENCES

Bernstein, D. P. (1986). A new stroke volume equation for thoracic electrical bioimpedance: theory and rationale. *Critical Care Medicine*, *14*(10), 904-909

Cohen, A., Kovacevic, J. (1996). Wavelets: the mathematical background. *Proceedings of the IEEE, 84,* 514-522

Dinh, H. A. N., Kumar, D. K., Pah, N. D., & Burton, P. (2001). Wavelets for QRS detection. *Proceedings of*

the 23rd Annual International Conference of the IEEE Engineering in Medicine and Biology Society, 2, 1883-1887.

Jensen, L., Yakimets, J., & Teo, K.K. (1995). A review of impedance cardiography. *Heart & Lung, 24*, 183-193

Koh, M. S., & Rodriguez-Marek, E. (2003). Generalized and parallelized ´a trous and Mallat algorithms to design non-uniform filter-banks. *Proceedings of the IEEE International Symposium on Signal Processing and Information*, Darmstadt, Germany, 38-41.

Kohler, B.U., Hennig, C., & Orglmeister, R. (2002). The principles of software QRS detection. *IEEE Eng. in Medicine and Biology*, *2,* 42-56

Kubicek, W. G., Kottke, F. J., Ramos, M. U., Patterson, R. P., Witsoe, D. A., Labree, J. W., et al. (1974). The Minnesota impedance cardiograph, theory and applications. *Biomedical Engineering, 9*, 410-416

Leski, J., & Tkacz, E. (1992). A new parallel concept for QRS complex detector. *Proceedings of the 14th Annual International. Conference. IEEE Eng. in medicine and Biology Society*, part 2 , Paris, France, 555-556

Mallat, S. G. (1989). A theory for multiresolution signal decomposition: the wavelet representation. *Transactions on Pattern Analysis and Machine Intelligence, 11*, 674-693

Pan, J., & Tompkins, W.J. (1984). A real-time QRS detection algorithm. *IEEE Trans. Biomed. Eng.*, *22,* 289-297

Patterson, R. P. (1989). Fundamentals of impedance cardiography. *IEEE Engineering in Medicine and Biology Magazine, 8*, 35-38

Rioul, O., & Duhamel, P. (1992). Fast algorithms for discrete and continuous wavelet transforms. *IEEE Trans. Information Theory, 38*(2), 569-586

Shensa, M.J. (1992). The discrete wavelet transform: wedding the a'trous and Mallat algorithms. *IEEE Trans. on signal processing, 40*, 2464-2482

Sramek, B. B. (1982). Cardiac output by electrical impedance. *Medical Electronics, 4*, 93-97

Sun, Y., Chan, K. L, & Krishnan, S. M. (2005). Characteristic wave detection in ECG signal using morphological transform. *BMC Cardiovascular Disorders, 5*, 28

Sun, Y., Suppappola, S., & Wrublewski, T.A. (1992). Microcontroller-based real-time QRS detection. *Biomed. Instr. Technol., 26*, 313-327

Suppappola, S., & Sun, Y. (1994). Nonlinear transforms of ECG signals for digital QRS detection: A qualitative analysis. *IEEE Trans. Biomed. Eng., 41*, 397-400

Treister, N., Wagner, K., & Jansen, P.R. (2005). Reproducibility of impedance cardiography parameters in outpatients with clinically stable coronary artery disease. *American Journal of hypertension, 18*, 44-50

Unser, M. (1994). Fast Gabor-like windowed Fourier and continuous wavelet transforms. *IEEE Signal Processing Letters*, *1*(4), 76-79

Unser, M., & Aldroubi A. (1996). A review of wavelets in biomedical application. *Proceedings of the IEEE*, *84*(4), 626-638

Yang, Li Y., Chenglin, P., Huafeng, W., Zhiqiang, Z., & Min, M. (2005). Using a'trous Algorithm and Modulus Maximum Lines to Detect R-wave of ECG Signal. *Proceedings of the 27th Annual Conference of the IEEE Engineering in Medicine and Biology,* Shanghai, China, 1270-1273.

Wang, X., Sun, H., & Van De Water, J. M. (1995). An advanced signal processing technique for impedance cardiography. *IEEE Trans. on Biomedical Engineering*, *42,* 224-230.

ECG SIGNAL DENOISING
Using Wavelet in Besov Spaces

Shi Zhao, Yiding Wang
Graduate University of Chinese Academy of Sciences, Zhongguancun East Road, Beijing, China
Zhaoshi05@mails.gucas.ac.cn, ydwang@gucas.ac.cn

Hong Yang
Graduate University of Chinese Academy of Sciences, Zhongguancun East Road, Beijing, China
yhong@mails.gucas.ac.cn

Keywords: ECG, noise reduction, wavelet, Besov, nonlinear shrinkage function.

Abstract: This paper proposes a novel technique to eliminate the noise in practical electrocardiogram (ECG) signals. Two state-of-the-art denoising techniques, which both based on wavelet bases, are combined together. The first one is discussing wavelet bases in Besov spaces. Compared to traditional algorithms, which discuss wavelets in $L^2(R)$ spaces, the proposed technique projects ECG signals onto Besov spaces for the first time. Besov space is a more sophisticated smoothness space. Determining the threshold of shrinkage function in Besov space could eliminate Gibbs phenomenon. In addition, instead of using linear shrinkage function, the proposed algorithm uses nonlinear hyper shrinkage function, which is proposed by Poornachandra. The function tends to keep a few larger coefficients representing the function while the noise coefficients tend to be reduced to zero. Combining the two techniques, we obtain a significant improvement over conventional ECG denoising algorithm.

1 INTRODUCTION

Removing noise is an pertinent problem in ECG signals processing. Usually, there are two kinds of noises in ECG, power line frequency noise and white noise. Power line frequency noise can be regarded as the result of an electromagnetic compatibility issues: background electromagnetic field interference from surrounding equipments and from buldings and power conductors. White noise is usually considered from the measure equipment.

Previously, different filters based on Fourier bases are used to eliminate the noises, such as notch filter. The problem of these methods is that they could not reduce the two kinds of noises at the same time. In addition, because the notch has a relatively large bandwidth, which means that the other frequency components around the desired null are severely attenuated, this method brings in signal distortions. In 1995, Donoho (David L Donoho, 1995) proposed a novel denoising algorithm based on wavelet shrinkage. It provides excellent performance and since then, wavelets became a state-of-the-art denoising method. Before long, P. M Agante (P M Agante, 1995) applied soft-threshold method in ECG and achieve good results. However, traditional wavelet method has its drawbacks. They are not shift invariant; therefore, for the signals not smooth enough, it will appear Gibbs Oscillation phenomenon at the location where the signal is sharp changed. In ECG signals, there are R waves, which change sharply. As a result, Traditional wavelet denoising algorithm brings in Gibbs oscillation after R waves.

In this paper, we apply two techniques to eliminate the noise and restrain the Gibbs phenomenon at the same time. First, we determine the threshold of wavelet shrinkage function in Besov spaces. Besov space $B_q^\alpha(L^P)$ is a smoothness space with $\sigma > 0$, $(p,q) \in [1,+\infty)^2$, it is defined by

$$B_q^\alpha(L^P) = \{f \in L^P(R) \mid \|f\|_{B_q^\alpha(L^P)} < \infty\} \quad (1)$$

Where the Besov seminorm $\|\cdot\|_{B_q^\alpha(L^P)}$ is linked to the smoothness modulus of the considered function. Besides that, in stead of linear shrinkage function, we use nonlinear shrinkage model (S. Poornachandra, 2007). Combining the two novel

techniques, we obtain a significant improvement over conventional wavelet denoising algorithm. In order to certify our idea, the noises in ECG signals in our experiment are not added by hand. They are from actual interfering. We collect the ECG signals with noises by our own devices.

2 INTRODUCTION TO WAVELET SHRINKAGE FUNCTION IN BESOV SPACE

Wavelet is defined as orthonormal basis functions for the expansion of functions belonging to various function spaces. Usually, it is the space of squared integrable real functions $L^2(R)$ (functions with finite energy). Recently, it has been shown that more sophisticated smoothness spaces, such as Besov spaces, provide a suitable and more refined characterization of real-life signals (Kathrin Berkner, 2000). The wavelet series representation of a function $f(t) \in L^2(R)$ could be express as

$$f(t) = \sum_{k \in Z}^{2^{j_0}-1} c_{j_0 k} \varphi_k(t) + \sum_{j=j_0}^{\infty} \sum_{k \in Z}^{2^{j_0}-1} d_{jk} \psi_{jk}(t) \tag{2}$$

φ is called farther wavelet and ψ is called mother wavelet. $\varphi_{j,k}(t)$ and $\psi_{j,k}(t)$ are the dilation and translation of the wavelet function.

$$\varphi_{j,k}(t) = 2^{j/2} \varphi(2^j - k) \tag{3}$$

$$\psi_{j,k}(t) = 2^{j/2} \psi(2^j - k) \tag{4}$$

j , k are the scaling and translation parameters respectively, $j,k \in Z$, $2^{j/2}$ could maintain the unity norm of the basis function at various scales. The coefficients $c_{j_0 k} = \langle g, \varphi_{j_0 k} \rangle$ and $d_{jk} = \langle g, \psi_{jk} \rangle$. Often we set $j_0 = 0$, and in that case there is only one scaling coefficient. The wavelet series are usually discussed in $L^2(R)$ spaces, but in our research, we use a more sophisticated set of functions, Besov spaces $B_q^{\alpha}(L^P)$ ($0 < \alpha < \infty$, $0 < p \le \infty$, $0 < q \le \infty$). In Besov spaces, for a function $f \in B_q^{\alpha}(L^P)$, its norm could be defined using its wavelet coefficients as (5) (Kathrin Berkner , 2000)

$$\| f \|_{B_q^{\alpha}(L^P)} = \left(\sum_k | c_{j_0 k} |^p \right)^{\frac{1}{p}} + \left(\sum_{j > j_0} \left(2^{j(\alpha p + p/2 - 1)} \sum_k | d_{jk} |^p \right)^{q/p} \right)^{\frac{1}{q}} \tag{5}$$

The three Besov parameters have natural interpretations: a p -norm of the wavelet coefficients is taken within each scale j , a weighted q -norm is taken across scale, and the smoothness parameter α controls the rate of decay of the d_{jk} , increasing α corresponds to increasing smoothness.

Based on reference (Antonin Chambolle, 1998), the denoising problem could be described as follow. Given a positive parameter λ and a signal f , find a function $\tilde{f}$ that minimize over all possible function the functional

$$\| f \|_{B_q^{\alpha}(L^P)}^q + \frac{\lambda}{2} \| f - f_0 \|_{L^2}^2 \tag{6}$$

Choose a proper λ , the $\tilde{f}$ could be the denoising signal of f . For simpleness, we set Besov parameters $p = q = 1$. Then the problem could be expressed as follow:

$$\min \sum_{j,k} 2^{j(\alpha - 1/2)} | d_{j,k} | + \frac{\lambda}{2} \sum_{j,k} \left(d_{j,k}^0 - d_{j,k} \right)^2 \tag{7}$$

That means for each j , k , we estimate the $\hat{d}$ use follow expression:

$$\begin{aligned} \hat{d} &= \arg\min_d \frac{\lambda}{2} (d_0 - \lambda)^2 + 2^{j(\alpha - 1/2)} | d | \\ &= sign(d_0) \cdot \max(| d_0 | - 2^{j(\alpha - 1/2)} / \lambda) \end{aligned} \tag{8}$$

That means the ECG signal has small Besov norm if the wavelet coefficient in each scale have small l_1 norms and those l_1 norms decay rapidly across scale.

Note that any wavelet basis having $r > \alpha$ vanishing moments can be used to measure a Besov norm (Hyeokho Choi, 2004).

3 INTRODUCTION TO NONLINEAR SHRINKAGE MODEL

Donoho and Johnstone were first to formalize the wavelet coefficient thresholding for removal of additive noise from deterministic signals (David L Donoho, 1995). Wavelet thresholding is based on the property that typical real-world signals have sparse representations in the wavelet domain. The small coefficients are usually correlated to noise. Therefore, by choosing an orthogonal basis, which could efficiently approximates the signal with few nonzero coefficients; we could choose a particular threshold and set the coefficient bellow the threshold to zero. Using these coefficients in an IDWT to reconstruct the data, we could kill the noise.

The shrinkage function proposed by Donoho and Johnstone are the hard and the soft shrinkage function. Hard thresholding simply sets the coefficients below a threshold T to zero, as (9). Soft thresholding first shrinks each coefficient by T and then hard thresholds, as (10).

$$\delta_T^H(x) = \begin{cases} 0, & |x| \le T \\ x, & |x| > T \end{cases} \tag{9}$$

$$\delta_T^S(x) = \mathrm{sgn}(x)\left(|x| - T\right)_+ \tag{10}$$

Both hard and soft shrinkages have their disadvantages. Due to the discontinuities of the shrinkage function, hard shrinkage estimate tends to have bigger variance and can be unstable, that is, sensitive to small changes in the data. The soft shrinkage estimate tends to have bigger bias, due to the shrinkage of large coefficients (S. Poornachandra, 2007).

To overcome the drawbacks of hard and soft shrinkage, we decide to use nonlinear shrinkage function. There are two kinds nonlinear shrinkage estimate in our experiment. The first is called nonnegative garrote shrinkage function (M. Vetterli, 1995), which was first introduced by Breiman (1995) as follow:

$$\delta_\lambda^G(x) = x\left[1 - (\lambda / x)^2\right]_+ \tag{11}$$

The shrinkage function $\delta_\lambda^G(x)$ is continuous and it provides a good compromise between the hard and the soft shrinkage functions. It is less sensitive than hard shrinkage to small fluctuations and less biased than soft shrinkage. The second shrinkage function is called hyper shrinkage, which is proposed by S. Poornachandra as follow:

$$\delta_\lambda^{hyp}(x) = \tanh(\rho * x)\left(|x| - t\right)_+ \tag{12}$$

The major advantage of hyper shrinkage is its nonlinearity, that is, the function in wavelet domain tends to keep a few larger coefficients representing the function while the noise coefficient tend to be reduced to zero.

4 NOISE REDUCTION BY OUR METHOD

The objective of this paper is to eliminate the noise buried in practical ECG signals. In our research, we combine the two techniques we mention above. First, we determined the threshold of shrinkage function for each level in Besov spaces. It is obviously that for each subband, the parameter α should be different. We set α_j for each level experimentally. Then we use the two kinds of nonlinear shrinkage functions to obtain the estimated coefficients. Finally, using these coefficients the original ECG signal is thus recovered. The general process is showed bellow. The decomposition level is 6.

Step 1. Choose db3 wavelets, and do DWT.

Step 2. Choose α at each level. For the fist level $\alpha_0 = 0.9$, and $\alpha_j = \alpha_0 + 0.25 * sqrt(\log(j+2))$ for each level.

Step 3. Determine the threshold based on the α_j.

Step 4. Apply hyper shrinkage function and the estimated coefficients obtained.

Step 5. IDWT use the estimated coefficients.

5 SIMULATIONS AND RESULTS

In our research, the ECG signals are obtained by our own devices. Each piece of signal is about 1 min long. The sampling rate is 1200Hz.

In our research, we use five different denoising methods. We show original signal and the processed 4 signals and their spectrums in Fig.1 to Fig.6. In order to see clearly, we show their details of the sample points around R waves. The method in Fig.2 determines the threshold in $L^2(R)$ spaces and use hard thresholding shrinkage function, while in Fig.3 the thresholds is determined in $L^2(R)$ spaces and use soft thresholding method. The other three discuss the thresholds in Besov spaces. Whereas Fig.4 uses soft shrinkage function, Fig.5 use nonnegative garrote shrinkage function and the last one uses hyper shrinkage function.

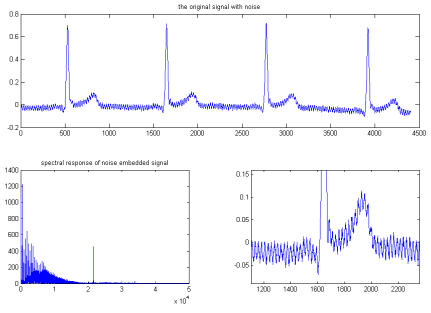

Figure 1: The original signal and its spectrum.

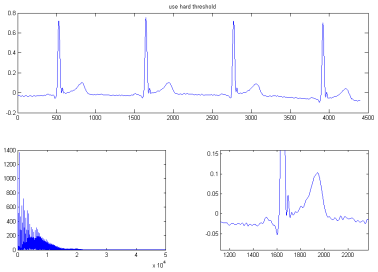

Figure 2: Determine the threshold in $L^2(R)$ and use hard thresholding.

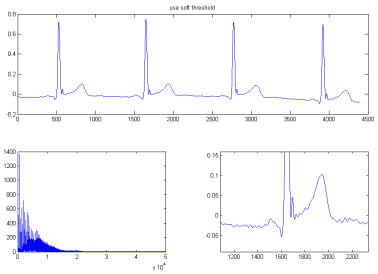

Figure 3: Determine the threshold in $L^2(R)$ and use soft thresholding.

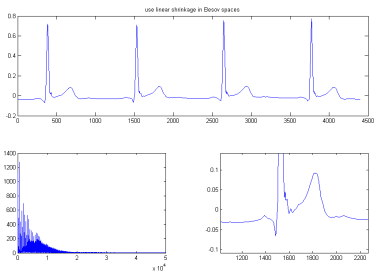

Figure 4: Determine the threshold in Besov spaces and use soft thresholding.

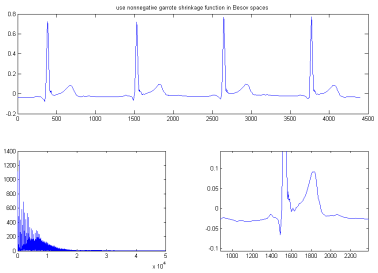

Figure 5: Determine the threshold in Besov spaces and use nonnegative garrote shrinkage function.

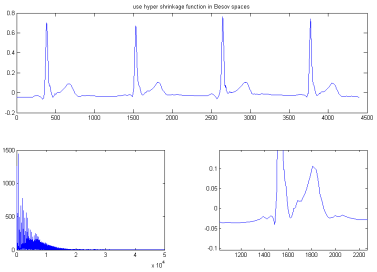

Figure 6: Determine the threshold in Besov spaces and use hyper shrinkage function.

As we seen from the pictures above, combined with threshold determined in Besov spaces and hyper shrinkage function, the recovered signal is the most visually pleasant. The proposed technique almost eliminate Gibbs phenomenon. To describe the oscillation of the recovered signal quantificational, we calculate the total variation of the six signals. Total variation for a uniform sampling discrete signal f is defined as (S. Mallat, 1998).

$$\| f_N \|_V = \sum_n | f_N[n] - f_N[n-1] | \tag{13}$$

Where $\| f_N \|_V$ is the Total Variation. In order to certify the effectiveness of the proposed method, we give 4 pieces of signals' Total Variation. They are show in Table 1.

Table 1: Total Variation of the signals.

	1	2	3	4	average
T1	0.3914	0.3747	0.3801	0.3875	0.3834
T2	0.1789	0.1654	0.1388	0.1252	0.1521
T3	0.1789	0.1654	0.1388	0.1252	0.1521
T4	0.1721	0.1517	0.1006	0.1177	0.1355
T5	0.1758	0.1504	0.1030	0.1206	0.1374
T6	0.1431	0.1371	0.0803	0.0919	0.1131

In the above table, T1 means the original signals' Total Variation. T2 to T6 correspond Fig.2 to Fig.5. In the table, we could notice easily that discussing threshold in Besov space and using nonlinear shrinkage function could obtain good results. And among those, hyper shrinkage is the most effective, it has the least oscillation.

6 CONCLUSIONS

This paper proposes a novel approach to eliminate the noises in practical ECG Signals. First, we use the characterization of Besov space, which is a smoothness spaces, through wavelet

decompositions. Then we apply nonlinear shrinkage function instead of linear shrinkage function. The experiment results show that the proposed algorithm is visually pleasant compared to traditional methods. It could eliminate the noise successfully, and at the same time, it suppresses Gibbs oscillation. The proposed technique has potential application in data acquisition systems, which are generally encountered by noise.

ACKNOWLEDGEMENTS

This research is supported by High Technology Research and Development Program of China (863 Program): 2006AA01Z133. The ECG signals collection device is designed by Shen Yadong, who is a graduate student in Tsinghua University, China.

REFERENCES

S. Poornachandra, N. Kumaravel, 2007. A novel method for the elimination of power line frequency in ECG signal using hyper shrinkage function. *Digital Signal Process*, doi:10.1016/j.dsp.2007.03.011.

S. Mallat, 1998. *A Wavelet Tour of Signal Processing*. Academic Press. San Diego, 2nd edition.

David L Donoho, 1995. De-noising by soft thresholding. *IEEE Transactions on Information Theory*, 41(3): 613-627.

P M Agante, J P Marques de Sa, 1995. ECG noise filtering using wavelets with soft-threshold method. *IEEE Computers in Cardiology*, 26:535-538.

M. Vetterli, J. Kovacevic, 1995. *Wavelet and Subband Coding*. Prentice Hall International, Englewood Cliffs, NJ.

Kathrin Berkner, Michael J. Gormish, Edward L. Schwartz, and Martin Boliek, 2000. A new wavelet-based approach to sharpening and smoothing of images in Besov spaces with applications to deblurring. *Proceedings. 2000 International Conference on Image Processing*, Vol 3: 10-13

Hyeokho Choi, Richard G. Baraniuk, 2004. Multiple wavelet basis image denoising using Besov ball projections. *IEEE signal processing letters*, Vol. 11. NO.9.

D. Leporini, J. C. Pesquet, 2000. Bayesian wavelet denoising: Besov priors and non-Gaussian noises. *Elsevier Science Signal Processing*,81: 55-67.

Alexandre Almeida, 2004. Wavelet bases in generalized Besov spaces. *Elsevier mathematical analysis and applications*, Appl.304: 198-211.

Antonin Chambolle, Ronald A. DeVore, Nam-yong Lee, and Bradley J. Lucier, 1998. Nonlinear wavelet image processing: variational problems, compression, and noise removal through wavelet shrinkage. *IEEE Transactions on image processing*, Vol. 7, NO.3.

WAVELET-BASED REAL-TIME ECG PROCESSING FOR A WEARABLE MONITORING SYSTEM

S. Zaunseder and W.-J. Fischer
Lifetronics, Fraunhofer Institute for Photonic Microsystems, Maria-Reiche-Strasse 2, 01109 Dresden, Germany
sebastian.zaunseder@ipms.fraunhofer.de

R. Poll and M. Rabenau
Institute of Biomedical Engineering, Dresden University of Technology, Dresden, Germany
Ruediger.Poll@tu-dresden.de

Keywords: ECG processing, wavelet transform, shift-invariance, quadratic spline, real time, ambulatory monitoring, wearable, ultra-low power microcontroller, MIT-BIH Arrhythmia Database.

Abstract: This paper presents a wavelet-based signal processing method developed for an ambulatory ECG monitoring system. The monitoring system comprises modern trends in ambulatory ECG monitoring like integration of hardware in clothing, the use of low-power components and wireless data transmission via Bluetooth. The signal processing is located close to the sensor, thus allowing increased variability for the subsequent data handling (i.e. data transmission in case of detected abnormalities). Due to the very limited computational resources (an ultra-low power microncontroller (μC)) and the relatively high demands upon signal processing, the need arises for a method which meets the special demands of the ambulatory application. Therefore, we developed a wavelet-based method for detecting QRS complexes, especially adapted to the real-time requirements. The novel idea of our approach was to incorporate information gained from a lower scale directly into the threshold applied for QRS detection in a higher scale. To date, all tests proved a very low computational load while simultaneously preserving the reliability of the analysis (Se=99,74%, +P=99,85% using the entire MIT-BIH Arrhythmia Database), thus pointing out the possibilities of real-time signal processing under ultra-low power conditions.

1 INTRODUCTION

Analysis of the electrocardiogram (ECG) is used for diagnosis in a wide range of cardiac diseases. Anomalous changes may indicate arising coronary diseases in an early stage. Further on, acute life-threatening situations can be observed in the ECG immediately after their incidence. Increasingly powerful hardware today allows ambulatory long-time monitoring of the ECG. Such recordings are especially useful to detect sporadically occurring events, which are not perceptible in short-time readings. Also, the online observation of patients with increased risk of cardiac breakdowns, due to preliminarily diseases or due to special physiological stress, is feasible. The available possibilities make the long-time ECG a very powerful tool for improved medical care. The Fraunhofer Institute for Photonic Microsystems (IPMS) focuses on the development of a complete system for ambulatory ECG monitoring. The signal processing is done in close proximity to the sensor to allow a high flexibility in further data handling. In particular, wireless data transmission can be reduced to situations of imminent risks, increasing the efficiency of the system to allow the long-time application (up to 7 days) of the system.

Due to the very limited resources of the employed ultra-low power μC and the often low signal quality, the demands on the signal processing are very high. The literature delivers a huge number of essays concerned with ECG processing: derivative based methods, digital filters, different transforms including the wavelet transform and neural networks, to name a few (Köhler, 2002). We designed a wavelet-based processing method especially suited for its real-time application. This paper describes the method and gives detailed information on the performance concerning detection rates as well as computational load.

The paper is organized as follows: Section 2 gives an introduction into the monitoring system and describes our algorithm based on considerations on the wavelet transform and its implementation in detail. Experimental results are reported in Section 3 and discussed in Section 4. Finally, Section 5 contains conclusions and some considerations concerning the future development of the system.

2 MATERIALS AND METHOD

2.1 Hardware

As carrier of the monitoring system we used a smart shirt. We integrated four electrodes to record a three-channel ECG based on Einthoven. Further on, a partially flexible printed circuit board was included. The board contains the hardware for analog preprocessing and further data handling. Sampling of the ECG is done at 1000 Hz and 12-Bit resolution. Data handling may include storage of data on a memory card and, optionally, the wireless data transmission via Bluetooth to a PDA. The PDA serves as gateway to communicate with medical personnel via internet. Signal processing done close to the sensor offers the possibility of wireless data transmission limited to situations of imminent risks. In this way, the actual data handling (storage and/or transmission) depends upon the outcome of the just-performed signal processing, thus rendering the overall system more flexible and improving its efficiency. All electronics as well as the signal processing is controlled by the ultra-low power μC MSP430F1611. Due to its low power consumption, such a controller is very suited for ambulatory applications. Of course, the low consumption accounts for a likewise low maximum clock frequency of 8 MHz. To handle this major drawback, an adequate signal processing method was developed. The underlying ideas, the implementation and performance results of the developed algorithm will be described next.

2.2 Signal Processing Method

2.2.1 Wavelet Basics

The wavelet transform (WT) decomposes a signal in scaled and translated versions $\psi_{a,t}(\tau)$ of a basis function called mother wavelet $\psi(\tau)$. The derivates of the mother wavelet are given by

$$\psi_{a,t}(\tau) = \frac{1}{\sqrt{|a|}}\psi\left(\frac{\tau - t}{a}\right) \quad \text{with} \quad a \in \mathbf{R}^+, t \in \mathbf{R} \qquad (1)$$

where a is a scale factor which is a measure of the current width of the applied wavelet and t is the translation parameter which describes the position of the wavelet in the time domain. The wavelet transform $X(a,t)$ results from the inner product of the signal and the scaled and translated wavelet

$$X(a,t) = \left\langle x, \psi_{a,t} \right\rangle = \int_{-\infty}^{+\infty} x(\tau)\frac{1}{\sqrt{|a|}}\psi^*\left(\frac{\tau - t}{a}\right)d\tau \qquad (2)$$

The resulting coefficients can be seen as a measure for the similarity of the examined signal segment specified by t, and a wavelet of varying width specified by a. The transformation of (2) to the frequency domain yields

$$X(a,t) = \frac{\sqrt{|a|}}{2\pi}\int_{-\infty}^{+\infty} X(\omega)\Psi^*(\omega)e^{j\omega t}d\omega \qquad (3)$$

where $X(\omega)$ and $\Psi(\omega)$ are the Fourier transforms of the signal and the wavelet, respectively. From (3) it can be seen that decomposing a signal by the WT is equivalent to the application of a filter bank. The bandwidth of each pass-band filter increases with higher center frequencies.

2.2.2 Calculated Transform

There are three usual ways to compute the wavelet transform: the so-called continuous WT (CWT), the dyadic WT (D_YWT) and the discrete WT (DWT). The schemes differ in the required computational resources, the resulting degree of redundancy and in some properties of the results like shift-invariance. In the D_YWT the scale a is sampled along a dyadic sampled grid while the translation remains scale independent. Thus, applying the D_YWT, the property of shift-invariance can be maintained while the degree of redundancy, and therefore the computational load, is reduced in comparison to the CWT. For the D_YWT the definition of $\psi_{a,t}(\tau)$ becomes

$$\psi_{2^m,t}(\tau) = \frac{1}{\sqrt{2^m}}\psi\left(\frac{\tau - t}{2^m}\right) \quad \text{with} \quad m \in \mathbb{Z}^+, t \in \mathbf{R} \qquad (4)$$

When using expressions like “scale 4”, we will refer to the scale $a=2^m=2^4$.

Fast computations of the DWT are done through the Mallat algorithm. In analogy to the “algorithme a trous” (Holschneider, 1989), it constitutes a recursive algorithm allowing the fast calculation of

the D_YWT. The highly advantageous property of shift invariance justifies an increased computational effort, rendering the use of the D_YWT optimal for our intended realization.

A wide range of different wavelets have been employed in the past for ECG processing. Referring to the choice of an adequate wavelet, the statements found in the literature disagree. For instance, Dinh et al. conclude that the cubic spline wavelet is best suited for the detection of QRS complexes (Dinh, 2001). Differing from this, Li et al. do not perceive substantial differences in the performance of the detection by using a spline of higher order than the quadratic spline wavelet (Li, 1995). The possible usage of different wavelets allows the utilization of other criterions searching for an adequate one. As our application aims at the real-time processing under extremely limited resources, the compactness of the chosen wavelet in the time domain is a crucial demand. The quadratic spline wavelet originally introduced by Mallat et al. (Mallat, 1992) meets this demand and is used in our implementation. In Figure 1, the transfer functions realized by the quadratic spline wavelet are shown.

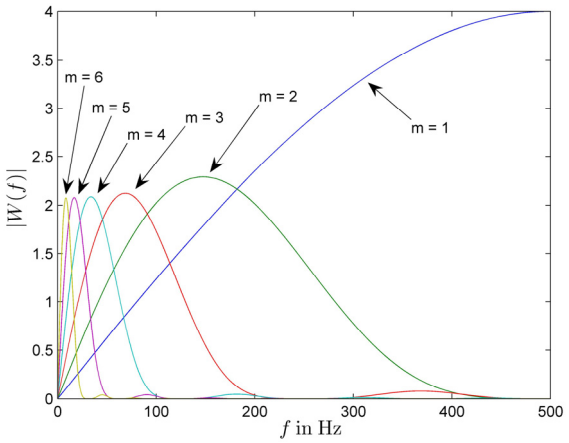

Figure 1: Transfer functions realized by the quadratic spline wavelet and a sampling frequency of 1000 Hz.

2.2.3 Underlying Idea of the Implemented Method

In the current stage of development we realized a QRS detector. The most commonly used principle of wavelet-based QRS detectors (employing the quadratic spline wavelet) is to search for modulus maximum pairs (MMP) (combination of local extreme values exceeding a threshold). To obtain a good performance the search typically is carried out across all scales, at least up to the scale assumed as most significant in regard to the main energy portions contained in QRS complexes. (Li, 1995), (Martinez, 2004)

An obviously possible solution to reduce the computational effort is not to incorporate all scales, but to do the detection based on only one scale. Such an approach does not take advantage of the multi-scale decomposition provided by the WT, but it constitutes a viable way to detect QRS complexes. Employing only one scale of the WT is similar to the usage of a single bandpass-filter. On the filtered signal the typical method of grouping extrema to MMP and assigning them to QRS complexes can be applied. In Section 3, some example results (*testing1* and *testing2,* see Table 1) using this methodology are given. Different rules to control the value of the thresholds were employed. In both cases, adaptive thresholds (see Appendix for details on the adaptation) were applied. In *testing2* the threshold is generally endued with an offset to lower the resulting value compared to the threshold in *testing1*. As expected, the performance of the methods varies in sensitivity and positive predictivity. Both methods offer, depending on the data set as well as on the observed signal portion within one data set, sections of varying detection quality. With regard to this, a method to influence automatically the valid threshold becomes a very interesting option. Such a procedure aims to take the advantages of a generalized lower or higher threshold according to the current signal state.

Our method detects QRS complexes in scale 5. Based on the number of threshold crossings within a sliding window in the scale 4 the threshold in scale 5 is controlled.

2.2.4 Structure of the Algorithm

The algorithm can be divided in three steps:

(1) Search for MMP and extract "relevant threshold crossings" in scale 4.
(2) Search for MMP in the scale 5 incorporating the information gained from the corresponding number of threshold crossings detected in the scale 4.
(3) Classification of MMP found in scale 5 as QRS complexes using a simplified regularity analysis

Step (1): With every incoming sample the search for local extrema, aimed at the grouping of a MMP, is continued. Different combinations of extrema can constitute a MMP. To detect the extrema, online-adaptive thresholds $\varepsilon^{\pm}_4$ are used. An adaptation of the thresholds is caused by the successful grouping of a MMP (see Appendix for details on the

adaptation). Based on $\varepsilon^{\pm}_4$ additional thresholds $\varepsilon^{\pm}_{cross}$ are created to excerpt all "relevant threshold crossings". "Relevant threshold crossings" refer to local extrema crossing the corresponding threshold $\varepsilon^{\pm}_{cross}$. This registration is not carried out in order to group the extrema as MMP, but to obtain a measure of the signal quality by counting the number of crossings N_{cross} within a window W_{cross} of 500 samples. Note that there is a major difference between the extrema searched for MMP grouping and the extrema detected using $\varepsilon^{\pm}_{cross}$, as the absolute value of $\varepsilon^{\pm}_{cross}$ is generally smaller or equal than $\varepsilon_4^{\pm}$ and found extrema are not discarded until their position has left the range of the sliding window.

Step (2): MMP are searched in scale 5 using the same routine as in scale 4. Also online adaptive thresholds $\varepsilon^{\pm}_5$ are existent. Differing from scale 4, for the MMP search in scale 5 not directly the online adaptive thresholds $\varepsilon^{\pm}_5$ are used, but a threshold changed by a correction factor κ. κ varies depending on the number of registered threshold crossings. The actual number of zero crossings N_{cross} can be interpreted as a measure for the degree of higher frequency noise or artifacts. According to this, κ converts the information contained in N_{cross} to a threshold operation in scale 5, referred as $\varepsilon^{\pm}_5 + \kappa$ (note that this is only a symbolic notation). In general, for noisy segments the threshold is increased whereas a reduction in sections of good signal quality is performed. Depending on the value of N_{cross}, the modification of threshold can be up to ±37.5% of the actual $\varepsilon^{\pm}_5$. It is important that the threshold be changed only for the search of local extrema, otherwise $\varepsilon^{\pm}_5$ doesn't suffer any changes. To allow the zero crossing window to be placed symmetrically around the scale 5 coefficient under observation, the scale 5 coefficients have to been delayed by 250 samples (taking into account the half window size), plus the delay introduced by the recursive online calculation of the WT.

Step (3): If a MMP is detected in scale 5 and a corresponding MMP in scale 4 is existent, a simplified regularity analysis based only on the amplitudes of the detected MMP is carried out. If no corresponding MMP is present at scale 4, the MMP of scale 5 is accepted as QRS without any regularity analysis.

Figure 2 shows an example containing an ECG segment, the corresponding scale 4 and scale 5 coefficients and the course of. Also showed is the course of the threshold values $\varepsilon^{\pm}_4$ (bright), $\varepsilon^{\pm}_{cross}$ (dark), $\varepsilon^{\pm}_5$ (bright), $\varepsilon^{\pm}_5 + \kappa$ (dark). The threshold adaptation after detections and the general dynamics of the correction factor are visible. N_{cross} exhibits the expected behaviour. An increase is visible during noisy segments whereas during uncorrupted segments only the QRS complexes have an influence (resulting in an oscillation between 0 and 2 detected crossings). $\varepsilon^{\pm}_5 + \kappa$ oscillates around $\varepsilon^{\pm}_5$).

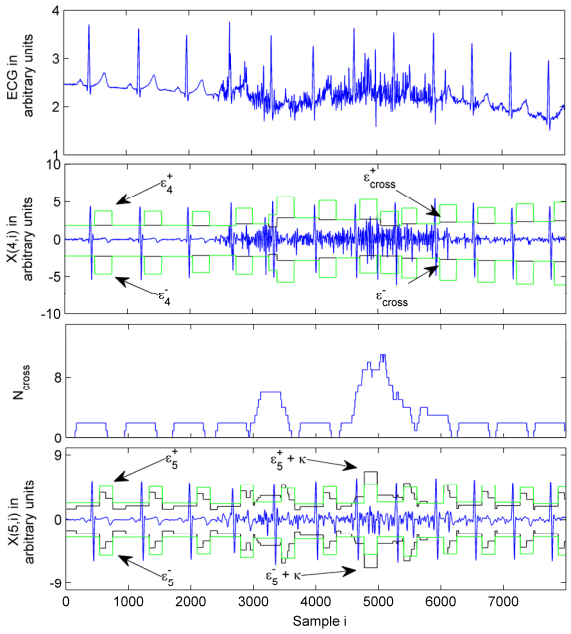

Figure 2: Example for the behavior of the algorithm.

2.2.5 Implementation

The algorithm was implemented in C. To minimize the required computational effort three fundamental concepts were incorporated in our implementation.

Simplicity of employed data types: the applied µC is a 16-Bit controller. This renders the application of 16 Bit fix-point operators very useful. Incoming data is sampled with a 12-bit resolution. 16-Bit fix-point numbers were used for the recorded ECG as well as for wavelet coefficients, scaling coefficients and threshold values. Considering the maximal values possibly appearing in the course of the WT, a multiplication of incoming data by 4 is possible. Therewith, the whole value range is involved and the inaccuracies introduced by rounding errors are reduced.

Simplicity of all employed operations: as mentioned before, the usage of the quadratic spline wavelet provides a low number of coefficients (namely 4 low-pass coefficients and 2 high-pass coefficients) thus fulfilling the first requirement on an effective real-time processing. Furthermore, the coefficients allow the calculation of the WT with only bit-shifts and additions. Also the adaptation of all threshold values was implemented by bit-

manipulations. All remaining steps of the algorithm are performed by logical instructions like comparisons. These operations also are characterized by their low computational load.

Avoidance of inappropriate processing methods: to provide a uniformly low computational load, often used undesirable steps as back-searchs were excluded. The applied windowing operation, also an improper medium for the real-time purpose, acts on a window of 500 samples, introducing a delay of 250 ms only. All values to be updated in periodic manner (for example the zero crossings within W_0, for which the removal or addition of crossings is demanded due to the sliding window) are arranged in circular buffers. This allows the algorithm to work continuously on every incoming sample.

3 RESULTS

3.1 Detection Performance

Table 1 yields the results of the performance evaluation accomplished under different conditions. Using the MIT-BIH Arrhythmia Database, all beats occurring beginning 5 minutes after the begin of the records until 30 minutes have been evaluated. This results in 90491 beats. As previously mentioned, the example trials *testing1* and *testing2* were carried out without any influence created by the usage of N_{cross}.

The quantitative evaluation of the complete method with own data (Table 1, *evalOwnData*) yielded a sensitivity (Se) of 99.85 % and a positive predictivity (+P) of 99.92 %. The annotation by a health professional was used as reference. The evaluation using the MIT-BIH Arrhythmia Database (Table 1, *evalMIT*) yielded a sensitivity and positive predictivity of 99,74 %, respectively 99,85 %. As the algorithm was designed for data sampled at 1000 Hz, the data was upsampled. Due to the contained frequency portions, the regularity analysis was skipped as a similarly easy regularity analysis (like accomplished for own data) no longer was possible.

Table 1: Performance of the QRS detector using different test configurations.

Identifier of the task	Number of beats	Se	+P
testing1	90941	99.31 %	99.80 %
testing2	90941	99,81 %	99,36 %
evalOwnData	8525	99,85 %	99,92 %
evalMIT	90941	99,74 %	99,85 %

Table 2: Required resources for signal processing.

Processing Step	Computational load (at 8 MHz)	
	required cycles	*required µs*
Calculation of WT	900	112.5
Search for MMP	400	50
N_{cross} maintanance	70	7.5
Over all	<2000	<250

Table 3: Memory coverage of the implemented method.

Code Memory	Data memory
<7900 byte	<4000 byte

3.2 Computational Load

Table 2 contains an outline of the required resources. Besides the overall amount of cycles, the equivalent processing time and the number of cycles concerning specific steps within the implemented method are given. The algorithm acts without any prefiltering of the signal and thus avoids additional computations other than the calculation of the WT and the subsequent feature extraction procedure. The step "Search for MMP" refers to the search for extremas and the grouping of detected combinations of extrema to a MMP. According to the structure of the algorithm, this step is called twice per input sample, once for scale 4 and once for scale 5. The whole detection procedure requires less than 250 µs (2000 cycles), leaving computing power to manage other functions.

Also of high interest considering the limited resources of the ultra-low power µC is the memory coverage. Table 3 shows the most important characteristics, proving the adequacy of the implemented method.

4 DISCUSSION

The evaluation of our method showed promising results in terms of the required computational load and the performance of the method. Note, that the only difference between the methods used in *testing1* and *evalMIT* is the correction of the threshold in scale 5, thus pointing out the effectiveness of the algorithm. Compared to the high-quality approaches of Li et al. (Li, 1995) and Martinez et al. (Martinez, 2004) the reached detection rates are slightly lower. However, a deeper

insight to the methods reveals in both cases strategies which are very impractical for a real-time calculation. For instance, Li et al. work on 600 samples of the ECG each time instead of on every incoming sample. Furthermore, two "real-time unfriendly" techniques (in the original paper referred to as "tactic 1" and "tactic 2") to exclude or accept detections based on foregoing and subsequent detections with the benefit of hindsight were incorporated. In turn, Martinez et al. incorporated in the computation of their scale-dependent thresholds the RMS calculated from 2^{16} values of the respective scale. The storage of that amount of data for one scale would exceed the data memory of the controller by a factor of 10. Taking this into account, our realization seems to be very appropriate for the application area. By incorporating the information on the latest detected QRS complexes, the performance of the method still can be slightly increased. Nevertheless, to reach the detection performance reported by Li et al. while maintaining a similarly low computational load like provided by our method seems to be very difficult.

In addition to the good results obtained by our method, the implemented method exhibits a high potential for future work. For instance, concerning the QRS delineation as well as P and T waves delineation, the already computed wavelet coefficients can be used as basis.

5 CONCLUSIONS

We developed a method especially suited to perform signal processing in close proximity to the sensor. The proposed algorithm is adapted to best meet the most important demands of the ambulatory application, which are low computational load and high reliability. Even for a sampling frequency of 1000 Hz the described method can be used on an ultra-low power µC, leaving computing power for other purposes. The physical proximity of the signal-processing hardware to the sensor provides increased flexibility for subsequent information handling and, combined with an ultra-low power architecture, is capable of significantly increasing the runtime of an ambulatory monitoring system.

Future work will focus on further signal processing steps. These steps may include detection of P and T-waves as well as the evaluation of the ST-segment. As it was shown by the literature this can be done based on the wavelet transform as well. The use of the wavelet coefficients for further signal processing purposes renders the wavelet-based method even more attractive for low-power microsystems with reduced hardware complexity.

REFERENCES

Dinh, H.; Kumar, D.; Pah, N. & Burton, P.: *'Wavelets for QRS detection'*, In Engineering in Medicine and Biology Society, 2001. Proceedings of the 23rd Annual International Conference of the IEEE, pp. 1883--1887.

Goldberger AL, Amaral LAN, Glass L, Hausdorff JM, Ivanov PCh, Mark RG, Mietus JE, Moody GB, Peng CK, Stanley HE. *PhysioBank, PhysioToolkit, and PhysioNet: Components of a New Research Resource for Complex Physiologic Signals.* Circulation 101(23):e215-e220 [Circulation Electronic Pages; http://circ.ahajournals.org/cgi/content/full/101/23/e215]; 2000 (June 13).

Holschneider, M.; Kronland-Martinez, R.; Morlet, J. Tchamitchian, P.: *'A Real-Time Algorithm for Signal Analysis with the Help of Wavelet Transform'*, Wavelets, Time-Frequency Methods and Phase Space, Springer Verlag, Berlin, 1989

Li, C.; Zheng, C. & Tai, C., 1995, *'Detection of ECG characteristic points using wavelet transforms.'*, IEEE Trans Biomed Eng 42(1), 21-28.

Köhler, B.; Hennig, C. & Orglmeister, R. *The principles of software QRS detection.* IEEE engineering in medicine and biology magazine : the quarterly magazine of the Engineering in Medicine & Biology Society., 2002, 21, 42-57

Mallat, S. & Hwang, W. , 1992*, 'Singularity detection and processing with wavelets',* IEEE Transactions on Information Theory 38, 617-643.

Martinez, J. P.; Almeida, R.; Olmos, S.; Rocha, A. P. & Laguna, P., 2004*, 'A wavelet-based ECG delineator: evaluation on standard databases.'*, IEEE Trans Biomed Eng 51(4), 570-581.

APPENDIX

Rules for threshold adaptation after a detected MMP (for lower thresholds ε_m^- "max" is replaced with the specific "min" values and ε_m^+ is replaced by ε_m^-):

$$\text{if } \max(X(2^m,i)) \geq 3*\varepsilon_m^+$$

$$\varepsilon_m^+ = 0.375*\max(X(2^m,i)) + 0.625*\varepsilon_m^+$$

$$\text{else if } \max(X(2^m,i)) \geq 3*\varepsilon_m^+$$

$$\varepsilon_m^+ = 0.5*\max(X(2^m,i)) + 0.5*\varepsilon_m^+$$

$$\text{else if } \max(X(2^m,i)) \geq 2*\varepsilon_m^+$$

$$\varepsilon_m^+ = 0.75*\max(X(2^m,i)) + 0.25*\varepsilon_m^+$$

$$\text{else}$$

$$\varepsilon_m^+ = 1.125*\max(X(2^m,i))$$

400 ms after an adaptation (to avoid mistakes introduced by T waves with higher frequency portions) the threshold is lowered by 50%.

MULTIDIMENSIONAL POLYNOMIAL POWERS OF SIGMOID (PPS) WAVELET NEURAL NETWORKS

João Fernando Marar
Department of Computing, Adaptive Systems and Computational Intelligence Laboratory
Faculdade de Ciências, São Paulo State University, Bauru, São Paulo, Brazil
fermarar@fc.unesp.br, fermarar@di.fc.ul.pt

Helder Coelho
Department of Informatics, Laboratory of Agent Modelling
Faculdade de Ciências, Lisbon University, Lisbon, Portugal
hcoelho@di.fc.ul.pt

Keywords: Artificial Neural Network, Function Approximation, Polynomial Powers of Sigmoid (PPS), Wavelets Functions, PPS-Wavelet Neural Networks, Activation Functions, Feedforward Networks.

Abstract: Wavelet functions have been used as the activation function in feedforward neural networks. An abundance of R&D has been produced on wavelet neural network area. Some successful algorithms and applications in wavelet neural network have been developed and reported in the literature. However, most of the aforementioned reports impose many restrictions in the classical backpropagation algorithm, such as low dimensionality, tensor product of wavelets, parameters initialization, and, in general, the output is one dimensional, etc. In order to remove some of these restrictions, a family of polynomial wavelets generated from powers of sigmoid functions is presented. We described how a multidimensional wavelet neural networks based on these functions can be constructed, trained and applied in pattern recognition tasks. As an example of application for the method proposed, it is studied the exclusive-or (XOR) problem.

1 INTRODUCTION

Wavelet functions have been successfully used in many problems as the activation function of feedforward neural networks. There are claims that many biological fundamental properties can emerge from wavelet transformation (Marar, 1997). An abundance of R&D has been produced on wavelet neural network area. Some successful algorithms and applications in wavelet neural network have been developed and reported in the literature (Zhang and Benveniste, 1992; Marar, 1997; Oussar and Dreyfus, 2000; Chen and Hewit, 2000; Zhang and San, 2004; Fan and Wang, 2005; Zhang and Pu, 2006; Chen et al., 2006; Avci, 2007; Jiang et al., 2007; Misra et al., 2007).

However, most of the aforementioned reports impose many restrictions in the classical backpropagation algorithm, such as low dimensionality, tensor product of wavelets, parameters initialization, and, in general, the output is one dimensional, etc.

In order to remove some of these restrictions, we develop a robust Three Layer PPS-Wavelet multidimensional strongly similar to classical Multilayer Perceptron. The great advantage of this new approach is that PPS-Wavelets offers the possibility choice of the function that will be used in the hidden layer, without need to develop a new learning algorithm. This is a very interesting property for the design of new wavelet neural networks architectures. This paper is organized as follows. Section 2 covers basic theoretical aspects in function approximation. Section 3 introduces the wavelet sigmoidal function. Section 4 presents the framework used in this research. Section 5 deals with application of exclusive-or (XOR) problem. Section 6 concludes this paper.

2 FUNCTION APPROXIMATION

Multilayer perceptron networks (MLP) have been intensely studied as efficient tools for arbitrary function approximation. Amongst the developments achieved in the theory of function approximation using MLP, the work carried out by Hecht-Nielsen resulted in an improved version for the superposition theorem defined by Sprecher (Hecht-Nilsen, 1987). Galant and White in 1988 showed that a feedforward network with one hidden layer of processing units that use flat

cosines as the activation function correspond to a special case of Fourier networks that can approximate a Fourier series for a given function. Cybenko developed a rigorous demonstration that MLPs with only one hidden layer of processing elements is sufficient to approximate any continuous function with support in a hypercube (Cybenko, 1989).

The theorem is directly applied to MLP. The sigmoid, radial basis and wavelets functions are a common choice for the network construction since it satisfies the conditions imposed in the theorem. The theorem of function approximation provides a mathematical basis that gives support to the approximation of any continuous arbitrary function. Furthermore, it defines for the case of MLP that a network composed of only one hidden layer neurons is sufficient to compute, in a given problem, a mapping from the input space to the output space, based on a set of training examples. However, with respect to training speed and ease of implementation, the theorem does not provide any insight about the solutions developed. The choice of activation functions and the learning algorithm defines which particular network is used. In any situation, the neurons operate as a set of functions that generate an arbitrary basis for function approximation which is defined based on the information extracted from the input-output pairs. For training a feedforward network, the backpropagation algorithm is one of the most frequently employed in practical applications and can be seen as an optimization.

3 WAVELET FUNCTIONS

Two categories of wavelet functions, namely, orthogonal wavelets and wavelet frames (or non-orthogonal), were developed separately by different interests. An orthogonal basis is a family of wavelets that are linearly independent and mutually orthogonal, this eliminates the redundancy in the representation. However, orthogonal wavelets bases are difficult to construct because the wavelet family must satisfy stringent criteria (Daubechies, 1992; Chui, 1992). This way, for these difficulties, orthogonal wavelets is a serious drawback for their application to function approximation and process modeling (Oussar and Dreyfus, 2000). Conversely, wavelet frames are constructed by simple operations of translation and dilation of a single fixed function called the mother wavelet, which must satisfy conditions that are less stringent than orthogonality conditions.

Let $\varphi_j(x)$ a wavelet, the relation:

$$\varphi_j(x) = \varphi\left(d_j.(x-t_j)\right)$$

where t_j is the translation factors and d_j is the dilation factors $\in \mathbf{R}$. The family of functions generated by $\mho$ can be defined as:

$$\mho = \left\{\varphi\left(d_j.(x-t_j)\right), t_j \text{ and } d_j \in \mathbf{R}\right\}$$

A family $\mho$ is said to be a frame of $L^2(\mathbf{R})$ if there exist two constants $c > 0$ and $C < \infty$ such that for any square integrable function f the following inequalities hold:

$$c\|f\|^2 \leq \sum_j |<\varphi_j, f>|^2 \leq C\|f\|^2$$

where $\varphi_j \in \mho$, $\|f\|$ denotes the norm of function f and $<\varphi_j, f>$ the inner product of functions. Families of wavelet frames of $L^2(\mathbf{R})$ are universal approximators (Zhang and Benveniste, 1992; Pati and Krishnaprasad, 1993). In this work, we will show that wavelet frames allow practical implementation of multidimensional wavelets. This is important when considering problems of large input and output dimension. For the modeling of multi-variable processes, such as, the artificial neural networks biologically plausible, multidimensional wavelets must be defined. In the present work, we use multidimensional wavelets constructed as linear combination of sigmoid, denominated Polynomial Powers of Sigmoid Wavelet (PPS-wavelet).

3.1 Sigmoidal Wavelet Functions

In (Funahashi, 1989) is showed that:

Let $s(x)$ a function different of the constant function, limited and monotonically increase. For any $0 < \alpha < \infty$ the function created by the combination of sigmoid is described in Equation 1:

$$g(x) = s(x+\alpha) - s(x-\alpha) \tag{1}$$

where $g(x) \in L^1(\mathbf{R})$, i.e,

$$\int_{-\infty}^{\infty} g(x) < \infty$$

in particular, the sigmoid function satisfies this property.

Using the property came from the Equation 1, in (Pati and Krishnaprasad, 1993) boundary suggest the construction of wavelets based on addition and subtraction of translated sigmoidal, which denominates wavelets of sigmoid. In the same article show a process of construction of sigmoid wavelet by the substitution of the function $s(x)$ by $\Upsilon(qx)$ in the Equation 1. So, the Equation 2 is the wavelet function created in (Pati and Krishnaprasad, 1993).

$$\psi(x) = g(x+r) - g(x-r) \tag{2}$$

where $r > 0$. By terms of sigmoid function, the Equation 2, $\psi(x)$ is given by:

$$\psi(x) = \Upsilon(qx+a+r) - \Upsilon(qx-a+r) - \Upsilon(qx+a-r) + \Upsilon(qx-a-r) \quad (3)$$

where $q > 0$ is a constant that control the curve of the sigmoid function and α and $r \in \mathbf{R} > 0$.

Pati and Krishnaprasad demonstrated that the function $\psi(x)$ satisfies the admissibility condition for wavelets (Daubechies, 1992; Chui, 1992). The Fourier Transform of the function $\psi(x)$ is given by the Equation 4:

$$\int_{-\infty}^{\infty} \psi(x) e^{-iwx} dx = -i\frac{4\pi}{q} \frac{sin(w\alpha)sin(wr)}{sinh(\frac{\pi w}{q})} \quad (4)$$

In particular, we accepted for analysis and practical applications the family of sigmoid wavelet generated by the parameters $q = 2$ and $\alpha = r$, as example. So, the Equation 3 can be rewritten the following form:

$$\psi(x) = \Upsilon(2x+m) - 2\Upsilon(2x) - \Upsilon(2x-m) \quad (5)$$

where $m = \alpha + r$.

Following, partially, this research line, we present in the next section a technique for construction of wavelets based on linear combination of sigmoid powers.

4 POLYNOMIAL POWERS OF SIGMOID

The Polynomial Powers of Sigmoid (PPS) is a class of functions that have been used in recent years to solve a wide range of problems related to image and signal processing (Marar, 1997). Let $\Upsilon : \mathbf{R} \rightarrow$ **[0,1]** be a sigmoid function defined by $\Upsilon(x) = \frac{1}{1+e^{-x}}$. The $n^{th}-$power of the sigmoid function is a function $\Upsilon^n : \mathbf{R} \rightarrow$ **[0,1]** defined by $\Upsilon^n(x) = \left(\frac{1}{1+e^{-x}}\right)^n$.

Let Θ be set of all power functions defined by (6):

$$\Theta = \{\Upsilon^0(x), \Upsilon^1(x), \Upsilon^2(x), \ldots, \Upsilon^n(x), \ldots\} \quad (6)$$

An important aspect is that the power these functions, still keeps the form of the letter *S*. Looking the form created by the power functions of sigmoid, suppose that the n^{th} power of the sigmoid function to be represented by the following form:

$$\Upsilon^n(x) = \frac{1}{a_0 + a_1 e^{-x} + a_2 e^{-2x} + \cdots + a_n e^{-nx}} \quad (7)$$

where $a_0, a_1, a_2, \ldots, a_n$ are some integer values. The extension of the sigmoid power can be viewed like lines of a Pascal′s triangle. The set of function written by linear combination of polynomial powers of sigmoid is defined as PPS function. The degree of the PPS is given by the biggest power of the sigmoid terms.

4.1 Polynomial Wavelet Family on PPS

The derivative of a function $f(x)$ on $x = x_0$ is defined by:

$$f'(x_0) = \lim_{\Delta x \rightarrow 0} \frac{f(x_0 + \Delta x) - f(x_0)}{\Delta x}$$

since the limits there is. So, if we do the computation of the Equation 8 :

$$\frac{f(x_0 + \Delta x) - f(x_0)}{\Delta x} \quad (8)$$

for a small value of Δx , showed have a good approximation for $f'(x_0)$. Naturally, Δx can be positive or negative. So, if is we use negative value for Δx, the expression will be:

$$\frac{f(x_0 - \Delta x) - f(x_0)}{-\Delta x} \quad (9)$$

This way, we can say that the arithmetic measure of the Equations 8 and 9 will be a good approximation for $f'(x_0)$ too. Then, we can write the following Equation 10:

$$f'(x_0) \simeq \frac{f(x_0 + \Delta x) - f(x_0 - \Delta x)}{2\Delta x} \quad (10)$$

By convenience, we consider $p = 2\Delta x$ and its substitution in the Equation 10. So, we have the Equation 11:

$$f'(x_0) \simeq \frac{f(x_0 + \frac{p}{2}) - f(x_0 - \frac{p}{2})}{p} \quad (11)$$

this point we computed an approximated value for the second derivative of $f(x)$ in $x = x_0$. From the Equation 11, changing $f(x)$ by $f'(x)$, we obtain the Equation 12 :

$$f''(x_0) \simeq \frac{f'(x_0 + \frac{p}{2}) - f'(x_0 - \frac{p}{2})}{p} \quad (12)$$

reusing the Equation 11, we can write:

$$f'(x_0 + \frac{p}{2}) \simeq \frac{f(x_0 + p) - f(x_0)}{p}$$

and

$$f'(x_0 - \frac{p}{2}) \simeq \frac{f(x_0) - f(x_0 - p)}{p}$$

using these results in the Equation12, we have an approximation of the second derivative of $f(x)$ in $x = x_0$ that is given by:

$$f''(x_0) \simeq \frac{f(x_0+p) - 2f(x_0) + f(x_0-p)}{p^2} \quad (13)$$

The approximation given by the Equation 13 is extremely adequate for the that $f(x)$ is a sigmoid function. Suppose that $f(x)$ is a sigmoid, for example, $\Upsilon(x)$. So, the second derivative of $\Upsilon(x)$ is approximated by the Equation 14:

$$\Upsilon''(x_0) \simeq \frac{\Upsilon(x_0+p) - 2\Upsilon(x_0) + \Upsilon(x_0-p)}{p^2} \quad (14)$$

Due the fact of the sigmoid function to be continuous and differentiable for any $x \in \mathbf{R}$, we can say that the Equation 14 is true for any x_0, then we can write the Equation 15, defined for all $x \in \mathbf{R}$.

$$\Upsilon''(x) \simeq \frac{\Upsilon(x_0+p) - 2\Upsilon(x) + \Upsilon(x-p)}{p^2} \quad (15)$$

Comparison the Equations 15 and 5, we do there analysis for the approximation of the second derivative of sigmoid function. The first for values of $p \geq 1$ and the second for values of $p < 1$.

Case $p \geq 1$:

It is clear that the function given by the sigmoid second derivative approximation, Equation 15, also will have the same form of the Pati and Krishnaprasad functions, except of a p^2 constant that divides their amplitude. So, the following result is true: when $p > 1$ always there is a sigmoid wavelet which integral of the admissibility condition (Daubechies, 1992; Chui, 1992) limited the same integral of the Equation 15. Therefore, the approximation of the second derivative of the sigmoid function is a wavelet too.

Case $p < 1$:

In this case, we will analyze when p is going to zero, i.e.,

$$\lim_{p\to 0} \frac{\Upsilon'(x_0+p) - 2\Upsilon(x) + \Upsilon'(x-p)}{p^2} \quad (16)$$

this limit tends to the second derivative of the function is given on PPS terms by:

$$\varphi_2(x) = 2\Upsilon(x)^3 - 3\Upsilon(x)^2 + \Upsilon(x) \quad (17)$$

where we denominated $\varphi_2(x)$ the first wavelet the sigmoid function. The others derivatives, begin on the second, we considered true by derivative property by Fourier Transform (Marar, 1997). The successive derivation process of sigmoid functions, allowed to join a family of wavelets polynomial functions. Among many applications for this family of PPS-wavelets, special one is that those functions can be used like activation functions in artificial neurons. The following results correspond to the the analytical functions for the elements $\varphi_3(x)$ and $\varphi_4(x)$ that are represented by:

$$\varphi_3(x) = -6\Upsilon^4(x) + 12\Upsilon^3(x) - 7\Upsilon^2(x) + \Upsilon(x)$$

$$\varphi_4(x) = 24\Upsilon^5(x) - 60\Upsilon^4(x) + 50\Upsilon^3(x) - 15\Upsilon^2(x) + \Upsilon(x)$$

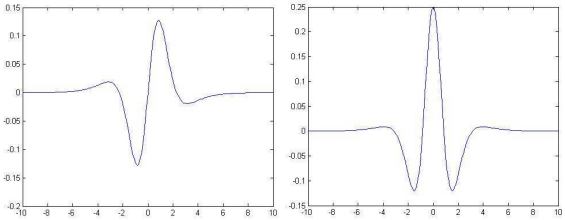

$\varphi_4(x)$ $\varphi_5(x)$

Figure 1: PPS-wavelets examples.

4.2 Estimating the Coefficients of PPS-wavelets

Considering j the number of wavelets that are to be defined, the algorithm below calculates a matrix of integer values that estimates the coefficients of the PPS-wavelets.

Step 1: Initialization

$$\begin{aligned} C_{1,1} &\leftarrow 1; \\ C_{1,2} &\leftarrow 1; \end{aligned}$$

The initial values are considered only auxiliary variables. The matrix of value associated with the process of wavelet construction is obtained from the second row.

Step 2: Calculate the coefficient of the PPS of the highest degree

$$\begin{aligned} n &\leftarrow 3; \\ n &\leftarrow n+1; \quad (n \leq j) \\ C_{n-1,n} &\leftarrow C_{n-2,n-1} * (n-1) * (-1)^{n+1}; \end{aligned}$$

Step 3: Calculate the coefficients of the remaining terms of the polynomial

$$\begin{aligned} k &\leftarrow n; \\ k &\leftarrow k-1; \quad (k>2) \\ C_{n-1,k-1} &\leftarrow C_{n-2,k-1}*(k-1)+ \\ & \quad C_{n-2,k-2}*(k-2)*(-1)^k; \end{aligned}$$

Step 4: Calculate the coefficients of the first power variable

$$C_{n-1,1} \leftarrow 1$$

It is important to notice that steps 2 and 3 are cascaded by an inherent dependence on variable n. By proceeding in above way, a family of polynomial wavelets are generated.

4.3 PPS Wavelet Neural Network

Let us consider the canonical structure of the multidimensional PPS-wavelet neural network (PPS-WNN), as shown in Figure 2.

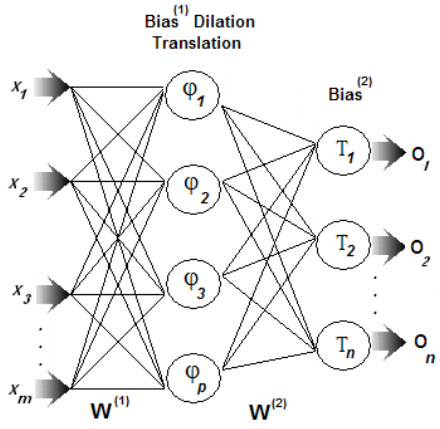

Figure 2: PPS-wavelet neural network Architectures.

For the PPS-WNN in Figure 2, when a input pattern $X=(x_1,x_2,\ldots,x_m)^T$ is applied at the input of the network, the output of the i^{th} neuron of output layer is represented as a function approximation problem, ie, $f:\mathbf{R}^m \rightarrow \mathbf{[0,1]}^n$, given by:

$$O_i(x) \simeq \Upsilon_i\left(\sum_{j=1}^{p} w_{ij}^{(2)}\varphi_j\left(d_j.\left(\sum_{k=1}^{m} w_{jk}^{(1)}x_k - b_j^{(1)}\right)-t_j\right)-b_i^{(2)}\right) \tag{18}$$

where p is number of hidden neurons, $\Upsilon(.)$ is sigmoid function, $\varphi(.)$ is the PPS-wavelet, $w^{(2)}$ are weight between the hidden layer to the output layer, $w^{(1)}$ are weights between the input to the hidden layer, d are dilation factors and t are translation factors of the PPS-wavelet, $b^{(1)}$ and $b^{(2)}$ are bias factors of the hidden layer and output layer, respectively.

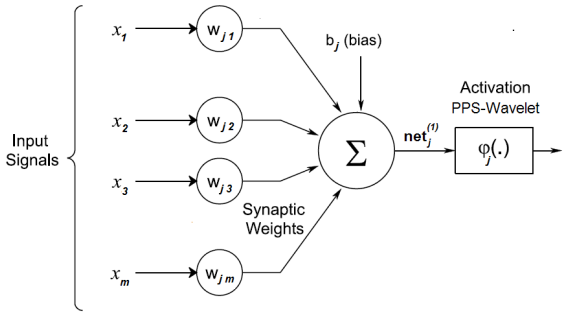

Figure 3: The Hidden Neuron of PPS-Wavelet Neural Network.

The PPS-WNN contains PPS-wavelets as the activation function in the hidden layer (Figure 3) and sigmoid function as the activation function in the output layer (Figure 4).

The output of the j^{th} PPS-wavelet hidden neuron (Figure 3) is given by :

$$\circledast_j = \varphi_j(d_j.(net_j^{(1)} - t_j))$$

where

$$net_j^{(1)} = \sum_{k=1}^{m} w_{jk}^{(1)}x_k - b_j^{(1)}$$

The output of the i^{th} output layer neuron (Figure 4)

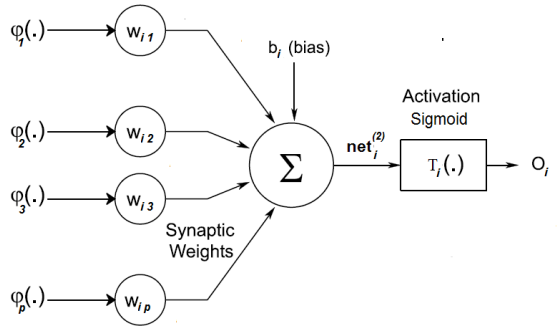

Figure 4: The Output Neuron of PPS-Wavelet Neural Network.

is given by:

$$\circledcirc_i = \frac{1}{1+exp(-net_i^{(2)})}$$

where

$$net_i^{(2)} = \sum_{j=1}^{p} w_{ij}^{(2)}\varphi_j(d_j.(net_j^{(1)} - t_j)) - b_i^{(2)}$$

The adaptive parameters of the PPS-WNN consist of all weights, bias, translations and dilation terms. The sole purpose of the training phase is to determine the "optimum" setting of the weights, bias, translations and dilation terms so as to minimize the difference between the network output and the target output. This difference is referred to as training error of the network. In the conventional backpropagation algorithm, the error function is defined as:

$$E = \frac{1}{2}\sum_{q=1}^{s}\sum_{i=1}^{n}(y_{qi} - o_{qi})^2 \quad (19)$$

where n is the dimension of output space, s is the number of training input patterns

The most popular and successful learning method for training the multilayer perceptrons is the backpropagation algorithm. The algorithm employs an iterative gradient descendent method of minimization which minimizes the mean squared error (L^2 norm) between the desired output (y_i) and network output (o_i). From Equations (18) and (19), we could deduce the partial derivatives of the error to each PPS-wavelet neural network parameter′s, which is given by:

Partial Equations of the Output Layer

$$\frac{\partial E}{\partial w_{ij}^{(2)}} = -\sum_{q=1}^{s}(y_{qi} - o_{qi}).o_{qi}.(1-o_{qi}).\varphi_j(d_j.(net_{qj}^{(1)} - t_j)) \quad (20)$$

$$\frac{\partial E}{\partial b_i^{(2)}} = \sum_{q=1}^{s}(y_{qi} - o_{qi}).o_{qi}.(1 - o_{qi}) \quad (21)$$

Partial Equations of the Hidden Layer

$$\frac{\partial E}{\partial w_{jk}^{(1)}} = -d_j.\sum_{q=1}^{s}[\varphi_j'(d_j.(net_{qj}^{(1)} - t_j)).x_{qk}.\sum_{i=1}^{n}(y_{qi} - o_{qi}).o_{qi}.(1-o_{qi}).w_{ij}^{(2)}] \quad (22)$$

$$\frac{\partial E}{\partial b_j^{(1)}} = \sum_{q=1}^{s}[\varphi_j'(d_j.(net_{qj}^{(1)} - t_j)).d_j.\sum_{i=1}^{n}(y_{qi} - o_{qi}).o_{qi}.(1-o_{qi}).w_{ij}^{(2)}] \quad (23)$$

Partial Equations of the PPS-Wavelet Parameters

$$\frac{\partial E}{\partial d_j} = \sum_{q=1}^{s}\{[\varphi_j'(d_j.(net_{qj}^{(1)} - t_j)).(net_{qj}^{(1)} - t_j)].\sum_{i=1}^{n}(y_{qi} - o_{qi}).o_{qi}.(1-o_{qi}).w_{ij}^{(2)}\} \quad (24)$$

$$\frac{\partial E}{\partial t_j} = d_j\sum_{q=1}^{s}[\varphi_j'(d_j.(net_{qj}^{(1)} - t_j)).\sum_{i=1}^{n}(y_{qi} - o_{qi}).o_{qi}.(1-o_{qi}).w_{ij}^{(2)}] \quad (25)$$

After computing all partial derivatives the network parameters are updated in the negative gradient direction. A learning constant γ defines the step length of the correction, r is the iteration and momentum factor is β. The corrections are given by:

$$w_{ij}^{(2)}(r+1) = w_{ij}^{(2)}(r) - \gamma.\frac{\partial E}{\partial w_{ij}^{(2)}} + \beta.(w_{ij}^{(2)}(r) - w_{ij}^{(2)}(r-1))$$

$$b_i^{(2)}(r+1) = b_i^{(2)}(r) - \gamma.\frac{\partial E}{\partial b_i^{(2)}} + \beta.(b_i^{(2)}(r) - b_i^{(2)}(r-1))$$

$$w_{jk}^{(1)}(r+1) = w_{jk}^{(1)}(r) - \gamma.\frac{\partial E}{\partial w_{jk}^{(1)}} + \beta.(w_{jk}^{(1)}(r) - w_{jk}^{(1)}(r-1))$$

$$b_j^{(1)}(r+1) = b_j^{(1)}(r) - \gamma.\frac{\partial E}{\partial b_j^{(1)}} + \beta.(b_j^{(1)}(r) - b_j^{(1)}(r-1))$$

$$d_j(r+1) = d_j(r) - \gamma.\frac{\partial E}{\partial d_j} + \beta.(d_j(r) - d_j(r-1))$$

$$t_j(r+1) = t_j(r) - \gamma.\frac{\partial E}{\partial t_j} + \beta.(t_j(r) - t_j(r-1))$$

4.4 Algorithm to PPS Wavelet Neural Network

In this section, the learning algorithm to the PPS-wavelet neural network is proposed by using the backpropagation method.

Begin

initialize-choice-PPS-function();

initialize-architecture();

initialize-weights();

initialize-PPSwavelet-neurons-dilatations();

initialize-PPSwavelet-neurons-translations();
initialize-neurons-bias();
Do-While ($epoch \leq epoch_{max}$)
or ($\frac{1}{2} total_{error} > acceptable_{error}$)
Begin$_{Do-While}$
$total_{error} \leftarrow 0$;
randomize-input-patter-order();
For pattern counter $q = 1..s$
Begin$_{for}$
read input pattern $x_{(q,j)} : j = 1..m$
read input target vector $y_{(q,i)} : i = 1..n$
acc-param-h-layer(); by Eqs. (22)- (25)
compute $O_{(q,i)}$ by Eq. (18)
acc-param-o-layer(); by Eqs. (20)- (21)
$total_{error} \leftarrow total_{error} + (y_{(p,k)} - O_{(p,k)})^2$
End$_{for}$
IF ($total_{error} > acceptable_{error}$) Then
Begin$_{Then}$
update-param-o-layer();
update-param-h-layer()
End$_{then}$
$epoch \leftarrow$ epoch+1
End$_{Do-While}$

End

where the initialization procedures, attribute random values on **[0,1]** to the parameters. However, improvements in the initialization process have been proposed by the selection of basic functions PPS-wavelet (de Queiroz and Marar, 2007).

5 PATTERN RECOGNITION AND THE XOR PROBLEM

The pattern recognition problem consists of designing algorithms that automatically classify feature vectors associated with specific patterns as belonging to one of a finite number of classes. A benchmark problem in the design of pattern recognition systems is the exclusive OR (XOR) problem. However, to solve this problem, effectively ended research interest in the area of Artificial Neural Networks for over 21 years, which highlights the importance of the XOR problem in the design of pattern recognition systems. The standard XOR problem is depicted in Figure 5:

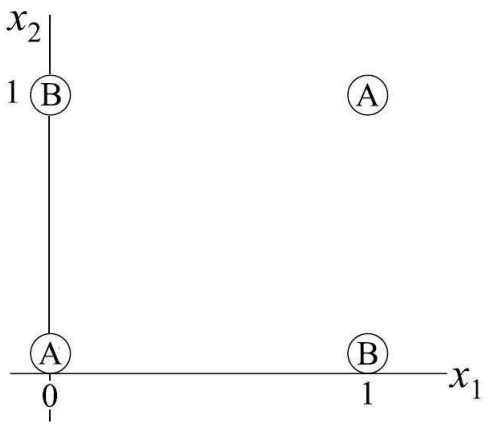

Figure 5: The exclusive or (XOR) problem: points (0,0) and (1,1) are members of class A; points (0,1) and (1,0) are members of class B.

Here the diagonally opposite corner-pairs of the unit square form two classes, A and B. From the Figure 5, it is clear that it is not possible to draw a single straight line which will separate the two classes. This observation is crucial in explaining the the complexity to solve this problem. This problem can be solved using multi-layer perceptrons (MLPs), or by using more elaborate single-layer artificial neural network such as the PPS Wavelet neural network, can be trained to solve this problem in a straightforward manner. In order to demonstrate the adaptive capacity of the PPS neural networks, we accomplished a study with the functions $\varphi_2(x)$ and $\varphi_5(x)$. The results are illustrated in Figures 6 and 7 respectively:

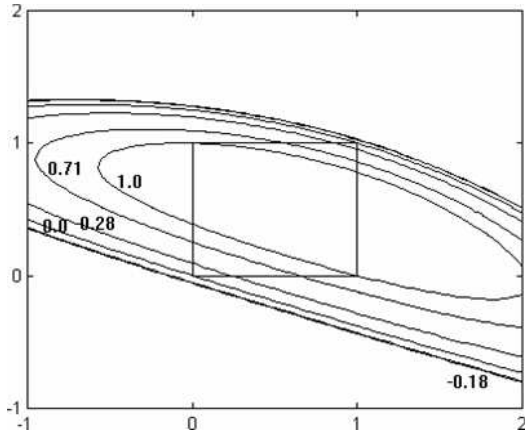

Figure 6: XOR problem based on $\varphi_2(x)$.

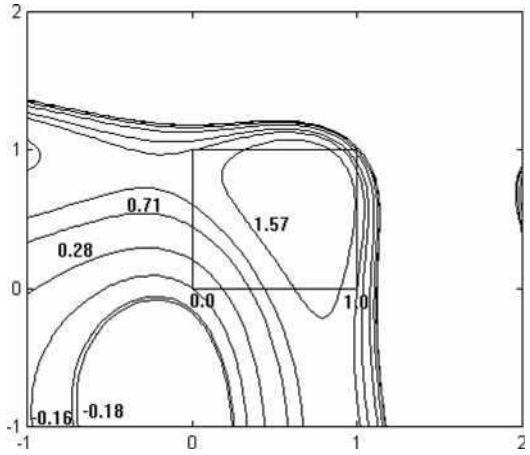

Figure 7: XOR problem based on $\varphi_5(x)$.

6 CONCLUSIONS

Neural networks and wavelet transform have been recently seen as attractive tools for developing efficient solutions for many real world problems in function approximation. The combination of neural networks and wavelet transform gives rise to an interesting and powerful technique for function approximation referred to as wavenets. Function approximation is a very important task in environments where computation has to be based on extracting information from data samples in the real world processes. So, mathematical model is a very important tool to guarantee the development of the neural network area.

ACKNOWLEDGEMENTS

We would like to thank the CAPES (Coordenação de Aperfeiçoamento de Pessoal de Nível Superior) process number $3634/06-0$ and the Lisbon University that supported this investigation.

REFERENCES

Avci, E. (2007). An expert system based on wavelet neural network-adaptive norm entropy for scale invariant texture classification. *Expert Systems with Applications*, 32:919–926.

Chen, H. and Hewit, J. (2000). Application of wavelet transform and neural networks to recognition and classivication of blemishes. *Mechatronics*, 10:699–711.

Chen, Y., Yang, B., and Dong, J. (2006). Time series prediction using a local linear wavelet neural network. *Neurocomputing*, (69):449–465.

Chui, C. (1992). *An Introduction to Wavelets*. Academic Press.

Cybenko, G. (1989). Approximation by superposition of a sigmoidal function. *Mathematics of Control, signals and Systems*, 3:303–314.

Daubechies, I. (1992). *Ten lecture on wavelets*. Society for Industrial and Applied Mathematics (SIAM).

de Queiroz, R. A. B. and Marar, J. F. (2007). Algorítmos heurísticos para a seleção de neurônios em redes neurais polinomios potências de sigmoide (pps)-wavelet. *TEMA Tend. Mat. Apl. Comput.*, 8(1):129–138.

Fan, J. and Wang, X. F. (2005). A wavelet view of small-world networks. *IEEE Transactions on Circuits and Systems*, pages 1–4.

Funahashi, K. (1989). On the approximate realization of continuos mappings by neural networks. *Neural Networks*, (2):183–192.

Hecht-Nilsen, R. (1987). Kolmogorov's mapping neural networks existence theorem. In *1st IEEE Inter. Conf. on Neural Networks*, volume 3, pages 11–14.

Jiang, X., Mahadevan1, S., and Adeli, H. (2007). Bayesian wavelet packet denoising for structural system identification. *Struct. Control Health Monit.*, 14:333–356.

Marar, J. F. (1997). *Polinomios Potências de Sigmoide (PPS): Uma nova Técnica para Aproximação de Funções, Construção de Wavenets e suas aplicações em Processamento de Imagens e Sinais*. PhD thesis, Universidade Federal de Pernambuco - Departamento de Informática.

Misra, B. B., Dash, P. K., and Panda, G. (2007). Pattern classification using local linear wavelet neural network. *International Conference on Information and Communication Technology*, pages 92–95.

Oussar, Y. and Dreyfus, G. (2000). Initialization by selection for wavelet neural traing. *Neurocomputing*, 34:131–143.

Pati, Y. and Krishnaprasad, P. (1993). Analysis and synthesis of feedforward neural networks using discrete affine wavelet transformations. *IEEE Transactions on Neural Networks*, 4(1):73–85.

Zhang, H. and Pu, J. (2006). A novel self-adaptive control framework via wavelet neural netwok. In *6th World congress on intelligent control and automation*, pages 2254–2258.

Zhang, Q. and Benveniste, A. (1992). Wavelet networks. *IEEE Transactions on Neural Networks*, 3(6):889–898.

Zhang, Z. and San, Y. (2004). Adaptive wavelet neural network for prediction of hourly nox and no2 concentrations. In *Winter Simulation Conference*, pages 1770–1778.

BIOMIMETIC FLOW IMAGING WITH AN ARTIFICIAL FISH LATERAL LINE

Nam Nguyen, Douglas Jones
Coordinated Science Laboratory, University of Illinois, Urbana Champaign, USA
nnguyen5@uiuc.edu, dl-jones@uiuc.edu

Saunvit Pandya, Yingchen Yang, Nannan Chen, Craig Tucker, Chang Liu
Micro and Nanotechnology Laboratory, University of Illinois, Urbana Champaign, USA
spandya2@uiuc.edu, yang10@uiuc.edu, nchen7@uiuc.edu, ctucker3@uiuc.edu, changliu@uiuc.edu

Keywords: Artificial lateral line, flow imaging, MEMS sensor array, calibration, adaptive beamforming, Capon beamforming, Cramer-Rao Lower Bound.

Abstract: Almost all fish possess a flow-sensing system along their body, called the lateral line, that allows them to perform various behaviours such as schooling, preying, and obstacle or predator avoidance. Inspired from this, our group has built artificial lateral lines from newly-developed flow sensors using Micro-Electro-Mechanical Systems (MEMS) technology. To make our lateral line a functional sensory system, we develop an adaptive beamforming algorithm (applying Capon's method) that provides our lateral line with the capability of imaging the locations of oscillating dipoles in a 3D underwater environment. To help our sensor arrays adapt to the environment for better performance, we introduce a self-calibration algorithm that significantly improves the image accuracy. Finally, we derive the Cramer-Rao Lower Bound (CRLB) that represents the fundamental perfomance limit of our system and provides guidance in optimizing artificial lateral-line systems.

1 INTRODUCTION

Biologists have discovered that almost all species of fish have a flow-sensing system, called the lateral line, consisting of cilium-like haircell sensors (Figure 1) (Dijkgraaf, 1963). Each haircell sensor in the lateral line measures local fluid flow velocity, and fish rely on their lateral lines to perform a wide range of activities including schooling, preying, navigation, and predator avoidance (Pitcher and Wardle, 1976; Coombs, 1994). Studies show that using its lateral lines, a fish can locate and track an acoustic dipole source (Coombs and Conley, 1997), which models the back-and-forth motion of the tail of smaller prey or other fish.

Inspired by the capability of the fish lateral lines, we are developing an equivalent engineered system, an artificial lateral line. Potential applications include maneuvering Autonomous Underwater Vehicles (AUV), dynamic imaging in an underwater environment, detecting corrosion or leaks inside pipes, and detecting and tracking intruders such as swimmers or submarines.

Recent advances in Micro-Electro-Mechanical Systems (MEMS) technology make it possible to build micrometer-scale sensors mimicking the function and structure of fish lateral lines. The first MEMS lateral line consists of a linear array of 16 hotwire amemometers (Fan et al., 2002). These sensors are capable of measuring flow magnitude but not direction. Recently, MEMS haircell flow sensors, which are sensitive to flow direction, have also been developed (Chen and Liu, 2003).

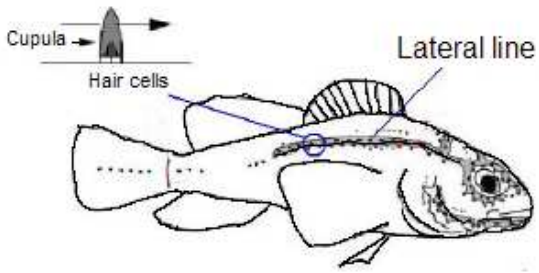

Figure 1: Hair cell sensor system in fish.

Along with development of sensors, signal-processing algorithms are also required to make a complete artificial lateral-line sensory system. Pre-

vious work in this area localizes and tracks an acoustic source using a ML estimator (Pandya et al., 2006) and introduces a new method for imaging all flow sources surrounding a sensor array (Pandya et al., 2007). In this paper, we extend the work in (Pandya et al., 2007) to cover mapping in three-dimentional space (3D imaging). In particular, we review the dipole model and modify the beamforming algorithm in (Pandya et al., 2007) to handle 3D imaging of dipoles using haircell sensors. Next, we present a self-calibration algorithm to adjust the gains across the sensors to improve estimation accuracy. Finally, we derive the Cramer-Rao Lower Bound (CRLB) for the dipole position estimate to find the fundamental performance limits of the system.

2 ARTIFICIAL LATERAL-LINE SENSORS

We have used three types of flow sensors to build artificial lateral lines: conventional hot-wire sensors, micromachined (MEMS) hot-wire sensors, and hair-cell sensors (Figure 2). Both types of hot-wire sensors operate on the heat dissipation principle. Voltage applied across a sensor heats up the wire. Movement of water or air particles across the hot wire carries away heat causing a change in the wire's resistance and in turn the current. The change in current reflects the speed of water or air particles moving across the wire.

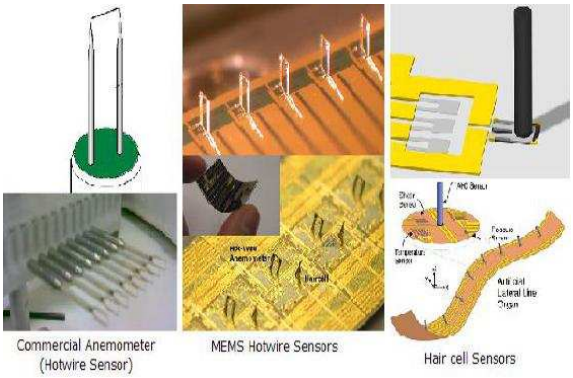

Figure 2: Three types of flow sensors for underwater acoustic signals.

Conventional hotwire sensors are bulky and costly. This makes it hard to form small and dense arrays of sensors for artificial lateral lines. To overcome those drawbacks, micromachined hotwire sensors have been developed (Chen et al., 2003). They can be integrated to form a lateral line in a canal as in fish or to form a dense array of sensors with 1mm spacing . However, the sensors are fragile and cannot distinguish the direction of flow. To avoid these problems, micromachined haircell sensors were invented that operate on the same principle as in fish. The hair of the sensor intercepts the flow, and the force applied on the hair is transformed into stress at the base of the hair. A piezo-electric strain gauge on a cantilever at the base translates the stress into an electronic signal (Yang et al., 2007). The advantages of the haircell sensors are robustness and directional sensing capability.

3 FLOW IMAGING USING A BEAMFORMING APPROACH

Our main goal is to estimate the locations of dipole sources using arrays of flow sensors in an underwater environment. In our laboratory experiment, the dipole source is a small sphere oscillating back and forth in a certain direction at a fixed frequency. We start with a dipole source since it is simple enough so that its surrounding flow field model is well established. Moreover, dipole-like flow sources are commonly encountered in nature, such as the waving tail of a fish. Biologists have extensively studied fish lateral-line response to acoustic dipoles and found that fish can locate the source of a dipole and track its movement, and at least some species treat it as prey (Coombs, 1994).

A model of an oscillating dipole source in fluid has been well studied in (Coombs, 2003). The flow velocity at a point in space near a dipole source is modeled as

$$\vec{v}_{flow}(r,\theta) = \left(a^3 U_o \frac{\cos(\theta)}{r^3}\right)\hat{\mathbf{r}} + \left(\frac{a^3 U_o}{2}\frac{\sin(\theta)}{r^3}\right)\hat{\theta}. \quad (1)$$

In the above equation, the flow velocity is a function of the dipole diameter a, the initial vibrational velocity amplitude U_o, and the observation distance r and angle θ as shown in Figure 3a. Also, $\hat{\mathbf{r}}$ and $\hat{\theta}$ are unit vectors of the dipole's spherical coordinates at the sensor's position.

The flow velocity in Equation (1) is, however, derived in the dipole's spherical coordinates. It is more convenient to compute flow velocity in the fish's Cartesian coordinates (Figure 3b) so that we can derive array patterns due to a dipole oscillating in a certain direction at some location in space. Transformed into the fish's Cartesian coordinates, the flow velocity is then

$$\vec{v}_{flow}(\vec{s}) = \frac{a^3 U_o}{2r^3}\left(3\cos(\theta)\hat{\mathbf{r}} - \hat{\mathbf{z}}_d\right) \quad (2)$$

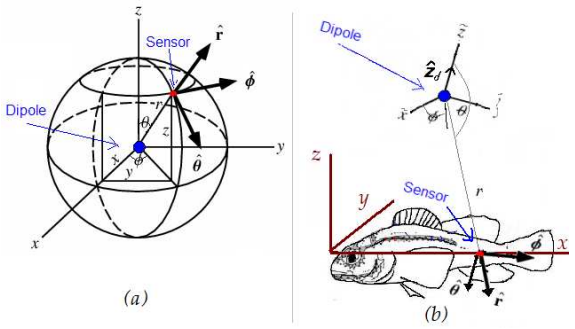

Figure 3: (a) Dipole's Spherical coodinates. (b) Fish's Cartesian coordinates.

where $\hat{\mathbf{z}}_d$ is now the unit vector on the oscillating axis of the dipole and $\vec{s} = (x_s, y_s, z_s)$ is the vector representing the position of the sensor in the fish's coordinates. If $\vec{d} = (x_d, y_d, z_d)$ is the vector that indicates the position of the dipole, then

$$r = \|\vec{s} - \vec{d}\| \text{ and } \hat{\mathbf{r}} = \frac{\vec{s} - \vec{d}}{\|\vec{s} - \vec{d}\|}$$

Researchers have studied how the lateral lines in fish respond to the fluid-flow field created by a dipole source. In (Curcic-Blake and van Netten, 2006), the excitation patterns along the lateral line of a ruffle fish (*Gymnocephalus cernuus* L.) were electrophysiologically measured, then compared to theoretical predictions and found to be in good agreement. The authors also applied a continuous wavelet transform (CWT) algorithm on the collected signals to produce a 2D-contour map of the area surrounding the dipole source. Although the region of the dipole source can be identified from the contour map, the map has poor resolution, making it difficult to visually locate the dipole's position or to see multiple simultaneous sources.

Approaching this problem from the engineering side, our research group has implemented artificial lateral lines with both conventional and MEMS hotwire sensors and used them to capture the signals in the flow field created by a dipole source. An adaptive beamforming approach using Capon's beamformer (Capon, 1969) yielded a much higher resolution spatial imaging of dipole source then the CWT (Pandya et al., 2007).

(Curcic-Blake and van Netten, 2006) and (Pandya et al., 2007) only focus on the case of two-dimensional imaging. That means that the dipole source and all the sensors are in the XY-plane, and the estimation is only concerned with the x and y coordinates. Moreover, (Pandya et al., 2007) used hotwire sensors that measure flow magnitude, not flow direction. In this case, the dipole model in Equation (2) reduces to

$$\begin{aligned} \|\vec{v}_{flow}(\vec{s})\| &= \frac{a^3 U_o}{2r^3} \|3\cos(\theta)\hat{\mathbf{r}} - \hat{\mathbf{z}}_d\| \\ &= \frac{a^3 U_o}{2r^3} \sqrt{3\cos^2(\theta) + 1}. \end{aligned} \quad (3)$$

In fact, Equation (3) is simplified further when the dipole's direction of oscillating $\hat{\mathbf{z}}_d$ is perpendicular to XY-plane

$$\|\vec{v}_{flow}(\vec{s})\| = \frac{a^3 U_o}{2r^3} \text{ since } \theta = \pi/2. \quad (4)$$

Equation (4) is used in (Pandya et al., 2007) to compute expected sensor readings for each position of dipole in the grid. However, this model no longer holds when we extend the problem to 3D imaging using haircell flow sensors.

3.1 3D Imaging with Haircell Sensors

Figure 4 illustrates how the flow velocity $\vec{v}_{flow}$ impacts on the hair of an artificial hair cell (AHC) sensor. A dipole source is located above the sensor in 3D space. The flow velocity is computed using Equation (2). Note that flow velocity now can be in any direction in 3D space. We neglect here any effects introduced by the structure to which the sensors are attached. Figure 4a shows the side view of the flow vector and Figure 4b shows the top view of it.

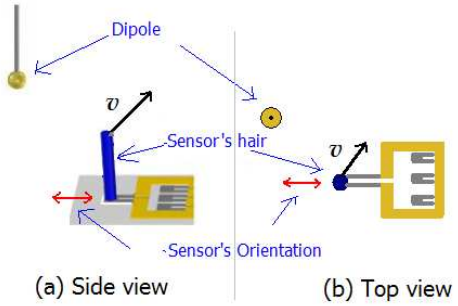

Figure 4: (a) Side view of sensor and dipole. (b) Top view of sensor and dipole.

A single AHC sensor can only measure flow parallel with the strain-guage cantilever. Therefore, an AHC sensor does not measure the magnitude and direction of the flow velocity $\vec{v}_{flow}$ but measures the projection of the flow velocity onto the sensor's orientation axis. The sensors' orientations are thus essential information to determine the sensor array response.

We extend the adaptive beamforming algorithm in (Pandya et al., 2007) to enable 3D imaging with AHC sensors via the steps summarized below:

- Step 1: Compute the expected sensor array pattern for each dipole position (x_d, y_d, z_d) in the 3D grid. For each sensor in the array, use Equation (2) to compute the flow velocity at that sensor, and then project the flow velocity onto the sensor's orientation axis. This produces a template of the array pattern including L sensor readings

$$\mathbf{s}_{(x_d,y_d,z_d)} = [s_1, s_2, \ldots, s_L].$$

  Note that the flow velocity in Equation (2) is determined by the sensor position vector $\vec{s}$, the dipole position vector $\vec{d} = (x_d, y_d, z_d)$, and the dipole oscillating vector $\hat{\mathbf{z}_d}$. $\hat{\mathbf{z}_d}$ is a unit vector defined by the azimuth angle θ_d and the zenith angle ϕ_d. So there are in total 5 parameters to define a dipole, namely x_d, y_d, z_d for position and θ_d, ϕ_d for oscillating direction.

- Step 2: Compute the outer-product from the sensor samples

$$\mathbf{R} = \frac{1}{N}\sum_{n=1}^{N} \mathbf{x}[n] * \mathbf{x}^T[n]$$

  where $\mathbf{x}[n]$ is the discrete-time vector of samples of the collected signals.

- Step 3: Using Capon's method, compute the energy level at each point in the grid

$$E = \frac{1}{\mathbf{s}_{\vec{d}}^H \mathbf{R}^{-1} \mathbf{s}_{\vec{d}}}$$

- Step 4: Plot a map of energy level E for each point in the 3D grid. The high-energy regions in the map correspond to the dipole sources' locations.

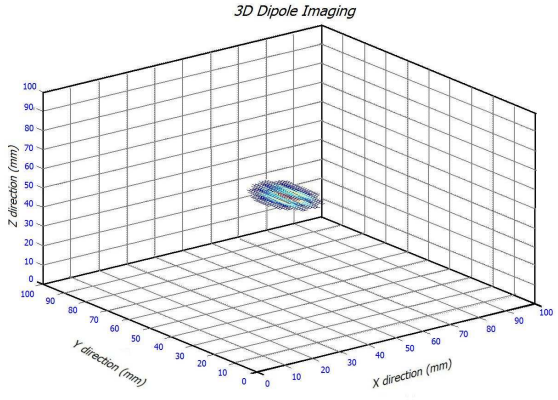

Figure 5: 3D Dipole Imaging with a dipole oscillating at (50,50,50).

The above algorithm is used in a 3D dipole imaging simulation, and the results are shown in Figure 5. In this case, we simulate 2 arrays in an L-shape pattern with a total of 21 haircell sensors on the x and z axes. On each of two axes, there are 11 sensors spaced 10 mm apart from 0 to 100 mm. A dipole is located at $(50, 50, 50)$. Figure 5 shows a sphere centered around the dipole source with different colour intensity. High intensity presents the energy level output (from Capon's formula) at the local point. That means the dipole is most likely there.

4 SELF-CALIBRATION ALGORITHM

Calibration of sensors is an important practical step before doing any signal analysis. Since each individual sensor's sensitivity gain can vary (especially for sensors still in the laboratory stage of development), poor calibration will lead to poor estimation performance. Biological systems have a remarkable ability to tune their response to environmental variation, growth, or injury. Self-tuning ability is equally desirable for an engineered system. In this section, we propose an effective way of doing sensor array calibration for this type of experiment.

A straightforward method for calibration of a sensor array is to sequentially place a dipole in front of each sensor in the array, then record readings of all the sensors, which form a series of array patterns. Ideally, all the patterns should have similar shape and magnitude with the peak at the sensor closest to the dipole. However, measured array patterns vary significantly due to the non-uniformity of sensor gains. Figure 6 displays an example of the measured array patterns before calibration.

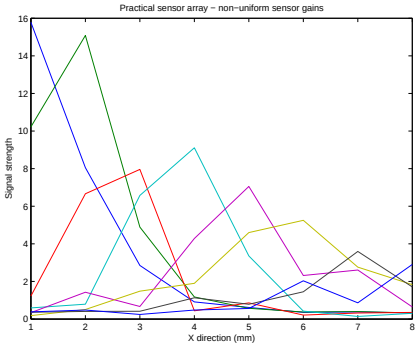

Figure 6: Measured sensor array patterns (non-uniform sensor gains).

Mathematically, the calibration problem can be formulated as follows. Consider a linear array of L evenly spaced sensors and a series of measurements

as the dipole travels a linear path at a constant distance from the sensor array. When the dipole is in front of Sensor 1, the ideal array pattern will be

$$[s_0, s_1, s_2, \ldots, s_{L-1}]$$

at Sensor 2, it will be $[s_{-1}, s_0, s_1, \ldots, s_{L-2}]$ and so on until sensor L, $[s_{-L+1}, s_{-L+2}, \ldots, s_0]$. Stacking those ideal array patterns together produces a Toeplitz matrix

$$A = \begin{bmatrix} s_0 & s_1 & s_2 & \ldots & \ldots & s_{L-1} \\ s_{-1} & s_0 & s_1 & \ddots & & s_{L-2} \\ s_{-2} & s_{-1} & \ddots & \ddots & \ddots & \vdots \\ \vdots & \ddots & \ddots & \ddots & s_1 & s_2 \\ \vdots & & \ddots & s_{-1} & s_0 & s_1 \\ s_{-(L-1)} & \ldots & \ldots & s_{-2} & s_{-1} & s_0 \end{bmatrix}$$

As each sensor i has a gain g_i, the matrix of array patterns with gains is

$$B = \begin{bmatrix} g_1 s_0 & g_2 s_1 & g_3 s_2 & \ldots & g_L s_{L-1} \\ g_1 s_{-1} & g_2 s_0 & g_3 s_1 & \ddots & g_L s_{L-2} \\ g_1 s_{-2} & g_2 s_{-1} & \ddots & \ddots & \vdots \\ \vdots & \ddots & \ddots & \ddots & g_L s_2 \\ \vdots & & \ddots & g_{(L-1)} s_0 & g_L s_1 \\ g_1 s_{-(L-1)} & \ldots & \ldots & g_{(L-1)} s_{-1} & g_L s_0 \end{bmatrix}$$

With noise included, the actual readings may be $C = B + N$, where C is the noisy version of B. Figure 6 shows the measured array patterns by plotting the rows of the matrix C. Although each pattern seems to have the peak at the sensor closest to the dipole, the shapes of the patterns are quite different due to non-uniform sensor gains. The aim of calibration is to find a set of sensor gains $[g_1, g_2, \ldots, g_L]$ and matrix A that approximate C as closely, as possible, i.e.

$$A * \begin{bmatrix} g_1 & 0 & \ldots & 0 \\ 0 & g_2 & \ddots & 0 \\ \vdots & & \ddots & \vdots \\ 0 & \ldots & 0 & g_L \end{bmatrix} \approx C$$

This is a bilinear least squares problem, which is a simple special case of a mixed linear-nonlinear least squares problem (Golub and Pereyra, 1973). Golub and Pereyra (Golub and Pereyra, 1973) show that the optimal linear coefficients in the globally optimal solution are simply the linear least-squares solution when the nonlinear coefficients are fixed at their globally optimum values; since the bilinear form is linear in both the sensor gains g_i and the shift-invariant dipole response pattern s_j when the other is held constant, this holds for both.

We apply the standard iterative solution approach in which we fix one set of coefficients, find the least-square optimal solution best fitting the measured data for the other, and iterate until convergence. (See, for example, (Bai and Liu, 2006) for recent convergence theorems for this algorithm for random inputs.) The algorithm is as follows:

- Step 1: Initialize with uniform gains $g_1 = g_2 = \ldots = g_L = 1$.
- Step 2: Fix the gains $[g_1, g_2, \ldots, g_L]$ and find the optimal least squares solution for the dipole response $[s_{(-L+1)}, s_{(-L+2)}, \ldots, s_0, \ldots, s_{(L-1)}]$. This is equivalent to summing matrix C diagonally and then dividing it by the sum of all gains corresponding to the column that the diagonal line crosses.
- Step 3: Fix the dipole response $[s_{(-L+1)}, s_{(-L+2)}, \ldots, s_0, \ldots, s_{(L-1)}]$ and find the optimal least squares solution for the gains $[g_1, g_2, \ldots, g_L]$. This is equivalent to summing up each column of C and dividing it by the sum of corresponding s_l that appeared in that column (see matrix B). For example, after summing up column 2, it is divided by the sum $(s_1 + s_0 + s_{-1} + \ldots + s_{(2-L)})$ to get g_2.
- Step 4: Go back to Step 2 with the new gains in Step 3. Repeat the process until convergence.

This method allows the on-line calibration of sensors from observation of a dipole source as it travels across the array. This can be exploited to develop a fully self-tuning system like biological systems.

Using the algorithm above, we show the improved results in Figure 7, using an array of 8 hotwire sensors positioned 12.5mm apart on the X-axis from 12.5mm to 100mm. A dipole is placed in front of each sensor and data are collected. Figure 7(A) displays the array patterns for these eight positions. As can be seen, these patterns do not look like a shifted version of each other. The calibration algorithm is applied to these patterns to produce the calibrated patterns in Figure 7(B). The improvement in the magnitude and shape of those patterns is clear. The effect of the calibration algorithm can be clearly seen as we run a 2D imaging test of estimating the location of a dipole located in front of sensor 4 (50 mm). The image in Figure 7(C) is the result of processing signals without calibration while the one in Figure 7(D) uses calibration. There is obviously a significant improvement in the accuracy of the image produced by using calibration.

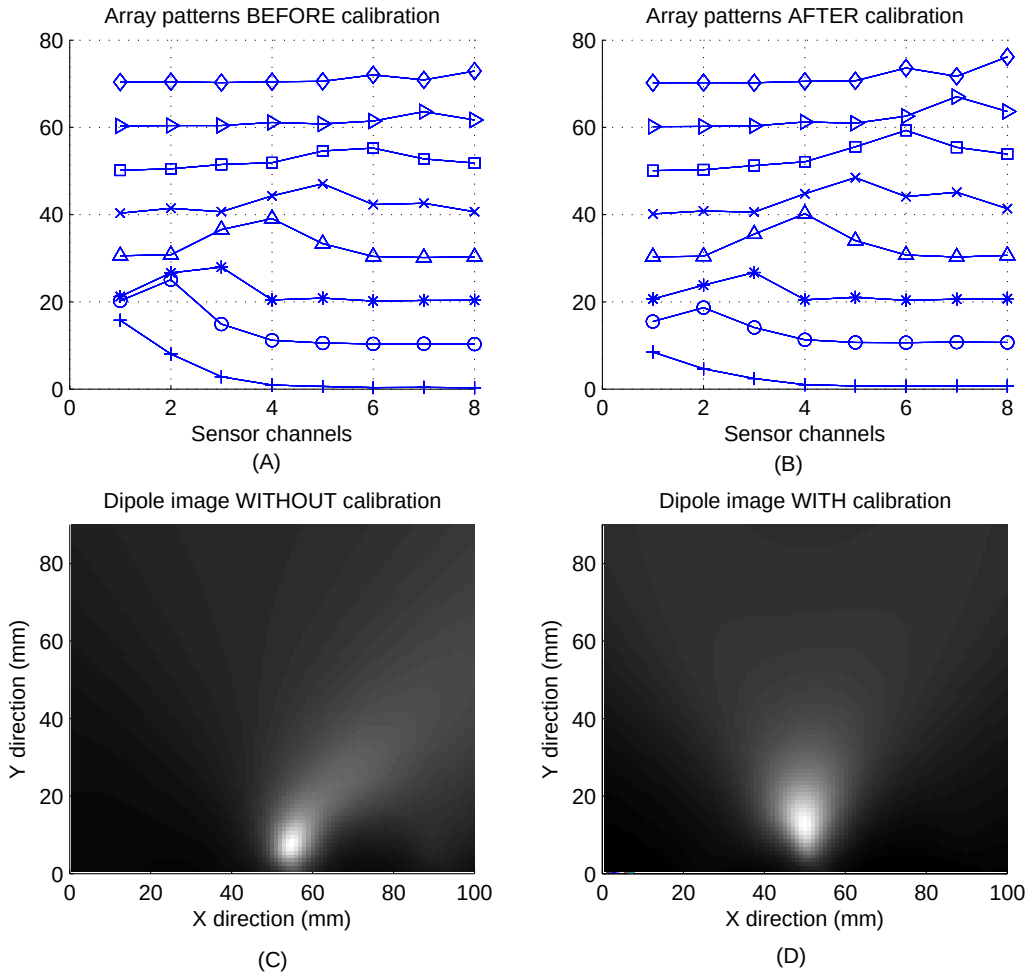

Figure 7: Effects of Self-calibration: (A) Measured array patterns (before calibration), (B) Calibrated array patterns, (C) 2D dipole imaging without calibration, (D) 2D dipole imaging with calibration.

5 CRAMER-RAO BOUND ON DIPOLE LOCALIZATION

Fundamental lower bounds on the error of the dipole position estimate for lateral-line sensors are very useful for evaluation of the estimator presented in Section 3.1, for finding the fundamental performance limit of a lateral line array, and for evaluating different sensor array configurations.

The signal captured by sensor k can be modeled as

$$s_k = f_k(\vec{d}) + N_k \tag{5}$$

where N_k is the additive Gaussian noise and $f_k(\vec{d})$ is the expected reading at sensor k produced by a dipole at location $\vec{d}$. For the case of 2D imaging ($\vec{d} = (x_d, y_d)$) using hotwire sensors, $f_k(\vec{d})$ is actually computed by Equation (3); i.e., $f_k(\vec{d}) = \|\vec{v}_{flow}(\vec{s}_k)\|$. For case of 3D imaging using AHC sensors, $f_k(\vec{d})$ is computed as described in Step 1 of the algorithm in Section 3.1.

If the noises at all sensors are assumed to be i.i.d. with zero mean and variance σ_N^2, the signal vector of the sensor array $\mathbf{s}$ is a Gaussian random vector $\mathcal{N}(\mathbf{f}(\vec{d}), \mathbf{I}\sigma_N^2)$. Using the standard procedure in (Poor, 1988), we can derive the Fisher Information Matrix for the case of 2D imaging as

$$\mathbf{F} = \frac{1}{\sigma_N^2} \begin{bmatrix} \sum_{k=1}^{L} \left(\frac{\partial f_k(x,y)}{\partial x}\right)^2 & \sum_{k=1}^{L} \frac{\partial f_k(x,y)}{\partial x}\frac{\partial f_k(x,y)}{\partial y} \\ \sum_{k=1}^{L} \frac{\partial f_k(x,y)}{\partial x}\frac{\partial f_k(x,y)}{\partial y} & \sum_{k=1}^{L} \left(\frac{\partial f_k(x,y)}{\partial y}\right)^2 \end{bmatrix} \tag{6}$$

then the CRLB is

$$Var[\vec{d}] \geq [\mathbf{F}]^{-1} \tag{7}$$

For the case of 2D imaging using hotwire sensors as in (Pandya et al., 2007), we have from Equation (3)

$$f_k(x,y) = \frac{a^3U_o}{2r^3} = \frac{a^3U_o}{2\|\vec{s_k}-\vec{d}\|^3} = \frac{a^3U_o}{2[(x-x_{s_k})^2+(y-y_{s_k})^2]^{\frac{3}{2}}}$$

then (6) becomes

$$\mathbf{F} = \frac{(\frac{3}{2}a^3U_o)^2}{\sigma_N^2} \times \begin{bmatrix} \Sigma_{k=1}^{L} \frac{(x-x_{s_k})^2}{[(x-x_{s_k})^2+(y-y_{s_k})^2]^5} & \Sigma_{k=1}^{L} \frac{(x-x_{s_k})(y-y_{s_k})}{[(x-x_{s_k})^2+(y-y_{s_k})^2]^5} \\ \Sigma_{k=1}^{L} \frac{(x-x_{s_k})(y-y_{s_k})}{[(x-x_{s_k})^2+(y-y_{s_k})^2]^5} & \Sigma_{k=1}^{L} \frac{(y-y_{s_k})^2}{[(x-x_{s_k})^2+(y-y_{s_k})^2]^5} \end{bmatrix} \quad (8)$$

We now compute the CRLB in Equation (8) for a system consisting of 16 hotwire sensors placed 6mm apart along the X-axis starting from 60mm to 90mm. The bounds on the estimation error's variance are represented by error ellipses in Figure 8. Each ellipse corresponds to a dipole located at its center. Note that the size of the ellipses grows larger as the dipole moves away from the array. This just agrees with the fact that as the dipole moves away from the sensor array, not only do the signals become weaker but also the array patterns flatten out. The CRLB shows that no signal processing algorithm can accurately estimate the location of dipoles at long range (more than about an array length) because the signals collected by sensors show almost no difference between dipole locations.

As the results show, the CLRB can be a source of design criteria to build a flow sensor array meeting requirements of image resolution and coverage range.

6 CONCLUSIONS

The adaptive beamforming approach to flow-field imaging can be generalized to produce an image of osccilating dipoles' locations in a three-dimensional underwater environment. The images' accuracy increases significantly when a self-calibration algorithm to tune the sensors' gains is applied. The calibration algorithm, which uses the bilinear least squares technique, is a good starting point to build a system with the self-tuning capability that biological systems always exhibit. Our final result, the Cramer-Rao Lower Bound, is a useful tool to evaluate the performance limits of a lateral line system. This helps in the design of a better system. The bounds also confirm that a lateral-line system is neccessarily a near-field sense.

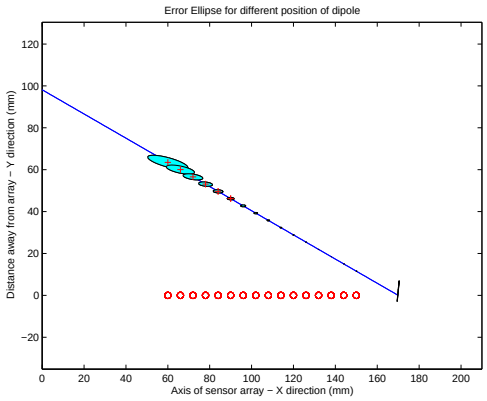

Figure 8: Error ellipse centered around different dipole positions, 16 sensors (the circles) are on the x-axis.

ACKNOWLEDGEMENTS

This work was supported by the DARPA BioSenSE Program under Grant FA-9550-05-1-0459.

REFERENCES

Bai, E. and Liu, Y. (2006). Least squares solutions of bilinear equations. *Systems & Control Letters*, 55(6):466–472.

Capon, J. (1969). High-resolution frequency-wavenumber spectrum analysis. *Proceedings of the IEEE*, 57(8):1408–1418.

Chen, J., Fan, Z., Zou, J., Engel, J., and Liu, C. (2003). Two-dimensional micromachined flow sensor array for fluid mechanics studies. *Journal of Aerospace Engineering*, 16:85.

Chen, J. and Liu, J. (2003). Development of polymer-based artificial haircell using surface micromachining and 3D assembly. *TRANSDUCERS, Solid-State Sensors, Actuators and Microsystems, 12th International Conference on, 2003*, 2.

Coombs, S. (1994). Nearfield detection of dipole sources by the Goldfish (CARASSIUS AURATUS) and the Mottled Sculpin (COTTUS BAIRDI). *Journal of Experimental Biology*, 190:109–129.

Coombs, S. (2003). Dipole 3d user guide. Technical report.

Coombs, S. and Conley, R. (1997). Dipole source localization by mottled sculpin. I-III. *Journal of Comparative Physiology A: Sensory, Neural, and Behavioral Physiology*, 180(4):387–399.

Curcic-Blake, B. and van Netten, S. (2006). Source location encoding in the fish lateral line canal. *Journal of Experimental Biology*, 209(8):1548–1559.

Dijkgraaf, S. (1963). The functioning and significance of lateral-line organs. *Biology Review*, 38:51–105.

Fan, Z., Chen, J., Zou, J., Bullen, D., Liu, C., and Delcomyn, F. (2002). Design and fabrication of artificial lateral line flow sensors. *Journal of Micromechanics and Microengineering*, 12(5):655–661.

Golub, G. and Pereyra, V. (1973). The differentiation of pseudo-inverses and nonlinear least squares problems whose variables separate. *SIAM Journal on Numerical Analysis*, 10(2):413–432.

Pandya, S., Yang, Y., Jones, D., Engel, J., and Liu, C. (2006). Multisensor processing algorithms for underwater dipole localization and tracking using MEMS artificial lateral-line sensors. *EURASIP Journal on Applied Signal Processing*.

Pandya, S., Yang, Y., Liu, C., and Jones, D. (2007). Biomimetic imaging of flow phenomena. *Proceeding of Acoustics, Speech and Signal Processing, 2007. ICASSP 2007*, 2:II–933 – II–936.

Pitcher, T. Patridge, B. and Wardle, C. (1976). A blind fish can school. *Science*, 194:963–965.

Poor, V. (1988). *An Introduction to Signal Detection and Estimation*. Springer-Verlag.

Yang, Y., Chen, N., Tucker, C., Engel, J., Pandya, S., and Liu, C. (2007). From artificial haircell sensor to artificial lateral line system: development and application. *MEMS 2007 20th IEEE International Conference on Micro Electro Mechanical Systems, Kobe, Japan*.

A HYBRID SEGMENTATION FRAMEWORK USING LEVEL SET METHOD FOR CONFOCAL MICROSCOPY IMAGES

Quan Xue[1], Severine Degrelle[2], JuhuiWang[1], Isabelle Hue[2] and Michel Guillomot[2]
[1]*INRA, MIA-jouy, Lab. of Applied Mathematics and Informatics, Jouy en Josas F-78350, France*
[2]*INRA, UMR 1198; ENVA; CNRS, FRE 2857, Biologie du Développement et Reproduction, Jouy en Josas F-78350, France*
{quan.xue, juhui.wang }@jouy.inra.fr

Keywords: Confocal microscopy, image segmentation, Level-Set, Fast Marching, Geodesic Active Contour.

Abstract: Based on variational and level set approaches, we present a hybrid framework with quality control for confocal microscopy image segmentation. First, nuclei are modelled as blobs with additive noise and a filter derived from the Laplacian of a Gaussian kernel is applied for blob detection. Second, nuclei segmentation is reformulated as a front propagation problem and the energy minimization is obtained near the boundaries of the nuclei with the Fast-Marching algorithm. For each blob, multiple locally optimized points are selected as the initial condition of the front propagation to avoid image under-segmentation. In order to achieve higher accuracy, a graphical interface is provided for users to manually correct the errors. Finally, the estimated nuclei centres are used to mesh the image with a Voronoi network. Each mesh is considered as a Geodesic Active Contour and evolves to fit the boundaries of the nuclei. Additional post-processing tools are provided to eliminate potential residual errors. The method is tested on confocal microscopy images obtained during trophoblast elongation in ruminants. Experimental results show that cell nuclei can be segmented with controlled accuracy and difficulties such as inhomogeneous background or cell coalescence can be overcome.

1 INTRODUCTION

Confocal microscopy imaging is one of the most important technologies used to observe the cellular developmental process. Image segmentation is a major step to interpret the obtained images. Correctly explored, it will provide important information about cellular shape and tissue organisation. Appropriate and automatic image segmentation tools are usually necessary to assist the analysis. However, segmenting confocal images is a complex and laborious task. Several factors might raise difficulties: (1) uneven background: Most of the tissues are fluctuating during the image acquisition and background is rarely uniform; (2) local intensity variation inside a nucleus. Due to imperfect staining during the experiment or intrinsic cellular structure, one nucleus may be split into two or more parts; (3) cell coalescence: Cell over-clustering makes it hard to tell the exact nuclei boundaries.

Many segmentation approaches relating to biological images have been proposed in the literature. Research shows that traditional image segmentation methods such as thresholding, region growing and edge-based approaches (Pitas, 2000) can not be successfully applied to microscopy images. Reported successful methods usually focused on a specific type of images without generality (Wu *et al.*, 2005). Watershed segmentation has been popular and considered as one effective method. Thomas (Thomas and Graham, 2007) modified watershed method to give more accuracy for identifying intracellular structures even in the presence of inhomogeneous background. Wahlby (Wahlby *et al.*, 2004) and Long (Long *et al.*, 2007) used both the intensity and geometry information to appropriately detect nuclei. Those methods are robust but the system is complicated and need more time to adjust and analyse the parameters to give the accurate result according to the characteristics of images. All modified watershed algorithms face over-segmentation phenomena and have to provide post processes to adjust the result, especially on cellular microscopy images with high noise and cell coalescence. Based on partial differential equations and variation models, Solorzano (Solorzano *et al.*, 2001), Chang (Chang *et*

al., 2007) and Dirk (Dirk *et al.*, 2006) provide another direction by using level set segmentation. The solution is derived by minimizing a global energy function. This method benefits from well founded mathematical theories which allow developers to analyze, understand, improve the existing methods and work in a continuous setting in higher dimensional space.

The paper is organized as follows: Section 2 introduces a hybrid structure supporting quality control. Section 3 illustrates segmentation approaches. The system is evaluated in Section 4. Finally, Section 5 draws a conclusion.

2 HYBRID FRAMEWORK

Drawing outlines of cells with a mouse, the result can be regarded as absolutely accurate and objective, but it is a hard work and difficult to repeated. Automatic methods are fast and convenient, but some errors occur. Therefore, the solution for image segmentation is a trade-off between precision and speed. When high accuracy is needed, the system needs interactivity with the analyzer or provides an automatic result with limited errors. To deal with a wide variety of biological microscopy images, a hybrid framework with quality control will be preferable.

We constructed such a hybrid framework combining PED-based level set approaches with selectable interaction which supports automatic and semi-automatic segmentation with a robust error-checking stage, as shown in Figure 1. The nuclei are firstly modelled into blobs with some additive noise and Laplacian of Gaussian (LoG) filter is regarded as a blob-detector. Using gradient information, a front propagation fast marching is applied to segment cellular nuclei. The result can be directly outputted after morphology filter or used to enhance the last result. An interactive module is provided to prevent error propagation and Voronoi meshing is created from those appropriate centres. From cellular shape information, geodesic active contour (GAC) is introduced to refine nuclei boundaries. Post processing methods are added as supplementary module to correct for potential errors.

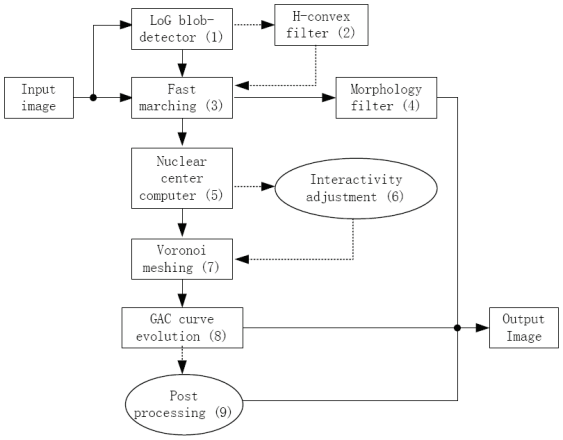

Figure 1: Diagram of hybrid framework.

3 METHOD DESCRIPTION

3.1 Blob Detection

On confocal images from ruminant trophoblast cells *e.g.* Figure. 2 (A), one sees that most nuclei are nearly round. Laplacian of Gaussian filter has been proved to be an effective blob-detector (Byun *et al.* 2006) since LoG filter is able to detect particular edges by determining the peak point of the ridge. Therefore, we aimed at detecting regions which are brighter than the surrounding to overcome inhomogeneous background.

Although the nuclei of trophoblast cells are not exactly round, our objective is focused on rotation invariance of objects, so that it is fitful to over-fit a circle model into the whole image. From the experimental results, we found that the diameter of LoG filter is proportional to nuclei average diameter and this initial value can be set in advance since the kind of cells are known, e.g. bovine or ovine trophoblast. LoG filter will get a smooth image local maximal values of which nearly correspond to the nuclei centres shown in Figure 2. (B).

After blob-detector, an H-convex filter is added for enhancing the local maximum. H-convex belongs to a kind of morphological method and has the effect of extracting objects that are brighter than background by at least H-intensity units. It is relatively straightforward and does not require homogeneity in the background. The enhanced local maximal result can be gotten in Figure 2. (C).

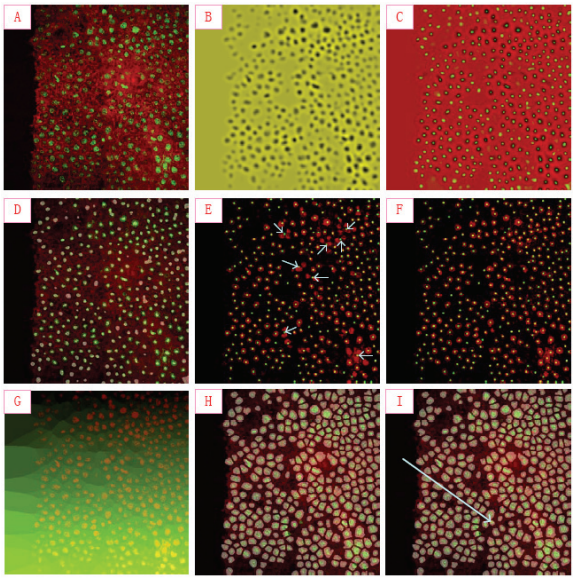

Figure 2: Results in each module.

3.2 Fast Marching

Fast marching method (Sethian, 1996) has monotonically advancing front with positive speed to build solutions outward from the boundary condition by choosing the smallest time in its evolution, until it adopts the form of the enclosing nuclei delineated by the staining. The segmentation result from fast marching is gotten in Figure 2 (D).

Our speed function is provided by sigmoid function:

$$S(I') = (Max - Min) \cdot \frac{1}{\left(1 + e^{-\left(\frac{I-\beta}{\alpha}\right)}\right)} + Min \quad (1)$$

where I is intensity of input pixel, I' is the intensity of output pixel, Min and Max are the minimum and maximum values of output image, α defines the width of input intensity range and β defines intensity around which the range is centred.

Since some cell nuclei are connected closely, segmentation results depend on initial seed positions, so that multiple seeds will have more chances not to miss objects. However, having seeds distributed inside the nuclei is not helpful for contour expansion. Therefore, instead of randomly selecting multiple points as initial condition, we searched the best seeds for each candidate by finding its local minimum through comparison with neighbours as shown in Figure 3.

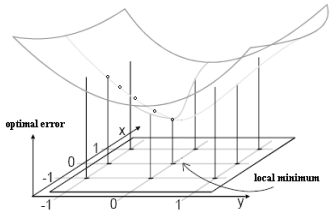

Figure 3: Seeds optimization by local searching.

The selection of optimal seeds gives a better result in detecting nuclei, and that this result is stable shown Table 1. The more seeds can be assigned nearby the edge of nuclei, the more precise the fast marching segmentation can be. Table 1 also shows that the number of initial seeds is important. If too many seeds are put in one image, many single nuclei will be divided into multiple parts due to local intensity variations. Normally the distances we have selected are 16 pixels in row, 16 pixels in column and a searching radius of 3 pixels. For some special trophoblast images we had to adjust these parameters carefully.

Table 1: Comparison between random and optimal seeds.

radius (pixels)	Number of nuclei	4×4	8×8	16×16	32×32	64×64
3	Optimal	398	360	337	339	310
	Random	419	364	332	319	307
5	Optimal	319	312	303	304	302
	Random	337	312	299	288	275

3.3 Interactivity

The centre of each nucleus can be estimated from the above results. Despite accuracy rate is averagely high, there is still a possibility of a few failures to occur as indicated by white arrows on Figure 2 (E). On our images, the error rate varies from 1% to 10%. If more than one seed is located inside a nucleus, this will cause over-segmentation, conversely when no seed is found within a nucleus, the object is lost. Therefore, the centres of nuclei are very important for the final result. In order to prevent error propagation, human interactivity is necessary to view and adjust results in this stage. Through an interface, the user can make decision based on visual examination of the nuclei, so that an immediate feedback enables the user to produce reliable results e.g. Figure 2 (F).

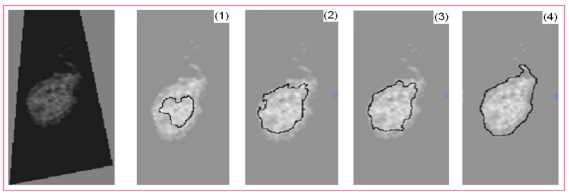

Figure 4: Refinement by GAC in one Voronoi mesh.

3.4 Geodesic Active Contour

From nuclei centres, Voronoi mesh is directly produced in Figure 2 (G), which can be regarded as a reference map in refining nuclei by geodesic active contours (Vicent *et al*. 1997). Since Voronoi mesh gives a limited small region to minimize the GAC energy function, it is sure that one nucleus is gotten just in one Voronoi-mesh. The refining result is shown in Figure 2 (H).

GAC consists of double forces which control the last shape and it is important to balance inside and outside forces. When the propagation term is set too high, the contour will go too far inside as illustrated in Figure 4. In our application to ruminant trophoblast cells, all nuclei are nearly rounded so that curvature term is responsible for smoothness.

3.5 Post Processing

When confocal images are very blurred or tightly clustered, a few errors cannot be avoided with automatic detection to correct these potential errors by human visual system. We provide a supplementary module. As an example (Figure 2: I), one lost nucleus has been recovered with this module.

4 EXPERIMENTS

This section describes how our hybrid framework is used to segment the nuclei on 2D confocal images from ruminant trophoblast. There are more than one thousand of images with varying cellular characteristics and varying background noise in dataset. Selecting different modules, four types of pipeline are designed shown in Table 2.

Table 2: Pipelines with different modules.

Module	1	2	3	4	5	6	7	8	9
Pipeline A	×	×	×	×					
Pipeline B	×	×	×		×		×	×	
Pipeline C	×	×	×		×	×	×	×	
Pipeline D	×	×	×		×	×	×	×	×

Figure 5 gives four typical images as examples to show the results of our framework. Our approach is compared with the existing methods in ITK and ImageJ which are using fast marching and K-means clustering individually. In row 1, when confocal images have good quality, all methods can be used successfully, with similar errors. However, when nuclei are clustered together (see row 2), our method keeps stable whereas the other methods lose the ability to separate each nucleus in the clusters. For example, ITK can only detect the whole cluster edge and cannot divide it further while ImageJ produces many connected regions. In row 3, when nuclei are organised in a special structure, the exiting methods (ITK and ImageJ) cannot identify the objects whereas the nuclei are correctly detected by our method and the contour is closer to the true shape. When there are many small nuclei and their size changes continuously (row 4), our result is also stable and useful.

Our framework is a scalable system with quality control through the selection of modules and the setting of the initial parameters based on the characteristics of the original image to balance terms in the energy function of level set. Through adjusting the parameters on propagation and smooth term, the nuclear edges can be detected and refined step by step by active contour as in Figure 6, from (a) to (d).

It is often necessary to complete a confocal image automatic segmentation with an acceptable error rate. Successful results can be obtained with our scalable procedure. Since the modules related to the human interaction are selectable, we can use the level set methods directly. Figure 7 gives an example. The first column comes from the fast marching following the blob-detector and we use morphology filter to enhance the result. In the second column, results from GAC without interactivity are provided. Some error is propagated from fast marching module because the gravity centre of the nuclei is wrongly estimated from fast marching segmentation. GAC can skip the false nuclei but will produce good results with coherent nuclei. So, the number of nuclei from GAC decreases for factual objects.

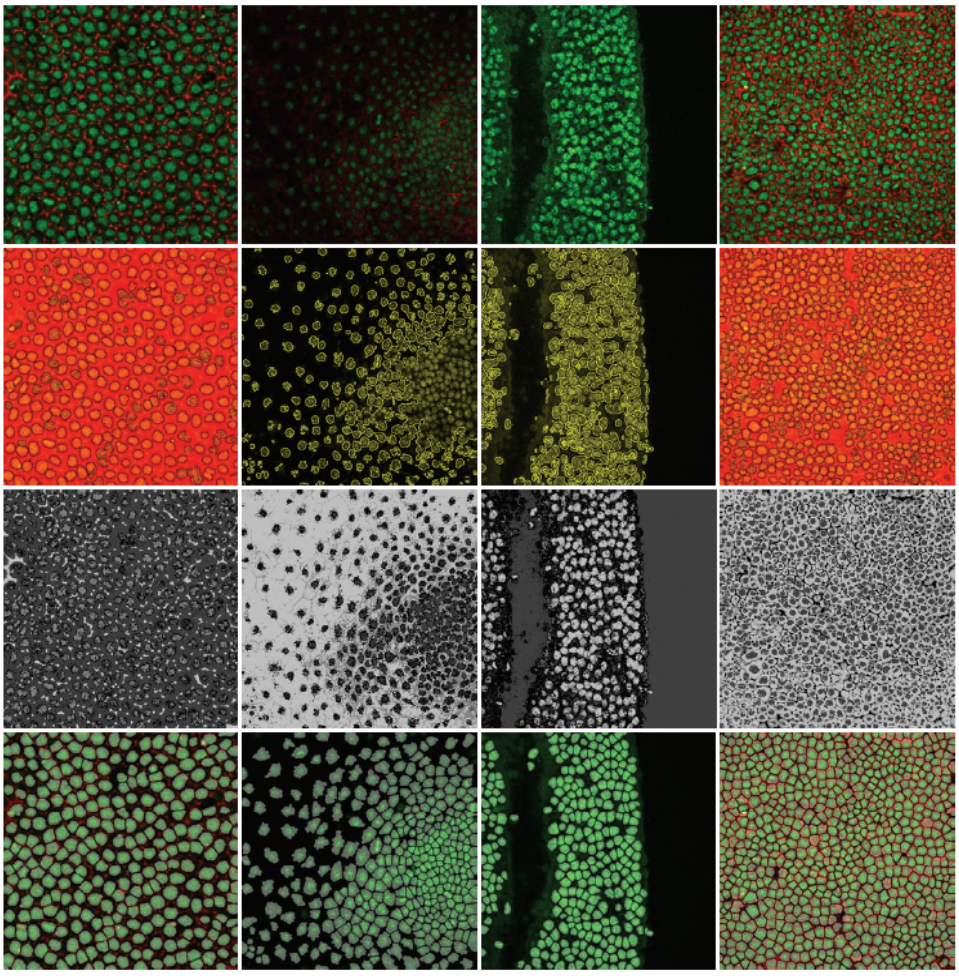

Figure 5: Comparison of proposed algorithm with fast marching in ITK and K-mean clustering in ImageJ (high quality, nuclei coalescence, special structure and low quality from left column to right column). The first row is the original confocal images. The second, the third and the fourth row respectively correspond segmentation results from ITK, ImageJ and proposed algorithm (Pipeline C).

Table 3: Segmentation results expressed as numbers of detected nuclei with each method.

Image	Actual number	Fast marching in ITK	K-means in ImageJ	FM with blob-detector (Pipeline A)	GAC without interactivity (Pipeline B)	GAC with interactivity (Pipeline C)	With post processing (Pipeline D)
(a)	280	253(-27)	265 (-15)	298 (+18)	294 (+14)	280 (+0)	280
(b)	378	281(-97)	347 (-31)	402 (+24)	373 (-5)	374 (-4)	378
(c)	294	236(-58)	179 (-115)	328 (+34)	318 (+24)	292 (-2)	294
(d)	704	544(-160)	652 (-52)	737 (+33)	729 (+25)	711 (+7)	704
Number	1656	1314 (-342)	1443 (-213)	1765 (+109)	1714 (+63,-5)	1657 (+7,-6)	1656
Error rates		20.65%	12.86%	6.58%	4.11%	0.79%	0%

In Table 3, we conclude and compare the error rates from all of the methods discussed above. "+" means over-segmented nuclei and "-" means under-segmented. Their sum is divided by factual total numbers to compute the error rate. Normally we do not use post processing module and the average error ratio is limited into 0.8%. The experimental results show that our hybrid segmentation framework is satisfactorily accurate.

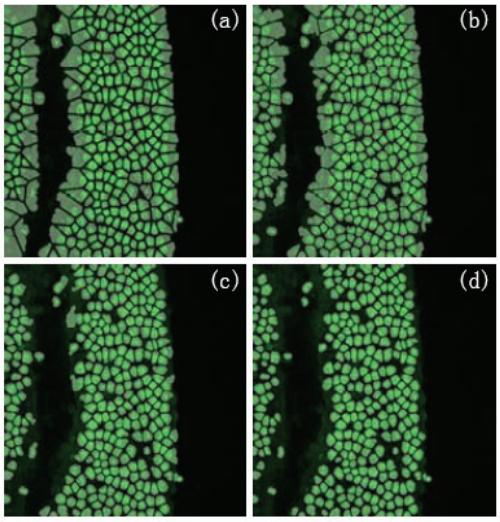

Figure 6: Refining boundary by GAC method with quantity control.

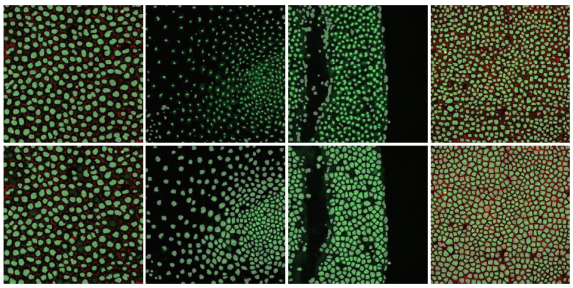

Figure 7: Automatic segmentation results by Pipeline A (first row) and Pipeline B (second row).

5 CONCLUSIONS

This paper demonstrates the effectiveness of a hybrid framework for cellular segmentation. It combines the efficiency of the automatic segmentation procedures with the accuracy of the human visual system. Based on confocal images of ruminant trophoblast, our experiments showed that the proposed approach provides reliable results and presents numerous advantages regarding to manual analysis or automatic methods in terms of objectivity and applicability.

ACKNOWLEDGEMENTS

QX and SD are respectively supported by an INRA and an Ile–de-France post-doctoral fellowship. Scientific financial support comes from an INRA AgroBi grant to JW and IH. We thank A Trubuil P Adenot* and G Lehmann* for helpful discussions (*INRA MIMA2 platform) and INRA experimental farms for embryo production.

REFERENCES

Byun. J.Y., Verardo. M.R., Sumengen. B., Lewis. G.P., Manjunath. B.S., Fisher. S.K., 2006. Automated tool for the detection of cell nuclei in digital microscopic images: Application to retinal images. *Molecular Vision*, pp.949-960. August 2006.

Chang. H., Park. C., Parvin. B., 2007. Quantitative representation of three-dimensinal cell culture models. In *ISBI'07, IEEE International Symposium on Biomedical Imaging: From Nano to Macro,* pp.536-539. April 12-15, 2007. Washington DC, USA.

Dirk. P., Jens. R, Nick. T., Badrinath. R., 2006. Spatio-Temporal Cell Cycle Phase Analysis Using Level Sets and Fast Marching Methods. In *MIAAB'06, 1st international workshop on Microscopic Image Analysis with Applications in Biology*. On 5th of October 2006. Copenhagen, Denmark, USA.

Long. F.L., Peng. H.C., Myers, E., 2007. Automatic segmentation of nuclei in 3D microscopy images of c.elegans. In *ISBI'07, IEEE International Symposium on Biomedical Imaging: From Nano to Macro*, pp.536-539. April 12-15, 2007. Washington DC, USA.

Pitas. I., 2000. *Digital image processing algorithms and applications.* Wiley-Interscience publication. New York, 1st edition

Sethian, J.A., 1996. *Level set methods and fast marching methods.* CAMBRIDE UNIVERSITY Press.

Solorzano. C.O., Malladi. R., Lelievre.S.A., Lockett. S.J., 2001. Segmentation of nuclei and cells using membrane related protein markers. *Journal of Microscopy*, Vol.201, Pt 3, pp.404-415, March 2001.

Thomas, J.G., Graham, W., 2007. WatershedCounting3D: A new method of segmenting and counting punctuate structures from confocal image data. *Blackwell Synergy - Traffic*, Volume 8 Issue 4 pp. 339-346, April 2007.

Vicent. C., Ron. K, Guillermo. S., 1997. Geodesic Active Contours. *International Journal of Computer Vision*, Vol.22 (1), pp.61-79, 1997.

Wahlby. C., Sintorn. I.M., Erlandsson. F., Borgefors. G., Bengtson. E., 2004. Combining intensity, edge, and shape information for 2D and 3D segmentation of cell nuclei in tissue sections. *Journal of Microscopy,* Vol.215, Pt 1, pp.67-76, July 2004.

Wu. H.S., Xu. R., Harpaz. N., Burstein. D., Gil. J., 2005. Segmentation of intestinal gland images with iterative region growing. *Journal of Microscopy,* Vol.220, Pt 3, pp.190-204, December 2005.

REALTIME NEOCORTICAL COLUMN VISUALIZATION

Pablo de Heras Ciechomski and Robin Mange
Visualbiotech, PSE-C EPFL, 1015 Ecublens, Switzerland
www.visualbiotech.ch
pablo@visualbiotech.ch, robin@visualbiotech.ch

Keywords: Realtime system, computer graphics, visualization, computational biology, neuroscience.

Abstract: This paper presents a method for real-time rendering of a neocortical column in the mouse brain with 10000 individually simulated neurons, as implemented in the software GabrielStudio (TM). It also presents how the same system is used to create movie sequences of scripted camera keyframes for high resolution outputs. The current system is running on an SGI Altix Prism Extreme with 16 parallel graphics cards and a shared memory of 300 GB. Gabrielstudio works as a virtual microscope for computational neuroscientists to analyze their simulations of neurons.

1 INTRODUCTION

In the field of computational neuroscience simulations of neurons arranged in circuits like the neocortex in the rat brain, are quite complex in the amount of data that is created for each simulation step. The simulation computes the electrical membrane potential of the neurons, at a detail level of each individual branch in its morphology (Carnevale and Hines, 2006). A typical neuron morphology consists of a spherical soma of 20 micro meters (see Figure 1), a tubular axon and tubular dendrites which in turn can be branched down to very fine segments of tissue and usually contribute 300 sections (Al-Kofahi et al., 2002), (Can et al., 1999), (Kuss et al., 2007). Each of these three basic morphological parts are also subpartitioned into electrical compartments, which on average are five per section depending on the length of the section. In order to analyze the fully detailed simulation at electrical compartment level on average 10000 neurons, times 300 sections, times five data points are inspected, which is 15 million data points in total per 10 millisecond simulation step. One real second of activity in the brain is quantized into steps of 10 milliseconds, so that there are 100 steps per real second of activity. Each such step can take minutes to compute even on an IBM Blue Gene (TM) super computer (BlueBrain, 2007).

Analyzing 15 million data points individually per time step is not reasonable, to simplify this, computational neuroscientists generally only have a look at the membrane potential at the soma level of the neurons. If a normal color map view is used (see Figure 2) the scientist analyzes the data where each column of data is one time step and each row is the voltage value for the soma of that neuron. In visualization terms the flat 2D view, maps data from four dimensions into two dimensions since the original neuronal data is in three physical dimensions (position) and one time dimension (the time step). Data loss is inevitable if one data point is supposed to represent on average 1500 points. One can argue that only the somas are important in neuronal research. As simulations get more complex and include dendrite and synapse details, debugging the simulation itself becomes next to impossible, if one cannot access all levels of importance (Westerhoff, 2003).

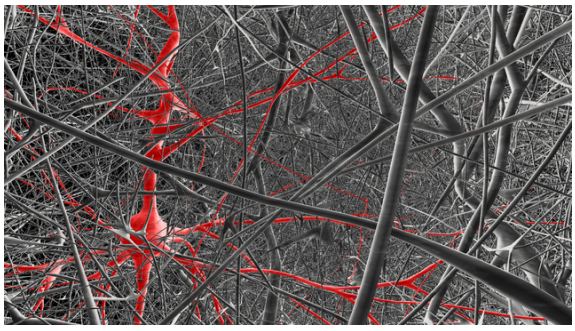

Figure 1: One neuron is highlighted as red in the column.

Using a 3D real-time view the user can explore the circuit without any simulation knowledge neces-

sary in the viewer itself. As an operator of this virtual microscope it is possible to stand in all positions and view the neocortical circuit from any angle or perspective. The amount of information is as overwhelming as before (15 million data points) but it is rendered in the positions where it belongs, so that electrical potentials for axons innerving nearby dendrites are close and visually connected. In this virtual microscope it is also possible to do virtual clamping in the full circuit enabling the user to follow and record the electrical history for a specific clamping point.

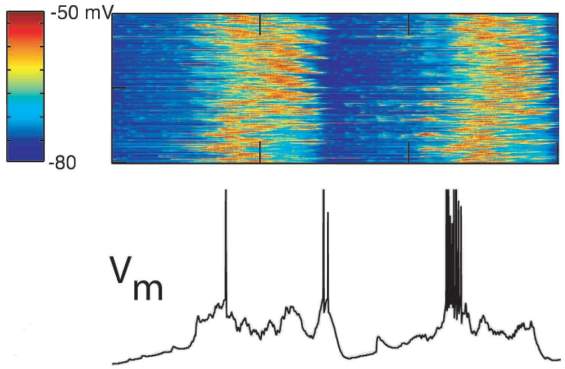

Figure 2: Each column is a time step and each row is the membrane potentials for the soma of one neuron. (Hill and Tononi, 2004).

The software library capable of rendering the neocortical column is called GabrielStudio. It is generic in terms of visualization for different areas of computational biology, and is the basis of the virtual microscope. Since this software is commercial only an older version of the software and the underlying algorithms are presented here, as the newest version is confidential. Nevertheless the authors are sharing some of the design decisions, rendering optimizations, adaptations to the SGI multi-pipe toolkit (MPK) and general interface decisions. The rendering engine is based on a target centric design where a target can be a set of neurons represented as triangle meshes, lines, segments (Melek et al., 2006), (Stoll et al., 2005) or soma billboards (Tarini et al., 2006), (Holm et al., 2005). Individual neurons can at all times be visible, invisible, colored independently and have simulation applied to them or not. The system is described in more detail in the following sections of the paper.

2 GABRIELSTUDIO

The rendering engine is based on the notion of targets where the total possible neurons to render is a set called the universe target. Each neuron has morphology which is a hierarchical description of a neuron in a directed acyclic graph manner (DAG), see Section 2.2.1. Several neurons share the same morphology where a circuit of 10 000 neurons usually contains 700 different morphologies of 100 000 or more triangles. To visuallize the column using a brute force rendering method, a total of one billion triangles per frame would have to be rendered. Given that a normal graphics card of 2007 can render 25 million triangles per second, this would take 40 seconds to render. Since the system is real-time an acceptable speed is 25 updates per second, which is 1000 times faster than one update every 40 seconds. Using the multiple pipes of an SGI Prism Extreme one can leverage this speed ten times, which gives us having to speed up the brute force method by a factor of 100. A factor of ten is always welcome. The solution proposed in this paper is the use of a regular grid, which is common in ray tracing and is a voxelization process on the triangle data.

2.1 Rendering Pipeline

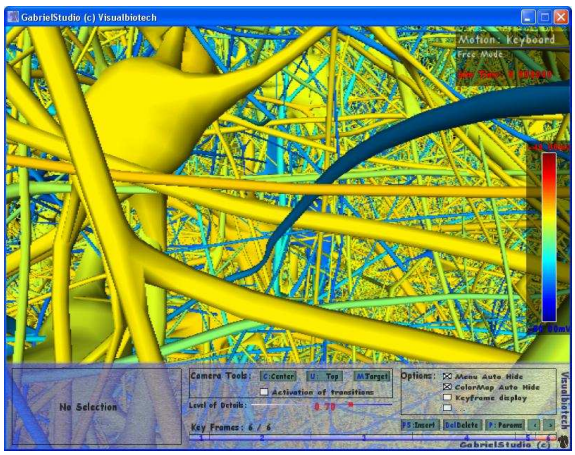

Figure 3: Action potential on neurons in the exploratory mode of GabrielStudio.

The neurons are inserted one by one, triangle by triangle, into the grid so that each grid cell contains a list of pointers to triangle data (3 vertices, uvs, normals and simulation information). Then the cells are re-allocated so that each cell contains an offset into a large continuous array of geometrical data. Depending on which neurons are part of the visible targets and level of detail (LOD), the index tables of the cell are appropriately called. Each cell has three LODs for each representation which is either triangle or mesh surface, diameter thick segments and one pixel wide lines. Two independent modes are rendered separately namely, the soma view using billboarded spheres and the synaptic view also using bill-

boards. The synapses are rendered connected to the hierarchy of the lines or branches that are visible.

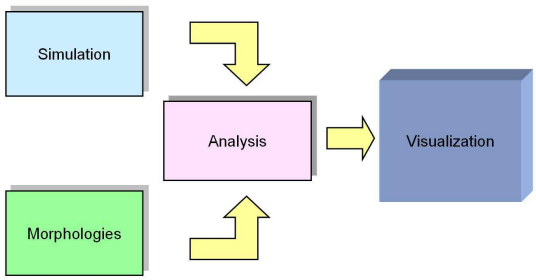

Figure 4: The visualization pipeline.

2.2 Regular Grid

The world of computer graphics consists mainly in tradeoffs between complexity and performance: level of detail (LOD) is a method offering such compromises and is explained in detail in the book (Luebke et al., 2002). Several examples of usage of this technique can also be seen in the papers (Gumhold et al., 2003) and (Schaufler and Stürzlinger, 1995) and Section 4 of this paper.

LODs are used to group branches in a priority order, going from always visible (LOD 0) to less important branches (LOD 2). Those LODs are computed when the neuron data is integrated into the regular grid with the help of a recursive algorithm which will be discussed later. This computation need to be done once, in an initialization phase at the launching of the program. During this phase, each neuron is inserted into the grid and its branches are distributed among the buffers of each LOD. Before going more in depth into the procedure, it is necessary to recall how a neuron is defined. It contains one root, from which several branches reach out, that in turn can be subbranched. They are organized in sections which allow representing the whole hierarchy of the neuron easily. More precisely, those sections indicate the linkage of each node going from the root to the extremities.

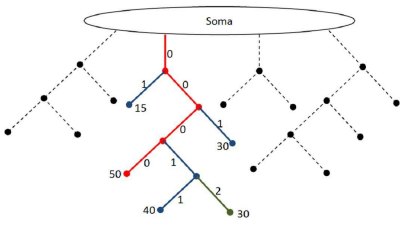

Figure 5: Neuron morphology branching numbering. Notice how at each branching only one section keeps the father number.

2.2.1 Insertion Into Lods

The insertion into LOD buffers is done according to a certain branch priority. The branching computation is done for each neuron morphology independently. It is made by going through each existing branch of a neuron, using the corresponding section map, and then attributing an index to each segment corresponding to the actual priority of its branch. To define this priority, a recursive algorithm is used, which looks at the depth of each branching and gives higher priorities to the longer ones. For a better understanding of this, it is possible to represent this scheme as a tree, where the nodes represent the splitting points between two branches taking as value the actual distance from the root (the neuron soma). Assuming the aim of the algorithm is to compute the sorting of one of the branches starting from the root; the path with the highest priority is going from the root to the extremity children with the largest distance; denoted as the longest branch of the tree (see Figure 5). Once this main branch is known, it starts from the root and goes through all the nodes of the tree. At intersection *i* (node *i*) it keeps the current priority for the longest branch of the sub-tree with node *i* as root and the other branch gets this priority increased by 1. Like that we will have branching index from 0 to a maximum of 255 (fixed limit). From those indices we can enter each vertices inside the corresponding LOD array respecting some ranges defined by the user (e.g. Lod-0: 0,1 / Lod-1: 2,3 / Lod-2: 4,...,255). Then each branch of a neuron will be rendered or not by comparing its LOD with the current LOD of the cell. In a similar manner synapses also need to be rendered conditionally to the LOD level.

2.2.2 Usage of the Lods

Employing a LOD system, allows splitting the rendering into several levels of detail yielding better performance. Those levels are defined by cells accordingly to the distance to the camera position, such that the closer cell to the viewer the better its definition is.

2.2.3 Update Function

Another particularity regarding the implementation of the regular grid is the use of an update target function which allows to have a per branch visibility capacity and a per cell representation mode. Each time a neuron state is changed (visibility or representation), the data is checked once and the right indices of the visible neurons are entered into the grid. The line buffer and the mesh buffer are used depending on the current cell representation. Since drawing is done using

arrays, it allows having the correct indices always directly for the rendering phase reducing the real-time computational expense.

2.3 Stylized Rendering

The implementation seen in the last section allows the use of different data representations. This is a necessary functionality since sometimes it is preferable to have a more simple representation using less details for a better global view. This is possible with the use of billboarding techniques which allows rendering neurons as spheres (using quadriliterals always in front of the camera, see Figure 6) and more somas are visible since no extra branches are occluding each other.

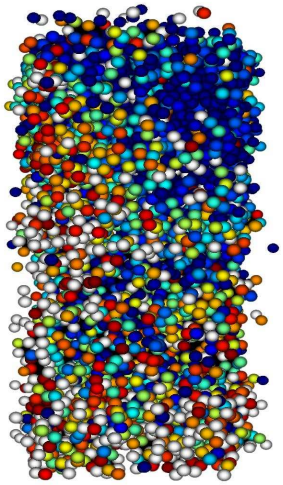

Figure 6: GabrielStudio also renders using billboards of somas.

2.4 User Interface

In order to interact dynamically with the rendering, a user interface was created. It offers several possibilities from camera centering to key frame editing. A lot of useful options are given to the user and allows having a good feeling about what is happening on the screen. There is an indication about the current selection, neuron or synapse and the simulation color mapping allowing to distinguish the current electrical value of each entity as well as the number of key frames kept for the movie creation, as depicted in Figure 9.

2.5 Scalable Rendering Architecture

The major difference between rendering on a single graphics card architecture available on most PCs and a parallel graphics pipeline, as the SGI Prism, is that several graphics contexts need to be tracked and updated simultaneously. Since the library uses GLEW to handle OpenGL extensions, it also keeps a separate MX GLEW context per graphics card. However recompiling such a library including a multi-pipe version of a helper library is not sufficient. This comes as the result that each function in the rendering engine that uses shaders, textures, vertex buffer objects, display lists or any other context specific data has a special structure sent to it containing the necessary data for that context. Each graphics card is assigned this context upon entry into that threads rendering loop.

3 CREATING MOVIES

Science needs to reach out and touch more interested minds through marketing, which is possible to do through the movie creation pipeline of GabrielStudio. Using such a software tool the user has the possibility to navigate through the scene, using the virtual microscope view and sample the interesting locations. A set of sampled view points or camera key frames are interpolated and rendered using a non-interactive mode for high resolution and detail as shown in Figure 7. Standard digital movie production pipelines are used for editing. In the off-line mode it is also possible to output stereo images for passive stereo outputs as displayed in Figure 1. These movies are shown to various visitors of our clients projects to give them a better picture of what neuroscience entails and reveal some of its mysteries. Movies are also shown at conferences for scientific discourses and presentations. It is also possible to do individual snapshots in high resolution for posters that require greater details.

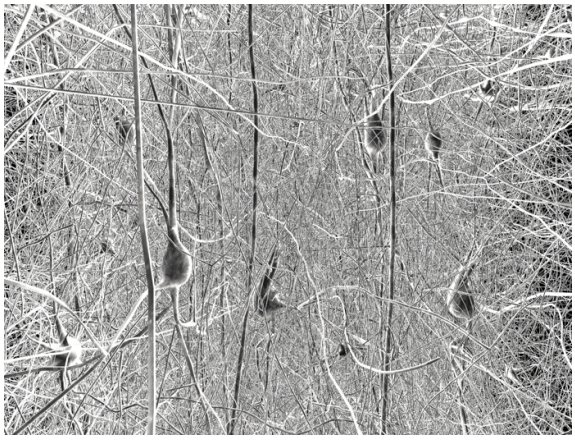

Figure 7: From a stereo flythrough sequence of the dendritic forest. The effect of having to dodge parts of neurons coming out of the screen is quite dramatic.

4 RESULTS

Rendering the neurons on a SGI Prism Extreme with 16 graphics cards, gives acceptable update rates of 15 frames per second with 5000 neurons in view. The viewer can observe the neurons from a distance or a closer range, while having the details preserved thanks to the employed LOD system.

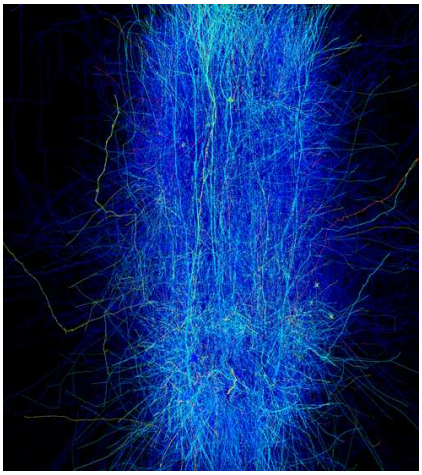

Figure 8: Simulation mapping applied.

When using the regular grid one must cope with some additional requirements. A typical example is the case when the viewer is far away from the column, such that the cells being just in front of the camera are rendered with a high level of detail i.e. all LODs are displayed. Those being near to the center of the column are represented using a lower definition, and some of the branches belonging to the LOD-2 are displayed in the front cells and not in the back ones. Since the branches appear not to be linked, the user gets a strange impression about the scene. One possible solution to such cases is to check for each branch whether one of its parts is drawn; if this is the case, this branch is rendered in each visible cell. In order to achieve such an implementation, a regular grid should be somehow replaced, since using the conditional tests increases the computational cost. Otherwise utilizing a regular grid leads to satisfying results even when employing the update target function since it is done only once per update and not per frame, at the rate of user interactions.

5 CONCLUSIONS

In this paper the software tool for real-time visualization of neurons has been presented. Acceptable rendering speeds are attained on large shared memory machines, where geometry duplication is not a limiting factor due to 300 GB memory banks. However, this is not useful on ordinary PCs, which is the next challenge for the authors. Using a regular grid gives a memory bound problem that is comfortable to render on a parallel rendering architecture. The movie mode of the described software GabrielStudio allows movie creation with ease. Finally the possibility of interacting and exploring the data in real-time, offers new perspectives to neuroscientists to observe their own simulations. Besides being a powerful tool for neurological process monitoring, the proposed software has additional applications for marketing purposes.

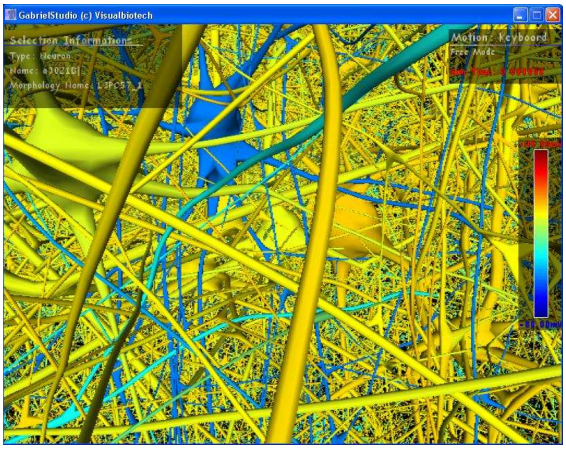

Figure 9: Selecting neurons in GabrielStudio.

ACKNOWLEDGEMENTS

Professor Henry Markram of the Blue Brain Project. Blue Brain Project for data. Sebastien Lasserre for the morphologies built in Maya.

REFERENCES

Al-Kofahi, K. A., Lasek, S., Szarowski, D. H., Pace, C. J., Nagy, G., Turner, J. N., and Roysam, B. (2002). Rapid automated three-dimensional tracing of neurons from confocal image stacks. *IEEE Transactions on Information Technology in Biomedicine*, 6(2):171–187.

BlueBrain (2007). A comoputational neuroscience project at ecole polytechnique federal de lausanne (epfl), lausanne, switzerland.

Can, A., Turner, J., Tanenbaum, H., and Roysam, B. (1999). Rapid automated tracing and feature extraction from live high-resolution retinal fundus images using direct exploratory algorithms.

Carnevale, N. T. and Hines, M. L. (2006). *The NEURON Book*. Cambridge University Press, New York, NY, USA.

Gumhold, S., Borodin, P., and Klein, R. (2003). Intersection free simplification. *International Journal of Shape Modeling (IJSM)*, 9(2):155–176.

Hill, S. L. and Tononi, G. (2004). Modeling sleep and wakefulness in the thalamocortical system. *Journal of Neurophysiology*, pages 1671–1698.

Holm, A., Offen, L., and Fellner, D. (2005). Biobrowser a framework for fast protein visualization. In *EUROVIS 2005 / IEEE VGTC Symposium on Visualization 2005*, pages 287–294.

Kuss, A., Hege, H.-C., Krofczik, S., and Borner, J. (2007). Pipeline for the creation of surface-based averaged brain atlases. accepted for publication.

Luebke, D., Watson, B., Cohen, J. D., Reddy, M., and Varshney, A. (2002). *Level of Detail for 3D Graphics*. Elsevier Science Inc., New York, NY, USA.

Melek, Z., Mayerich, D., Yuksel, C., and Keyser, J. (2006). Visualization of fibrous and thread-like data. *IEEE Transactions on Visualization and Computer Graphics*, 12(5):1165–1172.

Schaufler, G. and Stürzlinger, W. (1995). Generating multiple levels of detail from polygonal geometry models. In Göbel, M., editor, *Virtual Environments '95 (Eurographics Workshop)*, pages 33–41. Springer-Verlag: Heidelberg, Germany.

Stoll, C., Gumhold, S., and Seidel, H.-P. (2005). Visualization with stylized line primitives. In *IEEE Visualization*, page 88.

Tarini, M., Cignoni, P., and Montani, C. (2006). Ambient occlusion and edge cueing to enhance real time molecular visualization. *IEEE Transaction on Visualization and Computer Graphics*, 12(6).

Westerhoff, M. (2003). Efficient visualization and reconstruction of 3d geometric models from neurobiological confocal microscope scans. *Phd Thesis*.

MICROGLIA MODELLING AND ANALYSIS USING L-SYSTEMS GRAMMAR

Herbert F. Jelinek and Audrey Karperien
School of Community Health, Charles Sturt University, Albury, Australia
hjelinek@csu.edu.au, akarpe@telus.net

Keywords: Microglia, L-systems grammar, modelling, pathology.

Abstract: Medical image analysis requires in the first instance information on the extent of normal variation in a biological system in order to identify pathological changes. MicroMod is an L-systems based software package available through the World Wide Web that allows modelling of complex branching structures such as neurons and glia using deterministic or probabilistic algorithms. In addition, MicroMod includes software for assessing complex structures using methods such as fractal and lacunarity analysis. We demonstrated through fractal analysis of simulated microglia that MicroMod can be used for modelling and measuring different stages of microglial activation. The fractal dimensions of microglia visualised using histochemical techniques showed good agreement with our models made using MicroMod, and changes in complexity and heterogeneity as seen during activation and response to pathology were well emulated by modifying a few essential parameters (sub to parent branch length, sub to parent branch diameter, and sub branch number). These results indicate that MicroMod provides a useful adjunct to neuroscience research into understanding complex changes in structure associated with normal function and disease processes.

1 INTRODUCTION

The modelling programme described and discussed here was inspired from research into the morphology of a type of cell called *microglia*. These small cells are a critical component of the brain's immune system, and have been called the brain's "first line of defence" for the critical roles they play in mediating effects of injury and disease in the central nervous system. (Kreutzberg 1995)

The feature of microglia particularly relevant to this paper is their dynamic morphology. To explain, microglia normally reside in the brain in a highly branched resting morphology. In this form, microglial cell bodies are small and elongated or rounded, surrounded by multiple relatively thin extensions known as microglial processes that themselves branch to finer and finer levels of ramification, extending around neurons and other cells deep into the surrounding neural tissue, as illustrated in Figure 1.

Resting microglia are thus perfectly postured to continually sample their environment and respond to the earliest signs of insult or injury in the surrounding structures and milieu of the central nervous system, but their role goes beyond that of patrolling sentinel. If they detect problems, microglia can change dramatically from their

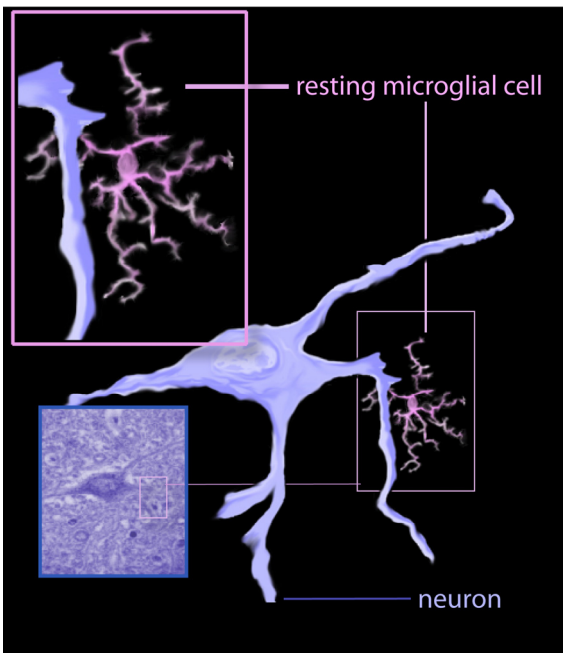

Figure 1: Resting microglia are highly branched immune system cells found in the brain.

highly ramified, resting sensor morphology to an unbranched, rounded to amoeboid form that is increasingly motile and phagocytic (Soltys, Orzylowska-Sliwinska et al. 2005). As illustrated in Figure 2, this change occurs along a continuum of subtle to obvious differences in morphology.

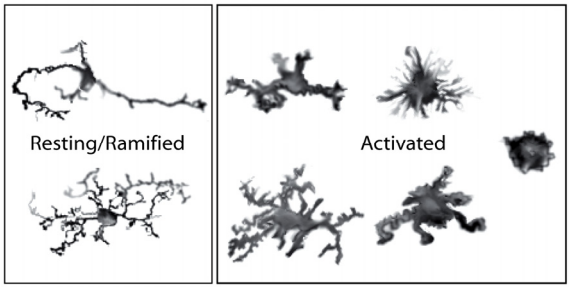

Figure 2: Typical microglial morphologies. Processes retract and the soma becomes rounder and expands as microglia become increasingly activated to respond to pathological changes.

The morphology a microglial cell might be found to adopt reflects variables such as the cell's position, surroundings, and motion, but also generally corresponds to differences in functional capacity and activity. Indeed, the relative amounts of microglial cells adopting certain morphological configurations vary in different diseases and in different stages of the progression of individual disease states (e.g., the overall profile of microglial morphology typical in schizophrenia can be differentiated from that in Alzheimer's disease) (Jelinek, Karperien et al. 2004). It is therefore essential to obtain a good understanding of even subtle changes in microglial form along the continuum of morphological variety, and to be able to relate these changes to cell characteristics (Cornforth, Jelinek et al. 2002).

1.1 The MicroMod Modelling Software

MicroModV6.0 is biological cell and fractal structure modelling software written in Java by one of the authors (AK), using the NetBeans IDE 3.5 on the Java 2 Platform v1.4.2 (Jelinek, Karperien et al. 2002). The programme has been tested on WindowsXP Pro, Windows2000, Windows98, and SUSE Linux. It is available as a stand-alone Java application from Charles Sturt University as MModLE.jar (source code is available on request). MicroMod contains 28,456 lines of code, 19,313 non-comment lines, and 7,818 comment lines of code. Features available in MicroMod are shown in Table 1.

In addition to the models described in the rest of this paper, MicroMod software renders for benchmarking and analysis statistical or deterministic, skinny or fat fractals, including quadric, Koch, Menger, and Sierpinski fractals; multifractals such as various Henon Maps; other iterated fractal structures (e.g., ferns); and diffusion limited aggregates.

Table 1: MicroMod Features.

MicroModsrc	Main package
MicroModsrc.GUI	Graphic user interface
MicroModsrc.Help	User's guide in html for swing browser
MicroModsrc.MakeStructure	Methods for generating random and deterministic fractals as well as branching structures for cell modelling
MicroModsrc.Utils	Utilities

Structures can be viewed on a display screen or saved to a hard drive as either images (.jpg or .png format) or MicroMod model files (.mod format). All models can be rendered and saved in coloured, shaded, gray-scale, and binary formats. Structures are generated from built-in configurations or loadable .mod files (some provided with MicroMod), or from parameters set by the user. Configurable options include structural parameters and various rendering options such as background colour or whether to view a structure grow or not. All models can be modified, saved, and reloaded, and can be used to generate single images or sets of multiple images.

MicroMod also includes a fractal analysis function. Structures can be assessed on the screen as they are generated or in batches of images from the user's hard drive. The analysis is delivered on screen and in detail in a text file that can be loaded in a spread sheet. The fractal analysis algorithms of MicroMod are also available in the *FracLac* software, a plug-in for *ImageJ* freely available from the US National Institutes of Health (Karperien 2007).

2 MODELLING WITH MICROMOD

To simulate biological structures such as microglia, MicroMod employs L-systems principles. As

illustrated in Figure 3, a variety of structures at different levels of complexity can be generated using L-systems.

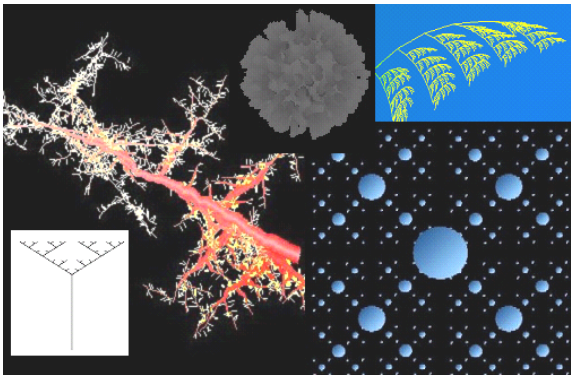

Figure 3: Examples of structures modelled in MicroMod using L-systems principles.

The fundamental algorithm used for modelling microglia is based on MicroMod's built-in branching model. The algorithm generates sets of symbols to be rendered on the computer screen. For modelling microglia, one set specifies features for one microglial process, where each point within each set specifies the size, shape, colour, and location of a structural element of the process, and rules set by the user are applied recursively to evolve each original set into a more complex structure.

To elaborate, the simplest branching model is a set of points representing straight lines, and the next level of complexity is a set with one level of sub-branches (Figure 4). Such a model can be altered by changing various parameters including the rate of acquiring branching points and the number of branches that sprout at each branching point; the ratio of the length and diameter of daughter branches to the length of the parent; and the taper for each branch.

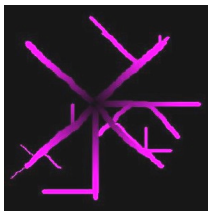

Figure 4: Radial model generated by specifying a minimum number of parameters.

Gross structural features such as the area and general shape of the central soma and the number, length, and diameter of primary branches can also be changed. In addition, directional features such as the probability of a branch continuing in a direction (related to the tortuousness of a process) and the angle of branching can be set. Moreover, to further explore variation within a cell or compare cells, the user can modify individual processes of a cell separately.

Furthermore, several of the parameters describing a process, such as branching rate and tortuousity, can be applied as probabilities rather than fixed values (Figure 5). Figure 5A, for instance, illustrates a simple radial model generated using a probability (rather than a deterministic value) for the number of branches along each primary branch, whereas Figure 5B shows a simple radial model rendered with a deterministic branching rate but probabilistic tortuousity features.

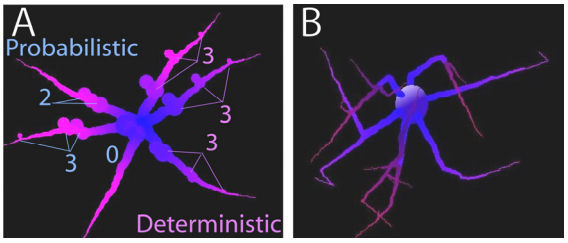

Figure 5: Simple branching models. Within each model, all branches are statistically identical. 5A. Random Variation in Branching Frequency. Nodes show locations for daughter branches on primary branches. All nodes were sprouted at one statistically identical rate; however, nodes on branches extending right were generated deterministically and on branches extending left were generated probabilistically. 5B. Random Variation in Branching Angle and Tortuousity. Daughter branches were sprouted at one deterministic rate on all primary branches, but their rate and angle of change in direction were determined probabilistically.

The significance of having probabilistic parameters available for modelling microglia is that the opportunity exists to generate each cell process as a statistically identical but unique structure. The user can, accordingly, explore overall features of a class of structures by generating groups of statistically identical but unique images from a single set of parameters (Figure 6).

Figure 6: Statistically identical but unique models of resting microglia generated using one set of parameters.

As was noted in the introduction, microglia adopt a wide variety of conformations when they respond to events in nervous tissue. For modelling microglia and other biological cells, MicroMod has several models in addition to the radial model just discussed. Examples of the MicroMod outputs of the Y-model, the bushy and narrow models, and the B-model are shown in Figure 7. The Y-model (top of Figure 7) provides large spherical to amorphous structures with short tapered and unbranched projections. The bushy model and the narrow model are similar, but allow branch diameters and the degree of sprouting to be set. These models specify how tortuous images are using the single angle functions in MicroMod. The B-Model includes options for multiple, bifurcating branches as well as for setting branch angle, length, tortuosity and twist. The number of branches and number of sprouts can be modified using the menus.

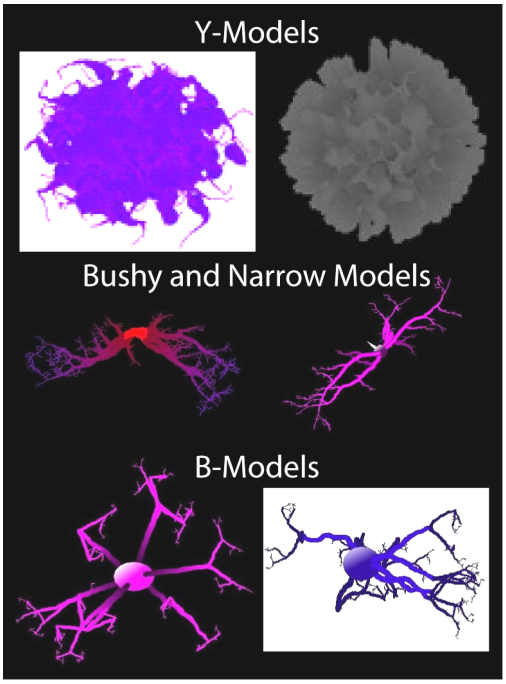

Figure 7: Modelling options for branched cell structures available in MicroMod.

3 ANALYSING MICROGLIAL ACTIVATION USING SIMULATED MICROGLIA

Populations of cells were modelled from real microglia, based on measurements such as the length and number of branches and the ratios of daughter to parent branch length and diameter. To most closely emulate real, dynamic microglia in their natural environment, cells were generated using probabilistic values. Using box-counting fractal analysis we compared the simulated cells to the real after converting digital images to binary in order to assess the complexity of the cell contour. As indicated in previous research, there was close agreement between simulated and real cells (Figure 8) on the box counting dimension (D_B). (Smith, Marks et al. 1989; Jelinek, Karperien et al. 2002)

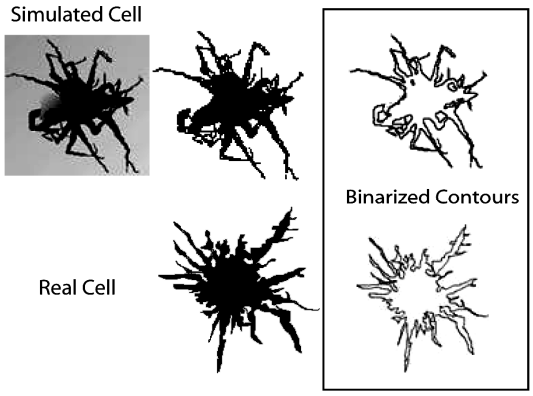

Figure 8: Real compared to simulated microglia. The real cell had a fractal dimension of 1.423 compared to the simulated of 1.425.

3.1 Scaling Features

To assess the sensitivity of MicroMod for modelling subtle morphological changes associated with different levels of microglial activation, we manipulated several features of the models and assessed both complexity as measured by the D_B and heterogeneity (lacunarity or Λ). Manipulating the size and shape of the modelled soma had essentially no effect on the D_B, but a slight effect on Λ, where in general models with larger and more elongated somata had lower values for Λ. Both the D_B and Λ were affected by changing the number of primary branches, but the effects were not consistent. Changing scaling features, in contrast, had several noteworthy effects. Changes were made in a manner consistent with fractal changes, as the results are predictable and therefore useful in judging the utility of the software.

Figure 9 shows that the D_B and Λ changed when the length of sub-branches relative to the parent branch was changed but the number of sprouts remained the same. Similarly manipulating the scale of sub to parent branch diameter and the number of new branches per branch affected the D_B.

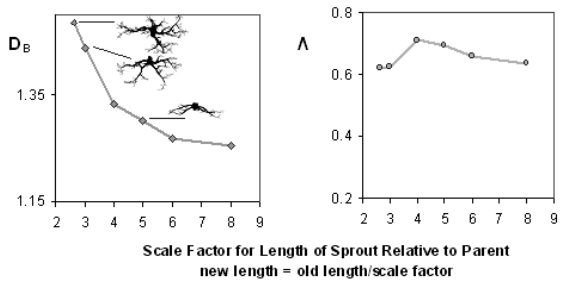

Figure 9: Effect of varying cell features on fractal dimension and lacunarity.

Changing the scaling of sub-branch diameter had no effect on either the D_B or Λ for models with narrow branches, owing to the finite limit on the smallest possible diameter of a branch. For models with larger starting diameters, however, the ratio of sub-branch to parent diameter affected the D_B. The D_B and Λ were strongly positively correlated for models with wider branches, but not as strongly for models having narrower branches. The D_B mainly decreased as the length of primary processes decreased, as when microglia withdraw their processes in response to noxious stimuli in their environment, for example. Although Λ decreased overall with decreasing primary process length, it initially increased for smaller branch diameters (i.e., models resembling resting more than activated cells).

Cells differing only in branch diameter were modelled to emulate process swelling in isolation from other changes—i.e., only the diameter of primary branches (measured where they leave the soma then allowed to taper according to a fixed rate) was manipulated. Both the D_B and Λ were affected by changing this feature, but there were some differences in the effects. As long as branch diameter remained relatively narrow compared to soma span, the D_B rose slightly as branch diameter increased. As branch diameter continued to increase, however, owing to crowding of "swollen" processes, some detail disappeared from the final binary patterns extracted from the images. In contrast, Λ decreased without increasing as branch diameter increased, and the effect was more noticeable at smaller diameters than it was for the D_B. In addition, models with greater tortuousity had higher D_B and lower Λ values.

4 CONCLUSIONS

Previous research has shown that microglial morphology can be modelled with high fidelity using MicroMod. In addition, recent investigations have revealed that the D_B and Λ can be used to measure the types of graded changes in microglial morphology typically associated with microglial activation. (Jelinek, Karperien et al. 2002) The work presented here goes a step further in describing how the progression from ramified to activated (i.e., nonpathological to pathological) in microglia can be accurately modelled and cellular complexity assessed by progressively changing a few essential parameters.

It is important to note that the modelling of microglial activation described here is deliberately subject to random variation. For perfect patterns extracted from perfect theoretical models, the D_B measures fundamental complexity and Λ measures heterogeneity. From a practical perspective applied to real cells, though, they will measure at once a composite of several features. Because of the considerable morphological variation attributable to not only activation but also the space microglia occupy and the orientation they assume at any point in time, variation is predictable when finding D_Bs even for cells in equivalent activation states having essentially the same branching ratios. As was shown here, despite that a microglial model's inherent complexity is specified by known recursively applied rules, an extracted pattern may not necessarily convey this fundamental pattern's original information fully and without distortion. In real cells, the underlying mechanisms of morphological transformation are also not necessarily conveyed in values extracted from real contexts. But microglia are biological structures we hope to understand and assess ultimately in their natural environs. Analyses that can be used in this way have practical advantages over assessments based on uncomplicated theoretical models, and modelling, as was shown here, helps bridge our knowledge of practical influences.

In conclusion, the work we report here may have important implications for understanding the events of microglial activation associated with different states of health and disease. Simulated cells, readily available in large numbers and extremely manipulable, increase the opportunities to objectively study morphological changes and random variation in microglia. MicroMod, thus, presents a useful adjunct to neuroscience research into understanding complex changes in structure associated with normal function and disease processes.

REFERENCES

Cornforth, D., H. F. Jelinek, et al. (2002). Fractop: a tool for automated biological image classification. 6th AI Australasia-Japan Joint Workshop, Australian National University, Canberra.

Jelinek, H. F., A. Karperien, et al. (2004). Differentiating grades of microglia activation with fractal analysis. Proceedings of the Complex Systems Conference, Cairns, Australia, IOS Press.

Jelinek, H. F., A. Karperien, et al. (2002). MicroMod - an L-systems approach to neuron modelling. 6th AI Australasia-Japan Joint Workshop, Australian National University, Canberra.

Karperien, A. (2007). FracLac for ImageJ. FracLac for ImageJ 2000-2007. Bethesda, Maryland, Research Services Branch, National Institutes of Health: Morphological digital image analysis software for fractal, multifractal, lacunarity, and other morphometrics.

Kreutzberg, G. W. (1995). "Microglia, the first line of defence in brain pathologies." Arzneimittelforschung 45(3A): 357-60.

Smith, T. G., W. B. Marks, et al. (1989). "A fractal analysis of cell images." Journal of Neuroscience Methods 27: 173-180.

Soltys, Z., O. Orzylowska-Sliwinska, et al. (2005). "Quantitative morphological study of microglia cells in the ischaemic rat brain using principle component analysis." Journal of Neuroscience Methods.

FINDING APPROXIMATE LANGUAGE PATTERNS

Samuel W. K. Chan
Dept. of Decision Sciences, The Chinese University of Hong Kong, Hong Kong
swkchan@cuhk.edu.hk

Keywords: Bio-inspired language parsing, semantic labelling.

Abstract: A two-phase annotation method for semantic labeling based on the edit distance is proposed. This dynamic programming approach stresses on a non-exact string matching technique that takes full advantage of the underlying grammatical structure of 65,000 parse trees in a Treebank. It is based on the assumption that human language understanding is relevant to concrete past language experiences rather than any abstract linguistic rules. This shallow technique is inspired by the research in the area of bio-molecular sequences analysis which advocates high sequence similarity usually implies significant function or structural similarity. Experimental results for recognizing various labels in 10,000 sentences are used to justify its significances.

1 INTRODUCTION

Automatic information extraction has received a great deal of attention in the latest development of information retrieval. While a plethora of issues relating to questions of accuracy and efficiency have been thoroughly discussed, the problem of extracting meaning from natural language has scarcely been addressed. When the size and quantity of documents available on the Internet are considered, the demand for a highly efficient system that identifies the semantic meaning is clear. Case frame is one of the most important structures that are used to represent the meaning of sentences (Fillmore, 1968). One could consider a case frame to be a special, or distinguishing, form of knowledge structure about sentences. Although several criteria for recognizing case frames in sentences have been considered in the past, none of the criteria serves as a completely adequate decision procedure. Most of the studies in natural language processing (NLP) do not provide any hints on how to map input sentences into case frames automatically. As a result, both the efficiency and robustness of the techniques used in information extraction is highly in doubt when they are applied to real world applications.

The objective of this research is twofold. First, a shallow but effective sentence chunking process is developed. The process is to extract all the phrases from the input sentences, without being bogged down into deep semantic parsing and understanding. Second, a novel semantic labeling technique that is based on the syntactic and semantic tags of the latest Treebank is being constructed (CKIP, 2004). One of our primary goals in this research is to design a shallow but robust mechanism which can annotate sentences using a set of semantic labels. While the classical syntactic and semantic analysis is extremely difficult, if not impossible, to systematize the current research in NLP, our approach does not require any deep linguistic analysis to be formalized. The annotation will provide piecemeal the underlying semantic labels of the sentence. The organization of the paper is as follows. The related work in semantic labeling and sentence chunking are first described in Section 2. In this research, each word in sentences has two attributes, i.e. part-of-speech (POS) and semantic classes (SC). Any input sentence is first transformed into a feature-enhanced string. A two-phase feature-enhanced string matching algorithm which is based on the edit distance is devised. Section 3 shows how the algorithm can be applied in the semantic labeling using 65,000 parse trees in a Treebank. The system has already been implemented using Java language. In order to demonstrate the capability of our system, an experiment with 10,000 sentences is conducted. A detailed evaluation is explained in Section 4 followed by a conclusion.

2 RELATED WORK

Following the framework of case grammar which is originally proposed by Fillmore in 1968, it has been accepted that every nominal constituent in every language bears a single syntactic–semantic case relation (Jackendoff, 1983; Dowty, 1991). In earlier systems, Somers describes a prototype computer program that attempts to map surface strings of English onto a formalism representing one level of a deep structure (Somers, 1982). Weischedel *et al*. (1993) predict the intended interpretation of an utterance when more than one interpretation satisfies all known syntactic and semantic constraints, and ascertain its semantic labels. It is on the basis that semantic features inherent in the main verb of a sentence can be used to infer the potential semantic labels of the sentence. Utsuro *et al*. (1993) describe a method for acquiring surface semantic labels of Japanese verbs from bilingual corpora. They make use of translation examples in two distinct languages that have quite different syntactic structures and word meanings. Similarly, Kurohashi and Nagao (1994) have developed a powerful parser for Japanese sentences based on the case frames encoded in a verb dictionary. The dictionary contains some typical example sentences for each case frame. The dictionary then tags the proper case frame for an input sentence based on the sentence similarities.

Any high level language understanding process, such as semantic labeling, must involve chunking sentences into segments. Motivated by the psycholinguistic evidence which demonstrates that intonation changes or pauses would affect the language understanding processes in humans (Gee & Grosjean, 1983), Abney (1991) proposes the concept of text chunking as a first step in the full parsing. A typical chunk of a text is defined as consisting of a single content word surrounded by a constellation of function words, matching a fixed template. Church also uses a simple model for finding base non-recursive NPs in sequence of POS tags (Church, 1988). Turning sentence chunking into a bracketing problem, Church calculates the probability of inserting both the open and close brackets between POS tags. Each chunking alternative is ranked and the best alternative is selected. Using transformation-based learning with rule-template referring to neighboring words, POS tags and chunk tags, Ramshaw & Marcus (1995) identify essentially the initial portions of non-recursive noun phrases up to the head, including determiners. These chunks are extracted from the Treebank parses, by selecting NPs that contain no nested NPs. While the above approaches have been proposed to recognize common subsequences and to produce some forms of chunked representation of an input sentence, the recognized structures do not include any recursively embedded NPs. As the result, the resultant fragments bear little resemblance to the kind of phrase structures that normally appear in our languages.

While it may be too computationally demanding to have a full syntactic and semantic analysis of every sentence in every text, Sima'an (2000) presents a Tree-gram model which integrates bilexical dependencies, and conditions its substitutions based on the structural relations of the trees that are involved. The Tree-gram model is a typical example of data-oriented parsing (DOP) advocated by Bod et al. (2003). The basic ideas of the Tree-gram model are to (i) take a corpus of utterances annotated with labeled trees; (ii) decompose every corpus tree into the bag of all its subtrees; (iii) treat the union of all these subtree bags as a stochastic tree substitution grammar, where the substitution probability of each subtree is estimated as the relative frequency of this subtree among the subtrees with the same root label. Inspired by the Tree-gram model, in this research, we propose a mechanism in shallow semantic labeling as well as sentence chunking by matching any input sentence with the trees in a Treebank through a two-phase feature-enhanced string matching. Different from the stochastic tree substitution grammar proposed in the Tree-gram model, our approach, characterized by an optimization technique, looks for a transformation with a minimum cost, or called edit distance. While the concept of edit distance is commonly found in the conventional pattern matching techniques (Gusfield, 1997; Tsay & Tsai, 1989), we take a step further in applying the technique in shallow semantic labeling. The detailed discussion of the algorithm is shown as follows.

3 TWO-PHASE FEATURE-ENHANCED STRING MATCHING ALGORITHM

Our labeling is defined as a two-phase feature-enhanced string matching using the edit operations. For every input sentence, a coarse-grained syntactic matching is conducted in our first phase of matching. The matching relies on a set of coarse-grained but global part-of-speech (POS) tags. The major objective of this phase is to shortlist all the potential trees among 65,000 parse trees in the CKIP Treebank, which are relevant to the input sentence,

without getting bogged down into computational complexity with other linguistic details. The second phase of the matching is followed to compute the dissimilarity measure between the input sentence and every short-listed candidate that is identified in the first phase. Detailed POS and semantic class (SC) tags will be employed. As a result, a candidate tree which has the minimum dissimilarity with the input sentence will be identified. The underlying semantic labels and phrases of the candidate tree are used to determine the shallow language patterns of the input sentence. The details of the two-phase matching are explained in the following.

3.1 Coarse-Grained Syntactic Matching

In the first phase of matching, each word is represented by its corresponding POS. Let S be an input sentence and the T be a tree in a Treebank, s_i and t_j be two tokens in S and T with attribute POS_i and POS_j respectively. We define the cost function for the *change* operation in the traditional edit operations (Wagner & Fischer, 1974) $s_i \rightarrow t_j$ to be

$$R(s_i \rightarrow t_j) = u(POS_i, POS_j) \quad (1)$$

where $u(POS_i, POS_j)$ defines the cost due to the difference between the POS of the two tokens. The POS tags from the Chinese Knowledge Information Processing Group (CKIP) of Academia Sinica are employed (Chen *et al*., 1996). The tags are subdivided into 46 major POS classes which are further refined into more than 150 subtypes. However, in this coarse-grained matching, only the major POS classes will be considered. To figure out the cost function $u(\cdot,\cdot)$ in the coarse-grained matching, all the major POS tags are organized into a hierarchical structure with an associated hard-coded cost function. Figure 1 shows the structure of notional words and describes the relative distances between the adjectives (`A`), verbs (`V`), status-verbs (`VH`), measure-words (`Nf`), nouns (`N`), position-words (`Ng`), time-words (`Nd`) and place-words (`Nc`). All notional words have definite meanings in the language. The cost function is based on their interchangeability, the degree of flexibility in placement in the syntax, and the similarity of their acceptable modifiers. For example, Chinese verbs and adjectives share a lot of common features syntactically, i.e. both can be predicates or modified by adverbs and the word, *not*. All these features fail to appear in nouns. The abbreviations in bracket indicate the original POS tags marked by the CKIP. The corresponding tree structure of the XML is shown in Figure 2.

```
<Head toll="5">
  <NodeB toll="2">
    <NodeC toll="2">
      <Adjective toll="5"/>
      <Verb toll="5"/>
    </NodeC>
    <Status-Verb toll="7"/>
  </NodeB>
  <NodeD toll="2">
    <Measure-Word toll="7"/>
    <NodeE toll="2">
      <Noun toll="5"/>
      <NodeF toll="2">
        <Position-word toll="3"/>
        <NodeG toll="1">
          <Time-word toll="2"/>
          <Place-word toll="2"/>
        ...
</Head>
```

Figure 1: XML illustrating the relative distances between 8 different types of POS.

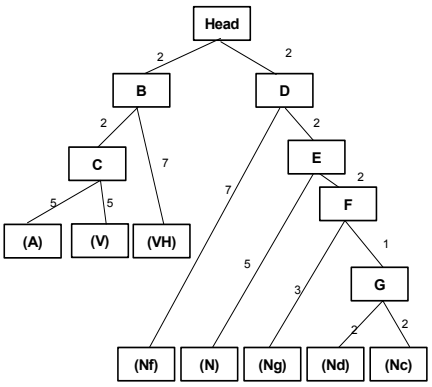

Figure 2: Corresponding tree structure of the XML shown in Figure1.

The cost function $u(\cdot,\cdot)$ reflects the difference based on the tag `toll` encoded in the XML as shown in Figure 1. The function also indicates the degree of alignment between the syntactic structure of the input sentence and the trees in the Treebank. Although two feature-enhanced strings with the same POS sequence do not imply they will share the same syntactic structure, this coarse-grained syntactic matching shortlists the potential trees by imposing a necessary, even not sufficient, constraint on its syntactic structure and limits the potential search space in the subsequent stage of semantic matching.

3.2 Computation of Semantic Dissimilarity

What this second phase matching basically does is to make a detailed comparison between the input sentence and the short-listed trees in its earlier stage. In this phase, each Chinese token has two attributes, i.e. a detailed part-of-speech (*POS*) and semantic class (*SC*). Similar to the approach in Section 3.1, we define the cost function for the *change* operation $s_i \rightarrow t_j$ to be

$$R(s_i \rightarrow t_j) = f\left(u(POS_i, POS_j), v(SC_i, SC_j)\right) \qquad (2)$$

where the function f is the dissimilarity function relied on two major components. The first component $u(POS_i, POS_j)$ defines the partial cost due to the difference between the detailed POS of the words. The detailed POS tags are organized in XML format, similar to the approach demonstrated in Figure 1. Figure 3 shows the further breakdown of the nouns (`Na`) which is divided into in-collective (`Nae`) and collective (`Na1`) nouns. The collective nouns are then subdivided into in-collective concrete uncountable nouns (`Naa`), in-collective concrete countable nouns (`Nab`), in-collective abstract countable nouns (`Nac`), in-collective abstract uncountable nouns (`Nad`). The figure associated with the arcs in the Figure 3 illustrates the cost function.

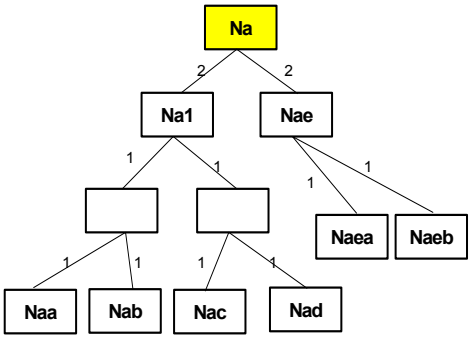

Figure 3: Tree structure of Nouns (`Na`) based on the CKIP Academia Sinica.

The second term in Eqn. (2) defines another partial cost due to the semantic differences. In our approach, the words in the input sentences and the trees are identified using a bilingual thesaurus similar to the Roget's Thesaurus. The *is-a* hierarchy in the bilingual thesaurus, shown the underlying ontology, can be viewed as a directed acyclic graph with a single root. Figure 4 shows one of the *is-a* hierarchies in the thesaurus using our Tree Editor. While the upward links correspond to generalization, the specialization is represented in the downward links. The hierarchies demonstrated in the thesaurus are based on the idea that linguists classify lexical items in terms of similarities and differences. They are used to structure or rank lexical items from more general to the more special.

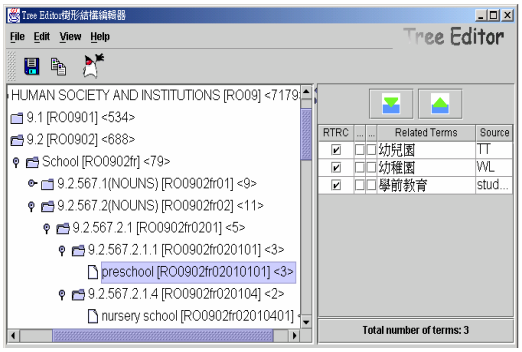

Figure 4: *is-a* hierarchy in the bilingual thesaurus.

Based on the *is-a* hierarchy in the thesaurus, we define the conceptual distance d between two notional words by their shortest path lengths. Given two words t_1 and t_2 in an *is-a* hierarchy of the thesaurus, the semantic distance d between the tokens is defined as follows:

$$d(t_1, t_2) = \text{minimal number of } \textit{is-a} \text{ relationships in the shortest path between } t_1 \text{ and } t_2 \qquad (3)$$

The shortest path lengths in *is-a* hierarchies are calculated. Initially, a search fans out through the *is-a* relationships from the original two nodes to all nodes pointed to by the originals, until a point of intersection is found. The paths from the original two nodes are concatenated to form a continuous path, which must be a shortest path between the originals. The number of links in the shortest path is counted. Since $d(t_1, t_2)$ is positive and symmetric, $d(t_1, t_2)$ is a metric which means (i) $d(t_1, t_1) = 0$; (ii) $d(t_1, t_2) = d(t_2, t_1)$; (iii) $d(t_1, t_2) + d(t_2, t_3) \geq d(t_1, t_3)$. At the same time, the semantic similarity measure between the items is defined by:

$$v(t_i, t_j) := \begin{cases} d(t_i, t_j) & \text{if } d(t_i, t_j) \leq d_{max} \\ MaxInt & \text{otherwise} \end{cases} \qquad (4)$$

where d_{max} is proportional to the number of lexical items in the system and *MaxInt* is a maximum integer of the system. This semantic similarity measure defines the degree of relatedness between the words. Obviously, strong degree of relatedness exists between the lexical tokens under the same nodes. On the other hand, for the cost of the *insert* and *delete* operations, we make use the concept of *collocation* that measures how likely two words are to co-occur in a window of text. To better

distinguish statistics based ratios, work in this area is often presented in terms of the mutual information (MI), which is defined as

$$MI(t_{j-1}, t_j) = \log_2 \frac{P(t_{j-1}, t_j)}{P(t_{j-1}) \times P(t_j)} \quad (5)$$

where t_{j-1} and t_j are two adjacent words. While $P(x, y)$ is the probability of observing x and y together, $P(x)$ and $P(y)$ are the probabilities of observing x and y anywhere in the text, whether individually or in conjunction. Note that tokens that have no association with each other and co-occur together according to chance will have a MI value close to zero. This leads to the cost function for insertion and deletion shown in Eqns. (6) and (7) respectively.

$$R(\lambda \to t_j) = \begin{cases} k \times e^{-z} & \text{if } z > \varepsilon > 0 \\ MaxInt & \text{otherwise} \end{cases} \quad (6)$$

where $z = \min \{MI(t_{j-1}, t_j), MI(t_j, t_{j+1})\}$

$$R(t_j \to \lambda) = \begin{cases} l \times e^{-MI(t_{j-1}, t_{j+1})} & \text{if } MI(t_{j-1}, t_{j+1}) > \varepsilon > 0 \\ MaxInt & \text{otherwise} \end{cases} \quad (7)$$

where k, l, ε are three constants relied on the size of the active corpus.

Obviously, the insertion operation will be penalized if the co-occurrence between the newly inserted word and its neighbors is low. Similarly, the deletion operation is most likely to happen if there is a high co-occurrence between the adjacent pairs after the deletion. Using the above cost functions for the three types of edit operations, the tree in the Treebank with minimum cost is being chosen to be the best approximation of the input sentence and its associated semantic labels will be adopted. Shallow language patterns are then extracted based on the recursive structures and semantic labels appeared in the Treebank. The experimental results of the semantic labeling are shown in the section below.

4 EXPERIMENTAL RESULTS

As mentioned in Eqn. (2), several approaches have been used to define the dissimilarity function f by combining the semantic differences and the detailed POS tags in our second phase feature-enhanced string matching. In our evaluations, five different types of dissimilarity function f are applied. They are

(i) $f_1(u, v) = u(POS_i, POS_j)$
(ii) $f_2(u, v) = v(SC_i, SC_j)$
(iii) $f_3(u, v) = u(POS_i, POS_j) + v(SC_i, SC_j)$
(iv) $f_4(u, v) = \min (u(POS_i, POS_j), v(SC_i, SC_j))$
(v) $f_5(u, v) = \max (u(POS_i, POS_j), v(SC_i, SC_j))$

Dissimilarity function $f_1(u, v)$ provides a detailed version of our coarse-grained syntactic matching. Detailed POS tags are used as the dissimilarity measure in the labeling. Similarly, $f_2(u, v)$ considers only the semantic class of the words. The other three combine both syntactic and semantic features in defining the dissimilarity measures. We have tested our shallow semantic labeling with 10,000 sentences with the Treebank. Since this research is concerning with shallow semantic labeling, we have no incentive to match the trees/subtrees in the Treebank with very complicated structures. The average sentence length is around 13.7 characters per sentence. Table 1 summarizes the results of our system evaluation. The third and fourth columns in the table are number of sentences in each range of edit distance and their average edit distances. The edit distance is defined as a minimum cost in transforming the input sentence with the closest sentence pattern in the Treebank. In other words, the smaller the distance, the higher similarity they have.

Table 1: Sentence analysis in the experiment. Edit distance is defined as a minimum cost in transforming the input sentence with the closest sentence pattern in the Treebank. The smaller the distance, the higher similarity they have.

Dissimilarity function f	Range of Edit distance	% of sentences	Average edit distance
$f_1(u, v)$	0-25	13.9	19.2
	26-50	16.3	40.5
	51-75	19.7	63.6
	76-100	27.9	89.6
	101-150	22.2	124.9
$f_2(u, v)$	0-25	11.3	19.3
	26-50	15.6	41.4
	51-75	17.7	65.2
	76-100	29.3	91.8
	101-150	26.1	125.7
$f_3(u, v)$	0-25	24.1	17.9
	26-50	31.6	38.2
	51-75	22.7	62.3
	76-100	12.8	85.5
	101-150	8.8	121.4
$f_4(u, v)$	0-25	18.6	19.1
	26-50	19.1	41.3
	51-75	30.2	64.7
	76-100	14.7	88.6
	101-150	17.4	124.2
$f_5(u, v)$	0-25	20.5	19.6
	26-50	22.4	40.9
	51-75	26.9	58.2
	76-100	15.3	87.9
	101-150	14.9	128.4

If it is considered as a good match where the edit distances are equal to or less than 50, then it can be observed, in Table 1, that the dissimilarity functions f_3, f_5 and f_4 all produce higher percentage of sentences with lower edit distance. This reflects both the information from syntactic tags and semantic classes provide useful clues in our shallow semantic labeling. Our experiments are not conducted with perfect information. It is worthwhile to mention that more than 530 sentences have incomplete information which mainly comes from proper nouns, or out-of-vocabulary (OOV) words. Both of them have neither defined POS nor semantic class. All these information will be annotated with a default value which will certainly induce errors in our labeling. While it is inevitable to have OOV words in any real corpus, the performance, due to the coverage of POS and semantic classes, does not deteriorate much in our system. The labeling is still feasible over the sentences with OOV words. This tolerance ability provides the graceful degradation in our shallow semantic labeling. While other systems are brittle and working only in all-or-none basis, the robustness of our system is guaranteed. At the same time, while real text tends to have grammatical mistakes and error-prone, these problems can be tackled with an acceptable tolerance in our system.

In our second evaluation, we have tested our algorithm in recognizing several major semantic labels that appear in our sentences. The semantic labels include `theme`, `goal`, `property`, `range`, `agent`, `predication`, `location`, `time`. As with other text analysis, the effectiveness of the system appears to be dictated by recall and precision parameters where recall (*R*) is a percentage of how many correct labels can be identified while precision (*P*) is the percentage of labels, tackled by our system, which are actually correct. In addition, a common parameter *F* is used as a single-figure measure of performance which combines recall (*R*) and precision (*P*) as in follows,

$$F = \frac{(\beta^2 + 1) \times P \times R}{\beta^2 \times P + R} \quad (8)$$

We set $\beta = 1$ to give no special preference to either recall or precision. The recall, precision and *F*-score for the semantic labels in dissimilarity function f_3 are shown in Table 2.

As shown in the last row in Table 2, the precision and recall of all semantic labels are calculated by considering all the semantic labels that appear in the sentences, rather than by averaging the measures for individual semantic labels. It is worth noting that the greatest differences in performance are the recall while the precision remains relatively steady in most semantic labels.

Table 2: Evaluation of different semantic labels in the dissimilarity function f_3. Brackets show the results obtained in the derivation subtrees.

	Elementary Subtree (Derivation		
Semantic Label	Recall	Precision	*F*-score
`theme`	0.79 (0.88)	0.82 (0.85)	0.805
`goal`	0.80 (0.78)	0.79 (0.76)	0.795
`property`	0.89 (0.78)	0.91 (0.83)	0.900
`range`	0.94 (0.93)	0.92 (0.91)	0.930
`agent`	0.92 (0.92)	0.87 (0.85)	0.894
`predication`	0.76 (0.80)	0.81 (0.78)	0.784
`location`	0.92 (0.92)	0.91 (0.89)	0.915
`Time`	0.93 (0.93)	0.95 (0.94)	0.940
`experiencer`	0.87 (0.89)	0.86 (0.88)	0.865
`manner`	0.79 (0.85)	0.84 (0.83)	0.814
`possessor`	0.91 (0.93)	0.88 (0.89)	0.895
`condition`	0.80 (0.84)	0.82 (0.81)	0.810
`all labels`	0.88 (0.84)	0.89 (0.88)	0.885

One possible explanation is that the low recall rates in some labels are due to less complete coverage of linguistic phenomena. In addition, we define an elementary subtree that spans only on a sequence of words, as well as a derivation subtree that contains at least one branch of elementary subtree. It may be expected the *F*-score of the derivation subtrees will be much worse than its counterpart, however, Table 2 shows surprisingly the differences in the overall accuracy in two main types of subtrees are not significant. An explanation is that we have approached chunking as well as assigning the most salient semantic label to the chunks based on the POS and semantic tags. Even though there may be some misclassification in the terminal nodes, this will not hinder the system to tag the semantic labels in the longer chunks. In other words, the longer chunks are less error prone in our semantic labeling. This shallow semantic labeling technique produces an output that abstract away the details but retains the core semantic structure of the actual sentence. Pure linguistic theories may well have solutions to the semantic labeling that tends to be highly theory-specific with less emphasis on real text. Our shallow approach does not focus on how well it explains various structural and interpretive phenomena in linguistics perceptive, but on how well it predicts the semantic label of sentences. It aims at theory-neutral annotation and derives linguistically-plausible semantic labels or short phrase structures using a Treebank. We have suggested that semantic labels can be detected by grouping sequences of words that occur together more often with high mutual information. While the approach has been

implemented successfully in the Chinese language as illustrated in our evaluation, the idea delineated certainly does not limit or tailor-made for any particular language. Only a minor modification is needed to apply the technique to other languages.

5 CONCLUSIONS

In this paper, we have illustrated a shallow technique in which semantic labels are extracted in forms of chunks of phrases or words using a two-phase feature-enhanced string matching algorithm. While the first phase is to shortlist the potential trees in the Treebank, chunks are further tagged with semantic labels in the second phase. Based on the linguist's conception of phrase structure, our approach does not require a full syntactic parse to pursue semantic analysis and the recursively embedded phrases can also be identified without pain. This shallow technique is inspired by the research in the area of bio-molecular sequences analysis which advocates *high sequence similarity usually implies significant function or structural similarity*. It is characteristic of biological systems that objects have a certain form that has arisen by evolution from related objects of similar but not identical form. This *sequence-to-structure* mapping is a tractable, though partly heuristic, way to search for functional or structural universality in biological systems. With the support from the results as shown, we conjecture this sequence-to-structure phenomenon appears in our sentences. The sentence sequence encodes and reflects the more complex linguistic structures and mechanisms described by linguists. While our system does not claim to deal with all aspects of language, we suggest an alternate, but plausible, way to handle the real corpus.

ACKNOWLEDGEMENTS

The work described in this paper was partially supported by the grants from the Research Grants Council of the Hong Kong Special Administrative Region, China (Project Nos. CUHK4438/04H and CUHK4706/05H).

REFERENCES

Abney, S. (1991). Parsing by chunks. In Berwick, R., Abney, S. & Tenny, C. (Eds.), *Principle-Based Parsing*. Kluwer Academic.

Bod, R., Scha, R., & Sima'an, K. (2003). *Data-Oriented Parsing*. Stanford: California, CSLI.

Chen, K.-J., Huang, C.-R., Chang, L.-P., & Hsu. H.-L. (1996). Sinica Corpus: Design Methodology for Balanced Corpora. *Proceedings of the 11th Pacific Asia Conference on Language, Information, and Computation (PACLIC II)*, Seoul Korea, 167-176.

Church, K. (1988). A stochastic parts program and noun phrase parser for unrestricted text. *Proceedings of Second Conference on Applied Natural Language Processing*, Austin, Texas.

CKIP (2004). *Sinica Chinese Treebank: An Introduction of Design Methodology*. Academic Sinica.

Dowty, D. (1991). Thematic proto-roles and argument selection. *Language*, 67, 547-619.

Fillmore, C.J. (1968). The case for case. In E. Bach & R.T. Harms (Eds.), *Universals in Linguistic Theory*, 1-90. Holt, Rinehart & Winston.

Gee, J., & Grosjean, F. (1983). Performance structures: A psycholinguistic and linguistic appraisal. *Cognitive Psychology*, 15, 4, 411-458.

Gusfield, D. (1997). *Algorithms on Strings, Trees, and Sequences: Computer Science and Computational Biology.* Cambridge University Press.

Jackendoff, R. (1983). *Semantics and Cognition*. MIT Press.

Kurohashi, S., and Nagao, M. (1994). A method of case structure analysis for Japanese sentences based on examples in case frame dictionary. *IEICE Transactions on Information and Systems*, vol. E77-D, no. 2, 227-239.

Ramshaw, L. A., & Marcus, M.P. (1995). Text chunking using transformation-based learning. *Proceedings of the Third Workshop on Very Large Corpora*, 82-94.

Sima'an, K. (2000). Tree-gram parsing: lexical dependencies and structural relations. *Proceedings of the 38th Annual Meeting of the Association for Computational Linguistics*, 53-60, Hong Kong.

Somers, H.L. (1982). The use of verb features in arriving at a 'meaning representation'. *Linguistics*, 20, 237-265.

Tsay, Y.T., & Tsai, W.H. (1989). Model-guided attributed string matching by split-and-merge for shape recognition. *International Journal of Pattern Recognition and Artificial Intelligence*, 3, 2, 159-179.

Utsuro, T., Matsumoto, Y., and Nagao, M. (1993). Verbal case frame acquisition from bilingual corpora. *Proceedings of the Thirteenth International Joint Conference on Artificial Intelligence*, vol. 2, 1150-1156.

Wagner, R.A., & Fischer, M.J. (1974). The string-to-string correction problem. *Journal of the Association for Computing Machinery*, 21, 1, 168-173.

Weischedel, R., Meteer, M., Schwartz, R., Ramshaw, L., Palmucci, J. (1993). Coping with ambiguity and unknown words through probabilistic models. *Computational Linguistics*, 19, 2, 359-382.

AN EVOLUTIONARY APPROACH TO MULTIVARIATE FEATURE SELECTION FOR FMRI PATTERN ANALYSIS

Malin Åberg, Line Löken and Johan Wessberg
Institute of Neuroscience and Physiology, Göteborg University, Box 432, SE-40530 Goteborg, Sweden
malin.aberg@neuro.gu.se, line.loken@neuro.gu.se, johan.wessberg@physiol.gu.se

Keywords: fMRI, pattern recognition, feature selection, evolutionary algorithms.

Abstract: Multivariate pattern recognition has recently gained in popularity as an alternative to univariate fMRI analyis, although the exceedingly high spatial dimensionality has proven problematic. Addressing this issue, we have explored the effectiveness of evolutionary algorithms in determining a limited number of voxels that, in combination, optimally discriminate between single volumes of fMRI. Using a simple multiple linear regression classifier in conjunction with as few as five evolutionarily selected voxels, a subject mean single trial binary prediction rate of 74.3% was achieved on data generated by tactile stimulation of the arm compared to rest. On the same data, feature selection based on statistical parametric mapping resulted in 63.8% correct classification. Our evolutionary feature selection approach thus illustrates how, using appropriate multivariate feature selection, surprising amounts of information can be extracted from very few voxels in single volumes of fMRI. Moreover, the resulting voxel discrimination relevance maps (VDRMs) showed considerable overlap with traditional statistical activation maps, providing a model-free alternative to statistical voxel activation detection.

1 INTRODUCTION

We recently showed that the evolutionary algorithm is an effective tool for classifier and feature subset optimization for single-trial discrimination of electroencephalography (EEG) (Åberg and Wessberg, 2007). In this study, we extend our approach to functional magnetic resonance imaging (fMRI).

Similar to the EEG, fMRI data is non-stationary, multivariate, noisy and very high-dimensional. These properties are typically dealt with by applying statistical parametric mapping (SPM) methods, where the average level of voxel activity is computed offline in a univariate, model-based fashion (Friston et al., 1994).

However, by being univariate, the SPM-based method is not appropriately sensitive to cognitive information that is encoded in the combined effect of numerous voxels. Pattern recognition approaches, on the other hand, provide tools that are multivariate, that is, based on the combined effect of several voxels. Moreover, trained pattern classifiers can be used in situations that demand real-time results, including online detection and identification of brain patterns. Several recent studies have established the feasibility of multivariate methods (Norman et al., 2006; Haynes and Rees, 2006).

Due to the vast spatial dimensionality (in the order of tens to hundreds of thousands of voxels), efficient feature selection has been identified as a major challenge in the development of pattern classification algorithms for fMRI (Norman et al., 2006). In this study we therefore present an algorithm based on evolutionary techniques, proven effective in numerous optimization areas, including feature subset selection (Hussein, 2001; Reeves and Rowe, 2002), that detects which number and combination of individual voxels that optimally carry information relevant to a stimulus. These voxels are used as features in a classifier, and we have chosen to use rudimentary multiple linear regression (MLR) to show that even a very simple classification scheme can detect and distinguish relevant cortical information in noisy fMRI data given proper feature selection.

Our algorithm also generates a voxel selection

frequency ranking, illustrating how relevant each voxel is in discriminating between given patterns. This ranking can be presented slicewise as a two-dimensional image, or what we propose to call a voxel discrimination relevance map (VDRM), showing the anatomical location of brain regions involved in the stimulus.

In this study we thus aim to evaluate the effectiveness of the evolutionary approach in automatic voxel subset selection, aspiring to improve single-volume discrimination of cortical patterns. We also explore how the results compare with established statistical methods for detecting activated areas of the brain. The data is acquired from a tactile stimulation experiment where the physiology of brain activation is reasonably well understood (Olausson et al., 2002). Part of the findings have been previously presented in abstract format (Åberg et al., 2006).

2 METHODS

Data Acquisition and Paradigm

A 1.5 T fMRI scanner (Philips Intera, Eindhoven, Netherlands) with a sense head coil (acceleration factor 1) and a BOLD (blood oxygenation level dependent) protocol with a T2*-weighted gradient echo-planar imaging sequence (TR 3.5 s; TE 51 ms; flip angle 90°) was used to acquire brain scans in six healthy human volunteers. The scanning planes (6 mm thickness, 2.3 x 2.3 mm in-plane resolution) were oriented parallel to the line between the anterior and posterior commissure and covered the brain from the top of the cortex to the base of the cerebellum. Each scan volume contained 25 slices at a spatial resolution of 128 x 128 voxels.

Following cues from the scanner, an experimenter stroked a 7 cm wide soft brush over a 16 cm distance in the distal direction on the right arm. Each brushing, lasting 3.5 seconds (one single scan volume), was repeated three times and rest periods of equal duration were interleaved. The Regional Ethical Review Board at Goteborg University approved the study, and the experiments were performed in accordance with the Declaration of Helsinki.

Data Pre-processing

Data pre-processing was carried out with software developed at the Montreal Neurological Institute (Montreal, Canada; available at http://www.bic.mni.mcgill.ca/software/). Functional data were motion corrected and low-pass filtered with a 6 mm full-width half-maximum Gaussian kernel.

Slices and voxels not containing brain matter were discarded. To correct for hemodynamic delay, the remaining data (slices 2-20) was shifted by one volume. An arm/rest data set containing 456 3.5 second patterns of each class was formed per subject and slice, and the samples were linearly normalized to the range [0 1]. The first 80% of the patterns were randomized and used in the evolutionary process (training data). The remaining volumes were exclusively used in estimating the prediction accuracy on already optimized classifiers (validation data).

Feature Selection using Evolutionary Algorithms

An evolutionary algorithm is an optimization scheme inspired by Darwinian evolution (Reeves and Rowe, 2002). The aim of the algorithm in this study is to select a limited number of voxels that, in combination with a classifier, are maximally optimal in discriminating between the brain states induced by brushing on the skin compared to rest.

Tournament selection is used here, where, for each parent, a subset of individuals is randomly chosen from the population and the fittest of these is selected. The tournament size is set to a third of the total population size. Reproduction is asexual, meaning that the offspring is identical copies of the parents.

The fitness is computed as the proportion of correctly classified patterns using multiple linear regression. In order to avoid overfitting, the classifier parameters are established on the training data, whereas a designated 25% of the training data (termed testing data) is used for fitness computation.

The only mutation operation is substitution of a voxel in the individual voxel subset with another, unused voxel. The frequency of mutation is regulated by a constant mutation rate parameter.

Due to the stochastic nature of evolutionary algorithms and the low signal-to-noise levels in the data, the algorithm is unlikely to evolve the same voxel subset at every attempt. To achieve robust results, the algorithm is thus run numerous times.

The algorithm was implemented in Matlab (The Mathworks, Massachusetts, USA) and C on a standard PC by one of the authors (M. Åberg).

Brain State Discrimination Performance

The prediction accuracy was evaluated on the validation data using the classifier and voxels from the run that achieved best results on the training and testing data. A discrimination accuracy of 50% corresponds to chance.

For comparison, the prediction accuracy using the voxels with highest activation according to a statistical parametric mapping (SPM) method was also determined. To this end, a statistical reference analysis was performed on the training data (Worsley et al., 2002).

Voxel Discrimination Relevance Maps

By aggregating the best feature subsets from each algorithm run a voxel discrimination relevance ranking, specifying the number of times each voxel has been selected, can be obtained. This can be presented as a slicewise two-dimensional voxel discrimination relevance map (VDRM).

In order to mimic a classic block-design study for comparison with the univariate SPM approach, all data were used in the training process and there was no prediction involved when generating the VDRMs.

3 RESULTS

Brain State Prediction Performance

The classification algorithm was applied to all subjects individually using five voxels and 500 runs. The prediction accuracies are well above chance (figure 1); a subject mean maximum prediction accuracy of 74.34% (range 65.79%-81.58%) was achieved. Using the five most active voxels as judged by the SPM analysis, the subject mean maximum prediction accuracy was significantly lower at 63.81% (Wilcoxon, p=0.031; range 59.21-73.68%). Random classification results in a prediction rate of 50%. Measuring the prediction success in terms of information bits (Krippendorf, 1986; Laubach et al., 2000), the difference between methods is even more apparent: the SPMt-based subject mean result is 0.094 bits (range 0.025-0.22 bits), whereas the EA-based approach achieves more than the double at 0.21 bits (range 0.077-0.32 bits).

The primary and secondary sensory cortices (SI and SII), expected to be activated by tactile stimuli, are approximately found in slices 4-7 and 11-12 (slice numbers in the dorsal-ventral direction). As shown in the bar chart in figure 2, the subject mean prediction accuracies obtained in these slices are markedly higher than in less relevant slices. Interestingly, the prediction trend is clearly similar to the behavior of the highest $|SPMt|$-value, a measure of brain activation (figure 2). It should be noted, however, that all data is analyzed individually in native space rather than at group level and that any anatomical congruence between subjects is approximate at best.

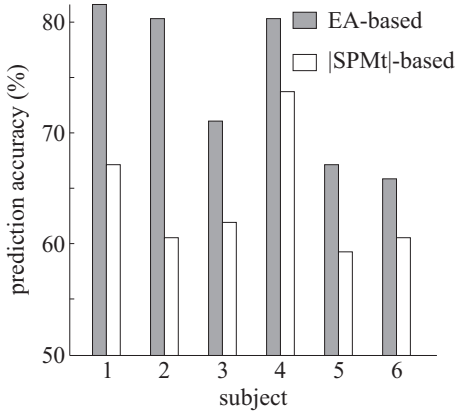

Figure 1: Brain state prediction accuracies for all subjects, as evaluated on the validation data set using the five best voxels and corresponding classifiers obtained after 500 training runs. The prediction accuracy using the five most activated voxels according to SPMt computations of the training data is also shown. The level of chance is 50%.

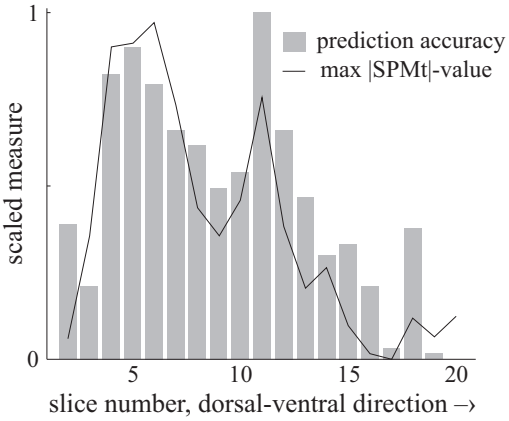

Figure 2: The subject mean brain state prediction performance and maximum $|SPMt|$-values per slice. The two variables show high correlation, and slices with voxels where a BOLD response was expected (SI: slices 4-7, SII: slices 11-12) show consistently higher values. The measures have been scaled to the range [0 1] within subjects to emphasize trends.

Voxel Discrimination Relevance Maps

The VDRMs also show striking visual similarity to the SPMt (figure 3), although the VDRMs appear less noisy overall. SI (slices 5-6), for example, is detected in the SPMt as well as in the VDRM. Similarly, the location of SII (slices 11-12) and also the insular cortex (slices 11), to which unmyelinated tactile afferents project (Olausson et al., 2002), is clear from either

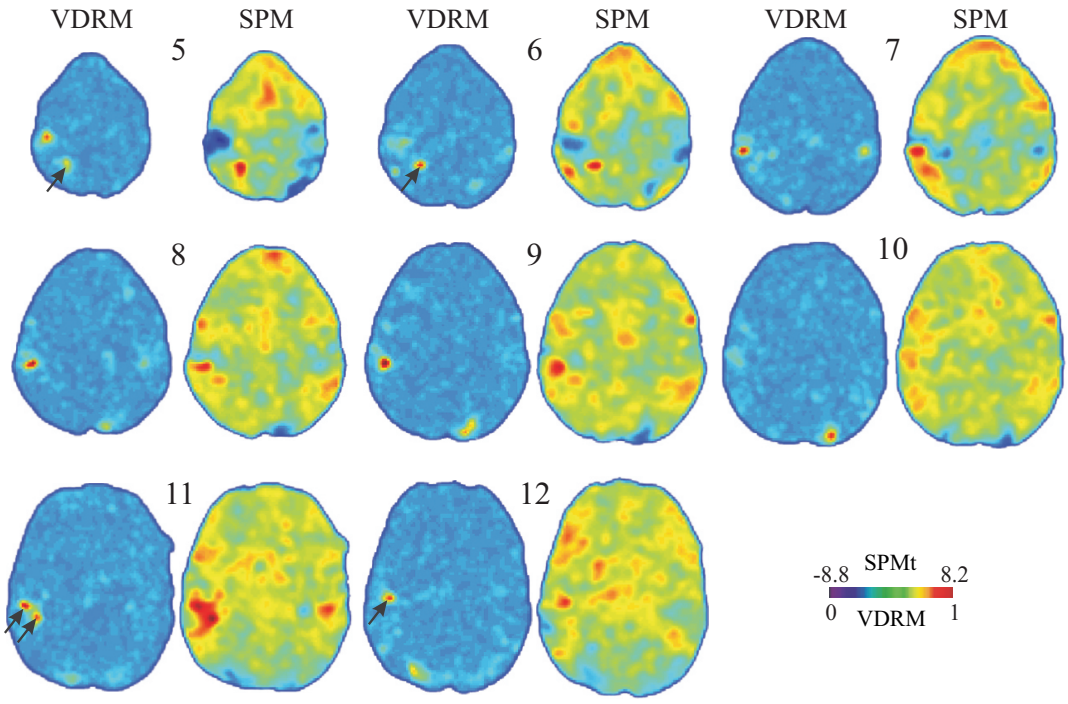

Figure 3: Voxel discrimination relevance maps for subject one, generated using five voxels over 500 runs, with corresponding SPMts. The VDRMs and SPMts are clearly correlated. The right side of the images corresponds to the right side of the brain.

map. The SPMt also suggests several activated areas that are not found in the VDRM. It should be noted, however, that the SPMt maps are not thresholded, and that all voxels with a $|t|$-value of less than 5.2 are below the required significance levels. The VDRM appears to detect highly activated negative and positive BOLD responses equally well, but does not distinguish between them (e.g. slice 5).

The Rffect of Voxel Subset Size

Including as few as two evolutionarily selected voxels yields voxel discrimination relevance maps where some visual correlation with the SPM is clear (figure 4A). Further addition of voxels results in more pronounced clustering at relevant sites, but also adds noise. At 30 voxels the noise levels render the map barely interpretable. Similarly, the subject mean evolution-based prediction accuracy (figure 4B), increases rapidly with the addition of up to three voxels, after which it levels out. Addition of more than 11 voxels decreases the performance drastically. SPMt-based voxel selection behaves differently: the performance for low numbers of voxels is poor, and increases linearly with addition of voxels. Note that the maximum number of available voxels is in the order of thousands.

4 DISCUSSION

This study demonstrates the effectiveness of evolutionary algorithms in selecting an optimal combination of voxels for highly accurate discrimination between single volumes of brain patterns — even in conjunction with an exceedingly simple classifier. Using as few as five evolutionarily selected voxels and a standard multiple linear regression classifier, a subject mean single-trial brain state prediction accuracy of over 74% was achieved. Moreover, the voxel discrimination relevance maps correlate clearly with statistical parametric maps, and the expected patterns of brain activation were detected. Not surprisingly, evolutionary feature selection achieved higher classification accuracy than voxel selection using SPM ranking. The latter approach merely selects voxels that show the largest individual average difference between brain states, whereas the evolutionary method determines a combination of voxels that is tailored for brain pattern discrimination. The feasibility of the multivariate approach is further established by the fact that the contribution of so little temporal and spatial information — 3.5 seconds worth of data from only five voxels — allows for accurate brain state prediction. The maximum prediction accuracy using evolutionary feature selection is achieved at drastically less

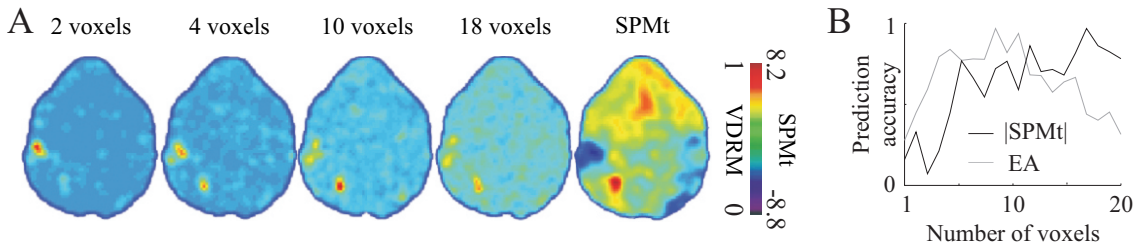

Figure 4: A: The effect of number of included voxels on the voxel discrimination relevance maps for subject one, slice five. The maximum number of possible voxels is in the order of thousands. B: Subject mean evolutionary and SPMt-based prediction accuracy as a function of voxels subset size. The SPMt-based feature selection peaks at 65 voxels. The data has been scaled within subjects to the range [0 1] to emphasize trends.

voxels than the SPMt approach (figure 4), indicating that a large number of SPMt voxels are irrelevant for the discrimination task. In addition, univariate fMRI-analysis requires averaging over time to overcome the inherently low signal quality, and lacks any prediction qualities.

Our approach is not limited to brain state identification, but also provides two distinct approaches to information localization. The fact that the slicewise prediction accuracy correlates very well with the corresponding maximum $|SPMt|$-value — the classical method of detecting activation — is a clear indication that the information revealed by the prediction performance is physiologically related to the stimulus (figure 2). The algorithm can be applied to voxel clusters of any size and shape, defined either beforehand or through evolution, thus optimizing the classification-based information localization. Alternatively, the voxel discrimination relevance maps serve as relative activation detection charts, visually showing which voxels are highly related to the stimulus. Significance levels akin to SPMt values can be computed using boot-strap statistical methods, involving data permutations, allowing for proper VDRM thresholding (Efron and Tibshirani, 1993). Although not done here, the algorithm can be applied to a whole head volume, resulting in a global rather than slicewise VDRM.

In combination with excessive amounts of data, typical for fMRI studies, the time taken to run an evolutionary algorithm can be staggering. However, in our design the number of included voxels is very small, and using a standard PC (3.20GHz processor, 3GB RAM) one five-voxel training run on one individual (20 slices) takes only approximately 1.5 minutes, whereas the validation is done in (biological) real-time. Furthermore, several refinements can be added to make the algorithm considerably more efficient.

The multiple linear regression method used for classification in this study is sensitive to noise and limited to linearly separable problems. In its simplicity, however, the MLR effectively illustrates the power of evolutionary algorithms in extracting relevant information buried in substantial amounts of noise. Pattern analysis using advanced non-linear algorithms, such as artificial neural networks, have been attempted and show promising results. Additional discrimination algorithms, such as support vector machines and other state-of-the-art classifiers, can easily be incorporated into the evolutionary scheme as required.

5 CONCLUSIONS

We have shown that evolutionary based multivoxel feature selection is effective in extracting relevant characterizing information from single volumes by utilizing the multivariate properties of fMRI. Moreover, our approach provides a data-driven alternative to voxel activation detection based on statistical methods.

ACKNOWLEDGEMENTS

This study was supported by the Swedish Research Council (grant 3548), the Sahlgrenska University Hospital (grant ALFGBG 3161), and the foundation of Magnus Bergvall.

REFERENCES

Åberg, M., Löken, L., and Wessberg, J. (2006). A multivariate pattern recognition approach to fMRI analysis using linear classifiers combined with evolutionary algorithms for voxel selection. *Society for Neuroscience 36th Annual Meeting, Atlanta, USA*, (492.11).

Åberg, M. and Wessberg, J. (2007). Evolutionary optimization of classifiers and features for single-trial eeg discrimination. *BioMedical Engineering OnLine*, 6(1):32.

Efron, B. and Tibshirani, R. (1993). *An introduction to the bootstrap*. Chapman & Hall Ltd.

Friston, K. J., Holmes, A. P., Worsley, K. J., Poline, J. P., Frith, C. D., and Frackowiak, R. S. J. (1994). Statistical parametric maps in functional imaging: A general linear approach. *Human Brain Mapping*, 2(4):189–210.

Haynes, J.-D. and Rees, G. (2006). Decoding mental states from brain activity in humans. *Nature Reviews Neuroscience*, 7(7):523–534.

Hussein, F. (2001). Genetic algorithms for feature selection and weighting, a review and study. In *ICDAR '01: Proceedings of the Sixth International Conference on Document Analysis and Recognition*, page 1240, Washington, DC, USA. IEEE Computer Society.

Krippendorf, K. (1986). *Information theory: Structural models for qualitative data*. Sage University Paper Series on Quantitative Applications in the Social Sciences.

Laubach, M., Wessberg, J., and Nicolelis, M. (2000). Cortical ensemble activity increasingly predicts behaviour outcomes during learning of a motor task. *Nature*, 405:567–571.

Norman, K. A., Polyn, S. M., Detre, G. J., and Haxby, J. V. (2006). Beyond mind-reading: multi-voxel pattern analysis of fmri data. *Trends in Cognitive Sciences*, 10(9):424–430.

Olausson, H., Lamarre, Y., Backlund, H., Morin, C., Wallin, B. G., Starck, G., Ekholm, S., Strigo, I., Worsley, K., Vallbo, A. B., and Bushnell, M. C. (2002). Unmyelinated tactile afferents signal touch and project to insular cortex. *Nature Neuroscience*, 5(9):900–904.

Reeves, C. R. and Rowe, J. E. (2002). *Genetic Algorithms - Principles and Perspectives: A Guide to GA Theory*. Kluwer Academic Publishers, Norwell, MA, USA.

Worsley, K. J., Liao, C. H., Aston, J., Petre, V., Duncan, G. H., Morales, F., and Evans, A. C. (2002). A general statistical analysis for fmri data. *NeuroImage*, 15(1):1–15.

DIMENSIONALITY REDUCTION FOR IMPROVED SOURCE SEPARATION IN FMRI DATA

Rudolph L. Mappus IV, David Minnen and Charles Lee Isbell Jr.
College of Computing, Georgia Tech, 85 Fifth St. NW, Atlanta, USA
cmappus@gatech.edu, minnen@cc.gatech.edu, isbell@cc.gatech.edu

Keywords: Dimensionality reduction, ICA, fMRI.

Abstract: Functional magnetic resonance imaging (fMRI) captures brain activity by measuring the hemodynamic response. It is often used to associate specific brain activity with specific behavior or tasks. The analysis of fMRI scans seeks to recover this association by differentiating between task and non-task related activation and by spatially isolating brain activity. In this paper, we frame the association problem as a convolution of activation patterns. We project fMRI scans into a low dimensional space using manifold learning techniques. In this subspace, we transform the time course of each projected fMRI volume into the frequency domain. We use independent component analysis to discover task related activations. The combination of these methods discovers sources that show stronger correlation with the activation reference function than previous methods.

1 INTRODUCTION

Functional magnetic resonance imaging (fMRI) captures neural activation patterns by measuring the hemodynamic response in cranial tissue through sampling discrete regions of the brain, referred to as voxels (Dogil et al., 2002). Each voxel represents the aggregate hemodynamic response of a region of neurons. Behavioral experiments using fMRI are designed to evoke activation in a hypothesized *region of interest* (ROI) in the brain. The ROI represents an anatomical region of the brain believed to be where functional processing of a specific behavioral task occurs. Experimental trials in these designs use a behavioral task meant to evoke activation in the ROI. Control trials do not evoke ROI activation.

Unfortunately, locating significant differences between active and non-active voxels is challenging because of the inherent latencies and artifacts in fMRI signal acquisition (Josephs et al., 1997). Furthermore, the hemodynamic activation level of neighboring voxels influences voxel activation, producing less accurate spatial activation maps.

Traditional analysis methods such as statistical parametric mapping (SPM) use statistical tests to demonstrate significant differences between the time course activation of particular voxels in the control and experimental tasks (Friston, 2003). By contrast, the objective of component analysis methods—such as independent components analysis (ICA)—is to recover components whose time course activation correlates with the task-based reference function: $\text{argmax}_{a \in \{A\}} \rho(r, a)$, where r is the reference activation time course that represents the ideal activation during the trial, and a is the component activation time course.

Although ICA has been shown to work for simple block experimental designs, it has some limitations. In particular, ICA has been used successfully when combined with *a priori* anatomical information about activation areas (McKeown et al., 1998). Furthermore, simple ICA does not account for the delayed composition effects that can arise in fMRI analysis.

The contribution of this work is to frame the problem of the combined latencies of the hemodynamic response and the signal acquisition process as a convolution of the hemodynamic response functions of spatially independent components. Framed this way, we can address these confounding spatial and temporal influences, by first using nonlinear manifold learning to constrain source separation and to remove voxels that do not help distinguish between task and non-task activation. We generate a frequency space representation of the reduced features for convolutive source separation using ICA. Our method allows us to handle delayed composition effects and to select ROIs

without specific a priori anatomical knowledge of the ROI. Thus, we are able to limit type II errors.

2 PREVIOUS WORK

Independent Components Analysis. Time domain independent component analysis (ICA) works on discrete time, linear dynamical systems where a latent process generates a set of observables (McKeown et al., 1998). A *k*-vector of random variables represents the state of the process at each time step. In such a system, latent variables are linearly mixed to give rise to the observable variables at each time step. First-order Markov dynamics govern state transitions within the process defined by a $k \times k$ matrix M (Roweis and Ghahramani, 1999).

Formally, $X = AS$, where X is a $k \times t$ *observation matrix*, A is a *mixing matrix* and S is the $k \times t$ matrix representing the time course evolution of the latent random variables. ICA recovers an *unmixing matrix* A^{-1} for the observation matrix X. A^{-1} produces a set of statistically independent components from the data. Under certain assumptions, the components represent the (possibly scaled) evolution of the original latent process. In this case, the mixing matrix A represents the degree to which a component participates in the generation of the observation data at each time step. For the analysis of fMRI scans, we assume that the separation problem in the reduced dimension problem is determined, which means that the number of sources is equal to the number of sensors (voxels). In the determined case, the discovered independent components can be interpreted as underlying *causes* of observations, especially when one believes that: (1) observed features are generated by the interaction of a set of independent hidden random variables, and (2) these hidden variables are likely to be kurtotic (*i.e.* discriminative and sparse). These assumptions are reasonable for fMRI analysis because of existing neurological evidence for functional modularity in the brain and the specific requirements of the experimental task.

Time domain applications of ICA assume an instantaneous linear mixture model at each time step. McKeown *et al.* (McKeown et al., 1998) applied ICA to fMRI data from a simple block-design experiment and found correlated activation signal for a component corresponding to the region of interest (McKeown et al., 1998).

Manifold Learning and fMRI. Manifold learning has been applied to fMRI time domain data directly (Shen and Meyer, 2006). In this case, the intrinsic dimensionality represents spatially independent voxel activations and the objective is to generate clusters matching ground truth classification. The intuition is that task related activated voxels will cluster together in the representation. The interpretation of the manifold is that it captures information about the geometry of the volume space. A key issue with direct application is that target signals in a behavioral study are often not the high ranking elements generated using principle components analysis (PCA) and ICA (McKeown et al., 1998). These less significant activations typically rank in the latter component quartiles.

Convolutional Blind Source Separation. Blind separation of convolutional sources has applications in a number of signal processing domains, including fMRI (Pederson et al., 2007; Anemuller et al., 2003). Here, we assume a linear convolution of sources in the time domain and model observations at time t as:

$$x(t) = \sum_{k=0}^{K-1} A_k s(t-k) + v(t) \qquad (1)$$

where K is the finite impulse response (FIR) length. In frequency space, source separation is performed for each frequency. For the purpose of analyzing fMRI data, where there is a relatively limited temporal extent, we choose a window function that minimizes band overlap.

$$\mathbf{W}(\omega) = \mathbf{A}(\omega)\mathbf{S}(\omega) + \mathbf{V}(\omega) \qquad (2)$$

3 COMBINED APPROACH

Our approach to fMRI analysis seeks to combine the strengths of manifold learning, convolution in frequency space, and complex ICA in order to improve the accuracy of recovered brain activity components.

Manifold learning has not been applied to time domain data as preprocessing for component analysis. Furthermore, manifold learning techniques reduce the dimensionality of the ROI, making component analysis more effective at source separation. In fact, much of the ROI is not significantly activated and correlated to the reference function. We want to reduce the dimensionality of these voxels before source separation.

Using ICA in the frequency domain allows us to treat convolution of components as a product, which in turn allows a computationally feasible algorithm to solve the convolutive blind source separation problem. Using this version of the source separation problem is important because voxels near each other in the brain may exhibit delayed influences during recording. Using a convolutive model instead of an instantaneous mixing model provides the ability to capture this influence and properly separate the components.

3.1 Manifold Learning

Before transformation into the frequency domain and subsequent component analysis, we apply a manifold learning algorithm to reduce the size of the voxel set. The dimensionality reduction serves two purposes. First, it reduces the computational burden of the relatively expensive ICA computation. More importantly, manifold learning allows researchers to include a large ROI in order to avoid Type II errors caused by failing to include a relevant voxel in the analysis. The dimensionality reduction algorithm can then reduce the region based on the observed activation levels, thereby achieving a manageable size while minimizing the risk of excluding relevant voxels.

We experiment with several different manifold learning methods: local linear embedding (LLE) (Roweis and Saul, 2000), isomap (Tenenbaum et al., 2000), Laplacian eigenmaps (Belkin and Niyogi, 2003) and diffusion maps (Coifman and Lafon, 2006). Diffusion maps were used in previous work with fMRI (Shen and Meyer, 2006), while LLE and isomap are both standard methods for manifold learning and provide a basis for comparison.

3.2 Complex ICA

In order to convert the time course of voxel activations into the frequency domain, we use the short–time Fourier transform (STFT) with a window size adapted for each dataset. In the case of the left/right dataset (described in detail in the following section), the window size equals the ratio of the hemodynamic response latency to volume acquisition latency. Each STFT generates frequency vectors for a specific temporal window, which are grouped into frequency vectors and analyzed via complex ICA. The Fourier transforms represent signals in each bin in the frequency domain as complex values. We apply complex-fastICA (Bingham and Hyvarinen, 2000) to each bin, so that the generated components are frequency specific.

3.3 Component Comparison

We select components with activation sharing high correlation to the reference activation function. We consider these components to be task related. In the time domain, application of ICA generates the activation of independent sources in the columns of the unmixing matrix A, and correlation of these columns to the reference function indicates task relatedness. In the frequency domain, where there STFT generates a set of frequency bins, the objective is to find components in each frequency bin that are task related. We generate the reference activation function using the same parameters (same spectral extent, same bin parameters) used to generate the STFT for the observation set. We use the standard distance measure for complex vectors: $\sum_i |x|^2$. For each bin, we find the highest correlated activation course: $\text{argmax}_a \rho(a,r)$.

4 EXPERIMENTS

Here, we present results of experiments comparing performance of the manifold learning techniques and complex source separation alone. The datasets are meant to demonstrate method performance in a simple, controlled task as well as actual study data.

4.1 Left/right Motor Task

To evaluate our method, we begin with a simple example: consider an fMRI scan sequence of a single subject performing a repetitive right- or left-hand finger movement task (Hurd, 2000). The objective is to find task related activated components of hand movements in the ROI. For the ROI, we selected a window of voxels in a region based on correlation values to the reference function using time domain ICA. In the motor task, 80 volumes were sampled at a constant rate for each task: left-hand/right-hand finger move. We defined a ROI in slices 13,14,15,16, loosely defined around the temporal area of the motor cortex. Scans of left hand tasks are concatenated to scans of right hand tasks, 160 scans total. Given this organization, the reference activation function for left hand tasks is defined as a delta function: $\delta(x \geq 80)$.

First, we want to test how manifold learning techniques assist in time domain separation. In this case, we compare the correlation of component activations recovered by ICA to reference function activation. We compare the best correlation values generated using ICA alone as well as with the various manifold learning techniques. These are all performed using the time domain data (see Table 1). The manifold learning methods do not recover correlated activation of components as well as using ICA alone in this case.

For the STFT, we use a parameterization for each dataset. In the case of the left/right dataset, the window size is the ratio of the hemodynamic response latency to volume acquisition latency. We consider the measured values of voxels v_i through time $t_{i\in\{1\ldots\tau\}}$. Each STFT generates frequency vectors for each window. We group frequency vectors from each STFT and apply component analysis to the resulting matrices. Computing the inverse transform of the compo-

Table 1: Comparison of correlation values to reference function using manifold learning in time domain.

Method	Max ρ	p-value
Diff Map	0.1407	0.1
Isomap	0.3470	0.001
LLE	0.2052	0.01
LE	0.2236	0.005
ICA	0.7395	0.0001

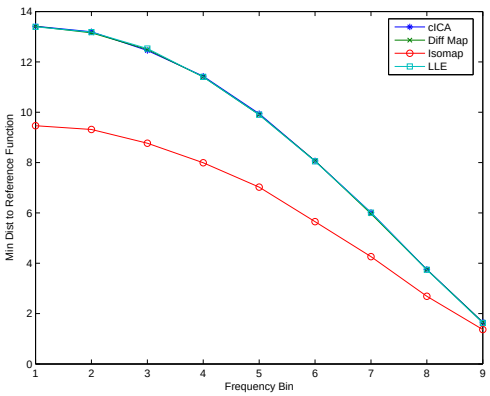

Figure 1: Comparison of minimum distances to reference function between manifold learning method preprocessing and complex ICA. Minimum distance for each method in each STFT frequency bin.

nent produces a time domain representation of the signal. However, due to the window overlap in the STFT, this time scale is not appropriate for comparison in the original observation space.

We compare the performance in the left/right task between the various manifold learning algorithms and complex ICA in the frequency domain without manifold learning (see Table 1). To compare methods, we use the minimum distance of component activation to reference function activation in each frequency bin. In this case, manifold learning using diffusion maps and local linear embedding perform slightly better than complex ICA alone.

4.2 Postle *et Al.* Study

Postle *et al.* (Postle et al., 2000) measured activation of five participants in four behavioral tasks: forward memory, manipulate memory, guided saccade, and a free saccade task. Subjects completed 96 trials: 8 blocks of 12 trials each. Within each block, subjects received an equal number of task trials, in random order. Subjects were presented with a static arrangement of squares on a screen. Signals were acquired using a GE 1.5T scanner with 3.75mm^2 in-plane resolution and 5mm inter-slice distance. Volumes were 21 slices, and volume acquisition time was 2s; 17 volumes were acquired per trial. Inter-trial time was 7s. By comparing voxel activation values in each experimental task in the ROI, Postle *et al.* showed no significant difference in voxel activations between control and experimental tasks.

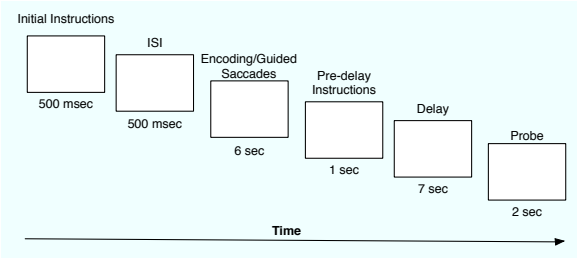

Figure 2: Trial event sequence (Postle et al., 2000). Initial instructions indicate what the memory task will be. After ISI, a sequence of highlighted boxes (see Figure 3) or fixation points appear. Pre-delay instructions indicate whether the memory task is "forward," "down to up," or "fixate." After the delay, the probe is shown.

Figure 2 shows the trial sequence. First, subjects are told what the trial task will be: "memory," "no memory," or "free eye movements." Following an interstimulus interval (ISI) of 500ms, subjects receive the sequence of highlighted squares (Figure 3) followed by further instructions: "forward," "down-to-up," or "fixate." After the return to baseline delay, subjects receive the probe: a highlighted square in the sequence.

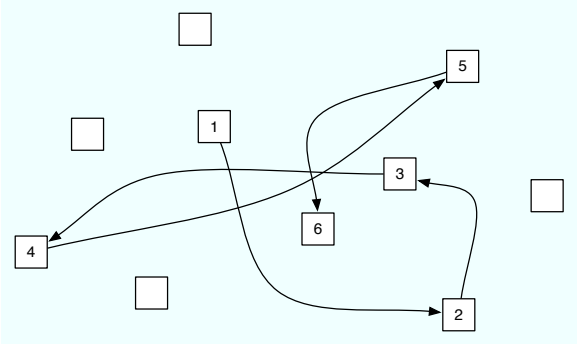

Figure 3: Memory task stimulus. A fixed number of squares are oriented on a screen. During memory tasks, a sequence of the squares are highlighted in a random order. An example highlight sequence for memory is shown.

Behavioral Tasks. During forward memory, manipulate memory, and guided saccade tasks, a sequence of squares was highlighted followed by a delay and then a task prompt (see Figures 2&3). In forward memory tasks, subjects were presented a sequence of highlighted squares. Then, given one of highlighted

Table 3: Comparison of minimum distances to reference function activation between manifold learning methods in combination with complex ICA and complex ICA alone. For each bin (columns), the minimum distance for each method is shown (*i.e.* the distance of the best matching components in each frequency bin).

	1	2	3	4	5	6	7	8	9
Subject H									
ICA	30.9077	29.5631	28.0292	25.5206	22.1484	18.0443	13.3546	8.1448	2.8922
Isomap	29.9395	29.4552	27.8957	25.4514	22.1252	18.0155	13.3221	8.1521	2.8443
Diff Map	30.2166	29.6940	28.1611	25.6646	22.3125	18.1816	13.4606	8.2916	2.9831
LLE	30.2003	29.6894	28.1652	25.6854	22.3254	18.1924	13.4682	8.2789	2.9805
Subject K									
ICA	30.1220	29.5681	28.0250	25.5203	22.1783	18.0569	13.3136	8.2129	2.9432
Isomap	30.1864	29.6640	28.1538	25.6675	22.2939	18.1749	13.4683	8.2771	2.9618
Diff Map	30.2093	29.7037	28.1519	25.6816	22.3158	18.2034	13.4654	8.2952	2.9904
LLE	30.2080	29.6818	28.1548	25.6716	22.3262	18.1962	13.4695	8.2875	2.9790
Subject S									
ICA	30.2240	29.7156	28.1836	25.6819	22.3365	18.2140	13.4956	8.3269	3.0025
Isomap	30.2044	29.7038	28.1697	25.6823	22.3215	18.2035	13.4576	8.2912	2.9832
Diff Map	30.2066	29.6898	28.1527	25.6871	22.3178	18.1870	13.4652	8.2941	2.9765
LLE	30.1965	29.6953	28.1583	25.6731	22.3160	18.1937	13.4655	8.2990	2.9525
Subject T									
ICA	30.2336	29.7114	28.1868	25.6938	22.3342	18.2210	13.4869	8.3183	3.0027
Isomap	30.2077	29.6922	28.1493	25.6869	22.3167	18.1991	13.4576	8.2959	2.9792
Diff Map	30.2115	29.6900	28.1641	25.6714	22.3120	18.1877	13.4735	8.2751	2.9868
LLE	30.2100	29.6754	28.1444	25.6737	22.3142	18.1942	13.4569	8.2977	2.9799
Subject W									
ICA	30.2307	29.7087	28.1928	25.7006	22.3436	18.2214	13.4755	8.3068	2.9984
Isomap	30.1833	29.6769	28.1525	25.6727	22.3140	18.1835	13.4538	8.2765	2.9460
Diff Map	30.2106	29.6915	28.1508	25.6780	22.3146	18.1972	13.4617	8.2923	2.9748
LLE	30.2044	29.6896	28.1588	25.6591	22.3199	18.1946	13.4617	8.3007	2.9805

Table 2: Time domain comparison using Postle *et al.* dataset. Correlation of power spectra for activation time courses generated for each subject using ICA and the various dimensionality reduction methods: ICA (ICA alone), Isomap (Isomap and ICA), LE (Laplacian eigenmap and ICA), and LLE (Local linear embedding and ICA).

Subject	ICA	Isomap	LE	LLE
H	0.7771	0.6944	0.8600	0.8774
K	0.9412	0.7288	0.8229	0.7897
S	0.8423	0.7319	n/a	0.8719
T	0.8903	0.7657	0.8274	0.8094
W	0.9262	0.7156	0.8268	0.8711

squares, subjects were asked to recreate the sequence from that point on. In the manipulate memory task, subjects were asked to reorder the highlighted sequence of squares from bottom to top, so that the lowest highlighted square should be first in the sequence and the highest should be last. In the guided saccade task, subjects were asked to simply follow another highlighted sequence on the screen. In the free saccade task, subjects were not shown a highlighted sequence, and were asked to simply saccade left and right repeatedly.

In these experiments, we consider a ROI based on the reported areas in each subject. We constrain the ROI to be even smaller. In this experiment, we use the manipulate memory task as the experimental task alone and generate the reference function for each subject.

Time Domain Experiment. We apply the method to time domain signals, as in the left/right task. In this case, dimensionality reduction methods produce signals that do not compare on the time axis. In this case, we compare the correlation of the power spectra from activation time courses to the reference power spectrum. Here we compare the first 50 frequency values, accounting for over 99% of the frequency content in the reference signal. ICA generated components are well correlated across subjects. However, local linear embedding appears to outperform ICA in subjects H and S (see Table 2).

Frequency Domain Experiment. We apply the method to the frequency domain signals using the same comparison method used in the left/right dataset. In this case, dimensionality reduction methods outperform ICA alone for most subjects. For sub-

ject H, Isomap appears to recover sources whose activation better matches the reference function. For subject K, ICA alone appears to outperform the manifold learning methods. For subjects S,T, and W, manifold learning appears to generate better source separation.

5 DISCUSSION

In our method, we motivate manifold learning as a pre-processing step to convolutive source separation by appealing to the need for dimensionality reduction. The idea in using manifold learning to reduce dimensionality is that we can automatically identify the voxels in the ROI that contain the most information about the activation sequence of the area. Furthermore, the frequency space representation of voxels results in much higher dimensionality; therefore, reducing the dimensionality is critical to feasible component analysis. The computational cost of filtering unneeded dimensions at component analysis time is far greater than at manifold learning time.

An additional side effect of manifold learning is that we not only find features representing the activation in an area, but we also space the data along these features so that we implicitly perform whitening of the data. In the normal use of time domain ICA one explicitly performs PCA as a first step in order to whiten the data. In the time domain this decorrelates the data, making the source separation task return better results.

We have shown improvement by using manifold learning as a preprocessing step to complex source separation. One benefit of this method is that the reduced dimensionality representation requires less computation by complex ICA. Furthermore, little prior information is needed to define the ROI. These results suggest that a more tightly integrated approach would lead to better separation performance.

REFERENCES

Anemuller, J., Sejnowski, T., and Makeig, S. (2003). Complex independent component analysis of frequency-domain electroencephalographic data. *Neural Networks*, 16:1311–1323.

Belkin, M. and Niyogi, P. (2003). Laplacian eigenmaps for dimensionality reduction and data representation. *Neural Computation*, 15:1373–1396.

Bingham, E. and Hyvarinen, A. (2000). A fast fixed-point algorithm for independent component analysis of complex valued signals. *International Journal of Neural Systems*, 10(1):1–8.

Coifman, R. R. and Lafon, S. (2006). Diffusion maps. *Applied and Computational Harmonic Analysis*, 21:5–30.

Dogil, G., Ackerman, H., Grodd, W., Haider, H., Kamp, H., Mayer, J., Reicker, A., and Wildgruber, D. (2002). The speaking brain: a tutorial introduction to fmri experiments in the production of speech, prosody, and syntax. *Journal of Neurolinguistics*, 15(1):59–90.

Friston, K. (2003). Experimental design and statistical parametric mapping. In et al., F., editor, *Human brain function*. Academic Press, 2nd edition.

Hurd, M. (2000). Functional neuroimaging motor study.

Josephs, O., Turner, R., and Friston, K. (1997). Event-related fmri. *Human Brain Mapping*, 5(4):243–248.

McKeown, M. J., Makeig, S., Brown, G. G., Jung, T. P., Kindermann, S. S., Bell, A. J., and Sejnowski, T. J. (1998). Analysis of fmri data by blind separation into independent spatial components. *Human Brain Mapping*, 6:160–188.

Pederson, M. S., Larsen, J., Kjerns, U., and Parra, L. C. (2007). *Springer handbook on speech processing and speech communication*, chapter A survey on convolutive blind source separation methods. Springer Press.

Postle, B. R., Berger, J. S., Taich, A. M., and D'Esposito, M. (2000). Activity in human frontal cortex associated with spatial working memory and saccadic behavior. *Journal of Cognitive Neuroscience*, 12 Supp. 2:2–14.

Roweis, S. and Ghahramani, Z. (1999). A unifying review of linear gaussian models. *Neural Computation*, 11:305–345.

Roweis, S. and Saul, L. (2000). Nonlinear dimensionality reduction by locally linear embedding. *Science*, 290(5500):2323–2326.

Shen, X. and Meyer, F. G. (2006). Nonlinear dimension reduction and activation detection for fmri dataset. In IEEE, editor, *Proceedings of 2006 conference on computer vision and pattern recognition workshop*. IEEE.

Tenenbaum, J., de Silva, V., and Langford, J. (2000). A global geometric framework for nonlinear dimensionality reduction. *Science*, 290(5500):2319–2323.

AN EVALUATION OF THE RELAXATION EFFECT OF MUSIC BASED ON THE RELATIONSHIPS BETWEEN THE CONDITION OF PULSE AND MUSIC TEMPO USING THE EEG AND HRV BASED INDICATORS

Genki Murayama*, Shohei Kato*, Hidenori Itoh* and Tsutomu Kunitachi**
*Dept. of Computer Science and Engineering, Graduate school of Nagoya Institute of Technology
Gokiso-cho, Showa-ku, Nagoya, 466-8555, Japan
**Dept. of Computer Science and Art, Daido Institute of Technology, 10-3 Takiharu-cho, Minami-ku, Nagoya, 457-8530, Japan
murayama@juno.ics.nitech.ac.jp, shohey@ics.nitech.ac.jp, itoh@ics.nitech.ac.jp, tomkuni@daido-it.ac.jp

Keywords: Music tempo, relaxation, EEG, HRV.

Abstract: This paper attempt to investigate the relationships between relaxation effect of music and rhythm of human body (in this paper fingerplethysmogram (so called ”pulse”) is adopted) using EEG and HRV based two relaxation indicators. We focus on following viewpoints: synchronization between pulse and music, the tendency of pulse beat and pulse-music tempo ratio (μ). This paper reports the experimental results that the pulse decreasing state is effective for EEG based indicator while HRV based indicator is high value at the pulse increasing state. Furthermore, we classify subjects into 3 groups by the analysis of synchronization between pulse and music tempo. This papar also reports the analysis of relationships between pulse-music tempo ratio (μ) and relaxation effect under the classification.

1 INTRODUCTION

Nowadays, ”Kansei” (emotion, feelings) evaluation has become more important keyword because many products are used by human and its feeling effects good or bad impression for the user. Many researchers are now researching the design and another factors bringing us better feelings. However, it is difficult to evaluate emotions because there are too many variations in ”emotion” and there is no general way to describe it. On the other hand, the objective way of evaluating emotion is studied in many institutes using bio signals. To evaluate the feelings, many indicators are adopted. For example, brain wave is popular one. Alpha wave of brain waves is usually adopted as a indicator of relaxation. In the ”Kansei” evaluation, a study about relaxation effect is performed flourishingly because many people needs relaxation in this demanding society. We focused on the relaxation effect of music because we can get the music relaxation easily sitting at the sofa in the house and no any special equipment is needed. (T. Nakamura, 2002) described the relationships between the tone of the sound and power spectrum of the alpha wave using electroencephalography (EEG). On the other hand, investigation on musical tempo and impression change using subjective valuation has been reported (K. Kurashima, 2004). In the other case, the substance in saliva is used as a indicator of stresses. Music research is also performed in many viewpoints because music has so many elements: rhythm, tempo, harmony, instrumental and more. Various researches focused on the music tempo has been reported. For example, synchronization between pulse and music tempo is described in (M. Fukumoto, 2004). The paper stated that synchronization effect is related to relaxation effect calculated from heart rate variability. In this paper, we try to investigate the relaxation effect of music based on the relationships between the rhythm of human body and music tempo in addition to synchronization effect, and report many empirical results about relaxation effect.

2 SUBJECT OF ANALYSIS

Relaxation indicators:
In this paper, we adopted electroencephalography (EEG) and heart rate variability (HRV) to calcualte relaxation indicators. EEG analysis was performed using the HSK central rhythm monitor system devel-

Figure 1: Brain wave and pulse sensor.

oped by Human Sensing Inc in Japan.

This equipment measures the Fp1 and Fp2 channels of the EEG and estimates the Comfortable-Degree (CD) (Yoshida, 2000). Ordinarily, EEG is measured with the International 10:20 method, but we adopted the method described in (Yoshida, 2000) because it lightens a burden of the subject. We used the content ratio of high frequency (HF) as the HRV indicator calculated from the finger plethysmogram (simply called, pulse).

- Comfortable-Degree
  We used Comfortable-Degree as an indicator of relaxation at brain. This indicator is calculated from the frequency fluctuation of the brain waves. Tomoyuki Yoshida tried to make a indicator of comfortable-feelings (Yoshida, 2000). He insisted that human psychological condition changes every time if the physical situation was same. So we have to evaluate the fluctuation of the human emotion in an objective way. The research groups performed the experiment that exhibit many good or bad smells, sounds and musics for the subject and investigated the fluctuation of the alpha wave frequency. According to the result, the gradient of the spectrum of brain waves in the left frontal area is get closed to 1.0 in the situation of comfortable. Conversely, that is get closed to 0 in the situation of uncomfortable. On the other hand, the gradient of the spectrum of brain wave in the right frontal area is get closed to 0 in the condition of subject felt awakening. As a result, the expression of comfortable degree is consisted below.

$$CD(\%) = \sqrt{{Fp1_{slope}}^2 + {Fp2_{slope}}^2}/2 * 100, \quad (1)$$

  where $Fp1_{slope}$ and $Fp2_{slope}$ mean the gradient of the spectrum of alpha wave in Fp1 and Fp2 channel, respectively.

- Content Ratio of HF
  Our heart beat is varying every time and R-R Interval (peak to peak) also changes every time. Many researches focused on this phenomenon clarified that the changes of R-R interval is related to autonomic nerve system (Task Force of the European Society of Cardiology, 1996). This evaluation method is called Heart Rate Variability (HRV). The method is performed following steps.

  – calculate R-R interval from pulse data (shown in Figure 2).

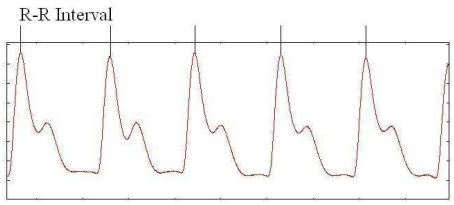

Figure 2: A sample of pulse data.

  – generate an interpolated R-R interval line (shown in Figure 3).

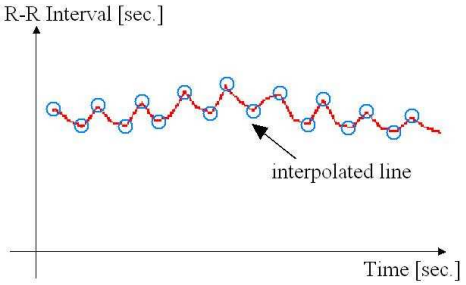

Figure 3: Interpolated R-R line.

  – Apply the Coarse Graining Spectral Analysis (CGSA) (Y. Yamamoto, 1991)(Y. Yamamoto, 1993) to make the indicator of autonomic nerve system clear.
  – In CGSA method, FFT is performed to obtain the frequency power spectrum.
  – separate the spectrum into Low frequency (From 0.024 Hz to 0.15 Hz) and High frequency (From 0.15 Hz to 0.6 Hz).

  We used Content Ratio of HF as an indicator of relaxation at body. LF/HF is used as an indicator of the sympathetic nervous system (SNS). Content ratio of HF, i.e., $HF/(HF+LF)$, is used as an indicator of the parasympathetic nervous system (PNS) that is also used as a relaxation indicator because parasympathetic nervous system is dominant during relaxation. We calculated the content ratio of HF by the HRV method from the pulse.

Relationships between pulse and music:

- Synchronization between pulse and music tempo
  (Y. Kusunoki, 2003) stated the synchronization phenomenon between pulse and music tempo

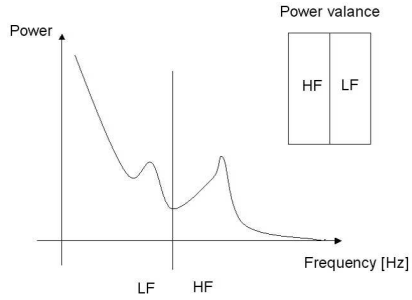

Figure 4: Spectrum of HF/LF valance (in rest).

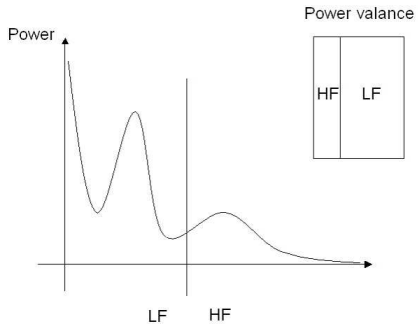

Figure 5: Spectrum of HF/LF valance (in tilt).

(Later, it is simply called as "synchronization") as a relationship between pulse and music tempo. (M. Fukumoto, 2004) explained that synchronization period is the period where the ratio between heart rate and the number of music beats is kept constant, and indicated that a total of the short synchronization periods in the music experiment were significantly larger than in the control experiment. For example, a state that the subject's pulse beats 3 times while a certain music played in one musical unit continues for a certain period of time (see Figure 6).

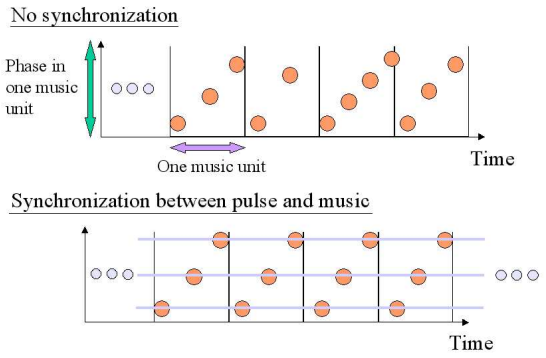

Figure 6: Example of synchronization.

To analyze the synchronization between pulse and music tempo, we adopted the method described in (Y. Kusunoki, 2003). The data (relaxation indicator) obtained are classified into three groups: no sound, no synchronization, pulse and music synchronization. In addition to this classification, no synchronization state is further more classified into two groups; pulse beat increased and pulse beat decreased.

- Pulse-Music Tempo Ratio
  In this paper, we introduce a scale that is called the pulse-music tempo ratio. By classifying the condition of the subject from the pulse-music tempo ratio, we can evaluate the relationships between relaxation indicator and the state of the subject' s pulse and the tempo of music. Musical tempo T in every minute is expressed by the sequence T_j ($j = t_m, t_{m+1}, ..., M$), where j is the minute with music presence, t_m is the starting minute of music presence, and M is the total minutes of measurement. Subject i' s average value of each indicator in the j-th minute is described as $CD_{i,j}$ and $HF_{i,j}$. The average value of each indicator in all listening terms is described as $\overline{CD}$ and $\overline{HF}$. Subject i' s average pulse beats in the j-th minute is described as $P_{i,j}$. Then, we denote the pulse-music tempo ratio as $\boldsymbol{\mu}_i$. The $\boldsymbol{\mu}_i$ value for subject i is calculated every minute using the following equation:

$$\boldsymbol{\mu}_i = \{\mu_{i,t_m}, \mu_{i,t_{m+1}}, ..., \mu_{i,M}\}, \tag{2}$$

where

$$\mu_{i,j} = P_{i,j}/T_j, \tag{3}$$

For example, (Reinhaldt, 1999) reported that synchronization is well observed in the 2:3 state of pulse and music tempo ratio. In this case, 2:3 state of the pulse-music tempo ratio corresponds to $\mu = 1.5$.

Finally, we define the efficiency values τ_{HF} and τ_{CD} for each indicator calculated from the following equations:

$$\tau_{HF}(\mu) = \frac{\Sigma_{i=1}^{N}\Sigma_{j=t_m}^{M}\{s(\mu_{i,j},\mu)comp(HF_{i,j},\overline{HF})\}}{\Sigma_{i=1}^{N}\Sigma_{j=t_m}^{M}\{s(\mu_{i,j},\mu)\}}, \tag{4}$$

$$\tau_{CD}(\mu) = \frac{\Sigma_{i=1}^{N}\Sigma_{j=t_m}^{M}\{s(\mu_{i,j},\mu)comp(HF_{i,j},\overline{HF})\}}{\Sigma_{i=1}^{N}\Sigma_{j=t_m}^{M}\{s(\mu_{i,j},\mu)\}}, \tag{5}$$

where N is the number of subjects, and

$$s(\mu_1,\mu_2) = \begin{cases} 1 & (0 \le \mu_1 - \mu_2 < K) \\ 0 & otherwise \end{cases}, \tag{6}$$

$$comp(a,b) = \begin{cases} 1 & (a > b) \\ 0 & otherwise \end{cases} \tag{7}$$

In this definition, τ is the ratio of the frequency where each indicator ($HF_{i,j}$, $CD_{i,j}$) is higher than its average value ($\overline{CD}$, $\overline{HF}$) to the frequency where $\mu_{i,j}$ is classified into μ. Function s classifies the condition of $\mu_{i,j}$ into each value of the pulse-music tempo ratio by the appropriate value K.

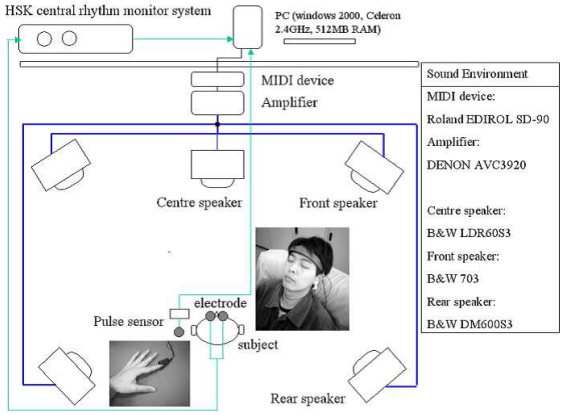

Figure 7: Experiment environment.

3 EXPERIMENT PROCEDURE

The subjects were 12 males in their 20s ($N = 12$). During the experiment, the subjects sat on a sofa and closed their eyes. The experiment consisted of two parts. In the first 4 min, no sound was presented, and then music was played for the next 10 min ($t_m = 5$ and $M = 14$). The experimental environment is shown in Figure 7. We presented an MIDI (Musical Instruments Data Interface) digital file 'Gymnopedie, No.1 (E. Satie)' as the musical stimulus, as used in (M. Fukumoto, 2004), and the tempo of the music was gradually decreased from 66 to 48 BPM every minute. The filter of the EEG analysis system was adjusted to the following settings; low pass filter: 13 Hz, high pass filter: 8 Hz. During the period of the experiment, a finger plethysmogram (simply called 'Pulse') that sampled at 500 Hz was measured from a subject's forefinger. The analog data obtained were translated to digital data and transferred to a PC through an USB port. To detect the synchronization of musical tempo and pulse, we adopted the method described in (Y. Kusunoki, 2003). The output signal from the MIDI device was transferred to the amplifier through a fibre optical cable. The volume of sound was fixed at a level that was not annoying for the subject.

4 RESULTS AND DISCUSSION

4.1 Analysis by Time

Measured average pulse tempo and presented music tempo is shown in Figure 8. Figure 8 indicate that the average value of pulse beat decreased 2.9 BPM in all the listening term, while the change of pulse beat includes the individual differences.

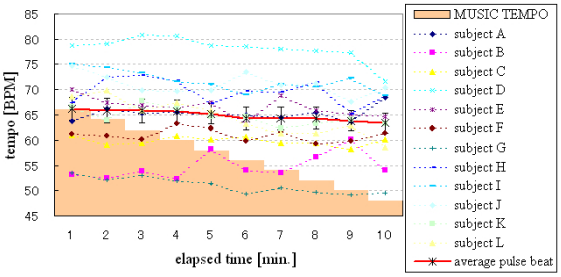

Figure 8: Music tempo and pulse tempo.

In next section we tried to analyze the relaxation indicator for each state of the subject using the pulse-music tempo ratio. According to the variance of the obtained pulse-music tempo ratio ($\mu_{i,j}$), we considered $K = 0.1$ to be appropriate to classify $\mu_{i,j}$ values in this experiment.

4.2 Analysis by Synchronization

The experimental results have some different tendencies of synchronization. So we classified observation type of synchronization into 3 groups (shown in Fig. 9): observed at low ratio, observed at high ratio and observed in wide range of ratio. In this paper "ratio" means the pulse-music tempo ratio.

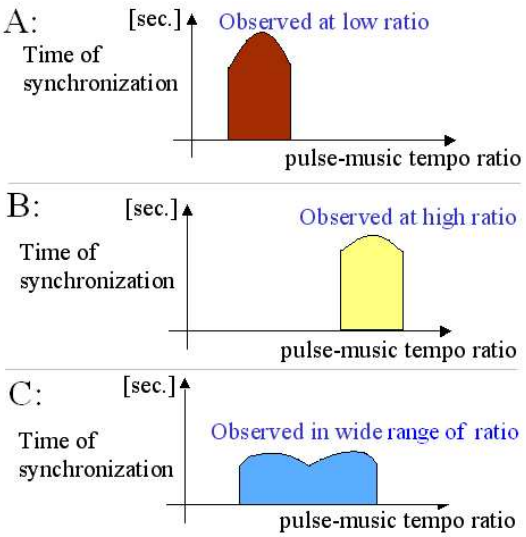

Figure 9: Classification of synchronization.

Experimental result of synchronization were classified into 3 groups shown in from Fig. 10 to Fig. 12. The number of person in each groups is following:

- group A(observed at low ratio): 4 subjects
- group B(observed at high ratio): 3 subjects
- group C(observed in wide range of ratio): 5 subjects

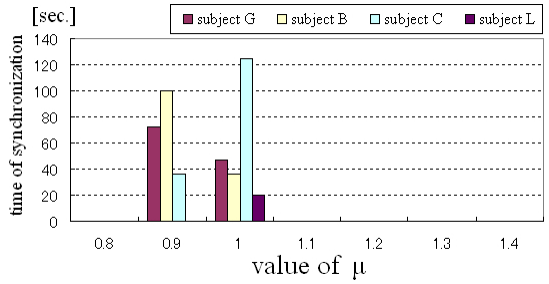

Figure 10: Synchronization observed at low ratio (type A).

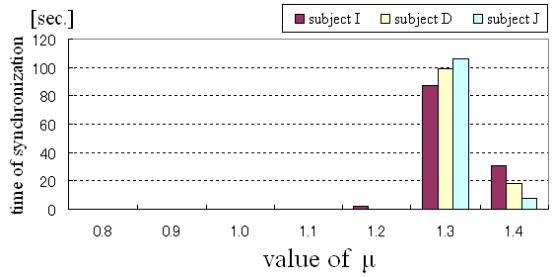

Figure 11: Synchronization observed at high ratio (type B).

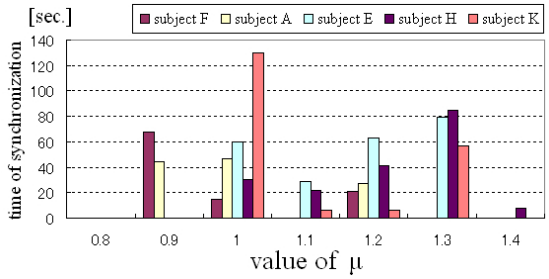

Figure 12: Synchronization observed at wide ratio (type C).

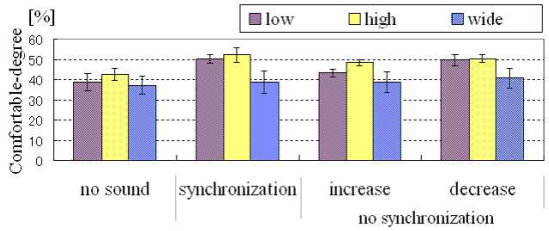

Figure 13: Synchronization and pulse tendencies and changes of *CD (each groups).*

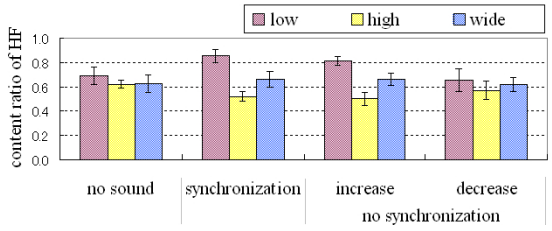

Figure 14: Synchronization and pulse tendencies and changes of *HF (each groups).*

Synchronization is observed in spread μ area as shown in figures. There is no correlation between synchronization occurrence and pulse-music tempo ratio. But the pulse-music tempo ratio that synchronization is well observed exists for each subject and the range has large individual differences (see Fig. 10, 11 and 12).

Next we considered the tendency of the pulse beat. In this paper, we adopted the gradient of the instantaneous pulse beats in every minute as an indicator of the pulse beat tendency as well as synchronization. Experimental result of Comfortable-degree and content ratio of HF were classified into four groups: no sound, tempo and pulse synchronization, pulse decrease at no synchronization, pulse increase at no synchronization, shown in Fig. 13 and 14.

In Figure 13, the changes of Comfortable-degree in type C ("observed in wide ratio" group) is smaller than the other groups. The results in Figure 13 says that Comfortable-degree is higher in both of synchronization state and pulse decreasing state. Furthermore, Comfortable-degree with listening to music (involves synchronization and no synchronization) is higher than no sound state. As well as Comfortable-degrees, Figure 14 indicates that the changes of content ratio of HF in type C group is smaller than any other groups. On the other hand, content ratio of HF is higher at the synchronization state same as reported in (M. Fukumoto, 2004). Comparing two indicators (Comfortable-degree and content ratio of HF), the tendency of content ratio of HF is uneven with Comfortable-degree. The relationships among relaxation effect and synchronization and pulse tendency in all group is shown in Figure 15 and 16.

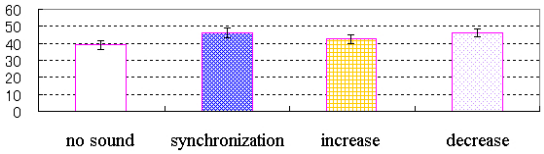

Figure 15: Sync. pulse tendency and *CD.*

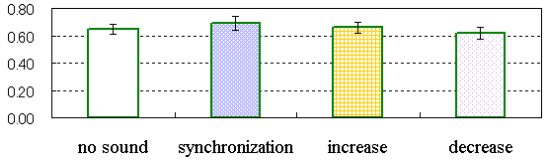

Figure 16: Sync. pulse tendency and *HF.*

We first considered the variance of each relaxation indicators. The result indicates that HF increases in the synchronization state, that is same as the result of each groups. However, the HF value in the no sound state is higher than that in the pulse decreasing state of no synchronization. On the other hand, Comfortable-degree in both the synchronization and no synchro-

nization was higher than that in the no sound state. This result implies that decreasing of the pulse tempo is as important as synchronization.

4.3 Analyze by Pulse-music Tempo Ratio

In this section, we calculated μ_i from the pulse tempo $P_{i,j}$ for all subjects and the musical tempo T_j, and the frequency ratios τ_{CD} and τ_{HF} from the relaxation indicators ($HF_{i,j}$,$CD_{i,j}$) for all subjects with the following μ values ($\mu = 0.8, 0.9, 1.0, ..., 1.4$).

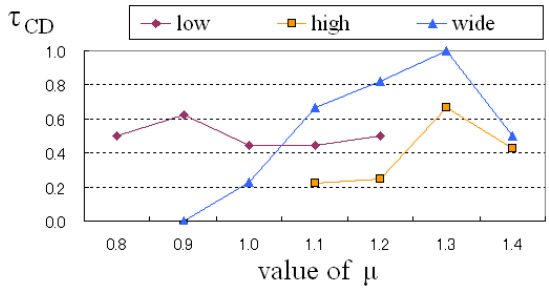

Figure 17: τ_{CD} in each group.

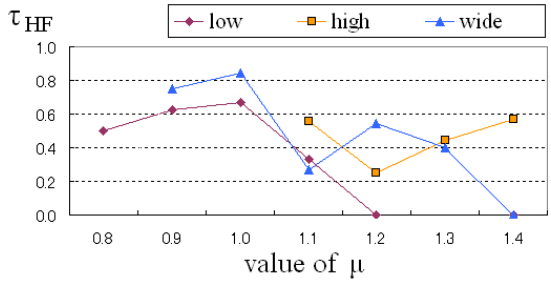

Figure 18: τ_{HF} in each group.

At first, the relationships between μ and τ_{CD}, τ_{HF} every groups (see Fig. 9) are shown in Figure 17 and Figure 18. The result in Figure 17 indicate that the effect for Comfortable-degree in type A group (”observed at low ratio”) changed constantly in observed pulse-music tempo ratio. In the other groups, Comfortable-degree was higher in the ratio around $\mu = 1.3$. In comparison with Comfortable-degree, content ratio of HF was more effective in lower pulse-music tempo ratio (around $\mu = 1.0$).

5 CONCLUSIONS

In this paper we reported the relationships among relaxation effect, pulse tempo and musical tempo based on two relaxation indicators. Experimental result indicate that the pulse decreasing state is effective for comfortable-degree calculated from brain waves as well as synchronization state. On The other hand, content ratio of HF calculated from pulse is high value in pulse increasing state. In analysis of synchronization, the tendency of synchronization occurrence is classified into 3 types. The analysis of pulse-music tempo ratio showed that each relaxation indicator has optimum μ value. According to these result, we suggest a new way of using music for relaxation. That is, selectively presenting music with slower tempo than the user’s pulse when the user wants the brain relaxation, or music with a tempo near to the user’s pulse when the user wants body relaxation. If there is a music music that has both two characteristics, that kind of music is better for us. In the future work, we will attempt to generate innovative music that depending on the tempo of the user’ s pulse at the beginning of music, the tempo of music is gradually decreased to $\mu = 1.3$. We will study whether that kind of music is effective for both content ratio of HF and Comfortable-degree.

REFERENCES

K. Kurashima, e. a. (2004). Influence of varying music tempos on musical perception and preference. *Information Processing Society of Japan (Special Interest Groups of Music) Technical Report*, 2004(111):125–130. (in Japanese).

M. Fukumoto, e. a. (2004). Synchronization between tempo of music and heart beat. *Journal of Japan Society of Kansei Engineering*, 4(2):17–24. (in Japanese).

Reinhaldt, U. (1999). Investigation into synchronization of heart rate and musical rhythm in a relaxation therapy in patients with cancer pain. *Research in Complementary Medicine*, 6(3):135–141. (in German).

T. Nakamura, e. a. (2002). Influence of the tone for brain wave. *Information Processing Society of Japan (Special Interest Groups of Music) Technical Report*, 2002(40):33–36. (in Japanese).

Task Force of the European Society of Cardiology, e. a. (1996). Heart rate variability standards of measurement, physiological interpretation, and clinical use. *European Heart Journal*, 17(3):354–381.

Y. Kusunoki, e. a. (2003). A statistical method of detecting synchronization for cardio-music synchrogram. *IEICE Trans. Fundamentals*, E86-A(9):2241–2247.

Y. Yamamoto, e. a. (1991). Coarse-graining spectral analysis. *J. Appl. Physiol.*, 71:1143–1150.

Y. Yamamoto, e. a. (1993). Extracting fractal components from time series. *Physica D*, 68:250–264.

Yoshida, T. (2000). 1/f like frequency fluctuation in frontal alpha wave as an indicator of emotion. In *Proceedings of the 2000 Spring Conference of KOSES & International Sensibility Ergonomics Symposium*, pages 99–103.

A NEW FRAMEWORK FOR REAL-TIME ADAPTIVE FUZZY MONITORING AND CONTROL FOR HUMANS UNDER PSYCHOPHYSIOLOGICAL STRESS

A. Nassef, C. H. Ting, M. Mahfouf, D. A. Linkens
Department of Automatic Control and Systems, The University of Sheffield, Sheffield, United Kingdom
(a.nassef, c.ting, m.mahfouf, d.linkens)@shef.ac.uk

P. Nickel, G. R. J. Hockey, A. C. Roberts
Department of Psychology, The University of Sheffield, Sheffield, United Kingdom
(p.nickel, g.r.j.hockey, a.roberts)@shef.ac.uk

Keywords: Adaptive Automation, Operator Functional State, Cardiovascular System, Electroencepharograph, Fuzzy Systems, Genetic Algorithms, Signal Processing.

Abstract: This paper proposes a new framework for the on-line monitoring and adaptive control of psychophysiological markers relating to humans under stress. The starting point of this framework relates to the assessment of the so-called operator functional state (OFS) using physical as well as psychological measures. An adaptive neural-fuzzy model linking Heart-Rate Variability (HRV) and Task Load Index (TLI) with the subjects' optimal performance has been elicited and validated via a series of real-life experiments involving process control tasks simulated on an Automation-Enhanced Cabin Air Management System (aCAMS). The elicited model has been used as the basis for an on-line control system, whereby the model predictions which indicate whether the actual system is in error or not, have been used to modify the level of automation which the system may operates under.

1 INTRODUCTION

With increasingly complex design of automation in safety-critical applications, there is a growing concern for the consequences of performance breakdown. This is because the human operator's role has become compromised with increasing operational demand, stress and fatigue, which all threaten safety and reliability (Hockey *et al.*, 2003). The approach taken to this problem in this paper is based on an 'Operator Functional State' (OFS) framework in which the performance of the operator is constrained by requirements to manage the automation tasks and his/her own personal state.

The OFS model should predict that, for a period before manifest breakdown occurs, the operator will be in a vulnerable state, because of reduced spare capacity to respond to emergencies. The goal of the current programme of work is to develop models for evaluating psychophysiological markers of this high risk strain state. If such states can be reliably detected, they can be used to trigger a switch of control from human to computer, through an adaptive automation (AA) interface, reducing the risk of operational breakdown (Kaber *et al.* 2001).

A likely marker is the 'task load index' (TLI) identified by Gevins and his group (Gevins and Smith, 1999). TLI is based on the presence of high levels of theta activity at frontal midline sites, with concomitant attenuation of alpha power in parietal sites [theta/alpha]. Observation of reduced frontal-midline theta power may reflect direct effects of fatigue or strategic disengagement from the executive requirements of the task management (Lorenz and Parasuraman, 2003).

To investigate this, a task known as automation-enhanced Cabin Air Management System (aCAMS) (Figure 1), developed by Hockey and colleagues (Hockey *et al.*, 1998, Lorenz, 2002) to simulate the atmospheric environment within a space capsule, is used. This semi-automatic system required operators to maintain an appropriate quantity and quality of breathable air by keeping system parameters (temperature, humidity, pressure, O_2, CO_2) within

normal ranges (primary task). The operators interacted with a dynamic visual display that provides data on system variables and functions via a range of controls and automation tools; this is a large mental burden to the operator.

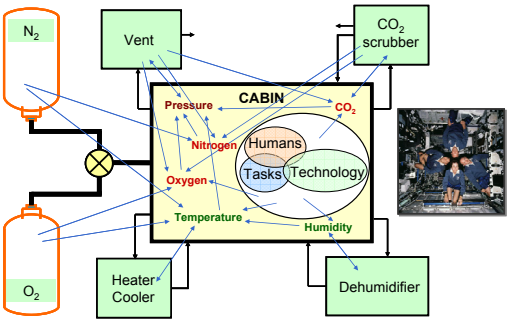

Figure 1: The aCAMS human-machine system.

The main objective of the research work presented in this paper is to propose a new framework for the on-line (real-time) monitoring of the human operator's performance for breakdown, stress or fatigure and the adaptive control of the level of automation. In order to achieve this a model that describes the input and output relationship between the psychophysiological measures (e.g. cardiovascular and EEG activities) and functional (i.e. cognitive, mental or psychological) states of the operator in a simulated process control environment is built first. The model can then be implemented in an adaptive automation control system to represent a kernel in OFS estimation. In the present investigation, the OFSs identification is achieved by using adaptive fuzzy modelling which requires the measured psychophysiological and primary task performance data only. The proposed modelling approaches are shown by simulation results to be capable of effectively exploiting the information contained in the measured physiological and performance data. By using this model the OFS may be identified or predicted by monitoring the changes in the psychophysiological and performance data, and hence the model output can be used as a bio-feedback signal in closed-loop automation control.

This paper is organised as follows: Section 2 will outline the chosen technical paradigm behind the intelligent systems-based modelling strategy. Section 3 will present the final models which were adopted and Section 4 shows how such models can be included in the real-time framework for monitoring and adaptive control. Finally, Section 5 will draw some conclusions in relation to this overall research study.

2 FUZZY MODELLING OF OPERATOR FUNCTIONAL STATE (OFS)

For the purpose of modelling fuzzy logic (Zadeh, 1965) was chosen as the main paradigm for characterising the input/output mappings because of its tolerance to uncertainties and also for the fact it can model human perception in a transparent way without a greater loss in accuracy. As a result, two types of fuzzy models were constructed and optimised automatically: one using neural networks leading to the Artificial Network Fuzzy Inference System (ANFIS) architecture (Jang, 1993) which utilises and the other using Genetic Algorithms (Goldberg, 1989) to estimate the parameters of the membership functions and the fuzzy rules of a Mamdani-type structure (Mamdani, 1974). In order to carry-out this modelling operation successfully it is important to first specify the variables associated with this input/output mapping and then carry-out the real-time experiments (Mahfouf *et al.,* 2006) which will enable one to collect the input/output data information as will be explained next.

2.1 Model Inputs and Output

The candidate inputs of the fuzzy model may include Heart Rate Variability (HRV) and EEG markers (TLI), which were found to be most sensitive to the changes in mental workload ((Fehrengerg and Wientjes, 2000);Nickel *et al*., 2005; Zhang *et al*., 2006). The optimal number of inputs selected from the above candidate inputs was determined by linear correlation analysis of the relationship between the input and output data. The single output of the model is '*Time in Range'* related to the primary task performance.

2.2 Data Acquisition and Analysis

The BioSemi® system (Biosemi, the Netherland) was used for EEG recording at 32 electrode sites defined by the international 10-20 system (Jasper, 1958). The electrodes were re-referenced to two linked mastoids. The EEG signal, sampled at a rate of 2048 Hz, was pre-processed with a band-pass filter between 1.6 and 25 Hz. The power in the three bands (i.e., theta, alpha and beta) for each of the selected electrode sites was calculated. The primary-task performance data ('Time in Range') were sampled every 1 min.

The heart rate (HR) signal was recorded every 1 s as soon as the aCAMS was started up. HRV_1 is defined as the average of the 0.1 Hz component

powers. HRV_2 is defined as the HR variation coefficient and given by the following expression:

$$HRV_2 = \frac{\sigma_{HR}}{\mu_{HR}} \quad (1)$$

where σ and μ denote the standard deviation and average of a HR segment of 7.5 min.

The TLI calculated using different EEG band powers was proposed in (Gevins et al., 1997). The TLI indices, TLI_1 and TLI_2 used in this paper, are given as follows:

$$\begin{cases} TLI_1 = \dfrac{P_{\theta,Fz}}{P_{\alpha,Pz}} \\ TLI_2 = \dfrac{P_{\theta,AF_z}}{P_{\alpha,CP_zPO_z}} \end{cases} \quad (2)$$

where P_θ and P_α denote the theta- and alpha-band power, respectively; the EEG frequency bands are defined in order as: θ, Fz: 6-7 Hz; α, Pz: 10-12 Hz; θ, AFz: 5-7 Hz; α, CPz: 8-10.5 Hz; α, POz: 10-13.5 Hz; and Fz, Pz, AFz, CPz, and POz are the five EEG electrode sites on the scalp introduced in the standard 10-20 system (Jasper, 1958).

3 RESULTS AND DISCUSSIONS

In this simulation the signal data sampling interval was taken to be 7.5 min and Gaussian MFs were used for both fuzzy models. The choice of the candidate input was mainly driven by the value of the input-output correlation factor (the higher the better), the training and testing data correlation factor (the higher the better) and the MSE values of the training and testing data. As a result, the two inputs HRV_1 and TLI_2 were selected for both fuzzy models. The training and testing data set was obtained from the 1st and 2nd experimental sessions, respectively. The ANFIS modelling result for P2 is shown in Figure 2.

Due to the large differences between the MSE values of the model output for each subject another index was introduced to differentiate between models. This index was named "Error Factor" and is defined by the ratio between the MSE of the model output when using the validating data and the MSE between the training and validating data as shown in Equ. (3).

$$\text{Error Factor} = \frac{MSE_{\text{model output-chk}}}{MSE_{\text{Tr-chk}}} \quad (3)$$

Using this new index it was found that Subjects P2, P4, and P10 led to the highest values, i.e. the worst performing models compared to the other subjects. So, those subjects' data have been chosen for the next study. The optimised rules of Mamdani-type fuzzy model and their weights are illustrated in Table 1. The optimal MFs and degrees of belief (rules' weight) in each rule are identified by using a GA approach. It is noted that the 1st, 2nd, 3rd, 11th, 12th, 13th, 15th and 16th rules (see Table 1 in 'bold' characters) are less important in terms of the smaller weights. The comparison of the model output and desired output is shown in Figure 3 for P2. Figure 4 illustrates the model output when HRV2 and TLI2 are used as inputs

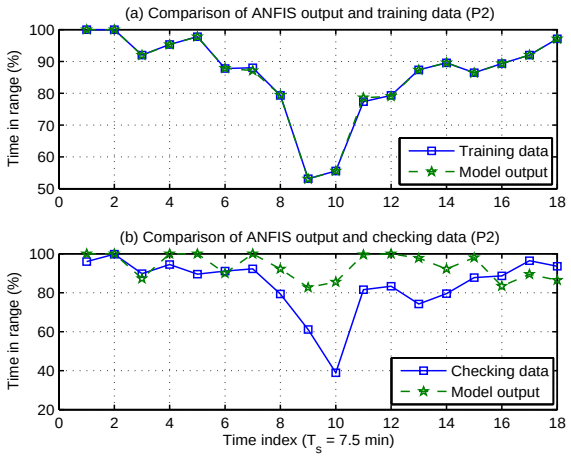

Figure 2: ANFIS modelling results for P2; HRV_1 and TLI_2 as inputs.

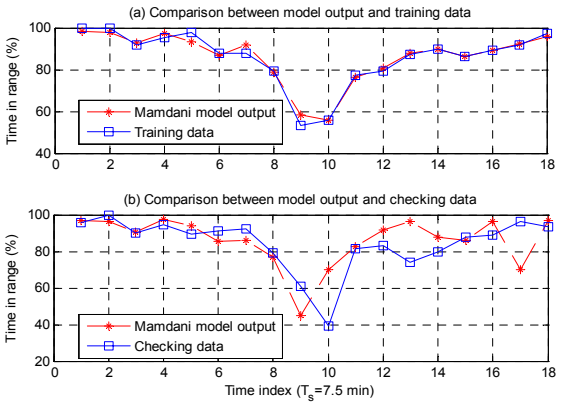

Figure 3: Modelling results via the GA-based Mamdani-type model for P2; HRV_1 and TLI_2 as inputs.

Table 1: The Mamdani-type fuzzy rules after optimization and their corresponding weights for P2 with the inputs HRV_1 and TLI_2.

No	Rule	
1	If HRV1 is M and TLI2 is S then TIR is VH	(**0.197**)
2	If HRV1 is M and TLI2 is S then TIR is VH	(**0.446**)
3	If HRV1 is M and TLI2 is M then TIR is H	(**0.159**)
4	If HRV1 is B and TLI2 is S then TIR is VH	(0.527)
5	If HRV1 is M and TLI2 is B then TIR is VH	(0.798)
6	If HRV1 is B and TLI2 is M then TIR is H	(0.983)
7	If HRV1 is M and TLI2 is B then TIR is H	(0.778)
8	If HRV1 is B and TLI2 is B then TIR is N	(0.470)
9	If HRV1 is S and TLI2 is B then TIR is L	(0.904)
10	If HRV1 is M and TLI2 is VB then TIR is L	(0.853)
11	If HRV1 is S and TLI2 is B then TIR is N	(**0.010**)
12	If HRV1 is S and TLI2 is B then TIR is N	(**0.013**)
13	If HRV1 is B and TLI2 is M then TIR is N	(**0.313**)
14	If HRV1 is B and TLI2 is VB then TIR is N	(0.864)
15	If HRV1 is B and TLI2 is B then TIR is N	(**0.331**)
16	If HRV1 is VB and TLI2 is M then TIR is N	(**0.352**)
17	If HRV1 is VB and TLI2 is M then TIR is N	(0.906)
18	If HRV1 is B and TLI2 is M then TIR is VH	(0.819)

Tables 2 and 3 show the model MSE's and the correlation factors for the three subjects data which only justify the initial choice of the criteria proposed for choosing the candidates' inputs and show that the model output is improved by using HRV_1 instead of HRV_2.

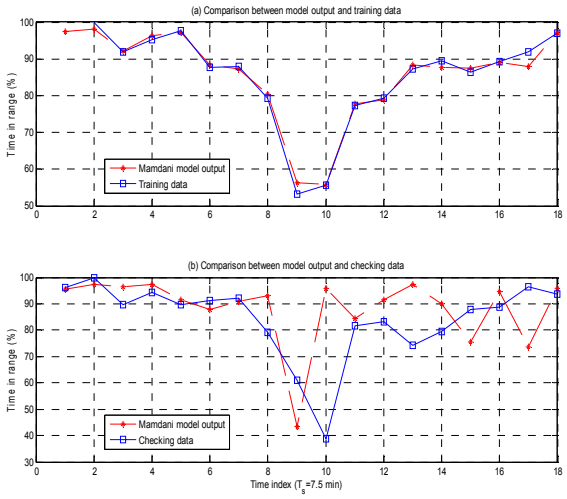

Figure 4: Model output of the GA Mamdani-type model of P2 for TLI_2 and HRV_2 as inputs.

Table 2: Training and testing MSEs and correlations of Mamdani fuzzy model for P2, P4 and P10 when inputs are HRV1and TLI2

No	MSE		Correlation		Error Factor
	Train	Check	Train	Check	2 inputs
P2	6.7506	130.340	0.983	0.712	2.931
P4	1.0860	93.672	0.997	0.8304	1.022
P10	8.4722	67.533	0.965	0.664	2.578

Table 3: Training and testing MSE and correlation values of the Mamdani fuzzy model for P2, P4 and P10 when the inputs are HRV2 andTLI2.

No	MSE		Correlation		Error Factor
	Train	Check	Train	Check	2 inputs
P2	7.213	194.930	0.981	0.518	4.383
P4	2.455	478.763	0.986	0.112	5.227
P10	2.840	130.624	0.988	0.541	4.987

4 THE NEW FRAMEWORK FOR REAL-TIME ADAPTIVE AUTOMATION

The adaptive fuzzy models developed previously allow for the OFSs to be used as bio-feedback signals in order to switch operations between human and machine. Hence, a conceptual adaptive automation control system built around aCAMS for the automation tasks is proposed as shown in Figure 5. The system was implemented using MFC (Visual C++ 8.0, Microsoft, USA) on a Window-XP computer. Psycho-physiological signals were collected using the BioSemi system with the recording scheme as described in Section 2.2. The two peripherals, aCAMS and BioSemi computers, communicate with the host system through Ethernet networking that uses the TCP/IP communication protocol.

Figure 6 shows a conceptual automation control system with the developed fuzzy OFS model for predictive control and primary task performance for immediate feedback reaction. The model analyzes psychophysiological responses every 128 s to provide information of how the system may drift into 'error'. Once a possible system abnormality is foreseen, the LOA Reallocator either switches system operation from human to machine or changes the level of automation (LOA). A "System in Error"

reported by aCAMS represents an anticipated system catastrophe if the system operation is not immediately intervened. The occurrence of such a fault elicits the LOA Reallocator for immediate automation intervention. This feedback correction is synchronized with aCAMS, 1 s in this case. Once an error occurs, the control is brought to a hysteresis loop which imposes a refractory duration to LOA commands to avoid adversary chattering effect. This coordinating scheme assures function allocation between human and machine for persistent system safety and operation performance.

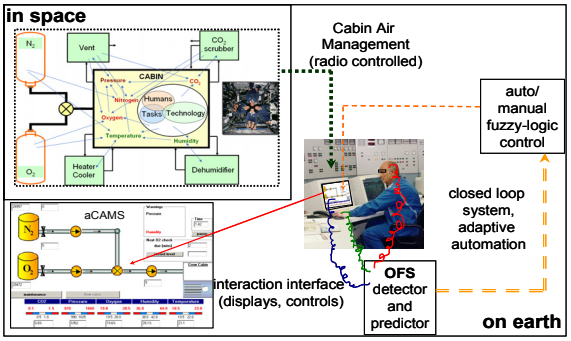

Figure 5: Conceptual adaptive automation control for the aCAMS human-machine system.

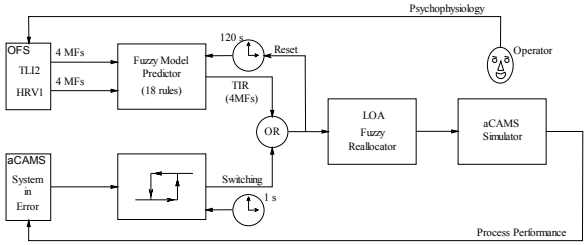

Figure 6: The control system of adaptive automation with OFS prediction and process feedback.

Figure 7 demonstrates the screenshot of a tentative experiment for which only the feedback correction loop of Figure 6 was activated. The screenshot shows aCAMS performance, psychophysiological responses, LOA allocation commands, subjective ratings, and system communication status on line. The automation controller took over the operation task from the operator and re-allocated LOA immediately responding to the occurrence of a system abnormality. The system operation recovered to a normal state subject to the LOA manipulation.

Figure 7: Screenshot of a tentative system operation. Top-left: aCAMS performance; top-right: psychophysiological response; bottom-left: LOA allocation; bottom-right: subjective ratings; status bar: monitoring of the system communication.

5 CONCLUSIONS

The first part of this paper related to the elicitation of ANFIS and Mamdani-type models for identifying OFSs using psychophysiological and performance measures. Model analyses revealed that the GA-based Mamdani-type model generalised better across the data used and that HRV_1 and TLI_2 represented the best correlating inputs to the performance output 'time in range'. The model represents a concise, transparent (easily understandable) and robust characterization of OFS and can be easily extended or modified to accommodate additional input variables, membership functions and fuzzy rules. The identification of these OFSs paved the way for proposing a new framework the real-time monitoring and adaptive control of automation in complex and safety-critical human-machine systems. Preliminary simulation studies using aCAMS, the OFSs predictor and the LOA fuzzy decision-maker showed that successful switching of system automation is possible. It is hoped that real-time experiments involving the same group of volunteers who partook in earlier experiments whose data were used for modelling will be conducted in the near future.

ACKNOWLEDGEMENTS

All authors wish to acknowledge financial support for this research work from the UK-EPSRC under Grant GR/S66985/01. A Nassef wishes to thank his sponsor; the Egyptian Cultural Bureau in London (UK), for its

financial support and C H Ting gratefully acknowledges the support of a research leave from The National Chiayi University, Taiwan.

REFERENCES

Fehrenberg, J., and Wientjes, C. W. J., 2000, 'Recording methods in applied environments' in *Engineering psychology: issues and applications*, ed. R. W. Backs & W. Boucsein W, Erlbaum, Mahawah, pp. 111-136.

Geveins, A. & Smith, M. E., 1999, 'Detecting transient cognitive impairment with EEG pattern recognition methods' *Aviation, Space, and Environmental Medicine*, vol. 70, pp. 1018-1024.

Gevins, A., Smith, E., McEvoy, L., & Yu, D., 1997, 'High-resolution EEG mapping of cortical activation related to working memory: Effects of task difficulty type of processing, and practice' *Cerebral Cortex*., vol. 7, pp. 374-385.

Goldberg, D. E., 1989, *Genetic Algorithms in Search, Optimization and Machine Learning*, Addison-Wesley.

Hockey, G. R. J., Gaillard, A. W. K. & Burov, O., 2003, *Operator functional State: the assessment and prediction of human performance degradation in complex tasks*, IOS Press, Amesterdam, The Netherlands.

Hockey, G. R. L., Wastell, D., & Saucer J., 1998, 'Effects of sleep deprivation and user-interface on complex performance: a multilevel analysis of compensatory control' *Human Factors*, vol. 40, pp. 233-253.

Jang, J., 1993, 'ANFIS: Adaptive-network-based fuzzy inference system' *IEEE Transations on Systems, Man and Cybernetics*, vol. 23, pp. 665-685.

Jasper, H. H., 1958, 'Report of the committee on methods of clinical examination in electroencephalography' *Electroencephalography and Clinical Neurophysiology*, vol. 10, pp. 370-375.

Kaber, D. B., Riley, J. M., Kheng-Wooi, T. & Endsley, M. R., 2001, 'On the design of adaptive automation for complex systems' *International Journal of Cognitive Ergonomics*, vol. 5, pp. 37-57.

Lorenz, B. and Parasuraman, R., 2003, 'Human operator functional state in automated systems: the role of compensatory control strategies' In *Operator functional State: the assessment and prediction of human performance degradation in complex tasks*, ed. G. R. J. Hokey, A. W. K. Gaillard & O. Burov, pp. 224-237, IOS Press, Amesterdam, The Netherlands.

Lorenz, B., 2002, 'Detection and prediction of an automation-induced state of impaired operator competence' In *Proceedings of NATO ARW on Operator Functional State*, Il Ciocco.

Mahfouf, M., Zhang, J., Linkens, D. A. Nassef, A., Nickel, P., Hockey, G. R. J., & Roberts, A.C., 2006, Adaptive Fuzzy Approaches to Modelling Operator Functional States in a Human-Machine Process Control System. In *Proceedings of FUZZIEEE2007*, London, UK, July 23-26..

Mamdani, E. H, 1974, 'Applications of fuzzy algorithms for control of simple dynamic plant' In *Proceedings IEEE,* (121), pp. 1585–1588.

Nickel, P., Roberts, A. C., & Hockey, G. R. J., 2005, Assessment of high risk operator functional state markers in dynamical systems – preliminary results and implications In *Proc. of Human Factors and Ergonomics Society Europe Chapter Annual Meeting 2005*, Turin, Italy, Oct. 26-28.

Zadeh, L. A., 1965, 'Fuzzy sets' *Information and Control*, vol. 8, pp. 338-353.

Zhang, J., Nassef, A., Mahfouf, M., Linkens, D. A., El-Samahy, E., Hockey, G. R. J., Nickel, P. & Roberts, A. C., 2006. Modelling and analysis of HRV under physical and mental workloads. In *Proc. of the 6th IFAC Symposium on Modelling and Control in Biomedical Systems*, Reims, France, Sept. 20-22, pp. 189-194.

DEVELOPMENT OF A PARTIAL SUPERVISION STRATEGY TO AUGMENT A NEAREST NEIGHBOUR CLUSTERING ALGORITHM FOR BIOMEDICAL DATA CLASSIFICATION

Sameh A. Salem, Nancy M. Salem and Asoke K. Nandi
Signal Processing and Communications Group
Department of Electrical Engineering and Electronics, The University of Liverpool
Brownlow Hill, L69 3GJ, Liverpool, UK
{sameh.salem, nancy.salem, a.nandi}@liverpool.ac.uk

Keywords: Data clustering, Partial supervision, Retinal blood vessels segmentation, Breast cancer classification.

Abstract: In this paper, a partial supervision strategy for a recently developed clustering algorithm *NNCA* (Salem et al., 2006), Nearest Neighbour Clustering Algorithm, is proposed. The proposed method (NNCA-PS) offers classification capability with smaller amount of a priori knowledge, where a small number of data objects from the entire dataset are used as labelled objects to guide the clustering process towards a better search space. Results from the proposed supervision method indicate its robustness in classification compared with other classifiers.

1 INTRODUCTION

Data clustering is a common technique for data analysis, which is used in many fields, including machine learning, data mining, pattern recognition, image analysis and bioinformatics. Clustering is the grouping of individuals in a population in order to discover structures in the data. In some sense, we would like the individuals within a group to be close or similar to one another, but dissimilar from the individuals in the other groups (Webb, 2003; Theodoridis and Koutroubas, 2003). Recently, a number of clustering algorithms has been proposed. The basic two types of clustering algorithms are partitional and hierarchical algorithms. Their main purpose (Xu and Wunsch, 2005; Jain et al., 1999; Jain and Dubes, 1988) is to evolve a $N_C \times n$ partition matrix $U(X)$ of a dataset X ($X = \{x_1, x_2, \ldots, x_n\}$) in R^p, representing its partitioning into a number of N_C clusters $(C_1, C_2, \ldots, C_{N_C})$. The partition matrix $U(X)$ may be represented as $U = [u_{mj}]$, $m = 1, \ldots, N_C$ and $j = 1, \ldots, n$, where u_{mj} is the membership of pattern x_j to cluster C_m. In hard partitioning of the data, the following conditions hold: $u_{mj} = 1$ if $x_j \in C_m$; otherwise, $u_{mj} = 0$.

Clustering is unsupervised classification where there are no predefined classes (labels) and no a priori knowledge of the data, while supervised classification requires a complete knowledge of the data where the class label and the number of classes (labels) are predefined (Bouchachia and Pedrycz, 2006). The process of labeling data objects is always an expensive and error-prone task that requires time and human intervention. In many situations, objects are neither perfectly labelled nor completely labelled. Therefore, the main idea of clustering with partial supervision strategy is to take the advantage of the smaller proportion of labelled objects to guide the clustering process of the unlabelled objects.

One of the typical applications of clustering with partial supervision is Computer-Aided Diagnosis (CAD) which has become one of the major research subjects in medical imaging and diagnostic radiology (Doi, 2005). The basic concept of CAD is to provide a computer output as a second opinion to assist radiologists' image interpretation by improving the accuracy and consistency of radiological diagnosis (Doi, 2005). The design of clustering with partial supervision in CAD can play an important role in improving CAD performance at small amount of knowledge, where only some labelled objects or regions of an image can assist in identification of any suspicious objects or regions.

This paper proposes a novel partial supervision strategy for the recently developed clustering algorithm *NNCA* (Salem et al., 2006). We examine its applicability and reliability using datasets from real-world problems, where the proposed method is used to segment the blood vessels in retinal images which

can help in early detection and diagnosis of many eye diseases, and it is used to classify breast tumors into either malignant or benign. Additionally, this paper presents a comparative evaluation of the proposed algorithm with some other algorithms.

2 THE NNCA CLUSTERING ALGORITHM

NNCA (Salem et al., 2006) is a modified version of the *KNN* classifier, and it is divided into two stages for creating N_C clusters. First stage is to select N objects randomly. Then non-overlapping clusters are created from these N objects, each of maximum size K_{init} objects (the choice of K_{init} ensures that more than N_C clusters are generated here). Afterwards an iterative control strategy is applied to update the clusters and their memberships by increasing the number of neighbours until N_C non-overlapping clusters are created. Second stage is to cluster the remaining objects. For each unclustered object q, K nearest clustered objects are found. Then, the cluster to which most of these K clustered objects belong is deemed to be one to which the object q belongs to.

The *NNCA* clustering algorithm is detailed in Algorithm 1. Let each object x be described by the feature vector:

$$< a_1(x)\, a_2(x), \ldots\ldots, a_p(x) >$$

where $a_r(x)$ is used to denote the values of the p-th attribute of data point x. If we consider two objects x_i and x_j, then the distance between them is defined as $d(x_i,x_j)$, which is expressed in Eq. 1.

$$d(x_i,x_j) = \sqrt{\sum_{r=1}^{p} (a_r(x_i) - a_r(x_j))^2} \qquad (1)$$

A fuzzy clustering, where all objects are allowed to belong to all clusters with different degrees of membership, is achieved by obtaining the mean value of the K nearest neighbours for each object in the dataset. Therefore, hard partition as well as soft partition can be obtained. For an object x_q to be clustered, let $x_1 \ldots x_K$ denote the nearest K clustered objects to x_q and $C(x_i) \in \{1, \ldots, N_C\}$ is the cluster index for object x_i. Hard partition value for x_q is:

$$C(x_q) = \arg\max_{n \in N_C} \sum_{r=1}^{K} \delta(n - C(x_r)), \qquad (2)$$

and soft partition vector is:

$$C(x_q) = \frac{\sum_{r=1}^{K} \delta(C(x_r) - C(x_i))}{K} \qquad (3)$$

Algorithm 1 Nearest Neighbour Clustering Algorithm (Salem et al., 2006)

Input (data, N, K_{init}, N_C, K) where:

$*$ N is the number of random objects to be clustered.

$*$ K_{init} is the nearest neighbour objects from N.

$*$ N_C is the user defined number of clusters.

$*$ K is the number of nearest clustered objects.

Step 1: Create N_C non-overlapped clusters
(a) Create initial clusters:
* Initially, all the N objects are unclustered.
let $M = 1$
For $i = 1$ to N
IF (object i is unclustered)
- Assign i and its unclustered neighbours (from N) of the K_{init} nearest neighbours to cluster # M.
- $M = M + 1$
End IF
End For

(b) Merge clusters:
* **DO**
- $K_{init} = K_{init} + 1$
- Assign each clustered object to the common cluster of the K_{init} nearest neighbours.
- Update the number of clusters $\rightarrow M$
WHILE ($M > N_C$)

Step 2: Find the nearest K neighbours for each remaining object
- Assign each unclustered object to the common cluster of the K nearest clustered objects.
- Use Eq. 2 to find hard partition and Eq. 3 to find soft partition.

Output (Hard partition vector, Soft partition matrix)

Figure 1 shows a sub-image from a colour retinal image and its ground truth along with the corresponding segmented sub-images after applying *NNCA*.

3 NNCA WITH PARTIAL SUPERVISION STRATEGY (NNCA-PS)

In this section, we propose to adapt *NNCA* algorithm with some labelled objects to guide the clustering process of the unlabelled objects, i.e., *NNCA* with partial supervision (*NNCA-PS*). The proposed method is divided into two stages. First stage is to select N_P objects randomly from the dataset to be labelled data ob-

(a) (b) (c)

Figure 1: (a) Original sub-image, (b) ground truth sub-image, and (b) sub-image with blood vessels clustered using *NNCA*.

jects and cluster these N_P objects into N_C clusters, as described in Sec. 2. Second stage is to classify each cluster according to the class label of the majority of its objects. For each labelled data object x_l of class C_i, assigned to cluster j ($1 \leq j \leq N_C$), if its cluster is classified to different class (label), then this data object will be assigned to the cluster that has the nearest objects and with the same label of it as in Eq. 4.

$$j = \begin{cases} j & if\ cluster\ j \in C_i \\ \arg\min\limits_{k \in C_i} \frac{\sum_{z \in k} d_{zx_l}}{|cluster\ k|} & if\ cluster\ j \notin C_i \end{cases} \quad (4)$$

where $|cluster\ k|$ is the number of objects in cluster k, and d_{zx_l} is the Euclidean distance between an object z and the labelled object x_l.
This process continues until all labelled objects within a cluster have the same class label. Then, the process continues to assign each unlabelled object x_u to the cluster that has the nearest labelled objects as in Eq. 5. Then, all the data objects that belong to different clusters with the same class labels can be assigned to that label.

$$j = \arg \min_{1 \leq k \leq N_C} \frac{\sum_{z \in k} d_{zx_u}}{|cluster\ k|} \quad (5)$$

where d_{zx_u} is the Euclidean distance between an object z and the unlabelled object x_u.
This proposed method will bias clustering towards a better search space. The proposed supervised method is detailed in Algorithm 2. Figure 2 shows two examples; abnormal (top) and normal (bottom) images and their results after blood vessels segmentation using *NNCA*, *NNCA-PS*, and *KNN* classifier.

A soft classification, where all objects are allowed in principle to belong to all classes with different degrees of membership, is achieved by adding the fuzzy memberships for each object with the clusters that belong to the same class label. Equations 6 and 7 show the fuzzy membership (u_{ix}) of object x to cluster i, and the soft membership ($U_{C_i x}$) of object x to class C_i respectively.

$$u_{ix} = \frac{1}{\sum\limits_{j=1}^{N_C} \left(\frac{d_{ix}}{d_{jx}} \right)^{2/(q-1)}} \quad (6)$$

$$U_{C_i x} = \sum_{j}^{N_C} u_{jx} \quad if\ cluster\ j \in class\ C_i \quad (7)$$

where d_{ix} is the distance from object x to the current cluster centre i (the average of all objects in cluster i), d_{jx} is the distance from object x and the other cluster centre j ($1 \leq j \leq N_C$), and q is the weighting exponent which controls the fuzziness of the resulting clusters ($q \geq 1$) (Webb, 2003). A value of $q = 1$ gives the hard membership, i.e. $u_{ix} = 1$ if $x \in$ cluster i; otherwise, $u_{ix} = 0$. In this study, $q = 1.5$ is used.

4 DATASETS

Two different types of real-world data are used to investigate whether the proposed algorithm scales well with the size and dimension of the dataset.

4.1 Retinal Images

For performance evaluation, a publicly available dataset is used (STARE,). The dataset consists of 20 images which are digitised slides captured by a TopCon TRV-50 fundus camera at 35° FOV. Each slide was digitized to produce a 605×700 pixels image, standard RGB, 8 bits per colour channel. Every image has been manually segmented by two observers to produce ground truth vessels segmentation. Ten of these images contain pathology and the other ten are normal, giving a good opportunity to test the proposed method in both normal and abnormal retinas.

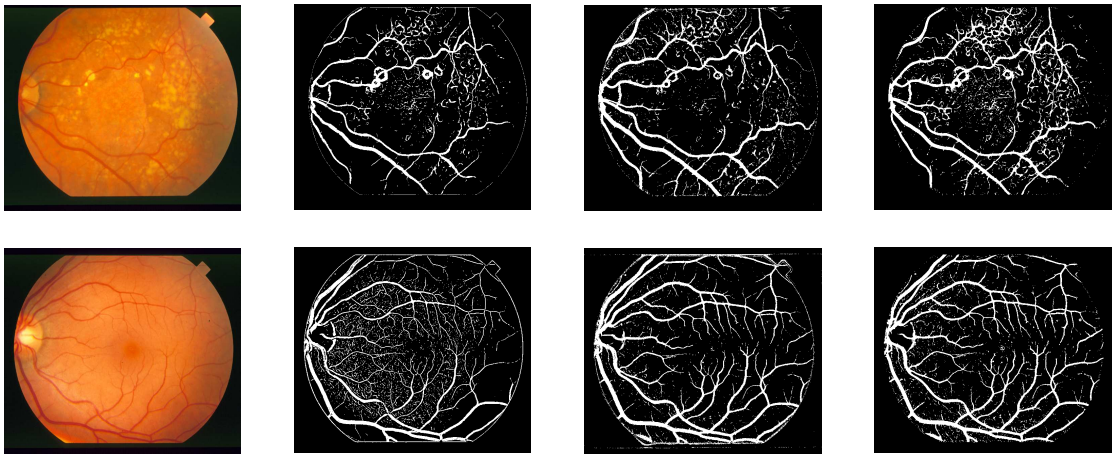

(a) (b) (c) (d)

Figure 2: (a) Original images, (b) output from the *NNCA* (hard decision), (c) output from the *NNCA-PS* (hard decision), and (d) output from the *KNN* classifier (hard decision).

Algorithm 2 *NNCA* with partial supervision strategy (*NNCA-PS*)

- *Step 1: Clustering using NNCA algorithm*
  1. Randomly select N_P points from the ground truth to be labelled objects.
  2. Cluster the N_P objects into N_C cluster using *NNCA* clustering algorithm.
- *Step 2: Apply the supervision strategy as follow:*
  1. Classify the clusters obtained by *NNCA* algorithm to the class of its most labelled objects.
  2. For each labelled object, if its cluster is classified to different class (label), then this object will be assigned to the cluster that has the nearest objects and with the same label of it.
  3. Each unlabelled object is assigned to the cluster that has the nearest objects and then classified to the class (label) of this cluster.

4.2 Breast Cancer Data

Two Wisconsin breast cancer datasets (UCI,) are considered in this paper. The first dataset contains 569 samples of 30 features each, and two classes: Benign (class 1 and 357 samples) and Malignant (class 2 and 212 samples). The second dataset contains 683 samples of 9 features each, and two classes: Benign (class 1 and 444 samples) and Malignant (class 2 and 239 samples).

5 EXPERIMENTAL RESULTS

5.1 Retinal Images

In our experiments, retinal blood vessels are segmented using the *NNCA* with partial supervised strategy (*NNCA-PS*). The performance is measured by the true and false positive rates. These rates are defined in the same way as in (Hoover et al., 2000), where the true (false) positive is any pixel which was hand-labelled as a vessel (not vessel), whose intensity after segmentation is above a given threshold. The true (false) positive rate is established by the dividing the number of true (false) positives by the total number of pixels hand-labelled as vessels (not vessels).

For purposes of comparison, we have compared the performance of *NNCA-PS* with *KNN* classifier (Salem and Nandi, 2006a) and *RACAL* with partial supervision strategy (Salem et al., 2007). For the *KNN* classifiers, two sets are required; one for training and the other for testing, so the dataset is randomly divided into two sets of images, each contains 5 normal and 5 abnormal images. The training set contains large number of training samples (423500 pixels/image), which is huge and is the main problem with this type of classifiers. To overcome such a problem, a random number of pixels are chosen from the field of view (FOV) of each image in the training set. The targets for these training samples are available from the manually segmented images. The testing

Table 1: *NNCA-PS*, *RACAL* and *KNN* hard decision results (average from 10 images (testing set)).

Image type	*NNCA-PS* Specificity %	*NNCA-PS* Sensitivity %	*RACAL* (Salem et al., 2007) Specificity %	*RACAL* (Salem et al., 2007) Sensitivity %	*KNN* (Salem and Nandi, 2006a) Specificity %	*KNN* (Salem and Nandi, 2006a) Sensitivity %
Normal	95.4%	90.2%	97.2%	85.9%	93.6%	88.6%
Abnormal	94.4%	87.8%	96.9%	80.3%	91.9%	82.4%
All images	94.8%	89.0%	97.0%	83.1%	92.7%	85.5%

Table 2: Average sensitivity at certain specificity values for 10 images.

Image type	Specificity %	*NNCA-PS* Sensitivity %	*RACAL* (Salem et al., 2007) Sensitivity %	*KNN* (Salem and Nandi, 2006a) Sensitivity %
Normal		90.8%	85.3%	86.6%
Abnormal	95%	86.7%	81.0%	76.2%
All images		88.8%	83.2%	81.4%
Normal		95.1%	92.9%	92.6%
Abnormal	90%	92.8%	93.5%	86.1%
All images		93.9%	93.2%	89.4%
Normal		96.9%	94.1%	95.1%
Abnormal	85%	95.4%	97.7%	90.9%
All images		96.1%	95.9%	92.9%
Normal		98.1%	98.1%	96.5%
Abnormal	80%	96.9%	96.6%	93.7%
All images		97.5%	97.4%	95.1%

set contains 10 images to test the performance of the classifier. The value of $K = 60$ and each feature is normalised to zero mean and unit standard deviation. While for *NNCA-PS* and *RACAL* with partial supervision strategy, only 30% of all the pixels are known (as vessels or non-vessels pixels) to demonstrate the advantage of using a small proportion of labelled pixels in clustering the unlabelled pixels.

For hard classification, the same set of images is used when comparing with the *KNN* classifier. As shown in Table 1, *NNCA-PS* achieves average sensitivity (true positive rate) of 89% at average specificity (1-false positive rate) of 94.8%, while the *KNN* classifier achieves sensitivity of 85.5% at average specificity of 92.7%. On average, the proposed *NNCA-PS* achieves better specificity as well as sensitivity than *KNN* classifier. On average, *RACAL* (Salem et al., 2007) achieves 2% higher specificity than *NNCA-PS*, but it offers 6% less sensitivity than *NNCA-PS*.

For soft classification as shown in Table 2, the soft classification results of the proposed *NNCA-PS* are compared with the soft results of *RACAL* and *KNN*. As shown, at 95% specificity, the proposed *NNCA-PS* achieves 5.5% and 4.2% higher sensitivity than *RACAL* and *KNN* respectively in case of normal images. Also in abnormal images at 95% specificity, *NNCA-PS* achieves 5.7% and 10.5% higher sensitivity than *RACAL* and *KNN* respectively. For higher specificity, *KNN* classifier achieves the lowest average sensitivity compared with *NNCA-PS* and *RACAL*, while both *NNCA-PS* and *RACAL* achieves on average comparable sensitivity.

5.2 Breast Cancer Datasets

For purposes of comparison, a series of experiments were carried out to examine the performance of *NNCA* when applying the proposed supervision strategy (*NNCA-PS*) on breast cancer datasets, where the classification results obtained by *NNCA* with the supervision strategy on breast cancer dataset 1 are compared with the results (Guo and Nandi, 2006) of different classifiers (*PCA/MDC* "Principal Component Analysis / Minimum Distance Classifier" (Theodoridis and Koutroubas, 2003; Cios et al., 1998), *FLDA/MDC* "Fisher Linear Discriminant Analysis / MDC" (Cios et al., 1998), *MLP* "Multi-Layer Percepton" (Duha et al., 2001), *SVM* "Support Vector Machine" (Hsu and Lin, 2002), and *GP/MDC* "Genetic Programming/ MDC" (Guo and Nandi, 2006; Kishore et al., 2002)). In order to achieve fair comparisons as in (Guo and Nandi, 2006), we randomly selected, without replacement, 100 samples (from the entire dataset) for training, and 100 samples for test-

Table 3: Comparison of classification accuracy (%) for breast cancer dataset 1 (testing set) using *NNCA-PS* and different classifiers, based on 100 experiments.

Algorithms		Best (%)	Average (%)	Std (%)
PCA/MDC	(Guo and Nandi, 2006)	88.7	88.6	N/A
FLDA/MDC	(Guo and Nandi, 2006)	88.9	88.6	N/A
MLP	(Guo and Nandi, 2006)	97.3	96.2	1.7
SVM	(Guo and Nandi, 2006)	96.7	96.3	0.8
GP/MDC	(Guo and Nandi, 2006)	98.9	97.4	1.5
NNCA-PS		99.5	97.2	1.2

ing; this process has been repeated 100 times. The target information, class labels, of the training samples is used to guide the clustering process of the testing samples using *NNCA-PS* algorithm. Table 3 shows comparison results of *NNCA-PS* along with different methods for classification. As shown, the best classification accuracy is achieved by *NNCA-PS* (99.5%), with the lowest being 88.7% obtained by *PCA/MDC* which gives comparable results as *FLDA/MDC*. Although the average classification accuracy obtained by *GP/MDC* are comparable with *NNCA-PS*, it gives 0.6% less than the best performance of *NNCA-PS* with higher standard deviation in classification accuracy. Therefore, the proposed method is more robust compared with other methods.

In order to reduce the amount of a priori knowledge, a small number of objects from the entire dataset are used as labelled objects. In these experiments, the effect of the number of labelled objects on the classification accuracy are investigated. We randomly selected a fraction from the entire dataset to be labelled objects. For each fraction, this process is repeated one hundred times without replacement. The best, average, and standard deviation of classification accuracy are obtained over one hundred runs for each fraction of labelled objects. For breast cancer dataset 1, as demonstrated in Table 4, the best and average classification accuracies increase with the increasing fraction of the labelled objects. As shown, the best and average classification accuracy of 98.2% and 96.3% respectively were achieved at 30% labelled objects, with the lowest being 96.2% and 91.5% for best and average accuracies respectively at 5% labelled objects. By examining the average and standard deviation of the classification performance, when 5% of the entire dataset are labelled, the average performance is the lowest, while it has the highest standard deviation compared with the other fractions of labelled objects. For breast cancer dataset 2 as recorded in Table 5, the standard deviations is lower than the standard deviations of breast cancer dataset 1. It is conjectured that the clusters on breast cancer dataset 2 are more compact with those in breast cancer dataset 1, as indicated in (Salem and Nandi, 2005). For 5% labelled objects and higher, the best classification accuracy is higher than 98% with a small decrease in the standard deviation and a significant increase in the average classification accuracy as demonstrated in Table 5.

Table 4: Classification accuracy (%) for breast cancer dataset 1 (entire dataset) using *NNCA* with partial supervision (*NNCA-PS*), based on 100 experiments.

labelled objects %	Best (%)	Average (%)	Std (%)
5	96.2	91.5	2.3
10	96.3	93.1	1.8
15	97.0	94.4	1.3
20	97.2	95.3	1.0
25	97.6	95.6	0.9
30	98.2	96.3	0.7

Table 5: Classification accuracy (%) for breast cancer dataset 2 (entire dataset) using *NNCA* with partial supervision (*NNCA-PS*), based on 100 experiments.

labelled objects %	Best (%)	Average (%)	Std (%)
5	98.0	96.0	1.2
10	98.1	96.3	1.1
15	98.5	96.7	0.9
20	98.7	97.0	0.8
25	98.7	97.4	0.7
30	99.2	97.9	0.5

When comparing the proposed *NNCA-PS* with *RACAL* for breast cancer data classification, where a small number of objects from the entire dataset are used as labelled objects. The average classification accuracy for breast cancer dataset 1 using *NNCA-PS* is 1% higher than *RACAL* algorithm while it achieves comparable accuracy for breast cancer dataset 2 as demonstrated in Tables 6 and 7. Moreover, the standard deviation of the classification performance of *NNCA-PS* for breast cancer dataset 1 is lower than *RACAL* which favors compact clusters,

Table 6: Comparison of classification accuracy (%) for breast cancer dataset 1 (entire dataset) using *NNCA* and *RACAL* with partial supervisions, based on 100 experiments.

labelled objects %	*NNCA-PS* Average(%) ± Std(%)	*RACAL* (Salem and Nandi, 2006b) Average(%) ± Std(%)
5	91.5 ± 2.3	90.6 ± 4.7
10	93.1 ± 1.8	92.1 ± 3.2
15	94.4 ± 1.3	93.5 ± 2.3
20	95.3 ± 1.0	94.4 ± 1.8
25	95.6 ± 0.9	94.9 ± 1.6
30	96.3 ± 0.7	95.2 ± 1.7

Table 7: Comparison of classification accuracy (%) for breast cancer dataset 2 (entire dataset) using NNCA and RACAL with partial supervisions, based on 100 experiments.

labelled objects %	*NNCA-PS* Average(%) ± Std(%)	*RACAL* (Salem and Nandi, 2006b) Average(%) ± Std(%)
5	98.0 ± 1.2	97.5 ± 1.4
10	98.1 ± 1.1	97.9 ± 0.3
15	98.5 ± 0.9	98.2 ± 0.3
20	98.7 ± 0.8	98.6 ± 0.3
25	98.7 ± 0.7	98.6 ± 0.3
30	99.2 ± 0.5	98.6 ± 0.3

while it achieves slightly higher standard deviations in breast cancer dataset 2. This may be the result of the *NNCA-PS* achieving clustering without any control of cluster sizes while *RACAL* is constrained with a radius parameter δ_0 which controls the size of the clusters.

6 CONCLUSIONS

In this paper, we have proposed a partial supervision strategy for a recently developed clustering algorithm (*NNCA*) to act as a classifier. We examined its applicability and reliability using datasets from real-world problems. As shown, the proposed *NNCA-PS* has the ability to classify pixels of retinal images into those belonging to blood vessels and others not belonging to blood vessels, and it also has the ability to classify breast tumors into either benign or malignant. Experimental results show that the proposed algorithm offers better classification accuracies compared with certain other classifiers.

REFERENCES

Bouchachia, A. and Pedrycz, W. (2006). Data clustering with partial supervision. *Data Mining and Knowledge Discovery*, 12:47–78.

Cios, K., Pedrycz, W., and Swiniarski, R. (1998). *Data Mining Methods for Knowledge Discovery*. Kluwer Academic, Boston.

Doi, K. (2005). Current status and future potential of computer-aided diagnosis in medical imaging. *The British Journal of Radiology*, 78:3–19.

Duha, R., Hart, P., and Stork, D. (2001). *Pattern Classification*. John Willey & Sons, Inc., Chichester.

Guo, H. and Nandi, A. (2006). Breast cancer diagnosis using genetic programming generated feature. *Pattern Recognition*, 39(5):980–987.

Hoover, A., Kouznetsova, V., and Goldbaum, M. (2000). Locating blood vessels in retinal images by piecewise thresholding probing of a matched filter response. *IEEE Transaction on Medical Imaging*, 19:203–210.

Hsu, C. and Lin, C. (2002). A comparison of methods for multiclass support vector machines. *IEEE Transactions on Neural Networks*, 13:415–425.

Jain, A. and Dubes, R. (1988). *Algorithms for Clustering Data*. Prentice Hall.

Jain, A., Murty, M., and Flyn, P. (1999). Data clustering: A review. *ACM Computing Surveys*, 31(3):264–323.

Kishore, J., Patnaik, L., Mani, V., and Arawal, V. (2002). Application of genetic programming for multicategory pattern classification. *IEEE Transaction on Evoluationary Computation*, 4:242–258.

Salem, N. and Nandi, A. (2006a). Segmentation of retinal blood vessels using scale space features and k-nearest neighbour classifier. In *The 31st International Conference on Acoustics, Speech, and Signal Processing (ICASSP 2006)*, Toulouse, France.

Salem, S. and Nandi, A. (2005). New assessment criteria for clustering algorithms. In *IEEE international workshop in Machine Learning For Signal Processing (MLSP 2005)*, pages 285–290, Mystic, CT, USA.

Salem, S. and Nandi, A. (2006b). Novel clustering algorithm (RACAL) and a partial supervision strategy for classification. In *IEEE international workshop in Machine Learning For Signal Processing (MLSP 2006)*, pages 313–318, Mynooth, Ireland.

Salem, S., Salem, N., and Nandi, A. (2006). Segmentation of retinal blood vessels using a novel clustering algorithm. In *14th European Signal Processing Conference (EUSIPCO 2006)*, Florence, Italy.

Salem, S., Salem, N., and Nandi, A. (2007). Segmentation of retinal blood vessels using a novel clustering algorithm (RACAL) with a partial supervision strategy. *Medical and Biological Engineering and Computing*, 45(3):261–273.

Theodoridis, S. and Koutroubas, K. (2003). *Pattern Recognition*. Academic Press, San Diego.

STARE. The STARE project. http://www.ces.clemson.edu/ ahoover/stare.

UCI. UCI repository of machine learning databases. http://www.ics.uci.edu/ mlearn/MLRepository.html.

Webb, A. (2003). *Statistical Pattern Recognition*. John Willey & Sons, Inc.

Xu, R. and Wunsch, D. (2005). Survey of clustering algorithms. *IEEE Transactions on Neural Networks*, 16(3):645–677.

BREAST CANCER DETECTION USING GENETIC PROGRAMMING

Hong Guo, Qing Zhang and Asoke K. Nandi
Department of Electrical Engineering and Electronics
The University of Liverpool, Brownlow Hill, Liverpool, L69 3GJ, U.K.
Hong.Guo@liv.ac.uk, john3000@liv.ac.uk, a.nandi@liv.ac.uk

Keywords: Genetic Programming, Feature Extraction, Classification, Breast Cancer Diagnosis.

Abstract: Breast cancer diagnosis have been investigated by different machine learning methods. This paper proposes a new method for breast cancer diagnosis using a single feature generated by Genetic Programming (GP). GP as an evolutionary mechanism that provides a training structure to generate features. The presented approach is experimentally compared with some kernel feature extraction methods: Kernel Principal Component Analysis (KPCA) and Kernel Generalised Discriminant Analysis (KGDA). Results demonstrate the capability of the proposed method to transform information from high dimensional feature space into one dimensional space for breast cancer diagnosis.

1 INTRODUCTION

Breast Cancer is the second most common cancer in the UK after non-melanoma skin cancer (Can). The early detection of breast cancer is becoming very important to ameliorate breast cancer survival rate. In recent years, various machine learning methods have been proposed for breast cancer diagnosis and prognosis. Yao and Liu described two neural network based approaches to breast cancer diagnosis; a feed-forward neural networks was evolved using evolutionary programming algorithm in the first approach, while the second approach was based on neural network ensembles (Yao and Liu, 1999). The performance of four fuzzy rule generation methods on Wisconsin breast cancer data was studied in (Jain and Abraham, 2004). In (Kermani et al., 1995), a hybrid genetic algorithm and neural network (GANN) was shown to extract the important features and train a NN in breast cancer classification. Guo and Nandi developed a modified Fisher criterion to help genetic programming optimism features for breast cancer diagnosis (Guo and Nandi, 2006). Nandi *et al.* used GP successfully for classification of breast masses in mammogram (Nandi et al., 2006).

In recent years, the application of genetic programming to pattern recognition problem has become increasingly common. Genetic Programming was first introduced by Koza (Koza, 1992), and has been proposed as a machine learning method in different fields. In (Benyahia and Potvin, 1998), GP technique was used to develop a decision support system for vehicle dispatching considering a population of utility functions that evaluate candidate vehicles for servicing requests. GP was tested in six medical diagnosis problems (Brameier and Banzhaf, 2001) and the results were compared with those obtained by neural networks. In (Kishore et al., 2000) the feasibility of applying GP to multi-category pattern classification problem was studied. Zhang et al. (Zhang et al., 2003) applied genetic programming for fault detection in machine condition monitoring field. However, in all the above applications (Benyahia and Potvin, 1998; Brameier and Banzhaf, 2001; Kishore et al., 2000; Zhang et al., 2003), GP was employed solely as a classifier based on manually developed features. In (Sherrah et al., 1997), GP-based feature extraction was used to improve the classification results and reduce the dimensionality of the data in the medical domain. GP exhibits pseudo-intelligent behaviour by deciding whether to perform feature extraction or feature selection during the evolutionary process. Unfortunately, the system is unable to sample adequately the search space for high-dimensional problems and

the main disadvantage lies in its computational complexity. Kotani et al. (Kotani et al., 1997) performed feature extraction using GP with a KNN classifier on one artificial task and one acoustic diagnosis experiment with the conclusion that the genetic programming is an effective tool for the feature extraction task.

In this paper, GP is employed to generate a single nonlinear feature to improve the classification accuracy for breast cancer diagnosis. As a machine learning method, GP exhibits intelligent behaviour to perform feature generation. During the evolutionary process, a new fitness function is developed to evaluate the effectiveness of each feature in helping GP select the best features by which the patterns from benign are well separated from patterns from malignant.

This paper is organized as follows: The data preparation of breast cancer is addressed in Section 2. Section 3 presents the proposed feature generator using genetic programming. Two kernel feature extraction methods kernel principal component analysis (KPCA) and kernel generalized discriminant analysis (KGDA) are briefly presented in section 4. Three classifiers Multi-Layer Prceptron (MLP), *k*-Nearest Neighbor (KNN) and Minimum Distance Classifier (MDC) are presented in section 5. In section 6, a number of experiments for breast cancer detection problems are reported using kernel Principal Component Analysis, kernel Generalized Discriminant Analysis extracted features and GP generated feature. Finally, based on the experimental results, conclusions on this proposed method are presented in section 7.

2 THE PROBLEM

It is of prime importance to be able to detect the breast cancer in early stages. In this paper, the Wisconsin diagnostic breast cancer (WDBC) dataset from the UCI Machine Learning repository (D.J. Newman and Merz, 1998) is used to examine the capability of GP for the breast cancer detection problem.

2.1 Image Preparation

The Wisconsin diagnostic breast cancer (WDBC) dataset was created by Wolberg et al., University of Wisconsin (Street et al., 1993). The diagnosis procedure begins by obtaining a small drop of fluid from a breast tumour using a fine needle. The image for digital analysis is generated by JVC TK-1070 colour video camera mounted atop an Olympus microscope and the image is projected into the camera with a $63\times$ objective and a $2.5\times$ ocular. The image is captured by a ComputerEyes/RT colour frame grabber board (Digital Vision, Inc., Dedham MA 02026) as a 512×480, 8-bit-per-pixel Targa file.

2.2 Data Preparation

An active model located in the actual boundary of cell nucleus is defined as a snake. The ten different features from the snake-generated cell nuclei boundaries are extracted by following techniques:

- ***Radius***: The radius of an individual nucleus is measured by averaging the length of the radial line segments defined by the centroid of the snake and the individual snake points.
- ***Perimeter***: The nuclear perimeter is defined by calculating the total distance between the snake points.
- ***Area***: The nuclear area is defined by counting the number of pixels on the interior of the snake and adding one-half of the pixels in the perimeter.
- ***Compactness***: The $perimeter^2/area$ is used as the compactness of the cell nuclei.
- ***Smoothness***: The smoothness of a nuclear contour is quantified by measuring of difference between the length of a radial line and the mean length of the lines surrounding it.
- ***Concavity***: Concavity is defined as the severity of indentations in a cell nucleus. For a line connecting any two non-adjacent snake points, if the actual boundary drop inside the line, an indentation occurs and the distance to the line is a measure of the severity.
- ***Concave Points***: This feature is similar to Concavity but measures only the number, rather than the magnitude, of contour concavities.
- ***Symmetry***: The length difference between lines perpendicular to the major axis to the cell boundary in both directions is defined as symmetry.
- ***Fractal Dimension***: The fractural dimension is an indication of the regularity of the nucleus. Higher values of the downward slops of the coastlines correspond to less regular contour and vice-versa.
- ***Texture***: The texture of the cell nucleus is defined by finding the variance of the gray scale intensities in the component pixels.

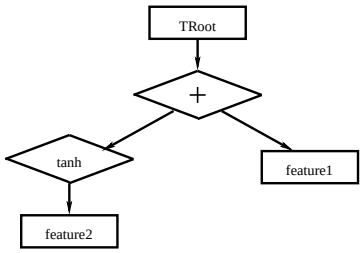

Figure 1: Tree Representation.

The mean value, largest value and standard error of each feature are computed for each image. A set of 569 images has been processed, yielding a database of 30-dimensional points (Street et al., 1993). In this paper, we randomly selected, without replacement, 100 samples for benign case, and 100 samples for malignant case respectively. Two 30×200 matrices are obtained for training and test datasets. One of them as the training dataset forms the terminator set to the GP. Another matrix is used as the test dataset. For each given pattern vector of training and test datasets, a corresponding vector is created in a matrix containing the target information.

3 GENETIC PROGRAMMING-BASED FEATURE GENERATOR

In this paper, we introduce a new method for a feature generator based on GP, for breast cancer detection problem. Genetic Programming, as a form of evolutionary algorithm and an extension of genetic algorithms, extracts the information from the real-valued parameter vector to create features based on the evolutionary algorithm. The surviving feature from the feature generator will be used to provide the solution to pattern recognition problems.

3.1 The Representation of Each Individual

Since expressions can be represented as trees ordered by operator precedence, GP systems in this paper evolve programs using tree representation. Each member can be written as a polynomial expression consisting of several non-linear functions up to a maximum specified depth. Using this function, each individual in the population is a mathematical formula that transforms the time series signals into a feature data. Formula $TRoot = tanh(feature1) + feature2$ can be represented by the Fig. 1.

3.2 Process of Genetic Programming

The GP-based feature extractor is used to extract useful information from the thirty features of breast cancer dataset in order to provide discriminating input features for the classifiers. The purpose of GP is to try to maximise the extra information content in the sample of the original feature set, and it implicitly maximises the separation between benign condition and malignant condition within the data. The evolutionary process of GP-based feature generation system is described by following steps. First, an initial population with a chosen number of individuals is generated on a random basis, meaning that there is no human influence or bias in the generation of original features. Original feature set are fed as the inputs to the initial population. Each individual represents a transformation network, which tries to transform dataset into information for classification.

In terms of the usefulness of each individual for classification, a fitness value is assigned to each individual by fitness function. The members with the best fitness values survive from the current generation and will be chosen as the origins of the next generation. In our design, only the elite will survive the natural selection. This mechanism allows the feature to evolve in a direction towards the best classification performance, thus achieving the automatic generation of features. At the beginning of the next generation, three operations - reproduction, crossover and mutation - are conducted to produce new members based on the surviving member. If the termination criterion is met, the best solution is preserved.

3.3 Fitness Function

The fitness function is one of the most important components. It determines the performance of the GP system. A good fitness function provides an improved solution by rating the performance of each member and giving the stronger one a better chance of surviving. It is well known that the computational demands are relatively high in training a classifier for each individual when the classification results are used as the fitness value for breast cancan diagnosis problem. Hence in this study it is decided that classification results are not used as a measure of fitness. This decision reduces the computational complexity of the proposed method significantly

Within the one-dimensional effective feature space, the achievable classification success is dependent upon the overlapping areas between classes. Usually, a threshold is set within the area to separate data belonging to different classes. However, it

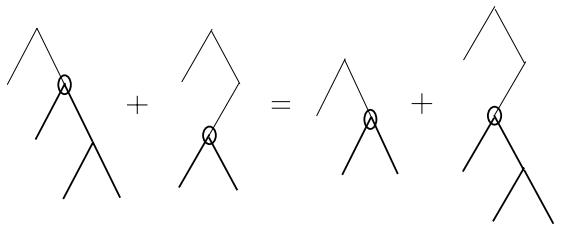

Figure 2: Crossover operation

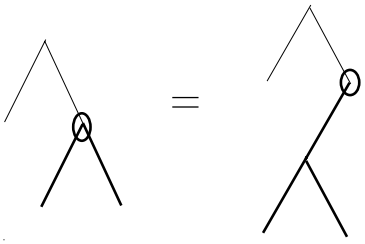

Figure 3: Mutation operation.

is inevitable that some data points are misclassified. Apparently the smaller the overlapping area, by the smaller number of data points within the overlapping area, the higher is the classification success. This rule is explored in our fitness function to reveal quickly and effectively the discriminating ability of the candidate features. Specifically, the higher boundary of the lower class and the lower boundary of the higher class are calculated. The number of data points present within these two boundaries are found out and then normalised by the total number of data points. A small percentage of the overlapping points is an indication how well the two classes can be separated.

3.4 Primitive Operations

Genetic programming evolves tree individuals representing possible solutions to the problem at hand. A population of such individuals is randomly created and then evolved by probability of genetic operations:

- Crossover: GP carries out a crossover operation to create new individuals with a probability P_c, which controls the occurrence of the crossover throughout generations. Two new individuals are generated by selecting compatible nodes randomly from each parent and swapping them, as illustrated in Fig. 2.
- Mutation: The mutation operation is performed by the creation of a subtree at a randomly selected node with the probability P_m. First, for a given parent, there is an index assigned to each node for identification. A random index number is generated to indicate the place where mutation will happen. The node is located, then the tree downstream from this node is deleted and a new subtree is generated from this node (see Fig. 3), exactly in the same way as growing initial population.
- Reproduction: The reproduction operation is performed by copying individuals to the next population without any change in terms of a certain probability P_r.

Table 1: The Operator sets for the GP.

Symbol	No. of Inputs	Description
+, -	2	Addition, Subtraction
*, /	2	Multiplication, Division
square, sqrt	1	Square, Square Root
sin, cos	1	Trigonometric functions
asin, acos	1	Trigonometric functions
tan, tanh	1	Trigonometric functions
reciprocal	1	Reciprocal
log	1	Natural Logarithm
abs, negator	1	Absolute, Change Sign

All these three operations happen within one generation based on three probabilities, such that:

$$P_c + P_m + P_r = 1 \tag{1}$$

3.5 Primitive Terminators

Terminators act as the interface between GP and the experimental dataset. They are required to collect related information as much as possible from the original feature set and to provide inputs to the feature generator. In our GP-based feature extractor, the terminator set is constructed by thirty original feature set (see Section 2) and some numerical values, which are randomly generated at the construction cycle of new individuals. These numerical values could be either integer or floating point numbers, both ranging from 1 to 100.

3.6 Primitive Operators

One of the main building blocks of the GP is the operator pool. The functions stored in the pool are mathematical operators that perform an operation on one or more inputs to give an output result. Table 1 lists the mathematical functions used as operators in this paper.

4 KERNEL FEATURE EXTRACTION METHODS

In recent years, kernel-based methods are becoming popular for their ability to solving nonlinear problems. It is first applied to overcome the computational and statistical difficultly of SVM classifier for seeking an optimal separating hyperplane in the feature space(E.Osuna et al., 1997). It is demonstrated to be able to represent complicated nonlinear relationship of the input data efficiently.

The Kernel Principal Component Analysis (KPCA) and Kernel Generalised Discriminant Analysis (KGDA) are two independent nonlinear feature extraction/selection methods, both of which perform the mapping in the feature space F with kernel functions and use a linear analysis algorithm to discover patterns in the kernel-defined space. The mapping function Φ is defined implicitly by specifying the form of the dot product in the feature space (Scholkopf et al., 1998).

4.1 Kernel Principal Component Analysis

Kernel PCA is the non-linear extension of the PCA in a kernel-defined feature space making use of the dual representation (Shawe-Taylor and Cristianini, 2004).

Given a set of observations $\{\vec{x}_i \in R^n : i = 1 \text{ to } N\}$, we first map the data into a feature space F and compute the covariance matrix(Muller et al., 2001):

$$C = \frac{1}{N}\sum_{j=1}^{N}\Phi(x_j)\Phi(x_j)^T \tag{2}$$

The $N \times N$ Kernel Matrix is defined as,

$$K_{ij} := \Phi(\vec{x}_i) \bullet \Phi(\vec{x}_j) = K(\vec{x}_i, \vec{x}_j); \quad i, j = 1, \ldots, N \tag{3}$$

The data need to be centred in the mapped feature space F

$$\tilde{K}_{ij} \equiv \tilde{\Phi}(\vec{x}_i) \bullet \tilde{\Phi}(\vec{x}_j) = K_{ij} - \frac{1}{N}\sum_{p=1}^{N}K_{ip} - \frac{1}{N}\sum_{q=1}^{N}K_{qj} + \frac{1}{N^2}\sum_{p,q=1}^{N}K_{pq} \tag{4}$$

Now the eigenvalue problem for the expansion coefficients α_i is solely dependent on the kernel function,

$$\lambda\alpha = \tilde{K}\alpha \tag{5}$$

Projects the mapped pattern $\Phi(x)$ onto V^k to extract features of new dataset x with kernel PCA.

$$(V^k \cdot \Phi(x)) = \sum_{i=1}^{N}\alpha_i^k(\Phi(x_i)\cdot\Phi(x)) = \sum_{i=1}^{N}\alpha_i^k K(x_i, x) \tag{6}$$

4.2 Kernel Generalized Discriminant Analysis (KGDA)

KGDA is derived from a linear version of the discriminant analysis, namely, Fisher linear discriminant analysis FLDA. FLDA is designed optimally with its ability to maximise the ratio of within-class scatter and between-class scatter of projected features. For c $(c > 2)$ classes, the ith observation vector from the class l is defined by x_{li}, where $1 \le l \le c$, $1 \le i \le N_l$, and N_l is the number of observations from class l. The within-class covariance matrix is given by

$$S_\omega = \sum_{l=1}^{c} S_l, \tag{7}$$

where

$$S_l = \sum_{i=1}^{N_l}(x_{li} - \mu_l)(x_{li} - \mu_l)^T \tag{8}$$

The between-class covariance matrix is defined by

$$S_b = \sum_{l=1}^{c} N_l(\mu_l - \mu)(\mu_l - \mu)^T \tag{9}$$

where μ_l is the mean of class l and μ is the global mean.

The idea of KGDA is to solve the problem of FLDA in a kernel feature space, thereby yielding a nonlinear discriminant in the input space. In term of the dot product, the optimisation problem for the KGDA in the feature space can be written as

$$J(\alpha) = \frac{\alpha^T S_b^\Phi \alpha}{\alpha^T S_\omega^\Phi \alpha} \tag{10}$$

where

$$S_b^\Phi = \sum_{l=1}^{c}[k_l k_l^T - kk^T] \tag{11}$$

$$S_\omega^\Phi = K^2 - \sum_{l=1}^{c} N_l k_l k_l^T \tag{12}$$

$$k_l = \frac{1}{N_l}\sum_{l=1}^{N_l}K_{ij} \quad i, j = 1, \ldots, N_l \tag{13}$$

$$k = \frac{1}{N}\sum_{i=1}^{N}K_{ij} \quad i, j = 1, \ldots, N \tag{14}$$

where k_l is the mean vector of kernel matrix of class l, k indicates the global mean vector of kernel matrix of K_{ij}.

The projection of the test dataset x into the discriminant is given by

$$W \cdot \Phi(x) = \sum_{i=1}^{N}\alpha_i k(x_i, x) \tag{15}$$

5 CLASSIFIERS

Three classifiers - Artificial Neural Networks (ANNs), K-Nearest Neighbour (KNN) and Minimum Distance Classifier (MDC) - are employed in this paper to evaluate the discriminating ability of features generated by GP and other kernel feature extraction methods discussed previously.

The Multi-Layer Peceptron (MLP) is chosen here as the structure of the network for its overall performance over other configurations. The MLP used here consists of one hidden layer varying between 1 and 14 neurons and one output layer, with the hidden layer having a logistic activation function and the output layer using a linear activation function. For training procedure, the back propagation algorithm with adaptive learning and momentum is used. The network is trained for 10000 epochs using each feature set.

KNN is a supervised learning algorithm to classify a test object based on majority of K-nearest neighbor category. Given that the version of $K = 1$ is often rather successful (Ripley, 2004). 1-NN is used as the classifier to examine the performance of features in this paper.

MDC is the simplest classification criterion. Basically, the method finds centres of classes and measures distances between these centres and the test data. The distance is defined as a measure of similarity so that the minimum distance indicates the maximum similarity. In this paper, Euclidean distance is used to investigate the capability of any feature extracted by this approach.

6 EXPERIMENTAL RESULTS

6.1 Feature Generation Result

Fig. 4 is obtained for detection of breast cancer by running GP-based feature extractor with population size 100, maximum tree depth 10 and terminating after the number of generations reaches 5000. Fig. 4 shows the output of a single feature, generated from the original feature set with 30 dimensions, for the training dataset and test dataset respectively. There are 200 examples in total from two conditions, with 100 examples in the benign case and 100 examples in the malignant case. It is clear from Figure 4 that the two conditions are perfectly separated from each other at training dataset, and three examples misclassified in test dataset.

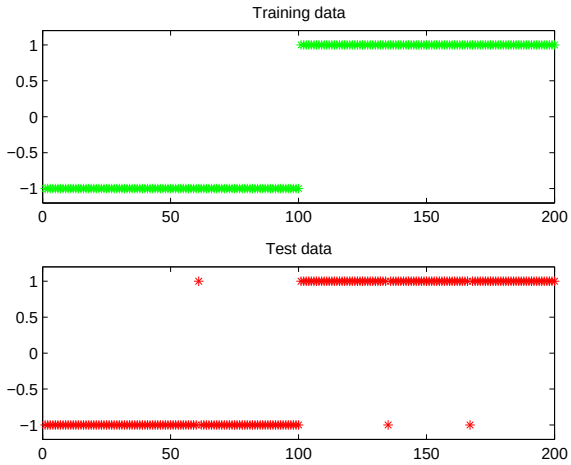

Figure 4: Output of a single feature, generated by GP from the original feature set with 30 dimensional breast cancer data, for the 200 examples in each of the training dataset and test dataset respectively.

6.2 Classification Results

A number of experiments were carried out to evaluate the discriminating ability of features generated by GP and other classical feature extraction methods in term of classification performance using MLP, 1-NN and the simplest classifier MDC respectively. Twenty runs of GP has been conducted for generating features. Also, fifty MLP have conducted using original features and feature extracted by KPCA, KGDA and GP respectively.

Table 2 presents the comparison results of classification success rate using feature set extracted by different method as the inputs to MLP, 1-NN and MDC. It can be seen that the best classification accuracy is achieved by MLP when thirty original features are used as input. One KPCA feature achieved the best 94.5% when MDC is use as the classifier. one KGDA feature with MLP and MDC achieved the same classification results 93.5%. When a GP extracted feature is employed, the improvement is significant compared with other classical feature extraction methods. Together with MLP, KNN and MDC, it performs the best with success rate at 98.5% among all of pattern recognition systems. From the best classification accuracy it can be seen that GP generated features are more robust compared with other methods.

Table 2: The best classification accuracy (%) using original features, one KPCA-extracted features, one KGDA-extracted features and one GP-generated features respectively, with a MLP, a KNN and a MDC classifier respectively on breast cancer dataset.

Classifier	Original Feature	KPCA Feature	KGDA Feature	GP Feature
MLP	97%	90%	93.5%	**98.5**%
KNN	87.5%	85.5%	93%	**98.5**%
MDC	84%	94.5%	93.5%	**98.5**%

7 CONCLUSIONS

It is now clear from Figure 4 that values of the single feature obtained from our proposed method cluster naturally into largely non-overlapping groups. Thus no computationally complex classifier may be needed for successful classification, instead some simple thresholds are enough. Summarizing all the results obtained from different approaches for breast cancer diagnosis problem, it can be said that performances from a single GP-generated feature are the most accurate and reliable in all experiments. From the results of different pattern recognition problems, GP is not only capable of reducing the dimensionality, but also achieving a significant improvement in the classification accuracy. Using the single feature generated by GP makes a significant contribution to the improvement in classification accuracy and robustness, compared with other sets of features extracted by KPCA and KGDA.

Generally in pattern recognition problems, there is a reliance on the classifier to find the discriminating information from a large feature set in case of standalone MLP. In this paper, GP as a machine learning method is proposed for nonlinear feature extraction for breast cancer diagnosis. This approach is able to learn directly from the data just like conventional methods (such as FLDA and PCA), but in an evolutionary process. Under this framework, an effective feature can be formed for pattern recognition problems without the knowledge of probabilistic distribution of data.

From the experimental results it can be seen that with the combination of a simple form of classifier MDC, GP outperforms the other two feature extractors which are using more sophisticate classifier MLP, indicating an overwhelming advantage of GP in feature extraction for breast cancer diagnosis.

ACKNOWLEDGEMENTS

H. Guo would like to acknowledge the financial support of the Overseas Research Studentship Committee, UK, the University of Liverpool and the University of Liverpool Graduates Association (HK)

REFERENCES

Cancer research UK.

Benyahia, I. and Potvin, J. (1998). Decision support for vehicle dispatching using genetic programming. *IEEE Trans. Syst., Man, Cybern. Part.A*, 28(3):306–314.

Brameier, M. and Banzhaf, W. (2001). A comparison of linear genetic programming and neural networks in medical data mining. *IEEE Trans. on Evolutionary Computation*, 5(1):17–26.

D.J. Newman, S. Hettich, C. B. and Merz, C. (1998). UCI repository of machine learning databases.

E.Osuna, Freund, R., and Girosi, F. (1997). *Support Vector Machines: Training and Applications*. MIT, Tech. Rep.

Guo, H. and Nandi, A. K. (2006). Breast cancer diagnosis using genetic programming generated feature. *Pattern Recognition*, 39(5):980–987.

Jain, R. and Abraham, A. (2004). A comparative study of fuzzy classification methods on breast cancer data. *Australas. Physical Engineering Sciences Medicine*, 27(4):213–218.

Kermani, B. G., White, M. W., and Nagle, H. T. (1995). feature extraction by genetic algorithms for nerual networks in breast cancer classification. volume 1, pages 831–832. New York, USA.

Kishore, J. K., Patnaik, L. M., Mani, V., and Arawal, V. K. (2000). Application of genetic programming for multicategory pattern classification. *IEEE Trans. on Evolutionary Computation*, 4(3):242–258.

Kotani, M., Ozawa, S., Nasak, M., and K.Akazawa (1997). Emergence of feature extraction function using genetic programming. In *Knowledge-Based Intelligent Information Engineering Systems, Third International Conference*, pages 149–152.

Koza, J. R. (1992). *Genetic Programming: On the Programming of Computers by Means of Natural Selection*. MIT Press, Cambridge.

Muller, K. R., Mika, S., Ratsch, G., Tsuda, K., and Scholkopf, B. (2001). An introduction to kernel-based learning algorithms. *IEEE Trans. on Neural Networks*, 12(2):181–201.

Nandi, R. J., Nandi, A. K., Rangayyan, R. M., and Scutt, D. (2006). Classification of breast masses in mammograms using genetic programming and feature selection. *Medical and Biological Emgineering and Computing*, 44(8):693–694.

Ripley, B. D. (2004). *Pattern Recognition and Neural Networks*. Cambridge Universith Press, Boston.

Scholkopf, B., Smola, A., and Muller, K. R. (1998). Nonlinear component analysis as a kernel eigenvalue problem. *Neural Computation*, 10(5):1299–1319.

Shawe-Taylor, J. and Cristianini, N. (2004). *Kernel Methods for Pattern Analysis*. Cambridge University Press.

Sherrah, J. R., Bogner, R. E., and Bouzerdoum, A. (1997). The evolutionary pre-processor: Automatic feature extraction for supervised classification using genetic programming. In *Proc. 2nd Int. Conf. Genetic Programming (GP-97)*, pages 304–312.

Street, W., Wolberg, W., and Mangasarian, O. (1993). Nuclear feature extraction for breast tumor diagnosis. In *International Symposium on Electronic Imaging: Science and Technology*, number 1905, pages 861–870. San Jose, CA.

Yao, X. and Liu, Y. (1999). Neural networks for breast cancer diagnosis. volume 3, pages 6–9.

Zhang, L., Jack, L. B., and Nandi, A. K. (2003). Fault detection using genetic progamming. *Mechanical Systems Signal Processing*.

BREAST CANCER DIAGNOSIS AND PROGNOSIS USING DIFFERENT KERNEL-BASED CLASSIFIERS

Tingting Mu and Asoke K. Nandi
Department of Electrical Engineering and Electronics, The University of Liverpool, Brownlow Hill, Liverpool, UK, L69 3GJ
tingting.mu@liverpool.ac.uk, a.nandi@liverpool.ac.uk

Keywords: Breast cancer, diagnosis, prognosis, pattern classification, kernel method.

Abstract: The medical applications of several advanced, kernel-based classifiers to breast cancer diagnosis and prognosis are studied and compared in this paper, including kernel Fisher's discriminative analysis, support vector machines (SVMs), multisurface proximal SVMs, as well as the pairwise Rayleigh quotient classifier and the strict 2-surface proximal classifier that we recently proposed. The radial basis function kernel is employed to incorporate nonlinearity. Studies are conducted with the Wisconsin diagnosis and prognosis breast cancer datasets generated from fine-needle-aspiration samples by image processing. Comparative analysis is provided in terms of classification accuracy, computing time, and sensitivity to the regularization parameters for the above classifiers.

1 INTRODUCTION

Despite the increasing public awareness and scientific research, breast cancer continues to be the most common form of cancer and the second most common cause of cancer deaths in females; the disease affects approximately 10% of all women at some stage of their life in the western world (Marshall, 1993). The long-term survival of a patient with breast cancer are improved by the early detection of the disease, which is enhanced by an accurate diagnosis. The choice of appropriate treatments following surgery is influenced by the expected long-term behavior of the disease, so-called prognosis.

Definitive diagnosis of a breast mass can only be established through fine-needle aspiration (FNA) biopsy, core needle biopsy, or excisional biopsy. Among these methods, FNA is the easiest and fastest method of obtaining a breast biopsy, and is effective for women who have fluid-filled cysts. Research works on the Wisconsin Diagnosis Breast Cancer (WDBC) data grew out of the desire of Dr. Wolberg to diagnose breast masses accurately based solely on FNA (Wolberg et al., 1993; Street et al., 1993). Later, a number of research projects have been developed with the WDBC dataset, focusing on computer-aided diagnosis (CAD) using machine learning techniques (Wolberg et al., 1994; Wolberg et al., 1995; Mangasarian et al., 1995; Guo and Nandi, 2006; Mu and Nandi, 2007). Breast cancer prognosis is a more difficult problem, that is, the long-term outlook for the disease for patients whose cancer has been surgically removed. Till now, few works have been developed on predicting the time to recur (TTR) for a patient for whom cancer has not recurred and may never recur (Wolberg et al., 1995; Mangasarian et al., 1995; Street et al., 1995). The detection of malignant breast tumors from a set of benign and malignant samples for diagnosis, and the simple prediction of patients as 'recurred' or 'not recurred' without predicting the TTR for prognosis, both belong to the pattern classification problems.

The idea of using kernel functions as inner product in a feature space was introduced into machine learning in 1964 by the work of Aizerman, Braverman and Rozonoer (Aizerman et al., 1964). Kernel methods to pattern analysis embeds the data in a suitable feature space, and then uses algorithms based on linear algebra, geometry, and statistics to discover patterns in the embedded data. Different kernel-based classifiers have been proposed. Boser, Guyon, and Vapnik (Boser et al., 1992) first combined the kernel function with the large margin hyperplanes, leading to support vector machines (SVMs) that are highly successful in solving various nonlinear and non-separable problems in machine learning. In addition to the original C-SVM learning method (Cortes and Vapnik, 1995), the ν-SVM learning method was proposed by Schölkopf et al. (Schölkopf et al., 2000), which is closely related to the C-SVM but with a different optimization risk. The famous Fisher's linear discriminant analysis (FLDA), dating back to 1936

(Fisher, 1936), seeks separating hyperplanes which best separate two or more classes of samples based on the Fisher criterion with the between- and within-class scatters built on individual samples. Mika et al. (Mika et al., 1999) combined kernels functions with FLDA leading to kernel Fisher's discriminant analysis (KFDA). Mu et al. (Mu et al., 2007a) proposed to seek the optimal separating hyperplane based on the pairwise Rayleigh quotient (PRQ) criterion with the between- and within- class scatters built on the pairwise information; they also proposed to combine kernels functions with the linear PRQ classifier leading to the nonlinear PRQ classifier. Multiplane learning is a comparatively new machine learning method developed in recent years. Mangasarian and Wild (Mangasarian and Wild, 2006) proposed the kernel-based multisurface proximal SVM (MPSVM) that seeks two cross proximal planes by optimizing a regularized optimization objective with Tikhonov regularization term employed. More recently, Mu et al. (Mu et al., 2007b) proposed the strict 2-surface proximal (S2SP) classifier that seeks two cross proximal planes by employing a "square of sum" optimization factor without any regularization term, which is mathematically stricter than the optimization objective of MPSVM; and kernel functions were employed to incorporate nonlinearity.

In this paper, studies are conduced on the WDBC and WPBC datasets to investigate the benefits of applying different kernel-based classifiers to breast cancer diagnosis and prognosis, including SVM, KFDA, PRQ classifier, MPSVM, regularized δ-MPSVM (Mangasarian and Wild, 2006), and S2SP classifier. The detecting accuracies, computing times, and sensitivities to regularization parameters are compared for the above kernel-based classifiers.

2 CLASSIFICATION METHODS

Given a set of l labeled training samples $z = \{(\boldsymbol{x}_i, y_i)\}_{i=1}^{l} \in (R^n \times Y)$, where R^n is the n-dimensional real feature space with a binary label space $Y = \{1, -1\}$, and $y_i \in Y$ is the label assigned to the sample $\boldsymbol{x}_i \in R^n$, the purpose of classification is to seek the best prediction of the label for an input sample $\boldsymbol{x}$. All the kernel-based classifiers are developed in the kernel-transformed feature space κ, with a nonlinear mapping $\phi : R^n \to \kappa$.

2.1 Discriminant Classification

The basic idea of the discriminant classification is to seek one optimal hyperplane that best separates the two classes of samples in a corresponding feature space. In the kernel-transformed feature space κ, by expanding the direction vector of the hyperplane into a linear summation of all training samples, the separating hyperplane can be given as

$$f(\boldsymbol{x}) = \sum_{i=1}^{l} \alpha_i K(\boldsymbol{x}_i, \boldsymbol{x}) + b, \tag{1}$$

where $\{\alpha_i\}_{i=1}^{l}$ denote the summating weights, b denotes the bias of the separating hyperplane, and $K(\cdot,\cdot)$ is a kernel function used to compute the inner product matrix, the so-called kernel matrix, on pairs of samples in the kernel-transformed feature space κ. Different classification methods lead to different ways to determine the optimal separating hyperplane $f^*(\boldsymbol{x})$. The label of a given test sample $\boldsymbol{x}$ can be predicted by

$$p(\boldsymbol{x}) = \mathrm{sgn}(f^*(\boldsymbol{x})), \tag{2}$$

where $\mathrm{sgn}(x)$ is equal to 1 when $x \geq 0$, and -1 otherwise.

2.1.1 Support Vector Machines

The basic idea of SVMs is to construct a separating hyperplane as the decision surface in such a way that the margin of separation between the positive and negative samples is maximized in an appropriate feature space. To determine $f^*(\boldsymbol{x})$ based on the maximal margin rule, the following constrained quadratic programming problem is solved (Cortes and Vapnik, 1995), as

$$O(\beta) = \sum_{i=1}^{l} \beta_i - \frac{1}{2} \sum_{i=1}^{l} \sum_{j=1}^{l} y_i y_j \beta i \beta_j K(\boldsymbol{x}_i, \boldsymbol{x}_j), \tag{3}$$

subject to

$$\sum_{i=1}^{l} y_i \beta_i = 0,$$

$$0 \leq \beta_i \leq C, i = 1, 2, \ldots, l,$$

where $\{\beta_i\}_{i=1}^{l}$ are Lagrange multipliers, and C is the regularization parameter set by the user. Letting $\{\beta_i^*\}_{i=1}^{l}$ denote the optimal solution of $O(\beta)$, the optimal value of the summating weights $\{\alpha_i\}_{i=1}^{l}$ and the bias b are obtained by

$$\alpha_i^* = y_i \beta_i^*, i = 1, 2, \ldots, l, \tag{4}$$

$$b^* = -\frac{1}{2S} \sum_{\boldsymbol{x} \in S_+ \bigcup S_-} \sum_{i=1}^{l} y_i \beta_i^* K(\boldsymbol{x}, \boldsymbol{x}_i), \tag{5}$$

where S_+ and S_- are two sets of support vectors with the same size of S but different labels of $+1$ and -1.

2.1.2 Kernel Fisher's Discriminant Analysis

KFDA determines $f^*(\boldsymbol{x})$ by maximizing the following Fisher criterion (Shawe-Taylor and Cristianini, 2004), as

$$O(f) = \frac{(\mu^+ - \mu^-)^2}{(\sigma^+)^2 + (\sigma^-)^2}, \tag{6}$$

where

$$\mu^+ = \frac{1}{l^+}\left(\sum_{i=1}^{l^+} f(\boldsymbol{x}_i)\right)^2,$$

$$\mu^- = \frac{1}{l^-}\left(\sum_{i=1}^{l^-} f(\boldsymbol{x}_i)\right)^2,$$

$$(\sigma^+)^2 = \frac{1}{l^+}\sum_{i=1}^{l^+}(f(\boldsymbol{x}_i) - \mu^+)^2,$$

$$(\sigma^-)^2 = \frac{1}{l^-}\sum_{i=1}^{l^-}(f(\boldsymbol{x}_i) - \mu^-)^2,$$

where μ^+ and μ^- denote the mean projections of the positive and negative samples, respectively; σ^+ and σ^- are the corresponding standard deviations; and l^+ and l^- denote the number of samples from the positive and negative classes, respectively. By incorporating Eq. (1) into Eq. (6), the optimal values of $\{\alpha_i\}_{i=1}^{l}$ and b can be calculated by solving a generalized eigenvalue problem (Shawe-Taylor and Cristianini, 2004).

2.1.3 Pairwise Rayleigh Quotient Classifier

The PRQ classifier helps in classification with insufficient training samples by employing pairwise constraints instead of individual samples. To determine the optimal separating hyperplane $f^*(\boldsymbol{x})$, the following PRQ criterion is maximized (Mu et al., 2007a), as

$$O(f) = \frac{\tilde{d}}{\tilde{d}^+ + \tilde{d}^-}, \tag{7}$$

where

$$\tilde{d} = \left[\sum_{i=1}^{m}\frac{1}{2}(1 - z_i)(f_{i1} - f_{i2})\right]^2,$$

$$\tilde{d}^+ = \frac{1}{l^+(l^+ - 1)}\sum_{i=1}^{m}\frac{1}{4}(1 + z_i)(1 + y_{i1})(f_{i1} - f_{i2})^2$$

$$\tilde{d}^- = \frac{1}{l^-(l^- - 1)}\sum_{i=1}^{m}\frac{1}{4}(1 + z_i)(1 - y_{i1})(f_{i1} - f_{i2})^2,$$

where $\tilde{d}$ denotes the differences of projections between samples from different classes; $\tilde{d}^+$ denotes the differences of projections between samples from the positive class; $\tilde{d}^-$ denotes the differences of projections between samples from the negative class; y_{i1} denotes the label of the sample $\boldsymbol{x}_{i1}$; $z_i \in \{1, -1\}$ is the pairwise constraint assigned to the two samples in the pair $(\boldsymbol{x}_{i1}, \boldsymbol{x}_{i2})$, and $z_i = 1$ if the two samples $(\boldsymbol{x}_{i1}, \boldsymbol{x}_{i2})$ belong to the same class, whereas $z_i = -1$ if the two samples $(\boldsymbol{x}_{i1}, \boldsymbol{x}_{i2})$ belong to different classes; f_{i1} and f_{i2} are used to denote $f(\boldsymbol{x}_{i1})$ and $f(\boldsymbol{x}_{i2})$; and m is the total number of available pairwise constraints. By incorporating Eq. (1) into Eq. (7), the optimal values of $\{\alpha_i\}_{i=1}^{l}$ and b can be simply calculated by matrix computation (Mu et al., 2007a). Compared with the Fisher criterion built on individual samples from a total number of l available samples, the PRQ criterion offers more possibilities by employing pairwise constraints from a total number of $l * (l - 1)$ available constraints.

2.2 Proximal Classification

The basic idea of proximal classification is to seek two proximal planes in a corresponding feature space, so that the first plane is as close to the points of the positive class while being as far as possible from the points of the negative class, whereas the second plane is as close to the points of the negative class while being as far as possible from the points of the positive class. In the kernel-transformed feature space κ, by expanding the direction vector of the hyperplane into a linear summation of all training samples, the two proximal hyperplanes are given as

$$f_1(\boldsymbol{x}) = \sum_{i=1}^{l}\alpha_{i1}K(\boldsymbol{x}_i, \boldsymbol{x}) + b_1, \tag{8}$$

$$f_2(\boldsymbol{x}) = \sum_{i=1}^{l}\alpha_{i2}K(\boldsymbol{x}_i, \boldsymbol{x}) + b_2, \tag{9}$$

where the subscripts 1 and 2 denote the first and second proximal plane, respectively. Let d_1 and d_2 denote the Euclidean distance between the sample and the two proximal planes, respectively, in the feature space κ. The label of a given test sample $\boldsymbol{x}$ can be predicted by considering values of d_1, d_2, and $\frac{d_1}{d_2}$ together using linear discriminant analysis.

2.2.1 Multisurface Proximal SVMs

MPSVMs obtain the first proximal hyperplane by maximizing the following objective function, as (Mangasarian and Wild, 2006)

$$O_1(\boldsymbol{\alpha}_1, b_1) = \frac{\|\mathbf{K}^-\boldsymbol{\alpha}_1 + \boldsymbol{e}b_1\|^2}{\|\mathbf{K}^+\boldsymbol{\alpha}_1 + \boldsymbol{e}b_1\|^2}; \tag{10}$$

and obtain the second proximal hyperplane by maximizing (Mangasarian and Wild, 2006)

$$O_2(\boldsymbol{\alpha}_2, b_2) = \frac{\|\mathbf{K}^+\boldsymbol{\alpha}_2 + \boldsymbol{e}b_2\|^2}{\|\mathbf{K}^-\boldsymbol{\alpha}_2 + \boldsymbol{e}b_2\|^2}, \qquad (11)$$

where $\boldsymbol{\alpha}_1$ and $\boldsymbol{\alpha}_2$ are two column vectors each with elements equal to $\{\alpha_{i1}\}_{i=1}^{l}$ and $\{\alpha_{i2}\}_{i=1}^{l}$, respectively; the $l^+ \times l$ matrix $\mathbf{K}^+$ represents the kernel matrix between the samples from the positive class and all the training samples; the $l^- \times l$ matrix $\mathbf{K}^-$ represents the kernel matrix between the samples from the negative class and all the training samples; and $\boldsymbol{e}$ is a column vector with all elements equal to one. The optimal values of $\boldsymbol{\alpha}_1$, b_1, $\boldsymbol{\alpha}_2$, and b_2 can be calculated by solving two generalized eigenvalue problems (Mangasarian and Wild, 2006), respectively.

Letting $\tilde{\boldsymbol{\alpha}}_1{}^T = \left[\boldsymbol{\alpha}_1^T, b_1\right]$, and $\tilde{\boldsymbol{\alpha}}_2{}^T = \left[\boldsymbol{\alpha}_2^T, b_2\right]$, to improve the classification performance of the MPSVMs, Mangasarian and Wild (Mangasarian and Wild, 2006) proposed to employ a Tikhonov regularization term, the two optimization objective shown in Eq. (10) and Eq. (11) become

$$O_1(\boldsymbol{\alpha}_1, b_1) = \frac{\|\mathbf{K}^-\boldsymbol{\alpha}_1 + \boldsymbol{e}b_1\|^2 + \delta\|\tilde{\boldsymbol{\alpha}}_1\|^2}{\|\mathbf{K}^+\boldsymbol{\alpha}_1 + \boldsymbol{e}b_1\|^2}, \qquad (12)$$

$$O_2(\boldsymbol{\alpha}_2, b_2) = \frac{\|\mathbf{K}^-\boldsymbol{\alpha}_2 + \boldsymbol{e}b_2\|^2 + \delta\|\tilde{\boldsymbol{\alpha}}_2\|^2}{\|\mathbf{K}^+\boldsymbol{\alpha}_2 + \boldsymbol{e}b_2\|^2}, \qquad (13)$$

where δ is a nonnegative regularization parameter set by the user. However, similar to the regularization parameter of the SVM, such as C for the C-SVM (Cortes and Vapnik, 1995) and ν for the ν-SVM (Schölkopf et al., 2000), performance of the above regularized δ-MPSVM is sensitive to the setting of the regularization parameter δ.

2.2.2 Strict 2-Surface Proximal Classifier

With consideration of the sign effect under the situation of misclassification with large projections onto the separating plane, the S2SP classifier eliminates the regularization term by employing the "square of sum" numerator. To obtain the first proximal hyperplane, the following objective function is to be maximized (Mu et al., 2007b), as

$$O_1(\boldsymbol{\alpha}_1, b_1) = \frac{\lceil\mathbf{K}^-\boldsymbol{\alpha}_1 + \boldsymbol{e}b_1\rceil^2}{\|\mathbf{K}^+\boldsymbol{\alpha}_1 + \boldsymbol{e}b_1\|^2}, \qquad (14)$$

and obtain the second proximal hyperplane by maximizing (Mu et al., 2007b)

$$O_2(\boldsymbol{\alpha}_2, b_2) = \frac{\lceil\mathbf{K}^+\boldsymbol{\alpha}_2 + \boldsymbol{e}b_2\rceil^2}{\|\mathbf{K}^-\boldsymbol{\alpha}_2 + \boldsymbol{e}b_2\|^2}, \qquad (15)$$

where $\lceil vector \rceil$ is used to denote the sum of the elements of the vector; and $\lceil matrix \rceil$ is used to denote a column vector with the sum of each row. The optimal values of $\boldsymbol{\alpha}_1$, b_1, $\boldsymbol{\alpha}_2$, and b_2 can be calculated by matrix computation (Mu et al., 2007b). There is no regularization parameter to be tuned for the S2SP classifier, which makes this method more convenient for the users, as compared with MPSVMs.

3 FEATURE PREPARATION

The WDBC and WPBC datasets were obtained from the University of Wisconsin Hospitals, Madison, of which the features were computed from digitized FNA samples. A portion of well-differentiated cells was scanned using a digital camera. The image analysis software system Xcyt was used to isolate individual nuclei (Wolberg et al., 1994; Wolberg et al., 1995; Mangasarian et al., 1995). In order to evaluate the size, shape, and texture of each cell nuclei, ten characteristics were derived and described as follows.

- **Radius** is computed by averaging the length of radial line segments from the center of mass of the boundary to each of the boundary points.
- **Perimeter** is measured as the sum of the distances between consecutive boundary points.
- **Area** is measured by counting the number of pixels on the interior of the boundary and adding one-half of the pixels on the perimeter, to correct for the error caused by digitization.
- **Compactness** combines the perimeter and area to give a measure of the compactness of the cell, calculated as $\frac{\text{perimeter}^2}{\text{area}}$.
- **Smoothness** is quantified by measuring the difference between the length of each radial line and the mean length of the two radial lines surrounding it, calculated by

  $$\frac{\sum_{\text{points}} |r_i - (r_i + r_{i+1})/2|}{\text{perimeter}},$$

  where r_i is the length of the line from the center of mass of the boundary to each boundary point.
- **Concavity** is captured by measuring the size of any indentations in the boundary of the cell nucleus.
- **Concave points** is similar to concavity, but counts only the number of boundary points lying on the concave regions of the boundary, rather than the magnitude of such concavities.
- **Symmetry** is measured by finding the relative difference in length between pairs of line segments

perpendicular to the major axis of the contour of the cell nucleus, calculated by

$$\text{symmetry} = \frac{\sum_i |\text{left}_i - \text{right}_i|}{\sum_i (\text{left}_i + \text{right}_i)},$$

where left_i and right_i denote the lengths of perpendicular segments on the left and right of the major axis, respectively.

- **Fractal dimension** is approximated using the "coastline approximation" described by Mandelbrot (Mandelbrot, 1997). The perimeter of the nucleus is measured using increasingly larger "rulers". As the ruler size increases, the precision of the measurement decreases, and the observed perimeter decreases. Plotting these values on a log-log scale and measuring the downward slope gives the negative of an approximation to the fractal dimension.
- **Texture** is measured by finding the variance of the gray-scale intensities in the component pixels.

The mean value, standard error, and the extreme (largest or "worst") value of each characteristic were computed for each image, which resulted in 30 features of 569 images, yielding a database of 569×30 samples representing 357 benign and 212 malignant cases, for the WDBC dataset; and 30 features of 198 images, yielding a database of 198×30 samples representing 151 nonrecurring and 47 recurring cases, for the WPBC dataset.

4 EXPERIMENTS

Experiments and comparative analysis were conducted on the WDBC and WPBC datasets, using SVM, KFDA, PRQ classifier, MPSVM, regularized δ-MPSVM, and S2SP classifier. The features were normalized to have zero mean and unit variance before being used as the input of a classifier. Classification performance is shown in terms of classification accuracy in percentage. The radial basis function (RBF) kernel was employed to calculate the inner-product matrix between samples in the kernel-transformed feature space, given as

$$K(\boldsymbol{x}_a, \boldsymbol{x}_b) = \exp\left(-\frac{\|\boldsymbol{x}_a - \boldsymbol{x}_b\|^2}{2\sigma^2}\right),$$

where σ is the kernel width set by the user. The SVM was trained by using the "SVM and kernel methods MATLAB toolbox" (Canu et al., 2003).

The 10-fold-cross validation was used to evaluate the classifiers, which was executed by randomly dividing all the available samples into ten subsets each with nearly the same number of samples. The same ten sets of training-test trials were employed for every classification method, each with one subset for test and the remaining nine subsets for training. Parameters of each classifier were selected by using the 5-fold-cross validation within the training set of the first trial. The same five sets of training-test trials were conducted to select parameters for each classification method. Finally, the mean value of the ten test classification accuracies with the selected parameters was used to represent the generalized performance.

Table 1: Performance comparison in percentage accuracy and computing time for different kernel-based classifiers.

	WDBC		WPBC	
Methods	Accu. (%)	Time (Sec.)	Accu. (%)	Time (Sec.)
SVM	98.8	0.09	76.3	0.08
KFDA	97.2	0.09	76.3	0.02
PRQ	97.7	8.02	76.3	1.07
MPSVM	85.3	0.90	75.3	0.21
δ-MPSVM	91.6	0.67	76.3	0.09
S2SP	99.2	0.10	77.3	0.02
Lam et al.	95.6	N/A	76.3	N/A

The classification performance and the corresponding computing time of each classifier are recorded in Table 1 using the WDBC and WPBC datasets; the results were also compared with the 10-fold-cross-validation performance obtained by the edited nearest-neighbor (ENN) with pure filtering (Lam et al., 2002) using the same datasets. The S2SP classifier provided the best classification accuracy of 99.2% as compared with the other five kernel-based classifiers. Nearly all of our obtained results (above 97%) were better than the published result of 95.6% (Lam et al., 2002) (see Table 1). For the more difficult WPBC dataset, the S2SP classifier provided the best classification accuracy of 77.3%. KFDA, SVM, δ-MPSVMs, and the PRQ classifier provided the same performance of 76.3% as that obtained by ENN (Lam et al., 2002) (see Table 1). KFDA, SVM, and the S2SP classifier possess faster training speed than MPSVMs, δ-MPSVMs, and the PRQ classifier, and performs better than MPSVMs and δ-MPSVMs. The classification performance of the PRQ classifier is comparable to those obtained by KFDA, SVM, and the S2SP classifier.

For a reasonable comparison of the classification capabilities, a score is calculated by averaging the classification performance over the two datasets and timing by 100 for each classifier, and recorded in Table 2. It can be seen from Table 2 that the S2SP classifier provides the highest score and requires

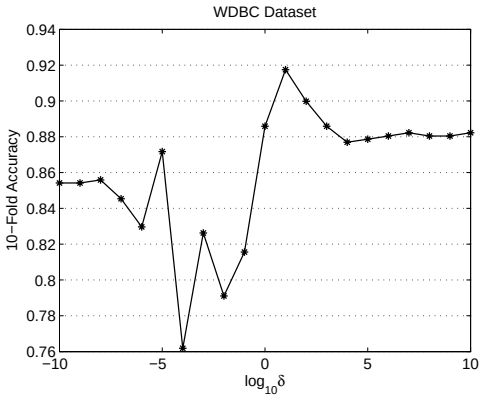

Figure 1: Performance variations of the δ-MPSVM classifier versus different values of $\log_{10}$ δ, with the RBF kernel width σ fixed as the selected values, for the WDBC dataset.

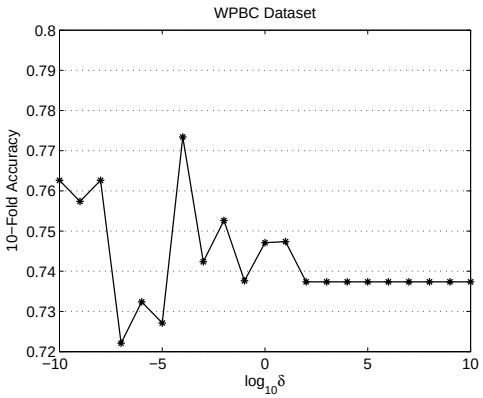

Figure 2: Performance variations of the δ-MPSVM classifier versus different values of $\log_{10}$ δ, with the RBF kernel width σ fixed as the selected values, for the WPBC dataset.

the least parameters to be tuned. Both the SVM and δ-MPSVM classifiers require to determine one extra regularization parameter. For SVM, C controls the tradeoff between the complexity of a SVM and the number of non-separable points. The SVM performance is not very sensitive to the setting of C. The performance variations of the δ-MPSVM are provided in Fig. 1 and Fig. 2, by varying the value of $\log_{10}\delta$ from -10 to 10, for the WDBC and WPBC datasets, respectively. It can be seen from Fig. 1 and Fig. 2 that performance of the δ-MPSVM classifier is sensitive to the setting of δ. Without using the regularization term, the average score of the MPSVM classifier falls down from 84.0 to 80.3 (see Table 2). However, tuning of the values of the kernel parameters is unavoidable for all these kernel-based classifiers.

Table 2: Comparison of classification capability in average percentage accuracy for different classifiers.

Rank	Classifiers	Score	Parameters
1	S2SP	88.3	1 (σ)
2	SVM	87.6	2 (σ, C)
3	PRQ	87.0	1 (σ)
4	KFDA	86.8	1(σ)
5	δ-MPSVM	84.0	2 (σ, δ)
6	MPSVM	80.3	1 (σ)

5 CONCLUSIONS

Five recently developed, kernel-based, nonlinear classifiers, including SVM, KFDA, PRQ classifier, MPSVMs (unregularized MPSVM and regularized δ-MPSVM), and S2SP classifier, have been applied to breast cancer diagnosis and prognosis. We have studied and compared the benefits of the above classifiers in terms of classification accuracy, computing time, and sensitivity to the regularization parameter. Studies were conducted with the WDBC and WPBC datasets. Experimental results demonstrate that the classification accuracies of SVM, KFDA, S2SP, and PRQ classifiers are comparable. However, the PRQ classifier possesses the slowest computing speed, as the PRQ criterion built on pairwise constrains leads to an increase of the computing speed by l^2 as the size (l) of the training samples increases. The classification performance of MPSVM is unsatisfactory, and sensitive to the setting of the regularization parameter δ. From an overall consideration, the S2SP classifier is more favorable to users with not only higher classification accuracy but also faster computing speed; furthermore, there is no regularization parameter to be tuned for the S2SP classifier.

ACKNOWLEDGEMENTS

T. Mu would like to acknowledge financial support from the Overseas Research Students Awards Scheme (ORSAS), the Hsiang Su Coppin Memorial Scholarship Fund, and the University of Liverpool, UK. We thank the Medical Research Council (the Interdisciplinary Bridging Awards), UK, for financial support.

REFERENCES

Aizerman, M., Braverman, E., and Rozonoer, L. (1964). Theoretical foundations of the potential

function method in pattern recognition learning. *Automation and Remote Control*, 25:821–837.

Boser, B. E., Guyon, I. M., and Vapnik, V. N. (1992). A training algorithm for optimal margin classifiers. In *Proc. of the 5th Annual ACM Workshop on Computational Learning Theory*, pages 144–152.

Canu, S., Grandvalet, Y., and Rakotomam, A. (2003). *SVM and Kernel Methods Matlab Toolbox*. Perception Systems et Information, INSA de Rouen, Rouen, France.

Cortes, C. and Vapnik, V. (1995). Support-vector networks. *Machine Learning*, 20(3):273–297.

Fisher, R. A. (1936). The use of multiple measurements in taxonomic problems. *Annals of Eugenics*, 7(2):179–188.

Guo, H. and Nandi, A. K. (2006). Breast cancer diagnosis using genetic programming generated feature. *Pattern Recognition*, 39:980–987.

Lam, W., Keung, C., and Ling, C. X. (2002). Learning good prototypes for classification using filtering and abstraction of instances. *Pattern Recognition*, 35(7):1491–1506.

Mandelbrot, B. B. (1997). *The Fractal Geometry of Nature, Chapter 5*. W. H. Freeman and Company, New York.

Mangasarian, O. L., Street, W. N., and Wolberg, W. H. (1995). Breast cancer diagnosis and prognosis via linear programming. *Operations Research*, 43(4):570–577.

Mangasarian, O. L. and Wild, E. W. (2006). Multisurface proximal support vector machine classification via generalized eigenvalues. *IEEE Transactions on Pattern Analysis and Machine Intelligence*, 28:69–74.

Marshall, E. (1993). Search for a killer: Focus shifts from fat to hormones in special report on breast cancer. *Science*, 259:618–621.

Mika, S., Rätsch, G., Weston, J., Schölkopf, B., and Muller, K. (1999). Fisher discriminant analysis with kernels. In *Proc. of IEEE Neural Networks for Signal Processing Workshop*, pages 41–48.

Mu, T. and Nandi, A. K. (2007). Breast cancer detection from FNA using SVM with different parameter tuning systems and SOM–RBF classifier. *Journal of the Franklin Institute*, 344(3-4):285–311.

Mu, T., Nandi, A. K., and Rangayyan, R. M. (2007a). Pairwise Rayleigh quotient classifier with application to the analysis of breast tumors. In *Proc. of the 4th IASTED Int'l Conf. on Signal Processing, Pattern Recognition, and Applications, SPPRA*, pages 356–361, Innsbruck, Austria.

Mu, T., Nandi, A. K., and Rangayyan, R. M. (2007b). Strict 2-surface proximal classifier with application to breast cancer detection in mammograms. In *Proc. of the 32nd Int'l Conf. on Acoustics, Speech, and Signal Processing, ICASSP*, volume 2, pages 477–480, Honolulu, HI.

Schölkopf, B., Smola, A. J., Williamson, R., and Bartlett, P. (2000). New support vector algorithms. *Neural Computation*, 12:1207–1245.

Shawe-Taylor, J. and Cristianini, N. (2004). *Kernel Methods for Pattern Analysis*. Cambridge University Press, Cambridge, UK.

Street, W. N., Mangasarian, O. L., and Wolberg, W. H. (1995). An inductive learning approach to prognostic prediction. In *Proc. of the 12th Int'l Conf. on Machine Learning, ICML*, pages 522–530, Morgan Kaufmann.

Street, W. N., Wolberg, W. H., and Mangasarian, O. L. (1993). Nuclear feature extraction for breast tumor diagnosis. In *Proc. of IST/SPIE Symposium on Electronic Imaging: Science and Technology*, volume 1905, pages 861–870, San Jose, CA.

Wolberg, W. H., Street, W. N., and Mangasarian, O. L. (1993). Breast cytology diagnosis via digital image analysis. *Analytical and Quantitative Cytology and Histology*, 15(6):396–404.

Wolberg, W. H., Street, W. N., and Mangasarian, O. L. (1994). Machine learning techniques to diagnose breast cancer from fine-needle aspirates. *Cancer Letter*, 77:163–171.

Wolberg, W. H., Street, W. N., and Mangasarian, O. L. (1995). Image analysis and machine learning applied to breast cancer diagnosis and prognosis. *Analytical and Quantitative Cytology and Histology*, 17(2):77–87.

COMPARATIVE STUDY OF BLIND SOURCE SEPARATION METHODS FOR RAMAN SPECTRA

Application on Numerical Dewaxing of Cutaneous Biopsies

Valeriu Vrabie[†], Cyril Gobinet[‡], Michel Herbin[†] and Michel Manfait[‡]
[†]*CReSTIC, Université de Reims Champagne-Ardenne, Chaussée du Port, 51000 Châlons-en-Champagne, France*
[‡]*MéDIAN, CNRS UMR 6142, Université de Reims Champagne-Ardenne, 51 rue Cognacq Jay, 51096 Reims, France*
cyril.gobinet@univ-reims.fr, michel.manfait@univ-reims.fr

Keywords: Raman Spectroscopy, Paraffin-Embedded Cutaneous Biopsies, Blind Source Separation, Independent Component Analysis, Non-negative Matrix Factorization, Maximum Likelihood Positive Source Separation.

Abstract: Raman spectroscopy is a powerful tool for the study of molecular composition of biological samples. Digital processing techniques are needed to separate the wealthy but complex information recorded by Raman spectra. Blind source separation methods can be used to efficiently extract the spectra of chemical constituents. We propose in this study to analyze the performances of four blind source separation methods. Two Independent Component Analysis methods using the JADE and FastICA algorithms are based uniquely on the independence of the spectra. The Non-Negative Matrix Factorization takes into account only the positivity of underlying spectra and mixing coefficients. The Maximum Likelihood Positive Source Separation assumes both the independence and positivity of the spectra. A realistic simulated dataset allows a quantitative study of these methods while a real dataset recorded on a paraffin-embedded skin biopsy provides a qualitative study.

1 INTRODUCTION

Raman spectroscopy is a light scattering technique used in numerous biomedical applications (Choo-Smith et al., 2002). For example, it was successfully used in oncology to discriminate between malignant and benign tumors (Haka et al., 2002; Gniadecka et al., 2004). Recording the Raman scattering of a laser on a biopsy, the Raman spectroscopy gives information about the vibrational modes of the analyzed sample. Based on the uniqueness of Raman signatures of each molecular constituent, this technique extracts wealthy but complex information about the molecular composition of biopsies.

To be studied in optimal and reproducible conditions by Raman spectroscopy, thin sections of biopsies are required. A conservative property of these biopsies is also needed for their storage in tissue banks (tumor banks in oncology) for further analysis. To satisfy these requirements, the biopsies are fixed by formalin and embedded into paraffin. However, the paraffin has a Raman signature made up of energetic peaks that strongly overlap the signature of the biopsy. Visual analysis of Raman bands (shape, wavelength localization, etc.) or classical signal processing methods such as Principal Component Analysis (Haka et al., 2002) will be biased for a signature extraction objective. A solution is to chemically dewax and rehydrate the biopsies before analyzing them by Raman spectroscopy. Nevertheless, this process has several drawbacks such as: it is time and reagent consuming, the biopsies are altered and a residual layer of paraffin may remain (Faoláin et al., 2005).
To overcome these problems, an advanced signal processing method based on Independent Component Analysis (ICA) was recently proposed (Vrabie et al., 2007). This method has been shown efficient to model the recorded spectra as a linear mixing of independent Raman spectra, allowing to extract the signatures of the paraffin and, thus, to numerically dewax the biopsies. It also allows to extract the spectrum of the underlying biopsy (human skin) and therefore to define molecular descriptors specific to melanomas and nevi. However, the extraction of Raman spectra is not perfect because some residual paraffin peaks remain on estimated spectra. This might be a consequence of estimated negative peaks, as this method does not take into account the positivity of the spectra and associ-

ated mixing coefficients.

In this paper we propose a comparative study of four methods of blind source separation for numerical dewaxing of paraffin-embedded skin biopsies. The first one employs the Joint Approximate Diagonalization of Eigenmatrices (JADE) algorithm (Cardoso and Souloumiac, 1993). The second one, named FastICA (Hyvärinen et al., 2001), uses a fast fixed-point algorithm. It is employed here in its deflation scheme in which the spectra are estimated one by one. These two methods are ICA-based methods that only assume the independence of the spectra to be estimated. Next, we consider the Non-Negative Matrix Factorization (NMF) which takes into account only the positivity of underlying spectra and mixing coefficients (Lee and Seung, 1999). Finally, the Maximum Likelihood Positive Source Separation (MLPSS) assumes both the independence and positivity of the spectra to be estimated and was developed for the blind separation of Raman spectra (Moussaoui, 2005). A quantitative study is proposed by considering the results given by these methods on a realistic simulated dataset, while a qualitative study is illustrated on a dataset recorded on a paraffin-embedded skin biopsy.

2 RAMAN SPECTRA

The Raman spectrum $\mathbf{R}_k$ is defined as a N_∇ dimensional vector made up by the Raman intensities recorded at different wavenumbers into a measurement point k. By scanning K points of a sample, the Raman spectroscopy provides a matrix dataset $\mathbf{R} = [\dots, \mathbf{R}_k, \dots] \in \mathbb{R}^{K \times N_\nabla}$.

The recorded dataset $\mathbf{R}$ can be modeled as a linear sum of spectra $\mathbf{S}_i \in \mathbb{R}^{N_\nabla}$ of chemical constituents, called also sources, weighted by the corresponding mixing coefficients $\mathbf{A}_i \in \mathbb{R}^K$, called also concentration profiles (Vrabie et al., 2007):

$$\mathbf{R} = \sum_{i=1}^{M} \mathbf{A}_i \mathbf{S}_i^T + \mathbf{N}_1 + \mathbf{N}_2 \,. \qquad (1)$$

The noise $\mathbf{N}_1$ describes a part of the noise that is made up by sources related to useless chemical constituents that might be present in acquisition or by a linear additive recorded noise. The noise $\mathbf{N}_2$ denotes a nonlinear additive noise (i.e. not having a linear behavior from a spectrum to another) made up principally by slow-varying parasitic fluorescence. Since they are generated by unrelated phenomena, the noise $\mathbf{N}_1$ is supposed decorrelated from the interesting spectra $\mathbf{S}_i$. Note that the spectra of the chemical constituents and the mixing coefficients admit only positive values by definition.

This model does not take into account the deforming effects that might appear in real acquisitions such as the spectral shifts or width variations of the Raman peaks. These deforming effects and the noise $\mathbf{N}_2$ can be removed from the recorded spectra by preprocessing techniques (Gobinet et al., 2007). We note thereafter with $\mathbf{R}_{sig} = \mathbf{R} - \mathbf{N}_2$ the subspace of dimension P obtained after the preprocessing, which is made up by the interesting spectra and the linear noise $\mathbf{N}_1$.

For paraffin-embedded biopsies, the value of M can be usually fixed at 5 for cases where the Raman signature of the fixation slide (as for example CaF_2 slide) is owing to the recorded spectral range or at 4 otherwise. Moreover, it was proved that the paraffin is completely described by three sources $\mathbf{S}_1, \mathbf{S}_2, \mathbf{S}_3$ having non-overlapping thin peaks (Vrabie et al., 2007). These sources being modeled as sparse and non-Gaussian, all higher-order cross cumulants of the M sources considered in (1) vanish, assuring the independence of these sources.

Retrieving the spectra of the chemical constituents can be thus formulated as a source separation problem based on the assumption that these sources are positive and independent.

3 BSS METHODS

Blind source separation (BSS) consists in recovering unobserved sources $\mathbf{S}_i$ from several observed mixtures $\mathbf{R}$ with no a priori information about the mixing coefficients $\mathbf{A}_i$. The lack of a priori knowledge about the mixture is compensated by physically plausible assumption on the sources such as decorrelation, independence and/or positivity. A review of the BSS approaches can be found in (Cardoso, 1998).

BSS methods usually suppose that the number of sources is smaller than the number of observed mixtures and that the dataset is noise-free. Generally, the number of recorded spectra (i.e. K in our case) being at least one hundred spectra, the first assumption holds. The second one is not respected by the subspace $\mathbf{R}_{sig}$ since the noise $\mathbf{N}_1$ remains after the preprocessing. Based on the assumption that this noise is decorrelated from the interesting spectra, it can be estimated and removed by decomposing the subspace $\mathbf{R}_{sig}$ in two orthogonal subspaces by the use of the Singular Value Decomposition (Vrabie et al., 2007):

$$\mathbf{R}_{sig} = \sum_{j=1}^{M} \delta_j \mathbf{U}_j \widetilde{\mathbf{S}}_j^T + \sum_{j=M+1}^{P} \delta_j \mathbf{U}_j \widetilde{\mathbf{S}}_j^T \,, \qquad (2)$$

Note that this decomposition can be linked with the well known Principal Component Analysis (PCA). The second subspace is an estimate of the noise

$\mathbf{N}_1$. The first subspace is constructed by decorrelated spectra $\widetilde{\mathbf{S}}_j$, which are still a linear mixing of interesting spectra, and fit the BSS model. The spectra of paraffin being modeled by independent sources, stronger criteria than decorrelation must be used to extract them. Note that this decomposition may introduce negative values in the first subspace, especially when the recorded intensities are weak, which is not usually the case in Raman spectroscopy. In these cases, the above subspace reduction can be replaced by a random projection of the dataset $\mathbf{R}_{sig}$ into a positive matrix having M lines (Moussaoui, 2005).

3.1 ICA

The Independent Component Analysis (ICA) is a computational technique for the BSS problem based on the only assumption that the sources are mutually independent and at most one is Gaussian. A detailed description can be found in (Hyvärinen et al., 2001). We focus here only on two ICA algorithms: JADE (Cardoso and Souloumiac, 1993) and FastICA (Hyvärinen et al., 2001).

ICA has two indeterminacies: the energies (variances) and the order of the independent components (estimated spectra) cannot be determined. The first ambiguity is avoided by estimating independent components of unit variances. This is not a restriction for this kind of application since we are interested to identify the spectrum of the biopsy in order to find molecular descriptors. Moreover, the ambiguity of the sign of the estimated spectra is not avoided, but this is insignificant since the sign can be found in the mixing coefficients. For these reasons and to simplify the theory and the algorithms, the dataset $\mathbf{R}_{sig}$ is centered by subtracting the mean of each spectrum. Each observation is also normalized to unit variance, ensuring that even weak-amplitude recorded observations are well represented within the input data.

3.1.1 JADE Algorithm

The 4^{th} order cross-cumulants of the decorrelated sources $\widetilde{\mathbf{S}}_j$ given by PCA in Eq. (2) are firstly computed. A $M \times M \times M \times M$ dimensional tensor is obtained, which must be diagonalized in order to find independent sources. The Joint Approximate Diagonalization of Eigenmatrices (JADE) algorithm (Cardoso and Souloumiac, 1993) uses the joint diagonalization of cumulant matrices obtained by unfolding the obtained 4^{th} order tensor. This step provides a $M \times M$ rotation matrix $\mathbf{B}$ that is used to find independent sources $\widehat{\mathbf{S}}_i$ by multiplying the matrix made up by the decorrelated sources $\widetilde{\mathbf{S}}_j$ with this matrix $\mathbf{B}$. The $\widehat{\mathbf{S}}_i$'s are centered and normalized estimators of the interesting spectra $\mathbf{S}_i$.

3.1.2 FastICA

The FastICA algorithm is based on a fixed-point iteration scheme for finding directions in which the negentropy is maximized. Beyond the very fast convergence of this algorithm (at least quadratic), the algorithm finds directly independent components of (practically) any non-Gaussian distribution using a nonlinearity g, so no estimate of the probability distribution function has to be first available. The nonlinearity can optimize the performance of the method allowing to obtain algorithms that are robust and/or of minimum variance. Moreover, the independent components can be estimated one by one, which is equivalent to a projection pursuit. A detailed description of this algorithm can be found in (Hyvärinen et al., 2001).

This algorithm was employed here in its deflation scheme. The algorithm iteratively finds directions in which the estimated independent components are maximally nongaussian. This technique is appropriate to initially estimate the spectra of the paraffin $\mathbf{S}_1, \mathbf{S}_2, \mathbf{S}_3$. The spectrum of the biopsy is hence obtained by deflation as the remaining source.

3.2 NMF

Broadly speaking, the Non-Negative Matrix Factorization (NMF) factorizes a matrix made up of non-negative values in two other matrices composed of non-negative values, which multiplied will approximately equalize the original result (Lee and Seung, 1999). The factorization algorithms are based on iterative updates which minimize a criterion such as the least squares error or generalized Kullback-Leibler divergence. These algorithms can only be guaranteed to find local minima, rather than a global minimum, and the obtained results depend on the initialization.

The NMF using a least squares error algorithm was used here in order to test if it is possible to find positive spectra $\mathbf{S}_i$ and mixing coefficients $\mathbf{A}_i$ from the dataset $\mathbf{R}_{sig}$ without further a priori information.

3.3 MLPSS

The Maximum Likelihood Positive Source Separation (MLPSS) assumes both the independence and positivity of the spectra to be estimated and has been developed especially for the blind separation of Raman spectra (Moussaoui, 2005). It models the positive independent spectra to be estimated by gamma probability density functions (pdf) with an α parameter

greater than one. This model is well adapted to spectra of the paraffin $\mathbf{S}_1, \mathbf{S}_2, \mathbf{S}_3$.

To solve this problem, two algorithms were proposed. The first one is based on the maximization of the likelihood by using a Monte-Carlo Expectation-Maximization scheme, while the second one combines the above assumptions and the maximum likelihood technique to derive a steepest gradient algorithm. This last algorithm was used here because it is faster and it is well adapted for cases where the noise is small, which is the case of large acquisitions after the noise removal by PCA.

3.4 Application

A quantitative study on a realistic simulated dataset is firstly presented followed by a qualitative study on a dataset recorded on a paraffin-embedded skin biopsy.

3.4.1 Simulated Dataset

We consider here four spectra $\mathbf{S}_1, \ldots, \mathbf{S}_4 \in \mathbb{R}^{990}$ represented in Figure 1. The first three were constructed from a recording on a paraffin block. The peaks were selected by the use of a Hanning window accordingly with the fact that the paraffin is defined by three spectra (Vrabie et al., 2007). The last one is the spectrum of the human skin estimated on a real dataset by an ICA-based BSS method. Note however that linear interpolations were used to eliminate the imperfections corresponding to contributions of paraffin peaks.

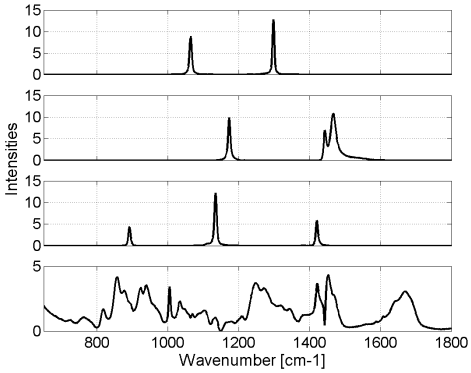

Figure 1: Simulated spectra.

These spectra were linearly mixed to construct $K = 250$ observations by randomly picking positive mixing coefficients from a mixing matrix obtained on a real dataset. Figure 2 shows one observation. The mixing coefficients of $\mathbf{S}_4$ are very low compared to the others, due to the energetic Raman signatures of the paraffin that are present in real acquisitions. Note that this dataset is free of noise, so the decomposition given in Eq. (2) was not performed here.

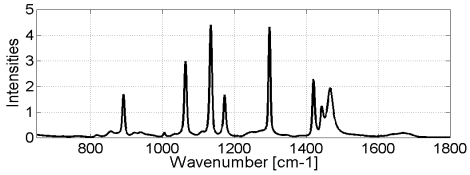

Figure 2: Example of one observation.

The number of sources to be estimated was set at $M = 4$ for all BSS methods. The dataset was centered and each observation normalized to unit variance before applying the ICA-based methods. A "pow3" nonlinearity g was chosen for the FastICA because it gives the best estimator for the last spectrum.

The threshold of the least squares error algorithm for NMF was set at 10^{-10}. As the convergence was very slow, a second stop condition was used: the variations of the least squares error from one iteration to other must be smaller than 10^{-5}. Even in this case the convergence was very slow, the number of iterations, which depends on the initialization, was about $6 \cdot 10^5$. Note that the results presented here are the best obtained for 20 different initializations of the NMF.

The gradient step size of the MLPSS method was set at 10^{-3}, which is a usual value for this kind of data. The MLPSS method has a faster convergence than NMF, around 10^4 iterations are necessary to obtain a good estimate of the spectra. However, the MLPSS did not have a convergence toward a stationary point, so it was stopped after $5 \cdot 10^5$ iterations.

Figure 3 shows the estimated spectra $\widehat{\mathbf{S}}_4$ of the last spectrum $\mathbf{S}_4$ by the presented BSS methods. We focus here only on this spectrum because it corresponds to the underlying biopsy in real applications and its estimation is of interest.

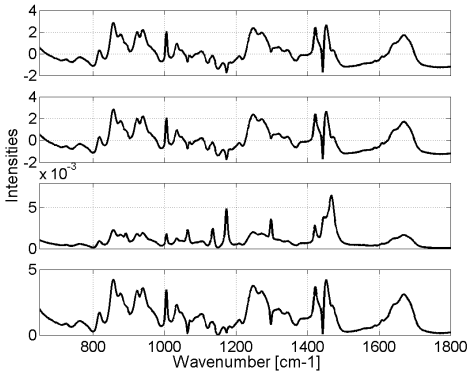

Figure 3: Estimators of the 4th spectrum. From top to bottom: JADE, FastICA, NMF and MLPSS.

As we can see, the NMF fails to estimate this spectrum. This is due to the fact that NMF requires the existence of a monomial submatrix in the dataset in order to ensure the convergence of the algorithm to the right solution (Moussaoui, 2005). The MLPSS

provides a good positive estimate with few imperfections corresponding to contributions of paraffin peaks at 1065 cm^{-1} and 1300 cm^{-1}. The two ICA-based methods give the same results. The estimated spectra have zero mean and unit variance and follow the shape of the original spectrum except some imperfections at 1175 cm^{-1} and 1470 cm^{-1}. Note that all estimated mixing coefficients have uniquely positive values, even for the ICA-based methods.

In order to provide a quantitative study we compute the root mean square error (RMSE):

$$\text{RMSE} = \left\| \overline{\mathbf{S}}_4 - \widehat{\mathbf{S}}_4 \right\| / \sqrt{N_{\overline{\nu}}} \qquad (3)$$

where $\|.\|$ denotes the Frobenius norm and $\overline{\mathbf{S}}_4$ the centered and normalized version of the original spectrum $\mathbf{S}_4$ used to construct the mixtures. $\widehat{\mathbf{S}}_4$ denotes either the spectra estimated by ICA-based methods or the centered and normalized versions of the spectra estimated by NMF or MLPSS.

The values of RMSEs obtained for the estimated spectra (see figure 3) are: 0.1605 for JADE, 0.1603 for FastICA, 0.8017 for NMF and 0.1264 for the MLPSS algorithm. These values confirm that ICA-based methods give practically the same results and that NMF fails to estimate this spectrum. Moreover, we can conclude that the MLPSS method gives the best estimate, which, additionally, has positive values.

In the following we consider the case where a linear noise $\mathbf{N}_1$, decorrelated from the interesting spectra, is added to the observations. We have chosen here a Gaussian noise for the sake of simplicity. This noise also simulates slight deforming effects on the peaks of paraffin that may remain after the preprocessing steps in real cases. This study is done by varying the signal-to-noise ratio (SNR):

$$\text{SNR} = 20\log_{10} \frac{\left\| \sum_{i=1}^{4} \mathbf{A}_i \mathbf{S}_i^T \right\|}{\|\mathbf{N}_1\|} \quad [dB] \qquad (4)$$

Note that the decomposition (2) does not completely remove the noise $\mathbf{N}_1$. After this step, a gain of $17dB$ is obtained for high values of SNR (i.e. SNR$=$ $50dB$). This gain linearly decreases with the SNR, a gain of $6.5dB$ being obtained for a SNR$=2.5dB$.

Figure 4 shows the evolutions of the RMSEs for the estimated spectrum $\widehat{\mathbf{S}}_4$ with respect to the SNR. These values are averaged over 4 independent realizations of the noise. The values obtained by the JADE algorithm (represented by "■") are superposed on those obtained for the FastICA (represented by "×"). These evolutions confirm the conclusion stated above even if, punctually, the RMSE of the MLPSS is larger than the ones obtained by ICA methods.

Although these results give the MLPSS as the best separation method, it is interesting to study the errors

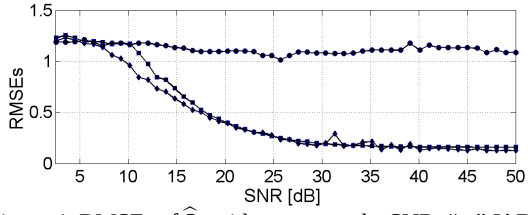

Figure 4: RMSEs of $\widehat{\mathbf{S}}_4$ with respect to the SNR: "■" JADE, "×" FastICA, "•" NMF, "♦" MLPSS.

of, for example, the estimator $\widehat{\mathbf{S}}_3$ of the third spectrum of the paraffin. These errors are shown in Figure 5.

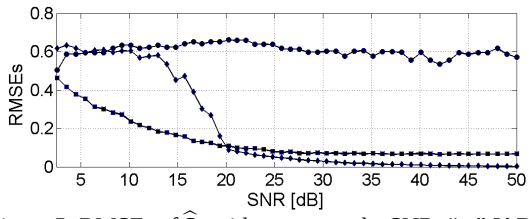

Figure 5: RMSEs of $\widehat{\mathbf{S}}_3$ with respect to the SNR: "■" JADE, "×" FastICA, "•" NMF, "♦" MLPSS.

The result obtained for the MLPSS method is due to the fact that the same peak of the paraffin is extracted by two estimators, $\widehat{\mathbf{S}}_2$ and $\widehat{\mathbf{S}}_3$. For real applications this effect can perturb the estimator of the biopsy, especially when the preprocessing does not completely compensate the deforming effects.

3.4.2 Real Dataset

The study is done on a dataset composed of $K = 1254$ Raman spectra acquired on a paraffin-embedded skin biopsy. Spectral data were recorded into $N_{\overline{\nu}} = 990$ points in the 650-1816 cm^{-1} range by using a Labram microspectrometer. The preprocessing techniques developed in (Gobinet et al., 2007) are firstly used in order to improve the estimated spectra.

Figures 6, 7 and 8 show the results obtained by the JADE, NMF and MLPSS algorithms. The results of the FastICA being the same with those given by JADE are not presented here. The same parameters as in the simulated case were used. Some residual peaks of paraffin, which sometimes are negative, are present on spectra estimated by the JADE algorithm. However, this technique provides positive mixing coefficients. The spectrum of the biopsy estimated by NMF contains more energetic residual peaks of the paraffin than the JADE estimator, whereas the spectra of the paraffin are not well estimated. Spectra estimated by MLPSS are close to the JADE results, but the same peak of the paraffin (1135 cm^{-1}) is extracted by two estimators as in the simulated case. Moreover, the application of this algorithm on another paraffin-embedded skin biopsy led to a wrong estimation of spectra, contrary to JADE.

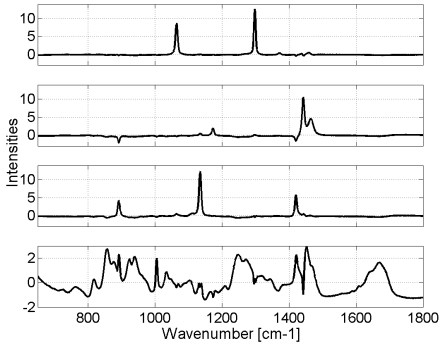

Figure 6: Spectra estimated by JADE.

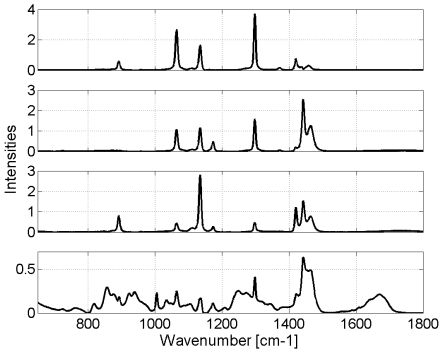

Figure 7: Spectra estimated by NMF.

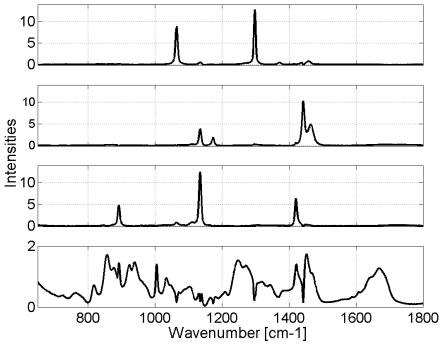

Figure 8: Spectra estimated by MLPSS.

4 CONCLUSIONS

Four BSS methods were studied on simulated and real datasets. Taking into account only the positivity, the NMF fails to estimate the interesting spectra. The positivity combined with the independence allows the MLPSS method to provide a good estimator for the biopsy, but artefacts are obtained for the paraffin for which the same peak is extracted by more than one estimator. Furthermore, the results obtained by this method depend on the analyzed biopsy. ICA-based methods give good estimators for all spectra, which do not depend on the biopsies, and extract positive mixing coefficients. These last methods can thus be employed as an efficient tool for the extraction of Raman spectra of chemical species and consequently for a numerical dewaxing of biopsies. However, all these methods allow to extract a unique spectrum of the skin, which might be insufficient for a classification purpose. Investigations are under way for the study of a numerical dewaxing based on least square methods, taking into account the Raman spectra of the parafin estimated on paraffin blocks.

REFERENCES

Cardoso, J.-F. (1998). Blind signal separation: statistical principles. *Proceedings of the IEEE*, 86:2009–2025.

Cardoso, J.-F. and Souloumiac, A. (1993). Blind beamforming for non-gaussian signals. *IEE Proceedings-F*, 140:362–370.

Choo-Smith, L.-P., Edwards, H., Endtz, H., Kros, J., Heule, P., Barr, H., Robinson, J., Bruining, H., and Puppels, G. (2002). Medical applications of Raman spectroscopy: from proof of principle to clinical implementation. *Biopolymers*, 67:1–9.

Faoláin, E., Hunter, M., Byrne, J., Kelehan, P., Lambkin, H., Byrne, H., and Lyng, F. (2005). Raman spectroscopic evaluation of efficacy of current paraffin wax section dewaxing agents. *Journal of Histochemistry and Cytochemistry*, 53:121–129.

Gniadecka, M., Philipsen, P., Sigurdsson, S., Wessel, S., Nielsen, O., Christensen, D., Hercogova, J., Rossen, K., Thomsen, H., Gniadecki, R., Hansen, L., and Wulf, H. (2004). Melanoma diagnosis by Raman spectroscopy and neural networks: Structure alterations in proteins and lipids in intact cancer tissue. *The Journal of Investigative Dermatology*, 122:443–449.

Gobinet, C., Vrabie, V., Tfayli, A., Piot, O., Huez, R., and Manfait, M. (2007). Pre-processing and source separation methods for Raman spectra analysis of biomedical samples. In *Proceedings of the 29th Annual International Conference of the IEEE Engineering in Medicine and Biology Society, Lyon, France*.

Haka, A., Shafer-Peltier, K., Fitzmaurice, M., Crowe, J., Dasari, R., and Feld, M. (2002). Identifying microcalcifications in benign and malignant breast lesions by probing differences in their chemical composition using Raman spectroscopy. *Cancer Research*, 62:5375–5380.

Hyvärinen, A., Karhunen, J., and Oja, E. (2001). *Independent Component Analysis*. Wiley, New York.

Lee, D. and Seung, H. (1999). Learning the parts of objects by non-negative matrix factorization. *Nature*, 401:788–791.

Moussaoui, S. (2005). *Séparation de sources non-négatives. Application au traitement des signaux de spectroscopie*. PhD thesis, CRAN INPL, Nancy, France.

Vrabie, V., Gobinet, C., Piot, O., Tfayli, A., Bernard, P., Huez, R., and Manfait, M. (2007). Independent component analysis of Raman spectra: Application on paraffin-embedded skin biopsies. *Biomedical Signal Processing and Control*, 2:40–50.

TREMOR CHARACTERIZATION
Algorithms for the Study of Tremor Time Series

E. Rocon, A. F. Ruiz, J. C. Moreno, J. L. Pons
Bioengineering group, IAI-CSIC, Ctra. Campo Real, km 0.200, Madrid, Spain
erocon@iai.csic.es

J. A. Miranda
Technaid S. L., Madrid, Spain
ja.miranda@technaid.com

A. Barrientos
Grupo de Robótica y Cibernética, UPM, Madrid, Spain
antonio.barrientos@upm.es

Keywords: Tremor, Empirical mode decomposition, Inertial sensors, Timefrequency analysis, Real-Time estimation.

Abstract: This paper introduces the work developed by the authors in the study of tremor time series. First, it introduces a novel technique for the study of tremor. The technique presented is a high-resolution technique that solves most of limitations of the Fourier Analysis (the standard technique to the study of tremor time series). This technique was used for the study of tremorous movement in joints of the upper limb. After, some conclusions about tremor behaviour in upper limb based on the technique introduces are presented. Furthermore, an algorithm able to estimated in real-time the voluntary and the tremorous movement was presented. This algorithm was validated in two contexts with successful results. Finally, some conclusions and future work are given.

1 INTRODUCTION

Tremor is a rhythmic, involuntary muscular contraction characterized by oscillations of a part of the body (Anouti and Koller, 1998). The oscillatory activities are related to various combinations of four basic mechanisms: (a)mechanically induced oscillations, (b) oscillations due to reflexes, (c) oscillations generated by neuronal generators in the central nervous system, (d) oscillations resulting from impaired feedforward and feedback loops.

It is well established that tremorous activity is composed of deterministic and stochastic components, (Timmer et al., 2000). The detection and quantification of tremor are of clinical interest for diagnosis of neurological disorders and objective evaluation of their treatment, (Gao and Wen-wen, 2002). Furthermore, the estimation of tremor is an important stage in systems that aim to control limb oscillations, and also in biofeedback studies. In this regard, estimation techniques have been developed for tremor suppression. Methods based on the Fourier transform (FT) are commonly employed for this purpose, specially because of the similarity between the tremor to a sine wave, (Elble and Koller, 1990). For instance, the weighted Fourier linear combiner (WFLC) characterizes the tremor based on its approximation by a sinusoidal waveform, (Riviere, 1995). Riviere also investigated the application of neural networks to augment manual precision by cancelling involuntary motion. Another example is the extraction of frequency parameters from the power spectrum (based on the FT) of the tremor for classification purposes, (Rocon et al., 2004).

This paper introduces an original study for tremor characterization. First, experiments were performed with 31 patients suffering from tremor diseases in order to study tremor characteristics. The data collected in this experiments were analyzed by means of a novel methodology for the study of tremor time series based on *Empirical Mode Decomposition*. This technique allows an automatic detection of tremorous movement and the study of nonlinear and nonstationary characteristics of tremor, (Rocon et al., 2006). Based on the information provided by this study, a novel algorithm able to estimate in real time and composed by two stages, one for the detection of voluntary movements and other for the estimation of

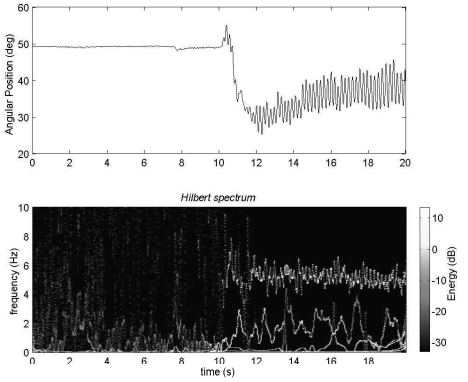

Figure 1: Hilbert Spectrum of an Essential tremor patient performing the task of Keeping the arms outstretched. The high levels of energy activities are perceived when the patient is performing the task.

tremorous movements, is presented. Finally, experiments for the validation of the algorithm presented are given.

2 THE EXPERIMENTAL PROTOCOL

In order to assess tremor characteristics we studied its behavior in 31 patients suffering from different pathologies. The average age of patients was 52.3 years old (ranging from 23 to 84 years old). All patients provided their written consent for the experiments.

The diagnosis of the condition of patients was given by the neurological staff of the General Hospital of Valencia (GHV, Spain) and the functional state of patients was evaluated by means of the Faher scale, (Fahn et al., 1998). Ethical approval for this research has been granted by the Ethical Committee of the GHV.

2.1 Sensors

The tremor was detected by a customized sensor, which is based on the combination of two independent gyroscopes placed distally and proximally to the joint of interest. The joint angular speed is obtained by subtraction of the angular speed measured by one gyroscope from the angular speed measured by the other one. The weight of the system is roughly 15 g, which is a low-mass system when compared to other sensors used in the field, (Rocon et al., 2004). The use of a low-mass sensor is important to reduce the effect of low-pass filtering on the detected signal. Gyroscopes were placed in order to estimate following movements of the upper limb: 1) Elbow flexion-extension, 2) Forearm pronation-supination, 3) Wrist flexion-extension, and 4) Wrist deviation.

2.2 Tasks

Six different tasks were employed for excitation of tremor: 1) Rest, 2) Reaching for an object, 3) Drawing a spiral, 4) Arm outstretched, 5) Touching nose, and 6) Moving a cup. In all tasks the patient was sitting on a chair. This set of tasks aims to stimulate all different types of tremor.

3 ANALYSIS OF TREMOROUS MOVEMENT

In order to analyze the tremorous movement acquired during the experiments, *Empirical Mode Decomposition* was used. This technique was proposed in (Rocon et al., 2006). This technique was identified as a very useful tool for an automatic decomposition of the signal into tremor and voluntary signal. Moreover, this technique enables the representation of the amplitude and the instantaneous frequency of the input signal as function of time in which the amplitude could be contoured on the time-frequency plane. The technique presented is a high-resolution technique that solves most of limitations of the Fourier Analysis (the standard technique to the study of tremor time series). This technique provides, in a time-frequency-energy plot, a clear visualization of local activities of tremor energy over the time, see figure 1.

Based on this technique, a study of the tremorous movement at different joints of the upper limb was developed. The study was performed with the data collect from the experiments introduced in the previous section and aim at understanding tremorous behaviour. The main conclusions of this study are the following: 1)the amplitude of the tremorous movement is larger in distal joints than in proximal joints, 2)the frequency of tremorous movements is comprised in the bandwidth between 3 and 8 Hz, 3)tremor frequency at different joints of the upper limb has very similar values, 4)tremor frequency is not related to the task performed by the patient, 5)the frequency of tremorous movement is constant during the execution of a task, nevertheless it could change during repetitions of the same task, 6)tremor activity is not always present during the experiments. Patients showed tremor activity just during 40% of the time measured, 7) sex and age does not influence tremor behaviour. The main novelty of this study is that it is centered in tremor at joint level while the majority of the studies presented in the literature are centered in the study of

tremor at finger tip. The main drawback of this technique is the impossibility to implement it in real-time (RT). In order to address this issue, next section describes the development of an algorithm able to distinguish in RT tremorous movement from voluntary movement.

4 TREMOR ESTIMATION

A number of estimation algorithms have been developed for tremor suppression. As a first approach, we evaluated robust algorithms based on IEEE-STD-1057, which is a standard for fitting sine waves to noisy discrete-time observations. In particular, the weighted-frequency Fourier linear combiner (WFLC) developed by Riviere, (Riviere, 1995), in the context of actively counteracting physiological tremor in microsurgery was implemented. The WFLC is an adaptive algorithm that estimates tremor using a sinusoidal model, estimating its time-varying frequency, amplitude, and phase. The WFLC can be described by equation 1. It assumes that the tremor can be mathematically modelled as a pure sinusoidal signal of frequency ω_0 plus M harmonics and computes the error, ε_k, between the motion, s_k, and its harmonic model.

$$\varepsilon_k = s_k - \sum_{r=1}^{M} [w_{r_k} \sin(r\omega_{0_k} k) + w_{r+M_k} \cos(r\omega_{0_k} k)] \quad (1)$$

In its recursive implementation, see equations 2 and 3, the WFLC can be used online to obtain estimations of both tremor frequency and amplitude, (Riviere, 1995).

$$w_{0_{k+1}} = w_{0_k} + 2\mu_0 \varepsilon_k \sum_{r=1}^{M} r\,(w_{r_k} x_{M+r_k} - w_{M+r_k} x_{r_k}) \quad (2)$$

where,

$$x_{rk} = \begin{cases} \sin(r\omega_0 k), & 1 \le r \le M \\ \cos((r-M)\omega_0 k), & M+1 \le r \le 2M \end{cases} \quad (3)$$

The WFLC algorithm was evaluated with the signals measured in the experiments described in previous section. In the completed trials, the algorithm was able to estimate the tremor movement of all the patients with accuracy always lower than 2 degrees, see figure 2. The main disadvantage of the WFLC is the need for a preliminary filtering stage to eliminate the voluntary component of the movement, (Riviere, 1995). This filtering stage introduces an undesired time lag for our system when estimating tremor movement, this time lag introduces a time delay that could considerably affect the implementation of the control strategies for tremor suppression.

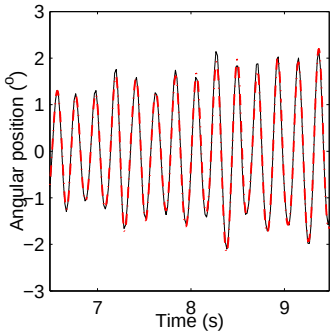

Figure 2: Estimation of tremor, solid line, based on WFLC algorithm, red dashed line.

4.1 Estimation of Voluntary Movement

The tremor literature indicates that voluntary movements and tremor movements are considerably different, (Elble and Koller, 1990). Voluntary movements are slower while tremor movements are brusquer. This indicates that adaptive algorithms to estimate and track movement would be useful when separating the two movements with an appropriate design. The underlying idea is to design the filters so that they only estimate the less dynamic component of the input signal, which in our case we consider to be voluntary movement, thereby filtering out the tremor movement.

A set of algorithms was considered for the estimation of the voluntary motion: two point-extrapolator, critically damped g-h estimator, Benedict-Bordner g-h estimator, and Kalman filter. These algorithms implement both estimation and filtering equations. The combination of these actions allows the algorithm to filter out the tremorous movement from the overall motion at the same time it reduces the phase lag introduced, (Bar-Shalom and Li, 1998). The equation parameters were adjusted to track the movements with lower dynamics (voluntary movement) since tremors present a behaviour characterised by quick movements. The performance of these algorithms were compared based on their accuracy when estimating voluntary movements of tremor time series from patients.

4.1.1 Two Points Extrapolator

It is the simplest tracking algorithm. This algorithm uses the current position measured, y_n, and the past measured position, y_{n-1}, to estimate the velocity, $\dot{x}^*_n$, and the future position x^*_{n+1}.

$$\dot{x}^*_n = \frac{y_n - Y_{n-1}}{T}, \quad (4)$$

$$x^*_{n+1} = y_n + T * \dot{x}^*_n, \quad (5)$$

where T is the sample time and "$*$" denotes an estimated value.

4.1.2 Critically Damped G-h Estimator

This estimation algorithm is a g-h filter composed by g-h track update equations and by g-h prediction equations

$$update \begin{cases} \dot{x}^*_{k,k} = \dot{x}^*_{k,k-1} + h_k \left(\frac{y_k - x^*_{k,k-1}}{T} \right) \\ x^*_{k,k} = x^*_{k,k-1} + g_k \left(y_k - x^*_{k,k-1} \right) \end{cases} \quad (6)$$

$$predict \begin{cases} \dot{x}^*_{k+1,k} = \dot{x}^*_{k,k} \\ x^*_{k+1,k} = x^*_{k,k} + T\dot{x}^*_{k+1,k} \end{cases} \quad (7)$$

The track update equations or estimation equations, 6, provide us the velocity and position of tremor at time kT after the measurement of the angular position of the joint, y_k. The estimated position is based on the use of the actual measurement as well as the past prediction. As a consequence of filtering, the measured noise is reduced. The predicted position is an estimate of x_{n+1} based on past states and prediction (equation 7), and take into account the current measurement by means of updated states.

4.1.3 Benedict-Bordner G-h Estimator

This estimation algorithm have the same equations that the Critically Damped g-h estimator but with different values in the parameters g-h, (Bar-Shalom and Li, 1998). The Benedict-Bordner estimator is designed to minimize the transient error. Filter g-h parameters are related by:

$$h = \frac{g^2}{2-g} \quad (8)$$

4.1.4 The Kalman Filter

The Kalman filter is a g-h filter where the weights g and h are a function of n and are updated recursively. This filter has the advantage of allowing the optimum use of the information if it is available. In addition, permits the use of the target dynamics information to optimize the filter parameters. More complete information about Kalman filter can be found in (Bar-Shalom and Li, 1998).

4.2 Figure of Merit

In order to quantitative compare the estimators proposed a metric, *Cinematic Estimation Error (CEE)*, was proposed. The equation that define this metrics is:

$$CEE = \sqrt{\varphi^2_{|b^*|} + \sigma^2_{\dot{x}^*}}, \quad (9)$$

where $\varphi^2_{|b^*|}$ is the mean square of errors of the estimators: $|b^*| = |x_k - x^*_{k,k-1}|$, and $\sigma^2_{\dot{x}^*}$ variance of the estimation.

CEE quantifies the transient response through $\varphi^2_{|b^*|}$ and, at the same time, the averaging or filtering capabilities of the filter through the term $\sigma^2_{\dot{x}^*}$. The accuracy and transient response of the estimation algorithms are important. Another important parameter taken into account in our analysis was the execution time of each algorithm in view of the fact that the system was designed to work in real time. The result of such analysis indicated that Benedict-Bordner filter presents the best results with the lowest computational cost.

4.3 Real-time Estimation of Voluntary and Tremorous Movement

The solution adopted was the development of an algorithm capable of estimating voluntary and tremorous motion with a small phase lag based on a two-stage algorithm. In the first stage, the Benedict-Bordner filter estimates the voluntary component of the movements. In the second stage, the estimated voluntary motion is removed from the overall motion and it is assumed that the remaining movement is tremor. After this, the WFLC was used in order to estimate tremor parameters. In this stage, the algorithm estimates both the amplitude and the time-varying frequency of the tremorous movement.

The algorithm proposed was evaluated with data obtained from the patients measured in our experiments. The estimation error of the first stage was 1.4 ± 1.3 degrees. The second stage algorithm has a convergence time always smaller than 2 s for all signals evaluated and the Mean Square Error (MSE) between the estimated tremor and the *real tremor*, after the convergence, is smaller than 1 degree. The combination of both techniques resulted in a very efficient algorithm with small processing cost for estimating in real time the voluntary and the tremorous components of the overall motion.

5 EXPERIMENTS AND RESULTS

The performance of the algorithm proposed was evaluated in two different contexts: 1)Tremor suppression based on exoskeleton devices, and 2)Filtering tremorous movement from PC mouse cursor.

5.1 Tremor Suppression based on Exoskeleton Devices

The algorithm for tremor estimation was incorporated to the WOTAS (Wearable Orthosis for Tremor Assessment and Suppression) active exoskeleton for tremor suppression, (Rocon et al., 2007). In order to evaluate the performance of the device developed to suppress tremor we have planned an experimental phase involving 10 patients suffering from different tremor diseases. During the first clinical trials the algorithm was able to measure and estimate tremor parameters, see Figure 3. The capacity of applying dynamic internal forces to the upper limb for tremor suppression (based on the information provided by the tremor estimation algorithm) was also evaluated. Based on this parameter it was found that the device could achieve a consistent 30% tremor power reduction, with reduction peaks in the order of 80% in the tremor power for patients exhibiting severe tremor, see Figure 3. Moreover, patients related that they felt small influence of the WOTAS device on their intended motion, which indicates a proper functioning of the algorithms proposed in the precious section, (Rocon et al., 2007).

5.2 Filtering Tremorous Movement From PC Mouse Cursor

In these experiments the algorithm was integrated in a device connected between the mouse and the computer that should remove tremorous movements from PC mouse cursor. These experiments were carried out in cooperation with Spanish Foundation of Multiple Sclerosis. Previously to the realization of the experiment, the operation of the system was explained to the user. After, the patient was asked to achieve a comfortable position in the chair and to grab and use the mouse as natural as possible. After a time of adaptation and relaxation, roughly 10 minutes, the patient was asked to perform 2 typical movements when using a computer mouse:

1. **Draw a spiral** - The patient was asked to follow with the cursor of the mouse a path with the form of a spiral drawn on the screen of the computer. The trajectory described by the user is not illustrated in the screen; with this approach it is possible to avoid the attempts of the user to correct the trajectory. The patient just has the reference of the model spiral on the screen. During this tasks the buttons are disabled and the trajectory described by the user was recorded by the software.

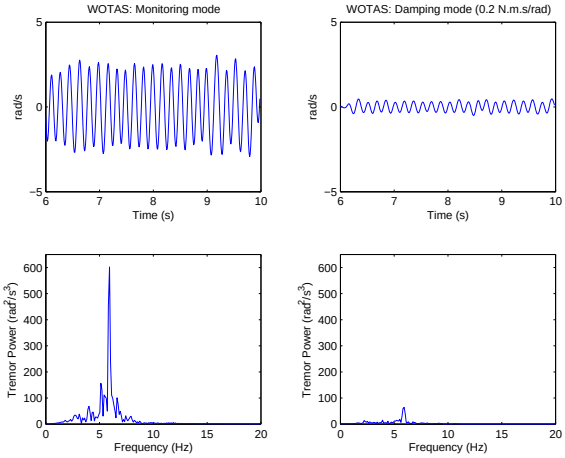

Figure 3: The graphics illustrated the reduction in the tremor power when WOTAS is applying viscosity to the tremorous movement.

2. **Goal and click** - To move the cursor over 10 icons that appear in a random sequence on the screen of the computer.The patient was asked to click over the picture every time he/she reaches it. In this way, the next picture will appear just after the patient click on the actual one. The trajectories and the number of erroneous clicks were recorded.

The total time of each experiment was 40 minutes and the main objective was to quantify the effectiveness of the device in tremor suppression. Each task was repeated 3 times, one with the filter disabled, another one with the filter activated and in the last trial, the filter is deactivated again. The order of trials was randomized. The figures of merit used to quantify the improvement in the ability of the patient in the realization of the tasks were:

1. The relation between the number of times the user leaves the boundaries of the path defined by the spiral, with and without the help of the algorithms, in the task *draw a spiral*, e_s.
2. The relation between the number of erroneous clicks, with and without the help of the algorithms, during the *click and goal* task, e_c.

Table 1: Results of the experiments.

Patient	e_s	e_c
1	20 %	44 %
2	33 %	100 %
3	30 %	28 %
4	50 %	33 %

Table 1 summarizes the results obtained in the data analysis. The results show that all patients improved their performance using the algorithm. In the

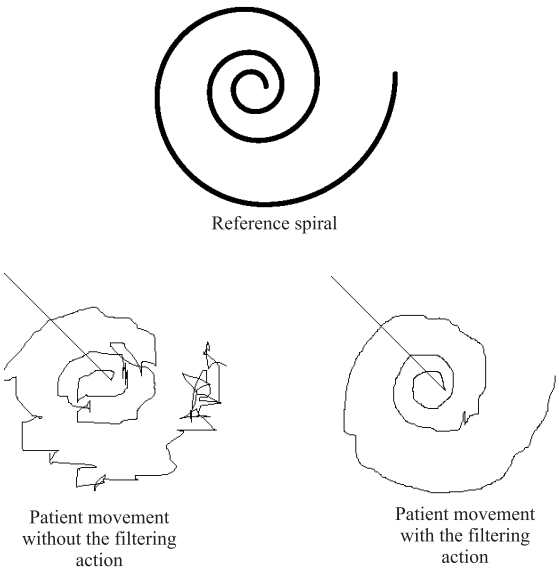

Figure 4: Results of a patient performing the task of drawing a spiral.

case of the *draw a espiral* task, the mean reduction in the error during the realization of the task was in order of 33,3%. This is a sign of a improvement of the patient ability in tracking a shape in the screen. The patients also presented a mean reduction of 52 % in the number of erroneous clicks during the execution of the *goal and click* task. These results indicates a consistent improvement in the ability of the patient in the execution of the tasks, see Figure 4. During the trials it was noticed that feedback of a smooth movement has a positive impact. Two patients spontaneously related that they felt a decrease in the amplitude of their tremorous movement.

6 CONCLUSIONS

This paper summarizes the work developed by the authors in the study of tremor time series. First, it introduces a novel technique for the study of tremor. The main advantage of this technique it that it allows an automatic estimate of the tremulous movement for different pathologies. The technique presented is a high-resolution technique that solves most of limitations of the Fourier Analysis (the standard technique to the study of tremor time series). This technique provides, in a time-frequency-energy plot, a clear visualization of local activities of tremor energy over the time.

The technique was used for the study of tremorous movement in joints of the upper limb. This study generates some conclusions about tremor behaviour in upper limb.

Furthermore, an algorithm able to estimated in real-time the voluntary and the tremorous movement was presented. This algorithm was validated in two contexts with successful results. The algorithm introduced presents a learning behavior that adapts to personal characteristics of each user. This algorithm was implemented in a novel device able to filter tremorous movement from a mouse cursor before it reaches computer interface. The device was successfully tested with patients. The results of the experiments showed an improvement of the patient ability in tracking a shape in the screen and a consistent improvement in the ability of the patient in the accomplishment of tasks, for instance, the number of erroneous clicks was reduced in 52%.

REFERENCES

Anouti, A. and Koller, W. (1998). Tremor disorders: diagnosis and management. *The Western Journal of Medicine*, 162(6):523–530.

Bar-Shalom, Y. and Li, X. (1998). *Estimation and Tracking: Principles, Techniques, and Software*. Artech House Publishers.

Elble, R. and Koller, W. (1990). *Tremor*. The Johns Hopkins University Press.

Fahn, S., Tolosa, E., and Marin, C. (1998). Clinical rating scale for tremor. In J. Jankovic, E. T., editor, *Parkinson's disease and movement disorders*. Urban & Schwarzenberg, Baltimore.

Gao, J. B. and Wen-wen, T. (2002). Pathological tremors as diffusional processes. *Biological Cybernetics*, 86:263–270.

Riviere, C. (1995). *Adaptive suppression of tremor for improved human-machine control*. PhD thesis, Johns Hopkins University.

Rocon, E., Andrade, A., J.L.Pons, Kyberd, P., and Nasuto, S. (2006). Empirical mode decomposition: a novel technique for the study of tremor time series. *Med Bio Eng Comput*, 44:569–582.

Rocon, E., Belda-Lois, J., Ruiz, A., Manto, M., Moreno, J., and J.L.Pons (2007). Design and validation of a rehabilitation robotic exoskeleton for tremor assessment and suppression. *IEEE Transactions on Neural Systems and Rehabilitation Engineering*, 15(3):367–378.

Rocon, E., Belda-Lois, J., Sanchez-Lacuesta, J., and J.L.Pons (2004). Pathological tremor management: Modelling,compensatory technology and evaluation. *Technology and Disability*, 16:3–18.

Timmer, J., Haubler, S., Lauk, M., and Lucking, C. (2000). Pathological tremors: Deterministic chaos or nonlinear stochastic oscillators? *Biological Cybernetics*, 78:349–357.

POSSIBILITY OF MENTAL HEALTH SELF-CHECKS USING DIVERGENCE PROPERTIES OF PULSE WAVES

Mayumi Oyama-Higa
Department of Integrated Psychological Science, Kwansei Gakuin University, Uegahara, Nishinomiya, Hyogo, Japan
oyama@kwansei.ac.jp

Tiejun Miao
CCI Corporation and Chaos Technology Research Laboratory, kitashinagawa, shinagawa-ku, Tokyo, Japan
t-miao@tokyo.cci-web.co.jp

Keywords: Chaotic analysis, divergence, fingertip pulse waves, Lyapunov exponent, PC mouse, mental health.

Abstract: We conducted a nonlinear analysis of fingertip pulse waves and found that the Lyapunov exponent having the "divergence" property of attractor trajectory was an effective index for estimating human mental health. We showed that this method is effective for an early detection of dementia and depression, as well as in the detection of changes in mental status. In addition, based on these results obtained from time series analysis of the recorded pulse waves, we developed an application device allowing easily installed and convenient measurement for daily check and monitoring mental/physical status. It was an easy-to-use and cost-less device installed in a PC mouse. Also, we studied a representation method of constellation graphs to disclose the fluctuation details of the Lyapunov exponents. In the representation, changes in mental status were assessed and graphically visible by using of the fluctuation factor of the Lyapunov exponents.

1 INTRODUCTION

Some serious mental health problems exist in Japan. For example, the number of annual suicides has reached 30,000 for three consecutive years 2004 to 2006.Most suicides are related to depressive symptoms. In addition, although Japan has the world's highest longevity rate, the cases of dementia increase along with the rapidly increase in the aged population, thereby leading to some social problems (ref. plala, http). Social and family responses are essential to help those with depression and dementia, but in most cases, these diseases progress without self-acknowledged, and hence need the necessary methods for an early detection and treatment.

It is generally necessary to check the status of behavior and mental health in daily life to detect the onset of depression and dementia. Subjective observation alone is insufficient; it is required to evaluate objective data using scientific methods. So far, scientific methods include the analysis of brain waves and image diagnosis of the brain, which require high levels of technology and knowledge; these are not simple measurement methods in terms of time or cost. Therefore, easy and economical measurement methods are required.

The Lyapunov exponent referencing the "divergence" of an attractor trajectory in the nonlinear analysis of fingertip pulse waves is an effective method for assessing mental health in humans (Tsuda 1992). In particular, it was found to be effective for the detection of dementia and the diagnosis of depression (Oyama-Higa 2006). In section 2, we describe the method used to calculate the "divergence value" using the nonlinear analysis of fingertip waves. In section 3, we explain the meaning of the use of fingertip pulse waves and the relation between the "divergence value" and cognitive psychology. In section 4, the relation between the Lyapunov exponent and mental health is explained. In section 5, we show the representation method of constellation graphs developed for mental health self-checks. Finally, we outline our future work, and make some discussions in relating to possible applications.

2 METHODS OF RECORDING AND ANALYSIS OF FINGERTIP PULSE WAVES

2.1 Recording Method of Fingertip Pulse Wave

Fingertip pulse waves were measured by photo-plethysmography method. Changes in the amount of hemoglobin flowing through the capillaries were measured by infrared photo-electric method (Fig. 1). The waveform is naturally synchronized with the beating of the heart. Dynamics changes in hemoglobin levels caused by the constriction of capillaries in the fingertip constitute time series data from a complex system that includes information from the sympathetic and parasympathetic nerve. Changes in hemoglobin levels in the capillaries are thought to be related to the baroreceptor, which are linked to the sympathetic and parasympathetic nerve via the brain stem and spinal cord (Figure. 2). Pulse wave data were collected at a sampling frequency of 200 Hz with a resolution of 12 bits. The measurement duration was variable, depending on the experimental conditions. Time series data consisting of 12,000 points can be obtained in 1 min of measurement.

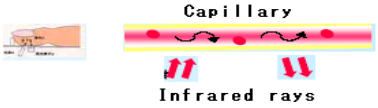

Figure 1: Measurement of pulse waves using infrared irradiation of capillaries.

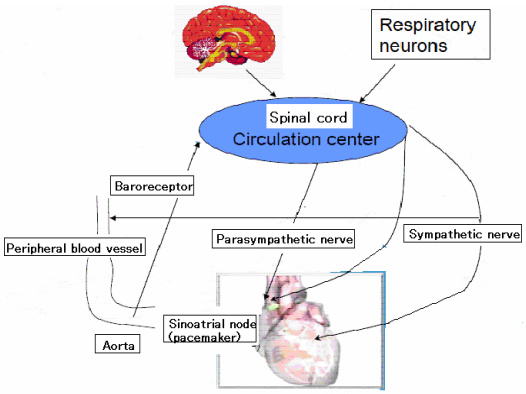

Figure 2: Diagrammatic representation of the interaction from brain stem to peripheral blood vessels through the action of sympathetic and parasympathetic nerves.

This is a convenient measurement method because it does not require special care with regard to room temperature, place of measurement, and measurement conditions. Moreover, because the measurement time is very short, the collection of data is not a burden to the subject.

2.2 Chaos Analysis of the Pulse Wave

Fingertip pulse waves were demonstrated to have chaotic characteristics (Tsuda1992, Sumida 2000, and Miao 2006). On the basis of chaotic analysis of time series, we analyzed the recorded data to determine divergence properties of the pulse waves.
In chaos analysis, the attractor was reconstructing using time delay method (Tarkens,1981,1985). The parameters used are delay time of 50 ms and embedding dimension 4.

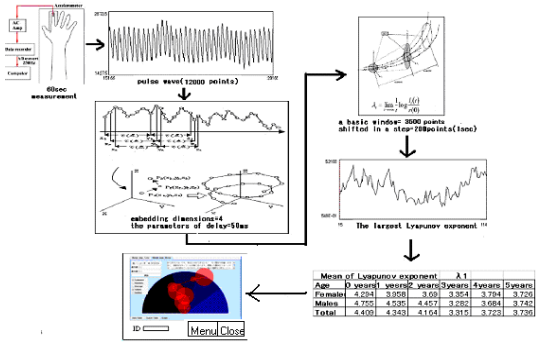

Figure 3: Procedure from measurement of pulse waves to Lyapunov exponent computations.

Beside of the effective information obtainable from the shape of the four-dimensional attractor, we calculated the Lyapunov exponent, which is an index of trajectory instability and a characteristic of chaos, using Sano and Sawada algorithm (Sano and Sawada 1985).
As shown in Figure 4, we used the following method to calculate the Lyapunov exponent. We assumed that a small sphere (hypersphere) of radius ε is the initial value for a three-dimensional chaotic dynamic system. After being mapped once, the sphere was stretched in the e1 direction and compressed in the e3 direction, and assumed the shape of an ellipsoid (Figure. 4). We designated the logarithm of the expansion rate per unit time along the directions e1, e2, and e3 as λ1, λ2, and λ3, respectively. Here, λ1, λ2, and λ3 are the Lyapunov exponents and their set is the Lyapunov spectrum. Because four embedded dimensions were set as the optimum number of dimensions for the pulse wave, w obtained the four Lyapunov exponents, λ1, λ2, λ3 and λ4, as the

Lyapunov spectrum. Of these, the largest Lyapunov exponent, λ1, was used in the calculation to prepare the constellation graphs.

The following equations show the method of calculating the Lyapunov exponent. For the time series data x(i), with i = 1, 2,…, N obtained from the fingertip pulse waves, the phase space was reconstructed using the method of time delays. Assuming that we create a d-dimensional phase space using a constant time delay τ, the vectors in the space are generated as d-tuples from the time series and are given by

$$\mathbf{X}(i) = (x(i),...,x(i-(d-1)\tau)) = \{x_k(i)\} \quad (1)$$

where $x_k(i) = x(i-(k-1)\tau)$, with k = 1, 2,..., d.

To reconstruct the phase space correctly, the parameters of delay (τ) and embedding dimensions (d) should be chosen optimally (Sano and Sawada, 1985). In time series data recorded from human finger photoplethysmograms, we chose the parameters τ = 50 ms and d = 4, as in (Tsuda, 1992) and (Sumida, 2000).

In the reconstructed phase space, one of the important measures of complexity is the largest Lyapunov exponent λ1. If $\mathbf{X}(t)$ is the evolution of some initial orbit $\mathbf{X}(0)$ in the phase space with time, then

$$\lambda_1 = \lim_{t\to\infty}\lim_{\varepsilon\to 0}\frac{1}{t}\ln\frac{|\delta\mathbf{X}_\varepsilon(t)|}{|\varepsilon|} \quad (2)$$

where

$$\delta\mathbf{X}_\varepsilon(t) = \mathbf{X}(t) - \mathbf{X}_\varepsilon(t) \text{ and } \varepsilon = \mathbf{X}(0) - \mathbf{X}_\varepsilon(0)$$

for almost all initial difference vectors $\varepsilon = \mathbf{X}(0) - \mathbf{X}_\varepsilon(0)$. We estimated λ_1 using the algorithm of Sano and Sawada (1985), where λ_1 describes the divergence and instability of the orbits in phase space.

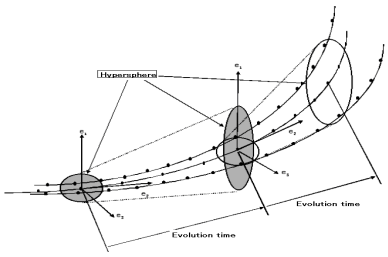

Figure 4: Method used to calculate the Lyapunov exponent.

The initial 8000 points of pulse wave data were taken as one window to calculate the largest Lyapunov exponent, λ1. In the next step, the window was shifted by 200 points and the exponent was calculated from the next window of 8000 points. This procedure was repeated until the pulse wave data were exhausted. Three minutes of measurement yielded 36,000 data points; therefore, we can obtain a (36,000 – 8000)/200 = 140-point time series of Lyapunov exponents. With 1 min of measurement, we can achieve a (12,000 – 8000)/200 = 20-point time series of Lyapunov exponents. The variation in the largest Lyapunov exponent is a measure of the variation in the trajectory of the four-dimensional attractor. The largest Lyapunov exponent is the divergence of the attractor trajectory and is an important value related to psychological indices (Oyama-Higa, 2005, 2006).

3 ESTIMATING PHYSIOLOGICAL AND PSYCHOLOGY STATUS

3.1 Outline of Self-checking Method

The subjects were asked to answer some simple questions to ensure the normal measurement of pulse waves. This information was used to interpret the observed divergence in measured values. The questions were status-checking items regarding physical conditions and a simple assessment of their mood at the time of measurement. Answers were chosen from one of three available levels (Table 1). In addition to these questions, the subjects were asked to describe their mood and condition at the time of the measurement in more definite terms (Table 1). This enabled the person to identify factors that can affect divergence values. Because these records were made in free-form style, key words alone could be used. However, when a subject is allowed to write freely, for example, about things that he or she had communicated to a friend, music he or she enjoyed, positive results in a sporting activity, and good or bad news that had been received, it is easier to study the relationships between these events and the divergence value.

The types of situations that elicit emotions such as delight, anger, sorrow, and pleasure differ from person to person. For example, a condition that creates a suitable level of divergence, such as listening to music or having a conversation with someone, must be recorded as data unique to that subject. In addition, extreme tension, fatigue, and low spirits also cause changes in divergence. Therefore, comparing the status recorded at the time

of measurement with the corresponding divergence values helps a person to assess his or her own mental status. The responses and simple comments on the subject's condition are stored so that they can be seen by clicking the corresponding divergence value on the graph. We plan to vary the simple questions asked according to the category of the subject, e.g., child, adult, or aged person.

Table 1: Checking items of subjective evaluation of subject's state.

Status	Good	Normal	Poor
Sleep	V		
Appetite		V	
Health	V		
Will to work		V	
Mental health			V
Current mood			V

Freestyle reporting: The subject enters a note on his or her condition at the time of measurement. These notes can be in the form of a descriptive comment on the subject's condition, keywords, and other comments.
Comment example 1: [Had a pleasant chat with a friend about hobbies.]
Comment example 2: [Feeling low after failing a test.]

3.2 Divergence Analysis for Various Physiological and Psychological Status

Biological systems are considered to be complex and fluctuating, with chaotic characteristics. Although chaotic systems appear to be extremely complicated and to behave in a random and unstable manner, they in fact change according to deterministic rules. Biological signals emanating from humans or vital signs come in many types, such as body temperature, blood pressure, and pulse rate. Fingertip pulse waves are biological signals that produce time series data with chaotic characteristics. Moreover, unlike cardiac waves, fingertip pulse waves contain various types of information, including information from the nervous system. In the field of psychology, several methods have been suggested as indices for assessing mental health. However, these methods are generally subjective and therefore intrinsically lacking in objectivity. Questionnaires have often been used as relatively simple psychological tests, and the measurement and analysis of brain waves can be used to objectively assess the neurological state at the time of measurement. However, the measurements are not simple and the analysis methods are not yet suitable for analyzing detailed psychological changes. Another possible method for measuring biological information is to analyze the R–R intervals of heartbeats and pulse waves. However, no analysis has attempted to take into account the chaotic characteristics of biological information.

The Lyapunov exponent is a property of chaotic systems that expresses the attractor and represents the "divergence" of the attractor trajectory. We focused on the Lyapunov exponent, which has not previously been evaluated quantitatively as an index of psychological change in humans, and investigated its relationships to dementia and communication skills (an ADL index) in aged persons (Oyama-Higa,2006), its relationship to error rate at work (Imanishi,2006), its relationship to diurnal changes and indices of cumulative fatigue in employees (Miao,2006),(Oyama-Higa,2006), and time series fluctuations in divergence in 0- to 5-year-old children, as well as the effects of parental affection toward children (Oyama-Higa,2006).

It became clear that suitable functioning and harmony of the sympathetic nerves, which are related to adaptability to the external environment and to society, as well as to flexibility, spontaneity, and cooperativeness of the mind, are important for humans to live in a mentally healthy state. These values were related to the largest Lyapunov exponent obtained using nonlinear analysis (Oyama-Higa, 2005, 2006). The largest Lyapunov exponent, which represents the time series variation in the attractor trajectory, is defined as the "divergence." When this value remains low continuously (i.e., when a long period with low divergence persists), the person has low ability to adapt to the external world in daily life and is incapable of maintaining a mentally healthy state. However, a continuously high level of divergence indicates an extremely tense or stressful state. A mentally healthy state also cannot be maintained in this situation. Normally in humans, a healthy state is indicated by the condition in which constant variation occurs in the divergence.

Emotions are a part of being human, and these are believed to cause the variation in divergence.

Physical immunity is critical for the maintenance of human health, and lowered immunity causes various diseases. Therefore, to prevent the lowering of physical immunity and to increase resistance and prevent diseases, we pay attention to what we eat and we rest, take medicine when necessary, and exercise to improve our stamina. However, mental toughness, as reflected in the ability to communicate in a positive manner, willingness to perform a given job, and the ability of mental toughness to withstand dramatic changes in the external world, are also very important. We can call these "mental immunity," but no methods have been developed to scientifically investigate this kind of immunity. We analyzed fingertip pulse waves using nonlinear analysis, examined their relationships to various psychological indices, and found that the largest Lyapunov exponent obtained through chaos analysis, which corresponds to the "divergence" of the attractor, was closely related to mental immunity. This value was also closely linked with the functioning of the sympathetic nerves of the autonomic nervous system.

For humans, a mentally healthy condition means having the ability to cope flexibly with external changes in "divergence." This can be considered mental flexibility or mental immunity, in contrast to physical immunity. Mental immunity represents adaptability to the external changes that a person has to face in his or her everyday life, including a person's ability to communicate and express oneself, and the suitability of psychological flexibility. When expressing themselves, humans skilfully fend off various types of changes, contacts, and assaults from the external environment, and deal with or cope with them. This is the essence of mental immunity. Change occurs constantly in day-to-day life. "Divergence," which represents a change in the state of mental immunity, is a critical index. At the same time, divergence varies depending on the condition of the person. For example, a long period without "divergence" suggests that the person is not in a normal state. In examples of the attractors of a mentally healthy person and patients with depressive psychosis, the depressed patients have low divergence (Figure. 5). In patients with dementia, the divergence becomes smaller as dementia advances (Figure. 6).

In a normal state, the level of divergence fluctuates constantly. During times of extreme tension and stress, the divergence will be continuously high. Afterward, however, a mentally healthy person naturally finds a way to relax, which brings the divergence back to its normal state. A low level of divergence would continue when a person is in a depressed state or when age-related dementia is present. This suggests that the person is incapable of bringing the divergence back to its natural level on his or her own, indicating decreased adaptability to the external environment.

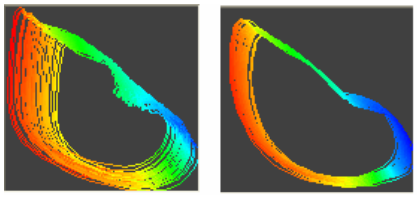

Healthy person Depressed patient

Figure 5: Attractors of a healthy person and a depressed patient prepared from 30 s of measurements.

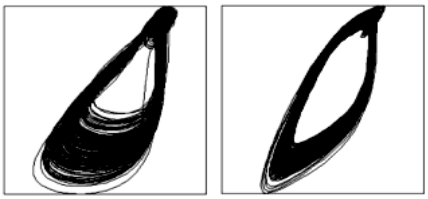

Figure 6: Attractors in elderly subjects with dementia of (severity = 0) and (severity = 4) severity.

4 CASE STUDIES AND A SYSTEM FOR MENTAL HEALTH

All measurements were taken after obtaining the informed consent of subjects.

4.1 Studies of Aged Subjects with Different Communication Skills

Subjects: Data were obtained from 179 subjects (40 males; 139 females) at three nursing homes for the aged in Shiga prefecture, Japan.

Date of measurement: August to November 2003. Measurement method: Fingertip pulse waves were measured three times for 3 min each. Systolic blood pressure, diastolic blood pressure, pulse, and body temperature were measured with the patient in a relaxed state at 25ºC (room temperature) prior to the measurement of pulse waves.

Indices: Five grades indicating the severity of dementia judged by a doctor. We obtained data for the ADL index of communication skills (three-

graded evaluation), composed of seven items and estimated by a care manager. We examined the relation between the data and the maximum Lyapunov exponent calculated from the fingertip pulse waves.

Results: There was a significant relation between the maximum Lyapunov exponent and communication skills (Figure 7 A) and severity of dementia (Figure 7 B). t-student test was used.

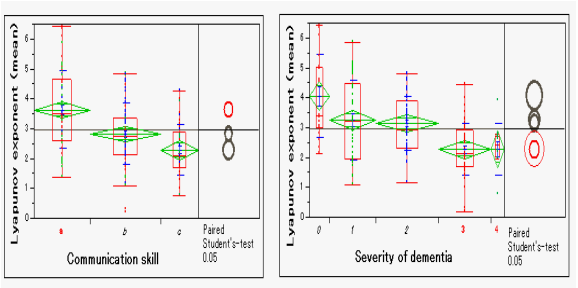

Figure 7: Relation of the Lyapunov exponent and (A) communication skills and (B) severity of dementia in elderly patients.

In constellation graphs, the right side indicates small Lyapunov exponents and the left side indicates large Lyapunov exponents (Figures. 7, 8). Because of the large quantity of data, five cases that were similar to the median of data for each rank in index (i.e., dementia, 0–4; communication skills, a–c) are shown.

Fifteen subjects with high cognition were selected and measurements were retaken after 9 months, in August 2004 (Figure. 10). Values of the Lyapunov exponent increased in some subjects and decreased in others compared to the first measurements taken in November 2003. These results indicate that changes in the Lyapunov exponent always occur. However, attention is needed to understand the causes of very low values.

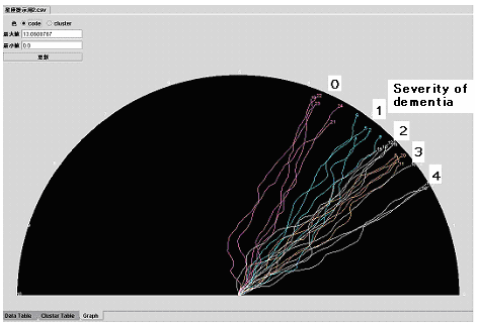

Figure 8: Relation between severity of dementia (0–4) and the Lyapunov exponent. One line indicates one subject.

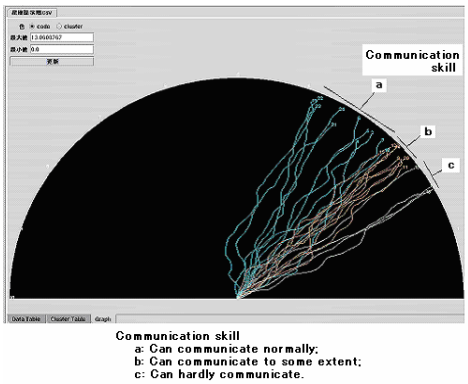

Figure 9: Relation between communication skills (a–c) and the Lyapunov exponent. One line indicates one subject.

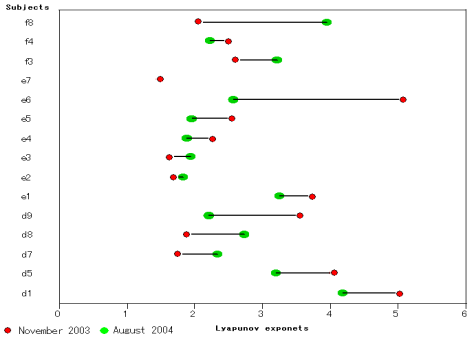

Figure 10: Results of the re-measurement of the Lyapunov exponent after 9 months (15 subjects). Subject e7 had died prior to the second measurement.

4.2 Case Studies of Maternal Attachment of Children

Subjects: Data were obtained from 242 children 0- to 5 years old from nurseries in Osaka and Himeji.

Date of measurement: January 2004–March 2005.

Measurement method: Fingertip pulse waves were measured twice for 1 min each.

Pulse waves were measured in a relaxed environment at 25ºC (room temperature). Within the age range of children tested, 3-year-olds had lower mean values in the largest Lyapunov exponent than ones of the other ages. There was a significant relation between mean values in the largest Lyapunov exponent and children ages ($p < 0.05$ using t-student test). Divergence was highest in 0-year-olds, followed by 1-year-olds and 2-year-olds, and was lowest in 3-year-olds (Fig. 11). For 3-year-old children, some widely held beliefs concerning their states and attachment seemed to correspond

scientifically to the divergence of the attractor trajectory in pulse waves.

Table 2: Relation between the age and number of children.

	Males	Females	Total
0-year old	2	5	7
1-year old	13	10	23
2-year old	19	13	32
3-year old	27	27	54
4-year old	44	25	69
5-year old	34	23	57
Total	139	103	242

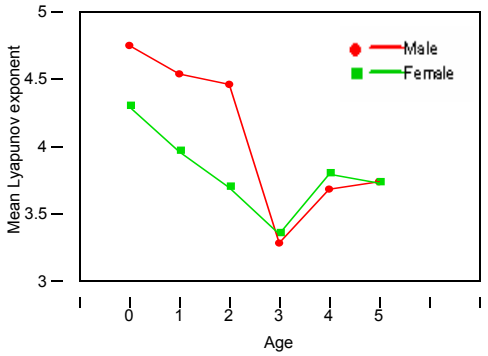

Figure 11: Relation between the Lyapunov exponent and the age of children (242 subjects).

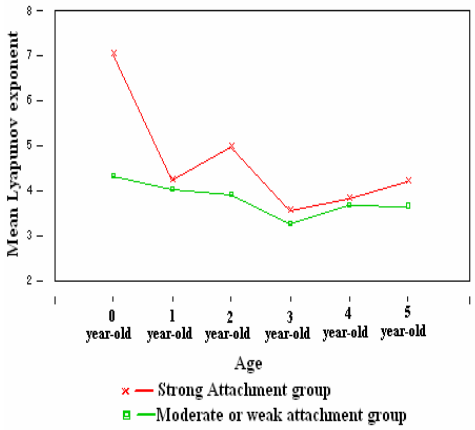

Figure 12: Relation between the Lyapunov exponent and maternal attachment to the child.

Additionally, questionnaires were completed by the mothers to study maternal attachment to the children (Index: Maternal Attachment Inventory MAI (Muller, 1994). After measurements were taken, the children were divided into two groups: a group with high maternal and a group with low maternal attachment. There was a significant relation between attachment and the Lyapunov exponent ($p < 0.05$ using t-student test; Fig. 12). These results indicate that problems of maternal attachment are also related to divergence in children, and could therefore be of help to mothers in child rearing.

4.3 Studies of Employees and the Tiredness Index

The Lyapunov exponents of 12 employees of a specific company were measured three times during the day: in the morning, immediately after arriving at the office; in the afternoon, 1 h after lunch; and in the evening, before leaving the office for the day. At the same time, the subjects were questioned to determine their tiredness index. We then examined the relation between the Lyapunov exponent and the tiredness index. Changes in the Lyapunov exponent with the time of day differed among the employees (Figure. 13). Because the management of mental health in business has caused many problems, including occurrences of depression, the Lyapunov exponent is a useful index not only for employees' self-management, but also for employers.

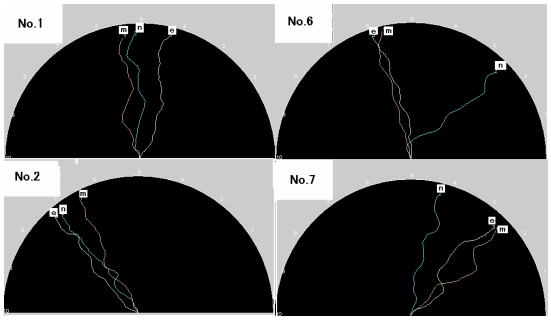

Figure 13: Changes in the Lyapunov exponents of employees of a specific company in the morning, afternoon, and evening.

The relation of the Lyapunov exponent to the tiredness index indicated that subjects with a low Lyapunov exponent in the afternoon tended to have depressive tendencies and strong anxiety (Table 3).

4.4 Experiments of Arithmetic Operations

Kraepelin tests that is addition work of numerical value were conducted twice for 15 min each on subjects in their 20s and 40s, and changes in the Lyapunov exponent were studied before and after the tests. The Lyapunov exponent increased in all subjects after the Kraepelin test. The subjects gave the impression that they felt better after the Kraepelin test than they did before the test (Fig. 14).

Table 3: Relation between the Lyapunov exponent in the afternoon and the tiredness index of employees. An inverse correlation greater than –0.7 means that a low Lyapunov exponent indicates a depressive tendency and a strong tendency toward anxiety.

	Willpower Decrement	Anxiety	State of Depression	Tiredness Accumulation	Lyapunov exponent Midday
Willpower Decrement	1	0.7235	0.7539	0.7496	-0.6385
Anxiety	0.7235	1	0.8455	0.9358	-0.7279
State of Depression	0.7539	0.8455	1	0.8420	-0.7014
Tiredness Accumulation	0.7496	0.9358	0.8420	1	-0.6305
Lyapunov exponent Midday	-0.6385	-0.7279	-0.7014	-0.6305	1

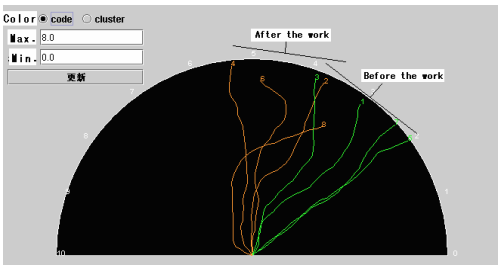

Figure 14: Changes in the Lyapunov exponent before and after the Kraepelin test.

4.5 Studies of Operation Error in Monitoring and Judgment Work

An apparatus used to simulate monitoring on a personal computer was developed to examine the relation between the Lyapunov exponent and the human error rate. The experiment was conducted by increasing the number of monitoring images from three to six, and then to nine images. In all cases, the error rate was high when the Lyapunov exponent was low (Figure. 15).

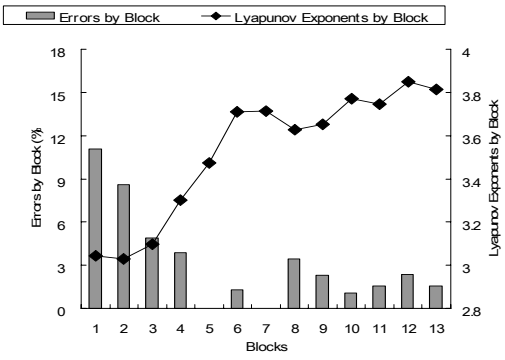

Figure 15: Relation between the Lyapunov exponent and human error rate in monitoring work over 30 min. Symbols and line indicate the Lyapunov exponent by block (3min); bars indicate the human error rates by block.

4.6 Studies of Painting Work

We measured the Lyapunov exponent when a certain artist did nothing and again 3 min after he began painting. The Lyapunov exponent increased while the artist painted (Figure. 16).

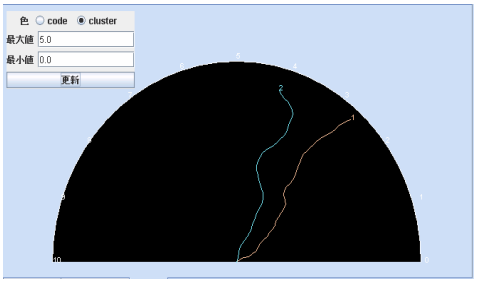

Figure 16: Changes in the Lyapunov exponent while painting. Orange, before painting; blue, during painting.

4.7 Studies of giving Birth Processes

The Lyapunov exponent was measured in seven pregnant women before and after giving birth (obstetrics and gynaecology in Nara city; Figure 17). Comparisons were made between the values measured within 1.5 h before birth and after birth. The Lyapunov exponent was significantly higher before birth than after birth (Student t-test, $p < 0.05$). Giving birth increased the functioning of the sympathetic nervous system.

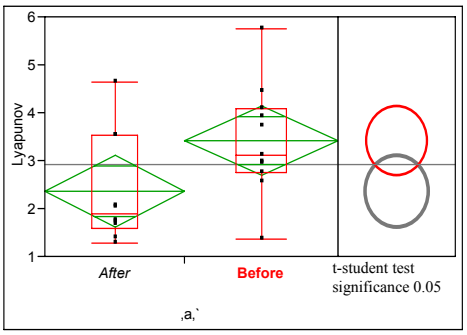

Figure 17: Comparison of the Lyapunov exponent measured in pregnant women within 1.5 h before and 1.5 h after giving birth.

5 SELF-CHECK SYSTEM

5.1 Equipment Components

A device that is easy to use and gives minimum burden on the subject is needed to measure the pulse

waves. It is not possible to check the mental health of a person through just one round of measurements. For these reasons, the device must be convenient to use. We took note of the fact many people often do their work with PCs, and therefore developed a device that can make these measurements using a mouse. The pulse wave sensor is installed on one side of the pulse wave mouse; measurements can be made by simply touching the sensor with a finger. The mouse is connected to the PC through a USB port and can also be used as an ordinary mouse (patent pending).
Software installed on the PC starts and ends the measurements, and sets their duration.

5.2 Representation System using Constellation Graphs in Mental Health Self-Checks

Previous studies indicated the possibility of using the Lyapunov exponent as a new psychological index. However, as noted above, it is dangerous to judge mental health using only one measurement. Therefore, even over the period of a single minute, several measurements are necessary to assess daily fluctuations. It is also necessary to prepare a self-feedback system to determine when changes in the values of the Lyapunov exponent can be observed.

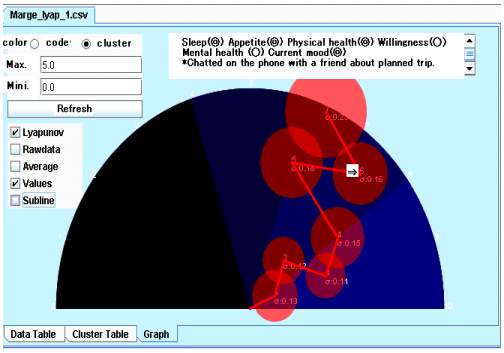

Figure 17: Example of a time series constellation graph for a self-diagnosis system. The right area of the graph indicates large Lyapunov exponents; the left area indicates small Lyapunov exponents. Changes among seven measurements are shown; circles indicate the standard deviation of the Lyapunov exponent for each measurement. If the point constitutes a change, the self-stated status at that point is shown.

To do this, a time series of the Lyapunov exponent must be recorded over several days and weeks to monitor natural variation, and the status of the pulse wave data should be recorded using simple words or keywords. To accomplish these measurements, the development of apparatus capable of taking measurements easily and of software that can indicate changes in mental health is necessary (Fig. 17).

5.3 Future Plan and Some Problems

There are three potential types of self-diagnosis system that use the divergence of fingertip pulse wave attractor. The first type is the personal computer (PC)-completed type, in which all operations from measurement to display are performed on one PC. In the second type, pulse wave data stored on a PC are transferred to a server via the Internet to construct a database. The software used to analyze the pulse waves on the server is either downloaded or pulse wave data are sent through the server. In the third type, a sensor for taking pulse wave measurements is installed on a cellular phone and the display of the results is provided as an image on the cellular phone. In this case, the Internet is also used. In the second and third types, results are accumulated in a database via the Internet, and a system is constructed for an available search. We expected that data will be accumulated through Internet use, enabling further advanced study. However, sufficient caution should be taken to protect the security of personal information.

If the self-management of mental health and early detection and treatment of diseases can be accomplished using this system, many people might be saved from terrible situations resulting from mental problems or instability. In addition, sending data regarding the mental indexes of humans using a network may lead to innovations in communication. However, sufficient care should be taken in the data management because of recent problems concerning the protection of personal information. However, in terms of the effectiveness in promoting further research, the accumulation of information would be extremely helpful for various future studies.

6 CONCLUSIONS

Mental management in humans is increasingly important as society continues to change. Accurate measurements have been difficult to obtain in the past using both subjective and objective methods, and the time and cost required to take brain measurements have imposed heavy burdens on patients. Measurement of pulse waves is simple and

has the merit of imposing a comparatively minor burden on the subjects.

The complete realm of information obtainable from pulse waves has not yet been fully elucidated, but we have found that the information is deeply related to the behavior of the autonomous system networked throughout the body via the spinal cord from the part of the brain stem responsible for much of human activity and responses. The divergence of pulse waves is thought to be the value most related to the function of the nervous system, including the sympathetic and parasympathetic nerves that are integrated with the brain stem. In the future, we plan to further document these relations through various experiments.

ACKNOWLEDGEMENTS

We thank all of the people who cooperated with us in taking measurements.

REFERENCES

http://www9.plala.or.jp/rescue/social.html, www.chihoucare.org/, http://dementia.prit.go.jp/

Oyama-Higa M., Miao T., and Mizuno-Matsumoto Y., 2006. Analysis of dementia in aged subjects through chaos analysis of fingertip pulse waves. 2006 IEEE Conference on Systems, Man, and Cybernetics, Taipei, Taiwan, 2863–2867.

Tsuda I., Tahara T., and Iwanaga I., 1992. Chaotic pulsation in capillary vessels and its dependence on mental and physical conditions. Int. J. Bifurcation and Chaos 2: 313–324.

Sumida T., Arimitu Y., Tahara T., and Iwanaga H., 2000. Mental conditions reflected by the chaos of pulsation in capillary vessels. Int. J. Bifurcation and Chaos 10: 2245–2255.

Sano M., and Sawada Y., 1985. Measurement of the Lyapunov spectrum from a chaotic time series. Phys. Rev. Lett. 55: 1082.

Miao T., Shimoyama O., and Oyama-Higa M., 2006. Modelling plethysmogram dynamics based on baroreflex under higher cerebral influences. 2006 IEEE Conference on Systems, Man, and Cybernetics, Taipei, Taiwan, 2868–2873.

Oyama-Higa M., and Miao T., 2005. Representation of a physio-psychological index through constellation graphs. ICNC'05–FSKD'05, http://dx.doi.org/10.1007/11539087_109.

Oyama-Higa M., and Miao T., 2006. Discovery and application of new index for cognitive psychology. 2006 IEEE Conference on Systems, Man, and Cybernetics, Taipei, Taiwan, 2040–2044.

Imanishi A., and Oyama-Higa M., 2006. The relation between observers' psychophysiological conditions and human errors during monitoring task. 2006 IEEE Conference on Systems, Man, and Cybernetics, Taipei, Taiwan, 2035–2039.

Oyama-Higa M., Tsujino J., and Tanabiki M., 2006. Does a mother's attachment to her child affect biological information provided by the child? Chaos analysis of fingertip pulse waves of children. 2006 IEEE Conference on Systems, Man, and Cybernetics, Taipei, Taiwan, 2030–2034.

Takens F., 1985. In: Braaksma B. L. J., Broer H. W., and Takens F., eds. Dynamical Systems and Bifurcations, Lecture Notes in Math. Vol. 1125. Springer, Heidelberg.

Takens F., 1981. Detecting Strange Attractors in Turbulence, Lecture Notes in Math. Vol. 898. Springer, New York.

Muller, M.E., 1994. Questionnaire to Measure Mother-to Attachment. Journal of Nursing Measurement, 2(2), 129-141.

MOUSE CONTROL THROUGH ELECTROMYOGRAPHY
Using Biosignals Towards New User Interface Paradigms

Vasco Vinhas
Faculdade de Engenharia da Universidade do Porto, Rua Dr. Roberto Frias s/n, Porto, Portugal
LIACC - Artificial Intelligence and Computer Science Laboratory, Rua Campo Alegre 823, Porto, Portugal
vasco.vinhas@fe.up.pt

Antonio Gomes
Faculdade de Engenharia da Universidade do Porto, Rua Dr. Roberto Frias s/n, Porto, Portugal
ee01198@fe.up.pt

Keywords: Medical Signal Acquisition, Analysis and Processing, Real-time Systems, User Interfaces.

Abstract: Recent technologic breakthroughs have enabled the usage of minimal invasive biometric hardware devices that no longer interfere with the audience immersion feeling. The usage of EMG to extend traditional mouse-oriented user interfaces is a proof-of-concept prototype integrated in a wider horizon project. A subset of the main project's architecture was reused, specially the communication middleware, as a stable development platform. An originally intended EEG hardware was adapted to perform EMG and therefore detect muscular activity. It was chosen, as a practical proof-of-concept, that it was desired to detect winking as a triggering device to perform a given traditional user interface action. The described application achieved extremely positive records with hit rates of around 90%. The volume of false positives and undetected desired actions are considered negligible due to both system development stage and application contextualization - non critical systems. The success and acceptance levels of the project are really encouraging not only to the enhancement of the proposed application but also to the global system continuous development.

1 INTRODUCTION

In this global scenario, the authors have defined and already started a research project precisely with the intention of using biosignals to assess user emotions and use this information to enable subconscious interaction. The contextualization of this work has numerous points of interest both in the academic community and in commercial applications. The usage of new hardware solutions and biosignals to enhance traditional user interface paradigms or even to enable new ones has managed to bring together multidisciplinary private organizations and research communities. In spite of the main project being still in an initial stage, several high-level decisions have already been taken and a high percentage of them have been either implemented or designed.

Perfectly integrated in this scope, it was decided to produce a spin-off application capable of testing the global architecture and, simultaneously, generate experimental results capable of test initial hypothesis and therefore confirm them or generate new discussion paths. The mouse control tool enabled trough EMG is a proof-of-concept project with two distinct sets of objectives.

The first encloses the goals directly related to the experimentation and test of new interaction paradigms by using innovative hardware solutions. More specifically, it is intended to trigger regular mouse interaction like right click or drag operations by detecting user winking. Once again, these defined actions have merely conceptualization purposes and can be easily altered.

The second group of objectives regards the reuse and consequent validation of the main project architecture, namely communication protocol and multiple sensors data integration. With this option, the authors are able to validate the defined approach by early producing research results.

This document is organized as follows: in the next section the current state of the art is presented, in section 3 the mouse control project is described, specially the most significant decisions are detailed and justified. In section 4, experimental results are presented and related conclusions are extracted in section 5 as well as future work areas are identified.

2 STATE OF THE ART

Regarding the main project nature, this section is structured in three wide components, namely, hardware solutions for emotion classification, biological data format standards and dynamic interaction paradigms.

2.1 Hardware Solutions

Since the beginning of the last century that there have been efforts to correlate biological signals to emotional states (Marston, 1917). The most traditional approaches are based on the standard polygraph where physiological variables such as blood pressure, pulse, respiration and skin conductivity are recorded in order to detect different levels of anxiety. Although the polygraph lie detection accuracy is arguable, the fact that it is an efficient tool to detect basic emotional states, especially individual related, anxiety levels, is not.

The human brain always performance an almost hypnotic attraction to several research fields, so in 1912, the Russian physiologist, Vladimir Vladimirovich Pravdich-Neminsky published the first EEG (Pravdich-Neminsky, 1913) and the evoked potential of the mammalian. This discover was only possible due to previous studies of Richard Caton that thirty years earlier presented his findings about electrical phenomena of the exposed cerebral hemispheres of rabbits and monkeys. In the 1950s, the English physician William Grey Walter developed an adjunct to EEG called EEG topography which allowed for the mapping of electrical activity across the surface of the brain. This enjoyed a brief period of popularity in the 1980s and seemed especially promising for psychiatry. It was never accepted by neurologists and remains primarily a research tool.

Due to the medical community skepticism, EEG, in clinical use, it is considered a *gross correlate of brain activity* (Ebersole, 2002). In spite of this reality, recent medical research studies (Pascalis, 1998)(Aftanas, 1997) have been trying to revert this scenario by suggesting that increased cortical dynamics, up to a certain level, are probably necessary for emotion functioning and by relating EEG activity and heart rate during recall of emotional events. Similar efforts, but using invasive technology like ECoG[1], have enable complex BCI[2] like playing a videogame or operating a robot (Leuthardt, 2004).

Some more recent studies have successfully used just EEG information for emotion assessment (K. Ishino, 2003). These approaches have the great advantage of being based on non-invasive solutions, enabling its usage in general population in a non-medical environment. Encouraged by these results, the current research direction seems to be the addition of other inexpensive, non-invasive hardware to the equation. Practical examples of this are the introduction of GSR[3] and oximeters by Takahashi (Takahashi, 2004) and Chanel et al(G. Chanel, 2005). The sensorial fusion, enabled by the conjugation of different equipments, have made possible to achieve a 40% accuracy in detecting six distinct emotional states and levels of about 90% in distinguishing positive from negative feelings. *These results indicate that using multi-modal bio-potential signals is feasible in emotion recognition* (Takahashi, 2004).

There also have been recorded serious commercial initiatives regarding automatic minimal-invasive emotion assessment. One of the most promising ones is being developed by NeuroSky, a startup company headquarted in Silicon Valley, which has already granted five million dollars, from diverse *business angels*, to perform research activities (Rachel Konrad, 2007). There are two cornerstone modules, still in the prototyping phase, yet already in the market. The first is the *ThinkGear* module with *Dry-Active* sensor, that basically is the product hardware component. Its main particularity resides in the usage of dry active sensors that do not use contact gels. Despite the intrinsic value of this module, the most innovative distinct factor is the *eSense* Algorithm Library that is a powerful signal processing unit that runs proprietary interpretation software to translate biosignals into useful logic commands.

As previously referred it is still a cutting edge technology, still in a development stage, nevertheless it has proven its fundamental worth through participation in several game conferences(Authors, 2007c).

2.2 Data Formats

As an intermediate project subject, one must refer to biological data format definition. This topic is particularly important to this project due to the absolute necessity of accessing, recording and processing, eventually in a distributed system, data which origin may vary from multiple hardware solutions. The European Data Format – EDF – is a simple digital format sup-

[1]Electrocorticography (ECoG) is the practice of using an electrode placed directly on the brain to record electrical activity directly from the cerebral cortex

[2]Brain-computer interface (BCI), also called direct neural interface, is a direct communication between a brain (or cell culture) and an external device.

[3]Galvanic skin response (GSR) is a method of measuring the electrical resistance of the skin.

porting the technical aspects of exchange and storage of polygraphic signals. This format dates from 1992 and, nowadays, is a widely accepted standard for exchange of electroencephalogram and polysomnogram data between different equipment and laboratories (Kemp, 1992). This data format's implementation is simple and independent of hardware or software environments and has the peculiarity of enabling both XML and raw text definition. This duality is especially important if there is any computing power limitation and/or interoperability is a project requirement.

Although the unquestionable positive points of EDF, hardly accommodates other investigations topics. In order to overcome this critical hurdle, EDF+ is presented in 2003 as a more flexible but still simple format which is compatible to EDF that can not only store annotations but also electromyography, evoked potentials, electroneurography, electrocardiography and many more types of investigations. Its authors believe that EDF+ offers a format for a wide range of neurophysiological investigations which can become a standard within a few years (Kemp, 2003).

2.3 User Interaction Paradigms

On the pure interactive multimedia systems domain, one must refer to the growing immersion sensation provided to the audience by several factors in diverse fields. As examples of this statement one must consider the success of new generation videogame consoles that have boosted audiovisual quality and brought new interaction paradigms. Also worldwide multimedia players, like Microsoft with table computer and Apple with iPhone have invested hard in the so-called "multi-touch" interfaces, which allow the user to move several fingers on a screen to manipulate data, rather than relying on a mouse and menus.

In spite of these advances, the mainstream entertainment industry has not changed the storyline linearity yet, but some promising research projects are trying to alter this reality. In this domain, one must refer to Glorianna Davenport's MIT Interactive Cinema Group (Authors, 2007b) that have been focusing its efforts on formal structures, construction methods, and social impact of highly distributed motion video stories.

Another recent interesting project is the apartment drama, 15-minute interactive story called *Faade* (Authors, 2007a), where two virtual characters powered by artificial intelligence techniques, allow them to change their emotional state in fairly complicated ways in response to the conversational english being typed in by the human player.

3 PROJECT DESCRIPTION

In this section both global and specific projects are described. With this intention, three subsections were designed: in the first global IT architecture is presented and depicted; afterwards the main decisions regarding the mouse control project are listed and detailed; and finally the key features of the action classifier are explained.

3.1 Global Architecture

In order to best understand the mouse control project, the main project IT design shall be considered and described as it is used and tested. The architecture's key concept regards the possibility to access biosig-

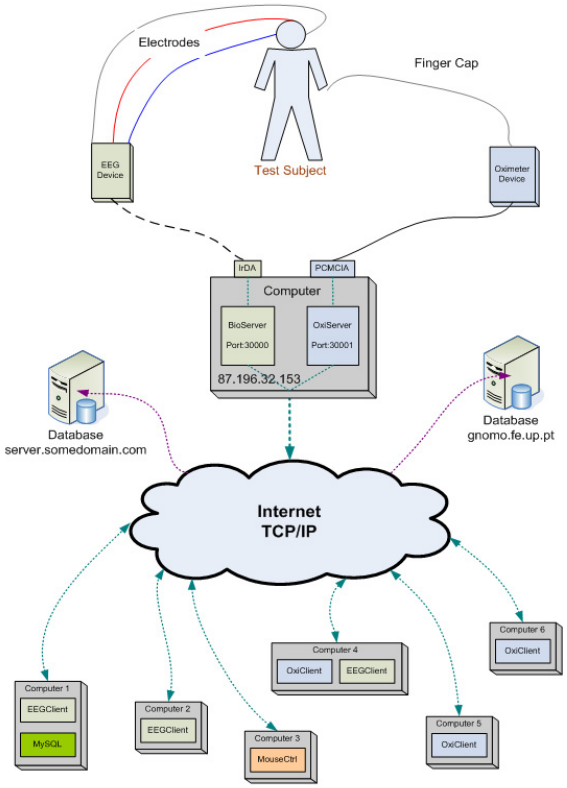

Figure 1: System Global Architecture.

nals independently of the resources physical location and nature. In other words, one must be able to read biosignals from a variety of equipments that might be connected to an arbitrary subject in a remote location without perceiving that other entities might be performing similar accesses, processing and actions.

With this concept in mind, Figure 1 is more understandable, as it shows the several project dimensions.

First, an arbitrary number and diversity of devices are connected to one or more subjects. Each device driver is encapsulated in a particular server software tool, responsible for signal diffusion, securing third-party code in a given logical compartment. These devices, as illustrated, might have distinct communication protocols but their are normalized to standard TCP/IP socket communication with a in-house developed logical protocol. Having this communication base established biosignal diffusion is possible to a wide kind of receivers that must explicitly connect to the broadcast server(s). These clients might have distinct objectives, namely signal visualization and/or processing; data storage; semantic extraction; etcetera.

3.2 Specific Decisions

Having the global system design being described in the previous subsection, the authors believed that a natural spin-off tool for proof of concept and test purposes would be materialized in a simple, yet effective, efficient and significant client application, capable of receiving realtime biosignals, process them and extract semantic information.

Two main specific decisions were taken. The first one resided in the choice of the base interaction mechanism. The decision fell to a traditional mouse hardware piece due to its simplicity and global usage. Two mouse functions/modes were selected for extension with the developed tool: right click and drag. Once the first is an operation less used than the left-click and some interaction paradigms do not contemplate it – original Macintosh machines – the second is a alternative mouse action with visual repercussions.

Regarding action classification, the authors chose *wink* detection, mainly, for three reasons: it is an action that most people are able to perform – at least with the non-dominant eye; it has a clear signal signature; and it stills remains as an unused potential interaction mechanism.

3.3 Action Classifier

The action classifier module resides its success in the correct detection of user *winking*. In order to achieve realtime high classification hit rates – and once again having in mind the concept decisions referred in the previous subsection – this module had to keep low levels of complexity without loosing its efficiency.

A signal study showed that muscular activity regarding quick *winks* had a very recognizable pattern with two consecutive signal peeks, having the second a lower strength. Figure 2 illustrates the shape of two possible consecutive *winks* delimited by the two vertical segments.

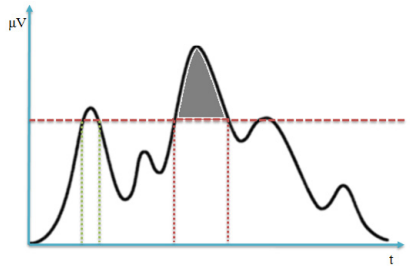

Figure 2: Classifier Parameters Appliance.

Once again keeping the approach simple enough to be enable realtime computation even in mobile devices, two distinct parameters where defined to, through signal monitoring, enable reliable action classification. These parameters were designated *peek value* and *time span* and are also visible in the referred illustration. The *peek value* can be understood as a threshold and is illustrated as the dotted horizontal line. Only signal values above this threshold are considered for further analysis. Again in Figure 2 it is visible that only to signal intervals respect this primary condition. The *time span* parameter is designed to prevent extemporary phenomenons like jitters and represent the minimum temporal interval that the signal must consistently be above the *peek value*. If a closer look is given to the reference illustration, one is able to perceive that the first *wink candidate* is discarded because its signal is too brief and only the second is valid. One important note is that either of these parameters is configurable to best fit the user natural abilities. More on this feature is elaborated in sections 4 and 5.

4 RESULTS

In this section experimental results are objectively presented. In the first subsection, experimental conditions are detailed and in the second, collected data is depicted and treated for analysis purposes.

4.1 Experimental Conditions

In order to perceive the accuracy and adequacy of the developed software tool, there were conducted several experiments. There were formed two distinct groups of subjects: one where users attended a fifteen minute theoretical formation, where the authors explained the tool's basics and how actions were detected. After these sessions, subjects had another ten

minutes to free practice and to get in touch with the application. The second group of users did not have any kind of training specific regarding the presented software. Experimental subjects were randomly selected among laboratory researchers and college students, constituting two groups os user with fifteen elements.

Test sessions were similar both to trained and untrained user groups. Each session was supervised by one of the authors and each subject was asked to close his non-dominant eye ten times, as winking, whenever the subjected wanted to perform a mouse action – either it was a right-click or activate drag mode operation. Environment conditions were similar to both groups either in terms of noise, illumination and time of day.

As sessions were defined in performing a given action ten times, or equal number of actions were detected – false positives – accuracy rates have been fractioned in steps of five percent.

4.2 Collected Data

As described in the previous subsection, experiments were conducted considering two sets of fifteen subjects, one with trained elements and the other with untrained ones. The thirty sessions have been completed in on week and the collected data distribution is illustrated in Figure 3. One must clearly refer that

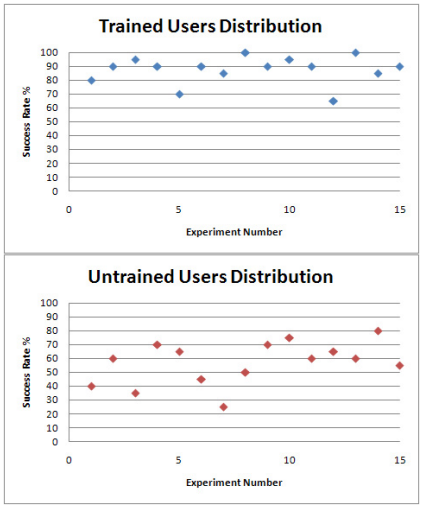

Figure 3: Experiment Result Distributions.

the trained users group has a greater performance with an average success rate of around ninety percent, minimum values of sixty-five and registry error free sessions. If we consider the untrained set, the average rate drops to less than sixty percent with lower bounds of twenty-five and maximum values of eighty percent.

These result distributions were translated into histograms, for analysis purposes, as visible through Figure 4. If a deeper study is conducted, one must refer that eighty percent of the trained subjects registered three or less errors. On the other hand, the untrained user group results are more distributed, although they are slightly concentrated in success rates between fifty-five and seventy percent.

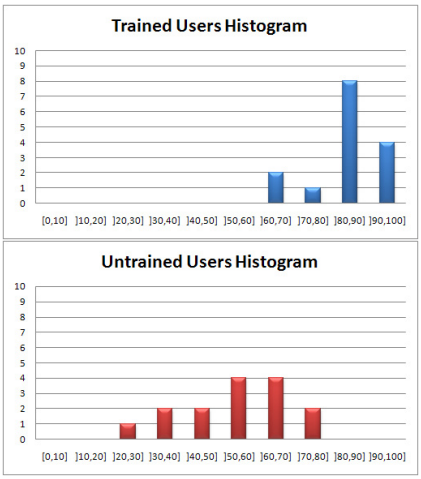

Figure 4: Experiment Result Histograms.

5 CONCLUSIONS

In this section, extracted conclusions are presented and future work topics are identified. Regarding the first theme, one must state that the objectives depicted at the beginning were completed achieved. In what concerns to the main project goals, the communication protocol was successfully tested, the IT architecture was used and validated and it was proved the versatile equipment usage, once again, sustaining the defined structural design. The specific project goals were also accomplished as it was proved the concept of utilizing biosignals to control interaction facets, even when this case study is merely a proof of concept.

Another important conclusion is the need of distinguish trained users from untrained ones, when considering the tool's usability values. One ought to refer that previous contact with the concept allied with a few minutes of practice enhances the software utilization success rates. However, even the untrained group of users has registered fair results. These can be rated as more than acceptable if one considers the whole project's intention.

Considering only the classification engine, a registered positive key point is the system ability to dis-

tinguish user winking from user blinking, especially if user specific parameterization is considered. However, even if this last feature is discarded, the default parameter values are sufficient to discard weaker signals that, with high probability, refer to blinking.

Despite the enunciated positive features and conclusions, there were identified some issues, namely the existence of false-positive results that refer to other user muscular activity. These faults are included in the numbers presented in section 4 and are, in most cases, related to sudden and wide head movements. On the other hand, some *winks* are not detected as it is necessary some *vigor*. However, this issue, as referred, can be suppressed by tuning classification parameters. At last, some minor occasional, application stability issues were detected, especially in what concerns the mapping between *wink* detection and action triggering, mainly due to the tool's lack of maturity. This last issue is development-oriented and does not have a negative impact in what concerns the main project's concept.

5.1 Future Work

The main future work topics are not related to this particular tool, once it is a proof of concept one, but rather with the main global project. With this in mind, there were identified the following areas:

- Reading Hardware Diversity Reinforcement: It is intended to handle a greater number and diversity of devices capable of acquiring biosignals so that information fusion, conjugation and complementary is possible;
- Semantic Leap: It is intended to use syntactic information – biological signal – to extract more complex information like emotions and simple commands;
- Software Control: The accomplishment of the previous item would enable both conscious and subconscious control of several tools and/or multimedia contents;
- IT Architecture and Network Reinforcement: Full-duplex data transfer would enhance user training and system adaptation levels.

Considering the main project's intentions and the future work topics referred, diverse practical applications come into sight. Some of them might be the videogame and virtual entertainment industry, multimedia contents adaptability, user interfaces enhancement, direct advertising, medical applications, namely in phobia treatments and psychological evaluations.

ACKNOWLEDGEMENTS

The authors would like to thank Professor Eugenio Oliveira for his guidance and support. A special mention is also due to LIACC for hardware purchase and excellent laboratory work conditions.

REFERENCES

Aftanas, L. (1997). Nonlinear forecasting measurements of the human eeg during evoked emotions. In *Brain Topography*, volume 10, pages 155–162.

Authors, V. (2007a). Faade a one-act interactive drama. In *Avaiable online at http://www.interactivestory.net/*.

Authors, V. (2007b). Mit interactive cinema group. In *Avaiable online at http://ic.media.mit.edu/*.

Authors, V. (2007c). Neurosky, do you mind fact sheet. In *Technical Report*.

Ebersole, J. (2002). *Current Practice of Clinical Electroencephalography*. Lippincott Williams & Wilkins.

G. Chanel, J. Kronegg, D. G. (2005). Emotion assessment: Arousal evalutation using eeg's and peripheral physiological signals. In *Technical Report*.

K. Ishino, M. H. (2003). A feeling estimation system using a simple electroencephalograph. In *Proceedings of 2003 IEEE International Conference on Systems, Man, and Cybernetics*, pages 4204–4209.

Kemp, B. (1992). A simple format for exchange of digitized polygraphic recordings. In *Electroencephalography and Clinical Neurophysiology*, pages 391–393.

Kemp, B. (2003). European data format 'plus' (edf+), an edf alike standard format for the exchange of physiological data. In *Clinical Neurophysiology*, pages 1755–1761.

Leuthardt, E. (2004). A braincomputer interface using electrocorticographic signals in humans. In *Journal of Neural Engineering*, pages 63–71.

Marston, W. (1917). Systolic blood pressure changes in deception. In *Journal of Experimental Psychology*, volume 2, pages 117–163.

Pascalis, V. D. (1998). Eeg activity and heart rate during recall of emotional events in hypnosis: relationships with hypnotizability and suggestibility. In *International Journal of Psychophysiology*, volume 29, pages 255–275.

Pravdich-Neminsky, V. V. (1913). Ein versuch der registrierung der elektrischen gehirnerscheinungen. In *Zbl Physiol*, pages 951–960.

Rachel Konrad, A. P. (2007). Next-generation toys read brain waves. In *Avaiable online at http://www.usatoday.com/tech/products/games/2007-04-29-mindreadingtoys_N.htm*.

Takahashi, K. (2004). Remarks on emotion recognition from bio-potencial signals. In *The second International Conference on Autonomous Robots and Agents*.

ENHANCED ANALYSIS OF UTERINE ACTIVTY USING SURFACE ELECTROMYOGRAPHY

A. Herzog, L. Reicke, M. Kröger
Institute of Dynamics and Vibration Research, Leibniz University Hannover, Germany
reicke@ids.uni-hannover.de, kroeger@ids.uni-hannover.de

C. Sohn, H. Maul
Obstetrics and Gynecology, UniversityHospital Heidelberg, Germany
holger.maul@med.uni-heidelberg.de

Keywords: Uterine, electromyography, pulse detection, stochastic analysis, Karhunen-Loève, principal component.

Abstract: This contribution presents a new approach for the enhanced analysis of uterine surface electromyography (EMG). First, a pulse detection separates the pulses, which contain the essential information about the uterine contractibility, from the flat line sections during relaxation. The functionality of this semi-automatic algorithm is controlled by two comprehensible parameters. Subsequently, the mean frequency, which serves as a criterion for imminent delivery, is evaluated from the extracted pulses. Although the pulse detection reduces the deviation of the mean frequency significantly, the results are still sensitive to parameter variations in the pulse detection. A stochastic analysis based on the Karhunen-Loève transform (KLT) derives generalised patterns, the eigenforms, from the pulse ensemble. The mean frequency of the first eigenform is less sensitive to parameter variations. Additionally, the correlation between the eigenforms of the left and right surface electrode can serve as a criterion for the measurement's quality.

1 INTRODUCTION

Even in modern obstetrics, the point of delivery cannot be precisely predicted. Although the majority of pregnancies passes without any complications, the significance of an enhanced analysis of uterine activity arises from the diagnosis of preterm labor as well as the treatment of delayed delivery.

The uterine muscle (myometrium), which has maintained a quiescent state during the majority of pregnancy, is prepared for labor by local contractions. These contractions, called training labors, improve the synchronisation between the single muscle cells in order to obtain a defined contraction sequence during delivery. Therefore, the identification of imminent labor requires an elaborate analysis and interpretation of this preparatory phase.

Several methods for the evaluation of uterine contractibility are commonly used: TOCO, IUPC and EMG. Uterine contractions cause variations in the abdomen's contour, which can be detected by pressure sensors. Due to the indirect measurement, this so-called external tocodynamometry (TOCO) is not sensitive and reliable enough. A more reliable approach consists of measuring the uterine's internal pressure (intrauterine pressure catheter, IUPC). The surface electromyography (EMG) combines the non-invasiveness property of TOCO with a sensitivity similar to that of the IUPC (Maul et al., 2004). The muscular activity is accompanied by variations of the electric potential at the neuromuscular junction between nerve and muscle cells. This potential can be picked up directly by needle electrodes and range from $-70\,\mathrm{mV}$ (relaxation) up to $+30\,\mathrm{mV}$ during contraction. In case of surface electrodes, the voltage has to be transmitted via the tissue to the skin, yielding to lower peak values as well as deformations in the time history of the voltage signal. For the measurement of the uterine contractions two surface electrodes are used. They are located on the right and left side of the abdomen. The time-history of a single electromyogram (EMG)-signal is displayed in Figure 1 above. The pulses, which belong to uterine contractions, are separated by flat line sections. Up to now, the frequency characteristics have been derived from large sections of its time history by means of the Fourier transform. Based on the assumption that ongoing synchronisation leads to an increase of the pulse's attack

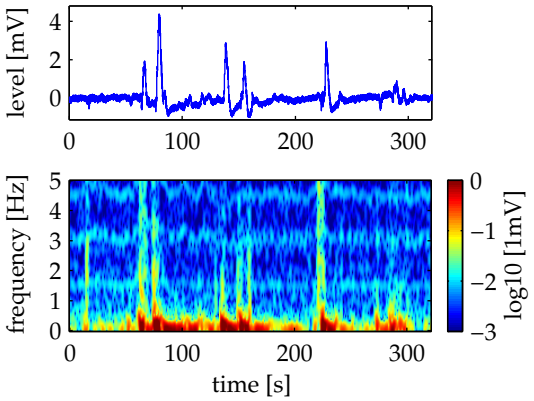

Figure 1: Surface Electromyogram: Time history (above) and its short-time Fourier transform (below).

and decay slope, the mean frequency of the calculated spectrum serves as a criterion to judge imminent delivery.

But a detailed analysis in the time-frequency domain reveals a strongly varying frequency content. This analysis is done by a discrete short-time Fourier transform (STFT) based on a Hann-Window 5 s long. An additional zero-padding and a logarithmic scaling of the resulting amplitude-coefficients unveils all the significant details. An introduction into the time-frequency transforms can be found in (Mertins, 1999), practical aspects are discussed e.g. in (Reicke et al., 2006).

The logarithmic representation of the STFT coefficients in Figure 1 does not only show the broad frequency content of the pulses, it even unveils the heart beat of the foetus at 1.6 Hz as well as its harmonics. Due to the fact that the pulses rather than the flat line sections contain the information about the uterine contractibility, the authors suggest an enhanced analysis which is restricted to the EMG-pulses. This new approach is supported by Figure 2. The diagram on the top shows the instantaneous mean frequency

$$f_{\mathrm{m}}(t) = \int_0^\infty f \cdot \frac{|X_{\mathrm{STFT}}(f,t)|^2}{||X_{\mathrm{STFT}}(t)||^2}\,\mathrm{d}f \qquad (1)$$

derived from the amplitude coefficients $X_{\mathrm{STFT}}(f,t)$ of the STFT. The norm $||X_{\mathrm{STFT}}(t)||$ denotes the instantaneous energy $\int |X_{\mathrm{STFT}}(f,t)^2|\,\mathrm{d}f$ of the STFT. The red line represents the level of the original EMG-signal. The lower diagram shows the evolution of the mean frequency's standard deviation

$$\sigma_f(t) = \sqrt{\int_0^\infty (f - f_{\mathrm{m}})^2 \cdot \frac{|X_{\mathrm{STFT}}(f,t)|^2}{||X_{\mathrm{STFT}}(t)||^2}\,\mathrm{d}f} \qquad (2)$$

over time. It underlines that a reliable estimation of the mean frequency is restricted to the pulses. Only in these time intervals, the standard deviation is less than 3 Hz.

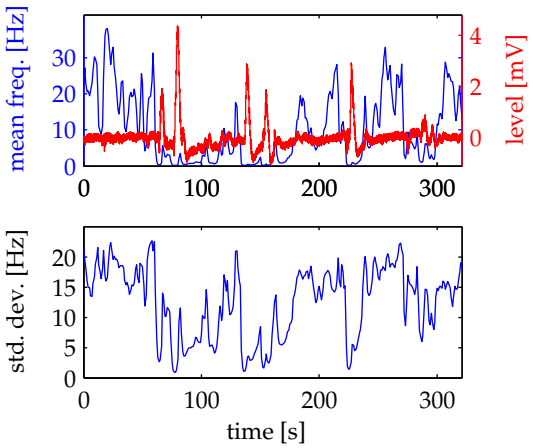

Figure 2: Instantaneous mean frequency (above) and its standard deviation (below) of the signal shown in Fig. 1.

As only the pulses contain the relevant information, it is convenient to analyse the pulses without the intervals of relaxation. This contribution presents a semi-automatic pulse detection, which extracts the pulses out of the measured EMG-signal. The expression *semi-automatic* underlines that the operation is controlled by the physician, whereas the algorithm undertakes the time-consuming and exhausting work of scanning through the signal searching for pulses. Additionally, the use of surface electrodes causes deformations of the pulse shape. Therefore, the pulses are processed by a stochastic method based on the Karhunen-Loève transform to evaluate a generalised pattern.

2 PULSE DETECTION

2.1 Conditioning

The surface-EMG signals are distorted by noise and a low frequency drift. A low-pass filter, which rejects frequencies higher than 7.5 Hz, is applied to attenuate the noise. The low frequency drift is reduced by a high-pass filter with a cut-off frequency of 0.1 Hz and a transition band of 0.2 Hz. Both are implemented as finite impulse response (FIR) filters based on a Kaiser window design (Oppenheim and Schafer, 1999). An additional noise-reduction is achieved by the pulse detection: the flat line intervals, which are characterised by a low signal-to-noise ratio, are excluded from the further analysis.

2.2 Pulse Detection

The pulse detection extracts those parts of the signal which contain the relevant information about the uterine contractibility. The localisation of the pulses is done regarding the magnitude of the signal. First, the global maximum and the mean value of the signal's magnitude as an approximation of the noise level are determined. All local peaks in the range between these two values can be considered as potential pulse centres. But only pulses whose peak values largely exceed the noise limit offer a sufficient signal-to-noise ratio. Therefore, the first parameter of the pulse detection, the *level value*, is introduced. This value determines the percentage of the range between noise level and global maximum which is added to the noise level in order to define the lower level limit. If the level value is chosen equal to zero, the lower level limit is identical to the noise level. Hence, any peak value higher than the noise level is considered as a pulse centre. In case of a level value equal to "1", the lower level limit reaches the global maximum and any peak except for the global maximum will be rejected. Figure 3 shows a particular lower level limit which corresponds to a level value of 0.3.

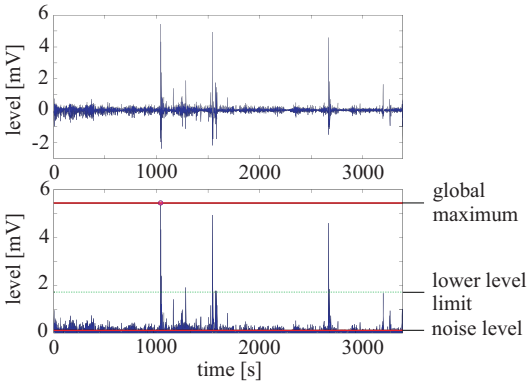

Figure 3: EMG-signal (above) and its magnitude with global maximum, noise level and a particular level value.

After the localisation of the pulse centres in the signal, the initial and end point of each pulse are determined. The pulse detection is based on the assumption that a pulse begins and ends at roots. Therefore, any low frequent drift has to be removed (cp. 2.1) before the execution of the pulse detection algorithm. Starting with the pulse centre, the adjoining roots temporary describe the initial and end points. In the following, this part of the pulse between these two roots is called the inner pulse. If these points were finally considered as the pulse's initial and end points, adjacent over- and undershoots, which might belong to the pulse and therefore contain valuable information, would not be extracted. Hence, the surroundings of the inner pulse have to be taken into consideration.

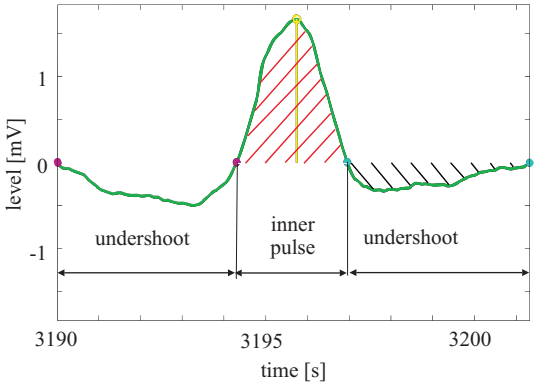

Figure 4: Evaluation of inner and outer area.

Figure 4 displays a pulse with a preceding and subsequent undershoot. To determine whether these undershoots are part of the pulse, the roots before and after the temporary initial and end points are considered. For example, the temporary end point and the root located on its right enclose the subsequent undershoot. Now, the area of the undershoot is calculated and related to the area of the inner pulse. In Figure 4, the area of the undershoot ("outer area") and the inner pulse ("inner area") are hatched in black and red, respectively. If the ratio of the outer and inner area exceeds a given value, the corresponding undershoot belongs to the pulse. If the right undershoot in Figure 4 fulfils this area criterion, the inner pulse is expanded by the right undershoot and the temporary end point is shifted by one root to the right.

This given value is called the *area value* and can be chosen anywhere between "0", which connects any adjacent undershoot to the inner pulse, and "1". In case of an area value equal to "1", only undershoots exhibiting an area greater than the inner area are attached to the pulse. The same procedure is done with the undershoot on the left. This algorithm goes on in both directions until the area of the current over- or undershoot is less than that of the original inner pulse. In this case, the temporary root becomes the final root, which borders the pulse to one side. As soon as the left and right final roots are determined, the pulse can be extracted from the signal. The detection of the next pulses follows the same algorithm. In order to avoid overlapping of closely neighbouring pulses, the extracted pulse data are replaced by zeros.

The level value influences the quantity of detected pulses. The lower the level value, the more peaks of the signal are regarded as pulse centres. The area value controls the lengths of the pulses. The greater the area value, the less over- and undershoots belong to the inner pulse and therefore the less pulses are

lengthened beyond their inner pulse. However, the area value has an influence on the quantity of the pulses, too. If the area value is very low, the pulses extracted from the signal are so long that less pulses can be detected in the remaining signal parts.

2.3 Characteristic Values

The pulse detection scans through the signal and cuts out single time histories belonging to those pulses whose shapes match the pattern specified by the level and area value. The extracted pulses are described in the time domain by their peak values and lengths. Additionally, each pulse is analysed in the frequency domain by the discrete Fourier transform (DFT). Contrary to the short-time Fourier transform $X_{\mathrm{STFT}}(f,t)$ of the entire signal, the spectrum $X_{\mathrm{pulse}}(f)$ of an individual pulse is not time-dependent. Hence, each pulse is characterised by two values in the frequency domain, the mean frequency f_m and the variance σ_f^2.

Based on a measured EMG-signal, Figure 5 shows the characteristic values of those pulses that fulfill a level value equal to "0.3", i.e. 30 % of the global maximum, and an area value of "0.4". In the diagrams, the horizontal line denotes the arithmetic mean. The third diagram exhibits a strong variation in the pulse length. Particularly, the 2nd and 4th pulse length strongly deviate from the mean of ≈ 650 samples. The 2nd pulse's mean frequency f_m largely exceeds the mean of ≈ 0.16 Hz. The reason may be the short duration of ≈ 200 Samples, which also increases the variance σ_f^2.

In order to demonstrate the influence of the two parameters *level value* and *area value* on the number, length and mean frequency of the pulses extracted from the EMG-signal, the results of five different pairs, shown in Table 1, are compared in Figures 6, 7 and 8.

Table 1: Pairs of parameters used for pulse detection.

parameter settings	level value	area value
E1	0.05	0.1
E2	0.1	0.1
E3	0.1	0.3
E4	0.3	0.4
E5	0.3	0.7

For each pair, denoted with E1 up to E5, the left and right bars represent the left and right channel of the electromyogram, respectively. With increasing level value, the number of pulses decreases because pulses with lower peak values are now rejected. A comparison between pair E2 and E3 as well as E4 and E5 unveils the influence of the area value on the length and number of pulses. An increasing area value leads to a shorter maximum pulse length. On the other hand, a higher level value increases the minimum pulse length because the pulses with low peak values, which are obviously shorter, are not considered anymore. As it is mentioned in 2.2, a more restrictive area value can resolve and separate closely neighbouring pulses into two individual pulse shapes.

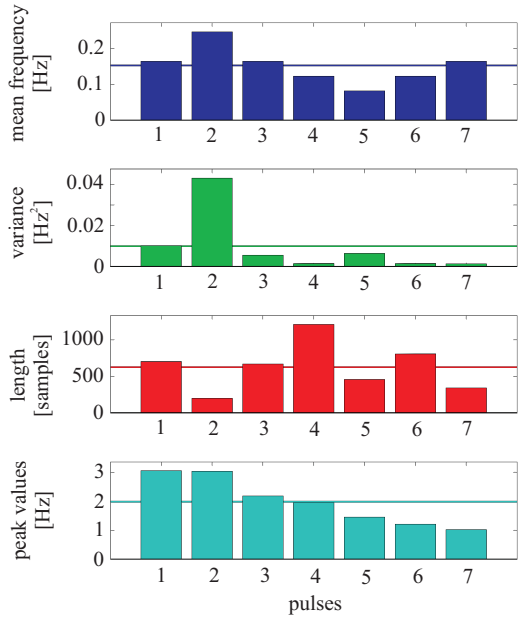

Figure 5: Characteristic values of a pulse ensemble cut out from a measured EMG-signal.

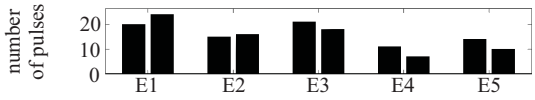

Figure 6: Influence of parameters in Table 1 on number of pulses extracted.

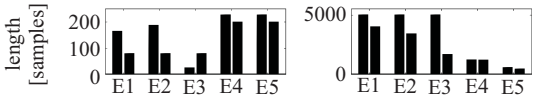

Figure 7: Influence of parameters in Table 1 on minimum and maximum pulse length.

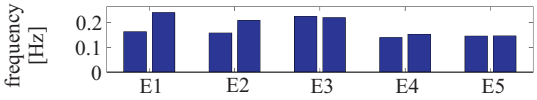

Figure 8: Influence of parameters in Table 1 on mean frequency.

The variation of the pulse length takes effect on the mean frequency, which is shown in Figure 8. It

reveals a strong sensitivity of the mean frequency to the given level and area values. This insufficient uncertainty motivated the authors to improve the analysis by a stochastic signal processing, which is described in the next section. Additionally, a criterion is required to give reliable information about the quality of the signal. A straightforward approach is the consideration of the signal-to-noise ratio, but this will not take into account any correlation between the two channels .

3 STOCHASTIC ANALYSIS

3.1 Karhunen-Loève Transform

The electric potential, which occurs at a neuromuscular junction, is transmitted via a quite complex electric network to the two electrodes at the abdomen's surface. This leads to an amplitude attenuation of $\approx -20\,\mathrm{dB}$ and deformations in the pulse shape. In addition, the location of the contraction is randomly distributed over the entire uterine muscle, which implies a random distortion of the EMG-signal with regard to the peak value and pulse shape.

Due to the fact that the measuring time of about 30 min is very short compared to the ongoing pregnancy, a stationary stochastic process is assumed. The individual pulse shapes extracted by the pulse detection are considered as the realisations of this stochastic process. The new approach uses the Karhunen-Loève transform (KLT), also referred to as Principal Component Analysis (PCA), to determine a characteristic pulse shape out of the pulse ensemble.

The Karhunen-Loève transform is a signal-depending decomposition based on the covariance matrix

$$\underline{R}_{\tilde{x}\tilde{x}} = \mathrm{E}\left\{\underline{\tilde{x}}\,\underline{\tilde{x}}^{\mathrm{T}}\right\}, \tag{3}$$

in which $\mathrm{E}\{\ \}$ denotes the statistic expectation and $\tilde{x}$ the stochastic process. The decomposition requires the eigenvectors $\underline{u}$ of the eigenvalue problem

$$\underline{R}_{\tilde{x}\tilde{x}}\,\underline{u} = \lambda\,\underline{u}. \tag{4}$$

The eigenvectors $\underline{u}$ can be regarded as the characteristic shapes of the stochastic process. The eigenvalue λ represents the degree of similarity between the corresponding eigenvector and the individual pulses. In the following, the product of eigenvector and eigenvalue is denoted as *eigenform*. The more similar the individual pulses of the ensemble are to each other, the more dominant becomes the first eigenform. If the ensemble consists of identical pulse shapes, the first eigenvalue will contain the whole variance of the stochastic process, while all other eigenvalues are equal to 0. A brief introduction into the Karhunen-Loève transform is given in (Mertins, 1999), a detailed description can be found in (Jolliffe, 2002).

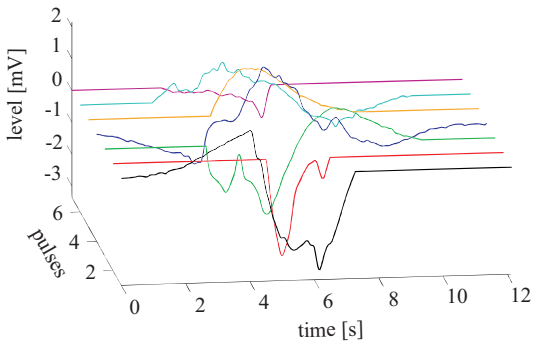

Figure 9: Ensemble of centred pulses.

For the stochastic analysis, a preprocessing of the pulses is necessary. The calculation of the covariance matrix requires an identical length of all the pulse shapes. Therefore, the pulses are centered with regard to their centres of area, followed by padding zeros on both sides to obtain an identical pulse length. The result of this preprocessing is shown in Figure 9, in which the longest pulse, the blue one, specifies the dimension of the covariance matrix. The other pulse shapes are shifted in such a way that all area centres coincide.

The result of the KLT of Figure 9 is displayed in Figure 10: The first and second eigenforms (EF) are dominant and contain $\approx 90\,\%$ of the process' variance. This can be seen from the time history on the left side as well as the loadings on the right. In this context, the loading denotes the normalised variance of the stochastic process.

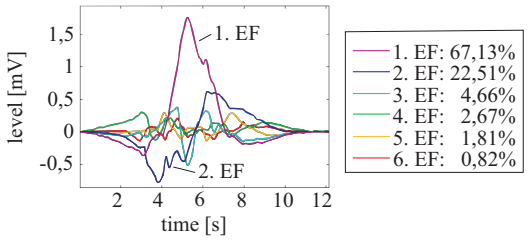

Figure 10: KLT: Eigenforms (left) and loadings (right).

Instead of deriving the mean frequency directly from the pulse ensemble (cp. subsection 2.3), the DFT of the first eigenform yields to a mean frequency which is less sensitive to parameter variations. On top of Figure 11, the global mean frequency, which is evaluated as the arithmetic mean of the individual eigenforms' mean frequencies, is displayed according to the parameter settings shown in Table 1. While

the global mean frequency is susceptible to parameter variations, the mean frequency derived from the first eigenform seems to be less sensitive. Here, research is in progress to confirm this observation.

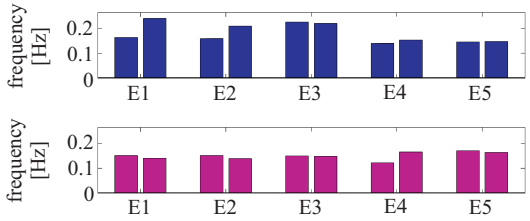

Figure 11: KLT: global mean frequency (above) and mean frequency of the first eigenform (below) for different parameter settings.

The Karhunen-Loève transform does not only extract a characteristic pulse pattern, the first eigenform, out of the pulse ensemble. It can also provide a reliable criterion of the electromyogram's reliability. If the first eigenvalue is dominant, the pattern of the first eigenform is similar to the shapes of the majority of pulses in the ensemble, while the other eigenforms represent the deformations in the pulse shapes.

3.2 Correlation Analysis

So far, the two channels of the electromyogram have been analysed separately. In case of a dominant eigenvalue (see subsection 3.1), the corresponding eigenform characterises the pulse pattern of the individual channel's pulse ensemble very well. Therefore, the correlation between the left and right EMG-channel can be evaluated by regarding their first eigenforms.

Even in case of identical pulse shapes, a time shift between the left and right eigenform can occur. This may be caused by different transmission delays from the neuromuscular junction to the surface electrodes in combination with the centring of the pulses before the KLT is performed.

In order to evaluate the similarities between the left and right eigenform $u_\ell(t)$ and $u_\mathrm{r}(t)$ the cross-correlation function (CCF)

$$R_{u_\ell u_\mathrm{r}}(\tau) = \int_{-\infty}^{\infty} u_\ell(t) \cdot u_\mathrm{r}(t+\tau)\,\mathrm{d}t \qquad (5)$$

is used. If the two eigenforms are of identical shape but shifted to each other, $u_\mathrm{r}(t) = u_\ell(t-\Delta t)$, the CCF resembles an autocorrelation function (ACF) whose maximum value is shifted along the time axis. Due to the fact that an ACF is symmetric to its origin $\tau = 0$, the CCF of two identical but shifted eigenforms is symmetric with regard to the time shift Δt:

$$R_{u_\ell u_\mathrm{r}}(\Delta t - \tau) = R_{u_\ell u_\mathrm{r}}(\Delta t + \tau)\,. \qquad (6)$$

Because the eigenvector's orientation is not specified by Equation 4, the left and right eigenforms can differ in their signs. Therefore, maximum correlation in the CCF appears at its global maximum or minimum. First of all, the time shift of the CCF is determined by its global extremum. Subsequently the CCF is divided into a symmetric

$$R_\mathrm{symm}(\tau) = \frac{R_{u_\ell u_\mathrm{r}}(\Delta t + \tau) + R_{u_\ell u_\mathrm{r}}(\Delta t - \tau)}{2} \qquad (7)$$

and antimetric

$$R_\mathrm{anti}(\tau) = \frac{R_{u_\ell u_\mathrm{r}}(\Delta t + \tau) - R_{u_\ell u_\mathrm{r}}(\Delta t - \tau)}{2} \qquad (8)$$

component. This decomposition is displayed in Figure 12. The extremum is located at ≈ 2000 samples, at which a vertical symmetry axis (dashed line) is drawn. According to Equations 7 and 8 the cross-correlation function (blue line) is decomposed into its symmetric (green line) and antimetric (red line) components.

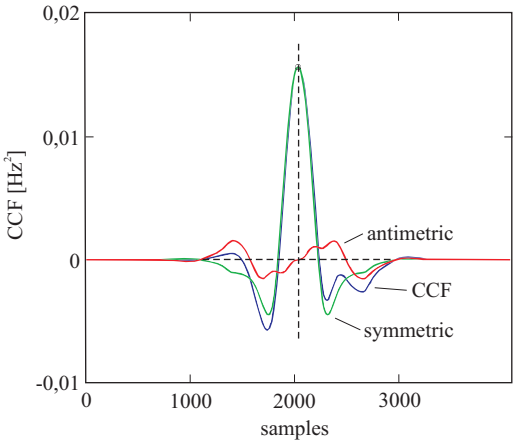

Figure 12: Decomposition of the CCF (blue) at its extremum into a symmetric (green) and antimetric (red) component.

Based on this decomposition a symmetry value

$$C_\mathrm{symm} = 1 - \frac{\int_{-\infty}^{\infty} \left(R_{u_\ell u_\mathrm{r}}(\tau) - R_\mathrm{symm}(\tau)\right)^2 \,\mathrm{d}\tau}{\int_{-\infty}^{\infty} R^2_{u_\ell u_\mathrm{r}}(\tau)\,\mathrm{d}\tau} \qquad (9)$$

can be specified as the square deviation of the CCF from its symmetric component. In case of full axis symmetry, the symmetric value in Equation 9 reaches "1" or 100 %. The cross-correlation function of the left and right eigenforms for the parameter settings

in Table 1 are displayed in Figure 13. The CCF's oscillations are caused by the under- and overshoots of the EMG-pulses. With an increasing area value, these parts diminish in the pulse shapes and eigenforms. The CCFs are dominated by their symmetric components, which is also confirmed in Table 2 by symmetry values close to 100 %.

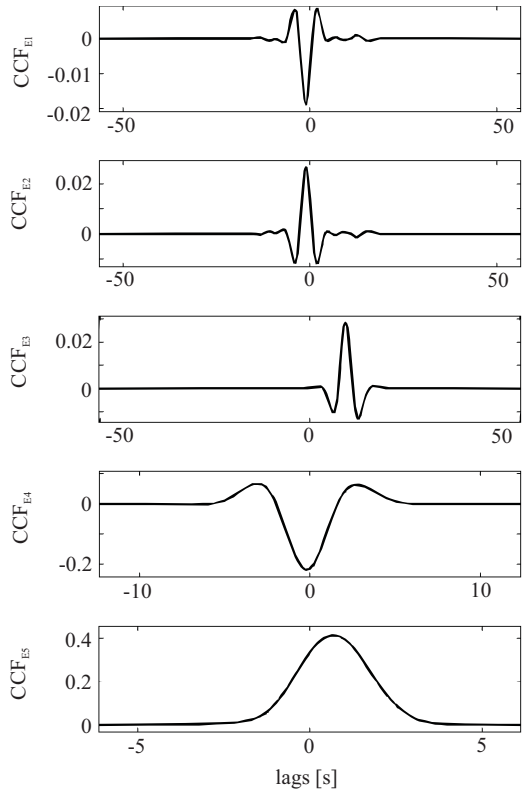

Figure 13: Cross-correlation functions for the parameter settings of Table 1.

Table 2: Symmetry values for parameter settings in Table 1.

parameter settings	symmetry value in %
E1	99.79
E2	99.74
E3	99.43
E4	99.97
E5	99.96

Figure 14 displays the eigenform's cross-correlation functions of another EMG-signal. The eigenforms are based on a pulse detection whose parameters are shown in Table 3. Due to a poorer signal-to-noise ratio, the minimum level value is set to 0.2. Only CCF_{E8}, the CCF for the third parameter set (level value of 0.2, area value equal to 0.7) seems quite symmetric. This assumption is confirmed by a symmetry value $C_{\text{symm}} = 0.9975$ in Table 3.

This means that the eigenforms of the second EMG-signal are more sensitive to variations of the pulse detection's parameters. This may be caused by an incorrect application of the surface sensors, which induces additional noise and deformations. Therefore, the combination of the eigenforms' loadings and the symmetry value indicates the quality of the measurement.

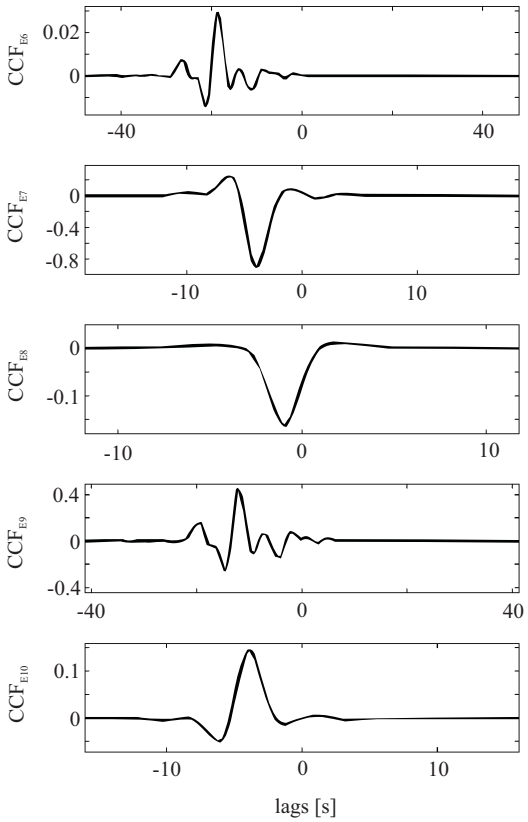

Figure 14: Cross-correlation function of another EMG-signal with parameter settings of Table 3.

Table 3: Symmetry values of the second EMG-signal.

parameter settings	level value	area value	symmetry value in %
E6	0.2	0.1	86.29
E7	0.2	0.4	97.16
E8	0.2	0.7	99.75
E9	0.3	0.1	77.23
E10	0.3	0.4	96.19

4 CONCLUSIONS

The existing methods for the analysis of EMG-signals are not precise enough for a reliable prediction of the point of delivery. The new approach presented in this contribution is based on the distinction between pulses (muscular contraction) and flat line sections during relaxation. A time-frequncy analysis reveals that only the pulses contain relevant information whereas the flat line sections can be neglected. For this reason, a semi-automatic pulse detection is developed. The physician controls the functionality of the pulse detection by adapting two comprehensible parameters, while the time-consuming work of pulse extraction is done automatically. The first parameter, the level value, influences the number of extracted pulses, whereas the second parameter, the area value, determines the length of the pulses. Therefore, the physician integrates his current observations as well as his medical experiences into the pulse detection.

The use of surface electrodes leads to deformations in the individual pulse shapes. In this approach, the pulses extracted by the pulse detection are treated as realisations of a stationary stochastic process. In order to derive a generalized pattern, a stochastic analysis, the Karhunen-Loève-Transform (KLT), is carried out. The KLT is based on the eigenvalue/eigenvector problem of the covariance matrix. While an eigenvector represents a generalised pattern, the corresponding eigenvalue specifies the degree of similarity with regard to the pulse ensemble. Eigenvalue and eigenvector yield to the eigenform. The more dominant the first eigenform is, the better it represents the pulses of the ensemble.

Until now, the mean frequency has been used for the prediction of the point of delivery. Although the pulse detection reduces the frequency deviation significantly, the mean frequency remains sensitive to variations of the pulse detection's parameters because the individual pulses are randomly distorted by conductivity effects. The first eigenform of the KLT is less susceptible to parameter variations. Particular in case of a dominant first eigenform, the mean frequency becomes a reliable criterion.

Furthermore, a new characteristic value is developed: the symmetry value. It is derived from the cross-correlation function of the first eigenforms of the left and right EMG-channel. If the quality of the electromyogram is high, the pulse ensembles of the left and right channel will yield to quite identical eigenforms and a symmetry value close to 100 %. Together with the eigenvalues of the KLT, the symmetry value serves as a criterion for the measurement's reliability.

In the future, the pulse detection combined with the stochastic analysis will be applied on a sufficiently large amount of electromyograms taken from various women during the last period of pregnancy. With these results, the reliability of this new approach as well as the improvement with regards to the present methods will be be quantified.

REFERENCES

Jolliffe, I. T. (2002). *Principal Component Analysis*. Springer, New York, 2nd edition.

Maul, H., Maner, W. L., Olson, G., Saade, G. R., and Garfield, R. E. (2004). Non-invasive transabdominal uterine electromyography correlates with the strength of intrauterine pressure and is predictive of labor and delivery. In *The Journal of Maternal-Fetal and Neonatal Medicine*. Parthenon Publishing.

Mertins, A. (1999). *Signal analysis: wavelets, filter banks, time-frequency transforms and applications*. Wiley, Chichester, 2nd edition.

Oppenheim, A. and Schafer, R. W. (1999). *Discrete-time signal processing*. Prentice Hall, Upper Saddle River, NJ, 2nd edition.

Reicke, L., Kaiser, I., and Kroeger, M. (2006). Identification of the running-state of railway wheelsets. In *ISMA2006, International Conference on Noise & Vibration Engineering*. Katholieke Universiteit Leuven, Department of Mechanical Engineering.

A MULTIMODAL PLATFORM FOR DATABASE RECORDING AND ELDERLY PEOPLE MONITORING

Hamid Medjahed, Dan Istrate
RMSE, ESIGETEL, 1 Rue du Port de Valvins, 77 215 Avon-Fontainebleau Cedex, France
hamid.medjahed@esigetel.fr, dan.istrate@esigetel.fr

Jerome Boudy, Jean-Louis Baldinger, Bernadette Dorizzi, Imad Belfeki, Vinicius Martins
EPH,INT, 9 rue Charles FOURIER,91011 Evry, France
{*jerome.boudy, jean-louis.baldinger, bernadette.dorizzi, imad.belfeki, vinicius.martin*}*@int-evry.fr*

François Steenkeste
U558, INSERM, Toulouse, France
steenkeste.f@chu-toulouse.fr

Rodrigo Andreao
Departamento de Engenharia Eltrica, Universidade Federal do Espirito Santo, Vitoria, Brazil
rodrigo@ele.ufes.br

Keywords: Medical Signal Acquisition, Biomedical multimodal database, Healthcare, Wearable Sensors and Systems, Acoustic Signal Processing, Telemedicine.

Abstract: This paper describes a new platform for monitoring elderly people living alone. An architecture is proposed, it includes three subsystems, with various types of sensors for different sensing modalities incorporated into a smart house. The originality of this system is the combination and the synchronization of three different televigilance modalities for acquiring and recording data. The paper focuses on the acquisition step of the system, usage and point out possibilities for future work.

1 INTRODUCTION

As the society is increasingly aging there is an important need to find an intelligent support system able to facilitate the maintenance at home of the disabled and/or old people with safety and providing their autonomy. The maintaining at home in safety of elderly people is a new major challenge to social and health government services: given limited resources, more and more elderly people living alone at home are particularly prone to accidents and falls in the home and can often lie injured and undiscovered for long periods of time. A statistical study indicates that 7% of elderly people have a home accident due to everyday life activity and in 84% of cases a fall occurs (B.Thélot, 2003). In practice all the industrialized countries are affected by this phenomenon.
Very few systems that support the home life and healthcare of elderly persons have been developed to improve quality of life and the alleviation of risk. Among established systems we can mention, the TelePat project (French RNTS Program) (Boudy et al., 2006) where certain physiological data and the person's activity are measured by different sensors connected to a microcontroller based computing unit, are sent through radio connection to a remote central server application for exploitation and alarm decision. Now, within the Tandem project (French RNTS Program), accelerometer sensors are added to this system for the detection of falls. In the framework of DESDHIS project a medical home monitoring system which use an accelerometer based sensor, infrared sensor, an oxymeter and a blood pressure device has been developed at Grenoble (G.L.Bellego et al., 2006). A system of multi-channel sound acquisition is presented in (D.Istrate et al., 2006a), to analyze in real time the sound environment of the home to detect abnormal noises (i.e., call for helps or screams).
In this article a new multimodal platform for a home remote monitoring is proposed, using a large number of sensors in order to reinforce the secure detection of abnormal situations, in particular patient's

fall event. Our software implementation gathers three subsystems which have been technically validated from end to end, through their hardware and software. This specific platform is multimodal since it allows us to record physiological data via the RFpat (J.L.Baldinger et al., 2004) subsystem, audio information via Anason (D.Istrate et al., 2006a) subsystem and patient's localization through infra-red sensors via Gardien (S.Banerjee et al., 2003) subsystem. An additional simulation process is added and will be integrated to our platform as a way to overcome the lack of experimental data required to design the decision part of the system, such as the cardiac frequency during distress situations.

2 MONITORING SYSTEM HARDWARE ARCHITECTURE

We define an intelligent environment as one that is able to acquire and apply knowledge about its inhabitants and their surroundings in order to adapt to the inhabitant and to improve its comfort and efficiency. To record the multimodal medical database our first aim is focused on providing such an environment. We consider our system as an intelligent agent, which perceives the state of the environment using sensors and acts consequently using device controllers. The first part of this intelligent environment was realized within the framework of TelePat project, in order to study the secure detection of patient's fall event. The present work is developed in the framework of the Tandem project.

Our platform is a surface of 20 m2 in our laboratory which is arranged in two rooms with a technical area in order to evaluate and to supervise the experiments. It integrate smart sensors (infra-red, audio, physiological,) linked to a smart PC .The two microphones for audio monitoring are linked to the PC through an external sound card, and can be interpreted as a single smart audio sensor for the Anason software. Eight infra-red sensors are fixed on specific places of the house (walls and ceiling) and connected to an acquisition card (ADAM) (F.Steenkeste et al., 1999), which is linked to the serial port of the PC. The card output is RS485 which is converted in RS232 in order to allow Gardien software to acquire the patient position at any time. The RFpat subsystem is composed of two main components: (1) a wearable terminal carried by the patient, continuously recording his physiological data and urgency call, (2) an in-door reception base station linked to the PC via RS232 serial link providing the information usually every 30 seconds. The layout of our house environment is shown in Figure 1.

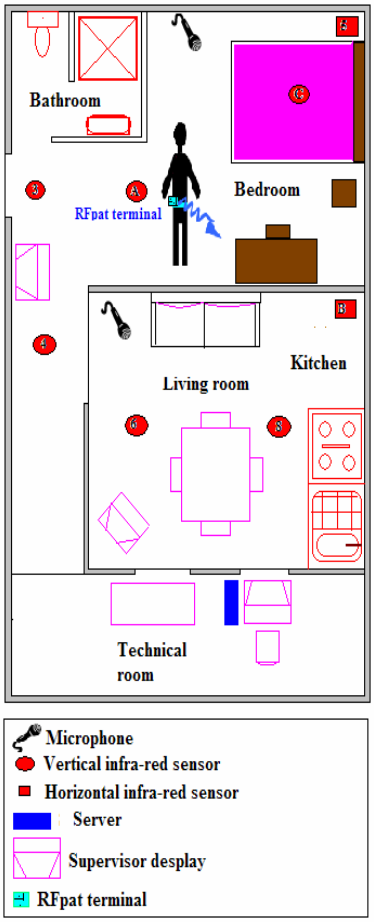

Figure 1: Layout of the house environment.

3 MONITORING SYSTEM SOFTWARE ARCHITECTURE

The multimodal system has three main subsystems like in Figure 2 and provides a general user interface which encapsulates the Anason subsystem. It is implemented under LabWindows/CVI software and communicates with RFpat subsystem and Gardien subsystem by client-server model using TCP/IP and appropriate application protocols. Gardien is implemented under C++ and recovers data every 500 milliseconds. RFpat is also implemented under C++ and receives data from receiver every 30 seconds. The use of the inter-module communication through TCP/IP socket allows each module (subsystem) to be run on a different computer, and to synchronize each televigilance modality channel. The user can interact with the system via internet navigator and supervises the different applications. For example, we use this web server to communicate with the person, who inter-

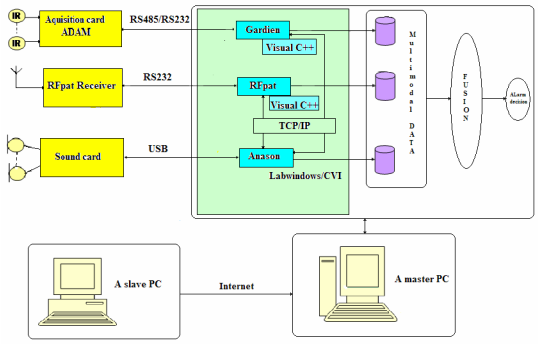

Figure 2: Software architecture of the system.

prets a patient's activity by displaying a reference scenario on the monitoring screen. This feedback can significantly help the system manipulation. The system flexibility obtained through TCP/IP socket communication allows to add others sensors like heart monitoring sensor (ECG).
Currently these three modalities work individually, we investigate multimodal data fusion methods by exploiting the measurements coming from the platform in order to increase reliability and to reinforce the secure detection of patient's distress events.

3.1 RFpat

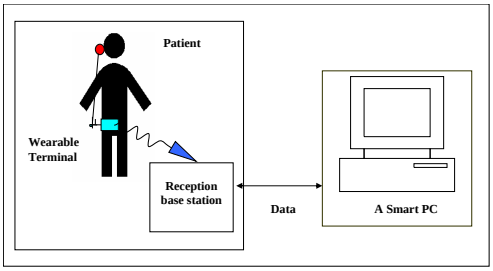

Figure 3: Architecture of RFpat system.

RFpat subsystem is composed of two fundamental elements (Figure 3):

- Wearable terminal carried out by the patient continuously recording his physiological and activity data.
- A reception base station (receptor connected to a PC), which receives signals from the patient's terminal, analyses data in order to generate an alarm after identification of an emergency situations.

All the sensors data are processed within the wireless portable device by using low consumption electronic components in order to face autonomy problems which are also crucial in that application. The circuit architecture is based on different micro-controllers devoted to acquisition, signal processing and emission. The wearable terminal includes chain of various physiological signals, their possible pre-processing in order to eliminate the power-line interference signal (50 Hz) and the various measurement noises, such as generated by the displacements of the sensors fixed on the patient's body. The latter type of noise is generally a factor limiting the use of such systems in ambulatory mode because the patient is often moving, even if slightly. In this system, the noise problem was solved in the acquisition stage of the portable device, by applying a digital noise reduction filter to the different sensors signals, movements, attitude and namely the pulse signal (heart rate). The performances of signal acquisition could be substantially improved when the patient performs movements. The noise reduction processing (J.L.Baldinger et al., 2004) reduces the variations of pulse measurement lower than 10%, even 5%, which remains in conformity with the recommendations of the health professionals.
The design of sensors and embedded processing has led to the realization of a remote wearable monitoring terminal, equipped with actimetry and physiological sensors, indicating the attitude of the patient (vertical/horizontal positions, activity) and his heart rate (pulse measurement); these specific sensors to recorded physical data type are, either integrated in the terminal, or externally fixed .
Data generated from the different sensors are transmitted, via an electronic signal conditioner, to a micro-controller based computing unit, embedded in the mobile terminal fixed on the patient's waist. Currently, a fall-impact detector sensor is added to this system for robustizing the detection of falls.

3.2 Anason

The sound remote monitoring subsystem analyzes the acoustical environment in real time and is made up of four main modules which are presented in the Figure 4 (D.Istrate et al., 2006b). The first module M1 continuously, supervises the sound environment in order to detect and extract useful sounds or speech from environmental noise. The signal extracted by the M1 module is classified like sound or speech by the M2 module. In the case of sound label, the sound recognition module M3.1 classifies the signal between eight predefined sound classes, while in the case of speech label, the extracted signal is analyzed by a speech recognition engine in order to detect distress sentences. For both cases, if an alarm situation has been identified (the sound or the sentence belong to an alarm class) this information is sent to the data fusion system.

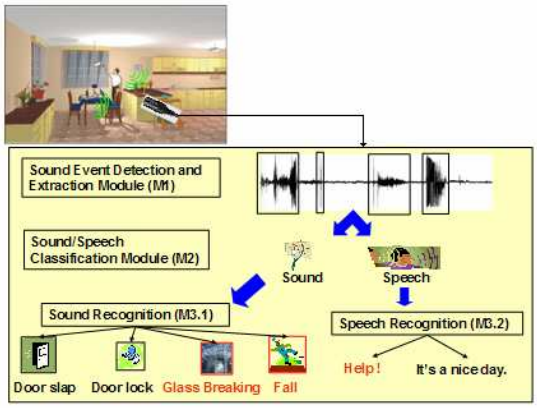

Figure 4: Sound monitoring architecture.

Sound Event Detection Module (M1). The sound flow is analyzed through a wavelet based algorithm aiming at sound event detection. This algorithm must be robust to noise like neighborhood environmental noise, water flow noise, ventilator or electric shaver. Therefore an algorithm based on energy of wavelet coefficients was proposed and evaluated in (D.Istrate et al., 2006a). This algorithm detects precisely the signal beginning and its end, using properties of wavelet transform.

Sound/Speech Classification Module (M2). The method used by this module is based on Gaussian Mixture Model (GMM) (D.A.Reynolds, 1995) (K-means followed by Expectation Maximisation in 20 steps). There are other possibilities for signal classification: Hidden Markov Model (HMM), Bayesian method, etc. Even if similar results have been obtained with other methods, their high complexity and high time consumption prevent from real-time implementation. A preliminary step before signal classification is the extraction of acoustic parameters: LFCC (Linear Frequency Cepstral Coefficients)-24 filters. The choice of this type of parameters relies on their properties: bank of filters with constant bandwidth, which leads to equal resolution at high frequencies often encountered in life sounds.
The BIC (Bayesian Information Criterion) is used in order to find the optimal number of Gaussians (G.Schwarz, 1978). The best performances have been obtained with 24 Gaussians.

Sound Recognition Module (M3.1). This module is based, also, on a GMM algorithm. The LFCC acoustical parameters have been used for the same reasons than for sound/speech module and with the same composition: 24 filters. The method BIC has been used in order to determine the optimum number of Gaussians: 12 in the case of sounds. A log-likelihood is computed for the unknown signal according to each predefined sound classes; the sound class with the biggest log likelihood is the output of this module.

Speech Recognition Module (M3.2). For Speech Recognition, the autonomous system RAPHAEL is used (M.Akbar and J.Caelen, 1998). The language model of this system is a medium vocabulary statistical model (around 11,000 words). This model is obtained by using textual information extracted from the Internet as described in (D.Vaufreydaz et al., 1999) and from "Le Monde" corpora. It is then optimized for the distress sentences of our corpus. In order to insure a good speaker independence, the training of the acoustic models of RAPHAEL has been made with large corpora recorded with near 300 French speakers (J.L.Gauvain et al., 1990): BREF80, BREF120 and BRAF100 corpora.

3.3 Gardien

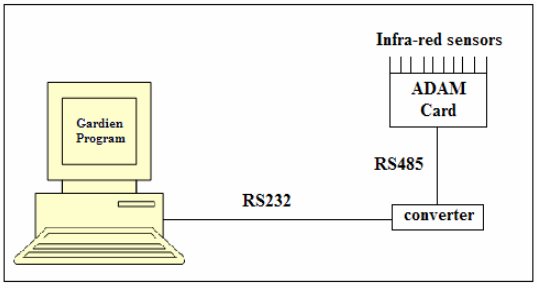

Figure 5: The Gardien system.

The subsystem knows as Gardien (Figure 5) consists of passive infra-red sensors placed in a residence and connected to a remote computer. All the sensors are connected through cables to an Input/Output parallel card (ADAM 4053) which is connected to a master PC. The computer automatically captures and registeres data obtained from the different sensors, with the help of Gardien software. Data corresponding to movements are collected twice per second, and stored with the time of the event in a specific file. When several consecutive data are identical, only the first instance is stored.
The sensors are activated by passage of person underneath, and remained activated as long as there is movement under that sensor and for an additional time period of $1/2$ seconds after the movement end.
The results from the automatic processing of this data are displayed in the form of list with all movements noted together with the time and each movement's

duration. Gardien is also able to display the data either in the form of graph (activity duration versus days) or as three-dimensional histograms (each sensor activation versus time). To validate the system, the results from the automatic processing are compared with manual analysis by an expert.

4 GENERAL INTERFACE OF THE SYSTEM

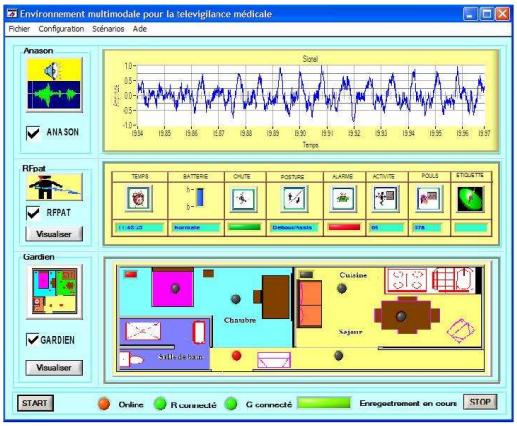

Figure 6: Main windows of the system during the acquisition step.

Figure 6 shows the front panel of the software system, where we can supervise the multimodal data acquisition step. The user must firstly select the modality to record and to configure its parameters. RFpat and Gardien need only to select the IP address and the TC/IP port number, while Anason requests the selection of the sound card (if two are present), the sampling rate and the location of the backup file.

5 THE BIOPHYSICAL SIGNALS SIMULATION STAGE (BSS)

The aim of this stage is to create pathological or critical situations for the patient at home. Indeed most of actual signals recorded on domotic platform are generally and hopefully in normal conditions. The simulator is based on the existing RFpat sensors device. The first main goal was to simulate cardiac pathological profiles such as in particular bradycardias: the design was done with the helpful collaboration of SAMU-92 (French emergencies service. In its implementation, are also foreseen functional stages for the actimetry simulation: patient's inclination (horizontal or vertical position), his body movement and

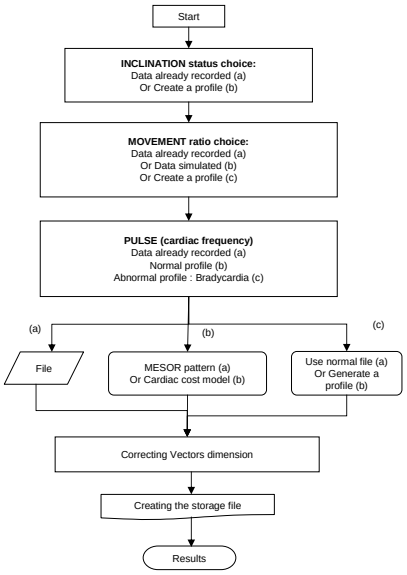

Figure 7: The Biophysical Signals Simulation.

in a larger extent patient's fall situations. The simulator software architecture is summarized in the Figure 7. For the cardiac frequency generation, three cases were proposed:

- A first normal cardiac category, based on the COSINOR method (F.Halberg, 1969), providing a global pulse variations trend within one day; this formula gives the cardiac frequency or pulse Fc in quiet situation under the following form: $Frest(t) = Fmoy + A\sin(2pi/24 * t)$, where Fmoy (around 70 bpm), A are respectively the average pulse or MESOR value and its maximal amplitude variation (about 6 bpm) along one circadian cycle; the Akrophase or maximal amplitude is statistically located around 16 hour.
- A second normal situation, called "Cost model", providing a pulse variation model, still denoted Fc, depending on the patient's activity; the formula is based on the pulse in a quiet situation (Fcrest) and the delta-variation due to patient efforts, namely representing the cardiac cost: $Fc(t) = Frest(t) + DFc(t)$. This part is developing stage.
- Bradycardia model corresponding to a situation met with elderly persons, by assuming no specific medication having a cardiac impact: the model is either artificially inserted inside an existing pulse signal sequence by taking into account the actual pulse variance, or is completely substituting the actual pulse sequence.

This tool is still open to other simulation process, namely for the actimetry where presently are per-

formed investigations on the potential correlations between the Cardiac cost model and the body movemenent. The BSS stage has been designed to be fully interfaced to the multimodal patient database.

6 APPLICATION

6.1 Recording of a Multimodal Medical Database

Most of monitoring systems use some form of learning method to discriminate between different types of normal and abnormal events. This methodology requires large amounts of training data that can be difficult to obtain especially data describing abnormal events that are by definition rare occurrences. An important issue for this problem, is to record a multimodal medical database which is the first application of our platform.

Data acquired from the patient are stored on the Master PC in a folder named with a code number corresponding to the patient. Each recording is composed from five files corresponding to the different subsystems.

The first one, named "personnel.xml", contains the patient's identifier and some personal information like age, native language, usual drugs treatments, etc. The second, named "scenario.xml ", describes the reference scenario. All these data relative to the tester are protected for his privacy and let to his agreement.

The sound data is saved in real time, in a wav file with 16 bit of resolution and a sampling rate of 16 KHz, a frequency usually used for speech applications.

The clinical data acquired from RFpat are saved in a separate file which contains information about patient's attitude (lied down or upright/seated), his agitation (between 0% and 100%), his cardiac frequency, fall events and emergency call in a binary type. The acquisition sample rate is $1/30$ seconds.

The data acquired every 500 milliseconds by Gardien subsystem are saved in a separate text file, fully respecting the original storage format of the GARDIEN application. Each line of this file contains the infrared sensors which are excited (they are represented by hexadecimal numbers from 1 to D) plus the corresponding date and hour.

To tackle the problem of the variety of each data sampling rates, a synchronization prototype between the three subsystems is obtained through TCP/IP protocol. RFpat is the master and supervise Gardien and Anason by TCP/IP commands.

Thus, our multimodal database acquisition software provides a very helpful and well-targeted application to elaborate and assess the data fusion-based decision methods. The low level data recorded by our system will be useful for the development of processing algorithms of each modality.

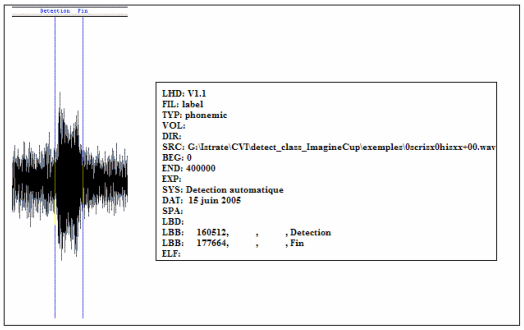

Figure 8: Sound file (*.wav) and its corresponding SAM file.

In order to index our multimodal database, we have retained the SAM standard indexing file (D.Well et al., 2004) generally used for Speech Databases descriptions. The SAM labeling of a sound file is shown in Figure 8; it indicates information about the sound file and describes this file by delimiting the useful part for analyzing and processing. For each modality of the database a corresponding indexing file is created, we have adapted this type of files to the specificities of each modality, and we have added another indexing file for the entire database.

6.2 The First Approach of Fusion: Bimodal Fusion between RFpat and Gardien

This work is a first step for a multi-modal experiment. Indeed, this was performed with only two of the televigilance modalities presented in this paper: the fixed infra-red sensors based Gardien system and the mobile sensors RFpat device. Its conclusions have motivated the extension of these modalities to the combination with the sound detector AnaSon through the current investigations led by ESIGETEL, INT and INSERM.

In this first step we have used a PCA analysis in order to preliminary determine potential correlation between the combined data and in order to obtain a data reduction. After preliminary evaluations with the K-Nearest Neighbors algorithm, the Gaussian Mixtures Models and Neural Network on RFPAT data, a Bimodal fusion was carried out by using the Neural Network .

6.2.1 Principal Components Analysis

The data resulting from RFpat subsystem and Gardien subsystem were analyzed simultaneously through their respective variables: posture, activity, cardiac frequency, exposure time under the infra-red sensor C3 (sensor indicating the input/output of the person in the home), and exposure time under the infra-red sensor C5 (sensor indicating the fall of the person). The analysis of the PCA algorithm results made it possible to propose a set of decision rules on several levels:

- To define an estimator in two levels: a "physiological" distance between two parameters (cardiac frequency, activity) normally correlated: normal state if they are close or pathological state if they are distant. Then, a "actimetric" distance (Slope, C5): normal if distant or pathological if close.
- There are a correlation between the cardiac frequency and the activity which will allow the fusion system to avoid a malfunction of one of the two sensors.

6.2.2 Application of the Neural Networks

The Neural Networks (NN) consist in an input layer, the sensors signals, several transition layers (denoted as hidden layers) and of an output layer delivering the classification of the data observed in situation either 'Normal', or critical 'detected Fall'. A classical NN structure was implemented by using a Multi-Layer Perceptron (MLP) based on only one hidden layer consisting in eight neurons after an optimal tuning.

Each neuron realizes a scalar product between its input vector and the weight vector, where a deviation is added, then operates an activation function in order to generate its output value y: $y = f(x.w + b)$.
The activation function must be strictly crescent and bounded. A classical function used in our experiment is the standard sigmoid function whose equation is reminded hereafter: $f(x) = \frac{tanh(x)+1}{2}$.
Two types of networks were compared, with respectively as input vector of the MLP first layer:

- Single actimetric data of RFpat in entry of the network, giving a rate of recognition of the order 84%.
- The actimetric data of RFpat and horizontal infared sensors of Gardien, providing a rate of 86%.

The improvement nevertheless remains quite limited. One improvement track is to increase the data corpus used for the learning phase, namely by recording more specific actual and simulated emergency situations thanks to the multi-modal recording tool previously described in this paper. Another main improvement track will be investigated by adding the AnaSon (abnormal sound detector) modality. Therefore that is why the need of a new multi-modal recording tool was considered as crucial for the follow-up. Thorough investigations will also be performed again on KNN and GMM techniques, namely by working on the data pre-processing (normalized, transformed input data).

7 CONCLUSIONS

This paper has focused on the technology used for implementing the acquisition step of the platform. Preliminary results are encouraging with the achievement a multimodal medical database including patient's clinical data, usual environment sounds and patient localization. The platform enables us to have a full and tightly controlled universe of data sets and to evaluate the decision part of remote monitoring systems.
Our platform is in the research phase targeting a prototype, the system will be completed and improved by adding a data fusion-based decision element exploiting the measurements coming from this platform in order to propose new processes to reinforce the secure detection of patient's distress events. In particular the fall situations are studied: indeed one or more televigilance modalities might be out of order, or a particular environmental situation (ambiant noise, bad wireless conditions, sensors disabilities ...) can hide one particular modality or more. This is a very challenging issue for hospital emergency units such as for instance SAMU in France or Telecare services providers in general. Studies of usability are planned, in order to test the satisfactoriness of patients towards this system and to get a standardization prototype for our platform. This constitutes indeed, a first concrete step before a prototype deployment. In actual situation, evaluation and connection to smart home system are also planed to be performed in the framework of a new European project.

REFERENCES

Boudy, J., JL.Baldinger, F.Delavault, Farin, D., R.Andreao, S.Torres-Muller, A.Serra, F.Rocaries, C.Dietrich, F.Steenkeste, A., Dr.M.Baer, Dr.Ozguler, and D.Gaiti (June 2006). Telemedecine for elderly patients at home. In *the TelePat project.ICOST conference ulster Belfast*.

B.Thélot (June 2003). Resultats de l'enquete permanente sur les accidents de la vie courante. In *Reseau*

EPAC,Institut de Veille Sanitaire,Departement maladies chroniques et traumatismes.

D.A.Reynolds (January 1995). Speaker identification and verification using gaussian mixture speaker models. *Speech Comm*, 17:91–108.

D.Istrate, E.Castelli, M.Vacher, L.Besacier, and J.F.Serignat (April 2006a). Information extraction from sound for medical telemonitoring. *Transactions on Information Technology in Biomedicine*, 10:264–274.

D.Istrate, M.Vacher, and F.Serignat, J. (Aug 30-Sept3, 2006b). Generic implementation of a distress sound extraction system for elder care. In *28th IEEE EMBS Annual International Conference,New York City, pp.3309-3312*. IEEE.

D.Vaufreydaz, J.Rouillard, and M.Akbar (December 1999). Internet documents: a rich source for spoken language modelling. *Workshop ASRU'99, Keystone-Colorado*, pages 277–281.

D.Well, J.Barry, W.Grice, M.Fourcin, and A.Gibbon (2004). Sam esprit project 2589-multilingual speech input/output assessmen,methodology and standardization. In *Final report. Technical Report SAM-UCL-G004, University CollegeLondon*.

F.Halberg (1969). Chronobiology. In *Ann Rev Physiol, vol.31,pp.675-725*.

F.Steenkeste, H.Bocquet, M.Chan, and B.Vellas (December 1999). Remote monitoring system for elders in a geriatric hospital. In *Promoting Independence and quality of life for older persons:an international conference on aging Arlington*.

G.L.Bellego, N.Noury, G.Virone, M.Mousseau, and J.Demongeot (January 2006). Measurement and model of the activity of a patient in his hospital suite. *TITB*, 10:92–99.

G.Schwarz (1978). Estimating the dimension of a model. *Annals of Statistics*, 6:461–464.

J.L.Baldinger, J.Boudy, B.Dorizzi, J.P.Levrey, R.Andreao, C.Perpre, F.Devault, F.Rocaries, and A.Lacombe, C. (Juillet 2004). Tele-surveillance system for patient at home: The medeville system. In *Congrs ICCHP 2004,Paris*.

J.L.Gauvain, L.F.Lamel, and M.Eskenazi (1990). Design considerations and text selection for bref, a large french read-speech corpus. In *ICSLP '90, pp. 1097-1100*.

M.Akbar and J.Caelen (1998). Parole et traduction automatique : le module de reconnaissance raphael. In *COLING-ACL'98, Montral, Quebec, vol.2, p. 36-40.*

S.Banerjee, F.Steenkeste, P.Couturier, M.Debray, and A.Franco (Septembre 2003). Telesurveillance of elderly patients by use of passive infra-red sensors in a smart room. In *Telemed Telecare*.

STANDING JUMP LOFT TIME MEASUREMENT
An Acceleration based Method

Susana Palma, Hugo Silva, Hugo Gamboa
Plux – Biosensor Engineering, Lisbon, Portugal
spalma@plux.info, hsilva@iplux.info; hgamboa@plux.info

Pedro Mil-Homens
Human Kinetics Faculty, Lisbon, Portugal
pmil@fmh.utl.pt

Keywords: Biomechanics, jump analysis, accelerometer, force platform, signal processing.

Abstract: This paper describes two methods for the measurement of loft time in vertical jumps using signals from an acceleration sensor. The vertical jump accelerometer characteristic curve is presented and notable regions corresponding to key stages of the kinetic activity are identified. Using the accelerometer signals along three dimensions two different algorithms were devised to compute the loft time. These algorithms are based on the morphology of the signal. The first uses the the maximum value of the curve during the landing stage; the second uses the time interval between minimum and maximum values of the acceleration during the flight and landing stages, respectively. To validate these algorithms, a standard algorithm to compute the loft time from force platform signals was employed and these values taken as ground truth. Performance assessment was performed by computing the relative errors between the loft time determined from the force signal and the values obtained with each of the proposed approaches. Preliminary results for a set of 60 jumps let to relative errors of 7.0% for the first method and 2.9% for the second method.

1 INTRODUCTION

Vertical jumps are part of a variety of sports. In athletic field vertical jump measurements are used both to optimize and measure the performance of various types of movements.

Performance of standing vertical jumps can be accessed by measuring the time the athlete is in the air – jump loft or flight time (Linthorne N. P., 2001). The typical approach for measuring the loft time uses force platform signals. With this approach the jump must be performed while standing on the force platform, that collects vertical force data. Force-time curves contain kinetic and temporal information that can be used to determine parameters that objectively measure the performance of athletic movements (Dowling, 1993). These platforms are rectangular metal plates provided with force sensors and connected by cabling to a data acquisition system and computer. Due to their weight (ranging from about 11 kg to 57 kg) and dimensions (usually between 0.4 m × 0.6 m and 1.2 m × 1.2 m) (amtiweb) the platforms are usually used only in laboratory work, restrained the outside work by the portability issues.

Acceleration data can be used to study the characteristics of human movement (Hassan, M. R., 2006) and assess parameters that identify one's state of physical activity. In jumping studies, acceleration signals are also an important source of information.

In this paper we present two different algorithms for determining vertical jumps loft times using a three axial accelerometer. In this case, the portability issues are lessened because the accelerometer and the acquisition system employed are light-weighted wireless devices.

The two algorithms were applied to a set of 60 vertical jumps and validated with a standard algorithm for computation of loft time from force platform signals.

Like on the vertical force curve, six interest regions can be identified on the acceleration-time curve: rest, preparation, take-off, flight, landing. and recovery. Following the last stage a rest period can also be present. Figure 1 shows the vertical force

and acceleration signals acquired during a vertical squat jump.

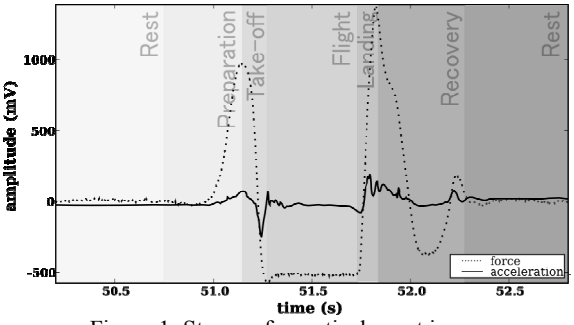

Figure 1: Stages of a vertical squat jump.

Some key points can be identified on the acceleration signal that are characteristic of the different stages of the jump and that are repeated as a pattern when a series of jumps is acquired. The biggest oscillations of the signal are noticed at the beginning of the flight stage and the landing stage - when the jumper leaves the ground and when his feet first contact the ground after the flight, respectively. A recovery phase follows the landing. During this period of time the acceleration oscillates and converges to its rest value which is reached when the jumper finishes the jump. The fact that the flight stage is clearly demarcated on the force curve is usually used to compute the duration of the flight – loft time. As we can see in Figure 1, the acceleration curve has also characteristic features that can be related with the loft time. Two of these features were used in this work to estimate the duration of the flight stage.

2 MATERIALS

The experimental set-up consisted of a bioPlux8 wireless electrophysiological data acquisition system (Silva, H., 2005, plux.info) to which we connected a xyzPlux triaxial accelerometer and a force platform (AMTI- LG 6-4-2000). With this apparatus force and acceleration (along three dimensions) were synchronously recorded during the vertical standing jumps.

The accelerometer was placed at the jumper's low back on the skin surface (Figure 2). The force platform signal was used for result comparison.

Figure 2: Placement of the accelerometer at the jumper's low back skin.

3 METHODS

The methodology for determining the flight time was based on the morphological analysis of the acceleration curves of a set of 60 jumps.

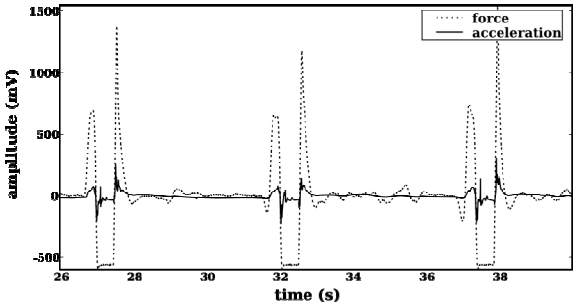

Figure 3: Acceleration and force curves of a series of 3 vertical jumps.

By comparing the acceleration curve of a set of jumps with the respective vertical force curve (Figure 3) we observe that some of the acceleration curve characteristic features seem to be related with the duration of the flight stage, namely at the flight and landing stages. Using notable points of these stages we devised two different algorithms to compute the loft time. The average acceleration curve was determined from the acceleration signals of the three dimensions and low passed using a moving average filter using a window of 250 points (Proakis J. G.,1995). Each of the algorithms uses different measurements of time and amplitude taken from this signal.

The first algorithm uses the landing stage curve amplitude (Figure 4). This stage is characterized by

sharp variations of the acceleration signal due to the vibration of the accelerometer when the feet first contact the force platform on the landing. The low-passed signal obtained from the smoothing still preserves this impact peak whose amplitude (v_{a1}) was measured and used as a predictor variable for the loft time.

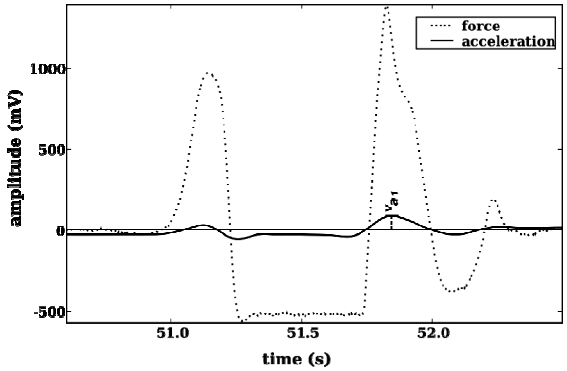

Figure 4: Jump parameter used on the first algorithm.

The second algorithm determines the time interval between the minimum of the smoothed signal on the flight stage and the impact peak. With this algorithm, a direct measure of the loft time is obtained (Figure 5).

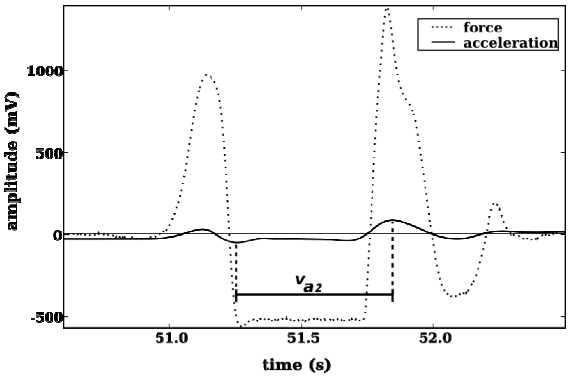

Figure 5: Jump parameter used on the second algorithm.

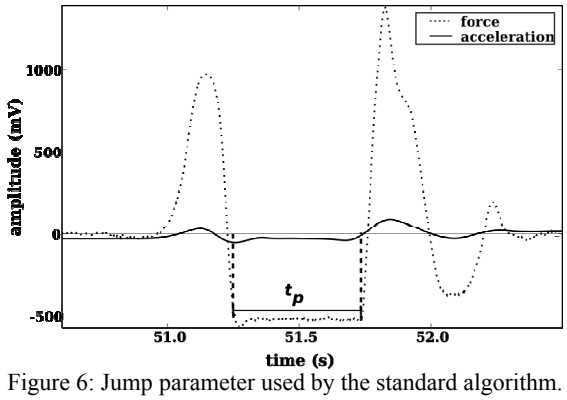

Figure 6: Jump parameter used by the standard algorithm.

For result comparison purposes, we determined the jump loft time of the 60 jumps from the force platform signal and took these values as ground truth. A standard algorithm was employed that computes the time during which the jumper is not touching the force platform - the time interval between the take-off and landing instants - where the force signal has a negative plateau (Figure 6).

4 RESULTS

The two independent variables measured on the acceleration signal (v_{ai}) were plotted against the loft time determined from the force platform signal (t_p). The scattergrams of these two variables are shown in Figure 7.

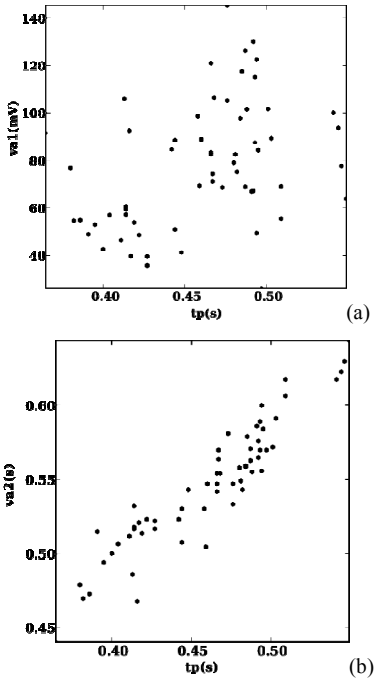

Figure 7: Scattergrams of the loft time measured with the standard algorithm versus (a) the variable measured with algorithm 1 and (b) the variable measured with algorithm 2.

A high correlation between the loft time measured from the force platform signal and the time interval measured from the acceleration curve (v_{a2}) can be seen is Figure 7b. This is a much better predictor of the flight time than the amplitude of the landing stage impact peak (r=0.382 and r=0.933 respectively). The regression equations for both variables are given by (1) and (2):

$$t_{p1} = 6{,}406 \times 10^{-4} v_{a1} + 4{,}102 \times 10^{-1} \text{ (s)} \quad (1)$$

$$t_{p2} = 0{,}967 v_{a2} - 0{,}068 \text{ (s)} \quad (2)$$

Using these equations we can obtain estimates of the loft time (t_{pi}) from the variables measured from the accelerometer signal (v_{ai}).

The loft time relative error associated with each of the algorithms *i* was determined for each jump *j* ($\delta_{\varepsilon ij}$), taking as "real" loft times the values measured from the force platform signal(t_{pj}).

$$\delta_{\varepsilon_{ij}} = \frac{\left(t_{p_j} - t_{p_{ij}}\right)}{t_{p_j}}, i = 1,2; j = 1,\ldots,60 \quad (3)$$

The accuracy of the algorithms was assessed by determining the corresponding average loft time relative errors:

$$\overline{\delta_{\varepsilon i}} = \frac{\sum \delta_{\varepsilon ij}}{n}, i = 1,2 \; j = 1,\ldots,60 \quad (4)$$

The results led to relative errors of 7,0% for the first algorithm and 2,9% for the second algorithm Taking as reference the mean loft time determined for the set of 60 jumps with the regression equations (1) and (2) these relative errors correspond to 32 ms and 13 ms, respectively.

Both algorithms are also affected by a common base error of 0.1% which is characteristic of the acquisition unit and inversely proportional to its sampling rate.

Usually, when the force platform is used to determine the loft time an associated error of 0,5% is introduced because the algorithm is susceptible of the parameters chosen by the user as the initial and final points of the flight stage. In contrast, the algorithms we propose are automatic.

5 CONCLUSIONS

The time interval between the minimum acceleration value of the flying stage and the maximum acceleration value of the landing stage is the best of the two devised measures, showing a good correlation with the real loft times (r=0.933 and δ_{ε}.=2,9%).

Although associated with errors, these preliminary results indicate that these algorithms are good alternative methods for the computation of loft time, taking advantage of the use of an accelerometer instead of a force platform, which is more expensive and less portable.

In addition to the flight time other parameters used to assess the performance of the jump can be found on the acceleration signal, such as the height of the jump. Furthermore, information on the dynamic behaviour of the jumper, namely during the flight stage can also be obtained from the acceleration signal, which is impossible to study with only the vertical force signal.

In the future, we plan to study the load distribution between inferior members during the take-off and landing stages by combining acceleration and force analysis and study the on-flight behaviour of the jumper.

REFERENCES

Dowling J., Vamos, L., 1993, J., *Identification of Kinetic and Temporal Factors Related to Vertical Jump Performance,* Applied Biomechanics, 9.

Linthorne, N. P., 2001, *Analysis of standing vertical jumps using a force platform,* Am. Journal of Phys., 69 (11).

Hassan R., Begg R. K., Khandoker A. H., Stokes R., 2006, *Automated Recognition of Human Movement in Stress Situations,* Proceedings of the 2nd Internationsl Workshop on Biosignal Procesing and Classification – BPC 2006, INSTICC Press.

Silva H., Gamboa H., Viegas V., Fred A., 2005, *Wireless Physiologic Data Acquisition Platform., 2005*. Proceedings of the 5th Conference on Telecomunications Confele.

http://www.plux.info

http://www.amtiweb.com/bio/force_platforms.htm

Proakis J. G., Manolakis D., 1995, *Digital Signal Processing: Principles, Algorithms and Applications,* Pearson US Import & PHIPEs, 3rd International Edition.

BIOSIGNAL ACQUISITION DEVICE
A Novel Topology for Wearable Signal Acquisition Devices

Luca Maggi, Luca Piccini, Sergio Parini, Giuseppe Andreoni
Dipartimento di Bioingegneria of Politecnico di Milano - Milan, Italy
luca.maggi@polimi.it, luca.piccini@polimi.it, sergio.parini@polimi.it, giuseppe.andreoni@polimi.it

Guido Panfili
SXT – Sistemi per telemedicina srl. – Lecco, Italy
g.panfili@sxt-telemed.it

Keywords: Wearable device, Brain Computer Interface, Amplifier, Signal Conditioning, Offset Recovery, Low Voltage Amplifier, Band Pass Filtering, ECG amplifier, EEG amplifier.

Abstract: The here presented work illustrates a novel circuit topology for the conditioning of biomedical signals. The system is composed of an amplification chain and relies on a double feedback path which assures the stability of the system, regardless of the amplification block gain and the order of the low-pass filter settings. During the normal operation, the offset recovery circuit has a linear transfer function, when it detects a saturation of the amplifier, it automatically switches to the fast recovery mode and restores the baseline in few milliseconds. The proposed configuration has been developed in order to make wearable biosignal acquisition devices more robust, simpler and smaller. Thanks to the used AC coupling method, very low high-pass cut-off frequencies, can be achieved even using small valued passive components with advantages in terms of circuit bulkiness. The noise rejection filter between the pre-amplification and the amplification stages eliminates the out-of-band noise before the amplification reducing the possibility of having clipping noise and minimizing the dynamic power consumption. The presented topology is currently used in a prototypal EEG acquisition device in a Brain Computer Interface (BCI) system, and in a commercial polygraph which will be soon certificated for clinical use.

1 INTRODUCTION

Wearable systems ought to be totally unobtrusive devices that allow physicians to overcome the limitations of standard ambulatory technology, aiming at providing a response to the need for monitoring individuals over weeks or even months without or limiting their usual behaviour. Such a systems typically rely on wireless, miniature sensors embedded in patches, bandages, or in items that can be worn, such as a ring or a shirt. They take advantage of hand-held units to temporarily store physiological data, which can be uploaded periodically to a database server through a wireless LAN or different gateways that allow Internet connection. The data sets recorded using these systems are then processed to detect events able to indicate a possible worsening of the patient's clinical situation or providing information explored to assess the impact of clinical interventions (Park, 2003).

Wearable devices are usually battery powered: low voltage supply and low power consumption are mandatory features for this kind of devices, in order to provide a good battery life to dimension ratio. In the last 10 years many garments with embedded sensors have been developed: the intrinsic characteristics of such electrodes and the possible instability of the contact make the design of wearable acquisition devices more difficult (Webster, 1991). The main aspects we have to take into account in the design of a wearable surface biopotential amplifier (e.g. Electrocardiogram-ECG, Electroencephalogram–EEG and Electromiogram-EMG) are:

- Dynamic reserve;
- Max offset rejection;
- Fast recovery from artefacts.

Although the operational amplifiers production technology has developed several low power and low cost devices, the development of dedicated

topologies is still necessary in order to maximize the overall circuit performance.

2 METHODS

2.1 Background

Figure 1 shows a typical, state of the art biosignal detection circuit which is composed of a set of independent stages connected in a chain. At the beginning there is a pre-filtering stage, the pre-amplification stage which is followed by the offset rejection circuit and by an amplification and filtering circuit.

This kind of solution is simple and effective when the wide power supply range provides a high dynamic reserve (avoiding clipping problems) and when the mechanical specifications allow the use of high capacity capacitor or the specific application doesn't require very low frequency high pass filter. It is worth to underline that the maximum tolerable offset is given by the following equation:

$$V_{Off}^{MAX} \cong \frac{1}{2} * \frac{(V_{\sup}^{+} - V_{\sup}^{-})}{G_{preamp}} \tag{1}$$

Where V_{sup} are the value of the supply rails and G_{preamp} is the gain of the preamplification stage.

It is worth noting that in case of a change in the input signal that causes the amplifier saturation, the output of the system will remain latched for a time which depends on the signal amplitude; it is possible to overcome this limitation by increasing the system complexity and inserting a baseline reset circuit which is activated by the saturation of the system itself.

2.2 General Description

The proposed system is composed of a differential pre-amplification stage P(s): usually realized using an Instrumentation Amplifier (INA). The F(s) block is a unity gain inverting filter (low-pass or low-pass plus notch filter) of any order. A(s) is an amplification stage, while I(s) is an offset compensation network. In the proposed version it is a non-linear circuit which acts as an attenuated inverting integrator when the Vin is inside the linear region and as an amplified inverting integrator when the signal is over threshold whose behaviour can be expressed as follow:

$$I = \begin{cases} -\frac{1}{a}\frac{1}{sRC} & if \quad V_{\sup}^{-} + Th < V_{in} < V_{\sup}^{+} - Th \\ -k\frac{1}{sRC} & otherwise \end{cases} \tag{2}$$

where Th is threshold value which identifies a saturated state, 'a' is an attenuation factor and 'k' the amplification factor.

The small signal transfer function and the G_{Loop} of the system are represented by the following equation:

$$TF(s) = P(s) \cdot \frac{F(s)A(s)}{1 - I(s)A(s)[F(s) - 1]} \tag{3}$$
$$G_{LOOP} = A(s)I(s)[1 - F(s)]$$

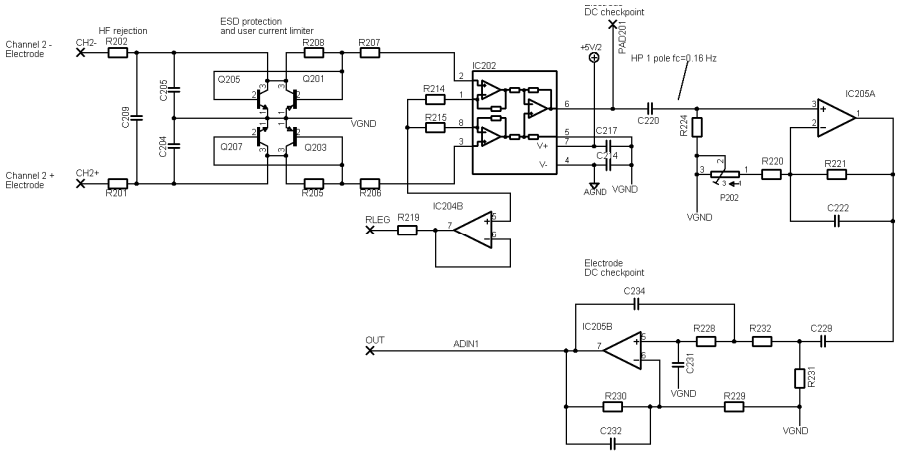

Figure 1: The amplification chain proposed by the OpenEEG project.

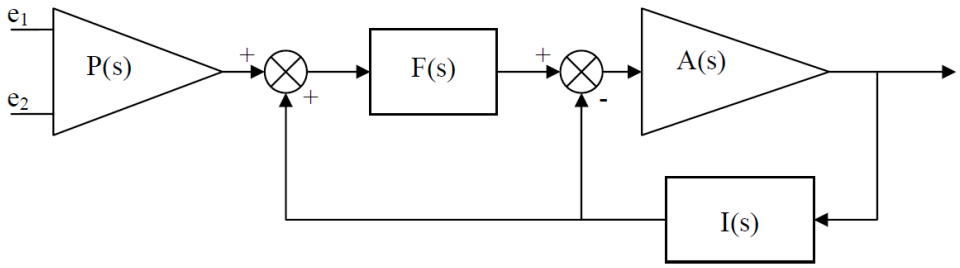

Figure 2: Block structure of the system.

considering that I(s) and F(s) are inverting the equation can be expressed as follows:

$$TF(s) = P(s) \cdot \frac{F(s)A(s)}{1 - |I(s)| \cdot A(s) \cdot [|F(s)| + 1]} \qquad (4)$$
$$G_{LOOP} = -|A(s)| \cdot I(s) \cdot [|F(s)| + 1]$$

The transfer function is a band-pass amplifier with a single pole high-pass and a low-pass whose shape depends on F(s). Figure 3 shows the bode diagram of a system with the following characteristics:

- F(s): 2nd order low pass at 75Hz;
- A(s): amplifier gain 100 V/V;
- P(s): pre-amplifier gain 5V/V;
- I(s): integrator 1/100 * 1/s.

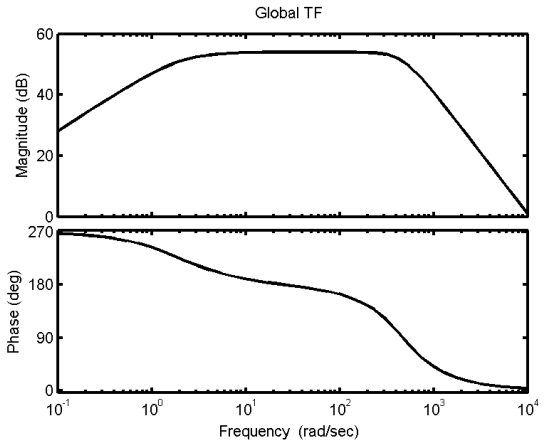

Figure 3: Frequency response of a sistem with 500V/V gain and a 2nd order low pass 75Hz filter.

2.3 Offset Compensation Issues

On the basis of the final output, the offset compensation value is fed both directly to the preamplifier P(s) reference pin, and by modifying polarization of the amplifier A(s). The proposed structure introduces a systemic offset compensation method which ensures that, thanks to the double feedback path, even when the pre-amplification output is close to the power supply rail, the following stages work inside the linear region this property doubles the maximum tolerable offset:

$$V_{Off}^{MAX} \cong \frac{(V_{sup}^{+} - V_{sup}^{-})}{G_{pream}} \qquad (5)$$

Thanks to this improvement it is possible to increase the gain of the pre-amplification stage taking major advantages of the qualities of the INA in terms of CMRR a noise figure.

As proposed in our previous work, the AC-coupling of the amplifier using a feedback integrator allows the tuning of the high-pass pole frequency just by varying the open loop gain of the system (Maggi, 2004). When setting the parameters for biosignals acquisition, it is useful to insert an attenuation factor in the I(s) block in order to compensate the amplifier gain: keeping the G_{loop} below the unity gain the high pass pole is moved to the lower frequencies.

The I(s) automatically identifies a saturation of the amplifier using a threshold method: if the value is outside a predefined interval, the attenuated integrator is switched into an amplified integrator that quickly brings the system output inside the linear interval.

The *k* value defines the delay of the offset recovery of the system: for example we can have a 0.05Hz high pass pole during the linear phase and switch it to a 100Hz one during the offset recovery phase, achieving a baseline recovery in about 10ms.

2.4 Stability of the Loop

During the normal operation the G_{loop} is usually kept low using the attenuation net of I(s) in order to achieve the desired high-pass frequency; when the

saturation occurs the I(s) is switched to a high gain configuration: in this section the stability of this configuration will be discussed both by considering the Bode Stability Criterion and the root-locus method.

2.4.1 Bode Stability Criterion

Provided that A(s) have a sufficient bandwidth to be considered like an ideal amplifier and that F(s) and I(s) are stable, the poles in F(s) and I(s) are the possible instability causes of the system. Considering the open-loop transfer function, the I(s) provides a single pole at low frequencies, while the F(s) put a variable number of poles at the higher bandwidth limit. Thanks to the second feedback path the poles of F(s) are compensated by the same number of zeroes. The figure 4 shows the Bode diagram of the original F(s) and the compensated one.

The newly created zeros must be very close to the F(s) poles in order to allow a difference between the DC gain and the high frequency one of just 6dB. The nearness of poles and zeroes makes the phase plot very flat: for any complexity of the filter the plot is between +90 and +270 degrees.

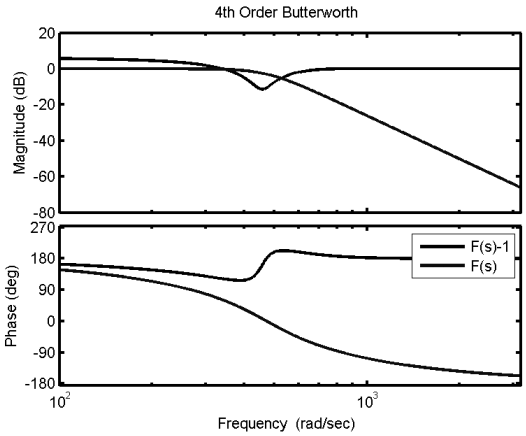

Figure 4: Bode plot of the compensate filter against the original one.

Figure 5 shows the phase diagram of the resulting G_{loop}, including the pole introduced by the integration process, it is possible to notice that it never cross the instability region.

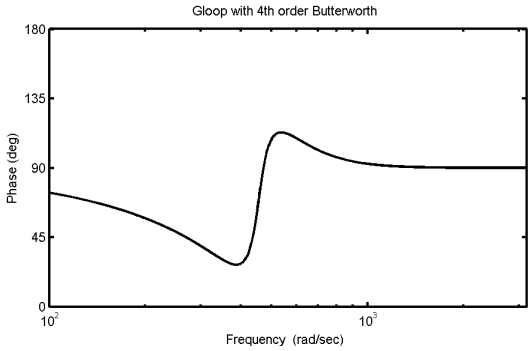

Figure 5: Phase diagram of the resulting Gloop.

2.4.2 Root Locus Study

The root locus (figure 6 and 7) show that the all the resulting closed loop poles are in the left semi-plane even with a 9th order low pass filter. For the higher open loop gains the phase margin can be less than 45 degrees, but during the nonlinear phase the overshoot can make the settling faster.

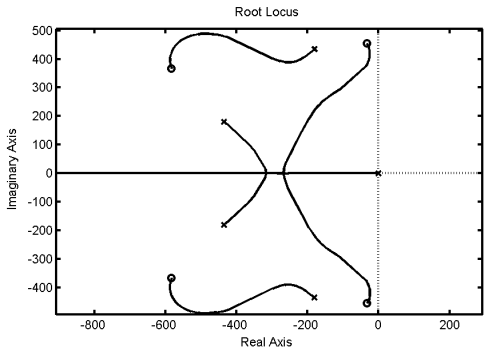

Figure 6: Root locus of a 4th order system.

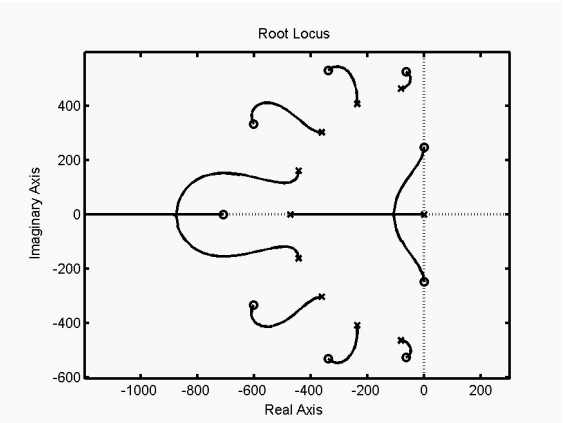

Figure 7: Root a 9th order filter system.

3 RESULTS

The configuration has been adopted both in a commercial wearable polygraph, in order to acquire the ECG signal and on a EEG acquisition prototype devoted to Brain Computer Interface applications. Figure 8 shows the proposed implementation for the EEG acquisition device. The system is 3,3V single supply powered using a li-ion battery and a low-dropout linear voltage regulator. The preamplification stage has a gain of 100V/V and P(s) is realized using a INA118 (Texas Instruments). The other four operational amplifiers are contained in a single integrated circuit (TLC2254, Texas Instruments).

The F(s) is an inverting double pole low pass filter, and A(s) is an amplification chain. The I(s) is composed by and attenuation network (R30 and R31), an inverting integrator (IC2B, C1 and R12) and the nonlinear activation network (K2, H2, R22, R23, R25, R27, R26).

The R27 and R26 network are used in order to set the intervention threshold of the offset recovery circuit: when the V_{be} of K2 and H2 are kept below 0,7 Volt the transistor are turned off. The Th parameter is defined also follows:

$$Th = 0{,}7V \cdot \frac{R27 + R26}{R27} \qquad (6)$$

K2 is switched on when the amplifier output voltage reaches the upper saturation limit, while H2 is switched on in case of lower saturation. When one of the transistor is turned on, it injects a current into the inverting integrator causing the fast offset recovery. R22, R23, R25 are necessary in order to limit the transistor current and avoid instabilities related to 2nd order effects of the components. The final amplification stage is optional an provides a last anti aliasing filtering.

The system circuit has been successfully used in a brain computer interface application (Piccini, 2005 and Maggi, 2006) and has an offset recovery time of less than 10ms.

4 DISCUSSION

The proposed architecture is a smart and cost effective solution to the problems related to the acquisition of biosignal in difficult acquisition situations based on an analog design; thanks to the evolution of modern digital devices, it is possible to adopt other method in order to achieve similar results.

The strength of the proposed topology is that a simple local solution doesn't require a full systemic redesign and support development of modular multiparametric wearable devices.

The discussion doesn't take into account second order effects related the components physical limitations: even if the architecture is robust and the frequency range of biosignals is reduced, the design of an amplifier based on the proposed topology should be approached with care.

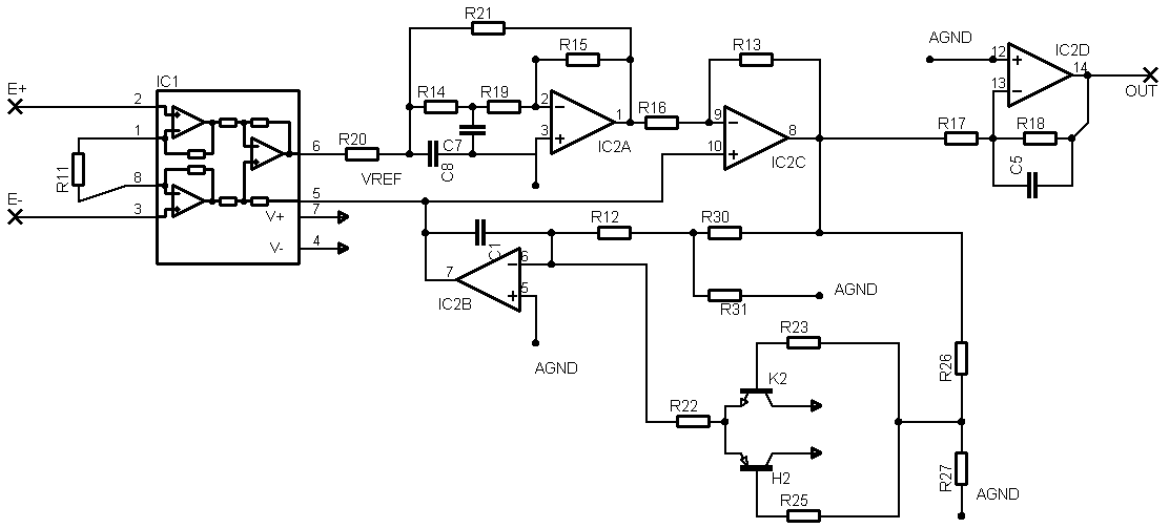

Figure 8: Schematic of the EEG amplification circuit.

5 CONCLUSIONS

The analysis proposed in this paper shows an interesting approach for providing a cost effective solution for AC coupled, low power amplifiers. Although born in a biomedical research laboratory, it faces problems related to a wide range of different applications. Also for this reason, this generic topology has been patented in Italy, and successfully revised by the European Patent Office for the PCT extension.

ACKNOWLEDGEMENTS

This work has been partially supported by ST Microelectronics and IIT Istituto Italiano di Tecnologia.

REFERENCES

Park, S., Sundaresan, J., 2003. IEEE Engineering in medicine and biology magazine, *Enhancing the quality of life trhough wearable technology*

Webster J. G., 1991. Innov. Tech. Biol Med. 12, n°spécial 1, pp. 39-45, *Noise sources in surfaces electrodes*

L.Maggi, L. Piccini, S. Parini, F. Beverina, S. Silvoni, G. Andreoni, 2004. Biomedizinsche Technik, v.49 pp.69-70, "*A portable electroencephalogram acquisition system dedicated to the brain computer interfaces*".

L.Piccini, L.Maggi, S.Parini, G.Andreoni, 2005. Shangai, Proceedings of EMBC. "*A Wearable Home BCI system: preliminary results with SSVEP protocol*".

L. Maggi, S. Parini, L.Piccini, G.Panfili and G.Andreoni, 2006. NY, Proceedings of EMBC. *"A four command BCI system based on the SSVEP protocol*.,

BIOSIG

Standardization and Quality Control in Biomedical Signal Processing using the BioSig Project

A. Schlögl, C. Vidaurre
Fraunhofer FIRST-IDA, Kekulestrasse 7, 12489, Berlin, Germany
alois.schloegl@first.fraunhofer.de, carmen.vidaurre@first.fraunhofer.de

Ernst Hofer, Thomas Wiener
Institute of Biophysics, Medical University of Graz, Harrachgasse 21, 8010, Graz, Austria
ernst.hofer@meduni-graz.at, thomas.wiener@meduni-graz.at

Clemens Brunner, Reinhold Scherer
Institute for Knowledge Discovery, University of Technology Graz, 8010, Graz, Austria
clemens.brunner@tugraz.at, reinhold.scherer@tugraz.at

Franco Chiarugi
Institute of Computer Science (ICS), Foundation for Research and Technology - Hellas (FORTH) P.O. Box 1385, Vassilika Vouton, GR 711 10 Heraklion, Crete, Greece
chiarugi@ics.forth.gr

Keywords: Standardization, Quality control, electroencephalogram, Brain Computer Interfaces, Free/libre open source software (FLOSS).

Abstract: Biomedical signal processing is an important but underestimated area of medical informatics. In order to overcome this limitation, the open source software library BioSig has been established. The tools can be used to compare the recordings of different equipment providers, it provides validated methods for artifact processing and supports over 40 different data formats (more than any other software in this area). BioSig provides reference implementations for biomedical signal processing questions and holds the top rank among all biomedical signal processing projects registered at SourceForge. Thus is provides standardization and quality control for the field of biomedical signal processing.

1 INTRODUCTION

Biomedical signal processing is an important area of medical informatics and is used in many subject area (neurology, psychiatry, cardiology, pulmology, cognitive neuroscience, psychology, biophysics, biomedical engineer etc) with many different applications. Unlike other areas of medical informatics (Imaging, labor diagnostics, patient information system etc.), biomedical signals are not well represented in health information systems.

A likely explanation is the fact that many different disciplines and many small groups do biomedical signal processing. The interaction between the various groups is not well organized; often the same well-known methods are implemented again and again, the wheel is re-invented again and again. In order to overcome this problem, the open source software project BioSig was founded with the aim to provide a software library for biomedical signal processing. Motivated by the successful development model of the Linux operating system, it was decided that the library should be also open source, everyone is invited to use and to contribute to BioSig, and the GNU General Purpose License (GPL) ensures that BioSig will stay open source.

Section 2, presents several subprojects that have been developed within BioSig. Section 3 provides some numbers about the success of BioSig, Sections 4 and 5 discuss open issues summarize the project.

2 METHOD

Software development and programming is an important aspect of biomedical signal processing. In order to address different needs, several programming languages are supported. The Matlab scripting language is widely used in biomedical signal processing and engineering. For this reason, the first part of BioSig has been implemented in Matlab language. Matlab is an proprietary software product from "The Mathworks Inc", short TMW, but there are also some open source alternatives available; Octave (http://www.octave.org) is probably the most widely known alternative. Special effort was undertaken to make the code also compatible to Octave. This part is now call "BioSig for Octave and Matlab", or short "BioSig4OctMat".

Moreover, C/C++ is a very flexible programming language and provides a very efficient (i.e. fast) software; although the software development takes more time. There is now a common C/C++ interface to access various data formats including the SCP-ECG standard (EN1064), the HL7aECG, GDF (Schlögl et al. 1999b, Schlögl, 2006b) and several other data formats.

Furthermore, projects for the languages Python (BioSig4Python) and Java (BioSig4Java) have been started.

2.1 Converter between SCP-ECG and HL7 aECG

SCP-ECG (Standard Communications Protocol for Computer-Assisted Electrocardiography) is a European standard (EN1064:2005) for interpretive resting ECG. This ECG Standard is the result of an EU supported project that European, American and Japanese Manufacturers and Users have jointly worked and agreed on (1989-1990). In 1993 it became a European ENV, later was positively balloted within AAMI (AAMI EC71), and finally became a European EN at the beginning of 2005.

In 2002 the FDA launched the need of having the full disclosure digital waveforms submitted for the support of clinical trials with a flexible XML schema and a rich set of annotations. The main

American manufacturers thus defined the so-called FDA XML Data Format Design Specification that was an FDA XML-based specification covering the design for the waveform data format as well as the relevant submission information. This specification of rising popularity, known also as Annotated ECG in XML, also became a part of HL7 V.3 currently balloted (HL7 aECG).

OpenECG is a world-wide network supporting interoperability in electrocardiography through the consistent implementation of standards. In 2007 it has about 850 members from more than 60 countries. The development of open source converters among ECG formats is supported and encouraged by OpenECG.

At the beginning of 2006 a international working group formed by people with different expertise was created by the OpenECG network, with the support of IEEE 1073 and CEN and the coordination of TU Graz and Biosig, for the development of an open source two way converter in C++ between the SCP-ECG and the HL7 aECG standards. In the conversion, GDF, the BioSig format was used as an intermediate form. ECG data sets available in the OpenECG portal (http://www.openecg.net) were used to test the converter in different environments included Linux and Cygwin.

Once the first version was available, there were some issues that remained open and most of them were related to an incomplete mapping between the two standards. This information was an important retrofit for the relevant Standard Developing Organizations and some actions in order to solve these open issues have already been done. In fact, a harmonization of the ECG lead standard terminology between the two standards has already been done leading to the creation of the SCP-ECG amendment (EN1064:2005+A1:2007) and a similar revision for the HL7 aECG standard.

The converter has been released as open source and is currently available in the Biosig Sourceforge site (http://biosig.sf.net/). Figure 1 shows SCP data that has been converted into the GDF v1 data format (Schlögl et al. 2007b).

2.2 BioSig for BCI Research

Brain computer interfacing is one topic closely related to EEG processing that needs of techniques capable to work under on-line conditions. Besides, efficient methods for artifact rejection and/or correction, online feature extraction techniques, classifiers, single trial analysis and performance measurements are important issues in this field.

A Brain Computer Interface (BCI) consists in general of 4 modules: EEG pre-processing, feature extraction, classification and feedback. Biosig provides useful tools for on-line artefact processing;

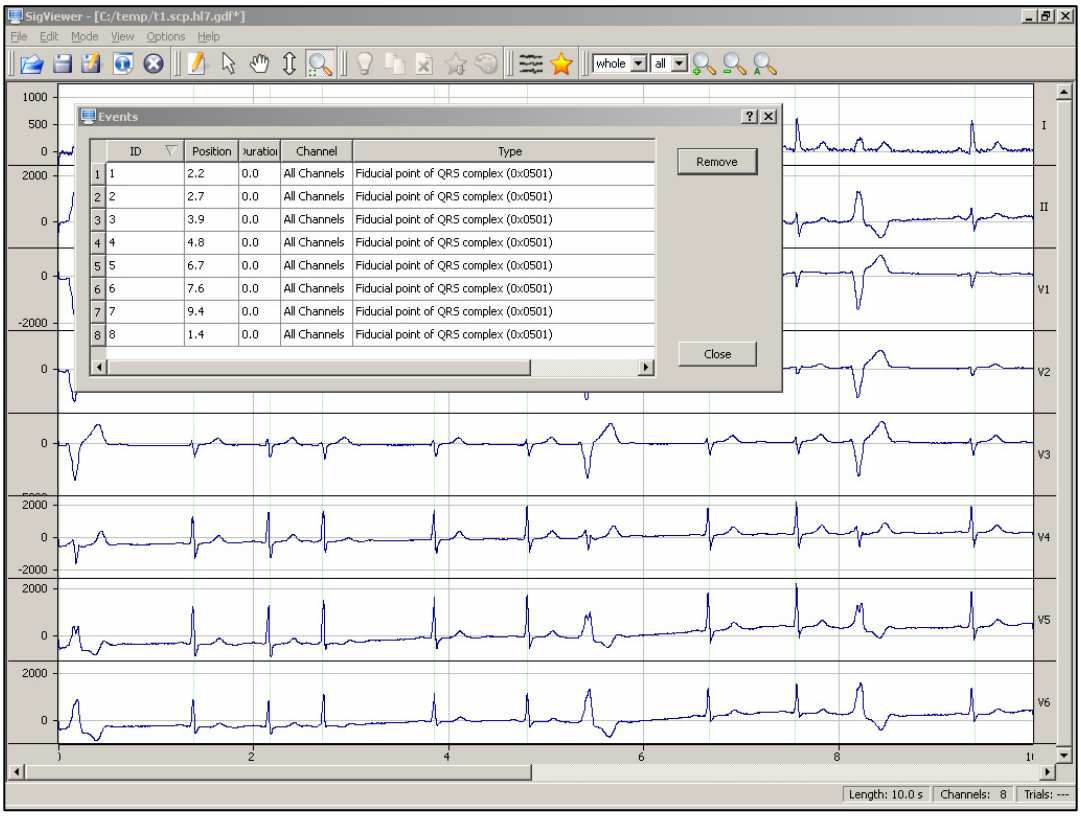

Figure 1: Screenshot of SigViewer showing 10s of 8-channel ECG data. The smaller "window" shows the editable event table. The data set was converted from the SCP (EN1064) to the GDF v1 (Schögl et al. 1999b) data format using BioSig4C++.

several on-line feature extractors are also available, such as adaptive autoregressive parameters or band power estimates. It also provides many classifiers (including but not limited to LDA, QDA/MDA, SVM, NBC, etc) and several single trial analysis methods to test the performance of systems/subjects. It can be used to provide initial conditions to all these modules before starting a BCI on-line session (see also for the section "rtsBCI below), in which the system is in general tuned for the subject. Also, it is especially useful for the analysis of experimental BCI data. BioSig was the reference tool for the development of on-line adaptive classifiers (which were tested in BCI experiments) (Vidaurre et al. 2006).

2.3 Artifact Processing and Quality Control

Biomedical signal recordings are often contaminated by various artifacts. BioSig provides several tools to address this issue. This include tools for (i) quality control and determining the saturation values of the recording systems are provided (Schlögl et al 1999a), (ii) a fully automated reduction methods of EOG artifacts in EEG recording (Schlögl et al 2007a), and (iii) inverse filtering for detecting muscle artifacts (Schlögl et al 2000).

2.4 Coupling Analyzing

In order to investigate the interaction and coupling between brain areas, various coupling measures like coherency, phase, partial coherence, partial directed coherence (PDC), directed transfer function (DTF) etc. can be used. As shown in Schlögl and Supp (2006), all these coupling measures can be derived from a multivariate autoregressive (MVAR) model. The MVAR estimator (Schlögl, 2006a) can be also applied to data with missing values, thus the various coupling measures can be obtained from data with missing values, too. BioSig supports also a non-parametric statistical analysis using a jackknife procedure (Efron, 1981) for estimating the confidence intervals of all the coupling measures.

2.5 QRS Detection and HRV Analysis

An important area of biomedical signal processing is analysing the electrocardiogram (ECG). BioSig contains several algorithms for QRS detection (Nygard et al, 1983, Afonso et al 1999), detecting extrasystoles and other irregular detections (Mateo and Lugano, 2003) and analyzing the heart rate variability (Taskforce, 1996). Furthermore, the efficient algorithm of Berger et al. (1986) for an equidistant sampling of the heart rate is implemented.

2.6 rtsBCI

The Graz-BCI open source software package rtsBCI provides a framework for the development and rapid prototyping of real-time BCI systems. The software is based on Matlab/Simulink (The Mathworks, Inc, Natick, MA, USA) running on Microsoft Windows (Microsoft Corporation, Redmond, WA, USA) and licensed under the GNU GPL. For hard real-time computing and the generation of stand-alone C code the Real-Time Windows Target (RTWT) and the Real-Time Workshop (RTW), respectively, are required. Both toolboxes are extensions of Simulink. Furthermore, BioSig for Octave and Matlab is needed for data format handling, and TCP/UDP/IP toolbox for network communication support. Additionally to these software requirements, a data acquisition device is indispensable.

After installation, all rtsBCI modules are listed in the Simulink Library Browser and can be used to design (model) the BCI system. Several Matlab functions and Simulink blocks for (i) data acquisition and conversion, (ii) storage, (iii) digital signal processing (e. g. band power feature estimation, Split-Radix discrete Fourier transform, adaptive autoregressive parameters (AAR) estimated with Kalman filtering, linear discriminant analysis, etc.), (iv) visualization (e. g. signal scope, presentation of cue information or feedback of a moving bar), (v) paradigm control (cue-based and self-paced operation mode) and (vi) network support (e. g. remote monitoring) are available.

Tunable parameters as well as other information relevant for the experiment (e.g. subject information, amplifier settings, electrode setup, paradigm timing) are stored in an individual configuration file (.INI file). Before a model is executed, the configuration is transferred to the model and stored altogether with the biosignals for further analysis. The division of model and parameters makes it very easy to deal with changes: For example, a new classifier requires only the replacement of the classification block. A new subject requires only the modification of the related data in the configuration file.

Modular architecture and rapid prototyping allow a fast extension and incorporation of new software as well as hardware components. This flexibility is a big advantage as is the fact that Matlab is very popular. The period of vocational adjustment is reduced, as well as the costs, because only a reduced number of toolboxes are required.

2.7 SigViewer

SigViewer is a powerful stand-alone viewing and scoring program for biosignals, originally designed to process electroencephalogram (EEG) signals. SigViewer has among its features the ability to load multi-channel signals such as EEG, ECG, EMG, and EOG recordings, and display these in various scales. At the moment, only GDF v1 (Schlögl et al. 1999b) is supported, but as a workaround, users can convert other data formats to GDF using the function "*save2gdf*" (available in BioSig4OctMat and BioSig4C++). Figure 1 shows a screenshot of SigViewer displaying ECG data.

The other major capability besides the viewing functions is the scoring of biosignals, which permits the user to make various annotations to the signals (e.g. mark segments as artifactious, mark specific events, like QRS-complexes, etc) and save this information into a file.

It is also possible to view basic information about a specific file (e.g. number of channels, sampling frequency, number of events, time of recording, and so on). In addition to graphically scoring the data, the event table is available as a list-based widget for viewing and deleting events and annotations (Figure 1).

SigViewer is written in C++ using the open-source platform-independent graphical user interface (GUI) toolkit Qt 4 (Trolltech®). SigViewer runs under many different operating systems such as Linux, Windows and Mac OS X – in other words, it is designed to be platform-independent (or more accurately cross platform). Moreover, it does not depend on any proprietary software, making it a truly free program. The source code does not have to be changed when compiling binaries for specific platforms, it is enough to take one and the same source tree and compile it on the target platform.

2.8 Analysis of Cardiac Near-Field (CNF) Signals

An ongoing research project is the investigation of the cardiac near-field (CNF) signal. The spatiotemporal electrical activation at the surface of heart tissue is assumed to propagate with a smooth elliptical wave front. Micro-obstacles like embedded connective tissue may affect the smoothness of the wave front which results in complex activation sequences at microscopic size scale. The investigation of these mechanisms by analysis of the local activation in microscopic dimensions is expected to gain deeper insight into structure-related arrhythmias. For this purpose electrophysiological in-vitro experiments have been carried out using autorhythmic or electrically stimulated heart tissue preparations from Rabbits or Guinea Pigs.

The gradient of electric potential at the cardiac surface, the Cardiac Near-Field (CNF), can be computed from four extra-cellular potentials $\Phi_1..\Phi_4$ recorded with ultra-densely placed electrodes (electrode spacing 50μm). Such a sensor with an appropriate data acquisition system (sampling rates of 100 kHz per channel) has been developed recently (Hofer et al. 2006). It has been shown that the multivariate signal $\mathbf{\Phi}= [\Phi_1, \Phi_2, \Phi_3, \Phi_4]^T$ can be used to determine local parameters of the propagating electrical activation, namely velocity and direction (Plank et al. 2000). Currently, research is aimed on developing robust procedures for the calculation of these parameters and the evaluation of their accuracy (Wiener et al. 2007). In practice, the two major problems are: First, the acquired signals are affected by inherent electrode noise and by stimulus artifacts. Second, in case of structural discontinuities in the underlying tissue, $\mathbf{\Phi}$ may be a composition of multiple local and distal electrical activation sequences. Therefore, the formation of the CNF in case of normal and complex activation sequences in the tissue has been extensively investigated in computer simulations (Plank et al. 2003).

The BioSig toolbox for Matlab is being used for off-line analysis of waveforms of $\mathbf{\Phi}$ obtained from experiments and computer simulations because it provides comprehensive procedures for time-frequency analysis of the multivariate stochastic process $\mathbf{\Phi}$. Moreover the implemented tools can deal with missing values due to the removal of stimulus artifacts. Developed signal processing procedures are being validated by applying them to noise-free waveforms $\mathbf{\Phi}$ obtained from computer simulations.

2.9 Miscellaneous

Many smaller algorithms are also included. Examples are the so-called “Paynter filter” (Bruce et al. 1977, Platt et al. 1998) to estimate the envelope of EMG power. There are also many EEG parameters like Hjorth parameters (Hjorth, 1975), Barlow parameters (Goncharova and Barlow, 1990), a global linear descriptor (Wackerman, 1999) and the brainrate parameter (Pop-Jordanova and Pop-Jordanov, 2005) supported. Furthermore, methods for multiple statistical tests for avoiding the problem of alpha inflation are supported (Hemmelmann et al. 2005), and many different plotting functions for EEG analysis, like the visualization of Coherence according to Nolte et al. (2004).

3 RESULTS

BioSig addresses all aspects of biomedical signal processing, starting with the support for over 40 different data formats, quality control and artifact processing, methods for signal processing and feature extraction classification of single trial EEG, and statistical tests including the multiple comparison problem. Currently, the main application areas are research on EEG-based Brain-Computer Interfaces, coupling analysis of EEG/ECoG/MEG, processing of EEG artifacts, conversion of different data formats.

BioSig provides reference implementations of many biomedical signal processing algorithms and for many application areas including, EEG, ECoG, MEG, ECG and HRV analysis, Brain Computer Interface research, analysing brain connectivity. The software algorithms can be copied, used, modified and distributed under the terms of the GNU GPL (http://www.gnu.org/copyleft/gpl.html). The open source *software library for biomedical signal processing BioSig* is available from http://biosig.sf.net.

An open source converter between ECG standardized ECG data formats SCP-ECG (EN1064) and HL7aECG and several other data formats is available. Future plans include the development of a common data format for all biomedical signals.

Table 1: Ranking of the Biosig project at SoureForge among various application areas. The 2nd column shows the ranking of BioSig and the total the number of projects for each application area.

Topic	**Ranking 2007-10-22 / number of projects**
SourceForge	456 / 160 049
Biosignals (keyword search: "EEG, ECG")	1 / 27
Medical Science applications	8 / 543
Human Machine Interfaces	2 / 612
Dataformats	20 / 2139

The BioSig software library is widely adopted. Currently, the download rate is far beyond 600 per month and increasing. As of Oct 2007, BioSig is the highest ranked project for biomedical signal processing (search term "EEG ECG") at SourceForge http://sourceforge.net, a platform that hosts over 160 000 open source projects. Within the last two years (Sep 2005 – Sep 2007), the monthly ranking fluctuated between 2906 (Jan 2007) and 380 (Aug 2007), the overall rank is within the top 2% of all hosted projects. Besides SourceForge, parts of BioSig have been incorporated in other projects (e.g. EEGLab http://www.sccn.ucsd.edu/eeglab/), which is not considered in the above statistics.

4 DISCUSSION

Although BioSig is routinely used in several application areas like BCI research, data conversion, coupling analysis, etc. there are several topics which are not or only suboptimally supported. Examples for the current limitations are the following.

(i) Two components (rtsBCI and SViewer) require proprietary software (Simulink and Matlab). It would be desirable to have a fully open source solution without this requirement. SViewer is going to be replaced by SigViewer, but it is still useful because SViewer supports more data formats. Nevertheless, many users do have Matlab anyway, therefore it is reasonable to distribute these tools.

(ii) The situation on the viewing and scoring software is not perfect. The SViewer requires the proprietary Matlab software and is relatively slow, SigViewer supports only very few data formats.

(iii) The conversion between different data formats is not always perfect, and can lose some information (demographic data, annotations, see also Schlögl et al. 2007b). For this reason, it is important to unify the various data formats for biomedical signal processing.

(iv) Support for many specialized application areas (like advanced ECG analysis, ...) depend on the contribution and evaluation of expert users. In order to maintain the growth of BioSig with the aim to become "the" software library for biomedical signal processing, participation of users and experts of the various areas of biomedical signal processing is crucial. We think of advanced ECG analysis (P- and T-wave detection, classification of arrhythmias), the source localization problem in EEG analysis, or analyzing the activity of spiking neurons.

5 CONCLUSIONS

The BioSig project contains many software tools for biomedical signal processing. Because BioSig provides an open source software library, there is no need to "re-invent the wheel", but the existing software algorithms can be used and improved. These algorithms provide reference implementations, and can be validated and improved by everyone. This is an efficient mechanism for standardization and quality control of software for biomedical signal processing.

The aim of BioSig providing *a* software library for biomedical signal processing has been already reached, BioSig is also the #1 project for biomedical signal processing on Sourceforge. The open question is not whether but how BioSig can help integrating biosignal analysis into the health information system.

ACKNOWLEDGEMENTS

This work was supported by the EU grant "BrainCom" (FP6-2004-Mobility-5 Grant No 024259) and the Austrian Science Fund FWF P-19993-N15.

REFERENCES

Afonso, V., Tompkins, W., Nguyen, T., Luo S. 1999. ECG beat detection using filter banks. *IEEE Trans. Biomed. Eng.* 46(2):192-202.

Berger R.D., Akselrod S., Gordon D., Cohen R.J. 1986. An efficient algorithm for spectral analysis of heart rate variability. IEEE Trans Biomed Eng. 33(9):900-4.

Bruce, E. N., M. D. Goldman, and J. Mead. A digital computer technique for analyzing respiratory muscle EMGs. J. Appl. Physiol. 43: 551-556, 1977

Efron, B. 1981. "Nonparametric estimates of standard error: The jackknife, the bootstrap and other methods", *Biometrika*, 68, 589-599.

EN1064 2005. Health informatics. Standard communication protocol. Computer-assisted electrocardiography

Goncharova, I.I. and Barlow, J.S. 1990. Changes in EEG mean frequency and spectral purity during spontaneous alpha blocking. *Electroencephalogr Clin Neurophysiol.* 76(3):197-204.

Hemmelmann C, Horn M, Suesse T, Vollandt R, Weiss S. 2005. New concepts of multiple tests and their use for evaluating high-dimensional EEG data. *J Neurosci Methods.* 142(2):209-17.

Hjorth, B. 1975. Time Domain Descriptors and their Relation to particulare Model for Generation of EEG activity. in G. Dolce, H. Kunkel: *CEAN Computerized EEG Analysis*, Gustav Fischer, p.3-8.

Hofer, E., Keplinger, F., Thurner, T., Wiener, T., Sanchez-Quintana, D., Climent, V., Plank, G., 2006. A new floating sensor array to detect electric near fields of beating heart preparations. In *Biosens. Bioelectron.*, vol. 21, pp 2232-2239.

Mateo, J., Laguna, P. 2003. Analysis of Heart Rate Variability in Presence of Ectopic Beats Using the Heart Timing Signal. *IEEE Transactions on biomedical engineering*, 50(3): 334-343.

Nolte G, Bai O, Wheaton L, Mari Z, Vorbach S, Hallett M. 2004. Identifying true brain interaction from EEG data using the imaginary part of coherency. *Clin Neurophysiol.*115(10):2292-307.

Nygards, M.-E. and Sörnmo, L. 1983. Delineation of the QRS complex using the envelope of the e.c.g.-*Med. & Biol. Eng. & Comput*., 21, 538-547.

Plank, G., Hofer, E., 2000. Model study of vector-loop morphology during electrical mapping of microscopic conduction in cardiac tissue. In *Ann. Biomed. Eng.*, vol. 28, pp 1244-1252.

Plank, G., Vigmond, E., Leon, L.J., Hofer, E., 2003. Cardiac near-field morphology during conduction around a microscopic obstacle – a computer simulation study. In *Ann. Biomed. Eng.*, vol. 31, pp 1206-1212.

Platt, R.S., Hajduk, E.A., Hulliger, M., Easton,P.A. 1998. A modified Bessel filter for amplitude demodulation of respiratory electromyograms. *J. Appl. Physiol.* 84(1): 378-388.

Pop-Jordanova, N. and Jordan Pop-Jordanov J. 2005. Spectrum-weighted EEG frequency ("Brainrate") as a quantitative indicator of arousal Contributions, Sec. Biol. Med. Sci., MASA, XXVI, 2: 35 - 42

Schlögl, A., Kemp, B., Penzel, T., Kunz, D., Himanen, S.-L., Värri, A., Dorffner, G., Pfurtscheller, G., 1999a. Quality Control of polysomnographic Sleep Data by Histogram and Entropy Analysis. *Clin. Neurophysiol.* 110(12): 2165 - 2170.

Schlögl, A., Filz, O., Ramoser, H., Pfurtscheller, G. 1999b. GDF version 1 - A general dataformat for biosignals, available at: http://www.dpmi.tugraz.at/schloegl/matlab/eeg/gdf4/TR_GDF.pdf

Schlögl, A. 2000. *The electroencephalogram and the adaptive autoregressive model: theory and applications.* Shaker Verlag, Aachen, Germany.

Schlögl, A. 2006a. Comparison of Multivariate Autoregressive Estimators. *Signal processing.* 86(9): 2426-9.

Schlögl, A. 2006b. GDF version 2 - A general dataformat for biosignals. http://arxiv.org/abs/cs.DB/0608052

Schlögl, A. and Supp, G. 2006. Analyzing event-related EEG data with multivariate autoregressive parameters. (Eds.) C. Neuper and W. Klimesch, *Event-related Dynamics of Brain Oscillations. Analysis of dynamics of brain oscillations: methodological advances.* Progress in Brain Research 159: 135 – 147.

Schlögl, A., Keinrath, C., Zimmermann, D., Scherer, R., Leeb, R., Pfurtscheller, G. 2007a. A fully automated correction method of EOG artifacts in EEG recordings. *Clin. Neurophys.* 118(1):98-104.

Schlögl, A., Chiarugi, F., Cervesato, E Apostolopoulos, E., Chronaki, C.E.. 2007b. Two-Way Converter between the HL7 aECG and SCP-ECG Data Formats Using BioSig.
Conference on Computers In Cardiology,

Taskforce Heart Rate Variability: Standards of Measurement, physilogical interpretation and clinical use. Taskforce of the European Society for Cardiology and the North American Society of Pacing and Electrophysiology. *European Heart Journal* (1996) 17, 354-381.

Vidaurre, C., Schlögl, A.,Cabeza, R., Scherer, R. Pfurtscheller, G. 2006. A fully on-line adaptive BCI, IEEE Trans. Biomed. Eng., 53(8): 1214–1219.

Wackermann, J. 1999. Towards a quantitative characterization of functional states of the brain: from the non-linear methodology to the global linear descriptor. *International Journal of Psychophysiology*, 34: 65-80.

Wiener, T., Thurner, T., Prassl, A.J., Plank, G., Hofer, E., 2007. Accuracy of local conduction velocity determination from non-fractionated cardiac activation signals. In *EMBC'07, 29th Annual International Conference of the IEEE Engineering in Medicine and Biology Society*.

DSP IMPLEMENTATION AND PERFORMANCES EVALUATION OF JPEG2000 WAVELET FILTERS

Ihsen Ben Hnia Gazzah, Chokri Souani and Kamel Besbes
Laboratoire Microélectronique et Instrumentation
Faculté des sciences de Monastir
gazzah.ihsen@yahoo.fr, chokri.souani@issatso.rnu.tn, kamel.besbes@fsm.rnu.tn

Keywords: Discrete wavelet transform, lifting scheme, filter banks, DSP.

Abstract: The lifting scheme wavelet Transform allows efficiency implementation improvement over filter banks model. In this paper, we present simulation results and DSP implementation results of Lifting scheme algorithm for 1D and 2D discrete wavelet transform (2D-DWT). The lossless and lossy wavelet filters 5/3 and 9/7, respectively, have been used to transform images. The transforms have been implemented in a float-point DSP chip and performances are evaluated. The DSP code was optimized at source code level and memory usage. The implemented code is optimized in different ways especially within memory usage.

1 INTRODUCTION

Since their introduction by Wim Sweldens in 1994 (Sweldens, 1996), the discrete lifting scheme (LS) wavelet transform has gained widely acceptance due to their ability to construct biorthogonal wavelets in the spatial domain independently of the Fourier transform (Daubechies et *al.*, 1998; Chendonga et *al.*, 2007; Delouille et *al.*, 2006). The lifting scheme was adopted as the base of the JPEG 2000 standard (Rabbani et *al.*, 2002). The image compression in the JPEG2000 standard is performed either by the 9/7 real values wavelet or by the 5/3 integer values wavelet.

The DWT has been implemented conventionally using the filter bank scheme (FBS). This solution implements filters with convolution technique. It requires both a large number of clock cycles and a large amount of storage memory. However, the lifting scheme requires less computations and less storage memory space. Recent studies tempted to compare between LS and FBS. In this context, Gnavi (Gnavi et *al.*, 2002) implemented both DWT methods and compared their performances for image coding task. He has found that the LS implementation run faster than the filter bank scheme. Special-purpose hardware is used to reduce the execution time of the DWT, Programmable processors, however, are preferable because they are more flexible. Furthermore, multimedia SIMD extensions (Shahbahrami et al., 2005) can be used to reduce the execution time of the DWT.

In this paper, we present simulation results of Lifting scheme algorithm using Matlab tool, and implementation results using a TMS320C6713 DSP processor. The code is optimized in order to reduce the execution time while performing the reconstruction quality. The lossless 5/3 and the lossy 9/7 lifting scheme transform were considered. The paper presents our contribution on the 2D-DWT-LS implementation into DSP processor. The paper is organized as follows: In section 2, a background of the lifting scheme is briefly explained, while an overview of our experimental results is given in section 3. Conclusions and future work are drawn in the end.

2 LIFTING SCHEME ALGORITHM

Lifting scheme decomposition consists on splitting the original signal into two subsets defined by the even and odd index signal samples, and then gradually a new wavelet coefficients set is built (Sweldens et *al.*, 1996) (figure 1). The decomposition is held in three steps:

- **Split:** This step is called "Lazy wavelet Transform (LWT)". It consists on decomposing the

original image S into two sub-images. The two sub-images are defined by the even ($Se_i=S_{2i}$) and the odd ($So_i=S_{2i+1}$) pixel image coefficients. The LWT is a simple function switching coefficients corresponding to their order (odd or even).

- **Primal Lifting step**: the original signal has even and odd index samples interspersed. If the signal has a local correlation structure, the even and odd samples will be highly correlated. In other words given one of the two sets, it should be possible to predict the other set with reasonable accuracy. The even set is always used to predict theo dd one which represents the wavelet coefficients (Daubechies et *al.*, 1998). H_i are the wavelet coefficients. So_i are the odd samples. P is the prediction polynom and Se_i are even samples (eq. 1)

$$H_i = So_i - P(Se_i) \quad (1)$$

- **Dual Lifting step**: The update operator U is applied to the wavelet coefficients computed H_i and then are addition with Se_i to compute L_i (eq. 2). L_i are the scaling coefficients.

$$L_i = Se_i + U(H_i) \quad (2)$$

3 EXPERIMENTATIONS AND RESULTS

In this section, we describe first the implementation of the DWT using lifting scheme into a DSP processor.

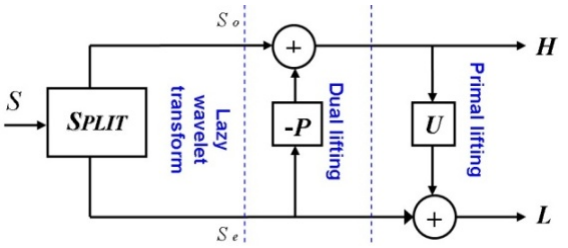

Figure 1: Basic structure of one dimensional Discrete Wavelet transform (1D-DWT) using lifting scheme (Ben Hnia Gazzah et *al.*, 2007).

3.1 Implementation

The 5/3 filter allows achieving lossless image compression and has short filter taps composed of 3/2 coefficients respectively to the 5 and 3 filter taps. The 9/7 filter is composed of 5/4 taps respectively. Figure2 shows the lifting scheme steps of the 5/3 wavelet filter. The Input samples x_{2k+1} and x_{2k} denote the odd and even samples, respectively, resulting from the split step provided by the Lazy Wavelet Transform (LWT). The prediction and updating steps are given by x'_{2k+1} and x'_{2k}. Coefficients x'_{2k+1} and x'_{2k} are the output coefficients obtained by the prediction task and the updating task respectively.

$$x'_{2k+1} = x_{2k+1} - \frac{1}{2}(x_{2k} + x_{2k+2}) \quad (3)$$

$$x'_{2k} = x_{2k} + \frac{1}{4}(x'_{2k-1} + x'_{2k+1}) \quad (4)$$

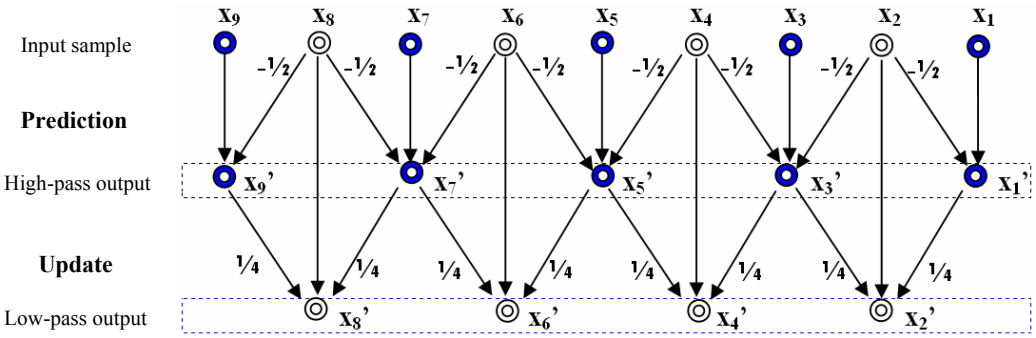

Figure 2: The lifting scheme set for 5/3 filter (Ben Hnia Gazzah et *al.*, 2007).

The 9/7 decomposition is computed within four steps (Daubechies et *al.*, 1998) as shown by equation 5-8:

$$x'_{2k+1} = x_{2k+1} + a*(x_{2k} + x_{2k+2}) \quad (5)$$

$$x'_{2k} = x_{2k} + b*(x'_{2k-1} + x'_{2k+1}) \quad (6)$$

$$x''_{2k+1} = x'_{2k+1} + c*(x'_{2k} + x'_{2k+2}) \quad (7)$$

$$x''_{2k} = x'_{2k} + d*(x''_{2k-1} + x''_{2k+1}) \quad (8)$$

The lifting coefficients (Jiang et *al.*, 2005) are: a=-1.5861, b=-0.0529, c=0.8829 and d=0.4435. The high-pass coefficients x''_{2k+1}, are normalized by a weight K_h=1.2302, and the low pass coefficients x''_{2k} are normalized by K_l=1/ K_h.

The implementation is held with the Texas Instrument TMS320C6713 floating-point processor. The TMS320C6713 processor is a fast special-purpose microprocessor with adequate architecture (figure 3) for signal processing (Texas Instrument, 2002).

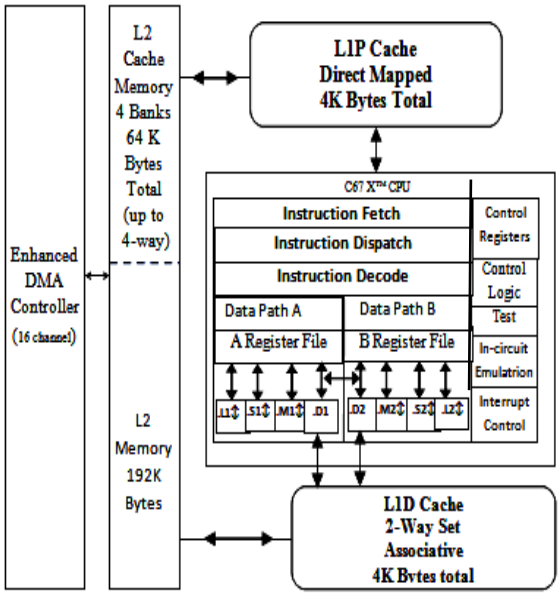

Figure 3: Functional bloc of TMS320C6713 and CPU diagram (Texas Instrument, 2002).

The TMS320C6713 is based on the VLIW architecture and its performance is rated at 1800 MIPS. The internal program memory is structured so that a total of eight instructions can be fetched every cycle. With a clock rate of 255 MHz the processor is capable of fetching eight 32-bit instructions every 4.44ns (Texas Instrument, 2001).

It is used only one storage memory block, in the algorithm description. In both prediction and update stages a new computed coefficient replaces the original input value without need to additional emplacements (in place calculus). The inverse transform is easily performed by inversing the steps of LS and the operations signs.

3.2 Experimental Results

The implementation performances are evaluated in term of execution time and cycle's number per computed pixel. Performance was measured using the cycle counters (Texas Instrument, 2002). Cycle counters provide a very precise tool for measuring the time that elapses between two different points in the execution of a program. Obviously the execution time depends on the image size (table1), the type of used memory (internal or external memory) and the number of steps of lifting scheme. The running time when using processor internal memory is shorter than that when using external memory. In our case, due to the limited size of the internal memory (256 KB), we are conducted to use the external memory (16 MB SDRAM) as a "buffer memory".

Table1 shows the execution time ratio of external memory to internal memory. The mean value ratio for 5/3 filter is about "21", however, the mean value is about "39" for the 9/7 filter. The mean value for 9/7 filter is two times higher then that for the 5/3 filter: this is due to the number of lifting scheme steps. The transforms with less lifting steps 5/3 tend to perform better than transforms with more lifting steps 9/7 in term of speed. In addition, we have implemented the 5/3 lifting scheme using only addition, subtraction, and shifting operations without multiplications.

The code optimization by using internal memory reduces the execution time. Obviously the internal memory access time is lower than that of external memory.

Figure 4 shows the running time using internal memory and figure 5 shows the running time using external memory.

Table 1: Cycle's number per pixel.

Samples number	64			256			512			1024			2048			4096		
Memory type*	ext	int	Ratio	ext	int	Ratio	ext	int	Ratio	ext	int	Ratio	ext	int	Ratio	ext	in	Ratio
5/3 filter	135	6	22.5	145	7	20.71	145	7	20.75	135	6	22.5	135	7	19.28	110	6	18.33
9/7 filter	274	7	39.14	273	7	39	274	7	39.14	275	7	39.28	275	7	39.28	275	7	39.29

*int = execution time of internal memory in cycles/pixel, ext = execution time of external memory in cycles/pixel

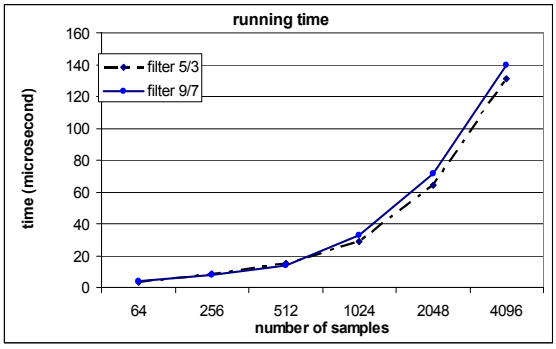

Figure 4: Running time using internal memory.

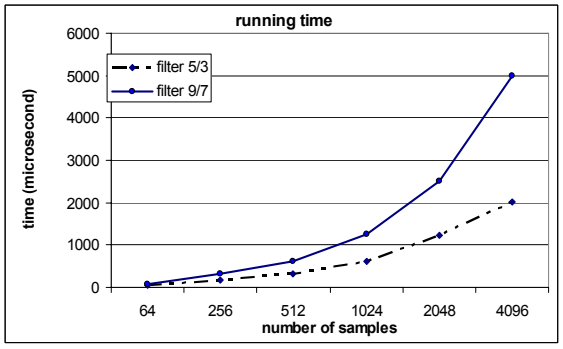

Figure 5: Running time using external memory (SDRAM).

Two sets of experiments of 1D- Discrete Wavelet lifting implementation were performed: in the first set, we used on-chip memory and external memory. In the second set, we used only external memory . Two programs have been implemented. They differ in the processing part. In the first program, the processing took place in the internal memory (on-chip memory), however in the second program, the processing part of the C-program is held in the external memory.

Execution time results (cycles/pixel) for both methods of the 1D- Discrete Wavelet lifting are shown in Table 2. The comparison of the execution time between both methods shows that the one using internal memory is about three times faster than the other using external memory SDRAM 16MB for the filtering operation.

We optimize the execution time of the lifting scheme by using internal memory for processing in three steps:

First, the image is divided into several blocks before storage into the SDRAM memory. Secondly, the blocs are transferred in the L2 cache internal memory. The filtering operation is performed by the lifting scheme algorithm. Finally the transformed image is transferred to the external memory (SDRAM) for result storage.

Similarly, the next blocks of image are transferred one after another into L2 cache where they are processed. The number of blocks depends on the image size. In the case of 256x256 image size, the size of each block is 64x256 pixels. Four successive blocks are to be used.

Table 2: Execution time of the 1D- Discrete Wavelet lifting for image (Baboon 256x256) using 5/3 filter.

	Execution time (Cycles/pixel)		**Ratio of B to A**
	Execution time A*	Execution time B**	
image(256*256 pixels) decomposition	43	135	3.14
image (256*256 pixels) reconstruction	43	134	3.16

*A : execution time using internal memory for processing.
**B : execution time using external memory for processing (SDRAM).

The reconstructed image was compared to the original image and the peak signal-to-noise ratio (PSNR) in decibels was computed for images to evaluate the performance of the wavelet lifting scheme transform program. In the case of an image whose intensity of the pixels lies between 0 and 255, the PSNR is given by the following formula:

$$PSNR = 10.\log_{10}\left(\frac{255^2}{\left[1/(M.N)\right].\sum_{i=1}^{M}\sum_{j=1}^{N}(x(i,j)-\tilde{x}(i,j))^2}\right) dB$$

where: M×N is image size computed in pixels

: (1<i<M) and (1<j<N) denote pixel indices.

We have founded a higher PSNR for wavelet lifting scheme transforms. This verifies a perfect reconstruction property of Wavelet lifting scheme transform. Table3 shows the PSNR and SNR results obtained by DSP implementation and MATLAB simulation using 2D wavelet lifting scheme transform for both 5, 3 and 9, 7 filters.

The 2-D discrete wavelet transform (DWT) based on a lifting scheme, is carried out as a separable transform by cascading two 1-D transforms in the horizontal and vertical direction. Each level of wavelet decomposition provides four sub-bands of decomposition images: LL, LH, HL and HH with halved resolution in both horizontal and vertical directions.

In our application we implemented the 2D-DWT on DSP using Lifting scheme until level three with different image sizes: Barbara (512x512), Cameraman (256x256), Lena (256x256), Baboon (512x512), goldhill (512x512), lena(512x512).

The same algorithm was simulated using Matlab language. We compared PSNR results of 2D lifting scheme at level three using different image sizes (table .3). Experimental and simulation results have almost the same performance.

The following figure represents three levels of the 2D-DWT with Lifting implemented on DSP using Barbara image (512 x 512 pixels).

Figure 6: 3-level 2D-DWT using lifting scheme with Barbara image 512x512 pixels.

Table 3: PSNR results of 2D lifting scheme implementation and MATLAB simulation (level three).

image	Perfor-mance	Wavelet CDF9/7		Wavelet LeGaull 5/3	
		Simulation results	Experimental results	Experimental results	Simulation results
Barbara 512*512	PSNR (dB)	307.929	∞	∞	∞
	SNR	301.522	∞	∞	∞
Baboon 512*512	PSNR (dB)	307.016	∞	∞	∞
	SNR	301.550	∞	∞	∞
lena 512*512	PSNR (dB)	307.171	∞	∞	∞
	SNR	301.514	∞	∞	∞
lena 256*256	PSNR (dB)	307.452	∞	∞	∞
	SNR	301.647	∞	∞	∞
Camera-man 256*256	PSNR (dB)	307.114	∞	∞	∞
	SNR	301.532	∞	∞	∞
Goldhill 512*512	PSNR(dB)	307.979	∞	∞	∞
	SNR	301.613	∞	∞	∞

4 CONCLUSIONS AND FUTURE WORK

In this paper, we reported the implementation of 2D-DWT using lifting scheme algorithm on the TMS320C6713 DSP, floating-point processor. We used 5/3 and 9/7 filters. We compared the implementation of the algorithm on DSP with the simulation using Matlab.

For both methods, we obtained high PSNR values of different images sizes confirming efficacy of the approach. The most important advantages of the lifting scheme (Ben Hnia Gazzah et *al*., 2007) for wavelet transform were verified which are: perfect reconstruction capability, in place computation.

We optimized speed execution time of DSP implementation of lifting scheme algorithm in different ways especially within memory usage.

Execution times of the two algorithms of 5/3 and 9/7 filters on a DSP have been compared. The corresponding C-program for a 1-level 1D DWT of 5/3 filter is up to 3x faster than of the 9/7. Integer to-integer transforms are often faster than real-to-real transforms, because the 5/3 wavelet filter requires

two lifting scheme steps, however the 9/7 wavelet filter requires four ones.

The future work will be optimizing speed execution time of lifting scheme algorithm using DMA.

REFERENCES

Ben Hnia Gazzah, I., Souani, C., and Besbes, K., 2007, "DSP implementation of lifting Scheme transform", *Journées scientifiques des jeunes chercheurs en Génie Electrique et Informatique*, pp 445-451.

Chendonga, D., Zhengjiab, H., and Hongkai, J., 2007, A sliding window feature extraction method for rotating machinery based on the lifting scheme, *Journal of Sound and Vibration*, vol. 299, pp 774–785.

Daubechies, I., and Sweldens, W., 1998, "Factoring wavelet transforms into lifting steps," *Journal of Fourier Analysis and Applications*, vol. 4, pp. 245–267.

Delouille, V., Jansen, M., and Von Sachs, R., 2006, Second-generation wavelet denoising methods for irregularly spaced data in two dimensions, *Signal Processing,* vol. 86, pp 1435–1450.

Gnavi, S., Penna, B., Grangetto, M., Magli, E., and Olmo, G., 2002, Wavelet Kernels on a DSP: A Comparison Between Lifting and Filter Banks for image Coding, *EURASIP Journal on Applied Signal Processing*, Hindawi Publishing Corporation: 9, 981–989.

Jiang, K., Dubois, E., 2005, Lifted wavelet-based image dataset compression with column random access for image-based virtual environment navigation, *IEEE International Workshop on Haptic Audio Visual Environments and their Applications*, Ottawa, Ontario, Canada.

Rabbani, M., and Josi, R., 2002, An Overviewof the the JPEG2000 Still Image Compression Standard Signal Processing: *Image Communication*, 17(1), pp.3-48.

Shahbahrami, A., Juurlink, B., and Vassiliadis, S., 2005 Performance Comparison of SIMD Implementations of the Discrete Wavelet Transform, *Proc. 16th IEEE Int. Conf. on Application-Specific Systems Architectures and Processors (ASAP),* Samos, Greece, July 23-25.

Sweldens, W., 1996, Wavelets and the lifting scheme, A 5 minute tour, *Zeitschrift für Angewandte Mathematik und Mechanik*, vol. 76 (Suppl. 2), pp. 41-44.

Sweldens, W., and Schröder, 1996, Building your own wavelets at home, in Wavelets in Computer Graphics, *ACM SIGGRAPH course notes*, pp. 15-87.

Texas Instrument, Revised November 2002, TMS320C6713 Floating-Point Digital Signal Processor, *Datasheet SPRS186B*

Texas Instrument, december 2001, TMS320C6713 Floating-Point Digital Signal Processor, *Datasheet SPRS186L*.

EVALUATION OF NOVEL ALGORITHM FOR SEARCH OF SIGNAL COMPLEXES TO DESCRIBE COMPLEX FRACTIONATED ATRIAL ELECTROGRAM

V. Kremen and L. Lhotska
Gerstner Laboratory, Department of Cybernetics, Czech Technical University in Prague, Technicka 2,Prague 6, CZ-166 27
vaclavkremen@seznam.cz, lenka.lhotska@fel.cvut.cz

Keywords: Wavelet transform, atrial fibrillation, atrial electrogram, signal complexes.

Abstract: Complex fractionated atrial electrograms (CFAEs) represent the electrophysiologic substrate for atrial fibrillation (AF). Progress in signal processing algorithms to identify CFAEs sites is crucial for the development of AF ablation strategies. Individual signal complexes in CFAEs reflect electrical activity of electrophysiologic substrate at given time. We developed and tested a novel algorithm based on wavelet transform. This algorithm enables to find individual signal complexes in CFAEs automatically and based on that the CFAEs complexity can be described in a novel way. The method was tested using a representative set of 1.5s A-EGMs (n = 113) ranked by an expert into 4 categories: 1 - organized atrial activity; 2 - mild; 3 - intermediate; 4 - high degree of fractionation. Individual signal complexes were marked by an expert in every A-EGM in the dataset. This ranking was used as gold standard for comparison with the novel automatic search method. Achieved results indicate that use of appropriate level of wavelet signal decomposition could carry high level of predictive information about the state of electrophysiologic substrate for AF and is efficient to help to describe the level of complexity of CFAEs in a novel way.

1 INTRODUCTION

Atrial fibrillation (AF) is a cardiac arrhythmia characterized by very rapid and uncoordinated atrial activation with a completely irregular ventricular response (Fuster et. al., 2006). Radiofrequency ablation of atrial areas that triggers or sustains AF is a nonfarmacological treatment available recently (Calkins and Brugada, 2007).

During AF, multiple wavefronts propagate continuously through the right and left atria, separated by anatomical and functional barriers (Houben and Allessie, 2006). This can be electrophysiologically manifested as hierarchical distribution of dominant frequency (Sanders and Berenfeld, 2005) or complex fractionated electrograms (CFAEs) (Nademanee and McKenzie, 2004) during endocardial mapping. Local dominant frequency analysis of AF is burdened by many methodological problems of spectral analysis (Kadish and Goldberger, 2006). Therefore the software support for electroanatomical mapping system is focused on objective description and space representation of CFAEs distribution most recently.

Algorithms for automatic classification (pattern recognition) are generally based on classification techniques or description of signal, using features extracted from recorded and preprocessed signals. Such algorithms, if they are implemented, could also suggest level of complexity or degree of fractionation of particular AEGM signals recorded during AF.

Till now there is only a single known approach. However it is not published in full scope, but only in company brochure (user manual) (Ensite NavX^{TM}, 2006). This algorithm assesses level of fractionation of AEGM signal using calculation and signal processing in time domain and describes signal by only one feature which relates to degree of fractionation of the signal.

We aim to describe AEGM signal in a new universal way, which helps us to extract features of the signal and to classify its complexity. There are signal complexes (figure 2) in every AEGM signal, which are related to electrical activation of electrophysiologic substrate during AF. These signal complexes (SCs) can be found automatically and then used for several features extraction (degrees of freedom of the signal), which could be used for

automatic evaluation of electrogram complexity (or level of fractionation) in next stages.

Therefore in this paper we want to introduce a new method of AEGM signal processing which enables to localize above mentioned SCs automatically with adequate efficacy. We describe a novel method for AEGM processing (searching of SCs), based on the wavelet transform signal analysis, which is a well known technique in the signal processing domain. We also introduce the design of a wavelet filter of AEGM signal which is used before search of SCs itself.

2 METHODOLOGY

We used a representative dataset (n = 113) of atrial electrograms (A-EGMs), which were pre-selected by an expert from a large database of A-EGMs. This database was recorded during AF mapping procedures. Signals were sampled by frequency 977 Hz during AF procedure and resampled to 1 kHz after that. Each pre-selected A-EGM signal in this dataset is 1500 ms long. The expert signal selection was driven by the intention to get a good quality signals with respect to low noise and high information value of signal for later evaluation of degree of A-EGMs fractionation by an expert. Although the degree of fractionation is supposed to be naturally continuous we decided to make a four degree set of classes (Figure 1.).

Three experts used these four categories for ranking (1 – organized atrial activity, n = 24; 2 – mild, n = 40; 3 – intermediate, n = 36; 4 - high degree of fractionation, n = 13.). Individual SCs (points of interest) were found manually by an expert in every A-EGM in dataset (Figure 2). The beginning and the end of every SC was marked by an expert for all found SCs thru the whole dataset of used CFAEs. This expert ranking of the beginnings and the ends of SCs was used as gold standard for comparison with outputs of the newly introduced automatic search method (ASM) and evaluation of ASM effectiveness.

In many applications the Continuous Wavelet Transform (CWT) is used to decompose a signal into wavelets, small oscillations that are highly localized in time. Whereas the Fourier transform decomposes a signal into infinite length sines and cosines, effectively losing all time-localization information, the CWT's basis functions are scaled and shifted versions of the time-localized mother wavelet. The CWT is used to construct a time-frequency representation of a signal that offers very good time and frequency localization. The CWT is an excellent tool for mapping the changing properties of non-stationary signals. When a signal is regarded non-stationary, the CWT can be used to identify stationary sections of the data stream.

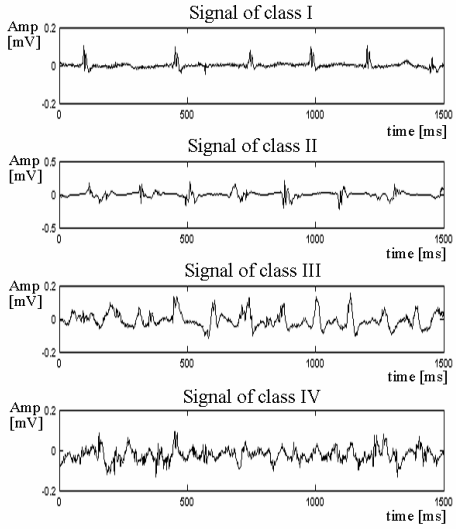

Figure 1: Four complex fractionated electrograms are shown. These are representatives of each ranking class of degree of fractionation ranked by an expert. From the top to bottom: 1 – organized atrial activity; 2 – mild, 3 – intermediate; 4 - high degree of fractionation.

The discrete wavelet transform (DWT) is an implementation of the wavelet transform using a discrete set of the wavelet scales and translations obeying some defined rules. In other words, this transform decomposes the signal into mutually orthogonal set of wavelets, which is the main difference from the CWT. The wavelet packet method is a generalization of wavelet decomposition that offers a richer range of possibilities for signal analysis.

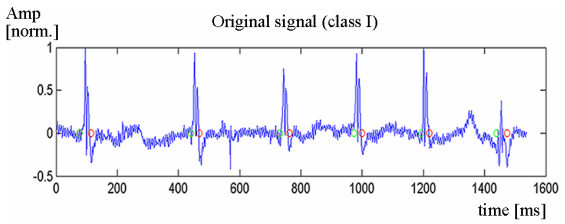

Figure 2: Original CFAE signal recorded during AF mapping procedure. Expert ranking of the signal is into class I. Depicted amplitude is normalized with respect to maximal absolute value of this particular CFAE signal. Green circles denote the beginnings of SCs and red circles the ends of SCs found automatically by ASM with optimized parameters.

We used such multilevel decomposition of CFAE signal for preprocessing (denoising) of the signal and for automatic detection of points of interests (SCs) in the signal. Simple and efficient algorithms exist for both wavelet packet decomposition and optimal decomposition selection. We chose the algorithm implemented and described in Matlab (function „wavedec“, „waveden“) (Matlab Wavelet Toolbox 3.0, 2006). As a mother wavelet we chose a Coiflet wavelet of order four. The selection of mother wavelet was driven by outcomes of optimization experiments performed using a Particle Swarm Optimalization algorithm (Lhotska and Macas, 2007) where this type of wavelet showed the best results for our purposes of signal preprocessing (filtering) and searching of SCs.

Filtering (de-noising) of CFAEs signals was performed using wavelet transform filter based on multilevel signal decomposition and thresholding of detailed coefficients (Mallat, 1999). The mentioned mother wavelet was used to decompose signal into 5 levels (Daubechies, 1992). Detail coefficients were thresholded by soft-thresholding (Donoho, 1995) with these settings of thresholds (level 1 to level 5): 0.02, 0.04, 0.008, 0.008 and 0.008. Reconstruction of the signal was computed by wavelet reconstruction based on the original approximation coefficients and the modified detail coefficients of levels from 1 to 5. Additional step of CFAEs signals preprocessing was done by thresholding of the signal with value of threshold 0.003 mV. Sample of CFAE signal ranked by an expert into class I, where described preprocessing technique was performed, is shown in Figure 4.

ASM itself was the next step. It was based again on wavelet multilevel decomposition of filtered signal. The signal was decomposed again into 5 levels using Coiflet wavelet of order four. The level 3 of detailed coefficients showed the best transform to find proper SCs (Figure 3). Therefore the reconstruction of the detailed coefficients of a signal (L3) of given wavelet decomposition structure was performed at level 3 (L3). Figure 3 shows the difference between L3 before and after signal preprocessing. Normalization of L3 was performed with respect to maximal absolute value of given L3 values to obtain uniform signals across the dataset for next stages of SCs detection. Thresholding of normalized L3 signal values was performed with value of threshold 0.014. Then all parts of the signal, where absolute value of amplitude was higher than 0, were marked as peaks with amplitude 1. These peaks were related to time localization of electrical activity of AF substrate in individual CFAE signals.

The last step of the algorithm consists in joining all peaks that lie very close to each other into one SC. Therefore all peaks whose inter-distance was closer than threshold 5 ms were joined together and they were marked as one individual SC (Figure 2 and 3).

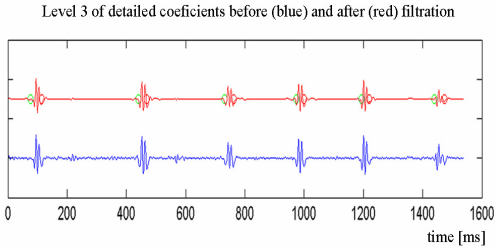

Figure 3: Reconstruction of the detailed coefficients of a signal from figure 1 of given wavelet decomposition structure performed at level 3 (L3). Blue signal shows L3 before wavelet filtering. Red signal is L3 reconstruction after filtering. Green circles denote the beginnings of SCs and red circles the ends of SCs found automatically by ASM with optimized parameters.

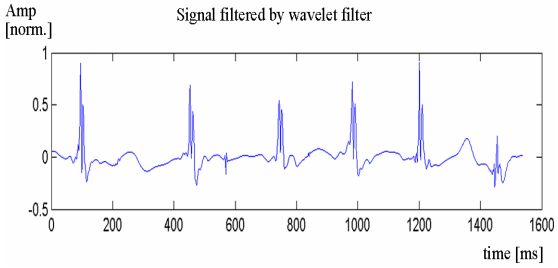

Figure 4: CFAE signal from figure 1 filtered by above mentioned wavelet filter. Depicted amplitude is normalized with respect to maximal absolute value of this particular CFAE signal.

All mentioned optional parameters of CFAE signal preprocessing algorithm and ASM itself (level used for searching of SCs and filtering, thresholds, and inter-segment distance threshold) were optimized by Particle Swarm Optimization algorithm (PSO), to get optimal parameters settings with respect to hit rate of ASM in comparison to expert marking of SC. The details and utilization of PSO is out of scope of this paper.

3 RESULTS

We evaluated the presented algorithm by calculating its hit rate, which was defined by using standard criteria of specificity. The overall results of ASM

sensitivity through all classes of CFAEs are shown in Table 1.

The best results were achieved in class I and II, where the signification of SCs can be performed very precisely by an expert. There is low sensitivity of ASM to approach the signals of class IV to find and confirm the SCs signified by an expert.

4 CONCLUSIONS

The newly introduced ASM is able to find SCs with high sensitivity in class I and II and is worse to approach the expert SC classification in classes III and IV in the used dataset. The expert can hardly see and relate the electropathologic AF substrate activation in signal of classes III and IV to individual SCs and he/she can hardly properly mark corresponding beginnings and ends of the SCs. That means there could be incorrective error of classifying SCs in the used gold standard. It could be pandering that ASM could disclose hidden characteristics of the CFAE signal related to electropathologic AF substrate. These could be hardly seen in time domain only, especially at signals of class III and IV.

We could therefore use the features extracted from found SCs for CFAE signal description and evaluation of CFAE signal complexity. Therefore it might be suitable to use description of CFAE signal based on such time domain characteristics. Good descriptor for separation of classes of CFAE signals could be an intersegment distance of SCs or SCs fractionation itself.

Table 1: Hit rate of ASM with optimal parameters setting for each class of AEGM signals separately. SCs of given dataset, marked by an expert were used as gold standard.

	Sensitivity
Class I	100%
Class II	98.2%
Class III	92.6%
Class IV	63.89%

But as the results suggest we could use also CFAEs signals descriptors based on characteristics of mentioned wavelet level decomposition. The decomposition can serve to find more hidden features of CFAE signals, which could help us to distinguish between CFAE classes. Especially class III and IV could be difficult to distinguish with features extracted in time domain only. Future work will show if this new approach of automatic description of level of complexity of CFAE signal will have good results comparable to expert ranking.

ACKNOWLEDGEMENTS

This work has been supported by the MEYS of the Czech Republic (under project No. MSM 6840770012 "Transdisciplinary Biomedical Engineering Research II").

REFERENCES

Fuster V, Ryden LE, Cannom DS, et al. ACC/AHA/ESC 2006. Guidelines for the management of patients with atrial fibrillation. Circulation 2006; 114:257-354.

Calkins H, Brugada J, Packer DL, et al. HRS/EHRA/ECAS expert consensus statement on catheter and surgical ablation of atrial fibrillation: recommendations for personnel, policy, procedures and follow-up. Heart Rhythm 2007;4:816-61.

Houben RPM, Allessie MA. Processing of intracardiac electrograms in atrial fibrillation. Diagnosis of electropathological substrate of AF. IEEE Eng Med Biol Mag 2006; 25: 40-51.

Sanders P, Berenfeld O, Hocini M, et al. Spectral analysis identifies sites of high-frequency activity maintaining atrial fibrillation in humans. Circulation 2005; 112:789-97.

Nademanee K, McKenzie J, Kosar E, et al. A new approach for catheter ablation of atrial fibrillation: mapping of the electrophysiologic substrate. J Am Coll Cardiol 2004; 43:2044-53.

Ng J, Kadish AH, Goldberger JJ. Effect of electrogram characteristics on the relationship of dominant frequency to atrial activation rate in atrial fibrillation. Heart Rhythm 2006; 3:1295-305.

Ensite NavX^{TM} Navigation and Visualisation Technology (Fractionation Mapping Tool Procedure Guide, Ensite 6), pp. 2-8, St. Jude Medical, 2006.

Matlab Wavelet Toolbox 3.0 reference manual. The MathWorks, Inc. 2006.

Lhotská, L. - Macaš, M.: Particle Swarm Optimization for Processing and Analysis of Biological Signals. In Proceedings of Workshop 2007. Prague: CTU, 2007.

Mallat, S. A Wavelet tour of Signal Processing**.** 2. edition. ISBN/ISSN:0-12-466606-X. Academic Press. 1999.

Daubechies I.: Ten lectures on Wavelts, CBMS-NSF, SIAM, 61, Philadelphia, Pennsylvania, USA, 1992.

Donoho, D.L. (1995), "De-noising by soft-thresholding," IEEE Trans. on Inf. Theory, 41, 3, pp. 613-62

AUTOMATED DETECTION OF SUPPORTING DEVICE POSITIONING IN RADIOGRAPHY

Chen Sheng, Li Li and Ying Jun
College of Mathematics and Science, Shanghai Normal University, Guilin Road 100, Shanghai, China
chnshn@hotmail.com

Keywords: Gaussian Filter, Contrast-Limited Adaptive Histogram Equalization (CLAHE), Hough Transform, Tube.

Abstract: Portable X-ray radiographs are heavily used in the ICU for detecting significant or unexpected conditions requiring immediate changes in patient management. One concern for effective patient management relates to the ability to detect the proper positioning of tubes that have been inserted into the patient. These include, for example, endo-tracheal tubes (ET), feeding tubes (FT), naso-gastric tubes (NT), and other tubes. Proper tube positioning can help to ensure delivery or disposal of liquids and air/gases to and from the patient during a treatment procedure. Improper tube positioning can cause patient discomfort, render a treatment ineffective, or can even be life-threatening. However, because the poor image quality in portable AP X-ray images due to the variability in patients, apparatus positioning, and X-ray exposure, it is often difficult for clinicians to visually detect the position of tube tips. Thus, there is a need for detecting and identifying tube position and type to assist clinicians. The purpose of this paper is to present a computer-aided method for automated detection of tubes and identification of tube types. Use of this method may allow clinicians to detect the tube tips more easily and accurately, thus improving the quality of patient management in the ICU.

1 INTRODUCTION

Computer-aided diagnosis is designed to help physicians improve the diagnostic accuracy of radiological images and for detection of the disease, and to explain the consistency, reduce the rate of misdiagnosis, and cause less opportunity for eye fatigue. The chest CAD system (Brem and Baum, 2003) and the Mammography CAD system (Bram and Bart, 2001) are both used in clinics. Clinical results show two aspects: Medical diagnostic radiology consults the CAD output and it is thus easier to find more features, such as micro-calcifications and the changes that have taken place in the tiny structures, greatly improving the efficiency and accuracy of diagnosis. We research the method of tube automatic detection for improving the quality of patient management in the Intensive Care Unit (ICU) (Doi and MacMahon, 1999).

ICU patients, particularly those with heart and lung diseases, rely on the existence of tubes to live and be treated. In the intensive care setting, catheters, tubes, and monitoring devices play an important role. Proper placement of these devices is crucial to their function Personnel are well aware of the need for timely medical ICU care for patients, correct placement of tubes, and the changes that need to be made around these tubes' positions. If the computer can automatically identify the location of tubes and their tips, and enhance medical images around tubes to provide diagnosis, it is a clear and very important improvement to their procedures.

ICU patients' chest X-ray images can be fuzzy, exhibit low contrast and noise, and contain many different types of tube connections on the image, such as the endo-tracheal tube, feeding tube, naso-gastric tube, pulmonary artery, central venous catheter, and other catheters required for the treatment of a variety of medical conditions. These bring a significant challenge to accurately detect tubes and their tips. Figure 1 shows a general original ICU chest image.

2 METHODS AND MATERIALS

We collected a database consisting of 107 portable X-ray images from 20 patients using Kodak's computed radiography (CR) system. An experienced

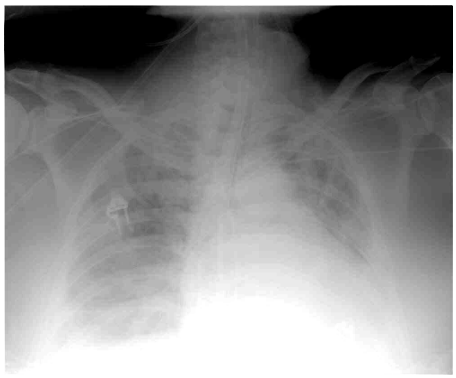

Figure 1: Original ICU chest X-ray image.

chest radiologist reviewed all the images from the 20 patients and provided a diagnosis for each image including the types of tubes and locations of their tips. The technique we developed here was evaluated for the detection of the three commonly used tubes in the ICU, the endo-tracheal tube, the feeding tube, and the naso-gastric tube. In this database, 33 images were identified to have endo-tracheal tubes, 54 with feeding tubes, and 22 with naso-gastric tubes. This technique will be used and evaluated for the detection of other tubes/lines in the future.

Figure 2 lists the steps used in the automated detection method. In the image-processing step, the contrast-limited adaptive histogram equalization (CLAHE) (Pizer and Amburn, 1987) (Zuiderveld) is used to enhance the contrast, and the anisotropic filtering is used to remove the noise prior to the generation of a gradient image. CLAHE can enhance the contrast details of the regions and avoid noise amplification as a result of histogram equalization in a similar region. As with the general histogram equalization, which can change the grey scale of the image to enhance the contrast, its distinction is that the operation region is a small region from which the whole image is divided, and then merged together again as the whole image and using bilinear interpolation between two neighbourhood intercropping to eliminate false results of the border reduced by histogram equalization. The combination of a canny filter (Parker, 1997 and Canny, 1986) and Hough transform (Kamat and Ganesan, 1998) is then applied to detect edges and lines on the tiles of an enhanced gradient image. A whole gradient image is divided into many tiles for performing Hough transform. The tube in a small tile can be considered a straight tube. The double-line/edge criteria are applied to identify potential tube candidates by paring a detected "left" edge with a "right" edge (See Fig.3). Theoretically, the paired left and right edges should have a fixed distance between them and each should have a gradient with an opposite direction (i.e., G, -G). Therefore, tubes' edges should be basically parallel so it can be determined which tube is the valid one (See Fig. 4). Further, we apply bilateral Hough transform to detect the missing lines between potential tube candidates.

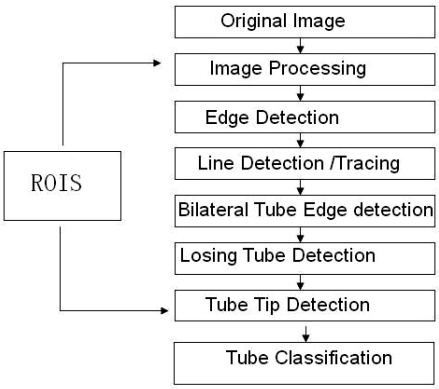

Figure 2: Tubes' automatic detection flowchart.

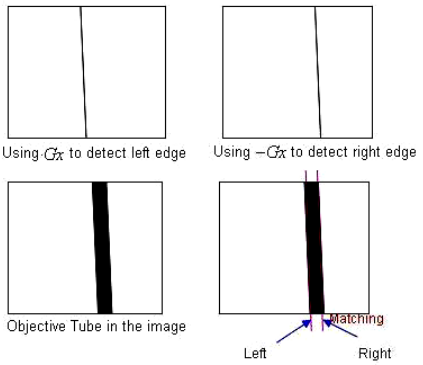

Figure 3: Tube matching.

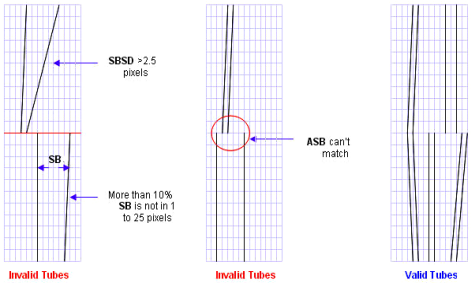

Figure 4: Determine the valid tube.

Note: SB is the abbreviation of Space Between. SBSD is the abbreviation of Space Between Standard Deviation. ABS is the average of SB.

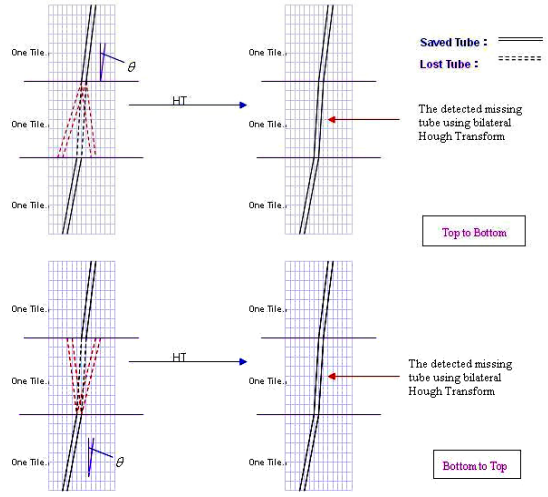

Figure 5: Bilateral Hough transform.

Figure 5 shows the detected missing/lost lines between the two potential tubes identified in the previous step. Bilateral HT: Using the tube's grey gradient (left is Gx and right is –Gx) to do bilateral Hough Transform. The paired left and right edges should have a fixed distance between the two edges and each should have a gradient with an opposite direction. The detected tube's size is assumed as the distance. Basing the detected tube's position, we do the bilateral Hough Transform to gradient image from top to bottom, then from bottom to top. After doing the bilateral Hough transform, we can locate the missing tubes.

In a small tile each to be linked with at least the boundary line is another small tile. In other words, the starting point of the boundary line and the end point of another boundary line must be in one pair of neighbouring tiles. The connective tubes' directive angle difference should be in pi/24. The tubes on the images are consistent. When detecting ET, only the isolated tube in the region of interest (ROI) upper part is valid. If a tube can connect with more than two tubes, we will choose the tube that bears a closer directive angle. See Fig. 6.

Tip detection is an important element of our work. Combining the region's information and anatomic structure, we use our algorithm (See Fig. 7). The tubes' edges should be crossing or the tube size should be less than the defined size (i.e., ET, NT: 3-10 pixels , FT: 15-25 pixels). (See Fig. 7: Case 1-2). We use the proper bilateral Hough Transform to stretch or shrink the tube for getting an accurate tip (See Fig. 7: Case 3).

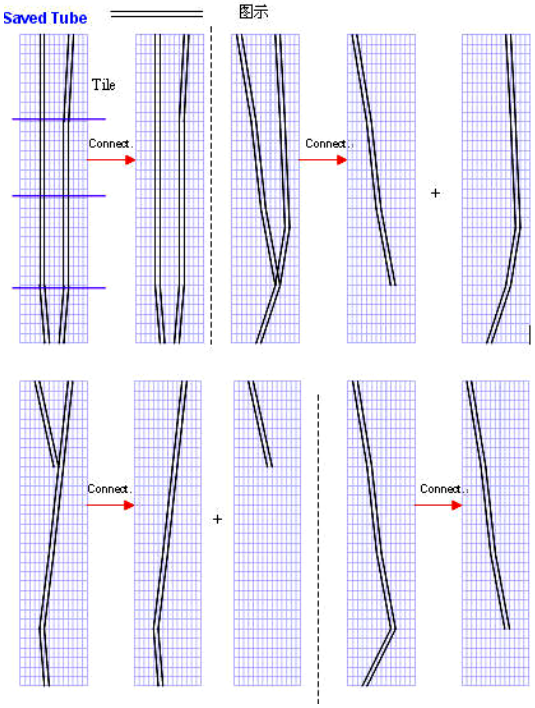

Figure 6: Tubes' connection.

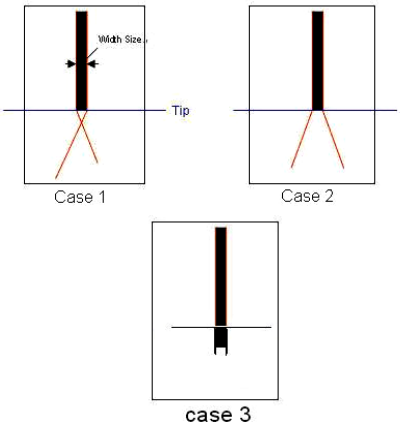

Figure 7: Tip detection.

After determining the tip, a classification step is executed to provide a decision on apparent tube type for the matched pairs of left and right edges. Information such as the length of the line, the location of the tube, and/or the tip relative to anatomic structures is used for classifying the tube types. The ROIs containing relevant anatomic structures, such as lung, mediastinum, and stomach, are identified and used to determine the relative position of tubes in the image. These ROIs serve as landmarks for tube detection and classification.

3 RESULTS

The detection result can be illuminated. See Fig.8-12. We evaluated the performance of the technique for ET, FT, and NT. Our preliminary results showed that use of the presented technique correctly detected the location for 94% of the 33 ET tubes, 82% of the 54 FT tubes, and 82% of the 22 NT tubes with no false positive detection (See Table 1). The performance is expected to improve when detection results from the same patient are used.

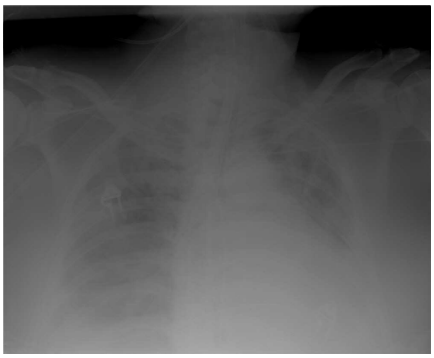

Figure 8: The original X-ray chest image.

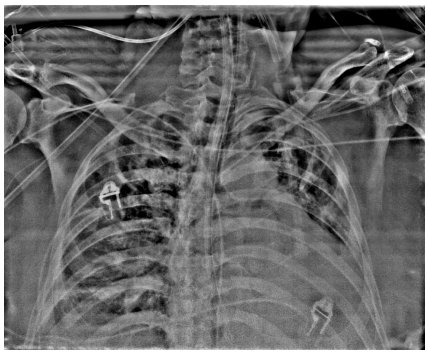

Figure 9: Image pre-processing (CLAHE)

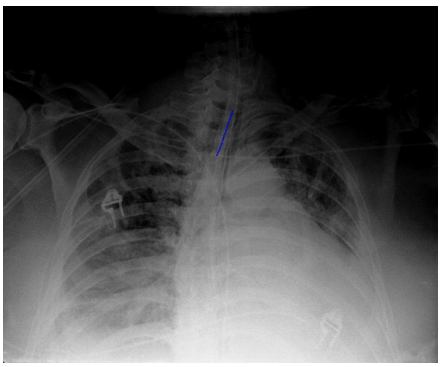

Figure 10: ET detection

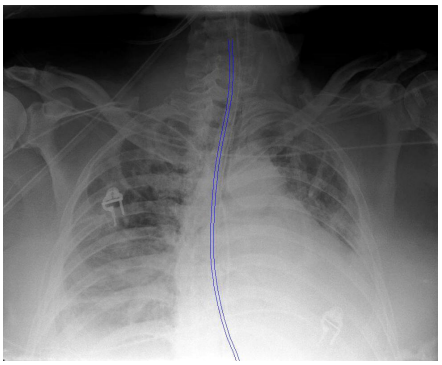

Figure 11: FT detection.

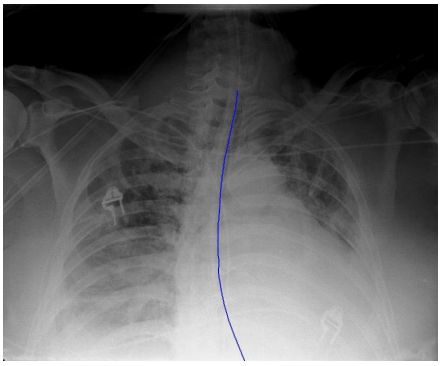

Figure 12: NT detection

Table 1: The result table.

107 images of 20 ICU patients, and the images were captured by portable CR system of Kodak			
	ET	FT	NT
Tube amount	33	54	22
Detection rate	94%	82%	82%

4 CONCLUSIONS

Our novel detection technique can accurately detect the tubes in ICU images at a high sensitivity level. A function of automated detection of tube placement can potentially improve the overall workflow and patient management in the ICU.

ACKNOWLEDGEMENTS

This paper is supported by Innovation Program of Shanghai Municipal Education Comission.

REFERENCES

J. Canny, 1986. “A computational approach to edge detection.” IEEE Trans Pattern Analysis and Machine Intelligence. Vol. 8, No. 6, pp. 679-689.

J. R. Parker, 1997. “Algorithm for image processing and computer vision.” New York, John Wiley & Sons, Inc., pp. 23-29.

K. Doi, H. MacMahon, S. Katsuragawa, 1999. “Computer-aided diagnosis in radiology: potential and pitfalls.” Euro. J. Radiology, pp. 97-109.

K. Zuiderveld. “Contrast limited adaptive histogram equalization.” Graphics Gems IV, pp. 474-485.

R. F. Brem, J. Baum, M. Lechner, 2003. “Improvement in sensitivity of screening mammography with computer-aided detection: a multi-institutional trial.” Am. J. Roentgenol, pp. 687-693.

S. M. Pizer, E. P. Amburn, J. D. Austin, R. Cromartie, 1987. “Adaptive histogram equalization and its variations.” Computer Vision, Graphics, and Image Processing (CVGIP), pp. 355-368.

V. G. Bram, M. H. Bart, 2001. Computer-aided diagnosis in chest radiography: a survey.” IEEE Trans. Med. Imag, Vol. 20, pp. 1228-1241.

V. Kamat, S. Ganesan, 1998. “A robust Hough Transform technique for description of multiple line segments in an image.” Proceedings of the 1998 IEEE International Conference on Image Processing (ICIP-98), Vol. 1, pp. 216-220.

MEASURING CHANGES OF 3D STRUCTURES IN HIGH-RESOLUTION μCT IMAGES OF TRABECULAR BONE

Norbert Marwan, Jürgen Kurths
Nonlinear Dynamics Group, Institute of Physics, University of Potsdam, 14415 Potsdam, Germany
marwan@agnld.uni-potsdam.de

Peter Saparin
Department of Biomaterials, Max Planck Institute of Colloids and Interfaces, 14424 Potsdam-Golm, Germany

Jesper S. Thomsen
Department of Biology, Institute of Anatomy, University of Aarhus, 8000 Århus, Denmark

Keywords: Measures of complexity, 3D image analysis, structural analysis, trabecular bone, osteoporosis.

Abstract: The appearances of pathological changes of bone can be various. Determination of apparent bone mineral density is commonly used for diagnosing bone pathological conditions. However, in the last years the structural changes of trabecular bone have received more attention because bone densitometry alone cannot explain all variation in bone strength. The rapid progress in high resolution 3D micro Computed Tomography (μCT) imaging facilitates the development of new 3D measures of complexity for assessing the spatial architecture of trabecular bone. We have developed a novel approach which is based on 3D complexity measures in order to quantify spatial geometrical properties of bone architecture. These measures evaluate different aspects of organization and complexity of trabecular bone, such as complexity of its surface, node complexity, or local surface curvature. In order to quantify the differences in the trabecular bone architecture at different stages of osteoporotic bone loss, the developed complexity measures were applied to 3D data sets acquired by μCT from human proximal tibiae and lumbar vertebrae. The results obtained by the complexity measures were compared with results provided by static histomorphometry. We have found clear relationships between the proposed measures and different aspects of bone architecture assessed by the histomorphometry.

1 INTRODUCTION

Bone is a dynamic tissue that adapts its architecture to the loading conditions it is subjected to. In addition, from the third decade of life the amount of bone tissue is gradually decreasing. However, in patients with osteopenia or osteoporosis or in astronauts staying in micro-gravity conditions for a long period of time, the bones may change so dramatic that they will lose a significant amount of their stability and the fracture risk increases. These changes may emerge on the one hand as the loss of bone, a decrease of the mineralization of bone, and on the other hand as a change in the micro-architecture of the interior spongy part of the bone called trabecular bone. Structural changes of trabecular bone have received more attention in the last years because the bone loss alone cannot explain all variation in bone strength. Moreover, the rapid progress in high resolution 3D Micro-Computed Tomography (μCT) imaging facilitates the investigation of the micro-architecture of bone.

The standard method for assessing the bone status and its micro-architecture is bone histomorphometry, which was developed for 2D (Parfitt et al., 1983) and recently extended for 3D analysis (Ito et al., 1998; Hildebrand et al., 1999). More recently developed methods for quantifying the complexity of trabecular structures includes methods using measures of complexity based on symbolic dynamics (Saparin et al., 1998; Saparin et al., 2005), fractal properties (Marwan et al., 2007b) and on recurrence (Marwan et al., 2007a), or using volumetric spatial decompositions (Stauber and Müller, 2006). By applying these approaches to 3D images of trabecular bone, it was shown that the bone micro-architecture changes substantially during the development of osteopenia/osteoporosis. The main conclusions in (Saparin et al., 2005; Marwan et al., 2007a) were that the complexity of the bone micro-architecture decreases with increasing bone loss and that the volume and surface of the trabecular structure changes in a different amount. This latter conclu-

sion confirms former findings that the shapes of the trabeculae change during bone loss, e. g., from plate-like structure to rod-like structure (Hildebrand et al., 1999).

In this study we develop new measures of complexity for quantifying the shape and the complexity of 3D structures. We use 3D geometrical properties like local ratio of bone volume to bone surface and the local configuration of the neighbourhood of the bone voxels. We apply these measures to 3D μCT images of human proximal tibial and vertebral bodies in order to investigate differences in trabecular bone structure at different stages of bone loss and compare the results with the outcome of the histomorphometrical evaluation of the same bone material.

2 MEASURES OF COMPLEXITY

The idea behind the quantification of a geometrical shape is based on the fact that different 3D objects of the same volume have different surfaces, depending on their geometrical shape. For example, a long cylinder (length is much larger than radius) has a larger surface than a cube of the same volume, and a sphere of the same volume has a smallest possible surface for the same given volume (Fig. 1).

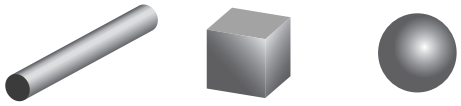

Figure 1: Long cylinder, cube and sphere of same volume ($V = 1000$) have different surface ($S_{\text{cylinder}} = 694$ (for this arbitrary proportion), $S_{\text{cube}} = 600$, $S_{\text{sphere}} = 484$).

Based on the relationship between surface and shape, we introduce measures using the local bone surface and local bone volume. Surface and volume of the trabecular bone are locally estimated in a small cubic box of size s, which moves through the entire 3D image.

Surface and volume could be estimated by a simple *Lego brick* approach. The number of voxels forming the bone structure is used as the volume, and the number of such bone voxels which are connected to the bone marrow (surface voxels) as the bone surface (Fig. 2A). However, this approach is rather problematic, because the amount of surface voxels is actually not a two-dimensional surface measure as it should be, but a three-dimensional volumetric measure. Moreover, the bone volume will be overestimated when such a simple voxel counting algorithm is used. Subsequent calculations based on this surface and volume estimation will lead to even more erroneous estimations. In order to get more precise results, we apply an *iso-surface* algorithm (Fig. 2B).

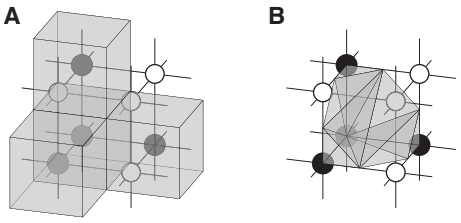

Figure 2: A fragment of data consisting of eight voxels including four bone voxels (black nodes) and four marrow voxels (white nodes). In the *Lego brick.* approach (A), the surface of bone is estimated by counting the number of bone voxels which are connected with marrow voxels (the top, front and right black nodes), and the volume is the number of all bone voxels. In the *iso-surface* approach (B), the surface is estimated by the sum of triangles which form an iso-surface between bone and marrow voxels; the volume is the sum of the tetrahedrons which can be filled between such iso-surface and the grid lines. The volume (gray shaded) will be overestimated by using the *Lego brick* approach (A), but will be calculated more precise by using the *iso-surface* approach (B).

An appropriate approach to construct iso-surface is the marching cubes algorithm (Lorensen and Cline, 1987) which is widely used for constructing iso-surfaces in 3D data visualisation. A marching cube (MC) consists of eight neighbouring voxels. If two neighbouring voxels of this MC have voxel values above and below a predefined threshold value (i. e. one is bone and another is non-bone voxel), the iso-surface will lie between these two voxels. In such MC the iso-surface is formed by a set of triangles, and the surface estimation is the sum of the areas of these triangles (Fig. 2B). Now we introduce the same approach for the estimation of the bone volume. The bone volume within the MC is filled with tetrahedrons in such a way, that the resulting surface equals the iso-surface, which is formed by triangles (Fig. 3). The sum of the volumes of these tetrahedrons is the estimated bone volume contained in the MC.

For the quantification of the 3D shape, we introduce at first the ratio between the local bone surface S_{bone} and the minimal possible surface of the given local bone volume V_{bone}, which is the surface of a sphere S_{sphere} containing this volume V_{bone}. We call this ratio *local shape index* σ_{loc}. Because the local bone volume V_{bone} depends on the size of the moving box s, the normalized local bone volume $\hat{V}_{\text{bone}} = V_{\text{bone}}/s^3$ is used ($\hat{V}$ corresponds to the local bone volume fraction or density $\text{BV/TV}_{\text{loc}}$). The local shape index

$$\sigma_{\text{loc}} = \frac{S_{\text{bone}}}{S_{\text{sphere}}} \quad \text{with} \quad S_{\text{sphere}} = \sqrt[3]{36\pi\hat{V}_{\text{bone}}^2} \qquad (1)$$

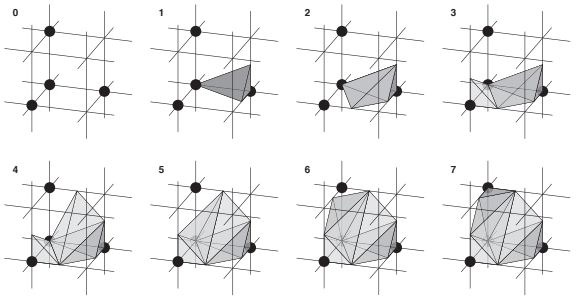

Figure 3: Same fragment as shown in Fig. 2, which is also called marching cube. For volume estimation, the marching cube is filled with tetrahedrons constructed between the isosurface and the grid lines.

distinguishes between different shapes with the same volume but whose surface differ, like plates and rods. In principle, the value of this index should be equal or larger than one, because the surface of a sphere is the smallest possible surface. However, the object could be cut by the faces of the moving box; these interfaces are not counted for the surface of the structure, resulting in a smaller surface. This can even result in a surface that is smaller than such of a sphere. However, this would mainly be the case if the structure is concave. Therefore, values of σ_{loc} smaller than one represent concave structures, whereas values larger than one represent convex structures.

Because σ_{loc} is computed within a small box while moving through the studied object, we get a frequency distribution of the shape index over the entire object $p(\sigma_{\mathrm{loc}})$. Based on this distribution, the *averaged shape index*

$$A_\sigma = \langle \sigma_{\mathrm{loc}} \rangle_{\mathrm{VOI}}, \tag{2}$$

which is the average of all σ_{loc} in the volume of interest (VOI); it measures the mean shape of the trabecular structures.

Next we define the *shape complexity* as the conditional entropy of the joint distribution $p(\sigma_{\mathrm{loc}}, V_{\mathrm{loc}})$ in a given bone volume V_{loc}

$$C_\sigma = -\sum_{\sigma_{\mathrm{loc}}, V_{\mathrm{loc}}} p(\sigma_{\mathrm{loc}}, V_{\mathrm{loc}}) \log \frac{p(\sigma_{\mathrm{loc}}, V_{\mathrm{loc}})}{p(V_{\mathrm{loc}})} \tag{3}$$

This measure quantifies the variety of different shapes for various bone volumes. If the bone surface changes in the same manner as the bone volume changes, i. e. the shape of the structure is roughly remaining, this measure will be low. If, however, the shape is changing more dramatically and perhaps irregularly due to changing bone volume, as it is the case for bone loss, C_σ will be high.

As already mentioned, an MC is formed from eight neighbouring voxels, arranged in the shape of a cube. The entire VOI is actually a composition of many such MCs. In each MC, depending on the positions of the bone voxels, there are 256 configurations possible; neglecting rotational and inversion symmetry, there are 15 unique and fundamental MC configurations (Lorensen and Cline, 1987). However, we will only consider rotational symmetry and ignore inversion, hence, we will deal with 21 pseudo-unique MC configurations (Fig. 4). A specific marching cube configuration corresponds to a specific bone surface configuration and, hence, it is related with the complexity of the surface. For all MCs composing the VOI we identify and count each MC configuration and can derive the probability $p(MC)$ with which a certain MC configuration occurs in the 3D architecture.

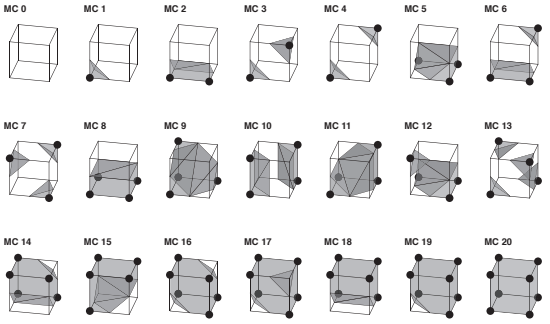

Figure 4: The 21 pseudo-unique marching cube configurations used for defining the *marching cubes entropy index*.

Since these pseudo-unique marching cube configurations (MC cases) are related with the surface complexity, we define an additional measure, the *marching cubes entropy index*

$$I_{\mathrm{MC}} = -\sum_{MC} p(MC) \log p(MC) \tag{4}$$

which is the Shannon entropy of the probability density $p(MC)$ of the marching cubes cases; it measures the complexity of the surface of the trabecular structures. Simple complex surfaces will result in low values of I_{MC}, whereas complex surfaces will result in high values of I_{MC}.

Note that shape complexity C_σ and marching cubes entropy index I_{MC} characterises different kinds of order in a structure. Whereas I_{MC} assesses a global order (or disorder) of bone surfaces, C_σ quantifies the order of certain structural shapes depending on the structure volume. Therefore, these two measures are not necessarily correlated with each other.

3 MATERIALS

These newly introduced measures, Eqs. (2), (3) and (4), are used for the assessment of structural changes

in trabecular bone due to bone loss in osteoporosis.

29 trabecular bone biopsies from proximal tibia bone specimens and 18 entire lumbar vertebral bodies L4 were obtained from the same set of donors. The proximal tibial bone biopsies were scanned at Scanco Medical AG (Bassersdorf, Switzerland) by using a *Scanco μCT 40* μCT scanner with a voxel size of 20 μm (Thomsen et al., 2005). The vertebral bodies were scanned at Scanco Medical AG by using a *Scanco μCT 80* with a voxel size of 37 μm. In order to get comparable images for both skeletal sites, proximal tibia images were downsampled to a voxel size of 40 μm. The analysed set of specimens includes normal, osteopenic (initial stage of osteoporosis) and osteoporotic bones.

Standardized volumes of interest (VOI) were applied to the μCT images for quantification of the 3D architecture: The VOI for the proximal tibial biopsies was located 5 mm below the cortical shell and were 10 mm long, whereas the VOI for the vertebra was a $25 \times 15 \times 10$ mm^3 cuboid with the center shifted 4.5 mm backwards from the center of the vertebra along its symmetry line (Fig. 5). The structural measures of complexity are then computed using these VOIs. In order to validate the developed measures, the results of the purposed 3D data evaluation were compared against conventional bone histomorphometry (Thomsen et al., 2000). Histomorphometric measures are discussed below.

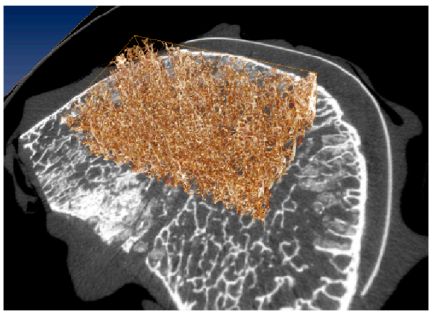

Figure 5: Volume of interest applied to a human lumbar vertebra. Analysed part of the trabecular structure is shown in brown, grey-scale image is the axial CT slice through the middle of the vertebral body.

4 RESULTS

Applying the introduced measures of complexity to the VOIs within the 3D μCT images, we perform an evaluation of the micro-architecture of the trabecular bone of 29 proximal tibial biopsies and 18 lumbar vertebrae representing different stages of bone loss in osteoporosis. The size of the moving box was chosen as $20 \times 20 \times 20$ voxels.

At first we study the differences of the trabecular structure due to bone loss and compare the trabecular bone architecture in proximal tibia and lumbar vertebra (Fig. 6). Bone volume to total volume ratio BV/TV (derived from histomorphometry) characterises the amount of bone material and is used as an indicator of bone loss. We find some remarkable differences between the proximal tibia and the lumbar vertebra.

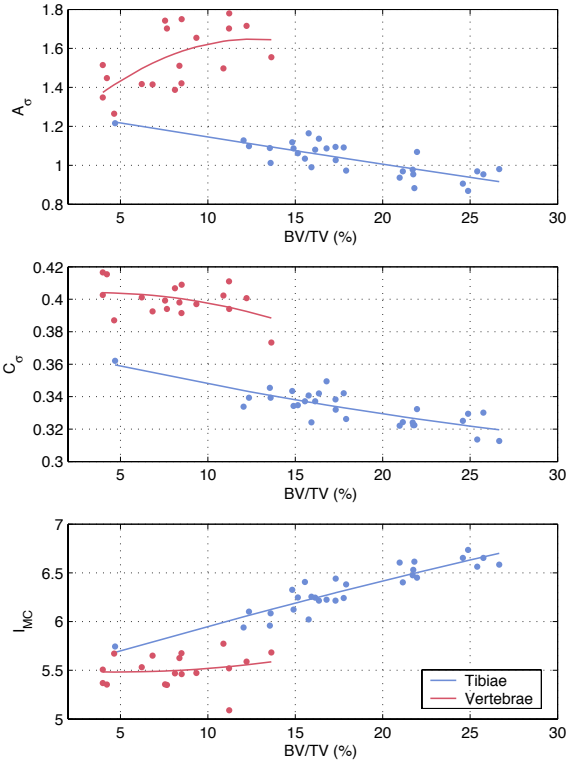

Figure 6: Measures of complexity vs. bone loss (represented by bone volume fraction BV/TV) for proximal tibiae (blue line) and lumbar vertebrae (red line). The lines are square-polynomial fits to guide the eye.

During bone loss, A_σ decreases in the vertebra, but increases in the proximal tibia. Moreover, for high density proximal tibiae (BV/TV $> 20\%$) its values are below one. This suggests that the normal trabecular bone in proximal tibial contains a large number of concave structures. Bone loss causes a shift from concave structures towards convex ones. A_σ for vertebra is higher than one. The Spearman's rank correlation coefficient between BV/TV and A_σ is $R = -0.75$ (proximal tibia) and $R = 0.57$ (vertebra). On a $p = 0.01$ significance level, the correlation for the proximal tibia is significant, but for the vertebrae it is not.

C_σ reveals the same trend for both proximal tibia and vertebra. I_{MC} reveals also the same trend for both skeletal sites. However, the direction of the correlations between C_σ and I_{MC} are opposite. The correlations are only significant for the proximal tibia. From the correlation between I_{MC} and BV/TV we infer that the complexity of the bone surface decreases during bone loss. The anti-correlation with C_σ suggests that the variety of shapes increases during bone loss, as it is the case when plate-like structures deteriorate towards rod-like structures, or rod-like structures become disconnected.

Next, we compare the introduced structural measures of complexity with some of the classical histomorphometrical measures (Tab. 1, Fig. 7). The majority of these measures are significantly correlated to the measures of complexity at the proximal tibia only. This is probably due to a higher variability of the shapes in proximal tibia.

The trabecular separation Tb.Sp measures the mean trabecular plate separation under the assumption that the bone tissue is distributed as parallel plates (Parfitt et al., 1983). At the vertebral body only A_σ is significantly correlated with Tb.Sp. At the proximal tibia both C_σ and I_{MC} are weakly correlated with Tb.Sp.

The nodes-termini ratio Nd/Tm represents the connectivity of the network as it appears on a 2D section (Garrahan et al., 1986). A change in the connectivity of the network causes a change in the complexity of bone surface. Therefore, at the proximal tibia we find that Nd/Tm is strongly correlated with I_{MC}. At the vertebral body Nd/Tm and I_{MC} are also correlated, but this correlation does not reach the level of significance.

A further common way to characterise the trabecular network is the trabecular bone pattern factor TBPf (Hahn et al., 1992). It is, like Nd/Tm, strongly related with the suggested measures of complexity, in particular with I_{MC}. Again, for vertebrae these correlations are not significant.

These results confirm that the averaged shape index A_σ, shape complexity C_σ and marching cubes entropy index I_{MC} express the shape and complexity of the trabecular micro-architecture. The different aspects of the introduced measures of complexity are clearly illustrated at the proximal tibia and by comparing tibia and vertebral trabecular bone architectures. We proved quantitatively that the architecture of the trabecular bone of lumbar vertebra is very different from that of the proximal tibia. This difference is also clearly emphasised by the new structural measures. Therefore, we infer that these measures reveal additional information about the bone structure, which are not included in BV/TV or any of the histomorphometric measures.

Table 1: Spearman's rank correlation coefficients between structural measures of complexity and bone volume fraction as well as histomorphometrical measures. Statistically significant values ($p = 0.01$) are black, non-significant values are gray.

	A_σ	C_σ	I_{MC}
Proximal Tibiae			
BV/TV	−0.75	−0.72	0.88
Tb.Sp	0.45	0.58	−0.64
Nd/Tm	−0.72	−0.65	0.88
TBPf	0.72	0.66	−0.90
Lumbar Vertebrae			
BV/TV	0.57	−0.27	0.25
Tb.Sp	−0.71	0.26	−0.19
Nd/Tm	0.38	−0.07	0.34
TBPf	−0.35	0.14	−0.41

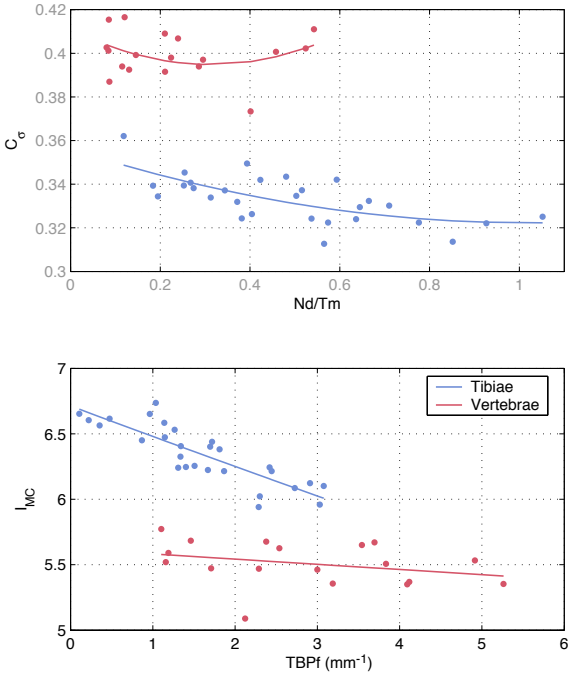

Figure 7: Measures of complexity vs. Nd/Tm and TBPf for proximal tibiae (blue line) and lumbar vertebrae (red line). The lines are squared fits to guide the eye.

The relationships we found between the developed measures and the bone architecture as well as the relation between the structural complexity measures and the histomorphometric parameters suggest that the proposed new measures of complexity are able to quantify 3D bone architecture. In addition, they contain important information about the trabecular geometry and can be used to describe changes in the spatial structure of trabecular bone.

5 CONCLUSIONS

Using the newly introduced measures, we were able to find significant differences in 3D bone architecture at different levels of bone loss including osteopenia and osteoporosis. We found that the trabecular bone of the proximal tibia contains more concave structures than of lumbar vertrebra. The amount of concave structures decreases during bone loss, while the proportion of convex structures increase. Similarly, the complexity of the bone surface is decreasing during bone loss. Although the complexity of the trabecular bone structure is higher in healthy bone, the order of the shapes of local structures depending on its volume is higher in healthy bone. This means that osteoporotic structural elements of a given volume have a higher variability in the shape than healthy bone.

The proposed new structural measures of complexity can be directly computed from 3D images and, thus, are non-invasive and non-destructive. They contain important information about the 3D structure of trabecular bone and can be used to describe the deterioration of the trabecular bone network that takes place during the development of osteopenia and osteoporosis.

ACKNOWLEDGEMENTS

This study was made possible in part by grants from the Microgravity Application Program/ Biotechnology from the Human Spaceflight Program of the European Space Agency (ESA) and support from Siemens AG and Scanco Medical AG. Scanco Medical AG is gratefully acknowledged for μCT scanning the bone samples. Erika May and Wolfgang Gowin, Carité Berlin, Campus Benjamin Franklin, are gratefully acknowledged for preparing the bone samples. Inger Vang Magnussen, University of Aarhus, is acknowledged for help preparing the bone samples for histomorphometry.

REFERENCES

Garrahan, N. J., Mellish, R. W. E., and Compston, J. E. A. (1986). A new method for the two-dimensional analysis of bone structure in human iliac crest biopsies. *Journal of Microscopy*, 142:341–349.

Hahn, M., Vogel, M., Pompesius-Kempa, M., and Delling, G. (1992). Trabecular bone pattern factor – a new parameter for simple quantification of bone microarchitecture. *Bone*, 13:327–330.

Hildebrand, T., Laib, A., Müller, R., Dequeker, J., and Rüegsegger, P. (1999). Direct Three-Dimensional Morphometric Analysis of Human Cancellous Bone: Microstructural Data from Spine, Femur, Iliac Crest, and Calcaneus. *Journal of Bone and Mineral Research*, 14:1167–1174.

Ito, M., Nakamura, T., Matsumoto, T., Tsurusaki, K., and Hayashi, K. (1998). Analysis of trabecular microarchitecture of human iliac bone using microcomputed tomography in patients with hip arthrosis with or without vertebral fracture. *Bone*, 23(2):163–169.

Lorensen, W. E. and Cline, H. E. (1987). Marching cubes: A high resolution 3d surface construction algorithm. *SIGGRAPH Comput. Graph.*, 21(4):163–169.

Marwan, N., Kurths, J., and Saparin, P. (2007a). Generalised Recurrence Plot Analysis for Spatial Data. *Physics Letters A*, 360(4–5):545–551.

Marwan, N., Saparin, P., and Kurths, J. (2007b). Measures of complexity for 3D image analysis of trabecular bone. *The European Physical Journal – Special Topics*, 143(1):109–116.

Parfitt, A. M., Mathews, C. H. E., Villanueva, A. R., Kleerekoper, M., Frame, B., and Rao, D. S. (1983). Relationships between Surface, Volume, and Thickness of Iliac Trabecular Bone in Aging and in Osteoporosis. *Journal of Clinical Investigation*, 72:1396–1409.

Saparin, P. I., Gowin, W., Kurths, J., and Felsenberg, D. (1998). Quantification of cancellous bone structure using symbolic dynamics and measures of complexity. *Physical Review E*, 58(5):6449.

Saparin, P. I., Thomsen, J. S., Prohaska, S., Zaikin, A., Kurths, J., Hege, H.-C., and Gowin, W. (2005). Quantification of spatial structure of human proximal tibial bone biopsies using 3D measures of complexity. *Acta Astronautica*, 56(9–12):820–830.

Stauber, M. and Müller, R. (2006). Volumetric spatial decomposition of trabecular bone into rods and plates – A new method for local bone morphometry. *Bone*, 38:475–484.

Thomsen, J. S., Ebbesen, E. N., and Mosekilde, L. (2000). A New Method of Comprehensive Static Histomorphometry Applied on Human Lumbar Vertebral Cancellous Bone. *Bone*, 27(1):129–138.

Thomsen, J. S., Laib, A., Koller, B., Prohaska, S., Mosekilde, L., and Gowin, W. (2005). Stereological measures of trabecular bone structure: comparison of 3D micro computed tomography with 2D histological sections in human proximal tibial bone biopsies. *Journal of Microscopy*, 218(2):171–179.

SINGLE PARTICLE DETECTION

A Diagnostic Tool for Particle Associated Diseases like Alzheimer's Disease and Creutzfeldt-Jakob Disease

Eva Birkmann*,**,[a], Susanne Aileen Funke**,[a], Detlev Riesner* and Dieter Willbold*,**
*Institut fuer Physikalische Biologie, Heinrich-Heine-Universitaet, Universitaetsstr. 1,40225 Dueselorf, Germany
**INB-2, Forschungszentrum Juelich, Juelich, Germany; [a] These authors contributed equally to this work.
birkmann@uni-duesseldorf.de, funke@fz-juelich.de, riesner@biophys.uni-duesseldorf.de,
dieter.willbold@uni-duesseldorf.de

Keywords: Fluorescence correlation spectroscopy, Alzheimer' disease, Creutzfeldt-Jakob disease, single particle detection.

Abstract: Neurodegenerative diseases like Alzheimer's disease (AD), prion diseases and others are progressive and lethal. High-molecular weight aggregates of the Amyloid-β-peptides (Aβ) or of the misfolded prion protein (PrP) are found in patients afflicted by AD or prion diseases, respectively. Despite of many attempts, neither a therapy for recovery, nor an early diagnosis at preclinical stages are available. Psychological tests and imaging approaches not directly related with a secure disease marker are in use only for late stages of the disease. The Creutzfeldt-Jakob-disease (CJD), a human prion disease, is caused by accumulation of aggregates consisting of an abnormally shaped version of PrP. CJD is diagnosed with certainty only by neuropathology *post mortem*. In this study a multidisciplinary development of a novel mode of single particle counting of immobilized Aβ and PrP aggregates as the most direct biomarkers for Alzheimer's disease and Prion diseases, respectively, is introduced. For ultrasensitive detection of aggregates, the suitable instrumentation as well as data acquisition and data analysis are developed using single molecule detection and advanced laser scanning fluorescence techniques. In the novel assay development effort biochemistry, detection and analysis were improved to detect single aggregates immobilised on a surface. First results show the improvement of single particle detection of PrP-aggregates of TSE-afflicted cattle and hamsters as well as synthetic Aβ-aggregates.

1 INTRODUCTION

In many neurodegenerative diseases e.g. prion diseases, Alzheimer's disease, Parkinson's disease, Huntington's Disease, protein aggregates are formed in the very beginning or in the progress of disease (Lee et al., 2005). Up to now it is not known, if these aggregates are causative agents or symptoms of the respective disease, but many studies show, that the aggregates or even oligomers of the according proteins are neurotoxic and therewith a reason of neurodegeneration. (Selkoe, 2003)

To understand the progression of these diseases, as well as disease associated or causative mechanisms and to monitor potential therapeutically approaches an ultrasensitive tool to quantify these disease related aggregates is required. A challenge for the analytic system is to reliably count only those aggregates or oligomers that consist of the specified protein or peptide. Monomeric molecules need to be clearly distinguished because they are present in healthy organism as well.

We developed a new method, which is able to count single protein aggregates bound by a capture-antibody to a surface (surface-FIDA) (Birkmann et al., 2007). Our new test system is based on fluorescence correlation spectroscopy (Eigen and Rigler, 1994). It is quantifying the number and size of aggregates simultaneously labelled by two different antibodies for dual colour fluorescence intensity distribution analysis (2D-FIDA) (Birkmann et al., 2006). Only aggregates and oligomers but not monomeric proteins are counted. To increase the sensitivity, particles were concentrated in the two-dimensional space by immobilizing it to capture antibodies on the surface of the slide. Laser beams are scanning the surface systematically, so even single particles are detected (Birkmann et al., 2007).

We report on the successful use of surface-FIDA as diagnostic tool for prion diseases. The infectious agents of prion diseases are composed primarily of the pathogenic isoform of the prion protein designated PrP^{Sc}, which is generated by a conformational change of the cellular isoform PrP^{C}. In contrast to its cellular isoform, the pathogenic isoform PrP^{Sc} forms insoluble aggregates. Hitherto accredited prion tests use the PK-resistance of PrP^{Sc} as a marker for the disease. Because of varying portions of disease related aggregated PrP, which is not PK-resistant, these prion tests offer only a limited sensitivity. Therefore prion protein aggregate detection, which does not rely on PK-digestion, is favourable for sensitive diagnosis. It allows detection of both, PK-resistant and PK-sensitive PrP^{Sc} aggregates.

Up to now, we could successfully verify the novel test system for correct diagnosis of Scrapie-infected hamsters as well as BSE-infected cattle in the clinical stages of diseases (Birkmann et al., 2007). Furthermore, we were able to detect PrP aggregates in the cerebrospinal fluid of cattle of BSE-infected cattle for the first time (Birkmann et al., 2007). During the next steps we will adopt the highly sensitive test system for diagnosis of human prion diseases like Creutzfeldt-Jakob disease and other aggregate related diseases, especially Alzheimer's disease.

In this study we apply surface-FIDA to different disease associated aggregates. First we show the single aggregate detection of prion protein aggregates purified from brain homogenates of Scrapie-infected hamsters and BSE-infected cattle to demonstrate the principal of surface-FIDA to detect single particles. In the second part of the work we show the transfer of surface-FIDA to the detection of single Aβ aggregates as diagnostic approach for Alzheimer's disease. Therefore we compared the detection of Aβ aggregates in solution with the application of surface-FIDA.

2 MATERIALS AND METHODS

2.1 Fluorescence Labelling of Antibodies

Antibodies R1 were kindly provided by S.B. Prusiner, UCSF, USA (Williamson et al., 1998). Antibodies 12F10 and Saf32 were obtained from SpiBio (Massy Cedex, France); antibody D18 was obtained from InPro (San Francisco, USA). For the detection of Aβ aggregates, antibodies 6E10 (Sigma Aldrich, Hamburg, Germany), 8G7, 19H11 and 4G8 (Calbiochem) were purchased.

Antibodies were labelled in free amino groups via reactive succinimidyl ester groups of Alexa-633 and Alexa-488 (Molecular Probes, Oregon, USA). For labelling, approximately 50 µg antibodies were incubated with 5 µg dye in carbonate buffer, pH 8.4 in a total volume of 100 µl for 1 hour. Conjugates were separated from free dye by gel filtration via NAP5-column (Pharmacia) with 10 mM TBS, pH 7.2 and 0.2 M NaCl as elution buffer. Labelled antibodies were stored in the dark at 4°C.

2.2 Fluorescence Correlation Spectroscopy

In fluorescence correlation spectroscopy (FCS) the fluorescence intensity is recorded in a very small volume, i.e. in the femtoliter range. Measurements were performed with the instrument FCS Olympus IX 50 (Evotec OAI, Hamburg, Germany) with a beam scanner unit in dual-colour mode with an Argon ion laser (excitation wavelength 488/514 nm) and a helium-neon laser (excitation wavelength 633 nm). The beam scanner unit allows the scanning of the sample for aggregates. In practice the detection volume is moved through the sample in horizontal and vertical dimensions. The beam scanner was used by moving 1 mm in one direction a rectangular deviation of 100 µm with a frequency of 50 Hz and an integration time of 50 µs. A piezo element was integrated in the optic of the FCS Olympus IX 50, which allowed a precise z-positioning of the focus in the 100 nm range.

2.3 Surface-FIDA

The surface-FIDA assay was carried out as described by earlier (Birkmann et al., 2007).

Briefly, 0.25 – 1 µg capture antibody was adhesively bound to poly-D-lysine activated glass surfaces. After blocking the unspecific binding sites with 10 % fetal calf serum, potentially present aggregates were bound to the capture by incubating 20 µl of a sample for at least two hours at 4 °C. After washing twice with PBS buffer (140 mM NaCl; 2.7 mM KCl; 10 mM Na_2HPO_4, pH 7.4), the fluorescence labelled detection antibodies were applied (0.1 µg/µl) and incubated for 1 h at 20 °C. After five washing steps with PBST (PBS with 0.1 % (w/w) Tween 20) and two washing steps with PBS, the measurements were carried out.

2.4 Preparation of Synthetic Aß-aggregates

Aβ(1-42) was purchased from JPT Peptide Technologies (Berlin, Germany). For aggregate preparation Aβ was dissolved in DMSO to 400 µM, diluted to 66 µM in PBS (140 mM NaCl; 2.7 mM KCl; 10 mM Na_2HPO_4) and incubated for five days at 37 °C. Aggregate formation was monitored using Thioflavin T (ThT) assay. For that, 10 mM ThT (Sigma, Hamburg, Germany) was added to the samples. Fluorescence was monitored with a microplate reader at excitation and emission wavelengths of 440 nm and 490 nm, respectively (Polarstar Optima, BMG, Offenburg, Germany).

For surface-FIDA, the aggregates were diluted 1:10 in pooled CSF of healthy people. CSF was obtained by Biochemed Services, Winchester, USA).

3 RESULTS

3.1 Methodical Setup

The new optical method for detection of protein aggregates is based on fluorescence intensity distribution analysis (FIDA). For detection of pathologic protein aggregates single molecule detection (SMD) combined with quantification of single aggregates immobilised on a relatively large surface was employed to achieve high sensitivity and specificity.

The new method, therefore, is called surface-FIDA. It is able to count single protein particles bound to a capture-antibody on the surface (fig. 1a) (Birkmann et al., 2007). Specific protein-particles are labelled simultaneously by two different antibodies for dual colour fluorescence intensity distribution analysis (2D-FIDA). Among the capture and both detection antibodies, at least two antibodies bind the same epitope. Thus, only aggregates but not monomers are counted. A laser beam scans the two-dimensional surface systematically in a double-meander mode. Thus, even single protein-particles are detected (fig. 1B). By utilising two lasers simultaneously two different fluorescence labels can be crosscorrelated. Only if the different labels are bound to the same aggregate both labels occur to the same time in small detection focus. A typical distribution of a coincident signal of double labelled aggregates is shown in fig. 1C.

3.2 Detection of Pathological Protein Particles with Surface-FIDA

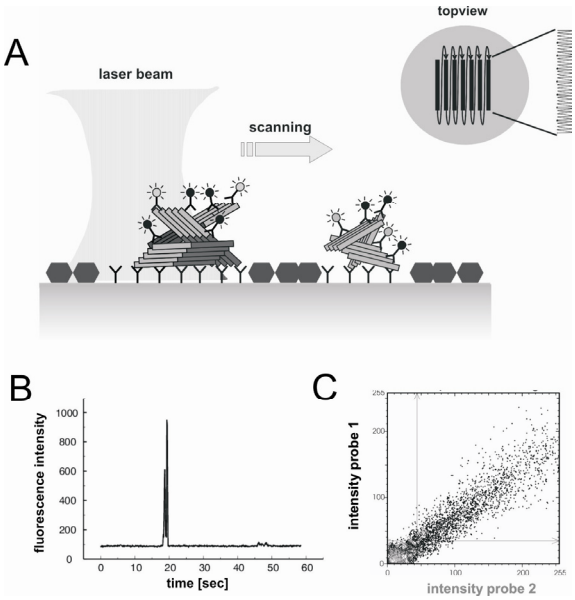

Figure 1: A) Scheme of surface-FIDA; B) fluorescence peak caused by the labelled aggregate: principal of particle counting; C) 2D-FIDA:Two probes with different fluorescence labels were used; Only simultaneous binding of both probes to the aggregates results in the specific diagonal signal distribution as shown in the plot

To observe, if the surface-FIDA setup is able to detect single aggregates different types of protein aggregates were tested.

3.2.1 PrP-particles Purified from Brain of Scrapie Infected Hamsters

Prion Protein aggregates were purified from brain homogenates of Scrapie infected hamsters in the clinical state of disease by NaPTA precipitation (Safar et al., 1998). The antibody R1 (Williamson et al., 1998) served as capture. The antibodies D13 and R1 were fluorescence labelled and utilized as detection probes. Same treated brain homogenates of healthy hamsters were used as control samples. The results of 2D-surface-FIDA in different distances to the surface are shown in fig. 2. In the samples of Scrapie infected hamsters at all distances between 10 µm and 20µm fluorescence peaks with high fluorescence intensity in both channels could be detected. At distances below 10 µm background signal in the control sample rise and in distances above 20 µm the signals of the Scrapie samples descended (data not shown).

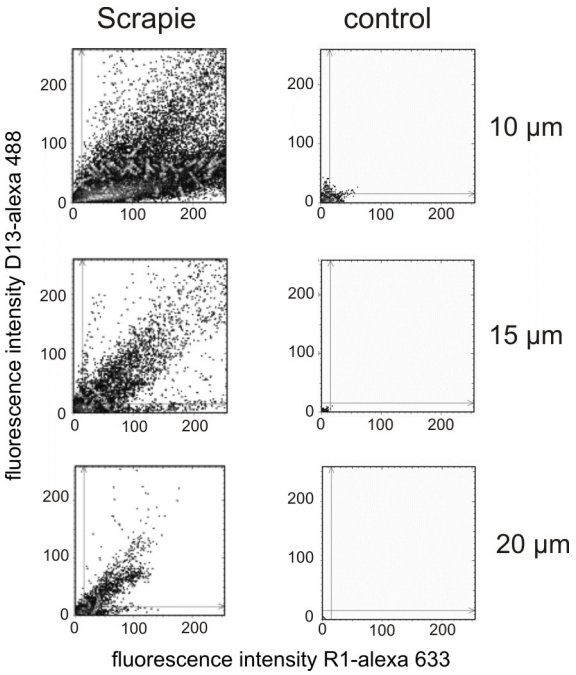

Figure 2: 2D-surface-FIDA of PrP-aggregates purified from brain homogenate of Scrapie infected hamsters and same treated brain homogenate of a healthy control in different distances to the surface 10-20 µm.

3.2.2 PrP-particles Purified from Brain of BSE Infected Cattle

Prion Protein aggregates were purified from brain homogenates of BSE infected cattle in the clinical state of disease by NaPTA precipitation (Safar et al., 2002). The antibody Saf32 (Krasemann et al., 1999) served as capture. The antibodies 12F10 and Saf32 were fluorescence labelled and utilized as detection probes. Same treated brain homogenates of healthy cattle were used as control samples. The results of 2D-surface-FIDA at different distances to the surface are shown in fig. 3.

3.2.3 Synthetic Aβ-Aggregates

As a first proof of principle, synthetical Aβ aggregates were used in the assay described above. First measurements were done in solution without immobilizing the aggregates. The antibodies 6E10 (N-terminal epitope) and 8G7 (C-terminal epitope) were fluorescence labelled and used as detection probes. Experiments were done in PBS. In the negative control, 0.2 % SDS was used to prevent Aβ aggregation, as monitored by ThT assay (data not shown). As expected, only aggregated Aβ resulted in fluorescence peaks as can be seen in fig. 4a.

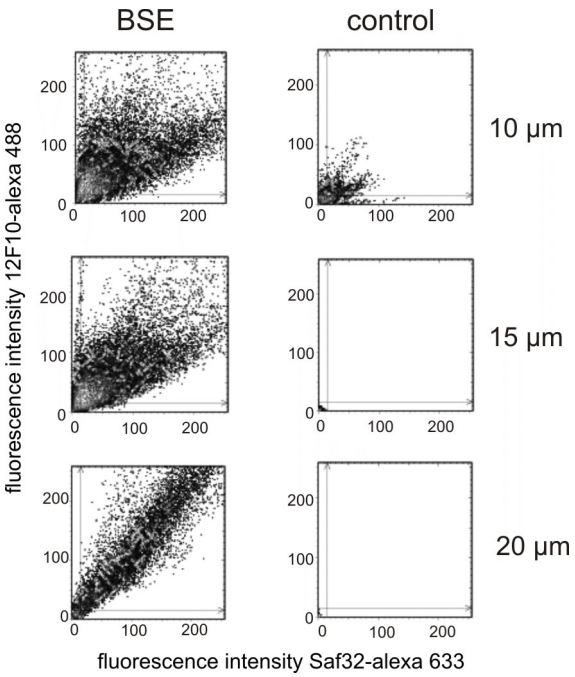

Figure 3: 2D-surface-FIDA of PrP-aggregates purified from brain homogenate of BSE infected cattle and same treated brain homogenate of a healthy control.

In a next step, Aβ aggregates diluted 1:10 in CSF to meet realistic conditions were immobilized on the surface of the slide. Antibody 4G8 (binding to amino acids 1-17 of Aβ) served as capture. The antibodies 6E10 and 19H11 were fluorescence labelled and served as detection probes. As both antibodies bind to the N-terminal part of Aβ, a simultaneous labelling of Aβ monomers was excluded. As controls, only CSF without additional Aβ aggregates was used in the immobilization procedure. The results of 2D-surface-FIDA are shown in fig. 4b. The measurements were done at 5 µm distance to the surface.

4 CONCLUSIONS

The proof of principle for the use of surface-FIDA to detect aggregates was shown for natural PrP-aggregates purified from brain of Scrapie infected hamsters, BSE infected cattle and for synthetic Aβ aggregates diluted in CSF.

Single particle counting as diagnostic tool is more sensitive as compared to measuring the integrated signal of all or many particles. “Single particle counting” allows measuring of multiple

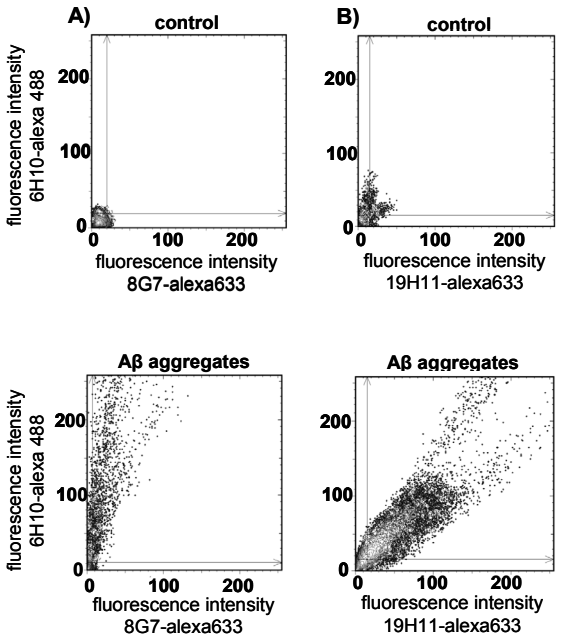

Figure 4: A) 2D-FIDA of synthetically prepared Aβ aggregates in solution (concentration 3,3 µM). Aβ, kept from aggregation by 0.2 % SDS, was used as control. B) 2D-surface-FIDA of synthetically prepared and in CSF diluted Aβ aggregates (concentration 6µM). CSF without additional Aβ aggregates was used as control. Measurements were done at 5 µm distance to the slide surface.

parameters of the individual particles are recorded like size, number of epitopes, different epitopes on the same particle etc. and those parameters can be used for improvement of specificity.

When the detection of single particles was carried out in suspension using the dual colour fluorescence intensity distribution analysis (2D-FIDA) (Birkmann et al., 2006), it was done in a small volume taken from a much larger sample volume by moving the laser detection focus through a cuvette. Diffusion of the particles and scanning of the volume were superimposed so that it was difficult to account quantitatively for all particles in the sample. Therefore the immobilisation of the particles on a surface had a major impact of the sensitivity of the whole assay, because it allows searching for the particles in a systematical way.

In the near future, we will develop surface-FIDA into an ultrasensitive diagnostic assay for particle associated disease, especially CJD and Alzheimer's disease. Such an assay will allow early diagnosis of AD and CJD using a minimally invasive approach in the living patient. In addition, such a diagnostic tool will be crucial for on line monitoring of disease progression and progress of a therapeutic approach.

Table 1: Sensitivity and Specificity Characteristics of surface-FIDA.

sensitivity	specificity
Concentration of particles on two dimensional surface	Simultaneous binding of three probes (one capture, two detection probes)
Single particle detection	Adjustable washing steps
Reproducible and complete counting of all aggregates by surface scanning	Detection of protein aggregates only, no monomers

ACKNOWLEDGEMENTS

This work was supported by the Ministry for Environment and Nature Protection, Agriculture and Consumer Protection of North Rhine-Westphalia (grant VI-1-17.90.01), Forschungs- und Innovationfonds of the Heinrich-Heine-University of Duesselsdorf and EU NoE Neuroprion. We gratefully acknowledge Dr. Prusiner for supplying the antibody R1, D13 and the scrapie brain material with negative controls. We would also like to thank Dr. M. Groschup, Friedrich-Loeffler-Institut (FLI), Institute for Novel and Emerging Infectious Diseases, for supplying BSE material of infected cattle and negative controls.

REFERENCES

Birkmann, E., Schäfer, O., Weinmann, N., Dumpitak, C., Beekes, M., Jackman, R., Thorne, L., Riesner, D., 2006. *Detection of prion particles in samples of BSE and scrapie by fluorescence correlation spectroscopy without proteinase K digestion.* Biol. Chem. 387, 95–102.

Birkmann, E., Henke, F., Weinmann, N., Dumpitak, C., Groschup, M., Funke A., Willbold, D., Riesner, D. 2007. *Counting of single prion particles bound to a capture-antibody surface (surface-FIDA)*
Vet. Microbiol. (2007), in press

Eigen, M. and Rigler, R. (1994). *Sorting single molecules – application to diagnostics and evolutionary biotechnology*. Proc. Natl. Acad. Sci. USA 91, 5740–
5747.

Krasemann S, Jurgens T, Bodemer W., 1999. *Generation of monoclonal antibodies against prion proteins with an unconventional nucleic acid-based immunization strategy*. J. Biotechnol. 73, 119-29.

Lee C, Yu MH., 2005 *Protein folding and diseases.* J Biochem Mol Biol. 2005; 38(3), 275-80

Safar, J., Wille, H., Itri, V., Groth, D., Serban, H., Torchia, M., Cohen, F.E., Prusiner, S.B., 1998. *Eight prion*

strains have PrP(Sc) molecules with different conformations Nat. Med. 10, 1157-1165.

Safar, J.G., Scott, M., Monaghan, J., Deering, C., Didorenko, S., Vergara, J., Ball, H., Legname, G., Leclerc, E., Solforosi, L., Serban, H., Groth, D., Burton, D.R., Prusiner, S.B., and Williamson, R.A., 2002. *Measuring prions causing bovine spongiform encephalopathy or chronic wasting disease by immunoassays and transgenic mice.* Nat. Biotechnol. 20, 1147-1150.

Selkoe, D.J. 2003, *Folding proteins in fatal ways* Nature 426; 900-904

Williamson, R.A., Peretz, D., Pinilla, C., Ball, H., Bastidas, R.B., Rozenshteyn, R., Houghten, R.A., Prusiner, S.B., Burton, D.R., 1998. *Mapping the prion protein using recombinant antibodies.* J. Virol. 72, 9413-8.

SPECTRAL AND CROSS-SPECTRAL ANALYSIS OF CONDUCTANCE CATHETER SIGNALS

New Indexes for Quantification of Mechanical Dyssinchrony

Sergio Valsecchi
Medtronic Italia, Rome, Italy
sergio.valsecchi@medtronic.com

Luigi Padeletti
University of Florence, Florence, Italy
lpadeletti@interfree.it

Giovanni Battista Perego
Istituto Auxologico Italiano, Ospedale S Luca, Milan, Italy
perego@auxologico.it

Federica Censi, Pietro Bartolini
Dept Technologies and Health - Italian National Institute of Health, Rome, Italy
federica.censi@iss.it, pietro.bartolini@iss.it

Jan J. Schreuder
Dept of Cardiac Surgery, San Raffaele Hospital, Milan, Italy
schreuder@libero.it

Keywords: Conductance catheter, spectral analysis, coherence function, heart failure, mechanical ventricular dyssynchrony.

Abstract: We hereby present novel index to quantify ventricular mechanical dyssynchrony by using spectral and cross-spectral analysis of conductance catheter volume signals. Conductance catheter is a volume measurement technique based on conductance measurement: the intraventricular volume, i.e. the time-varying volume of blood contained within the heart cavity, is estimated by measuring the electrical conductance of the blood employing a multi-pole catheter. Five segmental volume signals (SV_i, i=1,…5) can be acquired; total volume (TV) is estimated as the instantaneous sum of the segmental volumes. We implemented classical time-domain dyssynchrony indexes already utilized in conductance catheter signals analysis, and new frequency-domain indexes. Study population consisted of 15 heart failure (HF) patients with left bundle branch block and 12 patients with preserved left ventricular (LV) function. We found that spectral measures seem to out-perform classical time-domain parameters in differentiating atrial HF patients from no-HF group. These findings encourage the use of spectral analysis to obtain crucial quantitative information from conductance catheter signals.

1 INTRODUCTION

In a normal heart, mechanical activation of the ventricles occurs in a coordinated manner and depends on the rapid spread of electric signals via specialized fibers (His-Purkinje system) which branch out throughout the right ventricular (RV) and left ventricle (LV) endocardium (Uhley, 1960). When the activation is slowed-down or blocked, ventricle activation and contraction become dyssynchronous. Ventricular mechanical dyssynchrony is most commonly identified clinically by a prolonged QRS duration with left bundle-branch block (LBBB) morphology on surface

electrocardiogram but can also be detected by echocardiographic imaging of contraction timing.

Ventricular mechanical dyssynchrony plays a regulating role already in normal physiology (Brutsaert, 1987) but is especially important in pathological conditions, such as hypertrophy (Villari et al., 1996), ischemia (Heyndrickx and Paulus, 1990), infarction (Gepstein et al., 1998), or heart failure (HF) (Nelson, 2000). Dyssynchrony exacerbates heart failure (HF) in a variety of ways, generating cardiac inefficiency as well as pathologic changes at the biologic tissue, cellular, and molecular levels. Currently, the conductance catheter method has been extensively used to assess global systolic and diastolic ventricular function. More recently the ability of this instrument to pick-up multiple segmental volume signals has been used to quantify mechanical ventricular dyssynchrony.

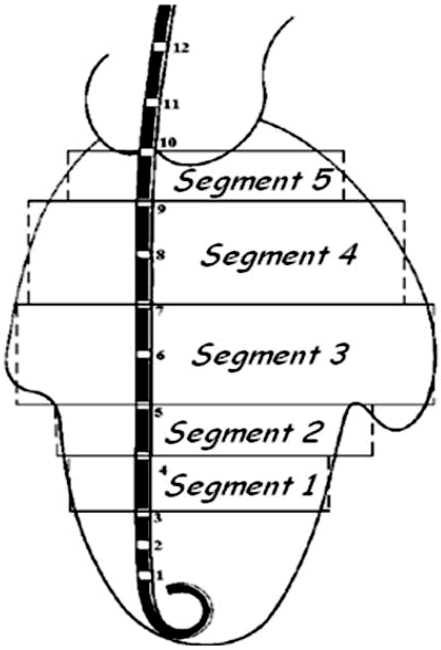

Figure 1: The conductance catheter positioning inside the left ventricle.

Conductance catheter was first introduced in 1981, by Baan and co-workers as a new volume measurement technique based on conductance measurement (Ban et al., 1981, Ban et al., 1984). Intraventricular volume, i.e. the time-varying volume of blood contained within the heart cavity, is estimated by measuring the electrical conductance of the blood employing a multi-pole catheter (conductance catether, Figure 1). The conductance catheter has 12 electrodes and should be positioned along the long axis of the LV in such a way that the electrode at the tip is situated within the apex and the proximal one just above the aortic valve. A weak alternating current (0.4 mA peak-to-peak, 20 kHz) is induced between the two most distal and two most proximal electrodes, in order to set up an electrical field within the ventricular cavity. Other 6 electrodes are used pair wise to measure segmental conductance signals. Two electrodes are used to record the intracardial ECG. A micromanometer measures real-time LV pressure. The induced voltage is then measured with six electrodes in between, yielding 5 segmental voltages. Since the conductance of the blood itself is constant (neglecting long term changes in haematocrite) the measured voltage will be proportional to blood resistivity, and thus inversely proportional to the conductance or amount of blood between the measuring (voltage) electrodes. This method has several advantages over other methods which determine intra-ventricular volumes. The results are obtained immediately, i.e. on-line, and precise geometric assumptions regarding the ventricle or labor-intensive analyses are not required. Recently, Steendijk et al., first introduced time-domain quantitative indexes of dyssynchrony based on volume signals acquired with the conductance catheter (Steendijk et al., 2004). Spectral analysis of conductance catheter signals has not been tempted yet. Frequency domain analysis has been extensively used to characterize a number of physiological signals, with promising results in terms of both classification schemes (Schumann et al., 2002, 1 Zywietz et al., 2004, Severi et al., 1997) and understanding of physiological mechanisms (Asyali et al., 2007, Cerutti et al., 1988, Montano et al., 2001). During ventricular dysfunction, segmental ventricular volumes experience abnormal changes which could result in unexpected spectral components. Also, the asynchrony and incoordination between ventricular segments, that seem to be quintessential to ventricular dysfunction, could be promisingly explored by cross-spectral analysis. The coherence spectrum is a frequency domain measure that may be used to make a quantitative comparison between activity of two heart regions. In the present study, coherence spectra have been used to quantify the relation between spectral components of ventricular volumes from different regions. The coherence spectrum would provide a measure of the synchrony and coordination between ventricular sites, and thus be indicative of the organization of electrical activity. Such a measure would be a useful tool in the

characterization and detection of synchronous contraction. Coherence measurements may provide a means to quantify the terms "synchronous" and "dissynchronous" as applied to ventricular contraction.

Aim of this paper is to characterize the conductance catheter signals in the frequency domain and to propose new indexes for ventricular mechanical dyssynchrony quantification.

2 METHODS AND MATERIALS

2.1 Study Population

The study population consisted of 27 consecutive patients with indications for electrophysiologic study or device implantation: 15 HF patients with left bundle branch block and 12 patients with preserved LV function. Table 1 shows the clinical characteristics of the study population. Age, sex and QRS duration were similar between groups. Subjects with a previously implanted device, valvular insufficiency or stenosis were excluded from analysis.

Table 1: Clinical characteristics of the study population.

	non-HF group (n=12)	HF group (n=15)
Male gender, n	7	11
Age, years	67±14	68±6
Ischemic Cardiomyopathy, n	-	7
NYHA Class	-	3.1±0.5
Ejection Fraction, %	57±9	26±6*
QRS duration, ms	88±21	167±24*
p-values: * < 0.05		

2.2 Experimental Protocols

A conductance catheter was placed in the LV via the femoral artery, and a temporary pacing lead was positioned in the right atrium. The conductance catheter enables online measurement of 5 segmental volume (SV_i, i=1,…,5) slices perpendicular to the LV long axis. We used 7-Fr combined pressure-conductance catheters with 1-cm interelectrode spacing (CD Leycom; Zoetermeer, The Netherlands). The catheter was connected to a Cardiac Function Lab (CD Leycom) for online display and acquisition (sample frequency 250 Hz) of segmental and LV total volumes (TV), LV pressure, and ECG. TV was obtained as the instantaneous sum of the segmental volumes.

Two stimulation protocols have been used, i.e. during spontaneous ventricular activation and atrial pacing. For this protocol, hemodynamic status was evaluated using multiple parameters. Indices of LV pressure, volume, and function were calculated and averaged over 8 to 10 beats at end expiration from the raw LV pressure and conductance volume data. Sequences of 30 s, i.e. 40-50 consecutive non-arrhythmic cardiac cycles at fixed heart rate induced by atrial pacing (at 10 bpm above the sinus rate) and steady-state conditions, were selected for off-line analysis using custom-designed software.

2.3 Classical Dyssynchrony Parameters Estimation

From the conductance catheter signals, we estimated the following classical time-domain parameters: mechanical segmental dyssynchrony (DYS), Internal flow fraction (IFF), Mechanical Dispersion (DISP), Cycle Efficiency (CE) and Time exceeding aortic closure (TExAC). See appendix for more details.

2.4 Spectral and Cross-Spectral Analysis

First we analysed the segmental and total volume signals in the frequency domain. For the spectral analysis, the periodogram of the signals was estimated. To reduce spectral leakage a Hamming window was applied after removal of the mean value. The length of segments was 1000 samples and a segment-overlap of 30% was used. Then we divided the signal bandwidth in 4 frequency bands (0-1 Hz, 1-5 Hz, 5-20 Hz and >20 Hz), and we estimated the percentage powers (PP) and the peak frequencies (PF) in each bands ($PP_{0\text{-}1Hz}$, $PP_{1\text{-}5Hz}$, $PP_{5\text{-}20Hz}$, $PP_{>20Hz}$ and $PF_{0\text{-}1Hz}$, $PF_{1\text{-}5Hz}$, $PF_{5\text{-}20Hz}$, $PF_{>20Hz}$, respectively).

The continually changing temporal or phase relationship between two volume signals has been quantified in the frequency domain by magnitude-squared coherence (Ropella et al., 1989). Magnitude-squared coherence (C(f)) between two recordings is defined as

$$C(f) = \frac{\left|S_{xy}(f)\right|^2}{S_{xx}(f)S_{yy}(f)}$$

Where x(t) and y(t) are two simultaneous recordings, Sxy is the cross power spectrum between signals x and y, and Sxx and Syy are the individual power spectra for signals x and y, respectively. C(f) is a measure of the linear relation between signals as a

function of frequency, f, and is a real quantity with value between zero and one. In other terms, C(f) measures the constancy of the time delay (phase) at a specific frequency between signals x and y. Two linearly related signals (in the absence of noise) will have a C(f) function equal to one at all frequencies present in both signals, while two random, uncorrelated signals will have a C(f) equal to zero at all frequencies. Any linear operation (multiplication by a constant or addition of a constant) on one or both of the signals will not alter the C(f) between x and y. However, additive, uncorrelated noise and system nonlinearities will reduce C(f) for two similar signals. C(f) may be estimated for sampled data using a method of overlapped and averaged FFT spectral estimates (Carter et al., 1973). Basically, estimates of Sxx, Syy and Sxy are determined using a periodogram technique (2048-samples long window, overlap 512 samples), and their estimates are then used in the definition of C(f).

The C(f) functions between each segmental volume SVi and the TV have been estimated. A Total Coherence function has been defined over the band 0-125 Hz by averaging the 5 C(f) functions. From the Total Coherence function, 5 new frequency domain indexes have been extracted:

- mean value of the Total Coherence over the band 0-125 Hz (Coh_{Tot})
- mean value of the Total Coherence from 0 to 1 Hz ($Coh_{0\text{-}1Hz}$),
- mean value of the Total Coherence from 1 to 5 Hz ($Coh_{1\text{-}5Hz}$),
- mean value of the Total Coherence from 5 to 20 Hz ($Coh_{5\text{-}20Hz}$),
- mean value of the Total Coherence from 20 to 125 Hz ($Coh_{>20Hz}$).

2.5 Statistical Analysis

All data are presented as means±SD. Differences between distributions were compared by a t-test for

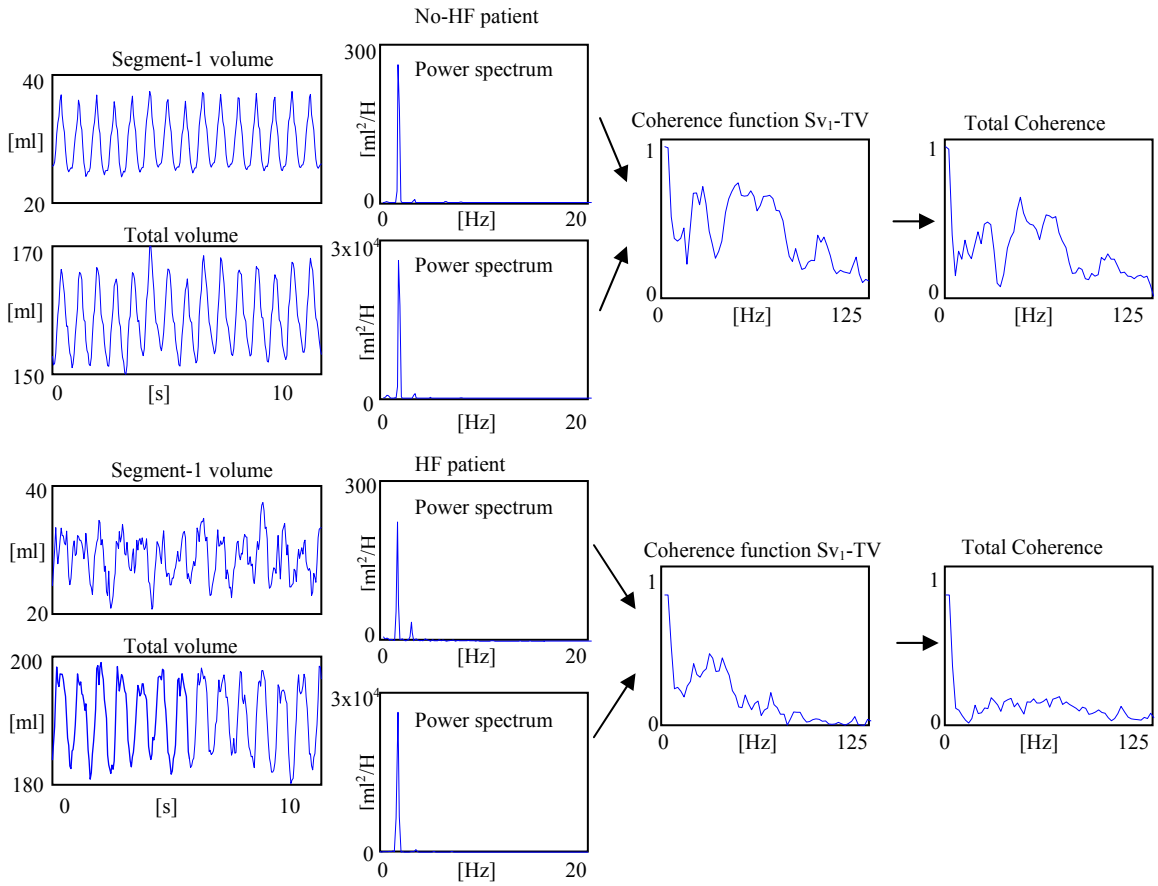

Figure 2: Examples of SV and TV time series and power spectra, for a no-HF patinet and a HF one. Coherence function between SV_1 and TV are showed, as well as the total coherence function.

Gaussian variables, and by Mann-Whitney nonparametric test for nongaussian variables. Statistical correlations between variables were tested by least-squares linear regression. A P value < 0.01 was considered significant. We performed receiver-operating characteristic (ROC) curve analysis to test the diagnostic performance of the indexes to discriminate the patient groups. Sensitivities and specificities at the optimal cut-off point were determined.

3 RESULTS

Example of the power spectrum of a TV signal are showed in figure 2, for a HF patient and a no-HF one. The coherence function between one SV and the TV and the Total coherence are also showed. The characteristics of the power spectrum of TV signals are reported in Table 2 (similar results were obtained for SVi signals, but were not reported). The majority of the signal power is in the band from 1 to 5 Hz (programmed heart rate during acquisition from 70 to 100 bpm). The components above 20Hz are associated to less than 1% of the total signal power. The frequency peak in the 0 – 1 Hz band matches with the respiratory rate and the power in this band seems higher in HF group. Table 3 summarizes the results of the comparison between groups for all indexes considered in the analysis, represented as mean ± standard deviation. Overall, 3 parameters permitted to discriminate the two groups ($p<0.01$): Coh1-5, Coh5-20 and CE. Table 4 shows the results of the ROC curve analysis. Sensitivity and specificity for Coh1-5 are 0.67 and 0.92, those obtained for Coh5-20 are 1.00 and 0.92 and those relatve to CE are 0.80 and 0.83, respectively. In Figure 3 the ROC curves are shown.

Table 2: Characteristics of the power spectrum of TV signal.

	no-HF	HF	p-values
$PP_{0\text{-}1Hz}$	4.34±6.26	9.12±12.00	0.071
$PF_{0\text{-}1Hz}$	0.41±0.17	0.45±0.12	0.488
$PP_{1\text{-}5Hz}$	93.24±6.45	88.44±11.85	0.194
$PF_{1\text{-}5Hz}$	1.52±0.20	1.44±0.13	0.301
$PP_{5\text{-}20Hz}$	2.16±1.84	2.21±1.34	0.946
$PF_{5\text{-}20Hz}$	8.37±0.88	7.63±0.80	0.036
$PP_{>20Hz}$	0.25±0.25	0.23±0.15	0.814
$PF_{>20Hz}$	37.59±5.12	44.14±7.59	0.013

4 DISCUSSION

Quantification of nonuniform mechanical function and dyssynchrony may lead to a more complete diagnosis of ventricular dysfunction (Schreuder wet al., 1997, Schreuder et al., 2000). Moreover, it may guide therapy, because patients with extensive dyssynchrony are likely to benefit from resynchronization therapy (Leclercq et al., 2002). The visualization of mechanical dyssynchrony provided by methods based on magnetic resonance imaging and echocardiography, although further emphasize the important role of mechanical dyssynchrony in cardiac dysfunction, requires laborious procedures and require substantial operator interaction and expertise.

Table 3: Indexes of mechanical dyssynchrony in no-HF and HF groups.

	no-HF	HF	p-values
DYS, %	26.0±7.2	32.6±3.9	0.012
IFF, %	25.8±18.8	40.8±13.6	0.033
DISP, ms	23.4±16.4	35.6±13.2	0.068
CohTot	0.44±0.07	0.37±0.10	0.016
Coh0-1	0.63±0.19	0.51±0.18	0.099
Coh1-5	0.69±0.10	0.57±0.10	0.004*
Coh5-20	0.47±0.07	0.32±0.04	0.000*
Coh>20	0.43±0.08	0.37±0.12	0.041
CE	0.78±0.12	0.58±0.16	0.000*
TExAC, ms	6.9±8.8	15.7±10.5	0.016

*p<0.01

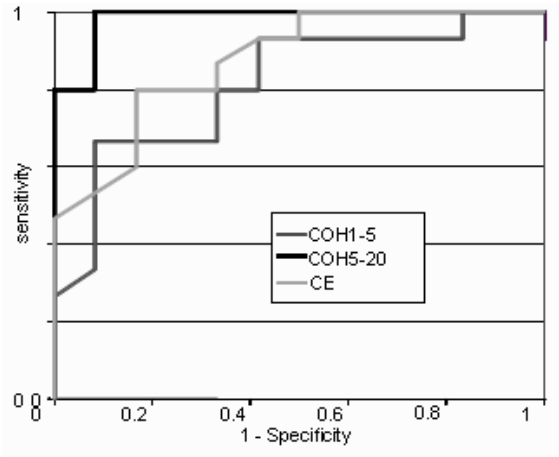

Figure 3: ROC curve analysis.

Table 4: ROC curve analysis of the tested variables.

	Area Under Curve (95% CI)	p-value	Cut-off
Coh1-5	0.81 (0.65-0.98)	0.006	0.57
Coh5-20	0.98 (0.94-1.02)	0.000	0.40
CE	0.88 (0.75-1.00)	0.001	0.70

Recently, novel indexes were introduce to quantify dyssynchrony based on volume signals acquired by the conductance catheter during cardiac catheterization (9). Such indexes were based on a time-domain approach and provided additional, new, and quantitative information on temporal and spatial aspects of mechanical dyssynchrony.

To our knowledge, conductance catheter volume signals have never been studied in the frequency domain. Since dyssynchrony refers to the organization of the mechanical contraction of the ventricle, it is natural to investigate such a phenomenon by spectral and cross-spectral analysis of ventricular segmental movements. The frequency-domain analysis can indeed discover particular aspects of interaction between volume signals beyond the temporal relationships.

Present analysis permitted to describe some characteristics of the conductance-volume signals. The frequency analysis evidenced the absence of relevant components above 20 Hz: this result corroborates the validation of segmental signals acquisition obtained by comparison with cine-computerized tomography (16), whose sampling rate has approximately the same value. The amplitude of the components in the range 0-1 Hz, attributable to the respiratory artefact, resulted markedly higher in HF patients, this may be due to the higher (mechanical) cardio-pulmonary interaction or to an altered vasovagal activity.

More interesting results have been obtained by cross-spectral analysis. The spectral coherence function provides a quantitative measure of that temporal synchrony and coordination between activities of ventricular regions. During synchronous mechanical contraction, multiple sites are activated in an coordinated manner, and the phase relation between activity from two sites is relatively unchanging, resulting in a high (close to 1) coherence. When ventricular contraction is dyssynchronous, the activity observed at one region is likely to be unrelated to the activity observed at other distant regions. Thus the coherence between two such sites would be very low at all frequencies due to a continually changing phase relation.

In the present study, the spectral coherence was confirmed to be significantly greater for ventricular contraction of no-HF patients than for HF ones. We found that the most significant parameters in the discrimination between HF and no-HF group were Coh1-5 and Coh5-20, with the latter reaching a sensitivity of 1 and a specificity of 0.92. Spectral measures seem to out-perform classical time-domain parameters (9) in differentiating atrial HF patients from no-HF group.

Since no previous studies have been performed on a similar topic, the frequency bands have been chosen on empirical basis. The choice of the optimal frequency bands in term of discriminating power would require larger population and/or modelling of ventricular contraction.

In conclusion, this paper encourages the use of spectral analysis to obtain crucial quantitative information from conductance catheter signals.

REFERENCES

Uhley H: Peripheral distribution of the canine A-V conduction system; observations on gross morphology. Am J Cardiol 5:688- 691, 1960.

Brutsaert DL. Nonuniformity: a physiologic modulator of contraction and relaxation of the normal heart. J Am Coll Cardiol 9: 341–348, 1987.

Villari B, Vassalli G, Betocchi S, Briguori C, Chiariello M, and Hess OM. Normalization of left ventricular nonuniformity late after valve replacement for aortic stenosis. Am J Cardiol 78: 66–71, 1996.

Heyndrickx GR and Paulus WJ. Effect of asynchrony on left ventricular relaxation. Circulation 81: 41–47, 1990.

Gepstein L, Goldin A, Lessick J, Hayam G, Shpun S, Schwartz Y, Hakim G, Shofty R, Turgeman A, Kirshenbaum D, and Ben-Haim S. A Electromechanical characterization of chronic myocardial infarction in the canine coronary occlusion model. Circulation 98: 2055–2064, 1998.

Nelson GS, Curry CW, Wyman BT, Kramer A, Declerck J, Talbot M, Douglas MR, Berger RD, McVeigh ER, and Kass DA. Predictors of systolic augmentation from left ventricular preexcitation in patients with dilated cardiomyopathy and intraventricular conduction delay. Circulation 101: 2703–2709, 2000.

Baan J, Jong TTA, Kerkhof PLM, et al. Continuous stroke volume and cardiac output from intraventricular dimensions obtained with impedance catheter. Cardivascular Research 1981;15:328-334.

Baan J, van der Velde ET, de Bruin HG, et al. Continuous measurement of left ventricular volume in animals and humans by conductance catheter. Circulation 1984;70:812-823.

Steendijk P, Tulner SAF, Schreuder JJ, et al. Quantification of left ventricular mechanical dyssynchrony by conductance catheter in heart failure patients. Am J Physiol 2004;286:H723-H730

Schumann A, Wessel N, Schirdewan A, Osterziel KJ, Voss A. Potential of feature selection methods in heart rate variability analysis for the classification of different cardiovascular diseases. Stat Med. 2002 Aug 15;21(15):2225-42.

Zywietz CW, Von Einem V, Widiger B, Joseph G. ECG analysis for sleep apnea detection. Methods Inf Med. 2004; 43(1):56-9.

Severi S, Cavalcanti S, Avanzolini G. Heart rate variability spectral indices for haemodynamic classification of haemodialysis patients. Physiol Meas. 1997 Nov; 18(4):339-53.

Asyali MH, Berry RB, Khoo MC, Altinok A. Determining a continuous marker for sleep depth. Comput Biol Med. 2007 Apr 12;

Cerutti S, Alberti M, Baselli G, Rimoldi O, Malliani A, Merri M, Pagani M. Automatic assessment of the interaction between respiration and heart rate variability signal. Med Prog Technol. 1988; 14(1):7-19.

Montano N, Porta A, Malliani A. Evidence for central organization of cardiovascular rhythms. Ann N Y Acad Sci. 2001 Jun;940:299-306. Review.

Ropella KM, Sahakian AV, Baerman JM, Swiryn S. The coherence spectrum. A quantitative discriminator of fibrillatory and nonfibrillatory cardiac rhythms. Circulation 1989;80:112-9.

Carter C, Knapp CH, Nuttall B. Estimation of the magnitudesquared coherence function via overlapped fast Fourier Transform processing. IEEE Trans Audio Electroacoustics. 1973;21:337-44.

Schreuder JJ, Steendijk P, Van der Veen FH, et al. Acute and short-term effects of partial left ventriculectomy in dilated cardiomyopathy: assessment by pressure-volume loops. J Am Coll Cardiol 2000;36:2104-2114.

Schreuder JJ, van der Veen FH, van der Velde ET, et al. Left ventricular pressure-volume relationships before and after cardiomyoplasty in patients with heart failure. Circulation. 1997;96:2978-2986.

Leclercq C, Kass DA. Retiming the failing heart: principles and current clinical status of cardiac resynchronization. J Am Coll Cardiol 39: 194–201, 2002.

APPENDIX

Mechanical dyssynchrony. At each time point, a segmental signal is defined as dyssynchronous if its change (i.e., dSV/dt) is opposite to the simultaneous change in the total LV volume (dTV/dt). Segmental dyssynchrony is quantified by calculating the percentage of time within the cardiac cycle that a segment is dyssynchronous. Overall LV dyssynchrony (DYS) is calculated as the mean of the segmental dyssynchronies. DYS may be calculated within each specified time interval, i.e. during systole and diastole, with systole defined as the period between the moments of dP/dtmax and dP/dtmin.

Internal flow. Nonuniform contraction and filling is associated with ineffective shifting of blood volume within the LV. This internal flow (IF) is quantified by calculating the sum of the absolute volume changes of all segments and subtracting the absolute total volume change:

$$IF(t) = \left[\sum \left|dSVi(t)/dt\right| - \left|dTV(t)/dt\right|\right]/2$$

Note that dTV(t)/dt represents the effective flow into or out of the LV. Thus IF measures the segment-to-segment blood volume shifts, which do not result in effective filling or ejection. Division by two takes into account that any non-effective segmental volume change is balanced by an equal but opposite volume change in the remaining segments. IF fraction (IFF) is calculated by integrating IF(t) over the full cardiac cycle and dividing by the integrated absolute effective flow.

Mechanical dispersion. In the HF patients, a substantial dispersion is present in the onset of contraction between the segments. This dispersion is assessed by segmental lag times which are determined by calculating the cross correlations between TV(t) and SV(t) for all systolic time points (i.e., between dP/dtmax and dP/dtmin). For each segment the lag which produces the highest linear correlation is determined. Mechanical dispersion (DISP) is defined as 2 standard deviation of the segmental lag times. Recently, new parameters have been introduced to quantify LV dyssynchrony with echocardiographic techniques. These indices can be directly applied to conductance method.

Cycle Efficiency. Calculated as previously described by the formula: CE=SW/[LVP* LV volume], with SW = stroke work, LVP = end-systolic – end-diastolic LV pressure. This index quantifies distortions in the shape of the pressure-volume diagram. The calculation assumes that the optimal contraction would have CE value near 1.0, corresponding to a rectangular pressure volume diagram. Decreases in cycle efficiency may be caused by multiple factors including isovolumic volume shifts as well as changes in afterload and ventricular stiffness. Similarly, regional cycle efficiency can be calculated from the most basal to the most apical segmental volume signal plotted against LV pressure. Differences in regional cycle efficiency during isovolumic filling or emptying may indicate inefficient patterns contraction or relaxation due to dyssynchrony.

Time exceeding aortic closure. In order to measure diastolic dyssynchrony and specifically to quantify LV contraction in diastolic phase, a new index was proposed, quantitatively reflecting the whole temporal amount spent by 12 LV segments in contracting after aortic valve closure. Using strain imaging that reflects myocardial deformation, the time of strain tracing exceeding aortic valve closure (ExcT) was measured in each segment as the interval between the marker of aortic closure and the nadir of the strain tracing. ExcT was considered 0 when the nadir of strain curve did not exceed aortic valve closure. The overall time of strain exceeding aortic valve closure (oExcT) was computed as the sum of the 12 segmental ExcTs. The index may be implemented in conductance method by considering each segment presenting a systolic phase (negative dSVi/dt) persisting during the phase of global diastole (positive dTV/dt). oExcT is estimated as the sum of these delays for all segments.

CARDIAC MAGNETIC FIELD MAP TOPOLOGY QUANTIFIED BY KULLBACK-LEIBLER ENTROPY IDENTIFIES PATIENTS WITH HYPERTROPHIC CARDIOMYOPATHY

A. Schirdewan, A. Gapelyuk, R. Fischer, L. Koch, H. Schütt, U. Zacharzowsky
R. Dietz, L. Thierfelder
Medical Faculty of the Charité, Franz-Volhard-Klinik, Helios Klinikum-Berlin, Wiltbergstr. 50, D-13125 Berlin, Germany

N. Wessel
Department of Physics, University of Potsdam, Am Neuen Palais 10, D-14415 Potsdam, Germany
wessel@agnld.uni-potsdam.de

Keywords: Patient screening, Cardiac magnetic field mapping, Kullback-Leibler entropy; Hypertrophic cardiomyopathy.

Abstract: Hypertrophic Cardiomyopathy (HCM) is defined clinically by the growing/thickening of especially the left heart muscle. In up to 70 % of cases, there is a family history of this condition. The individual risk for affected patients strongly varies and depends on the individual manifestation of the disease. Therefore, an early detection of the disease and identification of high-risk subforms is desirable. In this study we investigated the capability of cardiac magnetic field mapping (CMFM) to detect patients suffering from HCM (n=33, 43.8 ± 13 years, 13 women, 20 men; vs. a control group of healthy subjects, n=57, 39.6 ± 8.9 years; 22 women, 35 men; vs. patients with confirmed cardiac hypertrophy due to arterial hypertension, n=42, 49.7 ± 7.9 years, 15 women, 27 men). We introduce for the first time a combined diagnostic approach based on map topology quantification using Kullback-Leibler (KL) entropy and regional magnetic field strength parameters. The cardiac magnetic field was recorded over the anterior chest wall using a multichannel-LT-SQUID system. We show that our diagnostic approach allows not only detecting HCM affected individuals, but also discriminates different forms of the disease. Thus, CMFM including KL entropy based topology quantifications is a suitable tool for HCM screening.

1 INTRODUCTION

Hypertrophic cardiomyopathy (HCM) is a primary inherited cardiac muscle disorder characterized by hypertrophy, usually in the absence of other loading conditions, such as hypertension. In the general population, familial hypertrophic cardiomyopathy (FHCM) is the most common cardiovascular genetic disorder with a prevalence of about 1 in 500 adults. HCM is caused by mutations in several cardiac sarcomeric contractile protein genes. So far mutations in 11 different genes, including the cardiac ß-myosin heavy chain (ß-MHC), myosin-binding protein C (MyBP-C), cardiac troponins T and I, α-tropomyosin, myosin light chains and, more recently, titin and actin genes, have been identified (Seidman 1998, Thierfelder 1994). Histo-pathological hallmarks of HCM are myocyte hypertrophy with disarray and increased cardiac fibrosis, leading to electrical remodeling processes in the myocardium (Maron, 2004). The clinical course of the disease is heterogeneous. Clinical presentation of HCM ranges from minimal or no symptoms to the development of the most serious complications, including atrial fibrillation, heart failure, and sudden death, often at a young age and in the absence of previous symptoms (Spirito, 1989). One of the strongest predictors of disease progression to heart failure and finally death is the existence of a hemodynamic obstruction of the left ventricular outflow tract during systole, which per convention is defined by a pressure gradient ≥30 mmHg measured by continuous wave doppler echocardiography. Therefore, it is of clinical importance to distinguish between the obstructive (HOCM) and non obstructive (HNCM) form of the disease. Familial hypertrophic cardiomyopathy is

the most common structural cause of sudden cardiac death in individuals aged less than 35 years, especially in competitive athletes. Thus, an early recognition of the disease is useful for risk assessment and starting drug therapy and non-pharmacological treatment options to prevent prognostic fatal heart failure and mortality. The detection of affected patients remains still challenging. Genetic testing allows accurate diagnosis of HCM and its causing mutations, but has some limitations. First, DNA screening is not part of routine clinical evaluation, and identifies the mutation actually only in 50-60 % of patients. Secondly, as shown by DNA genotype-phenotype correlation studies, the disease expression varies not only between unrelated individuals but also within the same family. At present, clinical screening and risk stratification includes medical history, clinical examination, 12-lead ECG at rest and under physical exercise, Holter-ECG, echocardiography and cardiac magnetic resonance imaging. Follow-up examinations should be encouraged in affected patients on a 12-18 month basis. For their first degree relatives annual evaluations are recommended in the adolescence period and every 5 years beyond the age of 18.

Noninvasive electrophysiological diagnosis in patients suffering from HCM is usually done by electrocardiography, rarely by body surface potential mapping studies. However, information content from ECG signals seems to be limited and not disease specific (Maron, 1990). As an alternative to electrocardiography, magnetocardiography can be used for a study of cardiac electrophysiological phenomena, especially myocardial electrical remodeling processes. Changes in myocardial electrical properties were shown to be associated with the development of hypertrophic cardiomyopathy (Fananapazir, 1989). Multi channel cardiac magnetic field mapping (CMFM) reflects the magnetic fields generated by the myocardial electrical currents occurring during the cardiac cycle. CMFM signals have several advantages: (1) they are little influenced by the tissues between skin and heart; (2) they are sensitive to tangential currents that arise in the border zones of cardiac tissue with different electrophysiological properties; (3) they consider the track of electrical vortex currents; and (4) their properties make it possible to accurately localize intracardiac sources (Fenici, 2003).

We therefore investigated the capability of CMFM to detect patients suffering from HCM, including those who have a very mild phenotype or are asymptomatic. The purpose of the study was to develop a CMFM based diagnostic approach to improve screening/diagnosis of HCM. We introduced the calculation of Kullback-Leibler entropy as a parameter to quantify the topology of cardiac magnetic field distribution. We use the term map topology as a synonym for the two-dimensional distribution of cardiac magnetic field strength. Note that this term is therefore independent from field strength amplitudes. The mathematical method, first described by Kullback and Leibler in 1951, provides a value of the similarity between two probability distributions (Kullback).

We further analyzed, whether a combination of KL based topology quantification with regional field strength parameters improves the discrimination power of the automatic diagnostic algorithm.

Our study was done to address three questions:

1. Can CMFM distinguish between HCM individuals and healthy control subjects or patients with cardiac hypertrophy of other causes?
2. Is it possible to discriminate between the two main phenotype subgroups of HCM; patients with (HOCM) and without (HNCM) obstruction of the left ventricular outflow tract?
3. How do CMFM based classification algorithms perform, when prospectively applied for screening in HCM families with known genetic status?

2 METHODS

2.1 Patients

Thirty three patients (HCM, n=33, 43.8 ± 13 years, 13 women, 20 men) affected by hypertrophic cardiomyopathy were recruited from our hospital based cardiomyopathy-outpatient center. The diagnosis was confirmed by complex diagnostic tests including echocardiography and magnetic resonance imaging established on evidence-based guidelines. HCM was diagnosed by the presence of a non-dilated and hypertrophied left ventricle in the absence of another cardiac or systemic disease (e.g. hypertension or aortic stenosis) capable of producing the magnitude of hypertrophy observed. Nineteen patients suffered from the obstructive form and 14 patients from hypertrophic non obstructive cardiomyopathy.

The total number of subjects in the control group (NoHCM) was n=99. We recruited a healthy volunteers group from an occupational health center. The 57 healthy volunteers (age 39.6 ± 8.9 years; 35 men and 22 women) had normal findings in

echocardiography, bicycle ergometry, ECG and Holter-ECG for many years. No control subject had a history of cardiac diseases or symptoms. Forty two patients with essential arterial hypertension (HYP, n=42, 49.7 ± 7.9 years, 15 women and 27 men) were also included in this study, fulfilling the following criteria: known hypertension on pharmacological therapy; echocardiographicly estimated left ventricular hypertrophy (Framingham heart study classification FHC 1-2); no prior clinical manifestation or angiographic documentation of coronary artery disease; no evidence of prior myocardial infarction. The NoHCM group consists of both healthy volunteers and hypertensives (together n=99) to get a more realistic control group for familiar HCM screening.

Two families with genetically proofed HCM (ß-MHC, α-Tropomyosin; 4 HNCM, 1 HOCM, 22 family members in total) were investigated prospectively to check the accuracy of the MFM screening tool.

Our internal review board approved the study and written informed consent was obtained.

2.2 Magnetocardiographic Measurements

The cardiac magnetic field was recorded over the anterior chest wall using a seven channel magnetic measurement system (Cryoton Ltd, Moscow) based on low temperature Superconducting Quantum Interference Device (LT-SQUID), coupled with an axial second order gradiometer (baseline 5.5 cm, pickup coil diameter 2 cm). The component of the magnetic field perpendicular to the chest wall was registered in a 38 point grid (Fig. 1a). To improve the signal to noise ratio all measurements were done in a magnetically shielded room (VAC Akb3b) with a shielded factor better than 10000 at 10 Hz. Typical system performance in this environment was 7 fT in unit band. The measurements were done sequentially at six measurement positions (Fig. 1a) to cover a mapping area of 20x20 cm. Recording time was 30 seconds per point with an acquisition rate of 1000 Hz and a bandwidth of 0.01 – 130 Hz. The ECG lead II was recorded simultaneously as a time reference signal for further processing. Thereafter, signal averaging techniques and offset corrections were applied. Averaged data were then transformed from irregular measurement grid to the regular 6x6 point grid (20 cm width and height) using thin-plate-spline surface. Fig.1b shows averaged cardiac magnetic

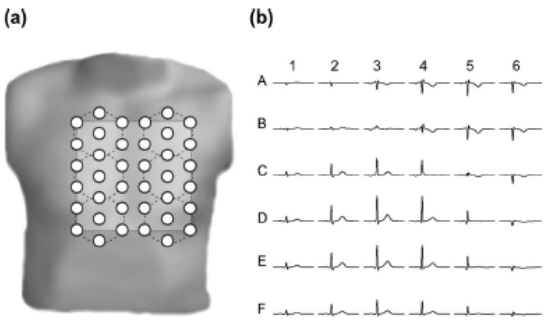

Figure 1: The layout of cardiac magnetic field map (CMFM) measurement: (a) CMFM measurement grid based on a seven channel system. The dashed lines denote six sequential measurement positions. (b) Cardiac magnetic field waveforms transformed into a regular grid (6x6) corresponding to the light grey square in panel (a).

signals for the regular grid. The strength of the cardiac magnetic field was in the range of 10 – 100 pT (picotesla, 10-12 Tesla). The MFM amplitude depends on the distance between measurement plane and patient heart. To compensate this effect we normalized magnetic field strength by the mean absolute value during QRS averaged over 36 points of rectangular grid.

2.3 Cardiac Magnetic Field Map Quantification

After averaging we obtained 1000 samples for each of the 36 measurement positions (Fig 1b), leading to 1000 different CMFM. Thus, the dimensionality of measured data is very high and therefore, we have to reduce it. One solution we present here is based on the concept of Kullback-Leibler entropy to quantify the topology of each map. Suppose that $Q=\{Q_i\}$ (i=1,..,36 – the number of measurement positions; 1: A1, …, 6: A6, 7: B1, …, 12: B6, …36: F6 in Fig 1b) is a given reference well-behaved probability distribution (all $Q_i>0$) and that $P=\{P_i\}$ (i=1,..,36) is some trial probability distribution. The difference of information content of P compared to the reference distribution Q is quantified by the Kullback-Leibler entropy

$$KL(P,Q) = \sum_{i=1}^{36} P_i * \ln \frac{P_i}{Q_i} \qquad (1)$$

The Kullback-Leibler (KL) entropy can be considered as a kind of distance between the two probability distributions, though it is not a real distance measure because it is not symmetric. In our study, KL entropy was used to quantify differences in topology between magnetic field maps of a single subject compared with a reference maps. For each

time point, the group mean CMFMs of subjects without HCM was used as a reference map. To quantify topology independent from amplitudes, each CMFM was normalized to get a probability distribution. For maps very similar to the reference we obtain a KL entropy value near zero, differences in topology lead to higher KL entropy values.

For each time point between the onset of QRS and the offset of T-wave, KL values describing differences in topology were calculated. In order to avoid inadequate comparisons due to interindividual differences in QRS and STT duration, we limited the considered time intervals to the shortest QRS and STT lengths in the study population. To identify sub segments with the highest differences in KL values between compared groups, we calculated the discriminant index (DI) for every time point as follows: the absolute differences of mean KL values in both groups were divided by the standard deviation of all cases. Mean KL values during QRS and STT subintervals with a DI value greater than 0.8 were considered as classification parameters KLQRS(DI>0.8) and KLSTT(DI>0.8).

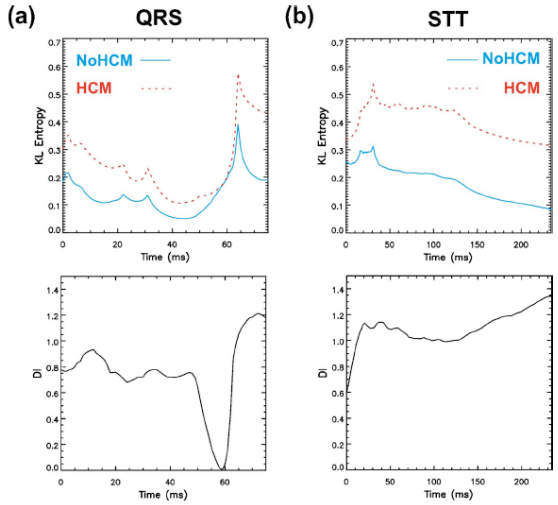

Figure 2: Mean group Kullback-Leibler (KL) entropy values over time during QRS (a) and STT (b). NoHCM group values are denoted with solid (blue) lines and HCM group values with dashed (red) lines (reference maps: NoHCM group). Lower panels give discriminant index (DI) values during QRS (a) and STT (b) intervals respectively: KL values for time intervals where DI was higher than 0.8 (dashed lines) are considered for KLQRS(DI>0.8) and KLSTT(DI>0.8) calculation.

To assess regional differences in magnetic field strength, which cannot be captured by topology, we calculated 36 regional parameters (QRSA1-F6, for positions see Fig. 1b) as mean values of magnetic field strength during QRS complex. Data processing was performed in two steps: classification rules were determined, firstly to discriminate between groups with and without HCM, and secondly to discriminate patients with different forms of HCM. For each step classification performance was tested for KL parameters, regional features and then for their combinations. Finally, the best set of predictors was prospectively applied to identify members of HCM families affected by the disease.

3 RESULTS

Discrimination of HCM Individuals from Healthy Control Subjects and Patients with Cardiac Hypertrophy of other Causes (NoHCM). The mean KL values of the HCM and NoHCM groups during QRS and STT interval are given in Fig. 2 (upper panels), with the corresponding DI values in the lower panels. Only the beginning and parts of the second half of the QRS are discriminating (DI>0.8) for these groups, whereas for STT almost the whole segment is distinctive. These subintervals were used to calculate KLQRS(DI>0.8) and KLSTT(DI>0.8). Mean values of these parameters differed significantly between the two groups (Tab. 1). LDA based on these two features yielded a sensitivity of 78.8 % and specificity of 86.9 % (Tab. 1) with an overall correct classification rate of 84.8 %. Next, we estimated discrimination power of regional parameters based on mean values of magnetic field strength in each grid position. Forward stepwise discriminant analysis was performed to select the best two feature set: QRSB3 and QRSF3. QRSB3 was positive in the NoHCM and negative in the HCM group (Tab. 1, $p < 10\text{-}8$). For QRSF3 mean values of both groups were comparable and not significantly different. However, this parameter was automatically selected by LDA because it provides orthogonal information to QRSB3 to separate both groups. The overall classification rate based on these two regional parameters was lower than with KL based: The specificity of 85.9 % was comparable with KL features but the sensitivity of 66.7 % (cross-validated only 63.6 %) was substantially lower (Tab. 1).

Table 1: Descriptive statistics of patient groups without HCM (NoHCM) and with HCM as well as their separability. Data are given as mean values ± SE and percentage of correctly classified (CC) cases. If 'leave one out' crossvalidated results of discriminant function analysis differ from the original results, they are shown in parentheses. P-values were obtained with the Mann-Whitney-U-test (univariate cases) and the Wilks-Lambda test (linear discriminant function). Three classification approaches were used: (a) KL: based on Kullback-Leibler entropy mean values for QRS and STT time intervals where discriminant index (DI) was higher than 0.8, (b) Regional: based on selected regional parameters, (c) KL+Regional: based on selected KL and regional parameters.

		NoHCM	HCM	P - value
KL	$KL_{QRS(DI>0.8)}$	0.14 ± 0.007	0.27 ± 0.019	$4.8*10^{-10}$
	$KL_{STT(DI>0.8)}$	0.11 ± 0.015	0.33 ± 0.03	$1.1*10^{-10}$
	CC	86.9 %	78.8 %	$3.9*10^{-17}$
Regional	QRS_{B3}	0.45 ± 0.07	-0.59 ± 0.14	$7.8*10^{-9}$
	QRS_{F3}	0.7 ± 0.05	0.68 ± 0.12	0.34
	CC	85.9 %	66.7 % (63.6 %)	$6.2*10^{-12}$
KL+Regional	QRS_{A6}*	-0.46 ± 0.02	-0.37 ± 0.06	0.44
	CC	88.9 %	84.8 %	$6.9*10^{-19}$

As a last step, we combined KL and regional features and applied forward stepwise LDA to find the best set of three parameters. This set included the KL parameters KLQRS(DI>0.8), KLSTT(DI>0.8) and the regional parameter QRSA6. The mean values of the latter parameter again did not significantly differ between both groups, but the combination of these three parameters improved the overall classification rate from 84.8 % to 87.9 % (sensitivity: 84.8 %, specificity: 88.9 %, area under ROC curve: 0.94). The correct classification rates for the subgroups included were 98.2 % in normal subjects, 76.2 % in hypertensive patients, 85.7 % in patients with HNCM and 84.2 % in patients with HOCM.

Discrimination of Obstructive from non Obstructive Forms of HCM. For this analysis, KL entropy was calculated using the averaged maps of the HOCM group as the reference. The mean KL values of HOCM and HNCM groups during QRS and STT interval are given in Fig. 3 (upper panels), with the corresponding DI values in the lower panels. Obviously, the only informative part to separate HOCM from HNCM is the time interval between 57 and 77 ms of the QRS (DI>0.8). Mean values of KLQRS(DI>0.8) differed significantly ($p<10^{-4}$) between both groups (Tab. 2). Using only this parameter, 78.8 % of patients were correctly classified (78.9 % from HOCM group and 78.6 % from HNCM group).

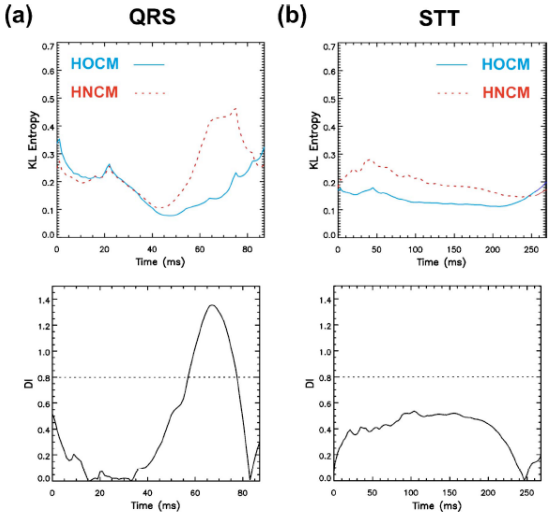

Figure 3: Mean group Kullback-Leibler (KL) entropy values over time during QRS (a) and STT (b). HOCM group values are denoted with solid (blue) lines and HNCM group values with dashed (red) lines (reference maps: HOCM group). Lower panels give discriminant index (DI) values during QRS (a) and STT (b) intervals respectively: KL values for time intervals where DI was higher than 0.8 (dashed lines) are considered for KLQRS(DI>0.8) calculation.

Table 2: Descriptive statistics of patients with HNCM and HOCM as well as their separability. Data are given as mean values ± SE and percentage of correctly classified (CC) cases. If 'leave one out' cross-validated results of discriminant function analysis differ from the original results, they are shown in parentheses. P-values were obtained with the Mann-Whitney-U-test (univariate cases) and the Wilks-Lambda test (linear discriminant function). Three classification approaches were used: (a) KL: based on Kullback-Leibler entropy mean values for QRS where discriminant index (DI) was higher than 0.8, (b) Regional: based on selected regional parameters, (c) KL+Regional: based on selected KL and regional parameters.

		HNCM	HOCM	P - value
KL	$KL_{QRS(DI>0.8)}$	0. 4 ± 0.04	0.16 ± 0.03	$5.1*10^{-5}$
	CC	78.6 %	78.9 %	$3.8*10^{-5}$
Regional	QRS_{F5}	0.67 ± 0.28	2.26 ± 0.34	$2*10^{-3}$
	CC	71.4 %	63.2 %	$1*10^{-3}$
KL+Regional	QRS_{A3}*	-0.73 ± 0.3	-1.31 ± 0.3	0.08
	CC	100 % (92.9 %)	94.7 % (89.5 %)	$1.5*10^{-7}$

Next, we estimated discrimination power of regional parameters, which were calculated for the same time

interval (57-77 ms of QRS). Forward stepwise discriminant analysis found QRSF5 to be the best discriminating parameter (Tab. 2). Overall classification rate using QRSF5 was 66.7 % (63.2 % patients from the HOCM group and 71.4 % from the HNCM group were correctly classified). Again, regional parameters demonstrated a lower classification power.

As the last step, we combined KL and regional parameters and performed a forward stepwise LDA. KLQRS(DI>0.8) and QRSA3 were selected. Overall classification rate for this parameter set was 97 % (94.7 % of HOCM and 100 % of HNCM patients were correctly classified, area under ROC curve: 0.97).

Prospective Screening of Two HCM Families. Application of the two classification algorithms based on the selected sets of combined KL and regional features yielded a correct classification of all 22 family members. This was true not only for detection of HCM affected individuals (5 out of 22 family members), but also for discrimination between different forms of the disease (1 HOCM vs. 4 HNCM).

4 CONCLUSIONS

This study investigated the capability of CMFM to detect patients affected by HCM. The most important findings are, that a KL based topology quantification of cardiac magnetic field distribution discriminates HCM from non HCM and distinguishes between different forms of HCM (HOCM and HNCM), and that a combination with regional field strength parameters improves the discrimination results to a level relevant for clinical application.

Discrimination of HCM Individuals from Healthy Control Subjects and Patients with Cardiac Hypertrophy of other Causes (NoHCM). Both the large variability of the disease expression and the resulting complexity of the CMFM raise difficulties for the magnetophysiologic diagnostic evaluation of HCM. The present paper proposes a new diagnostical approach based on CMFM. Different analysis techniques are currently used for evaluation of cardiac magnetic field maps. This includes for example the estimation of changes in magnetic field orientation through the cardiac cycle and the calculation of QRS-ST-T wave integrals (Van Leeuwen, 2006). We applied for the first time the methodology of Kullback-Leibler entropy for analysis of CMFM to investigate the diagnostic information content in topology related to the status “HCM affected or not”. As we could show, KL values increase with the deviation of map topology compared to the reference field distribution. The idea to use relative entropy measures to classify medical data had already successfully been applied to EEG, HRV and MRI-analyses. Using the KL approach, we found significant differences in map topology during QRS and STT interval between HCM patients and the mixed control group of healthy volunteers and hypertensives. For the process of depolarization the most significant differences were found during the early part (5-20 ms) and within the second half (62-75 ms) of this time period. In contrast, the same was true for nearly the whole repolarization period (STT interval) with marked map topology deviations of the HCM group, revealed by the discriminant index. The analysis of the CMFM using two parameters based on the Kullback-Leibler entropy measures correctly classified 84.8 % of the tested groups. As the control group contained also patients with cardiac hypertrophy due to arterial hypertension, our results strongly suggest that Kullback-Leibler based map quantification revealed specific topological features in HCM patients. They may originate from the pathognomonic ventricular remodeling process, which includes myocardial disarray, left ventricular hypertrophy (LV) and fibrosis. Typically, the LV hypertrophy shows asymmetric distribution with diffuse or segmental pattern of left ventricular wall thickening, most involving the septal region (Saumarez, 1992). This is accompanied by changes in the electrical properties especially at the initial and the last part of QRS, both due to a loss of electrical forces because of transmural myocardial fibrosis and abnormal electrical activation of hypertrophied ventricular septum (Dumont, 2006). Echocardiographic and MRI studies showed that the balance of these electrical forces is primarily a function of the relation of upper anterior septal thickness to right ventricular wall thickness and to upper left ventricular posterior wall thickness. In a non-invasive electrocardiographic imaging study of ventricular activation, Ramanathan et al. (2006) demonstrated an epicardial right ventricular breakthrough in the anterior paraseptal region during the earliest ventricular activation under physiological conditions in healthy volunteers. At the end of the ventricular activation sequence, an apex-to-base activation of the posterior left ventricle was displayed. Based on this description of the

ventricular activation sequence, our findings suggest that within the first 20 ms of the ventricular activation paraseptal parts of the right ventricle could contribute to the observed differences in CMFM topology. In contrast, the map topology differences at the end of the QRS could reflect the influence of regional LV wall hypertrophy and myocardial fibrosis on the electrophysiological myocardial properties, especially if the propagation wave front turns from apical to posterior basal LV. These findings are consistent with those from invasive electrophysiological and morphological LV studies (Schumacher, 2005). Myocardial scarring and its electrophysiological consequences like slowed and fragmented intraventricular conduction also contributed to the specific magneto-physiological HCM phenotype.

Changes in repolarization in HCM patients were also found in ECG studies (Barletta, 2005). The most common abnormalities are related to the ST-segment and the T-wave. This is in consistence with our findings of differences in KL entropy values at the STT interval. They probably emanate from myocardial disarray, fibrosis and small vessel disease leading to scarred myocardium due to regional ischemia (Basso, 2000). HCM does not affect the ventricles uniformly; it is likely that there are areas of diseased myocardium with abnormalities in conduction and refractoriness and heterogeneity of refractoriness, especially related to distal hypertrophy with craniocaudal asymmetry.

Compared with KL measurements, we also found significant regional deviations of magnetic field strengths during depolarization period (QRS), especially in the superior (sensor position B3) and inferior (sensor position F3) part of the mapped area. However, the overall classification rate using only these parameters was lower compared to the KL based set. Specificity was comparable with KL method but sensitivity was substantially lower. A possible explanation for the lower classification rate could be that regional parameters are more sensitive to measurement conditions, especially to the position of the patient's heart relative to the measurement system. Even with a presumed constant distance between sensors and thorax surface, the variations in patients' anatomy result in different heart-sensor distances. Automatic adjustments to solve this problem are under investigation (Burghoff, 2000).

In contrast to the lower efficacy of the mean values of magnetic field strength approach, the classification rate improved adding a regional parameter to the KL features. Since the crossvalidation did not differ from the original results the improvement in classification is due to a higher information content of the combined parameter set.

Discrimination of Obstructive from non Obstructive Forms of HCM. In order to find a discriminant function for separation of HCM subforms (HOCM vs. HNCM), we applied the same approach but now using the HOCM group maps as the reference for KL entropy calculation. As shown by high DI values, KL based topology differed only in a short time interval within the second part of depolarization process (57-77ms). The analysis of regional magnetic field differences revealed that most significant differences between these two HCM subforms exist in the inferior part of the mapped area (sensor position F5). HOCM is characterized by a predominantly septal hypertrophy, which leads to chronic obstruction of the left ventricular outflow tract and consecutively to an increase in wall stress, myocardial ischemia, increased cell death and fibrosis.

Using gadolinium contrast-enhanced MRI, Choudhury et al. found in asymptomatic or mildly symptomatic patients with HCM that the extent of scar increased significantly in relation to wall thickness on a regional basis. The electrophysiological consequences are regional prolongation of the bipolar endocardial potentials and the occurrence of fractionated and split potentials, which directly point to an underlying inhomogeneity of the myocardial excitation with a shift to earlier activation of the lateral LV wall due to septal conduction delay. This probably led to the observed deviation in CMFM map topology between HOCM and HNCM patients in the second part of the QRS interval, which could be quantified by using the KL entropy method. The alterations of regional electrophysiological properties at hypertrophic septal areas are responsible for the observed changes in the inferior mapped area.

Intended to detect HCM subforms, KL entropy measures were superior to the analysis of regional map differences. But, adding a regional parameter QRSA3 to KL entropy parameters, the classification result improved to 97 % with a sensitivity of 100 % for HNCM and a specificity of 94.7 % for HOCM.

Feasibility of the Approach and Conclusions. The correct classification of 5 HOCM and HNCM patients out of 22 family members, in which the diagnosis was confirmed by genetic testing, showed in a prospective part of the study the feasibility of the presented diagnostic algorithm. Our results give

evidence, that KL entropy as a natural distance measure between two probability distributions is an effective tool to obtain discrimination information from CMFM measurements. It is important to point out that the KL tool is applicable to CMFM analysis in a population characterized by a broad spectrum of magnetophysiological and clinical phenotype expression. Prospective screening of HCM family members is strongly recommended, including serial echocardiographic and electrocardiographic examinations (Maron, 2004).

In conclusion, a combined diagnostic algorithm based on KL entropy topology quantification and regional parameters of cardiac magnetic field maps is a suitable tool for HCM screening and discrimination between different forms of the disease.

REFERENCES

Barletta, G., Lazzeri, C., Franchi, F. et al. 2004, Hypertrophic cardiomyopathy: electrical abnormalities detected by the extended-length ECG and their relation to syncope. *Int J Cardiol* 97 (1): 43-8

Basso, C., Thiene, G., Corrado, D. et al. 2000, Hypertrophic cardiomyopathy and sudden death in the young: pathologic evidence of myocardial ischemia. *Hum Pathol* 31 (8): 988-98

Burghoff, M., Nenonen, J., Trahms, L. Katila T. 2000, Conversion of magnetocardiographic recordings between two different multichannel SQUID devices. *IEEE Trans Biomed Eng* 47 (7): 869-75

Dumont, C. A., Monserrat, L., Soler, R., et al. 2006, Interpretation of electrocardiographic abnormalities in hypertrophic cardiomyopathy with cardiac magnetic resonance. *Eur Heart J* 27 (14): 1725-31

Fananapazir, L., Tracy, C. M., Leon, M. B. et al. 1989, Electrophysiologic abnormalities in patients with hypertrophic cardiomyopathy. A consecutive analysis in 155 patients. *Circulation* 80 (5): 1259-68

Fenici, R. , Brisinda, D., Nenonen J., Fenici P. 2003, Phantom validation of multichannel magnetocardiography source localization. *Pacing Clin Electrophysiol* 26 (1 Pt 2): 426-30

Kullback S., Leibler R. A. 1951, On information and sufficiency. *Ann Math Stat* 22 (1): 79-86

Maron B. J. 1990, Q waves in hypertrophic cardiomyopathy: a reassessment. *J Am Coll Cardiol* 16 (2): 375-6

Maron, B. J., McKenna, W. J., Danielson, G. K. et al. 2003, Task Force on Clinical Expert Consensus Documents and the European Society of Cardiology Committee for Practice Guidelines. *J Am Coll Cardiol* 42 (9): 1687-713

Maron, B. J., Seidman J. G., Seidman C. E. 2004. Proposal for contemporary screening strategies in families with hypertrophic cardiomyopathy. *J Am Coll Cardiol* 44 (11): 2125-32

Ramanathan, C., Jia, P., Ghanem, R. et al. 2006, Activation and repolarization of the normal human heart under complete physiological conditions. *Proc Natl Acad Sci U S A* 103 (16): 6309-14

Saumarez, R. C., Camm, A. J. , Panagos, A.. et al. 1992, Ventricular fibrillation in hypertrophic cardiomyopathy is associated with increased fractionation of paced right ventricular electrograms. *Circulation* 86 (2): 467-74

Schumacher, B., Gietzen, F. H., Neuser, H. et al. 2005, Electrophysiological characteristics of septal hypertrophy in patients with hypertrophic obstructive cardiomyopathy and moderate to severe symptoms. *Circulation* 112 (14): 2096-101

Seidman C. E. and Seidman J. G. 1998 Molecular genetic studies of familial hypertrophic cardiomyopathy. *Basic Res Cardiol* 93 Suppl 3 13-6

Spirito, P., Chiarella, F., Carratino, L. et al. 1989, Clinical course and prognosis of hypertrophic cardiomyopathy in an outpatient population. *N Engl J Med* 320 (12): 749-55

Thierfelder, L. , Watkins, H., MacRae, C. et al. 1994 Alpha-tropomyosin and cardiac troponin T mutations cause familial hypertrophic cardiomyopathy: a disease of the sarcomere. *Cell* 77 (5): 701-12

Van Leeuwen, P., Hailer, B., Lange S., Gronemeyer , D. H. 2006, Identification of patients with coronary artery disease using magnetocardiographic signal analysis. *Biomed Tech (Berl)* 51 (2): 83-8

IMPROVING AN AUTOMATIC ARRHYTHMIAS RECOGNISER BASED IN ECG SIGNALS

Jorge Corsino, Carlos M. Travieso, Jesús B. Alonso and Miguel A. Ferrer
Technological Centre for Innovation in Communications (CeTIC), University of Las Palmas de Gran Canaria
Campus de Tafira, s/n, 35017, Las Palmas de Gran Canaria, Spain
jorge.corsino@gmail.com, ctravieso@dsc.ulpgc.es, jalonso@dsc.ulpgc.es, mferrer@dsc.ulpgc.es

Keywords: Automatic recognition of arrhythmias, electrocardiography, neural network, principal component analysis, wavelet transform.

Abstract: In the present work, we have developed and improved a tool for the automatic arrhythmias detection, based on neural network with the "more-voted" algorithm. Arrhythmia Database MIT has been used in the work in order to detect eight different states, seven are pathologies and one is normal. The unions of different blocks and its optimization have found an improvement of success rates. In particular, we have used wavelet transform in order to characterize the patron wave of electrocardiogram (ECG), and principal components analysis in order to improve the discrimination of the coefficients. Finally, a neural network with more-voted method has been applied.

1 INTRODUCTION

In Europe, cardiovascular diseases are one of most important causes of death, with a great repercussion in health assistance budget. For instance, to obtain an early exact cardiovascular diagnosis is one of the most important missions for the physicians. The electrocardiogram is the graphic description of the heart electric activity registered from the body surface and is a basic element in the diagnosis of different heart diseases.

The objective of this study is to make deeper in the extraction of characteristics and the later automatic classification of heart pathologies, analyzing every aspect that takes parting.

To carry on with this objective, we have developed Matlab software (Matlab, 2006), clear and easy, where users have three options to practise with all tools at their hands: making a pre-processing with wavelet transform and in order to play with the developed filing.

Wavelet transform (Romero-Legarreta, 2005) is a mathematics technique that has gained importance in the last years in all kind of applications related with non-stationary signal process.

Although the decomposition in well defined blocks in time and frequency, wavelet transform can characterise the local sign regularities. This skill allows distinguishing electrocardiogram waves (ECG) from noise and other artefacts.

In this paper, we establish the use of approximated wavelet coefficients taken out from the ECG signal in order to classify eight types of beat: normal pulse (N), extra-systole (L), premature ventricular contraction (R), premature auricular contraction (/), blockade left branch (A), blockade right branch paced beat (V), fusion of normal and paced beat (f) and fusion of normal and premature ventricular contraction (F).

The use of principal component analysis (PCA) (Bianchi, 2006) on the wavelet coefficients has improved their discrimination. Finally, we have used an automatic classification based on artificial neural networks (NN) (Bishop, 1995), (Juang, 1992). An improvement have been applied to NN, we have implemented the "more voted" method, obtaining better success rates.

2 WAVELET TRANSFORM: FEATURE EXTRACTION

The ECG features are extracted through a pre-processing stage in which the Wavelet transform is applied to original ECG signal.

The Discrete Wavelet Transform (DWT) is defined as follows:

$$C[j,k] = \sum_{n \in \mathbf{Z}} f[n] \psi_{j,k}[n] \quad (1)$$

where $\psi_{j,k}$ is the transform function:

$$\psi_{j,k}[n] = 2^{\frac{-j}{2}} \cdot \psi\left[2^{-j} n - k\right] \quad (2)$$

The application of different mother families on pre-processing (artefacts elimination) and on the feature extraction has got a set of good and discriminate parameters.

3 PRINCIPAL COMPONENT ANALYSIS

Principal components analysis (PCA) is a technique used to reduce multidimensional data sets to lower dimensions for analysis. The applications include exploratory data analysis data and for generating predictive models. PCA involves the computation of the eigenvalue decomposition or Singular value decomposition of a data set, usually after mean centering the data for each attribute. The results of a PCA are usually discussed in terms of scores and loadings. This process applied to ECG arrhythmias is named blind source separation, where there are fewer sources than input channels.

The blind source separation consists in several sources that are mixed in a system, these mixtures are recorded and then they have to be separated to obtain the estimations of the original sources. The following figure shows the mixing system:

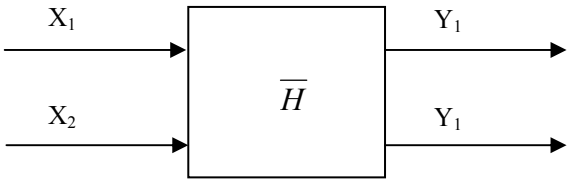

Figure 1: 2 Sources – 2 Mixtures system.

Generally, there are *n* source signals statistically independent $s(t) = [s_1(t),...,s_n(t)]$, and *m* observed mixtures that are linear and instantaneous combinations of the previous signals $x(t) = [x_1(t),...,x_n(t)]$. Beginning with the linear case, the simplest case, we have that the mixtures are:

$$x_i(t) = \sum_{j=1}^{n} h_{ij} \cdot s_j(t) \quad (3)$$

Now, we need to recover s(t) from x(t). It is necessary to estimate the inverse matrix of H, where h_{ij} are contained. Once we have this matrix:

$$y(t) = \overline{W} \cdot x(t) \quad (4)$$

Where y(t) contains the estimations of the original source signals, and is the inverse mixing matrix. Now we have defined the simplest case, it is time to explain the general case that involves convolutive mixtures. The process is defined as follows:

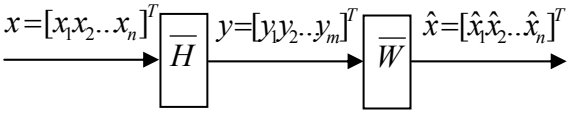

Figure 2: BSS General problem.

Where $\overline{H}$ is the mixing system:

$$\overline{H} = \begin{bmatrix} h_{11} & \dots & h_{1n} \\ \dots & \dots & \dots \\ h_{n1} & \dots & h_{nn} \end{bmatrix} \quad (5)$$

The h_{ij} are FIR filters, each one represents an acoustic transference multipath function from source, *i*, to sensor, *j*. *i* and *j* represent the number of sources and sensors.

4 NEURAL NETWORK

For this present work, we have implemented a supervised classification system for the discrete wavelet coefficients. Firstly, a neural network classification system using time intervals obtained from the previous extraction process is implemented.

This classifier has used a Feed-Forward Neural Network (NN) with a Back-propagation algorithm for training (Bishop, 1995), (Juang, 1992), where the number of input units is given by the dimension of the vector of features. And the number of output units is given by the number of pathologies to identify. Too, we have researched with different number of neurons in the hidden layer, in order to get the optimum recogniser.

Besides, the found success has been improved using the method of the 'more voted', where we have built a schedule with different neural networks (see figure 1).

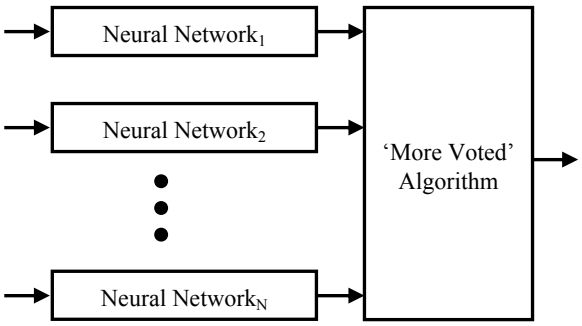

Figure 3: Classification System with 'more voted' algorithm, based on NN.

5 EXPERIMENTS

We have taken 24 signals from the MIT-BIH ARRHYTHMIA database (MITDB)(MIT-BIH, 2007), choosing 750 samples from each class, 6000 beats to classify; some of them are recognized by the MIT as difficult classifying signals. To remove noise from signals, the net interferences and the base line variations, we have use techniques proposed in (1). It consists in obtaining detail coefficients for different wavelet levels, to apply them a non-lineal form threshold, using a soft-thresholding calculated by the inverse transform to obtain the result signal. The threshold follows this expression: $\partial = \sqrt{2\log(N)\hat{\sigma}}$; where N is the number of decomposition levels and coefficients represent the details coefficients for the level to filter. In function of the wavelet family and the decomposition level, the result will change. In this work, we take Daubechies 3 of level 3 following our studies. Also we take different types of parameters as temporal as Fourier and Wavelet coefficients.

With temporal parameters took out from our previous works and algorithms (the time of Pwave, PR segment, QRS complex, QT segment and T wave, and the area of P wave, QRS complex and the T wave) we did not get to characterize any kind of beats, the same result were taken with Cosen Fourier Transform (DCT).

Hence we only select the approximation wavelet parameters like "in-parameters". The classification is realised with a neural networks using back-propagation. Once took out the wavelet coefficients with sym4 family and the third decomposition level, the neural networks has three layers. To obtain the number of neurons of the hidden layer, we tried with different numbers and with 45 we got the best result with an error of 26%. How the error is too much, we make principal components analysis, since with it, the network size and the computational cost are reduced. With this study the characteristic vector is ortogonalised to avoid the correlations of his components, is arranged and the components with less information are deleted. The algorithm is applied to the characteristic vector, the mean is established in cero and the standard deviation in one, after, the PCA is applied, in this case with 0,02%. The variations are showed in the next figures:

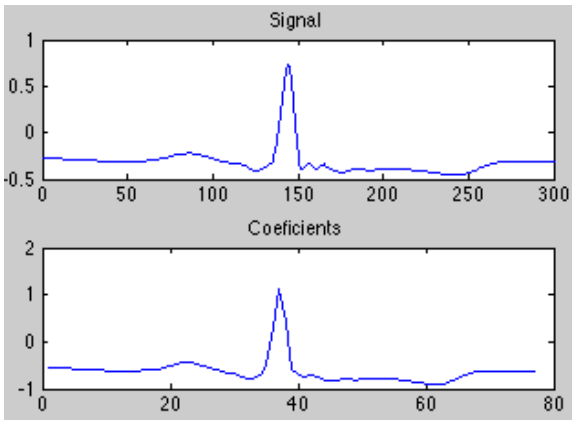

Figure 4: Signal and its coefficients.

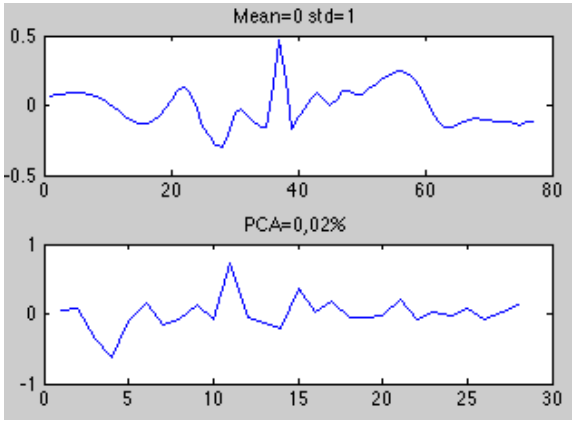

Figure 5: Modification of the coefficients.

With this technique, the network in trained again with the same conditions and the result with 55 neurons in the least error: 2,27%. This shows us a satisfactory study. Many trainings are realises where characteristics are: 3.000 beats (375 per class) for the training stage and the same quantity for the test stage, different PCA values (0,02%, 0,2 % and 2 %) the second, the third and the fourth decomposition level and ten wavelet families (Bior2.4, Bior5.5, Bior 6.8, Harr, Sym2, Sym4, Sym5, Sym8, rBio3.1, rBio5.5). With the result obtained we noticed is

better have a lot of approximation coefficients and alter make a PCA, instead of hace less quantity of approximation coefficients, then in better a low level and apply PCA. The best result were obtained with the wavelet rBio 3.1 at level 2 and PCA= 0,02% with 1,97% of error. "The most voted" technique is applied to boot the result. This model consist of select some networks an apply to all the same test in parallel. Finally, the results are compared and the result most voted is selected. In the figure 4 a double network is represented with only two parallel networks.

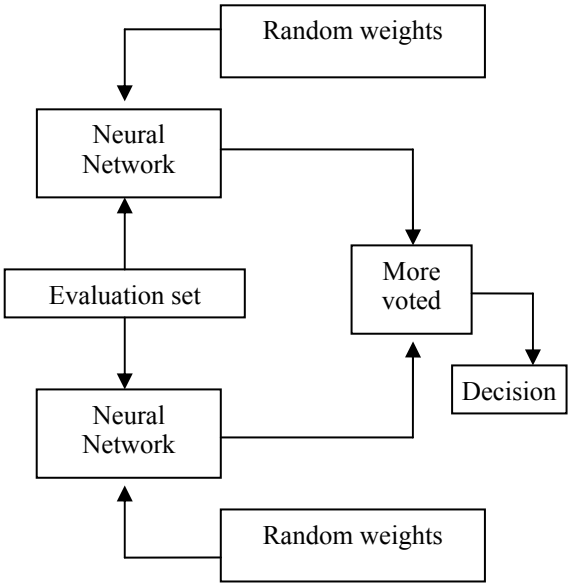

Figure 6: Parallel neural network.

With this new structure, the filing reduces error to 1.8% in the simulation and 1.4 in the train process. For the entire database, it has an error of 1.6%.

Table 1: Matrix confusion.

		OUTPUT CLASSES							
		N	L	R	/	A	V	f	F
INPUT CLASSES	N	375	0	0	0	0	0	0	0
	L	0	372	0	0	0	0	3	0
	R	1	0	372	0	2	0	0	0
	/	0	0	0	375	0	0	0	0
	A	16	0	3	2	351	1	1	1
	V	0	0	0	0	2	369	3	1
	f	0	0	0	4	0	0	371	0
	F	0	1	0	2	4	0	7	361

In the confusion matrix we can see, that the class that has more errors is the premature ventricular contraction, classifying this as normal beat, this is because the morphology of the auricular premature contraction is similar to the normal. Respect to the classification between normal and pathologic signals the filing detect the healthy signals whit a 100% and the pathologic signal with a 99,35 % being the total classification between this two classes a 99.7%. Respect to the computational time, we remember that the filing has three parts: the extractions of wavelet characteristics, the principal components analysis and the test process. This time are detailed in the table 2:

Table 2: Load times in seconds.

Process	**Computational Time**
Wavelet	0,010623 s
PCA	0,002571 s
Test	0. 111877 s
TOTAL	**0,1251 s**

Having in mind that a full beat has an approximated duration of 800 ms, the filing will classify the beat only 125 ms later, without the time of pre-processing and segmentation. These times are Matlab time. The part of classification depends on a well segmentation process, this is we propose to make a robust segmentation for noise and cardiac pathologies.

Finally, we have compared our results with other authors (Song, 2005), (Zimmerman, 2004), (Jankowski, 2003). The new blocks used for this application and with the optimization of the remainder of the blocks, we can observe as our results are better than the previous references.

6 CONCLUSIONS

It has been implemented and improved an automatic arrhythmias recogniser using a neural network with more voted algorithm. We have found error rate of 1.8% with independent samples, only using for the test (8 different classes); and an error rate of 0.3% for pathology or normal class.

The ECG signal used is from MIT arrhythmias database, and it has been parameterized with DWT coefficients and selected with PCA.

REFERENCES

Matlab 2006, http://www.mathworks.com. The Mathworks. Last Visit: 07-16-2006

Romero-Legarreta, I.,. Addison, P.S, Reed, M.J., Grubb, N.R., Clegg, G.R., Robertson, C.E., Watson, J.N., 2005. Continuous wavelet transform modulus maxima analysis of the electrocardiogram: Beat-to-beat characterization and beat-to-beat measurement, *Int. J. Wavelets, Multiresolution and Information Processing*, Vol.3, pp. 19-42.

Bianchi, M.F.de, Guido, R.C., Nogueira, A.L., Padovan, P., 2006. "A wavelet-PCA approach for content-based image retrieval" *Proceeding of the Thrity-Eighth Southeastern Symposium on System Theory*, pp. 439 – 442.

Bishop, C.M., 1995. *Neural Networks for Pattern Recognition*, Oxford University Press.

Juang, B.H., Rabiner, L.R., 1992. Spectral representations for speech recognition by neural networks-a tutorial" Proceedings of the *Proceedings of the Workshop Neural Networks for Signal Processing*, 1992, pp. 214 – 222.

MIT-BIH, 2007, http://www.physionet.org/physiobank/mitdb. MIT-BIH Arrhythmia Database. Last Visit: 07-16-2007.

Song, M.H., Lee, J., Cho, S.P., Lee, K.J., Yoo S.K, 2005. Support Vector Machine Based Arrhythmia Classification Using Reduced Features. *International Journal of Control, Automation, and Systems*. Vol. 3. nº. 4. 571-579.

Zimmerman, M.W., Povinelli, R.J., 2004. On Improving the Classification of Myocardial Ischemia Using Holter ECG Data. *Computers in Cardiology. Chicago. Illinois*, 377-380.

Jankowski, S., Oreziak, A., 2003. Learning System for Computer-Aided ECG Analysis Based on Support Vector Machines. *International Journal of Bioelectromagnetism*. Vol. 5. nº 1. 175–176.

NON-INVASIVE REAL-TIME FETAL ECG EXTRACTION
A Block-on-Line DSP Implementation based on the JADE Algorithm

Silvia Muceli, Danilo Pani and Luigi Raffo
DIEE - Dept. of Electrical and Electronic Engineering, University of Cagliari, Piazza d'Armi, 09123 Cagliari, Italy
pani@diee.unica.it, luigi@diee.unica.it

Keywords: Fetal monitoring, antenatal diagnosis, real-time processing, DSP.

Abstract: The possibility to access the fetal ECG non-invasively during the early stages of the pregnancy is a paramount requirement for cardiologists aiming to treat fetuses with congenital hearth diseases. Several research works have been presented during the past years to address this issue. In this paper we present a block-on-line blind source separation technique that combines the powerfulness of the batch JADE algorithm to the requirements of a separation able to adapt to a time-varying mixing process. To avoid estimated sources permutation, a simple preconditioning technique in conjunction with a proper parameters tuning has been developed and tested. The whole algorithm has been implemented on a powerful floating-point Digital Signal Processor, and it is ready to be embedded in an acquisition device for a deeper experimentation.

1 INTRODUCTION

Fetal electrocardiography would allow the early diagnosis of some fetal heart congenital diseases, effectively treatable by transplacental drugs administration, that cannot be discovered by means of other more expensive diagnostic instrumentation such as ultrasound-based devices. Fetal electrocardiogram (FECG) extraction from multichannel transabdominal maternal potential recordings can be accomplished resorting to Blind Source Separation (BSS) techniques. Off-line BSS methods exploiting fourth-order statistics have been proven to be more effective than other methods but they are very computationally intensive and unable to deal with long-lasting recordings with possibly time-varying mixing processes.

In this paper we present a possible solution to such problems introducing a block-on-line version of the famous JADE algorithm (Cardoso and Souloumiac, 1993), with the aim to take from it the high separation quality, at the same time allowing the processing in presence of a potentially time-varying mixing process. Estimated sources permutation was avoided by means of a preconditioning technique used in conjunction with a proper parameter tuning. To assess the actual real-time capabilities of the algorithm, we present its porting and simulation on a floating point Digital Signal Processor (DSP) by Texas Instruments (TI). Due to such implementation, which still preserves a great portability, the system is ready to be embedded in an acquisition device for a deeper experimentation. Separation quality results have been assessed on a publicly available database.

In Section 2 a short review of some related works is presented, whereas the proposed algorithm is described in Section 3. Section 4 deals with the DSP implementation of the system. Experimental results are presented in Section 5. Section 6 concludes this work.

2 STATE OF THE ART

Non-invasive fetal electrocardiography is not yet used in clinical practice because of the difficulty in extracting the signal of interest, particularly in real-time. Cutaneous recordings from a pregnant woman comprise fetal and maternal heart signals, electromyographic and breathing noises, and external interferences. Since FECG and maternal ECG (MECG) have overlapping spectra, they cannot be separated through conventional frequency selective filtering. Many methods yield an estimate of the maternal signal from her chest, then removing this contribution from the composite abdominal one to obtain the FECG. Widrow (Widrow and Stearns, 1985) proposed a method of adaptive filtering and noise cancelling but its performance is very dependent on the electrodes placement. Camps (Camps et al., 2001) provided an extension of Widrow's scheme by including in it a finite impulse response neural network. The drawback is the complexity of the choice of free pa-

rameters, whose number increases geometrically with the number of inputs, though without eliminating the problem of high sensitivity to electrodes placement. Kanjilal (Kanjilal et al., 1997) used Singular Value Decomposition (SVD) to recover fetal and maternal components from a single channel. Since this method is based on nearly periodicity of ECG signals, it is unsuitable to detect unexpected patterns. Mochimaru (Mochimaru et al., 2002) suggested a wavelet-based method, but this approach suffers in presence of overlapping maternal and fetal QRS complexes.

BSS aims to recover the source signals from a set of mixtures without a priori knowledge of the mixing process (blindly). Under the hypothesis that the mixing process is linear, if we denote with $\mathbf{s}$ the n-dimensional vector of sources, with $\mathbf{x}$ the m-dimensional vector of observed mixtures and with $\mathbf{A} \in R^{m \times n}$ the mixing matrix, the problem can be mathematically formulated as in (1):

$$\mathbf{x}(k) = \mathbf{A}\mathbf{s}(k) \tag{1}$$

where k represents a discrete time index. The solution consists in finding an unmixing matrix $\mathbf{B} \in R^{n \times m}$ such that $\hat{\mathbf{s}}(k) = \mathbf{B}\mathbf{x}(k)$ is a good estimation of $\mathbf{s}$ up to a permutation and a multiplicative constant (the two BSS ambiguities).

Source separation can be accomplished by Principal Component Analysis (PCA) and Independent Component Analysis (ICA). PCA looks for components which are uncorrelated, whereas ICA looks for components which are statistically independent, i.e. whose higher order cumulants are all diagonal tensors. Since uncorrelated sources are not necessarily independent, unless they have a Gaussian distribution, and ECG signals are known to be super-Gaussian, ICA is more appropriate than PCA, producing better results (Bacharakis et al., 1996). Sources involved in this application descend from different bioelectric phenomena and can be fairly considered statistically independent. It is also well-accepted that MECG gives rise to 3 source signals and FECG can be represented by means of 2 source signals (Nandi and Zarzoso, 1997). Hence it suffices to have a number of observed mixtures not lower than the number of sources to ensure the identifiability of ICA model. In the following, we assume $m = n$, then all vectors will be n-dimensional and all matrices will be $n \times n$.

Since De Lathauwer (De Lathauwer, 1995) has first used ICA to separate FECG successfully, many researchers resorted to the same approach, proved to perform better than the Widrow's method (Zarzoso and Nandi, 2001), and rather robust with respect to electrodes placement. De Lathauwer (De Lathauwer et al., 2000) showed ICA capability to reveal ectopic beats in a regular ECG, differently from other approaches making assumptions on the signal characteristics. This property makes BSS by means of ICA suitable for medical applications.

3 THE PROPOSED ALGORITHM

All the algorithms cited in Section 2 process data in batch mode, so they can be used only if the mixing process does not change over time. Since both mother and fetus can move, the separation algorithm must be able to track such changes. Some on-line solutions have been conceived but, unlike batch ones, the quality of the estimated sources is quite poor. We identified a good on-line algorithm in terms of separation quality in Mermaid (Marossero et al., 2003) but the main drawback is the parameter tuning, since several parameters have to be chosen empirically to achieve a good-quality signal. Balancing pros and cons of both batch and on-line techniques, we chose to derive a block-on-line method from a batch one: JADE (Cardoso and Souloumiac, 1993).

3.1 Background: The Jade Algorithm

In the JADE algorithm the ICA problem is solved by means of a two-stage procedure consisting of a preliminary processing performed by employing Second-Order Statistics (SOS) and a second one performed by resorting to Higher-Order Statistics (HOS). The first stage, multiplying by a whitening matrix $\mathbf{W}$ the observed mixtures, decorrelates and normalizes them; the second stage aims to obtain higher-order independence by multiplying decorrelated mixtures by an orthogonal rotation matrix $\mathbf{G}$ which minimizes the sum of squared fourth order cross cumulants of whitened observations:

$$\Psi = \sum_{ijkl \neq iikl} {K_{ijkl}}^2 \tag{2}$$

The $\mathbf{G}$ matrix is found by joint diagonalization of the cumulant matrices, efficiently performed by Jacobi method. This technique works by repeated sweeps of plane rotations, each one applied to a pair of rows of the cumulant matrices. During a sweep, for each pair (i, j) with $1 \leq i \leq n$, the Givens angle θ_{ij} which minimizes the contrast is calculated and if $\theta_{ij} > \theta_{th}$ (θ_{th} is a threshold angle whose value determines the optimization accuracy) the pair is rotated. The convergence is obtained when no pairs have been rotated over a sweep. This optimization procedure does not suffer from problems of convergence, as op-

posed to the gradient descent algorithm, and does not show the difficulty of parameters tuning.

The blind identifiability requires the diagonalization of the whole fourth-order cumulant set (n^2 cumulant matrices). The original JADE algorithm deals with complex signals and finds the **G** matrix by approximate joint diagonalization of the n most significant cumulant matrices, to reduce the computational load. Since we are dealing with real signals, we can exploit the symmetries of the cumulants to reduce to $n(n+1)/2$ the number of matrices to be diagonalized, without statistical loss (Cardoso, 1999).

3.2 On-Line Jade Implementation

For a batch algorithm, the permutation ambiguity is simply the obvious outcome of the mathematical formulation of the problem: the order of the sources is unpredictable and usually insignificant. It comes to be a critical problem in block-on-line algorithms, where the estimated sources can be differently ordered in different blocks, so that channels can swap producing meaningless signals. We solved this problem by combining a sliding window strategy (window length: L samples, overlap: $(L-T)$ samples) with a two-step HOS stage. First of all, the algorithm performs the preprocessing stage (SOS, i.e. centering and whitening) on a sample-by-sample basis. The data stream is subdivided into data blocks $\mathbf{X}$ of length T, with $\mathbf{X} = \{\mathbf{x}(k), 0 \leq k < T\}$. Recorded data of a block are centered subtracting their mean value by means of a running average given by:

$$\overline{\mathbf{x}}(k) = (1-\gamma)\overline{\mathbf{x}}(k-1) + \gamma\mathbf{x}(k), \tag{3}$$

where γ is a forgetting factor. We chose $\gamma = 1/L$ so that the memory depth is equal to the sliding window length. Centered data are whitened as follows:

$$\mathbf{z}(k) = \mathbf{W}(k)(\mathbf{x}(k) - \overline{\mathbf{x}}(k)) \tag{4}$$

and whitening matrix is updated using an approach adapted from (Cardoso and Laheld, 1996):

$$\begin{aligned}&\mathbf{W}(k+1) = \\ &= \mathbf{W}(k) - \frac{\lambda_0}{1+\lambda_0\mathbf{z}(k)^T\mathbf{z}(k)}(\mathbf{z}(k)\mathbf{z}(k)^T - \mathbf{I})\mathbf{W}(k)\end{aligned} \tag{5}$$

where λ_0 is a constant. The smaller λ_0 the slower the convergence, but with high values it is easier to incur in instability. The newest T preprocessed data are inserted in a L-wide window $\mathbf{Z} = \{\mathbf{z}(k), 0 \leq k < L\}$ with the last $L-T$ preprocessed samples.

After that, in the HOS stage, we precondition the rotation process by a coarse separation of the actual block of whitened mixtures with the rotation matrix of the previous block. This procedure considers that fetal movements can change the physical configuration and consequently the mixing matrix but, if T is chosen so that two consecutive blocks are close enough from a temporal point of view with respect to the dynamics of the mixing process, the coarse separation rotates whitened observations so that the basis vectors (the columns of the mixing matrix) of the current block are close to the basis vectors of the previous block. Coarse-separated mixtures are then used for the computation of the cumulant matrices and their joint diagonalization. At last, the fine separation matrix **G** is provided in output, the optimization process being carried out in the direction started from the coarse separation. The algorithm can be described by the following steps:

1. Acquire a block $\mathbf{X}$ of T new samples $\mathbf{X} = \{\mathbf{x}(k), 0 \leq k < T\}$;
2. For all k so that $0 \leq k < T$:
   (a) Center $\mathbf{x}(k)$ by subtracting $\overline{\mathbf{x}}(k)$ calculated as in (3), and keep $\overline{\mathbf{x}}(T-1)$ as the $\overline{\mathbf{x}}(-1)$ for the next block;
   (b) Whiten $(\mathbf{x}(k) - \overline{\mathbf{x}}(k))$ according to (4) to obtain $\mathbf{z}(k)$;
   (c) Update the whitening matrix following (5) and keep $\mathbf{W}(T-1)$ as the $\mathbf{W}(-1)$ for the next block;
   (d) Insert $\mathbf{z}(k)$ in $\mathbf{Z}(L-T+k)$;
3. Perform the coarse separation of $\mathbf{Z}$: $\mathbf{Y}' = \mathbf{Q}_{prev}\mathbf{Z}$;
4. Apply JADE algorithm to $\mathbf{Y}'$ to obtain the matrix **G**;
5. Perform the fine separation $\mathbf{Y} = \mathbf{G}\mathbf{Y}'$;
6. Update the rotation matrix $\mathbf{Q}_{cur} = \mathbf{G}\mathbf{Q}_{prev}$, $\mathbf{Q}_{prev} = \mathbf{Q}_{cur}$;
7. Go to 1 for another block.

3.3 Parameters Setting

The proposed algorithm has been applied to a real dataset consisting of $n = 8$ potential recordings, the first 5 abdominal and the last 3 thoracic. The dataset (BIOMED, 2005) is recorded at a sampling rate of 250 Hz, and it is composed of 2500 samples (Figure 1). It represents the benchmark used in most of research works about fetal ECG extraction. We set λ_0 to 0.001. The choice of L and T aims at achieving a good trade-off among permutation rejection, separation quality and computational efficiency. L and T are set to be 1024 and 256 respectively. A higher T gives rise to ECG channels swapping, a higher L increases the needed floating point operations (FLOPS) without improving the separation quality.

Figure 1: The real signal mixtures (BIOMED, 2005).

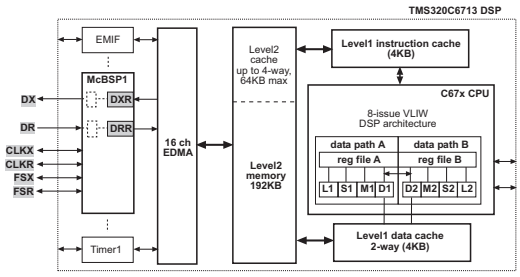

Figure 2: A block diagram of the simulated system.

4 THE DSP SYSTEM DESIGN

Modern electrocardiographs are based on DSPs, sometimes joined to a microcontroller for the user interface. The main problems of such implementations are the limited amount of memory available both on chip and on board and the low operating frequency, compared to PC processors. Conversely, DSPs are significantly less power hungry and highly optimized for signal processing operations. Almost all the devices on the market can be programmed in C or C++, so enhancing code portability. However, some performance improvements can be achieved only by exploiting at the most the architectural characteristics of the processor and then also assembly-written routines. All these aspects have been carefully taken into account in the proposed real-time system design.

The algorithm has been coded in C to work by file I/O on a PC, and then ported on a TMS320C6713 DSP, a TI 1800MFLOPS floating point VLIW processor up to 300MHz. Having to rely only on recorded signals, we avoided any hardware board implementation. To evaluate the real-time capabilities of the proposed DSP solution, it has been simulated under Code Composer Studio (CCS) 3.1, the Integrated Development Environment for the TI processors, with the Device Cycle Accurate Simulator as target. It is able to give an indication of the cycle count of the application with cycle accuracy even at peripherals level. The target DSP provides a rich set of on-chip advanced peripherals. Among them, we used one of the two Multi-channel Buffered Serial Ports (McBSP) available on chip, and the Enhanced Direct Memory Access Controller (EDMA).

Data enter the system through the McBSP1 in frames composed of 8 channels of the ECG, 16 bit/sample, with the proper sampling rate. The EDMA manages the acquisition performing a data ordering in an array placed in the internal L2 memory, so that at the end of a block acquisition such array is composed of 8 contiguous blocks of T samples, each one consisting only of the input samples for one channel. At the same time, the output samples are outputted through the same serial port with the inverse reordering procedure. The CCS Port Connect and Pin Connect features were used to provide the McBSP1 with the external clocks and frame syncs needed to correctly perform both the sample acquisition and the outputs collection, thus emulating a real hardware system. A simplified representation of the simulated system is depicted in Figure 2, where the externally driven pins (CLKX, CLKR, FSX, FSR) and ports (DXR and DRR) are shadowed. To guarantee stable input signals during the acquisition of a next block, EDMA performs automatic ping-pong buffering. The newest T samples $\mathbf{X}_i$ are acquired during the processing of the previous block $\mathbf{Z}_{i-1}$, so that the overall processing time must be less than $T_X = T/f_s$. This way the interrupt signal period is also equal to T_X. After sample-by-sample pre-processing, a Quick DMA (QDMA) call performs the sliding window mechanism needed for the HOS stage. We used fastRTS and DSPlib for highly optimized math functions and DSP array operations respectively. The access to the external memory dramatically increases the latency, whilst the wide data arrays substantially reduce the code space. With the chosen target, which comes with 256KB L2 internal RAM, and several optimizations, no external memory is required.

5 EXPERIMENTAL RESULTS

The sources estimated by means of the on-line algorithm are depicted in Figure 3. ECG channels do not suffer from the permutation problem, whereas there is a suspect permutation in the y_2 and y_4 noise channels. Such different robustness to permutations can be explained in the light of fact that cumulant based methods need a large number of samples to reach good separation results. The L value has been chosen so

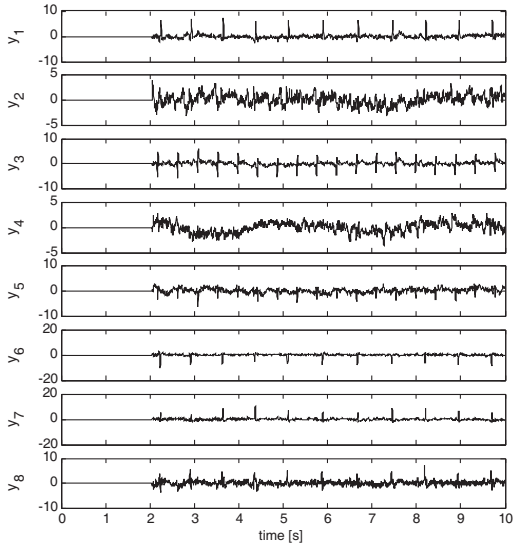

Figure 3: The sources estimated with the proposed on-line solution. The blanked parts of the signals at the beginning are due to the initialization of the on-line whitening procedure. Traces y_3 and y_5 clearly show the FECG, the hearth rate being almost twice the maternal one.

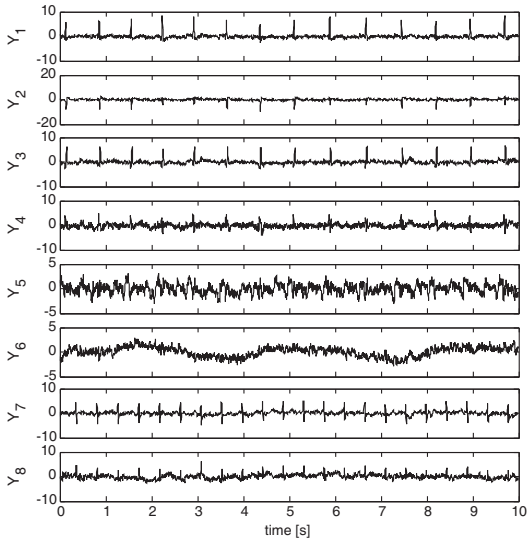

Figure 4: The sources estimated with the batch JADE algorithm. Traces Y_7 and Y_8 clearly show the FECG.

that a window contains some periods of ECG signals. Such noises can be interpreted as maternal respiration and electromyogram. Since respiration baseline wander is characterized by a pseudo-period higher than the one of ECG, we should work with a wider window to make up to a window containing some periods of fluctuation due to the maternal respiration, but this would increment the computational load. Furthermore some more unstructured noises could take no advantage of such resizing. Since our target are the ECG signals, we can disregard noise channels, maintaining $L = 1024$. With this choice, ECG waveforms are reconstructed with the same quality of the original JADE algorithm (Figure 4). To compare the performance of the two methods, we used the parameter proposed in (Bacharakis et al., 1996):

$$P_K = \frac{|K_{40}| + |K_{04}|}{\sum_{m+n=4} |K_{mn}|} \tag{6}$$

P_K represents the ratio between the sum of the modulus of the fourth-order auto-cumulants of two estimated sources and the sum of the modulus of all the fourth-order cumulants related to the same sources. If two components are really independent their cross-cumulants are close to 0, then the ratio tends to 1. In Table 1 are reported the cumulative results for all the signal couples, in terms of average value and standard deviation. It proves that the two methods allow to reach very similar source independence.

Table 1: Original batch JADE vs. block-on-line JADE. Average and standard deviation of the parameter P_K.

	avg	*STD*
Batch Algorithm	0.918	0.066
On-line Algorithm	0.912	0.109

5.1 Profiling Results

Performance have been also evaluated by means of cycle profiling to assess the real-time constraints satisfaction. From Table 2 we can see that the system largely respects the real-time requirements, since T_X is almost equal to 1 second and the DSP is running at 300 MHz. Hence, it will be possible either to add further pre/post processing to the actual implementation (such as signal enhancement, fetal QRS detection, fetal ECG delineation and measurement) and to safely reduce the clock rate. From Table 2 it is possible to notice that the time spent for the execution of the algorithm with the number of sweeps required (on the same block $\mathbf{Z}_i$), T_{tot}, represents about 8.3% of T_X, pre-processing requires less than 7% of T_{tot}, and the coarse separation plus $\mathbf{Q}_{prev}$ update less than 0.9% of T_{tot}. On the available records, we counted a maximum of 6 sweeps. In the HOS stage cycle count, there is a considerable offset due to the cumulant matrices computation that can be quantified in 21,399,260 clock cycles, 83.8% of T_{tot}. It can be estimated that every pairwise Givens rotation requires 13,534 clock cycles, 0.05% of T_{tot}. Hence, considering that 1 sweep, in the worst case, consists of maximum 28 Givens rotations, and that the coarse-separation dramatically reduces

Table 2: Profiling results for the DSP implementation: *(a).* for the whole algorithm on a single block allowing all the required sweeps, and *(b)* for only the 2^{nd} step of the HOS stage allowing a different (imposed) number of sweeps.

	Algorithm section	# ck ticks
(a)	Pre-processing	1,714,300
	Coarse-sep. + $\mathbf{Q}_{prev}$ update	220,258
	step of the HOS stage	23,599,929
(b)	1 sweep	21,557,940
	2 sweep	21,936,878
	6 sweeps (threshold control)	23,599,929

the need for many sweeps, the number of sweeps is not a performance limiter.

6 CONCLUSIONS

In this paper a block on-line version of the JADE algorithm and its real time implementation on a floating point DSP has been presented and evaluated in terms of both separation quality and profiling. Separation quality results are in line with those achievable with the batch JADE algorithm. This can be interpreted in the light of the considerations presented in Section 5 since the signal is extremely clear and stable so that it is possible to assume that mixing process does not changes a lot over time. At the same time, longer signals will benefit from the block-on-line implementation with preconditioning since the probability to have a stable mixing process over the whole recording is very low. The DSP implementation proved the possibility to use this algorithm in real-time on a portable device. The system is powerful enough to use only less than 10% of the overall available processing time to execute the algorithm, then leaving space for further processing actually required in a real implementation. The realization of a front-end analog circuitry for signals acquisition will enable the trial with custom databases.

ACKNOWLEDGEMENTS

The authors wish to thank Dr. R. Tumbarello (MD. Head, Division of Pediatric Cardiology) and Dr. S. Mura (Division of Gynecology and Obstetrics) of the Hospital “G. Brotzu”, Cagliari, Italy.

REFERENCES

Bacharakis, E., Nandi, A. K., and Zarzoso, V. (1996). Foetal ECG extraction using Blind Source Separation methods. In *Proc. EUSIPCO96*, pages 395–398.

BIOMED (2005). Katholieke Universiteit Leuven, Belgium, http://homes.esat.kuleuven.be/∼biomed/biosource/data006/foetal_ecg.dat.

Camps, G., Martinez, M., and Soria, E. (2001). Fetal ECG Extraction using an FIR Neural Network. *Computers in Cardiology*, pages 23–26.

Cardoso, J. and Souloumiac, A. (1993). Blind beamforming for non-Gaussian signals. In *IEEE PROCEEDINGS F*, volume 140, pages 362–370.

Cardoso, J. F. (1999). High-order contrasts for independent component analysis. *Neural Computation*, 11(1):157–192.

Cardoso, J. F. and Laheld, B. (1996). Equivariant adaptive source separation. *IEEE Trans. on S.P.*, 44(12):3017–3030.

De Lathauwer, L. (1995). Fetal Electrocardiogram Extraction by Source Subspace Separation. In *Proc. IEEE Workshop on HOS*, pages 134–138, Girona (Spain).

De Lathauwer, L., Moor, B. D., and Vandewalle, J. (2000). Fetal Electrocardiogram Extraction by Blind Source Subspace Separation. *IEEE Trans. on Biomedical Engineering*, 47(5):567–572.

Kanjilal, P. P., Palit, S., and Saha, G. (1997). Fetal ECG extraction from single-channel maternal ECG using singular value decomposition. *IEEE Transactions on Biomedical Engineering*, 44(1):51–59.

Marossero, D., Erdogmus, D., Euliano, N., Principe, J., and Hild, K. E. (2003). Independent component analysis for fetal electrocardiogram extraction: a case for the data efficient MERMAID algorithm. pages 399–408.

Mochimaru, F., Fujimoto, Y., and Ishikawa, Y. (2002). Detecting the fetal electrocardiogram by wavelet theory-based methods. *Progress in Biomedical Research*, 7(3):185–193.

Nandi, A. and Zarzoso, V. (1997). Foetal ECG separation. In *IEE Colloquium on the Use of Model Based Digital Signal Processing Techniques in the Analysis of Biomedical Signals (No. 1997/009)*, pages 8/1–8/6.

Widrow, B. and Stearns, S. D. (1985). *Adaptive Signal Processing*. Prentice-Hall Signal Processing Series.

Zarzoso, V. and Nandi, A. K. (2001). Noninvasive fetal electrocardiogram extraction: Blind separation versus adaptive noise cancellation. *IEEE Transactions on biomedical engineering*, 48(1).

ON THE FUTILITY OF INTERPRETING OVER-REPRESENTATION OF MOTIFS IN GENOMIC SEQUENCES AS FUNCTIONAL SIGNALS

Nikola Stojanovic
Department of Computer Science and Engineering, University of Texas at Arlington
Arlington, TX 76019, USA
nick@cse.uta.edu

Keywords: Transcriptional control signals, DNA motifs, Regulatory modules.

Abstract: Locating signals for the initiation of gene expression in DNA sequences is an important unsolved problem in genetics. Over more than two decades researchers have applied a large variety of sophisticated computational techniques in order to address it, but only with moderate success. In this paper we investigate the reasons for the relatively poor performance of the current models, and outline some possible directions for future work in this field.

1 INTRODUCTION

Eukaryotic gene expression is regulated by a complex network of protein–DNA and protein–protein interactions. The prevailing opinion, corroborated by many studies, is that most of these interactions take place within a few hundred bases upstream from the transcription start site, although this is still somewhat controversial (Nelson et al., 2004). In addition, sites important for the regulation of genes have been found in introns and in downstream sequences, as well as at distant loci, such as the β–globin LCR (Hardison et al., 1997b). Promoter regions in yeast are characterized by multiple occurrences of the same binding motif (van Helden et al., 1998), and this is also the case with many genes from other species. At present, relatively little is known about genetic pathways and the mechanisms of gene co-expression, but this situation is rapidly changing, especially with the advances in microarray technology and protein–protein interaction studies. However, while these advances provide an insight into expression patterns and associations, they do not tell anything about the mechanisms driving them, nor about the sites in DNA responsible for their regulation.

Despite of significant efforts over the last twenty years to computationally predict transcription factor binding signals in promoter and other regions of the genome, this remains an elusive goal. While early approaches relied on a rather naive assumption that the target sites for protein binding must feature information content sufficient for them to be uniquely recognized among all non–sites (Schneider et al., 1986), disillusionment soon followed, as any attempt to isolate functional elements in DNA resulted in an enormous number of false positives. Learning from that experience, and further experimental evidence, the bioinformatics community has widely adopted a view that the motifs for transcription factor binding in functional regions are grouped in regulatory modules, sometimes featuring multiple copies of individual sites. This idea is not new (Ackers et al., 1982; Mehldau and Myers, 1993; Kel et al., 1995), however in the recent years there has been an explosion of computational algorithms designed in an attempt to identify such modules (Hu et al., 2000; GuhaThakurta and Stormo, 2001; Rebeiz et al., 2002; Eskin and Pevzner, 2002; Jegga et al., 2002; Johansson et al., 2003; Sharan et al., 2003; Sinha et al., 2003; Aerts et al., 2004; Donaldson et al., 2005; Kundaje et al., 2005; Pierstorff et al., 2006; Papatsenko, 2007; Schones et al., 2007), to list just a few. Some of the methods also relied on the assumption that multiple copies of the same motif should be a component of these modules (Qin et al., 2003; van Helden, 2004). If a particular motif is over-represented, i.e. if it occurs in a genomic segment or a group of segments more often than expected by chance, it was anticipated that it should indicate a functional signal. Moreover, if multiple motifs in close proximity satisfy this condition, it was presumed to be a strong indication of function. Software developed for the location of such modules generally relied on previous information about the individual binding sites forming the modules. The ap-

proaches were based on the phylogenetic conservation (Jegga et al., 2002; Sharan et al., 2003; Sinha et al., 2004; Dieterich et al., 2004; Donaldson et al., 2005; Pierstorff et al., 2006) of homologous regions or promoters, approximate matching to known motif sequences acquired from databases such as TRANSFAC (Matys et al., 2006) or some combination of both. The search was performed for the statistically significant clusters of motifs (Johansson et al., 2003; Alkema et al., 2004; Kundaje et al., 2005; Schones et al., 2007), and it was often combined with matching them to conserved regions in alignments. This was necessary in order to reduce the search space, but it proved inaccurate. A regulatory module can contain elements that have not been included in the original set, but the elements which did get included were sometimes spurious, at least when binding *in vivo* is concerned. Indeed, over years evaluation studies have been consistently demonstrating that these tools have not been very effective (Fickett and Hatzigeorgiou, 1997; Tompa et al., 2005), despite of the progress in our understanding of the genome, advances in technology and sophistication of the models.

Many approaches were based on gene expression study results, and the postulated co-regulation. Promoter regions of such genes were considered simultaneously, and the programs used Gibbs sampling (Lawrence et al., 1993; Thijs et al., 2002), Bayesian clustering (Qin et al., 2003), Markov Models (Liu et al., 2001), Expectation Maximization (Bailey and Elkan, 1994), Shannon's entropy (Kundaje et al., 2005), simultaneous dyad motif discovery (Eskin and Pevzner, 2002), genetic algorithms (Aerts et al., 2004) and other techniques in order to isolate regulatory modules. Despite of the use of very sophisticated algorithms these methods have not achieved desired accuracy. Why?

2 TARGETING THE OVER–REPRESENTED MOTIFS

The use of motif over-representation for the prediction of transcription factor binding signals can be roughly divided into three categories:

1. Over-representation of single motifs in groups of related functional sequences.
2. Over-representation of motifs from a limited set, such as these recorded in the databases of DNA regulatory elements, in a single region under consideration.
3. Over-representation of phylogenetically conserved blocks in a genomic segment of interest.

Combinations of the above approaches are widely applied. We shall look at each one individually.

2.1 Single Motifs in Groups of Sequences

If the motifs recognized by transcription factor proteins were specific (such as these recognized by restriction enzymes, for instance), the search for systematically present short signals would show promise. It is commonly accepted that a transcription factor binding site consists of 5 to 25 nucleotides, and most experimentally confirmed cores tend to be on the shorter side of that range. Considering just 5 characters, and assuming that most transcriptional regulatory activity indeed happens within about 500 bases upstream of the gene start, under the simplistic model of each DNA base being equally likely, the probability of a chance occurrence of such motif at any single position would be $1/4^5 \approx 0.00098$. Within a window of 500 bases the expected number would thus be around 0.49. Using the Poisson distribution we can estimate the probability of seeing it at least once in any given window to be $1 - \mathrm{e}^{-0.49} \approx 0.39$. In consequence, if one would consider a set of just 4 *cis*–regulatory segments of co-expressed genes (determined by microarray experiments, for instance) in order to achieve statistical significance (i.e. a *p*–value of less than 0.05) and 5 to be highly significant (*p*–value < 0.01). This is encouraging, having in mind that the considered motifs are just 5 characters long, and that with 6 and more characters one can achieve statistical significance with regulatory sequences of just 2 co-expressed genes. If several motifs exhibit co-occurrence within a single set of regulatory sequences, that would almost certainly indicate a real signal, or at least a part of it (discarding for the moment the fact that such co-occurrences would also show up at many random places in the genome).

Even genes which are co-expressed under certain conditions may not be regulated in the same way. Their transcription initiation complexes may not be same, or even similar, or they may exhibit a weak similarity sufficient to yield co-expression only under certain circumstances. In addition, in any set of regulatory sequences any given motif may be absent from some, so the requirement that it should be found in all should be relaxed. Regardless of this, one can argue that when a set of regulatory sequences of co-expressed genes is available, one can determine the motifs unlikely to be shared by chance, and reliably identify at least these most common. Further studies can then be performed to identify proteins bound to these motifs, and their co-factors.

Unfortunately, nature does not follow simplistic models. Even as the core promoters lie upstream of the genes, most of their activity depends on the enhancer and other elements, which may be very far from the genes and regulating several of them simultaneously. In some cases, the co-expression pattern may stem from a group of genes affected by the *same* enhancer, rather than several enhancers featuring same motifs. Even when there are separate control elements targeted by same transcription factor proteins, and even if we assume that they would not function across domains, this expands the 500-base window to tens of thousands of bases, where only very long motifs would have a chance of achieving statistical significance.

Another problem is in that we may not even be able to detect a true binding signal present in all considered sequences. Transcription factors often feature a notorious lack of specificity, and within any given motif only certain positions, which need not be adjacent, may be important. The true transcription factor binding is determined by a very small number of bases, sometimes as small as 3. The use of position weight matrices (further referred to as PWMs) may be helpful in detecting these, but this method is far from perfect. Their biggest problem is in that they do not take into account the spatial structure of the motifs (such as positioning of the bases critical for binding within the major or minor grove of the DNA helix), which may be crucial in determining whether the specific nucleotide will interact with a protein or not. Alas, even the most recently published work, while allowing for non–contiguous critical residues, still fails to take into account anything but raw sequence information (Chakravarty et al., 2007).

2.2 Modules of Elements Retrieved from Databases

Researchers have spent many years meticulously collecting the experimental data concerning the binding of transcriptional proteins, and compiling the information about the bound motifs in databases such as TRANSFAC (Matys et al., 2006), Jaspar (Vlieghe et al., 2006) or Mapper (Marinescu et al., 2005). The consistency with which certain sequences are bound *in vitro* gives a strong support to the view that the exact nucleotide sequence is important, and that spatial and epigenetic factors may be more instrumental in blocking the sequences which are compositionally similar to the true binding targets, but which should not be used under the particular circumstances. Although it is still somewhat unclear how much of the binding effects *in vitro* would also happen *in vivo* (Jin et al., 2007), one can expect a reasonable correlation.

Concentrating on a motif recorded in a database rather than on any general one that may be repeated dramatically decreases the complexity of the search. In the extreme cases of long motifs with a strong consensus one can perform simple pattern matching and identify the targets uniquely in the genome. However, such motifs are not common, so the promise of this approach lies in the search for database motif clusters, i.e. regulatory modules. This still makes sense: TRANSFAC, the richest of the above mentioned resources, presently contains 7915 transcriptional binding sites, with consensus motifs organized into 398 position weight matrices. They come from different species, however one can use this number in rough calculations. Assuming the average length of a motif represented in a PWM to be around 9 (and for the moment discarding the fact that multiple motifs can match a single consensus) and the same random model as above, the number of possible motifs of this length would be $4^9 = 262144$. Consequently, one could estimate the probability that a motif from a set of 400 would start at any given position in the genome as $400/4^9 \approx 0.0015$. Within a window of 500 bases, putative regulatory region, the expected number of chance occurrences of a motif recorded in the database would roughly be around 0.76. Taking this number as the Poisson λ, one would need as few as 3 motifs recored in a database within a window of 500 bases (presumably serving as the anchoring for a regulatory module) in order to achieve statistical significance (p–value < 0.05). Such considerations have given rise to the creation of many software tools.

The first problem with this approach is that in a large genome such as human, even if we concentrate only on windows upstream of the known or predicted genes that would give us around 30 thousand regions, so with the p–value of 0.05 we would still get around 1500 false positive hits. Of course, for larger modules the p–values would be much lower, but one can hardly expect to locate very large clusters of sites, at least according to the current views on transcriptional regulation. If a module is shared among a few dozen regulatory sequences, and we would want to keep the specificity of the search at 0.5 or better, we would need to have the expected chance groupings at around, say, 50, which would dictate the p–value of 0.0017. Even under the above outlined simplified circumstances this would dictate literally dozens of motifs to participate in the module, forming a common core. Consequently, the poor performance of module searching software comes as no surprise.

The real–world situation is actually much worse: genomic sequences are not random assemblies of 4

letters, the regulatory module locations (moreover, locations that can be taken by individual participating motifs) are not limited to windows of length 500 immediately upstream of the genes, and many variants of a motif may match its consensus (as represented by the PWM). The currently available databases are neither complete nor accurate, and thresholds for matrix matching are set in a very *ad hoc*, heuristic fashion. In consequence, PWMs tend to match large groups of motifs, producing hits literally everywhere. Epigenetics phenomena may act in such fashion as to dramatically reduce the numbers of elements participating in a regulatory module, by making many instances of chance groupings resembling it inaccessible to transcriptional proteins, and many interactions within modules are taking place at the protein, not DNA level, further reducing the number of motifs in the genome that would need to be recognized in order to initiate transcription (and thus the size of the motif cluster corresponding to the module).

2.3 Phylogenetic Approaches

Another popular approach to identifying functional signals relies on phylogenetic conservation. Its basis is a very reasonable assumption that a functional constraint prevents mutations in DNA from becoming fixed in population, while sites which are not important are free to independently mutate and fix along separate branches of the evolutionary tree. This hypothesis has been amply confirmed by the study of coding sequences, and within them of the synonymous and non-synonymous substitutions. The encouraging results in the study of genes have led to the assumption that phylogenetic conservation can be exploited in the search for regulatory signals.

For this purpose, many investigators have turned attention to the identification of phylogenetic footprints, both in pair-wise sequence comparisons and multiple alignments. Studies have been performed in order to establish the most informative genetic distance between compared species, which have to be far apart so to minimize the noise coming from random conservation, but close enough to share similar regulatory signals (Hardison et al., 1997a; Miller, 2001), as well as the most informative additional species to place in a multiple alignment (Thomas et al., 2003). Pairwise, within the mammalian scope, sequences which have diverged about 70 million years ago (such as human and mouse) have shown greatest promise, although optimal phylogenetic distance for analysis tends to vary with the genomic locus (Hardison, 2000).

Even under the most favorable circumstances, when the effects of non-specific binding and permissible divergence in regulatory signal consensus, as well as these of inter–species differences, would be minimal, any short signal would not be sufficient to warrant significance, or it would require a multiple alignment of dozens of very close genomic sequences (Stojanovic, 2004). This is becoming feasible with bacterial, but not yet with eukaryotic genomes. Researchers have thus concentrated on the identification of clusters of conserved sites, guided by essentially the same reasoning as outlined in the previous sections. In relatively short segments of DNA it is unlikely that rearrangements would be taking place on a substantial scale, and the positional conservation of regulatory signals would lead to good alignments with short phylogenetic footprints clearly visible.

The probabilistic reasoning applied in this case relied on the strength of the signals (i.e. sequence conservation), the likelihood of seeing such conserved motif by chance, given the phylogenetic distance between the sequences, and, because the later is often difficult to establish, on the empirical determination of the background conservation within the alignment, as its sections which appear to stand out.

The first problem with this approach lies in the quality of the alignment itself: genetic regulatory signals are short and non-specific, and thus not very likely to be precisely positioned, although their relative offsets would probably be small. This, on one hand, may lead to an imprecise definition of motif boundaries, which often shows as only a partial overlap between the footprint and the experimentally confirmed binding site. On the other, the footprint itself may be difficult to identify, as its improperly aligned bases would both lower the signal and increase the neighboring region noise. In protein sequences one can at least partially exploit structural characteristics (such as α–helix signatures) in order to improve the alignment quality, but in DNA the only relatively reliable markers are the exons of genes. If one looks for their immediate upstream promoter regions this may be helpful, but unfortunately the 5' untranslated regions of variable lengths and weaker conservation (with some notable exceptions discussed below) tend to reduce the anchoring strength of the first exon.

Even when the alignment is reliable, the probability of random conservation in even distantly related sequences is too high to lend credibility to any but extremely large groupings of footprints, too large to be plausible anchor sites for the transcriptional complexes. Somewhat surprisingly, such large concentrations of footprints are not uncommon in higher eukaryotic genomes. In fact, many of these are so large that they can hardly be considered as groupings

of individual, discrete elements (Jones and Pevzner, 2006). The most dramatic example are the non-coding ultra-conserved segments, defined as blocks of 200 or more bases with absolute identity among all compared species. Within the human genome there are about 500 such blocks conserved among all sequenced mammals, but sometimes even among all vertebrates. The role of these elements is currently unknown, as many knock-out experiments have repeatedly failed to produce visible effects in model animals. Consequently, some researchers have postulated that the ultra-conservation (as well as conservation of other long non-coding blocks) may be a consequence of a regional repair mechanism of exceptional strength, but so far nobody was able to characterize what that mechanism might be, as well as why it would have been put in place at its target loci.

In order to quantify this phenomenon, we have looked at the patterns of conservation in mammalian *Hox* gene clusters (Stojanovic and Dewar, 2005), which are well preserved, and home to some of the mentioned ultra-conserved blocks. Interestingly, in *Hox* the highest overall conservation has been observed within the 5' UTR regions of genes, as illustrated in Table 1. While good conservation of untranslated regions is not common genome–wide, it has been observed in several other cases, such as mammalian casein genes (Rijnkels et al., 2003). In summary, this indicates that there is much more to phylogenetic conservation than a simple functional constraint. Before that mechanism is understood, some skepticism concerning the use of sequence conservation as a hallmark of a functional signal is warranted.

3 OVER-REPRESENTATION OF MOTIFS IN GENOMIC ENVIRONMENTS

The over-representation concept itself is problematic. It has been well known, and for a long time now, that genomic sequences, even in large "junk" areas, are not random assemblies of four letters. In order to quantify the genome-wide over-representation of short motifs, we have recently undertaken a systematic study (Singh et al., 2007) in which we have noted a remarkable over-representation of many short motifs throughout the presumably unique human genomic sequences, as well as (to a lesser extent), Markov model generated sequences trained on human chromosomes. As an example, the results counting the average number of repeated occurrences of motifs of lengths 4 through 9 measured in 6 datasets of 100 sequences of length 500 each are shown in Table 2. Our findings clearly indicated that, first, all genomic sequences feature dramatically higher numbers of repeated short motifs than one would expect by chance, and, second, that the differences in numbers of such motifs do not appear to be significant between random intergenic and presumably regulatory sequences upstream of the known genes, despite of the trend that one can notice in the last two columns of Table 2. Repeatedly, chi-square tests performed on these columns and other data could show only mild, but inconclusive, bias. This indicates that something else in addition to the functional signal is at play, but it is somewhat unclear what that might be.

In a series of studies started more than forty years ago (Waring and Britten, 1966) Britten, Davidson and others demonstrated that the nuclear genome of diverse eukaryotes contained a large fraction of repetitive DNA, and recent large–scale genome sequencing has established the ubiquitous existence of repeats. Many of them are of tandem nature, relatively easily recognizable, however the majority are the result of the repeated interspersed insertion of transposable elements, often not capable of further activity (Smit, 1999; Feschotte et al., 2002) — once integrated, these sequences will never transpose again and can be considered molecular fossils. Regardless of their origin and of the mechanisms responsible for their inactivation, it is widely accepted that fossilized transposons, as a whole, do not assume function to the host. Consequently, these inactive copies are progressively eroded by mutations accumulating at a neutral rate until they become unrecognizable. While more recent insertional events can be readily identified due to the high similarity of the copies, characterization of more ancient activity remains a challenge. In the human genome, almost half of the sequence is considered unique, but only a small fraction (about 5% of the total) is thought to be significant, whether coding or not. This leaves an open question about the origin and role of the presumably unique non-functional sequence, which is very likely to originate from ancient transpositions and duplications. Due to its degree of degeneracy, it would remain in the genomic segments under consideration after repeat masking, but it would also introduce a large number of seemingly over-represented motifs.

Therefore, many of the apparent clusters of conserved elements are likely just remnants of transposon insertions. While phylogeny–based approaches are less vulnerable to this effect, it can still be an issue when comparing sequences from species for which good repeat libraries have not yet been compiled. Regardless of the source, the micro-repetitive

Table 1: Fractions of the total number of *Hox* (*A, B, C* and *D* clusters) alignment columns in 7 distinct genomic environments contained in the regions of minimal length of 25 bp, of average conservation with p–value < 0.1 measured against the background conservation of the entire alignment. The intergenic data for *HoxD* have been parenthesized because of the Ensembl gene prediction at the location where many of these regions have been found. Overall, *HoxD* data are not as reliable because only a relatively small amount of high–quality sequence of this cluster was available in all considered species (human, baboon, mouse, rat, cow and pig) at the time of the study.

	500–1000bp 5'	200–500bp 5'	0–200bp 5'	Coding	Introns	0–1000bp 3'	Intergenic
HoxA	0.067	0.315	0.616	0.223	0.066	0.077	0.057
HoxB	0.115	0.342	0.788	0.639	0.071	0.145	0.024
HoxC	0.104	0.202	0.609	0.521	0.089	0.105	0.035
HoxD	0	0	0	0.061	0.026	0.066	(0.027)

Table 2: The mean numbers of repeated patterns of different lengths in different types of nucleotide sequences. Pattern counting has been done over 100 sequences of length 500 in each category.

Pattern Length	Expected Number	Random Synthetic	2^{nd} Order Markov M.	3^{rd} Order Markov M.	5^{th} Order Markov M.	Random Genomic	Upstream Regulatory
4	429.06	425.74	437.99	432.84	432.23	438.97	433.92
5	193.16	189.18	237.83	222.98	222.27	261.64	260.11
6	57.46	55.16	84.33	74.58	75.88	106.62	115.31
7	15.03	14.0	24.5	21.82	23.3	38.66	47.54
8	3.8	3.12	7.05	5.75	6.87	15.72	21.3
9	0.95	0.56	1.94	1.47	1.97	8.57	11.33

structure of genomic sequences of higher eukaryotes makes it very difficult to locate any feature through over-representation, simply because the background is highly non-random.

4 DISCUSSION

So far much of the computational search for genomic regulatory signals have been done using sequence information only, just because it was the most readily available. In the context of sequence analysis looking for statistical over–representation was indeed the most sensible approach. However, while the resulting combinatorial and probabilistic problems are challenging and mathematically interesting, biologically they are questionable. That does not mean that they are of no value whatsoever, only that they are currently not being used in the right way.

Much of the genome study is still in the data collecting phase. We are not yet in a position to build analytical models, and without them the quantification of their effects makes little sense. Over the last few years the scientific community has been increasingly turning attention to epigenetics, and there has recently been a significant increase in the accumulated knowledge about these phenomena. However, the computational community have so far mostly ignored these developments. At this time the study of binding signals in DNA should probably rely more on data mining approaches than on analytical models, although statistical analysis of the data will remain important.

When studying a potential regulatory role of a genomic sequence (or a group of sequences, in cases when co–regulation pattern of a group of genes is suspected), one should take into account, first of all, the specific experimentally confirmed knowledge about the region which can be mined from the literature using currently available technologies. Next, the specific biochemical information about methylation patterns and domain structure should be applied, before raw nucleotide information is considered. At the later stage the prediction and statistical evaluation should be incorporated, but structural data should still be taken into account, when available. Recent studies (Segal et al., 2006; Ioshikhes et al., 2006) have indicated that there may be specific histone proteins positioning codes in DNA, and if further evidence confirms this it would greatly help in the characterization of binding signals for other types of proteins, transcription factors in particular (through easier identification of potentially open chromatin domains). Only at this point one can concentrate on the motif–related considerations, looking for these recorded in databases and these that might be phy-

logenetically conserved. The over–representation *per se* may not be sufficient to provide useful information, but the appearance of similar motifs in areas otherwise postulated to share functionality (based on stronger evidence than just a correlation of expression in microarray experiments) may be indicative enough to warrant confidence.

The true discovery has always been through a well–coordinated combination of computational and experimental approaches. This takes time, although modern technologies are dramatically facilitating such efforts (Jin et al., 2007), so purely computational methods for genome–wide prediction of transcriptional regulatory signals will remain to be of interest. It is only that the methods will have to change in order to be really useful, and not just interesting.

ACKNOWLEDGEMENTS

The author would like to thank Cedric Feschotte of UTA Biology for useful discussions about the nature of DNA repeats, and Subhrangsu Mandal of UTA Biochemistry for the insights concerning epigenetic phenomena. Abanish Singh and David Levine of UTA Computer Science have provided computational infrastructure which generated data leading to our conclusions. This work has been partially supported by NIH grant 1R03LM009033-01A1.

REFERENCES

Ackers, G., A.D.Johnson, and M.A.Shea (1982). Quantitative model for gene regulation by lambda phage repressor. *Proc. Natl. Acad. Sci. USA*, 79:11291133.

Aerts, S., Van Loo, P., Moreau, Y., and De Moor, B. (2004). A genetic algorithm for the detection of new cis–regulatory modules in sets of co-regulated genes. *Bioinformatics.*, 20:1974–1976.

Alkema, W., Johansson, O., Lagergren, J., and Wasserman, W. (2004). MSCAN: identification of functional clusters of transcription factor binding sites. *Nucleic Acids Res.*, 32:W195–W198.

Bailey, T. and Elkan, C. (1994). Fitting a mixture model by expectation maximization to discover motifs in biopolymers. In *Proceedings of the Second International Conference on Intelligent Systems for Molecular Biology*, pages 28–36. AAAI Press.

Chakravarty, A., Carlson, J. M., Khetani, R. S., DeZiel, C. E., and Gross, R. H. (2007). SPACER: identification of *cis*–regulatory elements with non–contiguous critical residues. *Bioinformatics*, 23:1029–1031.

Dieterich, C., Rahmann, S., and Vingron, M. (2004). Functional inference from non-random distributions of conserved predicted transcription factor binding sites. *Bioinformatics.*, 20:i109–i115.

Donaldson, I. J., Chapman, M., and Gottgens, B. (2005). TFBScluster: a resource for the characterization of transcriptional regulatory networks. *Bioinformatics*, 21:3058–3059.

Eskin, E. and Pevzner, P. A. (2002). Finding composite regulatory patterns in DNA sequences. *Bioinformatics*, 18(S1):S354–S363.

Feschotte, C., Jiang, N., and Wessler, S. (2002). Plant transposable elements: where genetics meets genomics. *Nat. Rev. Genet.*, 3:329–341.

Fickett, J. and Hatzigeorgiou, A. (1997). Eukaryotic promoter recognition. *Genome Res.*, 7:861–878.

GuhaThakurta, D. and Stormo, G. (2001). Identifying target sites for cooperatively binding factors. *Bioinformatics*, 17:608–621.

Hardison, R., Oeltjen, J., and Miller, W. (1997a). Long human–mouse sequence alignments reveal novel regulatory elements: a reason to sequence the mouse genome. *Genome Res.*, 7:959–966.

Hardison, R., Slightom, J., Gumucio, D., Goodman, M., Stojanovic, N., and Miller, W. (1997b). Locus control regions of mamalian β–globin gene clusters: combining phylogenetic analyses and experimental results to gain functional insights. *Gene*, 205:73–94.

Hardison, R. C. (2000). Conserved noncoding sequences are reliable guides to regulatory elements. *Trends Genet.*, 16:369–372.

Hu, Y., Sandmeyer, S., McLaughlin, C., and Kibler, D. (2000). Combinatorial motif analysis and hypothesis generation on a genomic scale. *Bioinformatics*, 16:222–232.

Ioshikhes, I. P., Albert, I., Zanton, S. J., and Pugh, B. F. (2006). Nucleosome positions predicted through comparative genomicsenetic. *Nature Genetics*, 38:1210–1215.

Jegga, A., Sherwood, S., Carman, J., Pinski, A., Phillips, J., Pestian, J., and Aronow, B. (2002). Detection and visualization of compositionally similar *cis*–regulatory element clusters in orthologous and coordinatelly controlled genes. *Genome Res.*, 12:1408–1417.

Jin, V. X., O'Geen, H., Iyengar, S., Green, R., and Farnham, P. J. (2007). Identification of an OCT4 and SRY regulatory module using integrated computational and experimental genomics approaches. *Genome Res.*, 17:807–817.

Johansson, O., Alkema, W., Wasserman, W., and Lagergren, J. (2003). Identification of functional clusters of transcription factor binding motifs in genome sequences: the MSCAN algorithm. *Bioinformatics*, 19:i169–i176.

Jones, N. C. and Pevzner, P. A. (2006). Comparative genomics reveals unusually long motifs in mammalian genomes. *Bioinformatics*, 22:e236–e242.

Kel, O., Romaschenko, A., Kel, A., Wingender, E., and Kolchanov, N. (1995). A compilation of composite regulatory elements affecting gene transcription in vertebrates. *Nucleic Acids Res.*, 23:4097–4103.

Kundaje, A., Middendorf, M., Gao, F., Wiggins, C., and Leslie, C. (2005). Combining sequence and time series expression data to learn transcriptional modules. *IEEE/ACM Trans. Comput. Biol. Bioinform.*, 2:194–202.

Lawrence, C. E., Altschul, S. F., Boguski, M. S., Liu, J. S., Neuwald, A. F., and Wootton, J. C. (1993). Detecting subtle sequence signals: a Gibbs Sampling strategy for multiple alignment. *Science*, 262:208–214.

Liu, X., Brutlag, D., and Liu, J. (2001). Bioprospector: discovering conserved DNA motifs in upstream regulatory regions of co-expressed genes. In *Pac. Symp. Biocomput.*, pages 127–138.

Marinescu, V., Kohane, I., and Riva, A. (2005). The MAPPER database: a multi-genome catalog of putative transcription factor binding sites. *Nucleic Acids Res.*, 33D:D91–D97.

Matys, V., Kel–Margoulis, O.V., Fricke, E. *et al.* (2006). TRANSFAC®and its module TRANSCompel®: transcriptional gene regulation in eukaryotes. *Nucleic Acids Res.*, 34:D108–D110.

Mehldau, G. and Myers, G. (1993). A system for pattern matching applications on biosequences. *Comput. Appl. Biosci.*, 9:299–314.

Miller, W. (2001). Comparison of genomic DNA sequences: solved and unsolved problems. *Bioinformatics*, 17:391–397.

Nelson, C., Hersh, B., and Carroll, S. B. (2004). The regulatory content of intergenic DNA shapes genome architecture. *Genome Biol.*, 5:R25.

Papatsenko, D. (2007). ClusterDraw web server: a tool to identify and visualize clusters of binding motifs for transcription factors. *Bioinformatics*, 23:1032–1034.

Pierstorff, N., Bergman, C. M., and Wiehe, T. (2006). Identifying *cis*–regulatory modules by combining comparative and compositional analysis of DNA. *Bioinformatics*, 22:2858–2864.

Qin, Z., McCue, L., Thompson, W., Mayerhofer, L., Lawrence, C., and Liu, J. (2003). Identification of coregulated genes through Bayesian clustering of predicted regulatory binding sites. *Nature Biotechnology*, 21(4):435–439.

Rebeiz, M., Reeves, N. L., and Posakony, J. W. (2002). SCORE: A computational approach to the identification of *cis*–regulatory modules and target genes in whole–genome sequence data. *Proc. Natl. Acad. Sci. USA*, 99(15):9888–9893.

Rijnkels, M., Elnitski, L., Miller, W., and Rosen, J. M. (2003). Multispecies comparative analysis of a mammalian–specific genomic domain encoding secretory proteins. *Genomics*, 82:417–432.

Schneider, T. D., Stormo, G. D., Gold, L., and Ehrenfeucht, A. (1986). Information content of binding sites on nucleotide sequences. *J. Mol. Biol.*, 188:415–431.

Schones, D. E., Smith, A. D., and Zhang, M. Q. (2007). Statistical significance of cis-regulatory modules. *BMC Bioinformatics*, 8:19.

Segal, E., Fondufe–Mittendorf, Y., Chen, L., Thastrom, A., Field, Y., Moore, I. K., Wang, J.-P. Z., and Widom, J. (2006). A genomic code for nucleosome positioning. *Nature*, 442:772–778.

Sharan, R., Ovcharenko, I., Ben-Hur, A., and Karp, R. (2003). CREME: a framework for identifying *cis*–regulatory modules in human–mouse conserved segments. *Bioinformatics*, 19:i283–i291.

Singh, A., Feschotte, C., and Stojanovic, N. (2007). A study of the repetitive structure and distribution of short motifs in human genomic sequences. *Int. J. Bioinformatics Research and Applications*, 3:523–535.

Sinha, S., Schroeder, M., Unnerstall, U., Gaul, U., and Siggia, E. (2004). Cross–species comparison significantly improves genome–wide prediction of *cis*–regulatory modules in *drosophila*. *BMC Bioinformatics.*, 5:129.

Sinha, S., vanNimwegen, E., and Siggia, E. (2003). A probabilistic method to detect regulatory modules. *Bioinformatics*, 19:i292–i301.

Smit, A. (1999). Interspersed repeats and other mementos of transposable elements in mammalian genomes. *Curr. Opin. Genet. Dev.*, 9:657–663.

Stojanovic, N. (2004). Computational methods for the analysis of differential conservation in groups of similar DNA sequences. *Genome Informatics*, 15:21–30.

Stojanovic, N. and Dewar, K. (2005). A probabilistic approach to the assessment of phylogenetic conservation in mammalian *Hox* gene clusters. In *Proceedings of the BIOINFO 2005, International Joint Conference of InCoB, AASBi and KSBI*, pages 118–123.

Thijs, G., Marchal, K., Lescot, M., Rombauts, S., De Moor, B., Rouze, P., and Moreau, Y. (2002). A Gibbs sampling method to detect overrepresented motifs in the upstream regions of coexpressed genes. *J. Comput. Biol.*, 9(2):447–464.

Thomas, J.W., Touchman, J.W., Blakesley, R.W. *et al.* (2003). Comparative analysis of multi-species sequences from targeted genomic regions. *Nature*, 424:788–793.

Tompa, M., Li, N., and Bailey, T.L. *et al.* (2005). Assessing computational tools for the discovery of transcription factor binding sites. *Nature Biotechnology*, 23(1):137–144.

van Helden, J. (2004). Metrics for comparing regulatory sequences on the basis of pattern counts. *Bioinformatics*, 20:399–406.

van Helden, J., Andre, B., and Collado-Vides, J. (1998). Extracting regulatory sites from the upstream region of yeast genes by computational analysis of oligonucleotide frequencies. *J. Mol. Biol.*, 281:827–842.

Vlieghe, D., Sandelin, A., De Bleser, P. J., Vleminckx, K., Wasserman, W. W., van Roy, F., and Lenhard, B. (2006). A new generation of JASPAR, the open–access repository for transcription factor binding site profiles. *Nucleic Acids Res.*, 34:D95–D97.

Waring, M. and Britten, R. (1966). Nucleotide sequence repetition: a rapidly reassociating fraction of mouse DNA. *Science*, 154:791–794.

A DNA-INSPIRED ENCRYPTION METHODOLOGY FOR SECURE, MOBILE AD-HOC NETWORKS (MANET)

Harry C. Shaw and Sayed Hussein
NASA Goddard Space Flight Center, Greenbelt, MD, USA
Department of Electrical and Computer Engineering, George Washington University, Washington, DC, USA
Harry.c.shaw@nasa.gov, drsay@gwu.edu

Keywords: Encryption, DNA computing, MANET, Biomimetic, Molecular Cryptography, Steganography, Computational Biology.

Abstract: Molecular biology models such as DNA evolution can provide a basis for proprietary architectures that achieve high degrees of diffusion and confusion and resistance to cryptanalysis. Proprietary encryption products can serve both large and small applications and can exist at both application and network level. This paper briefly outlines the basis of the proprietary encryption mechanism which uses the principles of DNA replication and steganography (hidden word cryptography) to produce confidential data. The foundation of the approach includes: organization of coded words and messages using base pairs organized into genes, an expandable genome consisting of DNA-based chromosome keys, and a DNA-based message encoding, replication, and evolution process. Such an encryption model provides "Security by Obscurity".

1 INTRODUCTION

Mobile Ad-hoc Networks (MANET) require the ability to distinguish trusted peers, and transmit and receive information confidentially, yet tolerate the ingress and egress of nodes on an unscheduled, unpredictable basis. Because the networks by their very nature are mobile, self-organizing and self assembling, use of a Public Key Infrastructure (PKI), X.509 certificates, RSA and nonce exchanges becomes problematic if the ideal of MANET is to be achieved. The use of evolutionary computing and a DNA (Deoxyribonucleic acid) inspired approach are key in developing true MANET architectures. Future network organizations could include corporations, retail outlets, financial institutions organized into self-assembling MANETs of convenience, entering and leaving the network as necessary. Such networks might be better served by encryption approaches not widely available to the public.

This paper presents a new encryption technique which utilizes DNA-inspired coding, a dynamic fitness algorithm and trust metric vision for ad-hoc routing, and a rapidly evolving basis of encryption. Because of the dynamic, evolutionary nature of this approach, potential intruders must continually intercept decoding instructions between source and destination. Missing one generation of genome decryption information seriously corrupts the decryption process. Missing multiple generations eventually renders previous decryption analyses useless.

2 BACKGROUND OF DNA CRYPTOGRAPHY

The use of DNA as a cryptographic medium is not new. DNA encryption systems are one of the paths taken in the field of molecular computing. Systems using DNA as a one-time code pad (Gehani, 1999) in a steganographic approach have been described. An image compression –encryption system using a DNA-based alphabet (Bourbakis, 1997) was demonstrated including a genetic algorithm based compression scheme. Schemes utilizing DNA encryption utilizing dummy sequences of DNA have been published (Leier, 2000). The steganographic approach is highly desirable because DNA provides a natural template for the hidden message approach (Clelland, 1999). Clelland is a pioneer in this field. It also appears in recent applications such as DNA watermarks (Heider, 2007).

3 PROBLEM STATEMENT

Figure 1 displays a MANET routed message from Jack to Jill routed at two different times, through secure and potentially malicious nodes. A truly ad hoc network permits routing in the presence of un-trusted peers. In this case, message traffic is between Jack and Jill. Nodes A, B and C are trustworthy nodes at time t_1 and nodes α and β are potentially malicious nodes. At time t_2, the situation is reversed.

The problem of successful routing of messages over potentially un-trusted nodes requires:

- Routed messages arrive at the destination intact
- Routed messages remain confidential in transmission
- Cryptanalysis of message traffic passing through nodes other Jack or Jill is unlikely to be successful.
- Nodes enter and leave the network at will.

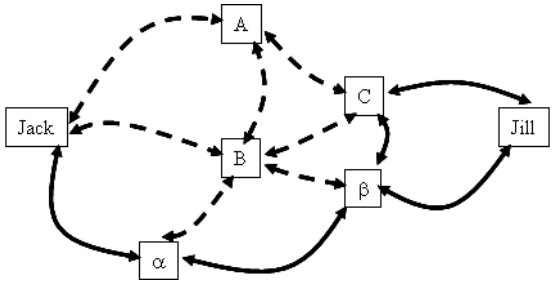

Figure 1: MANET routed over secure nodes at t_1 (—) and secure nodes at t_2 (---).

4 ENCRYPTION PROCESS

- Two or more users define a plaintext dictionary, and a DNA based dictionary. The users define the method by which plaintext is represented by the four DNA bases. The DNA dictionary is the is the source of messages and encryption keys (chromosomes)
- Messages are pre-coded from plaintext into DNA using a system of linear equations relating word position in the message and the ordinal position in the dictionary
- Chromosomes encrypt multiple permutations of the message
- The permutations are tested for fitness and the most fit permutation is selected for transmission by the source.
- The recipient decrypts the message with the same chromosomes
- The genome is expanded by mutating the chromosomes with each other or with message sequences.

The system is based upon operations upon words and not individual characters. The only individual characters that are encrypted are one character words.

Users of the DNA encryption tool are endowed with a starter genome which provides the equivalent of a small dictionary for initiating messages, an intended recipient capable of possessing a secret, shared key, and a secret encryption/decryption sequence to initiate communication. Chromosomes are "long" compared to message sequences.

Let D represent a dictionary (lexicographically ordered set) of all words such that D_0 represents the first word in the dictionary and that sender and receiver compose messages of W_i words (genes). A function U converts words to sequences of DNA bases B_q as shown below:

$$D_{i-1} < D_i < D_{i+1} \; \forall \; i < n \quad (1)$$

$$W_i, \subseteq D_n \quad (2)$$

$$D_i = U(W_i, B_q) \quad (3)$$

There exists a one-to-one mapping between the plaintext dictionary and DNA dictionary built from B_q={A,T,C,G} and. The binary coding for the bases is shown in table 1. Note that A and T, and C and G are inverses.

Table 1: DNA base coding.

Base	Binary value	Base	Binary value
Adenine	0011	Thymine	1100
Cytosine	1001	Guanine	0110

Given an alphabet of n characters, words of character length m, each plaintext word codes into a DNA word (gene) of x basepairs in length creating c_i possible combinations of DNA words for each plaintext word and Y total combinations DNA words for the dictionary as shown below.

$$\log_2 (n) = x \quad (4)$$

$$c_i = 2^{(x*m)} \quad (5)$$

$$Y = \Sigma \, c_i \, , \; i=1,\ldots,i_{max} \quad (6)$$

For n=8 with a character set consisting of {a,e,i,o,u,n,s,t}, and m= 3, there would be 584 total entries. Selected entries from such a dictionary are shown in table 2. Sequences of nonsense words can be inserted between plaintext words. As the character set and character length increases, the number of possible words (mostly nonsense words) increases exponentially. Actual words can be padded with interspersed nonsense words to increase security. Figure 2 shows displays the maximum size of the DNA dictionary for 8, 32 and 256 character

alphabets, word lengths ranging from 1 to 10 characters.

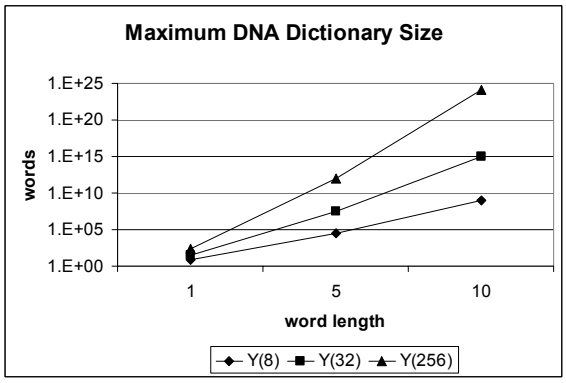

Figure 2: DNA Dictionary Size.

Table 2: Sample DNA dictionary entries.

ordinal	word	DNA code
146	i	TTT
147	ia	TTACAT
148	ie	TTATAT
452	san	ACACACGCC
453	sas	ACACAGAAG
454	sat	ACACATAAT
455	sea	ACCACACCC

The plaintext coding process yields message M consisting of a sense string M_{sense} of bases and $M_{anti\text{-}sense}$ string of bases. Chromosome ($C_{1,..j}$) sense and anti-sense strands generated from the DNA dictionary encrypt M_{sense} and $M_{anti\text{-}sense}$ to produce encrypted mutants. Given j chromosomes in the genome, m message basepairs, k chromosome basepairs, 2*j*(k-m) rounds of encryption on the sense and anti-sense message strands are possible. The message slides down the chromosome between rounds. One encrypted mutant is produced per round.

Table 3: Encryption Process.

Encrypt	$E(C,M) \rightarrow$Cipher
Anneal	$A(Cipher, B(q')) \rightarrow$ ACipher
Trust for p routes	$T_p(FREQ_p,RREQ_p) \rightarrow T_{max}$
Fitness(Diffusion & Confusion)	$D(M,ACipher),C(M,ACipher) \rightarrow F$
Select mutant	$S(g(F,T_{max})) \rightarrow$ Output

Encryption is a 5 step process as shown in table 3. The encryption step processes the message against the chromosome key to create a generation of two new mutants: A DNA fragment consisting of a sense strand from the message paired with a fragment of equivalent length from the sense strand of each chromosome moving from 5′to 3′ end, and a DNA fragment consisting of an anti-sense strand from the message paired with a fragment of equivalent length from the sense strand of each chromosome key moving from 3′to 5′ end. The process is summarized in figure 4. The chromosome is depicted as a series of segments. The functional output of the step is referred to as 'Cipher'

The process of aligning two dissimilar DNA strands results in numerous mismatches. Figure 5 demonstrates the annealing process via recombination and mutation by use of virtual bases B'_q = {a,t,c,g} Use of the transformation: A→g→T, C→a→G, T→c→A, G→t→C simplifies the evolution of the code and anneals mismatches. Mutations are induced by the chromosome (encryption key) onto the message (plaintext). The rule is simple: if mismatch between the chromosome base and a message base appears, the message is mutated to match the chromosome. For example, if a chromosome base 'A' is mismatched with either 'A', 'C' or 'G' on the corresponding message base, the message base is changed to a 'g' which mutates to a 'T'. The unused bit patterns in the 4-bit binary representations of the DNA hold special codes for this transformation. The advantage of this technique is that it allows for rapid merging of chromosome and message strands and provides a path for substituting new bases into the chromosome strand and mimics the activity of creating molecules which rely on the DNA structure but have substituted new monomer units into the structure. This technique could also be combined with crossover between chromosome and message strand. The functional output of this step is referred to as 'ACipher' for annealed ciphertext.

The sender of the message would like to know how much trust should be placed in each potential route to the destination. Determining the level of trust to be placed is a factor in determining the fitness of the encryption. The source of trust information in the methodology is querying the network and tabulating successful forward and return route request messages (FREQ, RREQ). The value of this information decays between successive queries. Given the assumption that any route is only as secure as the weakest link, a trust metric for p routes at a given point in time can be defined as:

$$T_p(FREQ_p,RREQ_p,\Delta t) = (e^{-\Delta t/\tau})*ZF_p*ZR_p \quad (7)$$

where ZF_p and ZR_p are the number of successful forward and return route requests over p routes and Δt is the delay from the baseline query. The rate of

decay in trust can be adjusted by the factor r to depending upon sender preference with the effects as shown in figure 3. The maximum value from all T_p represents the most desired route and is referred to as 'T_{max}'.

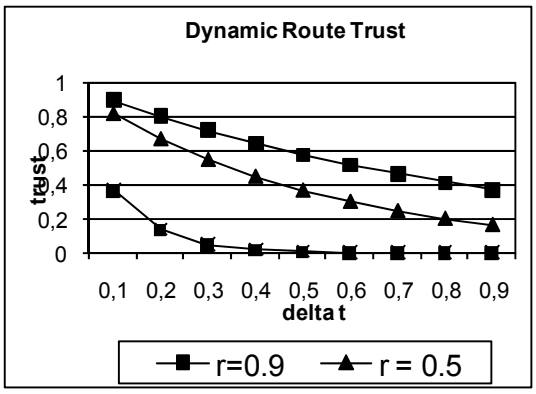

Figure 3: Temporal route trust.

A fitness algorithm defining the desired level of diffusion and confusion (Shannon, 1949) produces a means for evaluating each potential encryption. Diffusion ensure that redundancy or patterns in the plaintext message are dissipated into the long range statistics of the ciphertext message. Confusion ensures a complex relationship exists between the plaintext and ciphertext. Each encrypted mutant is compared to the plaintext message on this basis. The output of these functions produces a fitness value, 'F', for each mutant.

The source can define a fitness goal, $g(F,T_{max})$ such that only an encrypted mutant that exceeds the goal is selected by function S to become the transmitted message, referred to as the ' Output'.

Conceivably, if no mutant exceeded the fitness goal, the sender could select one of the following options:

a. Reduce the magnitude of the fitness parameters diffusion and confusion
b. Query the network again, re-compute T_{max} and determine if there is an encryption fit for transmission.
c. Conduct a second round of encryption by mating the most fit encrypted mutants, and re-compute their fitness parameters
d. Delay transmission of the encrypted message until a suitable T_{max} is achieved.

Figure 6 displays the transition from plaintext to a pair of DNA strands 54 base pairs long (M_{sense} and $M_{anti\text{-}sense}$) to a pair of encrypted and annealed mutants with a sense strand from message and chromosome for one mutant, and a anti-sense strand from message and chromosme for a second mutant. The 8 letter dictionary {a,e,i,o,u,n,s,t} and a chromosome designated as C4 having 1793 base pairs are used in this example.

5 MUTATION EFFECTS AND FITNESS

Life is intolerant of a high mutation rate in its genetic code. Ribonucleic acid (RNA) viruses have the highest mutation rate of any living species, 10^{-3} to 10^{-5} errors/nucleotide and replication cycle (Elena, 2006). The human DNA mutation rate has been approximated to be on the order of 10^{-8} errors/nucleotide and generation (Nachman, 2000). Injection of mutations into DNA encrypted messages is central to the encryption process.

In evolutionary biology, fitness is a characteristic that relates to the number of offspring produced from a given genome. From a population genetics point of a view the relative fitness of the mutant depends upon the number of descendants per wild-type descendant. In evolutionary computing, a fitness algorithm determines whether candidate solutions, in this case encrypted messages, are sufficiently encrypted to be transmitted.

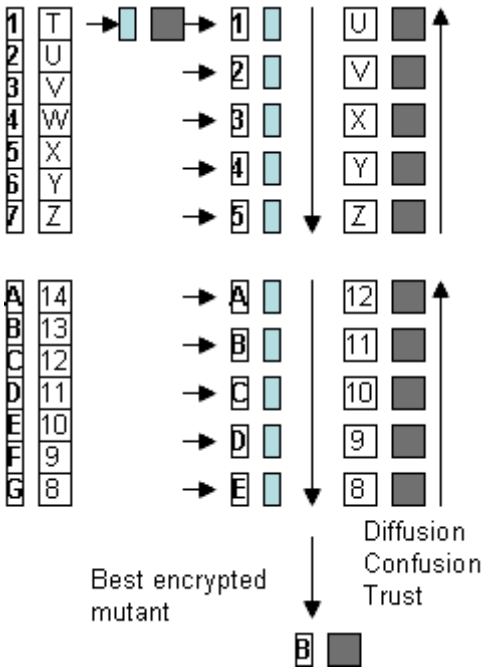

Figure 4: Mating of chromosome to message and subsequent selection.

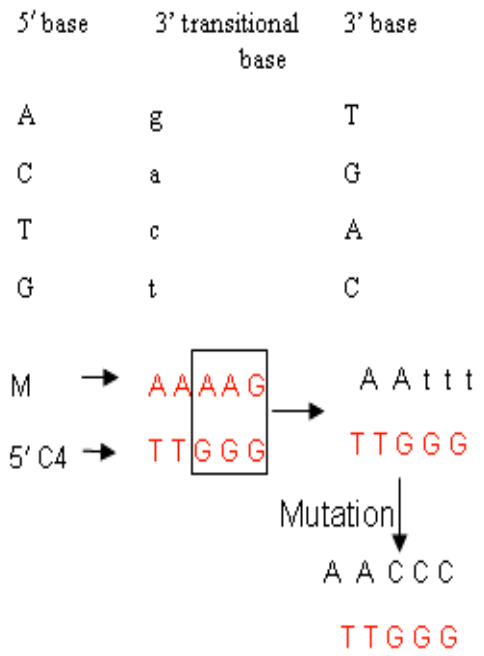

Figure 5: Anneal/mutation process.

By organizing the DNA dictionary into a codon based system and applying tools of evolutionary computing the encryption methodology can be adapted as a tool of computational biology for applications such as:

- Simulation of DNA mutations via crossover and translation
- Creation of DNA samples and mutagenic PCR (Polymerase Chain Reaction) primers for simulation
- Optimization of alignment of two DNA sequences
- Simulation of mutagenic agents on DNA
- Rate-based synthesis and mutation studies

Utilization of software based tools provides a fast, cost-effective means of testing strategies prior to performing laboratory analyses or cell-based techniques. DNA coding for biological applications require certain characteristics that are the opposite of those required for encryption. Diffusion and confusion must be minimized. Fitness would be defined in application specific parameters such as rate kinetics and reactant stoichiometry. Messages could be replaced by oligonucleotides of interest.

6 CONCLUSIONS

A DNA-inspired encryption technique that is highly resistant cryptographic analyses has been presented. It is a new variation on an ancient cryptography technique for use in mobile, ad-hoc networks and does not require the use of a public key infrastructure. To the best of the our knowledge, this approach to providing confidentiality in a MANET has not been previously published. The utility of a rapid evolving encryption genome using transitional annealing bases also represents a previously unpublished concept.

Encryption users define the plain text dictionary, the conversion into DNA sequences, the level of trust to be conferred on the MANET and the fitness characteristics of the message. The technique can be used within MANETs without decryption to establish cryptographic checksums for message integrity, authentication, and secure electronic transactions. It can be used within MANETs with decryption for message confidentiality.

The methodology is extensible to the realm of computational biology to perform computer aided diagnostics of DNA mutations. It is also extensible to other polymer based encryptions: peptide nucleic acids, silicones, polysilanes, block co-polymers, etc. It provides a path to simulating processes which could be used for encoding messages into physical molecules for a variety of applications.

ACKNOWLEDGEMENTS

This work was supported by NASA Goddard Space Flight Center and the Space Communications and Navigation Constellation Integration Project. Thanks to Deborah M. Preston of DuPont Analytical Solutions, Wilmington DE for reviewing this paper.

Figure 6: Sample plaintext, encrypted mutation, annealed mutation.

REFERENCES

A Gehani, TH LaBean, JH Reif, 1999, DNA-Based Cryptography, *5th DIMACS Workshop on DNA Based Computers*

Bourbakis, N.G., 1997, Image Data Compression-Encryption Using G-Scan Patterns, *Computational Cybernetics and Simulation., 1997 IEEE International Conference on*

A Leier, C Richter, W Banzhaf, H Rauhe, 2000, Cryptography with DNA binary strands, *BioSystems 57*, Elsevier

Catherine Taylor Clelland, Viviana Risca, Carter Bancroft, 1999, Hiding Messages in DNA microdots, *Nature,* Macmillan

Dominik Heider and Angelika Barnekow, 2007, DNA-based watermarks using the DNA-Crypt algorithm, *BMC Bioinformatics 2007*, BioMed Central

Shannon, Claude, 1949, Communication Theory of Secrecy Systems, *Bell System Technical Journal*

Santiago F Elena, Purificación Carrasco, José-Antonio Daròs, Rafael Sanjuán. 2006, Mechanisms of genetic robustness in RNA viruses. *EMBO Report*

Nachman MW, Crowell SL., 2000, Estimate of the mutation rate per nucleotide in humans. *Genetics*, Genetics Society of America

A NEW METHOD FOR THE DETECTION OF BRAIN STEM IN TRANSCRANIAL ULTRASOUND IMAGES

Josef Schreiber *, Eduard Sojka *, Lačezar Ličev *, Petra Škňouřilová †, Jan Gaura *
* *Department of Computer Science,* † *Department of Applied Mathematics*
VŠB - Technical University of Ostrava, 17. listopadu 15/2172
Ostrava - Poruba, Czech Republic
josef.schreiber@vsb.cz, eduard.sojka@vsb.cz, lacezar.licev@vsb.cz, petra.sknourilova@vsb.cz, jan.gaura.fei@vsb.cz

David Školoudík
Neurological clinic, Faculty Hospital in Ostrava-Poruba, 17.listopadu 1790, Ostrava - Poruba, Czech Republic
skoloudik@email.cz

Keywords: Ultrasound images, brain stem, detection, noise, speckle, Parkinson's disease, object recognition.

Abstract: Transcranial sonography is to date the only method able to detect structural damage of the brain tissue in the Parkinson's disease patients. The problem is that the images provided by this method often suffer from a very poor quality, which makes the final diagnosis strongly dependent on experience of examinating medical doctor. Our objective is to create a method that should help to minimize the physician's subjectivity in the final diagnosis and should provide more exact information about the processed ultrasound images. The method itself is divided into two phases. In the first one, we try to locate the position of a minimal window containing the brain stem in the analyzed image. In the second phase, we locate and measure the echogenic substantia nigra area.

1 PARKINSON'S DISEASE

Parkinson's disease (PD) belongs to the neurodegenerative diseases affecting mostly older people. It is a chronic progressive disease that occurs if the nerve cells in a part of the midbrain, called the substantia nigra, die or are impaired. These nerve cells produce dopamine, an important chemical messenger that transmits signals from the substantia nigra to other parts of the brain. These signals allow coordinated movement. If the dopamine-secreting cells in the substantia nigra die, the other movement control centers in the brain become unregulated. Neuroimaging methods are increasingly used as diagnostic tools in patients presenting with parkinsonism. However, brain computed tomography (CT) and magnetic resonance imaging (MRI) examinations are only able to detect other aetiology than PD (Ressner, 2007). This is why these traditional displaying methods like CT and MRI are not considered to be conclusive (Bogdahn, 1998).

In 1995 Becker et al. published a study dealing with the diagnostics of PD using transcranial sonography (Becker, 1995). They showed that increased echogenicity of substantia nigra is closely associated with PD. Later, their research was followed by other authors (Berg, 1999), (Berg, 2001). They proved that hyperechogenic substantia nigra can be found in more than 91% patients with PD. Nowadays the transcranial sonography is considered to be the best possible diagnostic tool for a detection of structural damage of brain tissue in Parkinson's disease patients. Ultrasonic imaging is based on detecting reflected and scattered waves arising as a response to the emitted wave with various frequencies. In general, the higher the frequency is, the better and more detailed output images can be obtained. Unfortunately, in the case of transcranial sonography, we need to deal with the scull that behaves as a barrier stopping all high-frequency waves. This means that only the low frequency probes (1-4 MHz) may be used. As a consequence of this, transcranial sonography provides images of significantly lower quality (see Figure 1).

The interpretation of ultrasound images is generally a difficult task and the opinion of different medical doctors is generally equivocal. The problem is even more serious in transcranial sonography. Even if the image is carefully evaluated by a physician, there

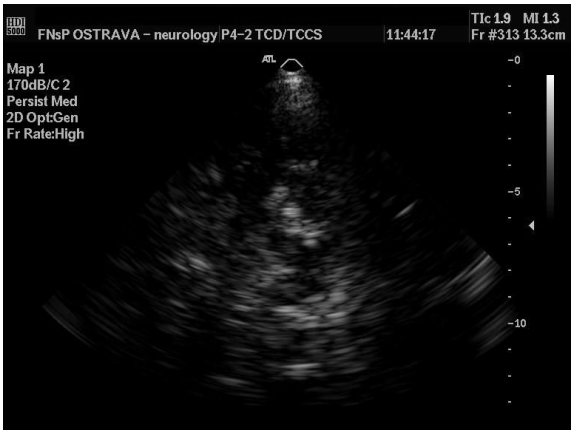

Figure 1: An example of processed sono image.

is a significant influence of subjectivity. By two different medical doctors, a different diagnosis may be determined from one image. Another problem is a long time treatment when the progress of the disease must be determined from old images and repeating of examination is no longer possible (Školoudík, 2007). That is why there appeared the demand to create a tool that would help physicians to objectivize the diagnosis process. The processing of ultrasound images is widely discussed in literature. Various methods were presented for an image segmentation (Noble, 2006), (Boukerroui, 2003), (Bosch, 2002), noise and speckle reduction (Magnin, 1982), (Rakotomamonjy, 2000), (Kerr, 1986) or image enhancement (Lee, 1980), (Sattar, 1997). However, according to our knowledge, there are no studies dealing with processing the brainstem transcranial images or with computerized recognition of objects in the substantia nigra area.

Since the image segmentation is strongly dependent on the character of the processed image we need to realize that the usage of classic ultrasound image segmentation methods will be limited. Still, some interesting studies dealing with ultrasound images were published. Ballard et al. (Ballard, 1982) presented region-based segmentation methods such as the region growing where they used the homogeneity of inner regions in the images. Such approach is obviously impropriate for transcranial images processing since the images contain too much ultrasound speckle. Mishra et al. (Mishra, 2006) presented the active contour method in combine with the genetic algorithms for the endocardial border detection. A slightly different approach was used by Mignotte (Mignotte, 2001). They used a statistical external energy in a discrete active contour for the segmentation of parasternal images. Their work was followed by many optimization efforts, e.g., Heitz (Heitz, 1994). The method provided relatively good results and is recommended for the noisy ultrasound images. Still,

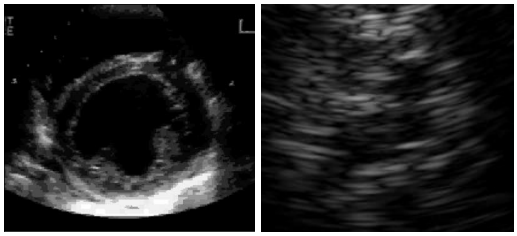

Figure 2: An endocardial (left) and transcranial (right)ultrasound image. The different level of noise is evident.

if we compare the level of noise in the images the method was tested on with transcranial ultrasound images, we see that our analysed images have significantly worse quality.

Another possible method for an ultrasound image segmentation are the level sets, using an adaption of the fast marching method. In 2003, Yan et al. (Yan, 2003) presented the purely edge-based version of this method for the endocardial boundary detection. It was later improved by Lin et al.(Lin, 2003). Their method combined an edge and a region information in a level set approach across spatial scales and it assumes that a boundary is a closed curve. The method is supposed to work well with the images of reasonably good quality. Klinger et al. (Klinger, 1988) presented a study dealing with the echocardiographic images, based on mathematical morphology. As well as the previous method, this one also assumes to work with good quality images. In 1999, Rekeczsky et al. (Rekeczky, 1999) and Binder et al. (Binder, 1999) came with the artificial neural network method. Binder used a 2-layer backpropagation network to identify a 7x7 pixels region with good results. Unfortunatly, we try to locate a region 120x120 pixels large which means a significant growth of input information for the neural network. Even if we decide to use only some important parts of the image to reduce the input, we still have to deal with the possiblity that the selected region is strongly covered by ultrasound speckle. Our proposed method is designed to use as much information from analysed image as possible to avoid being misled by the high level of ultrasound noise and speckle.

2 BRAIN STEM LOCALIZATION

The method we have developed for processing the brain-stem transcranial sono images is divided into two phases. In the first phase, we try to locate the position of a minimal window in the processed image containing the brain stem. To do so, we use a modified template matching algorithm. Since every human being is unique, the brain stems may slightly

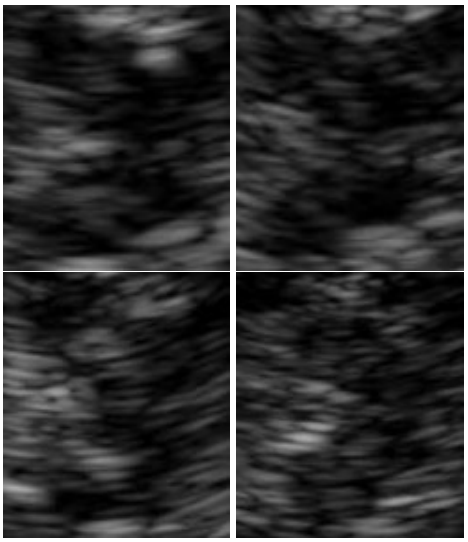

Figure 3: Examples of the images used for the template construction. For need of this paper, the images are displayed with the same size.

differ in shape and size. Moreover, the objects being sought inside the stem may have different position, size, and echogenicity, depending on the disease progress. Therefore, for creating the template of the stem, we choose several images that best represent, according to our opinion, various possible shapes and sizes of the stem. We also consider the seriousness of the disease by choosing images depicting the situation in various stages of the disease progress (from healthy persons to persons with an advanced stage of the disease). The selection of images that are used for the template construction is important in our method. Therefore, the selection of images was widely discussed with medical doctors to best fulfill previously mentioned parameters. Overall, there were 20 selected images used for the template construction. Four examples of these images can be seen in Figure 3.

We construct the template that is used for matching by simple averaging the particular selected images of the brain stem. Firstly, the images are normalized to the same size. In our experimental implementation, we use the size of 120×120 pixels. After normalizing the size, we normalize the images of stem also with respect to the mean value and the variance of brightness. We do so by using the following formula

$$b_n(\mathbf{x}) = a b_o(\mathbf{x}) + c, \tag{1}$$

where $b_n(\mathbf{x})$, $b_o(\mathbf{x})$ stand for the normalized and original brightness, respectively, at a pixel whose position is described by a two-dimensional vector $\mathbf{x}$, and a and c are constants that must be determined for each particular image. For determining them, the mean value of brightness, denoted by μ_{bo}, and the variance of brightness, denoted by σ^2_{bo}, in the original images are needed. Let Ω stand for the set of all pixels in the brain-stem image and let N be the size of this set. We have

$$\mu_{bo} = \frac{1}{N} \sum_{\mathbf{x} \in \Omega} b_o(\mathbf{x}), \tag{2}$$

$$\sigma^2_{bo} = \frac{1}{N} \sum_{\mathbf{x} \in \Omega} (b_o(\mathbf{x}) - \mu_{bo})^2. \tag{3}$$

In each normalized image, the normalization of brightness aims at achieving a certain required mean value, denoted by μ_{bn} and a required variance of brightness, denoted by σ^2_{bn}. Simple mathematics yields the following formulas for a and c

$$a = \frac{\sigma_{bn}}{\sigma_{bo}}, \; c = \mu_{bn} - a\mu_{bo}. \tag{4}$$

The effect of normalization can be seen in Figures 4, 5. In Figure 6, the set of example images from Figure 3 can be seen in normalized form. An example of the template that was obtained by averaging the brain-stem images using Equation 5 is depicted in Figure 7.

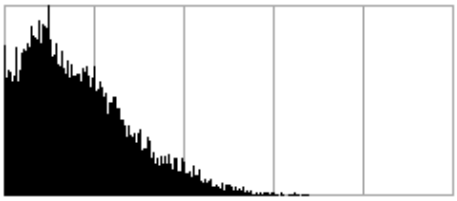

Figure 4: The histogram of original image.

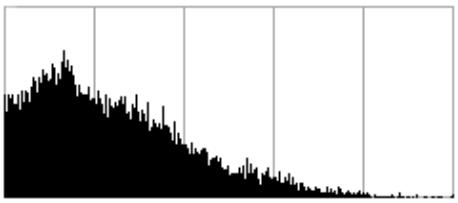

Figure 5: The histogram of normalized image.

In the pattern matching algorithm, we will also use the variance of brightness in particular pixels that can be expressed as follows

$$\mu_b(\mathbf{x}) = \frac{1}{M} \sum_{j=1}^{M} b_{nj}(\mathbf{x}), \tag{5}$$

$$\sigma^2_b(\mathbf{x}) = \frac{1}{M} \sum_{j=1}^{M} (b_{nj}(\mathbf{x}) - \mu_b(\mathbf{x}))^2. \tag{6}$$

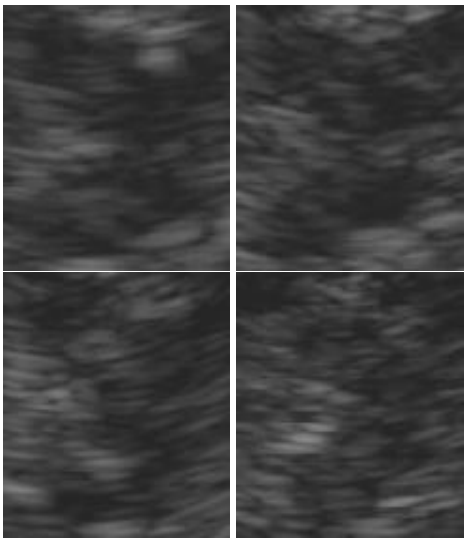

Figure 6: The brain-stem images from Figure 3 after the normalization process.

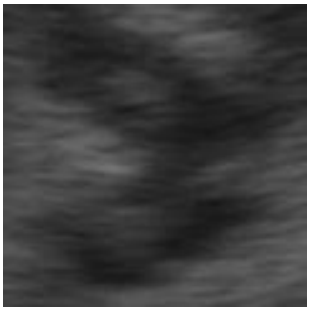

Figure 7: The constructed template.

In the above formulas, M is the number of particular normalized brain-stem images that are used for creating the template; b_{nj} stands for the j-th such image.

In the first step of our method, we try to locate the position of the brain stem. We introduce a possibility, denoted by $\pi(\mathbf{u}_k, \mathbf{x})$, of the event that the template point with the coordinates $\mathbf{x}$ corresponds to the image point with the coordinates $\mathbf{x}+\mathbf{u}_k$ (Sojka, 2006). This possibility may be determined from the difference of brightness

$$\Delta b = b(\mathbf{x}+\mathbf{u}_k) - t(\mathbf{x}), \tag{7}$$

where $b(\mathbf{x}+\mathbf{u}_k)$ is the brightness of the pixel with coordinates $\mathbf{x}+\mathbf{u}_k$ in processed image, and $t(\mathbf{x})$ is the brightness in the corresponding template pixel. Let it be pointed out that $\mathbf{u}_k$ characterizes the template position that is just being processed.

We suppose that the possibility distribution may be described by a certain chosen function φ. Figure 8 shows an example of such a function. For the construction of φ, we use the deviation $\sigma_b(\mathbf{x})$ that was determined in Equation 6.

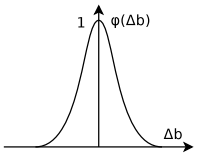

Figure 8: The distribution of possibility φ (we use the Gaussian function).

To obtain the possibility of the event that the image pixel just being processed corresponds to the pixel from the template, we use the following equation

$$\pi(\mathbf{u}_k, \mathbf{x}) = \varphi(b(\mathbf{x}+\mathbf{u}_k) - t(\mathbf{x}), \sigma_b(\mathbf{x})). \tag{8}$$

To characterize the quality of matching at the position $\mathbf{u}_k$, we introduce the quantity $S(\mathbf{u}_k)$ characterizing the number of pixels, i.e., the "net area" that can successfully be matched to the template. We have

$$S(\mathbf{u}_k) = \sum_{\mathbf{x}\in\Omega} \pi(\mathbf{u}_k, \mathbf{x}), \tag{9}$$

where Ω stands for the set of template pixels.

The final goal is to find the value of $\mathbf{u}$ that maximizes the value of $S(\mathbf{u}_k)$. The value of $\mathbf{u}$ then determines the position of the window that should contain the brain stem (Figure 9).

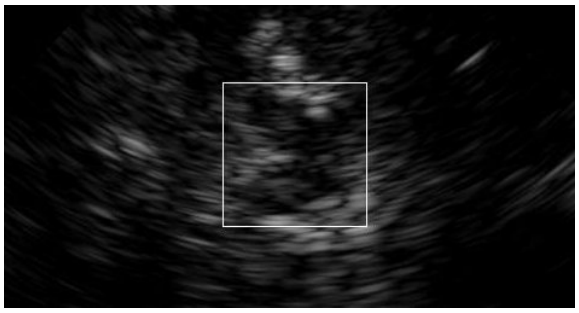

Figure 9: An image with the recognized brain-stem object.

It is obvious that during the brain-stem detection, each processed window from the analyzed image must be normalized in the same way as the images used for the template construction.

3 ANALYSIS OF BRAIN STEM

To obtain the information about the disease progress, we now need to locate and measure the objects inside the brain stem, which is the second step of our

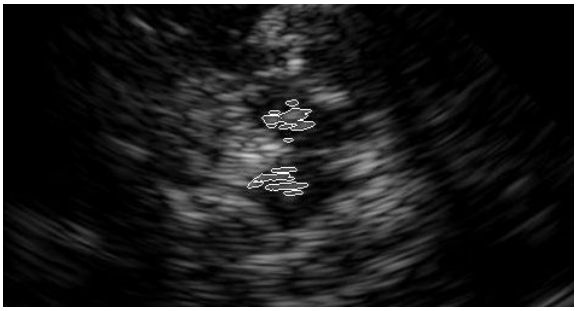

Figure 10: An image with the recognized brain stem and the highlighted objects.

method. In the image, these objects appear as the areas with a higher level of echogenicity inside the substantia nigra area. It is a difficult task to correctly identify these objects because the areas may have insufficient contrast.

We locate the objects in the brain stem as the areas with a higher level of brightness that are found using the region growing method. Homogenity of brightness is a criterion that is used for growing. After growing, the regions of interest are usually partitioned into several smaller areas (Figure 10). Therefore, morphological closing is carried out after growing to connect the sub-areas together. If it is required by a doctor, the convex hull of the found area may be computed too. The regions that have been found are then checked for the shape and size, which separates the objects of interest in the stem. The numerical characteristics are then computed. For all recognized objects, we determine the number of pixels the objects are composed of, their average brightness, and the location of their gravity centers. Besides computing the characteristics of the objects, they can also be highlighted in the images (Figure 10).

Naturally, there is also a possibility to correct the obtained results manually, if necessary, and remove possible unwanted objects that are considered to be only a noise, ultrasound speckle or possibly even a part that does not belong to the brain stem area.

4 ACHIEVED RESULTS

To test the succesfulness of our method in brain stem localization, we used a sample of 170 images in which we tried to locate the correct brain-stem position. The result (the quality of recognition) was classified with the marks between 1 and 3. The mark 1 means that the position was recognized correctly and accurately. The mark 2 means that the position was determined inaccurately but not completely incorrectly. In this case, the position was usually determined with an error up to 10-15 pixels. The mark 3 means that the method determined an incorrect position. For our set of test images, we obtained the results that are summarized in Table 1.

Table 1: The results of the brain-stem localization achieved by the presented method. The first column determines the quality of recognition. The second one shows the number of images recognized with corresponding quality and the last column displays the overall percentage.

Quality of recognition	Number of images	Results in %
1	129	75,9
2	4	2,3
3	37	21.8

The mark 1 was achieved in nearly 76% of images. This can be considered as a good result since we have to realize that the method must deal with images of various quality. The difference between the good and and bad image is shown in Figure 11. In the left image, we can clearly see the shape of the brain stem. For our method, the right image is very difficult to determine the correct brain-stem location.

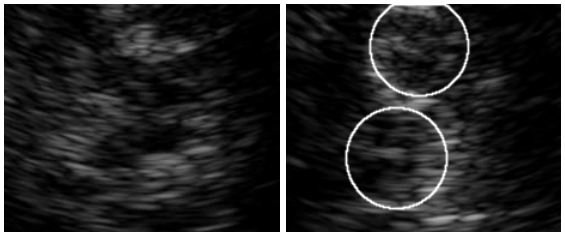

Figure 11: These images illustrate the difference between the good quality and the bad quality images. While in the left image, the shape and position of brain stem is obvious, in the right image, two places with similar shape to the brain stem may be found.

5 CONCLUSIONS

The computer processing of transcranial ultrasound images is a complicated task. Images often suffer from a very poor quality and they often have a high level of noise and speckle. The objects that were recognized are often discontinuous, in worse cases even incomplete. The objects inside the brain stem often have insufficient contrast and they are usually fragmented by ultrasound speckle. Still, the objective evaluation of these images can be very helpful in the Parkinson disease diagnostics and treatment. It can help the medical doctors to determine the correct diagnosis as well as the level of the disease progress.

The exact and objective information about the examination from particular date can especially help in longer time diagnostics when repeating of the examination is no longer possible.

Our method may be divided into two phases. At first, it attempts to correctly identify the position of brain stem in processed image. This phase is crucial in overall diagnostics and this paper focuses mostly on this part. In the second phase, we detect the objects of interest in the brain stem. The detection of existence, shape, size, and echogenicity of these objects is a valuable contribution to the diagnostics of Parkinson's disease.

Achieved results obtained during testing make us believe that the method we have developed for the detection and analysis of the brain stem in transcranial ultrasound images is successful. From the tested images, we obtained good results. In 76% of cases, the position of the brain stem was correctly determined.

ACKNOWLEDGEMENTS

Presented results had been obtained during solving the grant project code T401940412 supported by the Academy of Sciences of the Czech Republic.

REFERENCES

Ballard, D.H., B. C. (1982). *Computer vision*. Prentice-Hall, Englewood Cliffs, NJ.

Becker, G., B. U. G. C. e. a. (1995). Transcranial color-coded real-time sonography of intracranial veins. normal values of blood flow velocities and findings in superior sagittal sinus thrombosis. *Journal of Neuroimaging*, 5:87–94.

Berg, D., B. G. Z. B. T. O. H. E. e. a. (1999). Vulnerability of the nigrostriatal system as detected by transcranial ultrasound. *Neurology*, 53:1026–1031.

Berg, D., S. C. B. G. (2001). Echogenicity of the substantia nigra in parkinson's disease and its relation to clinical findings. *Journal of Neurology*, 248:684–689.

Binder, T., S. M. M. D. S. H. B. T. M. G. P. G. (1999). Artificial neural networks and spatial temporal contour linking for automated endocardial contour detection on echocardiograms: A novel approach to determine left ventricular contractile function. 25(7):1069–1076.

Bogdahn, U., B. G. S. F. (1998). *Echoenhancers and transcranial color duplex sonography*. Blackwell Science, Berlin.

Bosch, J.G., M. S. L. B. N. F. K. O. S. M. R. J. (2002). Automatic segmentation of echocardiographic sequences by active appearance motion models. 21(11):1374–1383.

Boukerroui, D., B. D. N. J. B. O. (2003). Segmentation of ultrasound images - multiresolution 2d and 3d algorithm based on global and local statistics. *Pattern Recognition Letters*, 24(4-5):779–790.

Heitz, F., P. P. B. P. (1994). Multiscale minimization of global energy functions in some visual recovery problems. 59:125–134.

Kerr, A.T., P. M. F. F. H. J. (1986). Speckle reduction in pulse echo imaging using phase insensitive and phase sensitive signal processing techniques. 8:11–28.

Klinger, J.W.J., V. C. F. T. A. L. T. (1988). Segmentation of echocardiographic images using mathematical morphology. 35(11):925–934.

Lee, J. (1980). Digital image enhancement and noise ltering by use of local statistics. PAMI-2(2):165–168.

Lin, N., Y. W. D. J. (2003). Combinative multi-scale level set framework for echocardiographic image segmentation. 7(4):529–537.

Magnin, P.A., v. R. O. T. F. (1982). Frequency compounding for speckle contrast reduction in phased array images. *Ultrasonic Imaging*, 4:267–281.

Mignotte, M., M. J. (2001). A multiscale optimization approach for the dynamic contour-based boundary detection issue. 25(3):265–275.

Mishra, A., D. P. G. M. K. (2006). A ga based approach for boundary detection of left ventricle with echocardiographic image sequences. 21(11):967–976.

Noble, J.A., B. D. (2006). Ultrasound image segmentation: A survey. *IEEE Transactions on medical imagining*, 25(8):987–1010.

Rakotomamonjy, A., D. P. M. P. (2000). Wavelet-based speckle noise reduction in ultrasound b-scan images. 22:73–94.

Rekeczky, C., T. A. V. Z. R. T. (1999). Cnn-based spatiotemporal nonlinear filtering and endocardial boundary detection in echocardiography. 27(1):171–207.

Ressner, P., v. D. H. P. K. P. (2007). Hyperechogenicity of the substantia nigra in parkinson's disease. *Journal of Neuroimaging*, 17(Issue 2):164–167.

Sattar, F., F. L. S. G. L. B. (1997). Image enhancement based on nonlinear multi-scale method. 6:888–895.

Sojka, E. (2006). A motion estimation method based on possibility theory. In *Proceedings of IEEE ICIP*, pages 1241–1244.

Školoudík, D., F. T. B. P. L. K. R. P. Z. O. H. P. H. R. K. P. (2007). Reproducibility of sonographic measurement of the substantia nigra. *Ultrasound in Medicine & Biology*, 33(9):1347–1352.

Yan, J.Y., Z. T. (2003). Applying improved fast marching method to endocardial boundary detection in echocardiographic images. 24(15):2777–2784.

AUTOMATIC DETECTION OF IN VITRO CAPILLARY TUBE NETWORK IN A MATRIGEL ANALYSIS

Eric Brassart [1], Cyril Drocourt [1], Jacques Rochette [2], Michel Slama [3] and Carole Amant [2]
[1] *LTI, Univerty of Picardie Jules Verne and IUT Amiens, France*
{eric.brassart, cyril.drocourt}@iut-amiens.fr
[2] *DMAG, EA 3901, Amiens, France;Univerty of Picardie Jules Verne, Amiens, France and CHU*
{carole.amant, jacques.rochette}@u-picardie.fr
[3] *INSERM, ERI-12, Amiens, France;Univerty of Picardie Jules Verne, Amiens, France and CHU*
slama.michel@chu-amiens.fr

Keywords: Angiogenesis, Image analysis, Capillary tube network.

Abstract: Angiogenesis, the formation of new capillary blood vessels from pre-existing vessel, has become an important area of scientific research. Numerous *in vivo* and *in vitro* angiogenesis assays have been developed in order to test molecules designed to cure deregulated angiogenesis. But unlike most animal models, most *in vitro* angiogenesis models are not yet automatically analysed and conclusion and data quantification depend on the observer's analysis. In our study, we will develop a new automatic *in vitro* matrigel angiogenesis analysis allowing tube length and the number of tubes per cell islets as well as cell islet and tubule mapping to be determined, percentage of vascularisation area, the determination of ratio of tubule length per number of cells in cell islet and, ratio length/width per tubule determination. This new method will also take image noise into account. Our method uses classical imaging quantification. For the first image processing we used image segmentation (Sobel type edge detection) and artefact erasing (morphologic operator). Subsequent image processing used Snakes: Active contour models in order to precisely detect cells or cell islets. We suggest that this new automated image analysis method for quantification of *in vitro* angiogenesis will give the researcher vascular specific quantified data that will help in the comparison of samples.

1 INTRODUCTION

Angiogenesis, a complex process whereby new blood vessels form from pre-existing vasculature in response to proangiogenic factors, is an essential physiological process required for growth and development (Folkman J. 1971 and 1992). Angiogenesis represents the unique process by which evolution tissue may be supplied in essential elements provided by blood. Angiogenesis is therefore involved in major physiological processes including embryonic development, female reproduction, wound healing and collateral generation in the myocardium. Dysregulated angiogenesis plays a critical role in various pathological mechanisms such as solid tumour formation, metastasis, childhood haemangioma, diabetic retinopathy, macular degeneration, psoriasis and in inflammation-related diseases such as rheumatoid arthritis, osteoarthritis and ulcerative colitis.

2 PRIOR AND RELATED WORK

In this way, drug design in order to cure dysregulated angiogenesis is evident. Many *in vivo* and *in vitro* angiogenesis model have been described. But unlike most animal models in which blood flow doppler analysis allows vascularisation quantification (Couffinhal T, 1999), most *in vitro* angiogenesis models are not yet automatically analysed and conclusion and quantification depend on observer analysis (Vincent L., 2003). most *in vitro* angiogenesis cannot be automatically quantified and require observer participation. The determination of the effect of drugs on vasculature development requires the comparison of samples and the use of data analysis standardization. In this

study, we focused on an *in vitro* endothelial cell differentiation matrigel assay automated image analysis methods for the quantification of angiogenesis. Most of the time, tube length and the number of tubes per cell islet are the only data in publication that can be found, and are quantified by the observer himself. Few publications have described an automatic image analysis approach. One of these publications, (Niemisto A., 2005) describes an automatic image analysis method for quantification of *in vitro* matrigel angiogenesis. But in our study we will develop a new automatic in vitro matrigel angiogenesis analysis allowing in addition cell islet and tubule mapping, percentage of vascularisation area determination, ratio of tubule length per number of cell in cell islet determination, and ratio length/width per tubule determination. In this study we will develop a new method in order to take image noise into account (particles, air bubbles included in the matrigel).

3 IMAGE ANALYSIS

3.1 Introduction

According to Nicolas Ayache, the problems encountered in the analysis of medical imagery can be separated into several categories:

- Restoration: this step consists of recreating an improved image, in which several faults connected with the physical acquisition process have been eliminated (noise reduction, ...).
- Segmentation: separation consists of extracting points, lines or regions which are then used as data in complimentary work such as realignment, measurement, analysis of movement, visualisation etc.
- Realignment: this a problem common to many tasks concerning the analysis of medical imagery, and is necessary to compare the images acquires from one single patient, or with varying modalities.
- Morphometry: this consists of studying the geometry of the forms, in particular the calculation of average forms and the variations around theses forms.

These treatments occur at different time and in different order. The reference image we were using in this article is in figure 1.

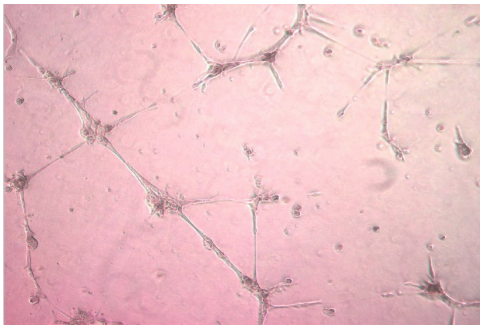

Figure 1: The reference image, to which all the developed processing will be applied in this article.

3.2 Segmentation

After having tested several methods of binarisation (Fisher, Otsu,) (Antti Niemistö 2005) we determined that this type of simple processing was not suitable, principally because of its sensitivity to the variation in luminosity within the image. Indeed, projections of light on to tissues are not homogenous, and often darker zones appear at the edges of the images acquired, leading to poor separation of classes in OTSU's formulation. We therefore chose to pre-process our images in several successive stages, allowing us to isolate only the cells and the background. These steps, undertaken one independently of the other correspond to traditional processing in digital imagery, but bring about an efficient solution:

- a detection of the contours by means of the use of a gradient operator($\vec{\nabla}$), and more specifically the norm of this operator.

$$\left|\vec{\nabla} I(x,y)\right| = \sqrt{\left(\frac{\partial I(x,y)}{\partial x}\right)^2 + \left(\frac{\partial I(x,y)}{\partial y}\right)^2}$$ with its

discreet estimation coming down to the calculation of two convolutions in the x and y directions. The operator we preferred is that of Sobel (Sobel, I 1973); see Figure 2.

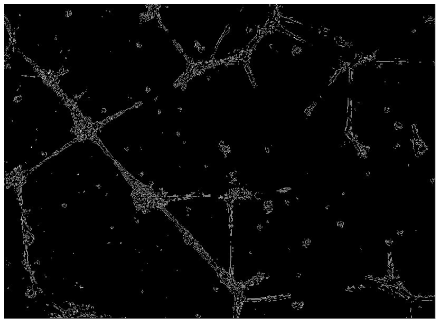

Figure 2 : Detection of the contours with Sobel's operator.

– Closure of the objects in the image which allows the joining of neighbouring pixels to close the contours and the unconnected surfaces. This allows us to make the "textured" surfaces homogenised and to create a complete, uniform object. (Figure 3),

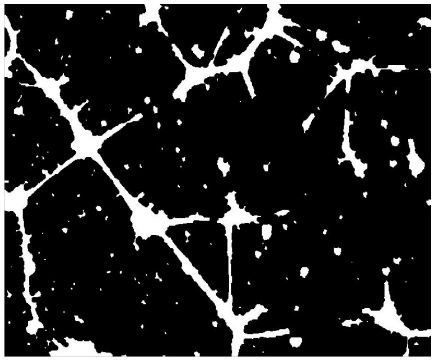

Figure 3 : Convolution and closure of the image

– Elimination of objects which are too small (Restoration phase). The aim here is to eradicate objects whose size does not satisfy the criterion of the average size of all the images composing the image. In the majority of the images contained in our library, this step permits us to attribute a sufficiently precise localisation of the network, without necessarily being able to identify the cells (or mass of cells) of the connecting tubes.

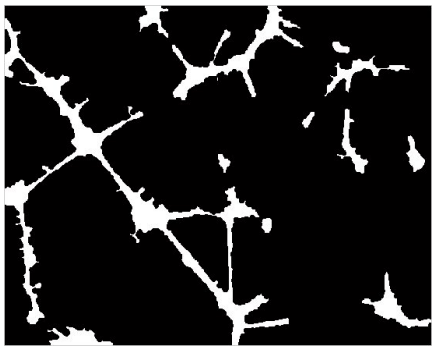

Figure 4 : Isolated network after noises elimination and the isolated elements.

The second phase of this study consists of extracting the different elements characteristic of what we will call the cells (or the mass of cells) from the image, and the tubes joining the cells, when they exist. The idea developed in this paper is firstly to isolate everyone which resembles cells, and then to try, from these latter, to establish the connections (tubes) which, after all, characterise the mesh of our network. The different stages put into place are the elimination of the various noises in the image, (reflection from bubbles of air in the network, particles, non-consideration of isolated cells; the elimination of tubes. From the resulting image, with the remaining lines, we are specifically looking for the exact contour of the cells or mass of cells. To do this, we used an algorithm based on the active contours, for which the initialisation of the starting points is done automatically.

Erosion of the picture descended of the previous stage permits to suppress the information of type tubes and to only keep information of type cells. This stage remains the most appreciable part of our algorithm because it is from this one that the set of cells will be initialized. (Figure 5),

Figure 5 : Erosion of the image and initialisation of the starting point characterising the cellular mass.

– Use of snakes

A snake (Kass M 93, Xu C 97) is an elasticised curve which can be modelled by a parametric shape normalised as follows:

$$s \rightarrow v(s) = \{x(s), y(s)\}$$

Where s is the curvilinear abscissa or the parameter on the curve $\in$ in the spatial domain Ω,

It ensues from the previous definition that a model of *snake* is a problem of optimisation of a functional.

– Several resolution approaches exist, let us quote a variation method which consists of resolving Euler's

$$\Omega = [0, 1] \rightarrow R^2$$

$v(s)$ is the vector of position of the point of contour of coordinates $x(s)$ and $y(s)$,

$v(1)$ and $v(0)$ are the vectors of position of the extremities of the contour.

The total energy of the contour which we try to minimize is represented by the following function (Kass M 93):

$$E_{snake} = \int_0^1 E_{snake}(v(s))\,ds = \int_0^1 E_{int}(v(s)) + E_{image}(v(s)) + E_{cont}(v(s))\,ds$$

Where E_{int} represents the internal energy of the snake, E_{image} is the energy derived of the image (contours, gradients) and E_{cont} represents the energy of constraints.

Initialisation of the detection process.

One of the major concerns which exist within the framework of the use of the active contours is the initialization. Indeed, in the majority of the applications using this technique, the initialization of snakes is done manually by asking the user to select points around the shape to detect what will constitute the initial contour. In our application each image zone corresponding to a cell is automatically framed by the max coordinates resulting from a labelling procedure The initial points correspond to the totality of points characterising the perimeter of each rectangle concerned (figure 6). The number of iteration points on the snakes is limited to 200, not to have a too long treatment on images. Of course, if the snake converges toward a solution before this maximum number the process stops on the usual criteria.

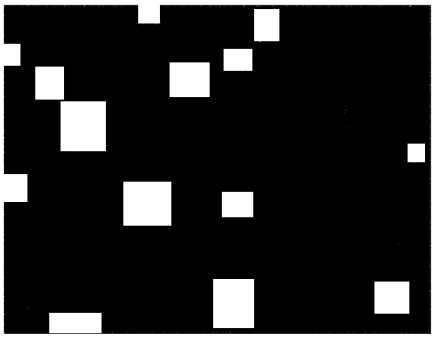

Figure 6 : Initialisation of the snake son the zones marked in white.

The use of the snakes permits to isolate precisely the surfaces associated with the cells (Figure 6). Finally the subtraction of the image obtained with that of the previous step to isolate the tubes (Figure 7).

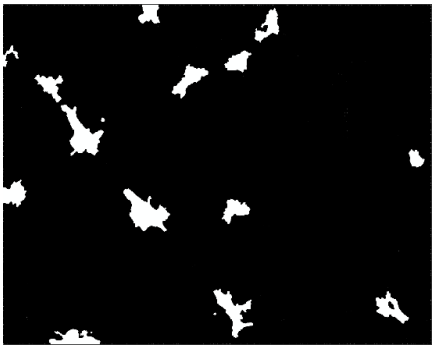

Figure 7: Initialisation of the snakes on the zones marked in white.

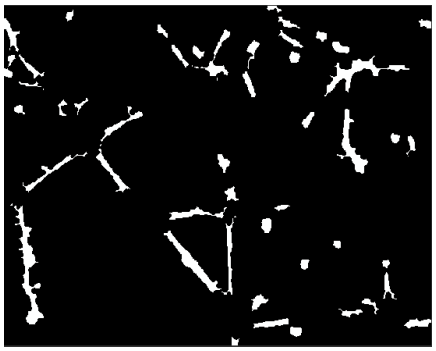

Figure 8: Detection of the tubes.

By carrying out a subtraction between the binarised images of the cells and those of the tubes we are now able to establish the network of cells, i.e. the cells and the tubes that connect them. To represent this network, we positioned the centre of theses cells by calculating the barycentre of each one of them. The result of this method is detailed in the following part of this article.

4 RESULTS

We have developed a new software for the processing of images, able to automatically analyse angiogenesis images. For this article a collection of 10 images of this type was used to validate the results obtained. This software was written under Matlab with the image processing toolbox. All the images were obtained using a light microscopy. The concern in these images acquirement is to obtain images having sufficient contrast to be able to clearly show the cells and the tubes, and the noise inherent to these images as at the lowest level as possible :

- homogenous light to avoid the effects of poor binarisations,

- particles and bubbles of air leading to the detection of objects capable of being assimilated with cells.

We will show in this part the results obtained with various processing on a reference image, but the reader will find the complete results obtained from all the samples used at the following address: www.iut-amiens.fr/Angio-results.
The first result given is to familiarize the practitioner with the vascularisation surface of the sample that has been imaged. On the image in figure 8, the percentage of vascularisation (%Sv) obtained is 10,247%. The values given are determined by the following ratio of surfaces :

The surface of the pixels within the contours (Sc) divided by the total pixel surface of the image (St).

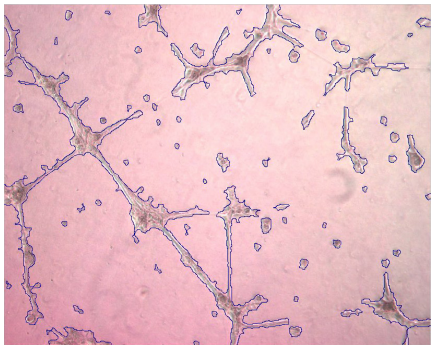

Figure 10: percentage of the vascularisation surface: %Sv = Sc/St.

The results obtained are given in the form of a ratio that the user of our program may consult following the processing. On one hand it is visual with the illustration in figure 9, on the other hand it is numerical by means of consultation of the statistics shown in the following table.

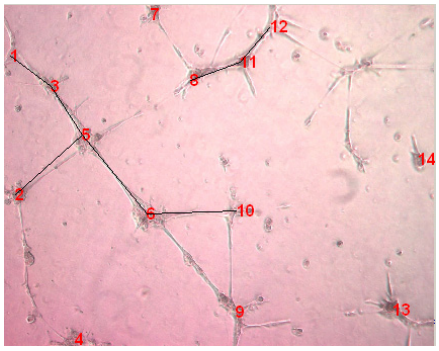

Figure 11: Aspect of the network corresponding to the cellular development.

Report of the detection:

Connection
1 connected with 3
2 connected with 6
3 connected with 6
6 connected with 10
8 connected with 11
11 connected with 12
Number of Cells: 14 :
Number of Tubes: 48
Number of Connections : 6
Mean tube length: 96,923 (in arbitrary units)
Surface of the cells: 4088 (in arbitrary units)

5 CONCLUSIONS

We have developed a new technique of automatic detection of a vascular network in a matrigel gel. This technique is based on basic image processing techniques such as the detection of contours, morphologic operators combined with more sophisticated processing such as the use of active contours. On this latter point we have developed the original idea of automatic placement of the initial points on the cells. In literature dealing with this aspect, there are very few methods avoiding the placement of these points manually. Our technique can be used to measure the length and size of tubular complexes automatically, to localize cell islet and tubule, to measure the percentage of the vascularisation area, the ratio of tubule length per number of cells in a cell islet and the ratio length/width per tubule. Our software also propose the structure of the capillary network.

Concerning the software, a certain number of developments still have to be completed. Indeed, during the detection of the cells in the image, a certain number of them are considered as noise or are ignored since the contrasts are not significant to allow automatic detection (the light is not adapted). In order to consider them as an integral part of the mesh, the practitioner must be able to make them active by manual intervention, and reintroduce them in the detection of the capillary network.

6 PERSPECTIVES

This software will help the researcher to quantify samples and to determine the effect of new anti-angiogenic or pro-angiogenic agents in deregulated

angiogenesis processing. An other application of these new *in vitro* angiogenesis quantification techniques in ischemic hind limb or ischemic myocardial cell therapy will be to test the ability of bone marrow stem cells or endothelial progenitor cells to differentiate in endothelial cells and to establish a vasculature shortly before the injection in the ischemic tissue.

REFERENCES

Antti Niemistö, Valerie Dunmire, Olli Yli-Harja, Wei Zhang, and Ilya Shmulevich 'Robust Quantification of *In Vitro* Angiogenesis through Image Analysis' IEEE Transactions on Medical Imaging, vol. 24, no. 4, April 2005 pp 549- 553.

Couffinhal T, Silver M, Kearney M, Sullivan A, Witzenbichler B, Magner M, Annex B, Peters K, Isner JM. "Impaired collateral vessel development associated with reduced expression of vascular endothelial growth factor in ApoE-/- mice." Circulation. 1999 Jun 22;99(24):3188-98.

Couffinhal T, Silver M, Kearney M, Sullivan A, Witzenbichler B, Magner M, Annex B, Peters K, Isner JM. "Impaired collateral vessel development associated with reduced expression of vascular endothelial growth factor in ApoE-/- mice." Circulation. 1999 Jun 22;99(24):3188-98.

Folkman J., "Tumor angiogenesis : therapeutic implications." N. Engl. J. Med. 1971 ; 285 : 1182-6.

Folkman J., Shing Y. "Angiogenesis. J. Biol. Chem. 1992; 267 : 10931-4.

Kass M, Witkin A and Terzopoulos D. "Snakes: Active contour models". Proc. 1st Int. Conference on Computer Vision, London, 1987, pp. 259-268.

Sobel, I., Feldman,G., "A 3x3 Isotropic Gradient Operator for Image Processing", presented at a talk at the Stanford Artificial Project in 1968, unpublished but often cited, orig. in Pattern Classification and Scene Analysis, Duda,R. and Hart,P., John Wiley and Sons,'73, pp271-2.

Spyridopoulos I, Brogi E, Kearney M, Sullivan AB, Cetrulo C, Isner JM, Losordo DW. "Vascular endothelial growth factor inhibits endothelial cell apoptosis induced by tumor necrosis factor-alpha: balance between growth and death signals." J Mol Cell Cardiol. 1997 May;29(5):1321-30.

Vincent L., Varet J., Pille JY., Bompais H ., Opolon P. , Maksimenko A., Malvy C., Mirshahi. M., Lu H., Vannier JP., Soria C., Li H. « Efficacy of dendrimer-mediated angiostatin and TIMP-2 gene delivery on inhibition of tumor growth and angiogenesis : in vitro and in vivo studies." Int. J. Cancer : 2003, 105 : 419-429.

Williams Donna J. and Shah Mubarak – "A Fast Algorithm For Active Contours and Curvature Estimation" – Image Understanding, Vol55, N°1, January 1992, pp14-26.

Xu C, and Prince J. L. . "Gradient Vector Flow: A New External Force for Snakes". *In IEEE Proc. Conf. on Comp. Vis. Patt. Recogn. (CVPR' 97).*

OTOLITH IMAGE ANALYSIS BY COMPUTER VISION

Anatole Chessel, Ronan Fablet
IFREMER/LASAA, France
anatole.chessel@ifremer.fr, ronan.fablet@ifremer.fr

Charles Kervrann, Frederic Cao
IRISA/VISTA, France
ckervran@irisa.fr, fcao@irisa.fr

Keywords: Computer vision, otolith, fish biology and ecology, biological image analysis, detection a contrario, variational methods.

Abstract: Otoliths are small stone located in fish inner ears and characterised by an accretionnary growth. They act as a biological archive and are of much use in marine biology and ecology. In this article a computer vision framework is presented which recover the successive shapes of the otolith and the significant ridges and valleys from a 2D grayscale image. Seeing vision processes as complex systems, an iterated process is presented using two perceptual information, contrast and good continuity. The successive concentric shapes of the otoliths are recovered as the level-sets of a dome shaped potential function, computed in a variational framework. Potential applications includes in particular fish age estimation, otoliths morphogenesis modelling, otolith proxy fusion.

1 INTRODUCTION

Otolith are small stones located in fish inner ears used for their spatial localisation. They grow continuously according to an accretionnary process. As the accretionary deposit is influenced both by physiological parameters and environmental conditions, fish otoliths can be viewed as biological archives from which a lot can be learned on fish biology and ecology. For instance, individual age data, which are among the key data for fish stock assessment, are estimated from the interpretation of fish otoliths.

The decoding of this biological archive is a difficult task, as the conditions influencing the accretion are numerous, and their effects not well known (Panfili et al., 2002). Various means of analysis of the physical and chemical properties of the stone can be used: microchemical analysis, mass or raman spectroscopy etc... Visual analysis of images of magnified otolith sections are also used but, being done by human operator, they would benefit a lot from computer vision techniques to improve automatising, robustness and quantitative evaluation. Such techniques would allow to fully consider the image as yet another mean of quantitative measurements similar for instance to chemical signatures (Panfili et al., 2002).

An otolith image can be seen in Figure 1. Concentric structures akin to the one found in tree trunk section can clearly be seen. Several works have tried to extract those curves, using multi-agent methods (Guillau et al., 2002) or active contours (Troadec et al., 2000). While yielding good results on the species considered as easy by expert (like plaice), they failed on more complicated images (like pollock or hake), because the hypothesis made were too restrictive.

The vision of concentric structures in otolith images are the result of complex global interactions between heterogeneous visual cues interpreted by the human vision system : what we see are continuous and smooth parallel concentric curves forming quasi-convex shapes. The analysis of low-level vision processes will lead to the definition of an original approach for the extraction of the relevant curves, and the recovery of the successive shapes of the otolith during its growth. Thus a novel framework for geometric images understanding applied to otoliths is proposed, the results of which can be seen in Fig. 1.

This paper is organized as follow. The next section presents a psychovisual analysis of otoliths and an overview of the framework with which we implement its conclusion. In section 3 the different steps are detailed. The last section details the implementation and shows results on several species.

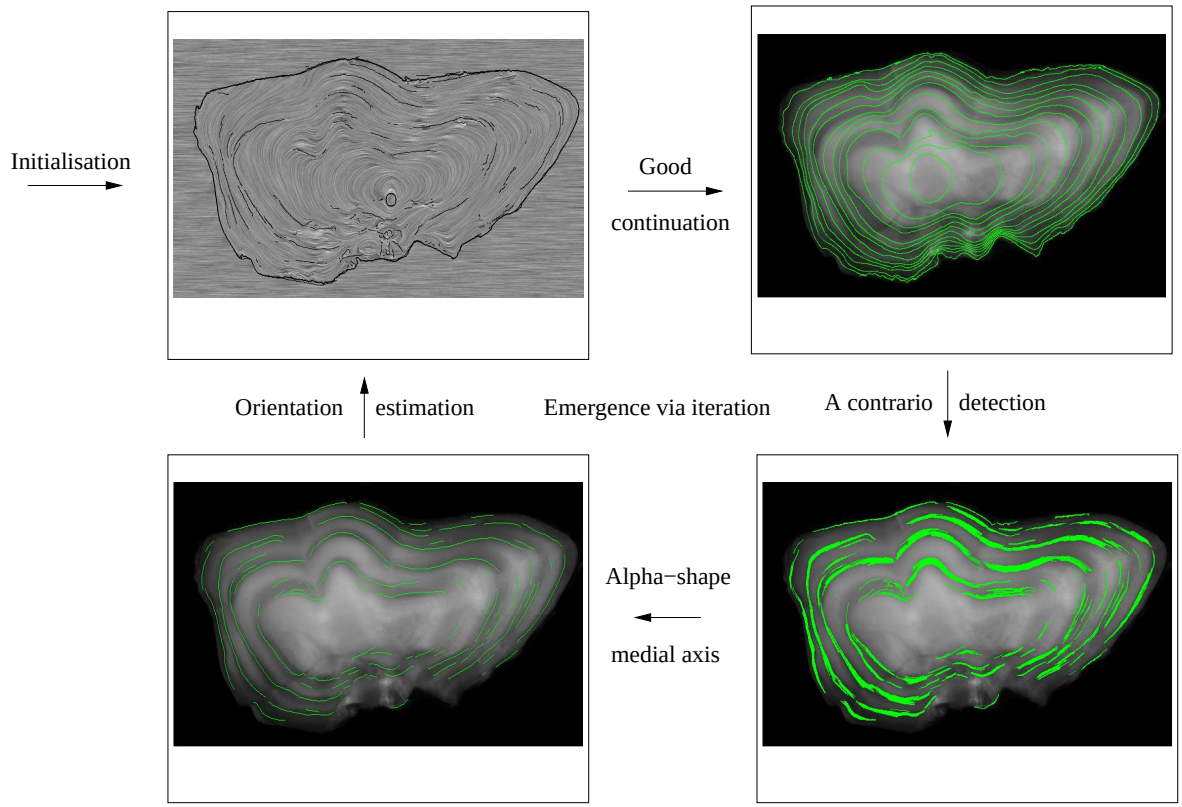

Figure 1: Overview of the process.

2 PSYCHOVISION AND CURVE EXTRACTION IN OTOLITHS

Psychovision is the study of vision from a subjective point of view: how do we manage to organize the wealth of information that reaches the retina into coherent structures? It is based on experiments where subjects are asked to describe how they perceive given stimuli. This section will be devoted to what psychovision can teach us about otolith images and how we can apply it in practice.

2.1 Perceptual Emergence from Interaction

Low-level vision is the part of vision (either biological or computer) that builds global structures (or percepts) i.e. curves, regions, depth perception, etc... from atomistic information, the pixels in one case and the cones and rods of the retina in the other. This process has been much studied, in particular by the Gestalt school of visual perception (Kanizsa, 1979).

They described the transition from local information to global percepts as the action of a number of grouping laws stating that individual cues having similar or compatible characteristics are seen as being part of the same group (Kanizsa, 1979). Those characteristics include color, direction, spatial proximity, global shape priors or specific structuring patterns like T-junction and X-junction.

But those laws interact one with the others, either reinforcing one another if they correspond to the same object, or inhibiting or masking one another if several interpretations of a scene are possible. Thus low-level vision can be seen as the process in which global percepts *emerge* from the complex interactions between perceptual cues and group of perceptual cues.

This description is based on the notion of emergence, which is characterised by the existence, in a hierarchy of organizational levels, of properties at a given level which are not explainable by/ reducible to the individual properties of elements of the lower levels. It is characteristic of *complex systems* (Benkirane, 2002). Such systems are notoriously difficult to understand and model because, every element being tied in non-linear ways with a great number of others, it is hard and/or unhelpful to try and study them separately.

2.2 Psychovisual Analysis of Otoliths

Otoliths are in some sense closer to artificial images used in psychovisual experiments than to natural ones. They are strongly organized geometrically in concentric curves alternatively darker and lighter which, despite a low contrast and various noises, are clearly seen event by an untrained eye. A number of grouping laws are involved in that perception: good continuation, concentricity and parallelism of the curves, quasi-convexity of the shapes, constant width of the rings. As all those informations describe the same structures, they reinforce one another, in positive feedback loops.

But most of those grouping laws work on a global scale. The problem might seem easy because otolith images are easily described subjectively as concentric curves, but saying so would be being triked by the ability of human vision to disregard all the cues that do not match its global view of an object. A careful analysis (or indeed any computer program which would lack that particular ability of the human eye) shows that there is locally a number of details that go against that interpretation, like flat zones, bubbles or isolated orthoradial structures. In the case of otoliths, two cues are mainly used: orientation, via the good continuation gestalt, and maxima of contrast. The proposed framework will alternatively use those two information and the coherence between them to find the global structure of the image.

2.3 Proposed Framework

The growth rings on otolith images correspond to ridges and valleys (together known as creases) in computer vision. Those are intuitively the relief curves of the landscape obtained when the image intensity is seen as a height map. As pointed out above, their perception is mainly the result of two grouping laws, one concerned about contrast, locating creases on local maxima or minima of intensity, the other being the good continuation, grouping together those loci forming curves long and smooth enough. In a first part of the algorithm the good continuation is exploited to compute a continuous orientation based family of curves, which in a second part is compared with contrast information to extract only the relevant creases. We should point out that both of those results are of interest for biological applications. While the computed family of curves correspond to the temporal history of the shapes of the otoliths, the extracted crease curves supply the actual growth rings. The different steps are outlined bellow, in relation with Figure 1, and will be detailed in the next section.

The first component of the proposed framework implements the good continuation principle for otoliths images. Good continuation is the grouping law that account for our viewing of continuous and smooth curves (Kanizsa, 1979). If perceptual cues have compatible directions, the curve to which they are all tangent will be seen as a unique curve. Orientation information has a key role and an interpolation based scheme is considered to estimate a dense orientation field. An example is shown Figure 1, top left. Details are in section 3.1. Then, given a prior model on accretionary growth, formalised as a dome-shaped potential function, the successive shapes of the otolith are reconstructed as being as tangent as possible to the orientation field. This model permits an embedding of time information in a third dimension satisfying both biological and psychovisual constraints. The result can be seen Figure 1, top right. The algorithm used will be detailed in section 3.2.

The implementation of the good continuation provides as an output a series of curves which are potential growth rings. A contrario detection is then exploited to combine this geometric information with a contrast based measure to detect crease curves. This step is illustrated figure 1, bottom right. Detail on a contrario detection and the measure used are found section 3.3. Intrinsically a contrario detection will detect several curves for a given growth rings, and an additional grouping law is required to fuse together the curves corresponding to a same structure. The result is seen Figure 1, bottom left. Section 3.4 will outline the algorithm used, full detail can be found in (Chessel, 2007).

As stressed previously, low level vision is about emergence by interaction. In the proposed implementation, those interactions comes from feedback loops, both positives and negatives. Section 3.5 describes how iteration can be used in place of those feedback loops to mimic the emergence process and allow for the progressive apparition of the structures we seek.

3 FROM GOOD CONTINUATION TO ITERATED MULTIMODAL A CONTRARIO DETECTION

3.1 Good Continuation via Orientation Interpolation

Good continuation has attracted much work in the computer vision community. Often an image of edgels -"edge elements", point supposed to be part of an curve along with the orientation of said curve

at that point- is taken as input, and continuous and smooth curves that link them are looked after (Parent and Zucker, 1989; Zweck and Williams, 2004).

Good continuation can be interpreted as an interpolation process. Either directly the interpolation of curves , Euler's elastica (Mumford, 1994) being then seen as a suitable and elegant solution, or through orientation interpolation. The idea is then to build, from a sparse edgel image, a dense orientation field where to each point is associated the tangent to an eventual structure going through that point. Curves in accordance with the good continuation principle are then the one the most tangent to that orientation field

In the case of otoliths, as outlined in the preceding section, such a field is particularly meaningful. The whole image can be described by concentric structures, and as such an orientation can be associated to each point. Furthermore, a biological interpretation can be associated: under the widely accepted hypothesis that variation of optical properties are linked to the biological growth, recovering the tangents to the structures means recovering the local direction of accretionary growth.

In (Chessel et al., 2006) two interpolation operators are presented. Orientation data belong to the unit circle $S^1 = \{x \in \mathcal{R}^2 \mid |x| = 1\}$. But extending data in S^1 poses additional challenges to extending scalar data. To the innate ambiguity of interpolation, one has to manage an ambiguity due to the periodic nature of S^1 and the need to use two maps to parametrize it. We then can distinguish two cases. Either the extension can be achieved by a laminar field, meaning one parametrisation is enough and the extension in S^1 is similar to the scalar case, or a turbulent field is needed and singularities are unavoidable. The hypothesis that can be made in the general case is that the field to be estimated is locally laminar: near each curvilinear structures a smooth field can be reconstructed, and far from them such an orientation field is meaningless. In the particular case of otoliths, a unique singularity is expected in the growth center.

The AMLE (Absolutely Minimizing Lipschitz Extension) is the extension operator used, it verifies an axiomatic approach (Chessel et al., 2006). It has been well studied mathematically. Existence and uniqueness has been proved in the scalar case ((Caselles et al., 1998) and its references). In particular, it verifies a maximality principle which guarantee that the solution is oscillation-free.

Let Ω be a subset of $\mathcal{R}^2$. Let S^1 be parametrise with the angle with the horizontal axis in $[0, pi[$. Let $D \subset \Omega$ be a set of points and/or curves and $\theta_0 : D \rightarrow S^1$. Then $\theta : \Omega \rightarrow S^1$ is the AMLE of θ_0 in Ω if:

$$\begin{cases} D^2\theta(D\theta, D\theta) = 0 \text{ in } \Omega, \\ \theta|_D = \theta_0 \text{ on } D, \end{cases} \quad (1)$$

i.e. if the second derivative in the direction of the gradient is equal to zero.

Numerically the equation was solved using the associated evolution problem. Because of the aforementioned ambiguity associated with the use of S^1, and the iterative nature of that scheme, a multi-resolution initialisation algorithm was used.

The set D of initial points can be obtained in various ways, as we will see later. An example of computed field can be seen Figure 1, the inital point being in black. The field is visualised via it's field lines using line integral convolition (Cabral and Leedom, 1993).

3.2 Recovering Shape Evolution

In this section is presented the representation of the otolith growth via its successive shapes and a way of computing such a representation from an image using the computed orientation field (Fablet et al., 2006). Such a representation stem from both biological modelling and computer vision constraint and algorithms. It is of interest both for itself, as the history of the shapes taken by the otolith, and as a mean of computing curves candidates to be growth rings, as used in the next section.

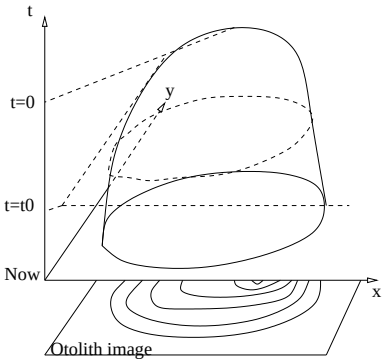

Figure 2: The successive shapes of the otoliths are represented as the level-lines of a dome shaped potential.

As suggested in the seminal work of D'arcy Thompson (D'arcy Thompson, 1917), we adopt a level-set setting to represent the accretionary growth process. It comes to introduce a potential function U defined over $\mathcal{R}^2$ such that the shape $\Gamma_t(U)$ of the considered biological structure within a given observation plane at time t is given by the level set of U,

$$\Gamma_t(U) = \{p \in \mathcal{R}^2 \text{ such that } U(p) = f(t)\}, \quad (2)$$

where f is a strictly monotonic continuous function (see Figure 2). Given U, the sequence of level sets $\{\Gamma_t(U)\}_{[0;T]}$ represents the evolution of the shape from time 0 to time T. This representation conforms to the classical assumption that accretionary growth is locally normal to the shape and thus that the shapes are included one in another (there is no reabsorbtion of the growth). But that representation also complies naturally to many of the low-level vision constraints defined earlier: thanks to it, we are bound to find smooth quasi-convex and concentric parallel curves.

The potential U is computed using a variational algorithm as the smooth potential following the previous definition that is the most tangent to θ, the orientation field computed section 3.1. Let I be the otolith image. Let θ be the computed orientation field with value in $[0,\pi[$. Then the hill-shaped potential function U, with minimum value 0 on the outline and maximum 1 in the center is computed as the minimum of an data driven regularized energy

$$U = \arg\min_U \int_{x\in\mathcal{R}^2} |\nabla U(x)|(1+\gamma\cdot\left\langle \frac{\nabla U(x)}{|\nabla U(x)|},\theta(x)\right\rangle^2)dx \quad (3)$$

It tends to align the tangents to the level-line of U to the computed field θ. The successive shapes of the otolith during its growth are then estimated via the successive and concentric level-sets of U.

3.3 A Contrario Detection

3.3.1 Principles

The a contrario detection relies on the Helmoltz principle, which states that a given geometrical structure in an image is perceptually meaningful if its probability of occurrence in a random image is low enough (Desolneux et al., 2003). Thus, given a collection of objects the assumption is made that they were randomly generated: a false random probability law is defined and meaningful objects are the ones that are unlikely enough with respect to this false model. It can be seen as an implementation of a perceptual grouping law, with the objects being the prospective perceptual groups and the random probability law defining the considered gestalt law.

Formally the a contrario detection is stated as follow. Let I be a grayscale image. Let $\mathcal{C}$ be a set of curves extracted from I and $\mathcal{C}_p$ the set of all pieces of curves from $\mathcal{C}$. Let M be a measure of creaseness (grayscale image) on I. Let $H(m) = \frac{1}{N}\#\{x|M(x) > m\}$, with $N = \#\{x \in I\}$, be the probability for a point of I to have a creaseness measure greater than m.

Definition 1 *Let $c \in \mathcal{C}_p$ be a curve of lenght l and $m = \min_{x\in c} M(x)$. The number of false alarms of that event is defined as*

$$NFA(c) = |\mathcal{C}_p| \times H(m)^l \quad (4)$$

Let $\varepsilon \in \mathcal{R}$. A given piece of curve c is said to be ε-meaningful if $NFA(c) < \varepsilon$.

Ultimately the detection is based on the length of the curves and the minimum of the creasness measure along them: between two curves with the same minimal contrast the more meaningful one will be the longer one.

The influence of ε has been shown to be small (Desolneux et al., 2003), such that a contrario detection can be considered to be parameterless.

The clear separation between the geometric structures being worked on and the random model telling us a contrario the relevant ones allows us to see the process as mutimodal (i.e. different cues brings in several distinct types of information). Indeed the geometric structures, which here are not generic but precomputed, are completely independent from the noise model, and are based on different geometric cues. Hence, if none the less a correlation between the two is detected, it stresses the existence of an underlying geometrical structure in the original image: what we are interested in is how much the two distinct informations ultimately describe the same object.

3.3.2 A Set of Candidate Curves

In the previous section was computed a continuous potential function U, implementing the good continuation principle. It will be used to give us a set of curves that are likely candidates for the growth rings we want to extract. Let $\Gamma_\lambda = \{x|U(x) = \lambda\}$ be the level-set of value λ of U, then if N is the wanted number of curves, we set

$$\mathcal{C} = \{\Gamma_\lambda|\lambda = \frac{k}{N}, k = 1...N\} \quad (5)$$

3.3.3 A Contrast based Measure

A lot of works have studied the local differential properties of images to define their ridges and valleys (Serrat et al., 2000; Sole et al., 2001). The two main criterion are maxima of intensity in the direction of the maximal curvature and maxima of level-line curvature.

Given the Hessian (the matrix of the second order derivatives), the chosen measure is the greatest hessian eigenvalue, or equivalently the greatest principal curvature. It is clear that it is maximal on the crease, it is not too localised contrary to the maxima of the level-line curvature and its sign allows us to differentiate ridges and valleys. The fact that it also responds

well on edges may be a drawback. But this is not problematic in our case as otoliths are rather flat images and the only edge in otolith image is the rim, which is treated separately anyway. So if λ_1 and λ_2 are the two eigenvalues of the hessian of I, associated with eigenvectors v_1 and v_2, $\lambda_1 > \lambda_2$, we define a ridge measure to be

$$M(x) = \lambda_1^+(x) = \begin{cases} \lambda_1(x) \text{ if } \lambda_1(x) > 0 \\ 0 \text{ else,} \end{cases} \quad (6)$$

and conversely λ_1^- for a valley measure.

3.4 Curve Fusion via Alpha Shapes

A contrario detection is about detection and not optimisation, thus a number of pieces of curves are detected as meaningful for a given crease. A step of grouping is necessary, which compute a unique curve from a given group. The detected curves are first regrouped into shapes, two curves being considered as in the same shape if their traces on the pixel grid are connex using 8-connexity. A regularized version of the shape is then computed by taking the α-*shape* of that boundary (Bernardini and Bajaj, 1997). That shape is then represented using triangulated polygon (Felzenszwalb, 2005) and the unique crease associated with a given group of detected curves is then defined as the medial axis of the triangulation. It will not be detailed further here, more details can be found in see (Chessel, 2007)),

3.5 Emergence via Iteration

It can be argued that both positive and negative feedback loops are a sine qua non condition of complex systems (Thomas and Thieffry, 1995). It is the fact that two or more perceptual cues can both reinforce and attenuate one another in non-linear and global ways that give rise to mid-level constructions, which in turn both give rise to global structures and get fed back to drive the individual cues interaction.

That process can be modelled using iterations, i.e. using the detected mid-level elements to drive the process of computing the global structure out of individual information. Contrarily to iterative schemes, used to solve partial differential equations for example, for which convergence and uniqueness results exist, complex systems are characterised by solutions that are difficult to predict analytically, but are rather simulated from given initial conditions.

Two perceptual information are used, orientation and contrast. The a contrario detection imposes to consider independent features, thus the feedback relies on orientation estimation only. The orientation interpolation step uses as input a set of points with known orientation. While initialisation is given by a simple filter, after an iteration of the proposed framework the extracted curves along with the tangent to these curves provides updated inputs to update the orientation field. Being the result of the combination of both perceptual informations, those tangents will allow us to compute orientation fields more closely following the structures, and thus to improve the results.

4 RESULTS

The presented algorithm were implemented in C/C++, using the Megawave2 (Froment, 1998) and the CGAL computational geometry library (CGAL Editorial Board, 2006) libraries. A simple filter selects interesting points to initialise the process. There are few parameters which are not crucial and can essentially be kept constant for a wide range of images.

Previous methods of 2D otoliths image analysis where limited to otolihs considered simple (like plaice, not shown here) and would fail on more complicated species like hake (Fig. 3 top). It is, as far as we known, the first time that reconstructing the history of the shapes as done here is attempted. Quantitative results with respect to synthetic data can found in (Chessel, 2007).

Results on otoliths from different fish species can be seen in Figures 3(a) and 3(b). For each are shown the dome shaped potential motolith, represented by its level lines, and the pieces of growth rings computed, both on top of the original image. Both are shown for the first iteration and after a few iterations.

The improvement over the iterations of the recovered shapes is clear. While at first cluttered by details not relevant with respect to the global structure sought after (on the left side of the hake otolith for exemple), a few iteration of comparing information from orientation and from contrast managed to disregard that local data and smooth the details out. On the growth rings however, that improvement is less visible. There may be two reasons. First those structure are less global than the whole shape evolution, and thus not as dependant over long range multimodal interaction. Second the probability law used in the a contrario detection is very conservative, being based on the minimum, and fail to recover long curves if they pass through a less contrasted part of the image.

5 CONCLUSIONS

Image analysis is one of the means of systematic analysis for the concentric structures found in otoliths. But automatic analysis is a challenge because of the noise and of the low contrast. Those structures are clear to human vision however, so a psychovisual analysis of low-level vision as a complex system was presented to understand how we manage to organise the atomistic information into a coherent whole.

It led us to an iterative algorithm which exploits the coherence between two distinct perceptual cues, orientation and contrast, to go back and forth between individual pixels and a global dome shaped potential. The results are good and biological applications that use them, including morphogenesis modelling and data fusion can be envisaged.

As far as computer vision is concerned, future work will in particular be focused a contrario laws that would allow for curve completion. Besides, the proposed level-sets representation of the otolith growth recover the geometry of the otolith, which provides a common framework for comparing and combining various otoliths features (opacity, growth, chemical signatures...) for the characterisation of individual life traits. To that end, statistical methods for comparing different features with respect to a given geometry will be needed.

To conclude, this work showed how specific computer vision development can be applied to a biological problem so that both computer vision and biology benefit from the cross-fertilisation such transdisciplinary studies induce.

REFERENCES

Benkirane, R., editor (2002). *La complexit, vertiges et promesses*. Le pommier.

Bernardini, F. and Bajaj, C. L. (1997). Sampling and reconstructing manifolds using alpha-shapes. In *Proc. 9th Canadian Conf. Computational Geometry*, pages 193–198.

Cabral, B. and Leedom, L. C. (1993). Imaging vector fields using line integral convolution. In *SIGGRAPH '93*, pages 263–270.

Caselles, V., Morel, J., and Sbert, C. (1998). An axiomatic approach to image interpolation. *IEEE Trans. Image Processing*, 7(3):376–386.

CGAL Editorial Board (2006). *CGAL-3.2 User and Reference Manual*.

Chessel, A. (2007). *Otolithe et Vision par Ordinateur*. PhD thesis, Universit de Rennes 1.

Chessel, A., Cao, F., and Fablet, R. (2006). Orientation interpolation: an axiomatic approach. In *European Conference on Conputer Vision*.

D'arcy Thompson, W. (1917). *On Growth and Form*. London press.

Desolneux, A., Moisan, L., and Morel, J.-M. (2003). A grouping principle and four applications. *PAMI*, 25(4):508–513.

Fablet, R., Pujolle, S., Chessel, A., Benzinou, A., and Cao, F. (2006). Variational level-set reconstruction of accretionary morphogenesis from images. In *IEEE International Conference on Image Processing*.

Felzenszwalb, P. F. (2005). Representation and detection of deformable shapes. *IEEE Transactions on Pattern Analysis and Machine Intelligence*, 27(2).

Froment, J. (1998). Megawave2. http://www.cmla.ens-cachan.fr/Cmla/Megawave/.

Guillau, A., Benzinou, A., Troadec, H., Rodin, V., and Le Bihan, J. (2002). Autonomous agents for edge detection and continuity perception on otolith images. *Image and Vision Computing*, 20(13):955–968.

Kanizsa, G. (1979). *Organization in Vision: Essays on Gestalt Perception*. Greenwood Publishing Group.

Mumford, D. (1994). Elastica and computer vision. In Bajaj, C., editor, *Algebraic Geometry and Its Applications*, pages 491–506. Springer-Verlag.

Panfili, J., de Pontual, H., Troadec, H., and Wright, P., editors (2002). *Manual of fish sclerochronology*. Ifremer-ird coedition.

Parent, P. and Zucker, W. (1989). Trace inference, curvature consistency, and curve detection. *IEEE Transactions on Pattern Analysis and Machine Intelligence*, 11(8):823–839.

Serrat, J., Lopez, A., and Lloret, D. (2000). On ridges and valleys. In *International Conference on Pattern Recognition ICPR'00*, pages 59–66.

Sole, A., Lopez, A., and Sapiro, G. (2001). Crease enhancement diffusion. *Comput. Vis. Image Underst.*, 84:241–248.

Thomas, R. and Thieffry, D. (1995). Les boucles de rtroaction, rouages des rseaux de rgulation biologiques. *Mdecine sciences*, 11(2):189–197.

Troadec, H., Benzinou, A., Rodin, V., and Le Bihan, J. (2000). Use of deformable template for two-dimensional growth ring detection of otoliths by digital image processing: - application to plaice (pleuronectes platessa) otoliths. *Fisheries Research*, 46(1):155–163.

Zweck, J. and Williams, L. (2004). Euclidian group invariant computation of stochastic completion fields using shiftable-twistable basis function. *J. Math. Imaging and Vision*, 21(2):135–154.

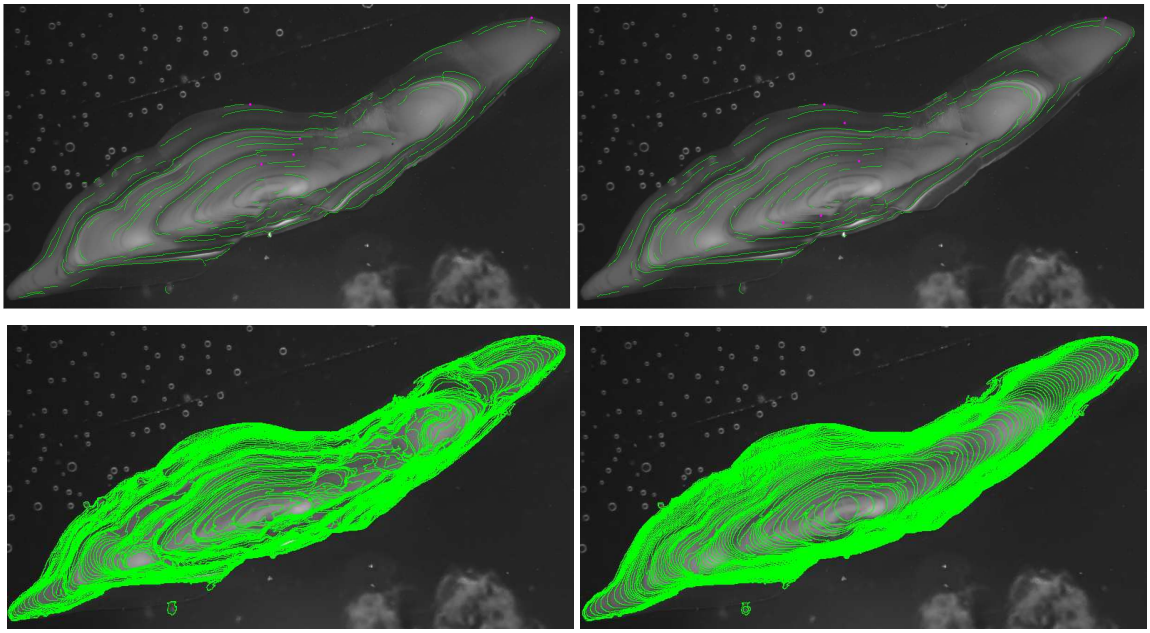

(a) A hake otolith, the recovered successive shapes (bottom), the extracted growth rings (top), first iteration (left), third iteration (right).

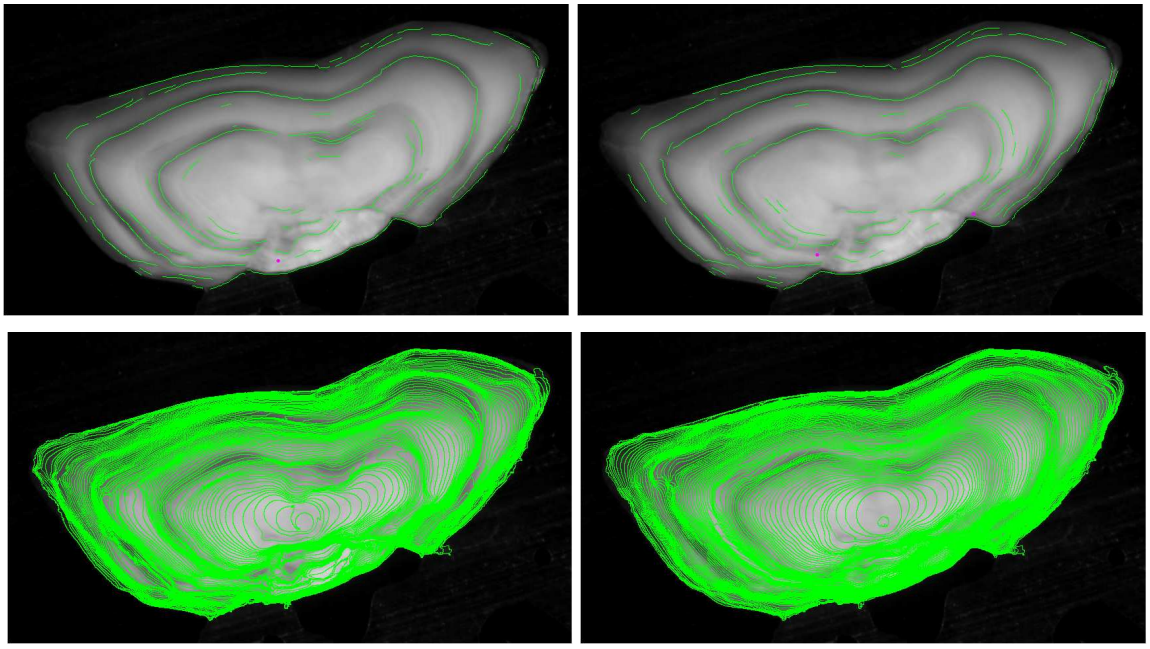

(b) A pollock otolith, the recovered successive shapes (bottom), the extracted growth rings (top), first iteration (left), third iteration (right).

Figure 3

NONLINEAR MODELLING AND CONTROL OF HEART RATE RESPONSE TO TREADMILL WALKING EXERCISE

Teddy M. Cheng, Andrey V. Savkin, Branko G. Celler
School of Electrical Engineering and Telecommunications, the University of New South Wales, Sydney, NSW 2052, Australia
t.cheng@ieee.org, a.savkin@unsw.edu.au, b.celler@unsw.edu.au

Steven W. Su
Faculty of Engineering, the University of Technology, Sydney, NSW 2007, Australia
steven.su@uts.edu.au

Lu Wang
School of Electrical Engineering and Telecommunications, the University of New South Wales, Sydney, NSW 2052, Australia
lwang@cochlear.com.au

Keywords: Heart rate modelling, heart rate control, nonlinear systems, exercise physiology.

Abstract: In this study, a nonlinear system was developed for the modelling of the heart rate response to treadmill walking exercise. The model is a feedback interconnected system which can represent the neural response and peripheral local response to exercise. The parameters of the model were identified from an experimental study which involved 6 healthy adult male subjects, each completed 3 sets of walking exercise at different speeds. The proposed model will be useful in explaining the cardiovascular response to exercise. Based on the model, a 2-degree-of-freedom controller was developed for the regulation of the heart rate response during exercise. The controller consists of a piecewise LQ and an H_∞ controllers. Simulation results showed that the proposed controller had the ability to regulate heart rate at a given target, indicating that the controller can play an important role in the design of exercise protocols for individuals.

1 INTRODUCTION

During dynamic exercise, the cardiovascular system increases the delivery of blood and oxygen to working muscles as the metabolic demand increases, resulting in an increase in heart rate (HR) and stroke volume. Obtaining a model that describes the HR response to exercise will improve our understanding of exercise physiology. Understanding the aetiology of HR response during, and recovery after an exercise, may also be beneficial to predicting cardiovascular disease mortality (Savonen et al., 2006) (Cole et al., 1999). This may also lead to an improvement in developing training protocols for athletics and more efficient weight loss protocols for the obese, and in facilitating assessment of physical fitness and health of individuals (Achten and Jeukendrup, 2003). Furthermore, knowing the cardiovascular system responses to the stress induced by physical exercise provides us another perspective on how this system functions. For instance, this may give us some measures for the prevention of cardiac failure from dialysis.

Studying and modelling of HR response during exercise have been carried out by a number of researchers (e.g. (Brodan et al., 1971; Hajek et al., 1980; Rowell, 1993; Coyle and Alonso, 2001; Su et al., 2007)). Broden et al. (Brodan et al., 1971) and Hajek et al. (Hajek et al., 1980) modelled the HR response from a regulation point of view. Their models are reliable for short duration exercises, but are not sufficient for explaining long duration exercises. As shown in, e.g. (Coyle and Alonso, 2001), HR will continue to increase during prolonged exercise. In reference (Su et al., 2007), exercising HR response was modelled by a Hammerstein system[1]. Besides modelling, they also studied the control of the HR response during exercise.

The ability to control the HR during exercise is of importance in the design of exercise protocols for patients with cardiovascular diseases and in developing rehabilitation exercises to aid patients recovering from cardiothoracic surgery. The control of heart rate response during exercise has been reported in the references (Kawada et al., 1999; Cooper et al., 1998; Su

[1] A system consists of a static nonlinearly cascaded at the input of a linear system.

et al., 2007). Among them, a number of different control strategies or algorithms have been successfully applied, e.g. classical PID control, H_∞ control, and model reference control. Each has its merits or disadvantages and therefore, it is interesting to investigate the usefulness of other control algorithms and techniques which have been developed by the control society.

The objective of this paper is twofold. First, a nonlinear model is proposed to describe the HR response to treadmill walking exercise during both the exercising and the recovery phases. We model the HR response from the neural and the local responses perspective. The advantage of this approach is that the model may describe the HR response over a longer exercise duration. Secondly, using the proposed model, we develop a controller-using the treadmill's speed as a control variable-that regulates the HR during exercise. The controller consists of feedforward and feedback components which provide better performance without trading off robustness.

2 THE MODEL

In this paper, we propose the following nonlinear state-space control systems to model the HR response to treadmill walking exercise:

$$\begin{aligned} \dot{x}_1(t) &= -a_1 x_1(t) + a_2 x_2(t) + a_2 u^2(t) \\ \dot{x}_2(t) &= -a_3 x_2(t) + \phi(x_1(t)) \\ y(t) &= x_1(t) \end{aligned} \tag{1}$$

where $\phi(x_1(t)) := \frac{a_4 x_1(t)}{1+\exp\left(-15(x_1(t)-a_5)\right)}$ and $x(0) = [x_1(0) \quad x_2(0)]^T = 0$, $y(t)$ describes the change in HR from rest, and $a_1, \ldots, a_5$ are positive scalars. The control input $u(t)$ represents the speed of the treadmill.

System (1) can be viewed as a feedback interconnected system, i.e. x_1 in the forward path and x_2 in the feedback path. The component $x_1(t)$ can be viewed as the change of HR due to the neural response to exercise, including both the parasympathetic and the sympathetic neural inputs (see e.g. (Rowell, 1993)). The component x_2 is utilised in describing the complex slow-acting peripheral effects from, e.g. the hormonal systems, the peripheral local metabolism, and/or the increase in body temperature, etc.. Generally, these effects cause vasodilatation and hence HR needs to be increased in order to maintain the arterial pressure (see (McArdle et al., 2007))). So, the feedback signal x_2, which can be thought of as a dynamic disturbance input to the x_1 subsystem, is a reaction to the peripheral local effects. By observing system (1), the input s drives the system nonlinearly, describing the nonlinear increase of the HR in response to the increase in walking speed. It has been observed that there is a curvilinear relationship between aerobic demand and walking speed (see, e.g. (McArdle et al., 2007)).

Table 1: Physical characteristics of the subjects: age, height, weight, and BMI (Body Mass Index).

	Age (yr)	Height (cm)	Weight (kg)	BMI (kg/m^{-2})
mean	29.3	174	68.5	22.5
std	5.8	3.4	12.6	3.4
range	23–38	169–178	53–85	18–27

2.1 Experimental Setup

The parameters in system (1) were identified from experimental data. The setup of the experiment is described in this section.

Subject. Six healthy male subjects were studied. The physical characteristics of the subjects are given in Table 1.

Procedure. Each subject completed three exercise sessions in separate occasions. In each session, a subject was requested to walk on a treadmill at a given speed (5km/h, 6km/h, and 7km/h) for 15 minutes with a recovery period of 15 minutes. After three sessions, each subject completed the treadmill walking exercise at the three different speeds.

Data Acquisition. In this study, the Powerjog fully motorised medical grade treadmill was used. The HR of the subjects was monitored by the wireless Polar system and recorded by LabVIEW. The Polar system generated pulses which were used to determine the HR. To remove noises, the HR measurements were then filtered using the moving average with a 5-second window.

Parameter Estimation. Using the measured HR data and the Levenberg-Marquardt method, the parameters in system (1) were estimated for each subject and for the average response of all subjects . Since there were three sets of input-output measurements for each subject (where the input is the speed of the treadmill and the output is the HR), we estimated the parameters as if the following multi-input multi-output system:

$$\dot{\mathbf{x}}(t) = \mathbf{f}(\mathbf{x}(t), a, u(t)), \quad y(t) = C\mathbf{x}(t), \quad \mathbf{x}(0) = 0 \tag{2}$$

where $C = \begin{bmatrix} 1 & 0 & 0 & 0 & 0 & 0 \\ 0 & 0 & 1 & 0 & 0 & 0 \\ 0 & 0 & 0 & 0 & 1 & 0 \end{bmatrix}$, $\mathbf{x} = [\mathbf{x_1} \quad \mathbf{x_2} \quad \mathbf{x_3}]^T \in \mathbb{R}^6$, $a = [a_1 \quad a_2 \ldots a_5]^T \in \mathbb{R}^5$, $u = [u_1 \quad u_2 \quad u_3]^T \in \mathbb{R}^3$ and $y = [y_1 \quad y_2 \quad y_3]^T \in \mathbb{R}^3$. For $i = 1,2,3$, the vector $\mathbf{x_i} := [x_{i,1} \quad x_{i,2}]^T$ and y_i are the state vector and the output from the input u_i. The unit of time t is in minute. To make the estimation process more robust, the speeds of the treadmill were normalised by 8 km/h, assuming the maximum walking speed was 8 km/h. In other words, the input vector u in (2) is in fact $u = [5/8 \quad 6/8 \quad 7/8]^T$. Similarly, the output $y_i(t)$ from the input $u_i(t)$ was defined as $y_i(t) = (HR_i(t) - 73.4)/60$, where $HR_i(t)$ is the absolute HR at time t, 73.4 bpm is the average resting HR for all the subjects[2], and 60 bpm is a normalising factor.

The objective function was chosen as

$$S(a) = \sum_{i=1}^{N} (y(t_i) - \hat{y}(t_i,a))^T Q (y(t_i) - \hat{y}(t_i,a)) \quad (3)$$

where, for $i = 1,2,\ldots,N$, $y(t_i)$ is the measurement of the output vector at time t_i, $\hat{y}(t_i,a)$ is the output of system (2) with the parameter vector a, and Q is a given diagonal weighting matrix. In this study, $Q := diag([2.5 \quad 1.5 \quad 1])$ was used. With the objective function (3), the Levenberg-Marquardt method was used to determine an estimate of a which was denoted as $\hat{a} := [\hat{a}_1 \quad \hat{a}_2 \ldots \hat{a}_5]^T$ (see, e.g. (Stortelder, 1996)). Based on a linear approximate method (see e.g. (Stortelder, 1996)), an approximate $100(1-\alpha)\%$ independent confidence interval for each estimate was given by $(\hat{a}_i - \delta a_i, \hat{a}_i + \delta a_i)$, for $i = 1,2,\ldots,5$. An α level of 0.05 was used for obtaining the confidence intervals of parameter estimates. Table 2 summaries the estimated parameters for each subject and it also shows the estimated parameters for the average response from all the subjects. The simulated HR responses with the proposed model based on the average response are shown in Figure 1.

Table 2: Estimated parameter values for 6 different subjects and the average response of all subjects.

Subject	Parameter estimates (Confidence intervals, δa)				
	$\hat{a}_1$	$\hat{a}_2$	$\hat{a}_3$	$\hat{a}_4$	$\hat{a}_5$
1	2.374 (0.180)	2.319 (0.161)	0.024 (0.014)	0.018 (0.003)	0.000 (0.308)
2	3.351 (0.334)	3.591 (0.340)	0.126 (0.008)	0.071 (0.004)	0.683 (0.009)
3	1.940 (0.180)	1.597 (0.138)	0.038 (0.007)	0.054 (0.004)	0.507 (0.010)
4	1.041 (0.078)	0.787 (0.052)	0.072 (0.011)	0.069 (0.007)	0.491 (0.015)
5	3.665 (0.489)	2.394 (0.304)	0.169 (0.023)	0.107 (0.013)	0.476 (0.029)
6	1.782 (0.166)	1.442 (0.123)	0.110 (0.009)	0.105 (0.007)	0.562 (0.013)
average response	1.858 (0.119)	1.655 (0.099)	0.057 (0.007)	0.046 (0.003)	0.550 (0.009)

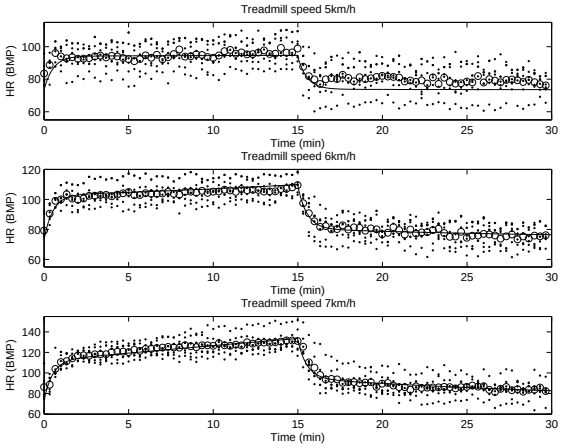

Figure 1: HR responses: actual responses from all subjects (dots), average response (circles) and simulated response (solid line).

3 CONTROLLER DESIGN

In the second part of this paper, a controller design is proposed for the regulation of HR. The controller essentially controls the speed of the treadmill and in turns controls the HR. It is desirable to design a controller that is suitable for all the subjects, rather than designing a controller for each individual subject. To design such a controller, the model for the average response was utilised (see Table 2). Substituting the parameters estimated from the average response, system (1) is written in the state-space form as follows:

$$\dot{x} = Ax + B_1\phi(x_1) + B_2 g(u), \quad y = Cx \quad (4)$$

where

$A = \begin{bmatrix} -1.858 & 1.655 \\ 0 & -0.057 \end{bmatrix}$, $B_1 = \begin{bmatrix} 0 \\ 1 \end{bmatrix}$, $B_2 = \begin{bmatrix} 1.655 \\ 0 \end{bmatrix}$, $x = \begin{bmatrix} x_1 & x_2 \end{bmatrix}^T$, $C = \begin{bmatrix} 1 & 0 \end{bmatrix}$, $g(u) := u^2$, $\phi(x_1) := \frac{0.046x_1}{1+\exp\left(-15(x_1-0.55)\right)}$.

System (4) is a nonlinear system with nonlinearity $\phi(x_1)$ and nonlinear control input $g(u)$. To overcome the control input nonlinearity, a transformed input $v = g(u)$ is defined. The function $\phi(x_1)$ can be

[2]Resting HR was estimated from the 3-minute resting period before exercise.

approximated by a piecewise linear function

$$\gamma(x_1) = \begin{cases} 0 & \text{if } x_1 \le 0.418 \\ 0.090x_1 - 0.038 & \text{if } x_1 > 0.418. \end{cases}$$

In fact, $\gamma(x_1)$ is obtained by linearising the function $\phi(x_1)$ at $x_1 = 0$ and 0.5. As a result, system (4) can be approximated by a piecewise affine system (see e.g. (Rantzer and Johansson, 2000)).

In this paper, we propose a two-degree-of-freedom (2-DOF) controller consisting of a piecewise linear quadratic (LQ) feedforward and a H_∞ feedback controllers, as shown in Figure 2, for the control and regulation of HR response.

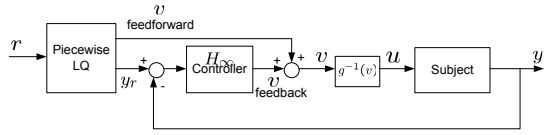

Figure 2: Control configuration.

3.1 LQ Feedforward Controller Design

First, we design the piecewise LQ feedforward controller using the piecewise LQ optimal control technique (Rantzer and Johansson, 2000). We also incorporate an integral action in the controller.

Define two partitions of the state space:

$$X_1 := \{[x_1 \ x_2]^T \in \mathbb{R}^2 \,\big|\, x_1 < 0.418\}$$
$$X_2 := \{[x_1 \ x_2]^T \in \mathbb{R}^2 \,\big|\, x_1 \ge 0.418\}$$

Next, define

$$\bar{A}_i = \begin{bmatrix} A_i & 0 & a_i \\ -C & 0 & 0 \\ 0_{n\times 1} & 0 & 0 \end{bmatrix}, \bar{B} = \begin{bmatrix} B_2 \\ 0 \\ 0 \end{bmatrix}, \bar{x} = \begin{bmatrix} x \\ e \\ 1 \end{bmatrix}$$

for $x \in X_i$ and $i = 1, 2$, where

$$A_1 = \begin{bmatrix} -1.858 & 1.655 \\ 0 & -0.057 \end{bmatrix}, A_2 = \begin{bmatrix} -1.858 & 1.655 \\ 0.090 & -0.057 \end{bmatrix},$$

$a_1 = \begin{bmatrix} 0 & 0 \end{bmatrix}^T$, $a_2 = \begin{bmatrix} 0 & -0.038 \end{bmatrix}^T$, $e(t) = \int_0^t (r - Cx(t))dt$ and r is the constant reference input. Therefore, we have

$$\dot{\bar{x}} = \bar{A}_i\bar{x} + \bar{B}v, \quad y = \bar{C}\bar{x}, \quad \text{for } x \in X_i. \qquad (5)$$

where $\bar{C} = [C \ 0 \ 0]$. Then, the control problem is to find a control law v that minimises the following cost function: $J = \int_0^\infty (\bar{x}^T\bar{Q}\bar{x} + v^T Rv)dt$, for any given $\bar{Q} \ge 0$ and $R > 0$. In the control design, the matrix $\bar{Q}$ and the value of R were chosen as follows: $\bar{Q} = diag([0 \ 0 \ 10 \ 0])$, $R = 0.5$. By using the technique in (Rantzer and Johansson, 2000), the minimising control law was $v(t) = L_i\bar{x}, x \in X_i$, $i = 1, 2$, where $L_1 = \begin{bmatrix} -1.457 & -0.989 & 4.471 & 0 \end{bmatrix}$, $L_2 = \begin{bmatrix} -1.48 & -1.001 & 4.471 & 0.009 \end{bmatrix}$. In turn, the LQ feedforward controller is in the form:

$$\dot{\bar{x}} = \bar{A}_i\bar{x} + \bar{B}v + B_r r, \quad y_r = \bar{C}\bar{x}, \quad v(t) = L_i\bar{x}, \qquad (6)$$

for $x \in X_i$ where $\bar{x}(0) = [0 \ 0 \ 0 \ 1]^T$, $B_r = [0 \ 0 \ 1 \ 0]^T$ and r is the reference input. In other words, the input to this feedforward controller is the reference r and the output are the feedforward control v and the "filtered" reference y_r.

3.2 H_∞ Controller Design

To cope with the uncertainty in the model, we design a feedback controller based on the H_∞ control technique (see e.g. (Petersen et al., 2000)). We first linearise the system (4) and then formulate the control problem as a mixed sensitivity problem (see e.g. (Skogestad and Postlethwaite, 1996) for details). In a mixed sensitivity problem, the idea is to choose some weighing functions, namely $W_1(s)$, $W_2(s)$ and $W_3(s)$ to reflect the control objectives. Generally, $W_1(s)$ is chosen to meet a performance specification and $W_3(s)$ is chosen to characterise the modelling errors. Whereas the weighing function $W_2(s)$ may be used to reflect some restrictions on the actuator signal.

In order to apply the mixed sensitivity technique, the system (4) was linearised at $x_0 = [0.5 \ 0.13]^T$, $v_0 = 0.43$, and the transfer function of the linearised model is given by

$$G(s) = \frac{1.655s + 0.094}{s^2 + 1.915s - 0.043} \qquad (7)$$

The weighting functions were then chosen as: $W_1(s) = \frac{0.02(s+5)}{(s+0.0001)}$, $W_2(s) = \frac{700(s+0.3)}{(s+2100)}$, $W_3(s) = \frac{100(s+7.13)}{(s+800)}$. By using MATLAB Robust Control Toolbox, we obtained a controller $K(s)$ that is fifth order, resulting in a complicated control strategy. In fact, by observing the Hankel singular values of the controller $K(s)$, a second order controller K_{reduced} was in fact adequate to approximate $K(s)$ and it is in the form

$$K_{\text{reduced}}(s) = \frac{0.927s + 0.009}{s^2 + 0.060s + 6.008 \times 10^{-6}} \qquad (8)$$

4 SIMULATION RESULTS

As shown in Figure 2, a 2-DOF controller were constructed by combining the LQ feedforward controllers (6) and the H_∞ feedback controller (8). Since both the feedforward and feedback controllers were

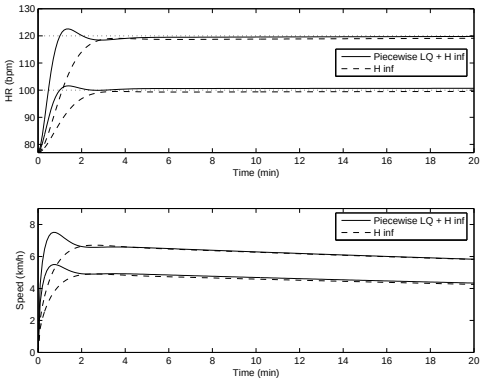

Figure 3: Subject 1–Simulation of HR regulation at 100 bpm and 120 bpm with H_∞ controller (dashed) and Piecewise LQ + H_∞ controller (solid).

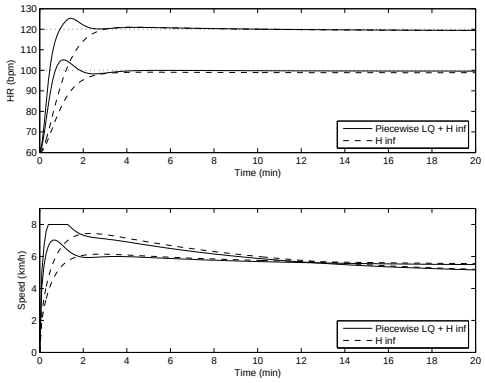

Figure 4: Subject 2–Simulation of HR regulation at 100 bpm and 120 bpm with H_∞ controller (dashed) and Piecewise LQ + H_∞ controller (solid).

obtained by considering the model of the average response from the six subjects, it would be realistic to validate the 2-DOF controller by applying it to each of the subject without re-tuning the control parameters for each subject. From the previous section, we have a model for each of the subject and the estimated parameters of the model are shown in Table 2.

We also assumed the treadmill speed was only allowed to be operated between 0 and 8 km/h, since speeds greater than 8 km/h may exceed the maximum walking speed of some subjects. For each subject, we tested the proposed controller by regulating the HRs at 2 levels, namely 100 and 120 bpm. In the simulations, the resting HR of each subject was assumed to be the average of the three resting HRs, since each subject performed 3 sets of walking exercise.

Figures 3–8 show the simulation results. Each figure shows the controlled HR responses and the speeds of the treadmill. It also shows the responses from the proposed 2-DOF controller and 1-DOF controller which consists of H_∞ feedback controller only. For each of the subject, the controlled HR was able to track the reference HR signals. By comparing the responses from the 2-DOF controller and the H_∞ controller, the proposed 2-DOF controller provides faster responses. It indicates that the proposed 2-DOF controller should give better performance than that of only H_∞ controller.

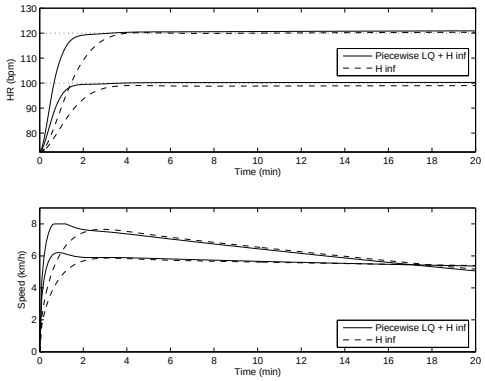

Figure 5: Subject 3–Simulation of HR regulation at 100 bpm and 120 bpm with H_∞ controller (dashed) and Piecewise LQ + H_∞ controller (solid).

5 CONCLUSIONS

In this study, a nonlinear model describing the HR response to the treadmill walking exercise is proposed. The proposed model is a feedback interconnected system, consisting of a subsystem in the forward path that can be used to describe the neural response, and a feedback subsystem can be utilised to describe the peripheral local response. Utilising this model, a 2-DOF controller was developed for the regulation of HR for treadmill walking exercise. The controller consists of a piecewise LQ feedforward and a H_∞ feedback controller. One of the benefits of introducing the feedforward control is to improve the performance, since robust control such as H_∞ controller is sometimes overly conservative that impedes performance. The controller was derived from the model of average response of the six participated subjects. Simulation results showed that the proposed controller had the ability to regulate HR for all the six subjects, without the need to re-tune the controller's parameters.

ACKNOWLEDGEMENTS

This work was supported by the Australian Research Council.

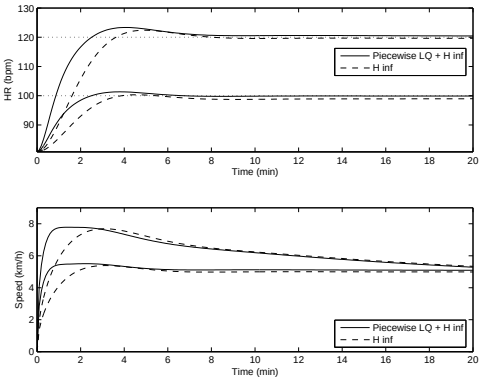

Figure 6: Subject 4–Simulation of HR regulation at 100 bpm and 120 bpm with H_∞ controller (dashed) and Piecewise LQ + H_∞ controller (solid).

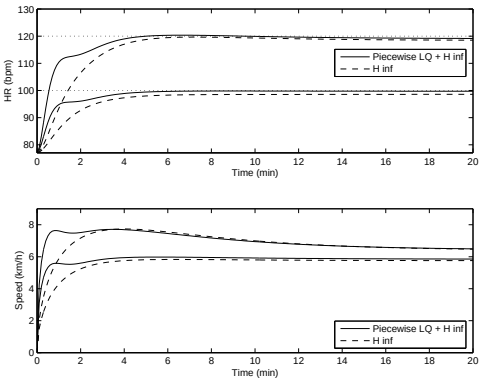

Figure 7: Subject 5–Simulation of HR regulation at 100 bpm and 120 bpm with H_∞ controller (dashed) and Piecewise LQ + H_∞ controller (solid).

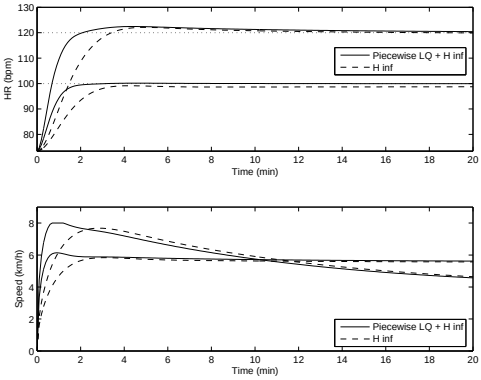

Figure 8: Subject 6–Simulation of HR regulation at 100 bpm and 120 bpm with H_∞ controller (dashed) and Piecewise LQ + H_∞ controller (solid).

REFERENCES

Achten, J. and Jeukendrup, A. E. (2003). Heart rate monitoring: Applications and limitations. *Sports Med.*, 33(7):517–538.

Brodan, V., Hajek, M., and Kuhn, E. (1971). An analog model of pulse rate during physical load and recovery. *Physiologia Bohemoslovaca*, 20:189–198.

Cole, C. R., Blackstone, E. H., F. J. Pashkow, C. E. S., and Lauer, M. S. (1999). Heart rate recovery immediately after exercise as a predictor of mortality. *The New England Journal of Medicine*, 341(18):1351–1357.

Cooper, R. A., Fletcher, T. L., and Robertson, R. N. (1998). Model reference adaptive control of heart rate during wheelchair ergometry. *IEEE Transactions on Control Systems Technology*, 6(4):507–514.

Coyle, E. F. and Alonso, G. (2001). Cardiovascular drift during prolonged exercise: New perspectives. *Exercise and Sports Science Review*, 29:88–92.

Hajek, M., Potucek, J., and Brodan, V. (1980). Mathematical model of heart rate regulation during exercise. *Automatica*, 16:191–195.

Kawada, T., Sunagawa, G., Takaki, H., Shishido, T., Miyano, H., Miyashita, H., Sato, T., Sugimachi, M., and Sunagawa, K. (1999). Development of a servocontroller of heart rate using a treadmill. *Japanese Circulation Journal*, 63:945–950.

McArdle, W. D., Katch, F. I., and Katch, V. L. (2007). *Exercise Physiology: Energy, Nutrition & Human Performance*. Lippincott Williams & Wilkins, Philadelphia, PA, 6 edition.

Petersen, I. R., Ugrinovskii, V. A., and Savkin, A. V. (2000). *Robust Control Design Using H$^\infty$ Methods*. Springer-Verlag, London.

Rantzer, A. and Johansson, M. (2000). Piecewise linear quadratic optimal control. *IEEE Transactions on Automatic Control*, 45(4):629–637.

Rowell, L. B. (1993). *Human Cardiovascular Control*. Oxford University Press, New York.

Savonen, K. P., Laka, T. A., Laukkanen, J. A., Halonen, P. M., Rauramaa, T. H., Salonen, J. T., and Rauramaa, R. (2006). Heart rate response during exercise test and cardiovascular mortality in middle-aged men. *European Heart Journal*, 27:582–588.

Skogestad, S. and Postlethwaite, I. (1996). *Multivariable Feedback Control*. Wiley, England.

Stortelder, W. J. H. (1996). Parameter estimation in dynamic systems. *Mathematics and Computers in Simulation*, 42:135–142.

Su, S. W., Wang, L., Celler, B. G., Savkin, A. V., and Guo, Y. (2007). Identification and control for heart rate regulation during treadmill exercise. *IEEE Transactions on Biomedical Engineering*, 54(7):1238–1246.

DELAYED RECOVERY OF CARDIOVASCULAR AUTONOMIC FUNCTION AFTER MITRAL VALVE SURGERY

Evidence for Direct Trauma?

R. Bauernschmitt[1], B. Retzlaff[1], N. Wessel[2], H. Malberg[3], G. Brockmann[1]
C. Uhl[1] and R Lange[1]
[1]*German Heart Center Munich,* [2]*University of Potsdam,* [3]*University of Karlsruhe*

Keywords: Biosignal processing, Baroreflex response, surgery.

Abstract: Baroreflex Sensivity (BRS) and heart rate variability (HRV) have significant influence on the patients' prognosis after cardiovascular events. The following study was performed to assess the differences in the postoperative recovery of the autonomic regulation after mitral valve (MV) surgery and aortic valve (AV) surgery with heart-lung machine. 43 consecutive male patients were enrolled in a prospective study; 26 underwent isolated aortic valve surgery and 17 isolated mitral valve surgery. Blood pressure, ECG and respiratory rate were recorded the day before, 24h after surgery and one week after surgery. BRS was calculated according to the Dual Sequence Method, time and frequency parameters of HRV were calculated using standard methods. There were no major differences between the two groups in the preoperative values. At 24 h a comparable depression of HRV and BRS in both groups was observed, while at 7 days there was partial recovery in AV-patients, which was absent in MV-patients: p (AV vs. MV)<0,001. While the response of the autonomic system to surgery is similar in AV- and MV-patients, there obviously is a decreased ability to recover in MV-patients, probably attributing to traumatic lesions of the autonomic nervous system by opening the atria. Ongoing research is required for further clarification of the pathophysiology of this phenomenon and to establish strategies to restore autonomic function.

1 INTRODUCTION

The well-known depression of cardiovascular autonomic function following cardiac surgery is related to a variety of reasons like anaesthesia and the use of the heart-lung-machine (Brown et al., 2003), (Bauernschmitt et al., 2004). The role of direct surgical trauma to the autonomic nerves (AN) is still unclear. The following study was performed comparing patients with isolated aortic valve replacement (AV, the surgical trauma to AN is considered to be low) or isolated mitral valve surgery (MV, high surgical trauma to AN is expected). With regard to the hypothesis that there is a traumatic lesion of the cardiovascular autonomic nervous system by opening the atria we observe the postoperative recovery of AV- and MV-patients.

2 METHODS

43 consecutive male patients were analysed. 26 of them underwent aortic valve surgery and 17 of them mitral valve surgery. The mean age of AV-patients was 63 +/- 13 years and the mean age of MV-patients 59 +/- 12 years. Patients with concomitant coronary heart disease were excluded for the known effects of atherosclerosis. Perioperative medication was standardized.

Anaesthesia was standardized; induction was performed with sufentanil and midazolam. For maintaining narcosis, a continuous infusion of propofol was given; muscle relaxation was achieved by pancuronium. Central venous pressure and pulmonary artery pressure were monitored by a Swan-Ganz catheter, arterial pressure by cannulation of the radial artery. All operations were carried out with cardiopulmonary bypass (CPB) in mild hypothermia (32-34°C) and pulsatile perfusion mode, cold crystalloid cardioplegia or blood cardioplegia (isolated bypass surgery) was used for cardiac arrest. After declamping, most of the patients needed one countershock to terminate ventricular fibrillation.

After 10-min equilibrations to the environment, non-invasive blood pressure signals were collected

from the radial artery by a tonometer (Colin Medical Instruments) at 1000 Hz. Data were channelled into a bed-side laptop after A/D-conversion and stored for analysis. Simultaneously, breathing excursions and a standard ECG were monitored. Data were sampled for a 30-min period the day before surgery, 24h and seven days after surgery on the ICU. Care was taken to perform the measurements during the same time of the day in each patient. From the recorded data the beat-to-beat intervals as well as the beat-to-beat systolic and diastolic values were extracted; premature beats, artifacts and noise were excluded using an adaptive filter considering the instantaneous variability.

Baroreflex Sensitivity (BRS): Dual Sequence Method (DSM). Using the DSM, the most relevant parameters for estimating the spontaneous baroreflex (BR) are the slopes as a measure of sensitivity. The DSM is based on standard sequence methods with several modifications: Two kinds of BBI responses were analyzed: bradycardic (an increase in systolic blood pressure (SBP)) that causes an increase in the following beat-to-beat-intervals (BBI) and tachycardic fluctuations (a decrease in SBP causes a decrease in BBI). Both types of fluctuations were analyzed both in a synchronous and in a 3-interbeat-shifted mode. The bradycardic fluctuations primarily represent the vagal spontaneous BR analysis of the tachycardic fluctuations represent the delayed responses of heart rate (shift 3) assigned to the beginning slower sympathetic regulation. The following parameter groups are calculated by DSM: (1) the total numbers of slopes in different sectors within 30 min; (2) the percentage of the slopes in relation to the total number of slopes in the different sectors; (3) the numbers of bradycardic and tachycardic slopes; (4) the shift operation from the first (sync mode) to the third (shift 3 mode) heartbeat triple; and (5) the average slopes of all fluctuations. DSM parameters are defined as described by Malberg et al (European Heart Journal, 1996).

Heart rate Variability (HRV). Respecting the suggestions by the Task Force HRV (Malberg et al., 2003), the following standard parameters are calculated from the time series: MeanNN (mean value of normal beat-to-beat intervals): Is inversely related to mean heart rate. sdNN (standard deviation of intervals between two normal R-peaks): Gives an impression of the overall circulatory variability. Rmssd (root mean square of successive RR-intervals):

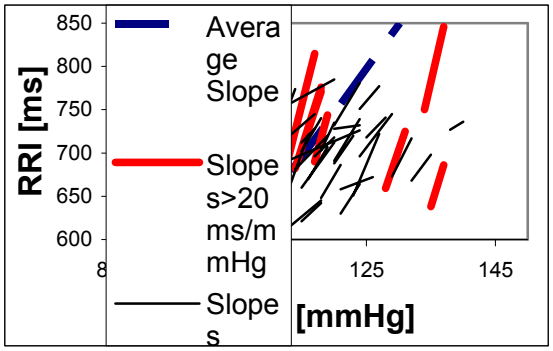

Figure 1: Schematic representation of the two main baroreflex parameters estimated by the Dual Sequence Method: the average slope (dotted line) of all baroreflex sequences as well as the total number of baroreflex slopes above 20 ms/mmHg (thick lines). The thin lines symbolize all baroreflex slopes below 20 ms/mmHg.

Higher values indicate higher vagal activity. Shannon (the Shannon entropy of the histogram): Quantification of RR-interval distribution. Apart from the time-domain parameters mentioned above, the HRV analysis focused on high-frequency components (HF, 0.15-0.4 Hz, high values indicate vagal activity) and low-frequency components (LF, 0.04-0.15 Hz, high values indicate sympathetic activity). The following ratios were considered: LFn – the normalized low frequency (LFn=LF/(LF+HF)), HP/P - the to the total power P normalized high frequency as well as LP/P - the P-normalized low frequency.

Nonlinear Dynamics. New parameters can be derived from methods of nonlinear dynamics, which describe complex processes and their interrelations. These methods provide additional information about the state and temporal changes in the autonomic tonus. Several new measures of non-linear dynamics in order to distinguish different types of heart rate dynamics as proposed by Kurths were used. The concept of symbolic dynamics is based on a coarse-graining of dynamics. The difference between the current value (BBI or systolic blood pressure) and the mean value of the whole series is transformed into an alphabet of four symbols (0; 1; 2; 3). Symbols '0' and '2' reflect low deviation (decrease or increase) from mean value, whereas '1' and '3' reflect a stronger deviation (decrease or increase over a predefined limit, for details see Voss et al. Subsequently, the symbol string is transformed to 'words' of three successive symbols explaining the nonlinear properties and thus the complexity of the system.

The Renyi entropy calculated from the distributions of words ('fwrenyi025' - a = 0.25) is a suitable measure for the complexity in the time series ('a' represents a threshold parameter). Higher values of entropy refers to higher complexity in the corresponding time series and lower values to lower ones. A high percentage of words consisting only of the symbols '0' and '2' ('wpsum02') reflects decreased HRV. The parameter 'Forbidden words (FW)' reflects the number of words which never or very rarely occur. A high number of forbidden words are typical for regular behaviour, while in highly complex time series, only very few forbidden words are found.

3 RESULTS

There were no major differences among the two groups preoperatively. At 24h after surgery, both groups showed a comparable depression of HRV and BRS. One week after surgery, however, marked differences were present: SDNN 15+/-6 (MV) vs. 42+/-33 (AV); p<0.001 (Fig. 1).

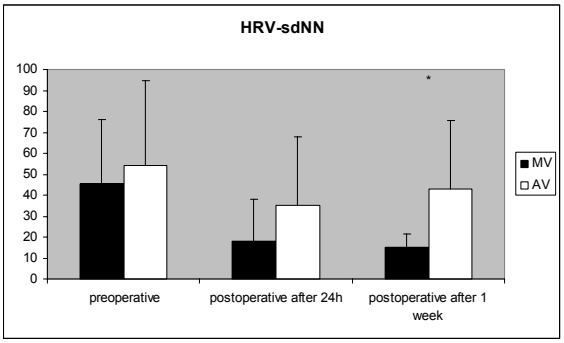

Figure 2: HRV-sdNN, heart rate variability - standard deviation of beat to beat intervals.

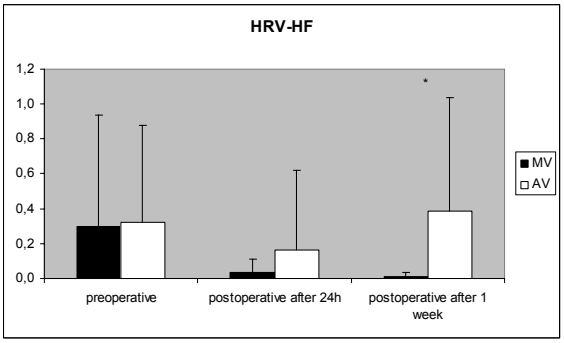

Figure 3: HRV-HF: heart rate variability – high frequency (indicator for parasympathetic regulation).

Similar kinetics were found for the High- and Low-Frequency components of HRV (HF 0.01+/- 0.02 (MV) vs. 0.38+/- 0.64 (AV); p<0.02 (Fig. 2, 3).

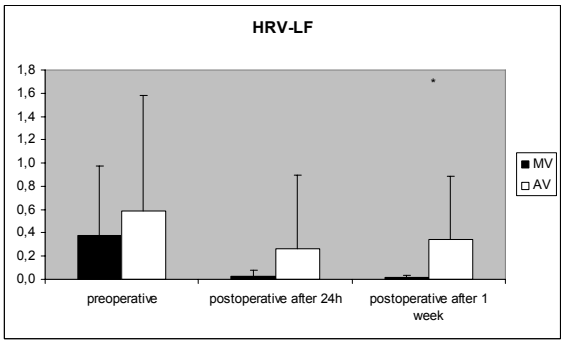

Figure 4: HRV, low-frequency.

Regarding the nonlinear parameters, there was a significant depression present already 24h after surgery with mitral patients more suppressed than aortic patients, these alterations being even more distinct after one week (Fig. 4).

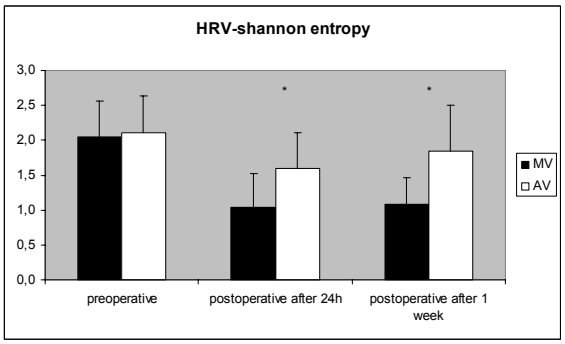

Figure 5: HRV, Shannon-entropy.

The baroreflex was impacted in a similar way for both the number and strength of regulations (BRS bradycardic 4.5+/-1.2 (MV) vs. 7.3+/-2.7 (AV); p<0.001 (Fig. 5, 6).

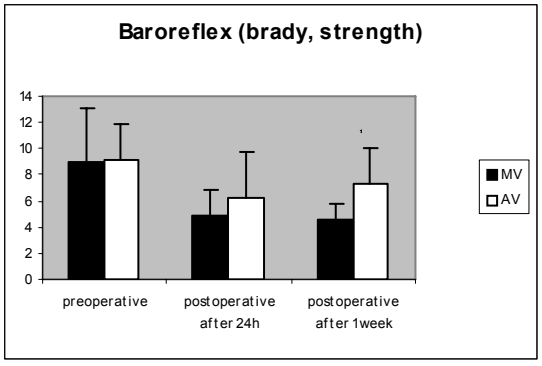

Figure 6: BRS, strength of bradycardic regulations.

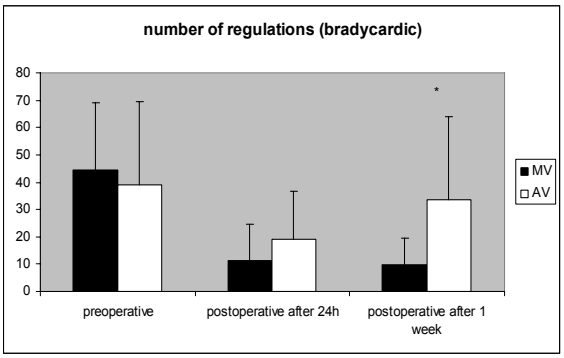

Figure 7: BRS, number of bradycardic regulations.

For the tachcardic part of the baroreflex, however, the differences among aortic and mitral patients failed significance after one week ($p<0.08$, data not shown).

4 DISCUSSION AND CONCLUSIONS

The last decade witnessed a strong increase in basic knowledge of the cardiovascular autonomic system. However, as far as alterations in the cardiac patient and in patients undergoing open heart surgery are concerned, we are still at the very start.

Meanwhile it is well known, that cardiac surgery leads to an early depression of autonomic function, and that there is potential for recovery after a certain time frame. The mechanisms for both phenomena are quite unclear, so the aim of the present study was to shed light on the precise role of direct surgical trauma. In contrast to earlier studies, where different preoperative conditions and different surgical procedures were mixed up, we focussed on patients with isolated aortic valve disease and isolated mitral valve disease, thus excluding the well known influences of atherosclerosis on cardiovascular autonomic function. On the other hand, the operative procedures done in these patients offer two entirely distinct entities of surgical trauma: while for aortic valve replacement the heart is left more or less untouched and the valve is approached by an incision in the anterior aspect of the ascending aorta only, in mitral valve operations, both the caval veins are extensively dissected, and the heart is opened by an incision right posterior to the interatrial groove, where an abundance of autonomic nerve endings are supposed to be.

The similar depression in both groups observed at 24h may reflect the effects of standardized anesthesia and perioperative treatment being comparable in all patients. While AV-patients showed a clear tendency to recover after one week, no recovery was recorded in MV-patients. In our opinion, this is a strong indicator of higher surgical trauma to AN, if the atria are dissected. Recovery of autonomic fibres is possible, even in heart transplant patients, as described earlier, so the next step will be investigating time and frequency parameters and baroreflex sensivity after six months to give evidence of the hypothesis of direct surgical trauma.

Summarizing, we were able to demonstrate for the first time, that direct surgical trauma can be one of the major mechanisms leading to depression of cardiovascular autonomic function. The diversity of results in earlier studies may be caused by the case-mix of patients, comprising different initial conditions as well as different extents of trauma.

ACKNOWLEDGEMENTS

This study was supported by grants from the Deutsche Forschungsgemeinschaft (DFG BA 1581/4-1, BR 1303/8-1, KU 837/20-1).

REFERENCES

Brown CA, Wolfe LA, Hains S, Ropchan G, Parlow J. Spontaneous baroreflex sensitivity after coronary artery bypass graft surgery as a function of gender and age. Can. J. Physiol. Pharmacol. 2003;(9): 894–902.

Bauernschmitt R, Malberg H, Wessel N, Kopp B, Schirmbeck EU, Lange R. Impairment of cardiovascular autonomic control in patients early after cardiac surgery. Eur J Cardiothorac Surg 2004; 25(3):320-326.

Heart rate variability Standards of measurement, physiological interpretation, and clinical use. Task Force of The European Society of Cardiology and The North American Society of Pacing and Electrophysiology. European Heart Journal 1996; 17: 354–381.

Malberg H, Bauernschmitt R, Meyerfeldt U, Schirdewan, A, Wessel N. Short-term heart rate turbulence analysis versus variability and baroreceptor sensitivity in patients with dilated cardiomyopathy. Z Kardiol 2003; 92(7):547-557.

AN INVERSE MODEL FOR LOCALIZATION OF LOW-DIFFUSIVITY REGIONS IN THE HEART USING ECG/MCG SENSOR ARRAYS

Ashraf Atalla and Aleksandar Jeremic
Department of Electrical and Computer Engineering, McMaster University, Hamilton, ON Canada
mohamasm@mcmaster.ca, jeremic@mcmaster.ca

Keywords: Biological system modeling, diffusion equations, parameter estimation.

Abstract: Cardiac activation and consequently performance of the heart can be severely affected by certain electrophysiological anomalies such as irregular patterns in the activation of the heart. Since the wavefront propagation occurs through the diffusion of ions (Na^+, K^+, etc.) the reduced mobility of ions can be equivalently represented as a reduction of ionic diffusivity causing irregularities in heartbeats. In this paper we propose models for the cardiac activation using inhomogeneous reaction-diffusion equations in the presence of diffusivity disorders. We also derive corresponding statistical signal processing algorithms for estimating (localizing) parameters describing these anomalies. We illustrate applicability of our techniques and demonstrate the identifiability of the parameters through numerical examples using a realistic geometry.

1 INTRODUCTION

The phases of myocardial action potentials and processes of myocardial depolarization and repolarization are well studied and described in most handbooks of electrophysiology and electrocardiography (Gulrajani, Malmivuo). The underlying processes controlling the (re)polarization in the cardiac activation can be described, on a molecular level, as diffusion of ions through various channels (Na, K, etc.) giving a rise to ionic current which in turn creates electromagnetic field on the torso surface which can be externally measured.

Modeling the cardiac activation on a cellular level (Gulrajani) has been a subject of considerable research interest resulting in numerous models related to membrane potential (e.g. Hodgkin-Huxley model). However, these models are mainly suitable for forward modeling in which the cardiac activation is simulated using *a priori* knowledge of various parameters. Complimentary to this approach is inverse modeling in which information on cardiac activation (and some physiological parameters) is deduced from ECG/MCG measurements.

One of the most important parameters controlling the activation wavefront propagation is the diffusivity (i.e., mobility of ions). Namely, significant loss of ionic mobility can cause occurrence of irregular activation patterns and lead to various pathological conditions such as arrhythmia, early after-depolarization, etc. From a physiological point of view, these changes usually occur due to ion depletion from a particular region of the heart. As a result, the diffusivity in this region becomes very small preventing the propagation of the activation wavefront and causing the aforementioned irregular patterns. Therefore, any algorithm capable of detecting these anomalies can potentially be useful to predict the onset of these cardiac physiopathologies.

In this paper we propose a new activation model based on the diffusion equation. Although the FitzHugh-Nagumo model is based on the diffusion equation its applicability to inverse approach and real data is limited because of its isotropic and homogeneous nature. In Section 2 we develop cardiac activation model based on the reaction-diffusion equation with non-homogeneous and anisotropic diffusion tensor. Such a model can be used for detecting different physiological conditions such as conductivity anomalies, which can predate onset of various pathological conditions such as cardiac arrhythmia, early after-depolarization, etc. In Section 3 we derive the statistical and measurements model using Geselowitz equations corresponding to our diffusion based source. Using these models we derive the generalized least squares (GLS) estimator for localizing conductivity anomalies/disorders. In Section 5 we demonstrate the applicability of our results using numerical simulations and in Section 6 we present conclusions.

2 PHYSICAL MODEL

During the spread of activation in the heart, the most significant bioelectric source is the large potential difference that exists across the moving wavefront that divides active (depolarized) from resting tissue. It has been proposed that the cardiac excitation can be modeled using reaction diffusion systems i.e., a set of nonlinear partial differential equations (Panfilov and Holden, 1997)

$$\frac{\partial u_i}{\partial t} = f_i(u) + \nabla \cdot (D_i \nabla u_i) \qquad i = 1, \dots n \quad (1)$$

where $u = [u_1, \dots u_n]^T$ is the state variable vector, f_i are excitations, and D_i diffusion tensors. Although the above models can be used to model the propagation even down to a cellular level, in order to develop an inverse model a simplified approach similar to (FitzHugh, 1961),(Rogers and McCulloch, 1994) is needed. Therefore, we propose a reaction diffusion model consisting of two state variables but with spatially dependent diffusivity tensor

$$\begin{aligned} \frac{\partial u_1(r,t)}{\partial t} &= \nabla \cdot (D(r) \nabla u_1(r,t)) + \\ &\quad + g^T(u(r,t)) A_1 g(u(r,t)) \\ \frac{\partial u_2(r,t)}{\partial t} &= u^T(r,t) A_2 u(r,t) \\ g(u(r,t)) &= [u_1^2(r,t), u_1(r,t), u_2(r,t), 1]^T \end{aligned}$$

where u_1 is the activation potential and u_2 is the resting potential.

The above model is the generalization of the existing models from at least two standpoints: a) by allowing the diffusivity matrix to be spatially dependent we can test for the presence of arbitrarily shaped anomalies, and b) by adding higher-order polynomial components we allow for wider range of dynamic behavior in the cardiac excitation. Note that in order to apply the above model to the realistic geometry we need to define boundary conditions. In our case we impose $\partial u_1 / \partial n$ on the epicardial surface of the heart. As for initial conditions, we define the active potential at time $t = 0$ as $u_1(r,0) = u_0 \delta(r - r_0)$ where $\delta()$ is a Dirac delta function and r_0 is the activation point in the myocardium. The initial condition for the inhibition (u_2) is set to zero.

To compute the electro-magnetic field on the torso surface we utilize the Geselowitz (Geselowtiz, 1970) equations that compute the potential $\phi(r,t)$ and magnetic field $B(r,t)$ at a location r on the torso surface at a time t from a given primary current distribution $J(r',t) = \nabla u_1(r,t)$ within the heart.We use a piecewise homogeneous torso model consisting of the following surfaces: the outer torso, the inner torso, and the heart. Therefore, we model the heart as a volume G of $M = 3$ homogeneous layers separated by closed surfaces $S_i, i = 1, \dots, M$. Let σ_i^- and σ_i^+ be the conductivities of the layers inside and outside S_i respectively. We will denote by G_i the regions of different conductivities, and by G_{M+1} the region outside the torso, which behaves as an insulator i.e, $\sigma_{M+1}^- = \sigma_M^+ = 0$.
It has been shown that in the case of a piecewise homogeneous torso model and using quasi-static assumption the magnetic field at a location r and time t is given by (Gulrajani, 1998) and (Malmivuo and Plonsey, 1995)

$$\begin{aligned} B(r,t) &= B_0(r,t) + \frac{\mu_0}{4\pi} \sum_{i=1}^{M} (\sigma_i^- - \sigma_i^+) \cdot \\ &\quad \cdot \int_{S_i} \phi(r',t) \frac{(r - r')}{\|r - r'\|^3} \times \mathrm{d}S(r') \\ B_0(r,t) &= \frac{\mu_0}{4\pi} \int_G \frac{J(r',t) \times (r - r')}{\|r - r'\|^3} \mathrm{d}^3 r', \quad (2) \end{aligned}$$

where μ_0 is the magnetic permeability of the vacuum. Similarly, the potential $\phi(r,t)$ is given by (Geselowitz)

$$\begin{aligned} \frac{\sigma_k^- + \sigma_k^+}{2} \phi(r,t) &= \phi_0(r)(\sigma_i^- - \sigma_i^+) + \\ &+ \frac{1}{4\pi} \sum_{i=1}^{M} (\sigma_i^- - \sigma_i^+) \int_{S_i} \phi(r',t) \frac{(r - r')}{\|r - r'\|^3} \cdot \mathrm{d}S(r'), \\ \phi_0(r,t) &= \frac{1}{4\pi} \int_G \frac{J(r',t) \cdot (r - r')}{\|r - r'\|^3} \mathrm{d}^3 r', \quad (3) \end{aligned}$$

where we k is chosen so that $r \in G_k$.

3 MEASUREMENT MODEL AND STATISTICAL MODEL

In this section we introduce our parametric description of the diffusion anomaly and measurement noise signals. To simplify the approach we assume that the anomaly region can be modeled with an ellipsoid i.e., the region $\mathcal{R}$ of anomaly is given by

$$\mathcal{R} = \{r : (r - r_a)^T F(a,b,c,\psi,\phi)^{-1} (r - r_a) \leq 1\}$$

where

$$F = T(\phi,\psi) \begin{bmatrix} a^2 & 0 & 0 \\ 0 & b^2 & 0 \\ 0 & 0 & c^2 \end{bmatrix} T^T(\phi,\psi)$$

where a, b, c are the axes of anomaly ellipsoid, r_a is the center, and ψ and ϕ are the orientation parameters (in 3D). The matrix $T(\phi,\psi)$ is the rotation matrix

given by

$$T(\phi,\psi)=\begin{bmatrix}\cos\phi & \sin\phi & 0\\ -\sin\phi & \cos\phi & 0\\ 0 & 0 & 1\end{bmatrix}\cdot\begin{bmatrix}\cos\psi & 0 & \sin\psi\\ 0 & 1 & 0\\ -\sin\psi & 0 & \cos\psi\end{bmatrix} \quad (4)$$

The diffusion tensor is then

$$D(r)=\begin{cases}0 & r\in\mathcal{R}\\ D & \text{otherwise.}\end{cases} \quad (5)$$

In the remainder of the myocardium tissue we assume homogeneous but possibly anisotropic diffusion tensor D.

Next, we assume that a bimodal array of n_{B} MCG and n_{E} ECG sensors is used for the measurements. Let $n=n_{\mathrm{B}}+n_{\mathrm{E}}$. We assume that the sensors are located at ρ_j, $j=1,\ldots,n$, and that time samples are taken at uniformly spaced time points $t_k, k=1,\ldots,n_{\mathrm{s}}$. In addition, we assume that data acquisition is repeated n_{c} times during several heart cycles in order to improve the signal-to-noise (SNR) ratio. Then, the n_{s}-dimensional measurement vector of this array obtained at time t_k in the lth cycle is

$$y_{lk}=f(\theta,t_k)+e_l(t_k), \quad (6)$$

where $y_{lk}=[y_{\mathrm{B}}^{\mathrm{T}}(t_k),y_{\mathrm{E}}^{\mathrm{T}}(t_k)]^{\mathrm{T}}$, θ is the collection of all the parameters $(a,b,c,r_0,\psi,\phi,u_0,D,A_1,A_2)$, $f(\theta,t_k)$ is the vector solution computed using finite elements, and $e_l(t_k)=[e_{\mathrm{B}}^{\mathrm{T}}(t_k),e_{\mathrm{E}}^{\mathrm{T}}(t_k)]^{\mathrm{T}}$ is additive noise. In the remainder of the paper we omit the subscript l whenever it is obvious that the samples belong to the same heart cycle. The subscripts B and E correspond to magnetic and electric components of the measurement vector (noise), respectively. We further assume that both magnetic and electric components of the noise are zero-mean Gaussian, uncorrelated in space and time with variances, σ_{B}^2 and σ_{E}^2, respectively.

4 PARAMETER ESTIMATION

We first start by splitting the unknown parameters θ into three groups: a) the unknown activation parameters $\theta_0=[u_0,r_a]^T$, and b) the unknown anomaly parameters $\theta_{\mathrm{a}}=[a,b,c,r_0,\phi,\psi]^T$. For simplicity in the remainder of the paper we assume that the heart parameters

$$\theta_{\mathrm{h}}=[\mathrm{vec}(D),\mathrm{vec}(A_1 1),\mathrm{vec}(A_2)]^T \quad (7)$$

where vec is the vector operator, are known. Note that some *in vitro* studies (Sachse, 2004) suggest that these parameters do not vary significantly between different subjects and thus can be easily estimated using data gathered from human subjects without any anomalies. Complicating the matter is the fact that the diffusion tensor in general is inhomogeneous. Namely, the ionic diffusion process is much larger along the myocardium fiber than across different fibers. Since the fiber orientations change in space the diffusion tensor should be spatially dependent. However, these changes are smooth in nature and can be easily modeled using a set of *a priori* known basis functions. Furthermore, information about fiber orientation can be easily obtained using cardiac diffusion MRI (et al., 2003).

To compute estimates $\hat{\theta}_0$ and $\hat{\theta}_a$ we use the generalized least squares (GLS) estimator which minimizes the following cost function (Vonesh and Chinchilli, 1997)

$$\begin{aligned}c(\theta_0,\theta_a,\hat{\sigma}_{\mathrm{E}}^2,\hat{\sigma}_{\mathrm{B}}^2) &= \sum_{k=1}^{n_{\mathrm{s}}}\sum_{l=1}^{q}\frac{1}{\hat{\sigma}_{\mathrm{E}}^2}\|y_{kl}^{\mathrm{E}}-f^{\mathrm{E}}(\theta_0,\theta_{\mathrm{a}},t_k)\|^2+\\ &\quad+\frac{1}{\hat{\sigma}_{\mathrm{B}}^2}\|y_{kl}^{\mathrm{B}}-f^{\mathrm{B}}(\theta_0,\theta_{\mathrm{a}},t_k)\|^2\\ \hat{\sigma}_{\mathrm{E}}^2 &= \frac{1}{n_{\mathrm{E}}n_{\mathrm{s}}q}\sum_{k=1}^{n_{\mathrm{s}}}\sum_{l=1}^{q}\|y_{kl}^{\mathrm{E}}-f^{\mathrm{E}}(\theta_0,\theta_{\mathrm{a}},t_k)\|^2\\ \hat{\sigma}_{\mathrm{B}}^2 &= \frac{1}{n_{\mathrm{B}}n_{\mathrm{s}}q}\sum_{k=1}^{n_{\mathrm{s}}}\sum_{l=1}^{q}\|y_{kl}^{\mathrm{B}}-f^{\mathrm{B}}(\theta_0,\theta_{\mathrm{a}},t_k)\|^2\end{aligned}$$

where we use superscripts E and B to denote electrical and magnetic, components of the measured field and solution vector.

The above GLS estimator is more efficient than the ordinary least squares estimator due to each contribution to the objective function is being normalized to the same unit variance (i.e., those measurements with less variation are given greater weight). The actual optimization can be done using any of the well known algorithms such as Davidson-Fletcher-Powell or Broyden-Fletcher-Goldfarb-Shanno. To further simplify the computational complexity, we propose to estimate θ_0 assuming that $a=b=c=0$ i.e. the diffusivity of the heart is homogeneous and using ordinary least squares. Then we can use this estimate as the initial guess for GLS estimation alghorithm.

5 NUMERICAL EXAMPLES

We now describe numerical study that demonstrates the applicability of the proposed algorithms. We used an anatomically correct mesh of the human torso that was kindly provided to us by Prof. McLeod, Utah University. In our model the Purkinje network was approximated by a set of nodes near the apex. To achieve higher precision we remeshed the original data into a new mesh (see Fig. 1). The volumetric

mesh was created using 15902 elements with 20830 degrees of freedom for the torso (electromagnetic) model and 1856 elements and 6190 degrees of freedom for the heart (diffusion) model. The computational model was developed using a general partial differential (PDE) toolbox in COMSOL software.
The torso conductivity was set to 5μS respectively as in (Malmivuo). To simplify the complexity of the numerical study we simulated the anomaly using $a = b = 2$cm , $c = 0.5$cm, and $\psi = \phi = 0$. The diffusion tensor was set to be isotropic with diagonal elements equal to 40cm^3/s. The diffusivity was chosen according to (Gulrajani) so that the activation wavefront propagates the whole heart in 0.2s. The control matrices A_1 and A_2 were chosen following the approach of (Rogers and Culloch). The heart rate was set to 72 beats per minute. We assume that the measurements are obtained using 64-channel ECG/MCG sensor array with sensors locations uniformly distributed on the chest. To evaluate the localization accuracy we use $\text{MSE}_{r_0} = \|r_0 - \hat{r_0}\|^2/\|r_0\|^2$, $\text{MSE}_a = \|a - \hat{a}\|^2/\|a\|^2$, and $\text{MSE}_c = \|c - \hat{c}\|^2/\|c\|^2$.

Figure 2 illustrates the activation wavefront in myocardium at approximately $t = 2T/3$ after the activation where T is the time length of the heart cycle. In Figure 3 we illustrate the body surface map of the electric field (voltage) on the torso surface. Similarly, Figure 4 illustrates the magnetic field map at the same time. In Figure 5 we illustrate the mean square error of the axis parameters with $c = a/10$ and $b = a$. The location of an anomaly was arbitrarily set to $r_0 = (0, 0.5, 0.75)$. As expected, due to the wavefront orientation as well as difference in size, the estimation accuracy of the cross-sectional axis parameters is much smaller. In Figure 6 we illustrate the localization accuracy i.e., MSE of r_0 as a function of noise. The SNR was defined as $SNR = 10\log(\sum \|y_{lk}\|^2/\sigma_{\text{E}}^2 + \sigma_{\text{B}}^2)$.

6 CONCLUSIONS

We addressed the problem of localizing the diffusivity disorder in the myocardium using ECG/MCG sensor arrays. To model the cardiac activation we considered an inhomogeneous reaction-diffusion model in a real human torso. To model a the loss we used a parametric model for an oblate spheroid and set its conductivity to zero. We assumed that the remainder of the myocardium tissue was homogeneous. The proposed algorithm can be easily extended to account for an arbitrary spatial variation in the diffusivity tensor using a set of *a priori* known basis functions. In addition the parametric shape of the anomaly can be extended to model an arbitrary region using a three-dimensional spatial Fourier transform. An effort should be made to examine the sensitivity of the proposed algorithms to the size of diffusivity difference between "regular" tissue and anomaly as well as the number of the unknown parameters needed to model arbitrary shapes.

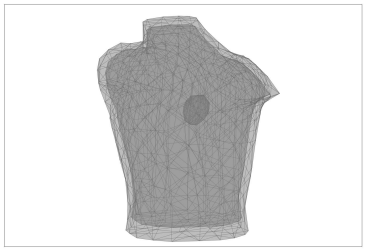

Figure 1: Mesh geometry used for numerical study.

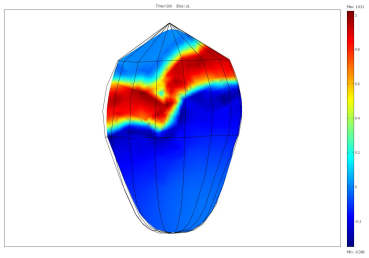

Figure 2: Activation wavefront, at $t = 2T/3$.

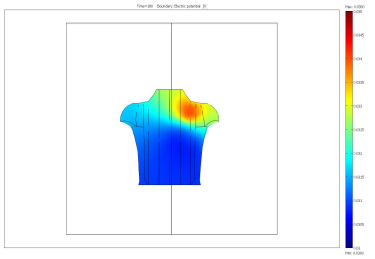

Figure 3: Body surface map of electric field at $t = 2T/3$.

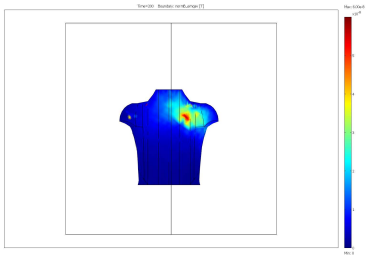

Figure 4: Body surface map of magnetic field at $t = 2T/3$.

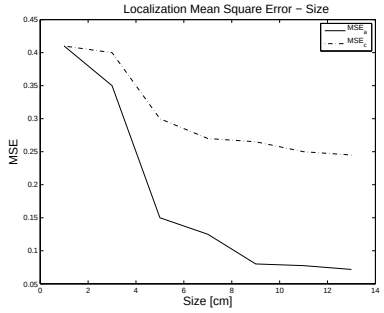

Figure 5: Mean square error for estimating the size of the anomaly.

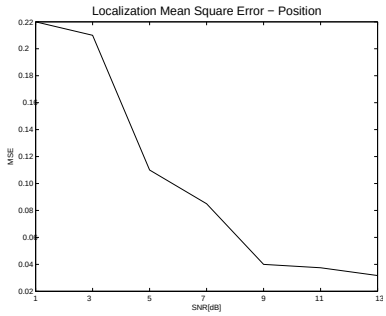

Figure 6: Mean square error for estimating the location of the anomaly.

REFERENCES

et al., L. Z. (2003). Heart-muscle fiber reconstruction from diffusion tensor mri. In *Proc. 14th IEEE Visualization Conference*. IEEE.

FitzHugh, R. A. (1961). Impulses and physiological states in theoretical models of nerve membrane. *Biophys. J.*

Geselowtiz, D. (1970). On the magnetic field generated outside an inhomogeneous volume conductor by internal current sources. *IEEE Trans. Magn.*, 6:346–347.

Gulrajani, R. M. (1998). *Bioelectricity and Biomagnetism*. John Wiley & Sons, New York.

Malmivuo, J. and Plonsey, R. (1995). *Bioelectromagnetism*. Oxford University Press, New York.

Panfilov, A. and Holden, A. V. (1997). *Computational Biology of the Heart*. John Wiley & Sons, Chichester, 1st edition.

Rogers, J. M. and McCulloch, A. D. (1994). A collocation-galerkin finite element model of cardiac action potential propagation. *IEEE Transactions on Biomedical Engineering*, 41:743–757.

Sachse, F. B. (2004). *Computational Cardiology*. Springer, Berlin.

Vonesh, F. and Chinchilli, V. M. (1997). *Linear and Nonlinear Models for the Analysis of Repeated Measurements*. Marcel Dekker, New York.

A BIO-INSPIRED CONTRAST ADAPTATION MODEL AND ITS APPLICATION FOR AUTOMATIC LANE MARKS DETECTION

Valiantsin Hardzeyeu and Frank Klefenz
Fraunhofer Institute for Digital Media Technology, Langewiesener str. 22, 98693, Ilmenau, Germany
{hrd, klz}@idmt.fraunhofer.de

Keywords: Retina, contrast adaptation, visual perception, fuzzy-like sets, lane marks detection.

Abstract: Even in significant light intensity fluctuations human beings still can sharply perceive the surrounding world under various light conditions: from starlight to sunlight. This process starts in the retina, a tiny tissue of a quarter of a millimeter thick. Based on retinal processing principles, a bio-inspired computational model for online contrast adaptation is presented. The proposed method is developed with the help of the fuzzy theory and corresponds to the models of the retinal layers, their interconnections and intercommunications, which have been described by neurobiologists. The retinal model has been coupled in the successive stage with the Hough transformation in order to create a robust lane marks detection system. The performance of the system has been evaluated with the number of test sets and showed good results.

1 INTRODUCTION

Human beings get a significant part of information through the visual perception system which consists of the retina, the visual nerve and the visual cortex in the midbrain. The retina in this sequence plays the role of a pre-processor and reduces the information delivered to the visual cortex. In this paper we like to point out how the retina adapts the intensity fluctuations that appear in the real-life situations and describe a method for the contrast adaptation with the help of the fuzzy–like sets.

According to the work that is presented in (Hubel, 1995) and (Masland, 2001), the retina is a part of the brain, which has been separated from it during the early stages of development, but having kept the connections to the brain through the optic nerve. Five different types of cells form the retina: photoreceptors, horizontal cells, bipolar cells, amacrine cells and ganglion cells. They all are organized in a layered structure and the visual data flows from the upper layer (photoreceptors) to the lower layer (ganglion cells) in a parallel manner. Their interconnections are well described in (Hubel, 1995). Among the other important functions of the retina, like edge extraction and motion detection (Olveczky et al., 2003), the real-time implementation of the contrast adaptation seems to be important for almost all image processing and robotic projects.

As described in (Smirnakis et al., 1997), the contrast adaptation process begins in the lower layers of the retina (amacrine and ganglion cells) and allows the retinal neurons to use their dynamic range more efficiently. The recovery time of the visual system after changing the ambient intensity is several seconds (Baccus and Meister, 2002) and in the (Solomon et al., 2004) were reported that when the mean intensity increase, the retina becomes less sensitive. These biological principles for the contrast adaptation were taken as a basis for the development.

As it pointed out in (Wilson, 1993), the contrast adaptation process which takes place in the retina can be described with help of differential equations. As an alternative, we found a method to describe this non-linear process with fuzzy-like sets and coupled the system with the Hough transform for lane marks detection.

2 RETINA MODEL FOR CONTRAST ADAPTATION

Five different layers (three vertical and two horizontal) build up the retina. Vertical layers are presented by photoreceptors (rods and cones), bipolar and ganglion cells and form the *direct pathway* of the visual data flow. Horizontal layers of the retina are presented by the horizontal and

amacrine cells and, together with the vertical layers form the *indirect pathway*. Both paths are needed for the sufficient visual information pre-processing and for forming the signals to the inner brain.

2.1 Two Layers, Three Processing Tasks

The cells in the inner retina are organized in a parallel manner and build together a highly distributed structure. In fig. 1 the digital representation of all five retinal cells and their interconnections is shown.

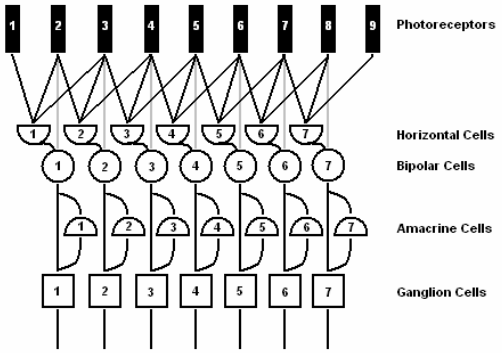

Figure 1: Digital representation of the retinal layers.

All retinal cells can be divided into two processing layers by their functionality. The first layer is presented by the photoreceptors, horizontal and bipolar cells, and performs the edge extraction (Hubel, 1995), (Olveczky et al., 2003), while the second layer, which is formed by the amacrine and ganglion cells, performs among other tasks the local motion detection and the direction of movement estimation (Masland, 2001), (Berry II et al., 1999). Since the contrast adaptation also begins in the lower retinal layers (amacrine and ganglion cells), it is important to understand the responses from the higher processing layers (photoreceptors – bipolars).

2.2 Modelling of the Bipolar Cells Response

The processing on the first layers starts from photoreceptors that sense the incoming light. Some of the photoreceptors are activated by the presence of light while others are activated when they do not detect light. All of them are arranged in a circular way so that one type is surrounded by other types (center–surround organization). In this paper we use the '*on–center*' surrounding organization scheme (Hubel, 1995).

On the next level, the horizontal cells get their input from the photoreceptors. They play a very important role in reducing the amount of information that is given to the inner brain and represent an additional mechanism which helps to adjust the retina response to the overall level of illumination. Their task is to measure the illumination across a broad region of photoreceptors and pass the average value further to the next level. Such calculation can be represented by Equation 1, where P_k is the output of each photoreceptor that is connected to a horizontal cell H_i ; n is the number of inputs of a certain horizontal cell.

$$H_i = \frac{\sum_{k=1}^{n} p_k}{n} \quad (1)$$

On the third level, the bipolar cells get their inputs from the center photoreceptors directly and from the surrounding photoreceptors indirectly through the horizontal cells. These two inputs build the *receptive field* of each bipolar cell.

The function of the bipolar cell involves a subtraction mechanism: it subtracts the value of the horizontal cell H from the value which is received from the center photoreceptors. Thus, the output of each bipolar cell B_i can be represented by the Equation 2, where B_{i1} is the input from the photoreceptors and the B_{i2} – is the input from the horizontal cell H_i.

$$B_i = B_{i1} - B_{i2} \quad (2)$$

The output of each bipolar cell forms the response from the whole receptive field and in this stage retina performs the edge extraction function (Olveczky et al., 2003). As it is known from the classical theory for image processing (Shapiro, 2001), the edge detection operators highlight the boundaries between regions of different intensities. This is, naturally, how human beings perceive the perimeter of an object, when it differs by its intensity from the background. In fig. 2 the stimuli with a step-change border and a simplified model of the first stages of the retina are presented. Here we assume that each photoreceptor corresponds to a single pixel in the image and each bipolar cell B is driven by the receptive field which is constructed by three photoreceptors – one for the center response and two for the surrounding. The receptive fields of the different bipolar cells overlap each other (Hubel, 1995) and, thus, each photoreceptor is fed not only to the single bipolar cell, but to a number of bipolar cells.

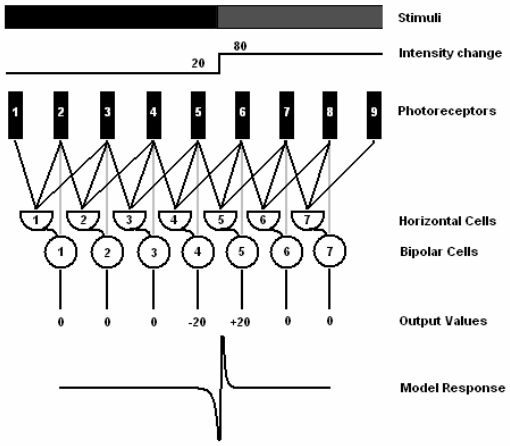

Figure 2: The model and its edge response.

In this example the stimuli change their intensities between the receptors 5 and 6 from 20 to 80. The model's response on the step-change border can be presented by the activities of the two peaks (negative and positive) exactly at the border between the two regions. The absolute values of the peaks are equal, but differ by the sign. Such bio-inspired edge extraction technique called *zero-crossing* has been confirmed by Marr (Marr, 1982) while investigating the neurobiological background of vision. Fig. 3 shows the response of the bipolar cells at vertical edges.

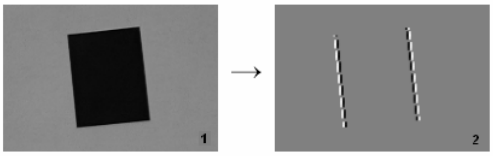

Figure 3: The stimuli and the bipolar cell's response at vertical edges.

The bipolar cells are fed to the amacrine and ganglion cells, but first the signal from the bipolar cell reaches the Contrast Adaptive Neuron.

2.3 Contrast Adaptive Neuron and its Function

According to (Smirnakis et al., 1997), when the mean intensity of ambient light increases, the retina becomes less sensitive. This process is organized with the help of the contrast adaptive neuron (*CAN*), which is located just after the bipolar cells and serves to adjust the input activity of the ganglion cells in order to use their dynamic range more efficiently. In fig. 4 the simplified model of the receptive field for a single 'on–center' ganglion cell with a *CAN* is presented.

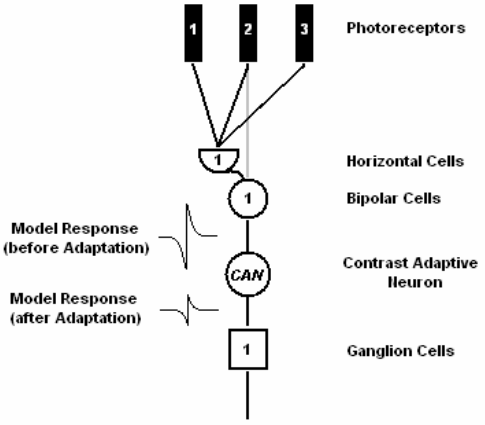

Figure 4: The model of the ganglion cells receptive field with *CAN*.

For fig. 4 we assume that the response generated by the bipolar cell lies above the ganglion cells dynamic range and the *CAN* brings the bipolar cell response back to the dynamic range of the ganglion cell by changing its amplitude value. However, the retina adapts the high and low intensities differently.

When the contrast changes from low to high (positive contrast change, e.g., going from normal light room conditions to the strong sun light at midday), in the first tens of a second the retina decreases the sensitivity of *CAN* dramatically, that results in a quick decrease of the ganglion cell's activity. Such first step of the adaptation process is called "*Fast adaptation*" and helps to bring the ganglion cell input nearly to its normal input range. After that the second "*Slow adaptation*" phase occurs and lasts for about ten-fifteen seconds. Its main task is to fine tune the input of the ganglion cell and bring it completely to the middle point of the ganglion cell's dynamic range.

In case, when the contrast changes from high to low (negative contrast change, e.g., going from sun light to the room with normal light conditions), the retina reacts differently. There is no fast adaptation process, but the retina increases step-by-step the sensitivity of the ganglion cells by scaling up their inputs (with help of *CAN*). It takes up to twenty-twenty five seconds till the inputs of the ganglion cells are in their dynamic range.

These two statements were confirmed by Solomon et al (Solomon et al., 2004) while observing the reaction of the isolated retina of a tiger salamander during contrast changes. Fig. 5 shows the adaptation process for negative and positive contrast changes.

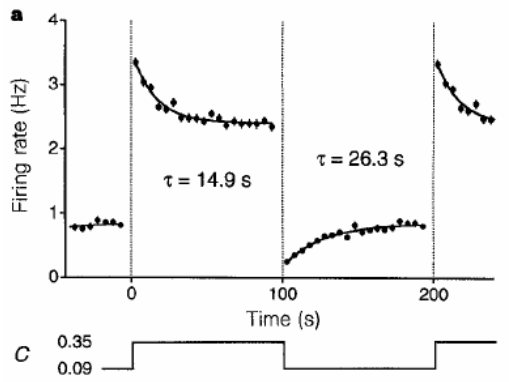

Figure 5: Contrast adaptation in salamander's retina from (Solomon et al., 2004).

In fig. 5 *C* depicts the contrast change values while the graphical representation shows the adaptation in the Salamanders retina on different contrast changes.

We investigated which functions might approximate the curves for "negative" and "positive" adaptation and found out that for the approximation of the "positive" contrast adaptation process (fig. 6a, upper image) a simple *rational function* (fig. 6b, upper image) can be used. "Negative" contrast adaptation curve (fig. 6a, lower image) can be approximated by the s*quare root* function, which is shown in fig. 6b (lower image).

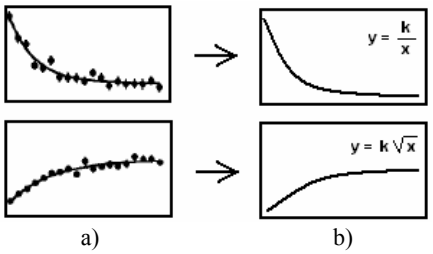

Figure 6: a) Natural adaptation curves (from (Solomon et al., 2004)) and b) their approximation functions.

Here, in both functions the coefficient *k* is a scaling factor, which is responsible for the *CAN's* selectivity. It controls how strong the adaptation should be in order to make the ganglion cells more or less sensitive, depending on the current light intensity situation. For instance, when the light intensity is high (e.g., in sunny midday) than the *CAN* should scale the intensity down by setting a rather large *k*; however, when the light intensity is just a bit above the dynamic range, the *CAN* should fine tune the contrast by setting a quite small value for the scaling coefficient. In this work we use the fuzzy-like sets for the definition of *CAN's* selectivity coefficient *k.*

3 USING FUZZY-LIKE SETS FOR CONTRAST ADAPTATION

In recent decades a number of applications were found for fuzzy logic in economics, mathematics and engineering. Firstly introduced in (Zadeh, 1965), it is very helpful for modelling highly nonlinear processes like natural contrast adaptation

3.1 Definition of a Fuzzy – like Set for Normal Contrast

For the graphical representation of the model's response we should declare, what the Normal contrast means and create a corresponding fuzzy – like set for its definition.

Since we are working with bio-inspired edge extraction based on zero-crossings, we assume here that the absolute zero, as it shown on the characteristic curve in fig. 2 will be equal to the intensity 128, which represents the middle point of the intensity spectrum. When model analyzes the border between object and background, on the graphical representation the response will drop down and then raise up by a certain value (e.g., dark and light vertical lines in fig. 3, image 2).

Then we analyzed which intensity differences can represent the Normal Contrast value (see fig.7).

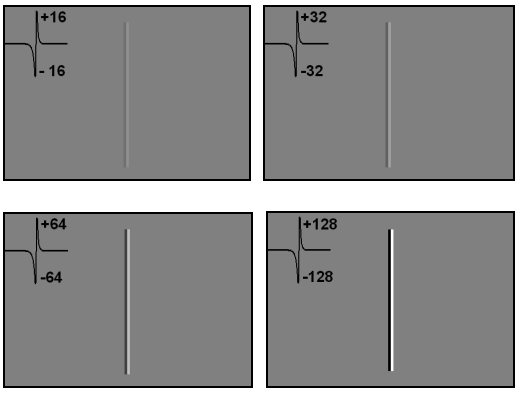

Figure 7: Biological edges with 16, 32, 64 and 128 intensity difference levels.

Fig. 7 shows four biological edges with intensities 16, 32, 64 and 128. The edges with the intensity differences of 16 and 32 do not have enough contrast and should be adapted. The edges with intensity difference of 64 and 128 do have enough contrast and thus there is no need for adaptation. However, in the real world situation the biological intensity difference of 128 is hardly possible, because it causes an intensity change of 255 levels at the object-background border (e.g.,

changing from black to white). Normally the contrast numbers, which can be detected in real images, lie in the range from 120 to 200, which caused the biological edge of [± 60 – ±100] to appear. That is why we do not have to adapt the high intensity values (e.g., from 180 to 255), we should only define such a process, which will adapt the edge values from the lower part of the intensity difference spectrum and bring them in to the middle region. Thus, only the "negative" contrast adaptation process should be used (fig. 6, lower images).

Following this, we introduce a Normal Contrast fuzzy variable which should adapt all the values that lie under the intensity 60. It is presented in fig. 8.

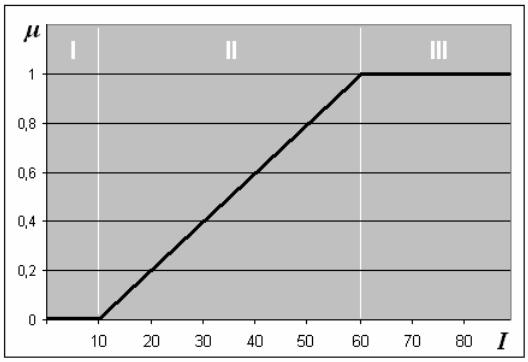

Figure 8: Fuzzy variable for Normal Contrast.

On this image, the X-axis represents the intensity change ***I*** on the biological edge and Y-axis shows the membership ***μ*** of a certain intensity value in the Normal Contrast variable.

There are three characteristic adaptation regions presented on this graphic. Since the fuzzy logic operates with linguistic variables, table 1 shows such a linguistic description and action which is needed for a certain region.

Table 1: Linguistic definition of the model.

Region	Intensity	Action needed
I	Low Intensity	Strong adaptation
II	Low–to–Normal Intensity	Adaptation based on the ***μ*** membership coefficient in order to control adaptation strength
III	Normal Intensity	No adaptation needed

When the bipolar cells deliver low intensities (values from 1 to 10), strong adaptation is needed; in the mid-range (values from 11 and 60), adaptation is also needed, but the system should control the strength of the adaptation by using the membership coefficient ***μ***; and when the intensity is normal (values above 61), then no adaptation is needed.

In order to create the system we should define the set of rules for each of the regions mathematically. Since we are using the "negative" adaptation process, a curve that will represent this process should have the shape of the s*quare root* function. Table 2 shows the mathematical representation for each action regions.

Table 2: Mathematical representation of the model.

Region	Intensity values	Representation
I	1 – 10	$K = 2 \cdot \sqrt{x}$ $I_{new} = I_i \cdot K$
II	11 – 60	$\mu = (2 \cdot I_i + 20) / 100$ $K = (2 - \mu) \cdot \sqrt{x}$ $I_{new} = I_i \cdot K$
III	61 – 127	$I_{new} = I_i$

The adaptation process in nature lasted for several seconds. Here this process is modelled with iteration mechanism and x represents current iteration; K is an adaptation coefficient and should be calculated differently for regions I, II and III. It represents the *CAN* selectivity and controls the input gain to the ganglion cells. I_i represents the input intensity of *CAN* and I_{new} is a new calculated value of the adapted intensity; μ is a membership coefficient, which influences the amplification factor and is calculated according to the equation of the characteristic line in region II (see fig. 8).

3.2 Adaptation Algorithm

The algorithm for the contrast adaptation involves all the definition for the variables that have been set early, like I_i, I_{low}, I_{normal}, I_{new}, μ, K and x which is initially set to 0. Firstly, based on the current intensity I_i, μ is calculated.

```
if (I_i>1&&I_i<=I_low){μ = 0}
if (I_i>I_low&&I_i<=I_normal){
     μ = (2·I_i+20)/100}
if (I_i>I_normal){μ = 1}
```

Then the adaptation coefficient K and the adapted intensity I_{new} based on the equations in table 2 is calculated.

```
if (μ<1){
    while (I_new<=I_normal){
          K = (2 - μ) · √x
          I_new = I_i · K
          x = x + 1;
     }
 }
```

```
else {Inew=Ii}
```

The process stops, when the calculated intensity I_{new} reaches the normal intensity I_{normal} that has been set to 60 empirically.

3.3 Adaptation Results

During the investigation and development the model has been tested on different types of images. Experiments were divided into three categories by the specific adaptation process:

- adaptation of the low contrast;
- adaptation of the low-to-normal contrast;
- adaptation of the real world images;

The first two categories were tested with synthetic images. Synthetic images were chosen because the results of the processing can be predicted in order to make the model's proof of concept under different conditions. To demonstrate it a number of images with different intensity changes were chosen. Fig. 9 represents two of them.

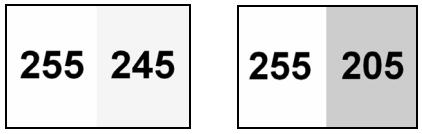

a) b)

Figure 9: Experimental data.

Fig. 9a shows the intensity change of 10 levels (from 255 to 245) and figure 9b corresponds to a change of 50 levels (from 255 to 205) of the intensity spectrum. The digits on the images represent just the absolute intensities and will not appear in the modelling results.

Fig. 10 shows the calculated bipolar cells activity for fig. 9a and 9b correspondently.

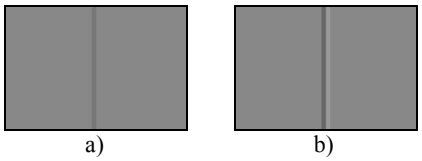

a) b)

Figure 10: Calculated bipolar cell's responses to the experimental data in fig. 9.

For the first experiment we took fig. 10a. The initial data (fig. 9a) shows minor intensity change at the object-background border, which causes a low contrast and hardly distinguished border response (fig. 10a). The initial intensity change I_i equals 3 (see equations 1 and 2), which corresponds to the low intensity region in fig. 8. Initial data: $I_i = 3$; $\mu = 0$, $=> K = 2 \cdot \sqrt{x}$.

For the adaptation of such a low intensity 104 iterations are needed. Table 3 shows some of them.

Table 3: First experiment data.

x	*K*	I_{new}	*Graphical representation*
1	*2*	*6*	
2	*2.82*	*8*	
3	*3.46*	*10*	
4	*4*	*12*	
	...		
101	*20.09*	*60*	
102	*20.19*	*60*	
103	*20.30*	*60*	
104	*20.40*	*61*	

The second experiment has been performed with fig. 10b. The initial intensity change here I_i is 16, which corresponds to the low-to-normal intensity region in fig. 8. Adaptation is still needed, but the strength of the adaptation should be controlled. Initial data: $I_i = 16$; $\mu = 0.12$, $=> K = (2 - \mu) \cdot \sqrt{x}$.

According to the algorithm, the adaptation of such intensity will be done in 5 iteration steps. Table 4 represents this process.

Table 4: Third experiment data.

x	*K*	I_{new}	*Graphical representation*
1	*1.88*	*30*	*x = 5, I_{new} = 67:*
2	*2.65*	*42*	
3	*3.25*	*52*	
4	*3.76*	*60*	
5	*4.20*	*67*	

As it can be seen on the results presented above, the contrast adaptation model shows the expected responses on the different stimuli with different adaptation time. The intensity change adaptation correlates with its natural representation (fig. 6, lower image). To confirm this, fig. 11 shows the adaptation curves for each experiment.

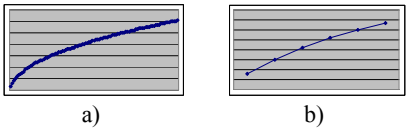

a) b)

Figure 11: Adaptation curves for all experiments.

3.4 Adaptation of the Real World Images

The model has been already tested on the synthetic images; the next step is to see how it will respond on the real world images. For this purpose we choose a number of images with the real road scenes that have been taken on a german highway. Some of these test images are shown in Fig. 12.

Figure 12: Real road scenes.

Then we processed the images first with the classical biological edge operator *without* the contrast adaptation mechanism. On the 2nd phase the same images have been processed with the bio-inspired edge operator and *with* the contrast adaptation module. Fig. 13 shows the results.

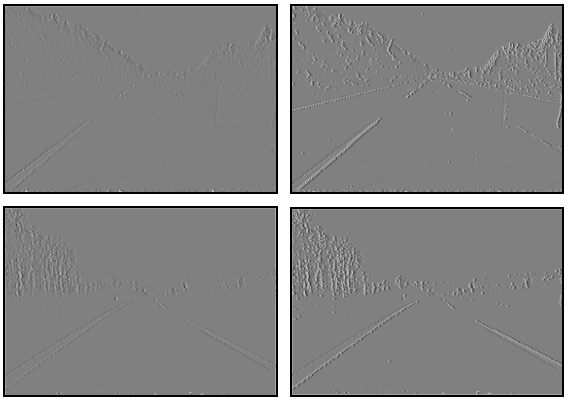

Figure 13: Calculated biological edge without (left) and with (right) contrast adaptation for fig. 12.

The difference between the adapted and the not adapted images can be clearly seen. The edges, that are even not fully visible on the left images, are well seen on the right ones. Besides, the initial images (fig. 12) were taken under slightly different illumination conditions: the first image was taken under bright sun light while the second one at early evening. Nevertheless, the adapted images show good results especially in underlining the lane road marks. This gives the possibility to use this contrast adaptation model for robust lane detection.

4 LANE DETECTION APPLICATION

Lane keeping assistant systems have been described in a number of recent publications, e.g. (Risack et al., 2000), (Chang et al., 2003). For such systems detection of the lane marks is a key feature for further processing. The lane marks form lines with certain slopes and thus, for its detection a good shape extraction method is needed.

The Hough transformation (Leavers, 1992) is a pattern recognition technique which is known for its performance in locating given shapes in images. Some researches have reported that the Hough transform correlates with the processes that happen in the striate cortex and in fact, reproduces the natural mechanism of objects contour extraction (Hubel, 1995), (Blasdel, 1992), (Ballard et al., 1983), (Brueckmann et al., 2004).

Very interesting state-of-the-art research work is presented in (Serre, 2007). The authors describe the usage of the midbrain biological mechanisms for the real world scene segmentation and objects recognition. Furthermore, they also use the Hough transformation as a shape localization method.

That is why we propose to use the Hough transform as a lane marks detection method together with the retina model with contrast adaptation as a preprocessing method. This gives the possibility to create a fully bio-inspired system for the lane mark detection. The architecture of such a system is shown in fig. 14.

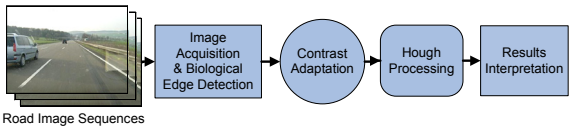

Figure 14: Architecture of the bio-inspired lane detection system.

The biological edge detection and contrast adaptation stages were well described above. In fig. 14, after contrast adaptation the Hough transformation takes place. Hough transformation involves a voting scheme for the shape detection. In particular, here we extract the lines of the different slopes. Fig. 15 represents the Hough spaces built from road edge picture (fig. 13, two right images) and then the maximas are marked.

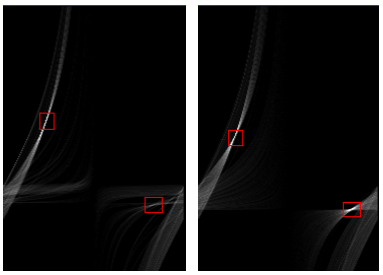

Figure 15: Hough spaces with local maximas.

After the maxima were detected, the interpretation of the results should be performed. Each maximum on the Hough space corresponds to the line with a certain slope in a Cartesian space and after processing the detected lane marks will be highlighted. Fig. 16 shows the final results.

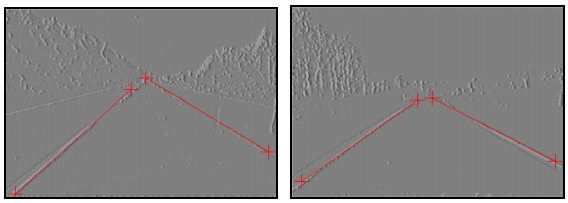

Figure 16: Detected lane marks in the adapted images.

5 CONCLUSIONS AND FUTURE WORK

In this paper a bio-inspired model for contrast adaptation has been presented. The model has been tested with different test sets and showed good results. Furthermore, the proposed contrast adaptation algorithm has been coupled with the Hough-based lane marks detector. This coupling showed good performance and full correspondence to the predicted behaviour.

Future work will concentrate on development of the lane keeping assistant system using the bio-inspired techniques further. In particular, for the preprocessing stage the colour perception model will be investigated, implemented and will be used for the road scenes segmentation and traffic signs detection.

Besides, for the post-processing and trajectory prediction stages time-to-lane crossing approach will be taken in to the account. It is likely possible that it might be modelled with the natural timing delay-computational maps. This problem will be also investigated and the results will be reported.

REFERENCES

David H. Hubel, Eye, Brain and Vision, Freeman, 1995.

Linda G. Shapiro, George C. Stockman, Computer Vision, Prentice-Hall , 2001.

Bence P. Ölveczky, Stephen A. Baccus & Markus Meister, “Segregation of the object and background motion in the retina,” Nature, Vol. 423, May 2003, pp. 401 – 408.

Richard H. Masland, “The fundamental plan of the Retina,” Nature Neuroscience, Vol.4 No. 9, September 2001, pp. 877 – 886.

Michael J. Berry II, Iman H. Brivanlou, Thomas A. Jordan & Markus Meister, “Anticipation of moving stimuli by the retina,“ Nature, Vol. 398,March 1999, pp. 334–338.

Hugh R. Wilson, “Nonlinear processes in the visual discrimination”, Proc. Natl. Acad. Sci. USA, Vol. 90, 1993, pp. 9785 – 9790.

Stelios M. Smirnakis, Michael J. Berry, David K. Warland, William Blalek & Markus Meister, “Adaptation of retinal processing to image contrast and spatial scale,” Nature, Vol. 386,March 1997,pp. 69–73

Stephan A. Baccus & Markus Meister, “Retina Versus Cortex: Contrast Adaptation in Parallel Visual Pathways”, Neuron, 2003, pp. 5 – 7.

Stephan A. Baccus & Markus Meister, “Fast and Slow Contrast Adaptation in Retinal Circuitry,” Neuron, Vol. 36, 2002, pp. 909 – 919.

Samuel Solomon, Jonathan Peirce, Neel Dhruv, Peter Lennie, “Profound Contrast Adaptation Early in the Visual Pathway”, Neuron, vol. 42, 2004, pp. 155–162

Zadeh L.A., “Fuzzy Sets”, Information and Control, 1965, vol. 8, pp. 338 - 353.

Marr D., Vision, Freeman, pp. 54 – 78. 1982.

Risack, R.; Mohler, N.; Enkelmann, W., A video-based lane keeping assistant, Intelligent Vehicles Symposium, 2000. Proceedings of the IEEE, pp. 356 – 361, 2000.

Tang-Hsien Chang; Chun-Hung Lin; Chih-Sheng Hsu; Yao-Jan Wu. A vision-based vehicle behavior monitoring and warning system Proceedings IEEE, Volume 1, pp. 448 – 453, 2003.

Leavers, V.F., Shape detection in Computer Vision using Hough Transform. Springer – Verlag, p.201, 1992.

Gary G. Blasdel, “Orientation Selectivity, Preference, and Continuity in Monkey Striate Cortex”, The Journal of Neuroscience, Aug. 1992, 12 (8): 3139 – 3161.

Ballard D., Hinton J., Sejnowski T., Parallel visual computation. Nature 306, pp. 21 – 26, 1983.

T. Serre, L. Wolf, S. Bileschi, M. Riesenhuber, and T. Poggio, “Robust Object Recognition with Cortex-like Mechanisms”, IEEE Trans. on Pattern Analysis and Machine Intelligence, vol. 29, no. 3, March 2007.

Brueckmann, A., Klefenz F., Wuensche, A. A neural Net for 2-D Slope and Sinusoidal Shape Detection. International Scientific Journal of Computing. Vol. 3 (1), pp. 21 – 26, 2004.

CREST LINES AND CORRELATION FILTER BASED LOCATION OF THE MACULA IN DIGITAL RETINAL IMAGES

C. Mariño, M. G. Penedo, S. Pena
VARPA Group, Faculty of Informatics, University of A Coruña, A Coruña, Spain
{*castormp,mgpenedo*}*@udc.es,infspp00@ucv.udc.es*

F. González
School of Medicine and Complejo Hospitalario Universitario of Santiago, University of Santiago de Compostela, Santiago de Compostela, Spain
francisco.gonzalez@usc.es

Keywords: Creases, correlation filter, macula, optic disk, deformable model.

Abstract: The fovea is a spot located in the center of the macula, and responsible for sharp central vision. In this paper a method to detect the macula location and size is presented, as a first step towards the fovea location.In the first stage of the process, the retinal vessel tree is extracted through a crest line detector. Then, the main vessel arc is fitted to a parabolic curve using a polynomial fitting process, which will allow for the computation of the area where the optic disc is located. The last stage consists in the segmentation of the optic disc, by means of the combination of morphological operations and a deformable model. Then, following the morphological properties of the eye, the macula location and size is determined by means of a new correlation filter. Search with this filter is performed in a reduced area of interest, whose size and position is determined by means, again, of the morphological properties of the eye. The algorithm has proven to be fast and accurate in the set of test images, composed of 135 digital retinal images.

1 INTRODUCTION

The retinal fundus photographs are widely used in the diagnosis of eye diseases. Processing automatically a large number of retinal images can help ophthalmologists to increase the efficiency in medical environments were big numbers of patients must be treated. The optic disk is the brightest area in images that do not have large areas of exudates and it is a slightly oval disk. It is the entrance region of vessels and its detection is very important since it works as a landmark for the other features in the retinal image. The macula is a commonly visible as a hazy dark area. This is the area with the highest number of cones and rods per unit area.

There are many previous works on optic disk localization. Goldbaum et al. (Goldbaum et al., 1996) extract the main features of the eye fundus (optic disk, vessels, blobs and fovea), through the combination of several templates, which work separately on the image color channels. Pinz et al. (Pinz et al., 1998) also obtain a map of the human retina using retinal angiographies, obtaining very good results. Lalonde et al. (Lalonde et al., 2001) extract the optic disk using Hausdorff based template matching and pyramidal decomposition. It is neither sufficiently sensitive nor specific enough for clinical application. On the other hand, strategies based on active contours (Mendels et al., 1999; Lowell et al., 2004; Chanwimluang and Fan, 2004) are used to detect the optic disk boundary in retinal images. These techniques are very robust against noise but their main disadvantage is their high computational cost.

A method for detecting the macular center was presented by Sinthanayothin (Sinthanayothin et al., 1999). In this approach a template based algorithm was used, combined with the morphological properties of the eye. The system showed an accuracy of 80.4% on 100 images. Li et al. (Li and Chutatape, 2004) presented a model based approach in which an snake was used to extract the vascular tree based on the location of the optic disk. Then, the information from the snake was used to find the macula center. The authors reported a 100% accuracy for optic disk localization and 100% for macula localization in 89 digital retinal images.

This paper presents an algorithm for the automatic localization and segmentation of the optic nerve head,

macula and fovea working on digital retinal fundus images. The optic nerve head is located and its shape is extracted without user intervention. Localization is achieved by means of a two stage process. In the first stage, creases are extracted and filtered, so that only the crest lines corresponding to the main vessel arc are not removed. Then a polynomial curve is fitted to the points in the crest lines, which will determine an area of interest where the optic disk will be located. In the second stage the shape of the optic disk is determined through the combination of two techniques: morphological operators and a deformable model. The final result is the optic disk shape and position. Once the optic disk position has been determined, macula and fovea are located using the morphological properties of the eye, which allow for the optimization of the search procedure, performed by means of a multi-scale correlation filter searching over a small area.

The setup of the paper is as follows. Section 2 provides details on the algorithm for the optic disk localization and segmentation. Section 3 describes the macula segmentation process. Experiments and results are given in section 4 for both the optic disk and macula localization and segmentation, and finally section 5 provides discussion and conclusions.

2 OPTIC DISK SEGMENTATION

The first stage of the process consists of locating the region where the optic disk is situated. This is performed by tracking the main crest lines, which converge in the optic disk. Then an accurate segmentation of the optic disk is obtained by means of a deformable model. This information, combined with the morphological properties of the eye, will be very useful in the process of locating and segmenting the macula.

2.1 Optic Disk Location

Analyzing the morphology of the retinal vessel tree (Figure 1), it is clear that the root of this tree is the optic disk, so by tracking the main vessels it is possible to arrive to the optic disk position. Following this approximation, an algorithm has been designed to obtain that position without the need of segmenting the whole retinal vessel tree.

Since the segmentation of the retinal vessel tree would be a costly process, only the crest lines of the main vessel arc are used in the detection of the optic disk position. To compute the crest lines, a geometric approach was used, the Multi-local Level Set

Figure 1: Digital retinal image acquisition. Note the convergence of the main vessels in the optic disk, fact which will be used in the detection of the optic disk position.

Extrinsic Curvature with the Structure Tensor filtering process (MLSEC-ST) (A. Lpez and Villanueva, 2000; Mariño et al., 2006). Using this method only the highest creases are preserved, and the main vessel arc creases are obtained, as shown in Figure 2.

However, in some of the images the crest lines obtained do not reach the optic disk due to the high filter levels applied, and it is necessary an interpolation method to compute the position of the optic disk (Figure 2, bottom). Analyzing the shape of the vessel arc, a parabolic fitting to the points in the creases seems to be the best approximation. But, from the results obtained, the two degree polynomial fitting showed to be inaccurate and a third level polynomial fitting was tried with satisfactory results. To obtain this curve, a least square fitting process was performed with the classic equation 1 and minimizing the expression in equation 2. In Figure 3 two examples of the result from the fitting process are depicted, with blue lines representing the curves interpolated from the crest lines.

$$y = ax^3 + bx^2 + cx + d \quad (1)$$

$$\sum_{i=1}^{n} [y_i - f(x_i)]^2 = \sum_{i=1}^{n} [y_i - (ax_i^3 + bx_i^2 + cx_i) + d]^2 \quad (2)$$

Once the optic disc is roughly located, an area of interest containing the optic disk is determined. This area will be centered in the coordinates where both branches of the main vessel arc crest lines converge, and its size will be two times the average optic disk size of all the images analyzed, so that every optic disk will be contained within this small area (the red rectangle in Figure 3). It is within this area where

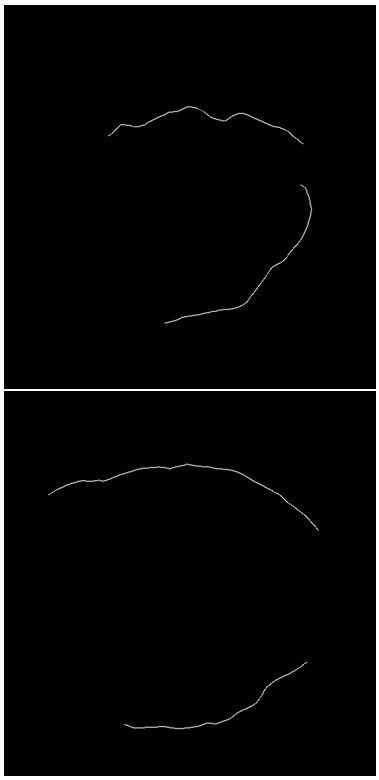

Figure 2: Crest lines obtained with the MLSEC-ST method. Top: crest lines reach the optic disk, so that its position is easily determined. Bottom: in some images, an interpolation method is necessary to reach the optic disc position.

the segmentation process will be performed, obtaining the shape and size of the optic disk.

2.2 Optic Disk Segmentation

Many works about the optic disk segmentation can be found in literature. Several methods were tried with the retinal images we are working with. The best results have been obtained with a deformable model-based segmentation process, based on the work by Hu et al. (Hu et al., 1998; Mariño et al., 2007). In this method, the deformable model is composed of a global model and a local model. The global model approximately fits the boundary of the optic disc. The local deformable model can get a more accurate fit to the characteristics of the boundary, keeping at the same time the shape of the model when the boundary does not exist or it is difficult to get. Optic disc segmentation is performed in three stages: in the first two stages the global model is fitted to the optic disc. In the third stage, starting from the result of the previous stages, the local model is accurately fitted to the particularities of the optic disk boundary. In Figure 4 two segmentation results are depicted, showing the accuracy of the method.

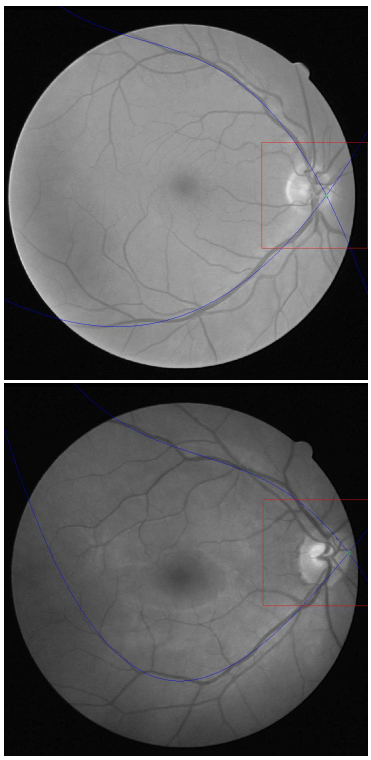

Figure 3: Results obtained from the third degree polynomial fitting applied to two different images. Blue lines represent the third degree polynomic curves fitted to the points of the creases.

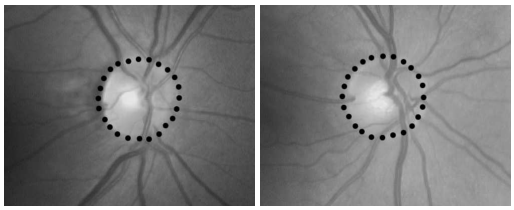

Figure 4: Results obtained from the segmentation process using the deformable model applied to two different retinal images.

Not that the optic disk has been located, the next step consists in licating the macula and fovea using the properties of the eye's morphology.

3 MACULA AND FOVEA DETECTION

The fovea is a small depression on the eye fundus. It is the darkest part in most of the retinal images, while

it is not obvious in some images due to high illumination or being covered by lesions. Its geometrical relation to other structures is employed to locate robustly the fovea. The method performs in two steps: first, a candidate area containing the macula is obtained, then, the macula size and position is located within this area through a matched filter.

3.1 Macula Candidate Region Selection

The candidate region for the fovea is defined as a circular area. Its center is located approximately at 2 disk diameters away from the optic disk center and its radius equals to the optic disk radius. Because the fovea is located about 2 times optic disk size temporal to the optic disk in the retinal images (Larsen, 1976), the candidate region is such defined in order to ensure that the fovea is within the region.

Since in section 2.2 we have computed the coordinates and diameter of the optic disk center, it is possible to obtain an accurate estimation of the fovea and macula position, by fitting a new parabolic curve to the main vessel arc, and taking the coordinates of the optic disk center as the parabola vertex. Following the work from Li et al. (Li and Chutatape, 2004), the parabolic shape is given by equation 3.

$$\begin{aligned}&[(x-x_c)\sin\theta+(y-y_c)\cos\theta]^2 = \\ &2p[(x-x_c)\cos\theta-(y-y_c)\sin\theta]\end{aligned} \tag{3}$$

where x_c, y_c are the vertex coordinates, x and y are the searched points, $p/2$ represents the focal length, and θ is the rotation angle of the directrix. Then a search by mean square error is performed. In this work the shape of the curve has been represented by the general form given by equation 4, much simpler and computationally more efficient.

$$y = ax^2 + bx + c \tag{4}$$

Although in equation 4 the rotation and the parabolic vertex are not represented, the least square error fitting is a very simple process. Vertex coordinates can be computed using equation 5.

$$\begin{aligned}x_v &= -b/2a \\ y_v &= c - b^2/4a\end{aligned} \tag{5}$$

where x_v, y_v are the coordinates of the vertex. If we impose the restriction that the vertex will always be the center of the optic disk, combining equations 4 and 5 the parabola will be given by equation 6, defined by the parameter a and the optic disk center coordinate, already known from the previous segmentation stage.

$$\begin{aligned}b &= -2x_v a \\ c &= ax_v^2 + y_v\end{aligned} \tag{6}$$

Figure 5 represents the parabolic fitting process.

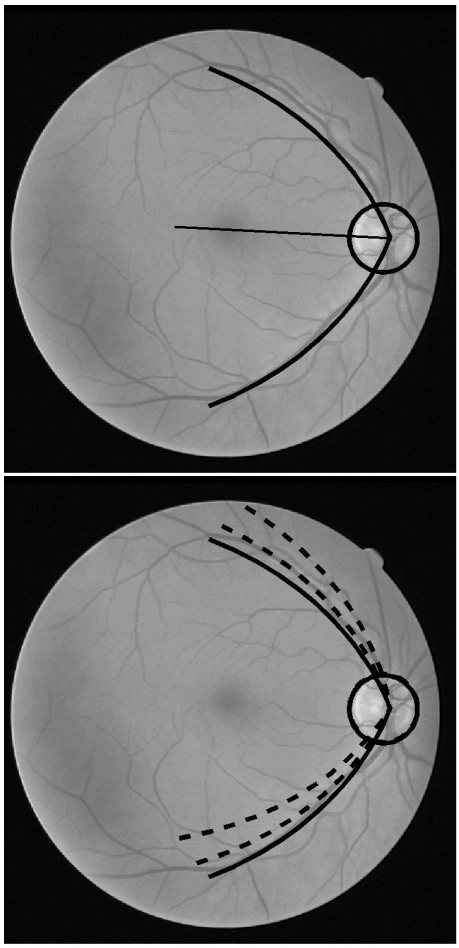

Figure 5: Representation of the parabolic model. Top: parabolic model with the directrix. Bottom: several iterations of the parabolic model searching for the best fit to the main arc vessels.

This way, following the parabola bisection two diameters away from the optic disk center, a search area can be defined, greatly reducing the search space where the macula is located. Figure 6 represents the process of determining this area of interest.

3.2 Fovea Location

Once the candidate area containing the macula has been located, a correlation filter is applied to the region in order to locate the macula and the fovea.

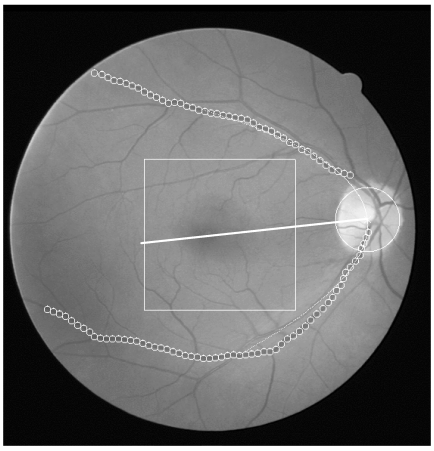

Figure 6: Computation of the candidate foveal region. Points from the creases (white circles) are fitted to the parabolic model and then, following the parabola directrix a fixed distance, the macula candidate search area is determined.

As previously stated, the fovea is a spot located in the center of the macula, and is responsible for the sharp central vision. The macula is commonly visible as a hazy dark area. To locate this dark area, a matched filter which consists of a Laplacian of Gaussian is used. The correlation filter is shown in Figure 7. The fovea will be located at the position where the response of the filter is maximum.

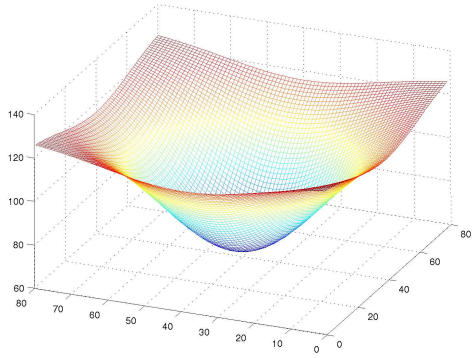

Figure 7: The correlation filter to locate the macula, where the template consists of a Laplacian of Gaussian.

The template is correlated with the intensity component of the retinal image. We use the full Pearson-R correlation to take variations in mean, intensity and contrast into account, as defined in Equation 7. The size of the filter is taken the same as the optic disk radius, since the diameter of the macula is about the same as the diameter of the optic disk (Larsen, 1976).

$$C_{i,j} = \frac{\sum_{x,y}(f(x,y) - \bar{f}(x,y))(w(x-i,y-j) - \bar{w})}{\sum_{x,y}(f(x,y) - f(x,y))^2 \sum_{x,y}(w(x-i,y-j) - \bar{w})^2} \quad (7)$$

The region of interest containing the macula is defined as an $n \times m$ rectangle whose center is the point with the higher response computed by means of the correlation filter. Figure 8 shows the result obtained by the macula segmentation process. The macula is marked as a white circle about the center of the image, while the fovea is marked with a cross in its center (optic disk segmentation result is also included, with its center marked as a red cross).

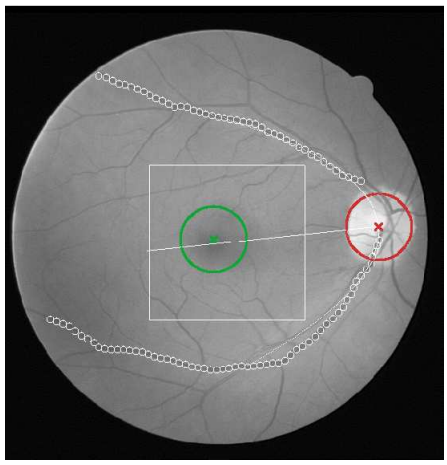

Figure 8: Result obtained by the macula segmentation process using the correlation matched filter in the image in Figure 6. Optic disk radius and center are marked in red, and fovea and macula contours are marked in green.

4 RESULTS

In order to test the accuracy of the method, several experiments have been designed, and the results have been validated by clinicians from the Complejo Hospitalario Universitario de Santiago (CHUS). The set of test images was composed of 135 retinal digital images with a resolution of 565×584 pixels. Table 1 contains the statistics for the test images, with average horizontal and vertical diameters of the optic disks (first and second column) and horizontal vs. vertical ratio (third column). This values will be used in the initialization stages of the deformable model, and will determine the size of the region of interest where the macula is located.

The main goal of this work is the macula location, and this task has been performed in two stages:

Table 1: Statistics (average, standard deviation, maximum and minimum) for the horizontal, vertical and ratio of the horizontal and vertical diameters (*horizontal/vertical*) for the images in the test set.

	Horizontal diameter	*Vertical diameter*	*Ratio Ratio*
Average	78,97	85,03	1,08
Standard deviation	7,34	8,36	0.09
Maximum	103	112	1,23
Minimum	65	70	0,77

the former determined an area of interest where the fovea will be searched, and in the latter the macula was segmented by means of a correlation filter. The results from the first stage are included in table 2. The location is considered *good* when the macula entirely contained within the area of interest. *Acceptable* results show the number of maculas from the set of test images partially contained in the area. A result is considered *bad* when the macula is mostly outside the area of interest. It is clear how the algorithm successfully detected the area of interest surrounding the macula in the 100% of the images in the test set.

Table 2: Results of the determination of the area of interest containing the macula.

Area of interest		
Good	*Acceptable*	*Bad*
100%	0%	0%
100%		0%

In the last stage of the process, the macula was segmented using a correlation filter. This process is very fast since the area where the search takes place is very small. Following the criteria of Goldbaum et al. (Goldbaum et al., 1996), there are three possible results in the segmentation:

1. *Good localization*: estimated center and real center (determined by an expert clinician) of the macula overlap.
2. *Acceptable localization*: estimated and real centers are not separated more than a mean radius (from table 1).
3. *Bad localization*: otherwise.

Following this categorization, the results obtained are depicted in table 3.

Figure 9 shows the results obtained in three different retinal images. The optic disk, the region containing the macula, the macula and the fovea have been marked in all of these images, showing the results commented in tables 2 and 3.

Table 3: Results for the macula location.

Macula location		
Good	*Acceptable*	*Bad*
97%	0%	3%
97%		3%

Table 4: Execution times for each one of the algorithm stages.

Stage	**Time (seconds)**
Creases extraction	0.537s
3rd. degree polynomic fit	0.020s
Optic disk segmentation	2.588s
Parabolic fit	0.033s
Macula location	0.324s
Total	3.502s

Finally, table 4 whows the execution times of each stage, from the creases computation to the macula location. These times were measured in a PIV 2.0GHz. From these times it is clear that a screening process involving thousands of people, which usually would take much time to the clinicians, could be greatly reduced with the help of a system like the one proposed in this paper.

5 CONCLUSIONS AND FURTHER WORK

In this work a methodology to locate and segment the optic disk and the macula has been presented. The algorithm performs in several stages, from the creases extraction, necessary for the optic disk location, to the macula location. Besides, high level domain knowledge is used to reduce the area where the macula is located once the optic disk has been detected. Still much work has to be done to improve the results of the process. A pyramidal search is being tried to obtain a better segmentation of the macula, and a higher number of images is necessary to validate the presented results. Moreover, tests with standard sets of images (like the DRIVE project (Staal et al., 2004)) need to be performed to obtain more reliable result statistics.

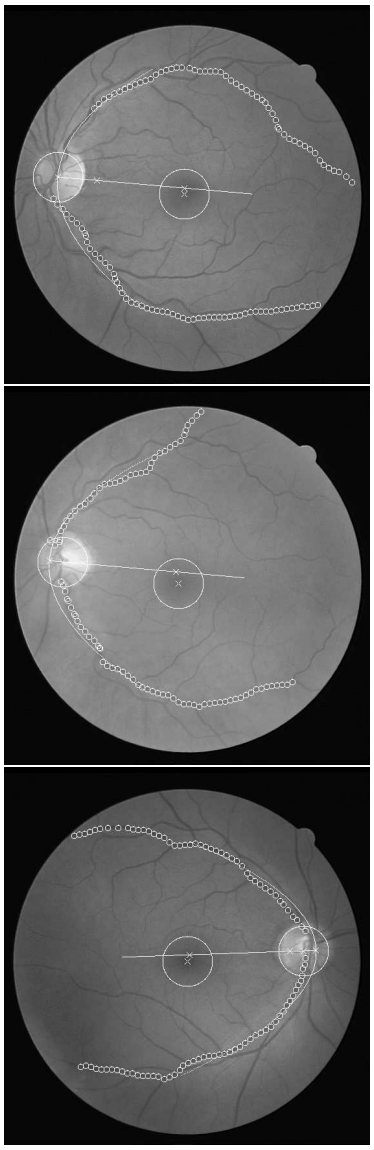

Figure 9: Results of the segmentation of the optic disk and the macula. These images show the results in three cases where the macula and optic disk were successfully located and segmented.

ACKNOWLEDGEMENTS

This paper has been partly funded by the Xunta de Galicia through the grant contract PGIDIT05SIN001E.

REFERENCES

A. Lpez, D. Lloret, J. S. and Villanueva, L. (2000). Multilocal creaseness based on the level set extrinsic curvature. *Computer Vision and Image Understanding*, 77:111–114.

Chanwimluang, T. and Fan, G. (2004). An efficient algorithm for extraction of anatomical structures in retinal images. *IEEE International Conference on Image Processing*, 23:1093–1096.

Goldbaum, M., Moezzi, S., Taylor, A., Chatterjee, S., Boyd, J., Hunter, E., and Jain, R. (1996). Automated diagnosis and image understanding with object extraction, object classification, and inferencing in retinal images. In *Proceedings of the International Conference on Image Processing*, volume 3, pages 695–698.

Hu, Y.-L., Rogers, W. L., Coast, D. A., Kramer, C. M., and Reicheck, N. (1998). Vessel boundary extraction based on a global and local deformable physical model with variable stiffness. *Magnetic Resonance Imaging*, 16:943–951.

Lalonde, M., Beaulieu, M., and Gagnon, L. (2001). Fast and robust optic disk detection using pyramidal decomposition and hausdorff–based template matching. *IEEE Transaction on Medical Imaging*, 20:1193–1200.

Larsen, H. W. (1976). *The Ocular Fundus: A Color Atlas*. Munksgaard.

Li, H. and Chutatape, O. (2004). Automated feature extraction in color retinal images by a model based approach. *IEEE Transactions on Medical Imaging*, 51(2):246–254.

Lowell, J., Hunter, A., Steel, D., Basu, A., Ryder, R., Fletcher, E., and Kennedy, L. (2004). Optic nerve head segmentation. *IEEE Transactions on medical Imaging*, 23:256–264.

Mariño, C., Barreira, N., Penedo, M. G., Ortas, M., Doncel, J. L., and Gómez-Ulla, F. (2007). Two stages optic disc segmentation in digital retinal images. *WSEAS Transactions on Information Science and Applications*, 4(4):771–778.

Mariño, C., Penedo, M. G., Penas, M., Carreora, M. J., and González, F. (2006). Personal authentication using digital retinal images. *Pattern Analysis and Applications*, (9):21–33.

Mendels, F., C., H., and J.P., T. (1999). Identification of the optic disk boundary in retinal images using active contours. *Proceedings of the Irish Machine Vision and Image Processing Conference*, pages 103–115.

Pinz, A., Bernögger, S., Datlinger, P., and Kruger, A. (1998). Mapping the human retina. *IEEE Transactions on Medical Imaging*, 17(4):606–619.

Sinthanayothin, C., Boyce, J., Cook, H., and Williamson, T. (1999). Automated localisation of the optic disc, fovea and retinal blood vessels from digital colour fundus images. *British Journal of Ophthalmology*, 83:902–910.

Staal, J., Abramoff, M., Niemeijer, M., Viergever, M., and van Ginneken, B. (2004). Ridge based vessel segmentation in color images of the retina. *IEEE Transactions on Medical Imaging*, 23:501–509. See also `http://www.isi.uu.nl/Research/Databases/DRIVE/`.

TOWARDS A UNIFIED MODEL FOR THE RETINA
Static vs Dynamic Integrate and Fire Models

Pedro Tomás, João Martins and Leonel Sousa
INESC-ID / IST TU Lisbon, Rua Alves Redol 9, 1000-029, Lisboa, Portugal
{*Pedro.Tomas, Joao.C.Martins, Leonel.Sousa*}*@inesc-id.pt*

Keywords: Retina Models, Stochastic Leaky Integrate and Fire, Poisson-based model, Dynamic model.

Abstract: Many models have been proposed to describe the visual processing mechanisms in the retina. The spike generation mechanism of the models is typically performed by a Poisson process. Alternatively, a more realistic approach can be used by implementing an integrate and fire mechanism. In this paper we show that the Stochastic Leaky Integrate and Fire (SLIF) model is equivalent to a non-linear Poisson-based model. Furthermore, it proposes a dynamic model for the retina visual processing path, achieved through modulations. For estimating this model a two-step approach is proposed: *i)* an initial estimation is computed by using a spike-triggered analysis, and *ii)* the likelihood of the spike train is maximised by gradient ascent.

1 INTRODUCTION

Vision is a fundamental sense in one's everyday life that gained even more relevance in the modern society; most of the information, art and entertainment relies on it. A continuously growing number of research groups have been dedicating their efforts to help visually impaired people by developing visual prostheses capable of conveying some kind of vision; a endeavour which demands the development of accurate and reliable retina models.

Retinal ganglion cells respond to visual stimuli by eliciting spikes whenever the inner-membrane voltage potential surpasses a given threshold. This response, $y(t)$, is characterised by the time spikes occurred; it can be mathematically represented as a sum of Dirac functions $\delta(t-t_k)$ centred at the time instants t_k, when the inner-membrane voltage potential surpassed the threshold: $y(t) = \sum \delta(t-t_k)$.

Several retina models, based mainly on general neuron models, have been proposed. Two of the most typical are the Poisson based model (Chichilnisky, 2001) and the Stochastic Leaky Integrate and Fire (SLIF) (Paninski, 2006) model. However, in this paper it is shown that, under some constraints, they are equivalent. Moreover, a dynamic model is proposed based on developed mathematical machinery used to prove the equivalence between these two models. This dynamic model modulates its output not only by the stimulus characteristics but also by the recent spike firing history. To estimate this model's parameters several other issues are addressed, such as the tuning and initialisation of this model, where it is used spike-triggered analysis. At the end some experimental results are provided.

This paper is organised as follows. Section 2 shows the equivalence between the SLIF model and a Poisson based model. Section 3 presents the proposed dynamic model and describes its tuning. Some experimental results are drawn in Section 4, and section 5 concludes the paper.

2 STOCHASTIC INTEGRATE AND FIRE MODEL

A typical approximation for the Hodgkin and Huxley neuron model assumes a leaky integrate and fire model. By adding a noise component to the model, it is possible to simulate the variability of real neurons (Keat et al., 2001). For a linear first order integrate and fire mechanism, the SLIF model is described by the stochastic differential equation (SDE):

$$dv(t) = -\frac{1}{\tau}v(t)dt + i(t)dt + \sigma\xi(t) \qquad (1)$$

where τ is a constant variable, $\xi(t)$ is standard white-noise and σ is a multiplicative term which defines the power of the noise source. The above SDE is valid until the subthreshold potential surpasses a given threshold V_{th}. Whenever this happens a spike is fired and the neuron enters a refractory period where no spike can be fired. Accordingly with the SLIF model, at the end of this period, which typically lasts a couple of

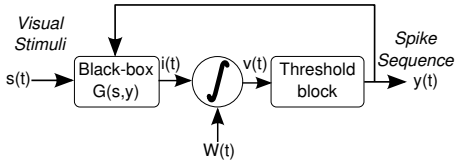

(a) General Stochastic Integrate and Fire model.

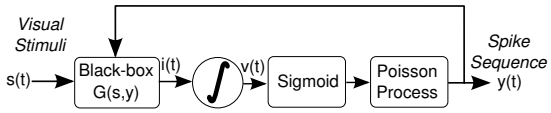

(b) Generalised Poisson model.

Figure 1: Changing the noise source in Integrate and Fire models.

milliseconds, the neuron is reset to a state where the subthreshold potential is v_0. Considering that the last spike was fired at time $t = t_0$, the solution to (1) is[1]:

$$v(t) = h_{IF}(t-t_0) * \left[i(t) + v_0\delta(t-t_0) + W(t) \right] \quad (2a)$$

$$W(t) \sim N(0,\sigma_t) \qquad , \sigma_t \equiv \sigma(t) \quad (2b)$$

where $*$ is the convolution operator and $h_{IF}(t)$ is the transfer function of a low pass filter with a pole in $\frac{1}{\tau}$:

$$h_{IF}(t) = \frac{1}{\tau} e^{-\frac{t}{\tau}} H(t) \quad (3)$$

where $H(t)$ is the Heaviside step function.

2.1 Equivalence between the Slif Model and the Poisson Based Model

Let us consider a SLIF model as shown in Figure 1(a), where $s(t)$ represents the visual stimulus, $y(t)$ is the spike response, and $G(s,y)$ is an arbitrary function that transforms the pair {stimulus, spike response sequence} into the SLIF input $i(t)$. The integrator block in the figure represents the linear filter $h_{IF}(t)$.

Under the SLIF model assumption, the noise source can be moved to the integrator output by modifying its statistics: $v(t) = u(t) + W'(t) \sim N(u(t), \sigma_t^2)$. Considering that after the refrationary period the subthreshold potential v follows a Gaussian distribution with standard deviation σ_0, and noting that the convolution is a linear operator, the output noise source remains Gaussian, with standard deviation:

$$\sigma_t^2 = H(t-t_0)\left[\sigma^2\frac{\tau}{2} + \left(\sigma_0^2 - \sigma^2\frac{\tau}{2}\right)e^{-2\frac{t-t_0}{\tau}}\right] \quad (4)$$

where t_0 represents the time instant of the last spike and σ is the standard deviation of the noise during the integration period, i.e. the Interspike Interval (ISI).

[1] Notice that (1) is similar to the Langevin's SDE.

Therefore, the probability for eliciting a spike at a given time instant t is given by the probability for the potential $v(t) = u(t) + W'(t)$ to surpass V_{th}:

$$\begin{aligned} P\Big(y(t)=1\Big) &= P\Big(u(t)+W'(t) \geq V_{th}\Big) = \\ &= P\Big(W'(t) \geq V_{th} - u(t)\Big) = \\ &= 1 - \mathrm{N}_{\mathrm{cdf}}(V_{th} - u(t) | 0, \sigma_t^2) = \\ &= \mathrm{N}_{\mathrm{cdf}}(u(t) | V_{th}, \sigma_t^2) \end{aligned} \quad (5)$$

where $\mathrm{N}_{\mathrm{cdf}}(x|\mu,\sigma_t^2)$ is the normal cumulative distribution function with mean μ and variance σ_t^2, evaluated at point x. The function $\mathrm{N}_{\mathrm{cdf}}$ defines a sigmoid where V_{th} controls the translation (centre of the sigmoid) and σ_t controls the expansion of the sigmoid.

Since the spiking probability of the SLIF model is given by a sigmoid function, the model in Figure 1(a) is equivalent to the Poisson based model in Figure 1(b), where the shape of the sigmoid depends on the noise statistic during the refractionary and integration periods; three cases can be considered:

(1) if $\sigma_0^2 = \sigma^2\frac{\tau}{2}$, the noise variance throughout the integration period is always the same;

(2) if $\sigma_0^2 < \sigma^2\frac{\tau}{2}$, the noise variance increases exponentially from σ_0^2, just after the refractory period, converging to $\sigma^2\frac{\tau}{2}$;

(3) if $\sigma_0^2 > \sigma^2\frac{\tau}{2}$, the noise variance decreases exponentially from σ_0^2, just after the refractory period, converging to $\sigma^2\frac{\tau}{2}$;

Equivalently, for a neuron described by the Poisson spike generation process presented in Figure 1(b), the change in noise variance is translated into a varying slope of the sigmoid – except in case (1). In case (2)/(3), the model variability increases/decreases as time from last spike progresses.

However it is worth to notice that this is not a true Poisson model, as the firing of a spike at a time instant depends on the recent spiking history. Since the integrator is reset whenever a new spike is fired, this is true even without the feedback path.

The above conversion thus shows that integrate-and-fire (IF) models improve the precision of neuron models by adding three important functions to the typical Poisson based model: *i)* a natural refractionary period given by the time for the integrator to recharge and fire a second spike; *ii)* a feedback mechanism; and *iii)* a sigmoid-like nonlinearity. While the feedback mechanism is not absolutely required to achieve a reasonable precision – see (Capela et al., 2007) –, the modelling of the feedback mechanism with a sufficiently variable filter allows for a considerable improvement on the precision of the model – see (Tomás and Sousa, 2007).

3 DYNAMIC MODEL

The typical modelling of neurons represents $G(s,y)$ in Figure 1 by a linear system dependent on the input stimuli $s(t)$ and on spike history $y(t)$:

$$G(s(t),y(t)) = \underbrace{(h_f * s)(t)}_{i_f(t)} + \underbrace{(h_b * y)(t)}_{i_b(t)} \quad (6)$$

where $h_f(t)$ and $h_b(t)$ represent the feedforward and feedback linear filters, respectively.

In some cases, driven by the necessity to model the contrast adaptation mechanisms existent in the retina, non-linear functions are included in the description of $G(s,y)$ (Baccus and Meister, 2002). These non-linearities can be, for instance, approximated by a Taylor series:

$$G(s(t),y(t)) = f_f(i_f(t)) + f_b(i_b(t)) \quad (7a)$$

$$f_x(y) = \sum_k a_k y^k \quad (7b)$$

Nevertheless, the inclusion of dynamics in neuron model is usually avoided, eventhough recent research suggest that they are required for effectively modelling the precise timing of neurons (Gerstner et al., 2006). This is particularly verified in IF neuron models where its natural non-linearities introduce local minimums, making the training process harder. In order to model the temporal dynamics of the retina circuitry, a model must be constructed where the transfer function changes with time, for instance by means of a modulation process. Typically, neural dynamics are considered only as a function of the stimuli – e.g. motion detection (Bialek and van Steveninck, 2005). However, as referred in section 2, if the precision of neuron models is improved by the inclusion of a feedback path, one should also consider the spike history for modelling neural dynamics.

The proposed model is divided into two parts: a static part and a dynamic part. Both parts have dependencies on the stimuli and the spike history. The static part is composed by a *static forward* filter $h_{sf}(t)$ and a *static backward* filter $h_{sb}(t)$:

$$i_{sf}(t) = (h_{sf} * s)(t) \quad (8a)$$

$$i_{sb}(t) = (h_{sb} * y)(t) \quad (8b)$$

The dynamic part is composed by a set of *dynamic forward* linear filters $h_{df}^{(k)}(t)$ and *dynamic backward* linear filters $h_{db}^{(k)}(t)$, whose amplitude is dynamically controlled by linear functions dependent of both the stimulus and the spike history:

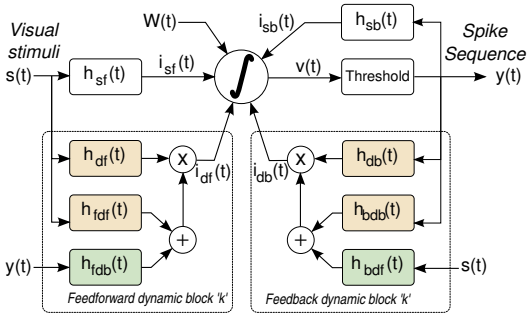

Figure 2: Dynamic model.

$$i_{df}^{(k)}(t) = c_{df}^{(k)}(t)(h_{df}^{(k)} * s)(t) \quad (9a)$$

$$i_{db}^{(k)}(t) = c_{db}^{(k)}(t)(h_{db}^{(k)} * y)(t) \quad (9b)$$

$$c_{df}^{(k)}(t) = \left[(h_{fdf}^{(k)} * s)(t) + (h_{fdb}^{(k)} * y)(t)\right] \quad (9c)$$

$$c_{db}^{(k)}(t) = \left[(h_{bdf}^{(k)} * s)(t) + (h_{bdb}^{(k)} * y)(t)\right] \quad (9d)$$

where $h_x^{(k)}(t)$ represents the linear filter x for component k and $i_{df}^{(k)}(t)$ and $i_{db}^{(k)}(t)$ are the outputs of the dynamic component k. The complete model is depicted in Figure 2.

The outputs of both the static and the dynamic components are then added in the integrator block:

$$i(t) = i_{sf}(t) + i_{sb}(t) + \sum_k i_{df}^{(k)}(t) + \sum_k i_{db}^{(k)}(t) \quad (10)$$

and the subthreshold potential, $v(t)$, follows (2).

3.1 Model Implementation

To implement the model and estimate its parameters, it was discretised in time steps of $T_s = 1$ ms, leading to a discrete representation $x_n \equiv x[n]$ of the continuous signal $x(t)$. Basis functions were used for describing each of the filters in the model. While one can simply estimate the value of the filter for each sample nT_s, the use of basis functions allows: *i)* to reduce the dimensionality of the problem, thus accelerating convergence; and *ii)* to decrease overfitting of the parameters to the data used during the training step.

Each of the filters in the static component $h_x(t)$, $x \in \{sf, sb\}$, or in its discretised form, $\mathbf{h}_x = \left[h_x[1], \cdots, h_x[M]\right]$, where M is the filter memory, is defined by means of the basis functions $\mathfrak{B} = [\mathfrak{B}_1^\mathsf{T}, \cdots, \mathfrak{B}_B^\mathsf{T}]^\mathsf{T}$, $\mathfrak{B}_k = [b_{k1}, \cdots, b_{kM}]$ as:

$$\mathbf{h}_x = \sum_{m=1}^{B} a_{xm}\mathfrak{B}_m = \mathbf{A}_x^\mathsf{T}\mathfrak{B} \quad (11)$$

where $\mathbf{A}_x = [a_{x1}, \cdots, a_{xB}]^T$. In the case of the filters in the dynamic components, $h_x^{(1)}(t), \cdots, h_x^{(C)}(t)$, $x \in \{df, db, fdf, fdb, bdf, bdb\}$, one can organise them in a matrix $\mathbf{H}_x = \left[\mathbf{h}_x^{(1)\mathsf{T}}, \cdots, \mathbf{h}_x^{(C)\mathsf{T}}\right]^\mathsf{T}$, $\mathbf{h}_x^{(k)} = \left[h_x^{(k)}[1], \cdots, h_x^{(k)}[M]\right]$, where the filters are organised in rows and the samples in columns. The filtering matrix $\mathbf{H}_x$ can be computed as:

$$\mathbf{H}_x = \mathbf{A}_x^\mathsf{T} \mathfrak{B} \tag{12}$$

For implementing the integrator linear filter, an infinite impulse response (IIR) description is used:

$$H_{IF}(z) = \frac{1-\beta}{1-\beta z^{-1}} \tag{13}$$

where β defines a pole in $s_{\text{pole}} = \frac{1}{T}\log\beta$ and $\log(x)$ is the natural logarithm of x. For the system to remain stable, $\beta \in \Re_{]0,1[}$, such that $s_{\text{pole}} < 0$.

Notice that unlike in the continuous version of the model, the filter is now normalised with unitary DC gain. Thus, the variance of the noise, σ_n^2, at instant n, given that the last spike event was fired at instant n_0, becomes:

$$\begin{aligned}\sigma_n^2 &= \beta^{2(n-n_0)}\sigma_0^2 + (1-\beta)^2\sigma^2 \sum_{k=0}^{n-n_0-1} \beta^{2k} = \\ &= \beta^{2(n-n_0)}\sigma_0^2 + (1-\beta)^2 \frac{1-\beta^{2(n-n_0)}}{1-\beta^2}\sigma^2\end{aligned} \tag{14}$$

3.2 Model Tuning

The complete set of parameters for the dynamic model in Figure 2 is:

$$\Big\{\mathbf{A}_{sf}, \mathbf{A}_{sb}, \mathbf{A}_{df}, \mathbf{A}_{db}, \mathbf{A}_{fdf}, \mathbf{A}_{fdb}, \mathbf{A}_{bdf}, \mathbf{A}_{bdb}, \beta, \sigma, \sigma_0, V_{th}, V_0\Big\} \tag{15}$$

However, some parameters depend on others. Namely, V_{th} and V_0 depend on the general gains of the model, $\mathbf{A}_x$. Changing their values implies changing the filter gains such that the total integration time for firing a spike remains the same. Also, modifying the value of β is similar to changing the shape of the other linear filters. Moreover, from our experience the initial noise variance σ_0^2 (the variance of the noise after the refractionary period) does not significatively influence the model tuning. Thus this parameter was removed from the learnable parameter set as well. The complete set of trainable parameters is therefore:

$$\Big\{\mathbf{A}_{sf}, \mathbf{A}_{sb}, \mathbf{A}_{df}, \mathbf{A}_{db}, \mathbf{A}_{fdf}, \mathbf{A}_{fdb}, \mathbf{A}_{bdf}, \mathbf{A}_{bdb}, \sigma\Big\} \tag{16}$$

which corresponds to the basis functions coefficients for each filter and the noise standard deviation. The non-trainable parameters were set to: $\beta = 0.9$, $\sigma_0 = 0$, $V_{th} = 1$ and $V_0 = 0$.

For the optimisation of the model parameters, a Bayesian approach was applied to compute the probability of the spike sequence (Tomás and Sousa, 2007). Afterwards, gradient ascent was applied to maximise this probability. Following (15) from (Tomás and Sousa, 2007), the non null gradients in order to the parameters in (16) are:

$$\frac{du_n}{d\mathbf{A}_{sf}} = \mathbf{s}_n * \mathfrak{B} * h_{IF} \tag{17a}$$

$$\frac{du_n}{d\mathbf{A}_{sb}} = \mathbf{y}_{n-1} * \mathfrak{B} * h_{IF} \tag{17b}$$

$$\frac{du_n}{d\mathbf{A}_{df}} = \left[(\mathbf{s}_n * \mathfrak{B})(\mathbf{c}_{df})_n^\mathsf{T}\right] * h_{IF} \tag{17c}$$

$$\frac{du_n}{d\mathbf{A}_{db}} = \left[(\mathbf{y}_{n-1} * \mathfrak{B})(\mathbf{c}_{db})_n^\mathsf{T}\right] * h_{IF} \tag{17d}$$

$$\frac{du_n}{d\mathbf{A}_{fdf}} = \left[(\mathbf{s}_n * \mathfrak{B})(\mathbf{s}_n * \mathbf{A}_{df}^\mathsf{T}\mathfrak{B})^\mathsf{T}\right] * h_{IF} \tag{17e}$$

$$\frac{du_n}{d\mathbf{A}_{fdb}} = \left[(\mathbf{y}_{n-1} * \mathfrak{B})(\mathbf{s}_n * \mathbf{A}_{df}^\mathsf{T}\mathfrak{B})^\mathsf{T}\right] * h_{IF} \tag{17f}$$

$$\frac{du_n}{d\mathbf{A}_{bdf}} = \left[(\mathbf{s}_n * \mathfrak{B})(\mathbf{s}_n * \mathbf{A}_{df}^\mathsf{T}\mathfrak{B})^\mathsf{T}\right] * h_{IF} \tag{17g}$$

$$\frac{du_n}{d\mathbf{A}_{bdb}} = \left[(\mathbf{y}_{n-1} * \mathfrak{B})(\mathbf{y}_{n-1} * \mathbf{A}_{df}^\mathsf{T}\mathfrak{B})^\mathsf{T}\right] * h_{IF} \tag{17h}$$

$$\frac{1}{\sigma_n}\frac{d\sigma_n}{d\sigma} = 2(1-\beta)^2 \frac{1-\beta^{2(n-n_0)}}{1-\beta^2}\sigma \tag{17i}$$

where $(\mathbf{c}_x)_n = [c_x^{(1)}[n], \cdots, c_x^{(C)}[n]]^\mathsf{T}$; the convolution, represented by the symbol $*$, operates along the columns of the operands; and the convolution with h_{IF} is performed using the IIR filter in (13), resetting the integration output to V_0 whenever a spike is fired.

However, unlike in static models, such as those described in (Tomás and Sousa, 2007), carefull initialisation is required in dynamic models. A method for doing this is to apply spike triggered analysis (Schwartz et al., 2002; Simoncelli et al., 2004). Eventhough this algorithm is valid under true Poisson neuron model, under IF models it becomes biased (Pillow and Simoncelli, 2003). This is mostly due to the IF natural non-linearities. However, since the estimation process of IF models has local minimums, it provides a good starting point.

Since the model includes feedforward and feedback dynamic mechanisms, Spike Triggered Average (STA) and Spike Triggered Covariance (STC) analysis were performed using both the stimuli and the spike history. The static filters h_{sf} and h_{sb} in Figure 2 were initially set with the shape of the feedforward and feedback STA, respectively. To adjust the initial

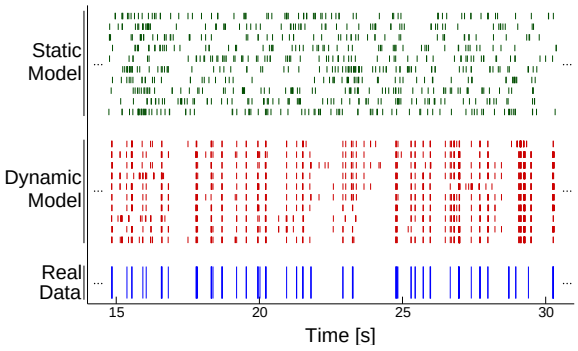

Figure 3: Spike response of the dynamic and static model *vs.* the response of real data (vertical lines represent the timing of the elicited spikes).

shape of the dynamic filters $h_{df}^{(k)}$ and $h_{db}^{(k)}$, excitatory and inhibitory directions can be extracted using STC analysis.

4 EXPERIMENTAL RESULTS

The proposed training algorithm was implemented and tested to estimate the responses of real rabbit retina ganglion cells. The data set consists of four trials of full field white noise stimulus, where each trial has a duration of $\approx$ 50s with an average count of 6.58 spikes per second. While the stimuli values for these four trials is the same, small differences exist in the stimulation time: on average stimulation changed with a new random value at every 152 ms; the standard deviation of stimuli change was 238 ms. The visual stimuli was normalised by subtracting its mean value and then by dividing it by the standard deviation of itself. The resulting stimuli, which corresponds to the input s_n given to the model, is therefore a sequence of normally distributed random values with zero mean and unitary standard deviation.

To estimate the dynamic model, many basis functions can be used to describe the linear filters. Typical examples are the Laguerre bases (Akçay and Ninness, 1999; Tomás and Sousa, 2007) or sinusoidal basis (Keat et al., 2001). However, they are typically unable to describe delayed filters well and, for the used data, it considerably deteriorated the results. Thus, in the present work simple Gaussian kernels were used. While these bases are not orthogonal, they allow to significatively reduce the number of trainable parameters, whilst allowing to achieve good results. A total of 31 kernels were employed each separated by 10 ms, and having a standard deviation of 5.6 ms.

As depicted in subsection 3.2, for model tuning

Table 1: Error measures between trained models and real responses.

		Spike Time	Inter Spike	NMSE
Static Model				
Training trial	mean	420.54	317.69	0.882
	std	10.39	7.05	
All four trials	mean	444.02	337.49	0.903
	std	12.03	6.95	
Dynamic Model				
Training trial	mean	251.63	242.62	0.625
	std	22.13	21.71	
All four trials	mean	325.85	281.32	0.808
	std	20.55	16.68	

mean - mean result std - standard deviation

the static filters h_{sf} and h_{sb} were initially set with the shape of the STA applyed to the stimuli and spike history, respectively. The dynamic filters h_{df} and h_{db} were set with the 5 most excitatory directions (extracted by using STC analysis); the experimental data showed no strong inhibitory directions. The modulating filters h_{fdf}, h_{fdb}, h_{bdf} and h_{bdb} were initially set to a small, non-zero value.

To compare the performance of the proposed dynamic model, we also performed fitting with a static model (the number of dynamic blocks in Figure 2 was set to zero). The training procedure was the same for both the static and the dynamic model. One of the ganglion cells' response trials was used for training. The other three were used for comparison. Again, stimulation times are not exactly the same for all trials, which leads to slightly different neuron responses.

For evaluating the performance of the models, 30 spike response trials were produced by using both the trained static and dynamic models. In Figure 3, we present the first 10 response trials obtained using the training data set. The figure also presents the real retina ganglion cells' response. Analysing the responses one can clearly see that the static model is unable to acquire the structure of the ganglion cells' response. On the other hand, the dynamic model is able to accurately reproduce the spike response pattern. However it does tend to fire 15% more spikes than the ganglion cell (average on the four trials).

For a better assessment of the response of the models, two error metrics proposed in (Victor and Purpura, 1997) were used. The first metric accounts for the cost associated with the absolute time of occurrence of neuronal events (Spike Time Metric). The second metric accounts for the cost of changing the

intervals between two spikes (Inter Spike Metric). The movement cost q was set to 50 s^{-1} – see (Victor and Purpura, 1997). A firing rate metric based on the normalised mean squared error (NMSE) (Berry II and Meister, 1998) was also applied. For that purpose, the firing rates where estimated for both the real and the estimated data, by convolving their PeriStimulus Time Histogram (PSTH) (Berry II and Meister, 1998) with a gaussian window of zero mean and 20ms of standard deviation.

Cross-evaluation between the models' responses and the real ganglion cells responses using the described error metrics are presented in Table 1. This table shows the results when comparing the training trial and the other trials. The presented error metrics confirm our analysis: the dynamic model is able to capture the dynamics of real retina ganglion cells which cannot be described by a simple set of a feedforward filter and a feedback filter. This can be seen by noticing that the mean values for all error metrics are much lower for the dynamic model than for the static model. The dynamic model also tends to achieve a higher degree of variability than the static model. However, this is due to the natural variability of the real data.

In the presented work, the number of dynamic components was fixed to five. However, for obtaining a more general model, one could start by using a larger number of dynamic components and then using feature selection – such as in (Tomás and Sousa, 2007) – to remove all unnecessary components.

5 CONCLUSIONS

Many researchers tend to classify SLIF models and Poisson-based models into different groups. However, as show in this paper, the former can be translated into the latest. One of the most important features of the SLIF model is the presence of feedback mechanisms. Given that this property helps to increase the spiking precision, we present a model whose coefficients are dynamic in time. Moreover we present a method to estimate its coefficients: it uses eigen-analysis to estimate the initial parameters and a gradient ascent technique for tuning the model. Presented results show that the proposed model is able to achieve better results than the simpler static models.

REFERENCES

Akçay, H. and Ninness, B. (1999). Orthonormal basis functions for modelling continuous-time systems. *Signal Processing*, 77(1):261–274.

Baccus, S. and Meister, M. (2002). Fast and Slow Contrast Adaptation in Retinal Circuitry. *Neuron*, 36(5):909–919.

Berry II, M. J. and Meister, M. (1998). Refractoriness and neural precision. *The Journal of Neuroscience*.

Bialek, W. and van Steveninck, R. (2005). Features and dimensions: Motion estimation in fly vision. *Arxiv preprint q-bio.NC/0505003*.

Capela, S., Tomás, P., and Sousa, L. (2007). Stochastic integrate-and-fire model for the retina. In *15th European Signal Processing Conference (EUSIPCO'2007)*.

Chichilnisky, E. J. (2001). A simple white noise analysis of neuronal light responses. *Network: Computation in Neural Systems*, 12(2):199–213.

Gerstner, W., Jolivet, R., Brette, R., Clopath, C., Rauch, A., and Luscher, H. (2006). Predicting Neuronal Activity with Simple Models of the Threshold Type. *Time (msec)*, 100:50.

Keat, J., Reinagel, P., Reid, R. C., and Meister, M. (2001). Predicting every spike: A model for the responses of visual neurons. *Neuron*, 30:803–817.

Paninski, L. (2006). The most likely voltage path and large deviations approximations for integrate-and-fire neurons. *Journal of Computational Neuroscience*, 21(1):71–87.

Pillow, J. and Simoncelli, E. (2003). Biases in white noise analysis due to non-Poisson spike generation. *Neurocomputing*, 52(54):109–115.

Schwartz, O., Chichilnisky, E. J., and Simoncelli, E. P. (2002). Characterizing neural gain control using spike-triggered covariance. In Dietterich, T. G., Becker, S., and Ghahramani, Z., editors, *Advances in Neural Information Processing Systems*, volume 14, pages 269–276, Cambridge, MA. MIT Press.

Simoncelli, E. P., Paninski, L., Pillow, J., and Schwartz, O. (2004). *Characterization of Neural Responses with Stochastic Stimuli*, chapter 23, pages 327–338. MIT Press.

Tomás, P. and Sousa, L. (2007). Feature selection for the stochastic integrate and fire model. In *2007 IEEE International Symposium on Intelligent Signal Processing (WISP'2007)*.

Victor, J. D. and Purpura, K. P. (1997). Metric-space analysis of spike trains: theory, algorithms and application. *Computation Neural Systems*, 8:127–164.

IDENTIFICATION OF HAND MOVEMENTS BASED ON MMG AND EMG SIGNALS

Pawel Prociow, Andrzej Wolczowski
Institute of Computer Engineering, Control and Robotics, Wroclaw University of Technology
ul. Wyb. Wyspianskiego 27,Wroclaw, Poland
pawel.prociow@pwr.wroc.pl, andrzej.wolczowski@pwr.wroc.pl

Tito G. Amaral, Octávio P. Dias, Joaquim Filipe
Escola Superior de Tecnologia de Setúbal, IPS, Campus do IPS, Setúbal, Portugal
tamaral@est.ips.pt, pdias@est.ips.pt, j.filipe@est.ips.pt

Keywords: Electromyography, mechanomyography, LVQ neural network, EMG and MMG signal classification, prosthesis.

Abstract: This paper proposes a methodology that analysis and classifies the EMG and MMG signals using neural networks to control prosthetic members. Finger motions discrimination is the key problem in this study. Thus the emphasis is put on myoelectric signal processing approaches in this paper. The EMG and MMG signals classification system was established using the LVQ neural network. The experimental results show a promising performance in classification of motions based on both EMG and MMG patterns.

1 INTRODUCTION

Biomedical signals means a set of electrical signals acquired from any organ that represents a physical variable of interest. These signals are normally a function of time and can be analysed in its amplitudes, frequency and phase. In the proposed method it is used two biomedical signals, electromyographic (EMG) and mechanomyographic (MMG) signals, to control the movement of prostheses.

Prosthesis systems for upper limb are mainly based on myoelectric control, recognizing EMG signals that occur during muscle contraction on the skin surface. Myoelectric control takes advantage of the fact that, after a hand amputation, great majority of the muscles that generate finger motion is left in the stump. The activity of these muscles still depends on the patient will, so biosignals that occur during it, can be used to control prosthesis motion (Asres, A., Dou, H. F., Zhou, Z. Y., Zhang, Y. L., and Zhu, S. C., 1996; Wołczowski, A., 2001).

In order to enhance functionality of such prosthesis another biosignal was researched. This signal is mechanical wave propagating in a contracting muscle (MMG) (Orizio, C., 1993). The nature and utility of MMG signals had already been studied namely in the control of a free-standing prosthetic hand (Goldenberg, M. S., Yack, H. J., Cerny F. J., and Burton, H. W., 1991; Ouamer, M., Boiteux, M., Petitjean, M., Travens, L., and Sal'es, A., 1999). A strategy to combine the MMG data and sensor fusion was proposed for the estimation and classification of muscle activity (Silva, J., Heim, W., and Chau, T., 2004). The fatigue of the biceps and brachioradialis muscles during sustained contraction was studied by (Tarata, M. T., 2003) using MMG signals. A linear classifier with a feature vector based on RMS power of the MMG signal was used to classify the finger movement in one of three possible groups (Grossman, A., Silva, J., and Chau, T., 2004).

In the proposed approach, an identification system will try to recognise a certain group of movements based on fusion of the mechanical and electrical signals (MMG and EMG signals) recorded on a patients arm. The features used are based on time and frequency histograms. The measurements were done on a specialized stand designed for such research.

2 MEASUREMENT STAND

Measurement set was created specially for obtaining signals from patients arm. The configuration used in the measurement contained 6 input channels (Figure 1). Input channels from 1 to 3 were connected to the microphone sensors and input channels from 4 to 6 were connected to EMG differential electrodes.

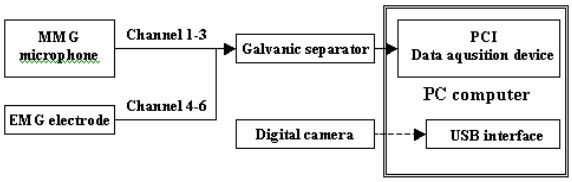

Figure 1: EMG and MMG acquisition system.

The microphone sensors are highly sensitive and are situated in a heavy brazen housing separating it from any external source of vibration. This microphone situated on the skin surface, records vibrations propagating in the tissue underneath it.

The microphone conditioning circuit filter out frequencies above 150 Hz as the frequency range of the mechanomyogram doesn't shows frequencies above this level (Orizio, C., 1993).

The EMG differential electrodes detect minimal potentials occurring on the skin over working muscles. It contains two contact poles situated 1 cm away from each other and amplifies only the difference between the two readings. Frequency of the electromyogram goes into range between 20-400 Hz (Krysztoforski, K. and Wołczowski A., 2005).

A digital camera can be used as an addition to the stand as feedback information. It allows extracting data from specific stages of movement.

3 METHODOLOGY

In the experiment sensor were attached to the patient's right arm. One set of microphone and electrode was positioned at the top of the forearm near the elbow. The second and the third pairs of microphone and electrode were positioned at the bottom of the forearm near the elbow and near the wrist, respectively. Table 1 shows the channels used in the acquisition of EMG and MMG signals.

During the measurements patient was repeating the same set of movements with various speeds and duration of the muscle contraction. Those movements were:

I – Hand closing;
II – Pointing with one finger;
III –Pointing with two fingers;
IV – Wrist flexion – down;
V – Wrist flexion – up;
VI – Pronation / suplination;
VII – Whole hand movement left / right;

All measurements were made with 1kHz probing density and lasted 5 sec. In each 5 second measurement the move was repeated two or three times.

Table 1: Channels used in the acquisition systems.

Sensor	Channel
MMG microphone	1
EMG electrode	4
MMG microphone	2
EMG electrode	5
MMG microphone	3
EMG electrode	6

3.1 Data Visualisation and Analysis

In order to create input for a classification system the data gathered during the measurements had to be analysed in search of the signal features. In figure 2 is shown typical MMG and EMG signals obtained during 5 seconds in channel 4. It can be seen that during these interval of time, one type of movement was repeated three times during the presented tests.

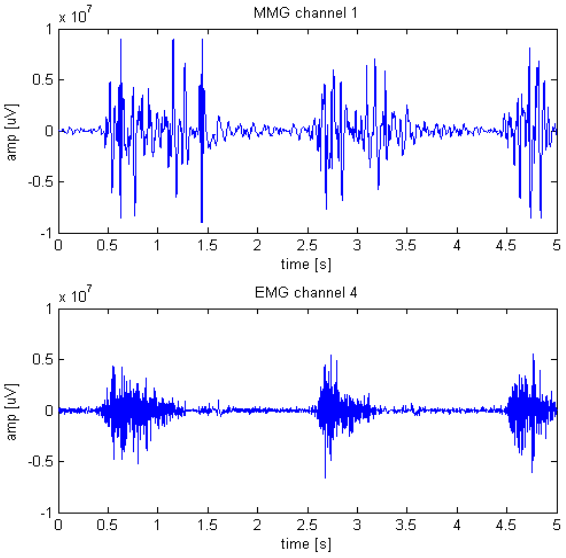

Figure 2: EMG and MMG signals.

The signal features were observed on a 3D histogram containing information in both time and frequency domains using Short Time Fourier Transform (STFT). An example of such histogram is shown on figures 3 and 4, for MMG and EMG signals obtained from one movement, respectively.

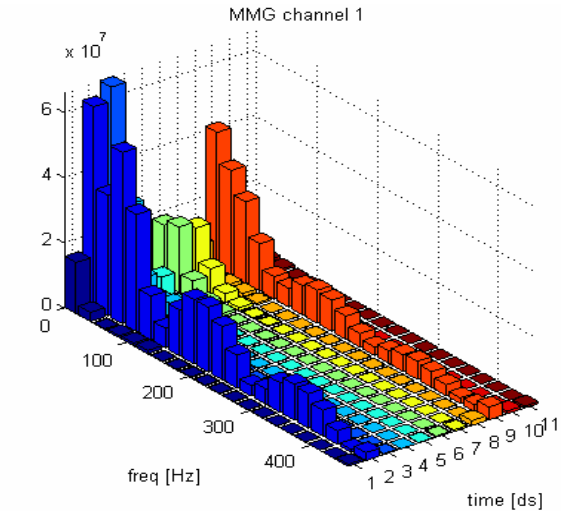

Figure 3: MMG frequency spectral density histogram.

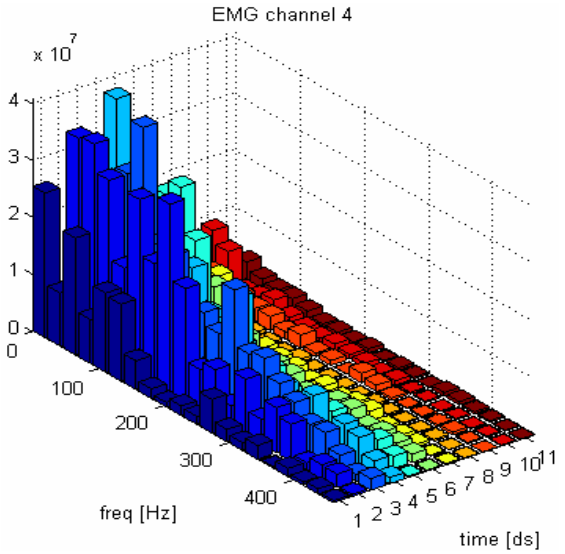

Figure 4: EMG frequency spectral density histogram.

It can be deducted from the histograms analysis, for every movement, that the MMG histogram has two peeks – in the beginning and at the end of the movement, whereas in the middle of the muscle activation spectral density is relatively low.

In the EMG histogram the signal is strongest while the muscle is kept contracted.

3.2 Feature Extraction

In the feature selection stage, the same number of features for each EMG and MMG channel are used.

The selection of the elements of the feature input vector has to take advantage of the knowledge about the signal features in the time and frequency domain.

Therefore the selection of the input vector elements is based on the time/frequency histograms. The proposed algorithm for selecting points is divided in five steps:

1- Extracting the movement part from every channel of 5s measurement record (Figure 5);

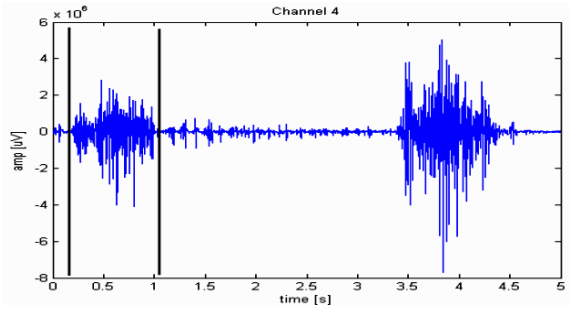

Figure 5: EMG signal obtained in channel 4.

2- Application of the STFT in the beginning (0.3t, where t is the movement time span), in the middle (0.5 t) and at the end (0.7 t) of the extracted movement;

3- In the frequency domain, in three specified moments of time, a set of n points is obtained (from the frequency range adequate to the channel type) (Figure 6).

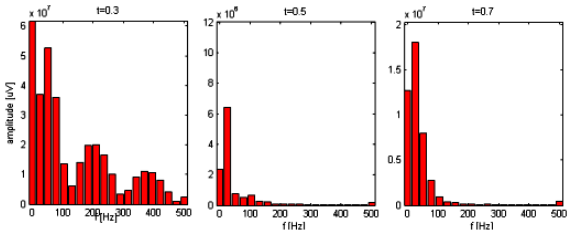

Figure 6: Frequency components in EMG signal.

4- Step 2 and 3 is repeated for every channel;

5- Normalization of the signals amplitude.

This procedure allows to create input vectors with an adjustable size. The minimum number of elements in the feature vector using 6 channels is 18. The minimum structure of these feature vector used as an input in the classifier based on a neural network is given by:

$$\left[A_{t1f}^{ch1}\ A_{t2f}^{ch1}\ A_{t3f}^{ch1} \ldots A_{t1f}^{ch6}\ A_{t2f}^{ch6}\ A_{t3f}^{ch6} \right] \quad (1)$$

The element A_{t1f}^{ch1} represents the signal amplitude in the channel 1 for the instant of time *t1* in the frequency *f*.

The minimum structure of the feature vector using only three channels (EMG or MMG) as 9 elements and is given by:

$$\left[A_{t1f}^{ch1}\ A_{t2f}^{ch1}\ A_{t3f}^{ch1} \ldots A_{t1f}^{ch3}\ A_{t2f}^{ch3}\ A_{t3f}^{ch3} \right] \quad (2)$$

3.3 Classification Method

The electromyographic and mechanomyographic signals are classified using the Learning Vector Quantization (LVQ) neural network. The LVQ network is a mutation of self-organizing Kohonen's maps. Unlike standard neural networks, it contains usually only one layer of neurons. Each neuron is subscribed to one class (Figure 7). The $[x_1, x_2, \ldots, x_n]$ is the feature vector and $[y_1, y_2, \ldots, y_n]$ represents each output movement. This kind of network proved to be efficient in biosignal recognition problem in previous research conducted by the authors (Wolczowski A. 2001, Krysztoforski, K. and Wołczowski A., 2005).

Usually there is more than one neuron for each class. Each neuron has its weight vector containing as many elements as data input (Kohonen, Teuvo K., 1995). During the teaching of the network, in every iteration, for each data vector a winning neuron is being settled based on the closeness (in Euclid's metrics) of the neuron weights to the data vector (Kohonen, Teuvo K., 1995).

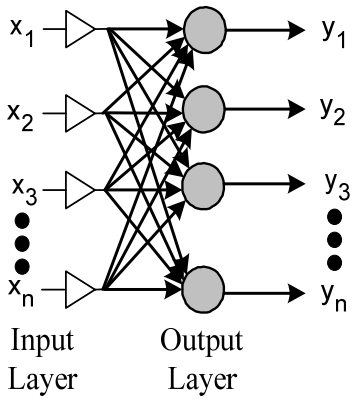

Figure 7: Neural Network architecture.

If the winning neuron represents the same class as the input vector, its weights are being changed to be even closer to this input. If the classes are different the weights are being pushed away.

The basic update algorithm is:

→ If **x** and $\mathbf{m_c}$ represent the same class then

$$\mathbf{m}_c(t+1) = \mathbf{m}_c(t) + \alpha(t)[\mathbf{x}(t) - \mathbf{m}_c(t)] \quad (3)$$

→ if **x** and $\mathbf{m_c}$ represent different classes then

$$\mathbf{m}_c(t+1) = \mathbf{m}_c(t) - \alpha(t)[\mathbf{x}(t) - \mathbf{m}_c(t)] \quad (4)$$

-> from $i \neq c$,

$$\mathbf{m}_i(t+1) = \mathbf{m}_i(t) \quad (5)$$

where **c** is the index of the winning neuron and $\alpha(t)$ is a teaching factor ($0 < \alpha(t) < 1$).

There is a different teaching factor for each neuron in the system and adapts during the process of teaching, starting from the initial value of 0.5 according with the following expression:

$$\alpha_c(t) = \frac{\alpha_c(t-1)}{1 + s(t)\alpha_c(t-1)} \quad (6)$$

Where:

$$s(t) = \begin{cases} 1, \textit{ if classification is correct}; \\ -1, \textit{ otherwise.} \end{cases} \quad (7)$$

An algorithm for handling unused neurons in every teaching epoch was applied.

4 EXPERIMENTAL RESULTS

Experiments were carried out in laboratory, and EMG and MMG signals were captured and recorded simultaneously during the motion of the subject's hand (Figure 8). The next step was extracting the features according to the proposed algorithm. Two sets of vectors (containing 36 or 90 element) were created. The vectors were divided into two groups – one for teaching and the other for testing, each one contained 81 vectors.

In each test the neural network was trained with 200 epochs using vectors from the teaching group. Training was followed by the classification process preformed on the vectors from the test group. The same procedure was repeated using vectors based

only on EMG signal features and vectors based only on MMG signal features in order to determine how useful is the combination of both biomedical signals.

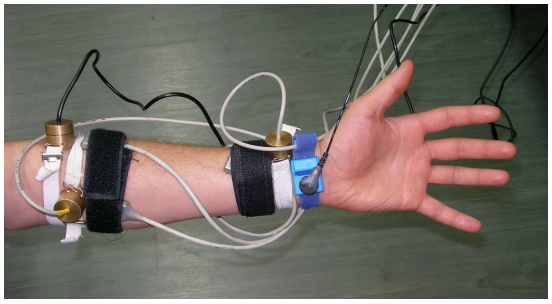

Figure 8: Patient's arm with attached sensors.

Figures 9 and 10, show the neural network error during the training stage when the input vector size is 36 and 90, respectively. The training error, for each epoch, is obtained by the mean value of the Euclidean distance between the current teaching example and the winning neuron.

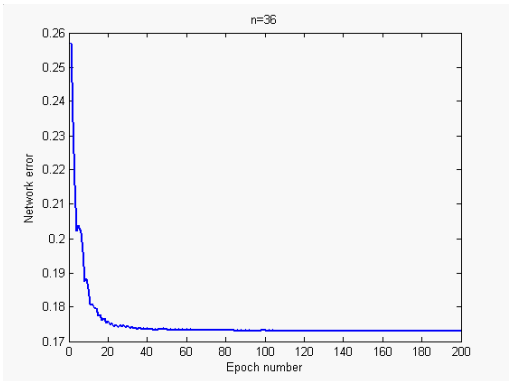

Figure 9: Training error for a vector size of 36.

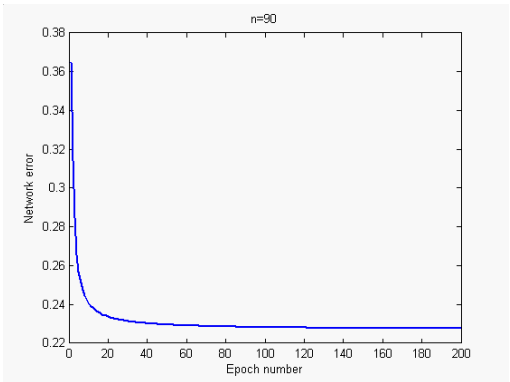

Figure 10: Training error for a vector size of 90.

Tables 2-3 and Table 4, show the results of the test vectors classification with the input vector size of 18 and 36, respectively. In the first row of each table it is represented the number of class movement indicated by the classification process. In the first column of each table are represented the class movements of the examples introduced in to the neural network. The test examples classified correctly are in bold.

Table 2: Classification based on MMG signals.

	1	2	3	4	5	6	7
1	**10**	0	2	0	0	0	0
2	2	**13**	3	0	0	0	0
3	0	0	**8**	0	1	0	0
4	0	0	0	**10**	0	0	0
5	0	0	0	0	**11**	0	3
6	0	0	0	0	0	**8**	1
7	1	0	0	0	0	2	**6**

Table 3: Classification based on EMG signals.

	1	2	3	4	5	6	7
1	**12**	0	1	0	0	0	0
2	0	**12**	1	0	0	0	0
3	1	0	**11**	0	0	0	1
4	0	0	0	**10**	0	0	0
5	0	0	0	0	**11**	0	0
6	0	0	0	0	0	**10**	1
7	0	1	0	0	1	0	**8**

Table 4: Classification based on EMG and MMG signals.

	1	2	3	4	5	6	7
1	**12**	0	1	0	0	0	0
2	0	**13**	1	0	0	0	0
3	1	0	**11**	0	0	0	0
4	0	0	0	**10**	0	0	0
5	0	0	0	0	**11**	0	0
6	0	0	0	0	0	**10**	1
7	0	0	0	0	1	0	**9**

The classification error obtained for the testing vectors group using only information form MMG channels was 18.52%. The error obtained using only the EMG signals in the input feature vectors was 8.64%. Finally, when features from both the EMG and MMG signals were used in the input vector, the classification error decreased to 6.17%.

The same tests were done using an input vectors with 45 and 90 elements. The results of the classification process are shown in Tables 5-6 and Table 7, respectively. The classification error obtained using only MMG signal features was 24.7%. The error obtained using only the EMG

signals in the input feature vector was 2.46%. When it is combined in the input vector, the features from both the EMG and MMG signals, the classification error decreased to 1.24%.

Table 5: Classification based on MMG signals.

	1	2	3	4	5	6	7
1	**9**	0	2	0	0	0	0
2	1	**9**	2	0	1	0	0
3	3	4	**9**	0	0	0	0
4	0	0	0	**10**	1	0	2
5	0	0	0	0	**10**	1	0
6	0	0	0	0	0	**7**	1
7	0	0	0	0	0	2	**7**

Table 6: Classification based on EMG signals.

	1	2	3	4	5	6	7
1	**13**	0	1	0	0	0	0
2	0	**13**	0	0	0	0	0
3	0	0	**12**	0	0	0	1
4	0	0	0	**10**	0	0	0
5	0	0	0	0	**12**	0	0
6	0	0	0	0	0	**10**	0
7	0	0	0	0	0	0	**9**

Table 7: Classification based on MMG and EMG signals.

	1	2	3	4	5	6	7
1	**13**	0	1	0	0	0	0
2	0	**13**	0	0	0	0	0
3	0	0	**12**	0	0	0	0
4	0	0	0	**10**	0	0	0
5	0	0	0	0	**12**	0	0
6	0	0	0	0	0	**10**	0
7	0	0	0	0	0	0	**10**

5 CONCLUSIONS

The results obtained during the experiment imply that efficient identifying hand movements based only on one MMG sensor is very difficult. Especially the first three movements are being confused during the identification process. The reason for such error is because those movements are caused by similar muscles and therefore sounds propagating during those movements are much alike.

The EMG based identification system gives much greater accuracy. The neural network taught with EMG based data badly recognizes only a small percent of test examples. Using the information obtained from both mechanomyogram and electromyogram improves results of the EMG-based recognition. Therefore it can be concluded that the mechanomyographic sensors can be used as a enhancement to a EMG prosthesis system improving the accuracy of identification and count of the supported range of movements. LVQ network proved produced sufficient and satisfactory recognition ratio, therefore proving its usefulness in the biosignal-based prosthesis control problem. Further improvement could be achieved by applying more complex neural network architectures in the recognition process and also by modifying the feature extraction algorithm. Those are the key areas for future investigation of the problem.

REFERENCES

Orizio, C., 1993, Muscle sound: Bases for the introduction of a Mechanomyographic signal in muscle studies, *Critical Reviews in Biomedical Engineering*, 21(3), pp. 201-243.

Asres, A., Dou, H. F., Zhou, Z. Y., Zhang, Y. L., Zhu, S. C., 1996, *A combination of AR and neural network technique for EMG pattern identification*, Proc. Ann. Int. Conference IEEE Eng. Med. Biol. Soc., vol. 4, pp. 1464-1465.

Grossman, A., Silva, J., and Chau, T., 2004, *Functional Mapping of Multiple Mechanomyographic Signals to Hand Kinematics*, Canadian Conference on Electrical and Computer Engineering, vol. 1, pp. 493-496.

Wołczowski, A., 2001, *Smart Hand: The Concept of Sensor based Control*, Proc. of 7th IEEE Int. Symp. on 'Methods and Models in Automation and Robotics', Międzyzdroje.

Goldenberg, M. S., Yack, H. J., Cerny F. J., and Burton, H. W., 1991, *Acoustic myography as an indicator of force during sustained contractions of a small hand muscle*, J. Appl. Physiol., vol. 70, nº. 1, pp. 87-91.

Silva, J., Heim, W., and Chau, T., 2004, *MMG-Based Classification of Muscle Activity for Prosthesis Control*, Proc. 26th Annual Int. Conference of the IEEE Engineering in Medicine and Biology Society, vol. 2, pp. 968-971.

Tarata, M. T., 2003, *Mechanomyography versus Electromyography, in monitoring the muscular fatigue*, BioMedical Engineering Online, 2:3.

Ouamer, M., Boiteux, M., Petitjean, M., Travens, L., and Sal'es, A., 1999, *Acoustic myography during voluntary isometric contraction reveals non-propagative lateral vibrations*, J. Biomech., vol. 32, nº. 12, pp. 1279-1285.

Krysztoforski, K., Wołczowski A., 2005, *Measurement stand for recording EMG signals* . Adv. of Robotics: Industrial and medical robotic systems, WKL, Warsaw.

Kohonen, Teuvo K., 1995, *Self-Organizing Maps*, Springer, Berlin.

FALL DETECTOR BASED ON NEURAL NETWORKS

Rubén Blasco, Roberto Casas, Álvaro Marco, Victorián Coarasa, Yolanda Garrido and Jorge L. Falcó
Instituto de Investigación en Ingeniería de Aragón, Universidad de Zaragoza, María de Luna 1, Zaragoza, Spain
{rblasco, rcasas, amarco, vcoarasa, ygarrido, jfalco}@unizar.es

Keywords: Fall detector, neural networks, ZigBee, wearable sensors, pattern recognition.

Abstract: Falls are one of the biggest concerns of elderly people. This paper addresses a fall detection system which uses an accelerometer to collect body accelerations, ZigBee to send relevant data when a fall might have happened and a neural network to recognize fall patterns. This method presents improved performance compared to traditional basic-threshold systems. Main advantage is that fall detection ratio is higher on neural network based systems. Another important issue is the high immunity to events not being falls, but with similar patterns (e.g. sitting in a sofa abruptly), usually confused with real falls. Minimization of these occurrences has big influence on the confidence the user has on the system.

1 INTRODUCTION

Aging of population is a well-known problem in developed countries. Nowadays, elderly people (+65 years old) represents in Spain more than 16% of the population (Eurostat, 2007). Falls are one of the major fears of the elderly and their relatives. Indeed, some authors estimate the amount of falls of people aged over 75 to be at least 30 percent per year (Sixsmith and Johnson, 2004). In the end, people's concern about falls and whether there will be someone there to help them in case of an emergency, prevent them to age at home (Rodriguez et al, 2005). As a result, people have to move to residences, usually causing negative effect in their health and happiness and resulting in high costs to the individual, their family or the Social Welfare System.

Fortunately, many initiatives are going on in order to increase the time people can stay at home. We will further see many fall detection systems enabling people to receive quickly assistance even when they are not able to request the assistance by themselves (e.g. immobilized or unconscious). Also, combination of these systems with telemedicine allows closer monitoring or collaboration of various experts in the diagnoses (Tunstall web, 2007).

Various methods have been described in order to detect falls in the elderly. Those based in a sensing infrastructure - infrared cameras (Alwan, et al., 2006), vision systems (Williams et al., 1998) or smart floors (Williams et al., 1998) - can be hardly used in many cases. We find wearable systems more appropriated in real scenarios because people refuse to have cameras everywhere in their homes and systems are much more expensive.

Inertial elements are mostly used for mobile monitoring, but still the perfect detector does not exist. Main reason is the difficulty in modelling a fall, it can happen in many different ways; it will not always be the typical big impact followed by inactivity and horizontality. Williams et al. use a shock sensor and a tilt switch to measure the inclination after the impact (Williams et al., 1998). Doughty et al. also use two sensors to perform the same two-stage-analysis (Doughty et al, 2000), which moreover is concreted in a commercial gadget from Tunstall (Nait-Charif and McKenna, 2004). Noury refines the procedure using an accelerometer to detect the shock, also a tilt switch, and adding a vibration sensor to estimate the physiological activity (Noury, 2002). Of course, the more variables measured, the more accurate the detection can be, but also the more complicated and expensive the hardware will be. Many actual works propose just using accelerometers to carry out the full detection (Noury, 2002; Degen et al, 2005; Chen et al., 2005). Main reasons are their low power consumption, reduced cost and versatility detecting different events -shocks, inclination and activity-. The devices presented in these works perform satisfactory fall detection: more of 80% of falls are correctly detected (Noury, 2002).

2 SYSTEM DESCRIPTION

Users must find fall detection systems trust-worthy and efficient in order to use them. Systems which detect all falls but generate many false alarms make users unconfident about it. Moreover, if we consider the difficulty of distinguishing between some kind of falls and ordinary movements in elderly people's life, threshold systems (those that generate an alert when acceleration rise above a fixed value) become not be reliable enough (Noury, 2002).

Figure 1.a. shows tri-axial acceleration when a person has a sideward fall. On the other hand, Figure 1.b. shows accelerations when a person sits down on a sofa abruptly. Both figures were obtained with a device which measures triaxial accelerations, hanged around the neck.

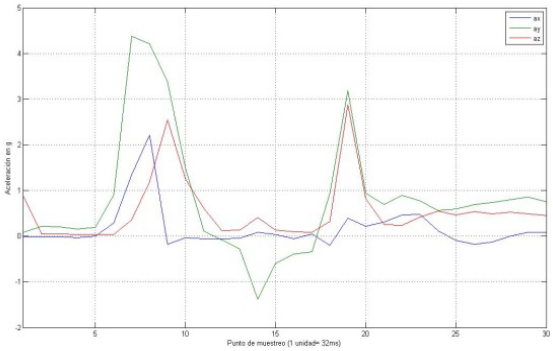

Figure 1a: Acceleration in three axes in a sideward fall.

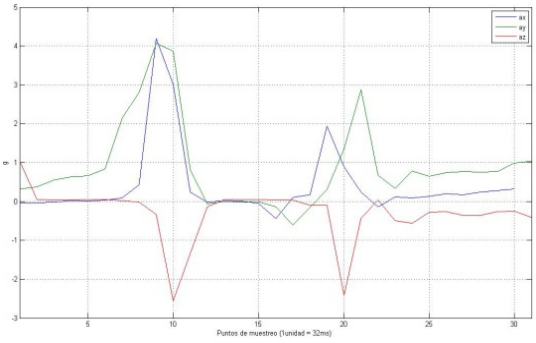

Figure 1b: Acceleration in three axes while sitting abruptly in a sofa.

As we can see, both figures have similar acceleration peaks being also the shapes pretty similar.

Our solution aims to distinguish falls from movements that have similar acceleration patterns not being falls using neural networks; that is to say, separate occurrences into true and false falls.

2.1 Blocks Diagram

The fall detector consists of a mobile device with an inertial sensor which is able to communicate through a ZigBee network. The system also needs a computer that analyzes data using a neural network. Figure 2 shows the portable device blocks: battery, sensor, microcontroller (µC), interface and Zigbee transceiver. Reduced size and low power consumption had been considered in the design process of every block.

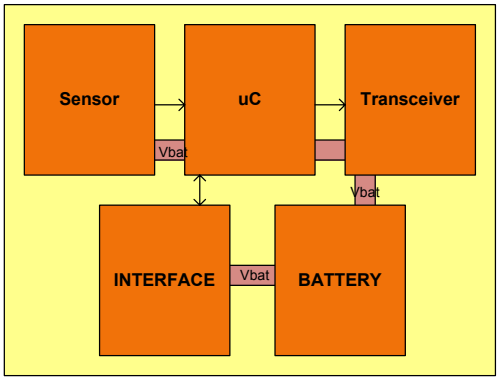

Figure 2: Blocks of the portable device.

The chosen sensor is MMA7260Q Freescale accelerometer because of its wide input voltage range (2,2 V - 3,6 V), current consumption (typically less than 500 µA and 3 µA in sleep mode) and reduced size (6x6x1,45mm). It also has three analog outputs that give the acceleration value in axis X, Y and Z. Its sensitivity is configured digitally into some ranges (1,5 g; 2 g; 4 g or 6 g). As some falls are above 4 g, our application uses the maximum range (6 g) and minimum sensitivity (200 mV/g).

The chosen microcontroller is Microchip's PIC16F688. It has eight A/D channels that can be configured to 10 bits. As well as working within a wide voltage supply range (2 V - 5,5 V), it also has very low current consumption (800 µA in active mode and 1 nA while sleeping).

Regarding communications, we discarded the development of a proprietary network for interoperability reasons. Other standard wireless protocols such as Bluetooth or WiFi consume too much energy as they are intended for higher data rates. We decided to use ZigBee because its adequate data rate (250 kbps), security (128 bits AES encryption), low latency (30 ms to join and 15 ms to access the network) and energy efficiency. Its interoperability with other potential applications (home control and automation), future projection of

the protocol, and its consequent cost reduction were other strategic reasons behind our decision (Geer, 2005).

The chosen ZigBee chip is ETRX2 from Telegesis. This is a ZigBee module on the 2,4 GHz ISM band based upon the Ember's EM250 chip. We used the development environment proposed by Ember to develop a ZigBee-compliant network following mesh topology (ZigBee Alliance, 2007). The chip consumes 30 mA when receiving or transmitting data and 10 µA in sleep mode. As we will use the radio exceptionally, just when are reasonable indications about a fall (when a threshold is exceeded), average power consumption due to communication is reduced.

The user interface consists of a single button and a buzzer for user interaction. Figure 3 shows the mobile device prototype. Its size, including battery, is 58x36x16 mm and it weights 30 gr.

Figure 3: Mobile device prototype.

In order to make the device useful is extremely important to keep it on working long time using the same set of batteries. That is why we gave preference to power-conservative and size of batteries among other designing requirements like transmission rate or processing time. Precise battery life estimation is very difficult because it will depende on the number of false alarms generated; every time the threshold is exceeded it sends data via ZigBee. Anycase, with the battery used (3 V, 1000 mA·h), it can last for several months daily sending several false falls to analize.

2.2 Software

As we said before, we designed a neural net to detect falls also aiming to minimize the number of false-falls compared to simple threshold based detectors.

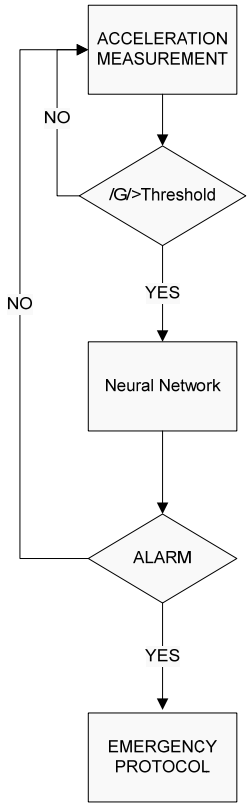

Figure 4: System's simplified flow diagram.

In our case, we use an acceleration threshold to get the "acceleration pattern" of the possible fall to be studied. Every 32 ms the device stores the current acceleration measurements. It keeps a buffer with the last 5 samples ($t_1 \approx 160$ ms). If the threshold is exceeded, a possible fall might have happened. Then we gather 25 samples more ($t_2 \approx 800$ ms) and all the data (960 ms) is sent via ZigBee to the PC. As we will see in section 3.2, those times and the threshold have been empirically set through acceleration pattern analysis of many falls and false-falls.

The "window time" ($t_w=t_1+t_2$) represents the time that the neural net analyzes the data in order to relation the detected event to a true fall.

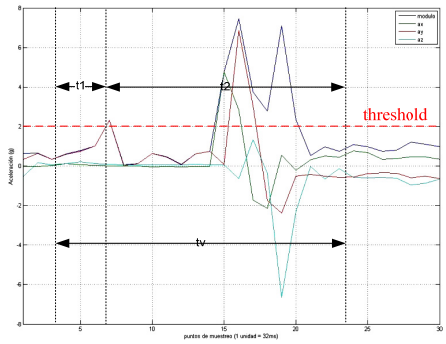

Figure 5: Window time.

In case the neural network detects a real fall, the PC asks the mobile device to buzz for one minute. During this time, the user can cancel the fall situation pressing the button; the user is okay and does not need assistance. In other case, an alert is sent to an assistance center asking for help.

3 NEURAL NETWORK DESIGN

We have chosen MLP (MultiLayer Perceptron) architecture because is the best neural network for pattern classification (Del Hoyo Alonso, 2003). MLPs are feedforward neural networks trained with the standard backpropagation algorithm. They are networks that learn how to transform input data into a desired response. As they are supervised, they require a set of known patterns with known responses to get trained. With one or two hidden layers, they can approximate virtually any input-output map. They have been shown to approximate the performance of optimal statistical classifiers in difficult problems (Neurosolution web, 2007).

Every acceleration point, within window time, is considered as input data to train neural network to distinguish between true and false falls (figures 1a and 1b). That is to say, if an event is represented by 30 samples for each axis (X, Y and Z), the number of inputs will be 90 (30x3). Consequently, it is the same as we give the net the whole graph to compare and classify.

We have decided to train the net with one hidden layer. To check if our choice is convenient or not, we have designed a test bench with different numbers of neurons, studying the absolute error in each case. To accelerate the training, we have chosen a bipolar sigmoid activation function for neurons of the hidden layer. The activation function of the output neuron is unipolar sigmoid so the output looks like a binary signal (1 = TRUE FALL; 0 = FALSE FALL).

The suitable number of neurons of the hidden layer is obtained doing simulations of different neural nets. Finally, we choose the one which produces the minimum absolute error. To reduce the number of simulations and to get patterns from the inputs able to generalize the results, we have defined a requirement: the number of inputs is greater than the number of neurons of the hidden layer.

3.1 Input Data Harvesting

Ten people of different ages, weight, height and sex imitated the movements of elderly people to create a data base of falls.

Table 1: Volunteers' characteristics.

Age range	25-40 years
Weight range	44-105 kg
Height range	1.58-1.90 m

To get the data as close to reality as possible, the volunteers had the acceleration detector hanged around the neck. Volunteers were asked to simulate true and false falls situations.

TRUE falls:

Every volunteer falls down 10 times on a straw mat. The fall intensity changed (rough and soft) and the way of falling down too (side, front, backwards), hitting the ground with their back, hip, knees, etc.

FALSE falls:

Every volunteer flings himself down 5 times on the center and 5 times on the side of a sofa.

Every volunteer stumbles and hits a wall without falling down 5 times.

Every volunteer walks around for 2 minutes doing normal movements like sitting up and down in chairs, picking up things, etc.

During the test, the fall detector continuously samples the three acceleration axes each 32 ms sending them to a PC working as a data logger. In the end, we get a file with all the acceleration samples in axis X, Y and Z for every volunteer. The resulting data base consists of 99 samples of true falls (we had one error while collecting data) and 150 of false falls.

3.2 Input Data Analysis

First of all, data analysis has determined the window time length. After studying all the falls, we decided that an event could be represented with 30 samples (tv = 960 ms; t1 = 160 ms; t2 = 800 ms). This means that the microcontroller has to store always in memory the last five samples to send, in case the acceleration threshold is exceeded, the event to the PC to be analyzed.

With the window time selected, the number of inputs to the neuronal network is set to 90. In order to reduce the number of network entries -and consequently the network size- we have done a PCA (Principal Component Analysis). This method lies in referencing input data to a new origin and coordinate base.

In the new reference, the main components are chosen to be those with the maximum variance among samples (those with the highest covariance).

Therefore, if we take the samples representing more than 95% of covariance, the number of input will be reduced without losing significant information. This leads to suppose that the greater is the variance of an input, the more information it gives.

The acceleration threshold was decided experimentally. At first, guided by most of the bibliography (Chen et al., 2005), we chose a 3 g value. Then 97 out of 99 true falls and 121 out of 150 false falls surpassed the selected threshold.

Missing true falls is far worse than over-detecting false falls, thus we reduced the threshold to 2 g to prevent losing any fall. As expected, we got all the falls, but the number of false falls which surpassed the threshold, increased to 241 because even normal movements triggered the detection process.

After using PCA analysis with the 340 events (99 falls plus 241 false-falls), the number of inputs was reduced from 90 to 55, keeping the 95% of the covariance of the original data.

3.3 Network Performance

The network was trained used Levenberg-Marquardt algorithm (Neural-toolbox in Matlab).

We trained different MLP architectures 55xMx1 (being M the number of neurons in the hidden layer, $5 \leq M \leq 35$). We repeated this process ten times in order to ensure the network design and its performance. Each test randomly selected 80% of the events for training and 20% for validating. That is to say, from the whole 340 events (99 falls plus 241 false-falls), the validation group had 20 true falls and 48 events that could be confused with falls. In the end, a neural net with 22 hidden neurons was able to classify falls correctly.

When interpreting the neural net output give precedence to the fall detection. Thus, we decided that if the output is above or equal to 0.3, a fall is detected. On the other hand, if the output is below 0.3, the analyzed event was not a true fall.
In table 2 we can see the network performance for the ten tests.

Table 2: Validation group detection results.

	Network fall detection / Fall events	Network fall detection / False-fall events
Test 1	20 / 20	0 / 48
Test 2	20 / 20	0 / 48
Test 3	20 / 20	1 / 48
Test 4	20 / 20	0 / 48
Test 5	18 / 20	1 / 48
Test 6	20 / 20	1 / 48
Test 7	16 / 20	1 / 48
Test 8	18 / 20	0 / 48
Test 9	17 / 20	1 / 48
Test 10	15 / 20	0 / 48

We can see how the network is able to detect 92% of all the falls and filter up 99% of the events that can be confused with falls.

In figure 6, we show the network output we got for the validating group in third test.

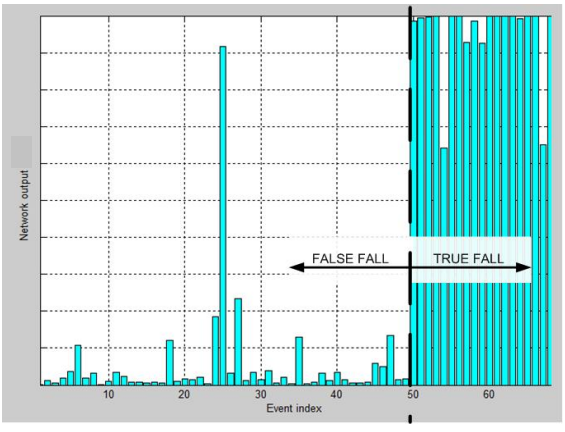

Figure 6: Network output for the third validation group.

4 CONCLUSIONS

The final results using MLP neural networks for fall detection have been quite satisfactory. The application classifies correctly 92% of the validation group falls, better performance than other detection methods: 80% in (Chen et al., 2005). Moreover, the number of false alarms is drastically reduced to 1%, which leads to enhance users trust on the fall detector. Nevertheless, a more extensive study with more users being also elderly has to be developed in order to gather more data and confirm the results.

Although the portable device can run for months with the same battery, the system needs a computer to analyze all the data. In order to reduce costs, it is possible to analyze the pattern remotely. As the amount of exchanged data is reduced, it could be sent via ADSL (if the person is at home), GPRS or even SMS to a service center. Anyhow our application gets better performance than others embedded in a microcontroller but a higher cost and complexity. To overcome this, we are currently minimizing the neural network size so it can run in a microcontroller or FPGA.

ACKNOWLEDGEMENTS

This work was supported by the Spanish MCYT under project Ambiennet (TIN2006-15617-C03-02) and by the EU under projects MonAmi (IST-5-0535147) and EasyLine+ .

REFERENCES

Alwan, M., et al., 2006. 'A Smart and Passive Floor-Vibration Based Fall Detector for Elderly'. Proc. The 2nd IEEE International Conference on Information & Communication Technologies: from Theory to Applications ICTTA'06, Damascus, Syria, April 2006.

Chen, J., et al., 2005. 'Wearable Sensors for Reliable Fall Detection'. Proc. 27th Annual International Conference of the Engineering in Medicine and Biology Society, IEEE-EMBS 2005, September 2005, pp. 3551–3554.

Degen, T., et al, 2005. 'SPEEDY: a fall detector in a wrist watch'. Proc 7th IEEE International Symposium on Wearable Computers, October 2005, pp. 184–187.

Del Hoyo Alonso, R. 2003. 'Supervised classification with Associative SOM.' IWANN 2003: 334-341

Doughty, K., et al, 2000. 'The design of a practical and reliable fall detector for community and institutional telecare', Journal of Telemedicine and Telecare, February 2000, 6, (1), pp. 150–154.

Eurostat web: http://epp.eurostat.ec.europa.eu/ last visited 2007

Geer, D., 2005. 'Users make a Beeline for ZigBee sensor technology'. IEEE Computer Magazine, 38, pp. 16–19.

Hansen, T.R., et al., 2005. 'Using smart sensors and a camera phone to detect and verify the fall of elderly persons'. Proc. European Medical & Biological Engineering Conference (EMBEC 2005), November 2005.

Nait-Charif, H., and McKenna, S. J., 2004. 'Activity Summarisation and Fall Detection in a Supportive Home Environment'. Proc. of the 17th international Conference on Pattern Recognition, (Icpr'04), Washington DC, August 2004, 4, pp. 323–326.

Neurosolution web.
http://www.nd.com/definitions/mlp.htm last visited 2007.

Noury, N., 2002. 'A Smart Sensor for the remote follow up of activity and fall detection of the elderly'. Proc. 2nd Annual International Special Topic Conference on Microtechnologies in Medicine & Biology, IEEE-MMB2002, Madison-USA, May 2002, pp. 314–317.

Rodriguez J.M., et al, 2005. 'Portable System for Patient Monitoring With Wireless Technologies'. The European Journal for the Information Professional, October 2005, 5, (5), pp. 46–52.

Sixsmith, A., and Johnson, N., 2004. 'A smart sensor to detect the falls of the elderly', IEEE Pervasive Computing, April-June 2004, 3, (2), pp. 42–47.

Tunstall web. http://www.tunstall.co.uk last visited 2007.

Williams, G., et al., 1998. 'A smart fall and activity monitor for telecare applications'. Proc. of the 20th IEEE Annual International Conference of the Engineering in Medicine and Biology Society, October 1998, 3, pp.1151–1154.

ZigBee Alliance: 'ZigBee Standard', 2007

USER TUNED FEATURE SELECTION IN KEYSTROKE DYNAMICS

Jyothi Bhaskarr Amarnadh
Dept of Electronics and Communications
Indian Institute of Technology, North Guwahati-781039, Guwahati, India
jyothi@iitg.ernet.in

Hugo Gamboa, Ana Fred
Instituto de Telecomunicações, Instituto Superior Técnico
IST - Torre Norte, Piso 10, Av. Rovisco Pais 1049-001 Lisboa, Portugal
hgamboa@lx.it.pt,afred@lx.it.pt

Keywords: Pattern recognition, Biometrics, Keystroke Dynamics, Feature selection.

Abstract: In this paper, we present a new approach for user biometric verification based on keystroke dynamics. In our approach, the performance of simple classifiers (namely KNN and Bayes classifiers) is tested in a user tuned feature selection method, based on a open password approach. The impact of the training set size is studied, obtaining good results in a preliminary study on a population of 20 users.

1 INTRODUCTION

Keystroke dynamics is part of a class of biometrics known as behavioral biometrics. Behavioral biometrics is related to the dynamic characteristic traits of a person which can be used to determine his/her identity. Examples are Handwriting, Voice, Speech, Language, Gesture and typing patterns, etc.

In comparison to the other biometric techniques, probably keystroke dynamics is one of the easiest technique to implement. The reason is keystroke recognition is completely software-based solution and there is no need for any additional hardware. The already existent basic hardware in the context of a user at his computer, namely the keyboard, is sufficient for this technique.

1.1 Keystroke Dynamics

Keystroke dynamics (or typing rhythms) (Monrose and Rubin, 2000) has been shown to be a useful behavioral biometric technique. This method analyzes the way a user types on a terminal, by monitoring the keyboard input. Typing characteristics have been firstly identified in telegraphic communications where it has been coined as the "fist of the sender" (Bartlow and Cukic, 2006) given that the Morse code operators could be distinguished one from another from their typing rhythms.

The interest in Keystroke Dynamics as a new format for biometric identification has been recognized from the growing number of publications with increasing performance, along with new approaches for biometric security systems. As a maturity indication of this technique, we note that the International Committee for Information Technology Standards (INCITS) has already produced standardization guidelines for data format for Keystroke dynamics(Friant, 2006). The document defines the format for interchange of keystroke data, containing information related to the type of keyboard (standard, laptop, pda-keypad or pda-touchscreen among other) and the keyboard country/layout identification. It also establishes how the events information will be kept in the file specifying the format of input code (like if it is ASCII or UNICODE) and the time resolution used.

The techniques being proposed in the context of Keystroke Dynamics, can be divided into two modes: short code (log-in verification) and long code (continuous verification). The first case the user will type his user name and/or his password and the system uses this non-free text information to try to verify the user identity (Modi, 2005). The continuous approach the user is in an already authenticated environment and continues to be monitored in a free-text approach where, if the keystroke dynamics varies too much from the user model, the user can be asked for some other strong biometric information (Shepherd, 1995) to regain access to the system.

Any biometric technique is usually accompanied by some metrics which evaluate its performance (Jain et al., 2004). The rate at which the attempts of genuine user are falsely classified as impostor and rejected by the biometric system is called false rejection rate (FRR). The rate at which the attempts of an intruder are falsely classified as genuine and accepted by the biometric system is called false acceptance rate (FAR). The FAR and FRR indicate the errors that could possibly occur while making decision by the biometric system. The equal error rate (EER) is the error rate when FAR equals FRR. The receiving oprating curve (ROC) is the graph of FAR as a function of FRR. All these metrics (FAR,FRR,EER,ROC) depend on the collected data ie. the population of users and samples per each user. These are typical reported performance measures in the biometrics field that we will use in the rest of the paper.

We address some of the works conduced during the last years in the area. In (Bergadano et al., 2002) a continuous mode verification implementation provided a result of Equal error rate (EER) of 1.75% in a population of 44 users (extracting 4 samples per user) and 110 impostors. The users had to write 300 characters text of in approximately 2 minute period of acquisition. In (Hocquet et al., 2005) a fusion experiment in a short code mode with 15 users, three different classification algorithms were developed and preformed a fusion of the results obtaining a final value of 1.8% EER. Another study (de Magalhaes et al., 2005; Revett et al., 2006), reports the construction of a system based on short code login reporting a 5.8 EER in a population of 43 users. The report with more users to date has been conduced in the base of log-in short code mode (Jiang et al., 2007) with a population of 56 users presenting the result of 2.54 EER. We note that the population size is yet in a order of magnitude lower than the sizes used in other more conventional biometric techniques.

1.2 Our Proposal - User Tuned Feature Selection

In this paper, we present a new approach for keystroke dynamics based on a open password (all the users are aware of pass sentence). We test the performance of KNN and Bayes classifiers for user recognition with all the features obtained (namely press times of keystrokes and latency times of keystrokes) with all the users typing a common sentence of 23 characters.

We selected a set of features for each user by sequential backward feature selection, thereby improving the performance considerably (Silva, 2007; Siedlencki and Sklansky, 1993).

Table 1: WIDAM Data message.

Field	Bytes
message ID	1
event ID	1
object ID	1
relative position X	2
relative position Y	2
absolute position X	2
absolute position Y	2
other information	4
timestamp	4

In the following section, we describe the architecture of the data acquisition system. Section 3 presents the classifiers for user recognition and feature selection. Experimental results obtained from collected data are presented in section 4. Section 5 presents the conclusions and future work.

2 DATA ACQUISITION SYSTEM

The Keystroke Dynamics data was acquired using a web-based acquisition system of human computer interaction developed by the research group. The system called Web Interaction Display and Monitoring (WIDAM) (Gamboa and Ferreira, 2003). The system has the capabilities of monitoring the events that occur in a particular web page. Examples of the events are the mouse movements and clicks, and more relevant to this biometric technique, the keypress and keyup events generated while entering text in a web page form. The data recorded in the WIDAM system is listed in table 1, but the information required for this implementation is the following: (1) the type of event (if it is a keyup or keydown); (2) the keycode; (3) the timestamp of when the event occured; (3) keyboard modifiers flags, idicating if a shift, ctrl or alt key is being pressed.

For the Keystroke Dynamics experience, the user is presented with a Web Page instructing to insert several times a specific sentence. The sentence is common to all the users that we called the open-password. This sentence is used as the genuine and impostor data given that all the collected data for on user can be used as impostor data for all the other.

The WIDAM Architecture is composed by a client and server applications as depicted in figure 1.

The user accesses the WIDAM application via a web browser that connects to the server. Then the server sends back to the user a web page that is capable of monitoring and displaying the user interaction. This page creates a connection to the server and selects one of the services provided by WIDAM. Then

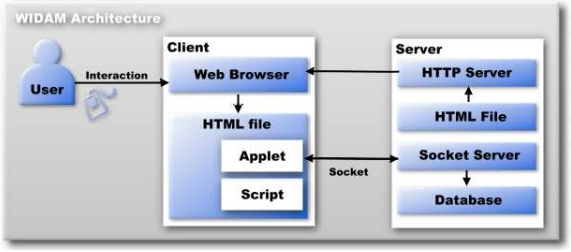

Figure 1: WIDAM architecture.

the client and the server exchange messages using a protocol defined by the authors.

In the server all the information is being recorded in a database in order to be accessed both on real time or off-line for the study of keystroke dynamics. In a previous work (Gamboa et al., 2007), the same structure was used to study the biometrics capabilities of the mouse movements dynamics.

3 RECOGNITION SYSTEM

The input to the recognition system is the press times of keystrokes and latency times of keystrokes from the users, recorded using the WIDAM module described previously.

3.1 Classifier System

We use the K nearest neighbor (KNN) (Duda et al., 2000) classifier at the first hand for user recognition. The nearest neighbors are determined based on the Euclidean distance of a testing sample from all the samples of the training data.

The Euclidean distance (d) between two samples $X = (x_1, x_2, x_3, ..., x_n)$ and $Y = (y_1, y_2, y_3, ..., y_n)$ is

$$d = \sqrt{\sum_{k=1}^{n} (x_k - y_k)^2} \tag{1}$$

We gather K nearest neighbors of a testing sample amongst all the samples from the training data, and depending on the majority of the nearest neighbors, we classify each attempt as either a genuine attempt or impostor attempt. If the majority of the nearest neighbors are from the training data of the genuine user, attempt is classified as genuine or else as an impostor attempt.

A Bayes classifier can be used if the distribution of training data is known. The technique of Bayes classifier is based on Bayesian theorem and is best suited when the size of training data is high. The posterior probabilities of each class for the measurement vector $\mathbf{X}$ and based on the maximum of all the posterior probabilities, we classify that $\mathbf{X}$ belongs to the class which has the maximum posterior probability, i.e. using the MAP rule.

$$\hat{w} = \arg\max_i p(w_i|\mathbf{X}) \tag{2}$$

The posterior probability that measurement vector $\mathbf{X}$ belongs to the class w_i is determined by

$$p(w_i|\mathbf{X}) = \frac{p(\mathbf{X}|w_i)p(w_i)}{p(\mathbf{X})} \tag{3}$$

where $p(\mathbf{X}|w_i)$ is the prior probability of the class membership. Since $p(\mathbf{X})$ is a scaling factor, the classification is based on maximum of the product $p(\mathbf{X}|w_i)p(w_i)$.

$$\hat{w} = \arg\max_i \{p(\mathbf{X}|w_i)p(w_i)\} \tag{4}$$

Since the measurement vector $\mathbf{X}$ is the set of all features, for simplicity of modeling we assume independence among the features conducing to the prior probability $p(\mathbf{X}|w_i)$ as follows:

$$p(\mathbf{X}|w_i) = \prod_{j=1}^{n} p(x_j|w_i) \tag{5}$$

where n is the total number of features.

3.2 Feature Selection

The classifiers described previously are implemented with the set of all the features and tested for performance. We select a subset of features from the set of all the features (all the press times of keystrokes and all the latency times of keystrokes) to best discriminate one user from the other (Jain and Ross, 2002).

For feature selection, we chose a set of features for each user which minimizes his/her performance metric M (we will detail latter the metrics used). To minimize M, sequential backward feature selection is used (Fukunaga, 1990). The algorithm for sequential backward feature selection is as follows:

1. Consider the set of all features $f = \{f_1, f_2, f_3, ..., f_n\}$ and M of f ie M_f.
2. Create a subset F_i by excluding the feature f_i from f and calculate M of F_i ie M_{Fi} for i=1,2,3,...,$n_{features}$ where $n_{features}$ is the number of features in f.
3. Choose F to be the set of features among all the sets F_i which has minimum M_{Fi} ; M_F is the minimum value of M_{Fi} for i=1,2,3,...,$n_{features}$.

4. If $M_F <= M_f$, then f=F and M_f=M_F and go to 2 ; else, go to 5.
5. The desired feature vector is $f_{desired}$=f and $M_{fdesired}$=M_f.

The performance metric M is FAR+αFRR in which α can be varied. We start feature selection by choosing $\alpha = 0$, so that M is FAR (ie. minimizing FAR alone) and we can increase α to infinity so that M is FRR (ie. minimizing FRR alone).We can achieve trade-off between FAR and FRR for intermediate values of α .

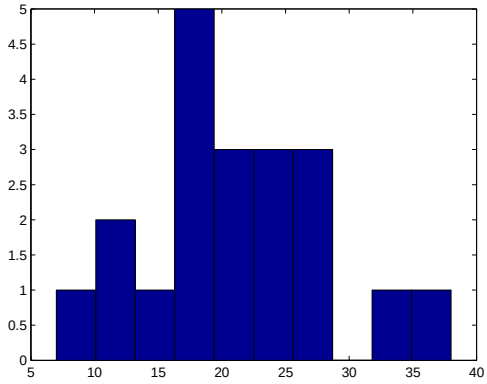

Figure 2: Histogram of length of feature vectors computed over 20 users.

4 RESULTS

We implemented KNN and Bayes classifiers for a system which contains 20 users and each of the user typing the keyword for 17 times. We tested with 9 of the 17 samples as training data and rest 8 samples as testing data. When testing the system for one user, an impostor is considered to be the one of the other users.

When KNN classifier applied for the above system with the set of all the features for various values of K, the optimum value of K for the system is found to be K=1 and for this value of K, the FAR obtained is 1.48% and FRR obtained is 28.125%. Similarly, the system when being tested with Bayes classifier with the set of all features assuming the distribution of training data to be gaussian, the FAR obtained is 2.13% and FRR obtained is 40.625%.

Since the performance of KNN classifier is better compared to Bayes classifier, we used the KNN classifier to select the set of features as described in the previous section, to improve the performance of the system. Feature selection has been done for each user separately and the KNN classifier is implemented for the set of features obtained from feature selection for the respective user. For the overall system, on implementing the KNN classifier with feature selection using M=FAR ($\alpha = 0$)and 9 training samples, the FAR is minimized to 0% and FRR obtained is 21.25% for the optimum value of K=1. More importance is placed on FAR because it is vital to minimize the rate at which an intruder successfully bypasses the authentication system as a genuine user for any biometric system.

Since it is not practical to have 9 samples as the training data (asking the user to type for 9 times to gather the training data), we reapplied the feature selection by considering only 4 samples per user as the training data and 13 samples per user as the testing data.On implementing the KNN classifier with feature selection and using M=FAR ($\alpha = 0$), ignoring FRR, the FAR obtained is 0.546% and FRR obtained is 56.59%. Since we cannot afford to have such a high FRR, we chose to have a trade-off between FAR and FRR ie. we decrease FRR at the expense of increasing FAR. This is achieved by applying sequential backward feature selection to minimize M=FAR+αFRR for a value of $\alpha > 0$.

Setting the limit for FRR to be 15%, on implementing feature selection for each user with the KNN classifier, the FAR obtained for the system is 0.8502% and FRR of the system is 15.00% for the value of $\alpha = 1$.

The average of length of features per user after feature selection is 21.35. Figure 1 represents the histogram of length of features computed over 20 users.

5 CONCLUSIONS

A novel approach has been presented based on behavioral biometric information obtained from Keystroke Dynamics. The technique identifies relevant keystroke typing patterns of a user by an user tuned feature selection. For the implementation of this technique, we used a system that includes a data acquisition module for the collection of keystroke data (time instances of key-up and key-down); the recognition module which includes classification system that uses the nearest K neighbors and decision rule for user recognition, and feature selection to identify user specific features to improve the performance of classification system.

The user authentication is based on the nearest neighbor method and initially all the features obtained from the data acquisition are used for recognition. A feature selection algorithm was applied which re-

duces the initial set of features to a subset of features which is unique for each user. Application of KNN classifier to the selected set of features for the respective users decides the authenticity of the user identity claim.

The results show that the proposed technique could be a competitive biometric technique which minimizes the rate at which an imposter bypasses the authentication system. Apart from that, as mentioned earlier, this technique does not require any additional hardware. The existent hardware namely keyboard is sufficient for this technique which makes it inexpensive.

The open password approach followed enabled a more complete study given that we had access to more impostor data, and validated the possibility of using a known sentence.

REFERENCES

Bartlow, N. and Cukic, B. (2006). Evaluating the reliability of credential hardening through keystroke dynamics. In *ISSRE '06: Proceedings of the 17th International Symposium on Software Reliability Engineering*, pages 117–126, Washington DC.

Bergadano, F., Gunetti, D., and Picardi, C. (2002). User authentication through keystroke dynamics. *ACM Trans. Inf. Syst. Secur.*, 5(4):367–397.

de Magalhaes, S. T., Revett, K., and Santos, H. M. D. (2005). Password secured sites: Stepping forward with keystroke dynamics. In *NWESP '05: Proceedings of the International Conference on Next Generation Web Services Practices*, page 293, Washington, DC, USA. IEEE Computer Society.

Duda, R. O., Hart, P. E., and Stork, D. G. (2000). *Pattern Classification*. Wiley-Interscience Publication.

Friant, D. (2006). Keystroke dynamics format for data interchange. Technical Report INCITS M1/06-0268, InterNational Committee for Information Technology Standards.

Fukunaga, K. (1990). *Introduction to statistical pattern recognition*. Academic Press Professional, Inc., San Diego, CA, USA.

Gamboa, H. and Ferreira, V. (2003). Widam - web interaction display and monitoring. In *5th International Conference on Enterprise Information Systems, ICEIS'2003*, pages 21–27, Anger, France. INSTICC Press.

Gamboa, H., Fred, A., and Jain, A. (2007). Webbiometrics: User verification via web interaction. In *Biometrics Symposium, BCC, Baltimore, USA*.

Hocquet, S., Ramel, J.-Y., and Cardot, H. (2005). Fusion of methods for keystroke dynamic authentication. *autoid*, 0:224–229.

Jain, A., Ross, A., and Prabhakar, S. (2004). An introduction to biometric recognition. *Circuits and Systems for Video Technology, IEEE Transactions on*, 14(1):4– 20.

Jain, A. K. and Ross, A. (2002). Learning user-specific parameters in a multibiometric system. In *Proc. of International Conference on Image Processing (ICIP)*.

Jiang, C.-H., Shieh, S., and Liu, J.-C. (2007). Keystroke statistical learning model for web authentication. In *ASIACCS '07: Proceedings of the 2nd ACM symposium on Information, computer and communications security*, pages 359–361, New York, NY, USA. ACM Press.

Modi, S. K. (2005). Keystroke dynamics verfication using spontaneous password. Master's thesis, Purdue University.

Monrose, F. and Rubin, A. D. (2000). Keystroke dynamics as a biometric for authentication. *Future Generation Computer Systems*, 16(4).

Revett, K., de Magalhães, S. T., and Santos, H. M. D. (2006). Enhancing login security through the use of keystroke input dynamics. In *Advances in Biometrics, International Conference, ICB 2006, Hong Kong, China, January 5-7, 2006, Proceedings*, pages 661–667.

Shepherd, S. J. (1995). Continuous authentication by analysis of keyboard typing characteristics. In *European Convention on Security and Detection (ECOS 95)*, pages 111–114.

Siedlencki, W. and Sklansky, J. (1993). On automatic feature selection. In Chen, C. H., Pau, L. F., and Wang, P. S. P., editors, *Handbook of Pattern Recognition and Computer Vision*. World Scientific.

Silva, H. (2007). Feature selection in pattern recognition systems. Master's thesis, UNIVERSIDADE Técnica de Lisboa, Instituto Superior Técnico.

PRINCIPAL COMPONENT ANALYSIS OF THE P-WAVE
Quantification of Not-Dipolar Components of Atrial Depolarization

Federica Censi, Giovanni Calcagnini, Pietro Bartolini
Department of Technologies and Health, Istituto Superiore di Sanità, Roma, Italy
federica.censi@iss.it , giovanni.calcagnini@iss.it, pietro.bartolini@iss.it

Chiara Ricci
Department of Statistics, Probability and Applied Statistics, Univ. of Rome "La Sapienza", Rome, Italy
chiara_ricci@hotmail.com

Renato Pietro Ricci, Massimo Santini
Department of Cardiology, San Filippo Neri Hospital, Roma, Italy
renatopietroricci@tin.it, m.santini@sanfilipponeri.roma.it

Keywords: Principal component analysis, atrial fibrillation, P-wave, not dipolar components.

Abstract: Aim of this study is to perform the principal component analysis (PCA) of the P-wave in patients prone to atrial fibrillation (AF). Eighteen patients affected by paroxysmal AF and implanted with dual chamber pacemakers were studied. Two 5-minute ECG recordings were performed: during spontaneous (SR) and paced rhythm (PR). ECG signals were acquired using a 32-lead mapping system (2048 Hz, 24 bit, 0-400 Hz bandwidth). For each patient, PCA of the averaged P-waves extracted in any of the 32 leads has been performed. We extracted PCA parameters related to the dipolar (using the first 3 PCs) and not dipolar (from the 4^{th} to the 32^{nd} PCs) components of the P-wave. The number of PCs according to the latent root criterion ranges between 2 and 3 during SR and between 2 and 4 during PR. PCA parameters related to the 3 largest PCs, and describing the dipolar component of the P-wave, did not significantly differ during SR and PR. The not dipolar components during SR were significantly lower than during PR (PCAres%: 0.03±0.06 vs 0.12±0.21, p=0.001; PCAres [mV^4]: 0.10±0.14 vs 0.49±0.73, p=0.001). Factor analysis showed that on average all leads contributes to the first principal component.

1 INTRODUCTION

Atrial fibrillation (AF) is the most commonly encountered arrhythmia in clinical practice. It is defined by the absence of coordinated atrial systole, since it results from multiple reentrant electrical wavelets that move randomly around the atria. Althought it is not a lethal disease, AF may increase mortality up to 2-fold, primarily due to embolic stroke.

Indeed, the lack of coordinated atrial contraction leads to unusual fluid flow states through the atrium that could favour the formation of thrombus at risk to embolize, expecially after return to normal sinus rhythm.

The incidence of atrial fibrillation increases significantly with advancing age. When a patient spontaneously alternates between AF and a normal rhythm, the condition is known as paroxysmal AF. When a patient continues with AF as the dominant cardiac rhythm without reversion to the normal rhythm, the condition is known as chronic AF. Two main electrophysiological conditions are indicated for AF initiation and perpetuation (Clavier et al., 2002): slower conduction velocity in some atrial areas and heterogeneity of cell refractory periods. This heterogeneity of structural and electrophysiologcal properties leads to a longer and more fragmented P-wave (Davies et al., 1963; Kawano et al., 1988; Dilaveris et al., 1998).

Thus, many studies focused on the analysis of the P-wave to extract parameters to recognize a patient with paroxymal AF as well as to predict the development of AF (Dilaveris et al., 1998; Jordaens et al., 1998; Dilaveris et al., 2001; Darbar et al., 2002; Dilaveris et al., 2002).

Given the technical difficulties to analyze the P-wave, and the different acquisition and processing

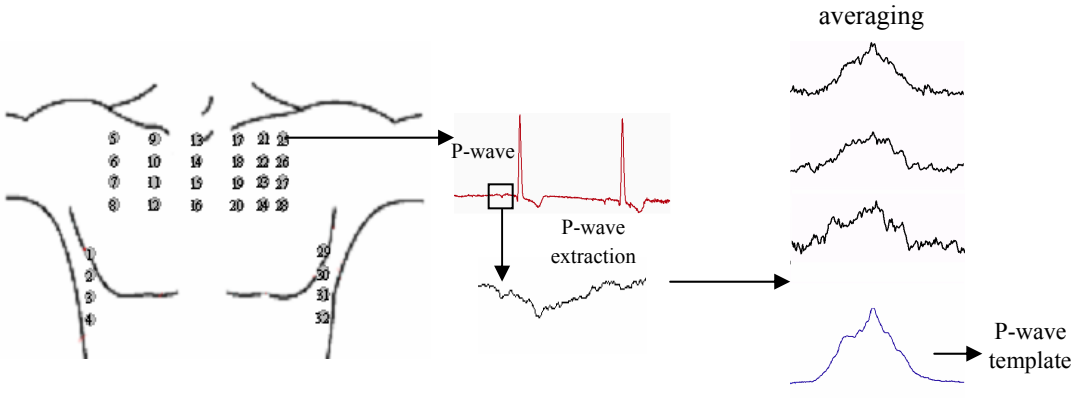

Figure 1: Scheme of the electrodes positioning and of the P-wave pre-processing procedure.

systems used, these studies often lead diverse and not-comparable results in terms of cutoff values. Indeed, the analysis of the T-wave, corresponding to the ventricular repolarization, has been extensively used to quantify repolarization inhomogeneity that may create an arrhythmogenic ventricular substrate. Promising results have been obtained by measuring the QT interval (QT dispersion) and by performing the principal component analysis of the T-wave (De Ambroggi et al., 1997; Acar et al, 1999; Malik et al., 2000; Kesek et al., 2004).

The former analysis have been already applied to the P-wave: P-wave dispersion (which is the difference between the maximum and the minimum P-wave duration recorded from the 12 standard leads), has been shown to distinguish patients with paroxymal AF (Dilaveris et al., 1998; Jordaens et al., 1998; Dilaveris et al., 2001; Darbar et al., 2002; Dilaveris et al., 2002).

PCA of the T-wave has been extensively used to quantify both the complexity and the not dipolar components of the T-wave (De Ambroggi et al., 1997; Acar et al, 1999; Malik et al., 2000; Kesek et al., 2004): particularly, if the ECG would be completely explained by a single electrical dipole, the three largest principal components (PCs), and their corresponding orthogonal eigenvectors, would span the real three dimensional space (dipolar components), while the remaining PCs (not dipolar components) would be zero (Kesek et al., 2004).

For the T-wave it has been demonstrated that the not dipolar components, quantified by the PCA, are not zero, and reflect local repolarization inhomogeneity (Kesek et al., 2004). PCA has never been applied to the P-wave.

Following the approach already used for the analysis of the T-wave, the aim of this study is to perform the PCA of the P-wave in patients prone to AF in order to: 1) evaluate how many principal components are necessary for an AF patient and in which way they are correlated with the ECG leads; 2) evaluate if and to which extent pacing affects the dipolar and the not dipolar components of the atrial depolarization (as quantified by PCA).

2 METHODS AND MATERIALS

2.1 Study Population

Nineteen patients with paroxysmal atrial fibrillation and permanent dual chamber pacemakers (AT500-Medtronic Inc., Minneapolis, MN, USA) were recruited from S. Filippo Neri Hospital, Rome, Italy.
The AT500 device combines atrial sensing and detection algorithms for monitoring and diagnostics, and atrial therapy delivery functions.
The system can store up to 35 episodes of atrial tachycardia/ flutter with electrograms and up to 128 episodes text summaries, without electrograms.

This pacemaker allows for accurate classification of atrial fibrillation episodes, with detailed information about episode instant of occurrence and duration, and further features three distinct programmable pacing algorithms that suppress atrial tachyarrhythmia trigger mechanisms.

When an episode occurs, the device is also programmed for arrhythmia termination. Three atrial pace-termination algorithms can recognise treatable atrial tachycardias and deliver antitachycardia pace-therapies to restore sinus rhythm.
The study population consisted of 9 female and 10 men, aged 72±10.

2.2 Experimental Protocols

Two five-minute recordings were performed for each subject. In the first recording the pacemaker was programmed in VVI mode, i.e. in single-chamber ventricular pacing mode set to a rate of 40/min, so that to have spontaneous rhythm.

In the second recording, pacemaker settings were changed back to the common operating DDD mode, i.e. with both atrial and ventricular pacing functions activated.

Recordings were made using a multi-lead mapping system for high-resolution biopotential measurement (ActiveTwo, Biosemi, The Netherlands).

The system is made of a battery powered isolated AD box that digitises the signals and transfers them to a PCI receiver on computer through a fibre-optic connection. The signals were digitised at a sampling rate of 2048 Hz and a resolution of 24 bits with a frequency response in the full DC-400Hz range.

No further filtering was applied to the data. Thirty-two leads were positioned on the thorax (figure 1), to allow accurate recordings of atrial signals.

ECG recordings were acquired as single-ended signals, with respect to a common reference position. Before starting the acquisition, signals were visualised on a computer screen to check for good electrode contact.

2.3 P-wave Pre-processing

Every lead signal was pre-processed and analysed to extract the average P-wave characteristic.

The first step is to isolate the P-waves from the acquired signals: after detecting the R-wave (using an algorithm similar to that proposed by Pan and Tompkins) (Pan and Tompkins, 1985), P-waves are extracted in a 200ms-long window (410 samples) starting 300ms before the R-wave (figure 1).

Secondly, a beat-by-beat linear piecewise interpolation was used to remove baseline wander, on each P-wave. Fiducial points for linear interpolation were taken from TP and PQ tracks of each beat.

Third, a P-wave template is constructed (figure 1) by averaging each extracted P-wave having a cross-correlation coefficient with the current template higher than 0.9.

In order to take into account the variations in PR interval and/or the inaccuracy in R-wave detection before averaging P-waves were aligned according to the lag at which the cross-correlation function between the current averaged P-wave and each single P-wave shows its maximum (coherent averaging procedure).

The coherent averaging procedure went on until 200 beats were included. If the residual noise level (measured in the isoelectric TP track) remained at more than 1μV even after averaging of 200 beats, averaging procedure continued until the noise level reached a value lower than 1μV.

If it was impossible, the lead was excluded from the study.

2.4 Principal Component Analysis – Measures of Atrial Depolarizatrion Characteristics

For each patient, PCA of the 32 averaged P-waves extracted from the 32 leads has been performed. Since PCA transforms the measured P-wave to virtual parameters that are mutually independent (orthogonal), the 3 largest PCs would contain all the information in the P-wave stemming from the vectorial concept of a single electrical dipole. Following an approach already applied to the T-wave (Kesek et al., 2004; Acar et al, 1999), the other principal components (in this case from the 4th to the 32nd) represent the not dipolar components of the atrial depolarization.

We thus extracted the following parameters:

$$PCA_1 = \frac{s_1}{\sqrt{\sum_{i=2}^{32} s_i^2}} x100$$

$$PCA_2 = \frac{s_2}{s_1} x100$$

$$PCA_3 = \frac{s_3}{s_1} x100$$

$$PCAres = \sum_{i=4}^{32} s_i^2$$

$$PCAres\% = \frac{PCAres}{\sum_{i=1}^{32} s_i^2}$$

where s_i denotes the i-th eingenvalue associated with the i-th principal component. We also extracted the number of principal components suggested by the latent root criterion (PCA number).

In addition, in order to estimate to which extent each lead contributes to the first principal component, factor loadings have been calculated. Analogous to Pearson's coefficient, the squared

Table 1: Results of the PCA parameters during spontaneous rhythm (SR) and during paced rhythm (PR) for all 18 patients.

	PCA number		PCA1 [%]		PCA2 [%]		PCA3 [%]		PCAres [mV^4]		PCAres% [%]	
patient	SR	PR	SR	PR	SR	PR	SR	PR	SR	PR	SR	PR
1	3	3	196.9	211.3	50.4	46.7	5.7	6.7	0.040	0.090	0.200	0.430
2	2	3	917.6	288.0	10.8	34.0	1.4	6.6	0.001	0.020	0.006	0.120
3	3	3	349.6	359.5	27.6	26.3	7.3	8.4	0.013	0.090	0.076	0.510
4	2	3	634.4	401.0	15.6	23.9	1.8	6.6	0.014	0.040	0.104	0.240
5	3	3	195.1	375.5	50.8	20.4	6.5	16.8	0.013	0.130	0.070	0.700
6	3	2	114.2	716.62	84.5	3.4	23.1	1.8	0.010	0.020	0.040	0.100
7	3	3	233.1	298.5	40.7	31.2	13.6	11.7	0.013	0.110	0.060	0.550
8	2	2	231.3	187.0	38.2	53.2	20.2	5.4	0.014	0.006	0.069	0.026
9	3	4	208.0	218.8	46.9	43.1	8.9	12.4	0.260	0.640	0.660	2.670
10	2	2	883.2	277.6	11.3	35.9	0.9	2.6	0.001	0.043	0.004	0.230
11	2	3	354.1	138.7	28.0	70.5	3.3	5.4	0.013	0.123	0.077	0.233
12	3	2	588.0	159.2	15.9	62.8	6.0	2.1	0.001	0.002	0.063	0.008
13	2	3	400.3	976.2	24.9	8.97	2.0	4.7	0.003	0.020	0.014	0.110
14	3	2	850.9	132.3	10.8	75.5	4.6	3.1	0.004	0.001	0.022	0.006
15	2	2	231.9	273.5	42.8	36.3	4.9	3.4	0.020	0.040	0.086	0.210
16	2	4	356.4	849.1	21.9	11.7	17.4	1.4	0.015	0.010	0.065	0.050
17	3	2	221.2	103.7	42.6	95.3	15.0	8.2	0.008	0.770	0.036	2.310
18	3	2	313.3	115.7	30.8	86.2	8.3	5.1	0.024	0.090	0.130	0.340
			404.4	337.9	33.0	42.5	8.4	6.2	0.03	0.12	0.10	0.49
			257.5	247.3	18.3	25.9	6.5	4.0	0.06	0.21	0.14	0.73
p-value (Wilcoxon test)				*0.472*		*0.306*		*0. 586*		*0.001*		*0.001*

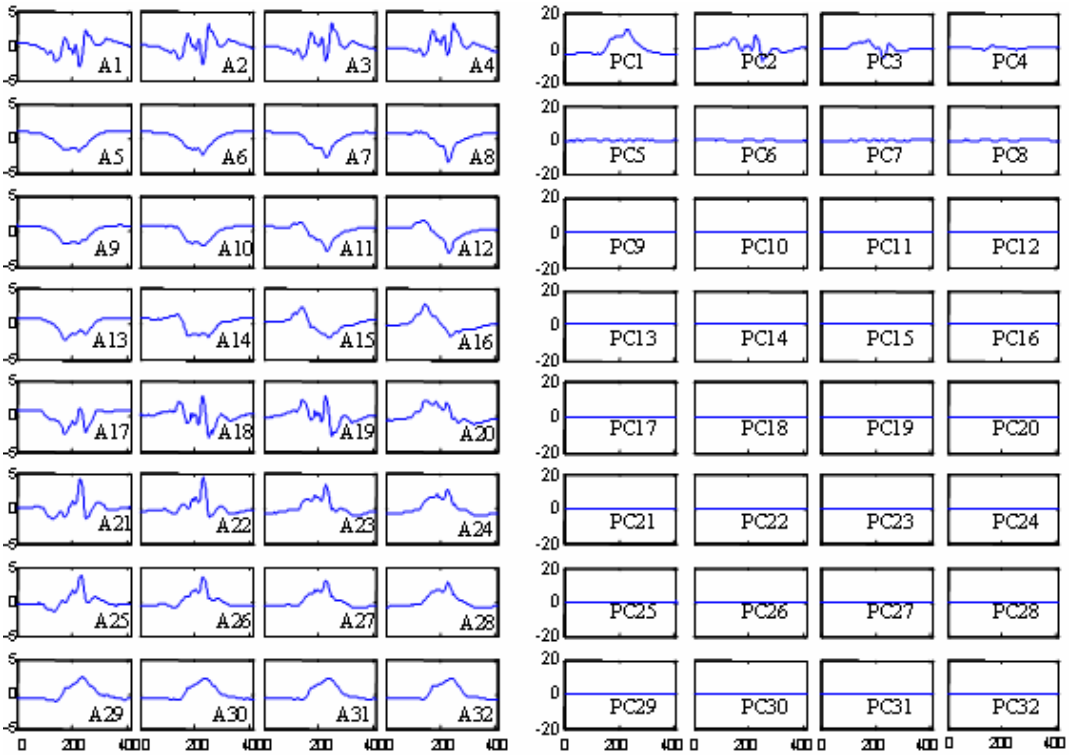

Figure 2: Example of the 32 P-wave templates and of the results of the PCA for one patient.

factor loading is the percent of variance in that variable explained by that PC (i.e the degree of correlation between the original data and the first principal component expressed in percentage).

In addition, in order to estimate to which extent each lead contributes to the first principal component, factor loadings have been calculated. Analogous to Pearson's coefficient, the squared factor loading is the percent of variance in that variable explained by that PC (i.e the degree of correlation between the original data and the first principal component expressed in percentage).

3 RESULTS

Figure 2 shows the 32 P-wave templates and the results of the PCA for one patient.

Table 1 summarizes the results obtained by the PCA parameters. The number of principal components according to the latent root criterion ranges between 2 and 3 (2,56±0,51) during spontaneous rhythm and between 2 and 4 during pacing (2,67±0,69, p=0,6).

PCA parameters related to the three largest PC (PCA_1[%], PCA_2[%] and PCA_3[%]), that describe the dipolar component of the P-wave, did not significantly differ during spontaneous and paced rhythm (table 1, Wilcoxon test for paired data). The not dipolar component (figure 3) as defined by both PCAres and PCAres% during spontaneous rhythm were significantly lower than during pacing (PCAres%: 0,03±0,06 vs 0,12±0,21, p=0,001; PCAres[mV^4]: 0,10±0,14 vs 0,49±0,73, p=0,001).

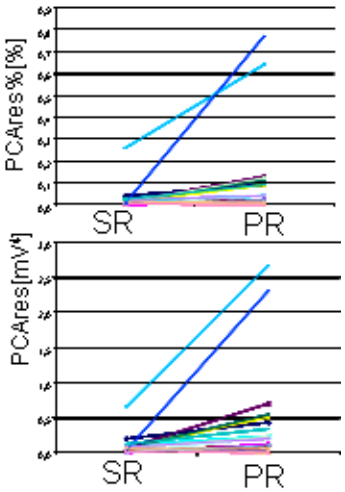

Figure 3: Notdipolar components as defined by both PCAres and PCAres% during spontaneous rhythm and during pacing.

Factor analysis showed that on average all leads contributes to the first principal components. Figure 4 shows the factor loadings averaged (in absolute values) all over the population during spontaneous rhythm and during pacing. Each lead but one in spontaneous rhythm (lead A17) correlates with the first principal component.

4 DISCUSSION

Analysis of the P-wave had been extensively developed to extract parameters related to atrial depolarization heterogeneities useful to recognize patients with paroxymal AF or to predict the development and the perpetuation of AF (Dilaveris et al., 1998; Jordaens et al., 1998; Dilaveris et al., 2001; darbar et al., 2002; Dilaveris et al., 2002). However, the technical difficulties to acquire and process the P-wave, had so far limited its clinical use. Indeed, promising results have been obtained by performing the PCA of the T-wave, in terms of quantification of ventricular repolarization inhomogeneity that may create an arrhythmogenic ventricular substrate (De Ambroggi et al., 1997; Acar et al, 1999; Malik et al., 2000; Kesek et al., 2004).

We hereby used an 32-lead ECG acquisition system particularly suitable for P-wave analysis, having 24 bit resolution and being DC-coupled. We performed the PCA of the P-wave in patients prone to AF. PCA has been applied to the average P-wave extracted in any of the 32 leads.

For each patient we extracted the same PCA parameters employed for the T-wave (Kesek et al., 2004; Acar et al, 1999). As for the T-wave, the PCA parameters related to the first three PCs are associated to the dipolar component of the P-wave, while the remaining PCs (form the 4^{th} to the 32^{nd}) are associated with the not dipolar component of the P-wave.

To our knowledge this is the first time the PCA is performed on the P-wave, thus physiological interpretation and critical discussion can be related only to previous experimental evidences of ventricular conduction disturbance (PCA of the T-wave) (Kesek et al., 2004; Acar et al, 1999).

The first important result is that pacing provokes a significant increase of the not dipolar components of the P-wave. Thus atrial pacing changes the atrial activation, disturbing the normal atrial depolarization process and generating additional paths not explainable by a single P-vector. Such a

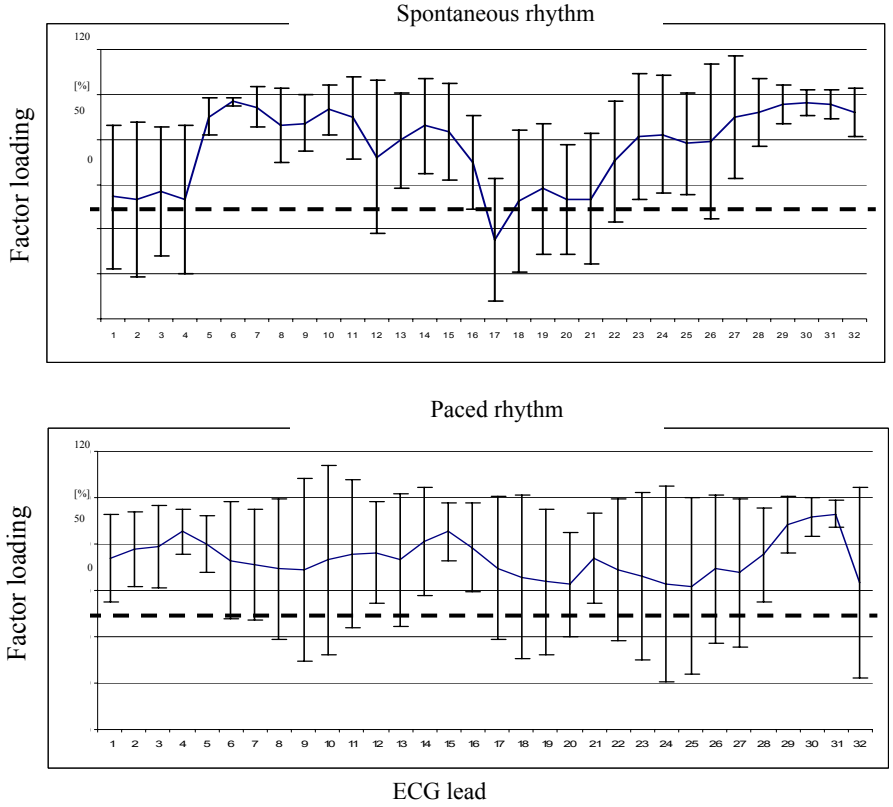

Figure 4: Factor loadings obtained during spontaneous rhythm and during pacing.

result is in agreement with previous studies showing an increase in P-wave duration and low-frequency energy during pacing respect to sinus rhythm in patients with AF (Keane et al., 1995). Non-dipolar components is plausible to be associated with local atrial depolarization inhomogeneity: pacing seems to provoke parts of the myocardium depolarized in a normal sequence and parts depolarized from an abnormal direction.

The second important results is that, on average, all the 32 leads contributes to the first PC, having a significant correlation coefficient with almost all variables.

Since any leads systematically show a not significant correlation with first PC, each lead seems to contribute to a similar extent to the dipolar component. However, we found an inter-patient variability for the factor loadings – some patients had not significant factor loadings in some leads. This result suggests that maps of the correlation with the first PC (or of the average correlation with the first 3 PCs) could help in identifying those leads (i.e. body surface zones) which mainly contribute to the dipolar component of the atrial depolarization.

In conclusion, the study of the dipolar and not dipolar components of the P-wave could provide important information not present in a classical ECG. If the assumption that the not dipolar signal is associated with local depolarization inhomogeneity of the atrium is correct, the PCA is a useful mathematic tool to deeply investigate the atrial conduction disturbances as well as the effects of pharmacological or electrical therapies. This first study tempting the PCA on the P-wave shows that pacing alters the atrial depolarization patterns, provoking an increase of the not dipolar component of the P-wave.

REFERENCES

Acar B, Yi G, Hnatkova K, Malik M. Spatial, temporal and wavefront direction characteristics of 12-lead T-wave morphology. Med Biol Eng Comput. 1999 Sep;37(5):574-84.

Clavier L, Boucher JM, Lepage R, Blanc JJ, Cornily JC. Automatic P-wave analysis of patients prone to atrial fibrillation. Med Biol Eng Comput. 2002 Jan;40(1):63-71.

Darbar D, Jahangir A, Hammill SC, Gersh BJ. P-wave signal-averaged electrocardiography to identify the risk for atrial fibrillation. Pace 2002; 25:1447-1453.

Davies LG, Ross IP. Abnormal P-waves and paroxysmal tachycardia Br Heart J. 1963 sep;25:570-4.

De Ambroggi L, Aimè E, Ceriotti C, Rovida M, Negroni S. Mapping of ventricular repolarization potentials in patients with arrhythmogenic right ventricular dysplasia: principal component analysis of the ST-T waves. Circulation. 1997 Dec 16;96(12):4314-8.

Dilaveris P, Gialafos J. Future concept in P-wave morphological analyses. Card Electrophysiol Rev 2002; 6:221-224.

Dilaveris PE, Gialafos JE, Sideris S. Simple electrocardiographic markers for the prediction of paroxysmal idiopathic atrial fibrillation. Am Heart J 1998;135:73-8.

Dilaveris PE, Gialafos JE. P-wave dispersion : a novel predictor of paroxysmal atrial fibrillation. A.N.E. 2001; 6:159-165.

Jordaens L, Tavernier R, Gorgov N, 'T Kindt H, Dimmer C, Clement D. Signal-averaged P-wave: predictor of atrial fibrillation. J cardiovasc Electrophysiol 1998; 9:S30-S34.

Kawano S, Hiraoka M, Sawanobori T. Electrocardiographic features of P waves from patients with transient atrial fibrillation. Jpn Heart J. 1988 Jan;29(1):57-67.

Keane D, Stafford P, Baker S, Lewis S, Jackson G, Vincent R. Signal-averaged electrocardiography of the sinus and paced P wave in sinus node disease. Pacing Clin Electrophysiol. 1995 Jul;18(7):1346-53.

Kesek M, Jernberg T, Lindahl B, Xue J, Englund A. Principal component analysis of the T wave in patients with chest pain and conduction disturbances. Pacing Clin Electrophysiol. 2004 Oct;27(10):1378-87.

Malik M, Acar B, Gang Y, Yap YG, Hnatkova K, Camm AJ. QT dispersion does not represent electrocardiographic interlead heterogeneity of ventricular repolarization. J Cardiovasc Electrophysiol. 2000 Aug;11(8):835-43.

Pan J, Tompkins WJ. A real-time QRS detection algorithm. IEEE Trans Biomed Eng. 1985 Mar;32(3):230-6.

EFFECTIVENESS FOR A SLEEPINESS TEST OF PUPIL SIZE ESTIMATION DURING BLINK

Minoru Nakayama
CRADLE (The Center for Research and Development of Educational Technolgy)
Tokyo Institute of Technology, O-okayama 2–12–1, Meguro-ku, Tokyo, 152–8552, Japan
nakayama@cradle.titech.ac.jp

Keiko Yamamoto, Fumio Kobayashi
Deapartment of Health and Psychosocial Medicine, Aichi Medical University
Karimata Yazako 21, Nagakute-cho, Aichi, 480–1195, Japan

Keywords: Pupil size, Estimation, Support Vector Regression, Sleepiness test, Pupil Unrest Index.

Abstract: Pupillary response has been used for an index of sleepiness, but the validity of the index is not clear. In this paper, the influence of blinks on the Pupillary Unrest Index (PUI) and the Power Spectrum Density (PSD) for the frequency range $0.01 < f < 0.8Hz$, as indices of pupil's instability during a sleepiness test, was examined. To estimate pupil size during blink, a procedure for collecting the clinical data was developed using Support Vector Regression (SVR). The values of PUI increased with experimental time, and the values and deviations of PUI for experimental observation were larger than the ones with SVR estimation. The blink time also increased with experimental time, and there were significant correlation relationships between the value of PUI and blink time. The mean PSD also correlated significantly with blink time. The relationship between pupillary indices and a subjective sleepiness index was not significant, as it was not in other previous works. These results provide evidence that pupillary indices were significantly affected by blink, and they did not reflect sleepiness correctly.

1 INTRODUCTION

Temporal observation of the human eye pupil is called as pupillography, and these observations can be used as an index for various human activities (Kuhlmann and Böttcher, 1999; Beatty, 1982). In particular, pupillography has been used for assessment of sleepiness and exhaustion using the eye sleepiness test, which consists of measuring the magnitude of pupillary change as a Pupil Unrest Index (PUI) and making readings of the frequency power spectrum. It is often applied to clinical observations or used in industrial engineering situations (Lüdtke et al., 1998; Wilhelm et al., 1998; Wilhelm et al., 1999). These indices have been applied to the evaluation of emotional change (Norrish and Dwyer, 2005); this analysis procedure is recognized as a significant measure.

Although these indices have also been applied to diagnostic procedures, a series of research studies of multiple sclerosis patients suggests that for healthy people there is no significant correlational relationship between PUI and subjective sleepiness indices such as the Stanford Sleepiness Score (Egg et al., 2002; Frauscher et al., 2005). This means that the evaluation procedure should be examined carefully.

A possible problem with observing the pupil is the influence of blink (Nakayama and Shimizu, 2001), because most methods of measuring pupil size are based upon processing the image of the eye. Blink can affect measurements due to the eye being obscured by the eye lid during blink. Blinks are usually discussed as an artifact in temporal observations such as mean pupil sizes or for results of frequency analysis (Nakayama and Shimizu, 2001; Nakayama and Shimizu, 2002). To resolve these problems, some methods of estimating pupil size during blink were developed (Nakayama and Shimizu, 2001; Nakayama, 2005), and the performance was examined (Nakayama, 2006).

However, the effectiveness of the estimation procedure for a diagnostic procedure (such as an eye sleepiness test) and the significance of pupil indices which include blinks have not been discussed sufficiently. In this paper, we address the influence of blink and the validity of pupillary indices by examining the effectiveness of estimating pupil size during

Table 1: Analysis condition.

Condition	Original method	This paper
Sampling		
Sampling rate	25Hz	60Hz
Pre-processing	moving average	moving average SVR
Average window size	0.4sec.	0.4sec.
PUI		
Segment length	2048(82sec.)	4096(68.3sec.)
Unit for segment	16(0.64sec.)	32(0.53sec.)
N of units	128	128
Sampling rate	1.560Hz	1.875Hz
FFT		
Data length	2048(82sec.)	4096(68.3sec.)
Frequency range	0.0<f<0.8Hz	0.01<f<0.8Hz, 4Hz

Original method:(Lüdtke et al., 1998; Wilhelm et al., 1999)

blink using the support vector regression (SVR) technique.

The purposes of this paper are as follows:

1. To develop an estimation procedure using SVR for clinical pupillary observation.
2. To examine the influence of blink on the pupillary indices.
3. To examine the relationship between pupil indices and subjective sleepiness scores, and the influence of blinks on them.

2 MEASURING PUPIL SIZE

2.1 Sleepiness Test

The most popular method to assess sleepiness is a procedure which has been proposed by Wilhelm et al. (Lüdtke et al., 1998; Wilhelm et al., 1999). The measuring procedure in this paper was based on the following method.

The measuring equipment was designed to be worn on the eyes as goggles (Hamamatsu photonics:C7364). The subjects were asked to wear this equipment and to gaze at a small red LED light (infrared wave length: 890 nm) through the goggles, with a CCD camera shooting an image of the pupil. The subjects were instructed to sit and to remain awake in a semi-dark room in a building during the experiment, and were also asked to close their eyes for one minute to promote sleepiness before starting the experiment. The experiment lasted 12 minutes. The pupil diameter size was measured at 60 Hz.

This experiment was conducted between 9 a.m. and 4 p.m. in the late summer. 35 healthy males joined the experiment, their average age was 37.9 years and the standard deviation was 4.1. They were volunteer subjects and signed an agreement on the experimental procedure before it commenced.

Some parameters of the analyzing procedure which were proposed by Wilhelm et al. (Lüdtke et al., 1998) depended on the measuring equipment. One example is the sampling rate of pupil size. The differences are summarized in Table 1.

2.2 Pre-processing

Pre-processing of pupil size during blink provides a possible pupil size from the temporal sizes. To examine the effectiveness of pre-processing, the following two pre-processings were created using moving average method (MOV) and support vector regression (SVR) (Smola and Scholkopf, 1998; Nakayama, 2005). SVR and the kernel method are often used for signal reconstruction or smoothening (Bishop, 1995; Smola and Scholkopf, 1998).

2.2.1 Experimental Observation (Exp.)

This data set consisted of experimental observations without any pre-processing. During the periods of blink, the pupil diameter shows that the size was measured as 0.

2.2.2 Moving Average (MOV)

Moving average method was applied to exclude a large deviation caused by blink and noise. Wilhelm et al. conducted this method for every data series of 0.4 *sec.* (Lüdtke et al., 1998; Wilhelm et al., 1999). This means that the sampling rate is reduced to 2.5 *Hz*.

2.2.3 Estimation with Svr

This processing provided estimation diameters during blink using support vector regression (SVR) with Gaussian kernel (Smola and Scholkopf, 1998). The estimation function was derived from the training data. This training data, as a prototype of pupil response, consisted of measured pupil diameters during the blink and estimated pupil sizes. To produce the training data, a set of data containing 5000 data points collected at the beginning of observations was prepared. To obtain an optimized model, the dimension n of input vector, and a precision $\varepsilon(eps)$ and $\sigma(std)$ of Gaussian kernel needed to be calculated. A practical calculation was conducted using the *SVMTorch* package (Collobert and Bengio, 2001), and parameters were optimized. As a result, the following parameters were provided: input dimension $= 45$; $\sigma = 40$;

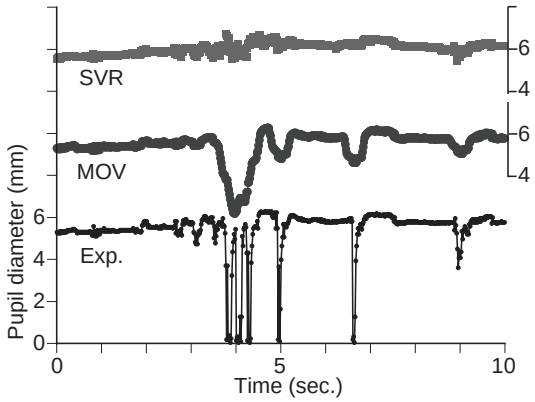

Figure 1: Example of pre-processing for pupillary change during blink.

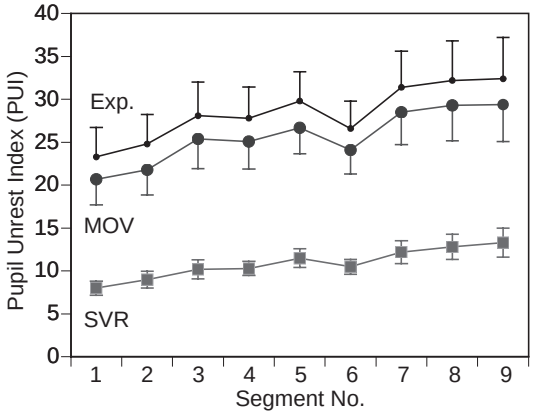

Figure 2: Result of PUIs across segments and pre-processing procedures.

$\varepsilon = 0.5$. Estimation accuracy was examined in the previous estimation experiments (Nakayama, 2006).

3 RESULTS

3.1 Results of Pre-processing

To examine the pupil size pre-processing performance, an example of experimental pupil size and processed data for 10 seconds is illustrated in Figure 1, listed from bottom to top as Exp., MOV and SVR. The horizontal axis shows time, the vertical axis shows pupil size with drops indicating blinks. Pre-processing with MOV shows that temporal changes are influenced by blink and all points are smoothened, although there is no null point during blink periods. On the other hand, SVR indicates the same pupil size without large blink drops and gives possible sizes of pupil diameters during blinks. As a result, an appropriate estimation procedure for clinical pupillography can be developed from this.

3.2 Results of Pupillary Unrest Index (PUI)

PUI as an index of instability of pupillography was calculated following a procedure which was modified from the original method using the parameters listed in Table 1. According to the definition of PUI as cumulative changes in pupil diameter (Lüdtke et al., 1998), firstly the data were reduced by calculating the average for periods of 32 (0.53 *sec*.) consecutive values, secondly the absolute values of the differences from one 32-value average to the next one were summarized for each 68.3 *sec*. data segment, namely 127 differences for one segment. Calculating the average prior to cumulation serves as a simple low pass filtering and excludes high frequency noise.

Average PUIs with standard error bars across the pre-processing procedure results were summarized in Figure 2. PUIs for Exp. and MOV conditions are significantly higher than the ones for SVR. According to the estimation procedure, PUI increases when pupillary temporal change includes blink drop. Therefore, PUIs for Exp. and MOV were relatively high.

Also, sleepiness may increase gradually with experimental time, so this suggests that the gradual increase may depend on sleepiness. According to the pre-processed PUI results and a previous work (Nakayama, 2006), the biggest factor in PUI change must be blink frequency, however.

3.3 Blink Time

Blink may influence a sleepiness index according to the results of PUI. Blink time is defined as the sum of blink drop duration of measured pupil diameters. Average blink times for each segment (68.3 *sec*.) were summarized as bar graphs with standard error bars in Figure 3. The figure shows that the blink time increases monotonically with the sequence number of the segment excepting segment 5. According to blink research, the estimated blink time may be around 1 minute per segment in the standard condition (Tada et al., 1991). It was suggested that the blink time after segment 5 was longer than the one for the standard condition.

These results also indicated that blink influenced PUIs. To examine the relationship between PUI and blink time, correlation coefficients were calculated across all segments and preprocessing procedures. The coefficients were summarized in Table 2. Most coefficients were significant ($p < 0.05$). During seg-

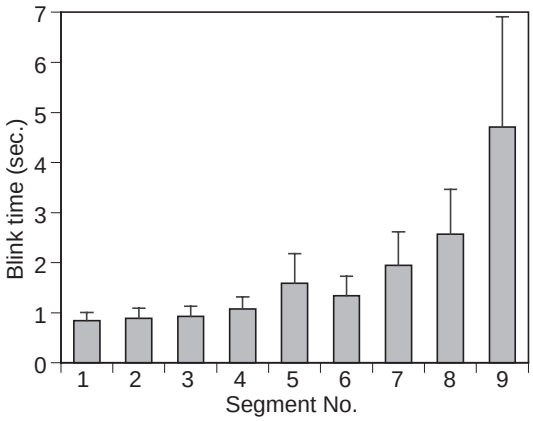

Figure 3: Average blink time for segments.

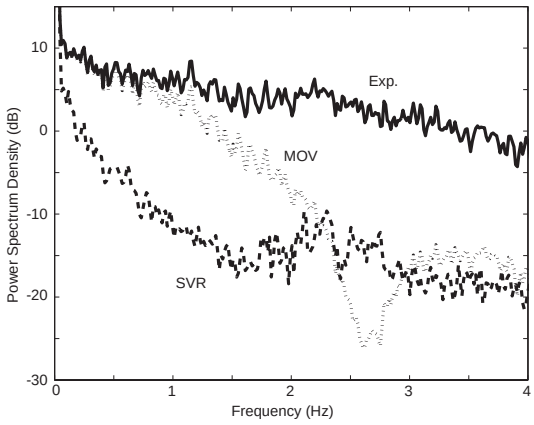

Figure 4: PSD of pupillography across pre-processing.

Table 2: Correlation coefficient between PUI and blink time.

Seg. No.	Exp.	MOV	SVR
1	0.95	0.95	0.42
2	0.91	0.92	0.71
3	0.93	0.92	(0.23)
4	0.90	0.92	0.41
5	0.42	0.45	0.41
6	0.64	0.65	0.34
7	0.55	0.58	0.63
8	0.69	0.70	0.58
9	(0.16)	(0.18)	0.35

N=35, ( ) not significant

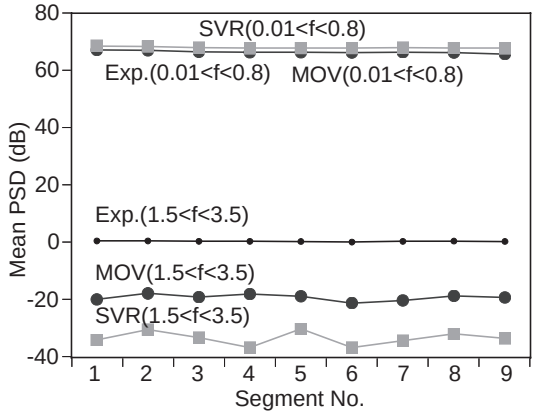

Figure 5: Averaged PSD of each segment for two frequency ranges.

ment numbers 1 to 4, there were large correlation coefficients for pupil diameters with blink times for Exp. and MOV rather than for correlation coefficients for SVR. Coefficients across all pre-processing stayed at same levels after segment number 5, when the blink times were longer than the ones in the standard condition.

These results showed that blink significantly affected PUI changes in the standard condition, and the effectiveness of pre-processing for pupils was examined while the blink times stayed at the standard level. The relationship was also affected by the incidence of additional blinking. Furthermore, these results suggested the blink time affected PUIs despite the conducting of estimations of pupil size during blink.

3.4 Frequency Analysis

Frequency power value of pupillary change, which is given by frequency analysis over 68.3 *sec*., can be used as another index of sleepiness (Lüdtke et al., 1998; Wilhelm et al., 1999). According to the procedure, the power spectrum of pupil diameter change was summarized. Figure 4 shows the results of Power Spectrum Density (PSD) for the first segment of one subject. PSD was estimated with *pwelch* function and Parzen window function of MATLAB (MathWorks Inc.). The vertical axis shows PSD in decibels (dB) and the horizontal axis shows frequency (Hz) from 0.01 to 4.0 Hz. DC component as frequency power was excepted in following analysis. The pupillary change has a low pass filter as low as 4 Hz because it is biological signal, and also pupilograms contain $0.05 \sim 0.3$ Hz components which are well known as pupillary noise (Tsukahara, 1976).

During sleepiness tests, the average power value for the frequency range ($0.01 < f < 0.8Hz$) is often evaluated as the index (Lüdtke et al., 1998; Wilhelm et al., 1999). The average PSD for frequency range ($0.01 < f < 0.8Hz$) for each segment was compared between pre-processing procedures. The results were summarized in Figure 5. According to the results of frequency analysis for the task evoked pupillography, PSDs of frequency range ($1.5 < f < 3.5Hz$) changed significantly in response to the task difficulty. Therefore, average PSDs for frequency range

Table 3: Correlation coefficients between PSDs and blink for two frequency ranges.

Seg. No.	$0.01 < f < 0.8Hz$ Exp.	MOV	SVR	$1.5 < f < 3.5Hz$ Exp.	MOV	SVR
1	-.36	-.36	(-.29)	0.81	0.86	0.44
2	-.38	-.38	(-.25)	0.86	0.87	0.65
3	-.35	-.36	(-.30)	0.65	0.77	(0.20)
4	-.53	-.53	-.51	0.57	0.63	(0.21)
5	-.42	-.42	-.37	(0.11)	(0.15)	(-.03)
6	-.47	-.46	-.47	(0.28)	0.37	(0.10)
7	-.52	-.52	-.46	(0.13)	(0.20)	(0.19)
8	-.55	-.55	-.53	(0.31)	0.45	(0.20)
9	-.62	-.62	(-.30)	(-.10)	(-.07)	(-.07)

N=35, ( ) not significant

($1.5 < f < 3.5Hz$) were also summarized in the same format in Figure 5. The figure shows that PSDs for ($0.01 < f < 0.8Hz$) are at the same level across segments and pre-processing procedures. The PSDs for ($1.5 < f < 3.5Hz$) have some differences amongst pre-processing, but they stay at the same levels during each experimental time point. This suggests that PSDs are not affected by a change in blink time, such as during a change in the level of sleepiness.

3.5 Blink Influence On Psd

To examine the influence of blink, correlation coefficients between blink time and average PSDs for two frequency ranges ($0.01 < f < 0.8Hz$ and $1.5 < f < 3.5Hz$) across pre-processing procedures were calculated. The results were summarized in Table 3.

All coefficients for the frequency range ($0.01 < f < 0.8Hz$) were negative values and significant except for some coefficients for SVR. There was no significant relationship between SVR and blink time during the first three segments, and some absolute values of coefficients for SVR were relatively smaller than the ones for Exp. and MOV. Most PSDs for frequency range ($0.01 < f < 0.8Hz$) correlated with blink time, however. This suggests that PSDs depend on blink time, and that the relationship is affected by the preprocessing procedure. Also, PSDs of Exp. and MOV for frequency range ($1.5 < f < 3.5Hz$) correlated with blink time during segments 1-4. There were no significant relationships between them after Segment No. 5, while blink time was longer than in the standard condition, however. These correlation relationships seem to be caused by blinks.

3.6 Relationship with a Subjective Score

Subjective sleepiness was measured for each subject using the Stanford Sleepiness Score (SSS) (Hoddes et al., 1973). 33 out of 35 subjects responded to this questionnaire. The scores were distributed from 2 to 4 on a 7 point scale. The correlation relationships of SSS with both PUIs and PSDs were examined. The absolute value of the correlation coefficients (r) were less than 0.15 and they were not significant ($p > 0.10$), because all subjects were healthy and scores were distributed in a narrow range. Therefore, indices of pupillography do not correlate with the subjective scores as well as in previous works (Egg et al., 2002; Frauscher et al., 2005).

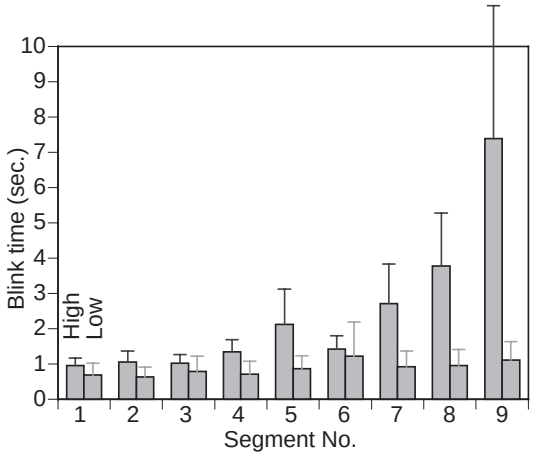

Figure 6: Averaged blink time across two sleepiness groups.

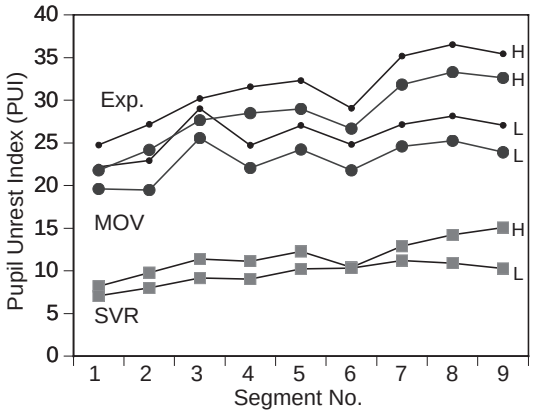

Figure 7: PUI changes with pre-processing procedures and two sleepiness groups.

4 DISCUSSION

The two observations and suggested causes which have been reported in this paper are examined here; there is an influence of blink on pupillary indices (Nakayama, 2005; Nakayama, 2006), and there is no-correlation between pupillary indices and subjective sleepiness (Egg et al., 2002; Frauscher et al., 2005). There was some distribution of subjective sleepiness

Table 4: Correlation coefficients between PSD and blink time across pre-processing procedures and two sleepiness groups.

	$0.01 < f < 0.8Hz$						$1.5 < f < 3.5Hz$					
Seg.	High sleepiness			Low sleepiness			High sleepiness			Low sleepiness		
No.	Exp.	MOV	SVR	Exp.	MOV	SVR	Exp.	MOV	SVR	Exp.	MOV	SVR
1	(-.25)	(-.25)	(-.15)	-.60	-.60	-.58	0.82	0.78	0.57	0.88	0.97	(0.18)
2	(-.33)	(-.33)	(-.15)	(-.53)	(-.53)	(-.52)	0.88	0.88	0.74	0.87	0.96	(0.19)
3	(-.35)	(-.35)	(-.29)	(-.37)	(-.37)	(-.31)	0.76	0.78	(0.04)	0.57	0.77	(0.38)
4	-.56	-.57	-.56	(-.51)	(-.51)	(-.44)	0.52	0.55	(0.15)	0.68	0.84	(0.27)
5	-.46	-.46	(-.41)	(-.51)	(-.51)	(-.47)	(0.04)	(0.07)	(-.12)	(0.54)	0.71	(0.13)
6	-.59	-.59	-.61	(-.50)	(-.50)	(-.47)	0.42	(0.47)	(0.01)	(0.20)	(0.31)	(0.18)
7	-.55	-.55	-.51	(-.55)	(-.55)	(-.48)	(0.09)	(0.14)	(0.31)	(0.35)	(0.48)	(0.20)
8	-.60	-.60	-.62	-.65	-.65	-.60	(0.34)	0.48	0.55	0.60	0.71	(0.19)
9	-.68	-.68	(-.37)	(-.32)	(-.32)	(-.31)	(-.17)	(-.14)	(-.15)	(0.45)	0.69	(0.11)

N=35, ( ) not significant

in this experiment, such as between 2 and 5 on the 7 point scale, therefore the effect of the difference in the subjective sleepiness on the indices was analyzed. Firstly, 33 responded subjects were divided into two groups; the low sleepiness group consisted of 13 subjects who answered 2 on the 7 point scale of sleepiness, and the high sleepiness group consisted of 20 subjects who answered 3 to 5 on the 7 point scale of sleepiness, with an average rate of 3.4.

Blink time for each segment was summarized across two groups in Figure 6 using the same format as in Figure 3. In Figure 6, bars show average blink times with error bars as standard errors. In comparing the two groups, the temporal change in segment sequences were quite different. Blink times for the high sleepiness group increased monotonically, and the standard errors also increased with the average. Blink times for the high sleepiness group in the 8th segment became 7 times the length of the time of the 1st segment. On the other hand, the average blink times for the low sleepiness group did not change during the experiment. There were no significant differences in blink time between the two groups because of the large deviation in blink time, however. If blink time reflects sleepiness, the differences in blink time between the two groups may significantly affect the variation in the subjective sleepiness score.

PUIs for two groups were summarized in Figure 7 using the same format as in Figure 2. Differences of PUIs for Exp. and MOV between the two groups increased with experimental time. Also, the differences in PUI for SVR between the two groups was small and almost constant during the experiment. There was no significant difference in PUI between the two groups and three pre-processing procedures because of the large deviation in PUI, particularly for the high sleepiness group. Although there was no significant difference between the two groups, it was noted that blink affected PUI values on pupil diameter observations when blinks were not processed appropriately.

To examine the relationship between PSDs and subjective sleepiness, correlation coefficients between averaged PSDs and blink times for the two groups were summarized in Table 4 using the same format as in Table 3. Comparing correlation coefficients between the two groups of subjective sleepiness ratings, the significance of coefficients for the frequency range $0.01 < f < 0.8$Hz changed across the two groups. Coefficients in the frequency rage $1.5 < f < 3.5Hz$ were relatively stable with the subjective sleepiness ratings. According to the results, coefficients between PSD and blink time depend on both the pre-processing procedure for blink and the subjective sleepiness rating. For coefficients in the frequency range $1.5 < f < 3.5Hz$, the effect of the subjective sleepiness rating was relatively smaller than the effect in the frequency range $0.01 < f < 0.8Hz$.

The results of analyzing pupil indices during the sleepiness test coincide with the clinical claims (Egg et al., 2002; Frauscher et al., 2005); PUI does not correlate with subjective sleepiness such as SSS. Although it was suggested that the frequency power of $0.01 < f < 0.8Hz$ reflected the subjective sleepiness (Lüdtke et al., 1998; Wilhelm et al., 1998; Wilhelm et al., 1999), the relationship was not confirmed in this experiment. Additionally, even the influence of blink when the blink drops during a temporal change of pupil size were removed was examined. Considering the empirical evidence from these clinical observations, a sleepiness evaluation procedure should be developed. A discussion of this will be the subject of our further study.

5 CONCLUSIONS

In this paper, we used pupillography to examine the influence of blink and validity of pupillary indices by analyzing a clinical sleepiness test.

The following results were achieved:

1. A pupil size during blink estimation procedure using the Support Vector Regression technique for clinical pupillary observation was developed and an appropriate level of performance was obtained.
2. The influence of blink in pupillary indices such as Pupil Unrest Index (PUI) and Power Spectrum Density (PSD) of pupillography was examined. In particular, it was shown that blink time increased monotonically with experimental time, therefore the influence of blink changed as the experiment progressed.
3. The relationship between pupil indices and subjective sleepiness scores such as the Stanford Sleepiness Score (SSS) was analyzed. There was no significant relationship, but there were some differences in pupil indices between high and low SSS groups.

Development of a sleepiness test evaluation procedure which considers blink and other factors will be the subject of our further study.

ACKNOWLEDGEMENTS

We would like to thank Dr. Misuzu Watanabe, Dr. Reiko Hori and Dr. Hirohito Tsuboi, Aichi Medical University, who kindly provided us with the opportunity to analyze pupillography data collected during their sleepiness tests.

REFERENCES

Beatty, J. (1982). Task-evoked pupillary response, processing load, and the structure of processing resources. *Psychological Bulletin*, 91(2):276–292.

Bishop, C. M., editor (1995). *Neural Networks for Pattern Recognition*. Oxford University Press, Oxford, UK.

Collobert, R. and Bengio, S. (2001). Svmtorch: Support vector machines for large-scale regression problems. *Journal of Machine Learning Research*, 1:143–160.

Egg, R., Högl, B., Glatzl, S., Beer, R., and Berger, T. (2002). Autonomic instability, as measured by pupillary unrest, is not associated with multiple sclerosis fatigue severity. *Multiple Sclerosis*, 8:256–260.

Frauscher, B., Egg, R., Brandauer, E., Ulmer, H., Berger, T., Poewe, W., and Högl, B. (2005). Daytime sleepiness is not increased in mild to moderate multiple sclerosis: a pupillographic study. *Sleep Medicine*, 6:543–547.

Hoddes, E., Zarcone, V., Smythe, H., Phillips, R., and Dement, W. C. (1973). Quantification of Sleepiness. *Psychlophysiology*, 10(4):431–436.

Kuhlmann, J. and Böttcher, M., editors (1999). *Pupillography: Principles, Methods and Applications*. W. Zuckschwerdt Verlag, Munchen, Germany.

Lüdtke, H., Wilhelm, B., Adler, M., Schaeffel, F., and Wilhelm, H. (1998). Mathematical procedures in data recording and processing of pupillary fatigue waves. *Vision Research*, 38:2889–2896.

Nakayama, M. (2005). Estimation of eye-pupil size during blink by support vector regression. In *Modelling Natural Action and Selection: Proc. of an International Workshop*, pages 121–126.

Nakayama, M. (2006). Influence of blink on pupillary indices. In *IEEE BioCAS 2006: Proceeding of Biomedical Circuits and Systems Conference*, pages 29–32.

Nakayama, M. and Shimizu, Y. (2001). An estimation model of pupil size for blink artifact in viewing TV programs. *IEICE Transactions*, J84-A:969–977.

Nakayama, M. and Shimizu, Y. (2002). An estimation model of pupil size for 'blink artifact' and it's applications. In *Proc. 10th European Symposium on Artificial Neural Networks, (ESANN '02)*, pages 251–256.

Norrish, M. I. K. and Dwyer, K. L. (2005). Preliminary investigation of the effect of peppermint oil on an objective measure of daytime sleepiness. *International Journal of Psychophysiology*, 55:291–298.

Smola, A. J. and Schölkopf, Y. (1998). A tutorial on support vector regression. NeuroCOLT2 Technical Report Series NC2-TR-1998-030.

Tada, H., Yamada, F., and Fukuda, K. (1991). *Psychological blink (in Japanese)*. Kita-Ouji-Shobo, Kyoto, Japan.

Tsukahara, N. (1976). *Control system of vertebrate and central nervous system (in Japanese)*, volume 6 of *Biological Science*. Asakura Shoten, Tokyo, Japan.

Wilhelm, B., Lüdtke, H., and Wilhelm, H. (1999). *Spontaneous pupillary oscillations*, Volume 18 of *Clinical Pharmacology*. W. Zuckschwerdt Verlag, Munchen, Germany.

Wilhelm, B., Wilhelm, H., Lüdtke, H., Streicher, P., and Adler, M. (1998). Pupillographic assessment of sleepiness in sleep–deprived healthy subjects. *SLEEP*, 21(3):258–265.

DO MOBILE PHONES AFFECT SLEEP?
Investigating Effects of Mobile Phone Exposure on Human Sleep EEG

Andrew Wood, Sarah Loughran, Rodney Croft, Con Stough
Australian Centre for Radiofrequency Bioeffects Research, Brain Sciences Institute
Swinburne University of Technology, Melbourne, Australia
awood@swin.edu.au

Bruce Thompson
Allergy, Immunology and Respiratory Medicine, The Alfred Hospital, Melbourne, Australia

Keywords: Mobile phone radiation, sleep, EEG analysis.

Abstract: This paper will summarize the results of a human volunteer study on the effects on sleep parameters of exposure to RF emissions from a mobile phone handset for 30min prior to going to sleep. A cohort of 55 volunteers were tested over 4 nights in a double-blind design. The significant outcomes were: Rapid Eye Movement (REM) sleep latency reduced by 16%; EEG alpha power enhanced by 8% during 1st non-REM period. These results are compared for overall internal consistency and with studies from other laboratories. Part of the program of the Australian Centre for Radiofrequency Bioeffects Research extending these studies is described.

1 INTRODUCTION

The issue of whether or not mobile phone handset radiofrequency (RF) and other emissions are able to alter sleep patterns is controversial. The World Health Organisation has a RF research agenda which highlighted the need to extend and replicate earlier studies which demonstrated effects on sleep [WHO http://www.who.int/peh-emf/research/rf03/en/ index2.html]. A series of experiments have been carried out at Swinburne University in the period 1999 – 2007 involving human volunteers on a range of immediate psychological and physiological consequences of use of mobile phone handsets, including sleep. In terms of health risk assessment, alterations of sleep quality may not appear to be as severe as possible links with cancer, but in terms of society's expectations, if phone emissions are linked to any biological changes, these need to be thoroughly understood. Although the basic research question we have asked is 'do the emissions from mobile phone handsets lead to an immediate change in ability to get a good night's sleep?', we have specific hypotheses formulated on the basis of previous research. A review of literature conducted at the start of the period (Hamblin and Wood, 2002) identified EEG alpha band power increase (both in awake and sleep experiments) as being the most consistent observation. The present experiment was designed to specifically examine the 'increased alpha power' hypothesis.

2 MATERIALS AND METHODS

2.1 Exposure

A popular handset (Nokia 6110) has been used throughout the series of experiments. The manufacturer's software is used to set into GSM pulsed 'test' mode (0.25 W average) via a serial cable which is then disconnected once the setting is complete. Since the current drawn from the battery follows the GSM pulsing scheme (217 Hz, 1/8 duty cycle), there is a strong extremely low-frequency magnetic field associated with this, in addition to the RF at 914 MHz. The other house-keeping pulses (including the blank 26th frame) were absent. Since all exposures were carried out with neither the participants nor those involved in administering cognitive tests aware or the exposure status, it is necessary to have independent verification that the phone was in the correct mode at each testing session. The RF output was checked i) by holding

the handset near to a landline phone and checking for a 'buzz' ii) direct connection of the antenna feedpoint to a RF power meter iii) by measurements in SAR phantom. The first of these was performed on each occasion, the second at six-monthly intervals to check the constancy of RF output over a 3-hour period and the third was performed once to determine the appropriate Specific Absorption Rate (SAR) in the users' heads.

The peak SAR was 0.19 ± 0.03 W/kg (based on 1g average). At the relevant moment during the testing the phone was attached to a cradle in a normal position next to cheek, with the antenna approximately 2 cm from the skin. The phone was set in one of two modes: i) turned on and transmitting (active); ii) turned off (sham). In other experiments in our series we also used handsets in 'standby' mode (turned on, but not emitting RF, except in intermittent bursts every few minutes or so). In order to ensure blinding, the phone was checked for audible cues from the phone circuitry, an important requirement in a quiet sleep laboratory. This was done by asking participants to indicate whether or not they thought the phone was transmitting. In order to fully prevent participants picking up the faint 'buzz' even with the loudspeaker disabled, a plastic foam pad was placed around the phone in a pouch. This also minimised the sensation of warmth when the phone was in active mode.

The phone exposure consisted of the handset being placed next to the participants' cheek for 30 min just prior to having monitoring electrodes attached and getting into bed.

2.2 Subjects

60 subjects were recruited to the study, but five of these withdrew after provision for their participation had been made. Five more were excluded because of confirmed apnoeic event during at least one of their nights in the study. The final study sample thus comprised 50 healthy volunteers aged from 18 to 60 years (Mean =27.9 SD = 10.9 years). Subjects were recruited from advertisements in local and state newspapers, and posters located at several universities and organizations in Melbourne. In the final sample there were 27 males and 23 females, 45 of whom were right handed. No participant reported any psychological or neurological condition, serious head injury or extended periods of unconsciousness.

The study took place at a purpose-made sleep laboratory (Eastern Sleep Disorders Service, Mitcham Private Hospital, Vic), which consisted of three individual bedrooms, a central monitoring room, together with a kitchen and a bathroom..

2.3 Design

A double blind crossover design was used to collect the data i.e. both the subject and the tester were blind to the exposure condition. Participants attended the sleep laboratory on Saturday and Sunday nights on two consecutive weekends. The Saturday nights were adaptation nights, to enable participants to become accustomed to sleeping in a strange environment and with monitoring sensors attached. Full sleep monitoring data were obtained and stored for these nights. On Sunday nights participants were required to sit for 30 min prior to getting into bed with the phone in either the transmitting condition or switched off, with the opposite condition the following Sunday. During this time the participants were instructed to look at a blank wall. At the cessation of real/sham exposure electrodes and sensors were attached, a task which normally occupied 15 – 20 min.

2.4 Measures

Sleep was recorded and stages were visually scored for 30 s epochs according to standard criteria (Rechtschaffen and Kales, 1968) by an experienced independent sleep technician who was blind to the experimental conditions. During sleep, EEG (C3 and C4), ECG, EOG, EMG, SaO2 and nasal airflow were monitored along with thoracic, abdominal, and leg movements, using the Compumedics™ E-series polysomnography system. All EEG electrode impedances were below 5 kΩ initially. Data were sampled as shown in Table 1. Data was stored in records of 1 second in duration in European Data Format (EDF). This format stores data points as 2 byte binary representation and as such can be converted into continuous data records for each channel. This was then exported to Matlab™ in order to resample the data for subsequent analysis using Neuroscan data processing software.

Table 1: Sample rates for all recorded channels.

Channel	Number of samples in each data record
EEG	250*
EEG(second)	250*
EOG(L)	50
EOG(R)	50
EMG	250
ECG	50
Leg(L)	50
Leg(R)	50
SaO2	5
Airflow	25
Thoracic Respiration	25
Abdominal Respiration	25
Sound	25
CPAP	25
Oxygen	1
Total	1131

*In some records the EEG was sampled at 125 Hz because of monitoring constraints: the EDF header provided the recording-specific information.

2.5 Analysis

The sleep staging was carried out in accordance with routine procedures followed by the Eastern Sleep Disorders Service. Each 30 s epoch of sleep was assigned to a stage using the standard R & K (Rechtschaffen and Kales, 1968) classification. This analysis also provided timing markers for subsequent analysis of EEG records. Matlab was used to extract the first 6 channels of each participant's EDF file (EEG1, EEG2, EOGleft, EOGright, EMG, and ECG). The individual channel files were then converted to continuous files and opened using Matlab, where they were re-sampled (due to the original acquisition rates being different) so that all channels had the same number of points. The individual files were then recombined in Matlab as an EDF file for subsequent spectral analysis using Neuroscan software. Using the staging data, the first NREM period (the time from sleep onset, defined as the first occurrence of stage 2, until the onset of the first REM sleep period) was extracted and artefact removal was performed by visual inspection (with the experimenter blind to the exposure condition). Only artefact free epochs were used for further analysis. The first 30 minutes of each file was taken and the two EEG channels (C3, C4, referenced to linked mastoids) were extracted and spectral analysis was performed on the average of the two channels for each 20 second epoch (FFT routine, Hanning window, averages of five 4-second epochs). Data was then exported to SPSS statistical package Version 11.5 for further statistical analysis. Spectral data, with a resolution of 0.25 Hz, was thus obtained for each 20 second epoch for the first 30 minutes from first stage 2 occurrence. The spectrum for each participant (and for each night) was an average of the spectra for 3 x 30 = 90 epochs. For each individual, the averaged spectrum on the active exposure night is then divided by the spectrum for the sham night an the ratio converted to a percentage. These intra-subject ratios are then averaged over the number of subjects (n = 50) and the overall percentage (± SEM) calculated. This is shown in Fig. 1 below, along with the overall averaged spectra for active and sham exposure nights.

3 RESULTS

3.1 Sleep Parameters

Of the 10 sleep parameters measured all were non-significant, except for REM latency, which was reduced 16% by exposure ($p = 0.02$) (Loughran et al., 2005). This was contrary to previous work which found a suppression of REM sleep (Mann and Röschke, 1996) and when corrected for multiple comparisons, the level of significance is marginal.

3.2 Spectral Analysis of EEG

As outlined above, the prior hypothesis was that EEG alpha power would be increased. Spectral analysis of the sleep EEG in the first 30 minutes of the first NREM period revealed no significant effects of EMF exposure on EEG power density in the alpha frequency range (8-13Hz) as a whole. Two alpha sub-bands (11.5-12.25Hz, 13.5-14Hz) that have previously shown effects in the first NREM period of an overnight polysomnography following EMF exposure (Huber et al., 2003) were also analysed. EEG power density was found to be significantly enhanced by around 8% in the 11.5 – 12.25 Hz frequency range following EMF exposure, $F(1,48) = 5.56$, $p = 0.022$ (Figure 1). No significant enhancement was found to be present in the 13.5 – 14 Hz frequency range. Effect sizes (partial eta squared) were also calculated for the 0-25 Hz region and are shown in Figure 2. This shows a raised effect size for the 13.5 – 14 Hz sub-band which failed to reach significance.

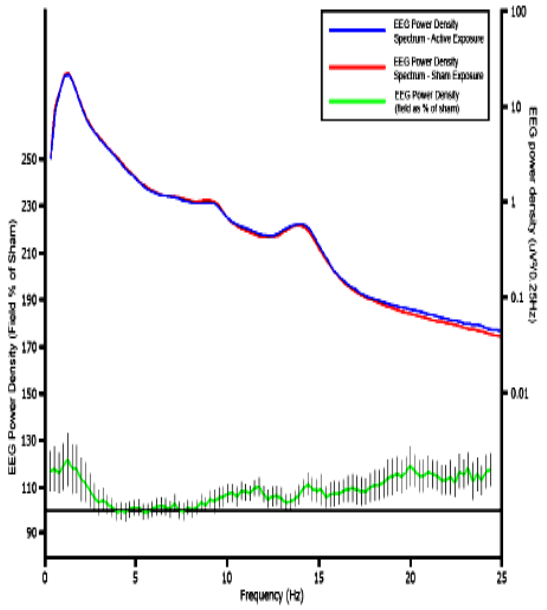

Figure 1: Upper: Averaged EEG spectra for active and sham exposure nights respectively (for 50 paricipants); Lower: Mean EEG Power Density Spectrum for real exposure as a % of sham. Bars represent Standard Error of Mean.

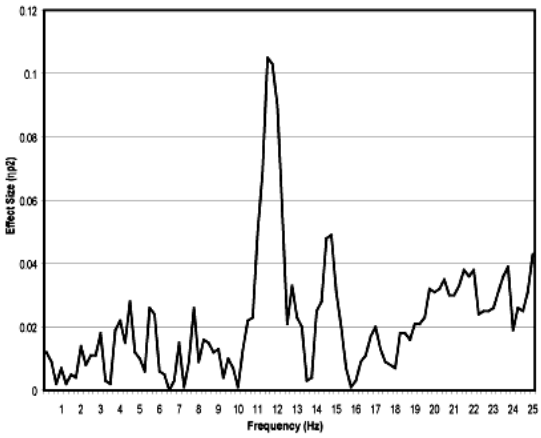

Figure 2: Effect sizes of EMF exposure on First 30 minutes of the first NREM period. Effect sizes for each 0.25 Hz bin (0 – 25 Hz) are illustrated and were calculated using the formula $\eta_p^2 = SS_{effect}/(SS_{effect} + SS_{error})$. (See Loughran et al. 2005).

It should be noted that in the region 0 – 3 Hz and 17 – 25 Hz there are enhancements of up to 20%, but as Figure 2 reveals, these are not statistically significant. Some of these data have previously been reported (Loughran et al., 2005). The averaged cross-participant spectra have a 1/f character (note log scale) with characteristic alpha and theta peaks shown. The differences in the spectra are only just distinguishable when plotted conventionally. Note that below 2 Hz the spectral estimates become unreliable.

4 DISCUSSION

Since our review paper which discusses papers published up to 2001 (Hamblin and Wood, 2002), we have continued to track the literature relating to reported EEG alpha band enhancements. Up to the end of 2006, we had noted that of the 18 papers reviewed, 9 showed data supporting alpha enhancement, 8 showed no effects, or a reduction and 1 showed both an enhancement and a reduction, based on gender. Although all reporting enhancement refer to the EEG band to be in the alpha region, further analysis shows that there is very little overlap between the actual sub-bands over which the significant changes were reported. In Figure 3 these bands are illustrated, in reverse chronological order of publication. Where multiple bands were shown to be significant in a single study these are shown as separate rows.

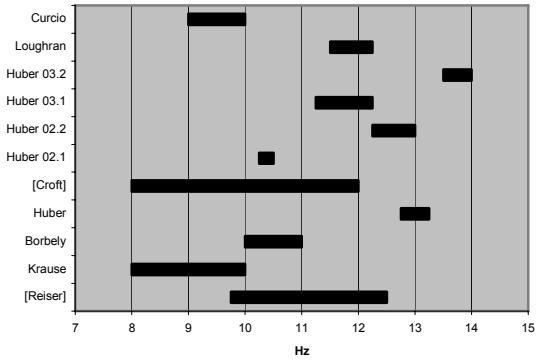

Figure 3: Frequency ranges over which increases in EEG power elicited by mobile phone radiation have been reported. In some cases, more than one sub-band was significantly enhanced. The studies are as follows: (Curcio et al., 2005, Huber et al., 2003*, Huber et al., 2002*, Croft et al., 2002, Huber et al., 2000*, Borbely et al., 1999*, Krause et al., 2000, Reiser et al., 1995. Those indicated thus (*) are during a non-REM period of sleep, the others were with awake subjects (Huber et al. 2002 showed increases with participants both awake and asleep.

5 FURTHER WORK

A repeat study is now underway in which 20 of the original cohort of 50 have repeated their participation. The aim is to discover if those who showed strong Alpha power changes in the first study show similar changes in the second. There has been some speculation that sensitivity to EMF may vary with the individual.

6 CONCLUSIONS

Alpha power findings are inconsistent across studies, but sleep studies may show slightly more consistency. The actual frequency range for significant increases varies between studies and even between studies from the same laboratory. Nevertheless, the preponderance is of reported increases in alpha power: this may relate to increased blood flow in superficial regions of the face or ear or increased tympanic membrane temperature. It is difficult however to envisage how these effects could persist several hours after exposure. Overall, the evidence is insufficiently strong to conclude that mobile phone emissions affect sleep.

ACKNOWLEDGEMENTS

Supported by the National Health and Medical Research Council of Australia, Grant No. 154905.

REFERENCES

Borbely, A. A., Huber, R., Graf, T., Fuchs, B., Gallmann, E. & Achermann, P. (1999) Pulsed high-frequency electromagnetic field affects human sleep and sleep electroencephalogram. *Neurosci Lett*, 275, 207-10.

Croft, R. J., Chandler, J. S., Burgess, A. P., Barry, R. J., Williams, J. D. & Clarke, A. R. (2002) Acute mobile phone operation affects neural function in humans. *Clin Neurophysiol*, 113, 1623-32.

Curcio, G., Ferrara, M., Moroni, F., D'inzeo, G., Bertini, M. & De Gennaro, L. (2005) Is the brain influenced by a phone call? An EEG study of resting wakefulness. *Neurosci Res*, 53, 265-70.

Hamblin, D. L., Anderson, V., Mcintosh, R. L., Mckenzie, R. J., Wood, A. W., Iskra, S. & Croft, R. J. (2007) EEG electrode caps can reduce SAR induced in the head by GSM900 mobile phones. *IEEE Trans Biomed Eng*, 54, 914-20.

Hamblin, D. L. & Wood, A. W. (2002) Effects of mobile phone emissions on human brain activity and sleep variables. *Int J Radiat Biol*, 78, 659-69.

Huber, R., Graf, T., Cote, K. A., Wittmann, L., Gallmann, E., Matter, D., Schuderer, J., Kuster, N., Borbely, A. A. & Achermann, P. (2000) Exposure to pulsed high-frequency electromagnetic field during waking affects human sleep EEG. *Neuroreport*, 11, 3321-5.

Huber, R., Schuderer, J., Graf, T., Jutz, K., Borbely, A. A., Kuster, N. & Achermann, P. (2003) Radio frequency electromagnetic field exposure in humans: Estimation of SAR distribution in the brain, effects on sleep and heart rate. *Bioelectromagnetics*, 24, 262-76.

Huber, R., Treyer, V., Borbely, A. A., Schuderer, J., Gottselig, J. M., Landolt, H. P., Werth, E., Berthold, T., Kuster, N., Buck, A. & Achermann, P. (2002) Electromagnetic fields, such as those from mobile phones, alter regional cerebral blood flow and sleep and waking EEG. *J Sleep Res*, 11, 289-95.

Krause, C. M., Sillanmaki, L., Koivisto, M., Haggqvist, A., Saarela, C., Revonsuo, A., Laine, M. & Hamalainen, H. (2000) Effects of electromagnetic field emitted by cellular phones on the EEG during a memory task. *Neuroreport*, 11, 761-4.

Loughran, S. P., Wood, A. W., Barton, J. M., Croft, R. J., Thompson, B. & Stough, C. (2005) The effect of electromagnetic fields emitted by mobile phones on human sleep. *Neuroreport*, 16, 1973-6.

Mann, K., Roschke, J. (1996) Effects of pulsed high-frequency electromagnetic fields on human sleep. *Neuropsychobiology*, 33, 41-47

Rechtschaffen, A. & Kales, A. (1968) *A manual of standardised terminology techniques and scoring system for sleep stages in human subjects*, Washington, DC, US Public Health Service.

Reiser, H., Dimpfel, W. & Schober, F. (1995) The influence of electromagnetic fields on human brain activity. *Eur J Med Res*, 1, 27-32.

SCREENING OF OBSTRUCTIVE SLEEP APNEA BY RR INTERVAL TIME SERIES USING A TIME SERIES NOVELTY DETECTION TECHNIQUE

A. P. Lemos, C. J. Tierra-Criollo and W. M. Caminhas
Department of Electrical Engineering, Universidade Federal de Minas Gerais, Antonio Carlos Av., 6627, Belo Horizonte, Brazil
andrepl@cpdee.ufmg.br, carjulio@cpdee.ufmg.br, caminhas@cpdee.ufmg.br

Keywords: Obstructive sleep apnea, RR interval time series, Time series novelty detection.

Abstract: This work proposes a methodology to screen obstructive sleep apnea (OSA) based on RR interval time series using a time series novelty detection technique. Initially, the RR interval is modeled using an autoregressive model. Next, for each data point of the time series, the model output, $\hat{x}(t)$, is compared with the observed value, x_t, and the prediction error is generated. The prediction error is then processed in order to detect novelties. Finally, the novelties detected are associated with apnea events. This methodology was applied to the Computers in Cardiology sleep apnea test data and correctly classified 29 out of 30 cases (96.67%) of both OSA and normal subjects, and correctly identified the presence of apnea events in 14078 out of 17268 minutes (81.53%) of the test data set.

1 INTRODUCTION

Obstructive sleep apnea (OSA) is a sleep disorder characterized by pauses in breathing during sleep with a reported prevalence in 4% in adult men and 2% in adult women (Young et al., 1993). Obstructive sleep apnea is associated with increased risks of high blood pressure, myocardial infarction, stroke, and with increased mortality rates.

According to the (AASM, 1999) patients are diagnosed with OSA if they have 5 or more events of apnea per hour of sleep during a full night sleep period. Each event is characterized by a respiratory pause during 10 seconds.

The definitive diagnosis of OSA is made by polysomnography (PSG). PSG is a multi-parametric test based on brain electrical activity (EEG), eye and jaw muscle movement, leg muscle movement, airflow, respiratory effort (chest and abdominal excursion), electrocardiography (ECG) and oxygen saturation. This exam is expensive and requires the patient to spend the night in the hospital.

In (Guilleminault et al., 1984) is reported that OSA can be characterized by cyclical variations on RR interval time series caused by progressive bradycardia, followed by abrupt tachycardia on resumption of breathing. This events are highly nonlinear and non stationary. Figure 1 illustrates a RR interval time series in two distinct time intervals, the first one, with no apnea events and, the second one, with these events.

If an automatic method is developed to screen the pathology using ECG monitoring instead of PSG, this can be done on basis of a portable and inexpensive device from patient home.

This paper proposes a methodology to detect OSA from RR interval time series based on a novelty detection technique. The normal behavior of a system can be characterized by a series of observations through the time. The problem of novelty detection consists in finding time periods where some characteristic of the monitored system has been changed.

An autoregressive model is used to model the RR interval time series using a subset without apnea events. For each data point of the time series, the model output is compared with the observed value and the prediction error is generated. The prediction error is then processed in order to detect novelties. Finally, the novelties detected are associated with apnea events, since based on information given by (Guilleminault et al., 1984), this events are nonlinear and non stationary.

This paper is divided as follows: in section 2 the RR interval time series is preprocessed in order to be modeled using an autoregressive model. Next, in section 3 the time series novelty detection technique is presented. In section 4 this technique is applied on Computers in Cardiology sleep apnea dataset (Goldberger et al., 2000) in order to detect OSA. Finally, section 5 presents conclusions and suggestions for further research.

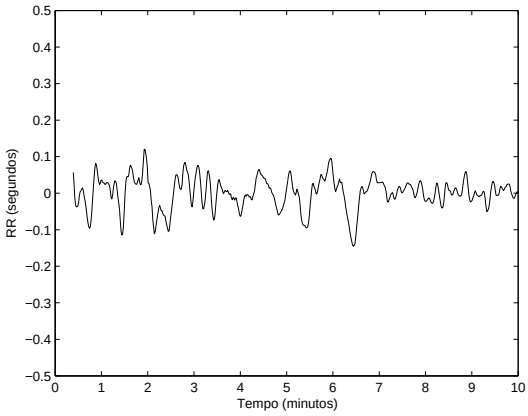

(a) Normal

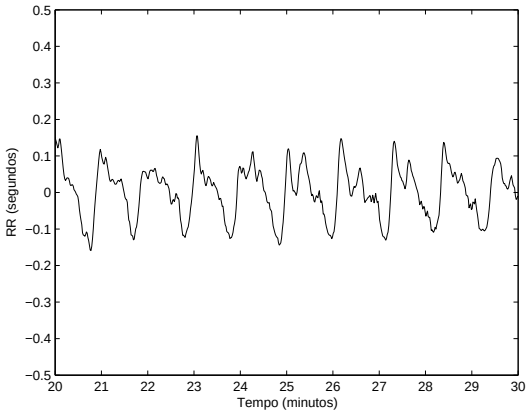

(b) Apnea events

Figure 1: A RR interval time series with and without apnea events.

2 RR INTERVAL TIME SERIES PREPROCESSING

In order to model the RR interval time series using an autoregressive model, the time series must be preprocessed to become stationary.

The preprocessing technique used in this work is similar with the one used on (Mietus et al., 2000) and is performed by the following steps:

1. The RR interval time series is extracted from ECG using an automated beat detection and classification algorithm selecting only normal sinus beats intervals in order to eliminate the effects of ectopic beats.
2. A moving average filter is applied to the signal in order to remove noise caused by beat detection and classification algorithm errors. For each set of 41 RR intervals, a local mean is computed excluding the central value and those values which lie outside the range of 0.4 to 2.0 sec. The central values is considered to be an outlier and is excluded if lies outside of 20% of the mean.
3. The signal is linearly resampled at 1 Hz.
4. The signal is smoothed. For each window of 5 points, the value of the central point is replaced by the average value over the window.
5. The signal is detrended. For each window of 81 points, the slope of the regression line over the window is calculated, and the value of this fit at the central point is subtracted from the actual value of this point.

Figure 2 illustrates a RR interval time series before and after the preprocessing.

3 TIME SERIES NOVELTY DETECTION TECHNIQUE

In this section the time series novelty detection technique used to detect OSA will be presented. This technique is based on a detector build on the variation of an autoregressive model prediction error.

3.1 Autoregressive Model

An autoregressive model of order p, $AR(p)$ estimates the current value of a stochastic process as a linear combination of its last p values and a white noise. The white noise process, a_t, is assumed to be Gaussian, independent and identically distributed (i.i.d), with zero mean and variance σ_a^2. This model can be written as:

$$X_t = \phi_1 X_{t-1} + \phi_2 X_{t-2} + \cdots + \phi_p X_{t-p} + a_t \quad (1)$$

where $\phi = \phi_1, \phi_2, \cdots, \phi_p$ and σ_a^2 are model parameters.

Given a time series that can be described as a stochastic process, to build a forecasting model for this series using (1) initially it is necessary to estimate the model parameters for several values of p and then evaluate which is the most suitable value for p using some statistical criterion.

The *Maximum Likelihood Estimator* for the model parameters, $\phi = \phi_1, \phi_2, \cdots, \phi_p$ and σ_a^2, is defined as (Box and Jenkins, 1990), (Davis and Vinter, 1985):

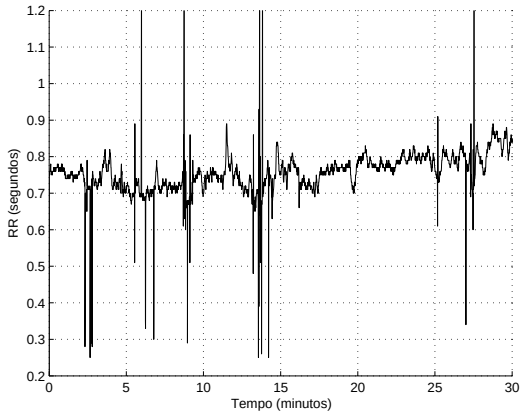

(a) Before

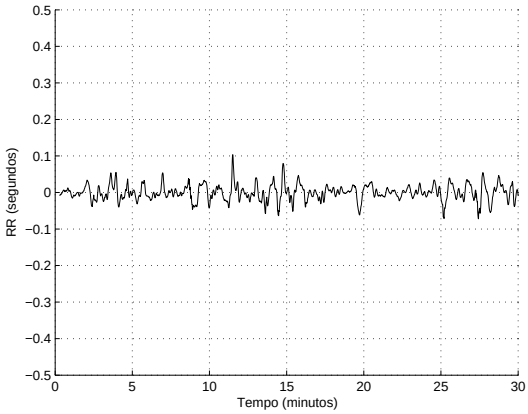

(b) After

Figure 2: RR interval time series before and after preprocessing.

$$\hat{\phi} = (X'X)^{-1}(X'Z) \quad (2)$$
$$\hat{\sigma_a}^2 = \hat{\tau}^{-1} = \frac{1}{N-p}(Z - X\hat{\phi})(Z - X\hat{\phi})^{-1}$$

where $Z = \begin{bmatrix} X_{p+1} \\ X_{p+2} \\ \vdots \\ X_N \end{bmatrix}$ e $X = \begin{bmatrix} X_p & \cdots & X_1 \\ X_{p-1} & \cdots & X_2 \\ \vdots & \vdots & \vdots \\ X_{N-1} & \cdots & X_{N-p} \end{bmatrix}$

Once the parameters of several $AR(p)$ models have been calculated, the most suitable value of p must be estimated. The *Scharwaz's Bayesian Information Criterion (BIC)* (Schwarz, 1978) is used to select the p value. The BIC is given by:

$$BIC = \log(\hat{\sigma_a}^2) + \frac{M\log(N)}{N} \quad (3)$$

where $M = p+1$ and N is the length of the time series.

3.2 The Detector

For each time series data point, the detector must be capable to distinguish between the following hypotheses:

$$H_0 : x_t \text{ is normal}$$
$$H_1 : x_t \text{ is a novelty}$$

For a given input x_t the detector must be capable to classify the point as normal meaning that it can be predicted by the forecasting model build for the time series, or novelty, the point can not be predicted by the model.

The detection probability P_D is the probability of the detector to classify the point as a novelty correctly, $P(H_1;H_1)$. The false alarm probability P_{FA} is the probability of the detector to classify the point as a novelty when the point is actually normal, $P(H_1;H_0)$.

Initially, the forecasting model parameters are estimated using a dataset of the time series assumed as normal. Then, for each new observed value of the time series x_t the statistical inference on the hypotheses is performed by the following steps:

1. The predicted value $\hat{x_t}$ is calculated using p last points of the time series.
2. The parameters of the predicted value distribution are estimated and the thresholds of the interval are calculated given a significance level α.
3. If the observed value of the time series x_t is inside the prediction interval, the null hypothesis is considered true.

The conditional probability density function of the forecasting model output when the null hypothesis is true, given the last p observations, is:

$$p(\hat{X}_t|x_{t-1},\cdots,x_{t-p};H_0) = \frac{1}{\sqrt{2\pi}\hat{\sigma_a}^2}\exp -\frac{1}{2\hat{\sigma_a}^2}(\hat{X}_t - \mu_t)^2 \quad (4)$$

where $\mu_t = \phi_1 x_{t-1} + \cdots + \phi_p x_{t-p}$.

The thresholds of the prediction interval given a significance level α is:

$$\mu_t \pm Q^{-1}\left(\frac{\alpha}{2}\right)\hat{\sigma_a} \quad (5)$$

where $Q(x)$ is the complementary cumulative distribution function of the normal distribution (Kay, 1993).

The false alarm rate P_{FA} is equal to the prediction interval significance level α. However the conditional novelty probability distribution $P(\hat{X}_t|x_{t-1},\cdots,x_{t-p};H_1)$ it is not know, so it is not possible to calculate the detection probability analytically.

3.3 Detector Output Processing

The detector classifies each point of the time series as a novelty or normal. However, the novelty to be detected, apnea events, is formed by a sequence of points. So, in order to use this detector it is proposed a technique to process the detector output using a sliding window of size W.

Given N detector outputs related to N data points of the time series, $N-W+1$ windows are generated. The first window is formed by the outputs on the interval $[1,W]$, the second on the interval $[2,W+1]$, and so on:

$$\begin{bmatrix} c(1) & c(2) & \cdots & c(W) \\ c(2) & c(3) & \cdots & c(W+1) \\ \vdots & \vdots & \ddots & \\ c(N-W+1) & c(N-W+2) & \cdots & c(N) \end{bmatrix}$$

where c_i is the detector output relative to the time series data point on time instant i and c_i is equal to 0 if the null hypothesis is true and 1 otherwise.

Each window is defined as an *event* $E_W(t)$ and its *1-norm* is given by:

$$|E_W(t)| = \sum_{i=0}^{i=W-1} c(t+i) \tag{6}$$

and measures how many novelties are found on the event.

Assuming that the detector output is an identical distributed Bernoulli variable, $|E_W(t)|$ will be a binomial random variable:

$$p_{|E_W|}(|e_W|) = \begin{cases} \begin{pmatrix} W \\ |e_W| \end{pmatrix} q^{|e_W(t)|}(1-q)^{n-|e_W(t)|} \\ \text{if } |e_W(t)| = 0\cdots W \\ 0 \text{ otherwise} \end{cases} \tag{7}$$

where q is the probability of occurrence of a novelty, and it is given by $q=\alpha$.

A unilateral confidence interval is built upon $p_{|E_W|}(|e_W|)$ and if the value of $|E_W(t)|$ is bigger than this interval, all the points present in this event (window W) are partially classified as novelties. The threshold of this confidence interval is calculated finding the smallest integer whose cumulative distribution function evaluated in this point is equal or exceeds the value of α.

After this procedure, each point of the interval $[W,N-W+1]$ will have W distinct partial classifications, since each one of these points appears on W windows. On the other hand, the first points of the interval $[1,W1]$ will have i distinct classifications, where i is its position on the interval. Finally the points of the interval $[N-W+2,N]$ will have j classifications, where $j=N-i$.

The final result for each point is obtained defining a percentage of partial novelties classifications that each point must have to be finally classified as a novelty. This constant is a parameter of the proposed algorithm defined as k and is defined for the interval $(0,1]$.

3.4 Parameters

The proposed time series novelty detection technique has the following parameters:

- The significance level α used to build the $AR(p)$ prediction intervals and the $p_{|E_W|}(|e_W|)$ confidence interval.
- The window size W used to process the detector output.
- The percentage of partial novelty classifications k that each point must have to be finally classified as a novelty.

4 EXPERIMENTS

In this section the time series novelty detection technique is used to detect OSA on Computers in Cardiology sleep apnea dataset.

4.1 Dataset

This dataset contains 70 records varying in length from almost 7 hours to nearly 10 hours of continuous digitized ECG signal and reference apnea annotations for each minute performed by human experts on the basis of simultaneously recorded respiration and related signals.

This dataset was used on a competition for development and evaluation of ECG-based apnea detectors (Penzel et al., 2002) and is divided in a learning set of 35 records and a test set containing the remaining records. All records were previously classified in three groups: a first group (A) with clear evidence

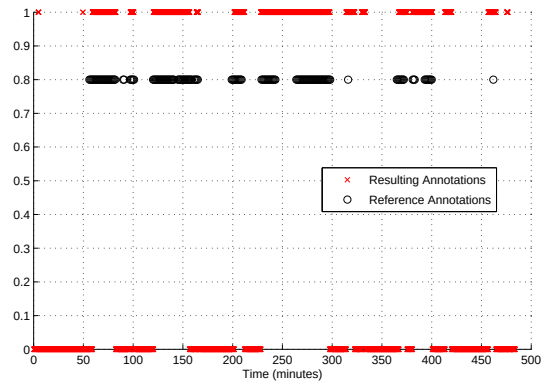

Figure 3: Reference and detector resulting annotations for each minute for the record a05 of the learning set.

of sleep apnea with more than 100 minutes of apnea events; a second group (B) with some degree of apnea, with 5 to 100 minutes of apnea events; and a third group (C) of healthy patients with less than 5 minutes of apnea events.

The competition consisted of two challenges. The first challenge was to distinguish between healthy patients (group C) and patients with OSA (group A). The second challenge was to label each minute of all records as either containing apnea events or not.

4.2 Methods

For each record, the RR interval time series was extracted from the ECG signal and preprocessed using the methodology described on section 2.

Next, 10 minutes of the resulting time series without apnea events where used to estimate the $AR(p)$ model parameters. The order of the model was set to $p = 17$, according to BIC.

Finally the time series novelty detection technique was used to label each minute of the signal as containing apnea (novelty) or not (normal). The parameters of the algorithm were set to $W = 240$ points (4 minutes), $\alpha = 0.01$ and $k = 1$.

The signal is sampled at 1 Hz, so in order to generate a label for each minute, if a window of 60 points have more than 10 points classified as novelty, the corresponding minute is labeled as apnea.

Figure 3 illustrates the detector resulting annotations and reference annotations for the record a05 of the learning set.

In order to distinguish between records of healthy patients and patients with OSA, if the record contain less than 50 minutes labeled as apnea the patient is considered to be healthy.

4.3 Results

The technique proposed was able to correctly distinguish between healthy and OSA patients on 57 out of 60 records (95.00%), 29 out of 30 (96.67%) of the learning set and 28 out of 30 (93.33%) from the test set.

When used to label each minute of the records, it correctly classified 28119 out of 34313 minutes (81.95%), 14041 out of 17045 of the learning set (82.38%) and 14078 out of 17268 (81.53%) of the test set.

5 CONCLUSIONS AND FUTURE WORK

Experiments shows that the technique proposed can be used to screen OSA based on RR interval time series. When compared with the 10 best results of the Computers in Cardiology magazine competition (Penzel et al., 2002), for the first challenge, the technique achieved similar results. For the second challenge, minute by minute apnea event annotations, the results were slightly lower than the best results of the competition. The technique was able to correctly classify 81.5% of the test set and the top 10 competition's techniques correctly classify 84.5% up to 96.2%.

Table 1 compares the results achieved by the methodology proposed with the results achieved by Physionet's apdet tool (Mietus et al., 2003) for the dataset described later.

Table 1: Comparison results.

Dataset	Challenge	Proposed Methodology	apdet
Train	1	96.7%	86.6%
	2	82.0%	82.1%
Test	1	93.3%	93.3%
	2	81.5%	84.5%

The main advantage of the technique proposed is the simplicity. The detection algorithm can be implemented in linear time and space, so it can run on cheap hardware. However, the main drawback of this technique is that it needs a dataset without apnea events in order to train the model. This dataset has to be achieved for each patient by a specialist or by another automatic methodology.

In order to use an $AR(p)$ model, the time series must be stationary, what was assumed for the RR interval time series preprocessed. However this is not completely true, so this technique can be improved using an adaptive autoregressive model.

The time series novelty detection technique presented is general purpose and can be used for screening other anomalies. It has already been used to detect ECG arrhythmias (Lemos et al., 2007).

The novelty detection technique proposed in this work can be integrated on a physiological remote monitoring system in order to reduce the amount of data transmitted. Those systems are used to monitor chronic patients biomedical signals (ECG, breathing frequency, temperature). At patient's location, some sensors are used to read biomedical signals. These signals are sent through a network to a remote station where the data is stored and analysed by specialists (Lin et al., 2004). The novelty detection technique proposed can be used to filter the data that needs to be sent to the remote station, where only data classified as novelty is sent.

REFERENCES

AASM (1999). Sleep-related breathing disorders in adults: recommendations for syndrome definition and measurement techniques in clinical research. *Sleep*, 22:667–689. American Academy of Sleep Medicine Task Force.

Box, G. E. P. and Jenkins, G. (1990). *Time Series Analysis, Forecasting and Control*. Holden-Day, Incorporated.

Davis, M. and Vinter, R. (1985). *Stochastic Modelling and Control*. Chapman Hall.

Goldberger, A. L., Amaral, L. A. N., Glass, L., Hausdorff, J. M., Ivanov, P. C., Mark, R. G., Mietus, J. E., Moody, G. B., Peng, C.-K., and Stanley, H. E. (2000). PhysioBank, PhysioToolkit, and PhysioNet: Components of a new research resource for complex physiologic signals. *Circulation*, 101(23):e215–e220.

Guilleminault, C., Connolly, S., Winkle, R., Melvin, K., and Tilkian, A. (1984). Cyclical variation of the heart rate in sleep apnoea syndrome. mechanisms, and usefulness of 24 h electrocardiography as a screening technique. *Lancet*, 1:126–131.

Kay, S. M. (1993). *Fundamentals of statistical signal processing: detection theory*. Prentice-Hall, Inc., Upper Saddle River, NJ, USA.

Lemos, A. P., Tierra-Criollo, C. J., and Caminhas, W. M. (2007). Ecg anomalies identification using a time series novelty detection technique. In *IV Latin American Congress on Biomedical Engineering*.

Lin, Y.-H., Jan, I.-C., Ko, P., Chen, Y.-Y., Wong, J.-M., and Jan, G.-J. (2004). A wireless pda-based physiological monitoring system for patient transport. *IEEE Transactions on Information Technology in Biomedicine*, 8(4):439–447.

Mietus, J. E., Peng, Ivanov, P., and Goldberger, A. (2003). Hilbert transform based sleep apnea detection using a single lead electrocardiogram (apdet). http://www.physionet.org/physiotools/apdet/.

Mietus, J. E., Peng, C. K., Ivanov, P. C., and Goldberger, A. L. (2000). Detection of obstructive sleep apnea from cardiac interbeat interval time series. *Computers in Cardiology*, 27:753–756.

Penzel, T., McNames, J., de Chazal, P., Raymond, B., Murray, A., and Moody, G. (2002). Systematic comparison of different algorithms for apnoea detection based on electrocardiogram recordings. *Medical & Biological Engineering & Computing*, 40:402–407.

Schwarz, G. (1978). Estimating the dimension of a model. *The Annals of Statistics*, 6:461–464.

Young, T., Palta, M., Dempsey, J., Skatrud, J., Weber, S., and Badr, S. (1993). The occurence of sleep-disordered breathing among middle-aged adults. *New England Journal of Medicine*, 328:1230–1235.

AUTHOR INDEX

AUTHOR INDEX (CONT.)

AUTHOR INDEX (CONT.)

AUTHOR INDEX (CONT.)

Proceedings of BIOSIGNALS 2008
International Conference on Bio-inspired Systems and Signal Processing
ISBN: 978-989-8111-18-0